11th Conference on Satellite Meteorology and Oceanography

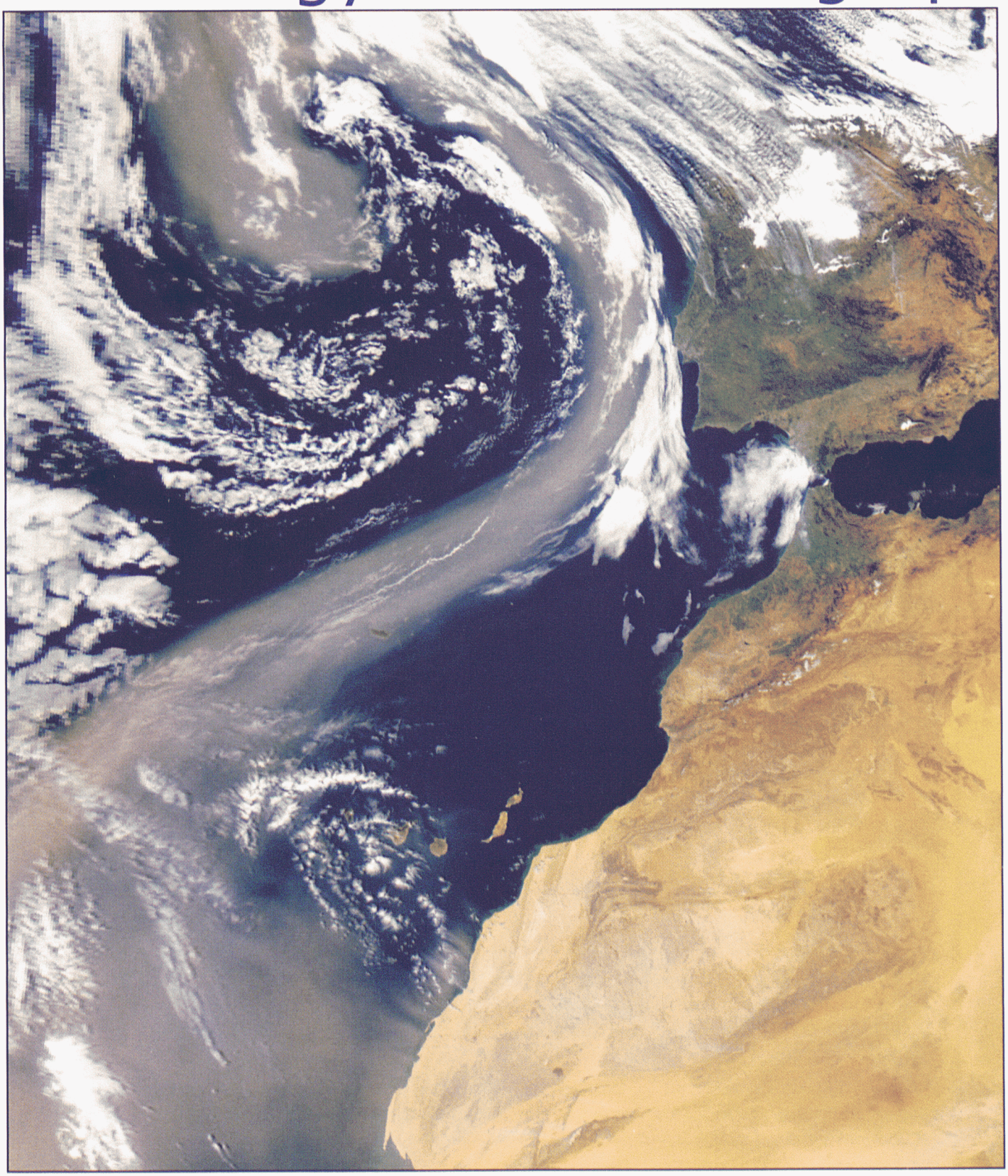

15–18 October 2001 Madison, Wisconsin

American Meteorological Society

Check out the AMS Journals Online now on the AMS Web site

AMS Journals Online

Now the complete contents of the AMS journals and Bulletin articles are available on the Web!

All users can view titles and abstracts of articles from the AMS journals (starting with the January 1997 issues), while subscribers will have the added ability to view the complete articles delivered in two forms—as HTML, optimized for on-screen viewing, and as Adobe Acrobat PDF files, for printing a precise "reprint" of the article as it appeared in the journal. The full text of *Bulletin* articles will be available free of charge to all users of the site.

- Flexible full-text and fielded search capability
- Journal contents available online *prior* to the print journal

- *Journal of the Atmospheric Sciences*
- *Journal of Climate*
- *Journal of Atmospheric and Oceanic Technology*
- *Monthly Weather Review*
- *Weather and Forecasting*
- *Journal of Applied Meteorology*
- *Journal of Physical Oceanography*
- *Bulletin of the American Meteorological Society*
- *Journal of Hydrometeorology*

Access the AMS Journals Online from the AMS Web site:
http://www.ametsoc.org/AMS

Subscriptions are available in the form of institutional network site licenses or individual subscriptions. See the AMS Web site for details, or write to the American Meteorological Society, 45 Beacon St., Boston, MA 02108.

11TH CONFERENCE ON SATELLITE METEOROLOGY AND OCEANOGRAPHY

15–18 OCTOBER 2001 MADISON, WISCONSIN

SPONSORED BY
AMERICAN METEOROLOGICAL SOCIETY

LIBRARY
JAN 4 2002
National Oceanic & Atmospheric Administration
U.S. Dept. of Commerce

TL
798
M4
C61
11th
2001

Front Cover: The cover is an OrbView-2 Sea-Viewing Wide Field-of-View Sensor (SeaWiFS) image collected at the Naval European Meteorology and Oceanography Center at Rota, Spain, 13 February 2001. This image was transmitted to the Naval Oceanographic Office and reprocessed by the Naval Research Laboratory. The image shows sand that has been blown off the African Sahara being entrained into a mid-latitude atmospheric low pressure system. The mid-latitude system is approaching the Iberian Peninsula. Image used with permission of ORBIMAGE.

The front cover was sponsored by the Naval Meteorology and Oceanography Command. For more information, please refer to paper number 3.5, page 234, entitled, "*Satellite Data Utilization by U.S. Navy Meteorology and Oceanography.*" by Don T. Conlee, Naval Meteorology and Oceanography Command, Stennis Space Center, MS; and R. L. Crout.

All Rights Reserved. No part of this publication may be reproduced or copied in any form or by any means—graphic, electronic, or mechanical, including photocopying, taping, or information storage and retrieval systems—without the prior written permission of the publisher. Contact AMS for permission pertaining to the overall collection. Authors retain their individual rights and should be contacted directly for permission to use their material separately. The manuscripts reproduced herein are unrefereed papers presented at the ***11th Conference on Satellite Meteorology and Oceanography***. Their appearance in this collection does not constitute formal publication.

AMERICAN METEOROLOGICAL SOCIETY
45 BEACON STREET, BOSTON, MASSACHUSETTS USA 02108-3693

National Oceanic and Atmospheric Administration
TIROS Satellites and Satellite Meteorology

ERRATA NOTICE

One or more conditions of the original document may affect the quality of the image, such as:

Discolored pages
Faded or light ink
Binding intrudes into the text

This has been a co-operative project between the NOAA Central Library and the Climate Database Modernization Program, National Climate Data Center (NCDC). To view the original document contact the NOAA Central Library in Silver Spring, MD at (301) 713-2607 x124 or Library.Reference@noaa.gov.

HOV Services
Imaging Contractor
12200 Kiln Court
Beltsville, MD 20704-1387
January 26, 2009

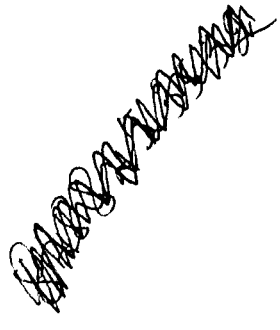

Blank page retained for pagination

FOREWORD

Welcome to Madison! We are pleased to present this preprint volume for the 11th Conference on Satellite Meteorology and Oceanography sponsored by the American Meteorological Society (AMS) and organized by the AMS Committee on Satellite Meteorology and Oceanography (CSMO). The conference is being held at the new Monona Terrace Convention Center, which was originally designed by the renowned architect Frank Lloyd Wright. The conference has been shortened to 4 days, and will run from October 15–18, 2001.

The CSMO program committee followed the successful format of the prior two conferences, emphasizing the poster sessions and a selection of invited oral presentations. The invited talks represent a wide-ranging set of topics related to satellite meteorology and oceanography, and provide the focus for the 5 chosen general themes of the conference and associated poster sessions: 1) Environmental Applications, 2) Climatologies, 3) Operational Applications, 4)Radiances, Clouds and Retrievals, and 5) New Technology. Each day of the conference we will focus on one or two of these themes. The invited talks will precede and follow each poster session. An evening session has also been scheduled featuring a panel discussion on the topic of "NESDIS Weather Products from Polar Satellites: Are We Meeting NOAA's Needs?"

Almost 300 abstracts were received in response to the call for papers. Students were encouraged to submit abstracts, and posters identified as student submissions were automatically entered into a student poster contest. The winners will be selected by a panel of CSMO judges, and will be provided certificates and cash prizes courtesy of the AMS. An exhibit program will be featured during the first three days, and a special NASA E-Theater presentation will take place on Wednesday evening. The Conference will officially end with a banquet to be held on Thursday night. We hope this program will provide a stimulating environment and forum for candid discussions inside and outside of the meeting venue.

I would like to express my appreciation to the CSMO Program Committee (listed below), and in particular the past program chairman Ralph Ferraro for his insight. Thanks goes out to Henry Reges of AMS and cohorts for program support and guidance, Terri Gregory of SSEC, John Chasten and colleagues of the Madison Convention and Visitors Bureau, and the Monona Terrace Convention Center. Finally, as the local host for this event, we are reminded of the late Verner Suomi, whose presence is forever felt here at the University of Wisconsin – SSEC/CIMSS.

Christopher S. Velden
Program Chairperson

AMS COMMITTEE ON SATELLITE METEOROLOGY AND OCEANOGRAPHY

Marie Colton, Chairperson
Daniel Birkenhauer, Tracy L.DeLiberty, Larry DiGirolamo, Ralph R. Ferraro, Jeffrey D. Hawkins, Kenneth Holmlund, Ronald G. Isaacs, Frank Monaldo, Christopher S. Velden and John V. Zapotocny

PROGRAM COMMITTEE

Christopher S. Velden, Chairperson
Daniel Birkenhauer, Larry DiGirolamo, Ralph R. Ferraro, Jeffrey D. Hawkins, John V. Zapotocny

Blank page retained for pagination

TABLE OF CONTENTS

11TH CONFERENCE ON SATELLITE METEOROLOGY AND OCEANOGRAPHY

PAGE

SESSION 1: ENVIRONMENTAL APPLICATIONS

* 1.1 OPERATIONAL SATELLITE OCEANOGRAPHY: DEVELOPING THE STRATEGIC VISION. Marie C. Colton, NOAA/NESDIS, Camp Springs, MD (*Invited Presentation*)

1 1.2 AN OVERVIEW OF ACTIVE FIRE DETECTION AND MONITORING USING METEOROLOGICAL SATELLITES. Elaine M. Prins, NOAA/NESDIS/ORA, Madison, WI; and J. M. Feltz and C. C. Schmidt (*Invited Presentation*)

9 1.3 HURRICANE HEAT POTENTIAL ESTIMATES FROM SATELLITE RADAR ALTIMETER MEASUREMENTS. Lynn K. Shay, Univ. of Miami/RSMAS, Miami, FL (*Invited Presentation*)

POSTER SESSION 1: ENVIRONMENTAL APPLICATIONS

17 P1.1 SNOW EMISSIVITY SIMULATED USING MIE THEORY. Banghua Yan, Decision Systems Technologies/RDC, Rockville, MD; and F. Weng

19 P1.2 SNOW COVER EXTENT OVER SOUTH AMERICA DERIVED FROM PASSIVE MICROWAVE AND VISIBLE/INFRARED OBSERVATIONS. Peter Romanov, NOAA/NESDIS/ORA, Camp Springs, MD; and D. Tarpley

23 P1.3 RETRIEVAL AND INTERPRETATION OF SNOW COVER PARAMETERS FROM MICROWAVE REMOTE SENSING DATA. Cezar E. Kongoli, QSS Group, Inc., Lanham, MD; and N. C. Grody

* P1.4 NEAR REAL TIME REMOTE SENSING OF LAKE SURFACE TEMPERATURE AND ICE COVER. John H. Marsham, Univ. of Edinburgh, Edinburgh, Scotland, UK; and C. J. Merchant

27 P1.5 MONITORING THE SEASONAL DECAY OF FIRST YEAR SEA ICE AT THE CANADIAN ICE SERVICE WITH NOAA AVHRR. Roger A. De Abreu, MSC/EC/Canadian Ice Service, Ottawa, ON, Canada; and M. Arkett and B. Ramsay

• P1.6 DIURNAL VARIATION OF GOES SST. Xiangqian Wu, CIMSS/Univ. of Wisconsin, Madison, WI; and W. P. Menzel

* P1.7 TROPICAL CYCLONE FORCING IN THE GULF OF MEXICO. Mark A. Bourassa, Florida State Univ., Tallahassee, FL; and S. L. Morey, J. Zavala, and J. J. O'Brien

31 P1.8 USING QUIKSCAT DATA TO DETERMINE THE STRENGTH OF A POLAR LOW. Boniface J. Mills, Univ. of Nebraska, Lincoln, NE

35 P1.9 AIR-SEA FLUXES FROM SYNTHETIC APERTURE RADAR: AN UPDATE. Todd D. Sikora, U.S. Naval Academy, Annapolis, MD; and D. R. Thompson

39 P1.10 REALTIME REMOTE SENSING-BASED MODELING AND IN SITU VALIDATION OF LAND SURFACE ENERGY AND WATER FLUXES. George R. Diak, CIMSS/Univ. of Wisconsin, Madison, WI; and J. R. Mecikalski, M. C. Anderson, J. M. Norman, R. D. Torn, and J. Hoss

43 P1.11 DESERT DUST STORMS AS DETECTED BY METEOSAT AND SEAWIFS MULTISPECTRAL IMAGERY. Steven D. Miller, NRL, Monterey, CA; and T. F. Lee

47 P1.12 CHARACTERIZATION OF CLOUDS, FIRES AND SMOKE PLUMES IN HYPERSPECTRAL IMAGES. Michael K. Griffin, MIT Lincoln Lab., Lexington, MA; and S. M. Hsu, H. K. Burke, and J. W. Snow

51 P1.13 A COMPARISON OF THE GOES-8 ABBA AND INPE AVHRR FIRE PRODUCTS FOR SOUTH AMERICA FROM 1995–2000. Joleen M. Feltz, CIMSS/Univ. of Wisconsin, Madison, WI; and E. M. Prins and A. W. Setzer

• Manuscript not available

TABLE OF CONTENTS

11TH CONFERENCE ON SATELLITE METEOROLOGY AND OCEANOGRAPHY

PAGE		
55	P1.14	PRINCIPAL COMPONENT IMAGE ANALYSIS OF MODIS FOR VOLCANIC ASH. Donald W. Hillger, NOAA/NESDIS/ORA and CIRA/Colorado State Univ., Fort Collins, CO; and J. Clark
61	P1.15	LOSS OF THE 12.0 μM "SPLIT WINDOW" BAND ON GOES-M: IMPACTS ON VOLCANIC ASH DETECTION. Gary P. Ellrod, NOAA/NESDIS/ORA, Camp Springs, MD
65	P1.16	RECENT MONITORING OF SUSPENDED SEDIMENT PATTERNS ALONG LOUISIANA'S COASTAL ZONE USING ER-2 BASED MAS DATA AND TERRA BASED MODIS DATA. Christopher C. Moeller, CIMSS/Univ. of Wisconsin, Madison, WI; and M. M. Gunshor, W. P. Menzel, O. K. Huh, N. D. Walker, and L. J. Rouse
	P1.17	PAPER WITHDRAWN
69	P1.18	MODIS OCEAN COLOR DATA FOR STUDYING OCEAN CIRCULATION FEATURES. K. S. Prasad, SeaSpace Corp., Poway, CA; and R. L. Bernstein
73	P1.19	TOPEX/POSEIDON ALTIMETRY REVEALS THE VIETNAM SUMMER RECIRCULATION. Eric J. Bayler, Univ. of Wisconsin, Madison, WI; and Z. Liu
75	P1.20	SEA SURFACE SALINITY FROM SPACE: SCIENCE GOALS AND MEASUREMENT APPROACH. C. J. Koblinsky, NASA/GSFC, Greenbelt, MD; and P. H. Hildebrand, Y. Chao, A. de Charon, W. Edelstein, G. Lagerloef, D. Le Vine, F. Pellerino, Y. Rahmat-Samii, C. Ruf, F. Wentz, W. Wilson, and S. Yueh
	P1.21	PAPER WITHDRAWN
79	P1.22	SPECTRAL TRANSFER OF HUMIDITY AND TEMPERATURE CORRELATIONS FOR INHOMOGENEOUS TURBULENCE FOR LAND AND AGRICULTURE PROCESSES. Sukaran R. Patel, Univ. Federal da Paraíba, Campina Grande, Brazil
81	P1.23	REFRACTIVE INDEX SPECTRAL TRANSFER IN INHOMOGENEOUS TURBULENCE IN ATMOSPHERIC/OCEANIC SURFACE LAYER. Sukaran R. Patel, Univ. Federal da Paraíba, Campina Grande, Brazil
83	P1.24	ASSIMILATION OF SOIL MOISTURE FROM SATELLITE-DERIVED SKIN TEMPERATURE WITHIN THE PENN STATE/NCAR MESOSCALE MODEL MM5. Jing Zhang, Univ. of Alaska, Fairbanks, AK; and J. S. Tilley
87	P1.25	A SYNERGISTIC SURFACE BRDF/ALBEDO RETRIEVAL WITH MODIS AND MISR OBSERVATIONS 1.INTERCOMPARISION. Yufang Jin, Boston Univ., Boston, MA; and F. Gao, C. Schaaf, A. Strahler, C. Bruegge, J. Martonchik, and D. Diner
91	P1.26	FRACTIONAL GREEN VEGETATION COVER OF THE CONTERMINOUS USA FOR USE IN NUMERICAL WEATHER MODELS. Kevin Gallo, NOAA/NESDIS, Sioux Falls, SD; and D. Tarpley, K. Mitchell, I. Csiszar, T. Owen, and B. Reed
93	P1.27	USING DMSP IMAGERY AND SSM/I DATA TO ANALYZE A VON KARMAN VORTEX OVER THE BLACK SEA. Boniface J. Mills, Univ. of Nebraska, Lincoln, NE; and P. J. McCrone
96	P1.28	STUDY OF FOG PROPERTIES USING LANDSAT DATA. Kenneth W. Fischer, Terabeam Labs., Redmond, WA; and M. Nunez, J. Ramaprasad, M. R. Witiw, and J. A. Baars
99	P1.29	INCORPORATING DATA FROM GOES AND POES PLATFORMS INTO AN INTEGRATED IN-FLIGHT ICING DIAGNOSTIC ALGORITHM FOR ALASKA. Jeffrey S. Tilley, Univ. of Alaska, Fairbanks, AK; and J. Long
*	P1.30	USE OF GOES SATELLITE DATA IN MESOSCALE SURFACE BOUNDARY CONDITIONS FOR A DESERT REGION. Elford G. Astling, West Desert Test Center, Salt Lake City, UT

* Manuscript not available

TABLE OF CONTENTS

11TH CONFERENCE ON SATELLITE METEOROLOGY AND OCEANOGRAPHY

PAGE

103 P1.31 ON PRECIPITATION MODIFICATION BY MAJOR URBAN AREAS: A NEW PERSPECTIVE FROM TRMM. J. Marshall Shepherd, NASA/GSFC, Greenbelt, MD; and H. Pierce

* P1.32 APPLICATION OF REMOTE-SENSING TECHNOLOGY IN ATMOSPHERIC ENVIRONMENT. Xuemei Wang, Zhongshan Univ., Guangzhou, China

SESSION 2: CLIMATOLOGY AND LONG-TERM SATELLITE STUDIES

107 2.1 THE ROLE OF PASSIVE MICROWAVE RADIOMETERS IN CLIMATE MONITORING. Roy W. Spencer, Univ.of Alabama, Huntsville, AL (*Invited Presentation*)

110 2.2 CHANGES IN THE EARTH'S RESOLVED OUTGOING LONGWAVE RADIATION FIELD AS SEEN FROM THE IRIS AND IMG INSTRUMENTS. Helen E. Brindley, Imperial College, London, UK; and P. J. Sagoo, R. J. Bantges, and J. E. Harries (*Invited Presentation*)

114 2.3 GLOBAL PRECIPITATION CLIMATOLOGIES AND THE ROLE OF SATELLITE OBSERVATIONS. Phillip A. Arkin, NOAA/Office of Global Programs, Silver Spring, MD; and P. Xie and J. Janowiak (*Invited Presentation*)

POSTER SESSION 1: CLIMATOLOGY AND LONG-TERM SATELLITE STUDIES

118 P2.1 SPECIFYING SATELLITE ORBITS FOR HIGH ACCURACY CLIMATE MONITORING. Daniel B. Kirk-Davidoff, Harvard Univ., Cambridge, MA; and R. M. Goody and J. G. Anderson

122 P2.2 LONGWAVE AND WINDOW ANGULAR DISTRIBUTION MODELS FROM CERES/TRMM RADIANCE MEASUREMENTS. Natividad Manalo-Smith, AS&M, Hampton, VA; and N. G. Loeb

126 P2.3 LIMB BIASES IN CO_2 CLOUD HEIGHT ALGORITHMS WITH RESPECT TO HIGH ALTITUDE CIRRUS. R. Lynn Rose, Aeromet, Inc., Tulsa, OK; and M. Bedrick, K. Swanson, and B. Morrison

128 P2.4 INTERNAL CONSISTENCY OF THE NVAP WATER VAPOR DATASET. Ronnie J. Suggs, NASA/MSFC, Huntsville, AL; and G. J. Jedlovec

132 P2.5 RADIATIVE IMPACT OF CLOUDS AND WATER VAPOR VARIATIONS ABOVE 300 MB FROM LONG-TERM NVAP AND ISCCP OBSERVATIONS. G. Garrett Campbell, CIRA/Colorado State Univ., Ft. Collins, CO; and T. H. Vonder Haar, J. Fosythe, A. Kankiewicz, R. Engelen, and S. Woo

136 P2.6 LONG TERM CHANGES IN CLOUD COVER DETECTED IN HIRS DATA. Donald Wylie, Univ. of Wisconsin, Madison, WI

* P2.7 AN ALTERNATIVE LONG TERM OLR DATA SET. Christopher Collimore, Univ. of Wisconsin, Madison, WI; and D. E. Waliser, G. L. Smith, T. D. Bess, D. F. Young, D. W. Martin, and K. A. Bush

* P2.8 A 10-YEAR CLIMATOLOGY OF CLOUD PROPERTIES AND RADIATION FLUXES BASED ON THE AVHRR POLAR PATHFINDER DATA SET. Xuanji Wang, CIMSS/Univ. of Wisconsin, Madison, WI; and J. R. Key and M. Pavolonis

138 P2.9 CLIMATE ANALYSIS WITH THE 21-YR HIRS PATHFINDER RADIANCE CLEAR-SKY DATA SET. Darren L. Jackson, CIRES/Univ. of Colorado, Boulder, CO; and J. J. Bates

141 P2.10 COMPARISONS OF CLOUD ANALYSES FROM INDEPENDENT INFRARED AND SOUNDER RETRIEVALS. Robert P. d'Entremont, AER, Lexington, MA; and D. P. Wylie

* Manuscript not available

TABLE OF CONTENTS

11TH CONFERENCE ON SATELLITE METEOROLOGY AND OCEANOGRAPHY

PAGE		
145	P2.11	CLOUD CLIMATE INVESTIGATIONS IN SCANDINAVIA DURING THE LAST DECADE USING HIGH-RESOLUTION NOAA AVHRR DATA. Karl-Göran Karlsson, SMHI, Norrköping, Sweden; and A. Dybbroe
149	P2.12	INITIATION OF A HIGH RESOLUTION TROPICAL CLOUD CLIMATOLOGY. Mary Bedrick, Aeromet, Inc., Tulsa, OK; and K. Swanson, L. Rose, and B. Morrison
153	P2.13	AN ANALYSIS OF CLOUD AND RAINFALL DISTRIBUTIONS OVER DEFORESTED AMAZONIA USING TRMM AND GOES MEASUREMENTS. Frédéric J. Chagnon, MIT, Cambridge, MA; and A. J. Negri, J. Wang, L. Xu, R. M. Adler, and R. L. Bras
157	P2.14	MESOSCALE SATELLITE CLIMATOLOGIES IN COSTA RICA. Bernadette H. Connell, CIRA/Colorado State Univ., Ft. Collins, CO; and V. Castro Leon
161	P2.15	PLUMES ABOVE THUNDERSTORMS ANVILS AND THEIR CONTRIBUTIONS TO CROSS TROPOPAUSE TRANSPORT OF WATER VAPOR IN MIDLATITUDES. Pao K. Wang, Univ. of Wisconsin, Madison, WI
165	P2.16	WIND REGIME GOES CLOUD COVER COMPOSITES FOR THE WAKEFIELD, VA COUNTY WARNING AREA. Cynthia L. Combs, CIRA/Colorado State Univ., Fort Collins, CO; and N. A. Stuart, M. DeMaria, and T. H. Vonder Haar
168	P2.17	INVESTIGATIONS OF LIQUID WATER PATH SPATIAL VARIABILITY USING MODIS. Robert Wood, Univ. of Washington, Seattle, WA; and D. L. Hartmann
172	P2.18	THE INFLUENCE OF ANTARCTIC CLOUD AND SURFACE PROPERTIES ON CLOUD RADIATIVE FORCING AT THE SURFACE. Michael J. Pavolonis, CIMSS/Univ. of Wisconsin, Madison, WI; and J. R. Key
*	P2.19	ENSO IN HIGHLY REFLECTIVE CLOUD: A FRESH LOOK. David W. Martin, SSEC/Univ. of Wisconsin, Madison, WI; and C. C. Collimore and M. H. Hitchman
176	P2.20	DEVELOPMENT OF A CLIMATOLOGY OF CLOUD PROPERTIES DERIVED FROM GOES OVER THE SOUTHEASTERN PACIFIC FOR PACS. J. Kirk Ayers, AS&M, Hampton, VA; and P. Minnis, D. F. Young, W. L. Smith, Jr., and L. Nguyen
180	P2.21	A PROTOTYPE BENCHMARK THERMAL RADIANCE MEASUREMENT. John A. Dykema, Harvard Univ., Cambridge, MA; and R. M. Goody, and J. G. Anderson
184	P2.22	AEROSOL OPTICAL DEPTH OVER LAND FROM THE AVHRR PATHFINDER ATMOSPHERE DATA SET. Kenneth R. Knapp, CIRA/NOAA/NESDIS/ORA, Camp Springs, MD
188	P2.23	TEMPORAL SCALES OF THE AREAL COVERAGE AND PRECIPITATION OF MONSOONAL CONVECTIVE CLOUD SYSTEMS OVER THE TROPICAL INDIAN OCEAN. Eric M. Wilcox, SIO/Univ. of California, La Jolla, CA
722	P2.24	WATER VAPOR TRANSPORT OVER THE TROPICAL OCEANS DURING EL NIÑO AND LA NIÑA AND ITS IMPLICATION FOR THE TROPICAL CIRCULATION: A SATELLITE APPROACH. Byung-Ju Sohn, Seoul National Univ., Seoul, Korea; and F. R. Robertson, E. A. Smith, and S.-C. Park
192	P2.25	VARIABILITY IN UTH AND WATER CYCLE DYNAMICS. John J. Bates, NOAA/ETL, Boulder, CO
*	P2.26	AN ASSESSMENT OF UPPER TROPOSPHERIC HUMIDITY MEASUREMENTS FROM THE ATMOSPHERIC RADIATION MEASUREMENT (ARM) PROGRAM. Brian J. Soden, NOAA/GFDL, Princeton, NJ; and D. Turner, R. Ferrare, B. Lesht, and J. Goldsmith

* Manuscript not available

TABLE OF CONTENTS

11TH CONFERENCE ON SATELLITE METEOROLOGY AND OCEANOGRAPHY

PAGE

196 P2.27 DIURNAL VARIABILITY OF SATELLITE DERIVED PRECIPITABLE WATER IN THE AMAZON BASIN. Tracy L. DeLiberty, Univ. of Delaware, Newark, DE; and J. A. Callahan

200 P2.28 TROPICAL PRECIPITABLE WATER CLIMATOLOGY FOR EQUATORIAL WAVES. Paul E. Roundy, Penn State Univ., University Park, PA

202 P2.29 DIFFERENCES IN THE RESPONSE OF SATELLITE PRECIPITATIONS ESTIMATES TO ENSO. Wesley Berg, Colorado State Univ., Fort Collins, CO; and C. Kummerow

206 P2.30 A TRMM-CALIBRATED INFRARED TECHNIQUE FOR CONVECTIVE AND STRATIFORM RAINFALL: ANALYSIS AND VALIDATION. Andrew J. Negri, NASA/GSFC, Greenbelt, MD; and L. Xu and R. F. Adler

* P2.31 GLOBAL TRENDS (1979 TO 2001) IN MEAN AND EXTREME RAINFALL FROM A NEW SATELLITE-GAUGE MERGED DATA SET. Scott Curtis, JCET/Univ. of Maryland Baltimore County, Greenbelt, MD; and R. F. Adler, G. J. Huffman, E. J. Nelkin, and D. T. Bolvin

210 P2.32 STANDARD ERRORS OF THE ESTIMATED TREND IN CHANNEL 2 OF THE MICROWAVE SOUNDING UNIT. David S. Crosby, NOAA/NESDIS/ORA, Camp Springs, MD; and M. D. Goldberg, T. Mo, and Z. Cheng

* P2.33 INTERANNUAL VARIATIONS IN HIRS OBSERVATIONS OF THE TEMPERATURE INVERSION OVER THE ANTARCTIC PLATEAU. Steven A. Ackerman, CIMSS/Univ. of Wisconsin, Madison, WI; and R. Frey and J. Key

212 P2.34 GLOBAL SATELLITE-BASED STUDY OF THE DIURNAL RANGE OF LAND SURFACE TEMPERATURE. Ivan Csiszar, CIRA and NOAA/NESDIS/ORA, Camp Springs, MD; and G. Gutman

SESSION 3: OPERATIONAL APPLICATIONS

216 3.1 WEATHER PREDICTION IMPROVEMENT USING ADVANCED SATELLITE TECHNOLOGY. Louis Uccellini, NOAA/NWS/NCEP, Camp Springs, MD; and F. Einaudi, J. Purdom, D. Rogers, R. Gelaro, J. Dodge, R. Atlas, and S. Lord (*Invited Presentation*)

220 3.2 USES OF SATELLITE DATA IN AIR FORCE WEATHER. John V. Zapotocny, Air Force Weather Agency, Offutt AFB, NE (*Invited Presentation*)

228 3.3 SATELLITE-BASED TROPICAL CYCLONE INTENSITY ESTIMATION USING NOAA-KLM SERIES ADVANCED MICROWAVE SOUNDING UNIT (AMSU). Kurt F. Brueske, U.S. Air Force Academy, U.S. Air Force Academy, CO; and C. S. Velden (*Invited Presentation*)

* 3.4 RECENT IMPACT OF SATELLITE DATA AT ECMWF. Graeme A. Kelly, ECMWF, Reading, Berks., UK (*Invited Presentation*)

234 3.5 SATELLITE DATA UTILIZATION BY U.S. NAVY METEOROLOGY AND OCEANOGRAPHY. Don T. Conlee, Naval Meteorology and Oceanography Command, Stennis Space Center, MS; and R. L. Crout (*Invited Presentation*)

240 3.6 SOME NEW OPERATIONAL APPLICATIONS OF METSAT OBSERVATIONS. Thomas H. Vonder Haar, CIRA/Colorado State Univ., Fort Collins, CO (*Invited Presentation*)

POSTER SESSION 3: OPERATIONAL APPLICATIONS

241 P3.1 UW-CIMSS SATELLITE WINDS ALGORITHM. Gail A. Dengel, CIMSS/Univ. of Wisconsin, Madison, WI; and C. S. Velden, T. L. Olander, D. A. Santek, and D. R. Stettner

* Manuscript not available

TABLE OF CONTENTS

11TH CONFERENCE ON SATELLITE METEOROLOGY AND OCEANOGRAPHY

PAGE		
244	P3.2	GWINDEX—GOES RAPID-SCAN WINDS EXPERIMENT: APPLICATIONS FOR WEST COAST FORECASTING. Christopher S. Velden, CIMSS/Univ. of Wisconsin, Madison, WI; and D. Stettner, J. Daniels, and W. Bresky
248	P3.3	VALIDATION OF GOES CLEAR-AIR WATER VAPOR WINDS. Jaime M. Daniels, NOAA/NESDIS/ORA, Camp Springs, MD; and W. Bresky
252	P3.4	WATER VAPOR WINDS IN VICINITY OF CONVECTION AND WINTER STORMS. Robert M. Rabin, NOAA/NSSL, Norman, OK; and J. Brunner, C. Hane, and J. Haynes
*	P3.5	CLOUD STEREO HEIGHTS AND MOTIONS FROM SATELLITES IMAGERY: EXAMPLES AND AUTOMATION. G. Garrett Campbell, Colorado State Univ., Boulder, CO; and T. H. VonderHaar and K. Eis
256	P3.6	EVALUATING THE POTENTIAL IMPACT OF THE ASSIMILATION OF SATELLITE DERIVED PRODUCTS ON A MESOSCALE FORECAST OF PACIFIC LANDFALLING JETS EXPERIMENT (PACJET) IOP 10. Michael C. Morgan, Univ. of Wisconsin, Madison, WI; and K. La Casse, D. T. Kleist, H. M. Kim, J. G. McLay, D. J. Posselt, J. R. Mecikalski, C. S. Velden, and D. Stettner
260	P3.7	ASSIMILATION OF GOES RAPID-SCAN WINDS INTO AN EXPERIMENTAL ETA MODEL DURING HURRICANE KEITH. Howard I. Berger, CIMSS/Univ. of Wisconsin, Madison, WI; and C. S. Velden
726	P3.8	*THE IMPACT OF SATELLITE WINDS ON TWO VERSIONS OF NCEP GLOBAL DATA ASSIMILATION AND* FORECAST SYSTEMS. Xiujuan Su, NOAA/EMC, Camp Springs, MD; and J. Derber and S. Lord
262	P3.9	AN IMPACT STUDY OF FIVE REMOTELY SENSED AND FIVE IN-SITU ETA DATA TYPES IN THE DATA ASSIMILATION SYSTEM. Tom H. Zapotocny, CIMSS/Univ. of Wisconsin, Madison, WI; and W. P. Menzel, J. P. Nelson III, and J. A. Jung
266	P3.10	ASSIMILATION OF GOES SOUNDER CLOUD TOP PRESSURE IN NCEP'S 48KM ETA MESOSCALE MODEL. James A. Jung, CIMSS/Univ. of Wisconsin, Madison, WI; and R. M. Aune, T. J. Schmit, and T. H. Zapotocny
270	P3.11	GPS-DERIVED INTEGRATED PRECIPITABLE WATER COMPARED WITH AFWA MM5 MODEL OUTPUT. Patricia A. Vollmer, Air Force Institute of Technology, Wright-Patterson AFB, OH; and G. R. Huffines
*	P3.12	*ASSIMILATION OF GOES LAND SURFACE DATA WITHIN A RAPID UPDATE CYCLE FORMAT: IMPACT ON MM5* WARM SEASON QPF. William M. Lapenta, NASA/MSFC, Huntsville, AL; and R. J. Suggs, G. Jedlovec, R. T. McNider, and S. R. Dembek
273	P3.13	UTILIZING VARIATIONAL METHODS TO INCORPORATE A VARIETY OF SATELLITE DATA IN THE LAPS *MOISTURE ANALYSIS. Daniel L. Birkenheuer, NOAA/FSL, Boulder, CO*
277	P3.14	ONE DIMENSIONAL VARIATIONAL ASSIMILATION EXPERIMENTS COMBINING GOES SOUNDER AND IMAGER *RADIANCE DATA. Dongsoo Kim, CIRES/Univ. of Colorado and NOAA/FSL, Boulder, CO; and D. Devenyi*
279	P3.15	THE ASSIMILATION OF SATELLITE OBSERVATIONS WITH THE NRL ATMOSPHERIC VARIATIONAL DATA ASSIMILATION SYSTEM (NAVDAS). Nancy L. Baker, NRL, Monterey, CA; and R. Daley, S. D. Swadley, J. Clark, E. H. Barker, J. S. Goerss, and K. Sashegyi
282	P3.16	IMPROVEMENTS TO U.S. AIR FORCE CLOUD FORECAST MODEL, ADVECT CLOUD. Steven J. Storch, Air Force Weather Agency, Offutt, NE; and D. G. McDonald
286	P3.17	ANALYSIS OF SUBTROPICAL CYCLONES USING NASA QUIKSCAT DATA. Paul J. McCrone, Air Force Weather Agency, Offutt AFB, NE

* Manuscript not available

TABLE OF CONTENTS

11TH CONFERENCE ON SATELLITE METEOROLOGY AND OCEANOGRAPHY

PAGE

290 P3.18 STATUS OF THE UW-CIMSS OBJECTIVE DVORAK TECHNIQUE (ODT). Timothy L. Olander, CIMSS/Univ. of Wisconsin, Madison, WI; and C. S. Velden

292 P3.19 PRELIMINARY OBJECTIVE ANALYSES USING THE NESDIS/CIRA TROPICAL CYCLONE INFRARED IMAGERY PART I: HURRICANE HARMONICS. James P. Kossin, CIRA/Colorado State Univ., Fort Collins, CO

296 P3.20 TROPICAL CYCLONE SURFACE WIND ANALYSIS USING SATELLITE SENSORS. Raymond M. Zehr, NOAA/NESDIS/ORA, Fort Collins, CO

300 P3.21 VALIDATION OF AN ADVANCED MICROWAVE SOUNDER UNIT (AMSU) TROPICAL CYCLONE INTENSITY AND SIZE ESTIMATION ALGORITHM. Mark DeMaria, NOAA/NESDIS/ORA, Fort Collins, CO; and J. L. Demuth and J. A. Knaff

304 P3.22 TRMM TMI VIEWS OF TROPICAL CYCLONES FOR TACTICAL RECONNAISSANCE. Thomas F. Lee, NRL, Monterey, CA; and F. J. Turk, J. D. Hawkins, and R. T. Edson

308 P3.23 MAPPING TROPICAL CYCLONE CHARACTERISTICS VIA PASSIVE MICROWAVE REMOTE SENSING. Jeffrey D. Hawkins, NRL, Monterey, CA; and T. F. Lee, J. F. Turk, K. Richardson, C. C. Sampson, and J. Kent

312 P3.24 THE REALTIME VALUE OF COMBINED UPPER TROPOSPHERIC INERTIAL STABILITY MEASUREMENTS AND SATELLITE-DERIVED WINDS ON TROPICAL CYCLONE AND CONVECTION FORECASTING. John R. Mecikalski, CIMSS/Univ. of Wisconsin, Madison, WI; and C. S. Velden

314 P3.25 SATELLITE APPLICATIONS FOR TROPICAL WAVE/TROPICAL CYCLONE TRACKING. Jason P. Dunion, NOAA/AOML/HRD, Miami, FL; and C. S. Velden

728 P3.26 VALIDATION OF GMS BRIGHTNESS TEMPERATURE DIFFERENCE TECHNIQUE FOR ESTIMATE OF CUMULONIMBUS IN TYPHOON BY TRMM PR DATA. Kotaro Bessho, MRI, Tsukuba, Ibaraki, Japan; and Y. Tanaka and T. Nakazawa

* P3.27 AN ASSESSMENT OF GLOBAL MODELS ABILITY TO ACCURATELY FORECAST DOWNSTREAM EXTRA-TROPICAL CYCLONE DEVELOPMENT IN THE SOUTHERN HEMISPHERE WINTER. Matthew A. Lazzara, Univ. of Wisconsin, Madison, WI; and J. G. McLay and S. G. Decker

318 P3.28 ANTARCTIC METEOROLOGY: SATELLITES AND WEATHER FORECASTING. Matthew A. Lazzara, Univ. of Wisconsin, Madison, WI; and L. M. Keller, C. R. Stearns, J. E. Thom, and G. A. Weidner

320 P3.29 CLOUD-DRIFT AND WATER VAPOR WINDS IN THE POLAR REGIONS FROM MODIS. Jeffrey R. Key, NOAA/NESDIS/ORA, Madison, WI; and D. Santek, C. S. Velden, and W. P. Menzel

324 P3.30 VIRTUAL LABORATORY FOR TRAINING IN SATELLITE METEOROLOGY. James F. W. Purdom, CIRA/Colorado State Univ, Ft. Collins, CO; and A. Mostek

328 P3.31 VIRTUAL INSTITUTE FOR SATELLITE INTEGRATION TRAINING - BRINGING TRAINING TO THE FORECASTERS USING VISITVIEW. Anthony Mostek, NOAA/NWS, Boulder, CO; and S. Bachmeier, T. Whittaker, D. Bikos, B. Motta, B. Zajac, J. Weaver, K. Schrab, B. Grant, and J. LaDue

332 P3.32 RECENT TRAINING FROM THE VIRTUAL INSTITUTE FOR SATELLITE INTEGRATION TRAINING. Brian Motta, CIRA/Colorado State Univ., Fort Collins, CO; and D. Bikos, B. Zajac, S. Bachmeier, T. Whittaker, B. Grant, J. LaDue, S. Jascourt, W. Bua, K. Schrab, M. Schichtel, S. Flood, D. Baumgardt, R. Grumm, P. Wolf, J. Weaver, and R. Zehr

* Manuscript not available

TABLE OF CONTENTS

11TH CONFERENCE ON SATELLITE METEOROLOGY AND OCEANOGRAPHY

PAGE		
336	P3.33	ATMOSPHERIC INSTABILITY PARAMETERS DERIVED FROM MSG SEVIRI OBSERVATIONS. Marianne Koenig, EUMETSAT, Darmstadt, Germany; and S. A. Tjemkes and J. Kerkmann
339	P3.34	ASSESSING THE QUALITY AND UTILITY OF HIGHER RESOLUTION GOES SOUNDER RETRIEVALS. Gary E. Gray, Raytheon, Lanham, MD; and J. Daniels
343	P3.35	AN ASSESSMENT OF THE TEMPORAL VALUE OF RETRIEVED PARAMETERS FROM THE GOES SOUNDER. Robert M. Aune, NOAA/NESDIS/ORA, Madison, WI; and R. Petersen
346	P3.36	CASE STUDIES USING HOURLY REAL-TIME GOES SOUNDER OZONE ESTIMATES. Christopher C. Schmidt, CIMSS/Univ. of Wisconsin, Madison, WI; and J. Li and A. J. Wimmers
348	P3.37	A VALIDATION STUDY OF THE GOES SOUNDER CLOUD TOP PRESSURE PRODUCT. James A. Hawkinson, CIMSS/Univ. of Wisconsin, Madison, WI and NOAA/NESDIS/ORA; and W. Feltz, T. J. Schmit, A. J. Schreiner, and S. A. Ackerman
351	P3.38	IS THE RESOLUTION OF GOES SOUNDER DATA SUFFICIENT TO SUPPORT SINGLE FIELD OF VIEW RETRIEVALS AND DERIVED PRODUCTS? Gail M. Bayler, CIMSS/Univ. of Wisconsin, Madison, WI; and S. Wetzel-Seemann, J. Li, and T. J. Schmit
355	P3.39	AN ANALYSIS OF PRE-TORNADIC LOW-LEVEL MOISTURE-FLUX CONVERGENCE AND THE UTILITY OF GOES AND GIFTS SOUNDER DATA. Ralph A. Petersen, NOAA/NWS/NCEP, Camp Springs,, MD; and W. F. Feltz and H.-L. Huang
359	P3.40	AN EVALUATION OF SEVERAL YEARS OF CIMSS AND NESDIS GOES SOUNDER DATA. James P. Nelson III, CIMSS/Univ. of Wisconsin, Madison, WI; and T. J. Schmit and W. P. Menzel
363	P3.41	A SUMMARY OF SATELLITE DATA USAGE IN THE NWS WESTERN REGION. Kevin J. Schrab, NOAA/NWS, Salt Lake City, UT
367	P3.42	USE OF ATOVS AND SSMI OBSERVATIONS AT MéTéO-FRANCE. Florence Rabier, Météo-France, Toulouse, France; and E. Gérard, Z. Sahlaoui, M. Dahoui, and R. Randriamampianina
*	P3.43	APPLICATION OF NOAA ADVANCED MICROWAVE SOUNDING UNIT (AMSU) DERIVED RAIN RATES TO SYNOPTIC EVENTS OVER THE UNITED STATES. Ralph Ferraro, NOAA/NESDIS, Camp Springs, MD; and P. Pellegrino, F. Weng, and L. Zhao
371	P3.44	A PHYSICALLY-BASED ALGORITHM TO DERIVE SURFACE RAINFALL RATE USING ADVANCED MICROWAVE SOUNDING UNIT-B (AMSU-B) MEASUREMENTS. Limin Zhao, NOAA/NESDIS/ORA, Camp Spring, MD; and F. Weng and R. Ferraro
375	P3.45	IMPROVEMENTS TO THE EXPERIMENTAL TROPICAL RAINFALL POTENTIAL (TRAP) TECHNIQUE. Stanley Q. Kidder, CIRA/Colorado State Univ., Fort Collins, CO; and S. J. Kusselson, J. A. Knaff, and R. J. Kuligowski
379	P3.46	VALIDATION OF GOES PRECIPITATION ESTIMATES OVER CENTRAL AMERICA. Rosario Alfaro, NOAA/NESDIS/ORA, Camp Springs, MD; and R. A. Scofield
383	P3.47	THE NESDIS SATELLITE QPE VERIFICATION PROGRAM. Robert J. Kuligowski, NOAA/NESDIS/ORA, Camp Springs, MD; and S. Qiu, R. A. Scofield, and A. Gruber
385	P3.48	THE SATELLITE IMAGERY DISPLAY AND ANALYSIS SYSTEM AT AIR FORCE WEATHER AGENCY. Charles R. Holliday, Air Force Weather Agency, Offutt AFB, NE; and M. D. Conner

* Manuscript not available

TABLE OF CONTENTS

11TH CONFERENCE ON SATELLITE METEOROLOGY AND OCEANOGRAPHY

PAGE		
720	P3.49	MEANDERING SEA SURFACE TEMPERATURE OF APRIL 2001. Serge Hagan-Deschamps, MSC, Dartmouth, NS, Canada
387	P3.50	FINDINGS FROM THE PRE-ASSIMILATION OF GOES IMAGER CHANNELS. Louis Garand, MSC, Dorval, PQ, Canada; and N. Wagneur
391	P3.51	VALIDATION OF GOES-11 DATA. Xiangqian Wu, CIMSS/Univ. of Wisconsin, Madison, WI; and T. J. Schmit
395	P3.52	LIFE CYCLE OF CONVECTIVE ACTIVITY IN TERMS OF CLOUD TYPE OBSERVED BY SPLIT WINDOW. Toshiro Inoue, MRI, Tsukuba, Ibaraki, Japan; and X. Wu and K. Bessho
397	P3.53	OBSERVATIONS OF A SEVERE SUPERCELL THUNDERSTORM ON 24 JULY 2000 USING GOES-11 SOUNDER AND IMAGERY. John F. Weaver, NOAA/NESDIS, Ft. Collins, CO; and J. A. Knaff, D. Bikos, J. M. Daniels, and G. S. Wade
402	P3.54	A CLOUD MODEL INTERPRETATION OF THE ENHANCED V AND OTHER SIGNATURES ATOP SEVERE THUNDERSTORMS. Pao K. Wang, Univ. of Wisconsin, Madison, WI; and H. Lin, S. Natali, S. Bachmeier, and R. Rabin
404	P3.55	A SATELLITE PERSPECTIVE OF THE PINE LAKE, ALBERTA TORNADO EVENT. A. Scott Bachmeier, CIMSS/Univ. of Wisconsin, Madison, WI; and J. P. Nelson III
408	P3.56	MCS DEVELOPMENT WITHIN CONTINENTAL-SCALE ELONGATED DRY FILAMENTS IN GOES WATER VAPOR IMAGES. Edward I. Tollerud, NOAA/FSL, Boulder, CO; and F. Caracena, A. Marroquin, S. E. Koch, J. L. Moody, and A. J. Wimmers
412	P3.57	OPERATIONAL CLOUD DETECTION IN GOES IMAGERY. Gary J. Jedlovec, NASA/MSFC, Huntsville, AL; and K. Laws
416	P3.58	A SATELLITE DIAGNOSTIC OF GLOBAL CONVECTION. Frederick R. Mosher, NOAA/NWS/AWC, Kansas City, MO
•	P3.59	VALIDATION OF A NEW GLOBAL OPERATIONAL CLOUD ANALYSIS AT AFWA. Gary B. Gustafson, AER, Lexington, MA; and D. C. Peduzzi
420	P3.60	DERIVED CLOUD PRODUCTS FROM THE GOES-M IMAGER. Anthony J. Schreiner, CIMSS/Univ. of Wisconsin, Madison, WI; and T. J. Schmit
424	P3.61	UPPER TROPOSPHERIC MOISTURE ASSIMILATION USING GOES OBSERVATIONS. William H. Raymond, CIMSS/Univ. of Wisconsin, Madison, WI; and G. S. Wade
428	P3.62	FUTURE SATELLITE INITIATIVES AT FLEET NUMERICAL METEOROLOGY AND OCEANOGRAPHY CENTER. Charles E. Skupniewicz, FNMOC, Monterey, CA; and J. Cornelius, J. Haferman, J. Vermeulen, and Y. Wang
431	P3.63	AN OPERATIONAL UNIFIED VALIDATION SYSTEM FOR SATELLITE DATA. Larry M. McMillin, NOAA/NESDIS/ORA, Camp Springs, MD; and H. Ding and J. Zhao
		SESSION 4: RADIANCES, CLOUDS, AND RETRIEVALS
*	4.1	ASSIMILATION OF SATELLITE SOUNDING RADIANCES IN NUMERICAL WEATHER PREDICTION. John Eyre, UK Met Office, Bracknell, Berks., UK (*Invited Presentation*)

• *Manuscript not available*

TABLE OF CONTENTS

11TH CONFERENCE ON SATELLITE METEOROLOGY AND OCEANOGRAPHY

PAGE

* 4.2 CLOUD PROPERTY RETRIEVALS USING INFRARED AND FAR-INFRARED MEASUREMENTS. Steven A. Ackerman, CIMSS/Univ. of Wisconsin, Madison, WI (*Invited Presentation*)

433 4.3 ESTIMATING THE PRIMARY ANALYSIS VARIABLES, TEMPERATURE, MOISTURE AND WIND, FROM SPACE—SCIENCE AND COOPERATION. John Le Marshall, BMRC, Melbourne, Vic., Australia (*Invited Presentation*)

POSTER SESSION 4: RADIANCES, CLOUDS, AND RETRIEVALS

P4.1 PAPER WITHDRAWN

438 P4.2 INTERCALIBRATION OF GEOSTATIONARY AND POLAR-ORBITING INFRARED WINDOW AND WATER VAPOR RADIANCES. Mathew M. Gunshor, CIMSS/Univ. of Wisconsin, Madison, WI; and T. J. Schmit and W. P. Menzel

442 P4.3 INTERCALIBRATION OF METEOROLOGICAL SATELLITE IMAGERS USING VIRS, ATSR-2, AND MODIS. Louis Nguyen, NASA/LARC, Hampton, VA; and P. Minnis, J. K. Ayers, and D. R. Doelling

* P4.4 *COMPARISON OF MODIS/TERRA RADIANCES WITH GOES-8, GOES-10, AND ARM CART SITE* OBSERVATIONS. Suzanne Wetzel-Seemann, CIMSS/Univ. of Wisconsin, Madison, WI; and D. Tobin, L. E. Gumley, C. C. Moeller, W. P. Menzel, T. J. Schmit, and M. M. Gunshor

446 P4.5 PHYSICAL DECOUPLING OF NEAR-INFRARED (3.9μM) SOLAR AND THERMAL RADIATION COMPONENTS THROUGH SATELLITE OBSERVATIONS OF TOTAL SOLAR ECLIPSES. Steven D. Miller, NRL, Monterey, CA

450 P4.6 ADVANCES IN THE BIAS CORRECTION OF SATELLITE RADIANCE DATA. William F. Campbell, NRL, Monterey, CA; and N. Baker

* P4.7 THE AIRS FORWARD MODEL AND SPECTRAL RESPONSE FUNCTIONS. Larrabee Strow, Univ. of Maryland Baltimore County, Baltimore, MD; and S. Hannon and H. Motteler

452 P4.8 CLOUD PROPERTIES FROM AMSU IN A SEMI-ARID REGION. Amy M. Doherty, CIMSS/Univ. of Wisconsin, Madison, WI

454 P4.9 EFFECTS OF CLOUD AND PRECIPITATION MICROPHYSICS ON AMSU MEASUREMENTS AS SIMULATED USING CLOUD RESOLVING MODEL OUTPUTS. Xiaofan Li, NOAA/NESDIS/ORA, Camp Springs, MD; and F. Weng

* P4.10 POLARIZATION OF MICROWAVE MEASUREMENTS FOR TEMPERATURE SOUNDING OF THE MESOSPHERE. Alan E. Lipton, AER, Lexington, MA

458 P4.11 COMBINING RADIO OCCULTATIONS AND IR/MW RADIANCES TO DERIVE TEMPERATURE AND MOISTURE PROFILES: A SIMULATION STUDY. Eva Borbas, Univ. of Wisconsin, Madison, WI; and P. Menzel and J. Li

460 P4.12 A SIMPLE DIAGNOSIS METHOD OF MOISTURE PROFILE FROM TMI/TPW. Tetsuo Nakazawa, MRI, Tsukuba, Ibaraki, Japan

462 P4.13 USE OF PASSIVE MICROWAVE OBSERVATIONS IN A RADAR RAINFALL PROFILING ALGORITHM. Mircea Grecu, Univ. of Connecticut, Storrs, CT; and E. N. Anagnostou

464 P4.14 STRUCTURE AND CHARACTERISTICS OF PRECIPITATION SYSTEMS OBSERVED BY TRMM. Steven J. Goodman, NASA/MSFC, Huntsville, AL; and D. J. Cecil

* Manuscript not available

TABLE OF CONTENTS

11TH CONFERENCE ON SATELLITE METEOROLOGY AND OCEANOGRAPHY

PAGE		
468	P4.15	AN IMPROVED LEVEL-3 OCEANIC RAINFALL ALGORITHM FOR THE TRMM MICROWAVE IMAGER (TMI) AND THE ADVANCED MICROWAVE SCANNING RADIOMETER (AMSR). T. T. Wilheit, Texas A&M Univ., College Station, TX; and J. Huang, K.-W. Jin, D. H. Lee, J. L. Thomas-Stahle, and R. Weitz
469	P4.16	WHAT ARE THE BENEFITS OF COMBINING VISIBLE, INFRARED, AND MICROWAVE SATELLITE DATA IN RETRIEVING CLOUD PHYSICAL PROPERTIES? Thomas J. Greenwald, CIRA/Colorado State Univ., Fort Collins, CO; and T. H. Vonder Haar
472	P4.17	DETERMINATION OF LIQUID WATER PATH AND EFFECTIVE RADIUS FOR WATER CLOUDS USING MICROWAVE AND VISIBLE MEASUREMENTS. Guosheng Liu, Florida State Univ., Tallahassee, FL; and H. Shao, M. Tschudi, and J. Haggerty
474	P4.18	THE SENSITIVITY OF COMPUTED MICROWAVE BRIGHTNESS TEMPERATURES FROM PRECIPITATING CLOUDS TO MODELS OF SPHERICAL MIXED-PHASE HYDROMETEORS. Benjamin T. Johnson, Univ. of Wisconsin, Madison, WI; and G. Petty
477	P4.19	A NEAR-REAL TIME METHOD FOR DERIVING CLOUD AND RADIATION PROPERTIES FROM SATELLITES FOR WEATHER AND CLIMATE STUDIES. Patrick Minnis, NASA/LRC, Hampton, VA; and W. L. Smith, Jr., D. F. Young, L. Nguyen, A. D. Rapp, P. W. Heck, S. Sun-Mack, Q. Z. Trepte, and Y. Chen
481	P4.20	VALIDATION OF GOES AND MODIS ATMOSPHERIC PRODUCTS AND RADIANCES USING DEPARTMENT OF ENERGY ATMOSPHERIC RADIATION (DOE ARM) MEASUREMENT DATA. Wayne F. Feltz, CIMSS/Univ. of Wisconsin, Madison, WI; and T. J. Schmit, J. Hawkinson, D. Tobin, and S. Wetzel-Seemann
484	P4.21	VALIDATION OF A GLOBAL CLOUD LIQUID WATER PRODUCT FROM AVHRR. Andrew K. Heidinger, NOAA/NESDIS/ORA, Washington, DC; and Q. Liu
488	P4.22	AEROSOL OPTICAL PROPERTY RETRIEVALS FROM VIS-SWIR DATA. J. W. Snow, MIT Lincoln Laboratory, Lexington, MA; and M. K. Griffin, H. K. Burke, and C. A. Upham
492	P4.23	THE CHESAPEAKE LIGHTHOUSE AND AIRCRAFT MEASUREMENTS FOR SATELLITES (CLAMS) EXPERIMENT. William L. Smith, Jr., NASA/LRC, Hampton, VA; and T. Charlock, B. A. Wielicki, R. Kahn, J. Vanderlei Martins, C. Gatebe, P. V. Hobbs, G. C. Purgold, J. Redemann, L. Remer, and K. Rutledge
	P4.24	PAPER WITHDRAWN
496	P4.25	SIMULTANEOUS RETRIEVAL OF CLOUD HEIGHT AND EFFECTIVE EMISSIVITY FROM HYPERSPECTRAL RADIANCE MEASUREMENTS. Hung-Lung Huang, CIMSS/Univ. of Wisconsin, Madison, WI; and X. Wu, J. Li, P. Antonelli, R. O. Knuteson, E. R. Olson, K. C. Baggett, and B. J. Osborne
500	P4.26	RETRIEVAL OF CIRRUS ICE-WATER PATH, PARTICLE SIZE, AND OPTICAL THICKNESS USING THERMAL INFRARED SATELLITE DATA. Robert P. d'Entremont, AER, Lexington, MA; and D. L. Mitchell
*	P4.27	A BAYESIAN ICE CLOUD PROPERTIES RETRIEVAL ALGORITHM. David A. Santek, CIMSS/Univ. of Wisconsin, Madison, WI; and H. Berger, K. F. Evans, R. Pincus, and S. A. Ackerman
504	P4.28	ESTIMATING THIN CLOUD PROPERTIES USING AN IMPROVED CO2 SLICING APPROACH. Hong Zhang, CIMSS/Univ. of Wisconsin, Madison, WI; and W. P. Menzel
*	P4.29	DEVELOPMENT OF CIRRUS MODELS FOR MODIS AND MISR. Sarah M. Thomas, Univ. of Wisconsin, Madison, WI; and B. A. Baum, S. L. Nasiri, A. Heymsfield, P. Yang, E. E. Clothiaux, R. Marchand, and J. Comstock
	P4.30	PAPER WITHDRAWN

* Manuscript not available

TABLE OF CONTENTS

11TH CONFERENCE ON SATELLITE METEOROLOGY AND OCEANOGRAPHY

PAGE

506 P4.31 STATISTICAL DEPENDENCE OF CLOUD FRACTION AS A FUNCTION OF VIEW ANGLE DERIVED FROM MISR DATA. Guangyu Zhao, Univ. of Illinois, Urbana, IL; and L. Di Girolamo

* P4.32 CLOUD DETECTION AND CLASSIFICATION USING HIGH-SPECTRAL INFRARED OBSERVATIONS. Kyle J. Leesman, CIMSS/Univ. of Wisconsin, Madison, WI; and S. Ackerman, H. Revercomb, and J. Spinhirne

508 P4.33 CONTRAIL COVER AND RADIATIVE PROPERTIES FROM HIGH-RESOLUTION SATELLITE DATA. Rabindra Palikonda, AS&M, Inc., Hampton, VA; and P. Minnis, P. W. Heck, S. Sun-Mack, Q. Z. Trepte, and H. Mannstein

* P4.34 MOPITT CO RETRIEVALS UNDER CLOUDY CONDITIONS. Juying X. Warner, NCAR, Boulder, CO; and J. Gille, D. Edwards, J. Drummond, M. Deeter, D. Grant, G. Francis, D. Ziskin, M. Smith, J. L. Attie, and J. Chen

* P4.35 CLOUD OVERLAPPING DETECTION ALGORITHM USING SOLAR AND IR WAVELENGTHS. Kazuaki Kawamoto, NASA/LRC, Hampton, VA; and P. Minnis and W. L. Smith, Jr.

512 P4.36 SURFACE EMISSIVITY DERIVED FOR INFRARED REMOTE SENSING FROM SATELLITES. Yan Chen, SAIC, Hampton, VA; and S. Sun-Mack, P. Minnis, W. L. Smith, Jr., and D. F. Young

516 P4.37 INTERCOMPARISON OF GOES-8 IMAGER AND SOUNDER SKIN TEMPERATURE RETRIEVALS. Stephanie L. Haines, Univ. of Alabama, Huntsville, AL; and R. J. Suggs and G. J. Jedlovec

520 P4.38 AN AEROSOL-DEPENDENT ALGORITHM FOR REMOTELY SENSED SEA SURFACE TEMPERATURES FROM THE NOAA AVHRR. Nicholas R. Nalli, CIRA/Colorado State Univ., Ft. Collins, CO; and L. L. Stowe

524 P4.39 COMPARISONS OF OBSERVED AND SIMULATED MICROWAVE IMAGES OF EXTRATROPICAL CYCLONES. Jui-Yuan C. Chiu, Purdue Univ., West Lafayette, IN; and G. W. Petty

SESSION 5: NEW TECHNOLOGY AND METHODS

* 5.1 REMOTE SENSING OF CLOUD, AEROSOL, AND WATER VAPOR PROPERTIES FROM MODIS. Michael D. King, NASA/GSFC, Greenbelt, MD (*Invited Presentation*)

* 5.2 NEAR REAL-TIME QUIKSCAT/SEAWINDS WIND VECTOR DATA AT NOAA/NESDIS. Paul S. Chang, NOAA/NESDIS, Camp Springs, MD; and L. Connor and E. Legg (*Invited Presentation*)

* 5.3 TRMM: STATUS OF PRECIPITATION ESTIMATES, SCIENCE HIGHLIGHTS, AND 3-HOUR GLOBAL, TROPICAL PRECIPITATION ESTIMATES. Robert F. Adler, NASA/GSFC, Greenbelt, MD (*Invited Presentation*)

528 5.4 COMBINING NEW SATELLITE TOOLS AND MODELS TO EXAMINE THE ROLE OF MESOSCALE INTERACTIONS IN FORMATION AND INTENSIFICATION OF TROPICAL CYCLONES. Joanne Simpson, NASA/GSFC, Greenbelt, MD; and E. Ritchie, W. T. Liu, C. S. Velden, K. Brueske, H. Pierce, and J. Halverson (*Invited Presentation*)

* 5.5 SATELLITE OCEANOGRAPHY IN THE 21ST CENTURY NAVY. Walt J. McKeown, Naval Atlantic Meteorological and Oceanographic Center, Norfolk, VA (*Invited Presentation*)

* 5.6 VALIDATION TOOLS FOR FUTURE SATELLITE OBSERVATIONS. H. E. Revercomb, Univ. of Wisconsin, Madison, WI; and D. C. Tobin, R. O. Knuteson, W. F. Feltz, W. P. Menzel, and W. L. Smith (*Invited Presentation*)

POSTER SESSION 5: NEW TECHNOLOGY AND METHODS

P5.1 PAPER WITHDRAWN

536 P5.2 NPOESS INSTRUMENTS: THE FUTURE OF METSAT OBSERVATIONS. John D. Cunningham, NOAA/NPOESS, Silver Spring, MD; and J. M. Haas and H. Swenson

* Manuscript not available

TABLE OF CONTENTS

11TH CONFERENCE ON SATELLITE METEOROLOGY AND OCEANOGRAPHY

PAGE		
540	P5.3	RECOMMENDATIONS FROM THE GOES USERS' CONFERENCE. James J. Gurka, NOAA/NESDIS, Suitland, MD; and G. J. Dittberner
544	P5.4	NOAA'S GOES SYSTEM—PLANS FOR NEW SENSORS. Gerald J. Dittberner, NOAA/NESDIS, Suitland, MD
547	P5.5	CHANNEL SELECTION FOR THE NEXT GENERATION GEOSTATIONARY ADVANCED IMAGERS. Timothy J. Schmit, NOAA/NESDIS/ORA, Madison, WI; and W. P. Menzel, M. M. Gunshor, and J. P. Nelson III
551	P5.6	CHANNEL SELECTION METHODS FOR INFRARED ATMOSPHERIC SOUNDING INTERFEROMETER RADIANCES. Nadia Fourrié, Meteo-France, Toulouse, France; and F. Rabier
555	P5.7	OPERATIONAL RADIANCE PRODUCTS FROM AIRS. Mitchell D. Goldberg, NOAA/NESDIS/ORA, Camp Springs, MD; and L. M. McMillin, W. Wolf, L. Zhou, Y. Qu, and M. Divakarla
559	P5.8	MEASUREMENT CONCEPT VALIDATION PLANS FOR GIFTS. David Tobin, CIMSS/Univ. of Wisconsin, Madison, WI; and C. S. Velden, N. Pougatchev, and W. Smith
563	P5.9	SIMULATION OF GIFTS DATA CUBES. David Tobin, CIMSS/Univ. of Wisconsin, Madison, WI; and K. Baggett, R. Garcia, H. Woolf, A. Huang, B. Knuteson, J. Mecikalski, E. Olson, B. Osborne, D. Posselt, and H. Revercomb
*	P5.10	VALIDATION OF THE SUBMILLIMETER CIRRUS REMOTE SENSING TECHNIQUE: IS IT READY FOR SPACE? K. Franklin Evans, Univ. of Colorado, Boulder, CO; and I. G. Nolt, M. D. Vanek, and C. Lee
566	P5.11	APPLICATION AND DESIGN OF SATELLITE INFRARED SPECTRAL IMAGING RADIOMETERS WITH UNCOOLED MICROBOLOMETER ARRAY DETECTORS. James D. Spinhirne, NASA/GSFC, Greenbelt, MD; and R. S. Lancaster and K. R. Maschhoff
570	P5.12	A PROPOSED MULTIANGLE SATELLITE DATASET USING GEO, LEO AND TRIANA. Helen Y. Yi, AS&M, Hampton, VA; and P. Minnis, L. Nguyen, and D. R. Doelling
574	P5.13	CLOUD DETECTION FROM MISR USING A BAND-DIFFERENCED ANGULAR SIGNATURE. Michael Wilson, Univ. of Illinois, Urbana, IL; and L. Di Girolamo
•	P5.14	MODIS CLOUD MASK: AN UPDATE AND VALIDATION. Richard Frey, CIMSS/Univ. of Wisconsin, Madison, WI; and S. A. Ackerman, W. P. Menzel, L. Gumley, C. Moeller, and S. Wetzel Seemann
•	P5.15	GLOBAL DAYTIME AND NIGHTTIME FREQUENCIES OF CLOUD THERMODYNAMIC PHASE AS A FUNCTION OF CLOUD TEMPERATURE USING MODIS DATA. Richard A. Frey, CIMSS/Univ. of Wisconsin, Madison, WI; and B. A. Baum, S. L. Nasiri, W. P. Menzel, S. A. Ackerman, and L. Gumley
579	P5.16	HIGH SPECTRAL RESOLUTION LIDAR VALIDATION OF MODIS DERIVED CLOUD PHASE AND ALTITUDE. R. E. Holz, Univ. of Wisconsin, Madison, WI; and S. Nasiri, R. E. Kuehn, R. Frey, B. Baum, and E. W. Eloranta
581	P5.17	CLOUD TOP ANALYSIS USING CLOUD MODEL SIMULATIONS AND SATELLITE OBSERVATIONS. Stefano Natali, Univ. of Ferrara, Italy; and P. K. Wang and H.-m. Lin
585	P5.18	NIGHTTIME CLOUD OVERLAP USING MODIS DATA. Monica K. Harkey, CIMSS/Univ. of Wisconsin, Madison, WI; and B. A. Baum
*	P5.19	DAYTIME CLOUD OVERLAP USING MODIS DATA. Shaima L. Nasiri, CIMSS/Univ. of Wisconsin, Madison, WI; and B. A. Baum

• Manuscript not available

TABLE OF CONTENTS

11TH CONFERENCE ON SATELLITE METEOROLOGY AND OCEANOGRAPHY

PAGE

588 P5.20 HIGH SPATIAL RESOLUTION SURFACE AND CLOUD TYPE CLASSIFICATION FROM MODIS MULTI-SPECTRAL BAND MEASUREMENTS. Jun Li, CIMSS/Univ. of Wisconsin, Madison, WI; and Z. Yang, H.-L. Huang, W. P. Menzel, R. A. Frey, and S. A. Ackerman

592 P5.21 LAND SURFACE ALBEDO, NADIR BRDF-ADJUSTED REFLECTANCE, AND BRDF PRODUCTS FROM THE MODERATE RESOLUTION IMAGING SPECTRORADIOMETER (MODIS). Crystal B. Schaaf, Boston Univ., Boston, MA; and F. Gao, A. H. Strahler, W. Lucht, X. Li, X. Zhang, Y. Jin, E. Tsvetsinskaya, J.-P. Muller, P. Lewis, M. Barnsley, G. Roberts, C. Doll, S. Liang, D. Roy, and J. L. Privette

596 P5.22 MODIS STATISTICAL STRUCTURE FUNCTION ANALYSIS. Tomoko Koyama, CIRA/Colorado State Univ., Fort Collins, CO; and D. W. Hillger and T. H. Vonder Haar

600 P5.23 SIMULATION OF GOES-M 5-BAND IMAGER USING MODIS DATA FOR VOLCANIC ASH. Donald W. Hillger, NOAA/NESDIS/ORA and CIRA/Colorado State Univ., Fort Collins, CO; and J. Clark

* P5.24 EVALUATION OF MODIS EMISSIVE BAND RADIOMETRIC PERFORMANCE USING MAS DATA COLLECTED DURING TX-2001. Christopher C. Moeller, CIMSS/Univ. of Wisconsin, Madison, WI; and D. D. LaPorte, W. P. Menzel, and H. E. Revercomb

• P5.25 MODIS DIRECT BROADCAST RECEPTION, PRODUCTS, AND APPLICATIONS. Liam E. Gumley, CIMSS/Univ. of Wisconsin, Madison, WI; and A. H. L. Huang, T. D. Rink, J. Li, and Z. Yang

604 P5.26 CORRELATED NOISE MODELING FOR SATELLITE RADIANCE SIMULATION. Thomas J. Kleespies, NOAA/NESDIS, Camp Springs, MD; and D. Crosby

606 P5.27 CERES/ARM VALIDATION EXPERIMENT(CAVE). David A. Rutan, AS&M, Hampton, VA; and F. G. Rose, N. Smith, and T. P. Charlock

610 P5.28 INTERCOMPARISON OF CERES SCANNING AND ERBS WFOV NON-SCANNING RADIOMETERS. David A. Rutan, AS&M, Hampton, VA; and G. L. Smith, R. B. Lee III, and T. Wong

614 P5.29 THE CALIBRATION OF NOAA-AVHRR VISIBLE RADIANCES WITH VIRS. David R. Doelling, AS&M, Hampton, VA; and V. Chakrapani, P. Minnis, and L. Nguyen

618 P5.30 USING POLARIMETRIC TWO-STREAM RADIATIVE TRANSFER MODEL TO STUDY MICROWAVE POLARIMETRIC SIGNATURES. Quanhua Liu, CIRA/Colorado State Univ., Ft. Collins, CO; and F. Weng

620 P5.31 A TEST OF THE PETTY AND KATSAROS (1994) INCIDENCE ANGLE CORRECTION IN A FORWARD MODEL. Clay B. Blankenship, NRL, Monterey, CA

622 P5.32 KCARTA: A FAST PSEUDO LINE-BY-LINE RADIATIVE TRANSFER CODE WITH SCATTERING. Sergio DeSouza-Machado, Univ. of Maryland Baltimore County, Baltimore, MD; and L. L. Strow, H. E. Motteler, and S. E. Hannon

• P5.33 OMPS—THE NEXT GENERATION U.S. OPERATIONAL OZONE MONITOR. Hal J. Bloom, NOAA/NPOESS/IPO, Silver Spring, MD; and F. Sanner

• P5.34 THE CROSS-TRACK INFRARED/MICROWAVE SOUNDER SUITE (CRIMSS): THE NEXT GENERATION OPERATIONAL POLAR ORBITING SOUNDER SYSTEM. Hal J. Bloom, NOAA/NESDIS, Silver Spring, MD; and R. Glumb

625 P5.35 NOAA/NESDIS OPERATIONAL ADVANCED-TOVS (ATOVS) POLAR ORBITER SOUNDING PRODUCTS. Anthony L. Reale, NOAA/NESDIS, Suitland, MD; and A. S. Allegrino

• Manuscript not available

TABLE OF CONTENTS

11TH CONFERENCE ON SATELLITE METEOROLOGY AND OCEANOGRAPHY

PAGE

629 P5.36 DERIVING ATMOSPHERIC TEMPERATURE AND HUMIDITY PROFILES FROM AMSU-A AND AMSU-B MEASUREMENTS USING NEURAL NETWORK TECHNIQUES. Lei Shi, SeaSpace Corp., Poway, CA

633 P5.37 AN OPTIMAL-ESTIMATION ALGORITHM FOR WATER VAPOR PROFILING USING AMSU. Darren S. McKague, CIRA/Colorado State Univ., Fort Collins, CO; and R. J. Engelen, J. M. Forsythe, S. Q. Kidder, and T. H. Vonder Haar

637 P5.38 RETRIEVAL OF ATMOSPHERIC INVERSIONS USING GEOSTATIONARY HIGH-SPECTRAL-RESOLUTION SOUNDER RADIANCE INFORMATION. Jun Li, CIMSS/Univ. of Wisconsin, Madison, WI; and T. J. Schmit, H.-L. Huang, and H. M. Woolf

640 P5.39 SSMIS UPPER ATMOSPHERE SOUNDING CALIBRATION AND VALIDATION PLANS. Steven D. Swadley, NRL, Monterey, CA

644 P5.40 AIR FORCE WEATHER AGENCY SPECIAL SENSOR MICROWAVE IMAGER/SOUNDER PROCESSING. David M. Paal, Air Force Weather Agency, Offutt AFB, NE; and T. J. Kopp

646 P5.41 IMAGERY INTERPRETATION OF MICROWAVE OBSERVATIONS FROM AMSU AND TMI OVER A COMPLEX TROPICAL REGION. Benjamin Ruston, Colorado State Univ., Ft. Collins, CO; and T. H. Vonder Haar and J. M. Forsythe

650 P5.42 EURAINSAT: EUROPEAN SATELLITE RAINFALL ANALYSIS AND MONITORING AT THE GEOSTATIONARY SCALE. Vincenzo Levizzani, Institute of Atmospheric and Oceanic Sciences, Bologna, Italy; and P. Bauer, A. Buzzi, D. H. Hinsman, A. Khain, C. Kidd, F. S. Marzano, F. Meneguzzo, A. Mugnai, J. P. V. Poiares-Baptista, F. Prodi, J. F. W. Purdom, D. Rosenfeld, J. Schmetz, E. A. Smith, F. Tampieri, F. J. Turk, and G. A. Vicente

654 P5.43 MICROWAVE SURFACE AND PRECIPITATION PRODUCTS SYSTEM (MSPPS)—AN APPLICATION OF AMSU DATA TO THE RETRIEVAL OF SURFACE GEOPHYSICAL PRODUCTS. Huan Meng, QSS Group, Inc., Lanham, MD; and D. A. Moore, L. Zhao, R. R. Ferraro, F. Weng, and N. Grody

• P5.44 SATELLITE MICROWAVE SENSORS: NEW TOOLS FOR MONITORING THE KINEMATICAL, THERMODYNAMICAL, AND CLOUD MICROPHYSICAL PROCESSES IN TROPICAL CYCLONES. Fuzhong Weng, NOAA/NWS/NESDIS/ORA, Camp Springs, MD

655 P5.45 MOTIVATING THE USE OF REMOTELY-SENSED DATA SOURCES FOR ESTIMATING CONVECTIVE MOMENTUM TRANSPORTS. John R. Mecikalski, CIMSS/Univ. of Wisconsin, Madison, WI

* P5.46 RAINFALL RETRIEVAL FROM LIGHTNING AND SATELLITE INFRARED OBSERVATIONS ADJUSTED WITH TRMM PRECIPITATION RADAR. Carlos Augusto Morales, Colorado State Univ., Fort Collins, CO; and E. Anagnostou and J. Weinman

* P5.47 TRACKING CONTINUOUS RAIN SYSTEMS USING A GENETIC BASED WAVELET IMAGE REGISTRATION TECHNIQUE. Jearanai Vongsaard, George Mason Univ., Fairfax, VA; and L. S. Chiu, T. El-Ghazawi, J. Weinman, and R. Yang

659 P5.48 COMPARISON OF INSTANTANEOUS TMI AND PR RAINFALL DATA FROM THE TRMM SATELLITE. John E. Stout, George Mason Univ., Fairfax, VA; and R. Meneghini

• P5.49 A NEW FINE-SCALE, QUASI-GLOBAL COMBINED PRECIPITATION ESTIMATE BASED ON TRMM. George J. Huffman, NASA/GSFC and SSAI, Greenbelt, MD; and R. F. Adler, D. T. Bolvin, and E. J. Nelkin

* Manuscript not available

TABLE OF CONTENTS

11TH CONFERENCE ON SATELLITE METEOROLOGY AND OCEANOGRAPHY

PAGE

662 P5.50 EVOLUTION OF THE NOAA/NESDIS SSM/I LAND RAINFALL ALGORITHM INTO THE TRMM AND AMSR ERA. Jeffrey R. McCollum, NOAA/NESDIS/ORA, Camp Springs, MD; and Univ.of Maryland, College Park, MD; and R. R. Ferraro

• P5.51 ADVANCES IN GLOBAL WATER CYCLE SCIENCE MADE POSSIBLE BY GLOBAL PRECIPITATION MISSION (GPM). Eric A. Smith, NASA/GSFC, Greenbelt, MD

666 P5.52 CO AND CH4 COLUMN RETRIEVAL FROM THE SCANNING HIGH RESOLUTION INTERFEROMETER SOUNDER (S-HIS). Kenneth Vinson, Univ. of Wisconsin, Madison, WI; and H. Revercomb, H. B. Howell, and R. Knuteson

670 P5.53 THE ROLE OF A PRIORI INFORMATION IN THE RETRIEVAL OF CO PROFILES FROM TERRA-MOPITT MEASUREMENTS. Shu-peng Ho, NCAR, Boulder, CO.; and J. C. Gille, D. P. Edwards, J.-L. Attie, M. N. Deeter, J. Warner, G. L. Francis, and D. Ziskin

* P5.54 MODIS/TERRA TOTAL PRECIPITABLE WATER AND OZONE PRODUCT COMPARISON WITH GOES, TOMS, AND ARM CART SITE OBSERVATIONS. Suzanne Wetzel-Seemann, CIMSS/Univ. of Wisconsin, Madison, WI; and J. Li, L. E. Gumley, T. J. Schmit, and W. P. Menzel

674 P5.55 APPLICATION OF MODIS DATA FOR DERIVING OCEAN SURFACE CURRENTS. R. L. Bernstein, SeaSpace Corp., Poway, CA; and K. S. Prasad

677 P5.56 STATISTICAL CHARACTERISTICS OF QUIKSCAT "REAL-TIME" OCEAN SURFACE WIND VECTOR RETRIEVALS. William H. Gemmill, NOAA/NWS/NCEP, Camp Springs, MD

• P5.57 NEAR-REALTIME WINDS AND SURFACE PRESSURES FROM SEAWINDS. David F. Zierden, Florida State Univ., Tallahassee, FL; and M. A. Bourassa, J. S. Tongue, J. J. O'Brien, and D. E. Weissman

681 P5.58 ATMOSPHERIC MOTION VECTORS WITH METEOSAT SECOND GENERATION. Kenneth Holmlund, EUMETSAT, Darmstadt, Germany

685 P5.59 FURTHER STUDY OF DERIVING SEA SURFACE TEMPERATURE FROM FUTURE GOES. Xiangqian Wu, CIMSS/Univ. of Wisconsin, Madison, WI; and A. Brisson, P. Le Borgne, A. Marsouin, and W. P. Menzel

688 P5.60 INFRARED LAND SURFACE EMISSIVITY RETRIEVAL FROM HIGH-SPECTRAL RESOLUTION UPWELLING RADIANCE. Robert Knuteson, Univ. of Wisconsin, Madison, WI; and B. Osborne, H. Revercomb, D. Tobin, and W. L. Smith

692 P5.61 QUALITY CONTROL AND PRELIMINARY DATA ANALYSIS OF THE INTERFEROMETRIC MONITOR FOR GREENHOUSE GASES (IMG) DATA SET. Robin L. Tanamachi, Univ. of Wisconsin, Madison, WI; and V. P. Walden, S. A. Ackerman, and R. O. Knuteson

* P5.62 VIIRS (VISIBLE INFRARED IMAGER RADIOMETER SUITE): A NEXT-GENERATION OPERATIONAL ENVIRONMENTAL SENSOR FOR NPOESS. Carol Welsch, U.S. Air Force and NPOESS/Integrated Program Office, Silver Spring, MD; and H. Swenson and J. M. Haas

696 P5.63 CALIBRATION AND INITIAL RESULTS FROM THE OSSE FOR NPOESS. Michiko Masutani, NOAA/NWS/NCEP, Camp Springs, MD; and J. C. Woollen, J. Terry, S. J. Lord, T. J. Kleespies, G. D. Emmitt, S. A. Wood, S. Greco, J. C. Derber, R. Atlas, and M. Goldberg

• Manuscript not available

TABLE OF CONTENTS

11TH CONFERENCE ON SATELLITE METEOROLOGY AND OCEANOGRAPHY

PAGE

* P5.64 ESTIMATION OF MESOSCALE ATMOSPHERIC LATENT HEATING PROFILES FROM TRMM RAIN STATISTICS UTILIZING A SIMPLE ONE-DIMENSIONAL MODEL. Robert Iacovazzi, Jr., SSAI, Lanham, MD; and C. Prabhakara

* P5.65 TRMM PRECIPITATION RADAR AND MICROWAVE IMAGER OBSERVATIONS. C. Prabhakara, NASA/GSFC, Greenbelt, MD; and R. Iacovazzi, Jr., J.-M. Yoo, and J. Weinman

SESSION 6: FUTURE ACTIVITIES

* 6.1 NPOESS: IMPROVING THE NATION'S SPACE-BASED, REMOTE SENSING CAPABILITIES. Gregory Withee, NOAA/NESDIS, Silver Spring, MD (*Invited Presentation*)

700 6.2 THE GEOSYNCHRONOUS IMAGING FOURIER TRANSFORM SPECTROMETER (GIFTS). W. L. Smith, Sr., NASA/LRC, Hampton, VA; F. Harrison, D. Hinton, J. Miller, M. Bythe, D. Zhou, H. Revercomb, F. Best, H. Huang, R. Knuteson, D. Tobin, C. S. Velden, G. Bingham, R. Huppi, A. Thurgood, L. Zollinger, R. Epslin, and R. Petersen (*Invited Presentation*)

708 6.3 METEOSAT SECOND GENERATION (MSG): CAPABILITIES AND APPLICATIONS. Johannes Schmetz, EUMETSAT, Darmstadt, Germany; and P. Pili, A. Ratier, S. Rota and S. Tjemkes (*Invited Presentation*)

714 6.4 WMO SATELLITE ACTIVITIES AND PERSPECTIVES. Donald E. Hinsman, WMO, Geneva, Switzerland (*Invited Presentation*)

* Manuscript not available

Blank page retained for pagination

AUTHOR INDEX

11TH CONFERENCE ON SATELLITE METEOROLOGY AND OCEANOGRAPHY

	PAPER #	PAGE
A		
Ackerman, S. A.	P2.33	*
Ackerman, S. A.	P3.37	348
Ackerman, S. A.	4.2	*
Ackerman, S. A.	P4.27	*
Ackerman, S. A.	P4.32	*
Ackerman, S. A.	P5.14	*
Ackerman, S. A.	P5.15	*
Ackerman, S. A.	P5.20	588
Ackerman, S. A.	P5.61	692
Adler, R. F.	P2.30	206
Adler, R. F.	P2.31	*
Adler, R. F.	5.3	*
Adler, R. F.	P5.49	*
Adler, R. M.	P2.13	153
Alfaro, R.	P3.46	379
Allegrino, A. S.	P5.35	625
Anagnostou, E. N.	P4.13	462
Anagnostou, E. N.	P5.46	*
Anderson, J. G.	P2.1	118
Anderson, J. G.	P2.21	180
Anderson, M. C.	P1.10	39
Antonelli, P.	P4.25	496
Arkett, M.	P1.5	27
Arkin, P. A.	2.3	114
Astling, E. G.	P1.30	*
Atlas, R.	3.1	216
Atlas, R.	P5.63	696
Attie, J.-L.	P4.34	*
Attie, J.-L.	P5.53	670
Aune, R. M.	P3.10	266
Aune, R. M.	P3.35	343
Ayers, J. K.	P2.20	176
Ayers, J. K.	P4.3	442
B		
Baars, J. A.	P1.28	96
Bachmeier, S.	P3.31	328
Bachmeier, S.	P3.32	332
Bachmeier, S.	P3.54	402
Bachmeier, S.	P3.55	404
Baggett, K. C.	P4.25	496
Baggett, K. C.	P5.9	563
Baker, N.	P3.15	279
Baker, N.	P4.6	450
Bantges, R. J.	2.2	110
Barker, E. H.	P3.15	279
Barnsley, M.	P5.21	592
B (Continued)		
Bates, J. J.	P2.9	138
Bates, J. J.	P2.25	192
Bauer, P.	P5.42	650
Baum, B. A.	P4.29	*
Baum, B. A.	P5.15	*
Baum, B. A.	P5.16	579
Baum, B. A.	P5.18	585
Baum, B. A.	P5.19	*
Baumgardt, D.	P3.32	332
Bayler, E. J.	P1.19	73
Bayler, G. M.	P3.38	351
Bedrick, M.	P2.3	126
Bedrick, M.	P2.12	149
Berg, W.	P2.29	202
Berger, H. I.	P3.7	260
Berger, H. I.	P4.27	*
Bernstein, R. L.	P1.18	69
Bernstein, R. L.	P5.55	674
Bess, T. D.	P2.7	*
Bessho, K.	P3.52	395
Bessho, K.	P3.26	728
Best, F.	6.2	700
Bikos, D.	P3.31	328
Bikos, D.	P3.32	332
Bikos, D.	P3.53	397
Bingham, G.	6.2	700
Birkenheuer, D. L.	P3.13	273
Blankenship, C. B.	P5.31	620
Bloom, H. J.	P5.33	*
Bloom, H. J.	P5.34	*
Bolvin, D. T.	P2.31	*
Bolvin, D. T.	P5.49	*
Borbas, E.	P4.11	458
Bourassa, M. A.	P1.7	*
Bourassa, M. A.	P5.57	*
Bras, R. L.	P2.13	153
Bresky, W.	P3.2	244
Bresky, W.	P3.3	248
Brindley, H. E.	2.2	110
Brisson, A.	P5.59	685
Bruegge, C.	P1.25	87
Brueske, K. F.	3.3	228
Brueske, K. F.	5.4	528
Brunner, J.	P3.4	252
Bua, W.	P3.32	332
Burke, H. K.	P1.12	47
Burke, H. K.	P4.22	488

* Manuscript not available

	PAPER #	PAGE
B (Continued)		
Bush, K. A.	P2.7	*
Buzzi, A.	P5.42	650
Bythe, M.	6.2	700
C		
Callahan, J. A.	P2.27	196
Campbell, G. G.	P2.5	132
Campbell, G. G.	P3.5	*
Campbell, W. F.	P4.6	450
Caracena, F.	P3.56	408
Castro Leon, V.	P2.14	157
Cecil, D. J.	P4.14	464
Chagnon, F. J.	P2.13	153
Chakrapani, V.	P5.29	614
Chang, P. S.	5.2	*
Chao, Y.	P1.20	75
Charlock, T. P.	P4.23	492
Charlock, T. P.	P5.27	606
Chen, J.	P4.34	*
Chen, Y.	P4.19	477
Chen, Y.	P4.36	512
Cheng, Z.	P2.32	210
Chiu, J.-Y. C.	P4.39	524
Chiu, L. S.	P5.47	*
Clark, J.	P1.14	55
Clark, J.	P3.15	279
Clark, J.	P5.23	600
Clothiaux, E. E.	P4.29	*
Collimore, C. C.	P2.7	*
Collimore, C. C.	P2.19	*
Colton, M. C.	1.1	*
Combs, C. L.	P2.16	165
Comstock, J.	P4.29	*
Conlee, D. T.	3.5	234
Connell, B. H.	P2.14	157
Conner, M. D.	P3.48	385
Connor, L.	5.2	*
Cornelius, J.	P3.62	428
Crosby, D. S.	P2.32	210
Crosby, D. S.	P5.26	604
Crout, R. L.	3.5	234
Csiszar, I.	P1.26	91
Csiszar, I.	P2.34	212
Cunningham, J. D.	P5.2	536
Curtis, S.	P2.31	*
D		
d'Entremont, R. P.	P2.10	141
d'Entremont, R. P.	P4.26	500
Dahoui, M.	P3.42	367
Daley, R.	P3.15	279
Daniels, J. M.	P3.2	244
Daniels, J. M.	P3.3	248
Daniels, J. M.	P3.34	339
Daniels, J. M.	P3.53	397
De Abreu, R. A.	P1.5	27
de Charon, A.	P1.20	75
Decker, S. G.	P3.27	*
Deeter, M. N.	P4.34	*
Deeter, M. N.	P5.53	670
DeLiberty, T. L.	P2.27	196
DeMaria, M.	P2.16	165
DeMaria, M.	P3.21	300
Dembek, S. R.	P3.12	*
Demuth, J. L.	P3.21	300
Dengel, G. A.	P3.1	241
Derber, J.	P3.8	726
Derber, J. C.	P5.63	696
DeSouza-Machado, S.	P5.32	622
Devenyi, D.	P3.14	277
Di Girolamo, L.	P4.31	506
Di Girolamo, L.	P5.13	574
Diak, G. R.	P1.10	39
Diner, D.	P1.25	87
Ding, H.	P3.63	431
Dittberner, G. J.	P5.3	540
Dittberner, G. J.	P5.4	544
Divakarla, M.	P5.7	555
Dodge, J.	3.1	216
Doelling, D. R.	P4.3	442
Doelling, D. R.	P5.12	570
Doelling, D. R.	P5.29	614
Doherty, A. M.	P4.8	452
Doll, C.	P5.21	592
Drummond, J.	P4.34	*
Dunion, J. P.	P3.25	314
Dybbroe, A.	P2.11	145
Dykema, J. A.	P2.21	180
E		
Edelstein, W.	P1.20	75
Edson, R. T.	P3.22	304
Edwards, D. P.	P4.34	*
Edwards, D. P.	P5.53	670

* Manuscript not available

	PAPER #	PAGE
E (Continued)		
Einaudi, F.	3.1	216
Eis, K.	P3.5	*
El-Ghazawi, T.	P5.47	*
Ellrod, G. P.	P1.15	61
Eloranta, E. W.	P5.16	579
Emmitt, G. D.	P5.63	696
Engelen, R. J.	P2.5	132
Engelen, R. J.	P5.37	633
Epslin, R.	6.2	700
Evans, K. F.	P4.27	*
Evans, K. F.	P5.10	*
Eyre, J.	4.1	*
F		
Feltz, J. M.	1.2	1
Feltz, J. M.	P1.13	51
Feltz, W. F.	P3.37	348
Feltz, W. F.	P3.39	355
Feltz, W. F.	P4.20	481
Feltz, W. F.	5.6	*
Ferrare, R. R.	P2.26	*
Ferraro, R. R.	P3.43	*
Ferraro, R. R.	P3.44	371
Ferraro, R. R.	P5.43	654
Ferraro, R. R.	P5.50	662
Fischer, K. W.	P1.28	96
Flood, S.	P3.32	332
Forsythe, J. M.	P2.5	132
Forsythe, J. M.	P5.37	633
Forsythe, J. M.	P5.41	646
Fourrié, N.	P5.6	551
Francis, G. L.	P4.34	*
Francis, G. L.	P5.53	670
Frey, R.	P2.33	*
Frey, R.	P5.14	*
Frey, R.	P5.15	*
Frey, R.	P5.16	579
Frey, R.	P5.20	588
G		
Gallo, K.	P1.26	91
Gao, F.	P1.25	87
Gao, F.	P5.21	592
Garand, L.	P3.50	387
Garcia, R.	P5.9	563
Gatebe, C.	P4.23	492
G (Continued)		
Gelaro, R.	3.1	216
Gemmill, W. H.	P5.56	677
Gille, J. C.	P4.34	*
Gille, J. C.	P5.53	670
Glumb, R.	P5.34	*
Goerss, J. S.	P3.15	279
Goldberg, M. D.	P2.32	210
Goldberg, M. D.	P5.7	555
Goldberg, M. D.	P5.63	696
Goldsmith, S. J.	P2.26	*
Goodman, S. J.	P4.14	464
Goody, R. M.	P2.1	118
Goody, R. M.	P2.21	180
Grant, B.	P3.31	328
Grant, B.	P3.32	332
Grant, D.	P4.34	*
Gray, G. E.	P3.34	339
Greco, S.	P5.63	696
Grecu, M.	P4.13	462
Greenwald, T. J.	P4.16	469
Griffin, M. K.	P1.12	47
Griffin, M. K.	P4.22	488
Grody, N. C.	P1.3	23
Grody, N. C.	P5.43	654
Gruber, A.	P3.47	383
Grumm, R.	P3.32	332
Gumley, L. E.	P4.4	*
Gumley, L. E.	P5.14	*
Gumley, L. E.	P5.15	*
Gumley, L. E.	P5.25	*
Gumley, L. E.	P5.54	*
Gunshor, M. M.	P1.16	65
Gunshor, M. M.	P4.2	438
Gunshor, M. M.	P4.4	*
Gunshor, M. M.	P5.5	547
Gurka, J. J.	P5.3	540
Gustafson, G. B.	P3.59	*
Gutman, G.	P2.34	212
Gérard, E.	P3.42	367
H		
Haas, J. M.	P5.2	536
Haas, J. M.	P5.62	*
Haferman, J.	P3.62	428
Hagan-Deschamps, S.	P3.49	720
Haggerty, J.	P4.17	472
Haines, S. L.	P4.37	516

* Manuscript not available

	PAPER #	PAGE
H *(Continued)*		
Halverson, J.	5.4	528
Hane, C.	P3.4	252
Hannon, S. E.	P4.7	*
Hannon, S. E.	P5.32	622
Harkey, M. K.	P5.18	585
Harries, J. E.	2.2	110
Harrison, F.	6.2	700
Hartmann, D. L.	P2.17	168
Hawkins, J. D.	P3.22	304
Hawkins, J. D.	P3.23	308
Hawkinson, J. A.	P3.37	348
Hawkinson, J. A.	P4.20	481
Haynes, J.	P3.4	252
Heck, P. W.	P4.19	477
Heck, P. W.	P4.33	508
Heidinger, A. K.	P4.21	484
Heymsfield, A.	P4.29	*
Hildebrand, P. H.	P1.20	75
Hillger, D. W.	P1.14	55
Hillger, D. W.	P5.22	596
Hillger, D. W.	P5.23	600
Hinsman, D. E.	6.4	714
Hinsman, D. H.	P5.42	650
Hinton, D.	6.2	700
Hitchman, M. H.	P2.19	*
Ho, S.-P.	P5.53	670
Hobbs, P. V.	P4.23	492
Holliday, C. R.	P3.48	385
Holmlund, K.	P5.58	681
Holz, R. E.	P5.16	579
Hoss, J.	P1.10	39
Howell, H. B.	P5.52	666
Hsu, S. M.	P1.12	47
Huang, H.-L.	P3.39	355
Huang, H.-L.	P4.25	496
Huang, H.-L.	P5.9	563
Huang, H.-L.	P5.20	588
Huang, H.-L.	P5.25	*
Huang, H.-L.	P5.38	637
Huang, H.-L.	6.2	700
Huang, J.	P4.15	468
Huffines, G. R.	P3.11	270
Huffman, G. J.	P2.31	*
Huffman, G. J.	P5.49	*
Huh, O. K.	P1.16	65
Huppi, R.	6.2	700

	PAPER #	PAGE
I		
Iacovazzi, Jr., R.	P5.64	*
Iacovazzi, Jr., R.	P5.65	*
Inoue, T.	P3.52	395
J		
Jackson, D. L.	P2.9	138
Janowiak, J.	2.3	114
Jascourt, S.	P3.32	332
Jedlovec, G. J.	P2.4	128
Jedlovec, G. J.	P3.12	*
Jedlovec, G. J.	P3.57	412412
Jedlovec, G. J.	P4.37	516
Jin, K.-W.	P4.15	468
Jin, Y.	P1.25	87
Jin, Y.	P5.21	592
Johnson, B. T.	P4.18	474
Jung, J. A.	P3.9	262
Jung, J. A.	P3.10	266
K		
Kahn, R.	P4.23	492
Kankiewicz, A.	P2.5	132
Karlsson, K.-G.	P2.11	145
Kawamoto, K.	P4.35	*
Keller, L. M.	P3.28	318
Kelly, G. A.	3.4	*
Kent, J.	P3.23	308
Kerkmann, J.	P3.33	336
Key, J. R.	P2.8	*
Key, J. R.	P2.18	172
Key, J. R.	P2.33	*
Key, J. R.	P3.29	320
Khain, A.	P5.42	650
Kidd, C.	P5.42	650
Kidder, S. Q.	P3.45	375
Kidder, S. Q.	P5.37	633
Kim, D.	P3.14	277
Kim, H. M.	P3.6	256
King, M. D.	5.1	*
Kirk-Davidoff, D. B.	P2.1	118
Kleespies, T. J.	P5.26	604
Kleespies, T. J.	P5.63	696
Kleist, D. T.	P3.6	256
Knaff, J. A.	P3.21	300
Knaff, J. A.	P3.45	375
Knaff, J. A.	P3.53	397

* Manuscript not available

	PAPER #	PAGE
K (Continued)		
Knapp, K. R.	P2.22	184
Knuteson, R.	P4.25	496
Knuteson, R.	5.6	*
Knuteson, R.	P5.9	563
Knuteson, R.	P5.52	666
Knuteson, R.	P5.60	688
Knuteson, R.	P5.61	692
Knuteson, R.	6.2	700
Koblinsky, C. J.	P1.20	75
Koch, S. E.	P3.56	408
Koenig, M.	P3.33	336
Kongoli, C. E.	P1.3	23
Kopp, T. J.	P5.40	644
Kossin, J. P.	P3.19	292
Koyama, T.	P5.22	596
Kuehn, R. E.	P5.16	579
Kuligowski, R. J.	P3.45	375
Kuligowski, R. J.	P3.47	383
Kummerow, C.	P2.29	202
Kusselson, S. J.	P3.45	375
L		
La Casse, K.	P3.6	256
LaDue, J.	P3.31	328
LaDue, J.	P3.32	332
Lagerloef, G.	P1.20	75
Lancaster, R. S.	P5.11	566
Lapenta, W. M.	P3.12	*
LaPorte, D. D.	P5.24	*
Laws, K.	P3.57	412
Lazzara, M. A.	P3.27	*
Lazzara, M. A.	P3.28	318
Le Borgne, P.	P5.59	685
Le Marshall, J.	4.3	433
Le Vine, D.	P1.20	75
Lee, C.	P5.10	*
Lee, D. H.	P4.15	468
Lee III, R. B.	P5.28	610
Lee, T. F.	P1.11	43
Lee, T. F.	P3.22	304
Lee, T. F.	P3.23	308
Leesman, K. J.	P4.32	*
Legg, E.	5.2	*
Lesht, B.	P2.26	*
Levizzani, V.	P5.42	650
Lewis, P.	P5.21	592
Li, J.	P3.36	346
L (Continued)		
Li, J.	P3.38	351
Li, J.	P4.11	458
Li, J.	P4.25	496
Li, J.	P5.20	588
Li, J.	P5.25	*
Li, J.	P5.38	637
Li, J.	P5.54	*
Li, X.	P4.9	454
Li, X.	P5.21	592
Liang, S.	P5.21	592
Lin, H.-M.	P3.54	402
Lin, H.-M.	P5.17	581
Lipton, A. E.	P4.10	*
Liu, G.	P4.17	472
Liu, Q.	P4.21	484
Liu, Q.	P5.30	618
Liu, W. T.	5.4	528
Liu, Z.	P1.19	73
Loeb, N. G.	P2.2	122
Long, J.	P1.29	99
Lord, S.	3.1	216
Lord, S.	P3.8	726
Lord, S. J.	P5.63	696
Lucht, W.	P5.21	592
M		
Manalo-Smith, N.	P2.2	122
Mannstein, H.	P4.33	508
Marchand, R.	P4.29	*
Marroquin, A.	P3.56	408
Marsham, J. H.	P1.4	*
Marsouin, A.	P5.59	685
Martin, D. W.	P2.7	*
Martin, D. W.	P2.19	*
Martonchik, J.	P1.25	87
Marzano, F. S.	P5.42	650
Maschhoff, K. R.	P5.11	566
Masutani, M.	P5.63	696
McCollum, J. R.	P5.50	662
McCrone, P. J.	P1.27	93
McCrone, P. J.	P3.17	286
McDonald, D. G.	P3.16	282
McKague, D. S.	P5.37	633
McKeown, W. J.	5.5	*
McLay, J. G.	P3.6	256
McLay, J. G.	P3.27	*
McMillin, L. M.	P3.63	431

* Manuscript not available

	PAPER #	PAGE
M (Continued)		
McMillin, L. M.	P5.7	555
McNider, R. T.	P3.12	*
Mecikalski, J.	P5.9	563
Mecikalski, J. R.	P1.10	39
Mecikalski, J. R.	P3.6	256
Mecikalski, J. R.	P3.24	312
Mecikalski, J. R.	P5.45	655
Meneghini, R.	P5.48	659
Meneguzzo, F.	P5.42	650
Meng, H.	P5.43	654
Menzel, P.	P4.11	458
Menzel, W. P.	P1.6	*
Menzel, W. P.	P1.16	65
Menzel, W. P.	P3.9	262
Menzel, W. P.	P3.29	320
Menzel, W. P.	P3.40	359
Menzel, W. P.	P4.2	438
Menzel, W. P.	P4.4	*
Menzel, W. P.	P4.28	504
Menzel, W. P.	P5.5	547
Menzel, W. P.	5.6	*
Menzel, W. P.	P5.14	*
Menzel, W. P.	P5.15	*
Menzel, W. P.	P5.20	588
Menzel, W. P.	P5.24	*
Menzel, W. P.	P5.54	*
Menzel, W. P.	P5.59	685
Merchant, C. J.	P1.4	*
Miller, J.	6.2	700
Miller, S. D.	P1.11	43
Miller, S. D.	P4.5	446
Mills, B. J.	P1.8	31
Mills, B. J.	P1.27	93
Minnis, P.	P2.20	176
Minnis, P.	P4.3	442
Minnis, P.	P4.19	477
Minnis, P.	P4.33	508
Minnis, P.	P4.35	*
Minnis, P.	P4.36	512
Minnis, P.	P5.12	570
Minnis, P.	P5.29	614
Mitchell, D. L.	P4.26	500
Mitchell, K.	P1.26	91
Mo, T.	P2.32	210
Moeller, C. C.	P1.16	65
Moeller, C. C.	P4.4	*
Moeller, C. C.	P5.14	*

	PAPER #	PAGE
M (Continued)		
Moeller, C. C.	P5.24	*
Moody, J. L.	P3.56	408
Moore, D. A.	P5.43	654
Morales, C. A.	P5.46	*
Morey, S. L.	P1.7	*
Morgan, M. C.	P3.6	256
Morrison, B.	P2.3	126
Morrison, B.	P2.12	149
Mosher, F. R.	P3.58	416
Mostek, A.	P3.30	324
Mostek, A.	P3.31	328
Motta, B.	P3.31	328
Motta, B.	P3.32	332
Motteler, H. E.	P4.7	*
Motteler, H. E.	P5.32	622
Mugnai, A.	P5.42	650
Muller, J.-P.	P5.21	592
N		
Nakazawa, T.	P4.12	460
Nakazawa, T.	P3.26	728
Nalli, N. R.	P4.38	520
Nasiri, S. L.	P4.29	*
Nasiri, S. L.	P5.15	*
Nasiri, S. L.	P5.19	*
Nasiri, S. L.	P5.16	579
Natali, S.	P3.54	402
Natali, S.	P5.17	581
Negri, A. J.	P2.13	153
Negri, A. J.	P2.30	206
Nelkin, E. J.	P2.31	*
Nelkin, E. J.	P5.49	*
Nelson III, J. P.	P3.9	262
Nelson III, J. P.	P3.40	359
Nelson III, J. P.	P3.55	404
Nelson III, J. P.	P5.5	547
Nguyen, L.	P2.20	176
Nguyen, L.	P4.3	442
Nguyen, L.	P4.19	477
Nguyen, L.	P5.12	570
Nguyen, L.	P5.29	614
Nolt, I. G.	P5.10	*
Norman, J. M.	P1.10	39
Nunez, M.	P1.28	96

* Manuscript not available

	PAPER #	PAGE
O		
O'Brien, J. J.	P1.7	*
O'Brien, J. J.	P5.57	*
Olander, T. L.	P3.1	241
Olander, T. L.	P3.18	290
Olson, E. R.	P4.25	496
Olson, E. R.	P5.9	563
Osborne, B. J.	P4.25	496
Osborne, B. J.	P5.9	563
Osborne, B. J.	P5.60	688
Owen, T.	P1.26	91
P		
Paal, D. M.	P5.40	644
Palikonda, R.	P4.33	508
Park, S.-C.	P2.24	722
Patel, S. R.	P1.22	79
Patel, S. R.	P1.23	81
Pavolonis, M. J.	P2.8	*
Pavolonis, M. J.	P2.18	172
Peduzzi, D. C.	P3.59	*
Pellegrino, P.	P3.43	*
Pellerino, F.	P1.20	75
Petersen, R. A.	P3.35	343
Petersen, R. A.	P3.39	355
Petersen, R. A.	6.2	700
Petty, G.	P4.18	474
Petty, G. W.	P4.39	524
Pierce, H.	P1.31	103
Pierce, H.	5.4	528
Pili, P.	6.3	708
Pincus, R.	P4.27	*
Poiares-Baptista, J. P. V.	P5.42	650
Posselt, D. J.	P3.6	256
Posselt, D. J.	P5.9	563
Pougatchev, N.	P5.8	559
Prabhakara, C.	P5.64	*
Prabhakara, C.	P5.65	*
Prasad, K. S.	P1.18	69
Prasad, K. S.	P5.55	674
Prins, E. M.	1.2	1
Prins, E. M.	P1.13	51
Privette, J. L.	P5.21	592
Prodi, F.	P5.42	650
Purdom, J. F. W.	3.1	216
Purdom, J. F. W.	P3.30	324
Purdom, J. F. W.	P5.42	650
Purgold, G. C.	P4.23	492
Q		
Qiu, S.	P3.47	383
Qu, Y.	P5.7	555
R		
Rabier, F.	P3.42	367
Rabier, F.	P5.6	551
Rabin, R. M.	P3.4	252
Rabin, R. M.	P3.54	402
Rahmat-Samii, Y.	P1.20	75
Ramaprasad, J.	P1.28	96
Ramsay, B.	P1.5	27
Randriamampianina, R.	P3.42	367
Rapp, A. D.	P4.19	477
Ratier, A.	6.3	708
Raymond, W. H.	P3.61	424
Reale, A. L.	P5.35	625
Redemann, J.	P4.23	492
Reed, B.	P1.26	91
Remer, L.	P4.23	492
Revercomb, H.	P4.32	*
Revercomb, H.	5.6	*
Revercomb, H.	P5.9	563
Revercomb, H.	P5.24	*
Revercomb, H.	P5.52	666
Revercomb, H.	P5.60	688
Revercomb, H.	6.2	700
Richardson, K. L.	P3.23	308
Rink, T. D.	P5.25	*
Ritchie, E.	5.4	528
Roberts, G.	P5.21	592
Robertson, F. R.	P2.24	722
Rogers, D.	3.1	216
Romanov, P.	P1.2	19
Rose, F. G.	P5.27	606
Rose, L.	P2.3	126
Rose, L.	P2.12	149
Rosenfeld, D.	P5.42	650
Rota, S.	6.3	708
Roundy, P. E.	P2.28	200
Rouse, L. J.	P1.16	65
Roy, D.	P5.21	592
Ruf, C.	P1.20	75
Ruston, B.	P5.41	646
Rutan, D. A.	P5.27	606
Rutan, D. A.	P5.28	610
Rutledge, K.	P4.23	492

* Manuscript not available

	PAPER #	PAGE
S		
Sagoo, P. J.	2.2	110
Sahlaoui, Z.	P3.42	367
Sampson, C. C.	P3.23	308
Sanner, F.	P5.33	*
Santek, D. A.	P3.1	241
Santek, D. A.	P3.29	320
Santek, D. A.	P4.27	*
Sashegyi, K.	P3.15	279
Schaaf, C. B.	P1.25	87
Schaaf, C. B.	P5.21	592
Schichtel, M.	P3.32	332
Schmetz, J.	P5.42	650
Schmetz, J.	6.3	708
Schmidt, C. C.	1.2	1
Schmidt, C. C.	P3.36	346
Schmit, T. J.	P3.10	266
Schmit, T. J.	P3.37	348
Schmit, T. J.	P3.38	351
Schmit, T. J.	P3.40	359
Schmit, T. J.	P3.51	391
Schmit, T. J.	P3.60	420
Schmit, T. J.	P4.2	438
Schmit, T. J.	P4.4	*
Schmit, T. J.	P4.20	481
Schmit, T. J.	P5.5	547
Schmit, T. J.	P5.38	637
Schmit, T. J.	P5.54	*
Schrab, K.	P3.31	328
Schrab, K.	P3.32	332
Schrab, K.	P3.41	363
Schreiner, A. J.	P3.37	348
Schreiner, A. J.	P3.60	420
Scofield, R. A.	P3.46	379
Scofield, R. A.	P3.47	383
Setzer, A. W.	P1.13	51
Shao, H.	P4.17	472
Shay, L. K.	1.3	9
Shepherd, J. M.	P1.31	103
Shi, L.	P5.36	629
Sikora, T. D.	P1.9	35
Simpson, J.	5.4	528
Skupniewicz, C. E.	P3.62	428
Smith, E. A.	P2.24	722
Smith, E. A.	P5.42	650
Smith, E. A.	P5.51	*
Smith, G. L.	P2.7	*
Smith, G. L.	P5.28	610
S (Continued)		
Smith, M.	P4.34	*
Smith, N.	P5.27	606
Smith, W. L.	5.6	*
Smith, W. L.	P5.8	559
Smith, W. L.	P5.60	688
Smith, Jr., W. L.,	P2.20	176
Smith, Jr., W. L.,	P4.19	477
Smith, Jr., W. L.,	P4.23	492
Smith, Jr., W. L.,	P4.35	*
Smith, Jr., W. L.,	P4.36	512
Smith, Jr., W. L.,	6.2	700
Snow, J. W.	P1.12	47
Snow, J. W.	P4.22	488
Soden, B. J.	P2.26	*
Sohn, B.-J.	P2.24	722
Spencer, R. W.	2.1	107
Spinhirne, J. D.	P4.32	*
Spinhirne, J. D.	P5.11	566
Stearns, C. R.	P3.28	318
Stettner, D. R.	P3.1	241
Stettner, D. R.	P3.2	244
Stettner, D. R.	P3.6	256
Storch, S. J.	P3.16	282
Stout, J. E.	P5.48	659
Stowe, L. L.	P4.38	520
Strahler, A. H.	P1.25	87
Strahler, A. H.	P5.21	592
Strow, L. L.	P4.7	*
Strow, L. L.	P5.32	622
Stuart, N. A.	P2.16	165
Su, X.	P3.8	726
Suggs, R. J.	P2.4	128
Suggs, R. J.	P3.12	*
Suggs, R. J.	P4.37	516
Sun-Mack, S.	P4.19	477
Sun-Mack, S.	P4.33	508
Sun-Mack, S.	P4.36	512
Swadley, S. D.	P3.15	279
Swadley, S. D.	P5.39	640
Swanson, K.	P2.3	126
Swanson, K.	P2.12	149
Swenson, H.	P5.2	536
Swenson, H.	P5.62	*
T		
Tampieri, F.	P5.42	650
Tanaka, Y.	P3.26	728

* Manuscript not available

	PAPER #	PAGE
T (Continued)		
Tanamachi, R. L.	P5.61	692
Tarpley, D.	P1.2	19
Tarpley, D.	P1.26	91
Terry, J.	P5.63	696
Thom, J. E.	P3.28	318
Thomas, S. M.	P4.29	*
Thomas-Stahle, J. L.	P4.15	468
Thompson, D. R.	P1.9	35
Thurgood, A.	6.2	700
Tilley, J. S.	P1.24	83
Tilley, J. S.	P1.29	99
Tjemkes, S.	6.3	708
Tjemkes, S. A.	P3.33	336
Tobin, D.	P4.4	•
Tobin, D.	P4.20	481
Tobin, D.	5.6	*
Tobin, D.	P5.8	559
Tobin, D.	P5.9	563
Tobin, D.	P5.60	688
Tobin, D.	6.2	700
Tollerud, E. I.	P3.56	408
Tongue, J. S.	P5.57	*
Torn, R. D.	P1.10	39
Trepte, Q. Z.	P4.19	477
Trepte, Q. Z.	P4.33	508
Tschudi, M.	P4.17	472
Tsvetsinskaya, E.	P5.21	592
Turk, F. J.	P3.22	304
Turk, F. J.	P3.23	308
Turk, F. J.	P5.42	650
Turner, D.	P2.26	*
U		
Uccellini, L.	3.1	216
Upham, C. A.	P4.22	488
V		
Vanderlei Martins, J.	P4.23	492
Vanek, M. D.	P5.10	*
Velden, C. S.	3.3	228
Velden, C. S.	P3.1	241
Velden, C. S.	P3.2	244
Velden, C. S.	P3.6	256
Velden, C. S.	P3.7	260
Velden, C. S.	P3.18	290
V (Continued)		
Velden, C. S.	P3.24	312
Velden, C. S.	P3.25	314
Velden, C. S.	P3.29	320
Velden, C. S.	5.4	528
Velden, C. S.	P5.8	559
Velden, C. S.	6.2	700
Vermeulen, J.	P3.62	428
Vicente, G. A.	P5.42	650
Vinson, K.	P5.52	666
Vollmer, P. A.	P3.11	270
Vonder Haar, T. H.	P2.5	132
Vonder Haar, T. H.	P2.16	165
Vonder Haar, T. H.	3.6	240
Vonder Haar, T. H.	P3.5	*
Vonder Haar, T. H.	P4.16	469
Vonder Haar, T. H.	P5.22	596
Vonder Haar, T. H.	P5.37	633
Vonder Haar, T. H.	P5.41	646
Vongsaard, J.	P5.47	*
W		
Wade, G. S.	P3.53	397
Wade, G. S.	P3.61	424
Wagneur, N.	P3.50	387
Walden, V. P.	P5.61	692
Waliser, D. E.	P2.7	•
Walker, N. D.	P1.16	65
Wang, J.	P2.13	153
Wang, P. K.	P2.15	161
Wang, P. K.	P3.54	402
Wang, P. K.	P5.17	581
Wang, X.	P1.32	*
Wang, X.	P2.8	*
Wang, Y.	P3.62	428
Warner, J.	P4.34	*
Warner, J.	P5.53	670
Weaver, J.	P3.31	328
Weaver, J.	P3.32	332
Weaver, J.	P3.53	397
Weidner, G. A.	P3.28	318
Weinman, J.	P5.46	*
Weinman, J.	P5.47	•
Weinman, J.	P5.65	*
Weissman, D. E.	P5.57	*
Weitz, R.	P4.15	468
Welsch, C.	P5.62	•
Weng, F.	P1.1	17

* Manuscript not available

AUTHOR INDEX

11TH CONFERENCE ON SATELLITE METEOROLOGY AND OCEANOGRAPHY

	PAPER #	PAGE
W (Continued)		
Weng, F.	P3.43	*
Weng, F.	P3.44	371
Weng, F.	P4.9	454
Weng, F.	P5.30	618
Weng, F.	P5.43	654
Weng, F.	P5.44	*
Wentz, F.	P1.20	75
Wetzel-Seemann, S.	P3.38	351
Wetzel-Seemann, S.	P4.4	*
Wetzel-Seemann, S.	P4.20	481
Wetzel-Seemann, S.	P5.14	*
Wetzel-Seemann, S.	P5.54	*
Whittaker, T.	P3.31	328
Whittaker, T.	P3.32	332
Wielicki, B. A.	P4.23	492
Wilcox, E. M.	P2.23	188
Wilheit, T. T.	P4.15	468
Wilson, M.	P5.13	574
Wilson, W.	P1.20	75
Wimmers, A. J.	P3.36	346
Wimmers, A. J.	P3.56	408
Withee, G.	6.1	*
Witiw, M. R.	P1.28	96
Wolf, P.	P3.32	332
Wolf, W.	P5.7	555
Wong, T.	P5.28	610
Woo, S.	P2.5	132
Wood, R.	P2.17	168
Wood, S. A.	P5.63	696
Woolf, H. M.	P5.9	563
Woolf, H. M.	P5.38	637
Woollen, J. C.	P5.63	696
Wu, X.	P1.6	*
Wu, X.	P3.51	391
Wu, X.	P3.52	395
Wu, X.	P4.25	496
Wu, X.	P5.59	685
Wylie, D. P.	P2.6	136
Wylie, D. P.	P2.10	141

	PAPER #	PAGE
X		
Xie, P.	2.3	114
Xu, L.	P2.13	153
Xu, L.	P2.30	206
Y		
Yan, B.	P1.1	17
Yang, P.	P4.29	*
Yang, R.	P5.47	*
Yang, Z.	P5.20	588
Yang, Z.	P5.25	*
Yi, H. Y.	P5.12	570
Yoo, J. -M.	P5.65	*
Young, D. F.	P2.7	*
Young, D. F.	P2.20	176
Young, D. F.	P4.19	477
Young, D. F.	P4.36	512
Yueh, S.	P1.20	75
Z		
Zajac, B.	P3.31	328
Zajac, B.	P3.32	332
Zapotocny, J. V.	3.2	220
Zapotocny, T. H.	P3.9	262
Zapotocny, T. H.	P3.10	266
Zavala, J.	P1.7	*
Zehr, R. M.	P3.20	296
Zehr, R. M.	P3.32	332
Zhang, H.	P4.28	504
Zhang, J.	P1.24	83
Zhang, X.	P5.21	592
Zhao, G.	P4.31	506
Zhao, J.	P3.63	431
Zhao, L.	P3.43	*
Zhao, L.	P3.44	371
Zhao, L.	P5.43	654
Zhou, D.	6.2	700
Zhou, L.	P5.7	555
Zierden, D. F.	P5.57	*
Ziskin, D.	P4.34	*
Ziskin, D.	P5.53	670
Zollinger, L.	6.2	700

* Manuscript not available

1.2

AN OVERVIEW OF ACTIVE FIRE DETECTION AND MONITORING USING METEOROLOGICAL SATELLITES

Elaine M. Prins*
NOAA/NESDIS, Office of Research and Applications, Advanced Satellite Products Team (ASPT)
Madison, WI

Joleen M. Feltz, Chris C. Schmidt
Cooperative Institute for Meteorological Satellite Studies (CIMSS), University of Wisconsin
Madison, WI

1. INTRODUCTION

Each year millions of acres of boreal and temperate forests and grasslands are consumed by wildfire resulting in loss of life and property with significant economic costs and environmental impacts. The 2000 fire season in the USA was the worst in nearly 50 years with over 8.4 million acres burned. The estimated cost of fire suppression alone was $1.3 billion. The cost of fire management and suppression is expected to increase, especially along the urban/wildland interface.

Throughout the world, fire also serves as a tool in deforestation, land clearing, grassland management, pest control, and other agricultural applications. Current estimates suggest that globally over 85% of all fires occur in the equatorial and subtropical regions primarily in Africa, South America, and Southeast Asia. Much of this activity is concentrated in developing countries where there are few resources to adequately document the extent of burning.

Biomass burning associated with naturally occurring forest fires, deforestation and other human activities is a distinct biogeochemical process that plays an important role in terrestrial ecosystem processes and regional and global climate change. Fire is a major source of trace gases such as NO, CO_2, CO, O_3, NO_x, N_2O, NH_3, SO_2, CH_3, and other nonmethane hydrocarbons. Preliminary global estimates indicate that biomass burning may be responsible for 38% of ozone in the troposphere, 32% of global carbon monoxide, 39% of the particulate organic carbon, and up to 40% of CO_2. Fire is also a significant source of aerosols (Crutzen et al., 1985; Andreae et al., 1988; Crutzen and Andreae, 1990; Levine, 1991). Studies have shown that the direct and indirect radiative effects of aerosols from biomass burning are a major factor in climate change calculations (Penner et al., 1992). Nationally and within the Framework Convention on Climate Change (FCCC), countries will need to report on their greenhouse gas emissions including those from biomass burning (Justice and Korontzi, 2001). In many countries, remote sensing may be the only economically feasible way to track fire activity.

* *Corresponding author address:* Elaine M. Prins, NOAA/NESDIS, 1225 W. Dayton St., Madison, WI 53706; email: Elaine.Prins@ssec.wisc.edu.

Over the past twenty years the international scientific research and environmental monitoring communities have recognized the vital role environmental satellites can play in detecting and monitoring active fires both regionally and around the world for hazards applications and to better understand the extent and impact of biomass burning on the global environment. Although the current suite of international polar orbiting and geostationary satellites do not meet all of the needs of the hazards and climate change community, routine generation of real-time fire products would be extremely valuable to both user communities. At the present time, consistent routine global fire products are not available in real time.

Remote sensing of biomass burning is currently the focus of two international efforts that bring together remotes sensing data providers and user communities, including climate change research scientists, resource managers, fire managers, and policy and decision makers. Although the primary focus of each effort is different, they both are dedicated to better utilization of environmental satellite data to detect and monitor active fires regionally and on a global scale. The Global Observation of Forest Cover (GOFC) is a coordinated effort that was originally developed as a pilot project by the Committee on Earth Observation Satellites (CEOS) as part of the Integrated Observing strategy (IGOS), and is now a panel of the Global Terrestrial Observing System (GTOS). Forest fire monitoring and mapping is one of three primary GOFC themes. The fire hazard team of the Disaster Management and Support Group (DMSG) is an ad hoc working group of CEOS focusing on current capabilities and requirements for space-based observations for fire management applications regionally and around the world. Both groups have stated the importance of utilizing operational meteorological satellites for routine fire products and long-term analyses (Dull and Lee, 2001; Gutman, et al.,2001; Justice and Korontzi, 2001).

2. OVERVIEW OF ENVIRONMENTAL SATELLITE FIRE DETECTION

Environmental satellites have been used for fire detection and monitoring for over 20 years. Some of the initial studies were performed using the National Oceanic and Atmospheric Administration (NOAA)-6

Advanced Very High Resolution Radiometer (AVHRR) (Matson and Dozier, 1981). This work showed how the different brightness temperature responses between the shortwave infrared (SWIR at 3.74 μm) and the longwave infrared windows (LWIR at 10.8 μm) can be used to locate fires and determine estimates of sub-pixel fire size and temperature. Typically the differences between the SWIR and LWIR bands are on the order of 2 to 4 K due to reflected solar radiation, surface emissivity differences, and water vapor attenuation. Larger differences occur when one part of the pixel is substantially warmer than the rest and in regions with enhanced solar reflection. Since the early 1980s, the AVHRR has been used to monitor fires around the globe using various algorithms ranging from single band image analyses and simple channel differencing to more complex automated contextual algorithms (Muirhead and Cracknell, 1985; Kaufman et al., 1990; Setzer and Pereira, 1991; Justice and Dowty, 1994; Flasse and Ceccato, 1996; Li et al., 2001).

Other polar orbiting sensors have been identified as appropriate for global fire detection including the Advanced Very High Resolution Radiometer (AVHRR), the ERS Along Track Scanning Radiometer (ATSR), the MODerate-resolution Imaging Spectroradiometer (MODIS), the Defense Meteorological Satellite Program (DMSP) Operational Linescan System (OLS), the Tropical Rainfall Measuring Mission (TRMM) Visible and Infrared Scanner (VIRS), and the ADvanced Earth Observing Satellite (ADEOS-II) Global Imager (GLI). In the mid-latitudes these instruments provide several observations of a given region each day. In the near future a suite of geostationary satellites will be available to complement the polar network by providing information on the diurnal timing, spatial distribution, and characteristics of sub-pixel fire activity around the globe. Currently geostationary active fire monitoring using the SWIR band is only feasible in the western hemisphere with the NOAA Geostationary Operational Environmental Satellites (GOES) (Prins et al, 2001). The remainder of this paper will focus on applications of geostationary data for fire detection and monitoring.

3. GOES FIRE MONITORING IN THE WESTERN HEMISPHERE

The current series of GOES satellites provide the unique opportunity to detect and monitor active fires every half hour throughout the western hemisphere. The GOES Imager has five spectral bands (see Table 1) including a broadband visible and 4 infrared bands (Menzel and Purdom, 1994). Several features of the GOES Imager are beneficial for fire monitoring. The oversampling of the instantaneous geometric field of views (IGFOV) in the east/west direction allows for increased opportunities to capture an entire fire within one field of view. The saturation temperature on the shortwave IR window band is significantly higher on GOES-8 (335K) than

Table 1: Geostationary Operational Environmental Satellite (GOES) Characteristics
Current Systems: GOES-8 and GOES-10
Position: GOES-8 at 75 °W and GOES-10 at 135 °W
Design Life: 3-5 years
Operating Agency: National Oceanic and Atmospheric Administration (NOAA)

Band	Wavelength (μm)	Resolution IGFOV (km)	Description
VIS	0.52-0.72	1	Broadband visible
IR 3.9	3.78-4.03	4	SW-R window
IR 6.7	6.47-7.02	8	Water Vapor
IR 10.7	10.2-11.2	4	IR Window
IR 12.0	11.5-12.5	4	Dirty Window

that on AVHRR (320K). If the saturation temperature were near 320K, over 80% of the fire pixels observed in South America would saturate the instrument. A higher saturation temperature allows for easier fire identification in regions with high background temperatures, the ability to monitor diurnal changes in fire size and intensity, and calculations of sub-pixel fire size and temperature estimates. At nadir, the minimum detectable instantaneous fire size burning at an average temperature of 750 K is 0.15ha and increases to 0.32 ha at 50°N (see figure 3 for more details) (Prins et al., 2001).

Throughout the western hemisphere, GOES is used to detect and monitor wildfires in real time for hazard applications and to document fires associated with deforestation and agricultural management (Prins et al, 1998; 2001; Alfaro et al., 1999; Molenar et al. 2000). At the University of Hawaii and the Colorado State University Cooperative Institute for Research in the Atmosphere (CIRA) image processing techniques, such as multispectral band differencing and multi-band image combinations, are used to create derived imagery that highlight regions of possible fire activities (Weaver et al., 1995; Harris, et al. 2000). These derived composite imagery products provide a valuable tool for near real-time fire identification for the trained user. At the University of Wisconsin Cooperative Institute for Meteorological Satellite Studies (CIMSS), multispectral imagery, ancillary data, and statistical and numerical techniques are incorporated in a complex algorithm that automatically locates hot spot pixels and provides estimates of sub-pixel fire characteristics. These products are used in real time for fire identification and monitoring and fire trend analysis activities and can be assimilated into climate change and pollutant transport models in real-time (Prins, et al., 2001). The following sections provide examples of GOES fire monitoring applications being conducted at CIMSS.

3.1 GOES Biomass Burning Trend Analysis in South America

The international scientific community has stressed the need for long-term monitoring of biomass burning for land-use/land-cover change analysis and global climate change research. The NOAA/NESDIS/ORA

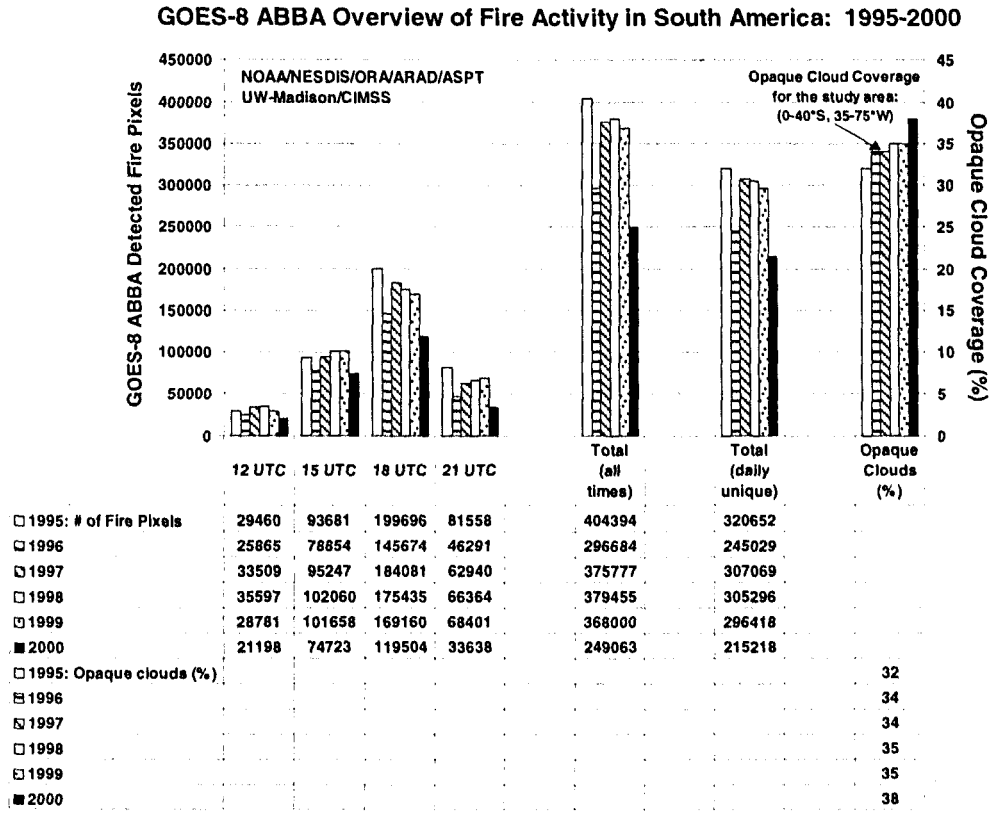

Figure 1. Summary of GOES-8 ABBA detected fire pixels in South America for 1995 to 2000.

Advanced Satellite Products Team (ASPT) and the Cooperative Institute for Meteorological Satellites Studies (CIMSS) developed two algorithms to monitor trends in fire, smoke, and clouds in South America using GOES-8 data. The GOES-8 Automated Biomass Burning Algorithm (ABBA) identifies and characterizes sub-pixel burning in GOES imagery (Prins and Menzel, 1994; Prins et al., 1998). It is a dynamic multispectral contextual algorithm which uses the visible, shortwave infrared window (3.9 μm) and longwave infrared window (10.7 μm) bands and ancillary data to locate fires in GOES imagery. Once a fire is found, numerical techniques are used to estimate sub-pixel fire size and temperature. The Merged Automated Cloud/Aerosol Detection Algorithm (MACADA) distinguishes smoke from various cloud types and catalogues smoke and cloud extent. The MACADA is a merged spectral/textural algorithm which uses multispectral GOES data (visible, 3.9, 10.7, 12.0 mm) to map smoke, aerosols, and clouds.

The 1995 fire season represented the first opportunity to quantitatively monitor diurnal fire activity from the GOES-8. It serves as the benchmark year in characterizing diurnal, spatial, seasonal and interannual trends in fire activity, clouds, and aerosols throughout South America. The GOES ABBA and MACADA were applied to 3-hourly (11:45, 14:45, 17:45, and 20:45 UTC) multispectral data collected from June through October in each year from 1995 to 2000. The study area extended from 0 to 40°S and from 35 to 75°W including portions of Brazil, Peru, Bolivia, Paraguay, Uruguay, and northern Argentina. Figure 1 provides an overview of the number of fire pixels detected at each time period and total burning for each year, along with the percent opaque cloud coverage. The opaque cloud coverage gives an indication if the interannual variability in the number of detected fire pixels is due to cloud coverage issues. From 1995 to 1999 the interannual differences in opaque cloud cover were less than 2% on average throughout the fire study area. Opaque cloud cover in the year 2000 was approximately 6% higher than in 1995.

The diurnal cycle is observed in all years with peak burning at 17:45 UTC. The sum of all fire pixels detected at all time periods for each year shows that 1995 was the peak year with over 400,000 fire pixels. The total number of fire pixels detected in 1996 at all time periods was 27% less than in 1995 with only a

slight increase in cloud coverage. In 1997 there was increased fire activity in north-central and northeastern Brazil primarily due to drought conditions associated with El Nino, although the total number of detected fire pixels was 7% less than in 1995. In 1998 the ABBA detected elevated burning in eastern Brazil with approximately 6% less fire pixels than in 1995. In 1999 enhanced fire activity was observed in southwestern Brazil, Paraguay, and Bolivia where wildfires raged out of control, although the number of fire pixels detected was 9% less than in 1995. The 2000 fire season showed a significant decrease in fire activity, nearly 38% less than in 1995. This change was accompanied by a 6% greater occurrence of opaque clouds in the study area.

Most fires in South America can be detected from satellite for only a few hours. The daily unique column shows that on average 82% of the fire pixels observed at a given time period were not observed at the other times in a day. In the year 2000, over 86% of the fires were observed in only one of the four time periods, possibly due to cloud obscuration in other time periods. This emphasizes the importance of high temporal observing systems to capture the short-lived fires and to have more opportunities for cloud-free viewing. Comparisons with the INPE AVHRR fire product for the 1995-2000 time period show that although both instruments detect similar patterns in burning, diurnal monitoring is necessary to monitor fires as they occur (Feltz, et al., 2001).

3.2 Applications of the Wildfire ABBA Throughout the Western Hemisphere

A new version of the GOES-8 ABBA was developed for fire detection and monitoring throughout the western hemisphere. The Wildfire ABBA enables fire monitoring in most ecosystems and was streamlined to allow for rapid processing of half-hourly GOES data. GOES-8 Wildfire ABBA composite fire products are created and posted on the Web in real time at the following web site: http://cimss.ssec.wisc.edu/goes/burn/wfabba.html. Initial evaluation of the Wildfire ABBA in Canada, Southeastern U.S., Mexico, and South America indicates improvements in identifying wildfires, distinguishing between fires and highly reflective surfaces and cloud edges, and a reduction in false alarms. In Canada preliminary studies have demonstrated the utility of high-temporal GOES data for early detection of large rapidly growing fires in remote regions of Quebec (Moreau, Personal Communication, 1999). In addition to applications in fire management, the Wildfire ABBA products are also being assimilated into the Navy Aerosol Analysis and Prediction System (NAAPS) as part of the Fire Locating and Modeling of Burning Emissions (FLAMBE) project (Prins et al., 2001).

Composites of the half-hourly Wildfire ABBA fire products provide a unique perspective regarding the prevalence and distribution of fire in the western hemisphere. Figure 2 is a composite of all fires detected in half-hourly GOES-8 imagery from 1 September 2000 through 28 February 2001. The most obvious feature of the 6-month composite is the that the vast majority of fires are located in South America, reflecting the extensive use of fire in deforestation and agricultural management. Although it is important to note that the study period did not include spring agricultural burning in Central America and the Southeast U.S.

Several areas of enhanced fire activity are outlined in North America. Clusters of fire pixels were detected in the plains of central Canada and North Dakota (location a). These fires were located in both cropland and forested regions. Although the major conflagrations in the western U.S. occurred in August of 2000, this composite shows wildfires burning in the western U.S. (location b) beyond August. Numerous fire pixels are identified along the Mississippi Delta region (location c) and are predominantly associated with agricultural activity. Fires in the southeastern U.S. (location d) are located in both cropland and forested areas. We have not been able to verify the cluster of fires in southern Florida (location e), but smoke plumes were observed in this region on a number of occasions. The fire pixels in Cuba (location f) and Central America (location g) are probably associated with agricultural burning.

The fires in the northwestern portion of South America, in the countries of Venezuela and Colombia (location h), are predominantly located in cattle ranching regions, although crops are grown here as well. Some of this fire activity is also located in forested regions. Numerous fire pixels were detected in the Guiana Highlands region of Venezuela, Guyana, and northern Brazil (location i). Thousands of fire pixels were located along the arc of deforestation in Brazil. The burning pattern is similar to what has been documented by the South American GOES-8 ABBA (Prins et al., 1998; 2001). The majority of these fires are associated with agricultural applications and deforestation activities. The composite shows distinct burning patterns along rivers and in areas with recent road construction (linear features) as observed at locations j, k, and l. The fires observed at location l represent a new region of expanding deforestation in western Amazonia associated with a new road being constructed over the Andes to link Brazil with Peruvian ports on the Pacific Coast. Fires in eastern Brazil and central Bolivia are primarily associated with ongoing agricultural management. The cluster of saturated fire pixels in south-central Argentina (location m) represents extensive fires that burned throughout December and January along the grassland/desert boundary. They produced large smoke palls that extended to the Atlantic Ocean. These fires were also observed in NOAA AVHRR imagery and were documented on the NOAA Operational Significant Events Imagery (OSEI) web site.

4. FUTURE GLOBAL GEOSTATIONARY FIRE CAPABILITIES

One of the goals of the international GOFC fire monitoring and mapping efforts is to promote and

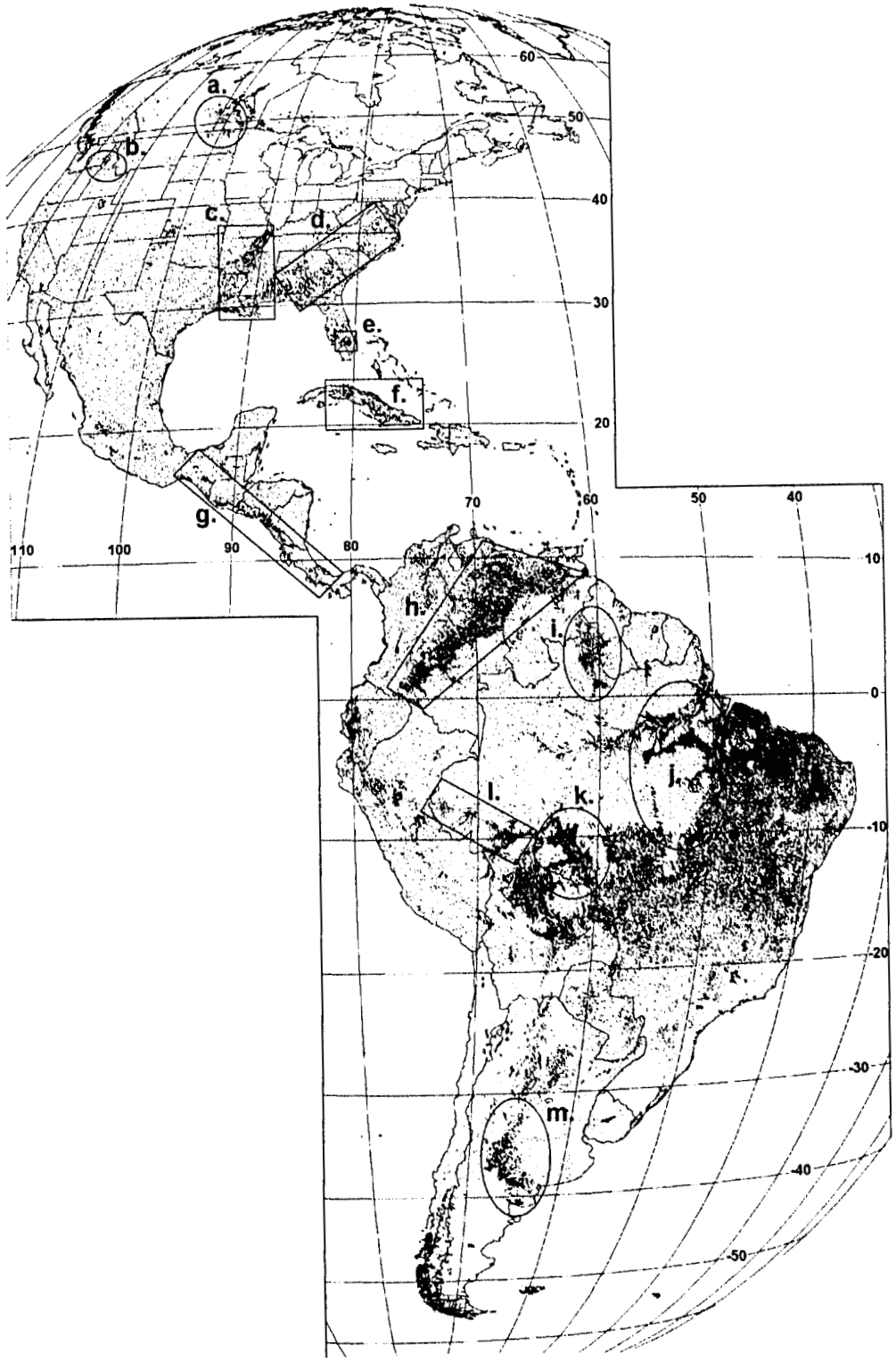

Figure 2. GOES-8 Wildfire ABBA composite of all half-hourly detected fire pixels for the time period 1 September 2000 through 28 February 2001.

support the development of a network of global geostationary satellites providing operational standard active fire products in near-real time and creating a long-term archive of fire data. A global geostationary fire network will be possible with the launch of the European Meteosat Second Generation(MSG) satellite in 2002 and the replacement Japanese Multi-functional Transport Satellite (MTSAT-1R) in 2003.

The MSG is a spin-stabilized satellite and will serve as the successor to the European Meteorological Satellite (Meteosat) series. The primary instrument on the MSG is the Spinning Enhanced Visible and Infrared Imager (SEVIRI) containing 3 visible bands (broadband centered at 0.75 μm, and bands at 0.63 and 0.81 μm), 1 near-infrared (NIR at 1.6 μm) and 8 infrared bands (3.9, 6.2, 7.3, 8.7, 9.7, 10.8, 12.0, and 13.4 μm) (see Table 2). Full disk imagery will be available every 15 minutes. The 3.9 μm band will enable sub-pixel fire monitoring in Europe and Africa with excellent coverage of the African forests. In addition, nighttime measured 1.6 μm radiance will provide quantitative observations of hot spots in the absence of reflected solar radiation contamination during the day, as demonstrated with the ATSR (Wooster and Rothery, 1997). The IGFOV at nadir will be approximately 1.6 km in the broadband visible and 4.8 km in the remaining bands, although all bands will be oversampled with a sampled resolution of 1 km in the broadband visible (HRV) and 3 km in all other bands. This oversampling can be used to enhance the spatial resolution and increases the opportunity to capture an entire fire within one field of view.

The elevated saturated temperature (>335 K) in the 3.9 μm band will minimize the impact of saturation and allow for sub-pixel fire characterization. Minimum detectable fire size estimates, presented in figure 3, indicate that MSG will be able to detect a 0.22 ha fire burning at 750 K at the equator and a 0.46 ha fire at 50°N.

MTSAT is a multi-functional three-axis stabilized satellite that is being produced by the Japan Meteorological Agency (JMA) and the Japan Civil Aviation Bureau (JCAB) to serve both a meteorological mission as the successor to the Geostationary Meteorological Satellite (GMS) series and an aeronautical mission (JMA, 1997). The initial MTSAT was lost during launch in the fall of 1999. Preliminary indications are that Japan will try to launch a replacement satellite MTSAT-1R in 2003.

The MTSAT-1R will include the Japanese Advanced Meteorological Imager (JAMI) which is similar to the GOES in terms of spectral coverage (Kigawa, 2000). This overview is based on current preliminary design specifications for the JAMI. The JAMI includes one visible band (broadband centered at 0.72 μm) and 4 infrared bands (3.75, 6.75, 10.8, and 12.0 μm). The current JAMI design specifies a spatial resolution at nadir of 0.5 km in the visible and 2 km in the infrared bands, although the data may be disseminated to the user community with the reduced resolution of 1 km in the visible and 4 km in the IR. The increased spatial resolution of MTSAT over GMS-5 and the addition of the 3.75 μm band will make geostationary diurnal fire monitoring in the western Pacific possible for the first time, with increased temporal resolution, providing coverage of the full disk region every 18 minutes.

The MTSAT-2, which is scheduled for launch in 2004, will be similar to the imager on the original MTSAT platform with a spatial resolution of 1 km in the visible and 4 km in the infrared bands. The infrared bands will have the same spectral configuration as the JAMI with half-hourly observations available for the entire full disk region. The saturation temperature in the 3.75 μm band on both MTSAT-1R and MTSAT-2 is expected to be near 320 K which will hinder sub-pixel fire characterization due to saturation, but saturation will still be less of an issue than with the current AVHRR 1 km Local Area Coverage (LAC) data.

The JAMI offers a unique opportunity to provide early warning in the detection of smaller fires which are not detectable by other geostationary platforms. Minimum detectable fire size estimates shown in figure 3 suggest that the spectral configuration and 2

Table 2: Meteosat Second Generation (MSG)
Launch Date: 2002
Position: Greenwich Meridian
Design Life: 7 years
Operating Agency: EUMETSAT

Band	Wavelength (μm)	Resolution IGFOV (km)	Description
HRV 0.75	0.60-0.90	1.6	Broadband visible
VIS 0.6	0.56-.71	4.8	Visible and Near IR
VIS 0.8	0.74-0.88	4.8	
IR 1.6	1.50-1.78	4.8	
IR 3.9	3.48-4.36	4.8	IR windows
IR 8.7	8.30-9.10	4.8	
IR 10.8	9.80-11.80	4.8	
IR 12.0	11.00-13.00	4.8	
IR 6.2	5.35-7.15	4.8	Water Vapor
IR 7.3	6.85-7.85	4.8	
IR 9.7	9.38-9.94	4.8	Ozone
IR 13.4	12.40-14.40	4.8	Carbon Dioxide

Table 3. Multi-functional Transport Satellite (MTSAT)
Launch Date: ~2003
Position: 140°E
Design Life: 5 years
Operating Agency: Japan Meteorological Agency (JMA) and the Japan Civil Aviation Bureau (JCAB)

Band	Wavelength (μm)	Resolution IGFOV (km)	Description
VIS 0.72	0.55-0.80	0.5	Broadband visible
IR 3.7	3.5-4.0	2	SWIR window
IR 6.7	6.5-7.0	2	Water Vapor IR
IR 10.8	10.3-11.3	2	IR Window
IR 12.0	11.5-12.5	2	Dirty Window

*Japan Meteorological Agency, 1997

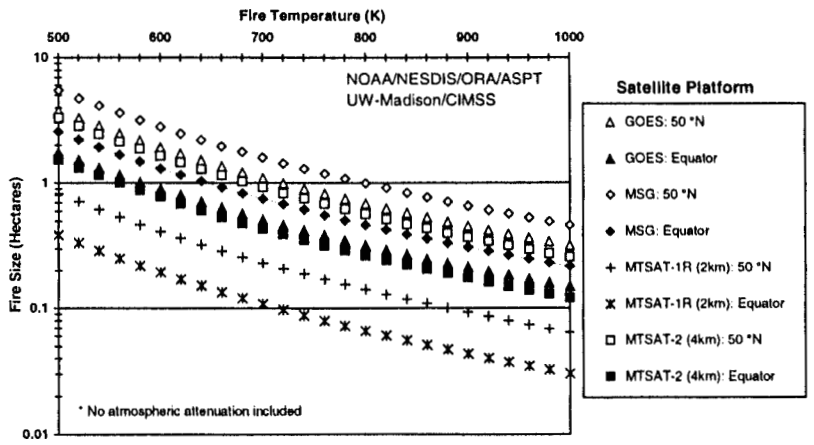

Figure 3. Minimum detectable fire size estimates for GOES, MSG, and MTSAT

km spatial resolution of the SWIR band on MTSAT-1R will allow it to detect significantly smaller fires than GOES-8. The MTSAT-1R will be able to detect a 0.03 ha fire burning at 750 K at the equator. The minimum detectable fire size at 50°N is 0.06 ha. This is 5 times smaller than the GOES minimum detectable fire size. The infrared spatial resolution of 4 km on MTSAT-2 will increase the minimum detectable fire size to 0.12 ha at the equator and 0.26 ha at 50°N for a fire burning at 750K.

5. CONCLUSIONS

Current international environmental meteorological satellites were not specifically designed for the purpose of fire monitoring and have limitations in this application. In spite of the limitations, studies have shown that they are a valuable resource for near real-time detection and monitoring of active fires. To date these satellites have been underutilized. International efforts are underway to better utilize environmental satellite data for detecting and monitoring active fires regionally and on a global scale for the wildfire management and climate change communities. In particular, operational satellites such as the NOAA POES, GOES, and DMSP platforms can provide consistent fire products from similar platforms over many years. Furthermore operational satellite data archives can be analyzed to study long-term trends in fire activity around the globe for climate applications. Within the next few years, an international suite of geostationary satellites will be able to monitor diurnal fire activity around the globe. Together with current and future meteorological/environmental polar-orbiting satellites, this suite of geostationary sensors will be able to detect and monitor fires as they occur and provide information on spatial, diurnal, seasonal, and interannual trends in biomass burning around the globe.

6. REFERENCES

Alfaro, R., W. Fernandez, and B. Connell, 1999: Detection of the forest fires of April 1997 in Guanacaste, Costa Rica, using GOES-8 images. *International Journal of Remote Sensing*. **20**(6), 1189-1195.

Andreae, M. O., E. V. Browell, M. Garstang, G. L. Gregory, R. C. Harriss, G. F. Hill,D. J. Jacob, M. C. Pereira, G. W. Sachse, A. W. Setzer, P. L. Silva Dias, R. W. Talbot, A. L. Torres and S. C. Wofsy, 1988: Biomass burning emissions and associated haze layers over Amazonia. *J. Geophys. Res.*, **93**, 1509-1527.

Crutzen, P.J., A. C. Delany, J. Greenburg, P. Haagensen, L. Heidt, R. Lueb, W. Pollock, W. Seilor, A. Wartburg, and P. Zimmerman, 1985: Tropospheric chemical composition measurements in Brazil during the dry season. *J. of Atmos. Chemistry*, **2**, 233-256.

Crutzen, P. J. and M. O. Andreae, 1990: Biomass burning in the tropics: impact on atmospheric chemistry and biogeochemical cycles. *Science*, **250**, 1669-1678.

Dull, C. W., and B. S. Lee, 2001: Satellite earth observation information requirements of the wildland fire management community. In Global and Regional Wildfire Monitoring: Current Status and Future Plans (F. J. Ahern, J. G. Goldammer, C. O. Justice, Eds.), SPB Academic Publishing , The Hague, Netherlands, pp. 19 - 33.

Feltz, J. M. and E. M. Prins, 2001: A comparison of the GOES-8 ABBA and INPE AVHRR fire products for South America from 1995 – 2000. Proceedings of the 11th Conference on Satellite Meteorology and Oceanography, Madison, WI, October 15-18, 2001, pp. TBD.

Flasse, S. P., and P. Ceccato, 1996: A contextual algorithm for AVHRR fire detection. *Int. J. Remote Sens.* **17**(2), 419-424.

Gutman, G., C. Elvidge, I. Csiszar, and P. Romanov, 2001: NOAA archives of data from meteorological satellites useful for fire products. In Global and Regional Wildfire Monitoring: Current Status and Future Plans (F. J. Ahern, J. G. Goldammer, C. O. Justice, Eds.), SPB Academic Publishing , The Hague, Netherlands, pp. 257-265.

Harris, A. J. L., L. P. Flynn, K. Dean, E. Pilger, M. Wooster, C. Okubo, P. Mouginis-Mark, H. Garbeil, C. Thornber, D. Rothery, and R. Wright, 2000: Real-time monitoring of volcanic hot spots with satellites. In *Remote Sensing Volcanism, AGU Monograph Series.* (P. Mouginis-Mark, J. Fink, J. Crisp, Eds.), pp. 139-159.

Japan Meteorological Agency (JMA), 1997: Meteorological observation with the Multi-functional Transport Satellite (MTSAT). Report produced by the Office of Meteorological Satellite Planning Administration Division, Observations Department, Japan Meteorological Agency, 4 pp.

Justice, C. O., and P. R. Dowty, 1994: Technical Report of the IGBP-DIS Satellite Fire Detection Algorithm Workshop. February, 1993, NASA/GSFC, Greenbelt, MD, Technical Report, IGBP-DIS Working Paper No. 9, IGBP, Paris.

Justice, C., and S. Korontzi, 2001: A review of satellite fire monitoring and requirements for global environmental change research. In Global and Regional Wildfire Monitoring: Current Status and Future Plans (F. J. Ahern, J. G. Goldammer, C. O. Justice, Eds.), SPB Academic Publishing , The Hague, Netherlands, pp. 1-18.

Kigawa, S., 2000: Overview of MTSAT-1R Imager. Japan Meteorological Satellite Center Technical Note No. 39, Japan Meteorological Agency, in press.

Kaufman, Y. J., C. J. Tucker, and I. Fung, 1990: Remote sensing of biomass burning in the tropics. *Jour. of Geophys. Res.,* **95**, 9,927-9,939.

Levine, J.S., 1991: Biomass burning: combustion emissions, satellite imagery, and biogenic emissions. In *Global Biomass Burning: Atmospheric,Climatic, and Biospheric Implications*, edited by J. S. Levine, The MIT Press, Cambridge, MA, pp. 264-271.

Li, Z., Y. J. Kaufman, C. Ichoku, R. Fraser, A. Trishchenko, L. Giglio, J-Z. Jin, and X. Yu, 2001: A review of AVHRR-based active fire detection algorithms: principles, limitations, and recommendations. In Global and Regional Wildfire Monitoring: Current Status and Future Plans (F. J. Ahern, J. G. Goldammer, C. O. Justice, Eds.), SPB Academic Publishing , The Hague, Netherlands, pp. 199 - 225.

Matson, M., and J. Dozier, 1981: Identification of subresolution high temperature sources using a thermal IR sensor. *Photo. Engr. and Rem. Sens.* **47**,1311-1318.

Menzel, W. P., and J. F. W. Purdom, 1994: Introducing GOES-I: the first of a new generation of geostationary operational environmental satellites. *Bull. Amer. Met. Soc.* **75**(5):757-781.

Molenar, D. A., K. J. Schrab, and J. F. W. Purdom, 2000: RAMSDIS contributions to NOAA satellite data utilization. *Bull. Amer. Met. Soc.* **81**(5), 1019-1030.

Moreau, M. , 1999: Personal Communication. Environment Canada/Meteorological Services/Quebec region. Ste-Foy, Quebec, Canada.

Muirhead, K, and A. Cracknell, 1985: Straw burning over Great Britain detected by AVHRR. *Intl. Jour. of Remote Sensing*, **8**, 827-833.

Penner, J. E., R. E. Dickinson, C. A. O'Neill, 1992: Effects of aerosol from biomass burning on the global radiation budget. *Science*, **256**, 1,432-1,433, 1992.

Prins, E. M., and W. P. Menzel, 1994: Trends in South American biomass burning detected with the GOES VAS from 1983-1991. *J. Geophys. Res.* **99**(D8), 16,719-16,735.

Prins, E. M., J. M. Feltz, W. P. Menzel, and D. E. Ward, 1998: An overview of GOES-8 diurnal fire and smoke results for SCAR-B and the 1995 fire season in South America. *Jour. of Geo. Res.* **103**(D24), 31,821-31,836.

Prins, E., J. Schmetz, L. Flynn, D. Hillger, J. Feltz, 2001: Overview of current and future diurnal active fire monitoring using a suite of international geostationary satellites. In Global and Regional Wildfire Monitoring: Current Status and Future Plans (F. J. Ahern, J. G. Goldammer, C. O. Justice, Eds.), SPB Academic Publishing , The Hague, Netherlands, pp. 145 - 170.

Schmetz, J., H. Woick, S. Tjemkes, and J. Rattenborg, 1998: From Meteosat to Meteosat Second Generation. Proceedings of the *Ninth Conference on Satellite Meteorology and Oceanography.* Paris, France, May 25-29, pp. 335-338.

Setzer, A. W. and M. C. Pereira, 1991: Amazonian biomass burnings in 1987 and an estimate of their tropospheric emission, *Ambio*, **20**, 19-22.

Weaver, J., J. Purdom, and T. Schneider, 1995: Observing forest fires with the GOES-8 3.9 μm imaging channel. *Weather and Forecasting.* **10**(4), 803-808.

Woick, H., J. Schmetz, and S. Tjemkes, 1997: An introduction to Meteosat Second Generation imagery and products. Presented at the 1997 Meteorological Data Users' Conference, Brussels, Belgium, Sep. 29- Oct. 3.

Wooster, M. J., and D. A. Rothery, 1997: Thermal monitoring of Lascar Volcano, Chile, using infrared data from the along-track scanning radiometer: a 1992-1995 time series. *Bull. Volcanol.* **58**, 566-579.

1.3 HURRICANE HEAT POTENTIAL ESTIMATES FROM SATELLITE RADAR ALTIMETER MEASUREMENTS

Lynn K. Shay
Division of Meteorology and Physical Oceanography
Rosenstiel School of Marine and Atmospheric Science
University of Miami

1. BACKGROUND

Tropical cyclone intensity forecasting has little skill in predicting storm strength particularly for rapid deepening storms (Elsberry *et al.* 1992). Based on deliberations from the Prospectus Development Team 5 (PDT5), tasked by the lead scientist of the United States Weather Research Program (USWRP) for NOAA and NSF (Marks *et al.* 1998), understanding and predicting intensity change requires the knowledge of: tropospheric interactions (troughs and ridges); internal core dynamics; and upper oceanic circulation which controls the upper ocean's heat potential.

Central to the upper ocean's effect on hurricane intensity is understanding the thermodynamics of the ocean mixed layer (OML) and the dynamical processes that modulate it such as the current field. An important example of this effect is the Gulf of Mexico basin since once a storm enters the semi-enclosed basin, it will make landfall along either the Mexican or United States coasts. The upper ocean's flow through the Yucatan Straits forces an annual variation in the Loop Current (Leipper and Volgenau 1972) (Fig. 1). This anticyclonically-rotating Loop Current has maximum flows of 1 to 1.5 m s^{-1} and intrudes 500 km northward into the Gulf of Mexico and transports subtropical water with a markedly different temperature and salinity relationship compared to the background Gulf of Mexico water. Since the depth of the 20°C isotherm occurs at 250 to 300 m in the subtropical water compared to 100 m for the Gulf common water, warmer subtropical waters extend several hundred meters deeper thereby increasing its heat potential. As this feature intrudes further north, warm core rings (WCR) having diameters of 100 to 200 km pinch off at 11 to 14 month intervals. Rings propagate westward at speeds of 3 to 5 km d^{-1} over a 9 to 12-month period, dissipating along the shelf break off Texas and Mexico. The anticyclonic circulation around the Loop Current flows through the Florida Straits between United States and Cuba forming the Florida Current. This deep, warm ribbon of high heat potential water then follows the eastern seaboard, and as it separates from the coast off North Carolina, it forms the core of the Gulf Stream. Central to the storm intensity issue is that since the warm water extends to depths exceeding 100 m, they represent heat reservoirs to fuel tropical and extratropical storms.

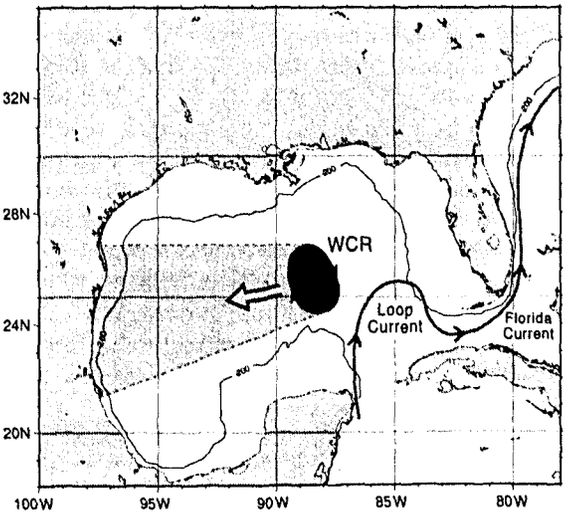

Figure 1: Cartoon of the Gulf of Mexico showing the mean boundaries of the Loop Current and the warm core rings (WCR) as they propagate westward.

Within this broader oceanographic context, the passage of hurricane Opal in 1995 in the Gulf of Mexico underscored inherent uncertainties in predicting sudden (and dramatic) wind-field changes. During hurricane Opal's intense deepening phase on 3 Oct 1995, surface winds increased from 35 m s^{-1} to more than 60 m s^{-1}. Vertical wind shear in the upper atmosphere was relatively weak; and, the cyclonic spin-up of Opal was maximized due to the approaching trough from

Corresponding Author Address: Lynn K. Shay, MPO, RSMAS, 4600 Rickenbacker Causeway, Miami, FL 33149. email: nick@erg.rsmas.miami.edu.

the northwest (Bosart *et al.* 2000). Atmospheric conditions were favorable for this intense deepening cycle starting late on 3 Oct. In this area of Opal's rapid deepening, the SST distribution in the Gulf of Mexico showed no apparent signs of any warm ocean feature as uniformly distributed SSTs exceeded 29°C. However, images from the NASA oceanographic TOPography EXperiment (TOPEX) mission and post-storm Advanced Very High Resolution Radiometer (AVHRR)-derived sea surface temperatures (SST) suggested that during this time Opal passed over a WCR (Shay *et al.* 2000; Hong *et al.* 2000). This rapid intensification ended on 4 Oct as Opal exited this WCR, and it encountered less favorable atmospheric conditions. This was fortunate for the Florida Panhandle residents as even a weakened Opal inflicted severe damage to the coastal community. Notwithstanding, the community learned a valuable lesson concerning rapid deepening. That is, oceanic heat potential associated with warm ocean features played a significant role in the rapid intensification of storms during neutral or favorable atmospheric conditions. This is important for the public who rely on advancements in intensity forecasts for evacuation purposes.

In this note, SSTs and oceanic heat potential are described and cast within a simple OML model. Upper ocean measurements, acquired during the 1999 and 2000 hurricane field program from NOAA WP-3D aircraft (listed in Table 1), are used to estimate oceanic heat potential in the Gulf of Mexico. The approach of estimating heat potential from satellite radar altimetry algorithms is described using the Gulf of Mexico as a test bed. This is followed by two recent storms where rapid intensification occurred relative to warm ocean features such as the Loop Current/WCR Complex. Recommendations for future research efforts are summarized in concluding remarks.

2. SST VERSUS HEAT POTENTIAL

Palmen (1948) noted that warm, pre-existing SSTs in excess of 26°C were a necessary, but insufficient condition for cyclogenesis. Once the tropical cyclone (TC) develops and translates over the tropical oceans, statistical models suggest that climatological SSTs (OML temperatures) describe a large fraction of the variance (40 to 70%) associated with wind speed increases (DeMaria and Kaplan 1994). However, these models neither account for layer depths where temperatures exceed the 26°C temperatures nor advective tendencies by basic-state oceanic currents.

A common perception of air-sea coupling in TCs is that SST represents the only important oceanic parameter for their maintenance (Palmen 1948). To illustrate that OML temperatures are important, a highly idealized case is considered where the surface buoyancy

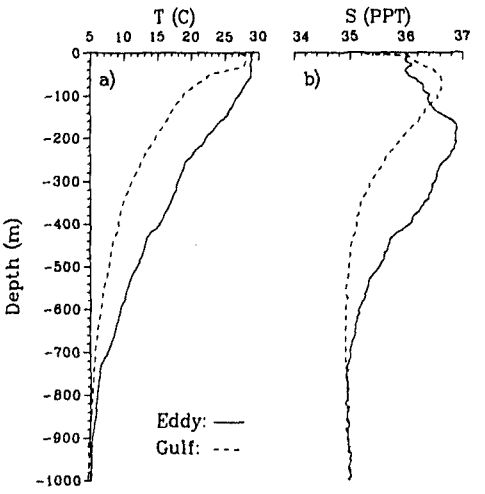

Figure 2: a) Temperature, and b) salinity profiles from two AXCTDs in the WCE/WCR (solid) and Gulf water (dash) deployed from the NOAA WP-3D.

flux is set to zero in a 1-dimensional, deepening mixed layer based upon Kraus and Turner (1967) given by:

$$\frac{dh}{dt} = \frac{1}{\Delta T}\left\{\frac{2}{\alpha g h}\left(\frac{\rho_a c_d}{\rho_o}\right)^{\frac{3}{2}} W^3\right\}, \qquad (1)$$

where h is the OML depth, ΔT is the temperature difference between an AVHRR-derived SST and the underlying OML temperature of 0.6°C (Shay *et al.* 1992), α is the thermal expansion coefficient (2.5 x 10^{-4} $°C^{-1}$), g is the acceleration of gravity (9.81 m s^{-2}), ρ_o is the water density (1.026 x 10^3 kg m^{-3}), ρ_a is the air density (1.2 kg m^{-3}), c_d is the bulk aerodynamic drag coefficient (1.3 x 10^{-3}), and W is the wind speed at 10 m.

This simple model is solved for the time required for nominal wind speeds of 4 to 10 m s^{-1} to erode thin SST layers of thicknesses 0.5 m, 1 m, and 3 m that usually overlie an OML. For a ΔT of 0.6°C, the time required to erode the thin layer from an AVHRR-derived SST ($\approx$ mm thick) is a fraction of an hour even for a 4 m s^{-1} wind speed. If the 3 m depth is chosen for the same wind condition, the time required to vertically mix it is 15 h. As the winds increase, however, the required time to erode even a 3 m layer decreases substantially from 2.7 h for a 7 m s^{-1} wind speed to less than an hour for a 10 m s^{-1} surface wind speed. As winds increase to gale force (> 17 m s^{-1}), the TC removes heat from the OML. The implication here is that the underlying oceanic structure has far more importance to the heat and moisture fluxes feeding the storm than just SST as observed in the hurricane Opal case (Shay

Date	AXBTs	AXCPs	AXCTDs
03 Aug 1999	46(3)	2(0)	2(1)
06 Aug 1999	18(0)	18(3)	16(2)
02 Oct 1999	14(0)	8(0)	8(1)
04 Oct 1999	8(2)	6(1)	5(1)
Success Rate	**94%**	**88%**	**84%**
10 Aug 2000	36(5)	1(0)	3(0)
13 Sept 2000	20(3)	16(3)	15(1)
21 Sept 2000	45(4)	0(0)	0(1)
01 Oct 2000	37(4)	9(2)	4(2)
Success Rate	**88%**	**81%**	**86%**

Table 1: Deployed probes during the 99 and 00 hurricane seasons. Numbers in parentheses indicate probe failures.

et al. 2000). Since the degree of upper ocean cooling is also a function of the OML depth, the regions of deep warm layers (i.e. WCR) thus provide more heat to the storm than regions of shallow OMLs (i.e. Gulf Common water).

3. RECENT IN SITU MEASUREMENTS

Research flights over the Loop Current in the eastern Gulf of Mexico were conducted on the NOAA WP-3D research aircraft over the past two seasons (Table 1). Grids of Airborne eXpendable Current Profilers (AXCPs), Airborne eXpendable Conductivity Temperature and Depth (AXCTDs) profilers and Airborne eXpendable Bathythermographs (AXBTs) were deployed during quiescent atmospheric conditions. As listed in Table 1, success rates exceeded 80%, including the deployment of the new AXCTDs, which provide conductivity (salinity) and temperature profiles to 1000 m. The AXCTDs provide salinity (via conductivity ratios) with accuracies of about 0.05 ppt and resolution of ± 0.03 ppt to 1000 m over vertical scales of 1 m.

As shown in Fig. 2, thermal structure profiles from the Gulf of Mexico indicated that the depth of the 20 and 26°C isotherms of the warm, subtropical water were located at 260 and 130 m, respectively or nearly twice that of Gulf Common water. In the WCR, salinity changed by 1 ppt over 200 m compared to the salinity change by 0.6 ppt over 60 m in the Gulf water. This salinity gradient, coupled with stronger thermal gradients caused the buoyancy frequency to be 12 to 15 cph in the Gulf Common water compared to 6 to 8 cph in the WCR water (not shown). In this regime, salinity is important to the upper ocean mixing and has similar characteristics to those observed in the western Pacific Ocean warm pool (Lukas and Lindstrom 1991).

Given the depth of warm ocean features, these deeper profilers are useful in determining the horizontal structure of heat potential and geostrophically balanced current fields (steady-state). Based on representative velocity (V) and length (L) scales, the advective time scale ($\frac{L}{V}$) is about 1.5 days in this oceanic regime. As shown in Fig. 3, the integrated oceanic heat potential estimates were objectively analyzed using temporal and spatial scales based on the hurricane Gilbert data set (Shay *et al.* 1992). As the depth of the 26°C isotherm depicts the top of the cooler thermocline water, subtropical water is distributed over deep layers ($\approx$ 130 m deep) compared to 35 to 40 m in the Gulf Common water. Given these differing depths, observed heat potential estimates of 130 KJ cm^{-2} in the Loop Current and WCR were well above those values in the Gulf Common water. Interestingly, the integrated heat potential estimates suggest a value of 1 KJ cm^{-2} m^{-1} at least in the Loop Current/WCR complex. These anomalously large values for heat potential represent a significant heat reservior for storms to tap. Note that the WCR separated from the Loop Current over a two-month period as suggested by the Oct 1999 observations.

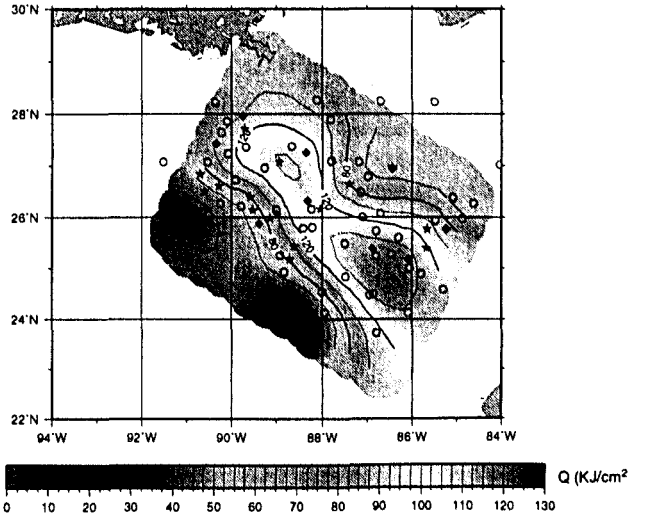

Figure 3: Ocean heat potential (color) and isotherm depth of the 26°C water (contour: m) based on AXCPs (star), AXCTDs (diamond), and AXBTs (circle) deployed in the eastern Gulf of Mexico in Aug 99 from a NOAA WP-3D flight.

4. RADAR ALTIMETRIC ESTIMATES OF HEAT POTENTIAL

Satellite altimetry data has proven to be a useful tool to study ring/eddy dynamics by acquiring continuous global coverage of surface height anomaly (SHA) fields (Goni *et al.* 1997). Unlike AVHRR imagery, altimeter data are unaffected by cloud obscuration

and can provide information on the vertical ocean structure if complemented by historical hydrographic data. Given the relatively slow translational speeds of mesoscale ocean features ($\approx$ a few km d^{-1}), the SHA data from the altimeter detects and locates warm mesoscale features, usually identified as positive SHA values. The data used in this study are derived from TOPEX/Poseidon and ERS-2 radar altimeters (Cheney *et al.* 1994). The TOPEX altimeter measures the sea level beneath its groundtrack at 7 km intervals every 9.9 days where adjacent tracks are separated by about 3° (300 km) in longitude. By contrast, the repeat cycle for ERS-2 is 35 days, but with much higher horizontal resolution as adjacent tracks are less than 100 km apart. The resulting SHA data are corrected for solid and ocean tides, wet and dry tropospheric effects, ionospheric processes, electro-magnetic bias and inverse barometric corrections. The SHA fields represent sea level heights at each satellite alongtrack location referenced to the mean sea level heights based on several years of measurements. The 7 km-alongtrack SHA are then smoothed using a 30 km running mean filter.

As shown in Fig. 4a,b, comparison of TOPEX and blended TOPEX/ERS-2 SHA fields have differing characteristics based on their ground tracks noted above. These ground tracks have consequences on resolving the mesoscale eddy field in the Gulf of Mexico where ring diameters are O(200 km). Using the parameter matrix scheme of Mariano and Brown (1992), and the parameters from the hurricane Gilbert data set (Shay *et al.* 1992), the SHA fields from TOPEX and blended (TOPEX/ERS-2) data set were objectively analyzed. This analysis technique consists of decomposing a scalar observation into a large-scale or trend field, natural field variability on the mesoscale or synoptic time scale and the combined effects of unresolved scales (i.e. subgrid-scale noise). The trend is calculated using a least-square plane fit to the data variable. Final field estimates are the sum of the trend field and a mapped deviation field. In Figs. 4c,d, the blended fields have higher resolution and smaller mapping errors than TOPEX only 0.8 (12 cm), due to the large diamonds between the ascending and decending tracks of 300 km. Understanding and mapping measurement uncertainties is an important step in the improvement for estimating heat potential from satellite data.

These analyzed altimeter-derived SHA data calibrated by hydrographic data (i.e. temperature and salinity climatology) are then used as a proxy to monitor the upper layer thickness based on a two-layer model approximation (Goni *et al.* 1997). Mean upper layer thickness along with historical temperature and salinity profiles are used here to monitor the upper layer heat potential relative to the depth of the 26°C isotherm (Shay *et al.* 2000). This value is chosen since it represents a threshold temperature suggested for hurricane genesis by Palmen (1948). Presumably, surface fluxes would be small below this value.

If the vertical ocean structure is approximated by a two-layer fluid, the upper layer thickness (h_1) can be estimated from the altimeter-derived SHA (η') field, provided that the mean upper layer thickness ($\overline{h}_1$) and reduced gravity (g') fields are known to a first-order from historical measurements based upon the expression:

$$h_1(x,y,t) = \overline{h}_1(x,y) + \frac{g}{g'(x,y)}\,\eta'(x,y,t), \qquad (2)$$

where $g' = \epsilon g$, g is the acceleration of gravity, and:

$$\epsilon(x,y) = \frac{\rho_2(x,y) - \rho_1(x,y)}{\rho_2(x,y)}, \qquad (3)$$

where $\rho_1(x,y)$ and $\rho_2(x,y)$ represent upper and lower layer densities, respectively. The upper layer thickness is defined from the sea surface to the depth of the 20°C isotherm. Early studies of the vertical structure of rings in the Gulf of Mexico show that the largest vertical temperature gradients are located between 15 and 21°C. Based upon temperature and salinity variability from hydrographic measurements, the choice of the 20°C isotherm depth is appropriate for the assumed two-layer ocean in this analysis. That is, the 20°C isotherm separates two layers of differing densities in and outside the WCR (see Fig. 4 in Shay *et al.* (1998)). However, in this two-layer approximation (Goni *et al.* 1997), the density is considered constant in the upper layer defined by the depth of the 20°C isotherm.

Climatology based upon Levitus (1984) is used to estimate both reduced gravity (g') and mean upper layer thicknesses ($\overline{h}_1$). Central to this question is the determination of an appropriate climatology of the upper layer thicknesses representing the depths of the 20°C and 26°C isotherms. Shay *et al.* (2000) used an annual climatology (Fig. 5) for the depth of the 26°C isotherm. These estimates oversmooth the penetration of the Loop Current into the Gulf of Mexico compared to a hurricane seasonal climatology (Fig. 6). Mainelli-Huber (2000) found improved agreements with in situ data with a hurricane (six-month average) climatology particularly during periods when the Loop Current was located well into the Gulf of Mexico. Deeper layer thicknesses exceeding 100 m are aligned with the axis of the Loop Current along 84°W. Generally, reduced gravities (not shown) range from 2 to 6 $\times 10^{-2}$ m s^{-2}, suggestive of a stratified ocean. Larger values of reduced gravities are associated with the core of the

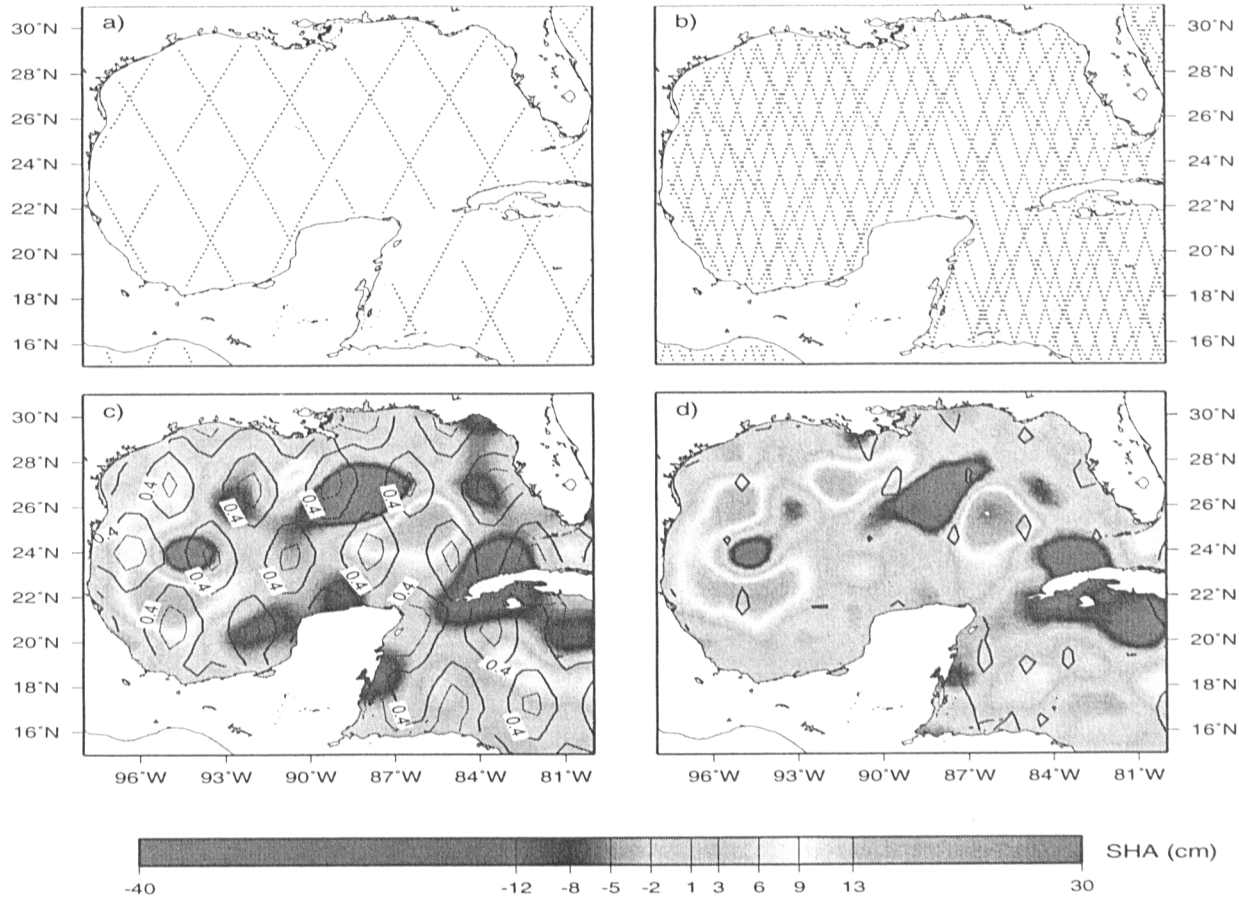

Figure 4: a) TOPEX and b) blended TOPEX/ERS-2 ground tracks in the Gulf of Mexico, objectively analyzed SHA fields (cm) and mapping errors for c) TOPEX and d) blended fields. A mapping error of 0.4 (darker contours) equates to a SHA error of 8 cm, 0.8 (lighter contours) represent 12 cm.

Loop Current, and the fresher water influx from the Mississippi River Delta along the shelf in the northern part of the basin. As indicated by Fig.2, the maximum upper layer thickness for the 20°C isotherm depth in the Loop Current exceeds 250 m north of the Yucatan Straits.

Hydrographic data from the Gulf of Mexico were used to determine an empirical relationship between the depth of the upper layer thicknesses (i.e. depth of the 20°C isotherm) and the depth of the 26°C isotherm (referred to as H), which is more relevant for hurricanes (Palmen 1948, DeMaria and Kaplan 1994). As a first approximation, a linear regression is made between H and h_1, yielding a relationship where the upper layer thickness is approximately twice the depth of the 26°C isotherm:

$$H(x,y,t) \;=\; 0.48\, h_1(x,y,t) - 5. \qquad (4)$$

This linear regression is correlated at a level of 0.77 over most of the Gulf of Mexico. A large fraction ($\approx$ 98%) of the data is within one standard deviation from the regression line. This procedure allows the conversion of the upper layer thickness field relative to h_1 based on the two-layer model to maps of H. Note that the relative ratios of these two isotherms do not necessarily agree with this empirical relationship outside of the Gulf of Mexico (Mainelli-Huber 2000).

The depth to which the temperature exceeds 26°C is proportional to the *hurricane heat potential* (Leipper and Volgenau 1972). This definition is arbitrary in the sense that the average air temperature is typically 24 to 26°C. In warm baroclinic structures, the 26°C water is distributed over deep layers ranging from 80 to 120 m deep (see Fig. 3). The heat potential of the upper layer relative to the depth of the 26°C isotherm:

$$Q(x,y,t) = \rho c_p \Delta T(x,y,t) \Delta z(x,y,t), \qquad (5)$$

where ρ is the average oceanic density taken as 1.026 g cm^{-3}, c_p is the specific heat at constant pressure taken as 1 cal gm^{-1} °C^{-1}, and ΔT is the difference between

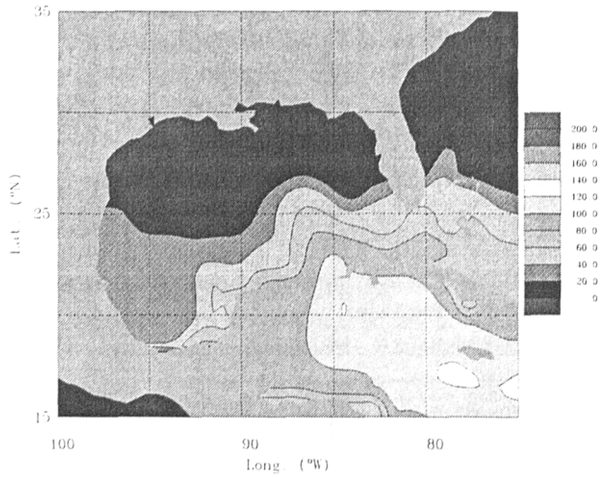

Figure 5: a) Annual climatology of the depth of the 26°C isotherm in the Gulf of Mexico (Mainelli-Huber 2000).

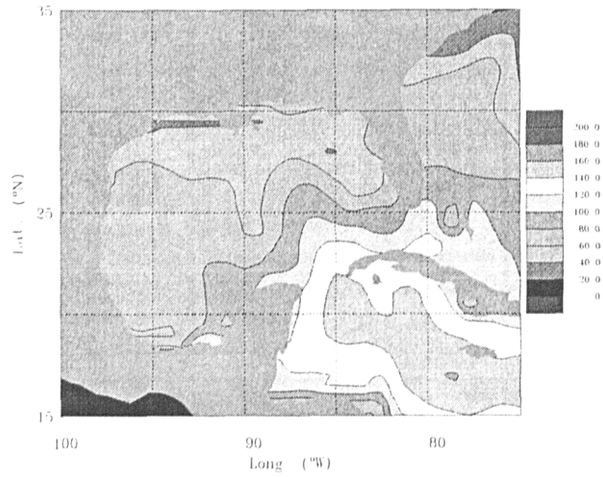

Figure 6: a) Hurricane season climatology of the depth of the 26°C isotherm in the Gulf of Mexico (Mainelli-Huber 2000).

the SST and 26°C summed over a depth interval Δz. If vertical structural measurements are available at a given depth interval, the heat potential expression is easily solved by vertical integration. However, *in situ* thermal and momentum structure observations are not always available, and in the summer months one of the setbacks is the spatially uniform SSTs above 29°C with little thermal contrast in the Gulf of Mexico (see Fig. 6 of Shay *et al.* 2000). From a bulk perspective, if Δz is taken as H, the depth of the 26°C isotherm, then (5) becomes:

$$Q(x,y,t) = A_1 \rho c_p \nabla_z T(x,y) H^2(x,y,t), \qquad (6)$$

where $\nabla_z T$ is the mean vertical temperature gradient between the surface and the 26°C isotherm obtained from AVHRR-derived SSTs and historical hydrographic data. Based on regression analyses, we have found a slope (A_1) of 0.8 to 0.85 between the satellite derived and the integrated thermal structure from the aircraft profiles (see Table 1). By multipling the expression by the regression slope (0.83) the gradient and integral methods begin to converge towards a realistic value of heat potential. Our approach is also being applied to available Lagrangian float data (T,S) in the western Atlantic Ocean basin to continue to refine this estimate through regression analyses.

5. STORM INTERACTIONS

Similar to the explosive nature of hurricane Opal, hurricanes Bret (August 1999) and Keith (October 2000) rapidly deepened from tropical storm status to category 4 storms in less than 24 hours. As shown in Fig. 7, Bret deepened to a category 4 storm over an area where two warm ocean features (heat potential > 80 KJ cm^{-2}) were located in the western Gulf of Mexico (Goni *et al.* 2000). By differencing pre and post-storm heat content data derived from the TOPEX-derived surface height anomaly field (SHA), normalized heat potential by the threshold value of 16.7 KJ cm^{-2} (Leipper and Volgenau 1972), changed by a factor of about 4 in this region. Thermal profiles from AXBTs also showed that 29°C water extended to 50 m depths. Hurricane Keith rapidly intensified from tropical storm to a category 4 storm in the northwestern Caribbean Sea where the heat potential exceeded 120 KJ cm^{-2} (Fig. 7b). These rapid-intensifiers occurred under favorable atmospheric conditions juxtaposed with high heat potential regimes. For ten storms over the past three hurricane seasons, Mainelli-Huber (2000) found maximum cross correlations between wind speed and heat potential changes ranging between 0.7 to 0.9. These heat potential changes (3 to 4 times the threshold) lead the wind speed by 12 to 18 h. Thus, mapping the heat potential is important even for slowly developing storms.

For this reason, oceanic and coupled models must have realistic ocean conditions to correctly simulate the response, and eventually forecast intensity. Jacob (2000) has showed that the choice of the entrainment mixing scheme is not only central to how the ocean mixed layer cools and deepens, but also affects the available heat to the storm via surface fluxes. By contrast, negative feedback occurs for a storm moving over regions of thin ocean mixed layers (i.e. shallow thermocline) where shear-induced mixing events cool the deepening layer at 1 to 2 radii of maximum winds in the storm's right-rear quadrant (Shay *et al.* 1998; Jacob *et al.* 2000). Understanding the impact of oceanic

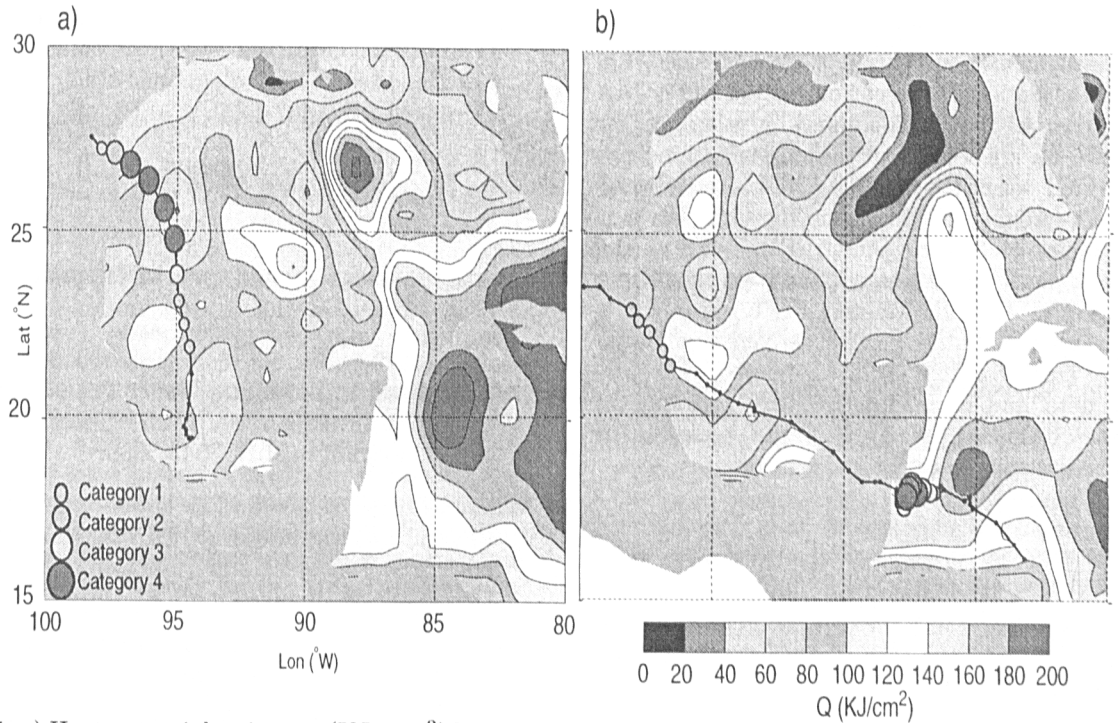

Figure 7: a) Heat potential estimates (KJ cm^{-2}) based on a hurricane climatology and the SHA field ftom TOPEX radar altimetry prior to hurricanes a) Bret (1999) and b) Keith (2000) relative to the track and intensity (legend in upper left of panel a). Notice that in panel a, WCR is just beginning to spin off the Loop Current at 28°N in the Gulf of Mexico in Aug 1999 (Images courtesy of M. Mainelli of TPC).

feedback is crucial to accurately forecasting storm intensity change. In this context, the OML structure and thermocline depth (including current and current shear) is fundamentally important to both feedback regimes as these processes modulate the amount of heat available to the storm.

6. CONCLUDING REMARKS

Observational (satellite and *in situ*) evidence supports the premise that when neutral or favorable atmospheric conditions (weak shear) are juxtaposed with high levels of oceanic heat potential, explosive deepening in hurricanes may occur as observed in recent hurricanes (Opal, Bret, and Keith). Even for weak storms encountering the Loop Current or WCRs, intensification was observed in Hurricane Gordon and Tropical Storm Helene (2000) despite unfavorable atmospheric conditions.

The key finding emerging from our research is the integrated thermal structure (heat potential) is a more effective measure of the ocean's influence on storm intensity than just SST. That is, the upper ocean structure must be accurately accounted for in the models with realistic ocean mixing parameterization schemes based on observations. Thin OML deepen and cool very quickly and may cause negative feedback to the atmosphere to occur. In regimes of deep OML, there is reduced negative feedback as the layer does not significantly cool and deepen. For example, the upper ocean (SST) cooled by less than 1°C in the WCR during Opal's passage as observed at a NOAA data buoy (Shay *et al.* 2000).

Implicit in these satellite algorithms is the acquisition of high-quality ocean structure measurements before, during and after hurricane passage. These data, including lagrangian float data, are needed to refine the algorithms to estimate heat potential. Three dimensional snapshots of the atmospheric and oceanic structure are not only important for the evaluation of remotely sensed signatures from radar altimetry (Shay *et al.* 2000; Mainelli-Huber 2000), but they are crucial in evaluating oceanic and coupled model simulations. An important ingredient in these coupled models is the parameterization of air-sea fluxes. Little is known about these fluxes in high wind conditions. Thus, to examine the physics of these processes, and to improve model parameteriztions, coupled observations are needed for rigorous, detailed comparisons to model generated fields. The TC community has now entered a **new era of hurricane intensity forecasting** where observed and modeled fields must be examined carefully to undertand these processes that

contribute to intensity (Marks *et al.* 1998).

Acknowledgments: Research effort has been supported by the National Science Foundation and NOAA through grant ATM-97-14885 and ATM-0108218. We are grateful for the efforts of the pilots, technicians, engineers and scientists at NOAA's Aircraft Operation Center (AOC) and Hurricane Research Division (HRD). James McFadden (AOC), Frank Marks and Peter Black (HRD) plan research flights on the NOAA heavy aircraft. Michelle Mainelli (TPC) kindly provided the heat potential images derived from radar altimetry, Daniel Jacob (RSMAS) objectively analyzed the data, and Tom Cook (RSMAS) provided the graphics. Bob Cheney (NOAA NESDES) provided the SHA anomaly fields from the radar altimeters.

7. REFERENCES

Bosart, L., , C. S. Veldon, W. E. Bracken, J. Molinari, and P. G. Black, 2000: Environmental influences on the rapid intensification of hurricane Opal(1995) over the Gulf of Mexico. *Mon. Wea. rev.*, **128**, 322-352.

DeMaria, M., and J. Kaplan, 1994: Sea surface temperature and the maximum intensity of Atlantic tropical cyclones. *J. Climate*, **7**, 1324-1334.

Elsberry, R. L., G. H. Holland, H. Gerrish, M. DeMaria, and C. P. Guard, 1992: Is there any hope for tropical cyclone prediction?- A panel discussion. *Bull. Amer. Meteor. Soc.*, **73**, 264-275.

Goni, G. J., S. L. Garzoli, A. Roubicek, D. B. Olson, and O. B. Brown, 1997: Agulhas ring dynamics from TOPEX/Poseidon satellite altimeter data. *J. Mar. Res.*, **55**, 861-883.

Goni, G., L. K. Shay, P. G. Black, S. D. Jacob, T. M. Cook, J. Cione, and E. Uhlhorn, 2000: Role of the upper ocean structure on the intensification of hurricane Bret from satellite altimetry, In *Proceedings of 24th Conference on Hurricanes and Tropical Meteorology*, 29 May-2 June, 2000, American Meteorological Society, Boston, Mass, J5-J6.

Hong, X., S. W. Chang, S. Raman, L. K. Shay, and R. Hodur, 2000: The interaction of hurricane Opal (1995) and a warm core ring in the Gulf of Mexico. *Mon. Wea. Rev.*, **128**, 1347-1365.

Jacob, S. D., 2000: The role of oceanic mesoscale variability on the tropical-cyclone induced response. **PhD Dissertation**, Rosenstiel School of Marine and Atmospheric Science, University of Miami, Miami, FL 33149, 169pp.

Jacob, D. S., L. K. Shay, A. J. Mariano, and P. G. Black, 2000: Mixed layer heat balance during hurricane Gilbert: A diagnostic study. *J. Phys. Oceanogr.* **30**, 1407-1429.

Leipper, D., and D. Volgenau, 1972: Hurricane heat potential of the Gulf of Mexico. *J. Phys. Oceanogr.*, **2**, 218-224.

Levitus, S., 1984: Annual cycle of temperature and heat storage in the world's ocean. *J. Phys. Oceanogr.*, **14**, 727-746.

Lukas, R., and E. Lindstrom, 1991: The mixed layer of the western equatorial Pacific Ocean. *J. Geophys. Res.*, **96(suppl)**, 3343-3358.

Mainelli-Huber, M., 2000: The upper ocean's role on tropical cyclone intensity. **MS Thesis**, Rosenstiel School of Marine and Atmospheric Science, University of Miami, Miami, FL 33149, 89pp.

Mariano, A.J., and O.B. Brown, 1992: Efficient objective analysis of heterogeneous and nonstationary fields via parameter matrix. *Deep Sea Res.*, **7**, 1255-1271.

Marks, F., L.K. Shay and PDT-5, 1998: Landfalling tropical cyclones: Forecast problems and associated research opportunities: Report of the 5th prospectus development team to the U.S. Weather Research Program, *BAMS*, **79**, 305-323.

Palmen, E., 1948: On the formation and structure of tropical cyclones. *Geophysics*, **3**, 26-38.

Shay, L. K., P. G. Black, A. J. Mariano, J. D. Hawkins, and R. L. Elsberry, 1992: Upper ocean response to hurricane Gilbert. *J. Geophys. Res.*, **97(12)**, 20,227-20,248.

Shay, L. K., A.J. Mariano, S. D. Jacob, and E. H. Ryan, 1998: Mean and near-inertial ocean current response to hurricane Gilbert. *J. Phys. Oceanogr.*, **28**, 859-889.

Shay, L. K., G. J. Goni, and P. G. Black, 2000: Effects of a warm oceanic feature on hurricane Opal. *Mon. Wea. Rev.*, **128**, 1366-1383.

P1.1 SNOW EMISSIVITY SIMULATED USING MIE THEORY

Banghua Yan[1*] and Fuzhong Weng[2]
[1]Decision Systems Technologies/RDC, Rockville, MD
[2]NOAA/NESDIS/Office of Research and Applications, Camp Springs, MD

1. INTRODUCTION

Satellite observations using microwave radiometers operating near the window regions are strongly affected by surface emissivity. Presently, the measurements obtained over land are not directly utilized in numerical weather prediction models because of uncertainties in estimating the emissivity. A model was developed to simulate the microwave emissivity over various land conditions by Weng et al. (2001). However, the discrepancy between simulated and observed emissivity on the snow conditions is quite significant especially for higher microwave frequencies due to inaccurate snow optical parameters based on the small perturbation method (SPM) developed by Tsang et al. (1985) that is valid only for lower frequencies. This study will develop a new method to compute the snow optical parameters using Mie theory. The coherent scattering due to closely spaced particles within a snow layer is taken into account in optical properties of snow layer by introducing an effective permittivity of the snow layer.

2. SNOW EMISSIVITY MODELING

A snow layer can be viewed as a homogeneous medium embedded densely with needle-shaped ice particles and be approximately modeled by a collection of spheres with an effective radius. Basing upon this model, the expressions of the extinction and scattering coefficients, and asymmetry factor for a snow layer can be determined by Mie theory as a function of snow parameters and incident frequency. The coherent scattering among ice particles has been taken into account in all of these optical parameters by introducing an effective permittivity of the snow layer that is a function of the volume fraction of ice particles in addition to the permittivities of both ice particle and its background medium. Using the land emissivity model developed by Weng et al. (2001), the snow emissivity is expressed as a function of the frequency and snow parameters, such as the effective particle size, particle volume fraction and snow depth. The optical parameters for snow medium are computed by Mie theory.

*Corresponding author address: Banghua Yan, NOAA Science Center, 5200 Auth Rd, Rm 601, Camp Springs, MD 20746

2.1 Snow Emissivity Spectrum

The incident frequency modulates the spectral dependency of snow emissivity. Figure 1 shows the simulated emissivities at both horizontal and vertical polarization as a function of the frequency. As a comparison, the simulated ones by employing the optical properties computed by the SPM are shown in the figure. Optical depth and single scattering albedo for the snow layer computed by Mie theory and SPM are also shown. One found that the emissivity decreases with frequency and that the emissivities simulated by employing the SPM optical properties decreases more quickly than ones by Mie theory at high frequencies.

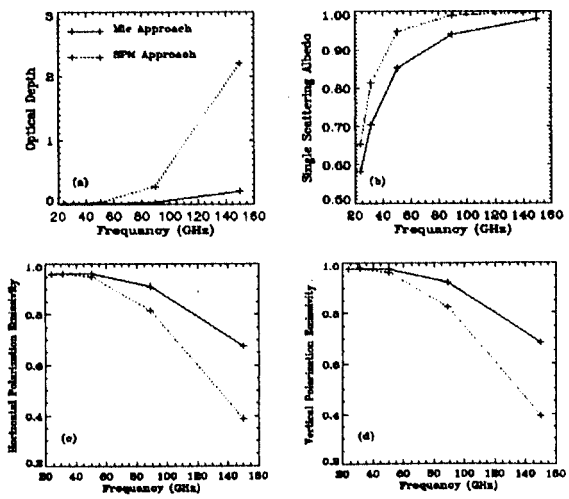

Fig.1 Simulated emissivities at both horizontal and vertical polarization as a function of the frequency, where the effective radius of ice particle is 0.3 mm, snow depth is 100 mm and volume fraction 0.1. (a) Extinction optical depth. (b) Single scattering albedo. (c) Horizontal polarization emissivity. (d) Vertical polarization emissivity.

The snow depth is an important snow parameter and influences the optical depth and then emissivity. Figure 2 is the simulated emissivity as a function of the snow depth at three different ice sizes. One found that a stronger depth-dependence is shown at high frequency or at larger ice size than that at lower frequencies or at smaller size.

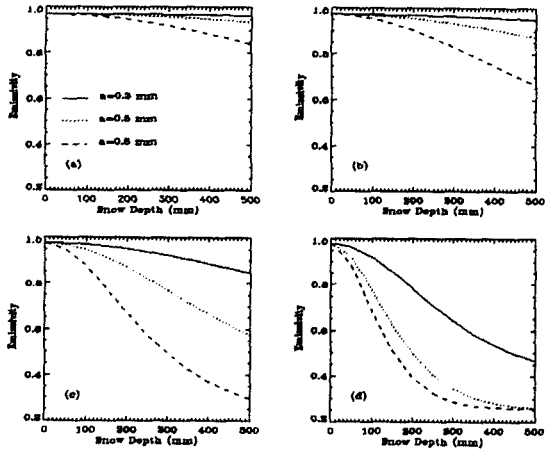

Fig. 2 Simulated emissivity as a function of the snow depth at three ice sizes where the volume fraction is 0.1. (a) 23.8 GHz. (b) 31.4 GHz. (c) 50.3 GHz. (d) 89.0 GHz.

The volume fraction affects the emission of the snow medium. Figure 3 is the simulated emissivity as a function of the volume fraction at four different frequencies. One found that at lower frequencies, the snow emissivity weakly depends on the volume fraction, and at high frequencies the snow emissivity first decreases and then increases with the volume fraction. A reason for this variation is due to that the effect resulting from the asymmetry factor is opposite to that from both the extinction optical depth and single scattering albedo on the volume fraction-dependency of the emissivity.

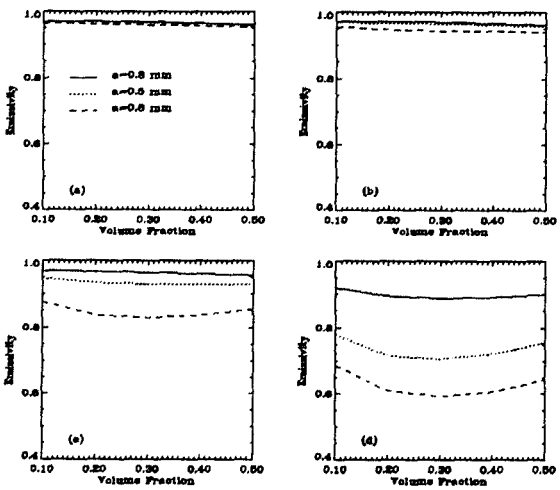

Fig. 3 Simulated emissivity as a function of the volume fraction at three ice sizes. (a) 23.8 GHz. (b) 31.4 GHz. (c) 50.3 GHz. (d) 89.0 GHz.

2.2 Intercomparison Of Simulations and Measurements

A simple comparison is carried out between the simulated and measured snow emissivity. The measured data is the ground-based measurements of snow emissivities obtained by Matzler at al. (1994). The simulated data are obtained using the microwave land emissivity model developed by Weng et al. (2001) with snow optical properties computed by the Mie theory. Fig. 4 is a comparison of the emissivity spectra over the snow condition in the range of 4.9 and 94 GHz between the simulations and measured results. Results by employing the snow optical properties computed by the SPM are shown in the figure. One found that the discrepancy between simulated and observed snow emissivities is reduced when optical properties computed by Mie theory are employed compared to these by employing the SPM data.

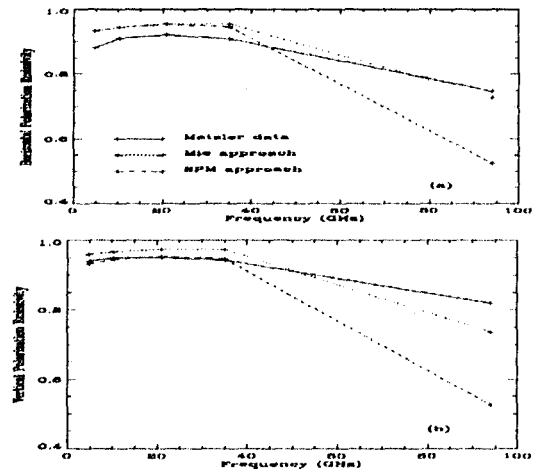

Fig. 4 Comparison of the emissivity spectra over snow condition in the range of 4.9 and 94 GHz between the simulations obtained using the model and the observations.

3. CONCLUSIONS

The snow emissivity model is derived as a function of the effective particle size, particle volume fraction and the snow depth. It is shown that the discrepancy between simulated and observed emissivity on the snow conditions is reduced by employing snow optical properties computed by Mie theory. More validations of snow emissivity need to be carried out.

Leung Tsang, J.A.Kong, R. T. Shin, 1985: Theory of microwave remote sensing. A Wiley-Interscience Publication.

Matzler, C., 1994: Passive microwave signatures of landscapes in winter, *Meteor. Atmos. Phys.*, **54**, 241-260.

Weng, F., B. Yan, and N. Grody, 2001: A microwave land emissivity model, *J. Geophy. Res.*, in press.

P1.2 SNOW COVER EXTENT OVER SOUTH AMERICA DERIVED FROM PASSIVE MICROWAVE AND VISIBLE/INFRARED OBSERVATIONS

Peter Romanov* and Dan Tarpley
NOAA/NESDIS, Office of Research and Applications, Camp Springs, MD 20746-4304

1. INTRODUCTION

Microwave measurements from polar orbiting satellites are an important element of the global snow cover monitoring system. The primary microwave snow product generated at the National Environmental Satellite and Data Information Service (NESDIS) of the National Oceanic and Atmocspheric Administration (NOAA) is based on observations from the Special Sensor Microwave Imager (SSM/I) onboard the Defense Meteorological Satellite Platform (DMSP). Snow maps are produced daily and cover the globe at a resolution of 30 km. For the Northern Hemisphere several other satellite-based snow products are available operationally, (Ramsay, 1998; Romanov, 2000), which explains the fact that microwave snow maps currently find a limited use in the current operational applications. In the Southern Hemisphere, and in particular over South America, where seasonal changes of snow cover are most substantial, SSM/I observations remain virtually the sole operational source of data on snow cover areal extent and spatial distribution. The fourteen year time series of SSM/I observations contain indispensable information on seasonal and interannual variability of snow cover in the Southern Hemisphere. However these data can be used for climatological analysis only after a proper validation of snow retrievals is made.

In this study we compare SSM/I snow retrievals over South America to another snow cover product, which is derived within a recently-developed automated snow monitoring system. The latter system is specially designed for mapping snow over South America and is based on observations in the visible, middle infrared and infrared (vis/mir/ir) from the Imager instrument onboard Geostationary Operational Environmental Satellite (GOES). The results of the comparison are used to assess the accuracy of microwave-based snow retrievals and their applicability for studies of seasonal and long-term changes of snow cover in South America.

2. MICROWAVE SNOW PRODUCT

Identification of snow cover from satellites using multispectral passive microwave measurements is based on a specific "scattering" spectral signature of snow, caused by decreasing emissivity and, hence, the decreasing brightness temperature of the emitted radiation, with increasing of the frequency. Non-precipitating clouds are essentially transparent in the microwave, which allows for practically all-weather snow cover monitoring. At NOAA/NESDIS a special technique was developed to derive global maps of snow cover from observations of a 7-channel SSM/I instrument onboard DMSP satellite (Grody and Basist, 1996). SSM/I-based snow maps are generated daily at a 30 km resolution and are available at http://orbit-net.nesdis.noaa.gov/arad2/html/microwave_daily.html). For climatological applications another microwave product was developed, where daily snow detection data are averaged on a monthly basis to derive frequency of occurrence of snow cover within $1^\circ \times 1^\circ$ cells. Daily snow maps are produced for every operational DMSP satellite, whereas data from only one satellite (currently DMSP F-13) are used in the monthly product. Daily and monthly snow maps are available since 1987, however the time series has a 1.5 years gap in 1990-1991 due to the failure of one of the SSM/I spectral channels critical for the snow detection.

The major deficiency of the microwave method is its inability to detect melting snow. This factor is responsible for a 10-15% average underestimate of the total snow area extent in the Northern Hemisphere. Furthermore, the spectral response of cold deserts (dry rocky soils) and precipitation is similar to snow, therefore these surfaces present a potential source of errors of snow identification in the microwave (Basist et al, 1996). The same problem is inherent to mixed snow-free land/water surfaces since their spectral response in the microwave is similar to the response of a layered perennial snow/ice cover, such as in Greenland and Antarctica (Grody and Basist, 1996).

3. SNOW MAPS FROM GOES IMAGER DATA

Multispectral measurements in the visible and middle infrared wavelengths have been extensively used to map snow for more than two decades. Most of the developed techniques have been applied to data from polar orbiting satellites (Key and Barry,1989; Hall et al., 1995). The advantage of geostationary satellites for snow cover monitoring consists in a high frequency of observations. It, first, allows to select the least cloud contaminated scene during a day and therefore to obtain a clearer view on a daily basis and, second, helps to more effectively detect clouds in the satellite imagery.

In a new automated snow mapping system developed at NOAA/NESDIS, snow maps over South America are generated using vis/mir/ir measurements from the Imager instrument onboard GOES satellite. Snow maps are produced daily at a spatial resolution of 4 km. The classification algorithm examines both spectral signatures and temporal variability of the reflectance and the brightness temperature in every

* Corresponding author address: Dr. Peter Romanov, NOAA/NESDIS, 5200 Auth Rd., Room 712, Camp Springs, MD 20746

image pixel to attribute it to one of three categories: snow cover, snow-free land surface and cloud. The daily snow cover map is then subjected to a blending procedure where pixels classified as cloudy are replaced by the most recent cloud clear data from the past observations. Therefore the final product is a binary map, which contains two categories: snow and snow-free land surface.

Daily GOES-based snow maps have been produced since May 2000 and are available on the Web at: http://orbit-net.nesdis.noaa.gov/crad/sat/surf/snow/html/snow_sa.htm. Validation of the vis/mir/ir snow product was performed primarily through visual analysis of satellite imagery, and involved a limited comparison with ground-based observations. The system was found to adequately reproduce the spatial distribution of large-scale perennial snow/glacier fields in the southern part of South America and changes in the seasonal snow cover in the middle latitudes. However it only occasionally detected snow fields and mountain ice caps with a size comparable or slightly exceeding the instrument field of view. Most of these glaciers are located in the tropical region. Poor identification of small snow/ice fields is mostly due to inaccuracy of the image navigation, which normally ranges within 4 to 6 km and due to clouds, which almost permanently mask tropical high-altitude glaciers and mountain ice caps in the daytime. It was also found, that due to a persistent cloud cover during snowfalls, a delay of one to three days may occur from the time of the snow cover onset to the time, when it is detected by the system.

4. COMPARISON OF THE SNOW PRODUCTS

The comparison of microwave and vis/mir/ir snow maps was performed over the time period from May 2000 to June 2001. Microwave snow maps were derived using data acquired at morning overpasses of DMSP F-13 satellite. Observations from one SSM/I instrument do not provide a complete coverage of the whole South America on a daily basis, therefore to compare the products we used monthly statistics of snow cover retrievals. Daily snow maps were compiled to derive monthly frequency of snow occurrence at spatial resolution of 30 km for SSM/I and 4 km for GOES Imager data. For convenience, monthly snow frequency was then converted into effective monthly average fractional snow cover, i.e., a map pixel identified as snow-covered 50% of time during the month was assigned a 0.5 monthly average fractional snow cover. Correspondingly, the monthly average snow-covered area was determined as a product of the fractional snow cover and the pixel area.

Figure 1 compares estimates of the monthly mean snow cover extent in South America derived from the vis/mir/ir and microwave products. The two data sets exhibit a good qualitative agreement on seasonal changes of snow cover. In particular, both time series reveal a double peak in the wintertime snow cover extent. However there is a significant difference in the absolute values of snow cover extent. Throughout the entire time series, the microwave product yields appreciably more snow than the GOES Imager product. At the peak of the snow season the difference amounts to about 400,000 km^2 (~400,000 km^2 vs 800,000 km^2) whereas in summer it decreases to approximately 200,000 km^2.

The comparison of maps of monthly snow frequency distribution (see Figure 2) makes it apparent, that much of the difference between estimates of the total snow covered area results from commission errors (false snow cover identification) over ocean coastlines in the microwave product. The removal of snow erroneously identified along the coastal line in microwave snow maps brings the two products to a closer agreement (see "SSM/I corrected" graph in Figure 1), however a substantial exceeding of the microwave-based snow cover area extent over the vis/mir/ir data still remains. Some of this residual difference may be explained by inability to correctly detect some of small snow/ice fields with the vis/mir/ir technique due to a persistent cloud cover. However, it is

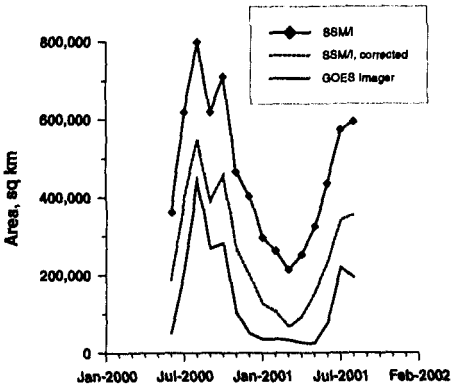

Fig.1 Snow covered area in South America estimated from SSM/I and GOES Imager data. In the "corrected" SSM/I-based snow area estimate snow cover detected along the coast line was removed

more likely that the problem lies in the microwave algorithm, which confuses snow-covered surfaces with cold snow-free rocky soils. First, a similar overestimation of snow cover extent in the microwave-derived snow product was noticed by Basist et al.(1996) in the mountainous regions of Europe, Asia and North America. The other reason to believe the overestimates are in the microwave product is based on the available information on the area of glaciers and permanent snow/ice fields in South America. The total ice-covered area in South America is estimated to be about 25,000 km^2 including about 20,000 km^2 of ice fields in Patagonia and Tierra del Fuego (Satellite Image Atlas of Glaciers, 1999). Even if snow cover erroneously detected along the coastal line is removed, the microwave product gives a much higher estimate of over 70,000 km^2 for the total summertime snow-covered area (see Figure 1). By contrast, the vis/mir/ir product offers a more reasonable estimate of ~20,000 km^2 for snow extent during the summer season.

It is worth noting that the microwave technique often fails to identify large glacierized fields located in

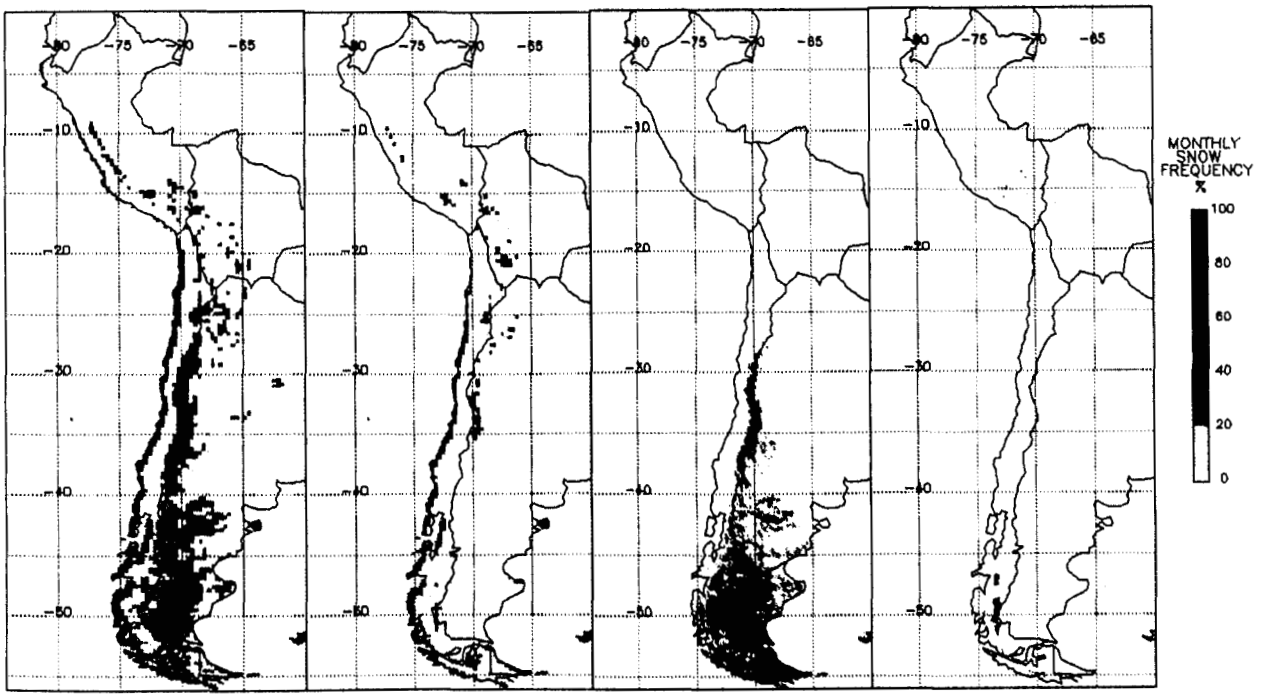

Fig.2 Monthly snow cover frequency for July 2000 and February 2001 derived from DMSP SSM/I and GOES Imager data

south of Chile. The glaciers are clearly seen in the February, 2001 snow frequency map derived from the GOES Imager data, but are hardly noticeable in the corresponding SSM/I-based snow product (see Figure 2). The failure to detect glaciers using microwave observations should be attributed to specific climatic conditions peculiar to this area, which keep the temperature of the glacier surface close to the melting point most of the year. Furthermore, precipitation in the very southern part of South America is frequent and usually comes in the form of rain or wet snow. Liquid water on top of the ice surface radically changes the spectral signature of the outgoing microwave radiation and prevents from detecting snow/ice cover.

A more detailed quantitative comparison between the vis/mir/ir and *microwave products* was performed using estimates of snow frequency compiled on a monthly basis for 1° x 1° grid boxes. A close correspondence between the two products with a correlation exceeding 0.9 and relative difference of less than 10% was found for a limited area in the southern part of South America. The area covers about 300,000 km^2 and confined to be south of Patagonia excluding glaciers and most of its mountainous section (see Figure 3). Good agreement of the two independent snow products can be viewed as an implicit indication of the consistency of SSM/I-based snow retrievals and hence, the validity of the microwave snow products in this area.

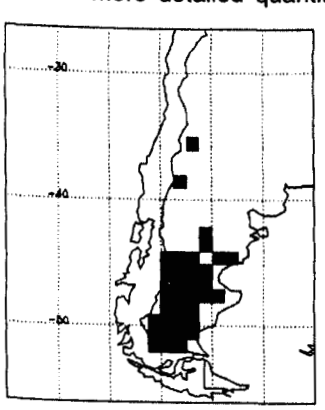

Fig.3 The area where SSM/I and GOES-based snow cover retrievals agree with each other.

5. ANALYSIS OF MULTIYEAR TIME SERIES

Time series of multiyear monthly SSM/I-based maps of snow cover frequency (converted to effective monthly average snow fraction) were processed to study seasonal and long-term changes of snow cover extent in South America. The analysis was confined to the area shown in Figure 3, where SSM/I snow retrievals proved to be consistent with the vis/mir/ir snow product.

Figure 4 shows that wintertime snow cover in the southern part of South America has experienced a significant variability during the last 14 years. The most

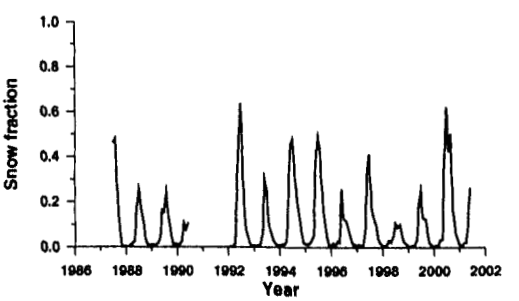

Fig 4. Time series of monthly average snow fraction for the test area in Patagonia, South America (see Fig.3) derived from SSM/I data.

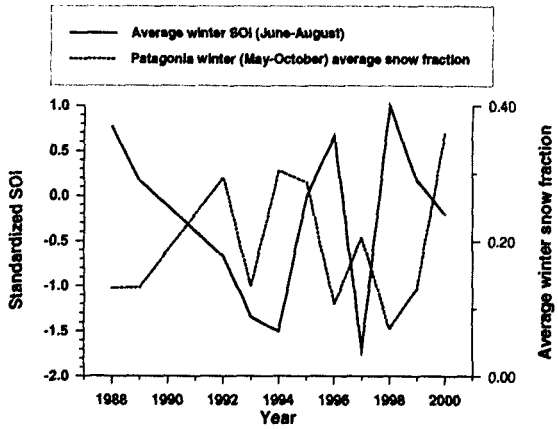

Fig.5 Time series of the average winter (May-October) snow fraction over Patagonia and the standardized values of the average winter (June-August) Southern Oscillation Index (SOI). Data for the years 1990 and 1991 are not shown because of unavailable snow retrievals during that time.

extensive snow cover was observed in 1992 and 2000, when it exceeded 60% of the study area. In 1998 the peak value of snow covered area reached only 10% of the region.

To elucidate a mechanism controlling year-to-year fluctuations of snow cover over the study area, we correlated the average area extent of snow cover for the winter season (May to October) with monthly and seasonal values of a standard Southern Oscillation Index (SOI), which is the Tahiti-Darwin surface pressure difference.

The results presented in Figure 5 reveal a distinct inverse relationship between wintertime (June-August) average SOI values and the snow cover areal extent. Data for all years except of the year 1993 fit into this pattern, i.e, periods of low SOI values are associated with a more extensive snow cover whereas the snow cover extent decreases during periods of higher SOI values. The correlation coefficient for the relationship is equal to –0.51. An even stronger negative correlation of –0.62 was found between the average winter season snow cover extent and SOI index for July. A negative correlation between SOI and snow cover extent was also reported by Cerveny et al. (1987) who analyzed NOAA/NESDIS weekly low-resolution snow maps for South America. The production of these maps was launched in 1974, but was discontinued 10 years later (see Dewey and Heim, 1983).

The possible reasons for the increase of winter snow cover associated with negative SOI values consist in the change of the wintertime atmospheric circulation pattern associated with fluctuations of SOI, which results in the increased precipitation and cooler temperatures over the southern part of South America.

5. CONCLUSIONS

The results of snow cover monitoring in South America with the new automated system based on GOES Imager observations were used to qualitatively and quantitatively evaluate snow cover retrievals from microwave measurements of the SSM/I instrument. The comparison of the microwave and the vis/mir/ir snow products revealed a significant overestimation of the snow cover areal extent in the microwave product. Overestimation occurs due to the physical limitations of the microwave snow detection method, which confuses snow covered surface with cold desert and mixed land/water surfaces. The other known deficiency of the microwave method i.e., its inability to detect melting snow or ice, results in a poor identification of large glacierized fields in South America. Therefore, available long-term SSM/I snow retrievals will be difficult to use for quantitative analysis of snow cover frequency of occurrence or its area extent at a continental scale.

We found a limited area in the southern part of South America, where microwave snow retrievals quantitatively agree with the vis/mir/ir product and adequately represent seasonal changes of the snow cover. A preliminary analysis of 14-years time series of SSM/I-based monthly snow cover statistics for this area revealed a strong inverted relationship between the winter snow cover area extent and the South Oscillation Index value.

References

Basist, A., D. Garrett, R. Ferraro, N.C. Grody, and D. Forsyth, 1996: A comparison between snow cover products derived from visible and microwave satellite observations. *J. Applied Meteor.*, **35**, 163 - 177.

Cerveny, R., B. Sketter and K.F. Dewey, 1987: A preliminary investigation of a relationship between South American snow cover and the Southern Oscillation. *Mon. Wea. Rev.*, **115**, 620-623

Dewey, K. and R. Heim, 1983: Satellite observations of variations in Southern Hemisphere snow cover. NOAA Technical Report Ness 87, US Govt. Printing Office, 20402; 83 p.

Grody, N.C. and A. Basist, 1996: Global identification of snow cover using SSM/I measurements. *IEEE Trans. Geo. Rem. Sens.*, **34**, 237 - 249.

Hall, D.K., G.A. Riggs, and V.V. Salomonson, 1995: Development of methods for mapping global snow cover using moderate resolution imaging spectroradiometer data. *Remote Sens. Env.*, 54, 127-140.

Key J. and R.G. Barry, 1989: Cloud cover analysis with arctic AVHRR data. 1. Cloud detection, *J. Geop. Res.*, 18,521-18,535

Ramsay, B., 1998: The interactive multisensor snow and ice mapping system. *Hydrological Processes*, **12**, 1537-1546.

Romanov P., G.Gutman and I.Csiszar, 2000: Automated monitoring of snow cover over North America with multispectral satellite data. *J. Appl. Met.* 39, 1866-1880.

Satellite Image Atlas of Glaciers of the World. South America, 1999: United States Geological Survey Professional Paper 1386-I Online Version 1.0 U.S. Geological Survey, U.S. Department of the Interior. Internet address: http://pubs.usgs.gov/prof/p1386i/. Ed. Williams, R.S., and J. G. Ferrigno U.S. Government Printing Office, Washington: 1999.

P1.3 RETRIEVAL AND INTERPRETATION OF SNOW COVER PARAMETERS FROM MICROWAVE REMOTE SENSING DATA

Cezar E. Kongoli [1*] and Norman C. Grody[2]

[1]QSS Group, Inc., Lanham, MD,
[2]NOAAA/NESDIS, Camp Springs, MD

1. INTRODUCTION

Snow cover is a vital component of the global energy budget and the hydrologic cycle. On average, approximately one sixth of the planet's surface is covered by snow and ice, containing about three quarters of the world's terrestrial water reserves. Due to its high albedo, high thermal emissivity and low thermal conductivity, snow cover strongly influences the overlying atmosphere (Chang et al., 1985). Snow depth and snow water equivalent (SWE) are critical snowpack parameters. The depth of snow regulates soil freezing (Flerchinger, 1991), with implications for snowmelt runoff and survival of certain crops (Kanneganti et al., 1998), while knowledge of SWE is essential for snowmelt runoff predictions. Deriving this information through satellites has several advantages over ground-based measurements provided by climate stations, the most obvious being better spatial coverage, consistency and lower cost. However, satellite retrieval of snow depth and SWE has proven to be a daunting challenge (Chang and Koike, 2000).

Passive microwave remote sensing technology provides a unique opportunity to address this challenge because of its all-weather capability and response to snow cover. Theoretically, there exists a distinct relationship between snow cover parameters and microwave brightness temperatures. Snow crystals are efficient scatters of microwave radiation. The deeper the snowpack, the more crystals are available to scatter energy away from the sensor, thus lowering the brightness temperature (Chang and Koike, 2000). However, interpretation of this relationship is severely complicated by the extremely dynamic nature of snow and spatial heterogeneity. Snow undergoes continuous structural and phase changes through the processes of accumulation, metamorphosis and compaction, stratification, and melt (US Army Corps of Engineers, 1953; Anderson, 1976), all of which are very difficult to analyze using theoretical models. For instance, the melting of the snowpack complicates the retrieval of snowdepth and SWE. At around 1.5% free water by volume, practically all information from the snowpack below the uppermost layer is lost (Edgerton et al., 1968). Under this condition, the snowpack acts more as an emitting surface than a scattering medium. The net result is an underestimation of snow depth or water equivalent, or even an estimate of no snow at all as the emission characteristics become almost indistinguishable from snow-free soil (Kunzi et al., 1982; Goodison and Walker, 1992). In contrast, the presence of depth hoar results in more scattering and lower brightness temperatures, the net result of which is an overestimation of snow depth. As a result of these ambiguities, existing algorithms are restricted to specific snow conditions, and thus they lack general validity (e.g., Foster et al., 1984; Tait, 1996; Kunzi et al., 1982; Hallikainen and Tiuri, 1982; Chang et al., 1985)

The ultimate objective of our project is to develop a snow depth retrieval algorithm based on the Advanced Microwave Sounding Unit (AMSU). This project is part of the Microwave Surface Precipitation Product System (MSPPS) ongoing project at NOAA/NESDIS. MSPPS is designed to provide operational near real time surface and precipitation products from AMSU data, critical for short and medium range weather forecasting and climate applications. A snow cover extent algorithm from AMSU data has been incorporated into MSPPS and is operational (Grody et al., 1996, 2000). However, a snow depth retrieval algorithm from satellites is still under development. Moreover, all current investigations of snow depth and SWE have been made with SSM/I data. This is the first study to report on the use of AMSU data for snow depth retrieval. The AMSU is a more recent instrument, which provides better spatial coverage and frequency range then SMM/I, but

*Corresponding Author Address: Cezar E. Kongoli, NOAA/NESDIS, 5200 Auth Rd., 601, Camp Springs, MD 20746- 4304; E-mail: Cezar.Kongoli@noaa.gov

lacks polarization information and has relative coarse resolution. A detailed review of the evolution of passive microwave sensors and their capabilities is provided by Grody et al., 2000. The results presented here provide preliminary statistics on the comparison of AMSU microwave brightness temperatures and surface observations of snow depth.

2. DATA AND METHOD OF ANALYSIS

Combinations of the NOAA-16 AMSU measurements in the 23.8 to 150 GHz range were compared with ground-based snow depth observations. Specifically, the following linear channel combinations were analyzed: TB23 - TB31, TB23 - TB89, TB89 – TB150, TB50.3, TB52.8, and TB53.7 GHz, where TB is brightness temperature measured at the indicated frequency. The first three combinations are a direct measure of the scattering of the microwave radiation by the snowpack, other variables are a measure of the surface and air temperature.

The region selected for analysis was a continuous area located between latitudes 34 and 50 north, and longitudes 89 and 100 degrees west. Daily snow depth reports across the US for the November 2000 - March 2001 season were obtained from the Cooperative Weather Stations Network of the National Weather Service. The snow depth observations represent point measurements following standard National Weather Service procedures (e.g., Doesken and Judson, 1996; Kongoli and Bland, 2000). Figure 1 shows a snapshot of the climate stations all across the US on January 21, 2001. As shown, the density of the network is spatially non-uniform. The density also varies with time, generally becoming sparser as less snow is on the ground.

Two methods of combining AMSU data with surface observations of snow depth were used. The "first method" matched each station location with the center of the corresponding pixel location of the AMSU measurements. To alleviate ambiguities resulting from melting snow, only nighttime passes were used. This approach resulted in a dataset containing match-ups of point snowdepth measurements and the microwave signatures averaged over the pixel size. The pixel size varies between approximately 50 and 150 km resolution, as the AMSU antenna scans from nadir to the limb position, respectively. Because of the non-uniformity of the spatial coverage of the climate stations, a one-to-many relationship between microwave signatures and snow depth measurements was observed to be a common occurrence. As such, clusters of climate stations as close as 20 km apart (e.g, Nebraska, Wisconsin, Montana, etc) resulted in different snow depth values corresponding to only one set of microwave signatures. To improve this sampling uncertainty, another approach was used.

In the "second method", daily snow depth measurements were averaged over an area of 1/2 degree in latitude and longitude from the center of the instrument pixel, and the average snow depth value was matched with the microwave signatures corresponding to that pixel. This resolution (approximately 100 km in size) is realistic because it reflects the average field of view of the instrument. In addition, the geographical region selected was relatively flat and homogeneous, so the within-pixel variability is smaller than in a region dominated by rugged relief. In this way, the resulting dataset contained only one-to-one match-ups between the areal snow depth average and the microwave signatures. To study spatial-temporal patterns of snow depth, the match-ups were analyzed statistically at different times of year within the period of investigation and for different areas within the selected region.

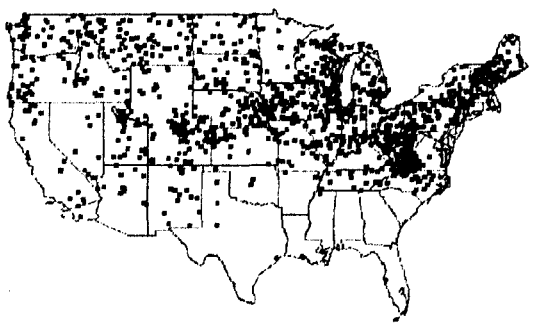

Figure 1. Climate stations on January 20, 2001

3. RESULTS AND DISCUSSION

The first sampling method gave poor correlation statistics with respect to snow depth, with overall correlation coefficient of 0.15 for the December 2000 - March 2001 period. November was left out because of a sparser climate stations network, and very shallow snow on the ground. The second method significantly improved overall and individual statistics (Tables 1 and 2). Overall, the TB23-TB31 combination was the single most significant variable to retrieve snow depth, with a multiplication coefficient value (C23-31) of 0.78 (Table 1). However, the value of this coefficient varies with month, the largest being in February. It

is interesting to note that the strength of the 23 - 89 GHz combination, the second independent variable, decreases as the snow season progresses, with the largest being in December. This demonstrates the ability of the 89 GHz channel to capture shallow snow, while lower frequencies are more suitable for retrieving deeper snow. Overall, the month of February gave the best correlation statistics. In February, most of the snowpack on the ground consists of old metamorphosed snow, captured by the TB23-TB31 GHz combination. Correlation of snow depth retrieval was higher when all six combinations (independent variables) were included in the analysis, with the highest correlation in February (Table 2). The correlation results reported here did not significantly change for specific areas within the selected region.

Table 1. Correlation statistics of snow depth retrieval (snow depth over 4 cm) based on the TB23-TB31 and TB23-TB89 GHz combinations.

	Dec.	Jan.	Feb.	Mar.	Dec .- Mar.
Mean Depth (cm)	19	23	27	28	24
Correlation	0.35	0.34	0.42	0.39	0.37
RMS error (cm)	12	14	17	16	15
C23-31	-0.67	0.03	1.8	1.01	0.78
C23-89	0.31	0.25	-0.18	-0.02	0.09
Intercept	4.82	5.32	4.65	3.92	5.39

Table 2. Multiple correlation coefficient of snow depth retrieval for specific dates and months with respect to the independent variables investigated.

Data/Month	All variables*	Two variables**
Dec. 15, 2000	0.48	0.22
Jan. 23, 2001	0.56	0.41
Feb. 19, 2001	0.51	0.46
Mar. 21, 2001	0.45	0.18
Dec. 2001	0.37	0.35
Jan. 2001	0.34	0.41
Feb. 2001	0.42	0.47
Mar. 2001	0.39	0.43
Dec.-March	0.35	0.39

** TB23-TB31 , TB23-TB89

* TB23-TB31, TB23-TB89, TB89-TB150, TB50, TB52, TB53

4. CONCLUSIONS

Snow depth and snow water equivalent (SWE) are critical snowpack parameters. However, their retrieval from satellites has proven to be a daunting challenge. Passive microwave remote sensing technology provides a unique opportunity to address this challenge because of its all-weather capability and response to snow cover. The ultimate objective of our project is to develop a snow depth retrieval algorithm based on the Advanced Microwave Sounding Unit (AMSU). This project is part of the Microwave Surface Precipitation Product System (MSPPS) ongoing project at NOAA/NESDIS. This study is the first to report on the AMSU data suitability for snow depth retrieval.

Comparison of AMSU data in the TB23-TB150 GHz range with surface observations of snow depth for the December 2000-March 2001 period revealed that the method of averaging snow depth over the pixel size of the AMSU instrument significantly improved snow depth retrieval statistics. Results showed that snow depth retrieval algorithm was different for different times of year. Overall, the TB23-TB 31 GHz combination was the most significant independent variable to retrieve snow depth, but its contribution varied through the snow season. Best retrieval results were for the month of February. Statistics improved significantly when the TB50.4, TB52.4, and TB53.7 GHz channels were included in the analysis. The contribution of the TB23 – TB89 GHz combination, the second independent variable, was small, except in December when shallow snow was more frequent than in the other months.

5. REFERENCES

Anderson, E.A., 1976: A point energy and mass balance model of snow cover. *NOAA Technical Report*, NWS **19**, US Department of Commerce, Silver Spring, Md.

Chang, A.T.C., J.L. Foster, M. Owe, D.K. Hall, and A. Rango, 1985: Passive and active microwave studies of wet snowpack properties. *Nordic Hydrology*, **16**, 57-66.

Chang, A., and T. Koike, 2000: Progress in AMSP snow algorithm development. Microw. Radiomet. Remote Sens. Earth's Surf. Atmosphere, 515-523.

Doesken, J.D., and Judsnon, A. 1996. The Snow Booklet. A Guide to the science, climatology, and measurement of snow in the United States. Colorado Climate Center,

Department of Atmospheric Sciences, Colorado State University, p. 85.

Edgerton, A.T., R.M. Mandle, G.A. Poe., J.E. Jenkins, F. Soltis, and S. Sakamato, 1968: Passive microwave measurements of snow, soils, and snow-ice-water systems. *Technical Report* N0. **4**, Office of Naval Research, Washington D.C.

Flerchinger, G.N., 1991: Sensitivity of soil freezing simulated by the SHAW model. *Transactions of the ASAE,* **34**(6), 2381- 2389.

Foster, J.L., D. K. Hall, A.T.C. Chang, and A. Rango, 1984: An overview of passive microwave snow research and results. *Review of Geophysics and Space Physics*, **22**(2), 195-208.

Goodison, B., and A.E. Walker, 1992: Data needs for detection of climate change: Some challenges. *Snow Watch '92, Report* GD-25, World Data Center A for Glaciology, 241-256.

Grody, N.C., and A.N. Basist, 1996: Global identification of snow cover using SMM/I measurements. *IEEE Transactions*, **34**(1), 237-249.

Grody, N.C., F. Weng, and R. Ferraro, 2000: Application of AMSU for obtaining hydrological parameters. *Microw. Remote Sens. Earth's Surf. Atmosphere*, pp. 339-351.

Hall, D.K., J.L. Foster, and A.T.C. Chang, 1984: Nimbus-7 SMMR polarization responses to snow depth in the Mid- western US. *Nordic Hydrology*, 15, 1-8

Hallikainen, M.T., and M.E. Tiuri, 1984: The Finnish approach to microwave remote sensing of snow. *Proceedings of lintegrated Approaches in Remote Sensing.* Guildford, UK, 8-11 April, 1984, pp. 81-87.

Kanneganti, V.R., W.L. Bland, and D.J. Undersander, 1998: Modeling freezing injury to calculate forage yield: II. Model validation and example simulations. *Agronomy Journal*, **90**, 698-704.

Kongoli, CE and W.L. Bland, 2000. Long-term snow depth simulations using a modified Atmosphere-Land Exchange model. *Agricultural and Forest Meteorology*, **104**(4), 273-287.

Kunzi, K.F., S. Patil, and H. Rott, 1982. Snow cover parameters retrieved from Nombus-7 Scanning Multichannel Microwave Radiomenter (SMMR) data. *IEEE Trans. Geosci. Remote Sens.*, 20(4), 452-467

Tait, A. 1996. Estimation of snow depth and snow water equivalent using passive microwave radiation dtata. (PhD). *University of Colorado*, Boulder, Colorado, USA.

US Army Corps of Engineers, 1956. Snow Hydrology. *US Army Corps of Engineers*, Portland, Oregon, USA.

1.5 MONITORING THE SEASONAL DECAY OF FIRST YEAR SEA ICE AT THE CANADIAN ICE SERVICE WITH NOAA AVHRR

Roger De Abreu*, Matthew Arkett and Bruce Ramsay
Canadian Ice Service -- MSC, Ottawa, Ontario, Canada.

1.0 INTRODUCTION

The Canadian Ice Service (CIS), a branch of the Meteorological Service of Canada (MSC), is mandated to continually monitor ice conditions in Canadian coastal areas in order to support ship navigation and other marine activities in waters where ice is present. Interpreting satellite image data is at the core of this monitoring task – NOAA AVHRR and RADARSAT-1 being the Service's primary data sources. The CIS receives and processes Local Area Coverage (LAC) Advanced Very High-Resolution Radiometer (AVHRR) (Kidwell, 1991) data several times daily. Although cloud cover limits the use of these data, clear sky data are routinely used to complement RADARSAT-1 coverage. The spring and summer melt of first year ice and the associated reduction in ice strength is a major determinant in the timing of Arctic marine activities in ice-covered waters. As such, the development of techniques whereby the state of Arctic first year sea ice melt can be reliably monitored with AVHRR and RADARSAT-1 is a high priority at the CIS.

This paper investigates the utility of AVHRR channel 1 and channel 2 data (hereafter AVHRR 1 and AVHRR 2 respectively) in the operational monitoring of the seasonal melt of Arctic first year ice. The sea ice volume's optical and thermal properties are modified significantly by melt-related physical changes. As a result, the appearance of first year sea ice in AVHRR data begins to change with the onset of melt conditions in the Arctic (De Abreu, 1996). This fact holds some promise for extracting information regarding the state of sea ice melt from these data.

2.0 STAGES OF FIRST YEAR SEA ICE MELT

The CIS is focusing on the following five stages of melt distilled from those proposed by Barber *et.al* (2001) : *Winter Ice, Snow Melt, Ponded Ice, Drained Ice and Rotten Ice*. The Winter Ice Stage is not a melt stage, but is useful as a baseline for detecting the onset of the melt process. During the Snow Melt Stage, liquid water content in the overlying snow volume steadily increases, snow grains increase in size and the snow volume may decrease in depth. Importantly, the strength of the ice volume begins its seasonal decline as the volume begins to warm and brine volumes increase. In a spatial sense, the icescape is still relatively homogeneous. The Ponded Ice stage is characterized by the appearance of melt ponds and the transformation of the surface into a heterogeneous mix of surface water and interstitial wet snow areas. The primary source of the melt water is the snow cover. The subsequent Drained Ice stage describes the drainage of surface water from both snow melt ponds and melted ice back to the ocean. The primary drainage paths are laterally into cracks and holes and vertically through the snow/ice volume. During the Ponded and Drained Ice Stages, the mechanical strength of the ice volume decreases dramatically (Johnston *et.al.*, 2001). As such, the detection of the onset of these two melt stages is critical from an operational perspective. The final stage, Rotten Ice, is characterized by a heterogeneous mix of open water and severely decayed ice dotted by saline melt ponds and thaw holes.

3.0 DATA AND METHODS

In order to support CIS operational analysis, AVHRR data are converted to an 8 bit product and registered to a standard projection for display and analysis. The 8 bit digital numbers (DNs) essentially represent raw counts of the reflected top of atmosphere (TOA) radiance. The data is not calibrated and the visible channels are not normalized to account for solar zenith angle dependence and/or anisotropic effects of the surface or intervening atmosphere. In order to facilitate temporal monitoring of melt conditions with these data, it is necessary to normalize these datasets. Towards this, the NOAA 14 data examined here were calibrated and nominally converted to TOA reflectance (Kidwell, 1991). In order to minimize the effects of scene anistropy, datasets were restricted to a specific sun-

* *Corresponding Author Address:* Roger De Abreu, Canadian Ice Service, Meteorological Service of Canada, Environment Canada, Ottawa, Ontario, Canada K1A 0H3
roger.deabreu@ec.gc.ca

scene-satellite geometry. Clear sky AVHRR scenes were identified manually by examining all five channels for cloud contamination and by utilizing surface-based cloud observations.

4.0 IDENTIFICATION OF ICE MELT STAGE

Operationally, the CIS requires the regular production of a chart which describes the stage of ice melt throughout the Canadian Arctic. This section assesses the potential of AVHRR data to accurately identify these melt stages. Figure 1 contains the average top-of-atmosphere reflectance calculated over a nine pixel subarea collected over the surface study area of the Collaborative Interdisciplinary Cryospheric Experiment 2000 (C-ICE '00) located in the central Canadian Arctic Archipelago (Figure 2). Of special interest is the seasonal transition of reflectance over this first-year ice study area and the possibility of identifying melt stages through the monitoring of AVHRR 1 and 2 reflectance values. Figure 2 contains subareas of AVHRR channel 1 data collected in the spring/summer of 2000.

Due to its higher sensitivity to changes in snow grain growth and increases in snow liquid water content (in the upper layers) (Warren, 1982), the departure from the Winter stage and the beginning of the Snow Melt period is first evident as a decrease in AVHRR 2 reflectance. From April 17 to June 14, AVHRR 2 reflectance decreased from 74% to 64%, while AVHRR 1 reflectance appeared to increase 2% (Figure1). However, as the snow volume thinned and a slush layer at the snow-ice interface appeared and grew, AVHRR 1 reflectance decreased to 67% by June 19, just prior to the appearance of melt ponds. The Snow Melt stage can also be identified by the increased difference between AVHRR 1 and 2 when compared to the Winter Stage. Operationally, this seasonal difference regularly manifests itself as a change in the colour of sea ice within a standard RGB colour display where AVHRR channels 1 and 2 are loaded.

Within the month of June, the transformation and removal of the highly reflective snow cover and the appearance of lower albedo melt ponds causes dramatic and distinctive changes in sea ice reflectance. In situ observations indicate that melt ponds first appeared at the C-ICE '00 site after June 19. During the Ponding stage, the relatively homogeneous sea ice surface was transformed into a heterogeneous mixture of light blue-coloured melt ponds and white interstitial snow/ice areas. As a result, AVHRR 1 and 2 reflectances decreased in magnitude and were more variable over the study area. The AVHRR 1 reflectance decreased due to the increasing coverage of dark melt pond areas at the expense of the brighter snow covered interstitial areas (Figure 2). AVHRR 2 is sensitive to the liquid pond surface and the surface characteristics of the interstitial areas. The wet pond surfaces and the large-grained interstitial snow/ice areas thus drive the AVHRR 2 reflectance. Between June 19 and June 21, AVHRR 1 and AVHRR 2 reflectance decreased from 67% to 50% and 47% to 29% respectively as the pond fraction increased from 0% to 45% (Figure 1). Unfortunately no clear-sky AVHRR data were available over the peak ponding period of June 22-24, but it is assumed that both AVHRR 1 and 2 reflectances continued to decrease as pond fraction increased.

In terms of sea ice field experiments, the Drainage stage has gone relatively unobserved. In C-ICE '00, an attempt was made to further the understanding of this melt stage by extending the field camp observations into early July and by returning later via a Coast Guard icebreaker. Surface melt water on sea ice begins to drain as soon as there is pathway to the underlying ocean. Spring first year ice is pocked with seal holes and cracks that efficiently drain surface melt water in the late Ponding stage and early Drainage stage. As the Drainage stage progresses, the enlarged brine pockets interconnect to form vertical drainage pathways that allow melt water to drain vertically through the ice. The immediate effect of drainage is a reduction in the fraction of the ice surface covered by surface water. The newly uncovered remnant ice surface is often crumbly, rough and dull white in colour.

In C-ICE '00, surface drainage was first observed on June 24 and resulted in a decrease in melt pond fraction. AVHRR 1 and 2 data indicated an increase in TOA reflectance from 29% (June 26) to 37% (June 29) (Figure 1), which is consistent with the decreasing melt pond fraction and the 'whitening' of the surface observed at the field site. The AVHRR dataset indicates another, larger increase in reflectance that begins after the first week in July. Both AVHRR 1 and 2 reflectances increased dramatically to at least 60% and 46% respectively, with this increase being observed throughout the region (Figure 2). Although field observations were not available during this period, it is possible that this rebound in reflectance was the result of the disappearance of surface water due to mass vertical drainage of the ice cover.

In 2000, observations in the last week of July from the Coast Guard icebreaker Louis St. Laurent coincided with what was estimated to be the beginning of the Rotten Ice stage. Arctic shipping and icebreaker support typically begins in this part of July when the ice is considered very weak. Ironically, this is the least understood stage from a remote sensing perspective - - likely due to the lack of dedicated field observations.

Ice in the Rotten Ice stage has lost much of its mass and strength. In 2000, numerous thaw holes were visible in the C-ICE '00 area, which could best be described as a mixture of deep, saline melt ponds and dry, non-saline raised hummock areas. AVHRR reflectances decreased from the Drainage Stage to Rotten Ice stage. This is consistent with the reappearance of melt ponds on the icescape, this time primarily saline in nature and at a lower areal coverage (visually estimated at 40%) than at the peak of the Ponding stage.

5.0 CONCLUSIONS

The seasonal decrease in AVHRR 1 and 2 reflectances is distinctive throughout the stages of first year ice melt and thus holds good potential in their mapping. Automatic classification of AVHRR 1 and 2 data into these stages will have to contend with cloud interference and will require the definition of reflectance thresholds for each stage. Future work will define these thresholds and investigate the use of channel AVHRR/3 3A to mask out clouds. A synergistic way to use AVHRR and microwave data (passive and active) to map the progression of these stages over first year sea ice is currently under development.

6.0 REFERENCES

Barber, D.G., J.J. Yackel, and J.M. Hanesiak (2001). Sea ice, RADARSAT-1 and Arctic Climate Processes; A Review and Update, *Canadian Journal of Remote Sensing*, Vol. 27(1):51-61.

De Abreu, R. (1996). In situ and satellite observations of the visible and infrared albedo of sea ice during spring melt. (Ph.D. Thesis -- Department of Geography), Waterloo, Ontario: University of Waterloo.

Johnston, M., R. Frederking, and G. Timco (2001). Decay-induced changes in the physical and mechanical properties of first year ice. Proceedings of the 16th International Conference on Port and Ocean Engineering Under Arctic Conditions, August 12-17, Ottawa, Ontario, Canada.

Kidwell, K.B. (1991). NOAA Polar Orbiter Data Users Guide. (NOAA NESDIS Technical Report), Washington, D.C.: U.S. Dept. of Commerce.

Warren, S.G. (1982). Optical properties of snow. *Reviews of Geophysics and Space Physics*. Vol. 20(1):67-89.

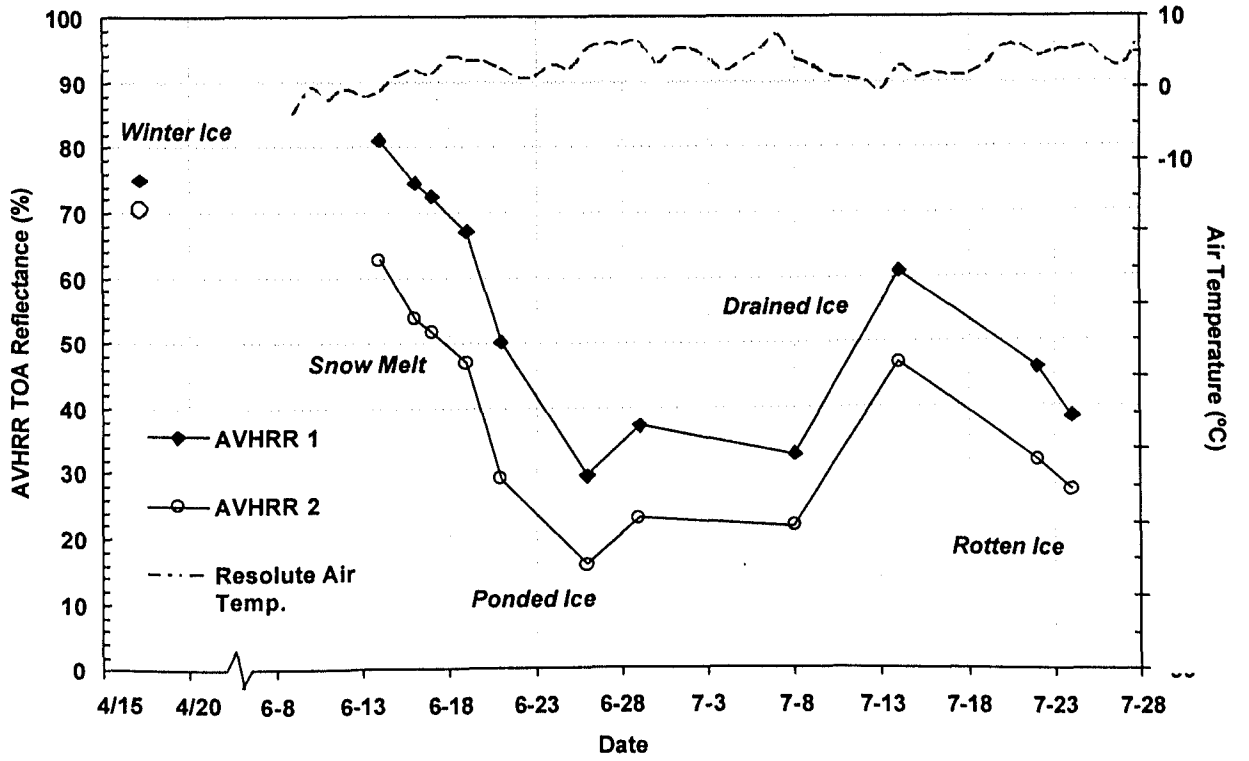

Figure 1. Seasonal variation in TOA AVHRR reflectance over fast first-year sea ice with Stages of Ice Melt, as determined by concurrent surface observations during C-ICE '00 . Air temperature measured at MSC weather station Resolute also shown.

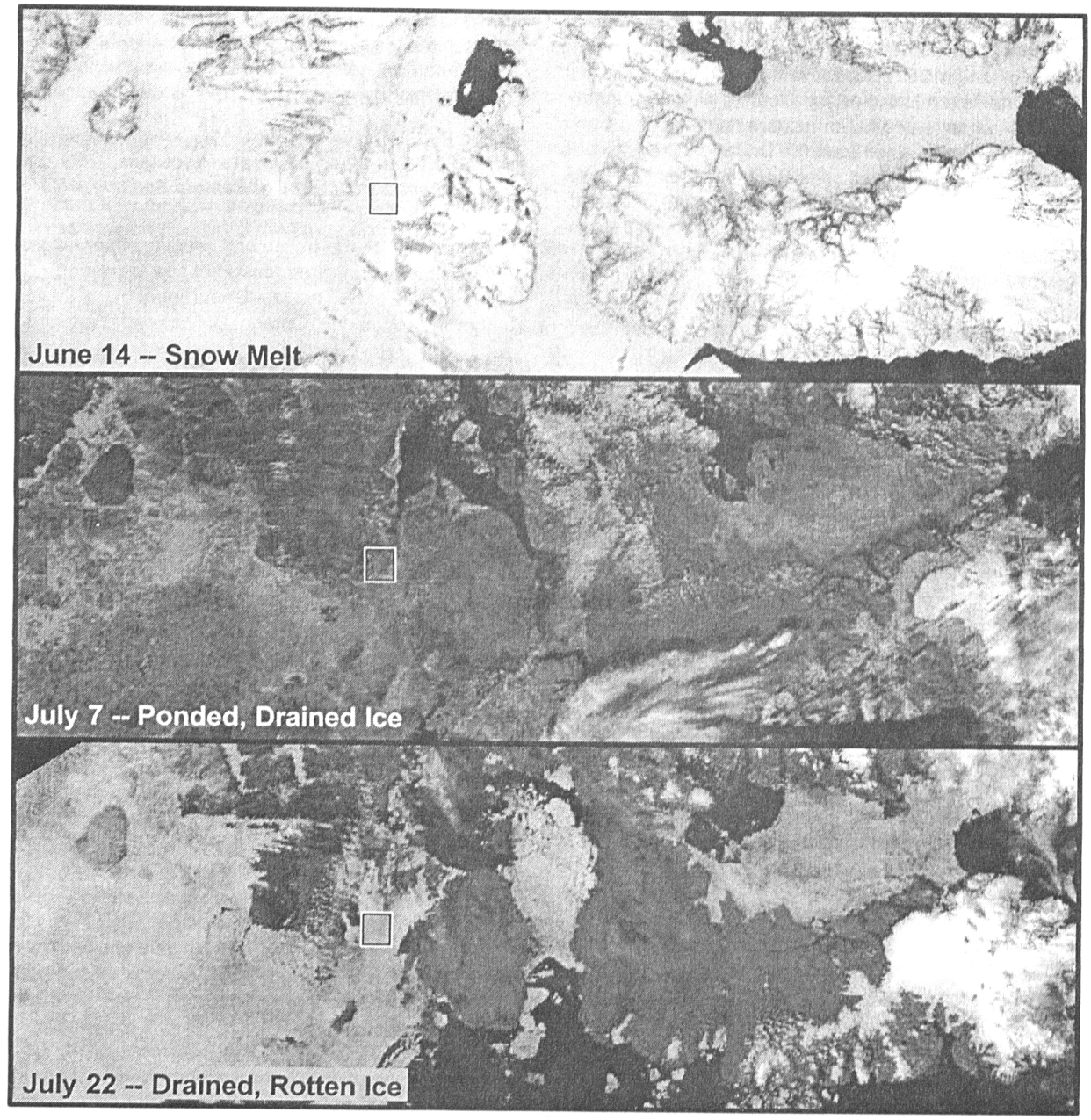

Figure 2. The transformation of TOA reflectance can be seen in these subareas of AVHRR 1 data collected during C-ICE '00 (location shown by inset box). The area is located in the Canadian Arctic Archipelago, specifically the waters off Barrow Strait and Lancaster Sound south of Devon Island, Cornwallis Island and Bathurst Island.

P1.8 Using QuikSCAT Data To Determine The Strength Of A Polar Low

Boniface J. Mills *

Department of Geosciences, Meteorology/Climatology Program
University of Nebraska – Lincoln, NE

Introduction

Intense subsynoptic winter storms, often referred to as polar lows, occur primarily over marine environments and in very cold air masses. Scientific understanding of these small weather systems was difficult because of the lack of data in the form of observations from remote areas and the short life span of these low pressure systems. Although small in size (<1000Km), the storms can produce hazards for ships and coastal boating. The hazards include gale to hurricane force winds, high sea waves, heavy and blowing snow and in some cases thunderstorm activity. Not all polar lows occur in the seas near Scandinavia. During the past three decades polar low activity has been detected over the North Pacific Ocean and the seas around Antarctica.

Improvements in satellite technology in the 1980s enabled meteorologists to actually observe the polar low phenomenon first hand either real time or within a few hours of development. Polar orbiting satellites like the NOAA series and the military's DMSP types have increased coverage as well as the resolution over areas where polar lows develop which tend to be in data sparse regions. Wind speed and direction cannot be determined by looking at a AVHRR or a thermal image. The strength of these subsynoptic maritime storms is of interest to forecasters. Satellite data can be used in conjunction with other forms of imagery to permit forecasters to see more polar lows in greater detail and issue forecasts accordingly.

NASA launched the Quick Scatterometer (QuikSCAT) satellite on June 19, 1999. The SeaWinds instrument onboard the QuikSCAT satellite is a 13.4 gigahertz microwave radar with a one meter diameter rotating dish. It measures near-surface wind speed and direction over global oceans under all cloud and weather conditions. QuikSCAT covers 90% of the Earth's surface in one day. Although the scientific objective is to acquire wind information over marine environments, its secondary or "operational objectives" include improved weather forecasts, storm warnings and monitoring near coastlines. This is accomplished by combining image information from polar orbiters and data from NASA's QuikSCAT satellite. More so, it can depict polar low wind speed and direction around its center.

* *Corresponding author address:* Boniface J. Mills, Univ. of Nebraska – Lincoln, Dept. of Geosciences, Bessey 214, P.O. Box 880340 Lincoln, NE 68588-0340; e-mail: bon@unlserve.unl.edu

Fig 1. The polar low near Kamchatka Peninsula on Feb. 20, 2001 at 1800 UTC with QuikSCAT wind data

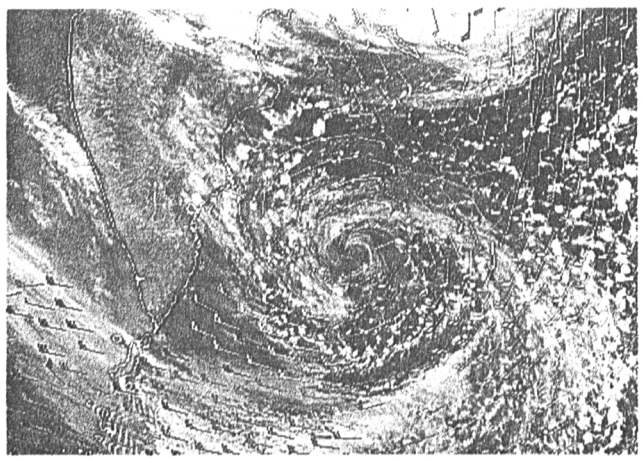

Fig 2. Polar low intensifying on Feb. 21, 2001 at 0000 UTC with QuikSCAT wind data

Data and Methodology

On February 20, 2001 northeastern Siberia was under the influence of high pressure. The temperature was extremely cold (-15F) and the Sea of Okhotsk was still frozen. A synoptic-scale low pressure system and associated frontal boundary had moved away from the Japanese and Kuril Islands. Cold-air advected behind the system over the Sea of Okhotsk, Kamchatka Peninsula and out over the warm Pacific Ocean.

The upper-air wave responsible for the synoptic scale system had deepened in the past 36hrs. An upper-level low had now formed and was located northeast of Karagin Island. Cold-air advection continued to pour over the warm Pacific Ocean at this time. Meanwhile, a circulation started to form off the coast of the Kamchatka Peninsula. Its size was less than 1000 kilometers. Using the Satellite Data Handling System (SDHS) and the Satellite Imagery Display and Analysis System (SIDAS) at the Air Force Weather Agency located at Offutt AFB Nebraska, both light and thermal smooth imagery from various DMSP satellites were retrieved and displayed for various times.

The Kamchatka polar low was short-lived, like most polar lows. The system was tracked between February 20th at approximately 1800 UTC thru February 21st at 1200 UTC. Observations around the polar low were scarce. The strength of the winds near the polar low's center was unknown.

One method of estimating winds in a remote location is by using QuikSCAT wind data. Once the image of interest is retrieved, QuickSCAT wind data for a given time period can be retrieved. Colorized wind barbs displaying various wind speed and direction are merged with the image. This new image shows the polar low 's features and associated winds around it.

Discussion and Conclusion

The polar low was tracked for a period of less than 24 hours. It was a quick developing subsynoptic storm. Most observations were from the Kamchatka coastal stations or from ship reports far from the center of the storm. DMSP satellite imagery was retrieved to follow the life history of this system. The polar low in its early stages resembled the "comma cloud" pattern as seen in Figure 1. The coastal observations at 1800 UTC on February 20 were recorded as northerly winds around

Fig 3. An image of the polar low as a spiral-form type on Feb. 21, 2001 at 0900 UTC.

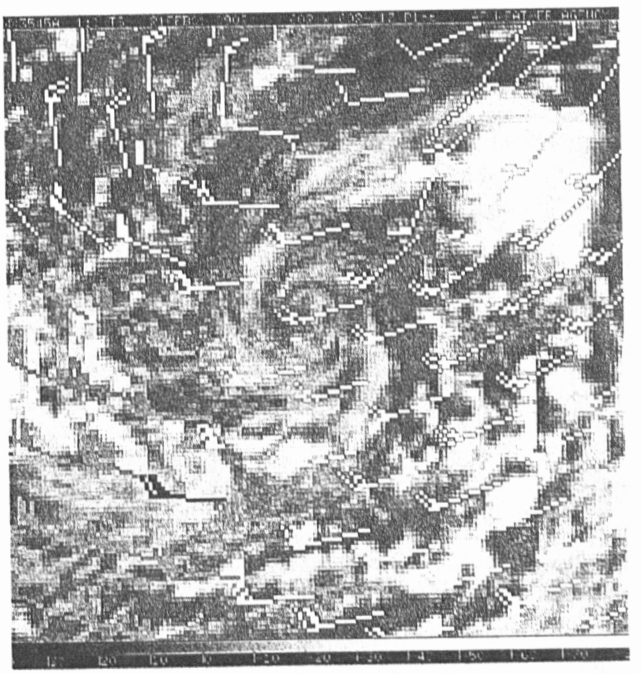

Fig 4. A magnified image of spiral-type polar low on Feb. 21, 2001 at 0900 UTC with QuikSCAT wind data.

10 to 25 knots. A ship southwest of the polar low recorded WNW winds at 30 knots. QuikSCAT winds plotted for the time period of 1600 thru 2000 UTC showed winds around 30 to 35 knots. Later, the polar low moved east-northeast into an observational sparse area over the Pacific Ocean.

Two ship observations at 0000 UTC on February 21st located southeast of the polar low, showed westerly winds at 30 knots. Another ship observation, southwest of the polar low near the Kuril Islands, recorded westerly winds at 40 knots. QuikSCAT winds plotted for the time period of 2300 thru 0000 UTC indicated winds similar to observational wind speed and direction.

The DMSP imagery for this time gave great detail of the polar low intensifying. The comma shape of the polar low at this time was more defined with new bands of clouds converging into the center (Fig. 2). Satellite wind data also showed wind speeds ranging from 25 to 40 knots near the storms center.

DMSP imagery over the area was not available until 0900 UTC on February 21st. The 0900 UTC imagery showed that the polar low had moved slowly east-southeast of its previous location. The polar low's shape had transformed from a comma to a spiral-form type (Fig. 3). The size of the polar low appeared to become smaller and more compact. The 0900 UTC thermal image suggested an eye associated with the storm.

There were no observations in the vicinity of the polar low. QuickSCAT winds plotted for the time period of 0600 to 1100 UTC indicated strong winds between 20 and 40 knots around the polar low (Fig. 4). By 1200 UTC on February 21st the polar low had weakened and was absorbed by a larger synoptic system in the area.

Overall, the QuikSCAT information provided reasonable insight about the storm's winds during the genesis, mature and decay stages. Although

observations were sparse, the observations in the vicinity of the polar low were in general agreement with the QuikSCAT wind data. Near real-time satellite imagery combined with QuikSCAT winds is a wonderful analysis tool for forecasters and researchers.

Acknowledgements

The author would like to thank Paul McCrone and the Air Force Weather Agency, Offutt AFB NE for providing the imagery and time on their computer systems.

References

Bromwich, D.H.,1987: A Case Study of Mesoscale Cyclogenesis over the Southwestern Ross Sea. Antarctica Journal of US, 22, 254-256.

Businger, S., 1987: The Synoptic Climatology of Polar Low Outbreaks over the Gulf of Alaska and Bering Sea. Tellus 39, 307-325.

Locatelli, J.D., P.V. Hobbs and J.A. Werth, 1982: Mesoscale Structures of Vorticies in Polar Air Streams. Monthly Weather Review. 110, 1417-1433.

NASA/JPL, 1999: QuikSCAT Science Data Product User's Manual. G. M. Shirtliffe, ed., JPL, California Institute of Technology. 43p

NASA/JPL, 2001: QuikSCAT Science Data Product User's Manual, Overview & Geophysical Data Products. Version 2.1. K. L. Perry, ed. 92p. Available On-Line: http://podacc.jplnasa.gov/quikscat/qscat_doc.html

Streten, N.A., and A. J. Troup. 1973: A Synoptic Climatology of Satellite Observed Cloud Vortices over the Southern Hemisphere. Quarterly Journal Royal Meteorological Society. 99, 56-72.

Reed, R.J.,1979: Cyclogenesis In Polar Air Streams. Monthly Weather Review.107, 38-52.

Reed, R.J., and W. Blier, 1986: A Case Study of Comma Cloud Development in the Eastern Pacific. Monthly Weather Review.114, 1681-1695

P1.9 AIR-SEA FLUXES FROM SYNTHETIC APERTURE RADAR: AN UPDATE

Todd D. Sikora
United States Naval Academy, Annapolis, MD 21402

And

Donald R. Thompson
The Johns Hopkins University Applied Physics Laboratory, Laurel, MD 20723

1. INTRODUCTION

Young et al. (2000) proposed and demonstrated a method to calculate diabatic wind speed and turbulence statistics from neutral wind speed imagery (Thompson and Beal, 2000) generated from synthetic aperture radar (SAR) data. Their method, referred to herein as the SAR method, is based on Monin-Obukhov and mixed layer similarity theory (Panofsky and Dutton, 1984; Stull, 1988). It relates the ratio of the mean to standard deviation wind speed, from the SAR-derived neutral wind speed imagery, to the static stability of the atmospheric surface layer. The scaling parameters arising from this relationship provide a stability correction to the neutral wind speed imagery in an iterative fashion. See Young et al. (2000) for an in-depth review of their method.

Upon completion of the stability correction, several of the resulting statistics (the Obukhov length ($\overline{L}$) and friction velocity ($\overline{u_*}$)) can be combined with an independent measure of the sea-surface virtual temperature ($\overline{T_v}$) to provide an estimate of the kinematic buoyancy flux ($\overline{B}$):

$$1) \quad \overline{B} = -\frac{\overline{u_*^3 T_v}}{\overline{L} k g},$$

where k is von Kármán's constant and g is the acceleration of gravity (overbars denote values averaged over a wind speed image sub-scene).

The demonstration of the SAR method by Young et al. (2000) was accomplished using *in situ* turbulence data gathered during the second High Resolution Remote Sensing (HI-RES 2) project as ground truth. The comparisons presented in Young et al. (2000) were for data collected during rather quiescent synoptic scale and statically unstable microscale atmospheric conditions (i.e., light winds and negative air-sea temperature differences).

Sikora et al. (2000) furthered the demonstration / testing of the SAR method by expanding the environmental conditions for such to more baroclinic regimes. Sikora et al. (2000) relied on National Ocean and Atmospheric Administration (NOAA) buoys to provide a means of ground truth and only investigated the performance of the SAR method in the calculation of $\overline{L}$ and the drag coefficient ($\overline{C_d}$). Although NOAA buoys do not provide such turbulence statistics, they do provide enough *in situ* data for input into the bulk flux algorithm arising from Tropical Ocean Global Atmosphere- Coupled Ocean Atmosphere Response Experiment (TOGA-COARE) (Fairall et al. 1996). The TOGA-COARE bulk flux algorithm, therefore, provided the "ground truth" for comparisons presented in Sikora et al. (2000).

Unlike the Young et al. (2000) study, the work reported in Sikora et al. (2000) did not include spectral filtering of the neutral wind speed imagery prior to the generation of their turbulence statistics. However, Sikora et al. (2000) smoothed the pixel size of the SAR imagery to 300 m. This choice of pixel size and smoothing arose from the study of Mourad et al. (2000), who found that doing so resulted in a close fit between the wind spectrum resulting from a SAR image and that developed using low-level turbulence measurements gathered from an aircraft flying over the imaged area.

The purpose of this paper is to report the results of the testing of the SAR method that has been accomplished since the publication of Sikora et al. (2000). The present research continues the work of Sikora et al. (2000), conducted using Radarsat-1 overpasses off the east coast of the United States between October 1996 and March 1997. While several of the case studies that we present below overlap with those presented in Sikora et al. (2000), we deviate from their work in that the results for the ratio of reference height (z) to $\overline{L}$ as well as for $\overline{B}$ are presented in place of $\overline{L}$ and $\overline{C_d}$.

2. DATA

The SAR data set employed in the present research comes from a 12-overpass Radarsat-1 narrow ScanSAR collection initiative by the Ocean Remote Sensing Group at the Johns Hopkins University Applied Physics Laboratory. All 12 overpasses can be seen at (http://fermi.jhuapl.edu/en_sar.html). For each overpass, we inspected data from all NOAA buoys located within the imaged area, as well as data from a Woods Hole Oceanographic Institution mooring operating in support of the Coastal Mixing and Optics (CMO) experiment, in order to choose sub-scenes for case studies. Case studies were chosen if the air-sea temperature difference at a reporting station was less than –1 °C at the time of the corresponding overpass. This criterion was chosen because the SAR method is intended for use in the presence of statically unstable environments. This selection process resulted in 13 cases studies from 9 overpasses.

Table 1 summarizes the air-sea temperature

Table 1. Summary of air-sea temperature difference and wind data gathered at the buoys for each of the 13 case studies.

Buoy	Date	Case Study	Delta T (°C)	Wind Speed (ms^{-1})	Wind Direction (°T)
44004	10/10/96	A	-1.4	9.0	262
41001	10/13/06	B	-4.4	3.9	016
44004	01/14/97	C	-9.4	8.7	290
44008	01/14/97	D	-4.1	8.1	285
CMO	01/14/97	E	-4.7	9.5	285
41001	01/17/97	F	-14.8	8.2	294
44025	01/17/97	G	-14.2	10.9	265
CMO	02/07/97	H	-1.9	7.0	290
41001	02/10/97	I	-3.6	11.0	123
44025	02/10/97	J	-3.4	5.7	290
44014	02/13/97	K	-2.5	8.5	084
41001	03/06/97	L	-4.4	12.1	295
44014	03/09/97	M	-2.2	5.7	086

difference and wind data gathered at the *in situ* stations for each of the 13 case studies. Because all SAR overpasses occurred around 2300 UT, the buoy data found in Table 1 is the 8-minute average reported by the National Data Buoy Center for that time for any particular case study. That for the CMO mooring is the 15-minute average reported for that time for any particular case study. A map of the buoy stations cited in Table 1 can be found at http://seaboard.ndbc.noaa.gov/. The CMO mooring was located at 40.5 N , -70.5 E.

The air-sea temperature difference ranged from –1.4 to -14.8 °C, the wind speed ranged from 3.9 to 12.1 ms^{-1}, and the wind directions covered every quadrant of the compass. Therefore, the environmental conditions for the present research were conducive for robust testing of SAR method.

Figure 1 shows imagettes of 10 m neutral wind speed from which each of the 13 sub-scenes were chosen. Each imagette is composed of 300 m pixels, has dimensions of 105 km by 105 km, and is oriented so that the top of the page is directed towards 348 °T. Notice that within many of these imagettes, the mottled SAR signature of cellular convection (Sikora et al., 1995; Zecchetto et al., 1998) is evident. These neutral wind speed imagettes were created following the procedure outlined in Thompson and Beal (2000). However, because calibration coefficients from the early Radarsat-1 imagery employed herein are in question, we first scaled the cross section from a 21 km square centered on the *in situ* station for each original SAR imagette such that resulting 10 m neutral wind speed, averaged over the 21 km square, equaled that from the corresponding *in situ* station.

The sub-scenes used for our case studies were developed from these imagettes by invoking Taylor's hypothesis using the wind speeds reported in Table 1, thus allowing the temporal data reported by the *in situ*

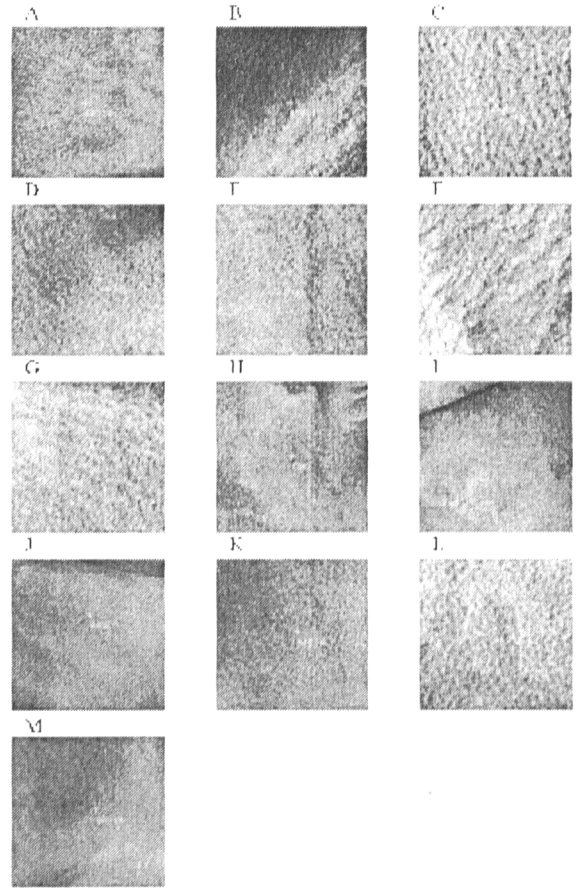

Figure 1. Imagettes of the 10 m neutral wind speed from which each of the 13 sub-scenes were chosen. Letters correspond to separate case studies found within Table 1.

stations to be compared to the spatial data found within the wind speed imagery. The average area of all 13 sub-scenes is 18 km^2. All sub-scenes were oriented such that one of their axes paralleled the average wind direction reported by the corresponding *in situ* station.

Unlike what was presented in Sikora et al. (2000), the results found below for the SAR method constitute average values of $z/\overline{L}$ and $\overline{B}$ for a 3-by-3 grid of sub-scenes centered on the *in situ* station for a particular case study. This was done in order to provide a more robust sample of both statistics while, at the same time, allowing us to assess their variability over the area of interest.

As was done by Sikora et al. (2000), ground truth turbulence data reported herein comes from the TOGA-COARE bulk flux algorithm, using the data reported by the *in situ* stations as input. Because humidity measurements were not reported by the NOAA buoys, but are required for calculation of the bulk statistics, we assumed 100% relative humidity for all of our case studies. We also used the *in situ* data and assumed

100% relative humidity when calculating $\overline{T_v}$ for input into equation 1.

3. RESULTS AND DISCUSSION

Figure 2 shows the TOGA-COARE / SAR method comparisons for $z/\overline{L}$ (a) and $\overline{B}$ (b). The slope and y intercept from simple linear regression are also shown on each plot. The overall correlation for both sets of comparisons is quite good. The correlation coefficient for $z/\overline{L}$ is 0.77 while that for $\overline{B}$ is 0.95. The mean difference and root mean square difference (COARE results – SAR results) for the $z/\overline{L}$ comparisons are –0.008 and 0.119 respectively. That for the $\overline{B}$ comparisons is 0.030 $ms^{-1}K$ (mean difference) and 0.039 $ms^{-1}K$ (root mean square difference).

Examining the two plots more closely and accepting the TOGA-COARE data as truth, one finds that the SAR method tends to underestimate $|z/\overline{L}|$ for weakly statically unstable environments and vice versa. Turing to the $\overline{B}$ comparisons, the SAR method tends to provide a slight underestimate for all ranges of static stability examined.

Scrutinizing the SAR method, we find that the value of $z/\overline{L}$ it produced, averaged over all 13 case studies, is –0.15. The standard deviation of $z/\overline{L}$ from the SAR method, averaged over all 13 case studies, is 0.11. The corresponding values for $\overline{B}$ are 0.046 $ms^{-1}K$ (average) and 0.034 $ms^{-1}K$ (standard deviation). Hence, there was quite a bit of relative variability in the output from SAR method for both statistics. This result was somewhat expected. By examining Figure 1, one can see that for several of the case studies, there was a large amount of variability in the degree of mottling seen in the neutral wind field about the buoys (e.g., large pattern changes are evident in Figure 1b). This lack of homogeneity resulted in large differences in the estimates of $z/\overline{L}$ and $\overline{B}$ from one of the 9 sub-scenes to another for the same case study. We cannot, therefore, simply attribute the large amount of variability noted in our results to some deficiency in the SAR method or our application of it. It may be that the observed variability is real.

Potential sources of error for the SAR method, beyond those discussed above, have been noted in Young et al. (2000) as well as in Sikora et al. (2000). Here, we outline the more probable candidates. For one, any extraneous variance in the wind speed imagery other than that owing to the wind (e.g., that due to oceanographic phenomena and speckle) will cause an incorrect assessment of the turbulence statistics. Implicit in the smoothing of the SAR imagery to 300 m was the attempt to diminish or remove such variance. However, degradation of the resolution of the SAR

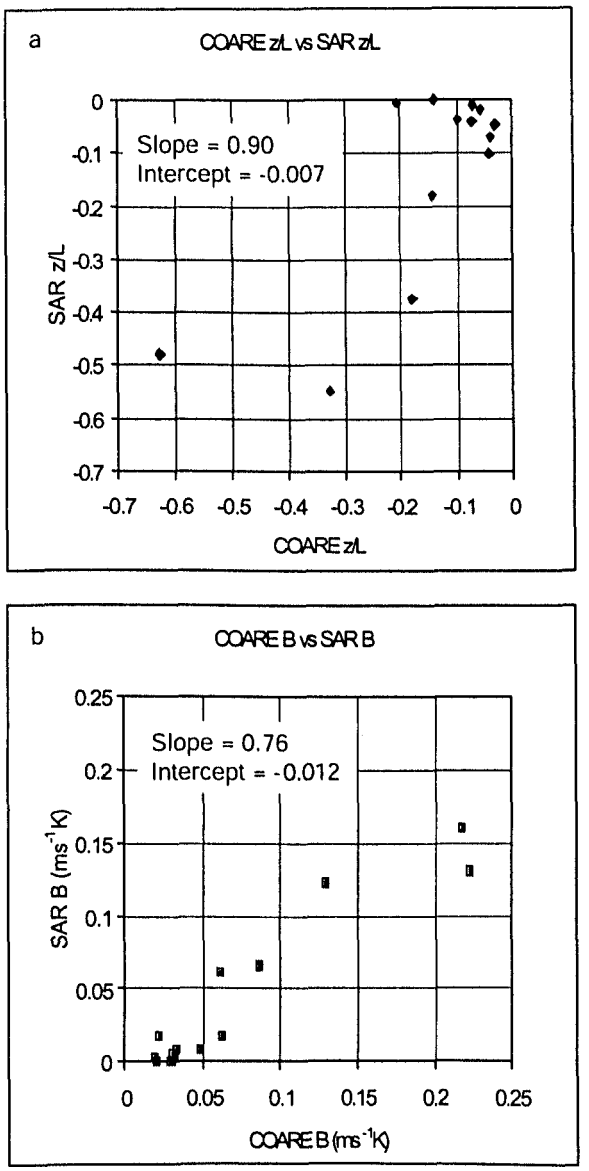

Figure 2. TOGA-COARE / Young et al. (2000) comparisons for (a) $z/\overline{L}$ and (b) $\overline{B}$.

imagery by smoothing to 300 m may inadvertently eliminate a significant amount of variance owing to the wind under certain circumstances. Only the limited Mourad et al. (2000) study justifies such an approach. Another potential source of error includes the presence certain sea states that can affect the near-surface turbulence in such a way as to cause a breakdown of Monin-Obukhov similarity theory (e.g., Drennan et al. 1999). Finally, the proper choice of $\overline{Z_i}$ is imperative for the correct assessment of $\overline{L}$, on which the SAR method hinges. To the best of our knowledge, there has been no systematic study addressing the ability of diagnosing

$\overline{Z_i}$ from SAR data beyond the study presented in Sikora et al. (1997).

4. SUMMARY

A similarity theory-based method (referred to as the SAR method) for calculating turbulence statistics from SAR-derived neutral wind speed imagery (first presented in Young et al. (2000)) was tested. We concentrated on its ability to yield proper estimates of the ratio of reference height to Obukhov length ($z/\overline{L}$) and kinematic buoyancy flux ($\overline{B}$), where the overbars denote averages over a sub-scene of the wind speed image. The TOGA-COARE bulk flux algorithm, fed with buoy and mooring data corresponding in space and time to the wind speed image sub-scenes, provided a comparison data set. The $z/\overline{L}$ and $\overline{B}$ values derived from the SAR method that are reported herein are averages from a 3-by-3 sub-scene grid centered on a particular *in situ* station. Thirteen cases studies were examined covering an air-sea temperature difference range of –1.4 to -14.8 °C and a wind speed range of 3.9 to 12.1 ms^{-1} (as measured by the *in situ* stations).

The correlation coefficient for the $z/\overline{L}$ comparison is 0.77 while that for $\overline{B}$ is 0.95. The mean difference and root mean square difference (COARE results – SAR results) for the $z/\overline{L}$ comparisons are –0.008 and 0.119 respectively. That for the $\overline{B}$ comparisons is 0.030 $ms^{-1}K$ (mean difference) and 0.039 $ms^{-1}K$ (root mean square difference).

Accepting the TOGA-COARE data as truth, the SAR method tends to underestimate $z/\overline{L}$ for weakly statically unstable environments and vice versa. For the $\overline{B}$ comparisons, the SAR method tends to provide a slight underestimate for all ranges of static stability examined. The value of $z/\overline{L}$ produced by the SAR method, averaged over all 13 case studies, is –0.15. The standard deviation of $z/\overline{L}$ from the SAR method, averaged over all 13 case studies, is 0.11. The corresponding values for $\overline{B}$ are 0.046 $ms^{-1}K$ (average) and 0.034 $ms^{-1}K$ (standard deviation).

Potential sources of error for the SAR method include the neutral wind estimates derived from the SAR imagery, the sea state, and the improper diagnosis of the mixed layer depth from the neutral wind speed imagery.

Acknowledgements. The research reported herein was funded by Office of Naval Research grants N00014-00-WR20021, N00014-01-WR20219, and N00014-01-1-0054 as well as National Aeronautics and Space Administration grant NAG5-10114. The Radarsat-1 images were made available through an ADRO grant from the Canadian Space Agency.

5. REFERENCES

Drennan, W. M., K. K. Khama, and M. A. Donelan, 1999: On momentum flux and velocity spectra over waves, *Boundary-Layer Meteorol.*, **92**, 489-515.

Fairall, C. W., E. F. Bradley, D. P. Rogers, J. B. Edson, G. S. Young, 1996: Bulk parameterization of the air-sea fluxes for tropical ocean-global atmosphere response experiment. *J. Geophys. Res.*, **101**, 3747-3764.

Mourad, P. D., D. R. Thompson, D. C. Vandemark, 2000: Extracting fine-scale wind fields from synthetic aperture radar Images of the ocean surface, *Johns Hopkins University APL Technical Digest*, **21**, 108-115.

Panofsky, H. A., and J. A. Dutton, 1984: *Atmospheric Turbulence.* Wiley-Interscience, 397 pp.

Sikora, T. D., G. S. Young, R. C. Beal, and J. B. Edson, 1995: On the use of spaceborne synthetic aperture radar imagery of the sea surface in detecting the presence and structure of the convective marine atmospheric boundary layer. *Mon. Wea. Rev.*, **123**, 3623-3632.

Sikora, T. D., G. S. Young, H. N. Shirer, and R. D. Chapman, 1997: Estimating convective boundary layer depth from microwave radar imagery of the sea surface. *J. Appl. Meteorol.*, **36**, 833-845.

Sikora, T. D., D. R. Thompson, and J. C. Bleidorn, 2000: Testing the diagnosis of marine atmospheric boundary layer structure from synthetic aperture radar, *Johns Hopkins University APL Technical Digest*, **21**, 94-99.

Stull, R. B., 1988: *An Introduction to Boundary Layer Meteorology.* Kluwer Academic Publishers, 666 pp.

Thompson, D. R., and R. C. Beal, 2000: Mapping mesoscale and submesoscale wind fields using synthetic aperture radar, *Johns Hopkins University APL Technical Digest*, **21**, 58-67.

Young, G. S., T. D. Sikora, and N. S. Winstead, 2000: Inferring marine atmospheric boundary layer properties from spectral characteristics of satellite-borne SAR imagery, *Mon. Wea. Rev.*, **128**, 1506-1520.

Zecchetto, S., P. Trivero, B. Fiscella, and P. Pavese, 1998: Wind stress structure in the unstable marine surface layer detected by SAR, *Boundary-Layer Meteorol.*, **86**, 1-28.

P1.10

REALTIME REMOTE SENSING-BASED MODELING AND IN SITU VALIDATION OF LAND SURFACE ENERGY AND WATER FLUXES

George R. Diak#, John R. Mecikalski#[1], Martha C. Anderson*, John M. Norman*, Ryan D. Torn#, and Jason Hoss*

#Cooperative Institute for Meteorological Satellite Studies
*Department of Soil Sciences
University of Wisconsin–Madison

Scott J. Richardson, and Jerry A. Brotzge
University of Oklahoma–Norman

1. INTRODUCTION

In Anderson et al. (1997) and Mecikalski et al. (1999), we detailed a method for evaluating fluxes of sensible and latent heat at the land surface using an Atmospheric Land-surface EXchange Inverse (ALEXI) model. The most important inputs to this model are the Normalized Vegetation Difference Index (NDVI, converted to a fraction vegetation cover), that can be obtained from the AVHRR satellite or other satellite sources, and the change in radiometric temperature of the land surface over a four-hour time interval in the morning. Currently, this time-change information is only available from the NOAA-GOES geostationary satellites.

ALEXI is a so-called "two-source" model, the two sources being soil and vegetated components of a satellite scene. Each of these scene subcomponents contributes to the radiometric temperature of the scene, taking into account the angle of view of the GOES observation and thus the relative amount of soil and vegetation viewed.

Through aerodynamic resistance laws of canopy and soil flux exchanges, surface fluxes are coupled to a atmospheric surface layer and ultimately a simple model of the growth of the Atmospheric Boundary Layer (ABL). This ABL model provides the energy closure needed to solve the ALEXI equation system, and is more robust than using an air temperature measured at shelter lever (2 m) to close the energy balance. In fact, through balancing of surface and ABL fluxes, ALEXI is able to *estimate* the air temperature at the top of the atmospheric surface layer, approximately 50 m. Using time-changes of radiometric temperature mitigates some of the problems involved with estimating emissivity and applying atmospheric corrections.

[1] *Corresponding author:* John R. Mecikalski, Cooperative Institute for Meteorological Satellite Studies, 1225 West Dayton Street, UW-Madison, Madison, WI 53607-1695. Email: *johnm@ssec.wisc.edu*

ALEXI also requires a modest amount of vegetation, land-use and atmospheric information that have been detailed in Mecikalski et al. (1999). Sources of the land-use and vegetation data are unchanged from those noted in that publication. The required atmospheric information is provided through analyses of surface synoptic data for wind speed and rawindsonde information for the atmospheric profiles needed for the ABL energy closure, a data- and computationally-intensive process over regional and continental scales. To alleviate this problem, we have adapted the forecast model component of CIMSS Regional Assimilation System (CRAS) to provide all the required atmospheric and selected other inputs to ALEXI. These inputs are vertical profiles of atmospheric temperature over the ALEXI region at the initial time, as well as wind speed, incident flux of solar radiation and net thermal radiation at both GOES observation times.

Two similar versions of ALEXI are being tested in real time. The first is identical to that described in Anderson et al. (1997). The second follows the mathematics of so-called "statistical interpolation" (see for example Diak et al. 1995) for a description of these principles applied to remote sensing of the surface energy balance). It has an advantage of being able to easily incorporate other "signals" of the surface energy flux balance, however none have been incorporated to date, and the results of the two methods are thus nearly identical.

2. APPLICATIONS OF THE ALEXI MODEL

a) Realtime Flux Estimation

As of 2000, the ALEXI model is being run in realtime to generate the four surface flux components (sensible, latent, and ground heats, and net radiation) over Oklahoma and the United States. These fluxes are computed at the end of a given day once GOES observations of surface radiometric temperature are available 5.5 hours after local sunrise across a domain. Currently, surface fluxes are computed on a 5 km-res-

a)

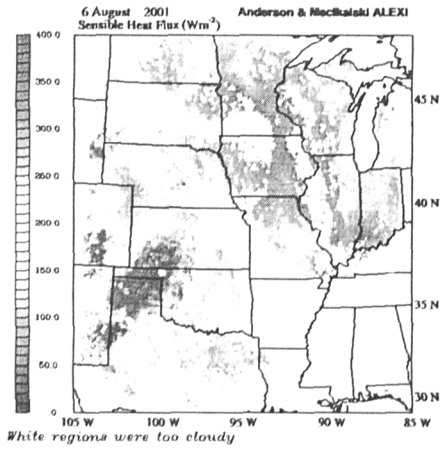

b)

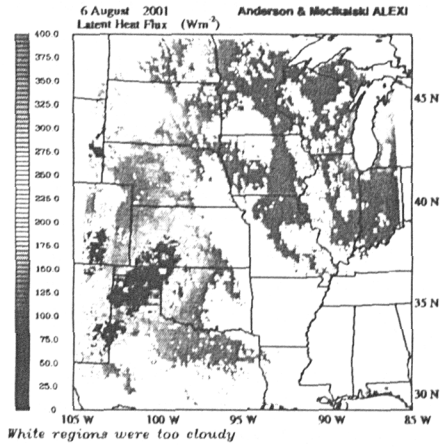

c)

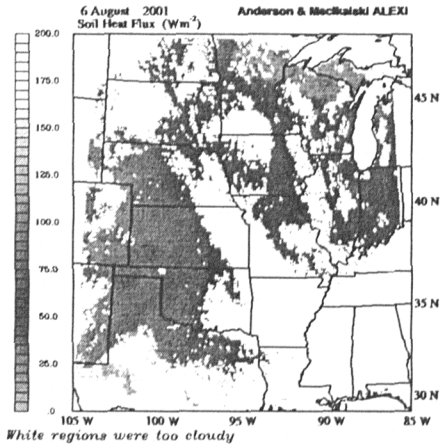

Figure 1: ALEXI-derived flux components for 6 August 2001. Fluxes are computed on a 10-km resolution domain and are available in realtime (computed between 00 and 06 UTC on the day after they are valid).

d)

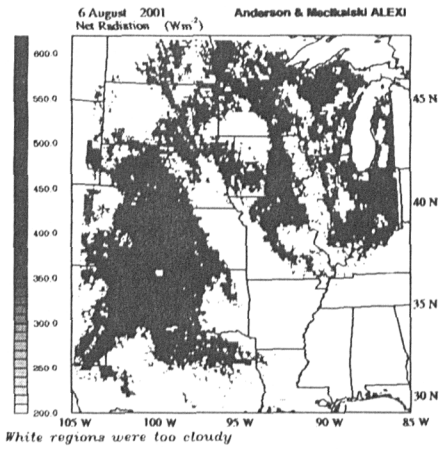

olution grid centered on Oklahoma, and on a 10-km resolution grid over the central US. The ALEXI flux estimates, along with all input variables, are displayed at: *http://cras.ssec.wisc.edu:8080/~jrm/alexi_us.html*.

Figure 1(a-d) show an example of the four flux components as derived by ALEXI for 6 August 2001. The method that estimates the fluxes shown in Fig. 1 is outlined in Mecikalski et al. (1999).

As of Summer 2001, software development, increased computational capabilities, and general improvements to the ALEXI method are allowing us to expand these flux computations to cover the entire United States, utilizing data from both the GOES-8 and GOES-10 satellite platforms. Plans for early 2002 are for 10-km flux estimated for both clear and cloud sky regions across the domain. Currently, all our methods are limited to clear sky conditions.

An algorithm has been developed to estimate fluxes on cloudy days, when GOES-based surface temperatures are corrupted and ALEXI cannot be used. For this method, it is assumed that on cloudy days, available water in the top 5 cm of soil and in the root zone is depleted by an amount consistent with the previous day's evapotranspiration (ET). Available water fractions in these water "pools" are used to estimate actual soil and canopy ET from potential values given by the Penman-Monteith equation. These available water fractions are subsequently updated by ALEXI every time a clear day is encountered. Updates reflect errors in depletion and any rainfall/drainage that may have occurred during the intervening cloudy period.

This algorithm is currently being tested with flux and surface temperature observations collected at several sites in Oklahoma during the Souther Great Plains (SGP) '97 field experiment. Preliminary results at the Little Washita site in southern Oklahoma are encouraging.

The overall goal of this portion of the ALEXI project will be to generate a climatology of fluxes across the US. From this, we may provide to numerical forecast models (like CRAS) estimates of soil moisture, as well as flux partitioning.

b) Oklahoma Mesonet Flux Validation

Collaboration with the University of Oklahoma and the researchers who collect and maintain the Oklahoma Mesonet has provided this project an excellent validation data set for our ALEXI results. For the 2000 and 2001 growing seasons, Mesonet fluxes for 24 clear days across Oklahoma region are being directly compared with ALEXI 5-km flux estimates.

Figure 2(a-b) presents the direct comparison of ALEXI sensible and latent heats with those obtained from the 114 station Mesonet for 23 May 2000. In Fig. 2, small circles denote data from the 10 Mesonet OASIS "Super Sites" which incorporate eddy correlation methods to obtain flux closure (i.e. sonic anemometers are used to obtain latent heat information); asterisks in Fig. 2 denote data collected from other 104 Mesonet stations that use Bowen ratio methods for obtaining flux closure. The high amount of scatter about the 1:1 line is characteristic of many attempts to validate point surface flux measurements with satellite-based energy flux estimation methods (see Campbell and Norman 1998). The reasons for this include: a) satellite sensing systems cannot account for all atmospheric effects, b) errors due to surface emissivity, and c) the errors caused by differences between the local land cover characteristics in the near-vicinity of a Mesonet station and the land cover characteristics specified as an average across a given 5 km ALEXI pixel.

In light of these concerns, the results presented in Fig. 2 are quite encouraging. Despite the scatter, there is no clear bias error in these results, suggesting that when many stations are considered, we are adequately representing the flux partitioning on scales near the GOES instrument's resolution. The results are generally in line with the 15-50% errors obtained from direct surface measurements.

c) Flux Disaggregation to 30-m Scales

As Fig. 2 demonstrates, there is a need to identify how well we can estimate land surface fluxes on the scales measured by the Oklahoma Mesonet stations, specifically, on scales from 30-100 m.

Considerable ongoing work is being done to disaggregate the 5- and 10-km fluxes to 30 meter scale fluxes. This procedure, termed "Disaggregated-ALEXI", or "DisALEXI", has been outlined by Norman et al. (1999) and is a method designed to incorporate inputs from high-resolution remote sensing platforms such as LandSat or aircraft. The motivation for the DisALEXI approach, in addition to direct validation of ALEXI, is attaining accurate ET estimates on scales near that of most farm fields and native ecosystems. In addition, the DisALEXI approach relinquishes the need for direct surface measurements while taking advantage of single-instrument remote sensing technologies.

The DisALEXI method is described as follows: 1) use 5-km values of radiometric temperature from GOES, atmospheric information (moisture and wind) as an average across a 5-km box, and a 5-km averaged

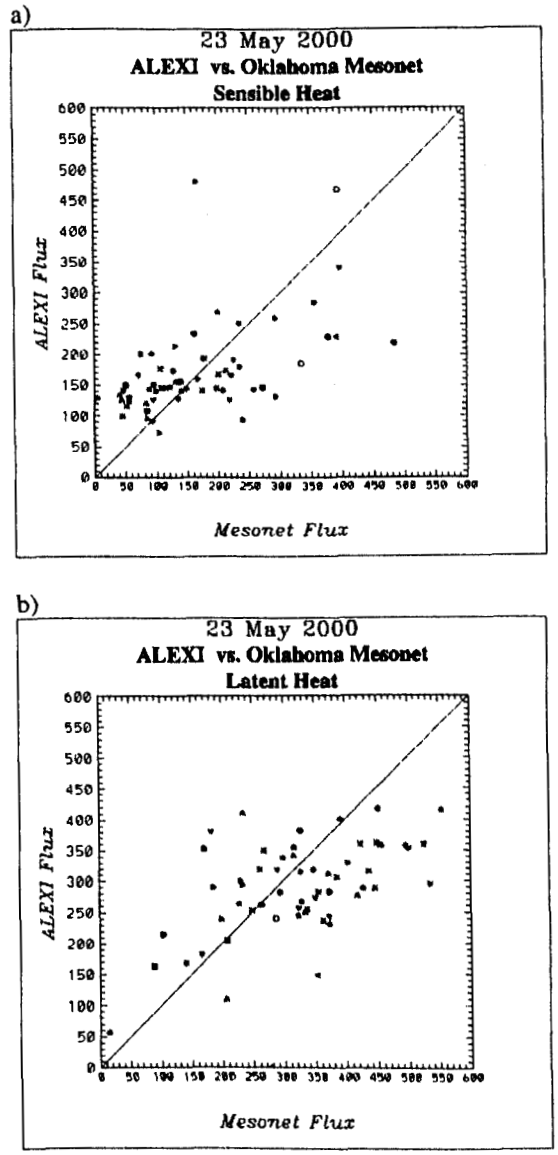

Figure 2: a) Sensible heat, and b) latent heat comparisons between 5-km estimates and 114 Oklahoma Mesonet stations for 23 May 2000. Circles denote data from the 10 Mesonet OASIS "Super Sites", while asterisks denote data from the other 104 stations.

vegetation cover observation from AVHRR to estimate an 5-km net radiation (R_{net}) and air temperature (T_a), 2) derived from LandSat 30 m resolution fraction vegetation cover and 60 m resolution radiometric temperature information (T_{radL}), 3) provided information on satellite and solar angles, R_{net}, T_a, and T_{radL}, use the two-source (Norman et al. 1995) model of turbulent heat and moisture exchange to derived sensible heat, latent energy, net radiation, and soil heat flux for each at the LandSat resolution.

From these 30-meter fluxes, we are then able to directly able to compare our remotely sensed flux estimates to measurements from the Oklahoma Mesonet stations. Aircraft flux data collected during the SGP '97 experiments is also being used to validate our ALEXI measurements via the DisALEXI procedure. As a final check, the 30-meter DisALEXI fluxes are re-aggregated back to 5-km ALEXI estimates.

Figure 3 displays the high-resolution scales of the DisALEXI processing with a 30-meter resolution images of LandSat-derived fraction vegetation covers over a 5 km x 5 km area. Figure 4 presents 30 meter sensible heats, the results of a DisALEXI simulation for 29 May 2000. One Mesonet station is located within this 5 km x 5 km box as shown in Fig. 4. Our flux validation via the DisALEXI method is limited to the acquisition of a LandSat image on a clear day over Oklahoma on a day for which Mesonet data is available. For a given LandSat image, only 10-15 Mesonet stations can be directly compared with DisALEXI simulated fluxes.

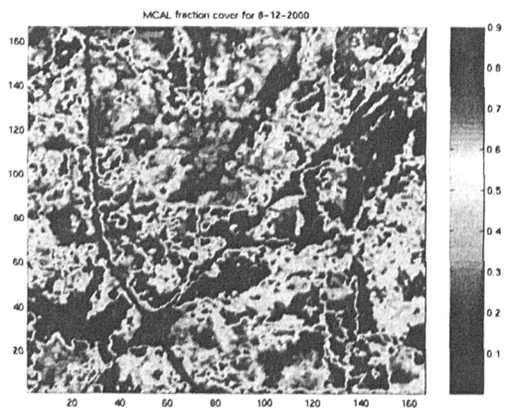

Figure 3: LandSat-derived fraction vegetation covers for a 5 km x 5 km (ALEXI pixel) region near the Mesonet station near McAlester, Oklahoma. The "clover leaf" pattern in the lower left of this image is the intersection of the "Indian Nation Turnpike" and US highway 69.

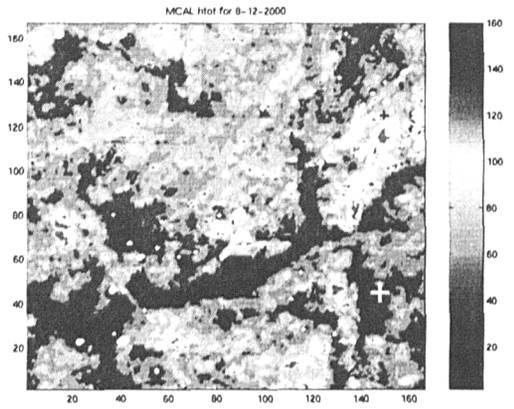

Figure 4: DisALEXI simulated sensible heat fluxes for the 5 km x 5 km box above for 29 May 2000. The "+" in the lower right of this image denotes the location of the the McAlester, Oklahoma (MCAL) Mesonet station.

3. Ongoing Work

Work with the ALEXI model continues in earnest. Through 2002, we plan on having ALEXI fluxes for the entire US, with the construction of the flux climatology now well underway. Formal reporting of the ALEXI-Oklahoma Mesonet flux validation and DisALEXI procedures is forthcoming. We also plan to explore the incorporation of our daily flux and soil moisture estimates as boundary conditions in numerical weather forecast model at CIMSS.

4. References

Anderson, M. C., J. M. Norman, G. R. Diak, W. P. Kustas, and J. R. Mecikalski, 1997: A two-source time-integrated model for estimating surface fluxes using thermal remote sensing. *Remote Sens. Environ.*, **60**, 195-216.

Campbell, G. S., and J. M. Norman, 1998: *An Introduction to Environmental Biophysics*, 2nd Ed. Springer, New York, 286 pp.

Diak, G. R., R. M. Rabin, K. P. Gallo, and C. M. Neale. 1995: Regional-scale comparisons of vegetation and soil wetness with surface energy budget properties from satellite and in-situ observations. *Remote Sens. Reviews.* **12**, 355-382.

Mecikalski, J. R., G. R. Diak, M. C. Anderson, and J. M. Norman, 1999: Estimating fluxes on continental scales using remotely-sensed data in an atmospheric-land exchange model. *J. Appl. Meteor.*, **38**, 1352-1369.

Norman, J. M., W. P. Kustas, and K. S. Humes. 1995: A two-source approach for estimating soil and vegetation energy fluxes from observations of directional radiometric surface temperature. *Ag. For. Meteorol.*, **77**, 153-166.

P1.11 DESERT DUST STORMS AS DETECTED BY METEOSAT AND SEAWIFS MULTISPECTRAL IMAGERY

Steven D. Miller* and Thomas F. Lee
Naval Research Laboratory, Monterey

1. INTRODUCTION

Lifted airborne by strong surface winds blowing across the dry, barren deserts of the world, dust produces a myriad of effects whose physics and feedbacks we are still only beginning to understand. In addition to their obvious detrimental effect upon surface visibility, significant atmospheric dust burdens pose a serious hazard to jet aircraft engines—factors of particular relevance to Navy tactical interests. Climatologically, dust modifies the energy budget of the earth by restructuring the radiative heating profile of the atmosphere. This includes shortwave (reflection) cooling and longwave (emission) warming at the surface and the opposite effect within atmospheric layer where the dust itself resides. Such perturbations have direct implications to the ensuing local atmospheric circulation (Miller and Tegen, 1988).

Dust can further influence the earth's radiation budget by altering the optical properties of clouds in terms of enhanced reflectivity (owing to a greater number of cloud condensation nuclei and a larger proportion of small, more reflective droplets) or enhanced absorption (multiple scattering within a cloud/dust layer increasing photon path lengths and hence the probability of absorption) (Twomey, 1972). Dust storms originating in the Sahara desert, transported thousands of kilometers across the Atlantic Ocean, have been linked to the atrophy of the coral reefs in the Caribbean (Shinn *et al.*, 2000). Perhaps more alarming, recent studies claim that these same storms may carry bacterial colonies that are detrimental to human health (e.g., Griffin *et al.*, 2001).

Considering these points, there exists a clear need for the monitoring of dust outbreaks on scales ranging from tens to thousands of km spatially and 1-min to several days (and possibly weeks) temporally. We appeal to satellites to provide this level of coverage and detail. This paper summarizes recent and ongoing efforts by the Naval Research Laboratory (NRL) to provide a near-real-time observational capability for dust storms using multispectral imager data from the Meteosat-7 and Sea-viewing Wide Field-of-view Sensor (SeaWiFS) instruments. The combination of geostationary and polar-orbiting platforms provides complimentary information on the spatial, spectral, and temporal characteristics of developing dust outbreaks. Combining visible and infrared imagery enables the identification and enhancement of these storms over both land and ocean backgrounds (e.g., Shenk and Curran, 1974; Lee, 1989).

* *Corresponding author address:* Steven D. Miller, Naval Research Laboratory, Monterey, CA 93943-5502;e-mail: miller@nrlmry.navy.mil

2. DATA

2.1 *SeaWiFS*

SeaWiFS, a scanning imager radiometer with 8 narrowband spectral channels between 412 and 865 nanometers (nm), is carried aboard the SeaStar spacecraft. Launched into a sun-synchronous orbit in August 1997, the instrument features a local area coverage (LAC) swath width of 2801-km (58.3° maximum scan angle) and spatial resolution of 1.1-km. Since no infrared channels are included, data are collected only during the daytime descending nodes. A varying sensor tilt of +/-19.8 degrees is used to avoid areas of sun glint. Typically there are to 3 passes per day over a given region at low to mid-latitudes. NRL is currently working with SeaWiFS data ingested at Navy Regional Centers (NRC) located in Bahrain, Yokosuka (Japan), and Rota (Spain) at 1-2 hour latency.

2.2 *Meteosat-7*

Meteosat-7 carries a scanning imager radiometer with channels in the visible, water vapor, and infrared window spectral regions. It was launched into a geostationary orbit at 0° longitude in July 1998. Data are available at 2-km resolution and half-hourly intervals, providing the capability to loop imagery and monitor both the temporal and spatial

evolution of dust storms during both day and night. In this way, Meteosat-7 compliments the fine-scale spectral and spatial resolution provided by SeaWiFS.

3. PROCEDURE

3.1 *SeaWiFS Processing*

The satellite-tracking antenna used to capture the SeaWiFS L-band telemetry is subject to surface clutter, especially near the horizons. The raw Level-0 data are calibrated (Level-1B) using SeaDAS software and then corrected for bad scan lines and spurious pixel noise owing to this clutter. Adjacent lines are use to replace bad scan lines, and noisy pixels are replaced by the mean of adjacent noise-free pixels. Rayleigh (molecular) scatter is then removed from all the SeaWiFS channels via a lookup table of pre-calculated solar reflectance data spanning all sun/sensor geometries. Post-calibration processing and product generation for SeaWiFS data are done using the Interactive Data Language (IDL) and TeraScan (SeaSpace) software packages.

"True color" images are created by assigning the SeaWiFS 412, 555, and 670 nm data to the blue, green, and red color palettes, respectively. The resultant image is similar but not identical to what the human eye would detect, with cloud-free ocean pixels appearing as blue (cyan in shallow waters), land surfaces as earth tones (with green vegetation), and clouds as white. Optically thick dust plumes over the ocean are discriminated easily from water/ice clouds by their yellow hue, strong contrast against the dark ocean background, and laminar spatial structure. Detection over the desert from visible imagery alone is more difficult, owing to the highly reflective background. Attempts to do so using measures of contrast reduction have met with varying degrees of success (e.g., Tanre and Legrand, 1991). The difficulty has been addressed in part here by appealing to the infrared sensing capability of Meteosat-7 described below.

As a further enhancement of any dust component present in the SeaWiFS data over the ocean, land areas are masked-out and the red channel in the aforementioned "true color" composite is replaced by a normalized spectral reflectance difference between 865 and 412 nm (SeaWiFS Channel 8 – Channel 1, or "8-1" hereafter). This produces negative values over the clear blue oceans, strong positive values over unvegetated land, and smaller positive values for clouds and airborne dust over the ocean. While both dust and clouds yield positive 8-1 values, their magnitudes relative to these same components of the 670 nm channel are such that the dust signal is made stronger and the cloud signal weaker. The dust component is therefore enhanced in the red color palette and clouds appear more a cyan than their usual white when combined with the unaltered blue and green channel data.

To reproduce white clouds in these scaled data, a simple cloud mask based on a minimum threshold on magnitude and maximum threshold on variance in the red, green, and blue channel reflectances is applied. The corresponding red channel data are substituted back into the 8-1 image such that clouds again appear white, while the dust component remains enhanced. While not required from the perspective of dust enhancement, this provides a more visually intuitive depiction of the overall scene. Masking the cloud field also allows for additional enhancement of the dust signal if desired. In the cases examined here this was not found to be necessary.

3.2 *Meteosat-7 Processing*

The Meteosat-7 dust enhancement algorithm takes advantage of thermal contrasts between airborne dust and the underlying surface. Following the discussion of Shenk and Curran (1974), during the middle of the day airborne dust that is cooler than the hot desert surface will produce depressed brightness temperatures with respect to the surrounding clear sky background. During the night any dust residing near the surface usually produces brightness temperatures very near the land background temperature, rendering detection nearly impossible. Detection over the ocean is achieved during the daytime by visible imagery.

NRL Monterey currently displays this contrast information in two ways. The first is a gray-scale image with visible channel data over the oceans and infrared over land (unless nighttime, then only infrared). The second

approach involves a red/green/blue composite where Meteosat-7 visible data are loaded into the red palette and the infrared channel into the blue and green palettes. In this case, land surfaces and dust-over-ocean appear as shades of yellow, and elevated dust over land will appear as various shades of blue against the bright yellow background.

4. CASE STUDY SUMMARIES

The following are two recent dust events captured by SeaWiFS and Meteosat-7.

4.1 *Saharan Dust Event*

Prolonged droughts in western Africa toward the end of the 20th century have lead to corresponding increases in the frequency and severity of Saharan dust storms. During February 12-13, 2001 a large cloud of Saharan dust streamed westward over the Central Eastern Atlantic. Carried by the prevailing winds, the plume streamed northward, skirting the Canary Islands, and finally wrapped into a low-pressure system off the coast of the Iberian Peninsula (reports of "mud-rains" in connection with these circumstances are not uncommon). At 1255 Z a SeaWiFS orbit (collected by the Rota NRC) captured this dramatic synoptic-scale dust feature near the center of its pass. Meteosat-7 data were available at half-hourly intervals over the duration of the event.

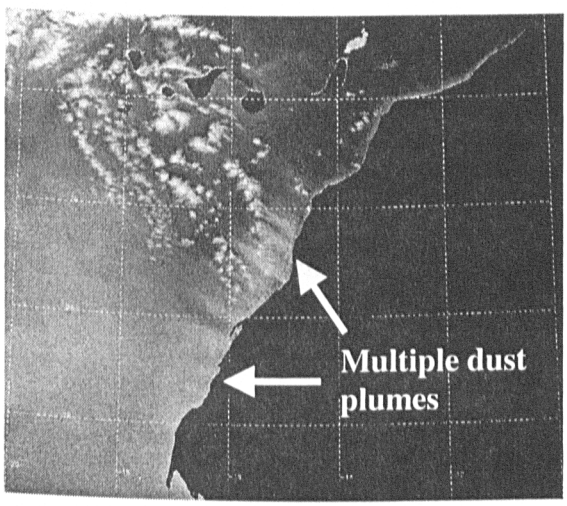

Fig. 1. SeaWiFS 8-1 dust enhancement for 2/13/01 at 1255 Z. Land regions have been masked out.

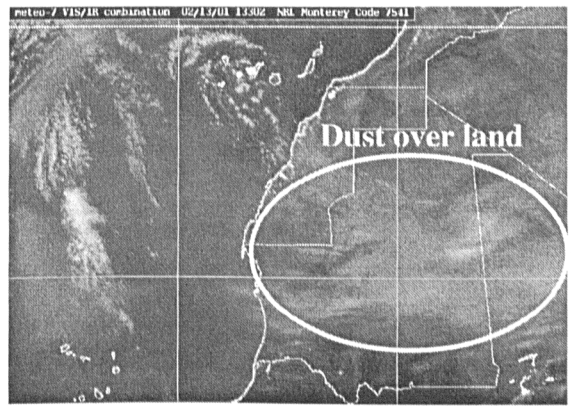

Fig. 2. Meteosat-7 vis/ir combination for 2/13/01 at 1330 Z.

Figure 1 shows a portion of the SeaWiFS-enhanced dust plume as it departed the Western Sahara coastline. Arrows indicate numerous distinct plumes of dust leaving the coastline at lower levels (as inferred from cloud shadows). The high resolution SeaWiFS data also reveals fine scale gravity waves in the stable boundary layer, with optically thicker bands corresponding to the convergent components of these waves.

The Meteosat-7 data revealed the full extent of the dust over a large portion of the northern African continent (Figure 2, with approximate region of dust-over-land indicated by an ellipse) and its progression from east to west over time. Tracking of the land component of the storms is best achieved using a time series. In the times series (not shown), the maximum contrast between the airborne dust and the underlying surface occurred near mid-day (maximum skin temperatures) and vanished almost completely by nightfall as the surface cooled rapidly.

4.2 *Shamal Dust Event*

From the Arabic word for "north," the Shamal is a low-level wind common to the Persian Gulf region during the summertime. Its existence is the consequence of the prevailing high pressure over northern Saudi Arabia, thermal low pressure over Pakistan and Afghanistan and lee trough associated with the Zagros mountain range of western Iran (Membery, 1983). The combined effect is a persistent north/northwesterly wind with a typical monthly mean of 19 knots that often is

responsible for loading the air over the Persian Gulf with copious amounts of dust.

On June 29, 2001 at 0819 Z a SeaWiFS pass (collected by the Bahrain NRC) occurred during the onset of a major Shamal dust event over the Persian Gulf. A plume of dust originating in the Tigris-Euphrates Valley can be seen clearly in the SeaWiFS enhancement (Figure 3). The Meteosat-7 vis/ir product (Figure 4) reveals distinct plumes of dust on the interior. By 1330 Z, the entire northwestern Gulf was consumed by airborne dust.

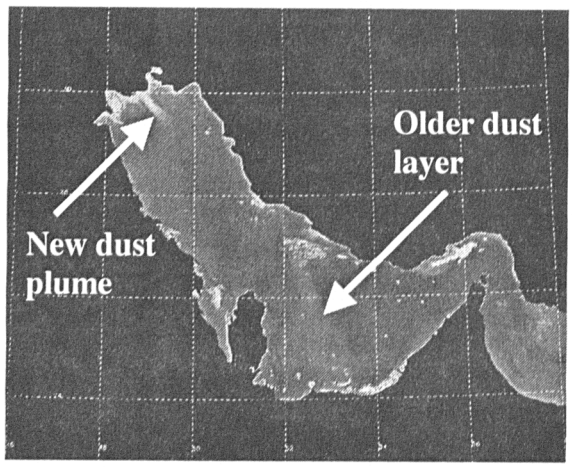

Fig. 3. SeaWiFS 8-1 dust enhancement at onset of Shamal 6/29/01 0819 Z. Land regions have been masked out.

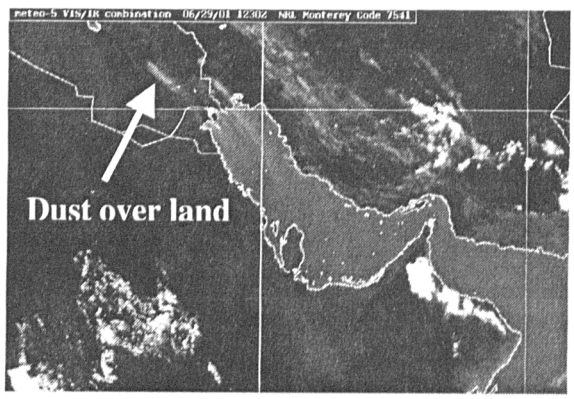

Fig. 4. Meteosat 7 vis/ir combination at 1330Z showing extensive dust coverage.

The transport of surface material by post-Shamal transitional winds has been studied in connection to the transport/dispersion of chemical nerve agents demolished in Southeastern Iraq in 1991 (Westphal *et al.*, 1998). Imagery from SeaWiFS and Meteosat can provide valuable tracer validation for such aerosol dispersion studies in the future.

5. CONCLUSION

Coincident Meteosat-7 and SeaWiFS data provide complimentary information in terms of spatial, spectral, and temporal resolution for detecting, enhancing, and monitoring desert dust storms. NRL Monterey currently processes these data in near real-time over areas of particular interest to Naval operations, and research with regard to dust detection and enhancement via multispectral imagery is ongoing.

6. REFERENCES

Griffin, D. W., et al., 2001: African desert dust in the Caribbean atmosphere: microbiology and public health. *Aerobiologica*, In press.

Membery, D. A., 1983: Low-level wind profiles during the Gulf shamal. *Weather*, **38**, 18—24.

Miller, R. L., and I. Tegen, 1988: Climate response to soil dust aerosols. *J. Climate*, **11**, 3247—3267.

Lee, T. F., 1989: Dust tracking using composite visible/IR images: a case study. *Wea. Forecasting*, **4**, 258—262.

Shenk, W. E., and R. J. Curran, 1974: The detection of dust storms over land and water with satellite visible and infrared measurements. *Mon. Wea. Rev.*, **102**, 830—837.

Shin E. A., et al., 2000: African dust and the demise of Caribbean coral reefs. *Geophys. Res. Lett.*, **27**, 3029—3032.

Twomey, S., 1972: The effect of cloud scattering on the absorption of solar radiation by atmospheric dust. *J. Atmos. Sci.*, **29**, 1156—1159.

Westphal, D. L. *et al.*, 1998: Meteorological reanalyses for the study of Gulf War Illnesses: Khamisiyah case study. *Wea. Forecasting*, **14**, 215—241.

7. ACKNOWLEDGEMENTS

The support of the research sponsor, the Oceanographer of the Navy through the program office Space and Naval Warfare Systems Command, PMW-155, under program element 0603207N is gratefully acknowledged.

P1.12 CHARACTERIZATION OF CLOUDS, FIRES AND SMOKE PLUMES IN HYPERSPECTRAL IMAGES

Michael K. Griffin*, Su May Hsu, Hsiao-hua K. Burke and J. William Snow
MIT Lincoln Laboratory, Lexington, MA

1. INTRODUCTION

Hyperspectral imaging (HSI) sensors have been used for more than a decade to aid in the detection and identification of diverse surface targets, topographical and geological features. Techniques for scene characterization can utilize individual or combinations of spectral bands to identify specific features in an image. This paper deals primarily with the problem of characterization of a partially smoke- or cloud-filled atmosphere. Proper analysis of the scene allows further sensing of underlying surface features such as actively burning and burn scarred regions. Both a physics-based and a semi-automated feature extraction (principal components analysis, PCA) approach are used for identifying and characterizing features in a set of AVIRIS scenes dominated by areas of smoke plumes, clouds and burning grassland as well as burnt vegetation. A combination of the two approaches is used to both discriminate (PCA) and classify (physics based) various features in a smoke/cloud filled scene.

An AVIRIS scene chosen for initial testing of the two algorithms was collected on 20 August 1992 in the foothills east of Linden, CA[1]. A typical AVIRIS scene covers a 10km x 10km area at 20m pixel resolution and 224 contiguous spectral bands of data over the range 400 to 2500 nm. The scene consists of a grass fire producing a thick plume of smoke extending toward the east (see Fig. 1a). A cloud produced by the thermal properties of the fire overlies the smoke plume. Northwest of the main fire, two smoldering fires produce a thin veil of smoke that covers much of the upper half of the scene. The southwest portion of the scene is cloud and smoke free. This scene (identified as the Linden scene in this paper) provides a variety of atmospheric and surface features from which to orient and characterize. A plot of the apparent reflectance (ratio of reflected to incoming solar radiance) of various identified features in the scene is shown in Fig. 1b. The legend displays the user identified features. The cloud is significantly brighter than the smoke over the entire spectral region. The hot area is brightest in the spectral region 2000 to 2500 nm, while the fire pixels are bright for wavelengths greater then 1150 nm.

2. PRINCIPAL COMPONENT ANALYSIS (PCA)

To reduce the HSI data dimensionality and therefore the computational complexity, feature extraction can be performed on the spectral data before application of image pixel clustering. Principal component analysis is generally used to de-correlate data and maximize the information content in a reduced number of features[2][3]. The covariance matrix is first computed over the pixel spectra contained in the HSI data cube of interest. Eigenvalues and eigenvectors are then obtained for the covariance matrix. Using the eigenvectors as a new coordinate system, the HSI data cube is then transformed into principal components, also called eigenimages. The eigenimages associated with large eigenvalues contain most of the information while the eigenimages associated with small eigenvalues are noise-dominated. Thus principal component transform allows determination of the inherent dimensionality and segregation of noise components of the HSI data. The components are ranked in descending order of the eigenvalues (image variances). Since backgrounds constitute the majority of information in the scene, they are contained in the first few principal components. Anomalies, which comprise only a small fraction of the scene, are in higher numbered principal components. Fig. 2 displays the 1st, 2nd and 5th principal components of the AVIRIS data for the Linden Scene. The first component shows the overall intensities of features such as bright clouds and smoke plumes over backgrounds. A dark area which appears to be the source of the thick smoke is apparent in the 2nd component. In the 5th component, a small fraction of the image pixels are in contrast to the image backgrounds.

Since the principal components are orthogonal and thus de-correlated, different image features can be separated from the components with appropriate thresholds to the pixel histogram distribution.

2.1 Physics-based analysis

Utilizing the diverse spectral and spatial information afforded by HSI observations of a scene, formulas can be developed relating the spectral measurements to discriminate and identify specific features in a scene (i.e., clouds, smoke, lakes, etc.). Equations for the discrimination of clouds, large and small particle smoke, high temperature surface regions and areas of burnt vegetation have been derived. A brief description of the phenomenology follows. Ultimately, these formulas can be used to classify regions identified by the PCA routine as having similar properties.

2.2 Clouds

Clouds are typically the brightest feature in an AVIRIS image. The reflectance from clouds is nearly invariant in the visible and near-IR window regions, since the size of the scatterers in the cloud are much larger (size parameter >> 1) than the sensor wavelengths. This is in contrast to atmospheric aerosols whose particle

* *Corresponding author's address:* Michael K. Griffin, S4-257, MIT Lincoln Laboratory, 244 Wood St., Lexington, MA 02420-9185, Voice: 781-981-0396, Email: griffin@ll.mit.edu

size tends to be at or near the observed wavelengths of radiation and therefore the scattering effects vary significantly with wavelength throughout the visible and near-IR. This information can be used to discriminate clouds from darker background objects and from bright but spectrally variable smoke plumes and fires.

A three step approach is used to isolate clouds in an AVIRIS scene. The first step removes dark background objects such as rivers, lakes and vegetation from consideration by applying a threshold to the 640 nm reflectance image. A threshold of 0.20 has been observed to eliminate a large portion of the background scene. The second step takes advantage of the spectral invariability of cloud. A ratio of the 640 and 860 nm reflectance images is obtained and all pixels with ratios less than 0.70 are eliminated. It has the effect of removing much of the smoke and vegetation that display distinct changes over the range of frequencies from 640 to 860 nm. Finally, to isolate the cloud from the surrounding thick smoke, a channel in the 1600 nm window region is used. A threshold of 0.35 was obtained from observation of the spectral characteristics in this region. Those remaining pixels with reflectance values above 0.35 were designated cloud.

2.3 Hot Spots

Areas of active burning or smoldering fires have distinct spectral characteristics of their own. Fig. 1b shows the effect high surface temperatures have on the measured radiance. Both the curves representative of the hot area and active fire display gradually increasing radiance (apparent reflectance) in the SWIR region. Non-physical reflectances greater than one in Fig. 1b are an indication of a combination of both solar and a significant thermal component to the measured radiance. A high surface temperature (> 400 K) is needed to produce a significant thermal component at these wavelengths[4]. Reflectance differences greater than 0.1 between channels in the SWIR (2200 nm) and the NIR (1095 nm) allowed the discrimination of these features.

2.4 Smoke plumes

As described above, the reflectance characteristics of smoke plumes vary systematically with wavelength. Also, smoke from smoldering fires may contain larger particles than that from more intense fires; the particles have had more time to coagulate. Therefore, it is useful to separate the smoke category into two subcategories: large and small particle smoke. In the Linden scene, small particle smoke is produced by the main fire near the center of the scene and is quite opaque in the visible and near-IR wavelengths. Observations of the spectral signature of small particle smoke indicate that a comparison of visible and SWIR channels provide a method of discrimination. When the difference between the reflectances at 490 nm and 2200 nm is greater than 0.02, small particle smoke is indicated.

Large particle smoke, observed as the large thin plume emanating from the two small fires in the upper left of the Linden scene, is relatively transparent to observations in the visible and near-IR. An empirical relationship was derived using visible channels only to isolate areas with large particle smoke. When the reflectance at 430 nm is greater than 0.18 and the ratio of the reflectance at 430 and 510 is greater than 1.2, then large particle smoke is indicated.

2.5 Burn Index

Biomass burning not only produces detectable smoke plumes but results in burn scars having spectral signatures that are distinct from that of undisturbed vegetation. Vegetation indices have been developed which highlight the change from low to high reflectance in the visible and near-IR spectral region. The Normalized Difference Vegetation Index (NDVI) is commonly used to categorize various surface vegetation types as well as separate vegetative from non-vegetative features (water, snow, etc.). The NDVI cannot be used under cloudy or smoky conditions since both tend to mask the underlying signal at these wavelengths. In an effort to obtain information about the spatial extent of biomass burning, a burn index (BI) was devised that can be used to detect areas of burnt vegetation using wavelengths that are more transparent to smoke. The formula used here for burn scar detection is

$$BI = \frac{\rho_{1100} - \rho_{2200}}{\rho_{1100} + \rho_{2200}}$$

where ρ_n represents the reflectance at a wavelength of n nanometers. Before application of the BI, a cloud and thick smoke mask is applied to the scene. The BI, like the NDVI, has the capability to discriminate between vegetation types, but with the added benefit of operating even under moderately smoky conditions. Fig. 3 shows the result of application of the BI to the Linden scene. A large burn scar is observed under the thin smoke plume in the upper left quadrant of the image.

3. COMPARISON OF RESULTS

Fig. 4 displays the results from application of the above two techniques to the Linden scene. Fig. 4b represents a composite of the results from applying the physics-based formulas to the AVIRIS data. Features identified in Fig. 4b were matched to classes derived from application of the PCA technique to the Linden scene and are shown in Fig. 4a. Two classes for which formulas have not been derived (visually identified as fire and shadow) are indicated in the PCA composite. Both techniques seem to provide good individual characterizations of the Linden scene, even to the differentiation of large particle (darker magenta) and small particle (lighter magenta) smoke.

4. SUMMARY

Two techniques for characterization of atmospheric features were applied to an AVIRIS scene. A feature extraction technique based upon principal component

analysis was used to separate distinct feature classes in an AVIRIS image. The PCA does not provide information on the identity of the resultant classes, only that they are distinguished in the analysis of the image. To identify these features, a physics based approach which utilizes the unique characteristics of the spectral signatures of the features is applied. Results are matched with the PCA classes to provide feature identification. The techniques were in agreement as to separation of classes and the general shape of the observed features for the Linden CA scene. It is likely a combination of the two techniques with the inclusion of the burn index, could provide a useful tool for the characterization and identification of scenes containing clouds, smoke and active fires from HSI data.

5. REFERENCES

[1] Gao, B.-C., Y. Kaufman and R. Green, "Remote Sensing of Smoke, Clouds and Fire Using AVIRIS Data," *Proc. of the Fifth Annual JPL Airborne GeoScience Workshop*, JPL Publication 93-16, Pasadena, CA, 1993, pp. 61-64.

[2] Geladi, P. and H. Grahn, Multivariate Image Analysis, John Wiley & Sons, New York, 1997.

[3] Richards, J., Remote Sensing Digital Image Analysis, Springer-Verlag, Berlin, 1994, 133 p..

[4] Green, R., "Estimation of Biomass Fire Temperature and Areal Extent from Calibrated AVIRIS Spectra," *Proc. of the Seventh Annual JPL Airborne GeoScience Workshop*, JPL Publication 96-16, Pasadena, CA, 1996, pp.105-113.

6. ACKNOWLEDGMENTS

The authors wish to thank CAPT Frank Garcia at DUSD (S&T), program manager for the Hyperspectral Technology Assessment Program (HTAP) at Lincoln Laboratory, and Dr. Ed Howard of the NOAA GOES program for their support of this effort. This work was sponsored by the Department of Air Force under Contract F19628-00-C-0002. Opinions, interpretations, conclusions and recommendations are those of the authors and not necessarily endorsed by the United States Air Force.

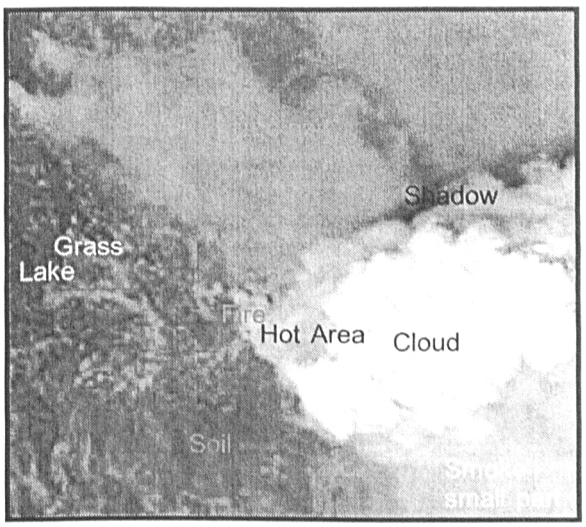

(a)

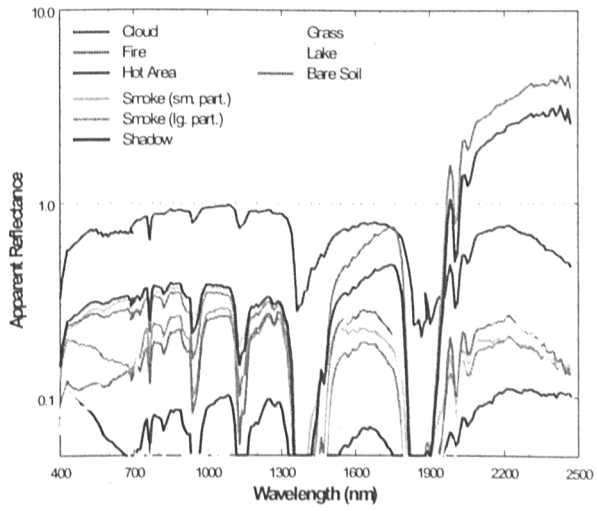

(b)

Figure 1. a) AVIRIS RGB image for the Linden, CA scene collected on 20-Aug-1992, denoting location of various features of interest and b) a plot of the spectral distribution of the apparent reflectance for those features.

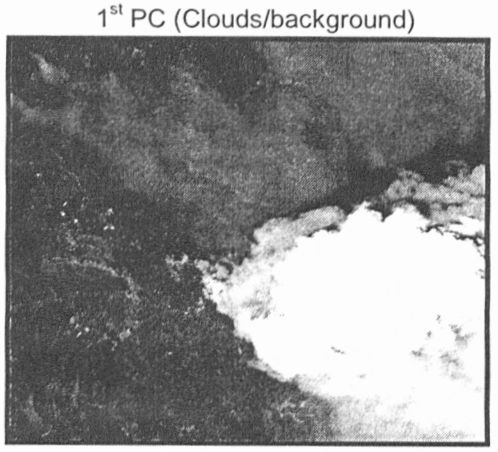

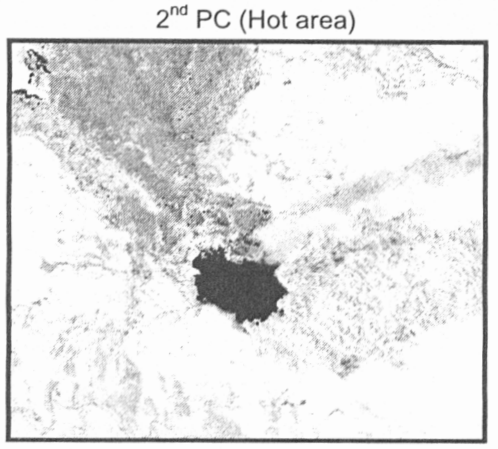

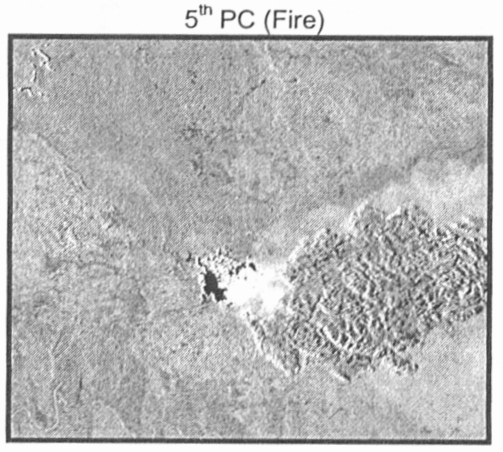

Figure 2. The 1st, 2nd and 5th principal components of AVIRIS data for the Linden scene.

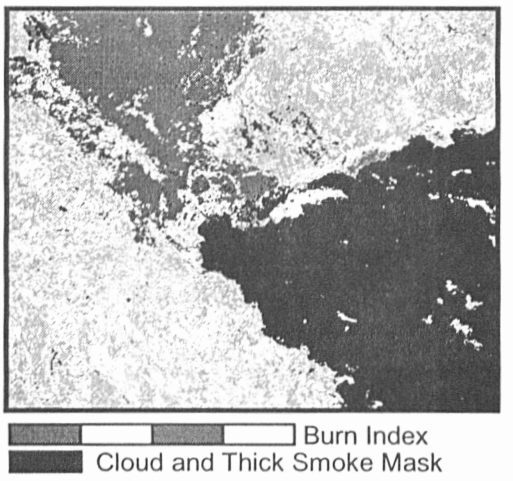

Figure 3. Application of the Burn Index to the Linden AVIRIS scene. Brown areas in upper left quadrant are indicative of burn scars. Cloud and thick smoke regions have been masked out (black).

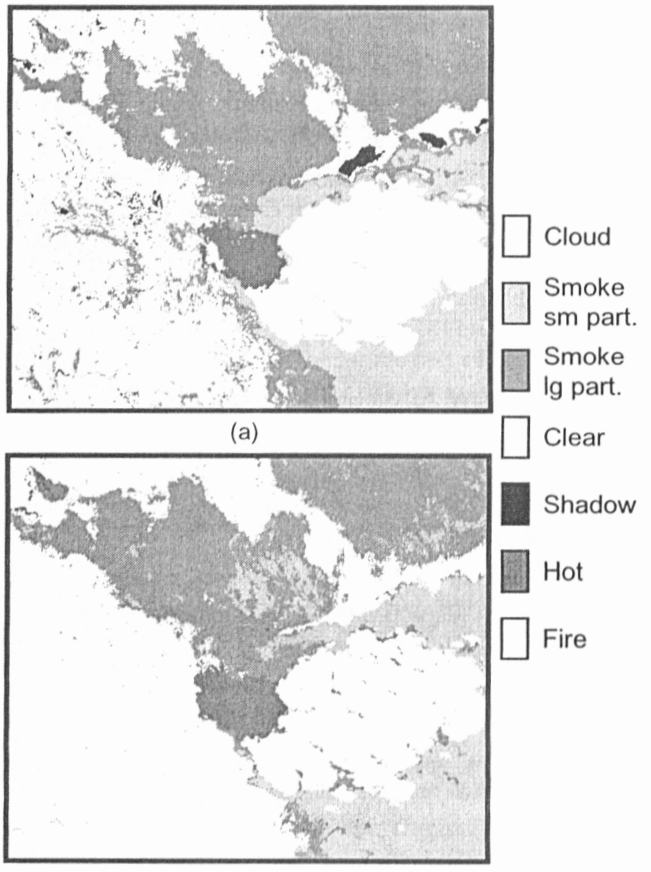

Figure 4. Composite results of the image characterization for the Linden AVIRIS image from (a) PCA and (b) physics based techniques.

P1.13

A COMPARISON OF THE GOES-8 ABBA AND INPE AVHRR FIRE PRODUCTS FOR SOUTH AMERICA FROM 1995-2000

Joleen M. Feltz*
Cooperative Institute for Meteorological Satellite Studies, University of Wisconsin, Madison, Wisconsin

Elaine M. Prins
NOAA/NESDIS/ORA Advanced Satellite Products Team, University of Wisconsin, Madison, Wisconsin

Alberto W. Setzer
Instituto Nacional de Pesquisas Espaciais, Sao Paulo, Brazil

1. INTRODUCTION

Since 1995 the Cooperative Institute for Meteorological Satellite Studies (CIMSS) at the University of Wisconsin - Madison has been using the Geostationary Operational Environmental Satellite (GOES)-8 Automated Biomass Burning Algorithm (ABBA) to monitor diurnal biomass burning activity throughout South America during the height of the fire season (June - October). The Brazil Instituto Nacional de Pesquisas Espaciais (INPE) has monitored fire activity in Brazil using the Advanced Very High Resolution Radiometer (AVHRR) sensor on board the NOAA-12 polar orbiting satellite since 1987. This paper presents a comparison of these two fire products during each fire season from 1995 to 2000. It will include an overview of the spatial and temporal observing characteristics of both the GOES and AVHRR instruments and discuss advantages of each system for fire identification in the region. This comparison will show that the higher temporal resolution of the GOES and the higher spatial resolution of the NOAA AVHRR provide complementary information about fire activity in South America.

2. THE GOES-8 ABBA AND NOAA AVHRR INPE FIRE PRODUCTS

The GOES-8 ABBA is a fully automatic fire detection algorithm which uses the visible (near 0.65 micron), short-wave infrared window (near 4 micron), and the long-wave infrared window (near 11 micron) data, along with moisture information from other data sets, to identify and characterize sub-pixel fire activity. The GOES-8 spatial resolution is 4 km at the sub-satellite point, but studies have shown that GOES-8 can accurately identify fires a few acres in size (Menzel and Prins, 1996a; 1996b; Prins and Menzel, 1996a; 1996b). The geostationary orbit of GOES-8 provides the opportunity to view and estimate fire activity over portions of South America every half-hour, with complete continental coverage at three-hour intervals. These data can then be studied individually or combined in a daily unique fire composite. Fire pixels from four different time periods (1145, 1445, 1745, and 2045 UTC) are combined in the daily unique fire composite. If a fire pixel is observed in more than one time period, only one occurrence of the fire pixel is selected for the daily unique fire pixel composite. Typically, over 80% of the fire pixels observed in one time period are not observed at any of the other three observation periods (Prins et al., 1998; 2000; 2001).

The AVHRR sensors on the NOAA polar orbiting series of satellites have a spatial resolution of 1 km at the sub-satellite point. Generally, INPE reports fire pixels from the NOAA-12 sensor with the exception of 1-14 August 1995, when the NOAA-14 sensor was used to report the fire pixels. The fire detection method employed by INPE is a digital nonsupervised clustering algorithm which selects pixels as burning if the AVHRR radiometric temperature exceeds 46°C (Setzer and Pereira, 1991). Data from the afternoon overpass are used to identify fire pixels. Fire counts from INPE are provided in a weekly email in grid format. They consist of a 7-day sum at 0.5-degree increments from 7°N to 40°S and 75°W to 34.5°W. A second receiving station, added in 1999, increased the observation region. However, the smaller region is used in this study for consistency between years.

Previous studies have characterized the GOES-8 observed diurnal, spatial, seasonal, and interannual trends in fire activity, clouds, and aerosols throughout South America for each fire season (June –October) from 1995 to 1999 (Prins et al., 1998; 2000). This study will focus on the combined spatial and temporal distribution of fires provided by GOES and AVHRR for the months of August-October 1995-2000. This captures the peak of the burning season and minimizes the number of missing days.

* *Corresponding author address:* Joleen M. Feltz, University of Wisconsin-Madison, Cooperative Institute for Meteorological Satellite Studies, 1225 W. Dayton, Madison, WI 53706; email: joleen.feltz@ssec.wisc.edu.

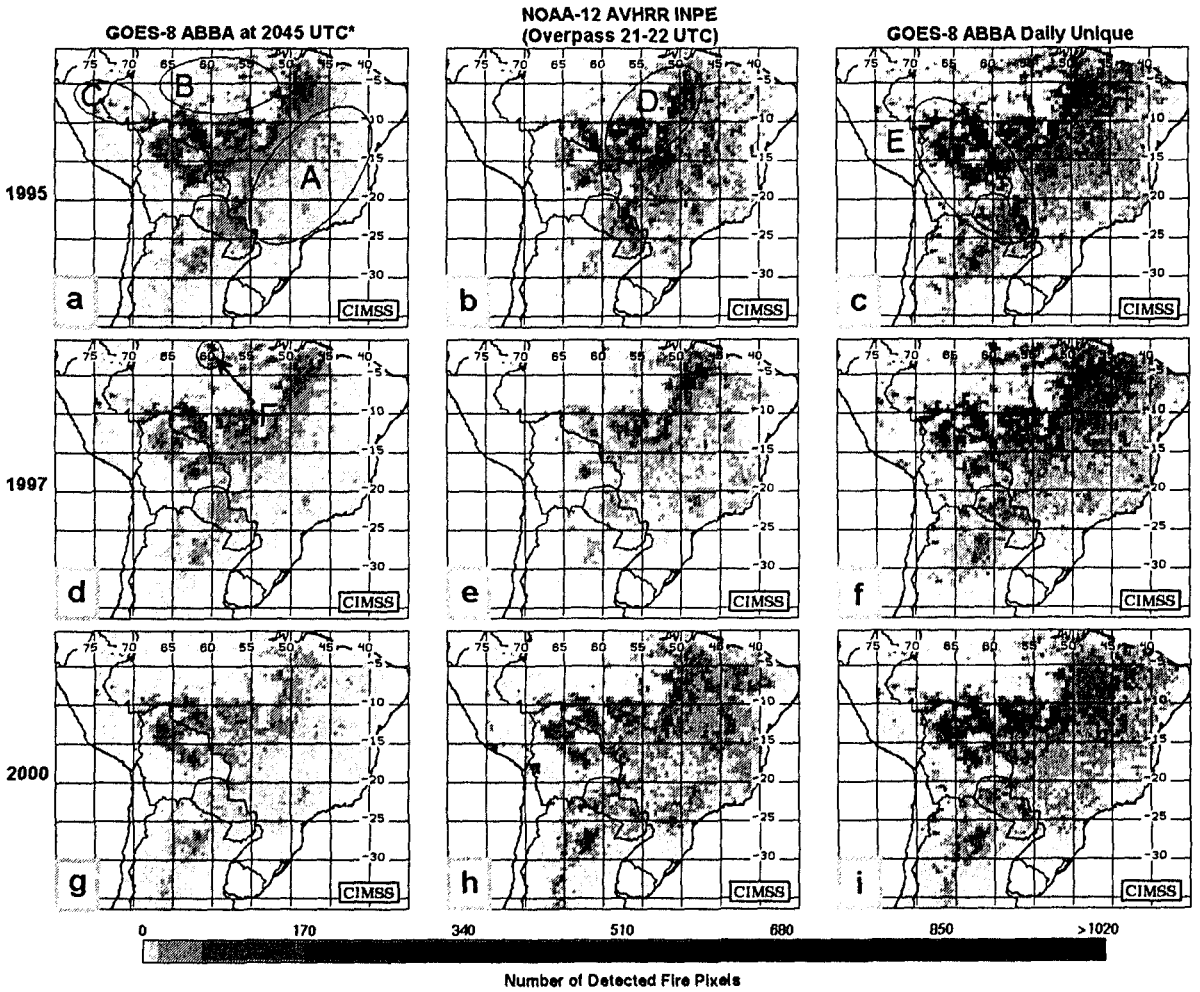

Figure 1: A comparison between the GOES-8 ABBA and NOAA-12 AVHRR INPE detected fire pixels for the months of August-October 1995, 1997, and 2000. The grid spacing is 0.5 degrees.

3. FIRE DISTRIBUTIONS IN SOUTH AMERICA AS OBSERVED BY GOES and NOAA AVHRR IN 1995, 1997, AND 2000

Fire distributions for all the years from 1995-2000 were plotted, and three representative years are shown in figure 1. The GOES-8 ABBA fire product at 2045 UTC (fig 1a, 1d, 1g), the NOAA-12 AVHRR INPE detected fire pixels from the afternoon overpass (fig 1b, 1e, 1h), and the GOES-8 ABBA daily unique fire product (fig 1c, 1f, 1i) are shown for comparison. The most active year was 1995 followed by 1997. The 1997 season was also selected to show the effect of drought in northern Amazonia. Both sensors observed less burning in 2000, providing an opportunity to compare a year with lower activity to the peak years. Examples from these three years show that satellite regional coverage, view angle, time of observation, and sensor spatial resolution all affect fire detection.

Overall, the NOAA-12 AVHRR INPE algorithm detects more fire pixels in a single time period than the GOES-8 ABBA at that same time period. This pattern is especially pronounced in the cerrado regions (region A) where narrow flame fronts are difficult to detect with GOES-8 due to its reduced spatial resolution. It is sometimes possible for GOES-8 to detect cerrado fires in the initial flaming stage, and the GOES-8 ABBA daily unique fire product shows many fires in the cerrado region which were missed in the 2045 UTC GOES-8 ABBA, but reported in the NOAA-12 AVHRR INPE fire pixel product. The two instruments tend to show the same patterns in regions where the view angle for both sensors is low and the coverage for AVHRR is good.

Burning along roads and the Amazon river (region B) is observed in all of the images, but the single time period distributions neither capture the extent nor the intensity of activity. Every year fires along the road being constructed west from Rondonia

(region C) to the Pacific coast appear in the GOES-8 ABBA fire composites. However, the road is not well defined in the NOAA-12 AVHRR INPE fire pixel product except in year 2000. The detection of burning along the road in 2000 by the AVHRR sensor resulted from the addition of a western receiving station providing more consistent information in western South America. The sensors also consistently show that most fire activity is concentrated in the "arc of deforestation" (region D). The GOES-8 ABBA also indicates that the borders between Bolivia and Rondonia, and Acre and Paraquay (region E) are places of more persistent activity. In peak years the GOES-8 ABBA 2045 UTC fire pixel product compares well with the NOAA-12 AVHRR INPE fire pixel product. However, the single time period quantities underestimate the number of fires reported throughout the day. In addition, the NOAA-12 AVHRR INPE product underestimates burning along the border regions as compared to the GOES-8 ABBA daily unique and in 1997 and 2000, the GOES-8 ABBA 2045 UTC data. It is near these border regions, close to the GOES-8 sub-satellite point of 0°N and 75°W, where the view angle for GOES-8 is optimal. The 1997 drought in Northern Amazonia caused a lake north of Manaus to dry (region F). The exposed timber on the bottom of the lakebed subsequently caught fire. Both sensors captured this event, but the AVHRR did not observe as many instances of that fire. The fire burned for days, but the AVHRR observed the Manaus region less than 2% of the time from August-October 1997.

4. COMPARISONS OF FIRE QUANTITIES DERIVED FROM GOES AND NOAA AVHRR FROM 1995-2000

The number of fires reported by both GOES and AVHRR are displayed in table 1. Since each year covers a different date range, the 1995 totals are a combination of two different time periods, and a second AVHRR receiving station was added in 1999, interannual comparisons of the totals are not possible. Two of these caveats produce results that are easily distinguished in the data shown in table 1. First, the contribution of the 1745 UTC period to the GOES-8 ABBA daily unique composite is significant. Therefore, the fire pixel totals for both GOES-8 ABBA at a single time period and the NOAA-12 AVHRR INPE are closer to the total fire pixel estimates of the ABBA daily unique algorithm in 1995 than in other years. Secondly, the 1999 and 2000 INPE totals are closer to the GOES-8 ABBA daily unique totals in the respective years, reflecting the extended coverage of the AVHRR.

The GOES-8 ABBA daily fire pixel counts range from 1.5 to 4.5 higher than the single time period NOAA-12 INPE AVHRR observations between 21-22 UTC. The ratio of ABBA daily unique fire pixels to the single time period ABBA estimates is even higher, ranging from 3 to 5. Grid subsets were used to allow a comparison between the GOES-8 ABBA daily unique and the NOAA-12 AVHRR INPE fire pixel products where the NOAA-12 AVHRR has better coverage (table 2).

Table 1

Year	Julian Day (NOAA Overpass)	INPE	GOES Single Time Period	GOES Daily Unique
1995	209-226 (17-18 UTC) 227-303 (19-22 UTC)	134417	86827	267584
1996	208-305 (19-22 UTC)	45137	42393	205293
1997	213-304 (19-22 UTC)	66097	56449	260696
1998	213-309 (19-22 UTC)	110675	60326	248018
1999	213-304 (19-22 UTC)	141516	62340	247583
2000	214-305 (19-22 UTC)	103272	29107	169095

Table 2

	Fire Pixel Counts (Ratio of GOES/INPE)		
	Entire Grid	60% Coverage	80% Coverage
1995	2.0	1.3	1.1
1996	4.5	3.0	2.5
1997	3.9	2.5	2.2
1998	2.2	1.6	1.4
1999	1.7	1.7	1.8
2000	1.6	1.6	1.6

When the NOAA-12 AVHRR views a region at least 60% of the time, the ratio of GOES-8 ABBA daily unique fire pixel observations to NOAA-12 AVHRR INPE fire pixels decreases to a ratio ranging from 1.3 to 3. At 80% coverage, the ratio is between 1.1 and 2.5. The lack of variability in the ratios for 1999 and 2000 are a result of the increased AVHRR coverage following the addition of the second receiving station. Prior to 1999, less than 30% of the study area had 60% or greater overpass coverage. This value increased to 50% in 1999 and to 91% in 2000.

The 1 km resolution of the NOAA-12 AVHRR generally provides the capability to detect more fires at a single time period, and provides enhanced information where the overpass coverage is high. However, the ability to capture fires as they burn throughout the day is also extremely important since previous studies have shown that many fire signatures are often only intense enough to be detected by satellite for a short time period (Prins et al, 1998; 2000).

5. CONCLUSIONS

Comparisons of the NOAA-12 AVHRR INPE and the GOES-8 ABBA fire pixel products show similar features in the spatial distribution of fires in South America. The higher spatial resolution of the NOAA-12 AVHRR results in more fire pixel observations at an instantaneous point in time and allows for the identification of fires with smaller flaming fronts. Since GOES-8 is in geostationary orbit, it can capture

the diurnal cycle of anthropogenic fires for better definition of regions with strong temporal signatures. It is also able to capture some fires in the flaming stages that are below the threshold of detection in later time periods. The consistent and complete continental coverage of GOES-8 allows it to observe fires in regions not adequately covered by a single overpass of the NOAA-12 satellite. The addition of the second NOAA polar orbiting satellite receiving station in 1999 made a significant impact on regional coverage. GOES-8 and AVHRR provide distinct and complementary capabilities for monitoring fire activity in South America.

6. REFERENCES

Menzel, W.P., and E.M. Prins, 1996a: Monitoring biomass burning and aerosol loading and transport utilizing multispectral GOES-8 data. 1996 International Symposium on Optical Science, Engineering, and Instrumentation, SPIE, Denver, Colo, August 4-9, 1996, pp. 50-59.

Menzel, W.P., and E.M. Prins, 1996b: Monitoring biomass burning with the new generation of geostationary satellites. In Biomass Burning and Global Change, edited by J.S. Levine, MIT press, Cambridge, MA, pp. 56-64,

Prins, E.M., and W.P. Menzel, 1996a: Monitoring biomass burning and aerosol loading and transport from a geostationary satellite perspective. Seventh Symposium on Global Change Studies, Am. Meteorol. Soc., Atlanta, Ga., Jan. 28 – Feb. 2, 1996, pp. 160-166.

Prins, E.M., and W.P. Menzel, 1996b: Investigation of biomass burning and aerosol loading and transport utilizing geostationary satellite data. In Biomass Burning and Global Change, edited by J.S. Levine, MIT press, Cambridge, MA, pp. 65-72.

Prins, E.M., W.P. Menzel, and J.M. Feltz, 1998: Characterizing spatial and temporal distributions of biomass burning using multi-spectral geostationary satellite data. Ninth Conference on Satellite Meteorology and Oceanography, Paris, France, May 25-29, 1998, pp. 94-98.

Prins, E.M., J. M. Feltz, R. A. Frey, C. C. Schmidt, W. P. Menzel, D. Wylie, 2000: A five-year trend analysis of biomass burning in South America Using GOES, Presented at the American Geophysical Union Spring Meeting, May 30 – June 2, 2000, Washington D.C.

Prins, E.M, J.M, Feltz, C.C. Schmidt, 2001: An overview of active fire detection and monitoring using meteorological satellites, Proceedings of the 11th Conference on Satellite Meteorology and Oceanography, Madison, WI, October 15-18, 2001, pp TBD.

Setzer, A.W., and M.C. Pereira, 1991: Amazonia biomass burnings in 1987 and an estimate of their tropospheric emissions. Ambio, 20, 19–22.

P1.14

Principal Component Image Analysis of MODIS for Volcanic Ash

Donald W. Hillger*
NOAA/NESDIS/ORA/RAMMT
CIRA / Colorado State University
Fort Collins CO

James Clark
NOAA/NESDIS/OSDPD/SSD
Satellite Analysis Branch
Camp Springs MD

1. Introduction

Current volcanic ash detection techniques rely heavily on split window differencing of the thermal longwave infrared bands (11 and 12 μm) on current operational satellites (Prata 1989). However this technique is not uniformly effective in properly classifying volcanic ash pixels in the satellite scene, often falsely interpreting meteorological cloud as volcanic ash clouds and conversely (Simpson et al 2000). A recommendation of that study is that new research-grade satellite remote sensing instruments employing multi-spectral observations of volcanic plumes in the thermal infrared be used to better characterize eruptive events and that the information be used to design improved volcanic ash cloud detection sensors. This will lead eventually to wider operational exploitation of these powerful and increasingly accessible technologies (Oppenheimer 1998).

One of the new satellite research sensors currently available is the Moderate Resolution Imaging Spectroradiometer (MODIS). MODIS imagery offers a multi-spectral advantage over Geostationary Operational Environmental Satellite (GOES) imagery for viewing volcanic ash plumes. The advantage is due to the larger number of spectral bands on MODIS (36 bands: 19 bands in the visible and near-infrared, and 17 bands in the longer-wavelength infrared). In comparison there are five bands in the GOES Imager. All of the thermal infrared bands of MODIS are available at 1 km spatial resolution (at nadir). This is a horizontal resolution advantage over 4 km GOES infrared data, but that is not the focus of this study. In addition, some of the MODIS bands are in portions of the spectrum not sensed by GOES. This spectral advantage however is offset by the lack of sufficient temporal resolution and continuity to follow rapidly-changing phenomena as is customary from geostationary orbit.

2. Principal Component Imagery

In their study of volcanic plumes, Dean et al (1994) found that satellite images analyzed using principal component techniques clearly distinguished the plume from the surrounding terrain. Their preferred analysis technique utilized three-color composites of principal component and spectral band images to show the extent of the plume as well as its opaque and transparent properties. While typically applied to remote sensing of earth resources, principal component analysis has been applied to GOES Imager and Sounder data to create Principal Component Images (PCIs) for the detection of atmospheric and surface features in multi-band imagery (Hillger* 1996, Hillger and Ellrod, 2000). In addition, the use of principal component analysis becomes increasingly important as the number of spectral bands increases.

Half-hourly GOES imagery is used by the Washington Volcanic Ash Advisory Center (VAAC) to routinely produce analyses of ash plumes. One of the image products used to generate the ash advisories is PCI analysis of GOES multi-spectral imagery, in use operationally since December 1999. The basic PCI product is based on the three infrared bands (bands 2, 4, and 5) of the GOES Imager. Each of the three component images is a linear combination of the input bands with weights applied based on the transformation of the original bands using eigenvector/eigenvalue analysis of the original imagery. For the GOES Imager, PCI-2 and PCI-3 have proven to be the most useful for volcanic hot spot and ash plume detection respectively. This is because the common or correlated information in the three GOES infrared bands is relegated to PCI-1. PCIs 2 and 3 contain band difference information that highlights features not seen in single-band imagery. PCI-2 is primarily a band 2/4 (shortwave/longwave difference) image, and PCI-3 is primarily a band 4/5

* Corresponding author address: Dr. Donald W. Hillger, NOAA/NESDIS/RAMMT, CIRA/Colorado State University, Fort Collins CO 80523-1375. E-mail: hillger@cira.colostate.edu

(longwave split window difference) image, with small contributions from the remaining band in each case.

3. Analysis of Volcanic Ash

The case analyzed for this study was a large eruption of ash from the Popocatepetl volcano (hereafter abbreviated Popo, 19.02°N, 98.62°W) at 5426 m elevation near Mexico City. One of the days with widespread ash was 20 December 2000. Figure 1 shows an analysis issued by the Washington VAAC (Operations 1999) giving the extent of the ash plume based on GOES multi-spectral imagery for 1715 UTC. This analysis time matches the time of the MODIS imagery that was analyzed using PCIs. The ash extends mainly south and east of the volcanic source, to as far away as the Yucatan Peninsula. In the ash analysis the plume is given in two parts, at different flight levels (FL250 [7600 m] and FL320 [9800 m]). These levels were estimated by effectively matching the derived vector motion of the ash as seen in GOES imagery to the appropriate height levels from the Mexico City upper-air sounding and a model sounding.

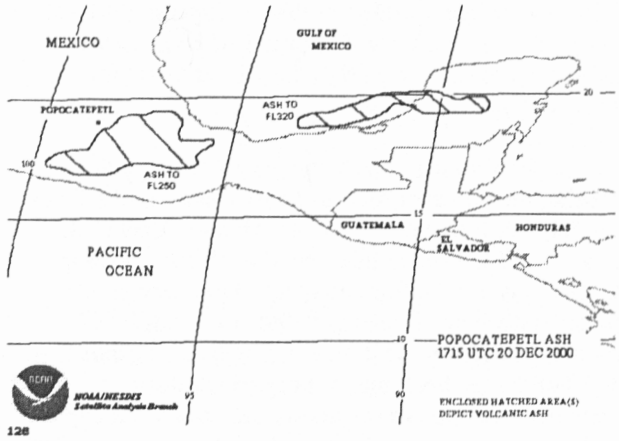

Figure 1: Volcanic ash analysis at 1715 UTC on 20 December 2000 for Popocatepetl volcano near Mexico City. Analysis based on GOES multi-spectral imagery by the Satellite Analysis Branch (SAB) Washington VAAC.

PCI-3 in Figure 2 is one of the GOES products used to generate the ash analysis in Figure 1. This product shows the ash cloud with good contrast to the image background, but with somewhat limited contrast to some of the other image features. The ash is mainly concentrated to the east and southeast of Popo. Ash extends east to a secondary maximum over Yucatan. The extent of the ash in both the ash analysis and PCI-3 serve as guides for the MODIS analysis to follow.

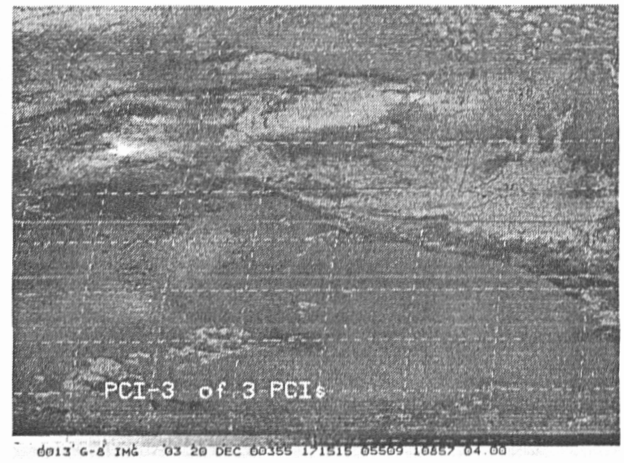

Figure 2: PCI-3 of 3 PCIs that were generated from the three thermal infrared bands (2, 4, and 5) of GOES for 1715 UTC on 20 December 2000. PCI-3 is one of the products used to generate the ash analysis in Figure 1. This product shows the ash cloud with significant contrast to the image background. This PCI is inverted black-to-white to make the ash plume white.

MODIS data for this volcanic ash case were available at 1715 UTC. None of the MODIS bands showed the relatively diffuse ash for this case when viewed alone. This is expected when the ash signal is subtle, appearing in contrast to the image background much more readily in multiple-image combinations. Ash that is associated with meteorological cloud can more easily be seen, but the ash content may be unknown. PCI analysis of the 17 MODIS thermal infrared bands provided several views of the ash plume. Table 1 shows the bandwidths and primary uses of MODIS thermal infrared bands used in the analysis.

The PCI analysis of the 17 thermal infrared bands of MODIS resulted in 17 PCIs. This paper will discuss only those PCIs that qualitatively show significant evidence of ash in contrast to the image background and other image features. This will lead into an analysis of the MODIS bands that contributed to those PCIs. The PCIs for this case are remapped from the MODIS polar-orbit projection into the GOES projection, to be more easily compared and contrasted with the ash analysis in Figure 1 and the GOES image in Figure 2.

Figure 3, showing the first PCI (PCI-1), which contains the majority (76%) of the information content (explained variance) in the 17 MODIS bands that went into the 17 PCIs, information common to all the thermal infrared bands. As such it gives an idea of the overall cloud conditions at the time of the event, the main features available in most of the thermal infrared bands.

The whitest areas are the highest clouds, low clouds are medium gray, and land surfaces are dark. Land surfaces vary in temperature from the blackest (hottest) to lighter gray (cooler). The area around but mainly to the north of Popo (which is marked by a label and an arrow pointing to the location of the volcano) contains some middle to higher-level clouds. Some of the white cloud mass nearest the volcano, appearing in PCI-1 as a result of appearing in most of the infrared bands, must be meteorological cloud. No ash plume is apparent in this image. Rather, the ash appears in higher-ordered PCIs where it becomes detectable by combining images from various portions of the spectrum.

Table 1: MODIS thermal infrared bands and bandwidths

Primary Use	MODIS Band	Bandwidth (μm)
Surface/Cloud Temperature (shortwave CO_2)	20	3.66-3.84
	21	3.929-3.989
	22	3.929-3.989
	23	4.02-4.08
Atmospheric Temperature (shortwave CO_2)	24	4.433-4.498
	25	4.482-4.549
Cirrus Clouds	26	1.36-1.39
Water Vapor	27	6.535-6.895
	28	7.175-7.475
	29	8.4-8.7
Ozone (O_3)	30	9.58-9.88
Surface/Cloud Temperature (split window)	31	10.78-11.28
	32	11.77-12.27
Cloud Top Altitude (longwave CO_2)	33	13.185-13.485
	34	13.485-13.785
	35	13.785-14.085
	36	14.085-14.385

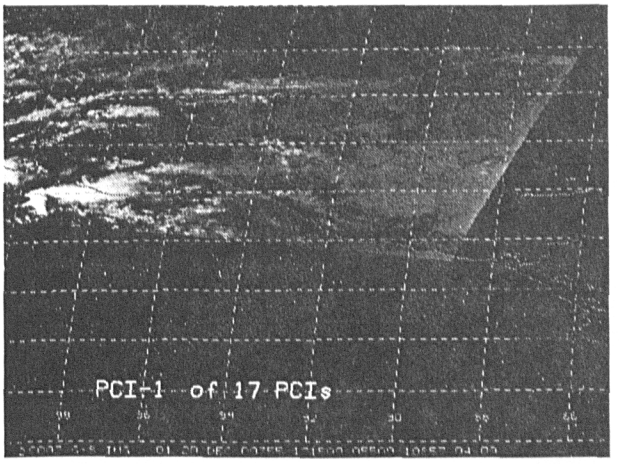

Figure 3: PCI-1 of 17 PCIs that were generated from the 17 thermal infrared bands of MODIS for 1715 UTC on 20 December 2000. PCI-1 shows the main cloud features common to all of the MODIS infrared bands.

3.1 Analysis of the PCIs That Show Ash

Of the remaining higher-ordered PCIs, only those in which the ash was detected with significant contrast to the image background and other image features will be discussed. The discussion will focus on where the ash was detected in each PCI, some of the relative qualities of those images for ash detection, and on the MODIS bands that contributed to those PCIs.

Table 2 summarizes details of the nine (of seventeen) PCIs that contained identifiable ash signal. The PCIs are listed in order of decreasing ash signal or contrast to the background and other features of the image. In the first three PCIs listed in the table the ash has much more contrast to surrounding regions than in the next three, and even more contrast than in the last three PCIs, which are of limited value for ash detection. The relative qualities of each PCI are given in the second column of Table 2. Detection problems, such as low contrast, noise, and confusion between ash cloud and non-ash features, are noted. Because of the decreasing ability to detect ash compared to the image background and other image features, it is increasingly hard to use more than the first six of these PCIs to determine the presence of ash for this case. Of those six PCIs, only the first three will be shown.

Each PCI consists of combinations of all input bands, but only a few of the original bands contribute heavily to the PCIs, as indicated by their much larger weight in the creation of the PCIs. After a discussion of the first three PCIs, in the order listed in Table 2, details summarizing the MODIS bands contributing to those PCIs will follow. In the last two columns of the table

are the percentage of the explained variance and the signal-to-noise ratio for each PCI. The signal-to-noise ratios were determined using spatial structure analysis (Hillger and Vonder Haar, 1988). A signal-to-noise ratio greater than 1.0 represents sufficient signal in the image to view features. (The top value in the last column, 1.70, means there is 70% more signal than noise in PCI-9). These two columns show that the information content of the PCIs is a very small fraction of the total signal in the MODIS bands, and that the signal in some of the PCIs is marginally above the noise level of the image. From these numbers it is clear that the best ash signal does not necessarily come from PCIs with larger explained variances or highest signal-to-noise ratios.

Table 2: PCIs in descending order of qualitative value for ash plume detection

PCI number (in descending qualitative value)	Qualitative assessment of ash contrast to the image background and features	PCI Explained Variance (%)	PCI Signal-to-Noise Ratio
9	Good ash concentration and extent	0.12	1.70
8	Good ash concentration and extent, noisy	0.18	1.26
16	Good ash concentration and extent, but cloud	0.002	3.30
14	Densest ash only, low contrast	0.012	1.48
4	Densest ash only, significant cloud contamination	2.7	6.55
10	Densest ash only, low contrast, noisy	0.07	1.26
13	Very weak, low contrast	0.027	1.20
15	Very weak, contaminated	0.003	1.70
7	Questionable value	0.39	3.71

PCI-9 in Figure 4a shows the volcanic ash as light gray in contrast to the image background. The ash also appears in PCI-8 in Figure 4b but with more noise than PCI-9. Table 2 gives a signal-to-noise ratio of 1.70 for PCI-9 and 1.26 for PCI-8. The signal-to-noise ratio is quite small for both PCIs, but there is sufficient signal above noise and contrast to the image background, so that the extent of the ash in both of these PCIs agrees well with the ash analysis in Figure 1. However, the increased signal-to-noise for PCI-9 gives the image a smoother-looking background, as opposed to the more apparent noise and line-to-line striping (due to multiple detectors in the MODIS instrument) in PCI-8. There is also one bad half-line of data near the middle of the MODIS band 30 image that was transferred into most of the PCIs as a dashed line similar to the latitude and longitude lines.

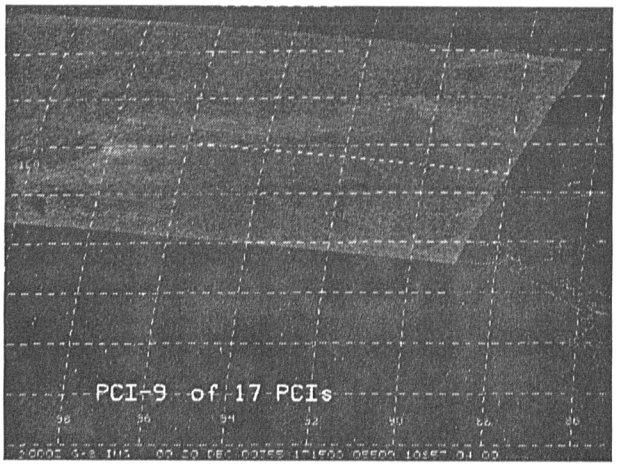

Figure 4a: PCI-9 of 17 PCIs that were generated from the 17 thermal infrared bands of MODIS for 1715 UTC on 20 December 2000. PCI-9 shows the ash plume as light gray, with good contrast to the image background and low noise.

In PCI-8 the portion of the ash plume not obscured by the clouds, as identified in PCI-1 in Figure 3, is denser to the east and southeast of the volcano. The ash also extends quite far east over the Yucatan Peninsula where there is a secondary maximum, due to an earlier exhalation of ash. The elongated west-east area of ash extending to the Yucatan may be slightly easier to identify in PCI-8, but there is increased chance of confusion between ash and low clouds to the south as seen in PCI-1. Also, another difference between the two PCIs is that the maximum ash concentration is east of Popo in PCI-8 and more southeast of Popo in PCI-9, probably due to variations in the height of the ash as noted in the analysis.

Figure 4c shows PCI-16, the next PCI in Table 2, with somewhat reduced ability to detect ash. The extent of the ash in PCI-16 is quite similar to that of GOES PCI-3 in Figure 2. PCI-16 is interesting because there is more connection between the primary ash maximum near Popo and the secondary ash maximum over Yucatan, highlighting this portion of the ash cloud. The secondary maximum also appears more intense

than in either PCI-9 or PCI-8. The variations are likely due to changes in the ash particle concentration and height of the ash in various parts of the plume. PCI-16 also contains more false ash-like signal. In particular, the thin line of ash-like signal just north of Popo, stretching from the western edge of the image eastward to 95°W, is identifiable as cirrus in PCI-1. Otherwise non-ash contamination in the signal can cause misidentification and either over- or under-estimation of the extent of the ash plume. This non-ash signal is probably the source of the increased signal-to-noise (3.3 from Table 2) for PCI-16, not the ash signal.

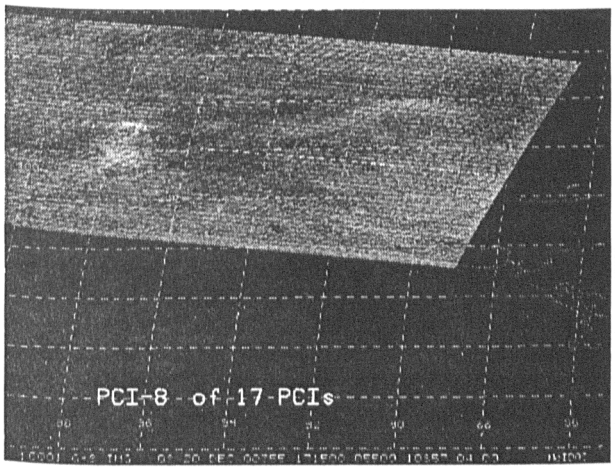

Figure 4b: Same as Figure 4a except PCI-8. PCI-8 shows the ash as white but contains significant image striping and noise from the MODIS instrument compared to PCI-9.

Table 3 gives information on the six MODIS bands that contributed the most to PCIs that were best at detecting the ash plume. Only the nine MODIS bands that contributed significantly to the first six PCIs are listed. For each of those bands the explained variance and sign are given for their contribution to each of the six PCIs. The explained variance is a measure of the magnitude of the contribution of each band and the sign is given to indicate whether the band contributed positively or negatively to a particular PCI. Whether the sign of a particular band is positive or negative is only important relative to the signs of the other bands, otherwise any PCI can be inverted along with the signs of all of the bands that contributed to it.

In Table 3 the two bands, one with the most positive and the other with the most negative explained variance, are bolded for each PCI. After the third PCI, the following row contains the sums of the explained variances for each band to the first three PCIs, regardless of the sign of the contribution. The bands that are considered most important for volcanic ash detection, with variances above 30%, are bolded. In this case the most important bands for overall ash detection are 25 (marginally), 30, 31, and 36. Likewise, the final row in the table gives the sums of the explained variances for each band to all six PCIs indicated as adequate for ash detection. This time the most important bands, with total explained variance over 50%, are bands 29 through 32, 34, and 36, leaving out band 25. The additional bands are important for locating more subtle variations in the ash plume density, such as seen in PCI-14. Thus these bands should not be excluded from ash analysis.

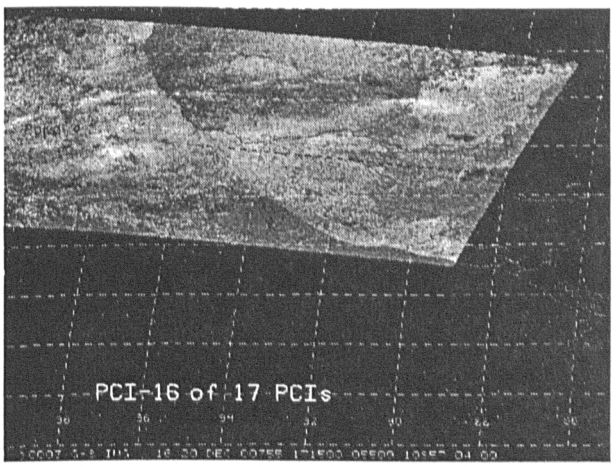

Figure 4c: Same as Figure 4a except PCI-16. PCI-16 shows the ash plume as lighter gray, but suffers from possible false ash signal due to cloud contamination.

The bands determined to be most important are combined in various ways to reveal the ash: PCI-9 is the difference between the ozone and longwave CO_2 bands at 9.7 μm and 14.2 μm respectively; PCI-8 is mainly the difference between shortwave and longwave CO_2 bands at 4.52 μm and 14.2 μm respectively; PCI-16 is the difference between a longwave window band and a nearby "dirty" window band at 11.0 μm and 12.0 μm respectively; and PCI-14 is primarily the difference between a water vapor band and a "dirty" window band at 8.6 μm and 12.0 μm respectively.

There is an emissivity minimum between 8.0 and 9.7 μm due to silicate rock, which is probably why the combination of bands in PCI-9 is the most important. Also, the 8.6 μm band is near the peak absorption for sulphate aerosols around 8.4 μm (Prata 1989), which is probably why the combination of bands in PCI-14 is important, in addition to the minimum in emissivity due to silicate in that portion of the spectrum.

Table 3: MODIS bands contributing heavily to the first six PCIs in Table 2 (in descending order of ash plume contrast to the image background and other image features)

PCI	Explained Variance (%) and Sign (negatives in parentheses) of MODIS Band Contributions								
	20	25	29	30	31	32	33	34	36
	3.75 μm	4.52 μm	8.6 μm	9.7 μm	11.0 μm	12.0 μm	13.3 μm	13.6 μm	14.2 μm
9	3	(11)	(~0)	51	~0	(~0)	1	1	(16)
8	4	(19)	2	9	1	~0	(2)	(6)	54
16	~0	~0	(7)	(~0)	63	(17)	(~0)	~0	~0
Sum of above	7	30	9	60	64	17	3	7	70
14	1	(2)	48	(4)	(2)	(36)	1	~0	(~0)
4	24	1	(17)	(1)	(6)	(6)	~0	6	12
10	(1)	(1)	1	~0	~0	(1)	(36)	43	(1)
Sum of all above	33	34	75	65	72	60	40	56	84

4. Summary and Conclusions

The abundance of bands available on MODIS requires sophisticated band-combination techniques such as PCIs to determine the bands that are most suitable for detection of volcanic ash. Even though the explained variance of most of the PCIs is generally small, several of these image products provided sufficient signal above noise to see the ash plume with good contrast to the image background and other image features. While many of the MODIS bands contribute to ash detection, various combinations of these bands, in the form of various PCIs, highlight variations in the ash plume height and/or density, where the ash occurs at different levels or has different particle concentrations. These applications of the PCI technique isolate MODIS band combinations that are the most useful and significant for qualitatively detecting both the extent and the concentration of the ash.

The multitude of MODIS bands gives much more flexibility for ash detection than the limited number of bands on the GOES Imager. The results of this study indicate that several of the MODIS bands are useful for volcanic ash detection, in particular, bands 29 through 32, in the water vapor and longwave portions of the spectrum. This includes the 7.0 to 9.7 μm portion of the spectrum known for volcanic ash signature. However, band 30 at 9.7 μm is neither available on the current GOES Imager nor planned for future GOES Imagers. Regardless, better ash plume detection will be available with the increased number of bands and good temporal resolution available from the Imagers planned for the GOES series.

Acknowledgements

The MODIS data for this study were provided by Chris Moeller of the CIMSS at the University of Wisconsin in Madison. Funding for this study is made available through NOAA Grant NA67RJ0152.

5. References

Dean, K., S.A. Bowling, G. Shaw, and H. Tanaka, 1994: Satellite analyses of movement and characteristics of the Redoubt volcano plume, January 8, 1990. *Journal of Volcanology and Geothermal Research*, 62, 339-352.

Hillger, D.W., and T.H. Vonder Haar, 1988: Estimating noise levels of remotely-sensed measurements from satellites using spatial structure analysis. *J. Atmos. Ocean. Tech., 5(2)*, April, 206-214.

Hillger, D.W., 1996: Meteorological analysis using principal component image transformation of GOES imagery. *International Radiation Symposium - IRS'96: Current Problems in Atmospheric Radiation*, (W.L. Smith and K. Stamnes, Editors; A. Deepak Publishing), 19-24 August, Fairbanks AK, 480-483.

Hillger, D.W., and G.P. Ellrod, 2000: Detection of unusual atmospheric and surface features by employing Principal Component Image transformation of GOES imagery, *Tenth Conference on Satellite Meteorology and Oceanography*, AMS, 9-14 January, Long Beach CA, 461-464.

Operations of the Washington Volcanic Ash Advisory Center, 1999: *Third Caribbean/South American Regional Air Navigation Meeting*, International Civil Aviation Organization, October 05-15, 5-p.

Oppenheimer, C., 1998: Volcanological applications of meteorological satellites, *International Journal of Remote Sensing*, 19, 2829-2864.

Prata, A.J., 1989: Observations of volcanic ash clouds in the 10-12 μm window using AVHRR/2 data, *International Journal of Remote Sensing*, 10, 751-761.

Simpson, J.J., G. Hufford, D. Pieri, and J. Berg, 2000: Failures in detecting volcanic ash from a satellite-based technique, *Remote Sensing of Environment*, 72, 191-217.

P 1.15

Loss of the 12.0 μm "Split Window" Band on GOES-M: Impacts on Volcanic Ash Detection

Gary P. Ellrod
Office of Research and Applications (NOAA/NESDIS)
Camp Springs, Maryland 20746

1. INTRODUCTION

Beginning with the Geostationary Operational Environmental Satellite (GOES)-M spacecraft (successfully launched on 23 July 2001) through GOES-Q (scheduled launch in 2007), a 12.0 μm "Split Window" InfraRed (SWIR) band (4 km resolution) on the Imager will be replaced by a 13.3 μm CO_2 absorption band (8 km resolution). Table 1 summarizes the changes planned for the reconfigured GOES Imagers. A more detailed description of GOES-M, with an assessment of effects on many environmental parameters, is available in Schmit et al, (2001).

Brightness temperature differences (BTD) between the IR window bands at 10.7 μm (Band 4 on GOES) and 12.0 μm (Band 5) have been successfully used in tracking hazardous volcanic ash clouds since they first became available on GOES-8 in 1994. Negative values of the Band 4 minus Band 5 BTD are typical of volcanic ash, while positive values denote meteorological clouds (e.g. Prata, 1989). This Two-Band Split Window (TBSW) product from GOES-8 is relied upon heavily at the Washington Volcanic Ash Advisory Center (VAAC), which is responsible for operational hazard monitoring of a large, volcanically-active portion of the Caribbean, and Central and South America. Other North American VAACs (Anchorage, Montreal) also employ the TBSW from GOES, but to a lesser extent.

The purpose of this paper is to describe the possible impact of the loss of this IR channel on volcanic ash detection within the GOES field-of-view, and discuss alternative strategies to mitigate this loss. The latter comprise: (1) maximum utilization of all remaining GOES channels, and (2) exploitation of the global constellation of polar orbiting meteorological satellites, including the operational National Oceanic and Atmospheric Administration (NOAA) series, and research satellites launched by the National Aeronautics and Space Administration (NASA).

2. DATA AND PROCEDURES

In order to assess the effect of the GOES-M+ Imager channel reconfiguration on volcanic ash detection, GOES-8 Imager or Sounder data from several prior eruptions were analyzed to see how volcanic ash coverage would look with and without the use of the 12.0 μm IR band. The GOES-8 Sounder (see Menzel et al, 1998) has all IR bands currently on the Imager, plus the 13.3 μm band, although at a lower resolution (10 km). The analysis was completed using principle component image software developed by Hillger (1996) which displays unique information available from the input IR wavelengths. The best principle component depiction of the ash cloud for each event was compared to a subjective best estimate of the actual ash cloud coverage based on: (1) analysis of all available GOES data, including visible images, (2) the evolution of the volcanic cloud from its eruption to image time, and (3) VAAC advisories. In one case (26 December 1997) a concurrent Total Ozone Mapping Spectrometer (TOMS) Aerosol Index image was obtained as a source of independent ash coverage.

In addition to qualitative comparisons, a quantitative parameter, termed "false pixel rate" (FPR) was determined. The FPR describes the percentage of the total image area (expressed in pixels) comprised of "false ash" (based on the subjective "true" ash plume described above). This can be described as:

$$FPR = (T - A) / N \qquad (1)$$

where T is the total of ash plus false pixels, A is the number of "true" ash pixels, and N is the total number of pixels in the image scene.

The six cases analyzed are summarized in Table 2, which contains information on the volcano name, date, time(s), type of data evaluated (Imager versus Sounder) and relative strength of the eruption. Analysis of the 26 December 1997 Soufriere Hills eruption is not complete. Two cases (Lascar, 20 July 2000 and Guagua Pichincha, 5 October 1999) were evaluated at hourly intervals for several hours. For some events that utilized only Sounder data, only single time periods are available due to the relatively infrequent Sounder scanning of volcanically active regions (once every six hours for the Caribbean, one to three hours for the Gulf of Mexico, none over South America).

Corresponding author address: Gary P. Ellrod, Room 601, E/RA2, WWB, 5200 Auth Road, Camp Springs, MD 20746 Email: gary.ellrod@noaa.gov

3. RESULTS

Preliminary results indicate that the loss of the SWIR band will result in an increase of mis-identified ("false") ash pixels which seem to vary diurnally. During the daytime, the increase in false pixel rate without SWIR will be minimal (~1-2%) due to the positive contribution of reflectance in the 3.9 μm shortwave IR band. At night, the false pixel rate increases by a factor of ~ 4, likely due to the loss of shortwave reflectance.

A representative daytime example is shown by the histogram in Figure 1 for the Guagua Pichincha eruption. At 2015 UTC (~1.5 hr after eruption), the FPR is >5 times larger using the SWIR than without its use. Use of the SWIR is less effective shortly after the eruption, due to the opacity of the volcanic cloud caused by large ash particles and considerable condensed water droplets and/or ice. At the later times (2115 and 2215 UTC) the FPR is ~3%, comparable to that obtained from the best image with no SWIR contribution. The increase in the latter to ~5% by 2215 UTC is due to less contribution from solar reflectance as sunset approaches. The role of reflectance at shortwave IR wavelengths has been described by Schneider and Rose (1994) for analysis of Spurr volcano ash samples in Alaska. An image comparison at 2215 UTC is shown in Figure 2.

A nighttime example from the GOES Sounder was obtained for an ash cloud from Popocatepetl volcano in Mexico that drifted across eastern Mexico on the night of 23 January 2001. The FPR values for the image that all four IR bands (including SWIR) are ~5 times less than for one that uses only the other IR bands. The latter were determined using the Sounder equivalents to Imager bands 2, 3, 4 and 2, 3, 4, and 6, respectively (Band 6 will be the new 13.3 μm IR). Inclusion of data from the 13.3 μm band appears to provide a slight positive impact, allowing for better discrimination of ash from thin cirrus clouds. A scatter plot of the Sounder data at this time for equivalent Bands 4 minus 6 vs Band 4 temperature (Figure 3) indicated a significantly higher BTD for cirrus clouds than for ash.

Subjective evaluation indicated that most of the mis-identified ash is not contiguous with the "true" ash plume or cloud, however, suggesting that a human analyst can successfully track an ash plume or cloud, and provide a reasonably good estimate of its area. The capability to animate GOES imagery at 15 to 30 min intervals provides valuable continuity in this analysis. Any gain achieved from the 13.3 μm IR data will be offset somewhat by its lower resolution (8 km), until GOES-O in 2005 when it will improve to 4 km.

4. ALTERNATIVE DATA SOURCES

In addition to the GOES Imager, the GOES Sounder provides 18 IR bands at 10 km resolution. The Sounder has limited spatial and temporal coverage however (current GOES operational scanning areas and schedules may be viewed at: http://www.ssd.noaa.gov). Nevertheless, if dedicated to view volcanic regions more often, the Sounder can provide useful TBSW-based image products (Ellrod, 1998).

The 12 μm IR channel will continue to be available at 1 km resolution from the Advanced Very High Resolution Radiometer (AVHRR) on the NOAA polar spacecraft The Moderate Resolution Infrared Spectrometer (MODIS) on the NASA Earth Observation Satellites (Aqua and Terra) will also have this spectral band , along with 35 others, also at 1 km. The Chinese Fun Yueng (FY)-1C has also recently become available to the Anchorage VAAC to fill some data gaps at high latitudes. The polar satellite data can provide better quality images to supplement (or calibrate) ash products generated from GOES. Merging of concurrent GOES and POES images is also a possibility.

5. SUMMARY AND CONCLUSIONS

GOES Imager and Sounder data were evaluated to determine the possible effects of losing the 12 μm Split Window IR band, on GOES-M (12) through Q (a period of at least 6 years). Principle component images with and without the SWIR were compared subjectively, and objectively using a false alarm rate parameter. GOES Sounder data were also evaluated in a few instances to assess any potential contributions from the new 13.3 μm Imager band. During periods of daylight, there was little difference in the quality of IR detection without the SWIR, likely due to the reflectance peak of ash near 3.9 μm. At night, the ash detection capability appeared to be somewhat worse, due to more interference from non-ash features, such as clouds or surface features. The effects of this performance on aviation operations could be an occasional increase in the area of analyzed ash coverage to err on the side of safety, resulting in somewhat longer enroute diversions. The 13.3 μm IR band should be useful in distinguishing ash from cirrus clouds, but not from low level water droplet cloud systems. In summary, we will still be able to observe and track significant volcanic ash clouds in the GOES-M through Q era (2002-2008+), but with some degradation that will be most significant at night.

6. REFERENCES

Ellrod, G. P., 1998: The use of GOES Sounder imagery for the detection of hazardous volcanic ash plumes. *National Weather Digest*, **22**, 3-9.

Hillger, D. W., 1996: Meteorological features from principle component image transformation of GOES imagery. Proceedings, Soc. of Photo-Optical Instr. Eng., 7-9 August 1996, Denver, Colorado, 111-121.

Menzel, W. P., F. C. Holt, T. J. Schmit, R. M. Aune, A. J. Schreiner, G. S. Wade, and D. G. Gray, 1998: Application of GOES-8/9 Soundings to Weather Forecasting and Nowcasting. *Bull. Amer. Meteor. Soc.*, **79**, 2059-2077.

Prata, A. J., 1989: Observations of volcanic ash clouds in the 10-12 μm window using AVHRR/2 data. *Int. J. Remote Sensing*, **10**, 751-761.-

Schneider, D. J. and W. I. Rose, 1991: Observations of the 1989-90 Redoubt Volcano Eruption Clouds Using AVHRR Satellite Imagery. *U. S. Geological Survey Bulletin 2047*, Proceedings of the First International Symposium on Volcanic Ash Detection and Aviation Safety, USGS, Reston, Virginia, 405-418.

Schmit, T. J., E. M. Prins, A. J. Schreiner, and J. J. Gurka, 2001: Introducing the GOES-M Imager. *National Weather Digest*, in press.

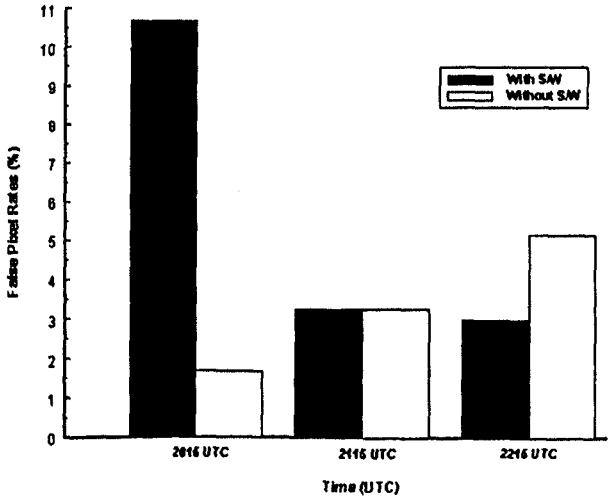

Figure 1. Histogram of False Pixel Rates (%) for Lascar eruption on 20 July 2000 with (black fill) and without (gray fill) the 12.0 μm IR band on the GOES Imager.

Table 1.
Imager Channel Configuration of GOES: Current vs GOES M-Q

	Current GOES (8-11)		GOES M-Q (2002-2008)		
Imager Band #	Wavelength (μm)	Resolution (km)	Wavelength (μm)	Resolution (km)	Description
1	0.6	1	0.6	1	Daytime visible
2	3.9	4	3.9	4	Shortwave IR
3	6.7	8	6.7	4	Water Vapor
4	10.7	4	10.7	4	Window IR
5	12.0	4	-	-	Split Window
6	-	-	13.3	8	CO2 absorption

Table 2.
Volcanic Eruption Cases Evaluated for GOES Ash Detection Capability

VOLCANO	DATE	TIMES	TYPE	INTENSITY
Soufriere Hills, Montserrat	29 Sep 97	1620 UTC	Sounder	Weak
Soufriere Hills, Montserrat	23 Sep 97	1520 UTC	Sounder	Weak
Popocatepetl, Mexico	23 Jan 01	0420 UTC	Sounder	Moderate
Guagua Pichincha, Ecuador	5 Oct 99	2015-2215 UTC	Imager	Moderate
Lascar, Chile	20 Jul 00	1539-1739 UTC	Imager	Moderate
Soufriere Hills, Montserrat	26 Dec 97	1520 UTC	Sounder	Strong

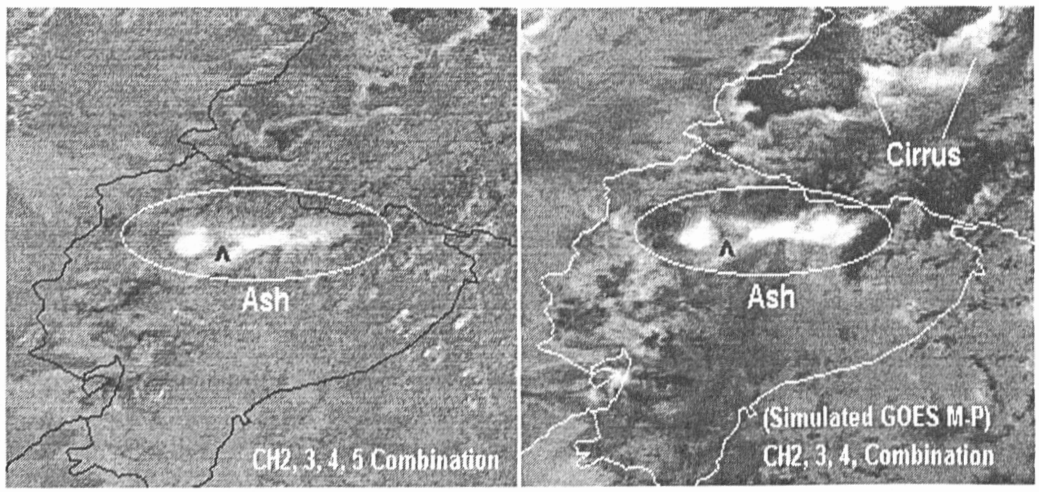

Figure 2. Comparison of ash cloud depiction from the GOES Imager on 5 October 1999 at 2215 UTC using all five IR bands, including 12 μm (left) versus only bands 2, 3, and 4 (right). The ash was produced by a moderate eruption of Guagua Pichincha volcano near Quito, Ecuador (shown by the ^) near 1945 UTC.

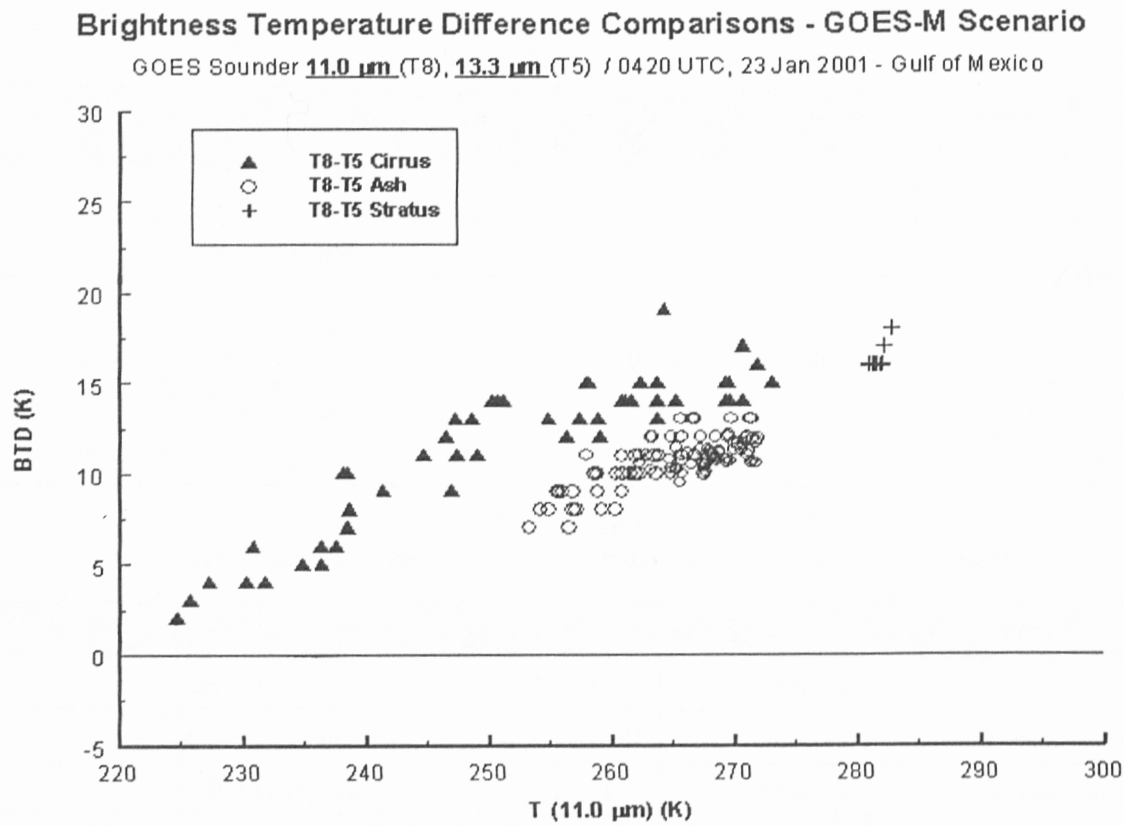

Figure 3. Scatter plot of GOES Sounder IR bands 8 - 5 BTD (equivalent to GOES-M Imager bands 4-6) versus Band 8 temperature (K) for volcanic ash (circles) and cirrus clouds (triangles) at 0420 UTC on 23 January 2001. Sounder bands 8 and 5 will be equivalent to GOES-M Imager bands 4 and 6, respectively.

P1.16 RECENT MONITORING OF SUSPENDED SEDIMENT PATTERNS ALONG LOUISIANA'S COASTAL ZONE USING ER-2 BASED MAS DATA AND TERRA BASED MODIS DATA.

Christopher C. Moeller* [1], M. M. Gunshor [1], W. P. Menzel [2], O.K. Huh [3], N. D. Walker [3], and L. J. Rouse [3]

[1] Cooperative Institute for Meteorological Satellite Studies
[2] NOAA/NESDIS/ORA
Madison, Wisconsin

[3] Coastal Studies Institute
Louisiana State University
Baton Rouge, Louisiana

1. INTRODUCTION

The University of Wisconsin and Louisiana State University have teamed to study the forcing of winter season cold frontal wind systems on sediment distribution patterns and geomorphology in the Louisiana coastal zone. Wind systems associated with cold fronts have been shown to modify coastal circulation and resuspend sediments along the micro tidal Louisiana coast (Roberts et al. 1987, Moeller et al. 1993). Remote sensing data is being used to map and track sediment distribution patterns for various wind conditions. Suspended sediment is a building material for coastal progradation and wetlands renewal, but also restricts access to marine nursery environments and impacts oyster bed health. Transferring a suspended sediment concentration (SSC) algorithm to EOS MODerate resolution Imaging Spectroradiometer (MODIS; Barnes et al. 1998) observations may enable estimates of SSC globally.

MODIS is a recent (spring, 2000) advance in global monitoring capability with its 36 VNIR-LWIR spectral bands and 250m–1000m spatial resolution. MODIS has distinct improved capability over heritage instruments (e.g. AVHRR, CZCS) for coastal monitoring. It contains two 250m resolution bands at 650nm and 860nm (2300 km swath), allowing daily monitoring of coastal sediment patterns from its sun synchronous orbit on the Terra platform (1030 LT overpass). MODIS was designed for assessing global change. Careful attention was given to radiometric calibration accuracy. MODIS has reflectance and radiance onboard sources to assure consistent spatial, spectral and radiometric characterization of global data sets. The multispectral complement of MODIS allows assessment of various atmospheric (e.g. aerosol content, cloud detection, moisture) and surface properties (e,g., land cover, SST vegetation, fluorescence) from the same platform.

Corresponding author address: Christopher C. Moeller; CIMSS, Univ. Wisconsin; 1225 West Dayton Street; Madison, WI 53706-1695

In spring, 2001 a NASA high altitude (20 km) ER-2 aircraft carrying the MODIS Airborne Simulator (MAS; King et al. 1996) flew missions over coastal Louisiana to monitor suspended sediment patterns in the Atchafalaya Bay region (Figure 1). The Atchafalaya Bay is a sediment rich estuary, especially in spring when snowmelt and spring rains annually swell the Atchafalaya River discharge into the bay. Sediment is distributed by micro tidal influences and wind driven currents in the nearshore zone, accumulating on the shallow subaqueous bottom or remaining in suspension over long distances in the prevailing currents. MAS 50m resolution (38 km swath) and MODIS 250m resolution VNIR data document the sediment patterns in existing wind conditions. Additional MODIS data sets document sediment patterns on other days, providing a resource of information on the response of sediment patterns to various wind forcing conditions.

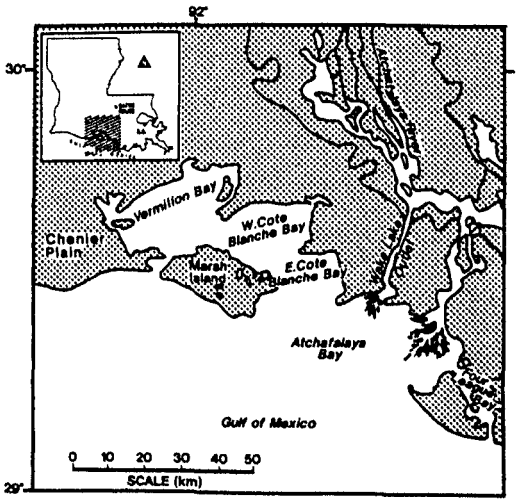

Figure 1. Louisiana coast study region. The Atchafalaya River, a distributary of the Mississippi River, flows into Atchafalaya Bay, carrying about 30% of the Mississippi River volume. New deltas are forming at the mouth of the Atchafalaya River and Wax Lake outlet.

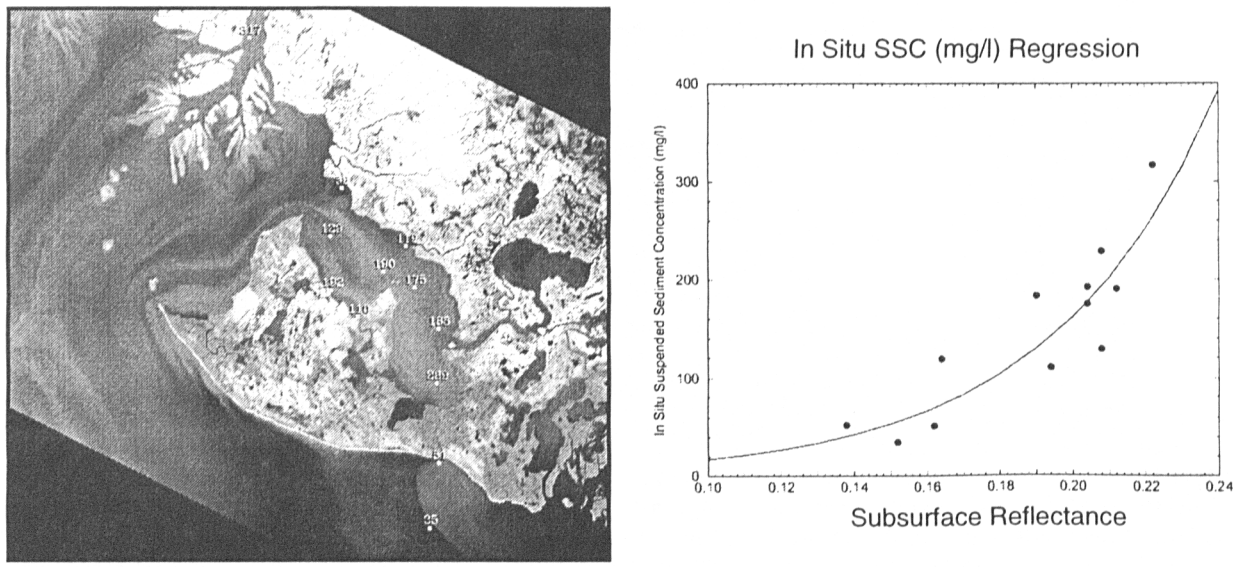

Figure 2. MAS 50m resolution near infrared (750 nm) image (left) of Atchafalaya Bay region on March 21, 2001 with in situ SSC (mg/l) data plotted at sampling locations. Atmospherically corrected MAS 660 nm reflectance is plotted against in situ SSC to define an SSC regression (right). RMS of the fit shown is 36 mg/l.

2. DATA COLLECTION

The ER-2 flew over the Atchafalaya Bay region of the Louisiana coast in spring 2001 during the Terra eXperiment – 2001 (TX-2001). On March 21, 36 hours after a cold front passage, the ER-2 flew multiple overpasses of the Atchafalaya Bay region of the central Louisiana coast while a boat team from LSU collected in situ water samples and the Terra satellite (with MODIS) passed overhead (1654 UTC). The boat team measurements included suspended sediment concentration (SSC, Figure 2), bulk temperature, salinity, secchi depth, and VNIR radiometer measurements of the upwelling reflectance out of the water column. The MAS data depicting the post-frontal conditions has been coupled with the in situ suspended sediment samples to produce an SSC estimation algorithm (Figure 2). This relationship will be transferred to co-registered MODIS 250m resolution observations for application to other days and coastal sites. The multiple MAS scenes of the Atchafalaya Bay region will be animated to derive water motion vectors, which when coupled with SSC estimates provide a sediment transport snapshot for the March 21 flight day.

Since first light (Feb, 2000), MODIS 250m resolution data has been collected on a routine basis for clear sky overpasses of the Louisiana coast. While many images are contaminated by cloud cover, clear sky cases are found throughout the annual cycle. Until the SSC estimation algorithm is transferred to MODIS data, these MODIS images can be used to provide a qualitative high-resolution (250m) snapshot of sediment patterns in response to prevailing wind conditions. Once incorporated, the SSC algorithm will benefit from the well-calibrated nature of MODIS data to extend SSC estimates to the global domain on a daily basis. This will be a valuable resource for extending analysis tools and findings to estuaries and deltas around the world.

3. SEDIMENT PATTERN OBSERVATIONS

As cold front systems approach and move downstream through the Gulf Coast of Louisiana, the coastal zone experiences pre-frontal southerly (blowing onshore) winds followed by a switch to northerlies after frontal passage. During each cycle of this wind pattern, sediment resuspension and transport results (Walker et al. 1997; Walker and Hammack, 2000). Offshore transport in the post-frontal phase exposes suspended sediment to longshore currents, resulting in downdrift transport. In the micro tidal Gulf coast, these winds have an important influence on existing water levels and circulation (Moeller et al. 1996).

The two 250m resolution reflectance bands (650 nm and 860 nm) are providing new

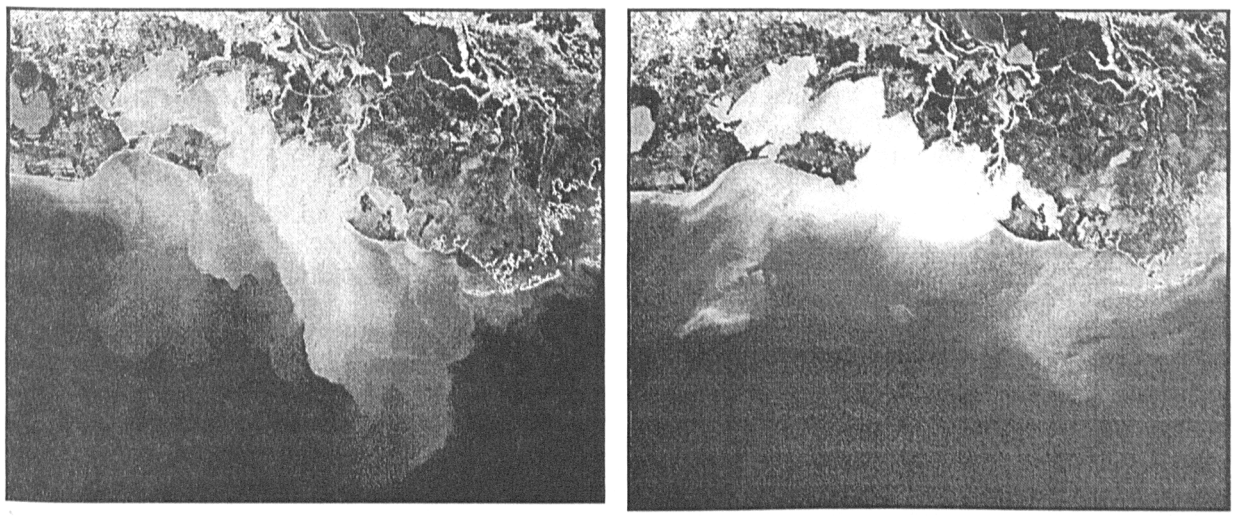

Figure 3. MODIS 250m resolution band 1 (650 nm) imagery on March 21 (left) and March 26, 2001 (right). The sediment plume from the Atchafalaya Bay (center of each image) is extended to the south and east on March 21, in keeping with the low level wind flow from the northwest. On March 26, winds had turned from the northeast pushing the sediment plume towards the southwest.

monitoring capability and insight on the spatial variability and temporal change of sediment distribution in the coastal zone. Figure 3 shows examples of sediment plume behavior on March 21 and 26, 2001. Surface wind energy (Figure 4) was primarily from the northwest on March 21, driving down water level in the Atchafalaya Bay and pushing the sediment plume out onto the inner continental shelf. This is contrasted to March 26, when wind energy was dominant from the northeast resulting in the sediment plume orienting towards the west-southwest, the prevailing direction of longshore currents off the Louisiana coast. The sediment plume areal coverage on March 21 is roughly 25–50% larger than on March 26. It is believed that sediment resuspension is an important contributing process to the sediment plume. Walker and Hammack (2000) have estimated that resuspension is contributing 75-80% of the material in the sediment plume during vigorous cold front events.

The variation of wind energy on a year to year basis, as a signature of short term climate variation, is expected to influence sediment transport from year to year. Variations of wind energy in the Louisiana coastal region may be influenced by El Nino (and La Nina) events. This is a topic of further investigation. Relationships between tropical and extra-tropical climate suggest mechanisms by which global climate change may influence sediment distribution along the Louisiana coast, and provide insight on future sediment transport behavior based on climate change predictions.

4. SUMMARY AND FUTURE WORK

Remote sensing provides an opportunity to monitor coastal zones on a regular basis. The advent of MODIS on Terra has enhanced the capability with high resolution (250m) daily coverage of the globe. Transfer of a suspended sediment concentration estimation algorithm from the ER-2 borne MAS instrument to MODIS observations would create a quantitative measure of sediment conditions, facilitating detection of short or long term change.

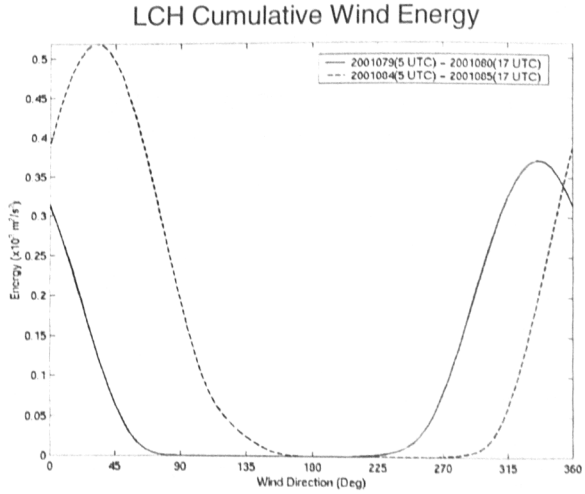

Figure 4. Lake Charles, LA cumulative surface wind energy for 36 hours leading up to MODIS imagery on March 21 (solid) and March 26 (dash), 2001 (see Figure 3 for imagery). Winds from northwest dominated on March 21, while northeast winds were prevalent on March 26.

Data collected during the spring 2001 TX-2001 field campaign show evidence of local wind influence on the sediment patterns along Louisiana's turbid central Gulf coast. In situ water sample measurements are being used to develop suspended sediment concentration estimation coefficients to quantify suspended material and transport (through animating co-registered imagery). MAS imagery will be atmospherically corrected for this procedure. The MAS SSC estimates will be co-located with MODIS data for transfer of the algorithm to MODIS. MODIS SSC estimates will be compared to new in situ measurements collected in 2002 for testing the algorithm.

The physical characteristics (particle size, shape, content) of sediments in the Atchafalaya Bay region will be used in a forward model to estimate water-leaving reflectance. This investigation will be used to gain insight on the sensitivity of water-leaving reflectance to the evolving characteristics of suspended sediment. It is expected to provide insight on the sediment characteristics of river effluents around the world, a step towards expanding the MODIS sediment estimation capability to the global domain.

MODIS data sets will continue to be collected in clear sky conditions for monitoring sediment plume behavior in the context of wind conditions along the Louisiana coast. The influence of wind will be evaluated on a seasonal basis for insight on response of sediment transport to short term climate variability.

5. REFERENCES

Barnes W. L., T. S. Pagano, and V. V. Salomonson, 1998: Prelaunch characteristics of the Moderate resolution Imaging Spectroradiometer (MODIS) on EOS-AM1. *IEEE Transactions on Geoscience and Remote Sensing*, **36**, No. 4, pp. 1088-1100.

King, M. D., W. P. Menzel, P. S. Grant, J. S. Myers, G. T. Arnold, S. E. Platnick, L. E. Gumley, S-C. Tsay, *C. C.* Moeller, M. Fitzgerald, K. S. Brown, and F. G. Osterwisch, 1996: Airborne scanning spectrometer for remote sensing of cloud, aerosol, water vapor, and surface properties. *Journal of Atmospheric and Oceanic Technology*, **13**, pp. 777-794.

Moeller, C. C., O. K. Huh, H. H. Roberts, L. E. Gumley, and W. P. Menzel, 1993: Response of Louisiana coastal environments to a cold front passage. *J. Coastal Res.*, Vol. **9**, No. 2, pp. 434-447.

Moeller, C. C., O. K. Huh, W. P. Menzel, and H. H. Roberts, 1996:The use of aircraft-borne MAS data for mapping sediment transport along the Louisiana Coast. *Second International Airborne Remote Sensing Conference and Exhibition*, 24-27 June 1996, San Francisco, CA, ERIM, Vol. II, pp. 673-682.

Roberts, H. H., O. K. Huh, S. A. Hsu, L. J. Rouse, Jr., and D. Rickman, 1987: Impact of cold-front passages on geomorphic evolution and sediment dynamics of the complex Louisiana coast. In *Coastal Sediments '87: Proceedings of Specialty Conference*, American Society of Civil Engineers, May 12-14, 1987, New Orleans, LA, pp. 1950-1963.

Walker, N. D., J. Day, N. Rabalais, O. Huh, A. Hammack, and R. Lane, 1997:Circulation, suspended sediment and chlorophyll distributions associated with the Atchafalaya River discharge plume, Louisiana. In *Proceedings, Fourth international Conference on Remote Sensing for Marine and Coastal Environments*, ERIM, March, 1997, Orlando, FL, Vol. I, pp. 277-286.

Walker, N. D., and A. B. Hammack, 2000: Impacts of winter storms on circulation and sediment transport: Atchafalaya-Vermillion Bay region, Louisiana, USA. *J. Coastal Res.*, Vol. 16, No. 4, pp. 996-1010.

P1.18 MODIS OCEAN COLOR DATA FOR STUDYING OCEAN CIRCULATION FEATURES

K.S. Prasad* and R.L. Bernstein
SeaSpace Corporation, Poway, CA 92064

1. INTRODUCTION

The Moderate Resolution Imaging Spectroradiometer (MODIS) has added a significant new capability for studying the abundance and distribution of phytoplankton chlorophyll. The relative levels of pigment concentrations of water masses, which compose eddies and other ocean circulation features has increased the utility of MODIS ocean color bands in open ocean and near coastal regions.

Data from the Coastal Zone Color Scanner (CZCS) provided the first ability to observe ocean phytoplankton chlorophyll from space (Feldman et al. 1989). The data from CZCS was used extensively to study ocean marine food webs and the ocean's role in biogeochemical cycles. CZCS ceased operating in 1986 and SeaWiFS (Sea-viewing Wide Field-of-view Sensor), a follow-on ocean color sensor, was launched in 1997 aboard the OrbView-2 satellite. In comparison to CZCS, SeaWiFS has additional bands in the blue, green, and near-IR regions of the electromagnetic spectrum. These bands were selected based on historical considerations, the spectral absorption characteristics of some common in-water constituents, and the spectral transmittance of atmospheric oxygen and water vapor constituents. The ocean color bands on MODIS are very similar to SeaWiFS bands, with the advantage that they are narrower than SeaWiFS. The narrower bands will enhance atmospheric correction. Therefore, in the visible region of the electromagnetic spectrum, MODIS builds upon the CZCS and SeaWiFS heritage with two important exceptions; absence of sensor tilt to avoid sun-glint and the instrument is designed to provide quantitative measurements of solar-stimulated fluorescence from chlorophyll *a* (Esaias et al. 1998). In terms of surface temperature, data from the Advanced Very High Resolution Radiometer (AVHRR), which has been operational have provided estimates of bulk sea surface temperature (SST) that were used extensively to study the upper ocean dynamics and the coupling between physical and biological ocean dynamics. The MODIS sensor was designed for visible and thermal imaging and specifically to fill both the primary needs established for SST and ocean color observations.

In this paper we briefly outline the MODIS calibration procedures using the International MODIS/AIRS processing Package (IMAPP) integrated with TeraScan image processing software. We show examples of ocean water-leaving radiance and chlorophyll *a* derived from MODIS ocean color bands employing SeaWiFS-type atmospheric correction procedures. We also demonstrate the utility of a sequence of color images to estimate ocean surface velocity.

The advent of the MODIS sensor, now flying on the NASA EOS Terra satellite (overpass time 10:30 AM/PM), and also on its sister satellite Aqua, scheduled for launch in late 2001 (overpass time 1:30 AM/PM), opens up new opportunities to apply the displacement technique for deriving ocean currents in addition to deriving routine ocean color products. In addition, two other ocean color sensors ,the Oceansat-1 OCM and Orbview-2 SeaWiFS provide data at local noon, exactly midway between Terra and Aqua.

2. METHODS

MODIS direct broadcast data is routinely acquired and processed at SeaSpace Corporation, Poway, California using an X-band downlink. Raw data is formatted to level 0 Production Data Set (PDS) according to NASA specifications. Data is calibrated to level 1b using IMAPP software integrated with TeraScan processing functions. The IMAPP routines produce calibrated Hierarchical Data Format (HDF) data sets at 250, 500 and 1000 m spatial resolution. The HDF data sets are converted to TeraScan Data Format (TDF) data sets and accurate earth-location is appended using a series of TeraScan functions. Data is then navigated and corrected for the MODIS sensor "bowtie effect" using the Terascan function *modis_bt*. The ocean color bands (MODIS

*Corresponding author address: K. S. Prasad, SeaSpace Corporation, 12120 Kear Place, Poway, CA 92064; e-mail: kprasad@seaspace.com

bands 8 through 16) are then extracted from the data set for level 2 data processing. A Terascan function called *modis_color* that implements the SeaWiFS-type atmospheric correction procedures is then employed to generate normalized water-leaving radiances (nLW's) for the 412, 443, 490, 530, and 550 nanometers (nm). Other variables produced are the aerosol radiances at 670, 865 and the aerosol optical thickness at 865 nm. Chlorophyll *a* concentration is derived using the following MODIS pre-launch bio-optical algorithm:

$$Log\ Chl\ a = -1.40(\log X) + 0.07$$

Where X is equal to a ratio of the following variables:

$$Lwn(443\ nm) / Lwn(550\ nm)$$

Figure 1. give the data processing steps

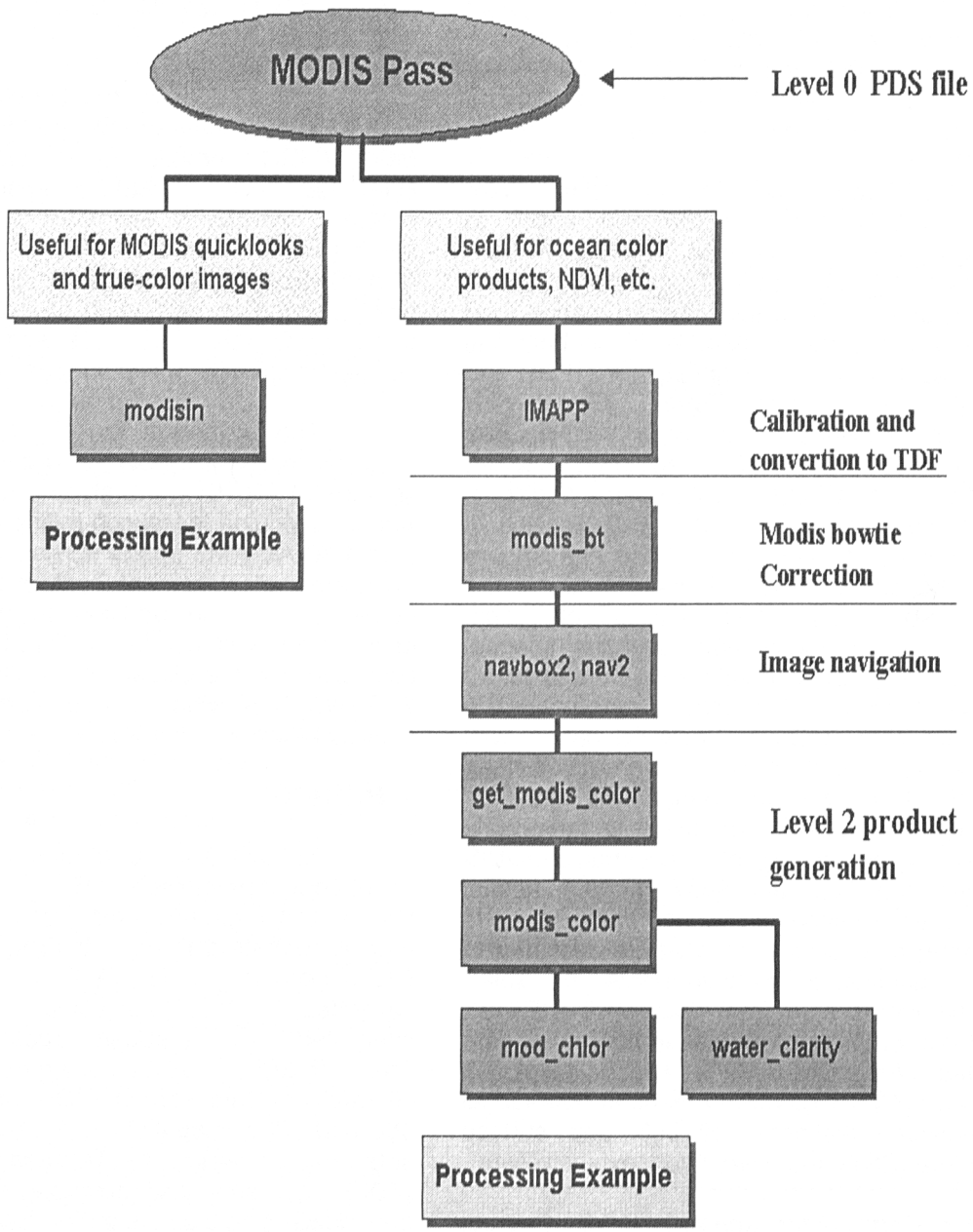

Figure 1. MODIS data processing flow chart

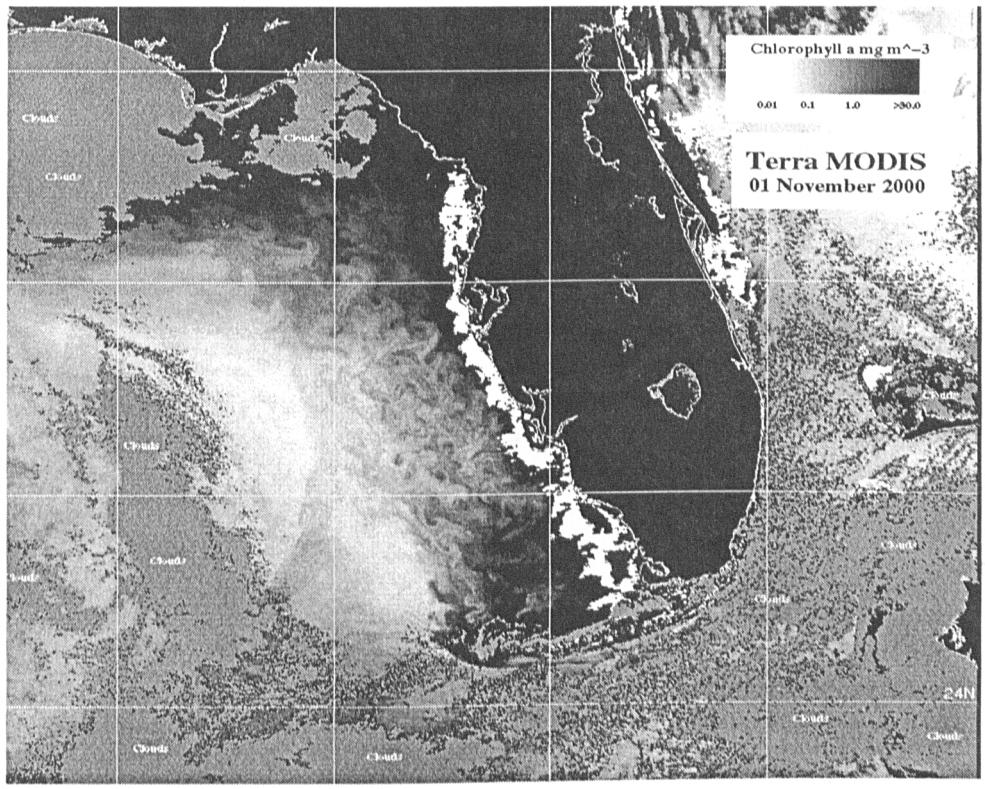

Figure 2. MODIS Chlorophyll a image from 1 Nov. 2000

involved in processing MODIS data from calibration through level 2 product generation.

3. RESULTS

Figure 2 shows a level 2 chlorophyll *a* image generated from a 1 November 2000 MODIS overpass over Florida. The image depicts fine ocean color patterns due to chlorophyll along the west Florida shelf, where a whole complex of eddies and other features appear. The grid overlay is 1 degree latitude/longitude, to provide spatial scale. It is apparent that there are a number of spiral eddies present, some with scales of order 25 km. Later this year, NASA will launch the second EOS, named Aqua, which will also carry a MODIS sensor and will have an overpass time of 1:30 PM, three hours after the Terra's overpass. SeaSpace Corporation is also presently acquiring data from Oceansat-1's OCM (Ocean Color Monitor), which flies at local noon and has the same excellent spectral channels for ocean color as does the MODIS, but at three to four times finer spatial resolution. Ideally there will be a sequence of three overpasses in rapid succession and will have the ability to (a) detect features such as are shown in figure 2, (b) a better, finer spatial resolution look at the features (300 m versus 1000 m), and (c) time evolution of the features from 10:30 AM, to noon, to 1:30 PM to estimate surface current. With reference to (c) above, a typical 0.25 m/s current would move features by about 2500 meters over the three hours from 10:30 AM to 1:30 PM. This should be readily observable with the spatial resolution of MODIS. The earth-location accuracy of MODIS is good to about 200 m, i.e. much better than the 1000 m spatial resolution of the sensor.

3.1 Ocean surface current estimation

Figures 3 and 4 show examples of ocean surface currents derived from a time sequence of normalized water-leaving radiance (nLw_443) images derived from MODIS and SeaWiFS. Both images were accurately earth-located and processed for

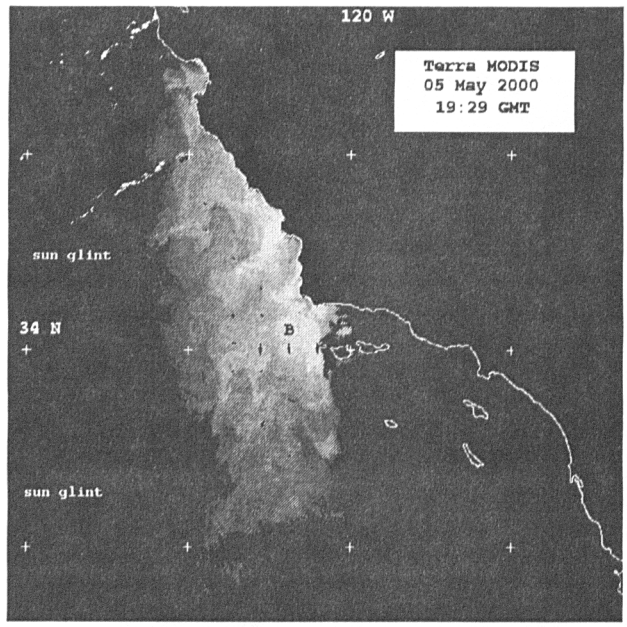

Figure 3. MODIS nLw_443 showing surface current vectors.

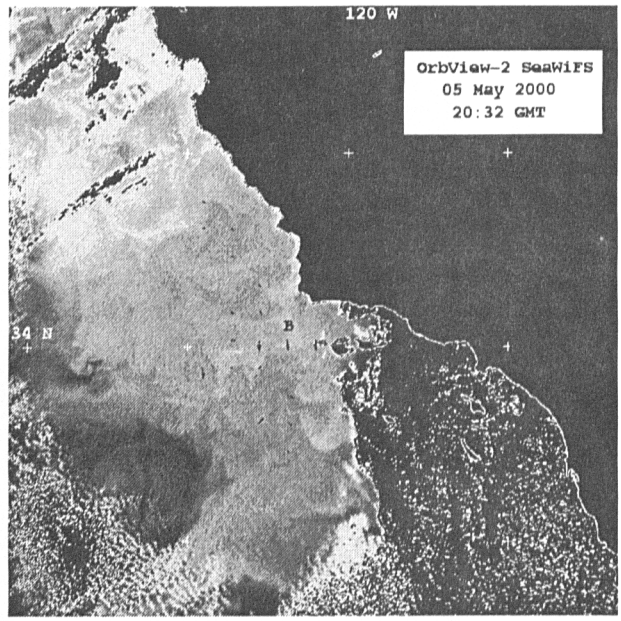

Figure 4. SeaWiFS nLw_443 showing surface current vectors

feature displacement using automated functions available in TeraScan. For further details on the actual methods and the techniques used for computing surface current velocity estimation please see extended abstract P5.55 (Bernstein and Prasad, same volume). SeaWiFS and MODIS overpasses are separated by approximately 3600 s. The nLw at 443 nm depicts excellent ocean surface current features due to absorption of chlorophyll in the blue region of the electromagnetic spectrum and shows a number of features that could be employed for feature tracking. We picked feature B and generated surface vectors using SeaWiFS as the reference image and MODIS as the search image. Image analysis revealed that the feature B was displaced about 6200 m, which approximately translates to a surface current velocity of 58 cm/s.

The study suggests that a sequence of three overpasses (MODIS, SeaWiFS and OCM) in succession can be used to detect features and study the time evolution of these features from 10:30 AM, to noon, to 1:30 PM to estimate surface currents. We found that both the nLw at 443 and chlorophyll *a* concentration provide good features for ocean surface current studies.

4. REFERENCES

Esaias, W.E. M.R. Abbot, I. Barton, O.B. Brown, J.W. Campbell, K.L. Carder, D.K. Clark, R.H. Evans, F.E. Hoge, H.R. Gordon, W.M. Balch, R. Letelier and P. J. Minnett. 1998. An overview of MODIS capabilities for ocean science observations. *IEEE. Trans. Geosci. Remote Sens.,* **36,** 1250-1265.

Feldman, G.C., N. Kuring, C. Ng, W. Esaias, C.R. McClain, J. Elrod, N. Maynard, D. Endres, R. Evans, J. Brown, S. Walsh, M. Carle, and G. Podesta. 1989. Ocean Color: Availability of the global data set, *EOS Trans. Amer. Geophys. Union,* **70,** 634-641.

P1.19 TOPEX/POSEIDON ALTIMETRY REVEALS THE VIETNAM SUMMER RECIRCULATION

Eric J. Bayler * and Zhengyu Liu
Department of Atmospheric and Oceanic Sciences / Center for Climatic Research
University of Wisconsin-Madison, Madison, Wisconsin

1. INTRODUCTION

Indications of seasonal recirculation near Vietnam in TOPEX/Poseidon (T/P) altimetry observations motivated this high-resolution modeling study of the southern South China Sea (SCS). Monsoon wind forcing dominates the circulation dynamics of the SCS, perpetually alternating the SCS between states that reverse the western boundary current. TOPEX/Poseidon altimetry data provides, for the first time, relatively high temporal resolution observations with near-simultaneous spatial coverage of the deep basin. The new data permit clearer identification of significant seasonal features.

During the southwest monsoon (spring-summer), the southern SCS develops an anticyclonic gyre with a northward western boundary current. This northward flow turns offshore along the coast of Vietnam as an easterly jet. With the easterly jet, a pair of recirculation cells form and remain, with the anticyclonic recirculation cell dominating the dynamics of the region until destroyed by the shift to the northeast monsoon (autumn-winter). This study demonstrates that the evolution of the anticyclonic recirculation cell near 12N 111E, hereafter the Vietnam Summer Recirculation (VSR), is governed by gyre-scale dynamics strongly influenced by topography, and that its seasonal destruction is caused by the migrating monsoon winds.

2. DATA

TOPEX / Poseidon (T/P) altimetry (WOCE, 1998a) is used to identify seasonal circulation features and to validate modeling results. Wind stress data derived from European Remote Sensing (ERS) satellite scatterometers are used to force the models. The ERS wind stress data (WOCE, 1998b), August 1991 through October 1999, completely overlaps the T/P altimetry span, allowing circulation modeling for which there are observations of both the forcing and the net response. The spatial and temporal resolutions of the data sets are similar. A biharmonic spline interpolated data to the ETOPO5 bathymetric data (NOAA_NGDC, 1988) grid selected for the model domain.

3. MODEL

The South China Sea is a semi-enclosed basin characterized by a well-defined deep basin. The 100-m contour defines the modeling domain, with vertical walls closing deep-water straits. Closing the Luzon Strait does not notably affect the southern SCS (Yang, et al., 2000). Both 1.5-layer reduced-gravity and 2.0-layer closed-basin versions of the primitive-equation, beta-plane Navy Layered Ocean Model (NLOM) (Wallcraft, 1991) were employed with 1/12th-degree zonal and meridional resolution. Two parallel wind forcing series, were examined: 1) steady ERS mean-summer wind forcing spin-up for highlighting processes; and 2) realistic sequential ERS winds for evaluating contributions to the annual cycle.

* *Corresponding author address*: Eric J. Bayler, Univ. of Wisconsin-Madison, Dept. of Atmospheric and Oceanic Sciences, 1225 W. Dayton St., Madison, WI 53706; e-mail: ericb@ssec.wisc.edu.

4. RESULTS

The general results are presented first and then factors contributing to the formation of the Vietnam Summer Recirculation (VSR) are examined, followed by an analysis of the VSR's destruction.

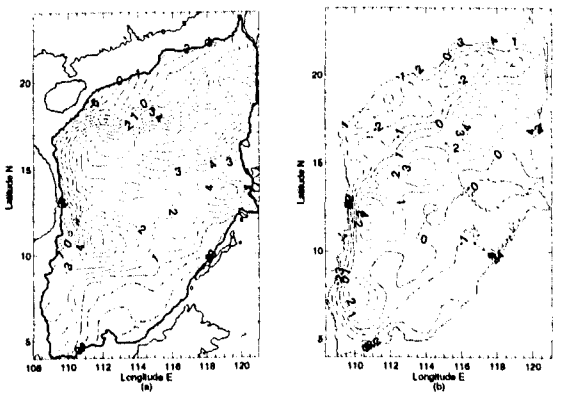

Fig. 1. Mean summer sea surface height anomalies (Contour interval = 1 cm; gray (dot-dash) < 0): (a) TOPEX/Poseidon, (b) model.

4.1 General Description

As defined by barotropic flow, the zonal and meridional extents of the VSR are about 110 E to 112 E and about 11 N to 13 N respectively. Persistent broader VSR upper-layer anticyclonic recirculation begins in March and continues through summer, achieving a mean summer magnitude of 4 Sv and vanishing in October and November. Mean VSR lower-layer anticyclonic flow is evident in the VSR region in all months except October and November, exceeding 2 Sv for the mean spring flow. VSR mean anticyclonic barotropic flow reaches its maximum in summer (over 5 Sv), vanishing in autumn and returning in winter.

4.2 Formation by Gyre-scale Dynamics

With the monsoon wind shift, a barotropic Rossby wave is immediately generated in the SCS, crossing the basin in several days. The initial circulation is barotropic Sverdrup flow. The basin completes its adjustment to the new monsoon regime when the baroclinic Rossby wave, generated at the eastern boundary subsequent to a wind shift, arrives at the western boundary. Based on the VSR latitude (12N) and a 200-m mean mixed-layer depth, this adjustment takes about 135 days. After the first baroclinic Rossby wave passes, the circulation evolves from barotropic to strongly baroclinic as the lower layer flow, now cut off from the wind forcing, begins to dissipate (Liu, et al., 1999). As expected from Cessi et al. (1987), the transport of the recirculation gyre (6 Sv) is three times larger than the theoretical Sverdrup transport (2 Sv). Western boundary Sverdrup return flow advects low-latitude potential vorticity (q) poleward, clearly driving the VSR from April through August.

4.3 Component Influences

Sensitivity cases highlight baroclinic / barotropic and topographic component contributions to the VSR. Wind-driven baroclinic flow defines the general circulation / recirculation pattern, with barotropic flow promoting stability and notably contributing to the location of recirculation. Simply including barotropic flow promotes anticyclonic recirculation centered on the VSR due to barotropic-baroclinic interaction. Adding topography produces additional competing barotropic / baroclinic recirculation effects. The baroclinic influences of topographically-constrained flow, destabilization of the offshore jet and drag, tend to offset barotropic tendencies resulting from the generation of mean bottom flow by eddy-topography interactions. An isolated topographic peak near the center of the VSR region focuses topographically-induced barotropic-baroclinic interactions, shifting recirculation northward and anchoring its position. A net anticyclonic barotropic-baroclinic interaction of about one Sv results, aided by closed potential vorticity contours that support anticyclonic flow around the VSR peak. Topography also appears to dampen fluctuations in the recirculation, providing indications of a free mode that are further supported by lower-level flow vectors.

4.4 Destruction by Migrating Winds

The SCS meets the three prerequisites for migrating winds to destroy recirculation (Liu, 1996). Different from an ocean basin, the narrow SCS allows both barotropic and baroclinic Rossby waves to have a time scale mismatch with advective development of the inertial recirculation. Consequently, the baroclinic mode amplifies rather than dampens recirculation destruction. Migration of the SCS wind forcing is best described as a pivoting zero-wind-curl line, with the pivot point anchored on the western boundary near 10N. The zero-wind-curl line migrates rapidly southward in July, with the migration range easily exceeding that needed to destroy recirculation (Liu, 1996). When the anticyclonic wind curl in the southern SCS suddenly disappears with the monsoon shift in late September, the strengthening equatorward western boundary current in the northern SCS is released to rapidly flow equatorward, reversing the western boundary current of the southern gyre. The rapidly advected cyclonic potential vorticity anomalies chaotically mix with the remnants of the recirculation, removing the injected anticyclonic potential vorticity anomaly, thereby, completely destroying the VSR recirculation by mid-October.

5. CONCLUSIONS

The VSR, a seasonal anticyclonic feature of the southern SCS, is driven by gyre-scale dynamics, principally Rossby wave adjustment and Sverdrup flow subject to strong topographic influence. Topography modifies and anchors the position of the VSR, providing closed potential vorticity contours conducive of an enhancing lower-layer anticyclonic free mode. Lower-level flow vectors and the dampening of flow fluctuations by topography provide evidence of a free mode. The barotropic Rossby wave generated by the semi-annual monsoon shift energizes the lower-level free mode with regular pulses. The migration of the monsoon wind forcing and chaotic mixing of q anomalies completely destroy the VSR each year.

6. REFERENCES

Cessi, P., 1988: A stratified model of the inertial recirculation. *J. Phys. Oceanogr.*, **18**, 662-682.

Liu, Z., 1996: Destruction of the inertial recirculation by the annual wind migration. *J. Phys. Oceanogr.*, **26**, 242-256.

National Oceanic and Atmospheric Administration, 1988: ETOPO5 digital relief of the surface of the earth, *Data Announcement 88-MGG-02*, National Geophysical Data Center, Boulder, Colorado.

Wallcraft, A. J., 1991: *The Navy layered ocean model users guide.* NOARL Report 35, Stennis Space Center, MS, 21 pp.

World Ocean Circulation Experiment (WOCE) Global Data, 1998a: TOPEX/Poseidon Sea Surface Height (1992-97) and AVHRR Sea Surface Temperature (1990-96), CD-ROM Version 1.1, JPL PODAAC, (extended to Aug 1999 via the Internet).

World Ocean Circulation Experiment (WOCE) Global Data, 1998b: Mean Surface Wind Fields from the ERS-AMI and ADEOS-NSCAT Microwave Scatterometers (91/08/05 to 98/03/01), CD-ROM, April 1998, Institut Francais pour l'Exploitation de la Mer (IFREMER) and the University of Hawaii, (extended to Nov 1999 via the Internet).

Yang, H., Z. Liu, and Q. Liu, 2000: Seasonal variability and dynamical mechanisms for the upper ocean circulation of the South China Sea. *J. Phys. Oceanogr.* (submitted).

P1.20

SEA SURFACE SALINITY FROM SPACE: SCIENCE GOALS AND MEASUREMENT APPROACH

C.J. Koblinsky[1], P. Hildebrand[1], Y. Chao[2], A. deCharon[7], W. Edelstein[2], G. Lagerloef[3], D. LeVine[1], F. Pellerano[1], Y. Rahmat-Samii[6], C. Ruf[4], F. Wentz[5], W. Wilson[2], and S. Yueh[2]

1 – NASA/Goddard, 2 – NASA/JPL, 3 – Earth and Space Research, Inc., 4 – Univ. Michigan, 5 – Remote Sensing Systems, Inc., 6 – UCLA, 7 – Bigelow Labs Ocean Sciences

1. SALINITY SCIENCE GOALS

The salinity of the ocean surface (Fig. 1) ranges from about 32 to 38 parts per thousand, reflecting the input of fresh water from precipitation, melting of ice and river runoff, the loss of water through evaporation, and the mixing and circulation of ocean surface water with deep water below. Globally, the sea surface salinity (SSS) is at a minimum near the equator (where there is considerable precipitation) and in polar regions (due to the melting of ice), and is enhanced in mid latitudes. (where there is reduced precipitation and enhanced evaporation).

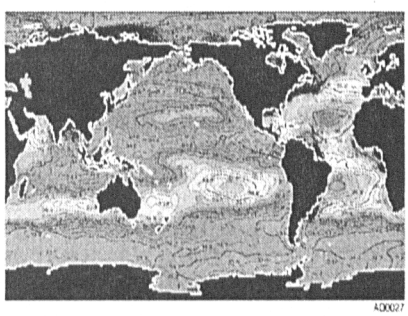

Fig.1. The estimated annual mean global SSS field from historical data, with salinities ranging from 32 (dark) to 37 (light). (After Levitus, et al, 1998)

Understanding the variability of oceanic salinity is extremely important to the full understanding of the relationship between ocean circulation and climate. This is because ocean buoyancy is a roughly equal function of sea water temperature and salinity. At the present time, only the sea surface temperature is adequately measured on a global scale. Additional inputs to ocean circulation include surface wind stress, and internal forces, including corriolis, frictional and waves. Global measurement of oceanic salinity will therefore enable understanding the buoyancy forcing of oceanic circulation.

1. Corresponding author address: Peter H. Hildebrand, NASA Goddard, Greenbelt, MD, 20771; peter.hildebrand@gsfc.nasa.gov

Improved understanding of the oceanic buoyancy field will improve our understanding of seasonal to interannual changes in ocean circulation and the feedback between ocean circulations and its feedback to the climate.

The depiction of SSS shown in Fig. 1 is based on averaging extensively over space and time (many years) and resolves only the largest, basin-scale salinity patterns. The knowledge of seasonal-to-interannual variability is much more poorly observed. This is because the actual measurements of SSS (Fig. 2) are limited; over 42% of the ocean has never been observed and for over 88% of the ocean there are fewer than 10 measurements over the past 125 years (Levitus, et al, 1998).

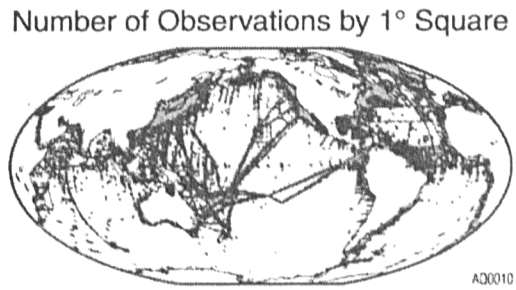

Fig. 2. Salinity observation density over past 125 years (Courtesy of F. Bingham based upon Levitus et al, 1998)

The salinity measurements that do exist suggest that at any one location the salinity varies by <1 psu, and the variability is frequently only a few tenths of a psu. Although there are only sketchy measurements, this same result comes from numerical modeling, the analysis of the underlying variability of salinity measurements at single locations, the observations of salinity anomalies (e.g. Dickson, et al, 1988; Belkin et al, 1998), studies of the effects of rainfall or runoff (e.g. Cronin and McPhaden, 1999) or from studies of seasonal to interannual salinity variability (e.g. Dessier and Donguy, 1994; Donguy and Meyers, 1996; Large and Nurser, 1997; Delcroix, 1998; Delcroix and McPhaden, 2001).

To provide global SSS measurements and meet these scientific challenges, we have proposed the Aquarius mission to the NASA Earth System Science Pathfinder Program. Aquarius measurements are designed to address

NASA Earth Science Enterprise goals concerning the global water cycle and the links between global ocean circulations to climate change. This will be done through providing the first ever observations of the global SSS basic state, plus observation of seasonal to interannual changes over the life of the program. The science goals of Aquarius are therefore to: a) provide the first, global mapping of the complete oceanic SSS field, b) to better describe the global thermohaline circulation, c) to improve understanding of the tropical ocean-climate feedback such as el Niño, and d) to facilitate investigations of the freshwater budget component of coupled ocean-atmosphere models. The temporal and spatial scales of important oceanographic phenomena and the measurement resolution capabilities of Aquarius are illustrated in Fig. 3. Also shown are the estimated amplitudes of the salinity variability for these phenomena in psu.

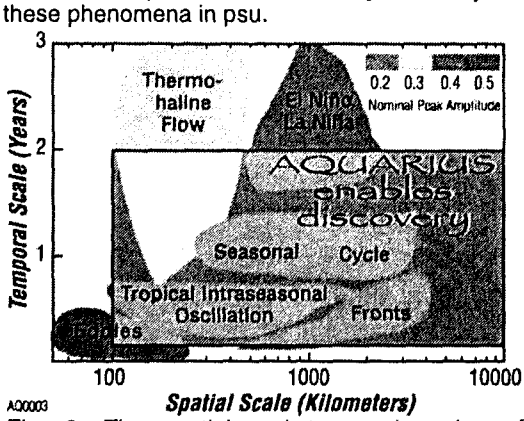

Fig. 3. The spatial and temporal scales of important oceanographic phenomena.

2. SALINITY MEASUREMENT GOALS

To meet the science goals, the Aquarius satellite must provide measurements of SSS to 0.2 – 0.4 psu, at a spatial sampling interval of 100 to 200 km and at a temporal sampling interval of 1 month. As illustrated in Figs 1 and 3, salinity measurements accurate to 0.2 psu are expected to be entirely accurate for the Aquarius science goals, and even measurements accurate to 0.3-0.5 psu would provide a major improvement in the current knowledge of SSS.

The Aquarius Salinity Measurement Satellite is therefore designed to measure global SSS with ~100 km resolution, every 8 days and will characterize salinity variability over a two year lifetime. With this coverage, salinity will be measured to an accuracy of ~0.2 psu in the tropics and ~0.3 psu at high latitudes, and over the range from 32 to 38 psu. The measurement domain will include the open ocean more than 150 km from coastal and sea ice boundaries.

3. RADIOMETRIC MEASUREMENT OF SALINITY

The underlying physics of salinity remote sensing from satellites is based on the sensitivity of the brightness temperature of sea water, T_b, to SSS and sea surface temperature, T_s. At microwave frequencies. T_b is related to SSS and T_s by the relation $T_b = e \bullet T_s$, where e is the emissivity of the sea surface, itself a function of SSS and T_s. This sensitivity is strongest in the frequency range from 0.5 to 1.5 GHz; the protected frequency band at 1.4 GHz (L-band) has been selected for Aquarius. For typical ranges of SSS and T_s over the open oceans, the T_b at L-band has a range of about 4-6K. The sensitivity of T_b to changes in SSS vs. T_s (Fig. 4) is greatest in warm water (0.7K/psu at 30°C) and least in cold (0.3K/psu at 0°C).

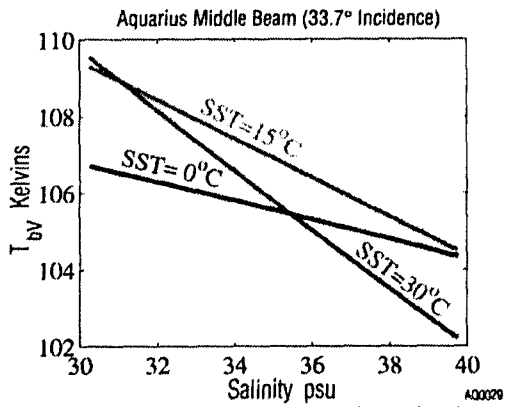

Fig. 4. Sensitivity of sea surface brightness temperature to Ts and salinity.

Measurement of salinity with this technique is complicated by several factors, the largest of which is the significant effect of sea surface roughness on microwave emission (Table 1). Sea surface roughness effects can produce a ΔT_b of up to ~5K, for very a rough sea surface. This effect dictates the need for an accurate means of measuring the sea surface roughness, which also must be accomplished simultaneously with the T_b measurements, due to the short time scale of sea surface wind variability.

Other contributions to the measured T_b at L-band include galactic emissions (ΔT_{bGAL} of ~2K), atmospheric emissions (ΔT_{bATM} ~2.4-2.8K), and emission from water vapor and cloud liquid water (both have a small effect on T_b). Additionally, the Faraday rotation of the polarized microwave emissions as the radiation passes through the ionosphere, needs to be corrected for. (Although there is no effect on (T_{bV}+T_{bH}), the individual T_{bV} and T_{bH} measurements can change by up to 5K.

The retrieval algorithm for SSS consists of two parts; a) evaluation of T_b at the sea surface and b) retrieval of SSS from T_b. The Aquarius instrument provides T_b at the satellite. Radiative transfer models allow correction for up- and down-welling emission from the atmosphere,

atmospheric and ionospheric attenuation and Faraday rotation. Down-welling galactic emissions are also taken into account using accurate maps. With these corrections, plus knowledge of the T_s and surface roughness, salinity can be calculated from T_b. Residual corrections to these data analysis algorithms will be carried out in a series of steps that have already begun with a series of aircraft test programs, plus laboratory and model developments. Algorithm refinement will continue with end-to-end simulation of the data algorithm system using ocean and atmospheric models, plus field experiment data. Finally, instrument calibration will include three major thrusts including deep space calibration maneuvers, detailed calibration corrections using highly accurate in-situ measurements of SSS, T_s, winds and roughness from buoy networks, plus error reduction approaches (e.g. Ruf, 2000; Wentz et al, 2000) that have been proven to be effective approaches to error reduction on other satellite data analysis systems.

4. AQUARIUS MEASUREMENT APPROACH

The first radiometric observations of salinity from space used an L-band radiometer on Skylab in the mid 1970s. Early design studies (e.g. Swift and McIntosh, 1983) detailed the conceptual design approach, and the required microwave emission model (Klein and Swift, 1977). Since then, aircraft instruments and flight programs have addressed the technical details of building the highly accurate L-band radiometer required to accurately measure SSS (Fig 5 and LeVine, et al, 1998 and 2001; Wilson, et al, 2001a,b). Based on these developments, the state of technology is now sufficient to produce an accurate L-band radiometer-scatterometer system that can be coupled with a planned global array of in situ salinity observations to provide the needed level of measurement accuracy.

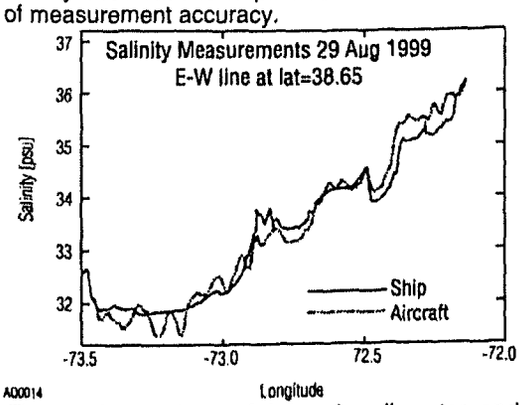

Fig. 5. Comparison of L-band radiometer and ship salinity measurements (Levine et al 1998).

The Aquarius design (Fig. 6) includes V- and H-polarized, 1.413 GHz radiometers and a 1.2 GHz scatterometer. A 3 m offset parabaloid reflector will be illuminated by three separate feeds to produce three beams with a 5.5° beamwidth and beam efficiencies of 95%. Each beam will include V- and H-polarization radiometers, plus an H-polarization scatterometer sampling of the ocean surface. The three beams will have incidence angles of 23.3°, 33.7°, and 41.7°. The resultant three-beam swath width of 250 km will give complete global coverage in 8 days and enough samples within a month to meet the accuracy requirement through averaging (see Table 1 and Yueh et al, 2001). The orbit will be a 6am/6pm orbit, with the beams directed toward the dark side of the earth in order to avoid reflected solar radiation.

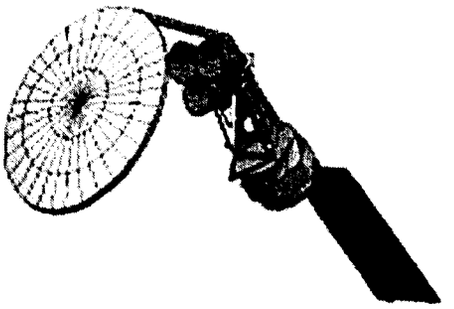

Fig. 6. Aquarius design concept showing the three feeds, the main reflector and the solar array.

The *Aquarius* instrument design was selected to meet the science needs within the constraints of measurement accuracy, spatial and temporal sampling requirements, global ocean coverage, and project risk and cost. The radiometer/scatterometer design is based on the lessons from integration of similar systems on the PALS systems (Wilson, et al, 2001a,b) and on the Advanced Water Vapor Radiometer (AWVR, Randa, et al, 2000) which has demonstrated radiometer stability of ~ 0.05K over 30 day time scales; more than a factor of two better than required for Aquarius.

5. REFERENCES

Belkin, I.M., S. Levitus, J. Antonov, and S.-A. Malmberg, 1998: Great Salinity Anomalies in the North Atlantic. *Prog. Oceanogr.* **41**, 1-68.

Cronin, M.F., and M.J. McPhaden, 1999: Diurnal cycle of rainfall and surface salinity in the western Pacific warm pool, *Geophys. Res. Letters*, **26**, 3465-3468.

Delcroix, T., 1998: Observed surface oceanic and atmospheric variability in the Tropical Pacific at seasonal and ENSO time scales: a tentative overview., *J. Geophys. Rev.*, **103**, 18611-18633.

Delcroix, T. and M.J. McPhaden, 2001: On SSS changes in the western Pacific warm pool during the 1992-1999 ENSO events., *J. Geophys. Res.*, (submitted)

Dessier, A. and J.-R. Donguy, 1994: The SSS in the tropical Atlantic between 10S and 30N—seasonal and interannual variations (1997-1989), *Deep Sea Res.*, **41**, 81-100.

Dickson, R.R., J. Meincke, S.-A. Malmberg and A.J. Lee, 1988: The Great Salinity Anomaly in the northern north Atlantic, 1968-1982, *Prog. Oceanogr.* **20**, 103-151.

Donguy, J.-R. and G. Meyers, 1996: Seasonal variations of sea-surface salinity and temperature in the tropical Indian Ocean. *Deep Sea Res.*, **43**, 117-138.

Levitus, S., T.P. Boyer, M.E. Conkright, T. O-Brien, J. Antonov, C. Stephens, L Statoplos, D. Johnson and R. Gelfeld, 1998: NOAA/NESDIS 18, World Ocean Database, **1**, 346pp.

Klein, L. and C. Swift, 1977: An improved model for the dielectric constant of sea water at microwave frequencies. *IEEE Trans. Antennas Propag.* **AP-25**, 104-111.

Large, W. and A. Nurser, 2001: Ocean surface water mass transformation. Eds.: J. Church and J. Gould. *Ocean Circulation and Climate,* 317-336.

LeVine, D., M. Kao, R. Garvine and T. Saunders, 1998: Remote sensing of ocean salinity: Results from the Delaware costal current experiment., *J. Atmos. Ocean. Technol.*,**15**, 1478-1484.

LeVine, D., C. Koblinsky, F. Pellerano, G. Lagerloef, Y. Chao, S. Yueh and W. Wilson, 2001: The measurement of salinity from space: Sensor concepts. *IGARSS 2001*, Sydney, Australia, July 2001.

Randa, J., L. Dunleavy and L. Terrell, 2000: Stability measurements on noise sources, *IEEE Trans. Inst. Meas.*, **50**, 368-372.

Ruf, C., 2000: Detection of calibration drifts in spaceborne microwave radiometers using a vicarious cold reference, *IEEE Trans, Geosci. Remote Sens.*, **38**, 44-52.

Swift, C. and R. McIntosh, 1983: Considerations for microwave remote sensing of ocean surface salinity, *IEEE Trans. Geosci. Remote Sens.*, **21**, 480-491.

Wentz, F., C. Gentemann, D. Smith, and D. Chelton, 2000: Satellite measurement of sea surface temperature through clouds, *Science*, **288**, 847-850.

Wilson, W, S. Yueh, S. Dinardo, S. Chazanoff, A. Kitiyakara and F. Li, 2001a: Passive-active L- and S-band (PALS) microwave sensor for ocean salinity and soil moisture measurements, *IEEE Trans. Geosci. Remote Sens.*, **39**, 1039-1048.

Wilson, W, S. Yueh, f. Li, S. Dinardo, Y. Chao, C. Koblinsky, G. Lagerloef, and S. Howden, 2001b: Ocean salinity remote sensing with the JPL Passive/Active L-/S-band (PALS) microwave instrument. *IGARSS 2001*, Sydney, Australia, July 2001.

Yuan, X., and L. Talley, 1992: Shallow salinity minima in the north Pacific, *J. Geophys, Oceanog.*, **22**, 1302-1316.

Yueh, S., R. West, W. Wilson, F. Li, E. Njoku, and Y. Rahmat-Samii, 2001: Error sources and feasibility for microwave remote sensing of SSS, *IEEE Trans. Geosci. Remote Sensing,* **39**, 1049-1060.

Table 1. Aquarius error analysis for sea surface salinity retrieval algorithm using T_{bv}.

Geophysical Parameter	Impact on T_{bv}	Supplementary Data Set For Correction	Residual Error in $T_{bv\,(K)}$	Salinity Error at mid Latitudes
Surface Roughness	< 5 K	Scatterometer (±2%)	0.10	0.18
SST	±0.14K/ 1°C SST	NCEP SST products (±0.5°C)	0.07	0.00
Dry Air	2.4-2.8K	NCEP air temperature (±2°C) and pressure (±5hPa)	0.07	0.13
Cloud Liquid Water	<0.1K	Operational integrated columnar water vapor (±0.15mm water)	0.04	0.07
Water Vapor	<0.01K	NA	0.005	0.01
Faraday Rotation	<5K	Polarimetric radiometer measurements provide <±0.2K error	0.02	0.04
Galactic	<2K + 3K bkgnd.	Sky survey with 1% accuracy	0.02	0.04
RSS of total geophysical error per observation			0.16	0.26
Radiometer calibration stability per observation			0.18	0.33
Radiometer NEΔT per observation			0.06	0.10
RSS of total error per observation			0.25	0.43
Average number of monthly Aquarius observations per 100 km grid cell				**9**
Aquarius monthly average accuracy, assuming 1/√n improvement (psu)				**0.14**

P1.22

SPECTRAL TRANSFER OF HUMIDITY AND TEMPERATURE CORRELATIONS FOR INHOMOGENEOUS TURBULENCE FOR LAND AND AGRICULTURE PROCESSES

Sukaran Ram Patel
Depatramento de Ciências Atmosféricas, Universidade Federal da Paraíba-UFPB
Campina Grande-PB, 58109-970, Caixa Postal 10027, Brazil

1.INTRODUCTION

Humidity and temperature measurements are not only intrinsically important as micrometeorological variables but also, because they are the components of the electromagnetic index of refraction, they govern the propagation of waves in the clear, turbulent atmosphere. Further, using optical scintillation measurements of inner scale and the refractive turbulence structure parameters, one may obtain complete micrometeorological characteristics of the surface layer and also the refractive index spectrum in the dissipation range is important to atmospheric optical propagation of studies of both weak and very strong scintillation. The Monin-Obukhov similarity theory is one of the most powerful tools in describing the atmospheric boundary layer; and the refractive index parameter is also considered as Monin-Obukhov quantity (Hill, 1989). There are several studies of similarity principles for homogeneous boundary layers but very few for horizontally inhomogeneous surfaces because of their obvious difficulties. Further very recently a number of applications of this theory for refractive index spectrum have been reported by Hill (1989), Andreas (1985, 1988, 1989, 1990) and others. These motivate to study the various aspects of the spectral transfer of humidity correlation and temperature correlation in homogeneous turbulent motion since they are the important parameters for determination of the refractive index parameter. In this study the two point spectral equations for humidity and temperature are constructed following Patel (2000) and it is shown that certain terms of these equations can be interpreted as transfer terms even for the general inhomogeneous turbulence. This is true for the case of homogeneous turbulence but does not seem obvious when the turbulence is not homogeneous since the condition of homogeneity is generally used in making the interpretation (Batchelor, 1953).

2. METHODOLOGY AND DISCUSSION

Following Patel (2000), the two point correlation eq. for the humidity correlation can be written as

$$\frac{\partial\overline{qq'}}{\partial t} = -U_k\frac{\partial\overline{qq'}}{\partial x_k} - U'_k\frac{\partial\overline{qq'}}{\partial x'_k} - \overline{u_k q'}\frac{\partial Q}{\partial x_k} - \overline{u'_k q}\frac{\partial Q'}{\partial x_k} - \frac{\partial\overline{q'u_k q}}{\partial x_k} - \frac{\partial\overline{qu'_k q'}}{\partial x_k} + D\left(\frac{\partial^2\overline{qq'}}{\partial x_k^{\,2}} + \frac{\partial^2\overline{qq'}}{\partial x'^{\,2}_k}\right) \qquad (1)$$

where the point P and P' are separated by a vector r (see Fig), the unprimed and unprimed quantities are measured at P and P' respectively, the over bar indicates an average quantity, the upper case and lower case u's and q's denote the corresponding mean and fluctuating quantities and D is molecular diffusivity for humidity. A similar equation for the temperature correlation can be obtained by replacing q by T and D by K (thermal diffusivity).

Now from the figure 1, one can have

$$\vec{x} + \vec{r} = \vec{x}' \text{ or } x_n = nx' + (1-n)x,$$
$$\text{or } r_k = x'_k - x_k, \quad (x_k)_n = n\,x'_k + (1-n)x_k \qquad (2)$$

where n is a number between 0 and 1. Now substituting eq (2) in eq. (1),one may have

$$\frac{\partial\overline{qq'}}{\partial t} = -\frac{\partial}{\partial r_k}(\overline{q'u'_k q} - \overline{q'u_k q}) - (U'_k - U_k)\cdot \frac{\partial\overline{qq'}}{\partial r_k} - \frac{\partial}{\partial(x_k)_n}[(1-n)U_k\overline{q'u_k q} + n\overline{q'u'_k q}] - [(1-n)U_k + nU'_{k]}\frac{\partial\overline{qq'}}{\partial(x_k)_n} + R \qquad (3)$$

where the right hand sides are respectively, the turbulence self-interaction, interaction of turbulence with mean flow, convection and R (sum of production and molecular diffusion term).

Similar equation can be obtained for the case of temperature correlation.

If $\Psi(\vec{\kappa}, \vec{x}_n)$ is the three dimensional Fourier transfer of the self interaction term, then one may have

$$-\frac{\partial}{\partial r_k}(\overline{q'u'_k q} - \overline{q'u_k q}) = \int_{-\infty}^{\infty}\Psi(\vec{\kappa}, \vec{x}_n)\,e^{(i\vec{\kappa}\cdot\vec{r})}d\vec{\kappa}$$

The corresponding three dimensional Fourier transfer of the self interaction term for the temperature correlation can be written as

$$-\frac{\partial}{\partial r_k}(\overline{\theta'u'_k\theta} - \overline{\theta'u_k\theta}) = \int_{-\infty}^{\infty}\Omega(\vec{\kappa}, \vec{x}_n)e^{(i\vec{\kappa}\cdot\vec{r})}d\vec{\kappa}$$

where $d\vec{\kappa} = d\kappa_1\,d\kappa_2\,d\kappa_3$ is the wave number vector. As in the case of homogeneous turbulence

$\partial(\overline{q'u'_k q} - \overline{q'u_k q})/\partial r_k$ and $\partial(\overline{\theta'u'_k} - \overline{\theta'u_k\theta})/\partial r_k$ for an inhomogeneous turbulence should be absolutely integrable over $\vec{r}$ in order for its Fourier transform to exist. For this it should be determined that Ψ and Ω should be interpreted as spectral transfer terms. So using eq. (2), and doing some simplification one may have

$$\int_{-\infty}^{\infty}\Psi(\vec{\kappa},x_n)e^{(i\vec{\kappa}\cdot\vec{r})}d\vec{\kappa} = -\overline{qu'_k}\frac{\partial q'}{\partial x'_k} - \overline{q'\frac{\partial u_k q}{\partial x_k}} + \\ + \frac{\partial}{\partial(x_k)_n}\left[n\overline{q'u'_k q} + (1-n)\overline{q'u_k q}\right] \qquad (4)$$

where the continuity equation is used. Further it can be seen after some simplification that eq (4) reduces to zero for the case of r=0, since for r=0, $x_k = x'_k$. Thus, even for a general inhomogeneous turbulence, Ψ when integrated over all wave numbers, gives zero contribution to the rate of change of $\overline{qq'}$. Thus, Ψ can only transfer Fourier components of $\overline{qq'}$ from one part of wavenumber space to another, as in the case of homogeneous turbulence. Similarly one prove that Ω when integrated over all wavenumbers, gives zero contribution to the rate of change of $\overline{\theta\theta'}$ even for the general inhomogeneous turbulence.

The second term of the right hand side of eq. (3), in contrast with the first is associated with the interaction of the turbulence with the mean flow. However both terms are related to transfer terms. So, if Ψ^* is the Fourier transform of the second term of the right hand side of eq. (3), then one may have

$$-(U'_k - U_k)\frac{\partial\overline{qq'}}{\partial r_k} = \int_{-\infty}^{\infty}\Psi^*(\vec{\kappa},\vec{x}_n)e^{(i\vec{\kappa}\cdot\vec{r})}d\vec{\kappa} \quad (5)$$

which for $\vec{r} = 0, U_k = U'_k$, reduces to

$$\int_{-\infty}^{\infty}\Psi^*(\vec{\kappa},\vec{x}_n)d\vec{\kappa} = 0 \qquad (6)$$

Thus, as in the case of $\Psi(\vec{\kappa},\vec{r}), \Psi^*(\vec{\kappa},\vec{r})$ gives zero total contribution to the rate of change of $\overline{qq'}$ and can only alter the distribution in wavenumber in wavenumber space of the contributions to $\overline{qq'}$. Similarly one may show that as in the case of $\Omega(\vec{\kappa},\vec{r}), \Omega^*(\vec{\kappa},\vec{r})$ gives zero distribution to the rate of change of $\overline{\theta\theta'}$ and only alter the distribution in the wavenumber in wavenumber space of the contributions to $\overline{\theta\theta'}$. Thus the first two terms of the right hand side of eq.(3) can be interpreted as transfer terms while other terms may be interpreted as production, convection and diffusion terms (Batchelor, 1953). Similar result holds for the corresponding eq. for the temperature correlation. It is hoped that this study will help better the understanding of the modeling of the refractive index spectrum for the land and the agriculture processes.

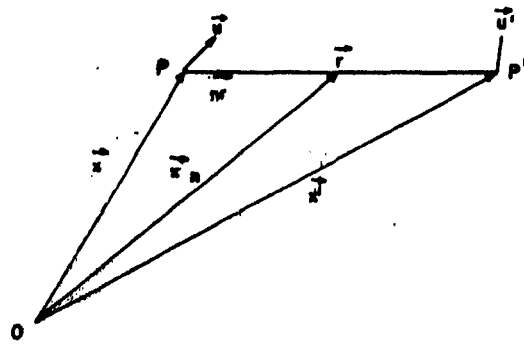

Fig. 1 vector configuration for two point correlation

3. REFERENCES

Batchelor, G. K., 1953: The theory of homogeneous turbulence, Cambridge University Press.

Endreas, E. L., 1988: Atmospheric stability from scintillation measurements, Appl. Opt. 27, 2241-2246.

Endreas, E. L., 1989: Two-wavelength method of measuring path-averaged turbulent heat fluxes, J. Atmos. Ocean. Tech. 6. 280-292.

Endreas, E. L., 1990: Three-wavelength method of measuring path-averaged turbulent heat fluxes, J. Atmos. Ocean. Tech., 7, 801-814.

Hill, R. J., 1989: Implication of Monin-Obukhov similarity theory for scalar quantities, J. Atmos. Sci., 46, 2236-2244.

Patel, S. R., 2000: Spectral transfer of velocity temperature correlation for inhomogeneous turbulence for atmosphere-land-interaction, in 24th Conference on Agriculture and Forest Meteorology, AMS, 14-18 August 2000, Davis California, U. S. A

P1.23

REFRACTIVE INDEX SPECTRAL TRANSFER IN INHOMOGENEOUS TURBULENCE IN ATMOSPHERIC/OCEANIC SURFACE LAYER

Sukaran Ram Patel
Departamento de Ciências Atmosfericas, Universidade Federal da Paraiba-PB
Campina Grande-PB, 58109-970, Caixa Postal 10027, Brazil

1. INTRODUCTION

Very recently the optical scintillation has been used in remotely sense many environmental parameters, such as wind components across the propagation path, rain rates and drop size distributions and the refractive index spectrum of turbulence. Using optical scintillation measurements of the inner scale and the refractive index turbulence structure, one may obtain complete micrometeorological characteristics of surface layer (Hill, 1992). Also the refractive index spectrum in the dissipation range is important to atmospheric optical propagation studies of both weak and very strong scintillation (Gerald and Hill, 1985). The Monin-Obukhov similarity theory is one of the most powerful tools in describing the physical properties of atmospheric/oceanic boundary layers and the refractive index parameters is also considered as Monin-Obukhov quantity (Hill, 1989).There are several studies of similarity principles for homogeneous boundary layer but very few for horizontally inhomogeneous surfaces because of their obvious difficulties. In this study, the two-point correlation equation for refractive index is constructed following Patel (2001) and it is shown that certain terms of this equation can be interpreted as transfer term even for a general inhomogeneous turbulence.

2. METHODOLOGY AND DISCUSSIONS

Following Hill (1978) the refractivity index variance of air, $\overline{m^2}$, when the pressure fluctuations and that the terms that are second order are neglected, may be written in the form

$$\overline{m^2} = a^2\,\overline{\theta^2} + b^2\,\overline{q^2} + 2ab\,\overline{q\theta} \qquad (1)$$

where a=(AP+CQ)/T^2, b=B-C/T, m is fluctuation in the refractive index, T is mean temperature, θ is the fluctuation of temperature, Q is mean specific humidity, q is fluctuation of humidity, P is the mean pressure; A, B and C are functions of wavelength. Now following Patel (2001) two-point correlation equation for refractve index may be written in the form

$$\frac{\partial}{\partial t}[a^2\overline{\theta\theta'} + b^2\overline{qq'} + 2ab\overline{q\theta}] = -\frac{\partial}{\partial r_k}[a^2(\overline{u'_k\,\theta\theta'} - \overline{u_k\theta\theta'}) + b^2(\overline{u'_k\,qq'} - \overline{u_kqq'}) + 2ab(\overline{u'_k\,q'\theta} - \overline{u_kq'\theta})] - (U'_k - U_k)\frac{\partial}{\partial r_k}(a^2\overline{\theta\theta'} + b^2\overline{qq'} + 2ab\overline{q'\theta}) - \frac{\partial}{\partial (x_k)_n}[a^2\{(1-n)\overline{u_k\theta\theta'} + n\overline{u'_k\,\theta\theta'}\} + b^2\{1-n)\overline{u_kqq'} + n\overline{u'_k\,qq'}\} + 2ab\{1-n)\overline{u_kq'\theta} + n\overline{u'_k\,q'\theta}\}] - [(1-n)U_k + nU'_k]\cdot\frac{\partial}{\partial (x_k)_n}[a^2\cdot\overline{\theta\theta'} + b^2\overline{qq'} + 2ab\overline{q'\theta}] + S \qquad (1)$$

where the right hand sides are respectively, the turbulent self interaction, interaction of turbulence with meam flow, diffusion, convection and S(sum of production, molecular diffusion of heat and specific humidity) terms. In eq.(1), the two points are separated by the vector r, the unprimed quantities are measured at point P and the primed quantities are measured at the point P', the over bar indicates an averaged quantity, the upper case and lower case denote the mean and fluctuating quantities respectively. Also referring the figure (Patel,2001) one may have $\vec{x} + \vec{r} = \vec{x}'$, $\vec{x} + n\vec{r} = \vec{x}_n$ from which it is easy to see that $\vec{x}_n = nx' + (1-n)x$, $r_k = x'_k - x_k$ and $(x_k)_n = nx'_n + (1-n)x_n$, where n is a number between 0 and 1. If $[a^2\Phi + b^2\Psi + 2ab\Omega]$ is the three dimensional Fourier transform of the self interaction term then one may have

$$-\frac{\partial}{\partial r_k}[a^2(\overline{u'_k\,\theta\theta'} - \overline{u_k\theta\theta'}) + b^2(\overline{u'_k\,qq'} - \overline{u_kqq'}) + 2ab(\overline{u'_k\,q'\theta} - \overline{u_kq'\theta})] = \int_{-\infty}^{\infty}[a^2\Phi(\vec{\kappa},\vec{x}_n) + b^2\Psi(\vec{\kappa},\vec{x}_n) + 2ab\Omega(\vec{\kappa},\vec{x}_n)]\exp(i\vec{\kappa}\cdot\vec{r})d\vec{\kappa} \qquad (2)$$

where $\vec{\kappa}$ is the wavenumber vector and $d\vec{\kappa} = d\kappa_1 d\kappa_2 d\kappa_3$. As in the homogeneous turbulent field $\partial[a^2(\overline{u'_k\,\theta\theta'} - \overline{u_k\theta\theta'}) + b^2(\overline{u'_k\,qq'} -$

$\overline{u_k qq'}) + 2ab(\overline{u'_k q'\theta} - \overline{u_k q\theta})]/\partial r_k$ for an inhomogeneous turbulence should be absolutely integrable over r in order for its Fourier transform to exist. Now our aim is to determine whether $[a^2\Phi+b^2\Psi+2ab\Omega]$ can be interpreted as spectral transfer term as in the case of homogeneous turbulence. Normally this is, true for the case of homogeneous turbulence (Batchelor, 1953) but here it is shown that this is true even for the case of inhomogeneous turbulence. To prove this, following Patel (2001) eq (2) can be simplified as

$$\int_{-\infty}^{\infty}[a^2\Phi(\vec{\kappa},\vec{x}_n)+b^2\Psi(\vec{\kappa},\vec{x}_n)+2ab\Omega(\vec{\kappa},\vec{x}_n)\cdot$$

$$\cdot e^{(i\vec{\kappa}\cdot\vec{r})}]d\vec{r} = a^2[\overline{u'_k\theta\frac{\partial\theta'}{\partial x'_k}} - \overline{\theta'\frac{\partial u_k\theta}{\partial x'_k}} + \frac{\partial}{\partial x_k}(n\cdot$$

$$\cdot\overline{u'_k\theta\theta''} + (1-n)\overline{u_k\theta\theta'})] + b^2[\overline{qu'_k\frac{\partial q'}{\partial x'_k}} -$$

$$-\overline{q'\frac{\partial u'_k q}{\partial x'_k}} + \frac{\partial}{\partial x_k}[n\overline{qq'u'_k} + (1-n)\overline{qq'u_k})] +$$

$$+2ab[\overline{q'u'_k\frac{\partial\theta}{\partial x'_k}} - \overline{\theta\frac{\partial q'u'_k}{\partial x'_k}} + \frac{\partial}{\partial x_k}\{n\overline{q'u'_k\theta}$$

$$-(1-n)\overline{q'u_k\theta}\}] \qquad (3)$$

where the continuity equation at P' and the fct that the quantities at one point are independent of the position of the other point, are used. Further, it can be shown, after some simplification that eq. (3) for r=0, reduces to zero; since for r=o, $x_k = x'_k$ in this case all the terms within the capital brackets in the right hand side become zero. Thus $[a^2\Phi+b^2\Psi+2ab\Omega]$ when integrated over all wavenumber gives zero contribution to the rate of change of the refractive index variance even for a general inhomogeneous turbulence. Thus, $[a^2\Phi+b^2\Psi+2ab\Omega]$ can only transfer the Fourier components of the refractive index correlation from one part of the wavenumber space to another, as in the case of homogeneous turbulence.

Now consider the second term of the right hand side of eq. (1), which is associated with the interaction of the refractive index variance with mean flow. This is different than the first term which, represents the interaction of the refractive index variance with turbulence. However both terms are related to the transfer term. So, if $[a^2\Phi^*+b^2\Psi^*+2ab\Omega^*]$ is the Fourier transform of second term of the right hand side of eq. (6), Then one may have

$$-(U'_k-U_k)\frac{\partial}{\partial r_k}(a^2\overline{\theta\theta'}+b^2\overline{qq'}+2ab\overline{q'\theta}) =$$

$$= \int_{-\infty}^{\infty}[a^2\Phi^*(\vec{\kappa},\vec{x}_n)+b^2\Psi^*(\vec{\kappa},\vec{x}_n)+2ab\cdot$$

$$\cdot\Omega^*(\vec{\kappa},\vec{x}_n)\exp(i\vec{\kappa}\cdot\vec{r})\,d\vec{\kappa} \qquad (4)$$

Considering r=0, one may have $U_k = U'_k$, in this case eq.(4) reduces to the form

$$\int_{-\infty}^{\infty}[a^2\Phi^*(\vec{\kappa},\vec{x}_n)+b^2\Psi^*(\vec{\kappa},\vec{x}_n)+2ab\cdot$$

$$\cdot\Omega^*(\vec{\kappa},\vec{x}_n)]\,d\vec{\kappa} = 0 \qquad (5)$$

Thus as in the case of $[a^2\Phi+b^2\Psi+2ab\Omega]$, $[a^2\Phi^*+b^2\Psi^*+2ab\Omega^*]$ also gives zero total contribution to the rate of change of refractive index $[a^2\overline{\theta^2}+b^2\overline{q^2}+2ab\overline{q\theta}]$ and can only change the distribution in the wavenumber space of contribution to refractive index $[a^2\overline{\theta^2}+b^2\overline{q^2}+2ab\overline{q\theta}]$. Thus the interaction of refractive index variance with the turbulent and the mean flow (the first two terms of the right hand side of eq. (1) appear to bo the only ones associated with the spectral transfer terms while other terms may be interpreted as production, convection and diffusion terms. It is hopes that this study will help better understanding of the modeling of refractive turbulence parameters in the atmospheric/oceanic surface layer.

3. REFERENCES

Batchelor, G. K., 1953: The theory of homogeneous turbulence, Cambridge University Press.

Hill, R. J., 1992: Review of optical scintillation methods of measuring the refractive-index spectrum, inner scale and surface fluxes, Waves in random media, 2, 179-201.

Hill, R. J., 1989 Implication of Monin-Obukhov similarity theory for scalar quantities, J. Atmos. Sci., 46,2236-2244.

Hill, R. J., 1978: Spectra of fluctuations in refractivity, temperature, humidity, and temperature-humidity cospectrum in the inertial and dissipation ranges, Radio Sci. 13, 953-961.

Patel, S. R., 2001: Spectral transfer ofhumidity and temperature correlations for inhomogeneous turbulence for land and agriculture processes, 11th Conference on Satellite Meteorology and Oceanography, AMS, 15-18 October 2001, Madison, WI. U. S. A., (in this issue . paper P1.22)

Priestley, J. T. and Hill, R. J., 1985: measuring high-frequency humidity, temperature and radio refractive index in surface layer, J. Atmos. Oceanic Tech. 2, 233-251.

P1.24

ASSIMILATION OF SOIL MOISTURE FROM SATELLITE-DERIVED SKIN TEMPERATURE WITHIN THE PENN STATE/NCAR MESOSCALE MODEL MM5

Jing Zhang and Jeffrey S. Tilley

Geophysical Institute, University of Alaska Fairbanks, Fairbanks, AK 99775-7320

1.Introduction

Studies of the influence of soil moisture on atmospheric circulation over a wide range of spatio-temporal scales have been performed by many investigators (e.g., Shukla and Mintz 1982; Sellers et. al 1988; Betts et. al 1996). The results demonstrated that an accurate initialization and evolution of soil moisture is essential for obtaining an appropriate depiction of atmosphere-surface interactions and the associated impacts on weather and climate. Due to a lack of observation data, especially in high latitudes, the initial soil moisture is specified poorly in current models.

In this study, we incorporate a satellite data assimilation method following Jones et al (1998) into version 3 of the Penn State/NCAR MM5 modeling system (Chen and Dudhia 2000) to retrieve soil moisture. As earlier studies have indicated that the surface temperature is most sensitive to the soil moisture (relative to other factors) during the mid-morning hours (e.g, Wetzel et. al 1984; Carlson 1986), we assume that the difference between simulated skin temperature and the observed one in mid-morning can be minimized by adjustments to the soil moisture. Thus the observed skin temperature is the key for this soil moisture initialization scheme.

Several methods of estimating surface temperature using thermal satellite data from the Advanced Very High Resolution Radiometer (AVHRR) on NOAA polar-orbiting platforms have been developed (e.g, Becker and Li 1990; Gutman 1994; Key et al 1997). In this study, we choose to employ the retrieval algorithm for clear-sky surface-temperature from Key et al (1997) which is developed specifically for high latitudes. In this algorithm, two 'split-window' infrared channels at approximately 11 μm and 12 μm from AVHRR are used.

In this paper, first we briefly introduce Key's algorithm for retrieving skin temperature from thermal satellite data. Then we present a description of our soil moisture assimilation scheme. In the last part of the paper, we give the results from case study simulation experiments using our implementation of the soil moisture assimilation scheme over high latitudes. By conducting experiments over an otherwise data sparse region, we hope to not only demonstrate the technique but its potential utility over such data sparse regions of significant hydrologic and climatic importance.

Corresponding Author : Jing Zhang, Geophysical Institute, University of Alaska Fairbanks, 903 Koyukuk Dr. P.O.Box 757320 Fairbanks, AK 99775-7320
email:jing@rathlin.iarc.uaf.edu

2. Brief Description of the Retrieval Algorithm for Skin Temperature

The retrieval of land surface skin temperature (LST) is much more complicated than for sea surface temperature (SST) because of the high spatial and temporal variability of surface emissivity and difficulties in detecting clouds over land surfaces. The basic approach of LST retrieval algorithms is to use the split window channels (4&5) of NOAA-AVHRR to develop relationships between surface temperature, split-window radiances and surface emissivity with radiative transfer model. The derivation scheme we adopted here is from Key et al (1997) (hereafter denoted the Key scheme). The Key scheme considers almost all the existing polar orbiting satellites (NOAA-7,9,11,12,14) and is optimized for high latitude surface temperature estimation, with spectrally dependent emissivity.

The relationship between surface temperature, infrared channel 4 & 5 brightness temperature and surface emissivity in the Key scheme is as follows:

$$T_s = a + b \times T_4 + c \times T_5 + d \times emiss4 + e \times emiss5$$

where a~e are coefficients as a function of temperature range and satellite number. T_4, T_5 are channel 4 & 5 brightness temperature. $emiss4$ (0.985), $emiss5$ (0.975) are surface emissitivity in channel 4 and 5 respectively.

For NOAA-12 and 14 satellites when T_4 > 260K, the coefficients are:

NOAA-12:	NOAA-14:
a=46.9049	a=45.9367
b=3.6529	b=3.3803
c=-2.6470	c=-2.3725
d=-181.5388	d=-166.7875
e=132.7192	e=118.6037

The scheme is applied only for clear sky condition; clouds are filtered out with the aid of both visible and IR channels following Czajkowski et al (1997). The satellite retrieval skin temperature is then assimilated into the model to retrieve soil moisture as described in the following section.

3. Summary of the Soil Moisture Assimilation Scheme

The core assumption of the assimilation approach is that the differences between the observed and simulated skin temperature arise from differences

between the actual and simulated latent heat fluxes (Jones et al., 1998). Under the same atmospheric conditions, such differences in the heat flux can be due only to differences in available soil moisture. The key to the method, then, is to use the difference in observed and simulated skin temperatures to adjust the model's energy balance (primarily the latent heat fluxes), which in turn is used to derive physically consistent values of soil moisture.

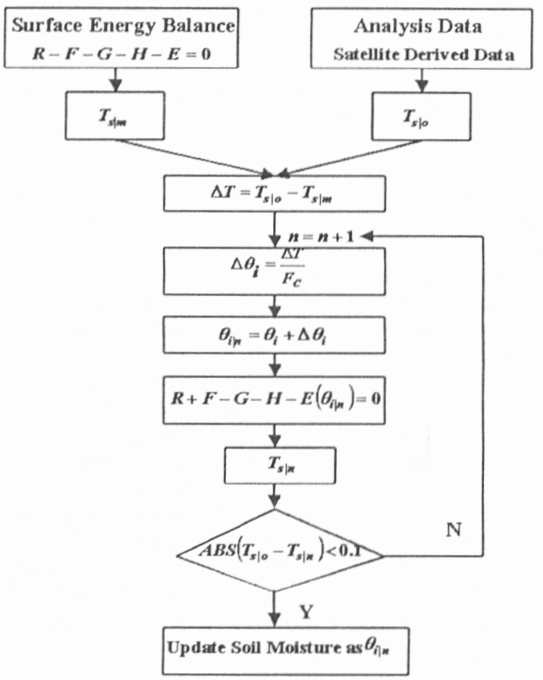

Where: R = *total atmospheric radiation*
F = *sfc. Longwave radiation*
G = *soil heat flux*
H = *sensible heat flux*
E = *latent heat flux*
T_s =*skin temp.(m:modeled; o:observed), and*
q_i = *soil moisture for the ith layer*

Figure 1. Flow chart depicting assimilation method

Figure 1 shows a flow chart summarizing the procedure used in our implementation. The modeled skin temperature is obtained via a surface energy balance computation, while the observed skin temperature is derived from either available observations or satellite data or analysis. An initial skin temperature difference is computed and then an iterative loop is entered. In this loop an adjustment is first made to the simulated soil moisture based on the skin temperature difference and a complex function F_c whose form is not presented here for brevity (see Tilley and Zhang 2001 for details). The adjusted soil moisture is then used to compute a new latent heat flux, which in turn enters a new surface energy balance computation. The result is an adjusted simulated skin temperature which is then compared with the observed value. If the new skin temperature difference is less than 0.1K, the method stops and the soil moisture is set to its most recent value. Otherwise, the loop repeats.

4. Experiment Design

The soil moisture assimilation method, as we have implemented it within MM5V3, can be applied not only to actual satellite-derived skin temperatures but also to surrogate datasets such as from a skin temperature analysis. For our tests of the method over Alaska and the Western Arctic, an area deemed fairly representative of the high latitude environment, we utilized both satellite derived skin temperature and NCEP/NCAR Reanalysis data in the experiments and compared their results. The use of reanalysis data has two advantages. First, there is ample contemporaneous skin temperature data from the reanalysis data over the entire domain of interest (Figure 2), something which can generally not be achieved from polar orbiting satellite data since the AVHRR swath width is a maximum of 2700km and the satellite only periodically scans at an optimal angle for domain-wide contemporaneous measurements. Second, analysis data allow us to determine the robustness of the scheme irrespective of satellite data quality issues; we may perturb the initial soil moisture values from the reanalysis and evaluate how well the method can retrieve an appropriate distribution in the course of the simulation.

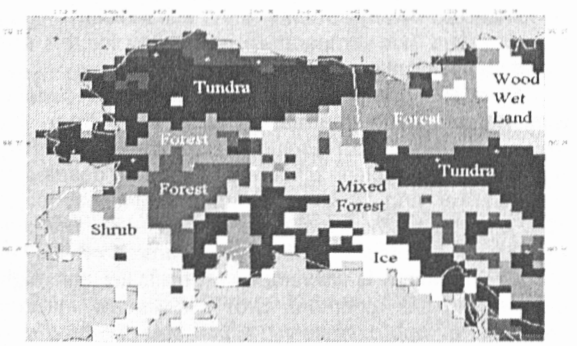

Figure 2. Domain and vegetation depiction used in the modeling experiments. The vegetation classes follow the USGS classification scheme. There are tundra, forest, wetland, shrub and glacial ice within this domain.

The model grid used in all experiments, shown in Figure 2, has a horizontal resolution of 45 km with a computational grid of 41 x47 x 23 vertical levels. A model time step of 150 seconds is used. In all experiments, we utilized the following physical parameterizations, all of which are standard options in MM5V3: the Dudhia (1989) simple ice microphysics scheme; the Grell (1993) cumulus scheme, the MRF

planetary boundary layer scheme (Hong and Pan 1996) and the Benjamin (1983) cloud radiative cooling scheme. NCEP/ NCAR reanalysis data are used to provide initial and boundary conditions to the atmospheric model as well as to the Chen and Dudhia (2000) MM5 Land Surface Model (LSM) derived from the Oregon State University model of Mahrt and Ek (1984).

We consider a mid-summer period, 4-7 July 1999. During this period there was only scattered light precipitation at a few locations; most of the domain shown in Figure 2 experienced no precipitation at all. Such a case was selected in order to avoid complications that precipitation would introduce into the latent heat flux adjustments as well as violate the basic assumptions underlying the scheme (see Jones et. al 1998 for details).

The following experiments, all for a 72 hour simulation period beginning at 00 UTC 4 July 1999, were conducted for this case study:

a) Control Run which does not utilize the assimilation scheme; initial soil moisture from the NCAR/NCEP analysis is applied

b) Dry Run where the initial soil moisture is reduced 10% volumetrically from the NCAR/NCEP analysis but the assimilation scheme is still not applied. This run effectively represents the potential errors that can result from a poor soil moisture initialization.

c) Assimilation Run 1 where the initial soil moisture is as in the Dry Run but the assimilation scheme with analysis skin temperature is applied at 10 am local time on the first simulation day.

d) Assimilation Run 2 which is same as Assimilation Run 1 except that the satellite derived skin temperature is used in the assimilation scheme.

The assimilation runs measure, effectively, the degree to which application of the assimilation scheme can mitigate the errors that would result from the poor soil initialization in the Dry Run.

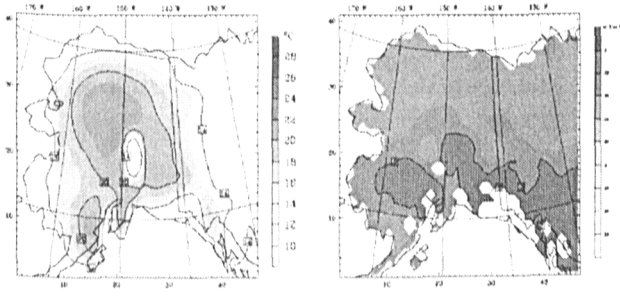

Figure 3. NCAR/NCEP Reanalysis fields at the initial simulation time (00 UTC 4 July 1999) for the Skin Temperature (°C; left panel) and Upper Layer (0-10cm) Soil Moisture (volumetric; right panel).

5. Results

Figure 3 shows the NCAR/NCEP Reanalysis fields for skin temperature and upper 10 cm soil moisture overt he domain at the initial time of the simulation (00 UTC 4 July 1999). The skin temperature field shows a maximum in Interior Alaska and the Brooks Range while the soil moisture indicates a sharp drop northward from the Gulf of Alaska coastline into Interior Alaska, followed by a more gradual decline to the North Slope region. These conditions are fairly typical for the warm season in Alaska, reflecting the influences of the maritime environment near the Gulf of Alaska and the more continental climate experienced in interior sections.

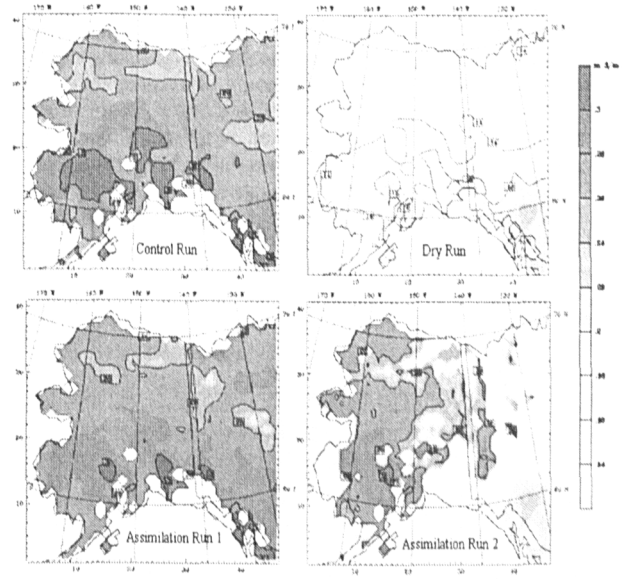

Figure 4. Upper layer volumetric soil moisture at 00 UTC 5 July for the Control, Dry and Assimilation Run 1 & 2 simulations.

Figure 4 depicts the simulated values for upper layer soil moisture in the Control, Dry and Assimilation 1&2 Runs at 00 UTC 5 July (24 hrs into the forecast). As would be anticipated, the Control Run results are not dissimilar to the analysis from the previous day. There is strong continuity of the upper layer soil moisture field.

The Dry Run results clearly reflect the effects of the 10% initial reduction in soil moisture from the analysis values. Skin temperature values (not shown) are 4-8°C higher over interior and northern Alaska, consistent (from an energy balance perspective) with soil moisture values that have remained essentially unchanged at the reduced initial values.

The results from Assimilation Run 1 show that the values of both skin temperature (not shown) and upper layer soil moisture at 24 hours into the simulation are reasonably close to those of the Control Run. This close correspondence of the Assimilation Run with both the Control Run and the Reanalysis soil moisture fields continues for most of the entire 72 hour simulation (figures not shown), even though the assimilation scheme is only applied once.

Soil moisture from the Assimilation Run 2 is retrieved reasonably over the part of the domain where there is no significant cloud cover (not shown). Recall that the Key scheme can only retrieve skin temperature from AVHRR satellite data under clear sky conditions for the assimilation scheme. Comparing the Assimilation Runs 1 & 2, the resultant soil moistures are very similar under the clear sky conditions.

Improvements in soil moisture from application of the assimilation scheme extend to boundary layer fluxes and structure as well. Figure 5 shows plots of planetary boundary layer (PBL) height at 00 UTC 6 July for the Dry Run and the Assimilation Runs 1 & 2. Differences of up to 1000 m in PBL height occur over Interior Alaska, the Brooks Range and the Yukon Territory, even though it is 42 hours after application of the scheme. Comparison with the Control Run results (not shown) show much closer agreement with the Assimilation Run 1 & 2 results. This further implies, considering the otherwise good agreement between the Control Run and Reanalysis, that the PBL heights in the Dry Run are too high and that the Assimilation Run provides a better simulation of boundary layer properties.

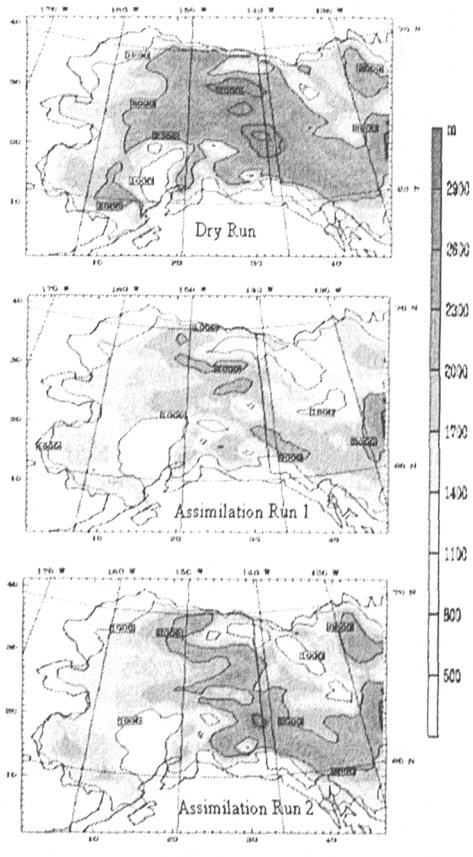

Figure 5. Planetary boundary layer height (m) at 00 UTC 6 July for the Dry Assimilation1&2 Runs.

6. References

Benjamin, S. G., 1983: Some effects of surface heating and topography on the regional severe storm environment. Ph.D. Thesis, Department of Mete-orology, The Pennsylvania State University, 265 pp.

Betts,A.K., J. B. Ball, A.C.M.Neljaars, M.J.Miller, and P.A. Viterbo, 1996:The land surface-atmosphere interaction: A review based on observation and global modeling perspectives. J.Geophys.Res., 101, 7209-7225.

Becker, F., and Z.-L. Li, 1990: Towards a local split window mehod over land surface. Int. J. Remote Sens., 11, 369-393.

Carlson, T.N., 1986: Regional scale estimates of surface moisture availability and thermal inertia using remote thermal measurements. Remote Sens. Rev., 1, 197-246.

Chen, F. and J. Dudhia, 2001: coupling an advanced land-surface hydrology model with the PSU/NCAR MM5 modeling system. Part I: Model description and implementation, Mon. Wea. Rev., 129, 569-585.

Dudhia, J., 1989: Numerical study of convection observed during the winter monsoon experiment using a mesoscale two-dimensional model. J.A tmos. Sci., 46, 3077-3107.

Grell, G., 1993: Prognostic evaluation of assumptions used by cumulus parameterizations. Mon. Wea. Rev., 121, 764-787.

Gutman, G. G., 1994: Global data on land surface parameters from NOAA AVHRR for use in numberical climate models. J. Clim., 7,669-680.

Hong, S. Y. and H-L. Pan 1996: Nonlocal boundary layer vertical diffusion in a medium-range forecast model. Mon. Wea. Rev., 124, 2322-2339.

Jones, A. S., I. C. Guch and T. H. Vonder Haar, 1998: Data assimilation of satellite diurnal heating rates as proxy surface wetness data into a regional atmospheric mesoscale model, Part I: Methodology. Mon. Wea. Rev., 126, 634- 645.

Key, J. R., J. B. Collins, C. Fowler and R. S. Stone, 1997: High-latitude surface temperature estimates from thermal satellite data. Remote Sens. Environ., 61,302-309.

Mahrt, L., and K. Ek, 1984: The influence of atmospheric stability on potential evaporation. J. Clim. Appl. Meteor., 23, 222-234.

Sellers,P.J., F.G.Hall, G.Asrar, D.E. Strebel, and R.E.Murphy, 1988: The first ISLSCP Field Experi-ment (FIFE). Bull. Amer. Meteor. Soc., 69, 22-27.

Shukla,J., and Y. Mintz, 1982: Influence of land-surface evapotranspiration on the earth's climate. Science, 215, 1498-1501.

Tilley, J. S. and J. Zhang, 2000: Testing methodologies for high latitude soil moisture initialization in the Penn State/NCAR MM5 Mesoscale Model. AGU Fall Meeting, San Francisco, 2000.

Wetzel, P.J., D.Atlas, and R.H.Woodward, 1984: Determining soil moisture from geosynchronous satellite infrared data: A feasibility study. J.Climate Appl. Meteor., 23, 375-391.

Acknowledgments:

The authors gratefully acknowledge Dr. Andrew Jones of Center for Geosciences, CSU for his helpful discussions. The work was sponsored by grants from the Dept. of Defense and Johns Hopkins University under the University Partnering for Operational Support Initiative.

P1.25

A SYNERGISTIC SURFACE BRDF/ALBEDO RETRIEVAL WITH MODIS AND MISR OBSERVATIONS 1. INTERCOMPARISON

Yufang Jin, Feng Gao, Crystal Schaaf, and Alan Strahler
Department of Geography, Boston University, Boston, Massachusetts

Carol Bruegge, John Martonchik, and David Diner
Jet Propulsion Laboratory, California Institute of Technology, Pasadena, California

1. INTRODUCTION

Surface albedo, the ratio of radiative energy reflected by land surface to incoming radiation, plays a key role in surface energy budget and hence has significant influences on climate. Satellite observations offer a great opportunity for global surface albedo retrieval from space. The acquisition of angular measurements by an individual sensor, however, is limited by its scanning configuration, the platform's orbital characteristics and cloud appearances. Surface Bidirectional Reflectance Distribution Function (BRDF) characterizes the anisotropy of surface reflectance and if specified accurately, can be used to retrieve surface albedo from limited directional observations of satellites (Wanner et al., 1997; Schaaf et al., 2001) .

The MODerate Resolution Imaging Spectro-radiometer (MODIS) and Multi-angle Imaging Spectroradiometer (MISR), on board the same TERRA platform, employ different observation concepts and both provide surface BRDF and albedo products with different retrieval algorithms. This paper intends to analyze the similarities and differences between MODIS and MISR surface bidirectional reflectance (BRF) and albedo products, as the first step in our ongoing effort to combine MODIS and MISR observations for better surface BRDF/albedo retrieval.

2. INSTRUMENT AND DATA

MODIS-TERRA is a cross-track imager and provides a near-daily global coverage. The directional samplings are accumulated through a time series of observations, and global surface BRDF and albedo are produced for each 16-day period. MISR, however, takes the novel approach of imaging the the earth almost simultaneously in nine different view directions (Diner et al., 1998). Its view angles range from 26.2° to 70° both in forward and afterward direction in addition to nadir looking. MISR scans along-track and hence complements MODIS in the azimuth dimension.

Daily atmospheric corrected surface directional reflectances are gridded into one kilometer resolution (Vermote et al., 2001) to serve as the input data for the MODIS BRDF/Albedo product and are used for this study. We reprojected and resampled the MISR level 2 surface products (Martonchik et al., 1998) and geometric parameter data from Space Oblique Macerator (SOM) to Integerized Sinusoidal Grid (ISG). Two ISG tiles acquired in early January and one in February 2001 were selected and four corresponding MISR swaths were extracted to represent different land cover types and sampling geometry (Table 1). Radiometric adjustments were applied to the first three swaths according to recent calibration data (Bruegge et al., 1997). The dominant land cover types are bare desert, semi-desert and shrubs. Figure 1 shows typical sampling geometries of MODIS and MISR over the

Table 1. Study areas represented by MODIS ISG tile number and MISR path/orbit as well as acquiring dates.

Lat., Lon.	Land type	MODIS tile (date)	MISR path, orbit (date)
30°~40°N 104°~130°W	Shrubland	h08, v05 1~16, Jan.	P042, O005569 3, Jan.
10°~20°N 0°~10°E	Desert	h18, v07 1~16, Jan.	P188, O005549 2, Jan.
		h18, v07 1~16, Jan.	P193, O005593 5, Jan.
20°-30°S 0°~10°E	Shrubland	h20, v11 2~17, Feb.	P174, O006218 17, Feb.

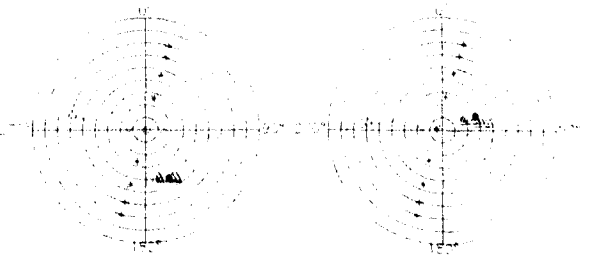

Figure 1. Angular sampling from MODIS and MISR observations in Sahel in early January (left) and in South Africa in early February (right). Radius of circles represents zenith angle with 10° increment (zero zenith angle is in the center) and polar angle represents azimuth (zero azimuth, North, is on the top). Diamond and asterisk: MODIS and MISR viewing direction; Triangle and solid dot: sun locations of MODIS and MISR overpass.

Corresponding author address: Yufang Jin, Boston Univ., Dept. Of Geography, Boston, MA 02215; email: yfj@crsa.bu.edu

Study areas. Both MODIS and MISR observations are between the principal plane (PP) and cross principal plane (CPP) over Sahel and California in early January. MODIS observations are closer to the PP while MISR observations fall between the PP and CPP in South Africa during early February. The change of solar zenith angles of MODIS observations during the 16 day periods are within 10° except for South Africa, where the solar zenith changes about 20°.

3. RESULTS

The anisotropy of surface reflectivity for shrubs on soil (Sahel) and on grass (South Africa) are demonstrated in both MODIS and MISR BRFs (Figure 2). Both MODIS accumulated angular observations and MISR simultaneous observations capture the characteristics of vegetation reflectance, such as the stronger backward scattering and hot spot effect. Surface directional reflectances of MODIS and MISR are very similar in tile h08v05 and h18v07, where both viewing azimuths are between the PP and CPP (Figure 2, top panels). The RossThickLiSparse-Reciprocal (RTLSR) BRDF model (Wanner et al., 1995) inverted with MODIS data predicts very well the shape of surface directional reflectance at MISR view geometry over these regions. However, surface reflectances observed from MODIS show larger angular variations than those from MISR in tile h20v11 (path 174), due to the fact that MODIS observations are closer to the PP in this tile during February (Figure 2, bottom panels). The decrease of predictability in tile h20v11 indicates that MISR observations can add extra angular information to MODIS observations when their sampling geometries are not equivalent.

Direct intercomparison of BRFs can not be made since MODIS and MISR acquire observations at different sampling geometry. Close to nadir, however, there are some possibilities that MODIS and MISR observing angles are similar. We extracted near nadir observations with viewing zenith and solar zenith difference less than 5° and relative azimuth difference less than 10°. The scatter plots of MODIS BRFs versus MISR BRFs at near nadir show a strong linear relationship, especially in red and green band (Figure 3, top panels). Normalized Difference Vegetation Index (NDVI) distribution demonstrates two modes with 0.15 as the break point. Pixels with NDVI higher than 0.15 are mostly from path 174 in South Africa, which is dominated by shrubs with grass underneath, and therefore its histograms of MODIS and MISR near-nadir BRFs were plotted separately from other swaths in Figure 3 (bottom panels). The shapes of histograms are very similar, indicating that both MODIS and MISR capture similar spatial variations of surface nadir reflectances.

In general MODIS BRFs agree very well with MISR in the green band for all pixels and are consistently lower by around 8 percent in the red. The largest difference is in the blue band, where MODIS BRFs are generally higher than MISR, due to the difficulty of aerosol retrieval and atmospheric correction in sparsely vegetated area. Theoretically, the difference between MODIS and MISR aerosol correction should lead to consistent differences between MODIS and MISR surface reflectance in the blue, green and red band. This is shown by the fact that the correlation between relative differences in red and blue is as high as 0.54. However, band center shifts might offset the expected differences. Both MODIS and MISR centers at 0.56 μm in green, and MODIS blue band center is 23 nm larger than MISR while red band center of MODIS is 26 nm less than MISR. We find that MODIS near nadir reflectance is close to MISR in tile h18v07 and h08v05, but is lower than MISR by 14 percent in tile h20v11 (South Africa). Further examination of MISR BRF images shows some distinct blocks in NIR and blue, where larger differences in NIR occur. It is recognized that the MISR algorithms were in updating period. In fact, the images of MISR surface products acquired beginning May 2001 is not spotty. Another possible reason is vegetation growth since MISR path 174 was acquired on February 17, the last day of the MODIS 16 day period in early February.

Another way to compare MODIS and MISR reflectance is to use a BRDF model to infer surface reflectance at geometries beyond observations. We inverted the RTLSR BRDF model with extracted MISR BRFs. The derived parameters were used to predict surface reflectance at the sampling geometry of MODIS at the same day. The scatter plots and histograms of MODIS BRFs against MISR concurrent predictions show similar results as those of near-nadir observations. The difference, however, increases for path 174 due to the same reasons discussed above.

Table 2. Correlation and differences (mean and standard deviation) between MODIS black sky albedo at MISR-overpass solar zenith angle and MISR directional hemispherical reflectance in tile h18v07.

Band	R	Difference	Relative Difference
NIR	0.88	-0.046 (0.068)	-7.3% (9.6%)
Red	0.96	-0.047 (0.033)	-10.0% (6.6%)
Green	0.96	-0.019 (0.020)	-6.2% (6.4%)
Blue	0.82	0.024 (0.017)	20.0% (15.3%)

The operational MODIS black sky albedo (BSA) is produced at local solar noon, while MISR directional hemispherical reflectance (DHR) is the direct beam albedo during the MISR overpass. We here therefore derived MODIS BSA at MISR-overpass solar zenith angle off-line instead of using MODIS operational BSA product. The similarity and difference of MISR DHR and MODIS black sky albedo again follow the pattern of near nadir reflectance although the magnitude of differences increases (Table 2). MISR DHR is derived

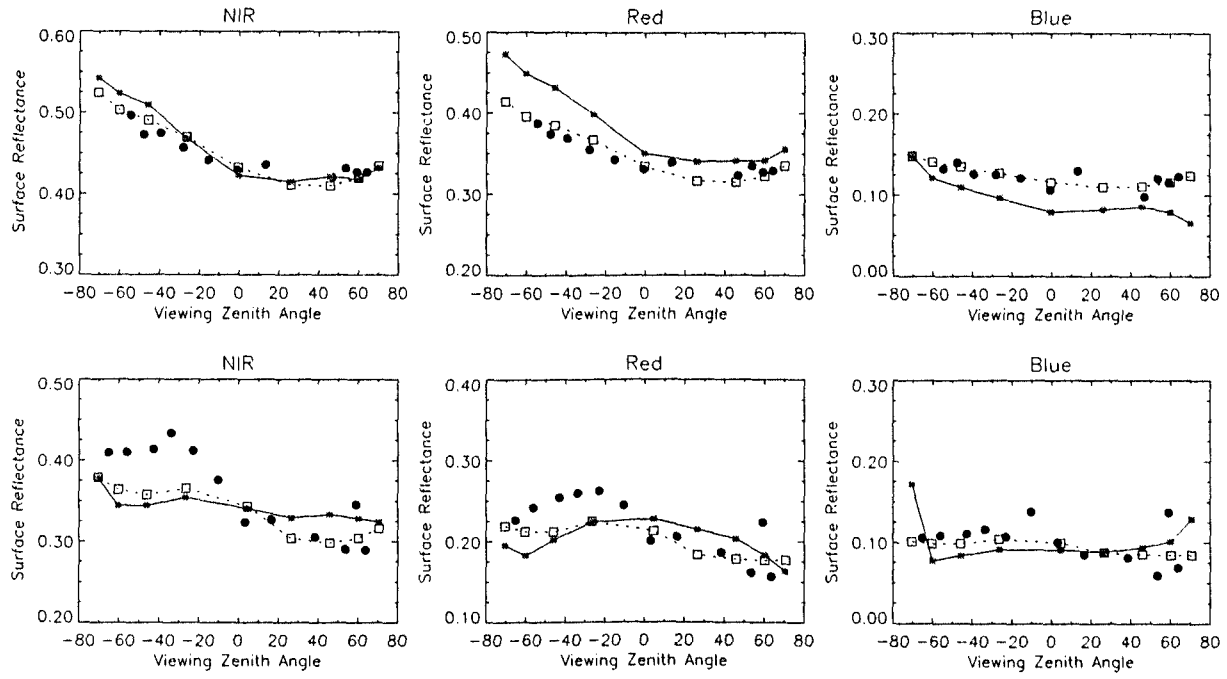

Figure 2. Surface directional reflectances observed from MODIS (dark solid dot) and MISR (light solid square, solid line) and predicted surface reflectance at MISR sampling geometry from MODIS observations (open square, dashed line). Top panel represents sparse shrubs on bare soil in Sahel, and bottom panel represents the shrubs on grass in South Africa.

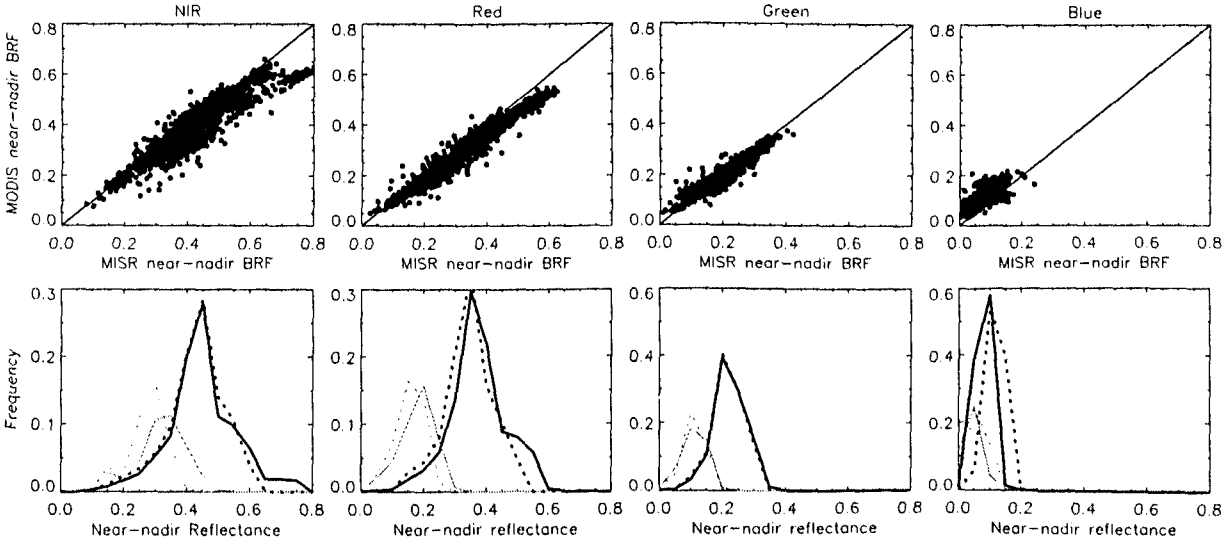

Figure 3. Scatter plots (top panels) and histograms (bottom panels) of MODIS versus MISR near nadir surface reflectances. Dashed line represents distributions of MODIS reflectances and solid line MISR reflectances. Light color is for tile h20v11 in South Africa (path 174) and dark color for other two tiles.

from retrieved surface hemispherical directional reflectances using a parameterized BRDF model (MRPV) (Engelsen et al., 1996), while MODIS albedo is based on RTLSR model. In order to examine the possible error induced by BRDF models, we generated surface albedo from MISR BRFs using MODIS algorithm and compared it with MISR DHR. The difference is within 3 percent, indicating that RTLSR and modified RPV model are similar in their ability to invert surface BRDF and to retrieve surface albedo as

previously demonstrated by Lucht (1998), Gao (2000), and Bicheron (2000).

4. CONCLUSIONS

We explored three intercomparisons between MODIS and MISR products with an aim of combining MODIS and MISR data to improve the retrieval of BRDF and albedo: near-nadir surface reflectance, surface reflectance at MODIS viewing geometry predicted by inversion of same day MISR observations, and MODIS black sky albedo under MISR-overpass solar zenith angle versus MISR directional hemispherical reflectance. Results show that

a) MODIS and MISR near-nadir BRF/DHR are very similar in the green band and MODIS BRF/DHR are generally 8 percent lower than MISR in the red band. MODIS BRF/DHR are around 20 percent higher than MISR in the blue band. Special attention should be paid to the NIR band, where differences may be dependent on vegetation status.

b) Largest relative differences appear in the blue band and the correlation between relative differences in the red band and blue band are as high as 0.54, indicating that these differences are probably due to the atmospheric correction differences.

c) Opposite band center shift seems to explain the opposite biases in blue and red of MODIS BRF/DHR relative to those of MISR. However, more studies about spectral differences need to be done in the future.

d) Information content of MODIS and MISR angular observations is very similar when observations of them are made between principal plane and cross principal plane. However, additional angular information can be added to other if they do not have equivalent angular samplings.

It should be noted that MODIS has started reprocessing a consistent one year product and that the MISR level 2 algorithms were being updated at the time of the intercomparison presented here. In the future, the most current data will be analyzed for various land cover types, sampling geometries and atmospheric conditions. TOA (top-of-atmosphere) radiance comparisons can be used to further determine if biases are caused by calibration or atmospheric correction.

REFERENCES

Diner, D. J., J. C. Beckert, T. H. Reilly, C. J. Bruegge, J. E. Conel, R. Kahn, J. V. Mortonchik, T. P. Ackerman, R. Davies, S. A. W. Gerstl, H. R. Gordon, J.-P. Muller, R. B. Myneni, P. J. Sellers, B. Pinty, and M. M. Verstraete, 1998: Multi-angle Imaging Spectro-Radiometer (MISR) instrument description and experiment overview, *IEEE Trans. Geosci. Remote Sens.*, 36, 1,072-1,085

Bicheron, P., and M. Leroy, 2000: Bidirectional Reflectance Distribution Function signatures of major biomes observed from space, *J. Geophys. Res.*, 105, 26,669-26,681

Bruegge, C. J., N. L. Chrien, R. Ando, and B. Chafin, 1997: In-flight radiometric calibration of the EOS/ MISR multicamera instrument. *Earth Observing System, Proc. SPIE 3117*, San Diego, CA, 28-29 July 1997

Engelsen, O., B. Pinty, M. M. Verstraete, and J. V. Martonchik, 1996:, Parametric bidirectional reflecance factor models: evaluations, improvements and applications, *Rep. EU 16426*, 114, Joint. Res. Cent. Eur. Comm., Ispra, Italy, 1996

Gao, F., X. Li, A. Strahler, and C. Schaaf, 2000: Evaluation of the LiTransit Kernel for BRDF modeling, *Remote Sens. Rev.*, 19, 205-224

Martonchik, J. M., D. J. Diner, R. A. Kahn, T. P. Ackerman, M. M. Verstraete, B. Pinty,H. R. Gordon, 1998: Techniques for the retrieval of aerosol properties over land ocean using multiangle imaging, *IEEE Trans. Geosci. Remote Sens.*, 36, 1,212-1,227

Schaaf, C. B., F. Gao, A. H. Strahler, W. Lucht, X. Li, T. Tsang, N. C. Strugnell, X. Zhang, Y. Jin, J.-P. Muller, P. Lewis, M. Barnsley, P. Hobson, M. Disney, G. Roberts, M. Dunderdale, C. Doll, R. d'Entremont, B. Hu, S. Liang, and J. L. Privette, 2001: First Operational BRDF, Albedo and Nadir Reflectance Products from MODIS, submitted to *Remote Sens. Environ.*

Wanner, W., A. H. Strahler, B. Hu, P. Lewis, J.-P. Muller, X. Li, C. B. Schaaf, and M. J. Barnsley, 1997: Global retrieval of bidirectional reflectance and albedo over land from EOS MODIS and MISR data: theory and algorithm, *J. Geophys. Res.*, 102, 17,143-17,162

Wanner, W., X. Li, and A.H. Strahler, 1995: On the derivation of kernels for kernel-driven models of bidirectional reflectance, *J. Geophys. Res.*, 100, 21,077-21,089

Lucht, W., 1998: Expected retrieval accuracies of bidirectional reflectance and albedo from EOS-MODIS and MISR angular sampling, *J. Geophys. Res.*, 103, 8,763-8,778

Vermote, E. F., N. Z. Saleous, and C. O. Justice, 2001: Atmospheric correction of MODIS data in the visible to middle infrared: First results, submitted to *Remote Sens. Environ.*

P1.26 FRACTIONAL GREEN VEGETATION COVER OF THE CONTERMINOUS USA FOR USE IN NUMERICAL WEATHER MODELS

Kevin Gallo[1,4,*] Dan Tarpley[1], Ken Mitchell[1], Ivan Csiszar[2], Tim Owen[3], and Brad Reed[4]
1) NOAA, Camp Springs, MD,
2) CIRA, Camp Springs, MD,
3) NOAA, National Climatic Data Center, Asheville, NC
4) EROS Data Center, Sioux Falls, SD.

1. INTRODUCTION

The land cover classes developed under the coordination of the International Geosphere-Biosphere Programme Data and Information System (IGBP-DIS) have been analyzed for a study area that includes the Conterminous United States and portions of Mexico and Canada. The 1-km resolution data have been analyzed to produce a gridded data set that includes within each 20-km grid cell: 1) the three most dominant land cover classes, 2) the fractional area associated with each of the three dominant classes, and 3) the fractional area covered by water. Additionally, the monthly fraction of green vegetation cover (fgreen) associated with each of the three dominant land cover classes per grid cell was derived from a 5-year climatology of 1-km resolution NOAA-AVHRR data. The fgreen values derived in this study provide a potential improvement over the use of monthly fgreen linked to a single land cover class per model grid cell, as currently used in some numerical weather models. The fgreen variable will be described and its relationship with land cover class will be discussed.

2. MODEL REPRESENTATION OF VEGETATION

The land surface variables in the land surface model component of the coupled Eta model include vegetation (land cover) type and fractional green vegetation cover (fgreen). Fgreen is defined as the fraction of horizontal area associated with the photosynthetically active green vegetation that occupies a model grid cell. Fgreen, as used by the National Centers for Environmental Prediction (NCEP) in the land surface model component in the Eta model, is varied through the growing season while a constant value of leaf area index (LAI) is utilized. The introduction of improved satellite-derived monthly values of fgreen into the Eta model resulted in improved model forecasts of land-surface fluxes and planetary boundary layer structure (Betts et al., 1997). The current land cover class and fgreen variables used in the Eta analysis are represented in the model as one (most dominant) land cover class per grid cell with monthly fgreen values derived as an average for the grid cell. The advantages of sub-grid cell vegetation information have been discussed by Koster and Suarez (1992) and demonstrated by Avissar and Pielke (1989) as well as others. The objectives of this study included development of land surface data sets for use in coupled land-atmosphere models that include sub-grid cell land classes and the seasonal characteristics of vegetation (fgreen) associated with each of those land classes for the Conterminous USA. A grid cell size of 20 km by 20 km was selected for this initial analysis as this is the nominal grid cell size in the current operational Eta model at NCEP.

The land cover information for this study was extracted from the IGBP_DIS 1 km land cover data set [Loveland and Belward, 1997] that was produced to make available a global data set with high spatial resolution and known accuracy. The 17 IGBP classes were condensed into 14 classes (CIGBP) by combining several of the classes, Additional information on the methodology can be found in Gallo et al. (2001).

3. FRACTION OF GREEN VEGETATION COVER

The fraction of green vegetation per grid cell (fgreen, Equation 1),

$$\text{fgreen} = (\text{NDVI} _ \text{NDVIo})/(\text{NDVIi} - \text{NDVIo}) \quad (1)$$

as described by Gutman and Ignatov (1998), and demonstrated useful in coupled land_atmosphere models (Betts et al., 1997), requires maximum and minimum thresholds of the normalized difference vegetation index (NDVI). Selection of the maximum (NDVIi) and minimum (NDVIo) thresholds of NDVI required for computation of fgreen was based on NDVI values of the biweekly Conterminous USA 1_km AVHRR data set (Eidenshink, 1992) in combination with the CIGBP land cover classes.

An interpolated mid_month NDVI data set was prepared from the biweekly Conterminous USA data set. All biweekly data available from 1993 and 1995 through 1998 were interpolated on a daily basis and temporally processed to remove fluctuations in the NDVI signal due to cloud or other contamination (Swets, et al.,

* Corresponding author address: Kevin P. Gallo, NOAA/NESDIS, EROS Data Center, Sioux Falls, SD 57198-0001; email: Kevin.P.Gallo@noaa.gov.

1999). The mid_month NDVI value was retained from the interpolated daily values. Data of 1994 were excluded from the analysis due to low solar elevation angles associated with the AVHRR data acquisitions during this year.

The mid_month NDVI values were averaged on a monthly basis over the 5 available years of data. Monthly values of fgreen were computed (equation 1) from the 5_year monthly NDVI values with NDVIo = 0.09 and NDVIi = 0.69. When observed NDVI values were less than 0.09 fgreen was assigned a value of 0.0, and when observed values were greater than 0.69 fgreen was assigned a value of 1.0.

4. RESULTS

One of the motivating factors for development of sub-grid cell information was the recognition that within vegetation cover transition zones a single land cover class per grid cell will likely misrepresent the surface conditions within the grid cell. Six grid cells that lie on an east-west transect from Eastern Arkansas through Tulsa, Oklahoma, to Western Oklahoma were intensively examined. This region represents a gradient of annual precipitation from over 127 cm for the eastern grid cell to less than 70 cm for the western grid cell. The crops associated with the Croplands dominated grid cells varied from cotton and rice (east) to wheat (west) (USDA, 1994). The fgreen values were examined for the three most dominant land covers of each grid cell. Some grid cells (e.g., Figure 1) displayed similar trends in fgreen for the three land covers, while trends within the other grid cells differed (e.g., Figure 2).

The overall impact of the use of three land cover classes and their associated monthly fgreen values was assessed for the entire study area. A significant difference in fgreen, defined as a difference greater than 0.1 (10%), between any of the land cover classes within a grid cell, was assessed for each grid cell on a monthly basis. Significant differences in fgreen were observed for over 57% of the non-water grid cells in the study area during at least one month. Over 6% of the grid cells exhibited significant differences in fgreen during all 12 months.

5. SUMMARY

The results suggest that for the CIGBP land cover classes, at a 20 km grid cell size, three land cover classes are sufficient to represent the land cover within a grid cell. The results also suggest that differences in fgreen between the classes within a grid cell are sufficient to warrant derivation of fgreen for each of the three land cover classes within a grid cell. Future analysis will include the variability in fgreen.

6. REFERENCES

Avissar, R. and R.A. Pielke, 1989: A Parameterization of Heterogeneous Land Surfaces for Atmospheric Numerical Models and Its Impact on Regional Meteorology. *Mon. Wea. Rev.* **117**, 2113-2136.

Betts, A., F. Chen, K. Mitchell, and Z. Janji, 1997: Assessment of Land surface and boundary layer models in two operational versions of the NCEP Eta model using FIFE data. *Mon. Wea. Rev.* **125**, 2896-2915.

Eidenshink, J.E., 1992: The 1990 Conterminous U.S. AVHRR Data Set. *Photogram. Engr. & Rem. Sensing.* **58**, 809-813.

Gallo, K., D. Tarpley, K. Mitchell, I. Csiszar, T. Owen, and B. Reed., 2000: Monthly Fractional Green Vegetation Cover Associated with Land Cover Classes of the Conterminous USA. *Geophys. Resr. L.*, **28**, 2089-2092.

Gutman, G. and A. Ignatov, 1998: The derivation of green vegetation fraction from NOAA/AVHRR data for use in numerical weather prediction models. *Intl. J. Remote Sensing*, **19**, 1533-1543.

Koster, R.D. and M.J. Suarez, 1992: Modeling the land surface boundary in climate models as a composite of independent vegetation stands. *J. Geophys. Resr.* **97**, 2697-2715.

Loveland, T.R. and A.S. Belward, 1997: The IGBP-DIS global 1 km land cover data set, DISCover: first results. *Intl. J. Remote Sensing*, **18**, 3289-3295.

Swets, D.L., B.C. Reed, J.D. Rowland and S.E. Marko, 1999: A Weighted Least-squares Approach to Temporal NDVI Smoothing. *Proceedings Amr. Soc. Photogram. Rem. Sens.* 17-21 May, Portland OR., ASPRS, Washington, D.C., 526-536.

USDA, 1994: Major world crop areas and climatic profiles. World Agriculture Outlook Board, U.S. Department of Agriculture. Washington, D.C.

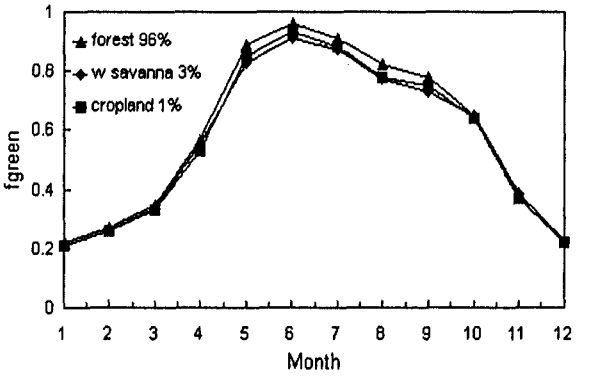

Figure 1. Five-year mean Fgreen for a forest dominated grid cell (36.1 °N, 94.9 °W). Note that the percentage of land area of each cover type, per grid cell, is also provided.

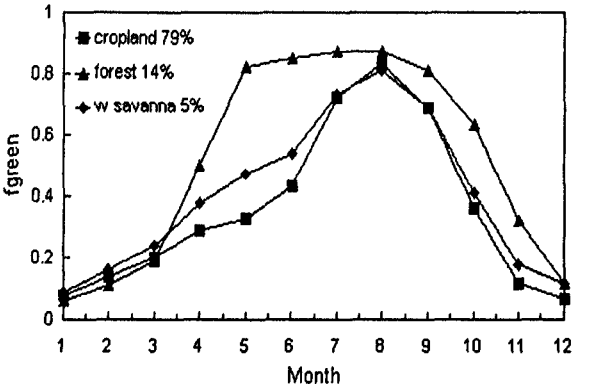

Figure 2. Five-year mean Fgreen for a cropland dominated grid cell (36.3 °N, 90.7 °W).

P1.27 Using DMSP Imagery And SSM/I Data To Analyze A von Karman Vortex Over The Black Sea

Boniface J. Mills *
Department of Geosciences, Meteorology/Climatology Program
University of Nebraska – Lincoln, NE

Paul J. McCrone
Meteorological Satellite Application Branch
Air Force Weather Agency (AFWA)
Offutt AFB, NE

Introduction

On January 24, 2001, high pressure was situated over the southern Ukraine and southwest Russia. A low pressure system was located over Turkey. A strong pressure gradient existed between the two systems producing strong, nearly geostrophic winds over extreme southern Ukraine and the Crimean Peninsula. The direction was east to west over the area. The wind speed was 15 to 35 knots decreasing southward over the Black Sea as shown in Figure 1.

A von Karman vortex had formed over the Black Sea southwest of the Crimean Peninsula and associated coastal mountains. A von Karman vortex forms when an object stands in the way of a fluid stream; the vortices generated will travel with the stream away from the object. Von Karman vortices form at all scales of fluid motion. This is usually a sign of turbulent atmospheric flow. Although von Karman vortices have been viewed by other spacecraft (e.g.

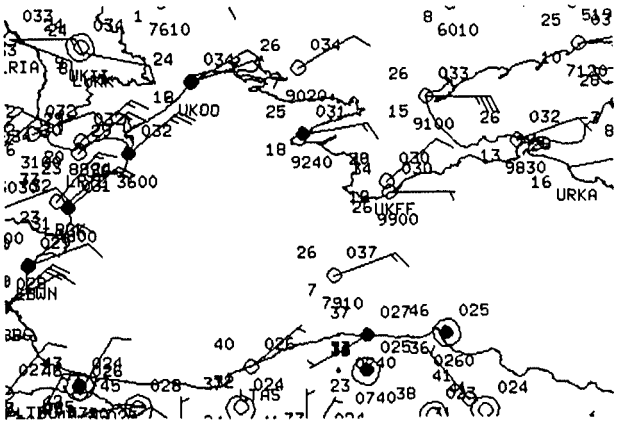

Figure 1. January 24, 2001 1200 UTC surface observations in the vicinity of the von Karman vortex.

NASA SeaWiFS and NOAA GOES) in other geographical areas, this is an unusual event over the Black Sea. Satellites of the Defense Meteorological Satellite Program (DMSP) recorded the event.

The von Karman vortex in this case was a mesoscale feature. It was visible because of stratocumulus clouds in the vicinity of the Crimean Peninsula. Favorable conditions for the vortex formation were due to the high winds flowing around a

* *Corresponding author address:* Boniface J. Mills, Univ. of Nebraska – Lincoln, Dept. of Geosciences, Bessey 214, P.O. Box 880340 Lincoln, NE 68588-0340; e-mail: bon@unlserve.unl.edu

tall, steep mountain range in southern part of the Crimean Peninsula. A more complete satellite analysis was done using DMSP imagery, including data from the Special Sensor Microwave Imager (SSM/I).

Data and Methodology

Visible and thermal imagery was obtained through the Satellite Data Handling System (SDHS) of the Air Force Weather Agency (AFWA). Additional DMSP imagery and SSM/I data was obtained from SDHS. Visible (fine) imagery was also retrieved and analyzed for examining details of the von Karman vortex because of its 0.3 nm resolution.

Infrared and visible imagery from DMSP were fused together using the multispectral imaging technique found in Klaes, d'Entremont and Thomanson (1992). This multi-channel image revealed low, stratiform clouds in yellow/green shades and high cirriform clouds depicted in blue. Convective clouds appeared white or off-white. This color shading helped identify important cloud features associated with this event.

All seven SSM/I channels were retrieved through SDHS. Specific SSM/I data can reveal the wind speed over open water where data is scarce. SSM/I wind estimates are a measure of ocean surface roughness and foam coverage. Frequent waves and foam dispersion at the air-sea interface allow more energy to pass (emissivity) from the sea surface. Therefore, higher brightness temperatures can be detected from space by sensors. The 19, 37 and 22 GHz channels are used for determining surface wind speed. The Goodberlet, Swift and Wilkerson algorithm (1989) was used. The formula for wind speed (WS) in meters/second is as follows:

$$WS = 147.90 + 1.0969 \cdot TB19v - 0.45555 \cdot TB22v - 1.7600 * TB37v + 0.7860 * TB37h$$

Where: TB= radiometric brightness temperature at frequency and polarization indicated

SSM/I data provides surface wind estimates with 50km (25nm) resolution up to gale force and beyond. Erroneous wind speeds can be produced by convective rainfall that lead to high wind speeds.

Results and Discussion

The DMSP imagery easily depicted the von Karman vortex (Fig.2). The feature was mesoscale in size showing a distinct curl of the cloud bands. The multispectral imagery (not shown) provided the viewer with a better contrast of clouds, water and land. Fine resolution (Fig.3) showed striations in the cloud cover as well as cloud streets north and west of the eddy, suggested strong winds. This image provided greater detail of the shape, size and fluid flow around the von Karman vortex because of its high (0.3nm) resolution.

The output of the SSM/I channels (not shown) revealed winds greater than 20 knots north of the Crimean Peninsula and west along the Black Sea coast. The observational data for that time frame confirm there was no precipitation in the vicinity of the von Karman vortex.

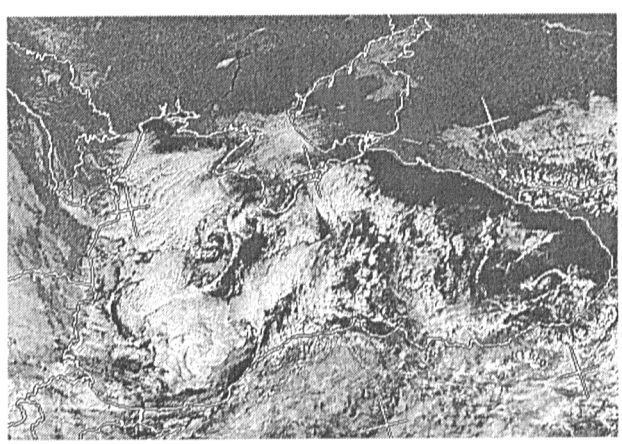

Figure 2. DMSP View of the von Karman vortex.

Figure 3. High resolution DMSP fine image of the von Karman vortex

The winds decreased rapidly southward especially in the vicinity of the von Karman vortex. Both the output of the Goodberlet et al. algorithm and the wind station observations for that time period agreed. The correct ingredients of geography and weather patterns helped produce this unusual event.

The general flow pattern around a large and tall mountain range helped create the von Karman vortex by preventing flow to penetrate southward. Thus the curl (vorticity) was created by the large variation in wind velocity. The resulting rotating motion caused a vertical motion of air that broke up the cloud cover around the center allowing the inner curl of the vortex to be viewed. The differential wind speed, from north to south, around an obstacle, and ideal cloud conditions set up the eddy formation to be visualized by satellite imagery.

Acknowledgements:

The authors would like to thank the Air Force Weather Agency, Offutt AFB NE for providing the imagery and time on their computer systems.

References

Goodberlet, M.A., C.T. Swift and J.C. Wilkerson, 1989: Remote sensing of ocean surface winds with the Special Sensor Microwave/Imager. J. of Geophys. Res., 94, 14547-14555.

Graham, J.R., 2000: Flow past a cylinder. Available On-Line: http://astron.berkeley.edu/~jrg/ay202/lectures/node18.html

Klaes, K.D., R.P. d'Entremont and L.W. Thomanson, 1992: Applying an 8-Bit Multispectral Color-Composite Image Simulation Technique to Operational Real-Time AVHHR Data. Bull. Amer. Meteor. Soc., 73, 766-772

NASA Goddard DACC, 2000: Various Views Of von Karman Vorticies. Available On-Line: http://dacc.gsfc.nasa.gov/CAMPAIGN_DOCS/OCDST/vonKarman_vorticies.html

STUDY OF FOG PROPERTIES USING LANDSAT DATA

Kenneth W. Fischer *[1], Manuel Nunez[2], Jaya Ramaprasad, Michael R. Witiw[1], Jeff Baars[1]

[1]Terabeam Labs, Redmond, Washington
[2]University of Tasmania, Hobart, Tasmania, Australia

1. INTRODUCTION

Recently, advances have been made in the analysis of fog and low clouds using satellite imagery. For example, NOAA/NESDIS has developed several experimental products derived from GOES infrared channels that describe low clouds and fog, giving the bases of low clouds as well as the thickness of the low cloud and fog layers (Ellrod, 1995; Lee, 1997).

In our research, LANDSAT imagery and, to a lesser extent, AVHRR imagery is used. LANDSAT Thematic Mapper (TM) images over the cities of Seattle and Chicago are analyzed to provide information on typical fog spatial structure and scale, and homogeneity and variability of liquid water content over the region of fog. Fog optical depths and visibility are mapped in the urban areas and then correlated with concurrent measurements taken in the nearby airports- Boeing Field International (BFI) near Seattle and Meigs Field near Chicago.

Radiative transfer calculations using MODTRAN have been developed to estimate top of atmosphere spectral reflectances as a function of total liquid water in a vertical path, and mean droplet radii. Using these calculations, the reflectances in the visible and near infrared channels of the LANDSAT images are used to derive liquid water content and radii. The liquid water content can be correlated with visibilities observed in the airports to formulate a relationship between the two parameters. Since we know one of the important variables in defining fog is the liquid water content, its relationship to visibility is a useful one to understand. We hope to apply the techniques to interpret the readily available daily GOES images to give us an ongoing database of visibility in middle and high cloud free areas.

2. BACKGROUND

Visibility in fog is known to be non-uniform, as fog is seen to take on a cellular structure similar to that of stratocumulus (Gerber, 1980; Welch, 1986). The distribution of this variability is important to the free space optics industry, as routine weather observations (even one minute ASOS observations) are inadequate to capture fog's spatial and temporal variability. Additionally, the relation of visibility to the liquid water content of fog could be a useful tool in determining expected fog visibilities.

3. DATA SOURCES

This study uses two types of satellite images of very different spatial resolutions and temporal sampling: Landsat and AVHRR. The Landsat imagery used was Bands 2 (λ=0.56μm) and 5 (λ=1.65μm) collected at 30 m spatial resolution. The AVHRR imagery used was Band 1 collected at 1 km resolution. Surface meteorological observations are used from Boeing Field (BFI) and Seattle-Tacoma Airport (SEA) to correlate reported visibilities with reflectances from the Seattle images. Surface meteorological observations from Meigs Field (CGX), O'Hare International Airport (ORD), and Midway Airport (MDW) are used to correlate reported visibilities with reflectances from the Chicago images.

4. ANALYSIS

Fog events at two major cities – Seattle and Chicago - were selected for case studies.

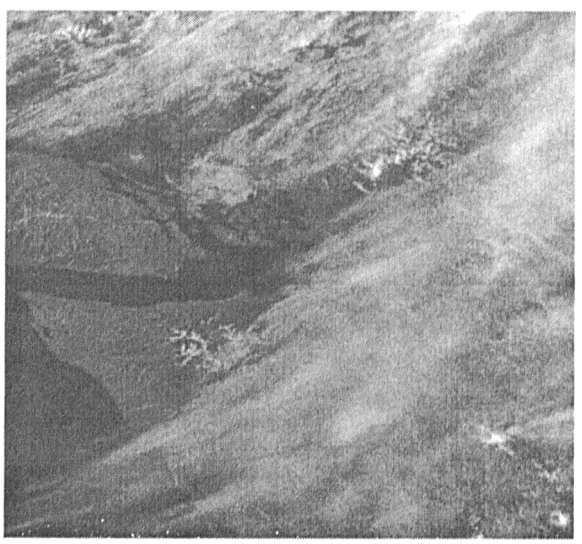

Figure 1. AVHRR Band 1 (λ=0.63μm) Image collected March 19, 1992 showing Puget Sound.

* *Corresponding author address:* Kenneth W. Fischer, Terabeam Labs, 14833 NE 87th St., Building C, Redmond, WA 98052; email: ken.fischer@terabeam.com

Figure 2. Landsat Band 5 (λ=1.65μm) image collected 3/19/92 showing fog and low clouds around downtown of Seattle area.

4.1 Seattle Case Study

On March 19, 1992, fog and low clouds were observed around the Seattle area during the morning hours. The AVHRR image collected at 1600 UTC (Figure 1) shows cirrus clouds over the southerly portion of Puget Sound. Dendritic patterns can be seen on the Olympic Peninsula (left center) and in the Cascade Range (right). Major bright feature in lower right corner is Mt. Rainier. The AVHHR 1 km resolution, however, is too coarse to adequately resolve the fog structures around downtown Seattle.

A Landsat image collected at 1730 UTC (Figure 2) shows cells of fog clustered around downtown Seattle area. Visibility observed at BFI showed visibility as low as 200 m during the hours immediately prior to the collection of this image. Observations at SeaTac (12 miles south of downtown Seattle) showed visibilities of 6000 m or better.

The fog cells ranged in size from 150 m up to 800 m. A key point in terms of the interest of mapping fog for FSO telecommunications, a fog event of this type might impact operations of optical telecommunications in downtown Seattle but the event would not be observed in AVHRR imagery or by other local airports such as SeaTac.

Several pixels from the image where fog was present were selected for analysis. MODTRAN was used calculate liquid water path based on the reflectivity for Landsat Bands 2 and 5 (Kuji, 2000). Results (Table 1) show a large variability in liquid water in the three sample pixels. The variability in liquid water is considerably larger than the standard error in the prediction relation (47 gm/m^2). This indicates that the variability is real and raises the possibility that there could be systematic regional differences in liquid water and visibility in the image.

Table 1. Calculated liquid water path from selected fog pixels from Landsat image in Figure 2.

Broadband Albedo	Band 2 Vis Reflectance (λ=0.56μm)	Band 5 IR Reflectance (λ=1.65μm)	Liquid water (g/m^2)
0.175	0.23	0.18	221
	0.17	0.14	129
	0.16	0.14	414

4.2 Chicago Case Study

During the morning of March 1, 1994, rolls of fog were observed over Chicago. Figure 3 shows a Landsat Band 2 image of Chicago and rolls of fog oriented WSW-ENE. The rolls of fog are Langmuir cells similar to stratocumulus clouds (Welch, 1986; Welch et al., 1988; Wielicki, 1986). The rolls are very regularly spaced at 1.4 km.

The northeast corner of the image shows higher brightness due to the underlying pack ice on Lake Michigan. As with the Seattle case study, the downtown Chicago area is under a blanket of fog while areas just south show clear skies.

Observations at Meigs Field just east of downtown right on Lake Michigan showed visibilities as low as 400 m at the surface. Midway and O'Hare Airports, both further from Lake Michigan, reported no ground fog, but both reported very low cloud ceilings. Midway (14 km from the lake) showed ceiling at 150 m while O'Hare (20 km from lake) showed ceiling at 270 m.

5. DISCUSSION

LANDSAT provides a superb nominal spatial resolution of 30 meters. However, the limited availability of the data and its expense make it difficult to complete extensive studies. In the past few years, new sensors on GOES 8-10, have allowed a spatial resolution of two kilometers. AVHRR can also be used at a slightly finer resolution (1 km) to detect fog. Although, this is still too large to detect the smallest cellular structure of fog, it is adequate to help determine some of the structure. After learning what we have from LANDSAT, exploring AVHRR and GOES data, with its reliable frequency may help to extend this study.

6. REFERENCES

Ellrod, G. P., 1995: Advances in the detection and analysis of fog at night using GOES multispectral infrared imagery. *Wea. and Forecasting.*, **10**, 606-619.

Gerber, H.E., 1980: The microstructure of fog. *J. Atmos. Sci.*, **38**, 454-458.

Kuji, M., T. Hayasaka, N. Kikuchi, T. Nakajima, M. Tanaka, 2000: The retrieval of effective particle radius and liquid water path of low-level marine clouds from NOAA AVHRR data. *J. Appl. Meteor.*, **39**, 999-1016.

Lee, T. F., J. Turk, K. Richardson, 1997: Stratus and fog products using GOES-8-9 3.9-μm data. *Wea. and Forecasting*, **12**, 664-677.

Welch, R. M., S. K. Sengupta, K. S. Kuo, 1988: Marine stratocumulus cloud fields off the coast of Southern California observed using Landsat imagery. Part II: Textural Analysis. *J. Appl. Meteor.*, **27**, 363-378.

Welch, R. M., B. Wielicki, 1986: The stratocumulus nature of fog. *J. Climate Appl. Meteor.*, **25**, 101-111.

Wielicki, B. A., R. M. Welch, 1986: Cumulus cloud properties derived using Landsat satellite data. *J. Climate Appl. Meteor.*, **25**, 261-276.

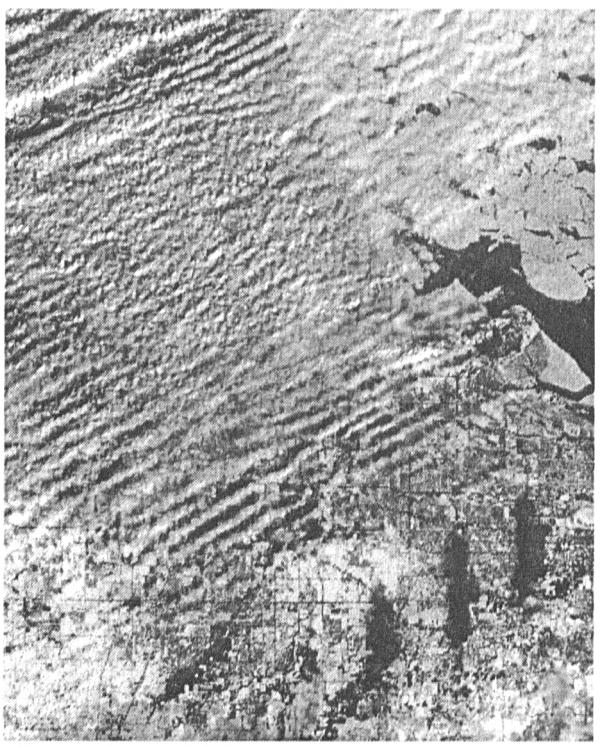

Figure 3. Landsat Band 2 (λ=0.56μm) image collected 3/1/94 showing rolls of fog over Chicago.

P1.29 INCORPORATING DATA FROM GOES AND POES PLATFORMS INTO AN INTEGRATED IN-FLIGHT ICING DIAGNOSTIC ALGORITHM FOR ALASKA

Jeffrey S. Tilley and James Long
Geophysical Institute, University of Alaska Fairbanks, Fairbanks, Alaska

1. INTRODUCTION

Though the aviation safety record in Alaska has improved in recent years, general aviation accidents continue to occur which are related to mesoscale in-flight icing conditions that are not well forecast with models and algorithms available to aviation forecasters. As part of the FAA's In-flight Icing Product Development Team, we have been developing a version of the National Center for Atmospheric Research/ Research Applications Program (NCAR/RAP) Integrated Icing Diagnostic Algorithm (IIDA; Bernstein *et al.* 2001) suitable for Alaskan application that utilizes the Penn State/NCAR MM5 mesoscale modeling system (e.g, Grell *et al.* 1994; Chen and Dudhia 2001).

In this paper we focus on the methodology of the Alaska-specific IIDA (hereafter referred to as the UAF IIDA) that we have developed at the University of Alaska Fairbanks, including the satellite aspects. We will describe the procedures used in incorporating data from the GOES-10 platform and merging this data with other data sources. We also briefly discuss possibilities for incorporating POES data, which, to achieve optimal icing diagnoses, will require a blending of data from GOES and POES along the appropriate POES swath at the time of interest.

2.OVERVIEW OF THE NCAR/RAP IIDA

Many elements of the UAF IIDA are heavily based upon the NCAR/RAP version. The NCAR/RAP version is fully described in Bernstein et al. (2001). Here we present a brief overview of the algorithm to provide a context for the modifications we have made, presented in the following section.

The NCAR/RAP IIDA utilizes several different types of meteorological data as input: a) output from the Rapid Update Cycle II model (RUCII) numerical weather prediction model; b) conventional surface observations (METARs); c) the national radar mosaic, d) pilot reports (PIREPs), and e) National Weather Service (NWS) GOES-8 satellite data including the visible (0.67 mm), short-wave infrared (3.7 μm), and long-wave infrared (10.8, 12.0μm) channels as well as the short-wave reflectance.

A combination of the GOES-8 data and model output is used to eliminate cloud-free areas from further consideration and determine cloud top temperature and cloud top height. METARs are introduced in a concentric scanning approach as the primary means of determining cloud base height. Once cloud parameters have been established, the METARs are again scanned for the occurrence of precipitation, with a focus on areas of freezing precipitation, frozen precipitation, rain and drizzle.

The next step in the algorithm is to apply the temperature, cloud top temperature and relative humidity to a series of 'interest maps'. This process utilizes fuzzy logic and is designed to relate the fields to the potential for the existence of supercooled liquid water (SLW) within a RUC II model grid column. SLW is a prime ingredient in many in-flight icing scenarios. The functional form of the maps is based on *in-situ* observations of various cloud types (e.g, Sassen *et al.*, 1985) and icing environments (e.g, Miller *et al.* 1998) as well as past experience with the performance of previous algorithms as validated by PIREPs (e.g., Schultz and Politovich 1992).

The likelihood of icing suggested by the interest maps is further modified based upon the particular meteorological scenario (thermodynamic structure, multiple cloud layers, etc.) and the information provided by surface observations of precipitation type and the radar mosaic, drawing from the current state of knowledge regarding the occurrence of aircraft icing in these situations. For icing diagnoses, positive icing PIREPs obtained within 60 minutes of the diagnosis time at a distance no greater than 150 km (300m) horizontally (vertically) from the RUCII grid cell are used to further enhance the icing potential. Detailed discussion of five common icing scenarios and how such modifications occur can be found in Bernstein *et al.* (2001).

Corresponding author address: Jeffrey S. Tilley, University of Alaska Fairbanks, Geophysical Institute, Fairbanks, AK 99709; Email: jeff@gi.alaska.edu

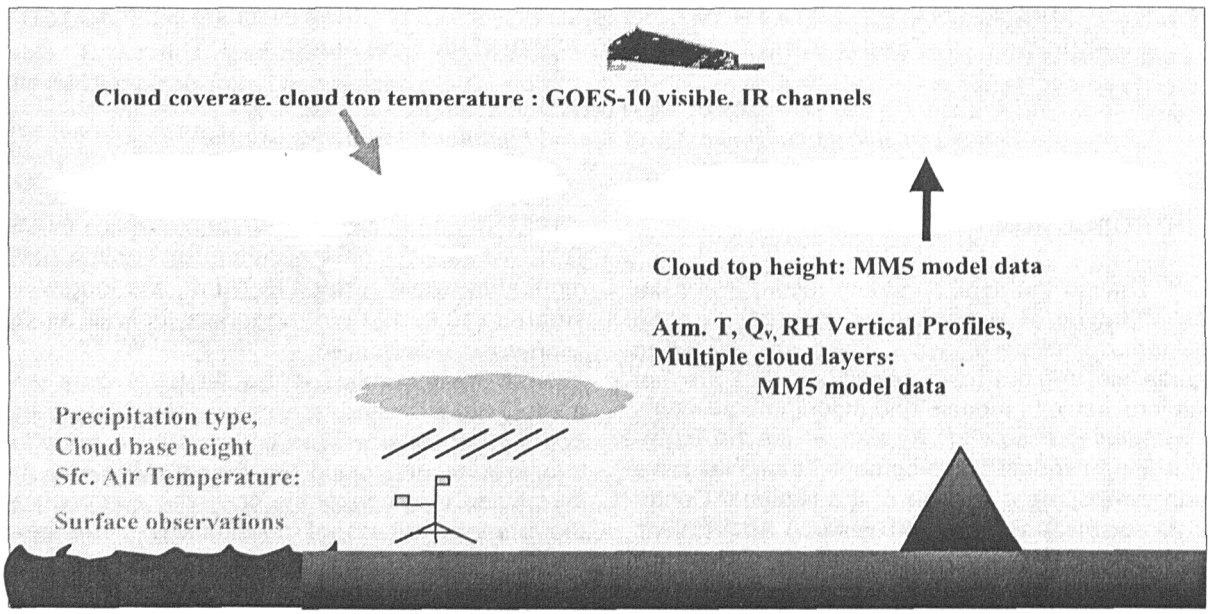

Figure 1. Schematic of UAF IIDA algorithm. See text for detailed description of elements.

3. UAF IIDA MODIFICATIONS

The current implementation of the NCAR/RAP IIDA has provided us with an excellent starting point for development of an Alaska-specific IIDA. However, some elements of the NCAR/RAP IIDA are not well suited for Alaska applications. Some of the data sources used in the NCAR IIDA are not available to the same extent or from the same platform. For example, while there are seven NEXRAD Doppler radars in the state, they are not geographically distributed to be utilized optimally by an icing algorithm, being concentrated in southern Alaska. Further, some of these sites have substantial terrain blocking to contend with, reducing considerably the volume of airspace for which useful radar information is available. In addition, the RUC II model is not available for Alaska, and GOES-8 satellite coverage does not extend far enough north or west to be useful.

Thus, to develop an IIDA that is optimal for Alaska, the NCAR IIDA must be modified. A schematic diagram of our algorithm is provided in Figure 1. The following paragraphs address our approach to dealing with each of the problems specific to Alaska applications.

First, while the RUC II model is not available for Alaska, there are versions of the Eta, Nested Grid Model, Aviation Model and the PSU/NCAR MM5 mesoscale model available in real to near-real-time. The first three of these models are available via the National Weather Service, whose

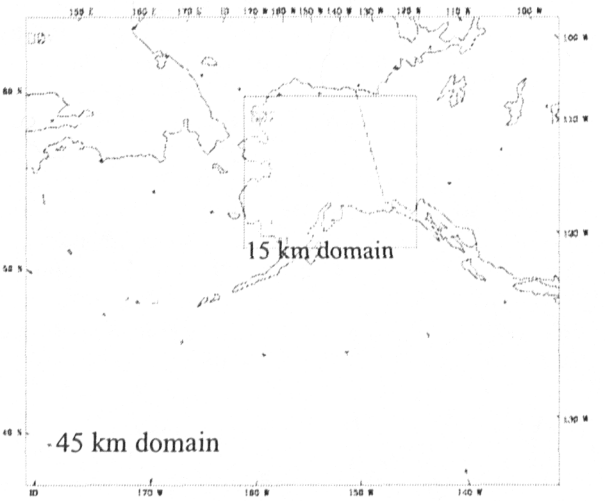

Figure 2. AFWA MM5 forecast domains at grid resolutions 45 km (no shading) and 15 km (shaded area) respectively. Only the 15 km domain is utilized in the UAF IIDA.

Fairbanks office is co-located with UAF. The latter model is run operationally over Alaska and vicinity by the Air Force Weather Agency (AFWA). The AFWA MM5 data are made available to UAF via a special arrangement with the Air Force for this work as well as other research. Given positive experience with the use of MM5 in forecasting for icing field studies such as the Winter Icing and Storms Project (e.g., Rasmussen *et al.*, 1992) and our own experience in evaluating MM5 predictions

of SLW (e.g., Tilley *et al.* 1999), we elected to utilize the MM5 model in the UAF IIDA.

Information on the MM5 model configuration employed by AFWA and used in the UAF IIDA is given in Tilley *et al.* (2001). Although this data is available over both a coarse grid of 45 km and a fine grid of 15 km (see Figure 2), we have elected to implement the UAF IIDA only on the 15 km grid. Our rationale for doing so involves the fact that routine icing forecasts for Alaska often involve large spatial areas for relatively long time periods (often 12 hours or more). Our objective in utilizing the finer scale data was to see how much reduction in areal and volume coverage of icing forecasts might be attainable by providing finer scale model input to the UAF IIDA. Our previous work (e.g, Tilley *et al.*, 1999) suggests that in some cases significant reductions in forecast icing volume might be possible.

Next, given relatively sparse quality radar data, we feel that more study is needed on the potential usefulness of this data before including it in an Alaska-specific IIDA. In addition to coverage issues, little observational work has been done on both cloud microphysics in high latitudes or the robustness of current radar retrieval algorithms in these environments.

As an alternative to using the actual NEXRAD datastream, in the UAF IIDA we utilize a calculation of simulated radar reflectivity from MM5 output mixing ratios of rain, snow and graupel developed by Mark Stoelinga at the University of Washington (e.g, Stoelinga, 2001).

Conventional surface observations are also relatively sparse over Alaska compared to the mid-latitudes. Further, many of these stations are sited in areas that are not necessarily representative, due to mesoscale topography, of the larger area comprising an MM5 grid box. As such, the 150 km search radius for the concentric scanning process may not be optimal. Further testing may suggest a better value for this parameter.

4. INCORPORATION OF GOES DATA

The GOES-8 satellite has insufficient geographic coverage for an Alaska-specific IIDA, though the Pacific-centered GOES-10 does provide coverage for much of our area of interest. We have modified the IIDA to accept this data.

GOES-10 data is received at UAF at the Alaska Data Visualization and Analysis Laboratory (ADVAL) and processed at ADVAL using a SeaSpace TeraScan system. During this initial processing, the data is prepared so that it may be used in the same way that GOES-8 data is used in the NCAR/RAP IIDA. TeraScan functions are used to: a) subset the data for Alaska (function "fastreg"), b) fix bad data points (function "outliers"), and c) compute latitude, longitude, satellite and solar zenith angles, and relative azimuth angles (function "angles"). Channel 2 reflectance data is computed closely following code developed by Greg Thompson for the NCAR IIDA (Thompson, pers. comm.) which follows the approach of Turk *et al.* (1998). Finally, the TDF format file output by this procedure is converted to an HDF format for use by the UAF IIDA.

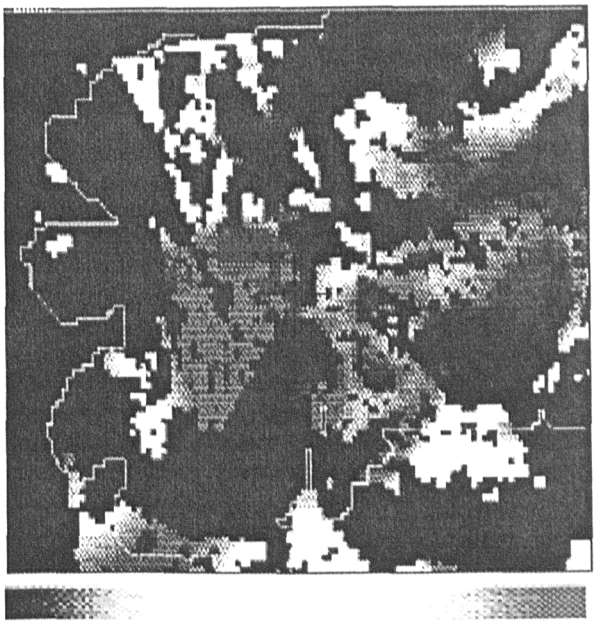

Figure 3. Sample icing potential field from the UAF IIDA for 14 May 2001 at ~ 4.6 k mAGL. Values of the icing potential can range from 0 to 1. In this test the maximum value is 0.56

While this input is sufficient for the initial UAF IIDA, we recognize that over much of our domain a geostationary satellite will be viewing the area from a large tangential angle, with increasing degradation in resolution with increasing latitude. Following a brief description of initial results in the next section, we present our future plans to deal with this shortcoming and its impact on the icing diagnosis as a whole.

5. RESULTS FROM A TEST CASE

Figure 3 shows a sample of IIDA output for a test period in spring of 2001 at approximately 4.6km above ground level. Some potential for in-flight icing exists over a substantial area of the state; values of the icing potential range from 0 to

0.56 out of a possible maximum value of 1. We are encouraged that the algorithm indicates the largest values of icing potential in areas that are climatologically reasonable for this time of year, namely the Prince William Sound/Gulf of Alaska, the North Slope and the Brooks Range passes. As of this writing we have not yet performed verification with PIREPs but will present results and verification from several interesting cases at the conference.

6. FUTURE PLANS: POES DATA

As latitude increases, each pixel of data in a GOES-10 image covers a larger geographical area due to the increased viewing angle from the vertical. For Alaska, this may mean a biased diagnosis of icing where the sideways viewing angle contributes to an inaccurately computed reflectance, primarily in the northern half of the State. To overcome this effect at high latitudes, it is desirable to incorporate polar orbiter (POES) AVHRR data for Alaska into the IIDA.

For most passes, POES data will not be available for the entire domain. We anticipate an approach where data from the two sources will be merged. Strictly, merging in time as well as space would be needed since the POES pass times rarely coincide exactly with an available GOES image. For initial inclusion of POES data we may elect to omit the temporal merging given that the difference in time between a POES pass and a corresponding GOES image should be under 15 minutes. Except for convective episodes, dramatic differences in cloud top temperature and height over such a time period should be relatively small and not impact the icing diagnosis.

Another issue is that the channels seen by the POES AVHRR sensor differ significantly from those on the GOES GVAR sensor. At present we do not know how such differences might manifest themselves in the IIDA. Further, a procedure needs to be devised to ensure proper registration of the POES swaths before blending with the GOES data. We will explore these issues further prior to implementation of POES AVHRR data in the UAF IIDA.

6. REFERENCES

Bernstein, B. C, F. McDonough, M. K. Politovich and B. G. Brown, 2001: IIDA: A physically-based, integrated approach to the diagnosis of in-flight aircraft icing. Part I: Description. Submitted to *Wea. Forecasting.*

Burk, S. D., and W. T. Thompson, 1989: A vertically nested regional numerical prediction model with second-order closure physics. *Mon. Wea. Rev.*, **117**, 2305-2324.

Chen, F. and J. Dudhia, 2001: Coupling an advanced land-surface/hydrology model with the Penn State/NCAR MM5 modeling system. Part I: Model description and implementation. *Mon. Wea. Rev.*, **129**, 569-585.

Dudhia, J. 1989: Numerical study of convection observed during winter monsoon experiment using a mesoscale two-dimensional model. *J. Atmos. Sci.*, **46**, 3077-3107.

Grell, G., 1993: Prognostic evaluation of assumptions used by cumulus parameterizations. *Mon. Wea. Rev.*, **121**, 764-787.

Grell, G. A., J. Dudhia, and D. R. Stauffer, 1994: A description of the fifth-Generation Penn State/NCAR mesoscale model (MM5). NCAR Technical Note, NCAR/TN-398+ST, 117pp.

Miller, D., T. Ratvasky, B. Bernstein, F. McDonough and J. W. Strapp, 1998: NASA/FAA/NCAR supercooled large droplet icing flight research: summary of winter 96-97 flight operations. *36th Aerospace Science Meeting and Exhibit, AIAA 98-0557, Reno, NV, AIAA*, 20 pp.

Rasmussen, R.M., M.K. Politovich, J. D. Marwitz, J. McGinley, J. Smart, W. Sand, G. Stossmeister, B. Bernstein, R. Pielke, D.Wesley, S. Rutledge, K. Elmore, E.R. Westwater, B.Stankov and D. Burrows, 1992: Winter Icing and Storms Project (WISP). *Bull. Amer. Meteor. Soc.*, **73**, 951-974.

Reisner, J., R. J. Rasmussen, and R. T. Bruintjes, 1998: Explicit forecasting of supercooled liquid water in winter storms using the MM5 mesoscale. *Quart. J. Roy. Meteor. Soc.* **124B**, 1071-1107.

Sassen, K., K. N. Liou, S. Kinne and M. Griffin, 1985: Highly supercooled cirrus cloud water: confirmation and climatic implications. *Science*, **227**, 411-413.

Schultz, P. and M. K. Politovich, 1992: Toward the improvement of aircraft-icing forecasts for the continental United States. *Wea. Forecasting*, **7**, 491-500.

Stoelinga, M., 2001: A user's guide to RIP Version 3.0. A program for visualizing PSU/NCAR mesoscale modeling system output. Available online: http://www.mmm.ucar.edu/mm5/mm5-home.html.

Tilley, J. S., D.-L. Wilkinson and M. K. Politovich, 1999: Application of mesoscale data to algorithms for in-flight icing over the Alaska region. *Preprints, 8th Conference on Aviation, Range and Aerospace Meteorology,* Dallas, TX, AMS, 452-456.

Tilley, J.S., J. Long, C. Weatherby and E. L'Herault, 2001: On the Performance of the AFWA version of the PSU/NCAR MM5 model for short-range forecasting in Alaska, the Western Arctic and North Pacific. *Preprints, 6th Conference on Polar Meteorology and Oceanography,* San Diego, CA, AMS, 367-370.

Turk, J., J. Vivekanandan, T. Lee, P. Durkee and K. Nielsen, 1998: Derivation and applications of near-infrared cloud reflectances from GOES-8 and GOES-9. *J. Appl. Meteor.*, 37, 819-831.

P1.31 On Precipitation Modification by Major Urban Areas: A New Perspective from TRMM

J. Marshall Shepherd
NASA-GSFC, Laboratory for Atmospheres, Greenbelt, Maryland

Harold Pierce
Science Systems and Applications, Inc. Lanham, Maryland

1. INTRODUCTION

By year 2025, 80% of the world's population will live in cities according to a 1999 United Nation's report. As cities continue to grow, urban sprawl creates unique challenges related to land use planning, transportation, agriculture, housing, pollution, and development. Urban expansion also has measurable impact on environmental process.

Urban areas modify boundary layer processes through the creation of "urban heat islands" or UHI. In cities, natural land surfaces are replaced by artificial surfaces that have very different thermal properties (e.g. heat capacity, specific heat, and thermal inertia). Such surfaces are typically more capable of storing solar energy and converting it to sensible heat. As sensible heat is transferred to the air, the temperature of the urban air tends to be 2-10 degrees higher than surrounding non-urban areas (fig, 1).

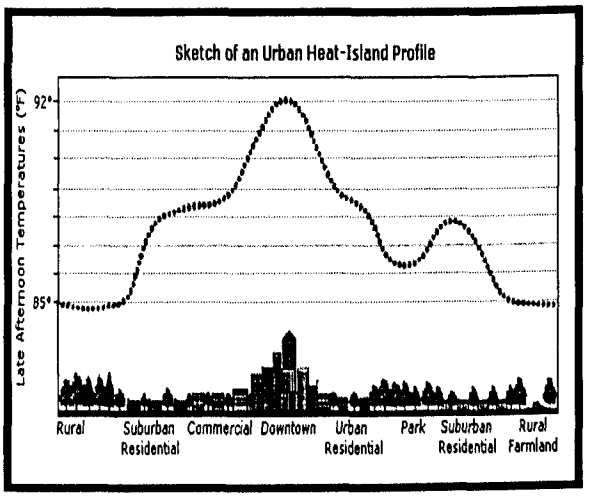

Fig.1-Typical Urban Heat Island Temperature Profile

In the past 30 years, several observational and climatological studies have theorized that the UHI can have a significant influence on mesoscale circulations and resulting convection.

* Corresponding author address: J. Marshall Shepherd, NASA-GSFC, Code 912.0, Greenbelt, MD 20771; shepherd@agnes.gsfc.nasa.gov

Early investigations (Changnon 1968; Landsberg 1970; Huff and Changnon 1972a and 1972b; Huff and Changnon 1973) found evidence of warm seasonal rainfall increases of 9 to 17% over and downwind of major urban cities. The Metropolitan Meteorological Experiment (METROMEX) was an extensive study that took place in the1970s in the United States (Changnon et al. 1977; Huff 1986) to further investigate modification of mesoscale and convective rainfall by major cities. In general, results from METROMEX have shown that urban effects lead to increased precipitation during the summer months. Increased precipitation was typically observed within and 50-75 km downwind of the city reflecting increases of 5%-25% over background values (Sanderson and Gorski 1978; Huff and Vogel 1978; Braham and Dungey 1978; Changnon 1979; Changnon et al. 1981; Changnon et al. 1991). Using a numerical model, Hjemfelt (1982) simulated the urban heat island of St. Louis and found positive vertical velocities downwind of the city. He suggested that the enhanced surface roughness convergence effect and the downwind shifting or enhancement of the UHI circulation by the synoptic flow were the cause (fig. 2). METROMEX results also suggested that areal extent and magnitude of urban and downwind precipitation anomalies were related to size of the urban area (Changnon 1992).

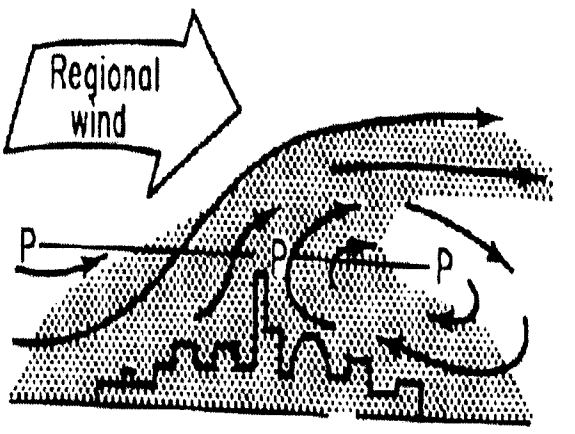

Fig. 2-Mesoscale Circulation Induced by UHI.

2. MOTIVATION and OBJECTIVES

More recent studies have continued to validate and extend the findings from pre- and post-METROMEX investigations. Balling and Brazel (1987) observed more frequent late afternoon storms in Phoenix during recent years of explosive population growth. Analysis by Bornstein and LeRoy (1990) found that New York City effects both summer daytime thunderstorm formation and movement. Jauregui and Romales (1996) observed that the daytime heat island seemed to be correlated with intensification of rainshowers during the wet season (May-October) in Mexico City. Selover (1997) found similar results for moving summer convective storms over Phoenix, Arizona. Bornstein and Lin (2000) examined data from an Atlanta meso-network to show that the UHI induced a convergence zone that initiated storms during the summer of 1999. Thielen et al. (2000) used a meso-gamma scale model to address the extent of influence of urban surfaces on the development of convective precipitation. The results showed that sensible heat fluxes and enhanced roughness due to the urban heat island can have considerable influence on convective rainfall.

The literature indicates that the signature of the "urban heat island effect" may be resolvable in rainfall patterns over and downwind of metropolitan areas. However, a recent U.S. Weather Research Program panel concluded that more observational and modeling research is needed in this area (Dabberdt et al 2000).

Objectives: Employ Tropical Rainfall Measuring Mission (TRMM) Precipitation Radar data:

a. To validate and extend ground-based observations of climatological rainfall patterns in major urban areas using satellite rain estimates.

b. To quantify the impact of urban areas on rainfall in and downwind of cities using satellite rain estimates.

c. To demonstrate the unique capabilities and opportunities to observe multiple urban rainfall climatologies over an extensive area (38 degrees North to 38 degrees South) using the TRMM PR data.

d. To validate an unanticipated application of TRMM PR data to urban-environmental issues.

[Note: The results discussed in this section can be found on the website that accompanies this extended abstract proceeding (http://rsd.gsfc.nasa.gov/912/urban). This website contains plots, figures, and graphs with more specifics details on the study.]

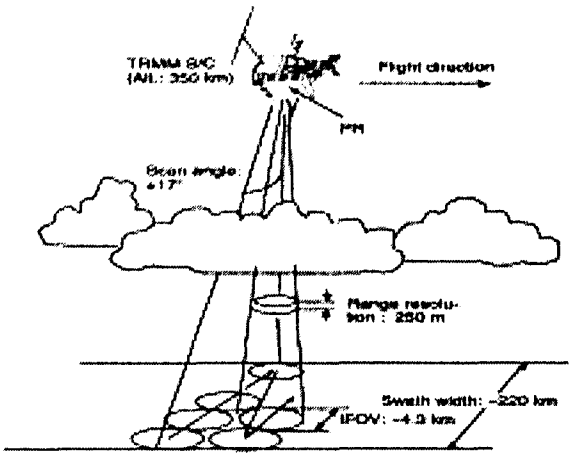

Fig. 3-TRMM Spacecraft and Scan Strategy

3. CONCLUSIONS and FUTURE WORK

The primary goal of part I of this study was to establish that a 3-year, warm season climatology of mean rainfall rates from the TRMM PR could be used to identify urban-induced rainfall anomalies. The study provides one of the first (possibly the first) published accounts of rainfall modification by urban cities that uses rainfall data from a satellite. It also illustrates a unique application of data from the first space-borne rain radar.

Prevailing wind was determined based on a 19-year climatology of geopotential heights, the results validated previous ground-based and modeling studies that identified urban-induced rainfall maxima over and downwind of cities. Using a 15-month climatology of mean rainfall rates at 2.0 km altitude, we examined the cities of Atlanta, Montgomery, Dallas, Waco, and San Antonio. We found that the average percentage increase in mean rainfall rate in the hypothesized "downwind maximum area" over the "upwind control area" was 28.4% with a range of 14.6%-51%. Over the urban area, the average change was smaller (+5.8%) but exhibited a range of –27.7%-24.7%. There was a slight indication that regions orthogonal and to the right of the mean prevailing flow (within 50 km) experienced relatively significant increases in rainfall (10.7%). However, the downwind region exhibited the most significant changes. Tabes 1 and 2 summarize key results. More extensive results can be found at the previously mentioned website.

We also demonstrated that the maximum rainfall rates found in the maximum impact area could exceed the mean value in the upwind control area by 48-116%. This maximum value was found at an average distance of 39 km from

the edge of the urban center or 64 km from the exact center. The range was 20-60 km downwind of the edge of the urban center. In general, the changes in rainfall and their location relative to the "non-urban" effect regions are extremely consistent with previous work related to METROMEX and other studies. This fact provides confidence that UHI-rainfall effects are real and satellite rainfall estimates from TRMM can detect them.

Future work will be published as a separate paper. Part II of the study will seek to establish a robust validation of TRMM rainfall estimates using special rain gauge networks around the key cities in the study. We are also interested in TRMM lightning data as an additional validation source. Additionally, we will seek to address the physical mechanisms that lead to the observed "city" and downwind maxima around cities during the warm season. We will use a cloud-mesoscale model to identify the role that the UHI plays in enhancing or creating mesoscale circulations. We will also seek to differentiate whether dynamic forcing related to the mesoscale circulation (e.g. destabilizing the boundary layer, enhanced vertical motion), surface convergence due to urban roughness, or a combination of both impact warm season rainfall development. We will also propose to develop a new urban land parameterization for the cloud-mesoscale models under study at NASA-Goddard.

The implications of the research presented herein are broad. The establishment of TRMM's ability to identify rainfall anomalies associated with urban areas provides a powerful tool to investigate urban effects due to cities around the world, particularly in areas with sparse ground-based rain measurement systems. The future space-based rainfall measuring missions (e.g. Global Precipitation Measurement) will extend TRMM-like measurements to the mid-latitudes thereby extending our approach to numerous major cities not located in sub-tropical and tropical latitudes that TRMM observed. As experimental and real-time weather prediction models continue to approach smaller spatial scales, this research may require mesoscale models to consider urban surfaces and their characteristics in surface/land parameterizations. This is particularly critical as urban growth continues to infringe upon green space at alarming rates. Additionally, the research has implications for policymakers, urban planners, water resource managers, and agriculture professionals who may use an understanding of urban rainfall climatology in the design of better drainage systems, planning of land-use, or identification of optimal areas for agricultural activity. Additionally, the study further demonstrates the impact of human development on environmental processes.

References available upon request.

City	Mean Rainrate in Maximum Impact Area (mm/hr)	Mean Rainrate in Upwind Control Area (mm/hr)	Mean Rainrate over Urban Center (mm/hr)	Percentage Change in Maximum Impact Area from Upwind Control Area	Percentage Change in Urban Center Area from Upwind Control Area
Atlanta, Georgia	4.23	3.54	3.81	19.5%	7.8%
Montgomery, Alabama	4.39	3.83	4.39	14.6%	9.9%
Dallas, Texas	4.00	3.03	3.78	32.0%	24.7%
Waco, Texas	3.33	2.17	2.49	51.1%	14.7%
San Antonio, Texas	3.29	2.63	1.90	25.0%	-27.7%

Mean Percentage Change in Maximum Impact Area=28.4%
Mean Percentage Change in Urban Center=5.8%
Mean Percentage Change in Northern Minimum Impact Area=1.1%
Mean Percentage Change in Southern Minimum Impact Area=10.7%

Table 1.0-Mean rainrates (mm/hr) from TRMM Precipitation Radar data (2.0 km height). The data is averaged over the specified upwind, downwind, and urban area for the warm season (May-September) for 1998-2000. The percentage change from the upwind control area is given for the "maximum impact" and urban center areas. Mean percentage change for each area is also shown for all cities in the study.

City	Maximum Rainrate Value in Maximum Impact Area (mm/hr)	Percentage Change in Maximun Value in Maximum Impact Area from Upwind Control Area	Distance Downwind of Maximum Rainrate Value from Urban Center Area
Atlanta, Georgia	5.86	65.0%	~60 km
Montgomery, Alabama	5.69	48.5%	~25 km
Dallas, Texas	4.52	49.1%	~20 km
Waco, Texas	4.74	116.0%	~50 km
San Antonio, Texas	5.45	107.0%	~40 km

Maximum rainrate value is found in the maximum impact area at a mean distances of ~39 km from the edge of the urban center (or ~64 km from the exact center).

Table 2.0-Maximum 3-year warm season rainrate (mm/hr) found in the maximum impact area. The table provides information on the distance and direction from the urban center to the value in column 1.

2.1 THE ROLE OF PASSIVE MICROWAVE RADIOMETERS IN CLIMATE MONITORING

Roy W. Spencer
Earth System Science Center
The University of Alabama in Huntsville
National Space Science and Technology Center
Huntsville, AL 35805

1. INTRODUCTION

Passive microwave radiometers have been at the forefront of the emerging field of climate applications of satellite data. Even though the pool of researchers is considerably smaller in passive microwave remote sensing than it is in visible and infrared remote sensing, the characteristics of microwave radiometers in some ways lend themselves more readily to climate applications. I will review some of the important advances this area has seen in the last thirty years, and what the future holds.

2. HISTORICAL CONTEXT

The first launch of a passive microwave radiometer for measurement of natural Earth emissions was accomplished by the U.S.S.R. on a Cosmos satellite in September, 1968. This followed the successful U.S. flyby mission past Venus with a microwave radiometer aboard Mariner-2 in December, 1962. On the U.S. side, these events were followed by a series of window-frequency and sounding (oxygen channel) frequency radiometers on the NASA Nimbus satellite series, starting with the Nimbus-5 Electrically Scanning Microwave Radiometer (ESMR-5) in 1972. ESMR-5 demonstrated the utility of microwave window frequencies (in this case, 19.35 GHz) to measure the warm thermal emission of rain cells against the low microwave emissivity ocean background (Wilheit et al., 1977), a concept first advanced by Buettner (1963). On the same satellite, the first temperature sounder, the Nimbus-E Microwave Spectrometer (NEMS) was flown to measure the emission by molecular oxygen at three frequencies near 60 GHz (e.g. Staelin, 1969). This set the stage for operational satellite monitoring of global atmospheric air temperatures.

Two important events in the eventual use of microwave radiometers for climate monitoring were the first launches of the Microwave Sounding Unit (MSU) in late 1978, and of the Special Sensor Microwave Imager (SSM/I) in mid-1987. Although designed for the day-to-day weather monitoring needs of NOAA and DoD, respectively, the design of these instruments turned out to be sufficiently well thought out, both in terms of calibration and longevity, to allow long-term monitoring of interannual to decadal climate variations. The MSUs, built by the Jet Propulsion Laboratory (JPL), followed on the heritage of the earlier, experimental microwave temperature sounders flown by NASA on the Nimbus-5, -6, and –7 satellites. The MSU was a four channel instrument with center frequencies at 50.3, 53.74, 54.96, and 57.95 GHz, allowing sensitivity to air temperatures from near the surface to the lower stratosphere.

Critical for climate applications, the MSUs had an "external" calibration design, which featured a two-point linear calibration strategy involving a view of the cosmic background at 2.7 K, and a high emissivity on-board warm target whose temperature was monitored with redundant platinum resistance thermometers (PRTs). These calibration measurements were made through the same antenna system (offset parabolic reflector and feedhorn) as were the Earth measurements. This design results in the variable thermal emissions by the radiometer hardware canceling out in the calibration equation. This is an important element in climate monitoring since the decaying or drifting orbit of a single satellite over the course of years causes long-term changes in the solar heating and thus temperature of the satellite and the radiometer. Monitoring and adjusting for these effects was found to be extremely difficult, e.g. in the case of the Nimbus-7 and SeaSat Scanning Multichannel Microwave Radiometer (SMMR). The use of the MSUs for monitoring decadal scale tropospheric temperature variations to about 0.01 deg. C per year was demonstrated by Spencer *et al.* (1990). But along with better sensors came a greater sensitivity to smaller instrument calibration effects. A small nonlinearity of the MSUs response caused instrument-temperature dependent biases, through the specification of the original calibration nonlinearity based upon a single gain state as measured pre-launch. Since the gain of the MSUs Dicke-style radiometer is directly related to the instrument temperature, as the orbits of the NOAA TIROS-N satellites drifted to different times of day, the instrument temperature changed. if not adjusted for, this causes a spurious drift on the long-term record of brightness temperatures (Christy *et al.*, 2000).

There are a series of temperature sounders on the DMSP satellites, also flying since 1979, called the Special Sensor Microwave Temperature (SSM/T) instruments. Partly because early data from these instruments were never archived, there are no climate products being investigated from them. A more recent raw data archive from SSM/T, since the mid-1980's, is kept by NOAA/NESDIS.

The SSM/I was an externally-calibrated window frequency radiometer, and was first flown on the DMSP F8 satellite. The SSM/I measures dual linear-polarized (H and V) brightness temperatures at 19.35, 22.235, 37, and 85.5 GHz. It features a

conical scan pattern, which results in a constant Earth incidence angle across the data swath. This allows more accurate retrieval of surface and atmospheric quantities since the variability of the Earth's microwave emissivity with incidence angle is complex, and not well understood. In the years following the launch of the first SSM/I, the field of satellite microwave remote sensing expanded considerably. What was once a field containing maybe two dozen researchers now numbers in the hundreds.

Obviously, a decadal-scale dataset requires one or more copies of an instrument to be operating during the time period. If multiple copies of the same instrument are flown, it is important to have at least one year of overlap between them to allow for accurate intercalibration while on-orbit.

Finally, the algorithms for turning calibrated satellite measurements into estimates of a geophysical parameter will always be imperfect. The climate demands on their accuracy are in some ways more stringent than for weather monitoring applications. For example, it is important that there be little algorithm "cross-talk" between different parameters. For example, an algorithm for the retrieval of any non-temperature parameter (e.g. sea ice) should have little change in the diagnosed sea ice parameter when only the temperature of the sea ice changes. Similarly, an algorithm for oceanic wind speed should be relatively insensitive to changes in water vapor.

3. THE MICROWAVE RADIOMETER "ADVANTAGE" FOR CLIMATE APPLICATIONS

An important practical aspect of all of these microwave radiometers that lend themselves well to climate monitoring is a low data rate. Since these instruments measure frequencies so much lower than visible or infrared radiometers, antennas of any practical size (generally from several centimeters to near 1 m in diameter) yield spatial resolutions from about 15km to over 100 km (depending on the channel frequency). Thus, not nearly as many radiometer measurements are required to cover the entire Earth. Since frequent reprocessing of multi-decadal satellite datasets is required to thoroughly understand their characteristics, current computer limitations give the data processing advantage to datasets whose volumes do not exceed tens of gigabytes of data. Clearly, as computer and data storage device access speeds increase, this will become less of an advantage.

A second, but arguable, advantage is the lack of cloud effects in the microwave temperature sounders. The "cloud-clearing" problem with infrared temperature sounders is a formidable one, and much work has been devoted to the removal of cloud effects from those measurements. The microwave sounder channels in the 50-60 GHz oxygen absorption region are insensitive to cirrus clouds, and are only slightly sensitive to cloud water contamination.

4. CLIMATE PRODUCTS AVAILABLE TODAY

While there are many researchers that now provide products from measurements made by several satellite microwave radiometer systems, we will highlight those few datasets that I am aware of that have been routinely available, and kept up-to-date with recent satellite data. Also, since strictly speaking a climate dataset could include as little as two months of data (from, say, two successive Januarys, thus allowing analysis of interannual variability) I will make special mention of only those datasets that span a decade or more. Times series of some of these datasets will be shown at the conference.

4.1 *from MSU*

The MSU global lower tropospheric and lower stratospheric deep-layer temperature datasets are now in their twenty-third data year, comprised of data from nine separate MSUs. The MSUs have now been replaced by the Advanced Microwave Sounding Units (AMSUs) on the NOAA-15 and NOAA-16 satellites. With fifteen temperature sounding channels instead of four, and higher spatial resolution (50 km versus 110 km for the MSU, both at nadir), the AMSUs are providing a rich source of new information, while allowing continuation of the time series started with the MSUs.

4. 2 *from SSM/I*

The dataset with the greatest heritage has been the "ocean product" suite developed by Wentz (1997). Available since shortly after the launch of the first SSM/I in 1987, these products include oceanic surface wind speed, total integrated cloud water, total integrated water vapor, and now precipitation rate. Because the emissivity variations of the ocean background are better understood, and therefore better modeled, than the land background, "ocean" products have a much longer heritage than do "land" products.

There are several researchers that now provide nearly complete rainfall retrieval records from the SSM/I instruments. This has been the area with possibly the greatest amount of research funding in recent years, and numerous investigators have developed their own algorithms, some of which provide routine products to the research community. Specifically, an SSMI-only dataset developed and maintained by NOAA/NESDIS, and a Global Precipitation Climatology Project (GPCP) dataset that includes SSM/I rainfall estimates, are worthy of mention. The precipitation products are particularly difficult to make an accurate long term record of since, generally speaking, the polar-orbiting spacecraft they come from are at different times during the diurnal cycle, and these times change as the satellites' orbits drift. This can cause the drift through the diurnal cycle in rainfall (even over the ocean) to be falsely interpreted as a climate trend in the rainfall estimates. To my knowledge, these

effects have not been adjusted for in any of the decadal-scale precipitation datasets from SSM/I. Indeed, the drift of "sun-synchronous" satellites through the diurnal cycle remains as possibly the largest single source of error in the use of these datasets for climate purposes.

The two best-known sea ice datasets that come from SSM/I (and even extend back to 1979 with SMMR) come from NASA. The so-called "NASA Team" algorithm (Cavalieri *et al.*, 1991) and the "bootstrap" algorithm (Comiso, 1995) have been applied to the SSM/I data record and have allowed estimates of decadal scale sea ice changes in the Arctic and around Antarctica.

Climate datasets of additional parameters (e.g. land surface temperature, snow cover, vegetation, soil wetness) will be addressed at the conference.

4.3 *TRMM*

Although designed as a three-year mission, the Tropical Rain Measuring Mission (TRMM) has been providing unique tropical measurements since late 1997. TRMM deserves special mention for several reasons. It carries the TRMM Microwave Imager (TMI), a modified SSM/I design, which includes the first externally calibrated channels below 11 GHz. This now allows sea surface temperature (SST) retrievals through clouds that could provide a basis for climate monitoring of cloudy SSTs from future microwave radiometers. There has been a recent decision to boost the TRMM satellite to a significantly higher orbit (from its nominal 350 km altitude) that will reduce atmospheric drag sufficiently that TRMM could conceivably provide a 10-year dataset before satellite reentry. Since TRMM is not sun-synchronous, it should provide important information on the diurnal cycle in tropical rainfall to allow diurnal adjustments to datasets built from the polar-orbiting radiometers. TRMMs first flight of a precipitation radar is providing a unique validation opportunity of the passive-microwave based precipitation datasets, and will pave the way for a future high-latitude orbiting radar as part of the NASA Global Precipitation Mission (GPM).

5. CLIMATE PRODUCTS IN THE FUTURE

There are more microwave radiometers in operational use now than ever before, and the situation will improve even further in the future. Within the next year or so, new satellite systems will include the research missions involving the Advanced Microwave Scanning Radiometer (AMSR), a Japanese-built instrument to be flown on the NASA Aqua satellite and on the Japanese ADEOS-II satellite. More operational copies of AMSU will be flown by NOAA and on the European MetOp satellite, as well as on Aqua. The first SSM/IS (an SSM/I-style instrument but with both temperature sounding and window channels) will be launched to begin replacing the SSM/I line of instruments. Farther in the future, probably after 2010, the National Polar Orbiting Environmental Satellite System (NPOESS) will carry a line of Conically-scanning Microwave Imager Sounders (CMIS), with 2 m antennas and frequencies ranging from 6 GHz to around 200 GHz, as well as a through-nadir scanning microwave temperature sounder.

In summary, the important elements necessary to the construction of useful decadal-scale datasets from sun-synchronous polar-orbiting satellites include:

1. stable calibration design
2. instrument longevity
3. overlap between successively launched copies of instruments (to allow intercalibration)
4. a stable orbit (or procedures for adjustment of the radiometer measurements for drift through the diurnal cycle)
5. well-designed retrieval algorithms with a minimum of cross-talk between different geophysical parameters.

6. REFERENCES

Buettner, K.J.K., Regenortung von wettersatelliten mit hilfe von zentimeterwellen (Rain localization from a weather satellite via centimeter waves). *Naturwiss.*, **50**, 591.

Cavalieri, D.J., J.P. Crawford, M.R. Drinkwater, D.T. Eppler, L.D. Farmer, R.R. Jentz, and C.C. Wackerman, 1991: Aircraft active and passive microwave validations of sea ice concentrations from the DMSP SSM/I. *J. Geophys. Res.*, **96**, 21989-22008

Christy, J.R., R.W. Spencer, and William D. Braswell, 2000: MSU tropospheric temperatures: Dataset construction and radiosonde comparisons. *J. Atmos. Ocean. Tech.*, **17**, 1153-1170.

Comiso, J.C., 1995: SSM/I (sea ice) concentrations using the bootstrap algorithm. NASA Ref. Pub. 1380, 40 pp.

Spencer, R.W., J.R. Christy, and N.C. Grody, 1990: Global atmospheric temperature monitoring with satellite passive microwave measurements: Methods and results 1979-84. *J. Climate*, **3**, 1111-1128.

Staelin, D.H., 1969: Passive remote sensing at microwave wavelengths. *Proc. IEEE*, **57**, no. 4.

Wentz, F.J. 1997. A well calibrated ocean algorithm for special sensor microwave/imager. *J. Geophys. Res.* **102(C4)**, 8703-8718

Wilheit, T.T., A.T.C. Chang, M.S.V. Rao, E.B. Rodgers, and J.S. Theon, 1977: A satellite technique for quantitatively mapping rainfall rates over the ocean. *J. Appl. Meteor.* **16**, 551-560.

2.2 CHANGES IN THE EARTH'S RESOLVED OUTGOING LONGWAVE RADIATION FIELD AS SEEN FROM THE IRIS AND IMG INSTRUMENTS

H.E. Brindley*, P.J. Sagoo, R. J. Bantges and J.E. Harries
Imperial College, London, UK

1. INTRODUCTION

Several authors have suggested the possibility of utilizing measurements of spectrally resolved outgoing longwave radiation (OLR) to monitor the climatic state (e.g. Goody et al., 1998). The idea is attractive since even a moderate degree of spectral resolution allows the assignation of changes seen in the OLR to a particular cause. However, its practical implementation has been hampered by a lack of suitable observational data.

Two data sets which have become available for analysis are provided by the Infrared Interferometer Spectrometer (IRIS), and the Interferometric Monitor for Greenhouse Gases (IMG). IRIS flew on the Nimbus 4 satellite, taking observations from April 1970 to January 1971 (Hanel et al., 1972). IMG, flying on the ADEOS satellite, produced a set of similar measurements spanning October 1996 to June 1997 (Kobayashi et al., 1999). A comparison of the data was reported by Harries et al (2001), and indicated that clear signatures of increases in greenhouse gases between the two measurement periods could be identified in the OLR difference spectrum.

Because of the length of the observational records used, the study by Harries et al. was limited to a comparison between two distinct periods in time. Given the variability within the climate system, a valid question to be addressed is the degree to which high frequency events may have influenced the magnitude of the signal reported. One obvious candidate that would be expected to exert a large influence on the temperature and water vapour fields at any given point in time is the El Nino Southern Oscillation (ENSO). Since the classic response of the climate system is seen within the equatorial Pacific we confine our attention to this region. By using model simulations of the resolved OLR over two extended time intervals centred on each measurement period the impact of short-term variability is assessed. In all cases, the simulations and data presented here correspond to clear-sky conditions only.

2. DATA CHARACTERISTICS AND PROCESSING

2.1 The IRIS Instrument

The IRIS-D Michelson interferometer provided measurements of the radiance leaving the top of the Earth's atmosphere over the spectral range 400 to 1600 cm^{-1} with a nominal apodized resolution of 2.8 cm^{-1}. The Sun-synchronous nature of the satellite orbit resulted in two global sweeps per day, with nominal equator crossing times of noon and midnight. The instrument had a circular field of view of approximate diameter 100 km. Every fifteenth and sixteenth interferogram was taken whilst viewing a warm blackbody and cold outer space respectively to achieve calibration. For one spectrum, the noise equivalent radiance is quoted as varying from 0.5 to 1.0 mW m^{-2} $(cm^{-1})^{-1}$ sr^{-1} from band centre to edge.

2.2 The IMG Instrument

A Michelson interferometer type instrument, IMG was designed to allow the retrieval of detailed greenhouse gas profiles from OLR measurements made in 3 spectral bands. For the purposes of this study band 3 data, running from 600 to 2000 cm^{-1}, was employed. The spectral resolution within this band increases from 0.25 cm^{-1} (at 1800 cm^{-1}) to 0.1 cm^{-1} (at 700 cm^{-1}) due to the alignment of the band 3 detector. Placed in a Sun-synchronous, 41-day recurrent polar orbit at 800 km, IMG had a field of view of 64 km^2. Radiometric calibration was achieved using observations of an internal warm blackbody and deep space after every six Earth views. For an individual spectrum, this is believed to provide a relative uncertainty of 0.20 - 0.27 mW m^{-2} $(cm^{-1})^{-1}$ sr^{-1}.

2.3 Quality control and cloud-clearing

Before accepting any of the spectra measured by either instrument strict quality control was performed on both sets of data. As a first step, spectra that had been classified as unreliable by the given science team were removed. The IMG data was then smoothed to match the

* *Corresponding author address:* Helen E. Brindley, Space and Atmospheric Physics Group, Imperial College, London, SW7 2BZ, UK; e-mail: h.brindley@ic.ac.uk

IRIS spectral resolution, and a small multiplicative correction was applied to the wavenumber scale to account for the effects of the different solid angles subtended at the two instruments. Radiances were then converted to equivalent brightness temperatures (BT).

Calculations on the remaining IMG data showed unacceptably high BT standard deviations at the centre of the 667 cm^{-1} CO_2 band and so it was decided to set the lower wavenumber limit for both instruments at 710 cm^{-1}. Similarly, the upper wavenumber was set at 1400 cm^{-1} since the noise in the IRIS data substantially increased at wavenumbers greater than this value.

Clear sky spectra were then derived for both instruments using a two-step brightness temperature threshold technique. The first step compared the BT at a wavenumber where the atmosphere is at its most transparent (1127.7 cm^{-1}) with the underlying sea surface temperature taken from NCEP reanalyses. If the magnitude of the difference in temperature was greater than a set threshold then the spectra was rejected as cloudy. Thresholds were selected by finding the value above which the standard deviation of the remaining spectra remained approximately constant across the window region (850-1250 cm^{-1}). Although this initial step should remove all but the warmest optically thick clouds, a second test was employed in an attempt to remove the effects of absorption due to thin cirrus. Following the example of Ackerman et al. (1990), this test compared the BT at 901.1 cm^{-1} (~ 11 μm) and 1197.2 cm^{-1} (~ 8 μm). Because of the absorption characteristics of ice it would be expected that if cirrus were present the BT difference (8 μm-11 μm: $BT_{(8-11)}$) should be greater than in the corresponding clear-sky situation. Given this, for each geographical region investigated, an optimum $BT_{(8-11)}$ was empirically selected. If the $BT_{(8-11)}$ for an individual spectrum exceeded this threshold the spectrum was rejected as cloudy. The thresholds were chosen based on the twin requirements to minimize the standard deviation across the window of the 'clear' spectra, whilst retaining enough spectra to form a statistically significant average. Sensitivity studies have indicated that the basic shapes of the final clear-sky difference spectra are relatively insensitive to the exact thresholds selected.

3. SIMULATION METHODOLOGY

Pentad mean global temperatures and specific humidity fields representative of two twenty-seven month intervals centred on the operational periods of the two instruments, running from April 1969 to June 1971, and April 1996 to June 1998 were generated using the Hadley Centre Atmospheric Model version 3 (HADAM3). HADAM3 comprises the atmospheric portion of the Hadley Centre Coupled Climate Model, with 19 levels in the vertical, and a horizontal resolution of 2.5° latitude x 3.75° longitude.

The model was forced by observed sea surface temperatures taken from the Global Sea Ice and Sea Surface Temperature (GISST) data set, and also included the effects of changes in trace gases, and a parameterisation of volcanic and solar forcing over the period considered. In order to quantify the impact of model uncertainties, four realizations of the atmospheric state were provided.

Using the model geophysical fields along with representative values of trace gas concentrations for each period, radiance spectra were calculated for each grid point and month at 1 cm^{-1} resolution over the wavenumber range 600-1400 cm^{-1} by the MODTRAN3.7 radiative transfer code. These 1 cm^{-1} radiances were then degraded to 2.8 cm^{-1} resolution using the IRIS instrument function and converted to the equivalent BT.

4. SAMPLING CHARACTERISTICS

The amount of noise on the radiance spectra presented here is reduced via temporal and spatial averaging of the individual spectra recorded by each instrument. Temporally, in an effort to remove the effects of seasonality from the results, only spectra from the months April, May and June (AMJ) in 1970 and 1997 are used to form the IRIS and IMG averages respectively. Nevertheless, the temporal distribution of the clear-sky spectra do show distinct differences between the two instruments in certain regions with, in general, IMG tending to provide more measurements in April relative to May and June, whilst IRIS observations are more uniformly scattered over the three months. This may in itself be an interesting consequence of changes in cloud pattern between the observational periods but obviously presents difficulties when attempting to compare a perfectly sampled model field with the data. By focusing on the equatorial Pacific, where the inter-monthly atmospheric variability should be at a minimum, we circumvent this problem. The two geographical regions considered span a latitude range of 10° S to 10° N, with longitudinal extent 160-215° E (West Pacific) and 215-270° E (East Pacific). Table 1 provides information concerning the number of samples used for each area and time.

TABLE 1. Number Of Clear-sky Spectra Used To Create Space/time Averages For IMG/IRIS

Spatial Region	IRIS	IMG
West Pacific	118	50
East Pacific	63	111

5. RESULTS

The observed 1997-1970 AMJ change in BT for the west Pacific and east Pacific regions are shown in figure 1. Also indicated on each plot is the envelope of maximum uncertainty associated with the difference plot, calculated by assuming that the quoted error on each spectrum is systematic in nature. The shape of the difference curves is remarkably consistent across both regions with spectral features due to CO_2 (710-740 cm^{-1}, 800 cm^{-1}), CFC11 (840-850 cm^{-1}), CFC12 (900-920 cm^{-1}), O_3 (1000-1070 cm^{-1}) and CH_4 (1280-1310 cm^{-1}) clearly apparent. Both curves also show enhanced emission over the atmospheric window with a clear break at the O_3 band. Differences shortwave of the band are consistently lower than those on the longwave side. Such a signature could be attributed to residual thin cloud in the nominally clear spectra. Given this, inferences concerning changes in surface temperature should be made with caution. Nonetheless, the larger increase in window BT over the east Pacific compared to that seen in the west is consistent with the phase of ENSO over the two measurement periods.

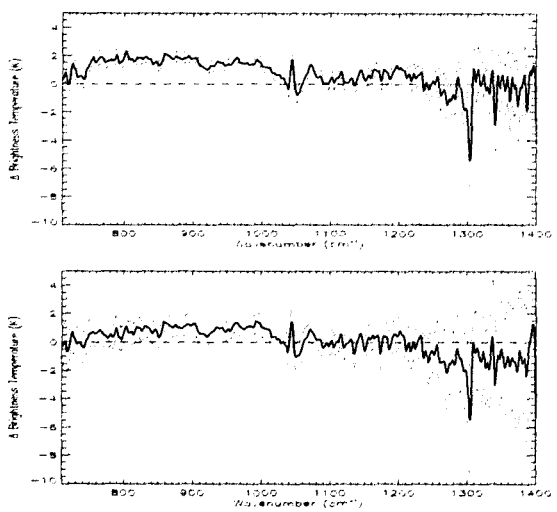

Figure 1. IMG-IRIS change in AMJ mean brightness temperature with associated uncertainty range. Top: East Pacific; Bottom: West Pacific

Figure 2 illustrates the changes between the 1970 and 1997 AMJ mean atmospheric temperature and humidity profiles generated by HADAM3. The crosses at each level highlight the 1-σ spread in these mean values over the 4 realisations considered. In both regions warming and moistening is predicted at all tropospheric levels. This moistening is sufficient to increase the level relative humidities by up to 10 %. In the stratosphere a strong ozone induced cooling is seen.

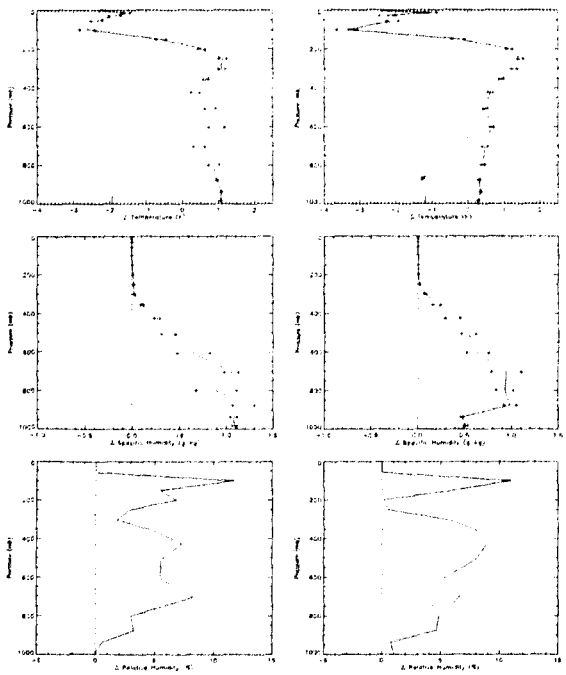

Figure 2. 1997-1970 AMJ mean changes in temperature and humidity derived from HADAM3. Left: East Pacific; Right: West Pacific

Simulated BT change spectra are presented in figures 3 and 4 for the east and west Pacific respectively. To investigate the relative role of the temperature and humidity changes the upper plot in both cases indicates the effect of only changing individual components on the BT difference, with the combined effect over-plotted in bold. For both regions the enhanced water vapour fields tend to dominate the BT response, strongly modulating the enhanced emission due to surface and tropospheric temperature increases in both shape and magnitude. Clearly however, considering changes in humidity and temperature alone cannot explain the shape of the observed BT difference spectra (fig. 1).

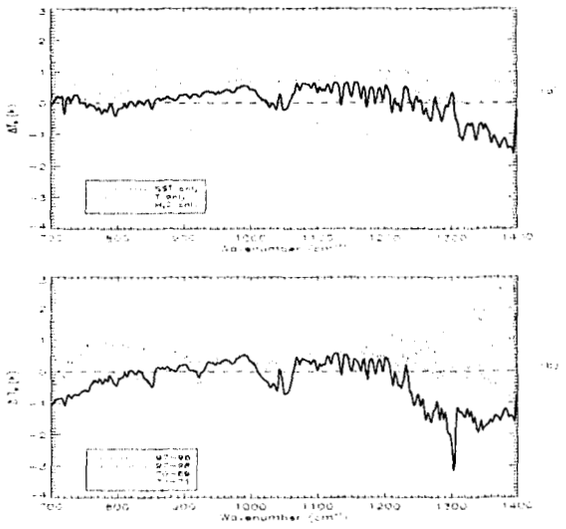

Figure 3. East Pacific: (a) Influence of SST, temperature and humidity on the simulated AMJ 97-70 difference; (b) Inter-annual variability in difference signal.

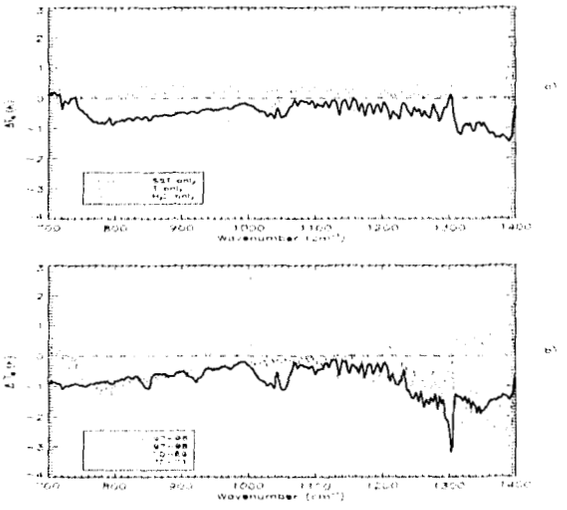

Figure 4. As figure 3 for the West Pacific.

The effects of including long-term changes in the trace gases CO_2, O_3, N_2O, CH_4, CFC11 and CFC12 are shown by the bold curve in figures 3(b) and 4(b). Now the absorption features seen in the observed data are apparent in the simulations, the latter having a comparable magnitude to the former given the measurement uncertainties (fig 1). The lighter curves also shown in figures 3(b) and 4(b) illustrate the mean AMJ year-year differences in BT over the two extended simulation time periods. Assuming that HADAM3 correctly captures atmospheric variability on monthly time scales, fluctuations in atmospheric temperature and humidity over an individual ENSO event are sufficient to produce BT changes over the window and water vapour vibration-rotation band that are at least of equal magnitude to those seen between AMJ 1997 and 1970. However, the distinctive trace gas signals can only be explained by long-term changes in atmospheric CO_2, O_3, CH4, CFC11 and CFC12.

5. CONCLUSIONS

By comparing spectrally resolved observations from the IRIS and IMG instruments we have identified clear signatures due to long term changes in trace gas amounts. Although these strongly affect the OLR the atmospheric temperature and humidity response cannot be unequivocally determined owing to the snapshot nature of the observations.

ACKNOWLEDGMENTS

We thank the NASDA for access to the IMG data set, L.Chen and R.Goody for supplying the IRIS data, and R. Allan for providing the HADAM3 fields.

REFERENCES

Ackerman, S., W. Smith, J. Spinhirne, and H. Revercomb, 1990: The 27-28 October 1986 FIRE IFO cirrus case study: spectral properties of cirrus cloud in the 8-12 μm window. *Mon. Wea. Rev.*, **118**, 2377-2388

Goody, R., J. Anderson, and G. North, 1998: Testing climate models: an approach. *Bull. Amer. Meteor. Soc.*, **79**, 2541-2549

Hanel, R.A, B.J. Conrath, V.G. Kunde, C. Prabhakara, I. Revah, V.V. Salomonson, and G. Wolford, 1972: The Nimbus 4 infrared spectroscopy experiment 1. Calibrated thermal emission spectra. *J. Geophys. Res.*, **77**, 2629-2641

Harries, J.E., H.E. Brindley, P.J. Sagoo, and R.J. Bantges, 2001, Increases in greenhouse forcing inferred from the outgoing longwave radiation spectra of the Earth in 1970 and 1997. *Nature*, **410**, 355-357

Kobayashi, H., A. Shimota, K. Kondo, E. Okumura, Y. Kameda, H. Shimoda, and T. Ogawa, 1999: Development and evaluation of the interferometric monitor for greenhouse gases: a high-throughput Fourier-transform infrared radiometer for nadir Earth observation. *Appl. Opt.*, **38**, 6801-6807

2.3 GLOBAL PRECIPITATION CLIMATOLOGIES AND THE ROLE OF SATELLITE OBSERVATIONS

Phillip A. Arkin*
NOAA/Office of Global Programs, Silver Spring, Maryland

Pingping Xie and John Janowiak
NOAA/NWS/NCEP/CPC, Camp Springs, Maryland

1. INTRODUCTION

Time series of global fields of precipitation are required for many purposes, including the validation of weather forecasts and climate model simulations, the monitoring and diagnosis of climate variations, and the assessment of global water budgets and the hydrologic cycle. Estimates of precipitation derived from satellite observations are central to any effort to produce such global fields. In this paper we will discuss recent attempts to create global climatologies of large-scale precipitation based on combinations of in-situ and remotely sensed observations. We will discuss the characteristics of the various data sources available, describe two procedures that have been developed, and show examples of the results.

2. DATA

The spatial and temporal distribution of area-averaged precipitation can be inferred with varying degrees of directness from many observations, including rain gauges, surface-based radars, satellite passive and active sensors, and even, through various models, from observations of temperature, winds and moisture in the atmosphere.

Rain gauges provide the most direct measurements for the exact location of the gauge. Gauges are subject to measurement errors related to the positioning of the instrument, the flow of air around it, and its shape and mechanism. However, for the purpose of estimating area-average precipitation, the sampling limitations for gauges are most significant. Most of the surface of the global is ocean, which has essentially no usable gauges, and a considerable portion of the rest is poorly sampled.

Observations from satellites have been used to estimate precipitation for nearly as long as they have been available. The single most important fact about such estimates is that they are all based on inferences from the radiation emitted from or reflected by the earth-atmosphere system. They are thus must less direct measurements of precipitation than are gauge observations. There are, however, significant differences among the various estimates available.

Infrared (IR) and visible imagery provide good evidence of the distribution in space of clouds. Brightness in the visible reveals something about the thickness of the clouds, and the IR temperature is a good indicator of the height of the top of the cloud. Both of these are related to precipitation, particularly convective precipitation in the tropics and mid-latitudes. A variety of estimates based on this have been developed and used over the years. The spatial and temporal coverage of geostationary imagery makes such estimates useful despite their modest physical basis. At the present, IR observations from geostationary satellites cover the globe up to about 50° of latitude, with a temporal resolution of 30-60 minutes.

Observations from satellite-based passive microwave radiometers have been available since mid-1987. Such observations are relatively insensitive to small water and ice particles such as comprise clouds, and much more sensitive to the large particles that constitute precipitation.

At lower frequencies, below about 50GHz, the observed brightness temperature is fairly directly related to the amount of water in large droplets in the column. When the surface below the column has a predictable character, a good estimate of total precipitation can be derived. In practice, this sort of estimate, often referred to as "emission", is possible only over oceanic regions. At higher frequencies, the amount of large ice particles in the column is related to the brightness temperature depression observed at the top of the atmosphere. This can be related, either statistically or through a model, to precipitation at the surface. These "scattering" estimates are possible over both land and ocean, and provide higher spatial resolution than the emission method. Since passive microwave observations are available only from polar-orbiting satellites, the coverage in both time and space is relatively limited.

Finally, one might consider observations of atmospheric parameters – temperature, winds, moisture throughout the depth of the atmosphere – as providing opportunities to infer the distribution of precipitation. This is precisely what numerical weather prediction models attempt, and there is evidence that such models do possess skill. Particularly in regions where gauge and satellite observations are scarce or problematic, model-derived products should eventually make a useful contribution.

3. ANALYSIS

* *Corresponding author address:* Phillip A. Arkin, NOAA Office of Global Programs, 1100 Wayne Ave., Suite 1215, Silver Spring, MD 20910; e-mail: Phil.Arkin@noaa.gov

This collection of information about precipitation must be combined in some sensible manner in order to produce global maps of area-averaged precipitation for given time periods. We will use the term "analysis" for this process, following conventional language from the weather prediction community. The challenge is to develop a systematic methodology that takes advantage of the strengths of each data source and minimizes their weaknesses. Unsurprisingly, many ways to go about this have been developed; here we will briefly describe two approaches.

The Global Precipitation Climatology Project (GPCP) of the World Climate Research Programme uses an approach developed by Huffman et al. (1997). They use estimates derived from geostationary IR (supplemented by estimates derived from polar orbiting IR instruments where geostationary data are unavailable), and passive microwave instruments. Microwave-based estimates are combined with geostationary IR estimates to combine the more frequent sampling of the latter with the more physically realistic microwave estimates. For periods before 1986 and in high latitudes where other data are not available, an estimate derived from TOVS observations is used (Susskind et al., 1997). This satellite-only, globally complete product can be used independently. However, it is likely to contain spatially and temporally varying bias, and so a final step adjusts the mean of the analysis over large areas to be identical to the mean of a gauge-only analysis over the region. The GPCP analysis is available for 5-day periods (pentads) and months beginning in January 1979 and continuing to the present.

The CPC Merged Analysis of Precipitation (CMAP; Xie and Arkin, 1996, 1997) uses most of the same data sources as the GPCP product, covers the same period, and exhibits similar characteristics (Gruber et al., 2000). The CMAP algorithm uses a linear combination of all available satellite estimates, with weights over land derived from a comparison to a gauge-only analysis. Over ocean, the weights are determined from retrospective analysis comparing the different satellite-derived estimates to atoll rain gauge observations. These weights are extrapolated into higher latitudes in a seasonally and latitudinally varying pattern based on the characteristics of each product. In regions where no usable satellite-based estimate is available, a version of CMAP using precipitation forecasts from the NCEP/NCAR Reanalysis (Kalnay et al., 1996) is created. The model-derived precipitation amounts are treated as another estimate, with weights derived in a manner similar to the others. This permits the creation of two products: one spatially complete and including information which is model-dependent to some degree, the other purely observation-based but with gaps. In both cases, the intermediate product is combined with a gauge-based analysis to minimize bias. The combination is done in such a manner as to preserve the gradients in the satellite combination while using the absolute value of the gauge analysis where sufficient gauges were available. The temporal coverage and resolution of the CMAP analysis is the same as for the GPCP product. The spatial resolution of both analyses is 2.5° latitude x 2.5° longitude. In the remainder of this paper we will present results from CMAP.

4. CLIMATOLOGY

The (usually implicit) definition of climatology in this context is the global mean field, in this case of precipitation, and the mean annual cycle at each point. When, as here, a full time series of the quantity is created, one might also add the time series of the global mean as an additional element. In this section we discuss the global climatology of CMAP over the 22-year period from 1979-2000.

Figure 1 shows the 22-year mean precipitation derived from the version of CMAP based only on satellite and gauge observations. In the lower panel is the time series of global mean precipitation over the period. Differences from the spatially complete version of CMAP are extremely small. The mean map is dominated by tropical features, with local maxima associated with Africa, South and Central America, and Southeastern Asia and the Maritime Continent. The oceanic Intertropical Convergence Zone (ITCZ) and several other convergence zones associated with the three maxima referred to above are also evident. The time series shows little evidence of trends or coherent large-scale variability.

Figure 2 shows the June-August and December-February 22-year means. The tendency of the various tropical features to move zonally toward the maximum seasonal heating is clear. The mid-latitude oceanic storm track precipitation maxima exhibit a noteworthy seasonal evolution.

Further results, including diagnostic descriptions of interannual variability associated with the El Niño/Southern Oscillation and the North Atlantic Oscillation, will be shown in the presentation.

5. REFERENCES

Gruber, A., and co-authors, 2000: The comparison of two merged rain gauge-satellite precipitation datasets. . *Bull. Amer. Met. Soc.*, **81,** 2631-2644.

Huffman, G.J., and co-authors, 1997: The Global Precipitation Climatology Project (GPCP) combined precipitation dataset. *Bull. Amer. Met. Soc.*, **78,** 5-20.

Kalnay, E., and co-authors, 1996: The NCEP/NCAR 40-yearre-analysis project. *Bull. Amer. Met. Soc.*, **77,** 437-472.

Susskind, J., and co-authors, 1997: Characteristics of the TOVS Pathfinder Path A dataset. . *Bull. Amer. Met. Soc.*, **78,** 1449-1472.

Xie, P. and P.A. Arkin, 1997: Global Precipitation: A 17-year monthly analysis based on gauge observations, satellite estimates, and numerical model predictions. *Bull. Amer. Met. Soc*, **78**, 2539-2558.

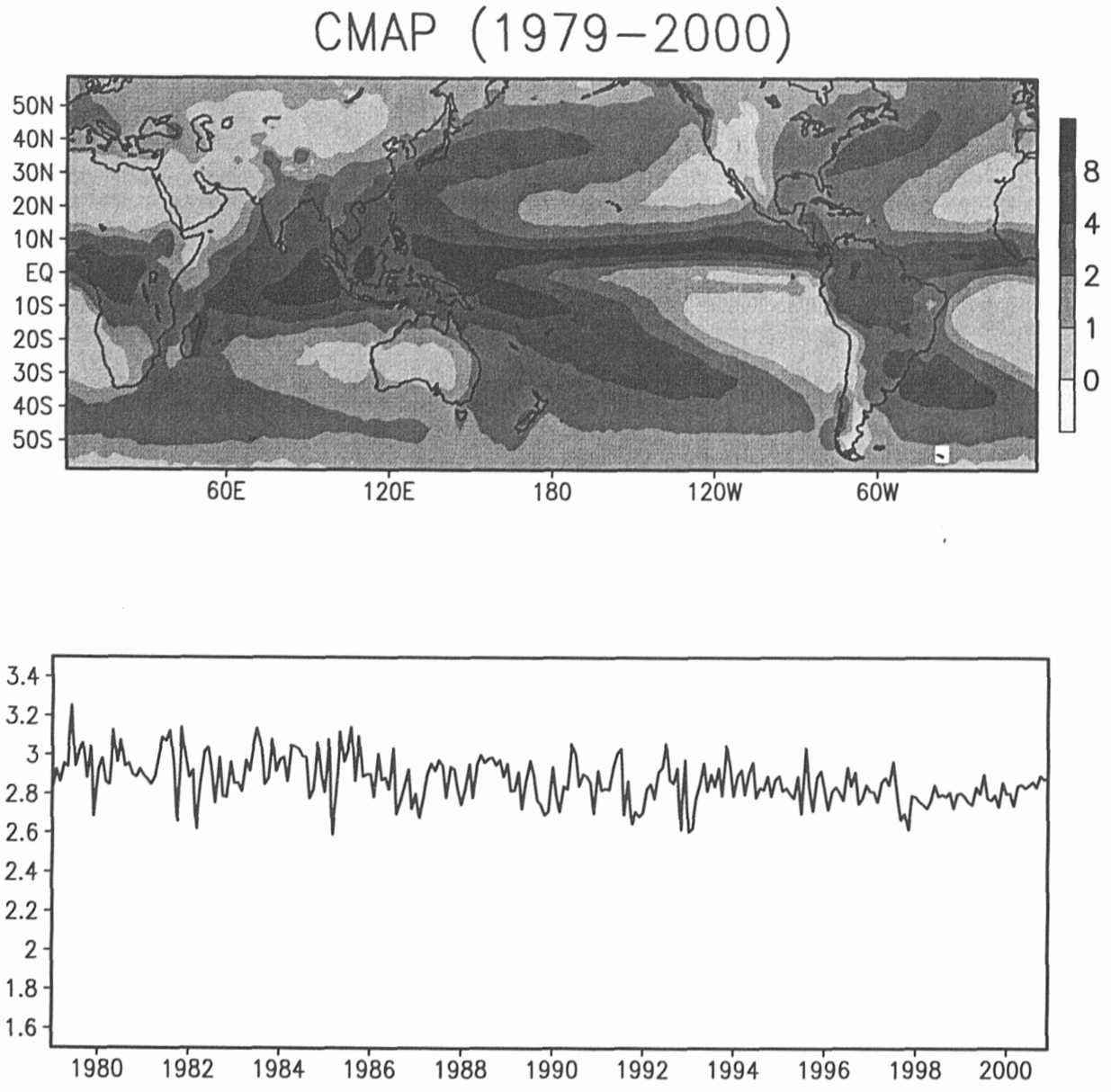

Fig.1 (top)
Distribution of the annual mean precipitation (mm/day) derived from the CMAP (observation only version) for the 22–year period from 1979 to 2000.

(bottom)
Time series of the CMAP global (60S–60N) mean precipitation (mm/day) for the 22–year period.

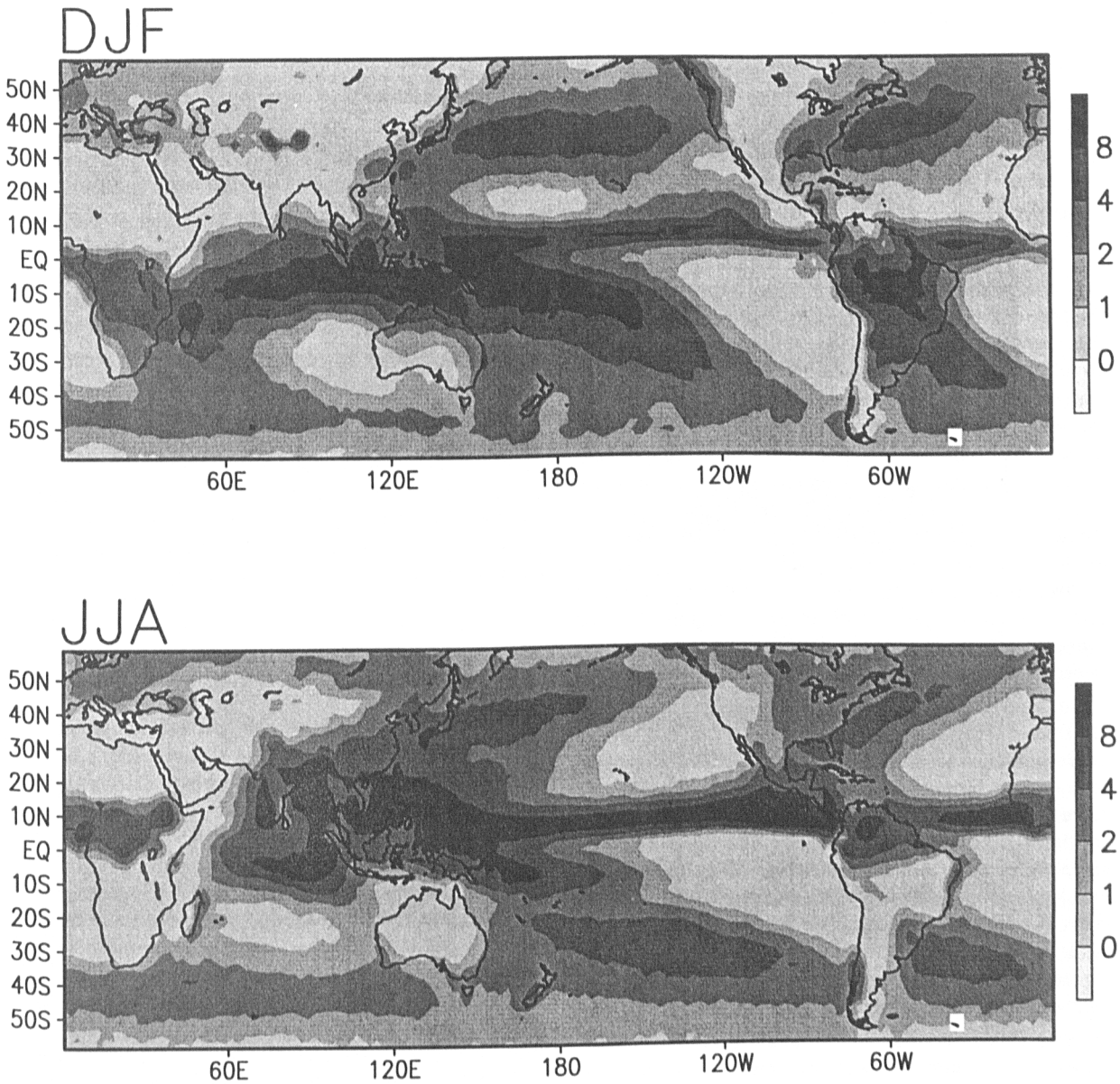

Fig.2 Distributions of mean precipitation (mm/day) for the DJF (top) and JJA (bottom) periods derived from the CMAP (observation only version) for the 22–year period from 1979 to 2000.

P2.1 SPECIFYING SATELLITE ORBITS FOR HIGH ACCURACY CLIMATE MONITORING

Daniel B. Kirk-Davidoff, Richard M. Goody and James G. Anderson
Harvard University
Cambridge, Massachusetts

I. Introduction

A crucial shortcoming of modern climate research is the lack of long-term benchmarks against which to test the rate of change of key climate indices. As part of an effort to design a system of small satellites to make benchmark observations of spectrally resolved infrared radiation emitted by the earth, we explore the impact of imperfect sampling on the ability of a suite of low earth orbiting satellites to reproduce mean radiance on a variety of spatial and temporal scales. Our aim is find those orbits which maximize the temporal and spatial resolution at which mean radiance can be measured to an accuracy of 0.1 K or better in brightness temperature. This level of accuracy is chosen to agree with the expected magnitude of decadal trends in temperature forced by changes in greenhouse gas concentration.

Our approach follows that of Salby and Callaghan (1997), who showed that significant errors in climate properties arise when polar orbiting satellites are used to construct short term averages of brightness temperature. They used geostationary satellite data as a proxy for the true brightness temperature, and simulated the sampling of polar orbiting satellites. They found that very large errors (in excess of 10 K) arose from sampling error of brightness temperature. We extend their work by defining the extent of spatial and temporal averaging necessary to overcome sparse sampling, and obtain highly accurate mean brightness temperatures.

Leroy (2001) considered the aliasing of the diurnal cycle onto satellite retrievals of annual mean surface temperature. He showed that for a diurnal temperature cycle with a peak-to-peak amplitude of 10 K, a single sun-synchronous nadir-sampling orbiter will have a bias of nearly 3 K in the retrieved global mean temperature. In extension of this work, we will consider the effect of diurnal biasing for retrieved brightness temperatures, and will show that, because the diurnal component of variations of brightness temperature is small compared to the surface temperature cycle, the bias in mean temperature by diurnal aliasing is smaller than in the case of surface temperature retrieval.

We model the sampling error of various potential satellite orbits and orbit combinations using the Salby Global Cloud Imagery (GCI) 11 micron brightness temperature data set to simulate real variations in radiance. We compare averages over space and time of the GCI data, and of the same data sampled along the paths traversed by a downlooking satellite footprint for each potential orbit, including the role of anticipated instrument error properties. We vary the inclination and altitude of orbits, to see how these affect retrieval accuracy. Maps of retrieval accuracy are formed for monthly mean and annual mean radiance. We show that for a suite of six sun-synchronous satellites, an accuracy of 0.1 K in brightness temperature can be achieved world-wide at a horizontal resolution of $22.5° \times 22°$. For three such satellites (the NPOESS configuration), 0.1 K accuracy can be achieved in most such grid squares, and in zonal means taken over 22.5 degree-wide bands.

II. Method

We consider the retrieval of brightness temperature by a highly accurate nadir-looking satellite with a field-of-view of 0.05 radians. Our method is to calculate the location of the sub-orbital point over the course of one year, and to use archived satellite brightness temperatures to simulate the brightness temperature retrieved by our simulated orbiter at each time. These brightness temperatures are grouped by location, and averaged together over the year, and then compared with the average of all the brightness temperatures in the archived data for that location. For our archive, we use the Salby Global Cloud Imagery data set (Salby et al., 1984), a re-gridded compilation of 11 μm brightness temperatures retrieved from geostationary and polar orbiting satellites. It has a spatial resolution of .35 degrees Latitude and 0.70 degrees Longitude, for a total of 512 X 512 grid points, and a temporal resolution of 3 hours. The 11 μm band has the advantage, for our purposes, of being one of the most highly variable bands in the terrestrial spectrum. Being minimally affected by water vapor or carbon dioxide, this band essentially measures the temperature of the highest cloud layer, or of the surface, in the absence of clouds. Other bands, which mostly represent emission by water vapor or carbon dioxide high in the atmosphere, have variances approximately three times smaller. Thus our estimates of sampling error represent the worst case over the terrestrial band, and a satellite or set of satellites that can accurately retrieve 11 μm brightness temperature can

certainly retrieve other bands to higher accuracy.

A satellite orbiting about the earth remains in a plane fixed with respect to the stars, except to the extent that this orbital plane is perturbed by such things as atmospheric drag, radiation pressure of sunlight, and the the earth's departures from perfect sphericity. We consider only the perturbation due to the first zonal harmonic perturbation to the earth's shape, J_2. Assuming a circular orbit, this perturbation will affect only the angular orientation of the satellite's plane of orbit with respect to the stars (Heiskanen and Moritz, 1967):

$$\Omega' = \frac{3na_e^2}{2a^2}\cos i \qquad (1)$$

, where Ω' is the rate of change of the angular orientation of the satellite's plane of orbit, n is the angular speed of the satellite along its orbit, where $n = (\frac{GM}{a^3})^{1/2}$, a_e is the earth's radius, a is the radius of the satellite's orbit, G is the gravitational constant, and M is the mass of the earth, and i is the inclination of the satellite's orbit with respect to the equator.

Once the satellite's orbital plane and its initial position is known, we can locate the region at surface sampled at any instant:

$$\phi = \arcsin(\sin i \cos d + \cos i \sin d) \qquad (2)$$

$$\lambda = \lambda_1 - \arctan(\frac{\sin d \cos i}{\cos d - \sin \phi \sin i}) + t * (\Omega - \Omega') \quad (3)$$

where ϕ is the latitude, λ is the longitude, λ_1 is the initial longitude, and Ω is the earth's angular rotation rate, equal to 7.292 s^{-1}. The initial position is assumed to be at $\phi = i$, $\lambda = \lambda_1$, and the initial motion to be purely zonal.

Our assumed field-of-view of 50 mrad gives a footprint of 40 km for an orbit altitude of 800 km. This is close to the 0.35 degree latitude, 0.7 degree longitude resolution of the GCI brightness temperature data. Thus, for simplicity, we assume that each satellite view combines all those grid points through which the suborbital point passes, during an assumed averaging period of 10 seconds. These satellite views are summed together on the same 512 by 512 grid used by the GCI data. We can then average adjoining grid point retrievals together over a larger region. This can reduce the sampling error if the adjoining points' brightness temperatures are correlated with one another, since in that case the number of samples increases faster than the number of independent data points to be sampled.

III. Results and Discussion

The sampling errors resulting from several simulated satellite orbital configurations are shown in Figures 2–4. Errors for single satellites in three different orbits are compared in Figure 2. We see that a polar orbiter has small errors at high latitudes, but relatively large errors in low latitudes. A low-latitude orbiter, with an inclination of 33° has small errors in the tropics, but no coverage outside the tropics. These orbital configurations have two important distinctions. The first is the obvious one: observations are concentrated in different regions. The polar orbiter visits each pole some 14 times each day, while the low-latitude orbiter never sees the poles, and has higher frequency of observations at any given location in the tropics. The second distinction is that, while the polar orbiter's plane of orbit remains fixed with respect to the stars (and thus results in a single annual cycle in the time of day of observations at any given location, the low-latitude orbiter's plane of

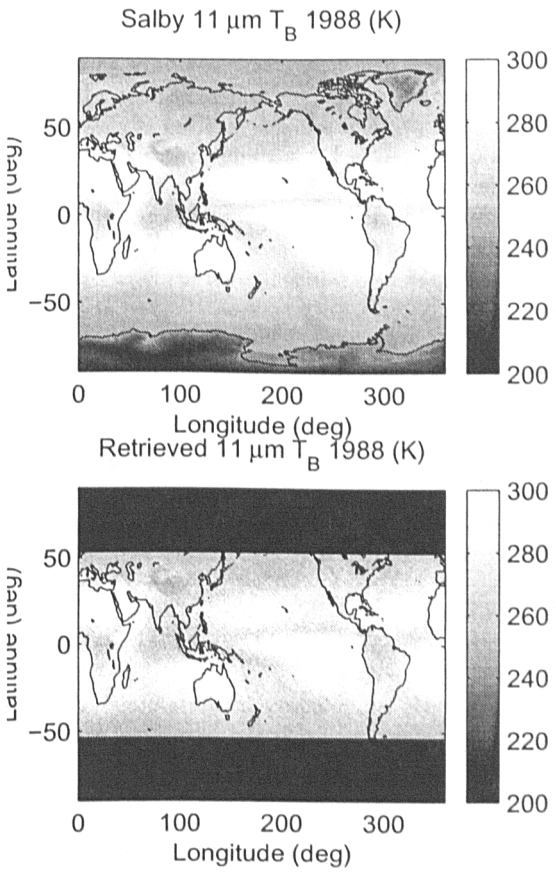

Figure 1: Top: Annual mean 11 μm brightness temperature for the year 1988 from the Salby GCI data. Bottom: Sample retrieval of this brightness temperature by a simulated precessing orbiter with an inclination of 53°.

orbit precesses six times about the earth in a period of a year. Further simulations show that a single annual cycle in the time of day of observations is in general a poor choice, especially for tropical regions. It turns out that a sun-synchronous orbit is a represents a good compromise between broad latitude coverage and accuracy in the tropical belt. Errors for a sun-synchronous orbit are shown in the bottom panel of Figure 2.

Although a single sun-synchronous orbiter can obtain brightness temperature retrievals that are reasonably accurate, it clearly does not attain a global accuracy of 0.1 K at 22.5 °re solution. To reach this goal of 0.1 K accuracy, we can add more satellites. Figure 3 shows retrieval errors for a suite of three equally spaced sun-synchronous orbiters. The top panel, for the year 1988, shows that brightness temperature is retrieved with 0.1 K accuracy over a majority of the earth. However, comparison with the bottom panel (1987) shows that the locations of 0.1K accuracy (denoted by *'s) are not the same from one year to the next.

Figure 4 shows two ways to obtain consistent accuracy over the whole earth. Addition of three satellites (for a total of six) allows 0.1 K accuracy at 22.5 °re solution over the great majority of the globe. Alternatively, one may compromise spatial resolution, and seek to measure zonal mean brightness temperatures. The bottom panel shows that accuracy of 0.1 K or better can be achieved by a suite of three sun-synchronous satellites, by a single low-latitude satellite, or by a single sun-synchronous satellite over a large portion of its latitude range. Similar regions of high-accuracy coverage are obtained for 1987.

IV. Conclusion

Our study has demonstrated that 0.1 K accuracy in the retrieval of zonal mean brightness temperature is attainable in the 11 μm band by a suite of 3 sun-synchronous satellites; that a suite of 6 sun-synchronous satellites can achieve this level of accuracy in each grid square of a $22.5^\circ \times 22.5^\circ$ longitude-latitude grid, and that a single polar orbiting satellite can obtain zonal mean brightness temperature in this band with an accuracy (accounting for sampling errors alone) of 0.2 K.

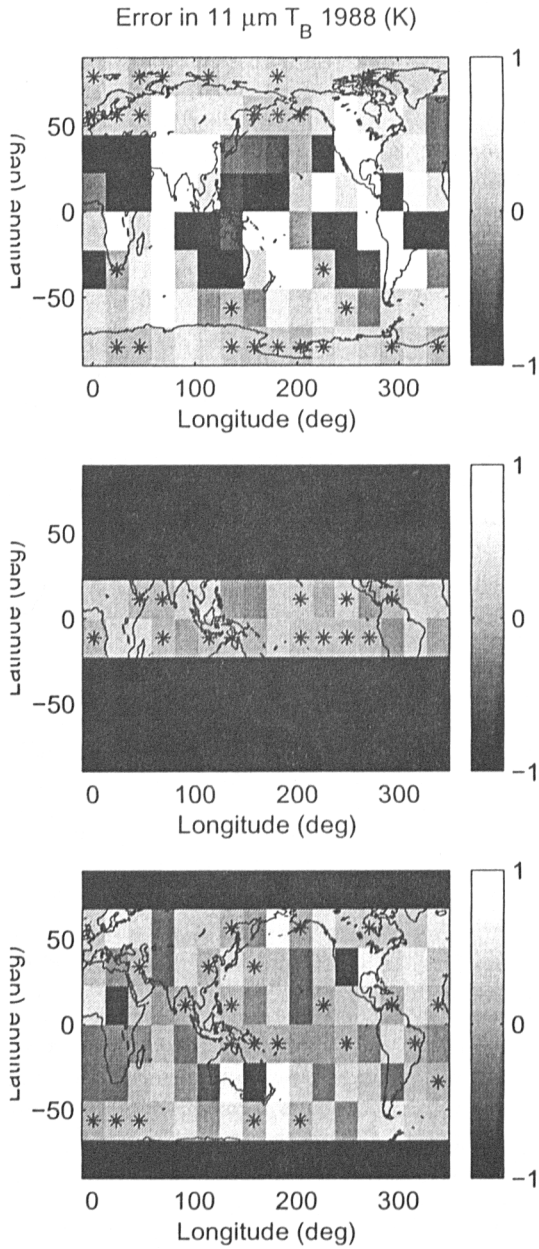

Figure 2: Top: Retrieval error of annual mean brightness temperature in the year 1988 due to sampling for a single polar orbiting satellite. Retrieved brightness temperatures are averaged over $22.5^\circ \times 22.5^\circ$gri d boxes. Those grid boxes where the sampling error is smaller than 0.1 K are marked by an asterisk ('*'). Middle: as in top, for a single precessing orbiter with an inclination of 33°. Bottom: as in top, for a single sun-synchronous orbiter.

References

Heiskanen, W.A., and H. Moritz, 1967: Physical Geodesy. W.H. Freeman and Company, New York. 364 pp.

LeRoy, S.S., 2001: The Effects of Orbital Precession on Remote Climate Monitoring. *Unpublished Manuscript.*

Salby, M.L, and P. Callaghan, 1997: Sampling Error in Climate Properties Derived from Satellite Measure-

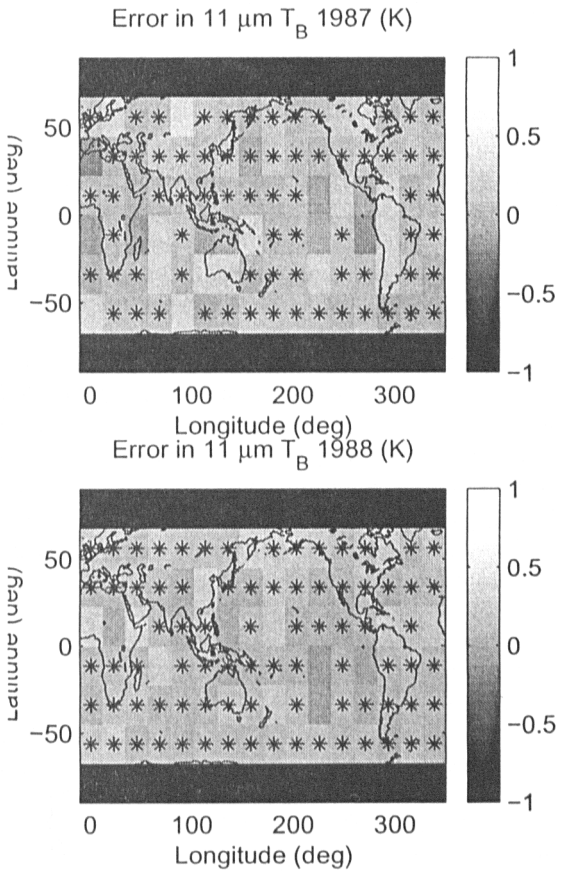

Figure 3: As in figure 2. Top: suite of three sun-synchronous orbiters, spaced equally in longitude around the earth, with inclinations of 98.765°, for the year 1988. Bottom: same configuration, for the year 1987.

ments: Consequences of Undersampled Diurnal Variability. *J. Climate*, **10**, 18-35.

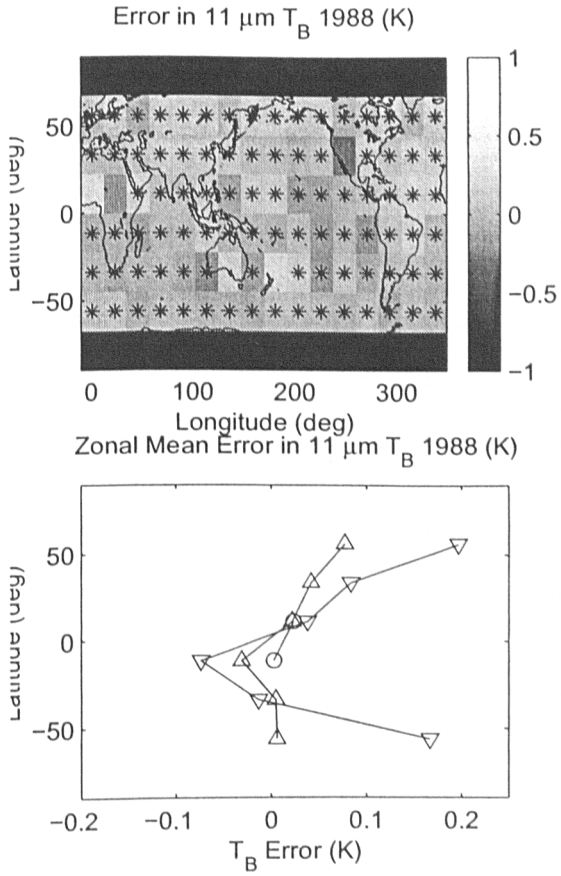

Figure 4: Top: As in figure 2, for a suite of six equally spaced sun-synchronous orbiters, for the year 1988. Bottom: Error of retrieved zonal mean brightness temperature for 1988 for three orbital configurations. Upward-pointing triangles: three sun-synchronous orbiters; downward-pointing triangles: a single sun-synchronous orbiter; circles: a single low-latitude (incl. 33°) orbiter.

P2.2 LONGWAVE AND WINDOW ANGULAR DISTRIBUTION MODELS FROM CERES/TRMM RADIANCE MEASUREMENTS

Natividad Manalo-Smtih
Analytical Services and Materials, Inc., Hampton, Virginia

Norman G. Loeb
Center for Atmospheric Research, Hampton University, Hampton, Virginia

1. INTRODUCTION

In order to improve our understanding of the Earth's climate, accurate retrievals of radiant fluxes at the top of the Earth's atmosphere (TOA) are essential. TOA radiant fluxes are inferred from satellite radiance observations by applying angular distribution models (ADMs) which account for the angular variation of the radiation field emerging from a scene. Because of the tremendous variability in Earth scenes, accurate TOA fluxes can only be obtained by accounting for the influence of clear-sky and cloud properties on the radiation anisotropy.

The Clouds and Earth's Radiant Energy System (CERES) [Wielicki,et al.,1996] represents a continuing effort, set forth by its predecessor, the Earth Radiation Budget Experiment (ERBE) [Barkstrom,1984, Smith, et. al.,1986], to produce highly accurate shortwave (SW) and longwave (LW) fluxes at the TOA. The CERES instrument together with the Visible Infrared Scanner (VIRS) aboard the Tropical Rainfall Measuring Mission (TRMM) satellite provide a unique data set for developing ADMs. The CERES instrument package also includes a window (WN) channel in the 8-12 micron region to measure the atmospheric "Greenhouse" effect [Ravel and Ramanathan, 1989]. In addition to scanning in the crosstrack direction, the CERES instrument can also scan in the alongtrack direction and in a rotating azimuth plane scan mode (RAPS), thereby providing multiangle radiance measurements of the same scene. In RAPS mode, CERES scans in elevation as it rotates in azimuth.

In this study, eight months of CERES/TRMM RAPS and alongtrack data from January-August 1998 are used to construct empirical LW and WN ADMs. The ADMs are determined for scene types defined by meteorological and imager-based cloud parameters that influence LW and WN radiance anisotropy. To ensure that there is consistent sampling in all angles for each scene type, the scene types are defined using percentile intervals of these parameters rather than discrete fixed intervals. The ADMs and their sensitivity to the selected parameters are presented.

* *Corresponding Author Address:* Natividad Manalo-Smith, Analytical Services and Materials, Inc. Hampton, VA 23666; e-mail: n.m.smith@larc.nasa.gov

2. THEORY AND IMPLEMENTATION

An instantaneous TOA radiant flux M is estimated from a satellite-measured radiance L as follows:

$$M = \frac{\pi L(\theta)}{R_j(\theta)} \quad (1)$$

where R_j is the anisotropic factor (or ADM) for the "j^{th}" scene type and θ is the viewing zenith angle. R_j is determined as follows:

$$R_j(\theta) = \frac{\pi \bar{L}(\theta)}{M_j} \quad (2)$$

where $\bar{L}_j(\theta)$ is the mean radiance obtained by compositing and averaging all available radiances for each scene type in each θ angular bin, and $\widehat{M}_j$ is determined from:

$$\widehat{M}_j = 2\pi \int_0^{\frac{\pi}{2}} \sin\theta \cos\theta \bar{L}(\theta) d\theta \quad (3)$$

Mean radiances in undersampled angular bins are extrapolated using theoretical model computations.

On TRMM, the CERES scene identification is based on collocated 2-km resolution VIRS measurements over a CERES footprint, which has a 10-km nadir resolution. These radiance measurements, along with VIRS scene information and meteorological and cloud property data, are

recorded on the Single Scanner Footprint TOA/ Surface Fluxes and Clouds (SSF) data product.

As shown in Tables 1 through 3, ADM scene types consist of a combination of surface type, cloud cover and fixed percentile intervals of atmospheric and cloud properties. The vertical temperature change describes the lapse rate in the first 300 mb of the atmosphere above the surface. For cloudy scenes, the cloud emissivity and the cloud-surface temperature difference are area-weighted in the case of multiple layered clouds.

3. RESULTS

The ADMs and their sensitivity to the scene type parameters are illustrated in Figures 1 through 8. The ADMs are represented as a function of viewing zenith angle and in terms of the ADM index *AI*, which is calculated by:

$$AI = \sqrt{\frac{\sum_{i=1}^{n} (R_{ji} - R_{Lamb})^2}{n}} \quad (4)$$

where the ADM index gives an indication of the RMS deviation from a Lambertian case ($R_{Lamb} = 1$) over the range of n view zenith angle bins for a scene type j. Anisotropy increases with ADM index.

Figure 1 shows that the anisotropy for a clear land scene increases as the vertical temperature change increases. The ADMs also exhibits an increase in anisotropy with precipitable water (Figure 2). The clear ocean cases (Figure 3) on the other hand, show little dependence on the vertical temperature change, but show increased limb darkening with precipitable water. A comparison between the day and night desert ADMs is shown on Figures 4 and 5, respectively. Daytime desert ADMs are significantly more anisotropic than the nighttime ADMs due to differences in the daytime and nighttime surface temperatures. Both cases show increased anisotropy with precipitable water. The dependence of overcast ADMs on cloud emissivity and surface-cloud temperature differences is shown in Figures 6 through 8. In general, anisotropy increases as the cloud emissivity decreases, particularly for thin ice clouds (large ΔT and small emissivity in Figure 6), The WN overcast ADM (Figure 8) exhibits a stronger limb darkening than the LW overcast ADMs (Figure 7). Similar results were obtained for other scene types. Examples of anisotropy from broken cloud fields are shown in Figure 9. In that case, ADMs show a large increase in anisotropy with cloud cover.

4. SUMMARY

A new set of angular distribution models have been developed for LW and WN channels from the CERES/TRMM data set. These models are stratified by clear and cloudy sky parameters that affect the anisotropy of Earth scenes.

5. REFERENCES

Barkstrom, B.R. 1984: The Earth Radiation Budget Experiment (ERBE), *Bull. Amer. Meteor. Soc, 65*, 1170-1186.

Ravel, A. and V. Ramanathan, 1989: Observational determination of the greenhouse effect., *Nature,* 342, 758-761.

Smith, G.L., R.N. Green, E. Raschke, L.M. Avis, J.T. Suttles, B.A. Wielicki, and R. Davies, 1986: Inversion Methods for Satellite Studies of the Earth's Radiation Budget: Development of Algorithms for the ERBE mission, *Rev. Geophys., 24,* No.2, 407-421.

Wielicki, B.A., B.R. Barkstrom, E.F. Harrison, R.B. Lee III, G.L.Smith, and J.E.Cooper,1996: Clouds and Earth's Radiant Energy System (CERES): An Earth Observing System experiment, *Bull. Amer. Meteor. Soc., 77*, 853-868.

ADM Category		Scene Type Stratification	Total
CLEAR- %cld<=0.1	Ocean Land Desert	3 Precipitable Water	45
		5 Vertical Temp. Change	
BROKEN CLOUD FIELD (4 cloud intervals)	Ocean/ Land Desert	3 Precipitable Water	288(O) 288(L) 288(D)
		6 T(surface-cloud)	
		4 IR Emissivity	
OVER- CAST	Ocean + Land/ Desert	3 Precipitable Water	126
		7 T(surface-cloud)	
		6 IR Emissivity	

Table 1: Preliminary Scene Types for CERES/TRMM LW and WN ADMs.

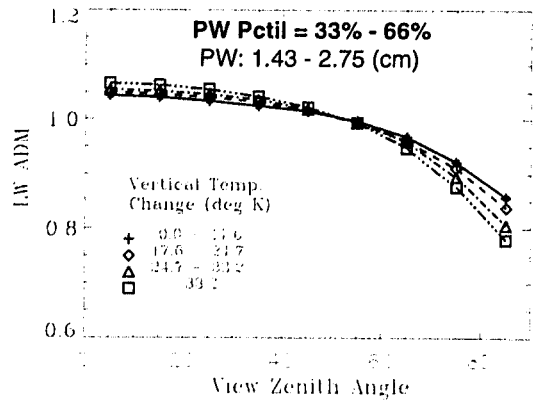

Figure 1. Variation of Clear Sky Land ADM (DAY) with PW and Vertical Temperature Change.

PW Pctile	Broken Cloud Fields			Overcast	
	Cloud Fraction %	ΔT Pctile	Cloud ε Pctile	ΔT (sfc-cld) Pctile	Cloud ε Pctile
< 33	0.1 - 25	ΔT < 0 deg	0 - 25	ΔT < 0 deg	0 -5
		0 -20	25 - 50	0 -20	5 - 10
		20 - 40		20 - 40	10 -25
33 - 66	25 - 50	40 - 60	50 - 75	40 - 60	25 - 50
	50 - 75	60 -80		60 -80	50 -75
> 66	75 - 99.9	> 80	> 75	80 - 90	> 75%
				> 90	

Table 2: ADM Scene Type Parameter Percentile Intervals for Cloudy Scenes.

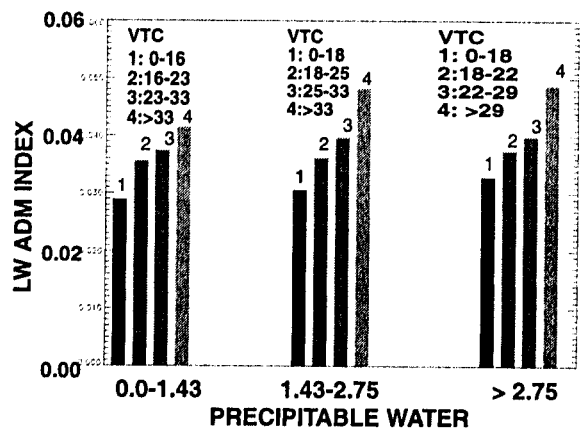

Figure 2. Clear Sky Land LW ADM Index vs. PW and Vertical Temperature Change.

PW Percentile Interval (%)	Vertical Temperature Change Interval (%)
0 - 33	VTC < 0 (deg)
	0- 25
33 - 66	25- 50
	50 - 75
66 - 100	75 -100

Table 3: ADM Scene Type Parameter Percentile Intervals for Clear Sky Scenes.

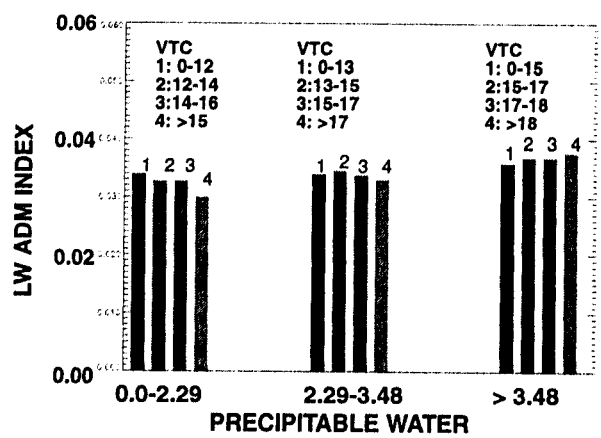

Figure 3. Clear Sky Ocean LW ADM Index vs. PW and Vertical Temperature Change.

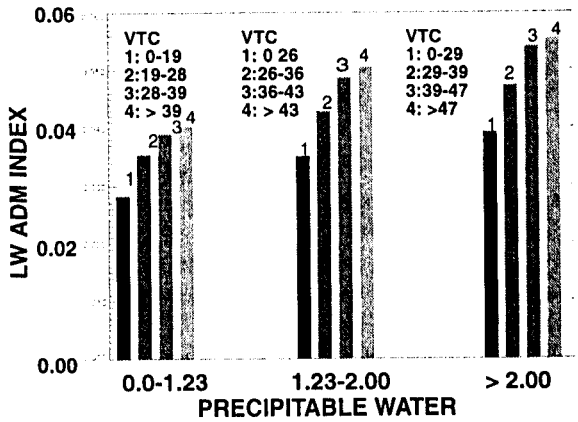

Figure 4. Clear Sky Desert (Day) LW ADM Index vs. PW and Vertical Temperature Change.

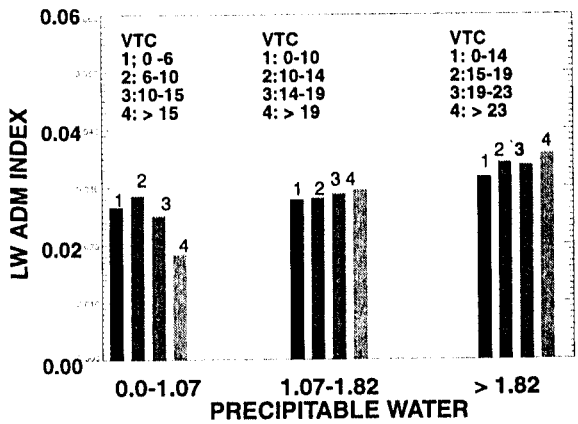

Figure 5. Clear Sky Desert (Night) LW ADM Index vs. PW and Vertical Temperature Change

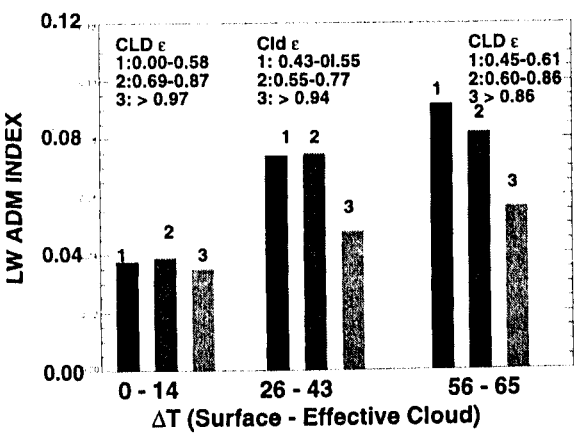

Figure 6. Overcast LW ADM Index vs. Cloud-Surface Temperature Difference and Cloud Emissivity.

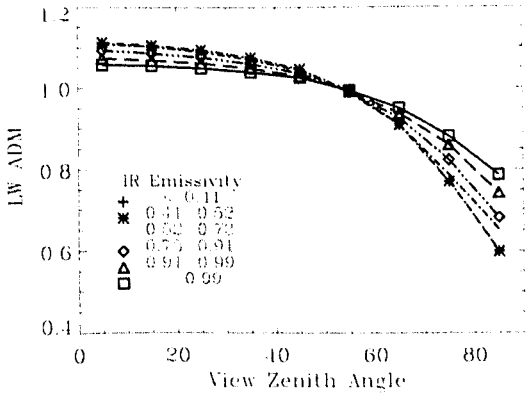

Figure 7. Variation of Overcast LW ADM with cloud emissivity for a given ΔT(33 - 46 K) and PW (> 4.63)

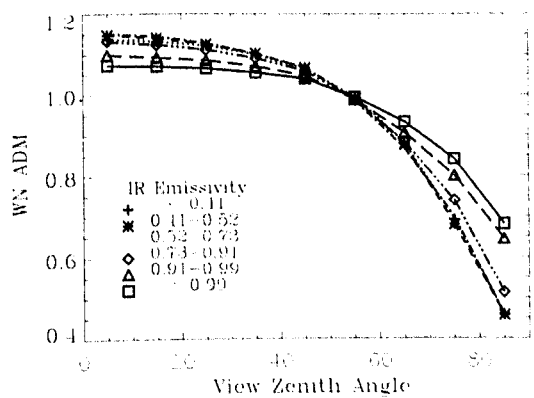

Figure 8. Variation of Overcast WN ADM with cloud emissivity for a given ΔT(33 - 46 K) and PW (> 4.63)

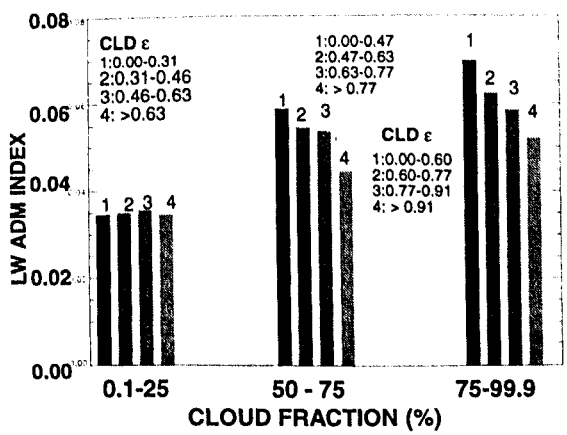

Figure 9. Broken Cloud Field (Land) LDM Index vs. Cloud Emissivity and Cloud Amount.

P2.3 LIMB BIASES IN CO_2 CLOUD HEIGHT ALGORITHMS WITH RESPECT TO HIGH ALTITUDE CIRRUS

R. Lynn Rose*, Mary Bedrick, Kirk Swanson**, Brian Morrison
Aeromet, Inc.

1. INTRODUCTION

Upper-level cirrus cloud climatologies have been composed from satellite-derived data sets using data collected from zenith angles of less than 10° (e.g. Wylie et al., 1994, and Wylie and Menzel, 1999). The cloud height data, obtained from Carbon Dioxide (CO_2) Slicing algorithms applied to National Oceanic and Atmospheric Administration (NOAA) polar orbiting High-resolution Infrared Radiation Sounder (HIRS) data, are used in the composition of the climatologies.

It is believed that data from the limbs can produce bogus clouds and cloud top heights although there does not seem to be a rule as to where reliable data begins and ends with respect to nadir (center of image). Several effects can contribute to bogus clouds and heights (Glahn, 1966). 1. Limb darkening refers to the change in the radiation received by the radiometer at the far limbs of its scan. Limb darkening appears as bright edges on images made from HIRS and AVHRR data. The limbs appear brighter (colder) because less radiation is received at the instrument than nadir. 2. The path through the atmosphere that radiation takes depends on the scan angle of the instrument. The shortest path is at nadir and the longest paths are at the limbs. On the limbs, a greater optical depth of the atmosphere is sampled. 3. Ambiguities in cloud heights can be found in isothermal regions. This would cause problems with the highest cirrus clouds since they are located near the tropopause. 4. Inaccurate temperature profiles could cause inaccurate cloud top height determination. 5. Instrument calibration errors.

Theoretically, limb darkening and the other effects have a large impact on properties derived from HIRS and AVHRR data (i.e., CO_2 derived cloud top heights). CO_2 Slicing algorithms derive clear pixels and cloud top heights from the HIRS infrared bands with partial CO_2 absorption (13 to 15μm), from the "window channel" (11μm) and from the water vapor channel (8.3μm). The clearest channel, 11μm, sees little atmosphere and mostly the surface. The CO_2 channels and water vapor channel, on the other hand, see only atmosphere. When the HIRS scans at an angle into the atmosphere, each CO_2 channel finds its mass of CO_2 higher in altitude than when it is looking from nadir. Since the algorithms find the mass higher, it is perceived as colder. Water vapor channels behave in the same way. Because of this limb darkening effect, it is thought that some of the very high cirrus detected at the limbs may be bogus.

In order to fully evaluate whether or not high clouds are present in the limbs, a long-term study between satellite derived cloud tops and in situ measurement by aircraft would be needed. Such studies as McFarquhar et al. (2000) and Booker and Stickel (1982) show that high thin cirrus is present at very high altitudes in the tropics. Since there is clear evidence of cirrus at high levels, this study will examine the differences between calculated cloud top heights at nadir and high scan angle measurements.

2. DATA AND METHODS

During February 2001, a unique data set was collected between Kwajalein, Republic of the Marshall Islands (8°44'N 167°44'E) and Wake Island, US Territory (19°17'N 166°39'E). NOAA-14 HIRS multispectral data were archived from both islands providing a look at oceanic data from 15°S to 40°N. This dataset is used to investigate any limb biases that may be present in the CO_2 cloud detection and height routine and the radiometer viewing pattern. Cloud heights are converted from pressure to height coordinates using the hydrostatic equation.

Using a Lagrangian framework, data is divided into three groups: left, center and right. Each scan-line of data has 56 bins of data. The left two bins, two center bins and right two bins are archived and used to make comparisons. Cloud height versus latitude are plotted for clouds above 12 km for nadir (Figure 1), left limb (Figure 2), and right limb (Figure 3). The plotted data appears in "bands" south of 20°N. This is due to the fact that the heights are originally calculated to the nearest 50 hPa and then converted hydrostatically to

*Corresponding author: R. Lynn Rose, Aeromet, Inc., P.O. Box 701767, Tulsa OK 74170-1767; e-mail: lynnr@aeromet.com
**Current affiliation: Architecture Technology Corp.

height coordinates. The authors believe that because the atmospheric temperature profile in the tropics is relatively constant from day to day, the data appear in these horizontal planes after the conversion to height coordinates.

3. DISCUSSION

Besides showing the amount and altitude of clouds detected at nadir and in the limbs, Figures 1, 2 and 3 have clear signatures of meteorological features. During February 2001, the subtropical high was anchored near 20°N. Mid-latitude systems were affecting areas to the north of Wake Island (north of 25°N).

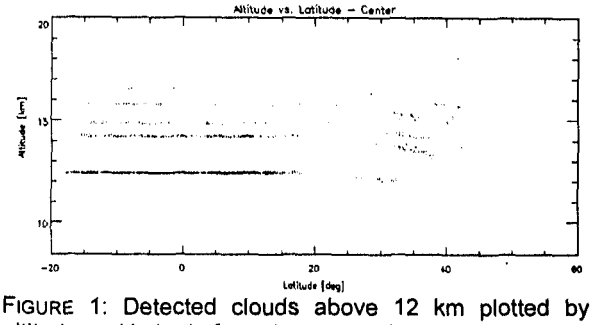

FIGURE 1: Detected clouds above 12 km plotted by altitude and latitude from the two nadir scan bins.

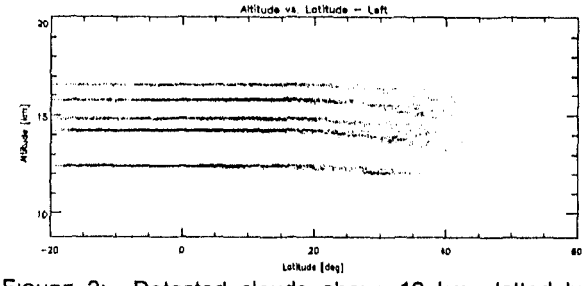

FIGURE 2: Detected clouds above 12 km plotted by altitude and latitude from the left limb scan bins.

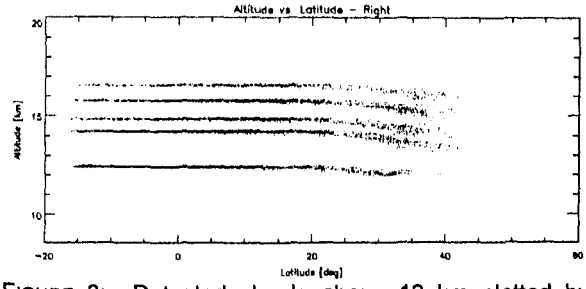

FIGURE 3: Detected clouds above 12 km plotted by altitude and latitude from the right limb scan bins.

The subtropical high is clearly visible in the nadir data (Figure 1) with only a scant few clouds detected above 12 km in the region of the subtropical high. The limb data (Figures 2 and 3) also show fewer incidents of cirrus detection around 20°N, but is not as pronounced as in the nadir data. The difference in detected high clouds could be due to the ability to better detect sub-visible cirrus in the limbs as the satellite samples a greater optical depth of the thin cirrus.

The transition from the tropics to the mid-latitudes is also apparent. Both nadir and limb data show a downward slope of the cirrus clouds from ~20°N toward the poles. This is associated with a decrease in altitude of the tropopause from the equator to the poles.

Upon closer inspection of the data, it appears that left and right limbs and nadir calculations all produce high clouds. There does not appear to be a significant difference in quantity and altitude of clouds detected between the right and left limbs. Nadir computations produce few very high clouds (above 13 km) as compared to the left and right limbs. Between 15° and 25°N, nadir computations produced very few cirrus clouds (above 12 km) but produced many more clouds below 12 km than the right and left limbs. Left and right limb computations also produce fewer high clouds in this region as compared to the areas south of 15°N. The number of cirrus clouds detected above 12 km decreases north of 25°N in both the right and left limbs and at nadir.

This paper illustrates the need for future study of high cloud detection and verification. High clouds are detected at nadir and in both of the limbs, but with far more counts in the limbs. It is not clear whether the limb data is over detecting, or if the nadir calculations are undercounting clouds. The difference could likely be a combination of both. These results indicate that global cloud climatologies composed from CO_2 Slicing analysis could be seriously underestimating global cirrus coverage.

Acknowledgements: The authors would like to thank Don Wylie for his CO_2 slicing code and for his helpful discussions on limb biases.

4. REFERENCES

Booker, D. R., and P. G. Stickel, 1982: High altitude tropical cirrus cloud observations. Preprints, *Conf. On Cloud Physics*, Chicago, IL. Amer. Meteor. Soc., 215-217.

Glahn, H. R., 1966: On the usefulness of satellite infrared measurements in determination of cloud top heights and areal coverage, *J. Appl. Meteor.*, **5**, 189-197.

McFarquhar, G. M., A. J. Heymsfield, J. S. Spinhirne, and B. Hart, 2000: Thin and subvisusual tropopause tropical cirrus: Observations and radiative impacts. *J. Atms. Sci.*, **57**, 1841-1853.

Wylie, D. P., and W. P. Menzel, 1999: Eight years of high cloud statistics using HIRS, *J. Climate*, **12**, 170-184.

Wylie, D. P., W. P. Menzel, H. M. Woolf, and K. I. Strabala, 1994: Four years of global cirrus cloud statistics using HIRS, *J. Climate*, **7**, 1972-1986.

P2.4 INTERNAL CONSISTENCY OF THE NVAP WATER VAPOR DATASET

Ronnie J. Suggs and Gary J. Jedlovec
Global Hydrology and Climate Center
MSFC/NASA, Huntsville, AL

1. INTRODUCTION

The NVAP (NASA Water Vapor Project) dataset is a global dataset at 1 x 1 degree spatial resolution consisting of daily, pentad, and monthly atmospheric total precipitable water (TPW) products (Randel et al. 1996). The analysis blends measurements from the Television and Infrared Operational Satellite (TIROS) Operational Vertical Sounder (TOVS), the Special Sensor Microwave/Imager (SSM/I), and radiosonde observations into a daily collage of TPW. The original dataset consisted of five years of data from 1988 to 1992. Recent updates have added five additional years (1993-1997).

Since each of the TPW sources (TOVS, SSM/I, and radiosonde) do not provide global coverage, the individual sources compliment one another by providing spatial coverage over regions and during times where the others are not available. *Over land regions TOVS is the primary data source.* Where there is a coincident radiosonde and satellite measurement the radiosonde measurement is used. Over the ocean where there is a collocated TOVS and SSM/I measurement, SSM/I is weighted by 10% of the TOVS measurement. Thus, *over the oceans SSM/I is the primary data source.* For this type of spatial and temporal blending to be successful, each of the source components should have similar or compatible accuracies. If this is not the case, regional and time varying biases may be manifested in the NVAP dataset. This study examines the consistency of the first 8 years of NVAP source data by comparing daily collocated TOVS and SSM/I TPW retrievals with collocated radiosonde TPW observations. The results of the comparison are used to explain differences seen between the NVAP and the National Centers for Environmental Prediction (NCEP) reanalysis TPW (Kalnay et al. 1996).

*Corresponding author address: Ron Suggs, Global Hydrology and Climate Center, NSSTC, 320 Sparkman Dr., Huntsville, AL 35805.
Email: ron.suggs@msfc.nasa.gov

2. NVAP AND NCEP COMPARISONS

Global averages of TPW from NVAP compare favorably with values from the NCEP reanalysis dataset (Fig. 1). The anomalies of both datasets, in general, describe similar interannual trends in TPW. Note that both data sets exhibit a dry period between 1992 and 1994 following the eruption of Mt. Pinatubo. This correlates with a cooling in the lower troposphere indicated by measurements from the Microwave Sounding Unit on the NOAA series of operational polar orbiting satellites (Christy et al. 1995). Also, the anomalies of both datasets indicate an essentially flat trend for the eight year period. There are also differences between the datasets. NVAP TPW exhibits a

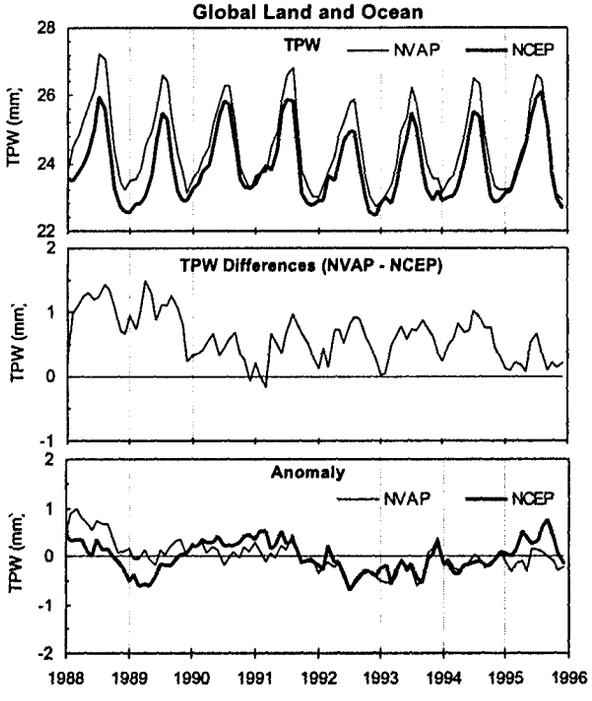

Figure 1. NVAP and NCEP global TPW time series comparison.

seasonal moist bias relative to the NCEP values for the summer months in the northern hemisphere. This time varying bias ranges from 0.0 mm to approximately 1.0 mm. The NVAP data indicates a moist anomaly during the first two years while the NCEP shows a mostly dry anomaly. From 1990-92 NCEP indicates a relative moist period (positive anomaly) while NVAP does not.

Differences between NVAP and NCEP TPW are more pronounced when different regions are examined. For example, comparisons over the NH land regions (Fig. 2) indicate seasonal biases between the datasets of approximately 1-3 mm. Note that during 1992, the NVAP anomaly indicates a deeper drying than NCEP associated with the Mt. Pinatubo effect. Moreover, NVAP exhibits a relative drying with respect to NCEP between 1990 and 1994 . This is seen in the TPW differences as well as in the anomaly differences (bottom panel Fig. 2). This characteristic drying is seen over the land regions in both the northern and southern hemispheres, and is not seen over the oceans except to a slight degree over the NH equatorial oceans.

Another regional example illustrating significant differences between the datasets is the northern midlatitude oceans (Fig. 3). Over this region NVAP exhibits a seasonal dry bias with respect to NCEP ranging from about 0.0 - 1.5 mm for the majority of the months during the first 5 years. Beginning in 1993 the bias amplitude increases to a moist bias of 1.5 mm in the summer months and a dry bias of approximately 2.0 mm in the winter months. The NVAP anomalies again show a deeper drying than NCEP during 1992 associated with the Mt. Pinatubo effect. Large differences are also seen between the anomalies beginning in 1993. During this period NVAP exhibits a seasonal varying anomaly indicating a dry bias during the winter months and a moist bias during the summer months. This is in contrast with the NVAP anomalies during the first 5 years and with the NCEP anomalies during the same period. These NVAP TPW characteristics are also seen in the southern hemisphere midlatitude ocean TPW time series as well, but not for the equatorial oceans.

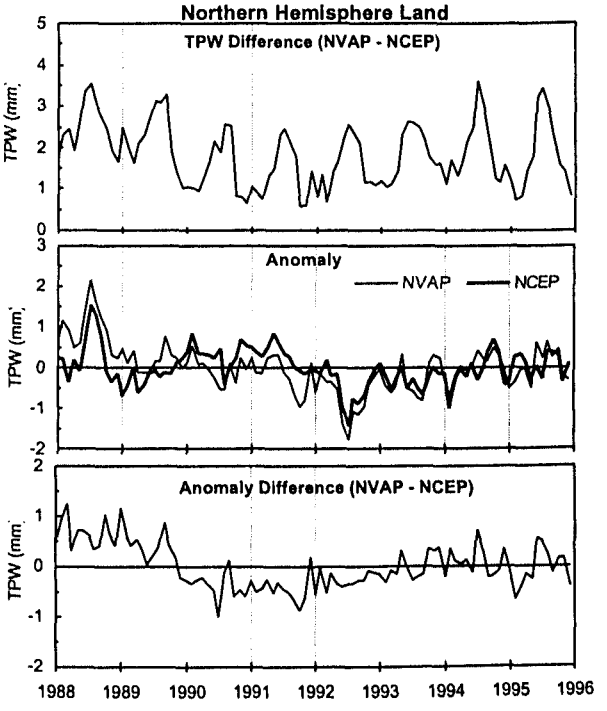

Figure 2. NVAP and NCEP TPW comparison over the northern hemisphere land regions.

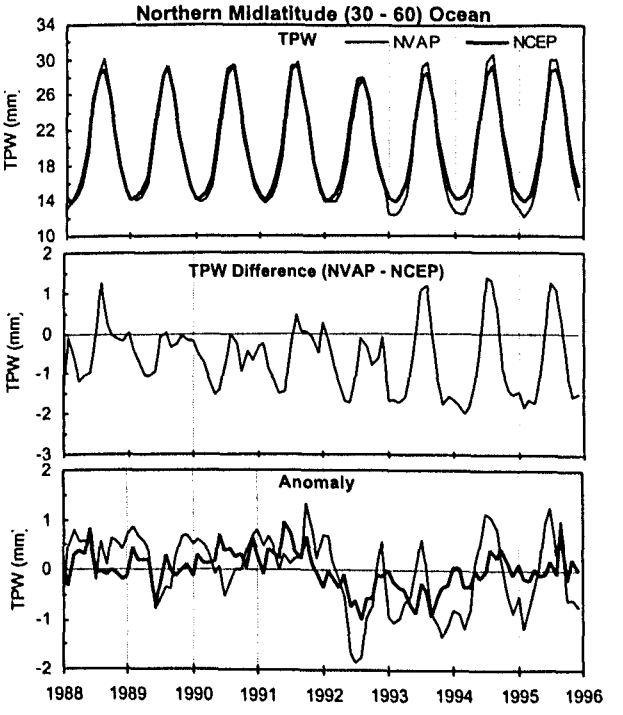

Figure 3. NVAP and NCEP TPW comparison over the mid-latitude ocean regions.

The differences seen between the datasets may be attributed to either dataset or both. In the NVAP/NCEP ocean comparison above, the discontinuity of the NVAP TPW time series (top panel Fig. 3) beginning in 1993 suggest that there was a change in the follow-on portion of the NVAP dataset. Also, one might infer that the departure of the NVAP TPW from the NCEP values suggests that the change had a negative impact on the NVAP dataset. Since the primary source of the NVAP TPW over the oceans is from SSM/I observations, the continuity of the SSM/I source data is in question.

In the above NVAP/NCEP northern hemisphere land comparison (Fig. 2), it is not apparent as to which dataset is responsible for the interannual discrepancy in the anomalies as seen in the anomaly difference plot (bottom panel Fig. 2). Since this anomaly characteristic is only observed over the land regions, it is reasonable to suspect the time consistency of the TOVS source data.

3. INTERCOMPARISON OF THE NVAP DATA SOURCES

The creators of the NVAP data set make available the individual component or source TPW datasets used to make the merged TPW daily product (Randel et al. 1996). Each component dataset is on the same grid as the combined dataset. The individual component datasets provide the daily average measurements that have also been averaged spatially within a one degree grid box. No interpolation is done for grid boxes containing no measurements. Though the satellite and radiosonde measurements represent the daily average TPW for a given grid box, there are differences associated with sampling. The radiosonde gridded daily measurements are usually comprised of an average of two measurements made at the synoptic times. Also, each grid box usually contains just one radiosonde location. The satellite grid boxes may contain, on occasion, only one time of day measurement dependent on the location and number of satellites, but also may be the average of several spatial measurements within a grid box. The time of radiosonde measurements are simultaneous through out the world while the time of the satellite measurements vary based on local equator crossing times of the particular satellite. These sampling differences as well as the accuracy of the measurements may also contribute to the variances in the daily comparisons.

In this analysis the TOVS and SSMI TPW daily grid point values were compared to collocated radiosonde grid values. For each daily - collocated radiosonde and satellite grid point value, the difference was calculated (satellite minus radiosonde). From these differences the mean difference and the standard deviation of the differences were calculated for a month of collocations. Also calculated was the mean TPW of the monthly sample from each source. In order to compare results easily between regions and instruments, the statistics are presented in terms of relative mean difference (RMD) and relative standard deviation (RSTD) with respect to a reference TPW. The radiosonde mean TPW was taken to be the reference for comparisons involving radiosonde measurements.

Figure 4 shows the NH comparison results for the TOVS and radiosonde case. The RMD is seen to vary with time with values of near zero to approximately 10%. TOVS is seen to exhibit an over all dry bias with respect to the radiosonde of approximately 5%. The cause of the varying accuracy of the TOVS TPW is unknown. Possible causes include algorithm processing changes, as well as satellite instrument and calibration effects. The onset of the accuracy change (approx. Nov. 1992) does not coincident with a new satellite launch. Note that the variation in the RMD has similar characteristics as the anomaly difference in Fig. 2. Moreover, the correlation coefficient between the two curves is 0.69. This comparison suggests that a TOVS dry bias is likely a major contributor to the NVAP/NCEP comparison differences over the land regions between 1990-1994.

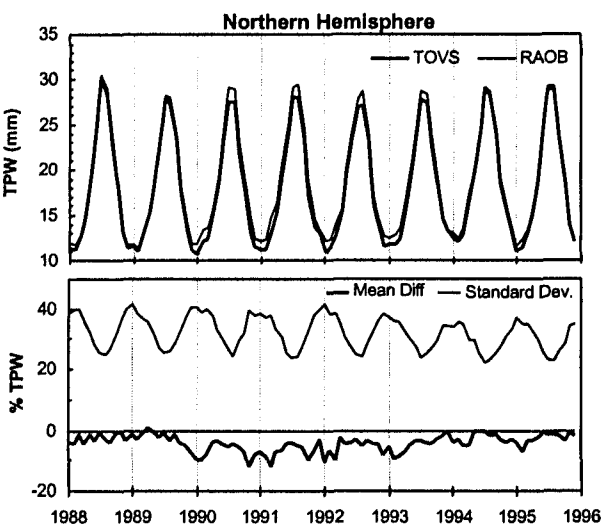

Figure 4. TOVS and radiosonde TPW collocation comparison over the northern hemisphere.

Figure 5 shows the comparison results for the SSM/I and radiosonde case. The radiosondes in this comparison are associated with launches from small islands and ships as well as radiosonde measurements along coast lines that may reside in a 1 degree grid box containing both land and water. It is seen that the RMD is quit large from 1988 to 1993. It has a seasonal variation from about 5% in the summer months to over 20% in the winter months. This SSM/I moist bias is seen to reduce significantly beginning in 1993 with a seasonal variation of less than 10%. Note that the RSTD is also reduced significantly for this period. The cause for the accuracy change was due to algorithm improvements put in place beginning with the 1993 dataset updates. The improvements include: a more robust precipitation check, improved land and ice contamination schemes, and the implementation of the 22 GHz channel in the retrieval process (D. L. Randel 2000, personal communication). The desired impact was to reduce the moist biases in the low TPW regions and seasons, which is confirmed in Fig. 5. Though the NVAP TPW departure from the NCEP TPW in Fig. 3 (top panel) suggests a possible NVAP degradation beginning 1993, the radiosonde comparison suggests that it is NCEP that has the TPW bias (moist). However, the improvement in the SSM/I processing causes a discontinuity in the TPW data. The result is a corrupted anomaly time series which does not reveal the correct climatological variability in TPW. Even though the NCEP TPW likely possesses a moist bias, its anomaly trend is more consistent with the TPW variations over the period.

4. CONCLUSIONS

Intercomparisons of the first 8 years of source data that is used in constructing the NVAP dataset indicates that there are data inconstancies in the SSM/I and TOVS data. In the case of the SSM/I data, an algorithm change implemented with the processing of the 1993 and later data produces a discontinuity in the TPW time series. Though the change appears to improve the TPW values as compared to radiosonde measurements, the TPW anomalies are effected adversely. This impact is mostly seen in the midlatitude regions.

For the case of the TOVS data, there is an observed drift in the accuracy of the TPW values from approximately 1990 through 1993 causing the TOVS TPW to be dry biased with respect to collocated radiosonde measurements. This dry bias is evident in TPW anomaly comparisons between NVAP and the NCEP reanalysis.

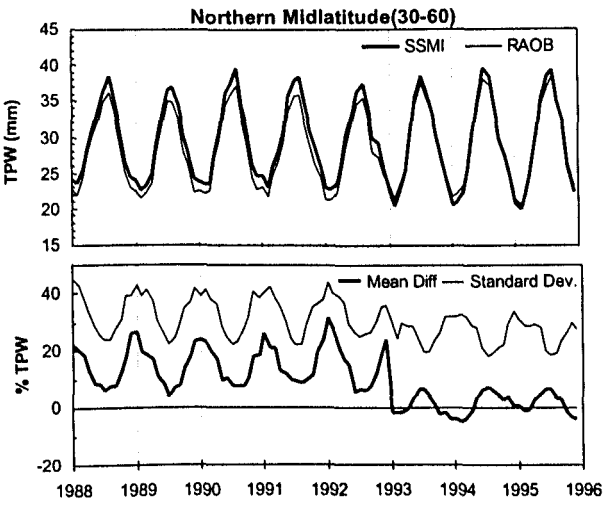

Figure 5. SSM/I and radiosonde TPW collocation comparison over the northern mid-latitudes.

Acknowledgements

This work is partially funded by NASA's Satellite Validation program under the auspices of Dr. James Dodge at NASA Headquarters. The NVAP data were obtained from the NASA Langely Research Center EOSDIS Distributed Active Archive Center.

5. REFERENCES

Christy, J. R., R. W. Spencer, and R. T. McNider, 1995: Reducing noise in the MSU daily lower-tropospheric global temperature dataset. *J. Climate*, 8, 888-896.

Kalnay, E. et al., 1996: The NCEP/NCAR 40-year reanalysis project. *Bull. Amer. Meteor. Soc.*, **77**, 437-471.

Randel, D. L., T. H. Vonder Haar, M. A. Ringerrud, G. L. Stephens, T. J. Greenwald, C. L. Combs, 1996: A new global water vapor data set. *Bull. Amer. Meteor. Soc*, **77**, 1233-1246.

P2.5 RADIATIVE IMPACT OF CLOUDS AND WATER VAPOR VARIATIONS ABOVE 300 MB FROM LONG-TERM NVAP AND ISCCP OBSERVATIONS

G.G. Campbell, T.H. Vonder Haar, J. Forsythe, A. Kankiewicz, R. Engelen[1] and S. Woo[2]

Cooperative Institute for Research in the Atmosphere
Colorado State Univ, Ft. Collins, CO

[1] Dept of Atmospheric Science, CSU
[2] Science and Tech Inc, Ft. Collins CO

The NASA Water Vapor Data set now includes an estimate of water vapor above 300 mb. Similarly the International Cloud Climatology Project and other cloud climatology estimates high-level clouds at those levels in the atmosphere. Using the day-to-day and month-to-month fluctuations in these fields we have estimated the radiative impact of these fluctuations around the mean climate situation. We see that changes in cloud properties dominate the radiative impact of water vapor on cloudy days. But that significant radiation changes occur on clear days due to water vapor changes. Ultimately this paper addresses the questions for cloud and water vapor feedback in the Earth's climate system.

1. INTRODUCTION

Here we report on an analysis of the radiative heating profiles estimated with a typical radiation code initialized by water vapor and cloud properties. The improved NASA Water Vapor Data set, NVAP, (Randel, 1996) includes an estimate of water vapor above 300 mb as well as 3 lower levels in the atmosphere. The International Satellite Cloud Climatology Project, ISCCP, (Rossow and Gardner, 1993) provides cloud amounts and liquid or ice water path measurements overlapping in time with the NVAP data set. Our goal is to estimate the radiative impact of real changes in the atmosphere in the period of the satellite record during the last two decades.

To begin, we initialized the radiative transfer model (Stephens et al 2002) with monthly observations and then perturbed those by 10% to see the relative impact of the various constituents. Because the monthly means are not instantaneous observations, the resulting heating rates are at best representative of the real atmosphere, but here we are interested in the changes around the climatology, not the absolute values. We believe, however, that the relative change is representative of the likely change in the atmosphere if that change were to have occurred. These toy experiments will lead to a better understanding of the relative importance of each component of the atmosphere and their climate impact. As this study evolves, we will attempt to estimate profiles of radiative heating over the last 10 years.

2. RESULTS

By adding water vapor to the upper atmosphere below the tropopause, one would expect heating to occur below because the water vapor will increase the downward IR flux since it is

warmer than space. In addition, it will cool the atmosphere above because it is colder than the atmosphere below. For our tests we calculated the heating rate profiles for average conditions and added 10% to the observed water vapor above 300 mb and recalculated the profile. Figure 1 is a super position of the difference of many heating profiles in a latitude band. Figure 2 shows that the infrared impact of the water is greatest in the stratosphere near the equator.

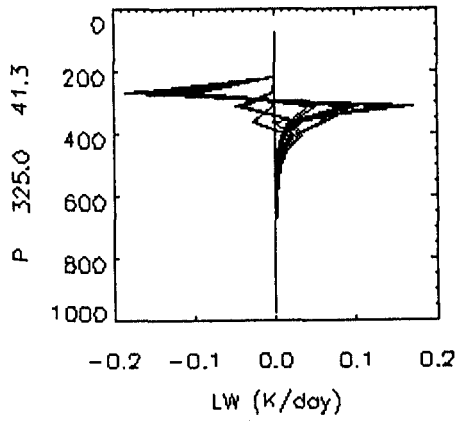

Figure 1 shows the Infra Red effects of adding 10% to the upper level water vapor. Many profile differences are superimposed at 41° North. This shows the expected result: cooling of the stratosphere and heating of the troposphere.

The interesting results come when cloud changes are compared to water vapor changes. ISCCP provides ice water path and mean pressure for cirrus clouds and liquid water path and pressure for stratus clouds. Again experiments were performed by calculating the heating profile with the mean conditions and then adding 10% to the water paths. Figure 3 shows both the infrared effects and short wave effects at noon in January. The short wave changes are comparable to the long wave changes at noon, but they are less if averaged over a diurnal cycle. At this time of year and at this latitude the changes would be comparable although the water vapor changes seem bigger.

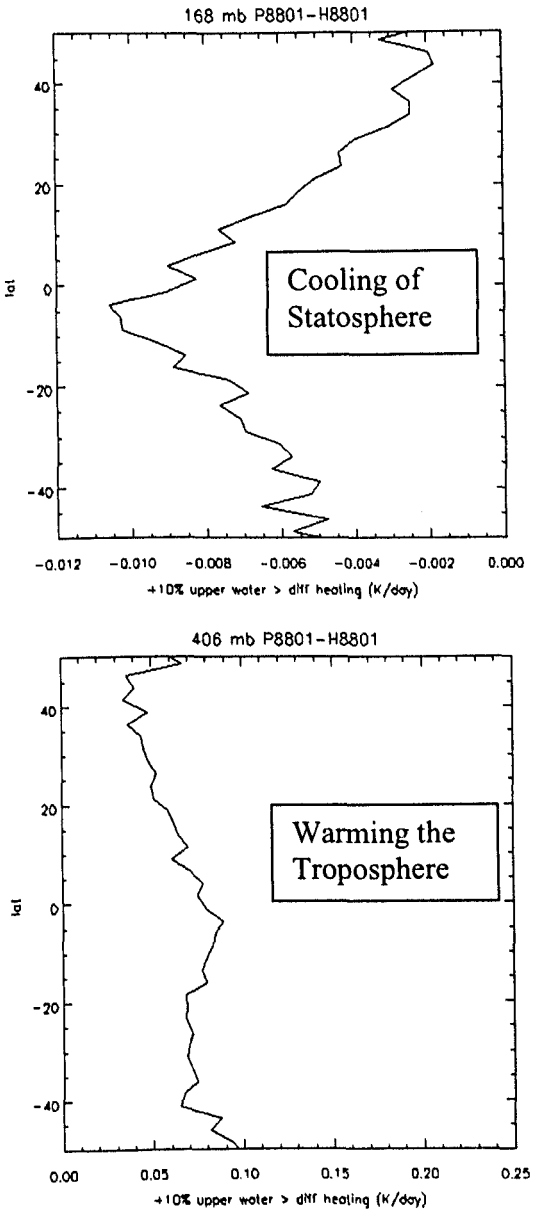

Figure 2 shows the zonal means at two different pressure levels. The results beyond 50 degrees are not accurate because there is very little vapor in the upper atmosphere.

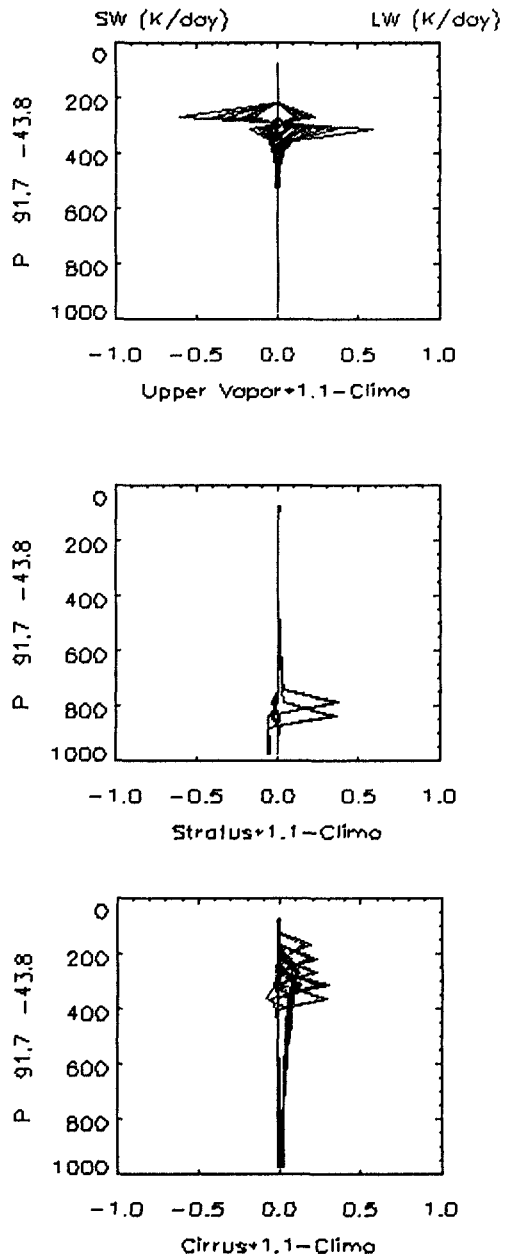

Figure 3 shows sample profiles with changes in water vapor, cirrus clouds and stratus clouds in the 43° South latitude band. These show a super position of many profiles. For the short wave results there are the noontime variations for January sun position.

To get some summary of these effects, we average the **maximum** difference in each profile. Our interest here it to decide which component is more important in the heating profile. It looks like changes in cirrus have the biggest impacts in the infrared and the visible. Stratus has a significant impact in the visible because changes in water path change the albedo.

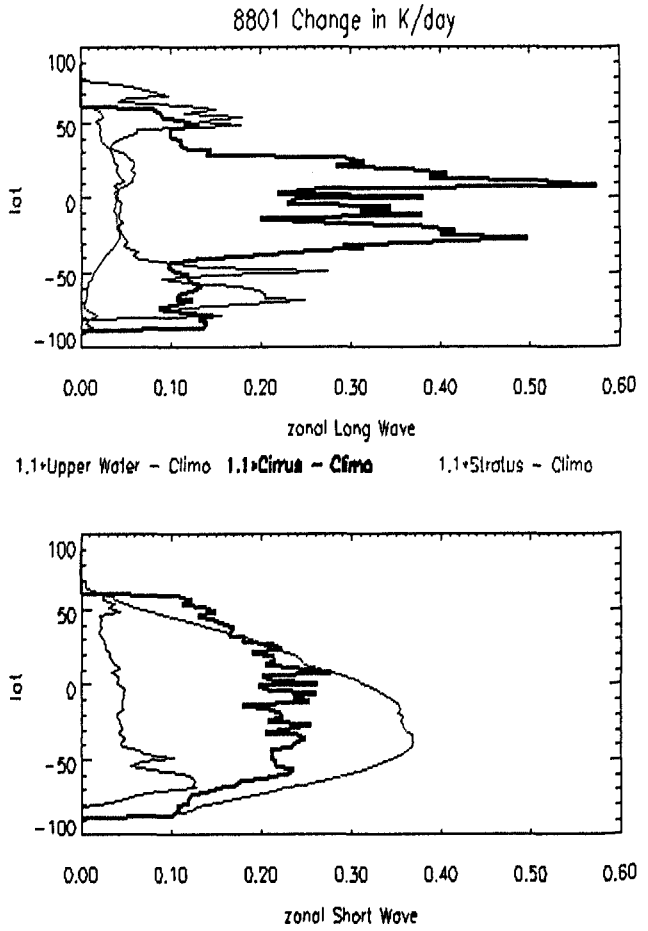

Figure 4 shows the zonal average of all the **maximum** differences. These are the average of the absolute values, so some deviations are negative.

Figure 5 shows the zonal average change at each pressure level and for each parameter. Although the shading is subtle, changes in the cirrus have an impact throughout the atmosphere whereas the water vapor and stratus changes are more local. In contrast Figure 6 factors in the cloud amount in each location the cirrus and stratus calculations. That reduces the impacts seen in figure 4 because the Earth is not covered by 100% cirrus or stratus. We have not yet run the diurnal cycle simulation to get the net effect, but it looks like the IR effects are dominating for the cirrus case.

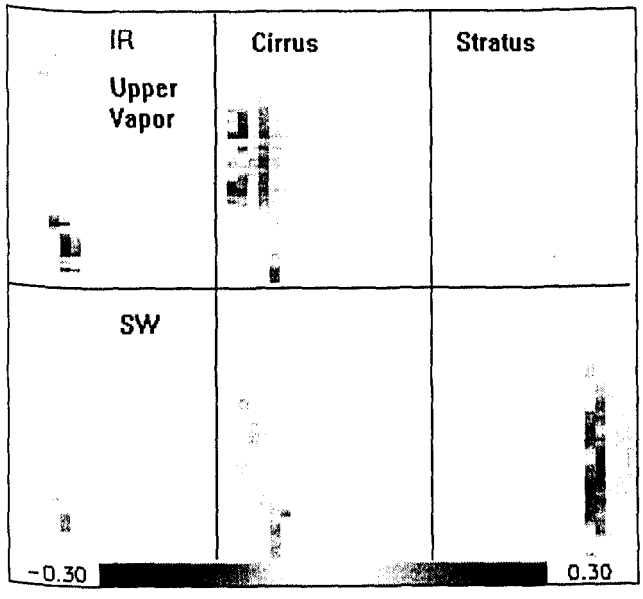

Figure 5: the zonal average change in heating (K/day) at different pressure levels and for the three components and short and long wave terms.

3. CONCLUSIONS

We started this research because of the startling conclusions of Lindzen et al (2001) who discussed observed water vapor changes. We have found that the effects of cloud changes are comparable in size to the water vapor effects especially for cirrus. Estimating water vapor feedbacks require detailed studies of the likely cloud changes as well as the water vapor changes.

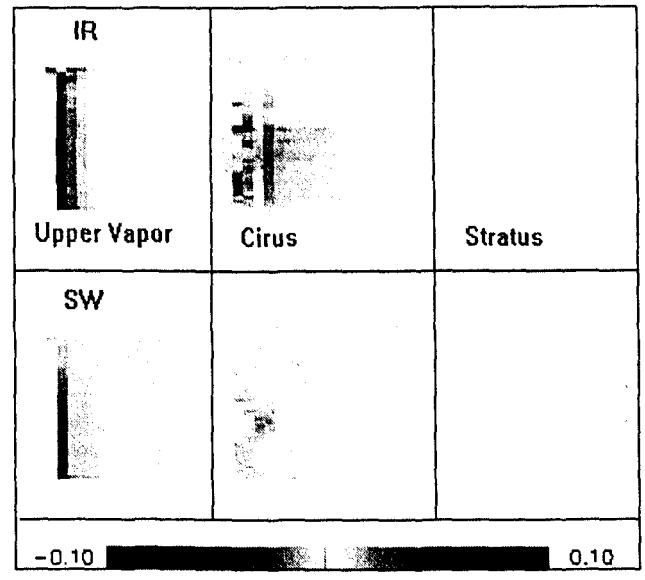

Figure 6: the zonal average change in heating (K/day) at different pressure levels and for the three components and short and long wave terms times the corresponding cloud amounts

4. ACKNOWLEDGEMENTS

The research was supported under the ISCCP Sector Processing Center project with NOAA support under grant #NA67RJ0152.

5. REFERENCES

Lindzen, R.S., Ming-Dah Chou and A. Y. Hou, 2001: Does the Earth Have an Adaptive Infrared Iris?, *BAMS*, **82**, 417-432.

Randel, D.L., T. H. Vonder Haar, M.A. Ringerud, G.L. Stephens, T.J. Greenwald, and C.L. Combs, 1996: A new global water vapor dataset. *Bull. Amer. Meteor. Soc,* **77**, 1233-1246.

Stephens, G. L., P. Gabriel, and P. T. Partain, 2002: Parameterization of atmospheric radiative transfer. I: Methods of solution. Accepted to *J. Atmos. Sci.*

P2.6 Long Term Changes in Cloud Cover Detected in HIRS Data

Donald Wylie
Space Science and Engineering Center
University of Wisconsin-Madison

Cloud cover has been globally monitored with HIRS data for the last 12 years at the University of Wisconsin. This record has covered two ENSO events and shown many inter-annual changes. Cloud cover increased in the early part of the record at the end of the 91-93 ENSO mainly in the northern hemisphere. The annual cycle of cloud cover in the southern hemisphere also became large in the mid-1990's. In the late 1990's cloud cover decreased in the northern hemisphere. The decrease was mainly from low altitude clouds while high clouds showed lesser changes. Comparisons also have been made to the ISCCP, 3-I, and SAGE cloud climatologies. The time trends are shown in Figures 1 and 2. Figure one covers most of the earth, 65 north to 65 south latitude while Figure 2 is restricted to the tropics, 20 north to 20 south latitude.

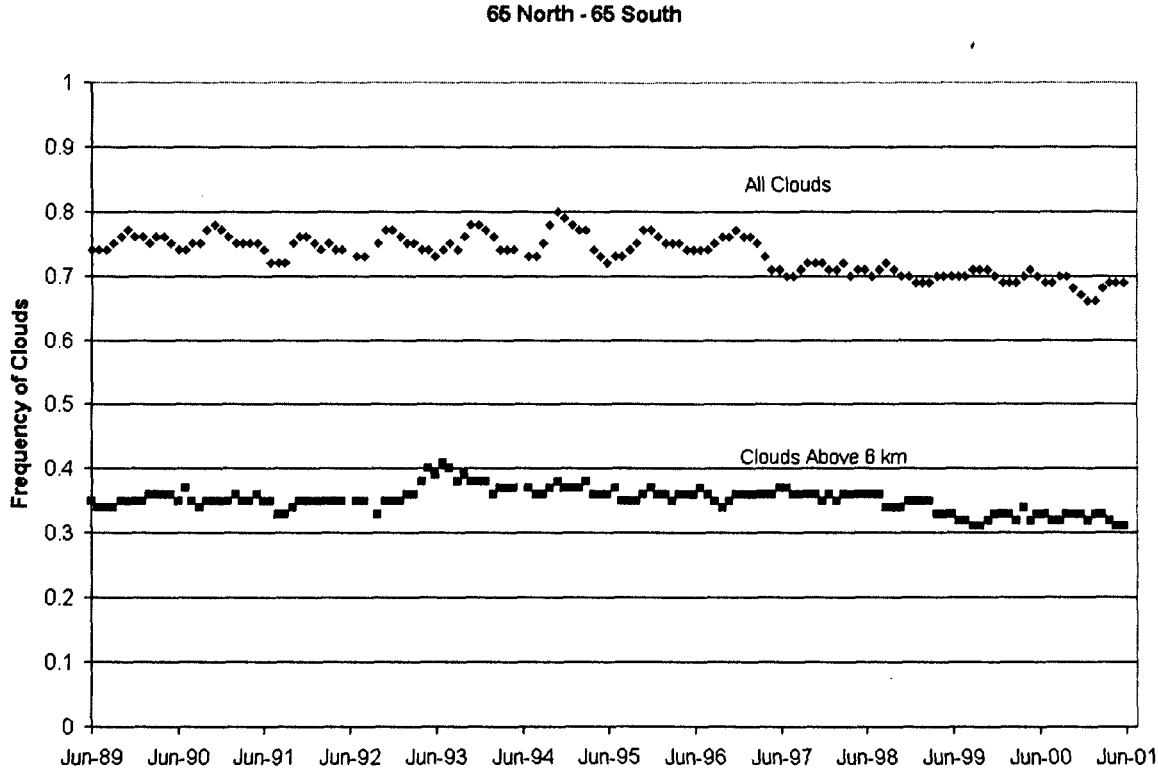

Figure 1: The cloud cover measured from the HIRS instruments on the NOAA polar orbiting satellites from June 1989 through June 2001, averaged from 65 north to 65 south latitude.

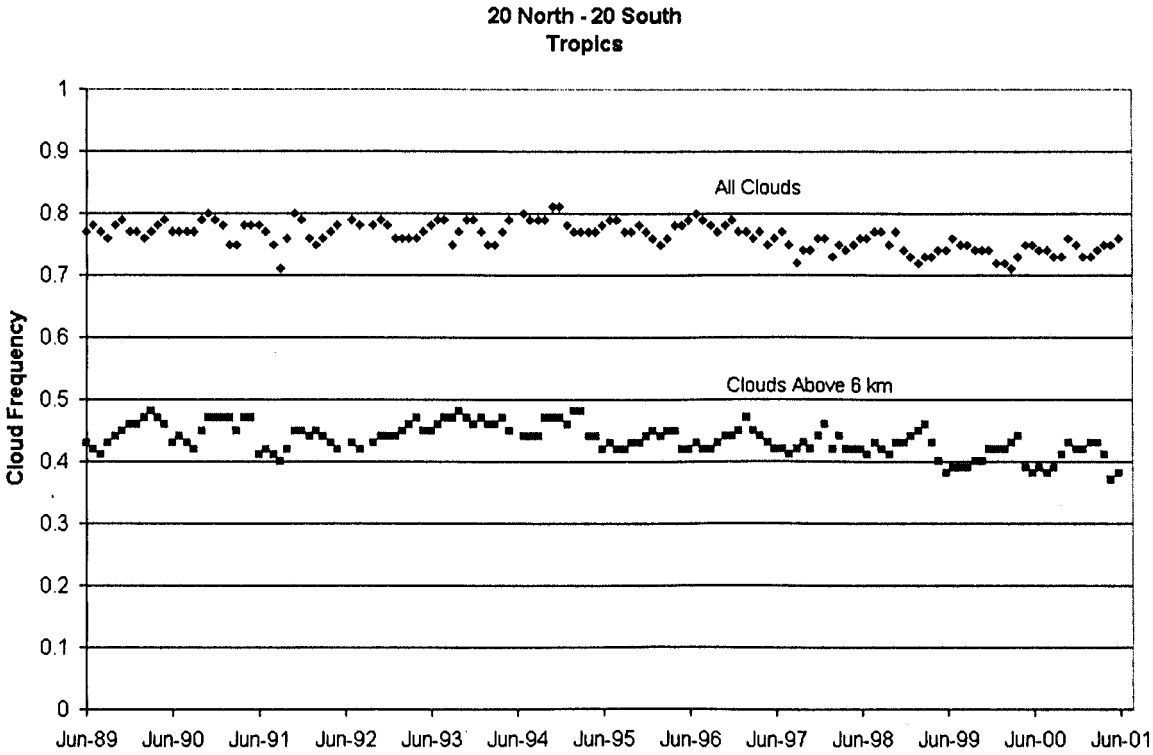

Figure 2: The cloud cover averaged from 20 North to 20 South latitude.

The technique for extracting cloud cover information from the HIRS is described in Wylie et al (1994) and Wylie and Menzel (1999).

Wylie, D. P., and W. P. Menzel, 1999: Eight years of cloud statistics using HIRS., J. Climate, **12**, 170-184.

Wylie, D. P., W. P. Menzel, H. M. Woolf and K. I. Strabala, 1994: Four years of global cirrus cloud statistics using HIRS., J. Climate, 7,1972-1986.

P2.9 CLIMATE ANALYSIS WITH THE 21-YR HIRS PATHFINDER RADIANCE CLEAR-SKY DATA SET

Darren L. Jackson*
Cooperative Institute for Research in Environmental Sciences, Boulder, CO

John J. Bates
NOAA/ERL Environmental Technology Laboratory, Boulder, CO

1. INTRODUCTION

The TOVS satellite sounding data provide the longest and most extensive global record of temperature and moisture profiles for the earth's atmosphere. Version 1 of the 21-yr HIRS clear-sky radiance data set has been constructed as a part of the TOVS Radiance Pathfinder project and provides the science community its first clear-sky radiance data set with a consistent quality control and cloud detection method throughout the entire HIRS period. These data will be beneficial for observational climate change studies and climate model/reanalysis validation studies.

2. METHOD

HIRS 1b data were first calibrated and converted to brightness temperature using the ITPP and AAPP packages from the University of Wisconsin and EUMETSAT respectively. Cloud detection was first described in Jackson and Bates (2000) and a brief overview is given here. The cloud/clear conditions were ascertained using the HIRS channel 8 surface channel. A limb correction was first applied to channel 8 to eliminate water vapor effects seen in tropical profiles. Surface temperature information was constructed by binning the maximum value all-sky channel 8 observations onto a 0.5 degree grid for each 6-hour period for each day. Each observation is compared to nearby grids, both in space and time, to determine if the observation was colder than the expected surface temperature. Pre-defined thresholds decide whether an observation is cold enough to be considered cloudy. The remaining clear-sky swath data were saved at the original resolution of the satellite observation. These swath data provide a unique high-resolution clear-sky data set that can be used to compose grid data at various time (daily, pentad, monthly) and spatial (1.0, 2.5 degree) resolutions. Other data products include all-sky brightness temperature statistics for each orbit, channel, and satellite. Table 1 highlights the data products currently available at NOAA ETL.

Table 1: Description of HIRS clear-sky data products.

Type	Size (Gb)	Description
Orbit	0.26	All-sky orbit statistics (mean, standard deviation, max, and min Tb) for each channel, satellite and orbit.
Grid	6.7	Monthly grids of mean, standard deviation and number of observations for each satellite and channel.
Swath	60	Original resolution with data records containing time, lat., lon., solar zenith, line number, scan position, altitude, reflectance, Tb.

3. RESULTS

Figure 1 gives a time series of the number of observations processed for each satellite and the number of remaining clear-sky observations after processing. Each satellite provides approximately $7x10^5$ observations per day and most of 21-yr period has coverage from two satellites collecting observations at four separate local times over the globe. Spikes indicate short periods where the data overlap between old and new satellites. The first nine years have several periods with coverage from only one satellite. The largest of these periods occurs in 1985-86 when the premature failure of NOAA-8 caused a significant gap in the morning satellite data. An extended period in 1997-98 where three satellites provide data is due to NOAA-11 satellite being reactivated after NOAA-12 HIRS data became suspect after May 1997 due to a filter wheel anomaly.

* *Corresponding author address*: Darren L. Jackson, NOAA/CIRES/ETL, 325 Broadway R/ET7, Boulder, CO 80303-3328; e-mail: Darren.L.Jackson@noaa.gov

A significant diurnal drift in NOAA-11 resulted in this satellite moving into the NOAA-12 morning position. The clear-sky data time series indicates nearly a 90% reduction in data from the all-sky data. Clear-sky comparisons with ISCCP/AVHRR data indicate a good agreement with only 2% of the Pathfinder clear-sky observations residing in ISCCP assigned cloud

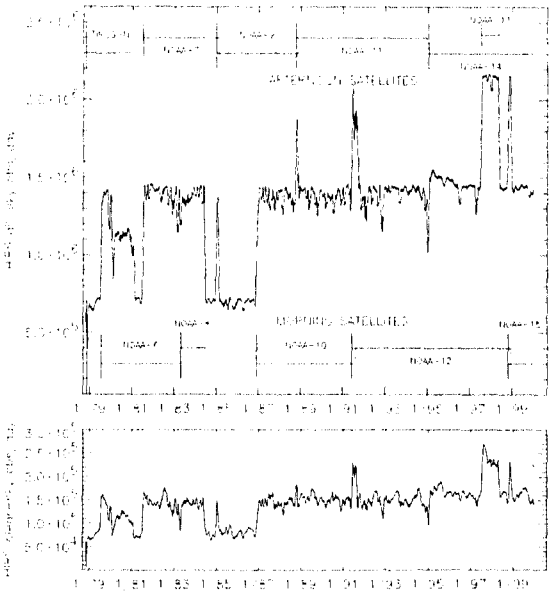

Figure 1: Time series of number of HIRS all-sky and clear-sky observations.

regions. However, the Pathfinder cloud detection uses a conservative approach that results in 13% of the ISCCP clear regions to be assigned cloudy.

Time series of 30N-30S brightness temperatures for channels 2 (14.70 μm), 4 (14.20 μm), 8 (11.10 μm) and 12 (6.70 μm) are presented in figure 2. Time series are shown from afternoon and morning satellites but from only two passes - the afternoon (15 LST) and evening (20 LST) passes. Channel 2 is a lower stratospheric temperature channel, channel 4 is an upper tropospheric temperature channel, channel 8 is a surface sensing temperature channel, and channel 12 is an upper tropospheric water vapor channel. Channel 2 results indicate an annual cycle with amplitude ~1.5 K and negative temperature trend for most of the record for both afternoon and evening passes. The direction and amplitude of the trend agrees well with the known cooling of the lower stratosphere detected by other satellites and ground-based instruments (Ramaswamy et al., 2001). Channel 4 time series indicates intersatellite bias of several degrees between the 10 satellites. This bias presumably is caused by small changes in the filter response functions and the central frequencies between the various satellites. Since this channel along with channels 5, 6 and 7 reside on edge of strong CO2 absorption region at 15 microns, the mean channel temperature is sensitive to small changes in these two parameters. The afternoon time series shows an artificial jump in 1985 caused by the transition from NOAA-7 to NOAA-9. Likewise, for the evening orbit in 1998 during the transition from NOAA-11 to NOAA-15. Channel 8 shows a noticeable decrease for both passes in 1991 following the eruption of Mt. Pinatubo. The afternoon pass shows a steady decrease from 1990 to 1995 demonstrating the drift of NOAA-11 from the afternoon to morning position. The large jump in January 1995 indicates the transition of afternoon satellites from NOAA-11 to NOAA-14. The afternoon data are warmer at all time periods since local observations near 15 LST result in the warmest temperatures over the desert regions. Channel 12 time series has high frequency variations and very little annual cycle for this domain. Intersatellite bias is most evident during the transition between NOAA-9 and NOAA-11 in the afternoon data in 1988.

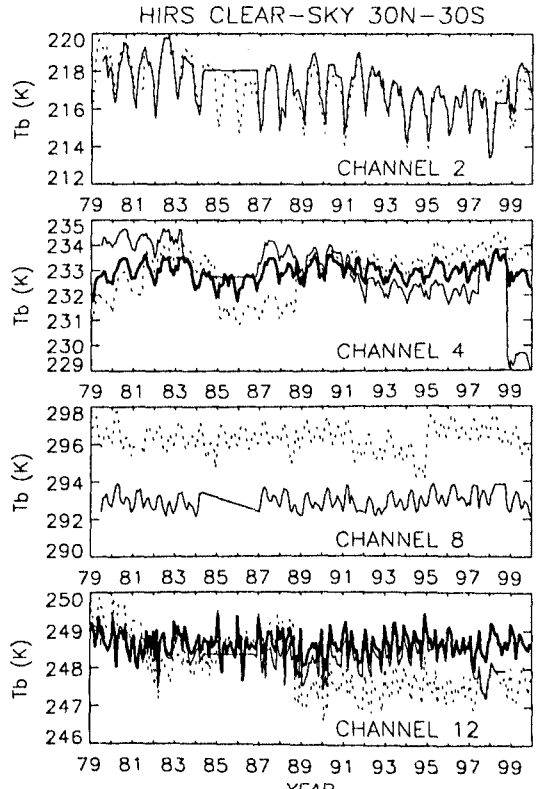

Figure 2: HIRS zonal mean time series of afternoon pass (dotted), evening pass (solid), and EDF-adjusted (thick curve) brightness temperatures for HIRS channels 2, 4, 8, and 12.

In light of the significant intersatellite bias in

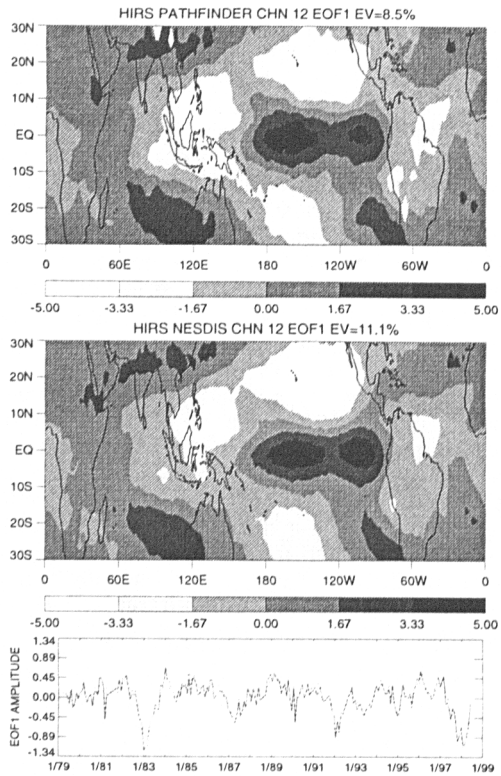

Figure 3: Leading EOF of clear-sky HIRS channel 12 data for the Pathfinder and NESDIS Operational. Time series of leading mode for Pathfinder (solid) and NESDIS (dotted) is given in bottom figure.

channels 4 and 12, an empirical dynamic function (EDF) analysis was applied to the data to eliminate intersatellite bias. This approach uses cumulative histograms of the interannual anomaly fields from the four local overpass periods and adjusts the results to a reference (evening) overpass time. Details of this technique are outlined in Bates et al. (1996). The EDF-adjusted brightness temperatures are shown by the thick curves for channel 4 and channel 12. The adjusted time series eliminate the artificial shifts created during satellite transitions. A physically based approach for explaining the intersatellite bias could not explain all of these transitions. This is likely due to inaccurate information about the instrument filter response or central frequency.

A comparison with NESDIS operational sounding data indicates HIRS channel 12 compares favorably for both the spatial variance and the time amplitude. The first EOF for channel 12 is given in figure 3. HIRS channel 12 indicates ENSO as the dominant mode of variability. The time series indicates this leading mode has its largest amplitude during El Niño events of 1983, 1987, 1992, and 1998. The moisture pattern indicates increased tropical moisture in the Central and Eastern tropical Pacific associated with tropical convection and significant dry regions over parts of Indonesia and the subtropical Eastern Pacific in the Northern Hemisphere.

4. CONCLUSIONS

Clear-sky HIRS data from the TOVS Pathfinder radiance project for the period from October 1978 to December 1999 indicate the temperature channels relate well with known changes in the temperature field for the lower stratosphere and lower troposphere. Middle and upper tropospheric channels suffer the largest intersatellite bias, but these biases were reduced using an empirical-based EDF approach for eliminating jumps between satellite periods. EOF Comparison with the NESDIS operational data products indicates good agreement for the moisture field and temperature fields (not shown).

Applications of these data include investigating the role of water vapor climatologies for GEWEX water vapor project, analysis of the role of water vapor in the monsoon/desert system for CLIVAR-GOALS, studies of upper tropospheric/lower stratospheric water vapor for SPARC and climate model/observation studies with AMIP-II. Future improvements to these data include providing all-sky data products, including cloud height and densities using the CO_2 cloud slicing method (Wylie and Menzel, 1999), and making these data available for users in a standard data format at a data center.

5. REFERENCES

Bates, J.J., X. Wu, and D.L. Jackson, 1996: Interannual variability of upper-tropospheric water vapor band brightness temperature. *J. Climate*, **9**, 427-438.

Jackson, D.L., and J.J. Bates, 2000: A 20-yr TOVS radiance Pathfinder data set for climate analysis. Proceedings, *10th Conference on Satellite Meteorology and Oceanography*, 426-429.

Ramaswamy, V., and co-authors, 2001: Stratospheric temperature trends: Observations and model simulations. *Rev. Geophys.*, **39**, 71-122.

Wylie, D.P., and W.P. Menzel, 1999: Eight years of high cloud statistics using HIRS. *J. Climate*, **12**, 170-18

P 2.10 **COMPARISONS OF CLOUD ANALYSES FROM INDEPENDENT INFRARED AND SOUNDER RETRIEVALS**

Robert P. d'Entremont
Satellite Meteorology Group
Atmospheric and Environmental Research, Inc.
131 Hartwell Ave, Lexington MA 02421 USA

Donald P. Wylie
Space Science and Engineering Center
University of Wisconsin / Madison
1225 West Dayton Street, Madison WI 53706 USA

1. Cirrus Properties

Many sources of passive satellite data are potentially useful for detection and analysis of cirrus attributes. TIROS satellites are equipped with the Advanced Very High Resolution Radiometer (AVHRR), a five-channel passive radiometer with detectors that measure upwelling visible (0.63 μm), near-infrared (near-IR, 0.86 μm), middle wavelength IR (MWIR, 3.7 μm), and split longwave thermal IR (TIR, 10.7 and 11.8 μm) energy both day and night. The geostationary GOES Imager also has five bands, positioned at 0.63, 3.9, 6.7 water-vapor (WV), 10.8, and 12 μm. The NOAA polar-orbiting sounder instruments collectively known as TOVS (TIROS Operational Vertical Sounder) also collect data in the wings of the 15-μm CO_2 absorption band that are useful for detection of thin cirrus and specification of their height.

Cirrus is recognized as one of the most poorly quantified of all clouds. Cloud altitude is difficult to specify, because cirrus consist typically of ice particles distributed over a considerable vertical extent with complex optical properties and microphysics. In addition to the wide variability in properties common for other cloud types, cirrus clouds are unique in exhibiting a range of transmissivity values t that span the entire possible domain $0< t <1$. The transmissive nature of cirrus cloud turns out to be its most important (in a climate sense) and elusive (in a retrieval sense) attribute to specify. Transmissive cirrus clouds both emit and transmit thermal energy. Emissions occur at a rate dependent on cirrus emissivity and temperature, while transmissions depend most strongly on cirrus transmissivity and the temperature of the underlying warmer surface (either a lower cloud or the ground). If the semi-transparent nature of cirrus clouds is not properly modeled, its altitude is consistently underestimated when using passive infrared brightness temperature data.

2. Cirrus Analysis Algorithms

In this study, comparison is made of cloud attributes, both spatial and radiative, obtained for the same cloud scenes using radiance measurements from the independent imagers and sounders onboard geostationary GOES and polar-orbiting TIROS platforms. Emphasis is placed on cirrus radiative and spatial attributes, including frequency of occurrence, optical thickness, and cloud temperature. Imager retrievals analyze multispectral thermal infrared (TIR) radiances in the 3.9, 6.7, and 10.8-μm window channels using an updated TIR cirrus analysis algorithm (TIRCA), adapted from that of d'Entremont et al. (1990, 1993; 2001 this preprint volume). The sounder retrievals incorporate the CO_2 slicing technique (Wylie and Menzel, 1989) in the 13-15-μm carbon dioxide absorption bands. Cloud emissivity and temperature are common to both the imager and sounder retrievals, and will be compared directly.

Comparison was made of cirrus cloud attributes, spatial and radiative, obtained for both GOES and TIROS cirrus cloud scenes over Wisconsin,

New England in September 1995, for a month-long analysis of polar-orbiting TIROS data over Florida in September 1996; and for a two-month period during the summer and fall of 2001 over the eastern US and western Atlantic.

Both the TIRCA and CO_2 slicing algorithms are designed to detect the presence of thin cirrus and to determine its radiative and spatial attributes. However, the capabilities of the two algorithms depart from each other in numerous respects. The most important differences between the two techniques are based on the differences in the spectral bands and the spatial resolutions of the sounder and imager sensors. Additionally, cloud altitude is retrieved independently of optical thickness by CO_2 slicing, whereas retrievals are coupled in the TIRCA algorithm. Thus the CO_2 slicing and TIRCA models mutually complement each other.

3. Comparisons with Radar

Nighttime AVHRR data for Channels 3, 4, and 5 were obtained over New England at ~2337 UTC on 16 September 1995, a time when surface-based radar observations of thin cirrus were available at Hanscom AFB as a part of an ongoing cirrus cloud field observation. The 35-GHz upward-pointing radar provides useful observations of cirrus cloud base and top against which satellite retrievals can be directly compared. Each satellite pixel has a resolution of approximately 1 km at nadir. Surface-based radar observations of the cirrus were collected for a period before, during, and after the NOAA satellite overpass time.

The emissivity and effective altitude estimates obtained for the Hanscom cirrus sample are plotted in Figure 1. Pixel-by-pixel retrievals were selected $\pm$30 minutes upwind and downwind of the radar site within the cirrus clouds. The TIRCA cloud altitudes for these pixels are consistent with TPQ-11 ground-based radar measurements of cirrus cloud base and top. The TPQ-11 radar measured cirrus base and tops in the 5.5 - 10 km range for the time period several hours before and after the 2337 UTC satellite overpass. The retrieved cirrus effective altitudes are not in dispute with the radar observations of cloud base and top, lending confidence that the transmissive characteristics of the thinner cirrus are being properly accounted for in the model.

With this data set it is not possible to verify the cirrus emissivity estimates except to say that if the effective cirrus altitudes retrievals are reasonable, then the emissivities are also likely to be reasonable since these two parameters are coupled in the TIRCA physical retrieval model.

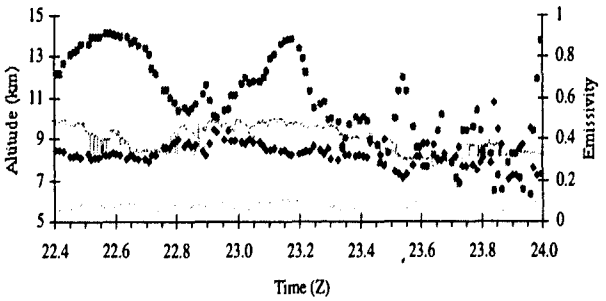

Figure 1. Enhanced cirrus cloud-top (diamonds) and emissivity (circles) retrievals over Hanscom AFB compared to TPQ-11-derived cloud top and base (solid lines)

4. CO_2-Slicing and TIRCA Analysis Inter-Comparisons

In recent years CO_2 slicing has been extensively applied to both TIROS and GOES data to obtain cirrus emissivity and altitude statistics on a global scale (Wylie, Menzel, and Woolf, 1991; Menzel, Wylie, and Strabala, 1992). Satellite data cloud climatologies produced thus far using the CO_2 slicing method have been extensive, focusing on determining the geographical, seasonal, and diurnal changes of cloud cover (Wylie and Menzel, 1989).

Because of this legacy, a comparison study was performed over Florida during September 1996 between CO_2 slicing and the imager-based TIRCA cloud retrievals. NOAA AVHRR and TOVS data were collected from September 1996 over Florida and the southeast U.S (Figure 2). Basic cloud-detection processing was performed using the SERCAA Phase 1 and 2 algorithms described by Gustafson et al. (1994). Further processing then was performed using the TIRCA cirrus altitude and emissivity retrieval algorithms. CO_2 Slicing was applied to the TOVS High-Resolution Infrared Sounder (HIRS) data and the SERCAA

AIRC model analyzed data from the AVHRR sensor. The final CO_2 Slicing and AIRC products are pixel-level representations of cloud altitude, pressure, and emissivity. Comparisons were made of cirrus cloud altitudes obtained for the same cloud scenes using measurements from the two independent sensors onboard the same NOAA TIROS polar orbiting satellites.

Figure 2. Data collection and analysis area for September 1996

AVHRR HRPT and coincident HIRS CO_2 sounder radiance data valid 4-23 September 1996 over the southeastern United States, the Gulf of Mexico, and the southwestern North Atlantic were analyzed for cirrus effective altitude. Figure 3 contains a frequency distribution of retrieved cirrus effective altitudes for the two independent analysis models. There is strong agreement between the altitude climatologies in the 7-to-13-km range. The largest differences between the two retrievals are in the 5-to-7 and greater-than-13-km range bins. The TIRCA analyses show more clouds at lower altitudes, and CO_2 slicing shows more clouds at higher altitudes. Stratified summary statistics show the same pattern both day and night, showing that algorithm diurnal biases of any sort are not responsible for the overall lack of agreement in the very low and very high cirrus. Reasons for this disagreement are under study.

5. Emissivity and Cloud Fraction

The TIRCA and CO_2 cirrus analysis models are useful for verifying independently derived cirrus characteristics within the same cloud scene. The CO_2 technique retrieves effective emissivity $N\varepsilon$, the product of cloud fraction "N" and emissivity "ε," and is capable of detecting thin cirrus at levels where the carbon-dioxide weighting functions peak. For each relatively coarse HIRS field of view a cirrus cloud fraction estimate "N" can be made from the AVHRR imager data using a multispectral cloud mask. The sounder emissivity ε can then be decoupled from the effective emissivity $N\varepsilon$ by dividing by "N." This in turn allows for direct comparison between the imager and sounder emissivity retrievals for those AVHRR cloudy pixels that lie within the HIRS sounder pixel.

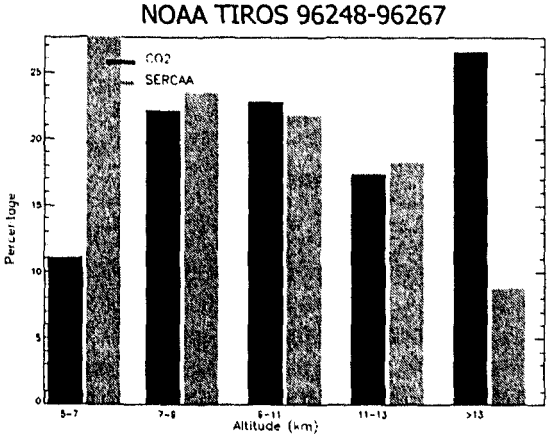

Figure 3. Frequency distribution of effective cirrus altitude for SERCAA and CO_2 Slicing

Figure 4 contains a scatter plot of the CO_2 effective emissivity $N\varepsilon_{CO2}$ vs. TIRCA cloud fraction N for a TIROS overpass above Wisconsin on 28 Oct 86. Points above the line $N\varepsilon = N$ are spurious because ε is constrained to be ≤ 1, and thus $N\varepsilon \leq N$. Visual inspection of the AVHRR image data show that the large majority of $N\varepsilon$ values above the $N\varepsilon = N$ line are from CO_2 opaque cloud reports ($N\varepsilon = 1$) in areas where TIRCA found little or no cirrus and where the CO_2 radiances detect no *transmissive* cloud (i.e., the cirrus fraction is zero but the cloud fraction N is one). Note from the scatter of $N\varepsilon$ vs. N that it is not proper to consider CO_2 Slicing $N\varepsilon$ analyses as representative of either cloud fraction or emissivity, but rather as a coupled product.

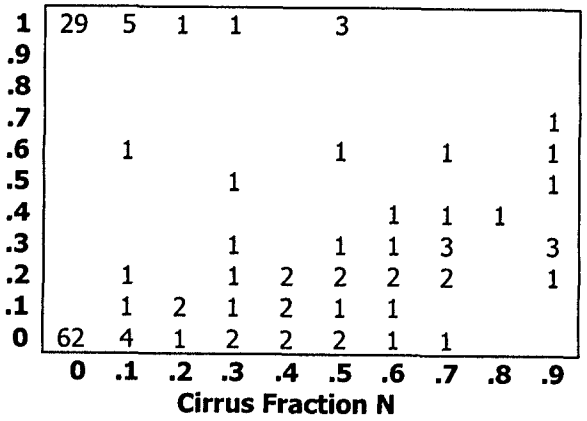

Figure 4. Scatter plot of CO_2-Slicing HIRS effective emissivity Nε (y axis) vs. AVHRR cloud fraction N. 62 HIRS FOVs were labeled "clear" by CO_2 Slicing and TIRCA

6. Eastern-US Climatology

As of this writing a new climatology comparison is underway over the eastern US and western North Atlantic. Analyses will be compared using techniques similar to those discussed in Section 4, and results will be presented at the poster conference. Particular emphasis will be placed on high-cirrus/low-cirrus differences, although it is suspected that with enhancements to both the CO_2 Slicing and TIRCA algorithms since the time of the Florida study, discrepancies may be small for cirrus at all levels.

7. Summary

SERCAA cloud analysis algorithms (Gustafson et al., 1994), complete with a multispectral infrared cirrus analysis technique (called here "TIRCA," see this preprint volume), were successfully applied to a large data set and compared to both CO_2 Slicing analyses and ground-based radar observations. The effective altitudes obtained by the CO_2 slicing and SERCAA models compare well for the cirrus and liquid water-droplet clouds observed during 4-23 September 1996 over Florida. The altitude summary statistics retrieved by the CO_2 slicing and SERCAA models are not in dispute with each other, after accounting for a high-cirrus bias evident in the CO_2 reports. The agreement between the two independent analyses of the same cirrus image scenes over a 20-day period provides an independent metric against which the performance and accuracy of CO_2 Slicing cirrus climatologies can be judged.

References

Barton, I. J., 1983: Upper Level Cloud Climatology from an Orbiting Satellite. *Journ. Atmos. Sci.*, **40**, 435 - 447.

d'Entremont, R. P., D. P. Wylie, S.-C. Ou, and K.-N. Liou, 1996: Retrieval of Cirrus Radiative and Spatial Properties Using Coincident Multispectral Imager and Sounder Data. *Preprints*, Eighth Conf. On Satellite Meteorology and Oceanography, Amer. Meteor. Soc., Atlanta, GA, 28 January - 2 February 1996, 377 - 381.

Gustafson, G.B., R.G. Isaacs, R.P. d'Entremont, J.M. Sparrow, T.M. Hamill, C. Grassotti, D.W. Johnson, C.P. Sarkisian, D.C. Peduzzi, B.T. Pearson, V.D. Jakabhazy, J.S. Belfiore, and A.S. Lisa, 1994: Support of Environmental Requirements for Cloud Analysis and Archive (SERCAA): Algorithm Descriptions. *PL-TR-94-2114*, Phillips Laboratory, Hanscom AFB, MA, ADA 283240.

Menzel, W. P., Donald P. Wylie, and K. I. Strabala, 1993: Trends in Global Cirrus Inferred From Three Years of HIRS Data. *Seventh Int'l. TOVS Conference,* Austria, 10-16 February 1993.

Menzel, W. P., Donald P. Wylie, and Katherine. I. Strabala, 1992: Seasonal and Diurnal Changes in Cirrus Clouds as Seen in Four Years of Observations with the VAS. *Journ. Appl. Meteor.*, **31**, 370 - 385.

Ou, S. C., K. N. Liou, W. M. Gooch, and Y. Takano, 1993: Remote Sensing of Cirrus Cloud Parameters Using Advanced Very High Resolution Radiometer 3.7- and 10.9-um Channels. *Appl. Optics*, **32**, 2171-2180.

Wylie, Donald P., and W. P. Menzel, 1989: Two Years of Cloud Cover Statistics Using VAS. *Journ. of Clim.*, **2**, 380 - 392.

P 2.11 CLOUD CLIMATE INVESTIGATIONS IN SCANDINAVIA DURING THE LAST DECADE USING HIGH-RESOLUTION NOAA AVHRR DATA

Karl-Göran Karlsson *
Adam Dybbroe
Swedish Meteorological and Hydrological Institute (SMHI)
Norrköping, Sweden

1 INTRODUCTION

The task to monitor the regional and global cloud climate has become increasingly depending on the existence of appropriate cloud data sets derived from satellite measurements. Many satellite-based cloud retrieval algorithms have now reached a maturity to permit the compilation of cloud climatologies with an acceptable quality. This paper describes a method for compilation of a ten-year high-resolution regional cloud climatology based on a systematic cloud classification of NOAA AVHRR scenes over the Scandinavian region. The paper also includes a comparison of results with cloud climatologies based on surface observations and other satellite data sets (e.g. ISCCP).

2 METHODOLOGY

The used approach for compilation of cloud climatologies has been to use archived results from the SCANDIA (SMHI Cloud ANalysis model using DIgital AVHRR data) cloud classification model (described in detail by Karlsson, 1996 and Karlsson, 1997) covering the period 1991-2000. SCANDIA uses the full five-channel NOAA AVHRR data set at maximum horizontal resolution. However, the cloud climatology results presented here have been utilizing a data set with a reduced resolution of 4 km.

SCANDIA results from four daily overpasses over the area (observing approximately at night, in the morning, in the afternoon and in the evening) have been used to define a daily mean of cloud cover over the area. Results have then been accumulated to define monthly, seasonal and yearly climatologies for the studied time period. Since SCANDIA makes a separation of many different cloud types, the data set permitted also studies of different cloud groups in addition to the central parameter total fractional cloud cover. Karlsson (2001) gives a full description of these results whereas this paper only reports on some results for the parameter total fractional cloud cover.

3 THE SATELLITE DATA SET

The studied NOAA AVHRR data set is composed by data from the satellites NOAA-10, NOAA-11, NOAA-12, NOAA-14 and NOAA-15. Consequently, except for a few months of data from NOAA-10, the data set consists entirely of data from the AVHRR/2 instrument. Due to technical constraints and problems (e.g., HRPT reception problems, tape failures and data gaps due to failures of the operational satellites NOAA-11 and NOAA-15), a complete satellite coverage during the period could not be achieved. The entire satellite data set consists of 12 470 satellite scenes which is 87 % of the theoretical maximum of useful scenes during the period.

4 RESULTS

4.1 SCANDIA climatologies

Figure 1 shows the period mean of cloud occurrence (cloud frequency in 4-km horizontal resolution) over the area for the selected months of January, April, July and October. Notice here that the vertical discontinuity in some of the result pictures is due to the use of different cloud detection thresholds in two different processing areas (see Karlsson, 2001).

Cloud conditions are shown to vary substantially according to season in Figure 1. Much higher cloud frequencies are found in the winter season than in the summer season for most places (except the Scandinavian mountain range and over the visible part of the Norwegian Sea). Over the Baltic Sea and over adjacent land areas, a substantial annual cycle in cloudiness is found. This is further illustrated in Figure 3 showing the annual course of cloud cover (estimated within a 36-by-36 km sub-area) at a position in the southern part of the Baltic Sea (at latitude 56N and longitude 18.5E). The yearly amplitude is estimated to approximately 40 % (40 % cloud frequency in summer and 80 % in winter).

* *Corresponding author address:* Karl-Göran Karlsson, SMHI, SE-601 76 Norrköping, Sweden; e-mail: Karl-Goran.Karlsson@smhi.se

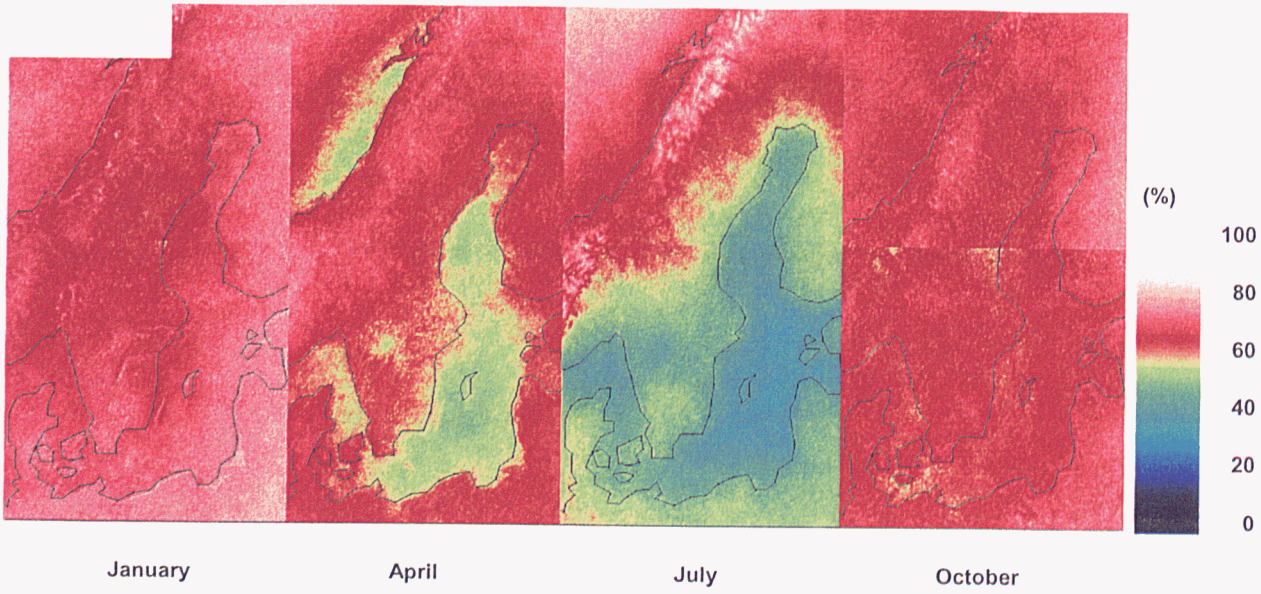

Figure 1 *Period mean (1991-2000) of cloud frequency in the Scandinavian area with 4 km horizontal resolution for the months of January, April, July and October.*

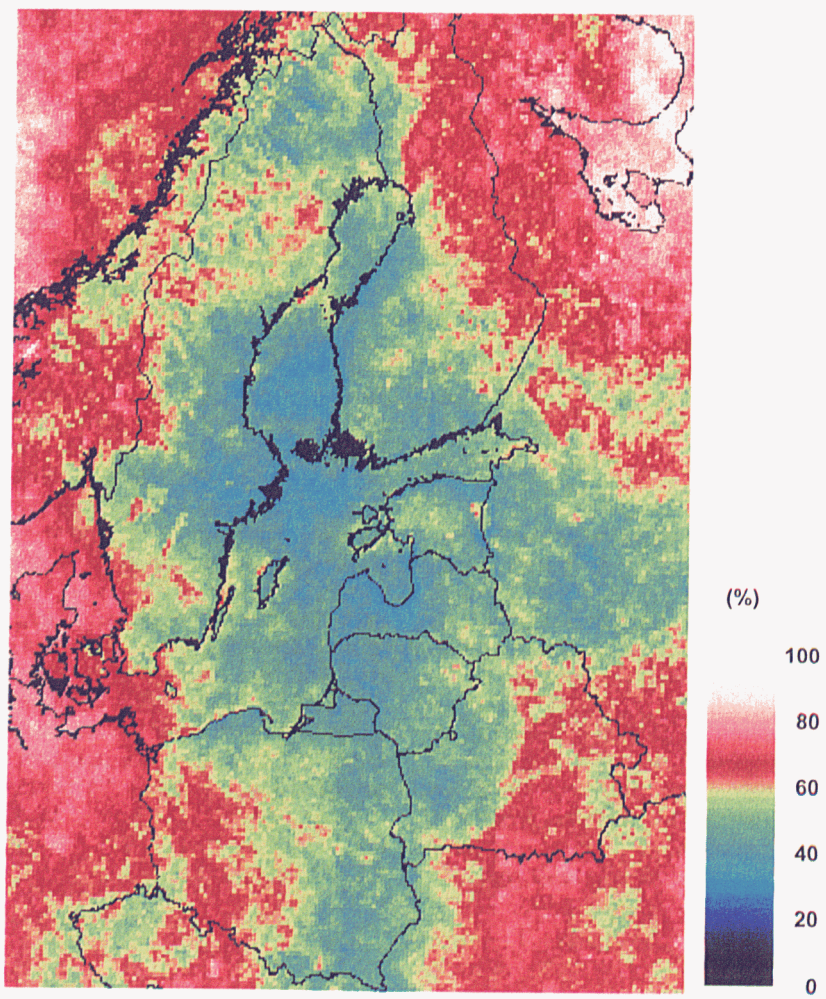

Figure 2 *Mean cloud frequencies in 10 km resolution over the Baltic Sea drainage basin derived from NOAA AVHRR afternoon passages in September 2000. See text for details.*

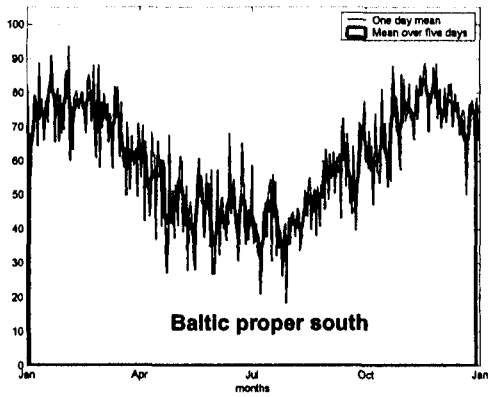

Figure 3 *The annual course of cloud cover (% - estimated in one-day and five-day intervals) for a position in the southern part of the Baltic Sea (56N, 18.5E).*

More detailed results (e.g., concerning the diurnal cycle of cloud cover and the contribution from ice and water clouds) are presented by Karlsson (2001).

4.2 *Comparison with other cloud data sets*

In order to validate the results of the SCANDIA cloud climatologies, a comparison with a corresponding cloud climatology based on surface observations (SYNOP) was carried out. Mean values of monthly cloud cover were compiled by use of SYNOP observations made at 00 UTC, 06 UTC, 12 UTC and 18 UTC for 28 Swedish SYNOP stations. The observations of total cloud cover from each SYNOP station were compared to corresponding estimations of SCANDIA cloud cover computed in 36-by-36 km sub-areas centered at the geographic location of each station. In total, more than 250 000 SYNOP observations were used and compared to corresponding satellite scenes.

Figure 4 shows an overall summary of validation results month by month in the period. Notice the sinusoidal variation in the bias error varying between +5-10 % in the winter season and –5-10 % in the summer season. Particular problems are indicated in the winter season having high positive bias errors, high RMS errors and low correlation coefficients. The low correlation coefficient in winter indicates that error structures are very complex. Several error sources seem to have importance, largely caused by the lack of useful visible information and the problematic temperature conditions near the surface with frequent temperature inversions making the use of infrared channels risky for cloud detection.

The indicated underestimation of cloudiness in summer was concluded to emanate entirely from deficiencies in the SYNOP observations. The relatively high correlation coefficient and the good experience from using the SCANDIA cloud classification in summer in operational weather forecasting support this conclusion.

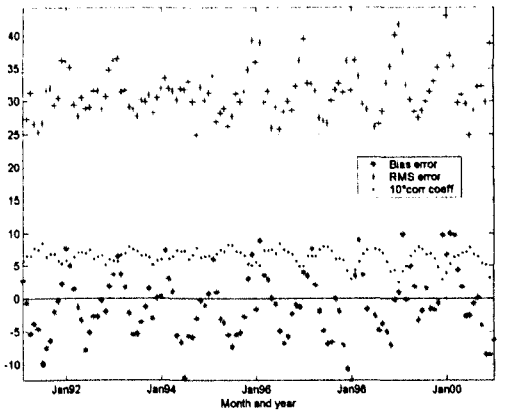

Figure 4 *Monthly averages of bias errors, RMS errors and correlation coefficients for the entire validation data set in the period 1991-2000.*

The SCANDIA climatologies were also compared to two international cloud data sets: CRU (New et al., 2000) and ISCCP (D2 series – described by Rossow and Schiffer, 1999). However, since the SYNOP based CRU data set is only available over land areas and since the ISCCP D2 series is not available yet for the entire ten-year period, the comparison here is limited to the years 1991-1993 only over land areas.

Figure 5 shows the comparison of monthly mean of cloud cover over land areas in the Scandinavian area of SCANDIA and the two other data sets. Noticeable is the larger dynamic range of cloud cover values for SCANDIA compared to the other two data sets. Especially the minimum values of cloud cover in the summer season are lower for SCANDIA. It can also be noticed that the agreement between SCANDIA and CRU is quite good in the beginning of the studied period. Basically the same pattern as previously found in the comparison with Swedish SYNOP stations (i.e., summertime SCANDIA underestimation and wintertime SCANDIA overestimation) were found. However, for the second half of the period deviations are very large. This is largely caused by lack of available SYNOP observations over the area in the CRU data set (basically now only giving a climatological mean of cloud cover over the area). The higher values of the the summertime minimum of cloudiness for the ISCCP data set were verified to exist also over sea areas in the region (see Karlsson, 2001).

5 DISCUSSION

The ten-year NOAA AVHRR cloud climatology shows that Scandinavian cloud conditions are largely influenced by the existence of the Baltic Sea. Conceptually, the Baltic Sea could be described as acting like a heat sink in the summer season (mainly caused by the springtime supply and accumulation of cold fresh water from melting snow in spring) suppressing convective clouds from forming over sea areas and adjacent land areas. However, the northern part of the region does not show a similar annual cycle of cloudiness. Here, cloud conditions remain practically the same throughout the year.

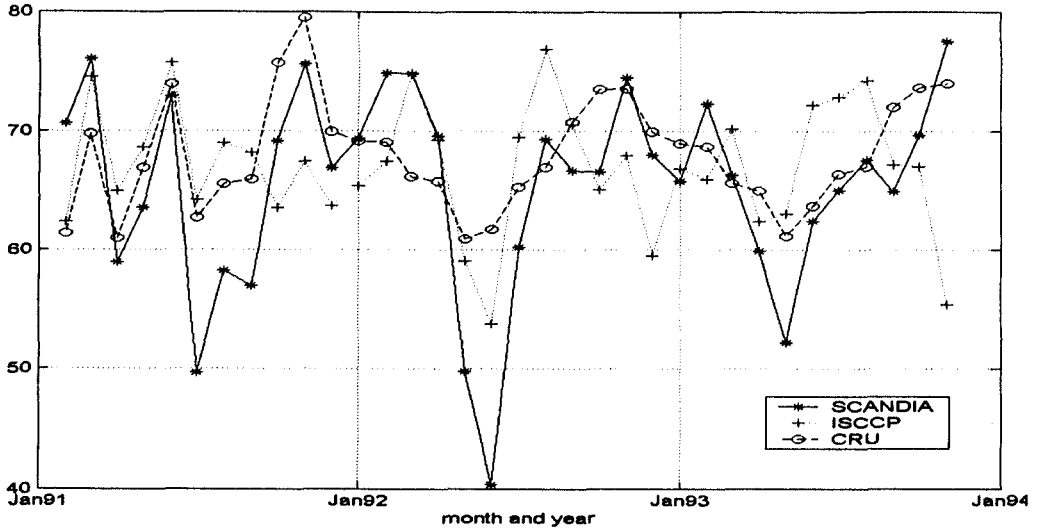

Figure 5 *Plot of monthly mean of cloud cover (%) over SCANDIA land points for SCANDIA (solid), the ISCCP D2 dataset (dotted) and the CRU data set (dashed) for the period February 1991 until November 1993.*

The NOAA AVHRR cloud climatology over the Scandinavian region was found to reproduce surface observed cloud climatology within +/- 5 % during all seasons except in winter. As for the SYNOP climatology, no particular trend in cloudiness could be seen over the period. A minimum in cloudiness was indicated in the middle of the period but this was partly exaggerated in the satellite data set due to problems with an inadequate compensation for the degradation of the visible AVHRR channels on the NOAA-12 satellite.

Comparisons with the CRU and ISCCP D2 data sets gave good agreement but SCANDIA showed generally lower cloud amounts in the summer season than the other data sets.

The future use of the SCANDIA cloud climatology will mainly be as a tool for validation of cloud information in climate simulation models (see Jones and Willén, 2001). The data set could be a valuable contribution to the BALTEX (Rashcke et al., 2001) and CLIWANET projects aimed for studies of the water and energy cycle of the Baltic Sea. Results from an improved cloud classification model have recently been compiled within the CLIWANET project (Dybbroe, 2001) and some preliminary results over the entire Baltic Sea drainage area are shown in Figure 2.

6 ACKNOWLEDGEMENTS

This work was sponsored by the Swedish National Space Board under contracts Dnr 59/95, Dnr 113/96 and Dnr 152/98.

7 REFERENCES

Dybbroe, A., Thoss, A. and Karlsson, K.-G., 2001: Mean cloudiness derived from satellite data over the Baltic Sea drainage basin during CLIWA-NET campaigns, To appear in *Proc of 3rd Study Conference on BALTEX, Mariehamn, Finland, 2-4 July, 2001.*

Dybbroe, A., Thoss, A. and Karlsson, K.-G., 2000: The AVHRR & AMSU products of the Nowcasting SAF, *Proc. 2000 EUMETSAT Meteorological Satellite Data Users' Conference, Bologna, Italy, 29 May–2 June 2000,* EUMETSAT, EUM P 29,729-736.

Jones, C. and Willén, U., 2001: The diurnal cycle of clouds and precipitation, To appear in *Proc of 3rd Study Conference on BALTEX, Mariehamn, Finland, 2-4 July, 2001.*

Karlsson, K.-G., 1996: Cloud classifications with the SCANDIA model, SMHI Reports on Meteorology and Climatology, No. 67, 36 pp. (Available from SMHI)

Karlsson, K.-G., 1997: Cloud climate investigations in the Nordic region using NOAA AVHRR data, *Theor. Appl. Climatol.*, **57**, 181-195.

Karlsson, K.-G., 2001: A NOAA AVHRR cloud climatology over Scandinavia covering the period 1991-2000, SMHI Reports on Meteorology and Climatology, No. 67, 36 pp. (Available from SMHI)

New, M., Hulme, M. and Jones, P., 2000: Representing twentieth-century space-time climate variability. Part II: Development of 1901-96 monthly grids of terrestrial surface climate, *J. Climate,* **13**, 2217-2238.

E. Raschke, J. Meywerk, K. Warrach, U. Andrae, S. Bergström, F. Beyrich, F. Bosveld, C. Fortelius, L.P. Graham, S.-E. Gryning, S. Halldin, L. Hasse, M. Heikinheimo, H.-J. Isemer, D. Jacob, I. Jauja, K.-G. Karlsson, S. Keevallik, J. Koistinen, A. van Lammeren, U. Lass, J. Launiainen, A. Lehmann, B. Liljebladh, M. Lobmeyr, W. Matthäus, T. Mengelkamp, D. B. Michelson, J. Napiórkowski, A. Omstedt, J. Piechura, B. Rockel, F. Rubel, E. Ruprecht, A.-S. Smedman, A. Stigebrandt (2001) BALTEX (Baltic Sea Experiment): A European Contribution to Investigate the Energy and Water Cycle over a Large Drainage Basin, in press, to appear in *Bull. Amer. Meteor. Soc.*

Rossow, W. B. and Schiffer, R. A., 1999: Advances in understanding clouds from ISCCP, *Bull. Amer. Meteor. Soc.*, 80, 2261-2287.

P2.12 INITIATION OF A HIGH RESOLUTION TROPICAL CLOUD CLIMATOLOGY

Mary Bedrick*, Kirk Swanson**, Lynn Rose, Brian Morrison
Aeromet, Inc.

1. INTRODUCTION

Clouds play an important role in the tropics. Globally, high clouds have two effects on the global radiation budget. They reflect solar radiation and absorb and re-radiate terrestrial radiation. Deep convective clouds act to affect the temperature profile of the atmosphere through diabatic processes.

Several global cirrus climatologies have been composed (e.g. Wylie et al., 1994, and Wylie and Menzel, 1999) using National Oceanic and Atmospheric Administration (NOAA) polar-orbiting satellite High Resolution Infrared Radiation Sounder (HIRS) multispectral data. Global cloud cover is detected by a Carbon Dioxide (CO_2) slicing method. The algorithms calculate cloud top pressures and emissivity from radiative transfer principles. For these climatologies, information was sampled only from every third Field of View (FOV) with a zenith angle less than 10° from every third line of data. This represents less than 2% of the total data available.

Since October 1999, NOAA polar-orbiting HIRS multispectral data have been archived from Kwajalein, Republic of the Marshall Islands (RMI) (Table 1). The number of passes greatly decreased when NOAA-12 HIRS data became unavailable. Cloud occurrence, height, and effective emissivity are determined through CO_2 slicing techniques for the area between 5°S and 30°N, 155°E and the international date line. Unlike previous global climatologies, this tropical study uses data from every available FOV for NOAA-12 and -14.

2. DATA AND METHODS

Daily passes are collected, processed and archived. Archived data is divided into morning and evening cycles, which is further divided into different layers for the heights of the calculated cloud tops. Low clouds extend from 1000 to 700 hPa (near the surface to 3 km), medium clouds from 700 to 400 hPa (3 to 9.5 km), and high clouds exist above 400 hPa (9.5 km). The choices for the different levels of clouds is rather arbitrary because a very robust cumulonimbus cloud would be placed in the high cloud group, although most of its characteristics are that of low and medium altitude clouds. Morning and evening passes are also grouped together and counted in a total cloud count cycle.

Each cycle also has a grid of data that has been calculated as clear. Each cloud layer is sub-divided into thickness categories: Thin, Thick and Opaque. Calculated emissivity values range between 0.0 (fully clear) and 1.0 (fully opaque). Thin clouds are defined as those with emissivity values less than 0.5, while Thick clouds have emissivity values between 0.5 and 0.95. Opaque clouds are defined as those with emissivity values greater than 0.95. These data are stored in ¼° latitude-longitude grid squares. Total counts of clouds are stored at each grid point. Since the CO_2 algorithms detect clouds from the top layer towards the surface of the earth, only the first encountered layer of cloud top heights are processed. The data set is, in this sense, biased toward the higher clouds.

In this paper, only daily total results of all high, medium, low and all clouds will be evaluated. Time of day and cloud opacity are not taken into consideration in this portion of the study. Since the traditional climatological four seasons does not apply to Kwajalein's tropical location, the data for each level is divided into two seasons. The high wind (low precipitation) season extends from December through May. The low wind (high precipitation) season runs from June through November.

TABLE 1. Number of passes archived from Kwajalein, RMI.

Month	Number of passes
October, 1999	117
November, 1999	127
December, 1999	183
January, 2000	147
February, 2000	146
March, 2000	140
April, 2000	141
May, 2000	187
June, 2000	124
July, 2000	143
August, 2000	144
September, 2000	153
October, 2000	140
November, 2000	138
December, 2000	113
January, 2001	92
February, 2001	73
March, 2001	40
April, 2001	48

3. PRELIMINARY RESULTS

Initial results of the climatology show interesting features for the high wind season (Figure 1a) and low wind season (Figure 2a). The maximum in total observed clouds is found between the equator and 10°N for both season, but the maximum is located more

*Corresponding author: Mary Bedrick, Aeromet, Inc., P.O. Box 701767, Tulsa OK 74170-1767; e-mail: maryb@aeromet.com
**Current affiliation: Architecture Technology Corp.

poleward and over a broader region during the low wind season. A second maxima in clouds looks to start near 5°S with a relative minima near the equator in all seasons. In the high wind season, another maxima in total clouds is seen in the northern portion of the domain. The relative lack of clouds found between 10° and 25° N in the high wind season hints at the position and intensity of the subtropical high.

A majority of the total observed clouds are in the high cloud group. This is not surprising because of the CO_2 slicing algorithm's top down cloud finding approach. There does appear to be a "sloshing" of the concentration of high clouds from the western portion of the domain to the center of the domain from the high wind season (Figure 1b) to the low wind season (Figure 2b).

Part of this "sloshing" effect may be a residual of our choice for groupings of high clouds. In the high wind season just to the east of the cloud maxima along 5°N, there is a maxima in the medium cloud group (Figure 1c). A similar but less pronounced pattern can be seen in the low wind season middle cloud group (Figure 2c). It appears that a majority of the total cloud maxima found at the northern part of the domain during the fast wind months is due to medium layer clouds.

The highest concentration of low clouds is found outside of the regions of high concentrations of medium, and high level clouds. In the high wind season (Figure 1d) low level clouds are concentrated between 10° and 25°N. In the low wind season (Figure 2d), most low levels clouds are found between 15°N and the northern portion of the domain. Interestingly, more low cloud tops are detected in both seasons (and every individual month) than medium cloud tops.

4. DISCUSSION

Many of the features presented in this study can be correlated with known meteorological features. The broad band of clouds and its movement between the equator and 15°N can be associated with the intertropical convergence zone and its movements. There are hints of a second cloud band in the southern hemisphere from this climatology. The maxima in clouds located in the northern portion of the domain during the high wind season can be correlated to the movement of mid-latitude cold fronts into sub-tropical regions during the cold months. This is supported by the presence of more medium and low-level clouds in these maxima, which would correspond to the stratus type clouds often associated with cold fronts.

The preliminary results of this 19-month study compare well to the Wisconsin HIRS 6.5 Year Global Cloud Climatology prepared by Don Wylie (http://www.ssec.wisc.edu/~donw/PAGE/CLIMATE.HTM). The 6.5 year climatology also has the movement of total cloud concentrations poleward in our domain area in the low wind season and broadening of the maximum region. It also shows the encroachment from mid-latitude systems in winter months into the northern part of our domain. The 6.5 year climatology does not show the bi-model equatorial cloud band seen in this study. This difference could be due to either our small number of months or to the higher resolution of our data set

This paper presents the preliminary data gathered in an ongoing climatology. As more data is gathered, it is hoped that annual and seasonal trends will become more apparent. Finer scale features will be available from this data set as compared to the current global cloud climatologies. Soon, cloud height data from NOAA-16 will be added to the study. The paucity of data in the medium cloud layer will be investigated. Since the problem may come from the definitions of cloud heights, the separation of clouds into different layers will also be examined. The problem may actually be that too many cloud free grid points are being classified as containing low-level clouds. This could be caused by poorly initiating low level temperature profiles (sea surface temperatures).

Acknowledgements: The authors would like to thank Don Wylie for his CO_2 slicing code and for his helpful discussions on the procedures used for the analyses.

5. REFERENCES

Wylie, D. P., and W. P. Menzel, 1999: Eight years of high cloud statistics using HIRS, *J. Climate*, **12**, 170-184.

____, ____, H. M. Woolf, and K. I. Strabala, 1994: Four years of global cirrus cloud statistics using HIRS, *J. Climate*, **7**, 1972-1986.

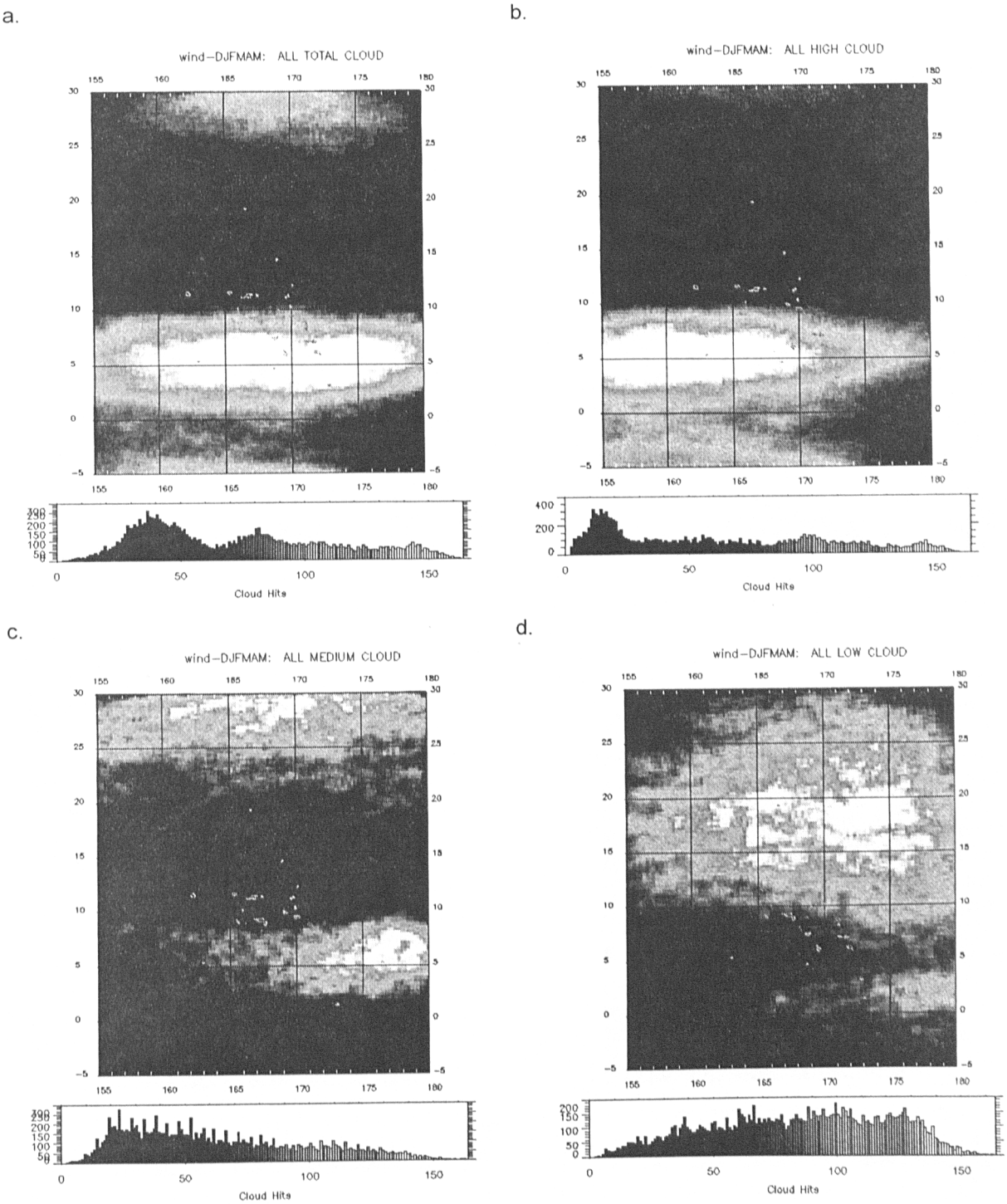

FIGURE 1: Plots of cloud counts for the high wind (DJFMAM) season with histograms of the number of ¼° by ¼° latitude-longitude bins with a particular number of cloud counts for a. all clouds, b. all high clouds (>400 hPa), c. all medium clouds (400 – 700 hPa), and d. all low clouds (<700 hPa).

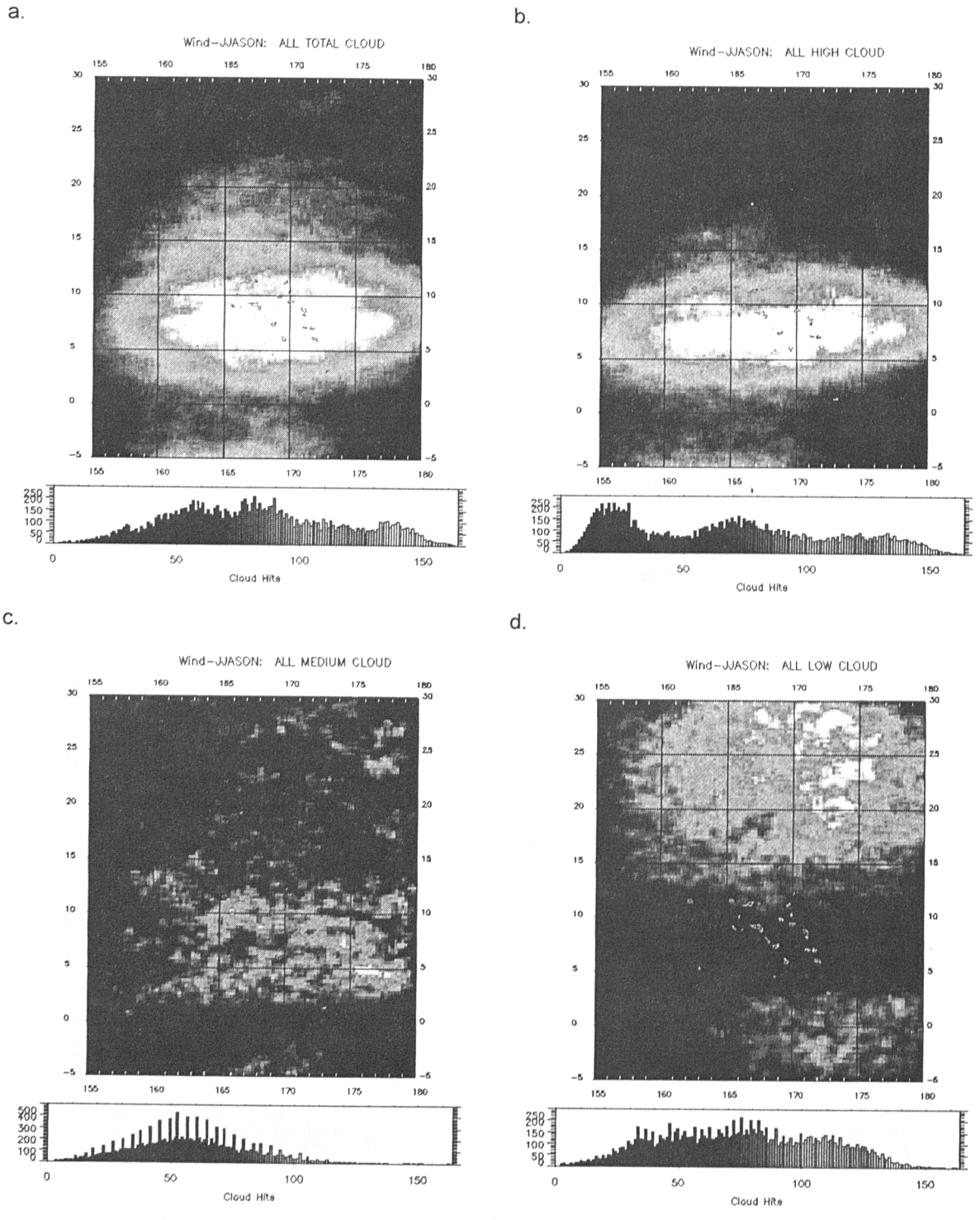

FIGURE 2: Same as Figure 1 except for the low wind (JJASON) season.

P2.13

AN ANALYSIS OF CLOUD AND RAINFALL DISTRIBUTIONS OVER DEFORESTED AMAZONIA USING TRMM AND GOES MEASUREMENTS

Frédéric J. Chagnon *[1], Andrew J. Negri [2], Jingfeng Wang [1], Liming Xu [2], Robert M. Adler [2], and Rafael L. Bras [1]

[1]Ralph M. Parsons Laboratory, M.I.T. [2] NASA Goddard Space Flight Center

1 INTRODUCTION

The advent of remote sensing in hydrology presents great opportunities to further our knowledge and understanding of the Earth's dynamic natural system. One such area of interest is the impact of tropical deforestation on global and regional climatic circulation. In this paper, we use data from the Tropical Rainfall Measuring Mission (TRMM) and Geostationary Operational Environmental Satellite (GOES) to study precipitation intensity and shallow cloud patterns over Amazonia under the current state of deforestation.

Recent studies on the impact of large-scale deforestation on climate in the Amazon basin have demonstrated the importance that such land-use changes have on the regional and global scales. General Circulation Model (GCM) simulation results of Amazonian deforestation undertaken by Salati *et al.* (1991) suggested that the equilibrium climate for grassy vegetation in Amazonia would be one of significantly reduced precipitation. Using GCM simulations, Nobre *et al.* (1991) found that when the Amazonian tropical forest was replaced by pasture, there was a significant increase in the mean surface temperature (~2.5°C), and decreases in the annual evapotranspiration (30%), precipitation (25%) and runoff (20%). The relative decreases in the latter three variables indicated a decrease in the regional moisture convergence. The simulations of Nobre *et al.* (1991) showed that the greatest differences occurred during the dry season. A large-scale (~2,500 km) simulation of the response of the tropical atmosphere to deforestation undertaken by Eltahir & Bras (1993a) also showed an increase in mean surface temperature and a decrease in precipitation. These results, it was discussed, are competitive, and hence make predictions of resulting runoff highly sensitive to their relative scales.

*Corresponding author address: Frédéric J. Chagnon, Mass. Inst. of Tech., Dept. of Civil & Environmental Engineering, Cambridge, MA 02139; email: frederic@mit.edu

McGuffie *et al.* (1995) studied the global-scale climate sensitivity to tropical deforestation using a modified version of the NCAR Community Climate Model coupled with a land-surface hydrology scheme (the Biosphere Atmosphere Transfer Scheme, BATS). Their experiment consisted of replacing the tropical forest in the Amazon, S.E. Asia and tropical Africa with grassland. Their results in Amazonia showed marked decreases in precipitation, evaporation and moisture convergence. They also showed that tropical deforestation impacted the Asian monsoon, as well as climate in the middle and high latitudes.

Recently, studies have been undertaken on the impacts of deforestation on climatic circulation at regional and local scales. A numerical mesoscale circulation model (Penn State/NCAR MM4) was used in conjunction with BATS to study the sensitivity of climate to deforestation at the regional scale (~250 km.) New parameterizations for rainfall interception and rainfall spatial coverage were developed to aid this study, and are described by Eltahir & Bras (1993b,c.) The modeling exercises of this study showed a decrease in net surface radiation, evaporation and rainfall, and an increase in surface temperature. The model results concurred with observed net radiation over forested and deforested areas (Eltathir & Bras, 1994.)

Looking at the local impacts of land-use change, Rabin *et al.* (1990) used GOES visible and infrared images over Oklahoma and observed that, under weak synoptic forcing, clouds formed earlier over mesoscale-sized areas of harvested wheat than over the actively growing vegetation of adjacent areas. They also observed that shallow clouds were suppressed downwind of small human-made lakes and over areas dominated by heavy tree cover. Following this study, Cutrim *et al.* (1995) a cumulus cloud recognition algorithm that uses GOES visible and infrared image pairs, and applied it twice-daily over Amazonia during August 1988. They found an enhanced frequency of afternoon cumulus clouds over

areas where the forest had been cleared.
Rabin *et al.* (1996) used the same cumulus recognition algorithm as the previous paper to study the frequency of cumulus clouds over the central United States for two periods: July 1988, which was a drought year, and July 1987, which is the control. The observed that cumulus clouds occurred more often over lightly vegetated than heavily vegetated surfaces in southern and central Illinois.
The impact of observed deforestation at local scales (~10 km) on the spatial distribution of rainfall and clouds was studied using the Penn State/NCAR MM5 numerical weather model to a sub-region of Rondonia (Wang *et al.*, 2000.) Synoptic forcing was shown to dominate mesoscale circulation during the wet season (December - April). However, during the dry season (May - August) and the break-period (September - November), mesoscale circulation had an impact over the deforested area. An enhancement in low-level clouds was seen, although there was little or no effect on rainfall amounts.

2 OBJECTIVES

The objectives of this study are to determine and quantify the local effect of deforestation on shallow cumulus and rainfall intensity climatologies in the Amazon basin. The goal is to quantitatively validate past observational and numerical studies.

3 DATA & PROCESSING

For this study, shallow cumulus cloud maps are produced three-times daily over the Amazon basin. The shallow cumulus were detected using a modified version of the algorithm first developed by Cutrim *et al.* (1995). The algorithm employs a series of thresholds which must all be met to determine whether a pixel is occupied by a shallow cumulus. Table 1 presents the state that is determined by the threshold, the parameter on which the threshold is applied, and the threshold values.
Rainfall intensities are derived 48 times daily using the Convective Stratiform Technique (CST) with GOES infrared images. The derived rain rates are calibrated a priori with rainrates derived from four months of TRMM Microwave Imager (TMI) data. The reader is referred to Negri *et al.* (2001) for a more detailed treatment of the rainfall intensity retrieval process.

Table 1: Shallow Cloud Detection Algorithm

	Land vs. Cloud	Deep vs. Shallow	Stratus vs. Cumulus	Association to Deep Convection
Parameter	Relative Albedo (%)	Infrared Temperature (K)	Albedo Contrast (%)	Proximity to Deep Convection (km)
Low Threshold	20	280	10	8
High Threshold	100	330	100	N/A

4 PRELIMINARY RESULTS

Shallow cumuli and rainfall intensities were studied over two regions of 200 km to the side. These regions are characterized by a strong contrast in land surface cover: the contrast in one is between the Amazon river and tropical forest, while the other shows a long strip of deforested land flanked by dense tropical forest. Both regions are void of topographical features.
The probability that the shallow cloud density over the forest exceeds that over the contrasting land cover was computed for each month. A Monte-Carlo simulation of a completely spatially random (CSR) cloud field was used to determine the statistical significance of the difference in cloud densities observed over contrasting land surface covers. Figure 1 shows that the difference in shallow cumulus density over the river/forest contrast is statistically significant to a level of 95% for all months studied, whereas that difference is significant only for the month of November 2000 over the region characterized by the forest/deforest contrast. NCEP/NCAR re-analyses were used to study the synoptic meteorological conditions during days of high cloud density contrast (i.e. contrast values that exceed the mean monthly contrast by one standard deviation), and it is observed that the mean mid and lower level winds are significantly weaker when a high contrast in cloud density over differeing land covers is observed (see Figure 2.)

5 PRELIMINARY CONCLUSIONS

The preliminary analyses of shallow clouds over the Amazon basin demonstrates that land cover significantly affects shallow convection. The mean monthly cloud cover density over the surface characterized by water (the Amazon river) is significantly lower than over Forest for all months studied. The mean monthly cloud cover density over the deforested surface is significantly higher than over the forest for the

Figure 1: Probability that Cloud Density over Deforest/River Exceeds/Lags that over Forest

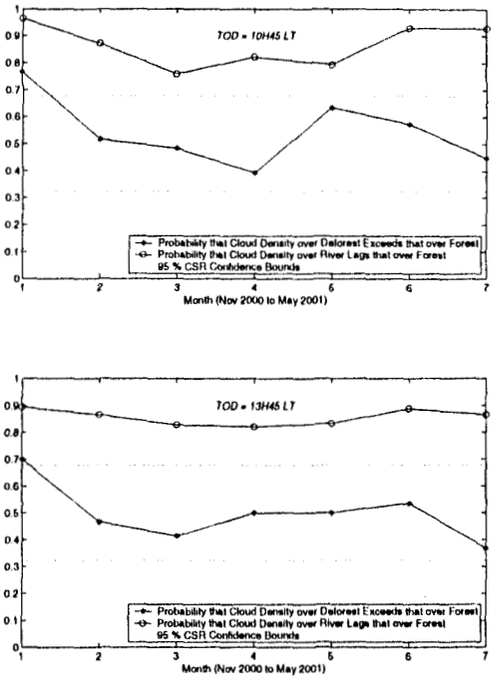

Figure 2: Mean Monthly Wind Speeds: Periods of High vs. Low Cloud Density Contrast

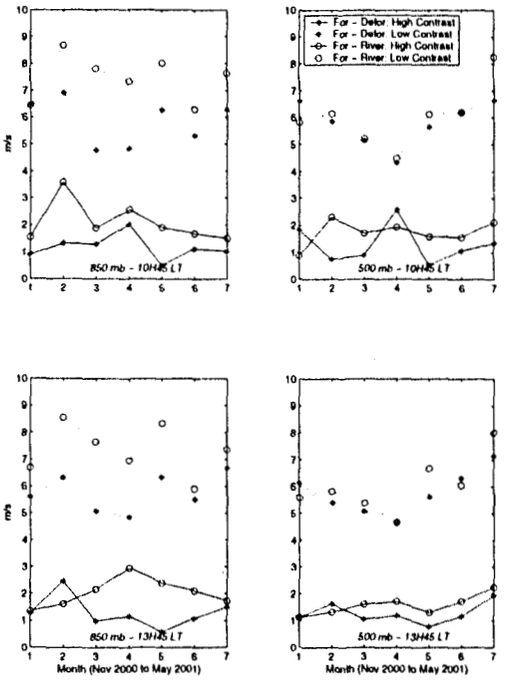

month of November 2000, which is the "break period" between the dry and wet seasons, and is characterized by weak synoptic flow. It is also observed that the higher contrasts in cloud cover densities occur when the mid and lower levels winds are weak.

6 ON-GOING WORK

The process of analyzing GOES data and producing shallow cloud maps over the amazon is on-going. A lenghtier climatology of the shallow clouds will improve our understanding of the impacts of land cover change on local atmospheric circulation under differing synoptic condidtions.

Instantaneous rainrates derived half-hourly (Negri *et al.*, 2001) are being studied over the same two regions in the Amazon to determine whether there is a statistically significant impact of the land cover on rainfall.

Acknowledgements: This work was supported by the NASA TRMM project under grant NAG5-3726.

7 REFERENCES

[1] Cutrim, E., D. W. Martin, and R. Rabin, 1995: Enhancement of cumulus clouds over deforested lands in Amazonia, Bull. Amer. Meteor. Soc., **76**, 1801-1805.

[2] Eltahir, E. A. B., and R. L. Bras, 1994: Sensitivity of Regional Climate to Deforestation in the Amazon Basin, Advances in Water Resources, **17**, 101-115.

[3] Eltahir, E. A. B., and R. L. Bras, 1993a: Estimation of the fractional Coverage of rainfall in Climate Models, J. Climate, **6**, 639-644.

[4] Eltahir, E. A. B., and R. L. Bras, 1993b: A Description of Rainfall Interception over Large-areas, J. Climate, **6**, 1002-1008.

[5] Eltahir, E. A. B., and R. L. Bras, 1993c: On the Response of the Tropical Atmosphere to Large-scale Deforestation, Quart. J. Roy. Meteor. Soc., **119**, 779-793.

[6] McGuffie, K., A. Hendersonsellers, H. Zhang, T. B. Durbridge, and A. J. Pitman, 1995: Global Climate Sensitivity to Tropical Deforestation, Global and Planetary Change, **10**, 97-128.

[7] Negri, A. J., L. Xu, and R. M. Adler, 2001: ,J. Geophys. Res., in press.
[8] Nobre, C. A., P. J. Sellers, and J. Shukla, 1991: Amazonian Deforestation and Regional Climate Change, J. Climate, **4**, 957-988.
[9] Rabin, R. M., S. Stadler, P. J. Wetzel, D. J. Stensrud, and M. Gregory, 1990: Observed effects of landscape variability on convective clouds, Bull. Amer. Meteor. Soc., **71**, 272-280.
[10] Rabin, R. M., and D. W. Martin, 1996: Satellite observations of shallow cumulus coverage over the central United States: an exploration of land use impact on cloud cover, J. Geophys. Res., **101**, 7149-7155.
[11] Salati, E., and C. A. Nobre, 1991: Possible Climatic Impacts of Tropical Deforestation, Climatic Change, **19**, 177-196.
[12] Wang, J., R. L. Bras, and E. A. B. Eltahir, 2000: The Impact of Observed Deforestation on the Mesoscale Distribution of Rainfall and Clouds in Amazonia, J. Hydrometeorology, **1**, 267-287.

P2.14 MESOSCALE SATELLITE CLIMATOLOGIES IN COSTA RICA

Bernadette H. Connell*
Cooperative Institute for Research in the Atmosphere (CIRA)
Colorado State University, Fort Collins, Colorado

Vilma Castro Leon
Universidad de Costa Rica
San José, Costa Rica

1. INTRODUCTION

Costa Rica is a small tropical country with an area of approximately 50,200 sq. km centered at 10 deg N. Latitude and 84 deg. W. Longitude. Four mountain ranges run from the northwest to the southeast across the center of the country separating the Altantic and Pacific regions. The Cordillera de Guanacaste and Cordillera de Tilaran to the northwest attain average heights of 1000-1500 m with a few peaks reaching 1900 m, while the central and southeastern mountains (Cordillera Central and Cordilla de Talamanca) attain average heights of 2000 – 3000 m with many peaks reaching 3300 to 3800 m. See Figure 1 for a topography map of the area. The drier season in Costa Rica is generally acknowledged to extend from December to April with the wetter season extending from May through November (Chacón and Fernández 1985, Fernández et al. 1996). However, the extent of the seasons and the precipitation measured in various parts of the country can vary considerably due to significant terrain interaction.

The studies by Chacon and Fernández (1985) and Fernández et al. (1996) have used rain gage information to look at the rainfall distribution with altitude for a river basin on the Atlantic side of Costa Rica and for a southwest-northeast cross section across the country. Both these studies were conducted in a part of the country with the highest mountains. Their findings show that there is a large variation of rainfall with height and that the rainfall maxima occur at intermediate altitudes rather than on mountaintops. Chacón and Fernández (1985) descriptively differentiate between orographic and convective rains by their duration and intensity. The convective rain is of short duration (1 to 6 hours), of great intensity, and occurs more often during the wetter season. The orographic rain occurs mainly during the dry season, lasts for several days (1 to 5 days) and is of low intensity. Chacón and Fernández (1985) do point out that orographic rain is convective in the initial stages.

Studies conducted in conjunction with ecosystem research at the Monteverde Cloud Forest Preserve in the Cordilla de Tilaran have measured precipitation with a standard rain gage at an elevation of 1480 m (Clark et al. 2000). Annual precipitation collected in 1991-92 was 3192 mm. An additional 886 mm or 22% of hydrologic inputs was collected with a cloud water collector used to simulate wind-driven precipitation.

Each of the orographic, convective or wind-driven inputs is important in quantifying the totoal hydrologic inputs, especially in a country that relies on hydroelectric power. Knowing the amount and duration of orographic and convective precipitation is also important for predicting flash flood potential. Although cloud frequency composites do not directly provide rainfall information, they can provide a broader picture of the types and distribution of clouds and their variations from one season to the next and one year to the next. The results presented here take a preliminary look at these variations.

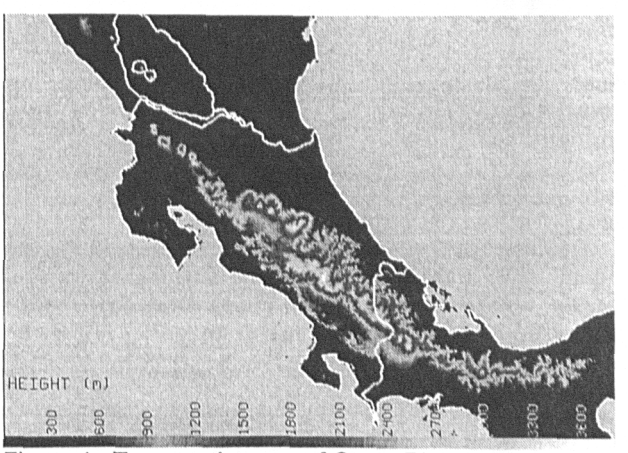

Figure 1. Topography map of Costa Rica.

2. DATA

Hourly GOES-8 full resolution visible imagery (1 km) centered over Costa Rica were used to look at cloud frequency distribution for the drier months of January, and February of 1998 – 1999. Most of the rain processes during these months result from cold air outbreaks from North America and upper tropospheric troughs in the midlatitude westerlies that propulgate into

*Corresponding author address: Bernadette Connell, CIRA, CIRA Bldg., W. La Porte Ave., Colorado State University, Fort Collins, CO 80523-1375; e-mail: connell@cira.colostate.edu

Central America and interact with the topography of the region (Fernández et al. 1996) The observed cloud types appear as stratus and small cumulus. The cloud top temperatures are often above freezing and are difficult to detect from background mountain surface temperatures in the 10.7 μm imagery. Smaller clouds are more readily detected in the 1 km higher resolution visible imagery than in the 4 km resolution 10.7 μm imagery.

Infrared imagery (10.7 μm) were used to look at cloud frequency distribution during the wetter months of June and July 1998 – 1999. Most of the rain processes during these months are a result of the influence of the Intertropical Convergence Zone, or interaction with easterly waves and tropical cyclones (Fernández el al. 1996). The deep convective cloud type dominates during this period. Visible imagery were not used because of problems with sun glint and also because cloud cover often reaches 100% in the afternoon over much of the study area.

The imagery were collected and archived at the Cooperative Institute for Research in the Atmosphere (CIRA). Image processing and analysis was done on Personal Computers with the Man Computer Interactive Data and Analysis System (McIDAS) software. McIDAS is the software backbone for the RAMM Advanced Demonstration and Interpretation System (RAMSDIS) which has been demonstrated at several National Weather Service (NWS) Offices.

After checking for correct navigation cloud/no cloud image products were created. The visible product was created by a threshold technique in which a background cloud-free image is compared with a normal visible scene to discriminate between cloudy and cloud-free areas (Reinke et al. 1992, Connell el al. 2001). The infrared product was created by a simpler threshold technique that utilizes the brightness temperature to distinguish between cloudy and cloud-free regions. A threshold of 273 K was used to capture as many high and low level clouds as possible. Both the visible and infrared threshold techniques do not distinguish between low or high level clouds, or type of cloud such as convective or stratiform.

The compositing was done hour by hour for each month. Hours 1415 UTC – 2115 UTC were processed for the visible imagery, while hours 0015-2315 were processed for the 10.7 μm infrared imagery. For each hour, the number of pixels containing clouds is summed on a pixel by pixel basis, divided by the total number of days and then multiplied by 100 to obtain the cloud frequency. The output is then placed into a digital image and stretched between 50 and 250 brightness counts.

3. RESULTS

Visible cloud frequency composites for the months of January and February for 1998 and 1999 are shown in Figure 2. During these months in 1998, an El Niño event was occurring. During 1999, La Niña was building. From the images in Figure 2, the strong influence of the mountains in the formation of clouds is readily apparent. Notice in January and February of 1998, mountains higher than 2500 m (in the center of the country) distinctly show 20 – 40% less cloud cover than regions between 1000 and 2500 m in elevation. Data for 1999 show similar patterns but with higher cloud frequencies in many mountainous regions, and with higher frequencies along the Atlantic side of Costa Rica.

The northwest part of Costa Rica (on the Pacific side of the mountains) shows lower cloud frequency in both January and February for 1998 and 1999. This is a common occurrence during the dry season.

Although the data are not presented here, cloud frequencies derived by infrared threshold technique for 273 K, show less than 10% cloud frequency for January 1998, less than 20% cloud frequency for February 1998 and January 1999, and less than 35% cloud frequency for February 1999. The 4 km infrared cloud frequencies also do not show the detail that can be seen in the 1 km cloud frequencies.

Infrared cloud frequencies by temperature threshold for cloud tops colder than 273 K are shown in Figure 3 for June and July, 1998 and 1999, for Costa Rica and the surrounding countries. June is typically wetter over many parts of Costa Rica than July. This is more readily seen in 1999 than in 1998. It is believed that the El Niño influence in 1998 delayed the start of the rainy season. Data for May 1998 (not shown) also shows lower cloud frequencies than other years.

Because the infrared data are at a courser resolution than the visible imagery, small clouds are not readily detected. The infrared imagery however, has the advantage of use both during the day and at night. Although the monthly composites are useful to show regional scale variations, diurnal composites are also helpful to indicate preferred regions of cloud formation throughout the day. Figure 4 shows a morning hourly composite for 1515 UTC for June 1999. It shows that cloud frequency is concentrated along the Atlantic coast at this time. In contrast, later in the day at 0115 UTC, cloud frequency is concentrated over the mountains and along the Pacific coast. While these generalizations in the relative placement of clouds for the region during this month are not new, the details on the seasonal, monthly, and annual variations will add new information in analyzing the rainfall patterns for the region.

4. CONCLUDING REMARKS

The preliminary results show that using both high (spatial) resolution visible and infrared imagery at high temporal resolution will significantly add to the understanding of the observed rainfall patterns in Costa Rica and the surrounding region. Further study of the monthly, seasonal, and annual variations in association with changes in parameters such as sea surface temperature will lead to a better understanding of impacts of weather occurrences such as El Niño and La Niña on the region.

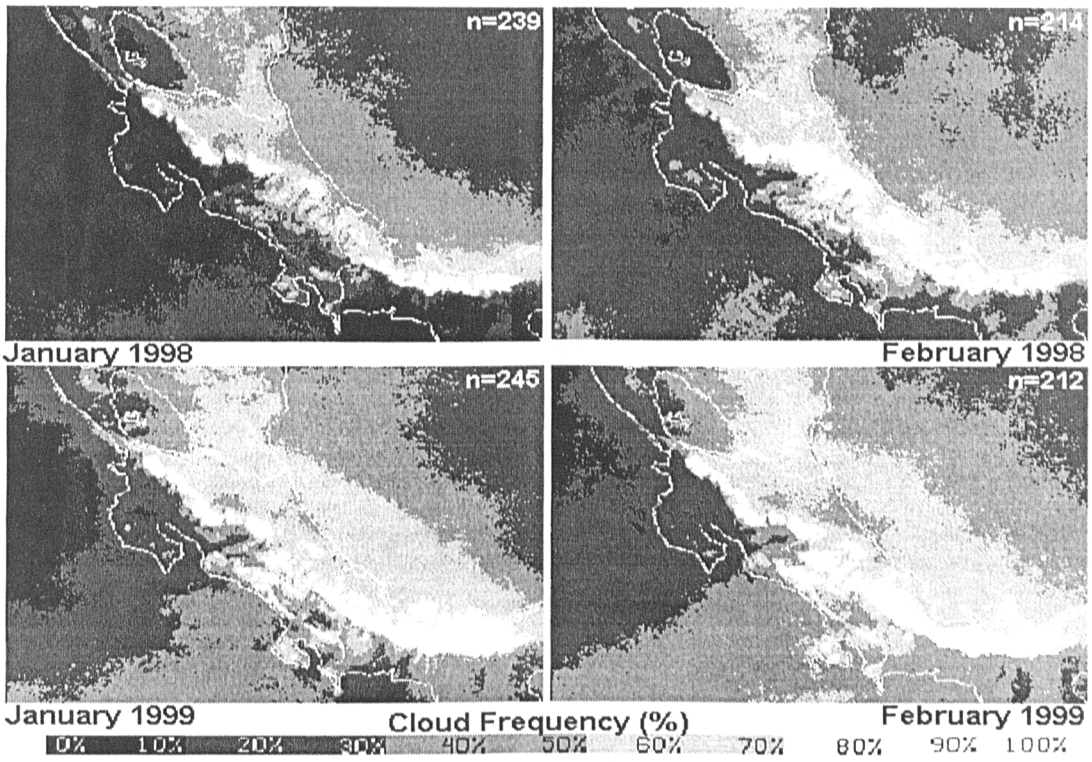

Figure 2: GOES-8 monthly visible cloud frequency composites for January and February, 1998 and 1999, centered over Costa Rica. Data are composited for 1415 –2214 UTC. (n=sample size)

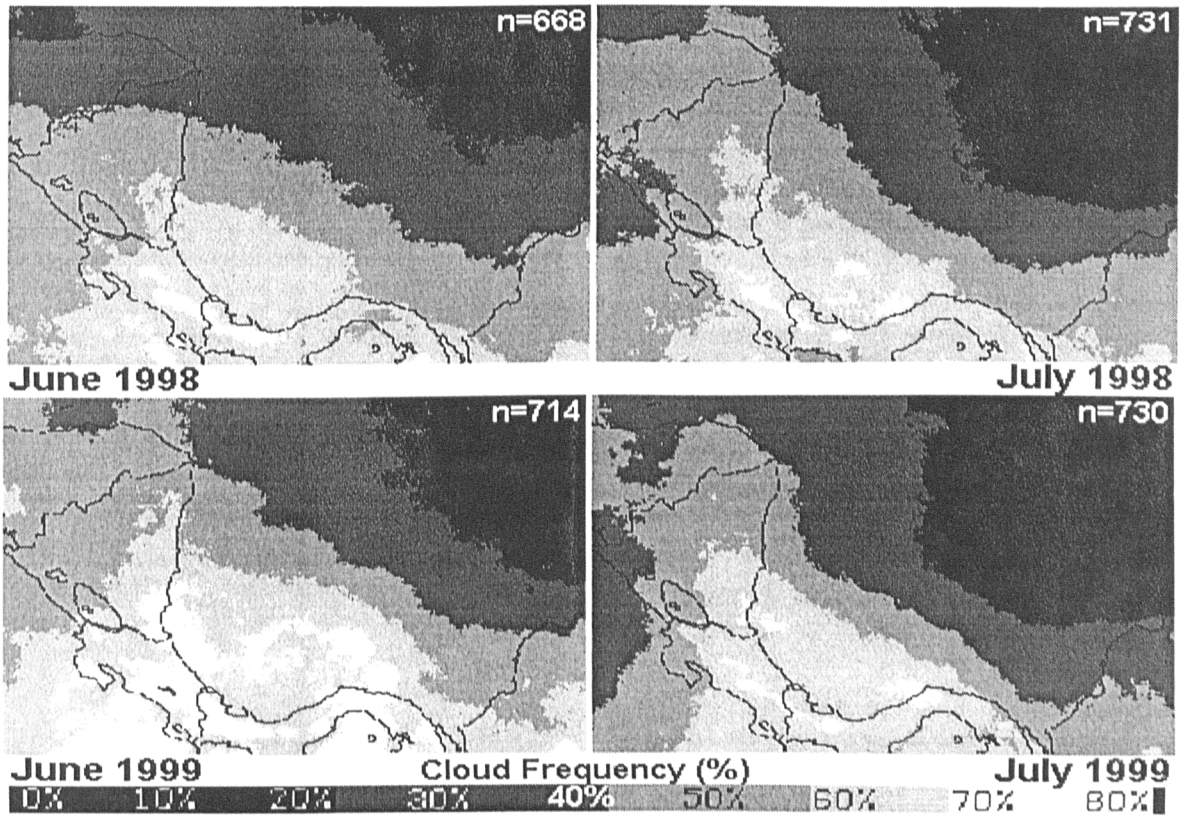

Figure 3. GOES-8 infrared cloud frequency composites (temperature threshold = 273 K) for June and July, 1998 and 1999 for Costa Rica and the surrounding countries. Data are composited for 0015 – 2315 UTC. (n= sample size)

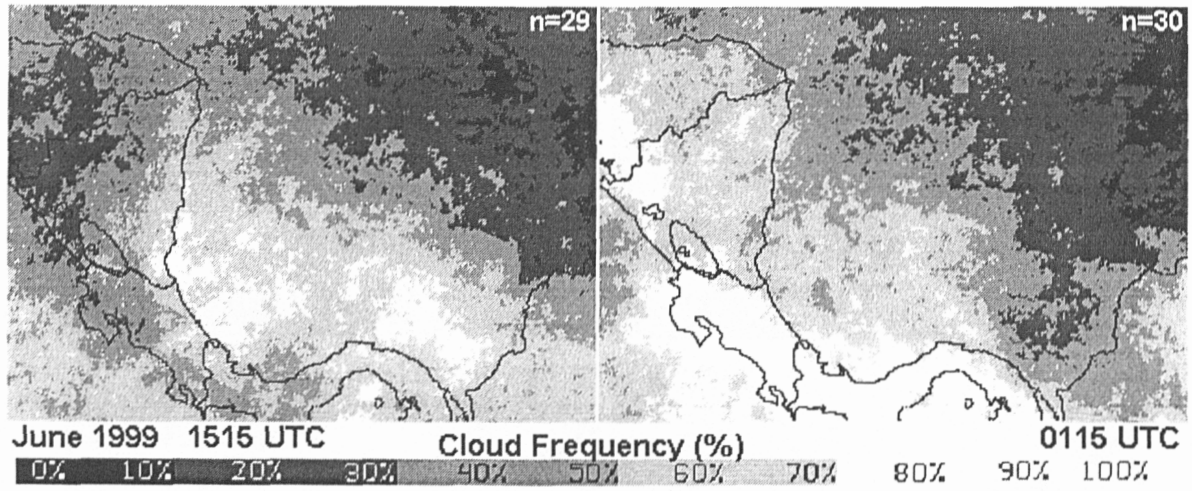

Figure 4. GOES-8 infrared cloud frequency composites (threshold temperature = 273 K) for hours 1515 and 0115 UTC in June 1999. (n=sample size)

5. ACKNOWLEDGMENTS

This work is supported by NOAA Grant NA67RJ0152.

6. REFERENCES

Chacón, R. E. and W. Fernández, 1985. Temporal and spatial rainfall variability in the mountainous region of the Reventazón River basin, Costa Rica. *J. Climatol*, **5**, 175-188.

Clark, K. L., R. O. Lawton, and P. R. Butler, 2000. The Physical Environment. *Monteverde Ecology and Conservation of a Tropical Cloud Forest*, N. M. Nadkarni and N. T. Wheelwright, Eds., Oxford University Press, 15-20.

Connell, B. H., K. J. Gould, and J. F. W. Purdom, 2001. High Resolution GOES-8 Visible and Infrared Cloud Frequency Composites Over Northern Florida During the Summers 1996-1999. accepted for publication in *Weather and Forecasting*.

Fernández, W., R. E. Chacón, J. W. Melgarejo, 1996. On the Rainfall Distribution with Altitude over Costa Rica. *Revista Geofisica*, **44**, 57-72.

Reinke, D. L., C. L. Combs, S. Q. Kidder, and T. H. Vonder Haar, 1992: Satellite Cloud Composite Climatologies: A New High-Resolution Tool in Atmospheric Research and Forecasting. *Bull. Amer. Meteor. Soc.*, **77**, 883-890.

P2.15 PLUMES ABOVE THUNDERSTORM ANVILS AND THEIR CONTRIBUTIONS TO CROSS TROPOPAUSE TRANSPORT OF WATER VAPOR IN MIDLATITUDES

Pao K. Wang*
Department of Atmospheric and Oceanic Sciences
University of Wisconsin-Madison
Madison, WI

1. INTRODUCTION

Water vapor is important to the radiative budget to the atmosphere, and hence to climate studies, because of its strong absorption of infrared (IR) radiation (e.g., *Liou*, 1984; *Goody and Yung*, 1989). It is also the main source of ozone-destroying HO_x radicals in the lower stratosphere. In the condensed phase, as exemplified by the recently observed anvil-top plumes (*Setvak and Doswell*, 1991; *Levizzani and Setvak*, 1996) to be discussed in detail later, it serves as a catalytic surface for heterogeneous reactions involving NO_x and halogen species (e.g., *Solomon*, 1999). It is clear that the distribution of water substance in the upper troposphere/lower stratosphere (UT/LS) region has significant impacts on the global climate process.

In order to assess the impact of water vapor, we need to understand how it is transported in the stratosphere. At present, the global scale transport of water vapor in the lower stratosphere is thought to be due to the *extratropical pumping* mechanism generated by breaking Rossby waves and related potential-vorticity-transporting motions in the midlatitude atmosphere (*Holton et al.*, 1995). In this scenario, the main source of lower stratospheric water vapor is the deep tropical convective clouds that pump water vapor from the troposphere to the stratosphere. Oxidation of methane may represent a minor water vapor source in the lower stratosphere. The tropical stratospheric water vapor is then transported poleward by the midlatitude "pumps" so that the middle and higher latitudes are basically a water vapor sink. However, recent observations suggest that this simple mechanism may be inadequate for explaining finer details of the water vapor transport. For example, aircraft measurements done by *Foot* (1984) over 45-65°N indicated that the midlatitude lower-stratospheric water vapor concentration is much higher than can be explained solely by tropical entry of air. There are also seasonal and hemispheric variations of lower-stratospheric water vapor that cannot be explained by the mean circulation scenario alone. Also, results of ER-2 research aircrafts measurements during the Airborne Antarctic Ozone Experiment (AAOE) and the Airborne Arctic Stratospheric Expedition (AASE) showed that the wintertime water vapor fields in the lower stratosphere display a hemispheric asymmetry, with much lower early spring values in the southern hemisphere (SH) than the northern hemispheric (NH) (*Kelly et al.*, 1990). Export of dehydrated air from the polar vortex was investigated as the possible mechanism for the asymmetry.

Using water vapor data from the Stratospheric Photochemistry, Aerosols and Dynamics Expedition (SPADE), *Hintsa et al.* (1994) found higher water vapor concentration in the NH in fall than in spring. Further analyses of water vapor profile measurements during SPADE (*Dessler et al.*, 1995) show that water vapor mixing ratios in the lowermost stratosphere are consistent with a significant influx of air into the lowermost stratosphere from the extratropical upper troposphere. *Pan et al.* (1997), using Stratospheric Aerosol and Gas Experiment II (SAGE II) data, found a strong seasonal cycle of the water vapor mixing ratio on the 320-K isentropic surface for both hemispheres, with maximum values in summer and minimum values in early spring. By also analyzing SAGE II ozone data, they inferred from both water vapor and ozone data that extratropical UT/LS exchange has a significant influence on the lowermost stratosphere, especially in the NH summer season.

2. SATELLITE OBSERVATIONS OF PLUMES ABOVE THUNDERSTORM ANVILS

* *Corresponding author address*: Pao K. Wang
Department of Atmospheric and Oceanic Sciences
University of Wisconsin-Madison
Madison, WI 53706. Email: Pao@windy.meteor.wisc.edu

The observations mentioned in the preceding section are mainly concerned with stratospheric water vapor measurements but do not pinpoint its possible transport mechanisms. A few other observations, on the other hand, provide some clues. *Roach* (1967) and *Fujita* (1982) pointed out observations of cirrus clouds atop the anvils of some severe thunderstorms, and mentioned that they were produced by collapsing overshooting tops, although the source of water vapor was not clear. More recently, *Setvak and Doswell* (1991) and *Levizzani and Setvak* (1996) reported the observation of plume-like features on top of some convective storms in Advanced Very High Resolution Radiometer (AVHRR) satellite imagery of the US National Oceanographic and Atmospheric Administration (NOAA) polar orbiters. Examples of the anvil-top plumes are shown in Fig. 1. These studies were based on the AVHRR channels 2 (0.625-1.1 μm), 3 (3.55-3.93 μm), and 4 (10.3-11.3 μm) but some visible characteristics in channel 1 (visible) are also included. Some of the major characteristics listed below, based on *Levizzani and Setvak* (1996), are common to all plumes whereas others hold only in specific cases:

(a) A small bright spot in channel 2 a few pixels across, i.e., a few kilometers, in the form of an oval cloud, is detected as the plume's source. The shadow cast by this rounded cloud appears much longer than that of the plume, suggesting a higher altitude. The source spot is normally shifted downwind from the coldest area, and collocated with the storm's embedded warm area.

(b) These cloud plumes spread downwind, resembling smoke plumes from a chimney. The estimated height in one case is about 15 km.

(c) They are vertically separated from the underlying anvils, as deduced from the shadows they cast on the anvils.

(d) Plumes are partially transparent in channels 1 and 2, and one can often see through them and discern some features on the underlying anvil. This indicates that the plumes are usually very thin and tenuous.

(e) The structure of the plume is more or less preserved in channel 4, indicating a temperature difference between the particles of the plume and the surroundings.

(f) Sometimes the plume splits into two very bright splinters with a cyclonically curved northern branch and *anticyclonic* southern branch. The source of the split plume appears to be in the distant warm area.

It is the purpose of this paper to show that the plume formation is closely linked to the strong updraft and overshooting of a severe thunderstorm. The requisite water vapor comes from the storm below, hence representing a transport of water vapor from the troposphere to the lower stratosphere. This conclusion is achieved by using a three-dimensional (3D) numerical cloud model capable of simulating the evolution of major dynamical and microphysical processes in a deep convective storm. Careful analysis of the simulation results reveals cloud features strikingly similar to the aforementioned plume characteristics as reported by *Levizzani and Setvak* (1996).

3. DESCRIPTION OF THE CLOUD MODEL WISCDYMM

The cloud model utilized for the present study is the Wisconsin Dynamical/Microphysical Model (WISCDYMM), which is a 3D quasi-compressible, time-dependent, non-hydrostatic cloud model developed at the University of Wisconsin-Madison by the author's group. The governing equations and microphysical parameters are given in *Straka* (1989) and Johnson et al. (1994).

4. THE 2 AUG 1981 CCOPE SUPERCELL

The simulated storm for illustrating the plume-formation mechanism is a supercell that passed through the center of the Cooperative Convective Precipitation Experiment (CCOPE) (*Knight*, 1982) observational network in southeastern Montana on 2 August 1981. The storm and its environment were intensively observed for more than 5 h by a combination of seven Doppler radars, seven research aircraft, six rawinsonde stations and 123 surface recording stations as it moved east-southeastward across the CCOPE network. This storm case was chosen because it provides much detailed observational data for comparison with model results in dynamics and cloud physics, and the author's group has obtained successful simulations of it previously.

5. RESULTS AND DISCUSSIONS

Simulations were performed using three different resolutions: 1 x 1 x 0.5 km^3, 1 x 1 x 0.2 km^3, and 0.5 x 0.5 x 0.2 km^3. All three simulations show the plume phenomenon well in that they all exhibit similar plume characteristics. The overall features for the latter two grids are quite similar, except that the one with refined horizontal resolution shows more detailed midlevel horizontal structure than the other two runs. Since the utmost concern in this study is the vertical transport, it was decided to choose the simulation results with the refined vertical resolution (1 x 1 x 0.2 km) for analysis here. The overall dynamical and microphysical characteristics of the new results, being very similar to those reported by *Johnson et al.*(1994), will not be discussed here.

The original 1746 MDT Knowlton, Montana sounding did not contain moisture information above 300 mb. The simulation of *Johnson et al.* (1994) was performed under the assumption of no water vapor above 300 mb initially (hereafter called the "dry-

case"). But since the present study is concerned with water vapor transport, this assumption may be inappropriate. To ensure that the upper level (above 300 mb) moisture is properly represented, two additional options modifying the upper level dewpoint profile were made and tested: (1) using an average August 1999 Halogen Occultation Experiment (HALOE) water vapor profile over midlatitudes (40°-60°N) to represent the upper level humidity, (2) shifting the upper level T_d profile of option 1 to the right so that the 300 mb level is exactly saturated with respect to liquid water (not shown). The simulation results with option 2 do not show clear plume structure and therefore will not be considered further. The results of option 1 do not differ significantly from the dry case.

Central Cross-section Features

Figure 1 shows a series of snapshots of the vertical profiles of *relative humidity with respect to ice*, RHi, in the central west-east cross-section (y = 27 km) where the storm activity is usually the most vigorous. The reason to use RHi profiles rather than RHw, the relative humidity with respect to liquid water, is that ice formation is more relevant in the cloud top due to the prevailing cold temperatures there. Note that only the portion of the storm above 10 km is shown in each panel. A comparison between the water vapor mixing ratio q_v and RHi profiles shows that the two are very similar. Hence the RHi profile can be viewed as essentially the same as the q_v profile. The range in Fig. 4 are windowed to 10-20 km vertically and 20-55 km horizonatally, with the vertical scale stretched by ~ 35% in these views.

No obvious plume structure is discernible before 20 min into the simulated storm activity. At 24 min, strong gravity wave motions at the cloud top are visible. There is a large surge of high humidity region above the second wave crest (to the east of the main updraft column) that seems to propagate upward and westward (i.e., towards upstream relative to the upper level wind direction) into the stratosphere. At 32 min, this moist surge appears to be nearly detached from the anvil of the storm and forms a separate moist layer in the stratosphere. At 36 min, the surge appears to break into two parts; the one to the west seems to merge with the uprising overshooting dome, while the one to the east seems to form a separate plume-like structure. This latter plume, sloping downward almost parallel to the slope of the anvil, appears to gradually dissipate with time into much more diffuse moist layer. This surge mechanism may be responsible for the formation of the stratospheric cirrus as observed by *Fujita* (1982), who stated that "One of the most striking features seen repeatedly above the anvil top is the formation of cirrus cloud which jumps upward from behind the overshooting dome as it collapses violently into the anvil cloud". Some more details of this phenomenon will be examined in the next section. While this mechanism may form some cirrus in the stratosphere, it does not seem to produce the main plumes as seen in the satellite images. However, it may be responsible for the formation of plumes in the "distant warm area" as described in Point (f) in Sec. 2.

At 48 min, a "blob" of moist air appears on top of the overshooting dome of the storm. The size of this blob fluctuates at first, but it eventually becomes larger and, beginning at 80 min, it gradually takes on the shape of a chimney plume, much as described in Sec. 2. The stretching of the plume downwind is apparently caused by the upper-level winds, which are predominantly westerly. The maximum RHi humidity in the core of the plume sometimes exceeds 100%. At 112 min, the plume has reached the east boundary of the computational domain. Its altitude is between 15 and16 km, roughly the same as that observed by *Levizzani and Setvak* (1996). The plume associated with the gravity wave crest, on the other hand, is located at 12 -13 km. Thus there may be more than one layer of plumes at a given time. The thickness of the plumes depends on the choice of critical RHi for defining their boundaries. If we use 90% RHi, then the thickness can range from several hundred meters to about 1 km. A choice of smaller critical RHi will naturally lead to a somewhat thicker plume layer. Judging from the extremely small amount of water vapor mixing ratio in the plume, any condensed water would also have extremely small concentrations and hence be semi-transparent. It is also clear from the pictures that there is a shallow dry layer immediately above the anvil. This dry layer is about 1 ~ 1.5 km thick and apparently extends to the whole length of the anvil in the computational domain.

Other notable cloud top features

There are other notable cloud top features related to the plume phenomenon and they will be reported during the conference. The possible mechanism responsible for plume formation will also be discussed at that time.

Acknowledgments. I am grateful to Susan Solomon for pointing out relevant references and for her encouraging and helpful comments, to Liwen Pan for sharing the SAGE II data, to Hsin-mu Lin and Yulien Chu for helping processing the model data, and to Robert Schlesinger and David Martin for many helpful comments. This study was first inspired by a discussion with Vincenzo Levizzani and Martin Setvak. This work is partially supported by NSF Grants ATM-9907761 ATM-9633424, and NASA Grant NAG5-7605.

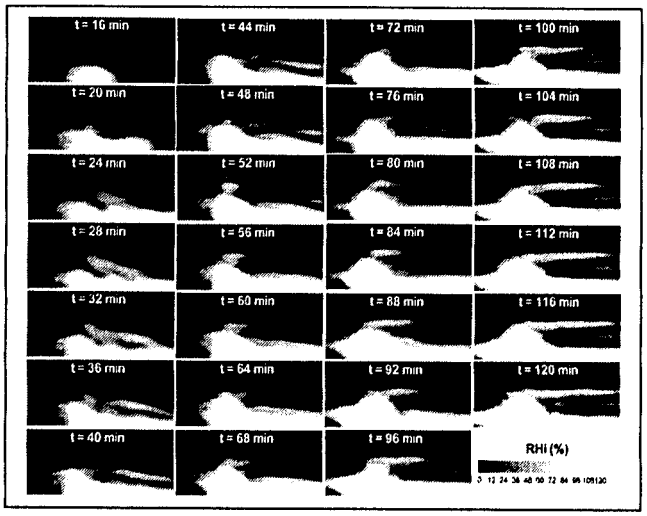

Fig. 1. Snapshots of vertical RHi (relative humidity with respect to ice) profiles every 4 min in the central east-west cross-section (y = 27 km), showing the plume feature above the anvil. The vertical axis range is 10-20 km and horizontal axis range 20-55 km.

REFERENCES

Foot, J. S., 1984: Aircraft measurements of the humidity in the lower startosphere from 1977 to 1980 between 45N and 65N, *Q. J. Royal Meteor. Soc.*, 110, 303-319..

Fujita, T. T., 1982: Principle of stereographic height computations and their application to stratospheric cirrus over severe thunderstorms, *J. Meteor. Soc. Japan.*, 60, 355-368.

Goody, R. M., and Y. L. Yung, 1989: *Atmospheric Radiation: Theoretical Basis.* Oxford University Press.

Hintsa, E. J., E. M. Weinstock, A. E. Dessler, J. G. Anderson, M. Lowenstein, and J. R. Podolske, 1994:SPADE H2O measurements and the seasonal cycle of stratospheric water vapor. *Geophys. Res. Lett.*, 21, 2559-2562, 1994.

Holton, J. R., P. H. Haynes, M. E. McIntyre, A. R. Douglass, R. B. Rood, and L. Pfister, 1995:Stratospheric-tropospheric exchange. *Rev. Geophys.*, 33, 403-439.

Johnson, D. E., and P. K. Wang, and J. M. Straka, 1994: A study of microphysical processes in the 2 August 1981 CCOPE supercell storm. *Atmos. Res.* 33, 93-123.

Kelly, K. K., A. F. Tuck, L. E. Heidt, M. Loewenstein. J. R. Poldoske, S. E. Strahan, and J. F. Vedder, 1990: A comparison of ER-2 measuremnts of stratospheric water vapor between the 1987 Antarctic and 1989 Arctic Airborne Missions. *Geophys. Res. Lett.*, 17, 465-468.

Knight, C. A., Ed., 1982:The Cooperative Convective Precipitation Experiment (CCOPE), 18 May-7 August 1981. *Bull. Amer. Meteor. Soc.*, 63, 386-398.

Levizzani, V., and M. Setvak, 1996: Multispectral, high resolution satellite observations of plumes on top of convective storms. *J. Atmos. Sci.*, 53, 361-369.

Liou, K.N., 1992: *Radiation and Cloud Processes in the Atmosphere: Theory, Observation, and Modeling.* Oxford University Press, New York, 487 pp.

Pan, L., S. Soloman, W. Randel, J-F. Larmarque, P. Hess, J. Gille, E. Chiou, and M. P. McCormick, 1997: Hemispheric symmetries and seasonal variations of the lowermost stratospheric water vapor and ozone derived from SAGE II data. *J. Geophys. Res.*, 102, 28177-28184.

Pan, L. L., E. J. Hinsta, E. M. Stone, E. M. Weinstock, and W. J. Randel, 2000: The seasonal cycle of water vapor and saturation vapor mixing ratio in the extratropical lowest stratosphere. *J. Geophys. Res.*, 105, 26519-26530.

Roach, W. T., 1967: On the nature of the summit areas of severe storms in Oklahoma, *Q. J. Royal Meteor. Soc.*, 93, 318-336.

Setvak, M. and C. A. Doswell III, 1991: The AVHRR channel 3 cloud top reflectivity of convective storms. *Mon. Wea. Rev.*, 119, 841-847.

Solomon, S., 1999: Stratospheric ozone depletion: A review of concept and history. *Rev. Geophys.*,37, 275-316.

Straka, J. M., 1989: *Hail growth in a highly glaciated central high plains multi-cellular hailstorm.* Ph.D thesis, University of Wisocnsin-Madison, 413pp.

P2.16 WIND REGIME GOES CLOUD COVER COMPOSITES FOR THE WAKEFIELD, VA COUNTY WARNING AREA

Cynthia L. Combs *
CIRA/Colorado State University

Neil A. Stuart
NOAA/NWS Wakefield, VA

Mark DeMaria
NESDIS/ORA/RAMMT
CIRA/Colorado State University

Thomas H. Vonder Haar
CIRA/Colorado State University

1. INTRODUCTION

Predicting the location and timing of the onset of convective precipitation remains a challenging forecasting task. For example, the 24-hr Quantitative Precipitation Forecasts (QPF) from the Hydrometeorological Prediction Center (HPC) in the summer typically have less than half the skill of the corresponding winter forecasts (HPC verification statistics available at www.hpc.ncep.noaa.gov). Numerical modeling studies suggest that surface characteristics (land-sea contrasts, land usage, topography, etc) play an important role in the formation of convection (e.g., Doyle 1997, Pielke, et al, 1999). These studies also indicate that models can sometimes realistically simulate small-scale flow features even when initialized with very smooth initial conditions, provided that the surface boundary conditions are adequately resolved. These modeling results suggest that forecast information on convective initiation and development can be obtained from knowledge of the synoptic-scale flow and the surface characteristics.

Connell and Gould (2000) have shown that hourly cloud frequency composites divided into various wind regime categories are useful in forecasting sea breeze convection in the Florida Panhandle. In this study, cloud frequency composites are developed for the county warning area of Wakefield, VA National Weather Service (NWS) forecast office. The goal of the study is to determine the utility of the satellite composite in another part of the U.S. with different concerns and local terrain.

2. DATA AND METHODOLOGY

For this project, visible (channel 1) images from the Geostationary Operational Environmental Satellite (GOES) were taken from an archive collected at CIRA. The GOES 8 images were collected hourly during the daylight period for May through October, 1998-2000, cover the eastern United States, and are sampled to 4 km resolution. Each image was sectorized to cover the Mid-Atlantic states region, then grouped by hour for further processing.

In order to estimate percentage of cloud cover for a given month over a given area, a visible channel threshold method as described in Reinke, et al (1992) was used. First, a set of visible images for a given month and hour are quality checked for noise lines or other problems. Then for each pixel location within the sector, all the images in the set are compared and the minimum value (excluding values within suspected cloud shadow regions) is found. The results form a cloud-free image called a "background". It provides later algorithms with the brightness temperature values to expect for clear conditions and thus be able to better detect abnormally bright (i.e. clouds values).

The next step is to categorize each image by wind regime. For each day, the 1000 - 700mb Mean Layer Vector Wind (MLVW) is determined. First, the 12 UTC ETA model analysis fields are used to derive a 'sounding' over the Wakefield, VA vicinity. The MLVW is then calculated using PC-Gridded Interactive Display and Diagnostic System (PC-GRIDDS) software. Using the MLVW value, the image is then designated into one of nine generalized regimes. These cover the eight points of the compass and a calm (< 5 m/s) regime, as listed in the table below.

The cloud frequencies within a given wind regime are determined by comparing each image with the previously determined background image for that hour and month. For each pixel location, the image value is compared to the background plus a given threshold value. If the image value is greater than the background and threshold, that pixel is tagged as cloudy. If the image value is less, it is considered clear. As the

* *Corresponding author address*: Cynthia Combs, CIRA/Colorado State University, W. Laporte Avenue, Foothills Campus, Fort Collins, CO 80523-1375; e-mail: combs@cira.colostate.edu

images from the set are processed, the number of cloudy pixels for each pixel location are tallied. Then the number of cloudy pixels is divided by the total number of pixels considered for that location to produce a cloud cover percentage.

Table 1

	Wind regimes
1	Calm (< 5m/s)
2	North
3	Northeast
4	East
5	Southeast
6	South
7	Southwest
8	West
9	Northwest

This procedure was implemented for each month, hour and wind regime with in the time period. Since one hour of one month divided into potentially nine wind regimes does not allow for many cases in each category, the resulting monthly composites are combined according to hour and wind regime for a given period. In this study, we were interested in three time periods during 1998-2000: the entire warm season from May through October; the warmer, more convectively active period of May through July within the previous period; and the cooler August through October period. The last processing step was to sectorize the final composites down to the Wakefield, VA County Warning Area (CWA).

4. PRELIMINARY ANALYSIS

In order to be called a true climatology, many years worth of cases are required to be statistically significant. Since our study only covers three years, which include both an El Nino and a La Nina year, it can only provide us with a hint of the climate for this region. This is especially true for wind regimes that occur less often. While onshore wind cases, including the NE, E, and SE regimes, usually are very important to the Wakefield Terminal Areodome Forecast (TAF), none of these categories have enough cases to enable us to draw conclusions. (see Table 2). As expected, wind regimes more in line with the prevailing wind, such as SW, W, and NW, have more cases while the Calm category has the most. It will be features from these regimes that we will concentrate on.

Some of the most interesting features can be seen in the Calm regime composites. The complex coastline around the Chesapeake Bay and the Atlantic ocean are most prominent in this regime, especially in the May-July period (Figure 1). In fact, minimums can be discerned over the rivers. This supports previous research that there are small-scale boundaries around the rivers (Stuart et al. 1998), with local ascent on the peninsulas enhancing clouds, and local descent over the rivers negating clouds. Some of these coastline features can also be seen in the W and NW composites, especially during the warm months May-July.

In addition, both the W and NW regime composites, overall, have a lower percentage of cloudiness, especially when compared to the SW composites. A good example is found by comparing two composites from 1645 UTC for May-July. Most locations in Figure 2, the NW case, has cloud percentage values approximately 20 % lower than corresponding locations in the SW case (Figure 3). This is probably due to the fact that NW winds are generally downslope for this area. From the time-series loop, it appears that part of the cloudiness of the SW case is due to convection drifting off the mountains. The areas of higher cloud percentage in the NW case appear over the peninsulas, much like the previously discussed Calm case.

Another feature of interest for the Wakefield region is "Bay Plumes/Streamers", an enhanced convective line over the Chesapeake Bay usually seen during the cool season. These plumes can sometimes enhance other convection in the area and trigger severe weather such as waterspouts. Since northerly winds are one of the conditions for setting up a bay plume, the N wind regime for the August-October was examined (Figure 4). While the N regime has only an average of 36 cases per hour, a hint of the bay plume can be seen during the morning in the lower Chesapeake Bay, southwest the lower Eastern Shore tip.

All of these figures, plus additional the hourly composite loops, may be seen in color at our website: http://www.cira.colostate.edu/RAMM/clim/Wakefield/windr.html

5. FUTURE WORK

There is still much to be analyzed concerning these composites. For instance, timing of cloud formation and peak coverage for S through W directions are important for convection development and timing of clouds in TAFs. The hourly composite loops for each regime are very usefully in viewing cloud development during the day. They should help identify location and frequency, hopefully providing new insight. In addition, we would like to incorporate the wind regime composites so that a forecaster only has to identify the current wind regime,

Table 2: Average Number of Cases for Each Hour during 1998-2000

Period	Calm	North	NE	East	SE	South	SW	West	NW
May-Oct	133	54	24	11	6	20	68	98	83
May-Jul	69	19	9	4	1	10	40	60	44
Aug-Oct	64	36	15	7	5	10	28	38	39

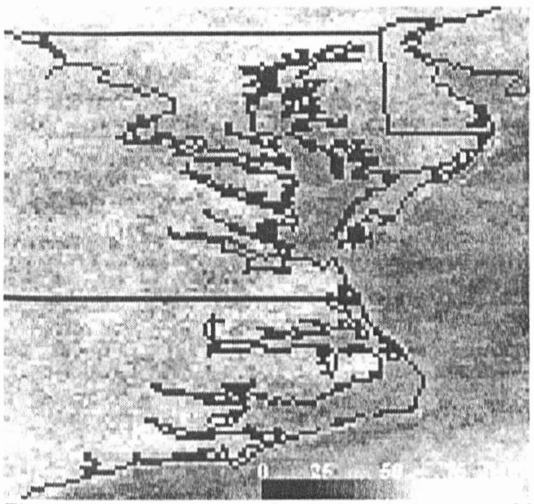

Figure 1: % cloud cover for Calm wind regime, May-July, 1998-2000, 1645 UTC

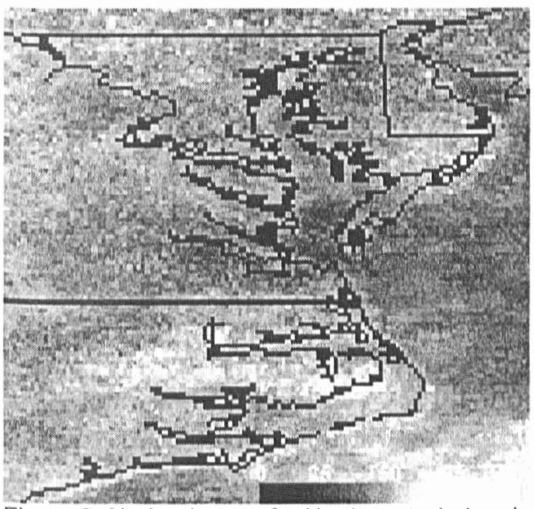

Figure 2: % cloud cover for Northwest wind regime, May-July, 1998-2000, 1645 UTC

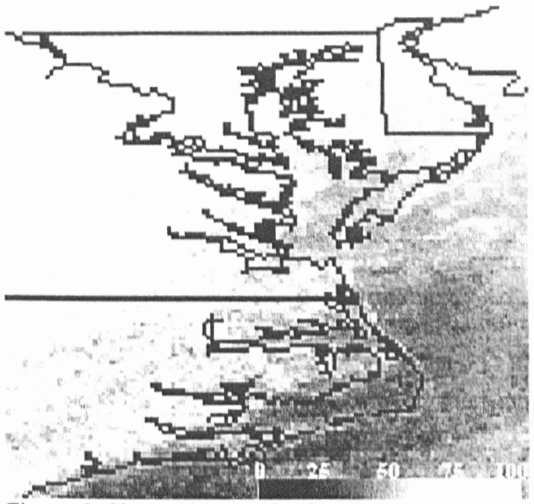

Figure 3: % cloud cover for Southwest wind regime, May-July, 1998-2000, 1645 UTC

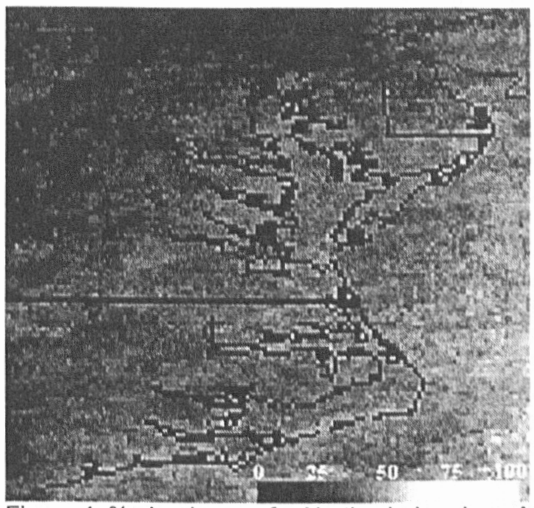

Figure 4: % cloud cover for North wind regime, Aug-Oct, 1998-2000, 1245 UTC

possibly through AWIPS, and see the time series for that regime.

6. ACKNOWLEDGMENTS

This work was funded by Cooperative Program for Operational Meteorology, Education and Training(COMET) Partners Project, S00-24228.

7. REFERENCES

Connell, B. H., and K. J. Gould, 2000: GOES-8 visible cloud frequency composites of the convectively active sea breeze under stratified synoptic flow over the Florida Panhandle. Preprints, *Tenth Conf. on Satellite Meteorology and Oceanography*, Long Beach, CA, Amer. Meteor. Soc., 438-441.

Doyle, J. D., 1997: The influence of mesoscale orography on a coastal jet and rainband. *Mon. Wea. Rev.*, **125**, 1465-1488.

Pielke, R. A., R. L. Walko, L.T. Steyart, P.L. Vidale, G.E. Liston, W. A. Lyons, and T. N. Chase, 1999: The influence of antropogenic landscape changes on weather in South Florida. *Mon. Wea. Rev.*, **127**, 1663-1673.

Reinke, D. L., C. L. Combs, S. Q. Kidder, and T. H. Vonder Haar, 1992: Satellite cloud composite climatologies: A new high-resolution tool in Atmospheric research and Forecasting. *Bull. Amer. Meteor. Soc.* **73**, 278 - 285.

Stuart, N. A., H. D. Cobb, W. F. Albright, A.T. Anderson, J. B. Browder, 1998: Correlating thunderstorm lightning patterns with WSR-88D signatures and resultant benefits for utility companies: A preliminary investigation of the Hampton Roads "hot spot", Preprints, *19th Conf. on Severe Local Storms*, Mineapolis, MN, Amer. Meteor. Soc., 424-427

P2.17 INVESTIGATIONS OF LIQUID WATER PATH SPATIAL VARIABILITY USING MODIS

Robert Wood* and Dennis L. Hartmann
University of Washington, Seattle, Washington

1. Introduction

Boundary layer cloud structure is never homogenenous. Heterogeneities occur on all scales (e.g. Lovejoy 1982, Cahalan and Snider 1989, Kostinski and Shaw 2001) Two important points related to cloud heterogeneity are:

(i) a complete understanding of the convective processes driving the organisation and structure of marine boundary layer clouds has not yet been attained (see Atkinson and Zhang 1996). One approach to elucidating possible mechanisms for mesoscale cellular convection (MCC) is to characterise the types of cloud structures over large areas and couple this with synoptic data to examine statistical relationships between large-scale forcings and cloud structural properties;

(ii) models of boundary layer clouds do not explicitly resolve processes that are occurring on scales smaller than the grid-box size. Two processes of particular importance to climate are radiative transfer (Cahalan et al. 1994) and precipitation generation (Albrecht 1989). Both processes have non-linear relationships between local cloud properties (optical thickness, liquid water path) and the process variable of interest (albedo, precipitation rate). For any process that depends nonlinearly upon a local cloud property, using the mean value of the cloud property will result in an erroneous estimation of the mean value of the process (e.g. Pincus and Klein 2000). The mean short wave reflectance of a cloudy domain is always less for a heterogeneous cloud than for a homogeneous cloud. For precipitation rates this is reversed.

In this study we:

(i) examine MODIS data from both the Californian and Peruvian regions to assess characteristics of the spatial variability in marine boundary layer clouds;

(ii) estimate the dominant spatial scales and MCC characteristics of boundary layer clouds;

(iii) estimate the potential magnitudes of precipitation biases in climate models if cloud spatial variability is not accounted for.

2. Data analysis

Data from the Moderate Resolution Imagining Spectroradiometer (MODIS) on the recently launched Terra satellite are used to assess liquid water path characteristics in regions dominated by warm low-level clouds. From measurements of optical thickness and effective radius (King et al. 1997) it is possible to estimate (e.g. Brenguier et al. 2000) liquid water path and droplet concentration: parameters of more relevance to cloud microphysical processes. Spatial resolution is 1km. All MODIS images used are collected at approximately 10-11 AM local time.

3. Characteristics of spatial variability

To investigate the climatology of mesoscale cellular convection we need a measure of the convective cell characteristic lengthscale and to know if the convection is open or closed cellular in form. To investigate the likely magnitude of process rate biases requires knowledge of the moments of the pdf of the relevant cloud properties.

Here we use 2-D Fourier analysis on 256x256 km MODIS scenes to determine the spatial scaling in the LWP fields. Fig. 1 shows the method used to determine the dominant spatial scale of convective cells. After detrending the 2D LWP field by removing the best fit planar surface, the 2D power spectrum P_{LWP} is generated as a function of the combined wavenumber k, where $k^2 = k_x^2 + k_y^2$. Horizontal asymmetry information is therefore discarded. In Fig. 1 the power spectra are shown for three cases. Note how the characteristic convective cell size corresponds well to a peak in the power spectrum with an associated power-law energy cascade at smaller scales. However, automatically selecting the wavenumber of the peak from a noisy, multi-peaked signal proved to be more complicated than anticipated. We found that a reasonable method was to calculate a second characteristic lengthscale λ_0 (marked by solid triangles on the abscissae in Fig. 1) from P_{LWP} using

$$\lambda_0^{-1} = \int_0^\infty k P_{LWP} dk \qquad (1)$$

We found by inspection that λ_0 itself is not a particularly good measure of the scale of the convective cells because it is too heavily dependent upon the power spectrum at larger scales which are poorly sampled. However, when a power-law fit to the spectrum for $k > 1.5/\lambda_0$ is calculated, this generally fits the energy cascade region of the spectrum well (dotted straight line in Fig. 1). The peak scale is then determined by first binning P_{LWP} using logarithmically spaced bins (filled circles) and calculating the 95% confidence limits (dotted curves). We determine the convective cell scale λ as the inverse of the wavenumber at which the upper confidence limit falls below the power-law fit, i.e. the smallest scale at which the observed power spectrum deviates at the 95% level from the power-law (vertical dashed lines). Note that in (a) there is no scale for which

* *Corresponding author address*: Dr. Robert Wood, Atmospheric Sciences, University of Washington, Seattle, WA; *e-mail: robwood@atmos.washington.edu.*

this criterion is fulfilled. We find that in almost all these cases of failure (<5% of total scenes processed), the peak in the power spectrum is located at small scales (<5-10 km), which is close to the Nyquist scale (2km). For cases (b) and (c) the derived cell scales are 10.3 and 48.2 km, which are in good agreement with those chosen by visual inspection.

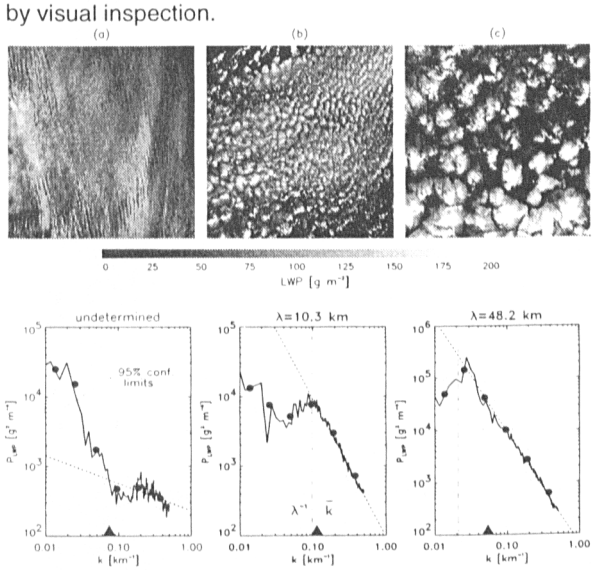

Figure 1: *Example showing LWP power spectra used to determine the dominant spatial scale of the MCC.*

The LWP pdf is derived for the cloudy pixels in each scene. The pdf and the power spectrum are used to classify scenes as containing open cellular, closed cellular or homogeneous cloud. Open cellular convection has more skewed pdfs and more power at small scales (P_{small}, the integrated power for $0.2 < k < 0.5$ km^{-1}). Closed and open MCC cannot be diagnosed based upon cloud fraction alone because closed cellular convection covering only a small portion of the scene would be misdiagnosed as open celled convection. Fig. 2 shows an example of the diagnosis of open and closed cells. We diagnose open cellular convection as having (a) skewness larger than 1.8; (b) $P_{small} > 250$ g^2 m^{-4}; (c) cloud fraction $0.1 < CF < 0.75$. Of the remaining scenes, those with $\lambda > 10$ km and $CF > 0.1$ are classified as closed cellular convection. Those with $\lambda \leq 10$ km and $CF > 0.1$ are classified as homogeneous cloud. Finally, those with $CF < 0.1$ are unclassified. These could either be scattered trade with cumulus or edges of extensive stratocumulus.

4. Frequencies and scales of cellular convection

Fig. 3 shows the freqeuncies of homogeneous, open and closed MCC for the Californian and Peruvian regions during SON. Close to the Calfornian coast homogeneous and closed cellular convection dominate. Close to the S. American coast there is less homogeneous cloud and more closed cells (over 90% in places) which most likely reflects the deeper boundary layers found close to the S. American coast. There is also an interesting band

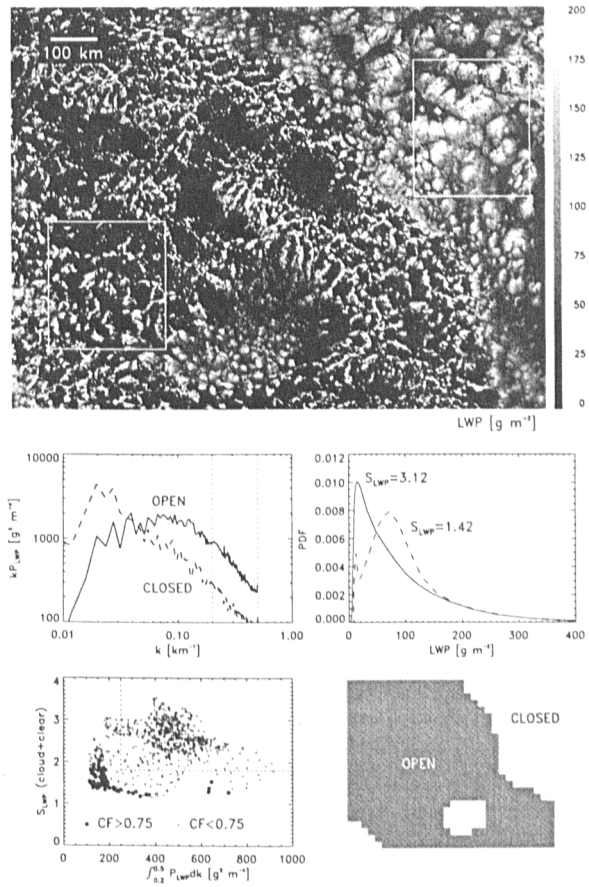

Figure 2: *Diagnosis of open/closed cellular convection. Two example scenes are chosen from larger image (top). Second row shows LWP power spectra and pdfs. Third row shows small scale power plotted against skewness (see text), and location of where open and closed cellular convection has been diagnosed in upper image.*

of closed MCC just south of the equator where equatorial upwelling is prevalent. Open MCC dominates further westwards in the subtropical regions.

Spatial scales of the closed MCC are shown in Fig. 4. The median λ for the closed MCC is 26.1 and 24.2 km for the Californian and Peruvian regions respectively. There is a tendency for the integral scale to underpredict the cell sizes for open MCC and so these are not presented.

Convective cell scales increase with distance away from the coast in the Californian region, while the largest cells are typically found close to the S. American coast. The reason for this is not yet clear although one might expect that the cell diameter would scale with the depth of the boundary layer. Accurate MODIS cloud top temperatures have only recently become available; we will examine cell scaling relationships as this data becomes available.

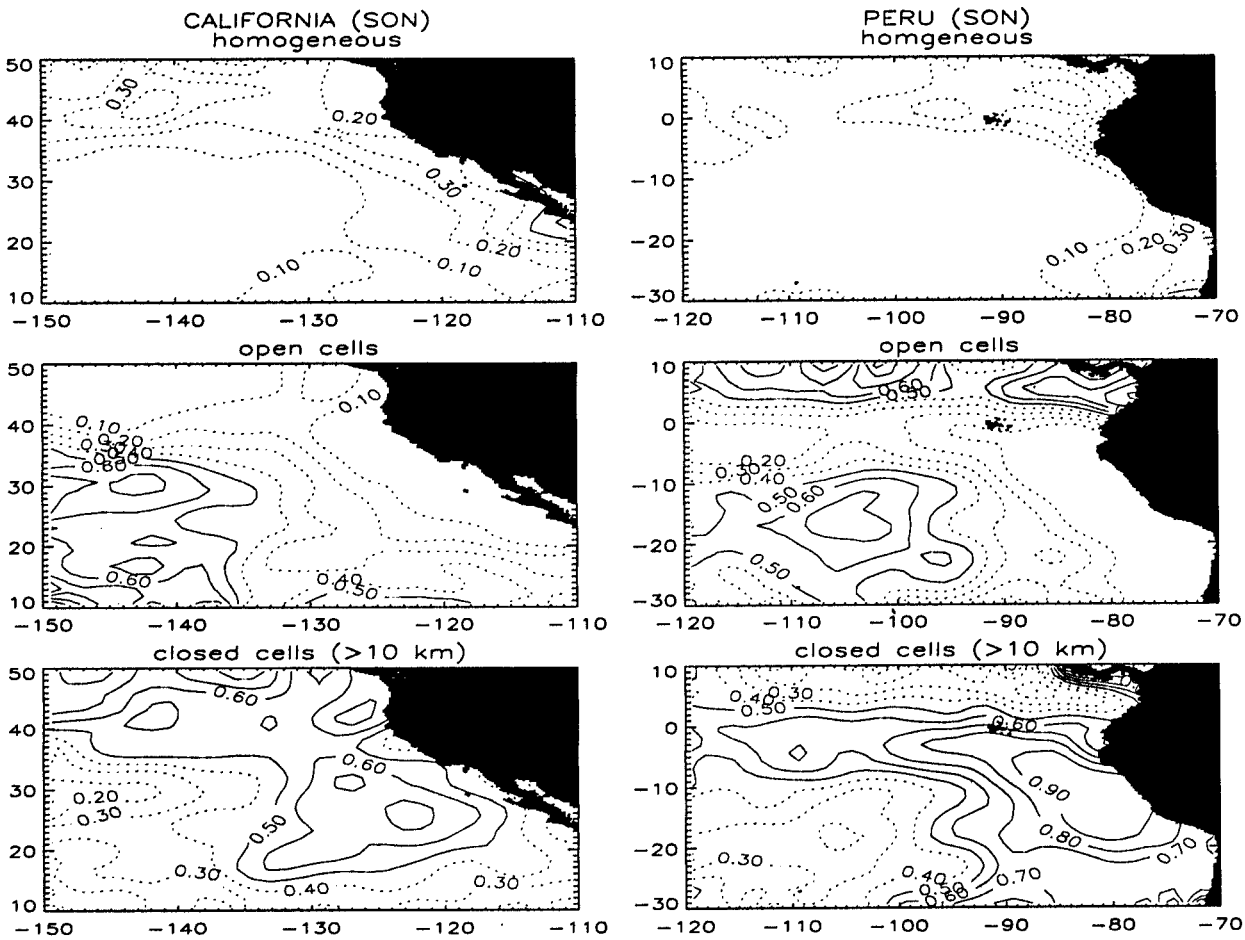

Figure 3: *Diagnosed homogeneous, open and closed cellular convection frequencies for Californian and Peruvian regions during SON.*

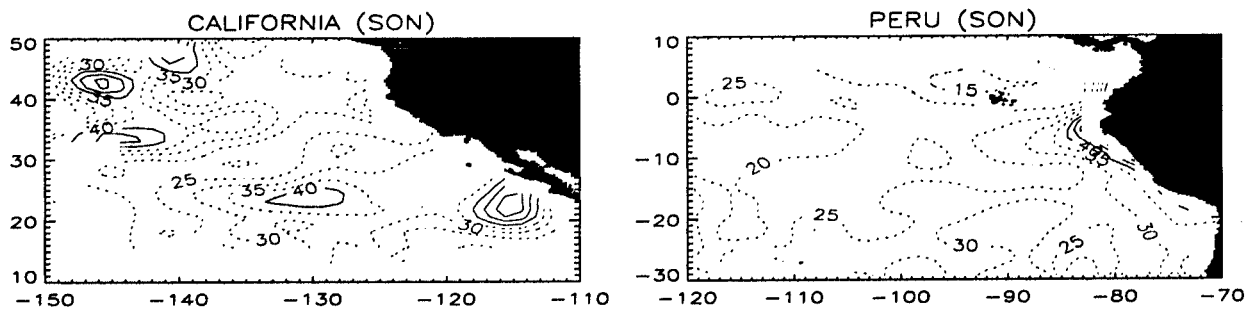

Figure 4: *Median integral scale of closed cells.*

5. LWP and precipitation variability

The role of precipitation in controlling the distribution of liquid water within boundary layer clouds remains uncertain. The dependence of drizzle rate upon liquid water content and droplet concentration is not quantitatively known with any accuracy. Here, we present a simple model which can be used to examine precipitation rate variability in warm boundary layer clouds. The model is a simple one dimensional equilibrium model which models drizzle formation through the processes of autoconversion, accretion and sedimentation. The model has been used to assess the merits of various autoconversion and accretion schemes. Fairly good agreement between modelled and observed precipitation rates is obtained when the Khairoutdinov and Kogan (2000) parameterisations for autoconversion, accretion and sedimentation are used.

The assumption is made that the cloud liquid water content and droplet concentration profiles do not change with time, i.e. the precipitation flux is balanced by the moisture flux into the cloud through the base and top. This may be a reasonable approximation for stratocumulus with moderate amounts of drizzle where observations suggest that the profiles of liquid water content remain fairly adiabatic.

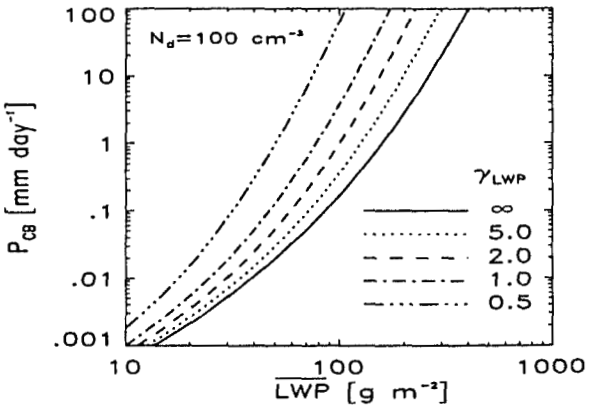

Figure 5: *Mean cloud-base precipitation rate as a function of $\overline{LWP}$ and γ_{LWP}. Droplet concentration is 100 cm^{-3}.*

The LWP pdf is well represented using a Gamma distribution (two free parameters). Using this the precipitation rate at cloud base is calculated for inhomogeneous clouds with different $\overline{LWP}$ and γ_{LWP}, where $\gamma_{LWP} = (\overline{LWP}/\sigma_{LWP})^2$. The domain size is 256x256 km. For a given $\overline{LWP}$ clouds with higher levels of heterogeneity (lower γ_{LWP}) have higher mean cloud base precipitation rates (Fig. 5). This is because the autoconversion rate has a strongly non-linear dependence upon cloud liquid water content. Thus a bias is introduced if the cloud is assumed to be homogeneous (e.g. Pincus and Klein 2000). This bias can be significant. For the dataset median $\overline{LWP} = 80$ g m^{-2} and $\gamma_{LWP} = 1.0$, the heterogeneous mean cloud base precipitation rate P_{CB} is a factor of 11.6 higher than the rate P_{PPH} calculated for a plane parallel homogeneous cloud. Biases become greater at higher values of $\overline{LWP}$ because at higher cloud liquid water contents the accretion term amplifies biases in autoconversion rates.

The geographical distribution of the precipitation bias $(P_{CB} - P_{PPH})/P_{PPH}$ is shown in Fig. 6. The estimated biases are smallest (< 5) where there is a prevalence of relatively homogeneous stratus clouds close to the N. and S. American coastlines. Even here however, the biases are not negligible. Further from the coast in the transition/cumulus regions, the biases can become very large.

6. Conclusions

Early data have been presented from the MODIS instument, which are being used to investigate cloud spatial inhomogeneity characterised using power spectra and pdfs. Diagnosis of the type of convection and the scales of the cells will be used to determine the synoptic conditions for the formation of MCC. The width of the LWP pdf is important in determining the mean cloud base precipitation rate for a given area of heterogeneous cloud. All GCMs use a plane parallel (PPH) homogeneous model for calculating precipitation. A simple model to account for cloud spatial variability suggests that the PPH assumption can result in considerable underprediction of drizzle rates.

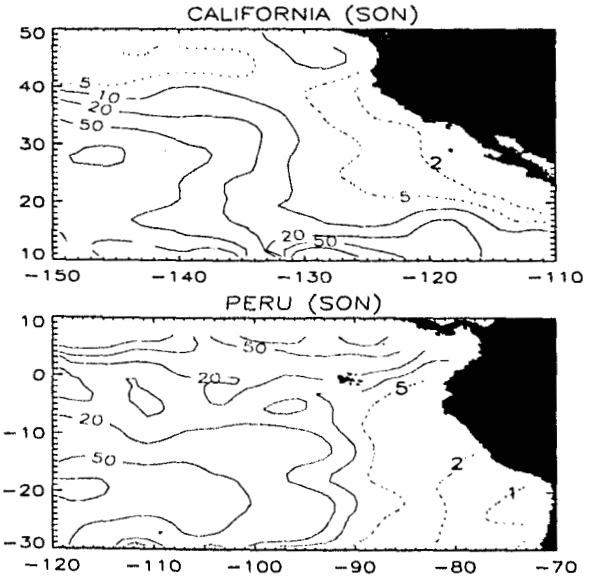

Figure 6: *Median precipitation rate biases*

References

Albrecht, B. A., (1989): Aerosols, cloud microphysics and fractional cloudiness. *Science*, **245**, 1227-1230.

Atkinson, B. W. and J. Wu Zhang, 1996: Mesoscale shallow convection in the atmosphere. *Rev. Geophys.*, **34**, 403-431.

Brenguier, J.-L., H. Pawlowska, L. Schuller, R. Preusker, J. Fischer, Y. Fouquart, 2000: Radiative properties of boundary layer clouds: droplet effectvie radius versus number concentrations, *J. Atmos. Sci.*, **57**, 803-821.

Cahalan, R. F. and J. B. Snider, 1989: Marine statocumulus structure, *Remote Sens. Environ.*, **28**, 95-107.

Cahalan, R. F., W. Ridgway, W. J. Wiscombe, T. L. Bell, J. B. Snider, 1994: The albedo of fractal stratocumulus clouds, *J. Atmos. Sci.*, **51**, 2434-2460.

Khairoutdinov, M. and Y. Kogan, 2000: A new cloud physics parameterization in a large-eddy simulation model of marine stratocumulus. *Mon. Wea. Rev.*, **128**, 229-243.

King, M. D., S-C. Tsay, S. E. Platnick, M. Wang, K-N. Liou, 1997: Cloud retriveal algorithms for MODIS. Optical thickness, effective particle radius, and thermodynamic phase. *MODIS Algorithm Theoretical Basis document No. ATBD-MOD-05*, NASA.

Kostinski, A. B. and R. A. Shaw, 2001: Scale-dependent droplet clustering in turbulent clouds. *J. Fluid. Mech.*, **434**, 389-398.

Lovejoy, S. D., 1982: The area-perimeter relationship for rain and cloud areas, *Science*, **216**, 185-187.

Pincus, R. and S. A. Klein, 2000: Unresolved spatial variability and microphysical process rates in large-scale models. *J. Geophys. Res.*, **105**, 27059-27065.

P2.18 THE INFLUENCE OF ANTARCTIC CLOUD AND SURFACE PROPERITES ON CLOUD RADIATIVE FORCING AT THE SURFACE

Michael J. Pavolonis *
Cooperative Institute for Meteorological Satellite Studies
University of Wisconsin, Madison, Wisconsin

Jeffrey R. Key
Office of Research and Applications, NOAA/NESDIS, Madison, Wisconsin

1. INTRODUCTION

Model simulations have shown that the radiative properties of clouds over the Antarctic influence not only the south polar climate but global climate as well. Changes in cloud and surface properties can result in changes in the surface energy budget which in turn can alter the regional atmospheric and oceanic dynamics of the Antarctic. Lubin et al. (1998) showed that any significant warming or cooling at the surface over Antarctica will cause changes in temperature gradients that may then lead to changes in regional transport mechanisms. Another consideration of surface warming/cooling is the feedback on cloud properties and cloud amount. The purpose of this work is to learn how changes in cloud and surface properties affect the surface radiative budget in the Antarctic.

There are several factors that can influence the radiative effect of clouds (cloud "forcing") at the surface such as cloud optical depth, surface albedo, cloud amount, cloud temperature, and surface temperature. The net radiative effect of clouds on the surface will vary, in large part, according to the aforementioned parameters. However, it would be useful to determine which of those parameters most dramatically alter the net effect of clouds on the surface radiation budget if it were to change.

In this study, cloud and surface properties from the International Cloud Climatology Project (ISCCP) "D1" data set were used as input to a radiative transfer model which computed shortwave and longwave surface cloud radiative forcing. For more information about the ISCCP D-series data set refer to Rossow et al. (1996). The period 1989 to 1991 and the area between about 60°S and 90°S latitude were examined. Spatial and temporal variability of surface cloud forcing were then analyzed and model sensitivity studies were performed in order to access the relative importance of different surface and cloud properties.

2. METHODS

Cloud, atmospheric, and surface parameters from the ISCCP 3-hourly data set (D1) were used as input to FluxNet, a neural network implementation of the two-stream radiative transfer model Streamer (Key and Schweiger, 1998). Temperature and humidity profiles from the TOVS Pathfinder "Path-P" data set were used when and where available, primarily over the ocean around the Antarctic continent. Shortwave and longwave fluxes and cloud forcing at the surface and top of the atmosphere were computed with FluxNet because of its computational efficiency: it is up to 10,000 times faster than Streamer. Sensitivity studies were performed with Streamer.

Cloud forcing is calculated as the difference between the net fluxes for cloudy or partly cloudy conditions and clear skies:

$$CF = F(A_c) - F(0)$$

where CF is cloud forcing, F is the net shortwave, longwave, or all-wave flux, and A_c is the cloud amount.

3. SPATIAL AND TEMPORAL VARIABILTY

In order to evaluate both spatial and temporal trends in cloud forcing, zonal averages were calculated for each 2.5 degree latitude interval from 59.75°S to 88.75°S in the ISCCP data set and for each month. As can be seen in Figure 1, the presence of clouds leads to the greatest amount of surface cooling in the summer months at latitudes north (equatorward) of 70°S. In the figure, the dark line marks the boundary between negative and positive values of cloud forcing. This is no surprise since the days are much longer and the surface is less reflective due to ice melt. However, the most prominent feature of the net cloud forcing is that at latitudes poleward of about 80°S clouds were found to have a warming effect on the surface every month of the year. While clouds have a warming effect on the surface in the longwave and a cooling effect in the shortwave, the decrease in downwelling shortwave radiation due to reflection by clouds is much smaller because the bright surface increases the downwelling shortwave flux through multiple surface-cloud reflections. This year-round warming effect of clouds is not seen at comparable latitudes in the northern hemisphere.

4. SENSITIVITY ANALYSIS

Using Streamer, model sensitivity studies were conducted to determine the relative importance of various cloud and surface properties on the longwave and shortwave cloud forcing. More specifically, the

* Corresponding author address: Michael Pavolonis Univ. of Wisconsin - CIMSS, 1225 West Dayton St., Madison, WI 53706; Email: mpav@ssec.wisc.edu

sensitivity of cloud forcing to cloud fraction, cloud top temperature, cloud optical depth, surface albedo, and surface temperature were examined. For the baseline case, spatially averaged (88.75°S to 59.75°S) ISCCP cloud and surface parameters from the month of December were used when possible. The solar zenith angle was taken to be 60 degrees. An ice cloud with an effective particle radius of 30 microns and a ice water content of 0.07 g/m^3 was used in all simulations except when the cloud top temperature exceeded 258 K, where a liquid cloud with an effective particle radius of 10 microns and a liquid water content of 0.2 g/m^3 was used. These are the same effective particle sizes and concentrations used in the ISCCP processing. Table 1 shows the specific model input parameters.

Cloud fraction, cloud top temperature, cloud optical depth, surface reflectance, and surface temperature were varied so that cloud and surface properties characteristic of both the Antarctic continent and the ocean poleward of 60°S degrees would be accounted for. Table 2 shows the results of this sensitivity analysis including the difference between each case and the baseline case.

In the sensitivity studies, cloud amount was decreased from 50% to 10%. The increase in the shortwave cloud forcing (SWCF) was about twice as much as the decrease in longwave cloud forcing (LWCF), although both the SWCF and the LWCF are very sensitive to a 40% decrease in cloud amount. With 100% cloud cover the SWCF decreased by roughly 68 W/m^2 and the LWCF increased by about half as much. It should be noted that high cloud amounts are more typical of the ocean area surrounding Antarctica and lower cloud amounts are common over the Antarctic continent.

Table 1. Cloud and surface input parameters for baseline case.

Parameter	Value
Solar zenith angle	60 degrees
Cloud Fraction	0.50
Cloud top temperature	250 K
Cloud optical depth	10.0
Surface reflectance	0.60
Surface temperature	260 K
Effective particle size (ice)	30 microns
Ice water concentration	0.07 g/m^3
Effective particle size (liquid)	10 microns
Liquid water concentration	0.2 g/m^3

Next cloud top temperature was decreased by 35 K to 215 K. As expected, the change in the SWCF is small and insignificant. The LWCF decreases but by less than 3 W/m^2. Similarly, when the cloud top temperature is increased by 25 K the change in SWCF is negligible. The increase in the LWCF is larger than the decrease when cloud top temperature was decreased by 35 K, but it was still less than 3 W/m^2. Thus, neither the shortwave nor longwave cloud forcing are particularly sensitive to large changes in

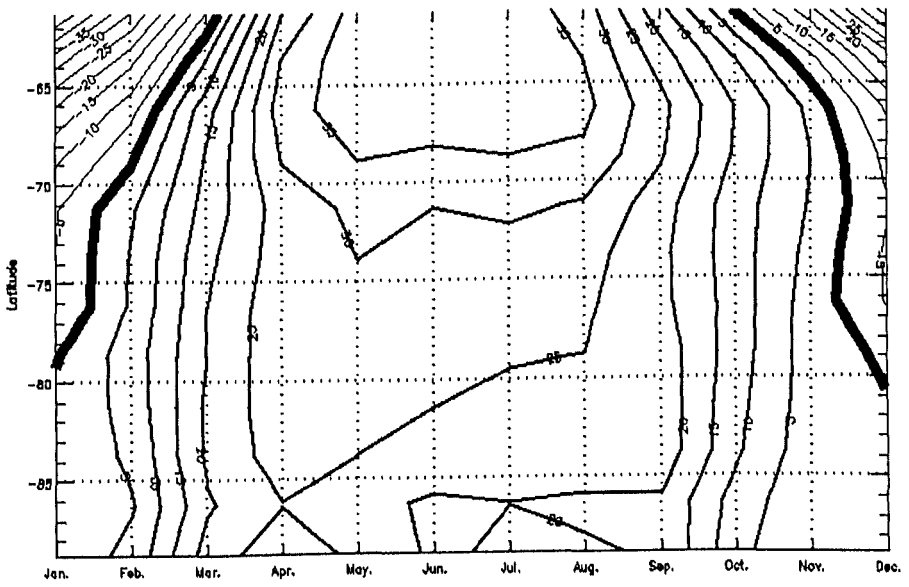

Fig. 1. Spatial and temporal distribution of net cloud forcing for the Antarctic (W/m^2).

cloud top temperature.

Table 2. Sensitivity of surface cloud forcing (W/m^2) to changes in cloud and surface parameters. Changes from the basline case are indicated for each parameter along with the actual values in parentheses. Shortwave (SWCF), longwave (LWCF), and net (NETCF) cloud forcing values are given along with their corresponding difference (diff) from the baseline case.

	SWCF	diff	LWCF	diff	NETCF	diff
Baseline case	−67.81	-----	34.32	-----	−33.59	-----
Cloud fraction						
−0.4 (0.1)	−13.58	+54.33	6.86	−27.46	−6.72	+26.87
+0.5 (1.0)	−135.82	−67.91	68.64	+34.32	−67.18	−33.59
Cloud top temperature						
−35 K (215 K)	−67.68	+0.23	32.27	−2.05	−35.41	−1.82
+25 K (275 K)	−68.49	−0.58	36.63	+2.31	−31.86	+1.73
Cloud optical depth						
−9.0 (1.0)	−16.81	+51.10	17.40	−16.92	0.59	+34.18
+20.0 (30.0)	−103.34	−35.43	37.20	+2.88	−66.14	−32.55
Surface albedo						
−0.4 (0.2)	−124.16	−56.25	34.32	0.00	−89.84	−56.25
+0.3 (0.9)	−36.04	+31.87	34.32	0.00	−1.72	+31.87
Surface temperature						
−35 K (225 K)	−67.91	0.00	33.81	−0.51	−34.10	−0.51
+20 K (280 K)	−67.91	0.00	34.79	+0.47	−33.12	+0.47

The sensitivity of cloud forcing to cloud visible optical depth was tested by first decreasing the optical depth from 10.0 to 1.0. Both the shortwave and longwave cloud forcing are sensitive to the decrease in optical depth, with the decrease in SWCF being about 15 W/m^2 greater than the increase in LWCF. When the cloud optical depth was increased from 10.0 to 30.0 the changes in both the SWCF and LWCF are much smaller than when the optical depth was decreased from 10.0 to 1.0. This is due to the logarithmic relationship between cloud optical depth and cloud forcing. In the shortwave, model runs reveal that the greatest changes in cloud forcing per unit change in optical depth occur at optical depths less than 10.0. In the longwave, the greatest variability occurs for optical depths less than 5.0. Hence, the sensitivity of cloud forcing to cloud optical depth is highly dependent on the magnitude of the optical depth, not the unit change in optical depth.

Only the SWCF will be sensitive to changes in surface reflectance. When the surface reflectance is reduced to from 0.6 to 0.2, which is a typical albedo for open water surfaces south of 60°S, the SWCF is decreased by about 56 W/m^2. Conversely, when the surface reflectance was increased to 0.9, which is typical of the Antarctic continent, the SWCF increased significantly. As can be seen in Table 2, surface albedos as large as 0.9 result in values of SWCF that are much smaller in magnitude as so the net cloud forcing approaches zero or becomes positive. This is the case over the Antarctic continent. In addition, one of the main reasons for the sharp gradient in the net cloud forcing in the summer months north of 70°S is the abrupt change in surface albedo due to sea ice melt (Figure 1).

Finally, changes in cloud forcing due to changes in surface temperature were examined. As expected, the SWCF is unaffected by changes in surface temperature. Similarly, even large changes in surface temperature produce negligible changes in the LWCF. This is probably due to the fact that changes in surface temperature will bring about changes in atmospheric temperatures which almost completely compensate for any increase or decrease in surface temperature.

It is apparent from this sensitivity analysis that any changes in the net cloud forcing due to changes in the cloud top temperature and surface temperature are negligible and can be ignored. It is also clear that the SWCF is much more sensitive to changes in cloud fraction and cloud optical depth than the LWCF. Thus,

changes in cloud fraction and cloud optical depth during the daylight months will lead to large changes in the net cloud forcing even though the changes in the SWCF and LWCF are opposite in sign. However, changes in the net cloud forcing due to changes in optical depth can vary significantly depending on the magnitude of the optical depth. Changes in surface albedo will also produce fairly large changes in the net cloud forcing.

5. SUMMARY

Cloud fraction, cloud optical depth, and surface reflectance have a significant influence on the surface radiation budget of Antarctica. Any changes in these parameters can mean the difference between clouds having a warming or a cooling effect on the surface. Over much of the Antarctic continent these parameters combine such that clouds have a warming effect on the surface year-round. This effect is unique to the Antarctic.

ACKNOWLEDGEMENTS

This work was supported by NSF grant OPP-0096085.

6. REFERENCES

Key, J., and A.J. Schweiger, 1998: Tools for Atmospheric Radiative Transfer: Streamer and FluxNet, *Computers and Geosciences*, **24**(5), 443-451.

Lubin, D., B. Chen, D.H. Bromwich, R.C.J. Somerville, W. Lee, and K.M. Hines, 1998: The Impact of Antarctic Cloud Radiative Properties on a GCM Climate Simulation, *J. Climate*, **11**, 447-462.

Rossow, B.W., Walker, A.W., Beuschel, D.E., and Roiter, M.D., 1996: International Satellite Cloud Climatology Project (ISCCP) documentation of cloud data, World Climate Research Programme, WMO.

P2.20 DEVELOPMENT OF A CLIMATOLOGY OF CLOUD PROPERTIES DERIVED FROM GOES OVER THE SOUTHEASTERN PACIFIC FOR PACS

J. Kirk Ayers*
Analytical Services & Materials Inc., Hampton, VA

Patrick Minnis, David F. Young, William L. Smith, Jr., and Louis Nguyen
Atmospheric Sciences, NASA-Langley Research Center, Hampton, VA

1. INTRODUCTION

A goal of the NOAA Pan American Climate Studies (PACS) Program is to understand the role of the trade winds, sea surface temperature, and the subtropical stratocumulus systems, especially over the southeastern Pacific (SEP), in the maintenance and variability of the eastern Pacific intertropical convergence zone (ITCZ). Determination of the cloud properties and their interaction with the radiation budget and SST are crucial to understanding the relationship between the subtropical highs and the deep convection over the eastern Pacific. This paper presents the results of an initial analysis of 3-hourly multispectral GOES-8 data to derive cloud macrophysical and microphysical properties as well as the radiation budget over the SEP and adjacent continental areas. Cloud amount, height, phase, effective particle size, optical depth, and liquid/ice water path are derived along with shortwave SW albedo, and the top-of-atmosphere (TOA) longwave flux on a 1.0° latitude-longitude grid for a domain encompassed by 20°N, 40°S, 60°W, and 115°W, shown in Fig. 1. The initial analyses focus on the period between October and November 1999 when research ships from Chile and the USA were operating in the domain. Data from radar and a ceilometer aboard the ships are used to validate the retrievals from GOES-8. These analyses are the first steps in the process of developing climatologies of cloud and radiation properties for use in meso- and large-scale models of the circulation in the southeastern Pacific.

2. METHODOLOGY

This study utilizes the Visible Infrared Solar-Infrared Split Window Technique (VISST) to determine cloud properties. VISST is a 4-channel model-matching method for plane parallel clouds. It is discussed further by Minnis et al. (2001). VISST requires 4-km pixel resolution GOES-8 satellite images and uses the following channels: 0.65 μm (VIS), 3.9 μm (SIR), 10.8 μm (IR), and 12.0 μm (SWC). The GOES-8 data for each channel were calibrated by Minnis et al. (2001) using coincident data from the Visible Infrared Radiometer (VIRS) on the Tropical Rainfall Measuring Mission satellite (TRMM). No changes were made to the nominal GOES-8 SIR, IR, and SWC data.

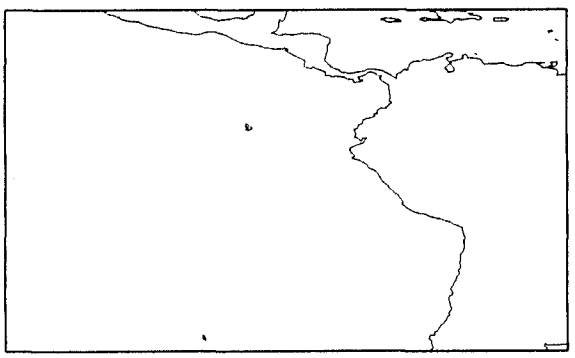

Figure 1. Analysis domain.

Several additional inputs are required to facilitate satellite retrievals. Atmospheric profiles (1° resolution) derived from ECMWF 6-hourly model runs are used for skin temperature, cloud height calculation, and humidity profiles. Surface type is based on the IGBP 10-minute resolution surface map, remapped to an albedo representation. Clear-sky reflectances, and ice and snow masks developed for the Clouds and the Earth's Radiant Energy System (CERES) program are used for additional surface characterization (Trepte et al. 1999). Narrowband-to-broadband flux conversion functions, developed from correlations of coincident ERBE-scanner broadband and GOES narrowband fluxes are used to compute broadband shortwave and longwave fluxes from the GOES data.

3. MONTHLY SUMMARIES

Several examples of monthly mean cloud products for November 1999 are shown in Figs. 2 - 7. Mean cloud coverage and cloud-top heights for the month are shown in Figs. 2 and 3, respectively. The areas of deep convection, identified by mean cloud heights over 5 km, are primarily located over South and Central America. The ITCZ over the Pacific is apparent in the elevated cloud amounts near 10°N, but deep convection is not as frequent there as over Central America because the mean cloud heights do not exceed 4 km. Nevertheless, the northern part of the ITCZ where cloud tops are higher is probably a region where rainfall occurs. The smallest cloud amounts are found over the Atacama Desert while the greatest cloud amounts are found over the

* *Corresponding Author Address*: J. K. Ayers, AS&M, Inc., 1 Enterprise Parkway Hampton, VA 23666;
E-mail: j.k.ayers@larc.nasa.gov.

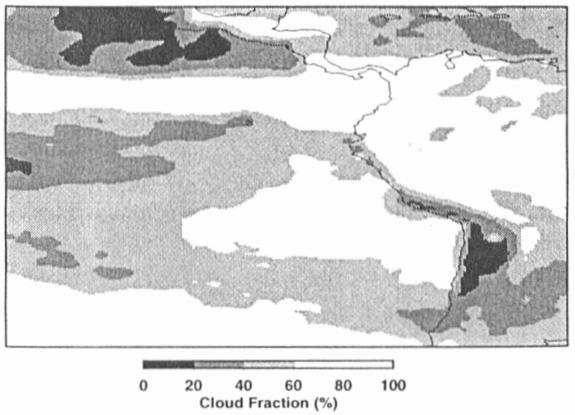

Fig. 2. November 1999 mean cloud fraction.

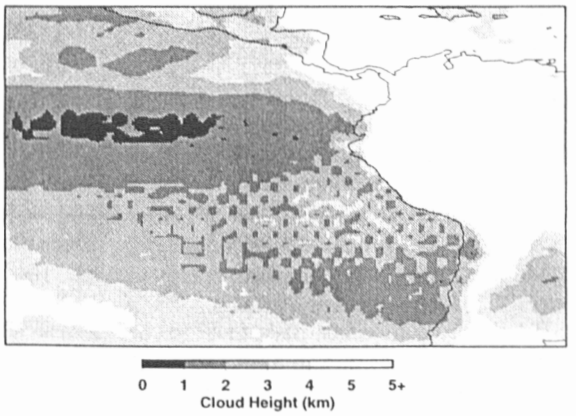

Fig. 3. November 1999 mean cloud-top height.

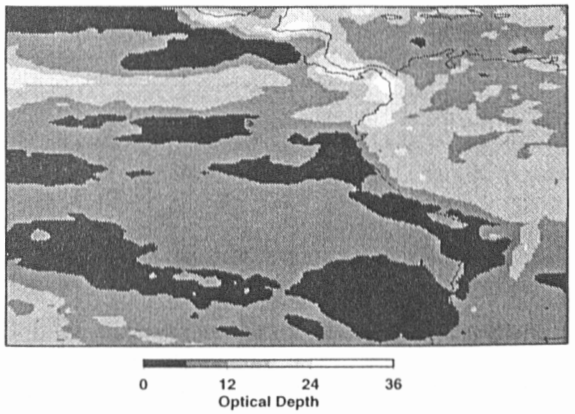

Fig. 4. November 1999 mean optical depth.

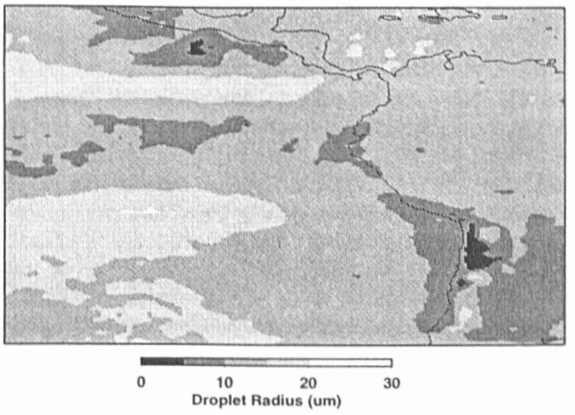

Fig. 5. November 1999 mean water droplet radius.

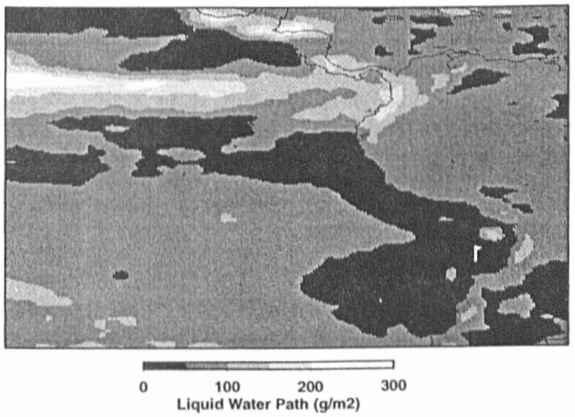

Fig. 6. November 1999 mean liquid water path.

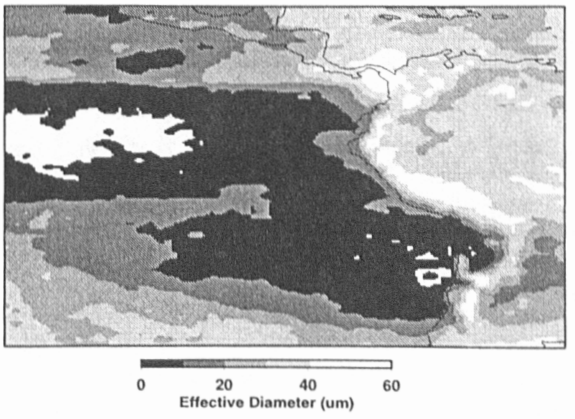

Fig. 7. November 1999 mean ice crystal effective diameter.

Amazon Basin and the stratocumulus region off the western coast of Chile. Increased cloud fraction over the Southern Hemispheric storm track is visible in the southernmost portion of the figure. Cloud tops are lowest just south of the ITCZ and near the Chilean coast. The mottled pattern in Fig. 3 over the ocean is an artifact of the gridded soundings and SSTs used in the analysis.

Mean optical depth τ, shown in Fig. 4, varies from 3 over some ocean areas to nearly 35 over Panama. The heavier cloud cover in the ITCZ has relatively larger values of τ. The SEP stratocumulus region shows τ

decreasing around its edges. The mean water droplet radius r_e distribution for the analysis domain in Fig. 5 reveals smaller droplets near the Mexican and Chilean coasts and also south of the ITCZ. The smaller effective radii over the SEP tend to follow the cold current into the ITCZ. Larger droplets are found over the Amazon Basin, the ITCZ, and in the western part of the SEP stratocumulus region. The mean r_e for the ITCZ is in the 15 to 20 μm range, which is usually associated with precipitation. The westward increase in r_e from the Chilean coast was also observed during October 1999 from GOES-8 (Garreaud et al. 2001).

The mean liquid water path *LWP* for the domain in Fig. 6 shows values ranging from 150 to 300 gm^{-2} over the ITCZ. The smallest values are found along the cold current and north of the ITCZ as a result of the small values of r_e and τ for the region.

The mean ice crystal effective diameters D_e are shown in Fig. 7. The light gray region near the center of the western edge of the domain is an area where no ice retrievals were found. Many of the small values of D_e over the SEP are probably underestimated because most of the retrievals were affected by the low clouds underneath the thin cirrus. The ice particle sizes over the Andes and the ITCZ are more accurate and larger because the clouds are optically thick and the 3.9-μm radiance is unaffected by the lower clouds. Examination of individual scenes reveals larger ice crystals for thin cirrus over an otherwise cloud-free ocean. The mean ice water path *IWP* (not shown) varies from 0 to over 300 gm^{-2}; the largest values are found over the areas of deep convection. The percentage of the observed clouds that were identified as ice clouds is shown in Fig. 8. More than half of the cloudiness over the entire Amazon Basin and Caribbean Sea is composed of ice. A smaller percentage of ice occurs over the ITCZ while very few ice clouds were observed over the SEP stratocumulus area (black in the figure).

4. VALIDATION

During November 1999 the NOAA *R/V Ron Brown* cruised the region, 8°N - 8°S, 95°W - 110°W, collecting a wide range of meteorological and oceanographic data, (http://www.ogp.noaa.gov/mpe/clivar/pacs/fy99/fairall/fairall99.htm). Data from the ceilometer, cloud radar, and microwave radiometer aboard the *Ron Brown* are used for assessing the satellite retrievals. The validation is effected by comparing VISST cloud properties averaged for a 0.5° box centered on the ship with half-hourly means from the ship data. Cloud amount is computed from the ceilometer data by dividing the number of cloud returns by the total number of shots. Cloud-top height is derived from the radar data and the *LWP* is computed from the microwave radiometer measurements.

Cloud Fraction

Overall the mean cloud fraction from VISST is 36.8% compared to 39.7% from the ceilometer. The standard deviation of the differences is 19%. The cloud amounts are in good agreement when the cloud fraction is either less than 20% or greater than 80% (Table 1). The approximately 30% of the time when the agreement is poor can be attributed to several factors. In a few cases, the column directly over the Brown was clear but, from the satellite imagery, clouds were obviously present in the box. Mid and high level clouds, which can be observed by satellite but not by the ceilometer, could contribute to the scatter. Those cloud types may account for the VISST values in the 40-60% range for the nearly clear ship observations,

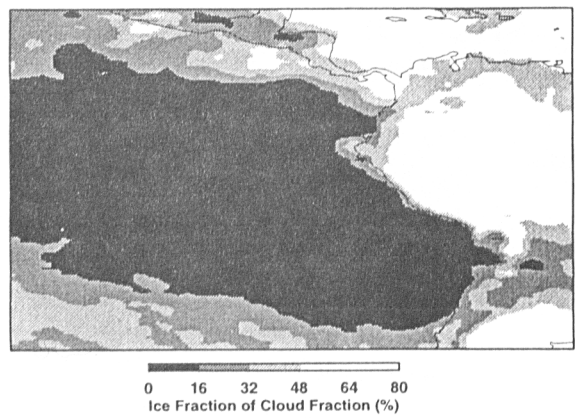

Fig. 8. Percentage of observed cloud amount classified as ice cloud.

Cloud Height

The VISST and radar cloud-top heights are compared in Fig. 9. The non-filled circles are a direct comparison of all coincident data. The resulting curve fit shows that the radar measurements are somewhat higher than those from VISST for $z_c < 1.5$ km, but the agreement is better for higher clouds. Overall, z_c(GOES) is 0.15 ± 0.55 km lower than z_c(radar). This level of agreement is similar to that found over the southeastern Pacific by Garreaud et al. (2001) for a comparison of GOES-8 data analyzed with VISST over the southeastern Pacific during October 1999. The largest contributors to the difference here are multi-level clouds and multiple inversions. If only single layer clouds are considered (filled circles), the agreement is even better.

Liquid Water Path

VISST-derived and ship microwave LWP amounts are compared in Fig. 10. The two datasets are reasonably well correlated but appear to have an offset. The mean microwave LWP is 87.2 gm^{-2} which is 13.5 gm^{-2} greater than the VISST average. These results were obtained using a global baseline of 10 gm^{-2} for the microwave data. Work is in progress to correct a diurnal cycling problem and to adjust the baseline of the microwave LWP retrievals (C. F. Fairall, personal communication). New LWP values might improve the correlation.

Table 1. Comparison of *R/V Ron Brown* ceilometer and VISST cloud fractions.

	VISST				
R. Brown	0-20	20-40	40-60	60-80	80-100
0-20	19	1	5	0	0
20-40	4	1	1	0	0
40-60	0	0	1	0	0
60-80	0	0	1	0	0
80-100	0	1	1	1	12

5. CONCLUDING REMARKS

The SEP contains a variety of interesting features that should be reproduced in climate or regional forecast models. For example, variations in cloud particle size may be correlated with SST, the intensity of the subtropical high, or the availability of cloud condensation nuclei. Significant changes in cloud amount, optical depth, and *LWP* occur as a function of local time (not shown). Thus, the relatively static picture presented here does not capture one of the main features of clouds in this part of the world. Such characteristics should be taken into account when modeling the atmosphere in this area.

The initial validations from this study indicate that the VISST method applied to GOES data can produce reliable cloud macrophysical and microphysical properties over the PACS region. The ship observations will be refined further to obtain final validation for this particular cruise. Additional study using ship observations from other *R/V Ron Brown* cruises in the same area will be analyzed to improve the statistical reliability of the validations and to better understand the retrievals. Concurrently, the GOES-8 data will be analyzed continuously for a long time period beginning in 1996 to determine the differences in the SEP cloud features during and after El Ninos.

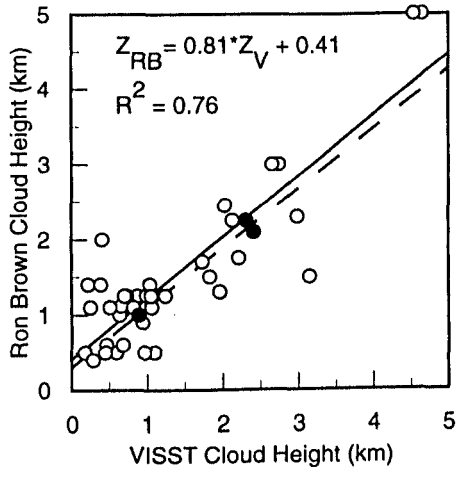

Fig. 9. Comparison of radar and VISST cloud heights.

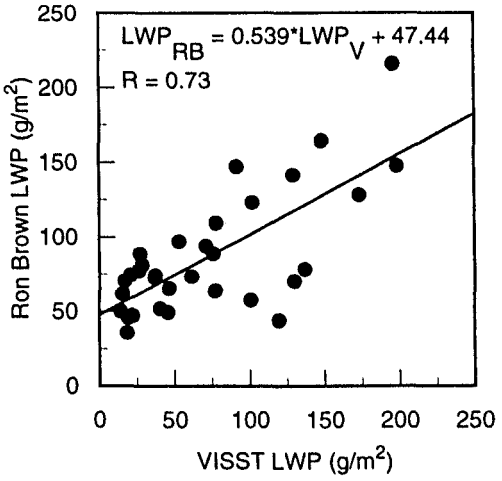

Fig. 10. Comparison of VISST and microwave LWP.

Acknowledgments

This work was supported by the NOAA PACS Program under NOAA agreement NA00AANRG0330. Many thanks to Dr. Chris Fairall for providing the preliminary data from the *R/V Ron Brown*, and to Pat Heck, Anita Rapp, Mandana Khaiyer, and David Doelling for helping to implement the satellite analysis programs. The atmospheric profiles were generated by the CERES Meteorological, Ozone, and Aerosols group and obtained from the NASA Langley Atmospheric Sciences Data Center.

References

Garreaud, R. D., J. Rutllant, J. Quintana, J. Carrasco, and P. Minnis, 2001: CIMAR-5: A snapshot of the lower troposphere over the subtropical southeast Pacific. *Bull. Amer. Meteorol. Soc.*, October issue.

Minnis, P., L. Nguyen, D. F. Young, D. R. Doelling and W. F. Miller, 2001: Rapid calibration of Operational and research meteorological satellite imagers, Part I: Use of the TRMM VIRS or ERS-2 ATSR-2 as a reference. Submitted to *J. Atmos. Oceanic Technol.*

Minnis, P.,et al., 2001: A near-real time method for deriving cloud and radiation properties from satellites for wether and climate studies. *Proc. AMS 11th Conf. Satellite Meteor. and Oceanogr.*, Madison, WI, October 15-18.

Trepte, Q., Y. Chen, S. Sun-Mack, P. Minnis, D. F. Young, B. A. Baum, and P. W. Heck, 1999: Scene identification for the CERES cloud analysis subsystem. *Proc. AMS 10th Conf. Atmos. Rad.*, Madison, WI, June 28 – July 2, 1999, 169-172.

P2.21

A Prototype Benchmark Thermal Radiance Measurement

John A. Dykema, James G. Anderson and R.M. Goody
Harvard University, Divsion of Engineering and Applied Sciences, Cambridge MA

1. Introduction

The NOAA Science Advisory Board's Panel on Strategies for Climate Monitoring prioritizes the development of a set of Benchmark measurements for monitoring long-term changes in climate. As defined by the Panel, Benchmark measurements adhere to principles requiring demonstrable accuracy tied to metrological standards on a limited set of climate variables relevant to decadal-to-century scale climate change. An illustrative example of a Benchmark measurement is the baseline CO_2 monitoring effort maintained by CMDL. Spectrally resolved, thermal radiance measurements from space constitute a key Benchmark measurement that is well-studied (Harries *et al.* 2001) and capable of early deployment. The realization of this benchmark measurement requires scientific infrastructure which is singularly focused on the radiometric accuracy target. This infrastructure connects precision measurements in the laboratory through identical hardware to on-orbit diagnostics in the satellite.

We present a numerical model which quantifies the expected radiometric performance of a prototype instrument for a benchmark radiance measurement. The model calculates the systematic error as a function of observed brightness temperature and wavenumber. The model is based on a design for a low-cost, lightweight satellite. This design includes two bore-sighted Michelson interferometers covering the spectral window from 250 to 2000 cm^{-1} (40 to 5 μm) at a spectral resolution of ~ 0.5 cm^{-1}, with an accuracy goal of 0.1 K on at 250 K brightness temperature at 750 cm^{-1}. This level of accuracy in a space-based measurement represents a significant challenge. Because the satellite must satisfy the objective of convincing future investigators of accuracy, radiometric performance must be clearly documented.

The calibration strategy for this Benchmark measurement is based on the principles of precision metrology (Keith and Anderson 2001). Every source of systematic error that is significant at the 10 mK level will be measured independently. The end-to-end performance of the instrument will then be carefully quantified, and analyzed for its agreement with the constituent error sources. The model under development presented here provides a quantitative simulation of these systematic errors. The model is designed to both simulate the errors independently and calculate their effect as they would occur together in the real instrument. The parameters utilized by the model reflect the actual performance of instrumental subsystems as determined both by emipirical measurements and from engineering specifications. The model converts the subsytem parameters into their associated systematic radiometric errors, expressed in units of equivalent temperature. Errors related to the calibration standards (blackbodies) and instrumental optical performance are treated, including blackbody thermometry and emissivity, out of field of view optical sensitivity, infrared detector and signal chain nonlinearity, and polarization effects. These errors have been treated for other infrared radiometers (Fennelly *et al.* 2001, Best *et al.* 1997, Mason *et al.* 1996). The following table shows the design values for the individual errors simulated in this model (Anderson *et al.* 1995).

Systematic Error	Value
Absolute Thermometry	0.030 K
Blackbody Inhomogeneity	0.035 K
Blackbody Emissivty	0.9997
Polarization Error	0.0011*scene temperature contrast
Out-of-Field of View (FOV) Sensitivity	0.01%
Signal Chain Nonlinearity	0.0001

These errors are treated with the goal of providing a performance baseline for critical analysis of on-orbit accuracy and to evaluate effects of the space environment on the measurement calibration.

2. Numerical Model

A calibrating, spectrally resolving radiometer requires three basic components: calibration standards, a means of spectral dispersion, and a radiation detector. The candidate radiometer simulated by this model has three calibration standards: two blackbody cavities and a deep space view, to allow overdetermination of the calibration (assuming the radiometer has a linear response to incident flux). The level of measurement accuracy achieved during flight can therefore be critically analyzed by intercomparing the three calibration standards.

The blackbodies are composed of deep cylindrical cavities coated with very low reflectivity coating, which yields emissivity very near (but not perfectly) unity. The cavities are maintained at a stable temperature by closed loop control, monitored by redundant temperature sensors. For accurate determination of radiometric zero, a deep space view is included as a calibration standard. The systematic errors due to the blackbodies are related

Corresponding author address: John A. Dykema, Anderson Group/CCB, Harvard University, 12 Oxford St., Cambridge, MA 02138; e-mail: dykema@fas.harvard.edu

to differences between the true photon flux provided by the blackbody and the estimated photon flux from the measured thermometric temperature and the estimated emissivity.

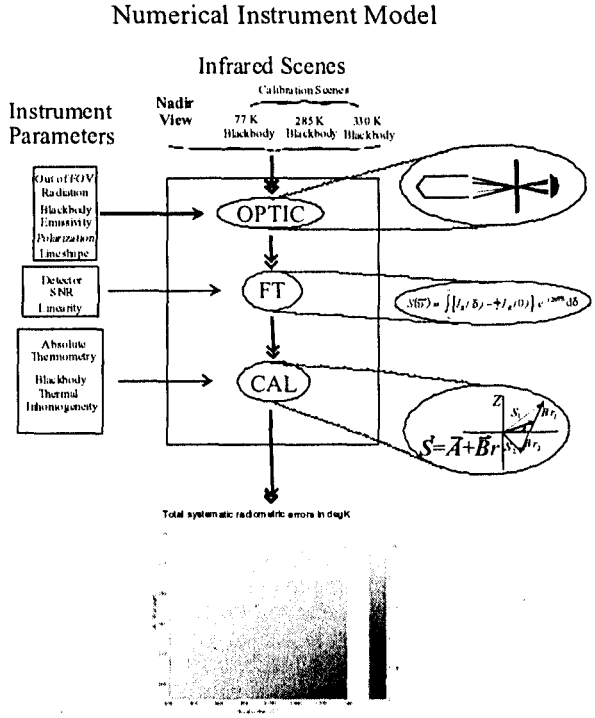

Figure 1: A flow chart of the numerical model of the prototype Benchmark spectrometer. Radiation scenes undergo sequential operations simulating the systematic errors specified by the characteristics of the actual instrumental hardware. The large central rectangle represents the numerical model; the left hand column represents the instrument subsystem parameters, which determine the magnitude of the systematic errors. The ellipses on the right hand side represent the internal calculations of the model. An observed scene plus two calibration scenes are processed from top to bottom, finally producing a calibrated output scene, from which the systematic errors are determined, as shown in the bottom plot.

A corner cube, four port FTS provides spectral dispersion. The input port that views the scene (either calibration scene or atmospheric scene) is differenced against a stable radiometric standard. An optical pointing system is required to select the light that is directed into this input port. This action is accomplished via a pointing mirror. The systematic errors due to the spectral disperser and optical system are related to stray light which is directed into the observation scene, and to changes in optical efficiency due to polarization effects as the pointing mirror rotates relative to the FTS beamsplitter.

At each detector port, a pyroelectric detector senses the interferometric signal. Although pyroelectric detectors have relatively low detectivity (D*) and thus lower signal-to-noise ratio (SNR) than quantum detectors such as mercury cadmium telluride (MCT) detectors, they have a much more linear response and cover a wider spectral window with nearly constant responsivity. The systematic errors associated with the detector are due to nonlinearities in its response and within the signal chain. The noise intrinsic to the detector (as measured by D*) adds a random noise component to the spectral measurement.

As shown in figure 1, the model performs sequential operations that simulate the changes to the observed radiation field due to the characteristics of the instrument. To calculate the error for a given observation scene, three spectral acquisitions are simulated: the observation scene itself, and two calibration scenes. The calibration scenes are necessary to derive the calibration coefficients as per Revercomb *et al* (1988).

The first module of the model simulates the optical properties of the spectrometer. For blackbody calibration scenes, the radiance is calculated from the planck function for the chosen calibration temperature. Calibration temperatures are chosen to bracket the expected range of observation temperatures, which are expected to be between 180 K and 320 K. This radiance is then multiplied by a factor less than one to simulate the imperfect emissivity of the blackbody cavity.

$$r_{bb} = \varepsilon r_{planck}(T)$$

Here a constant value of ε for all wavenumbers is used, although a factor which is a function of wavenumber may be used if detailed measurements show significant frequency-dependent emissivity. The value of ε used for this work was 0.9997. This emissivity may be readily achieved by utilizing Enhanced Martin Black coating in a cavity with a diameter to aperture ratio of 3.

The next step is to simulate stray radiation which is modulated by the interferometer and enters the infrared detector. (Laboratory observations indicate radiation from outside the field of view is well approximated by thermal radiation at ambient instrument temperature). The observed radiation is modeled as a linear combination of the scene radiation from the previous operation and blackbody radiation at the temperature of the instrument optics.

$$r_{scene} = (1-\beta) r_{scene} + \beta\, r_{ambient}(t,T)$$

The value of the out of field sensitivity β used for this work was 0.01%. Because this ambient radiation represents an offset to the scene radiance, the calibration procedure will compensate for it if it is stable over an acquisition cycle. If it varies between acquisitions of calibration and observation scenes, an error will be introduced. To simulate this property, the model varies the temperature of the ambient radiation and the reference input between data acquisitions. This introduces the thermal stability of the instrument as a significant source of systematic error. The thermal stability of the reference input was 400 min/K. The thermal stability of the emission temperature of the ambient (stray) radiation was 80 min/K.

The next step simulates the polarization effect due to changes in orientation between the optical axes of the pointing mirror and the beamsplitter. The reflectivity of the pointing mirror is slightly different for radiation polarized parallel and perpendicular to the plane of reflection (called s- and p-reflectivities). The correction takes the form:

$$r_{pol} = \rho \cos(2\theta)(r_{scene} - r_{PM}) + r_{scene}$$

where r_{pol} is the scene radiation transformed by the polarization effect, ρ is a parameter measured empirically or derived from the known optical properties of the pointing mirror and beamsplittter θ is the angle between the plane of reflection at the pointing mirror and the optical axes of the beamsplitter, and r_{scene} is the scene radiation from the previous model step. The value for ρ here is 0.0011, taken from measurements on INTESA (Keith *et al* 2001). This value creates a radiometric error of about one part per thousand in the mid-infrared. This error may be measured by viewing a fixed scene over a range of pointing mirror angles. This procedure can be accomplished in a satellite by viewing deep space over a range for 45°, producing a value for ρ. This value can then be used with the above equation to correct the measured radiance.

As stated above, the spectrometer model is based on a four-port interferometer with two input ports and two output ports. A radiometric reference is placed at the second input port (the first being dedicated to scene radiation selected by the pointing mirror). The radiation detected at the interferometer output ports is then a difference spectrum created by the difference of the scene radiation and the reference radiation. This characteristic is simulated by subtracting blackbody radiance for the temperature of the reference input (typically 5 K below ambient temperature) from the scene radiation.

This difference spectrum is next converted into an interferogram by an inverse Fourier transform. A nonlinear response in the detector signal chain may be approximated by a power series in the interferogram (Abrams *et al.* 1994). For the small nonlinearities required for this spectrometer, inclusion of a quadratic term is sufficient. The interferogram is thus transformed:

$$I_{nl} = I_{obs} + \alpha I_{obs}^2$$

Since the candidate detector for this spectrometer is pyroelectric, the interferogram consists only of an AC modulated signal. Pyroelectric detectors only detect time-changing signals (Porter 1981). The nonlinearity in this model reduces the centerburst magnitude of the brightest scene by 0.01%.

Quantum photodetectors which are sensitive to DC background radiation require an offset term:

$$I_{nl} = (I_{obs} + \Phi_{DC}) + \alpha(I_{obs} + \Phi_{DC})^2$$

This DC flux creates an additional radiometric error which is proportional to the scene radiance.

After the nonlinearity is simulated, the scene is returned to spectral form via a Fourier transform. The radiometric error on the scene may now be calculated by following the calibration procedure, which incorporates errors due to absolute thermometry and blackbody thermal inhomogeneity.

The systematic errors associated with this module arise due to differences between the predicted blackbody radiation flux and actual blackbody radiation flux that are constant in equivalent temperature. These errors arise from temperature gradients in the blackbody cavity, temperature differences between the location of the temperature sensor and the emitting surface, and from inaccuracies in measurement by the temperature sensors themselves.

The calibration coefficients are calculated by solving the system of equations:

$$S_{i,\tilde{\nu}} = A_{i,\tilde{\nu}} + B_{i,\tilde{\nu}} r_{i,\tilde{\nu}}$$

where S is the observed radiance signal for each blackbody i and channel $\tilde{\nu}$, and r is the true radiance calculated from the Planck function. A and B are the calibration coefficients, computed for each wavenumber channel. A represents the optical offset vector, B represents the instrument gain. The thermometry errors are simulated by computing a blackbody radiance r for a temperature differing from the blackbody scene temperature by some error dT.

$$r_{i,\tilde{\nu}} = r_{planck}(T - dT)$$

The value for the thermometry error dT used for this work is 0.065 K. This value includes 0.03 K absolute thermometry error (inaccuracy of the temperature sensor) plus 0.035 K blackbody inhomogeneity error (spatial temperature inhomogeneity of the blackbody, difference between temperature of emitting surface and region of temperature sensor).

Results

The calculation of the radiometric error in equivalent temperature units was performed for brightness temperatures ranging from 210 K to 325 K, for frequencies from 200 cm^{-1} to 1600 cm^{-1}. The results for these calculations are shown in figure 2. This figure shows that the highest levels of accuracy are achieved in the middle of the instrument's spectral window, between 500 cm^{-1} and 1000 cm^{-1}. This spectral region covers several important radiative forcings, including CO_2, CFC-11 and CFC-12 and O_3. CH4 and water vapor have strong radiative forcings nearby between 1100-1300 cm^{-1}, where radiometric accuracy is also good except for very cold equivalent temperatures.

The errors at warm temperatures are dominated by the nonzero reflectivity of the blackbodies. This effect produces a warm bias on the measurement, which is most pronounced for the hottest scenes and is near zero for very cold scenes. At cold temperatures, the errors are dominated by stray light effects, which are largest at higher frequencies. Because cold scenes emit a relatively low quantity of radiation at these frequencies, stray radiation from warm scenes has an exaggerated effect. The nonlinearity errors are most pronounced at the edges of the spectral window, where the ratio of aliased radiance to real radiance is largest. Thermometry errors create a radiometric error that is nearly equal in equivalent temperature across the window. Polarization errors are largest for scenes that are either very hot or very cold, since they are proportional to the temperature contrast between the pointing mirror and the scene.

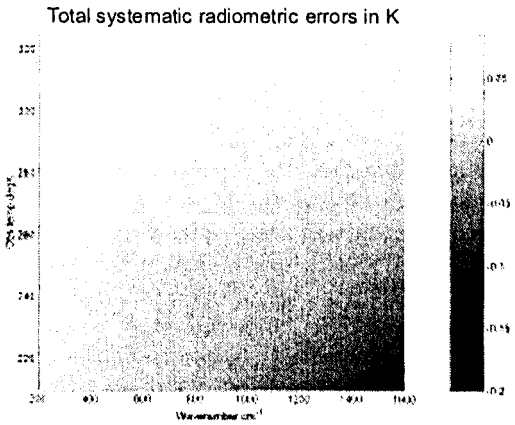

Figure 2 Results of model calculation for error budget given in table 1. The calculations predict that the instrument will demonstrate better than 0.1 K radiometric accuracy for frequencies between 500-1000 cm^{-1} for all brightness temperatures between 210-325 K. Between 1100-1400 cm^{-1}, better than 0.1 K accuracy is achieved for brightness temperatures above 240 K. This performance meets the requirements for monitoring the decadal-scale trends in the radiative forcing due to the key greenhouse gases CO_2, CH_4, H_2O, N_2O, O_3, CFC-11, and CFC-12.

Conclusions

The radiometric performance of a prototype spectroradiometer for long-term climate monitoring may be simulated by a set of simple calculations that utilize parameters from engineering specifications and laboratory experiments. These calculations reveal significant spectral variation in the achieved radiometric accuracy, which also depends considerably on scene temperature. These results may be used as a tool to optimize instrumental design to efficiently monitor long-term changes in climate.

References

Abrams, M. C., Toon, G. C., Schindler, R. A., 1994: Practical example of the correction of Fourier-transform spectra for detector nonlinearity. *Applied Optics*, **33**, 6307-6314.

Anderson, J. G., Keith, D. W., Goody, R.G., and Coauthors, 1996: Arrhenius: A small satellite for climate research. A proposal submitted to NASA-HQ December 1996, No. ESSP-II-0030, 160 pp. [Available from the authors]

Best, F., H. Revercomb, D. LaPorte, R. Knuteson, and W. Smith, Accurately Calibrated Airborne and Ground-based Fourier Transform Spectrometers II:HIS and AERI Calibration Techniques, Traceability, and Testing, in *Council for Optical Radiation Measurements (CORM) 1997 Annual Meeting*, National Institute of Standards and Technology (NIST), Gaithersburg, MD, 1997.

Fennelly, J., J.E. Jenney, D. Jordan, and P. Mantica, Challenges in calibration of operation fourier transform spectrometers for space-based nadir sounding of the earth's atmosphere, in *Fourier Transform Spectroscopy And Optical Remote Sensing of the Atmosphere*, Optical Society of America, Couer d'Alene, ID, 2001.

Harries, J.E., H.E. Brindley, P.J. Sagoo, and R.J. Bantges, Increases in greenhouse forcing inferred from the outgoing longwave radiation spectra of the Earth in 1970 and 1997, *Nature*, *410*, 355-357, 2001.

Keith, D. W., and Anderson, J.G., 2001: Accurate Spectrally Resolved Infrared Radiance Observation from Space: Implications for the Detection of Decade-to-Century–Scale Climatic Change, *Journal of Climate*, **14**, 979–990.

Keith, D.W., J.A. Dykema, H. Hu, L. Lapson, and J.G. Anderson, An Airborne Interferometer for Atmospheric Emission and Solar Absorption, *Applied Optics*, in press

Mason, I.M., P.H. Sheather, J.A. Bowles, and G. Davies, Blackbody calibration sources of high accuracy for a spaceborne infrared instrument: The Along Track Scanning Radiometer, *Applied Optics*, *35* (4), 629-639, 1996.

Porter, S.G., A brief guide to pyroelectric detectors, *Ferroelectrics*, *33* (1-4), 193-206, 1981.

Revercomb, H.E., H. Buijs, H.B. Howell, D.D. Laporte, W.L. Smith, and L.A. Sromovsky, 1988: Radiometric calibration of IR Fourier-transform spectrometers - solution to a problem with the high-resolution interferometer sounder, *Appied Optics*, **27**, 3210-3218.

P2.22 AEROSOL OPTICAL DEPTH OVER LAND FROM THE AVHRR PATHFINDER ATMOSPHERE DATA SET

Kenneth R. Knapp*
CIRA –NOAA/NESDIS/ORA

1. INTRODUCTION

With the reprocessing of AVHRR data back to 1981 by the AVHRR Pathfinder Atmosphere (PATMOS) project at NOAA/NESDIS (Jacobowitz, 1999), cloud-free radiance statistics exist for each day on a global 110 km grid for all five channels of AVHRR. Ocean grid cell data have been processed with the NOAA operational aerosol retrieval algorithm to create the most extensive record of aerosol optical depth (τ) ever compiled. However, as theoretical climate model studies indicate, the most significant concentrations and radiative effects of aerosols occur over land. To assist these climate studies, as well as the Global Aerosol Climatology Project, we are developing a τ retrieval algorithm over land comparable to the one over oceans when and where an aerosol signal is present in the 0.63μm reflectance channel of AVHRR.

The first step of this research was to determine an aerosol signal in the PATMOS data, where a signal was found, but is strongly dependent on the surface bidirectional reflectance distribution function (BRDF). The research presented herein is the preliminary results of retrieving aerosol optical depth from top-of-the-atmosphere (TOA) AVHRR PATMOS reflectances.

2. DATA

Two data sources are used in this study: the PATMOS data set provides cloud-free TOA reflectance observations and the Aerosol Robotic Network (AERONET) data provide ground-truth aerosol optical depths.

2.1 PATMOS Data

The Advanced Very High Resolution Radiometer (AVHRR) has flown nearly continuously on numerous NOAA satellites since 1981. This vast amount of data is condensed into a useable format in the PATMOS data set (Jacobowitz et al., 2001; Stowe et al., 2001). The volume of the Global Area Coverage (GAC) AVHRR data has been significantly reduced from terabytes to gigabytes by statistically decreasing the spatial resolution. The GAC data are binned into 110×110 km^2 quasi-equal area grid cells where statistics are calculated for each AVHRR channel for each grid cell.

The PATMOS daily-radiance data set (PATMOS-1) includes 71 parameters for each grid cell. 54 parameters are direct variables of AVHRR measurements. Four statistical categories are used for each channel: All pixels, clear sky, aerosol burden and cloudy. Statistics for each category (generally, the mean and standard deviation) are recorded for each channel. The parameter used in this study is the channel 1 (0.63μm) reflectance (R_{sat}) deemed cloud-free by the CLAVR-1 algorithm (Stowe et al., 1999).

For this study, the PATMOS-1 data from 1993 through 1999 are used to compare with AERONET observations of τ.

2.2 AERONET Data

The AERONET provides the ground truth validation for this research. AERONET is a federation of sun-sky radiometers independently owned with centrally archived data, which can measure aerosol optical depth to an accuracy of ±0.02 (Holben et al., 1998). Data used in this study utilizes only those sites where the data have been cloud filtered as well as post-calibrated (i.e., level 2 data).

3. AEROSOL RETRIEVAL METHOD

The retrieval of aerosol information from PATMOS data over land is a three-step process. First, reflectances for numerous conditions are calculated from a radiative transfer model and stored in look-up tables (LUT). These tables are then used to retrieve the surface BRDF from the PATMOS data. The surface BRDF data are then used to retrieve τ from the PATMOS data using LUT for that BRDF. This method is developed and further test by Knapp and Stowe (2001).

3.1 Step 1: Look-Up Table Calculation

The DISORT radiative transfer model version 2 (Tsay et al. 2000) is used to produce theoretical TOA reflectances. TOA reflectances (R_{LUT}) were simulated at 13 solar zenith angles, θ_1: 10°-70°, 15 satellite zenith angles, θ_2: 0°-70° and 19 azimuth

* Corresponding author address: Kenneth Knapp; CIRA-NOAA/NESDIS/ORA; Room 711c; 5200 Auth Rd.; Camp Springs, MD, 20746-4304; email: Ken.Knapp@noaa.gov

angles, ϕ_1-ϕ_2: 0°-180°. Atmospheric effects were held constant during the calculations, with ozone absorption and Rayleigh scattering characteristic of a tropical atmosphere.

Privette et al. (1997) compare different BRDF models and conclude that the model described by Rahman et al. (1993) describes a multitude of surfaces with higher accuracy than other models. Therefore, it was used in this research to model the surface; it uses three terms to describe the surface: the magnitude of the surface reflectance, ρ; the Henyey-Greenstein function parameter, Θ; and the level of anisotropy, k. For each viewing geometry in the LUT, calculations were performed at 1100 BRDF combinations, with ρ: 0.001 to 0.09, Θ: -1 to 1, and k: 0.0 to 1. Each BRDF was used in a DISORT run to calculate the R_{sat} due to the surface BRDF and Rayleigh scattering for each of the 3705 possible geometries.

Lastly, aerosol scattering and absorption are included in these calculations via the continental aerosol described by Kaufman et al (1997). One look-up table is computed with τ = 0.05. This is the assumed to be the minimum τ observed during the composite time period. LUTs area also calculated at other τ values, the interpolation between which allows the τ retrieval.

3.2 Step 2: Surface BRDF Retrieval

The surface BRDF is estimated by compositing PATMOS reflectances. The satellite repeat cycle of the NOAA series of satellites is nine days. Thus, over the course of 24 days it is possible to composite 3 observations from each look angle (given plenty of cloud-free observations). However at some sites, cloudy skies limit the number of observations, so the time period is allowed to vary from 24 to 48 days. Circles in figure 1 show an example of 24 days of cloud-free channel 1 reflectances from the Patmos-1 data. It is clear that a significant trend as a function of view zenith angle is present and that there is noise in this trend. Assuming that the presence of aerosol increases the reflectance (i.e., that the aerosol absorption is low), then the darkest of these points in the composite is likely to have the lowest τ.

The LUT with τ = 0.05 is used to determine the surface BRDF. First, the LUT is interpolated for the viewing geometry of each of the points. This narrows the possible solutions to the 3705 combinations of BRDF parameters. A cost function is then used to retrieve the best-fit BRDF parameters.

An example BRDF retrieval is also shown in figure 1. The circles represent PATMOS observations over Cuiaba, Brazil. The squares represent the TOA reflectances given the retrieved BRDF. In general, the squares compare well with the darkest observed reflectances.

This BRDF retrieval method is not limited to AERONET locations since the retrieval of BRDF parameters uses only the PATMOS data. It can be used over the entire world regardless of ground-truth location. However, the accuracy of the aerosol retrieval will depend on location so current retrievals are limited to AERONET sites.

3.3 Step 3: Aerosol Optical Depth Retrieval

Once the BRDF parameters have been determined, the τ retrieval is performed. The LUTs for each $\tau$are interpolated to the corresponding BRDF parameters and viewing geometry. Finally, τ is retrieved by matching the R_{sat} within the LUT to the corresponding τ. Before discussing the retrieval results, the uncertainty in these comparisons should be considered.

4. UNCERTAINTIES

Perhaps the most significant is the sampling of cloud-free pixels in the PATMOS grid cell. The surface viewed each day varies with the spatial distribution of cloud. So for spatially inhomogeneous areas, the day-to-day variation in the observed surface can be large.

Another source of noise is the difference of the AERONET instrument field-of-view of the Sun and the 110×110km^2 spatial resolution of the PATMOS data. Thus, spatial variations in τ will increase noise in the comparison.

Other uncertainties result from departure of the actual conditions from those assumed in the LUT, which include variations in:

- aerosol optical properties (spatially and temporally)
- column ozone amount
- Rayleigh scattering optical depth
- cloud contamination in the PATMOS cloud-free reflectances
- the lowest observed τ (because 0.05 is assumed)
- the discrepancy between the modeled BRDF and the actual BRDF

5. RESULTS

Retrievals are applied to PATMOS land grid cells nearest to 122 of the AERONET sites around the world between 1993 and 1999 (which covers the seven years of level-2 AERONET data).

The validation of the Cuiaba retrieval is shown in figure 2. Currently, the retrieval validation is filtered for:

- Standard deviation of the PATMOS cloud-free reflectances > 0.05: too large of a spatial variance
- View Zenith Angle < 0°: Staying away from the backscatter peak reflectance
- Fraction of cloud free pixels in the grid cell: Requires the cloud free pixels to be greater than one-third the number of all pixels.

These restraints on the validation with ground truth decrease the noise when verifying with the AERONET point measurement. For Cuiaba, the correlation, r, is 0.88 with a root-mean-square difference of 0.15. There is a negative bias (i.e., slope of 0.78) likely due to the larger absorption of the typical biomass-burning aerosol than the continental aerosol of the LUT.

Grouping all the AERONET sites in South America provides more insight to the retrieval performance (figure 3). A similar low bias (with a slope of 0.63) and correlation (r = 0.87) is found. However, the retrieval shows significant errors during August and September (the burning season) when the assumed background τ (0.05) is likely wrong. Error analysis, together with independent observations and models of the surface and atmosphere, will allow us to analyze error sources and increase the accuracy of the retrieval method.

Further grouping of results into ten regions provides analysis for sites over the globe. These results are preliminary; yet still suggest where this approach is appropriate. Statistics for the ten regions are presented in Table 1. It is clear that the best results are in South America where the surface reflectance has small temporal and spatial variations and the aerosol is relatively constant (aerosol here are primarily from biomass burning). Other regions with high correlations include southern Africa, Central Canada and parts of the U.S.

5. CONCLUSIONS

The surface BRDF is retrieved from PATMOS channel 1 cloud-free reflectance data and used to retrieve the aerosol optical depth. Comparisons of retrieved τ to ground-truth show positive correlation in all defined regions of the globe. However, the correlations are weak in some areas, likely due to:

- Desert areas have a brighter reflectance than used in the LUT BRDF calculations
- TOA reflectance is less sensitive to aerosols over brighter areas.
- Other uncertainty sources as described in section 4.

Further research will include:

- More error analysis to determine error sources.
- Inclusion of multiple aerosol types in the LUTs to remove regional biases.
- Inclusion of other ground-truth data sets, e.g., the Multi-Filter Rotating Shadowband Radiometer (MFRSR) AOD dataset
- Inclusion of surface information from channel 2 (0.83μm)

The addition of this information should increase the accuracy (and thus, value) of the retrieval of AOD from the PATMOS data set.

The current results are encouraging. The retrieval of aerosol optical depth over land has been very limited and these results suggest the possibility of quantifying spatial and temporal variation of aerosol optical depth over some land areas within the 20-year record of the PATMOS data set.

ACKNOWLEDGMENTS

This work is supported by the NASA/Global Aerosol Climatology Project (GACP, Michael Mishchenko, Principal Scientist). We acknowledge Brent Holben of NASA and the Principle Investigators of each AERONET site for the use of their data, which is available at http://aeronet.gsfc.nasa.gov:8080/ and the personnel of NOAA Satellite Active Archive where the PATMOS data can be acquired (http://www.saa.noaa.gov/).

REFERENCES

Holben, B. N. et al., 1998: AERONET – A Federated Instrument Network and Data Archive for Aerosol Characterization, Remote Sens. Environ., 66, 1-16.

Jacobowitz, H., L. Stowe, G. Ohring, K. Knapp and N. Nalli, 2001: The Advanced Very High Resolution Radiometer Pathfinder Atmosphere Data Set, submitted to *Bull. Amer. Meteor. Soc.*

Kaufman, Y. J., D. Tanré, L. A. Remer, E. F. Vermote, A. Chu and B. N. Holben,1997: Operational remote sensing of tropospheric aerosol over land from EOS moderate resolution imaging spectro-radiometer, J. Geophys. Res., 102, 17051-17068.

Knapp, K. R. and L. L. Stowe, 2001: Evaluating the potential for retrieving aerosol optical depth over land from AVHRR Pathfinder Atmosphere data, accepted to *J. Atmos. Sci.*

Privette, J. L., T. F. Eck and D. W. Deering, 1997: Estimating spectral albedo and nadir reflectance through inversion of simple BRDF models with AVHRR/MODIS-like data, J. Geophys. Res., 102, 29529-29542.

Rahman, H., B. Pinty and M. M. Verstraete, 1993: Coupled Surface-Atmosphere Reflectance Model 2. Semiempirical Surface Model Usable with NOAA Advanced Very High Resolution Radiometer Data, J. Geophys. Res., 98, 20791-20801.

Stowe, L. L., P. A. Davis and E. P. McClain, 1999: Scientific Basis and Initial Evaluation of the CLAVR-1 Global Clear/Cloud Classification Algorithm for the Advanced Very High Resolution Radiometer, J. Atm. Oceanic Tech., 16, 656-681.

Stowe, L. L., H. Jacobowitz, G. Ohring, K. Knapp and N. Nalli, 2001: The Advanced Very High Resolution Radiometer Pathfinder Atmosphere Data Set, submitted to *J. Climate*.

Tsay, Si-C., K. Stamnes, W. Wiscombe, and I. Laszlo, 2000: General Purpose Fortran Program for Discrete-Ordinate-Method Radiative Transfer in Scattering and Emitting Layered Media: An Update of DISORT, presented at the International Radiation Symposium 2000, in St. Petersburg, Russia.

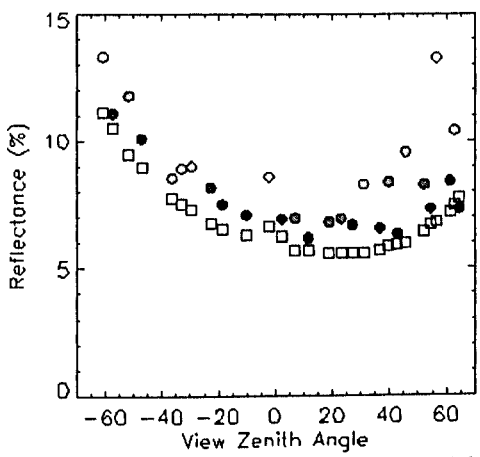

Figure 1 – Example fit of PATMOS cloud-free observations (circles) to a BRDF (squares) at Cuiaba, Brazil. The retrieved parameters BRDF are ρ = 0.03, k = 0.1, and Θ = 0.1. Negative viewing angle corresponds to viewing away from the Sun.

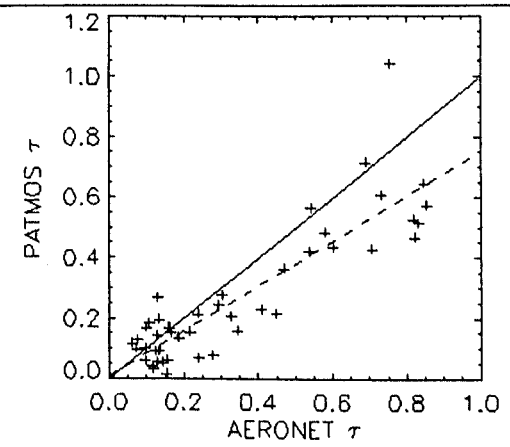

Figure 2 – Validation of filtered PATMOS AOD with AERONET AOD at Cuiaba. The linear regression best fit (dashed line) is: y=0.78x + 0.01 with r = 0.88 (for 47 points)

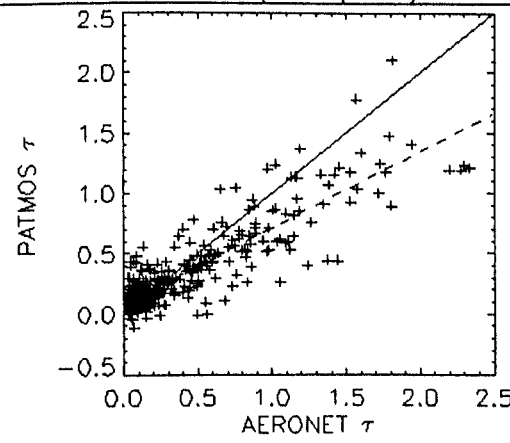

Figure 3 – Validation of filtered PATMOS AOD with AERONET AOD for South America. The linear regression best fit (dashed line) is: y=0.63x + 0.08 with r = 0.87 (for 396 points)

Table 1 – Statistics of the filtered validation of AOD estimation for different regions of the world.

Region	n	r	Slope	Offset
South America	**396**	**0.87**	**0.63**	**0.08**
Northwestern U.S.	101	0.33	0.81	0.11
Southwestern U.S.	293	0.16	0.75	0.27
Midwestern U.S.	**216**	**0.55**	**0.75**	**0.11**
Eastern U.S.	431	0.49	0.47	0.14
Central Canada	**240**	**0.87**	**0.75**	**0.06**
Europe	208	0.49	0.53	0.13
Western Africa	374	0.29	0.71	0.44
Southern Africa	**249**	**0.66**	**0.55**	**0.09**
Other*	468	0.15	0.80	0.60

* All other sites outside the defined regions

P2.23

TEMPORAL SCALES OF THE AREAL COVERAGE AND PRECIPITATION OF MONSOONAL CONVECTIVE CLOUD SYSTEMS OVER THE TROPICAL INDIAN OCEAN

Eric M. Wilcox
Center for Atmospheric Sciences, Scripps Institution of Oceanography
University of California, San Diego, La Jolla, CA

1. INTRODUCTION

Cloud processes continue to be a significant source of uncertainty in the modeling of the general circulation of the atmosphere. The physics associated with the production of clouds and precipitation critically impacts the radiative forcing of the climate system and the scavenging of trace gases and aerosols, among other effects. Gaining confidence in model predictions requires careful validation against observational cloud climatologies. Development of a comprehensive cloud climatology, however, is hindered by the complex temporal and spatial variability of natural cloud systems.

The typical approach to cloud climatology studies is to prepare time and space-averaged fields of cloud coverage and cloud properties. For the purposes of model validation, these observations are then compared with similar fields generated by a model. This approach ignores the fact that clouds are dynamical entities that evolve with time. Thus the cloud coverage observations in traditional cloud climatologies are often integrations over the temporal and spatial variability associated with several cloud systems.

As an alternative to these studies, a Lagrangian approach is adopted in this study whereby individual clouds are identified and tracked in time using geostationary satellite imagery. A database of the areal coverage and lifetimes of an ensemble of clouds spanning a broad range of time and space scales is produced. The boundaries of each cloud are determined such that they encompass both the active regions of precipitating convection within the cloud as well as the extended decks of anvil and cirrus cloud resulting from convection. Preliminary estimates of rain rate throughout the lifecycles of the observed clouds are made from infrared brightness temperatures in order to investigate the temporal scales of precipitation within evolving cloud systems. The statistical description of cloud spatial and temporal properties that results from this analysis is offered as an additional tool for the validation of cloud parameterizations that can be compared to similar statistics determined for an ensemble of clouds predicted in general circulation model simulations.

The analysis presented here reveals that wintertime monsoonal cloudiness over the tropical Indian Ocean is dominated by giant decks of semi-permanent overcast cloudiness that can cover millions of square kilometers and persist for days to weeks. The evolution of the areal coverage and precipitation of such clouds is modulated by such processes as planetary wave dynamics, moist convection and microphysics. Comparing the evolution of observed clouds to that of modeled clouds will help reveal how well current parameterizations approximate cloud physical processes.

2. DATA AND METHODOLOGY

The temporal and spatial scales of clouds over the tropical Indian Ocean are determined using half-hourly METEOSAT-5 images during the period 1 January through 9 February 1999. Image pixels (gridded at 0.25 deg. lat-lon) are roughly classified by cloud type based on infrared window and water vapor channel brightness temperatures (T_{IR} and T_{WV} respectively). The classification scheme, summarized in Table 1, aims to classify only overcast pixels. Pixels that do not meet the criteria in Table 1 are either clear-sky or only

Table 1. METEOSAT-5 pixel classification scheme

classification	brightness temperature (K)
deep convection/anvil	$T_{IR} < 240$
shallow conv./thick cirrus	$240 <= T_{IR} < 280$
thin cirrus	$T_{IR} >= 280$, $T_{WV} < 245$

Corresponding author address: Eric M. Wilcox, Center for Atmospheric Sciences, Scripps Institution of Oceanography, University of California, San Diego, 9500 Gilman Dr., La Jolla CA 92093-0221; email:ewilcox@ucsd.edu.

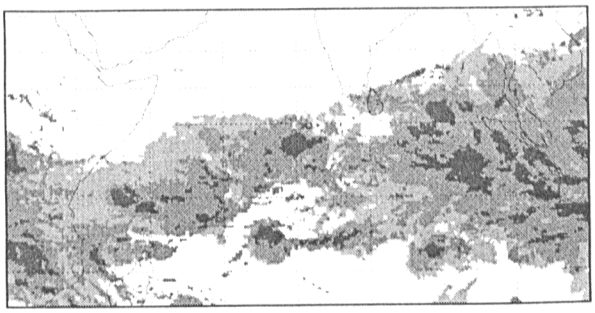

Fig. 1. METEOSAT-5 cloud map from 1100 GMT, 18 Jan. 1999. Black: deep convection/anvil; dark gray: shallow convection/thick cirrus; light gray: thin cirrus.

partially covered by cloud and are disregarded.

Following classification, a cloud-clustering algorithm similar to that described in Mapes and Houze (1993) is applied whereby adjacent overcast pixels are grouped into a single cloud. Overcast pixels must share a side to be included in the same cloud. For the purposes of this study, the term "cloud" refers to a cluster of adjacent overcast pixels.

Once cloud maps have been constructed for a series of consecutive images, an automated cloud-tracking algorithm is applied to them that identifies clouds containing pixels that overlap in consecutive images. A cloud may overlap with several clouds from the preceding image or the subsequent image because of splitting and merging behavior. In such cases, a decision is made about which pair of overlapping clouds are the same cloud by finding the pair whose fractional area of overlap is greatest.

Surface rain rate estimates, averaged over the area of each cloud, are made using a variation of the GOES Precipitation Index technique of Arkin and Meisner (1987). Rain rate (R) is related to f_{240}, the fraction of the area of each cloud with T_{IR}<240K according to the following expression:

$$R(\mathrm{mm/hr}) = Gf_{240}$$

where the coefficient, G, is calibrated by passive microwave rain rate measurements from collocated passes of the TRMM satellite. The value of G is 1.28 mm/hr based on a regression between cloud area-averaged rain rate measured by TRMM and f_{240} from METEOSAT-5 for a set of nearly 200 clouds exceeding 5 X 10^5 km^2. The correlation coefficient of the regression is 0.7. The resulting rain estimates are expected to be biased low owing to a small amount of precipitation observed from clouds with temperatures warmer than 240K. The rain estimates are preliminary. More sophisticated IR techniques will be applied in the future.

3. RESULTS

3.1 Cloud Spatial and Temporal Scales

Figure 1 is an example of a METEOSAT-5 image following the classification step in the analysis. The image shown corresponds to a period of widespread convection along the Intertropical Convergence Zone. The dominant feature of the image is a single cloud characterized by a giant overcast deck extending across the ocean basin. Within the overcast deck are numerous areas of active deep convection that provide the cloud material for extended decks of anvil and cirrus cloud that act as bridges connecting the convective regions. During the 40 days of the analysis, a few clouds such as the one shown in Fig. 1 dominate the integrated cloud cover. The dominance comes not only from their large spatial coverage, but also because such giant overcast decks can persist for several days to several weeks.

Fig. 2a shows the number distribution of

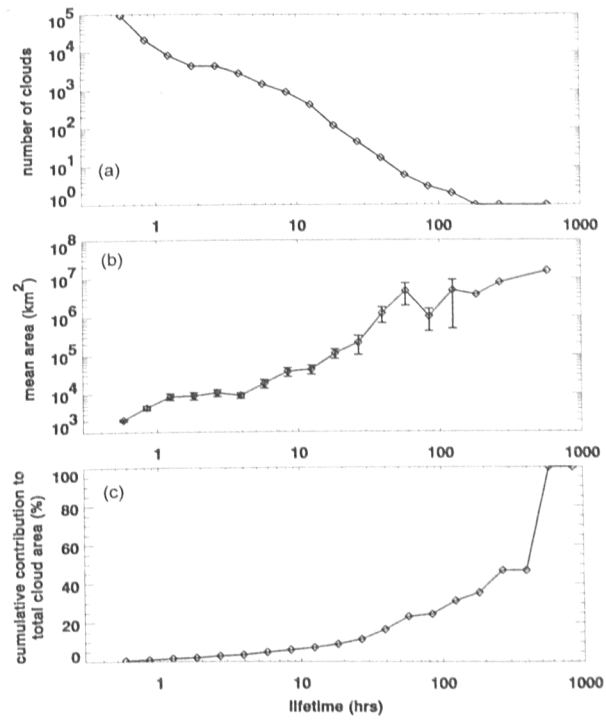

Fig. 2. (a) Number of clouds. (b) Mean area of cloud averaged over cloud lifetime. (c) Cumulative contribution to total overcast cloudiness. All are shown as a function of cloud lifetime. Error bars indicate one standard deviation of the mean.

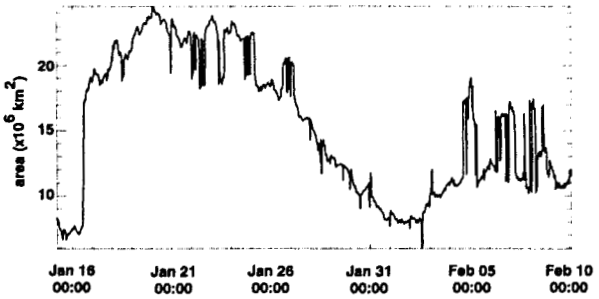

Fig. 3. Temporal evolution of the areal coverage of the longest living cloud observed. An image of this cloud on Jan. 18 appears in Fig. 1.

clouds as a function of cloud lifetime. While over 40 000 individual clouds were tracked for at least 1 hour, only five clouds where found to last for greater than 100 hours. They are also the five largest clouds observed. Averaged over their lifetimes, 4 of the 5 longest living clouds exceed one million km^2 as illustrated in Fig. 2b. The cumulative contribution to the total observed cloud cover is presented in Fig. 2c. Over 75% of the total cloud coverage is attributable to just those clouds that persist for greater than 100 hours.

3.2 Internal Temporal Variability

The temporal evolution of the cloud pictured in Fig. 1 is shown in Fig. 3 over a 26-day period. The size of the cloud demonstrates variability on a number of important time scales. First, there is the growth and decay cycle on a time scale of weeks that is likely a result of planetary wave modulation of deep convection or other large-scale forcing events. The scale of this cloud is so large, however, that it extends across the entire satellite image for a considerable length of time and always borders at least one boundary of the image. Thus the long time-scale evolution of the cloud's area could simply result from movement of the cloud off of the image (such as into the western Pacific Ocean, for example). The second most obvious variation in the evolution of this cloud's area is the fast time-scale flickering, often growing or shrinking by millions of km^2 in a single half-hour time step. Such flickering results from splitting and merging behavior that is especially prevalent when a tenuous bridge of cirrus cloud exists between two large, geographically separated regions of intense convection.

Cloud size varies strongly on the diurnal time scale. Figure 4a is the same as Fig. 3 but for a 7-day period of the lifecycle of another cloud. The area of the cloud oscillates diurnally over 4 days before beginning to dissipate. Figure 4b shows

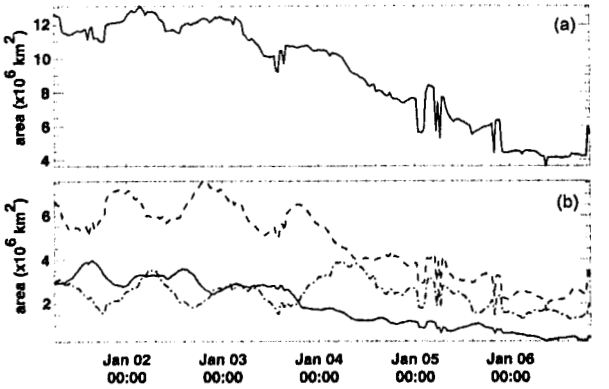

Fig. 4. (a) Temporal evolution of the areal coverage of another cloud. (b) Temporal evolution of the areal coverage of each cloud type within the cloud. Solid line: deep convection/anvil; dashed line: shallow convection/thick cirrus; dash-dot line: thin cirrus.

the area of the cloud that is attributable to each cloud type (the sum of each of the three lines in Fig. 4b is the curve shown in Fig. 4a). Deep convection and anvil cloudiness within this cloud tend to peak in the afternoon as illustrated by the area colder than 240K (solid line). The area covered by thin cirrus (dash-dot line) peaks 12-15 hours later and the intermediate cloud class (dashed line) peaks in between. While convection varies on a diurnal time scale, the lag between the peak in convection and the peak in cirrus cloud cover help explain how giant overcast decks persist.

3.3 Precipitation Statistics

The amount of condensate that falls out is a constraint on the amount of condensate available to detrain as anvil and cirrus cloud. Furthermore rain rate and the spatiotemporal scales of precipitation control the amount of soluble trace gas and aerosol that is scavenged. The dependence of precipitation processes upon the temporal scales of clouds is presented in Fig. 5. Rain rate, averaged over the area and lifecycle of the cloud, increases strongly with cloud duration (Fig. 5a). Precipitation is predominantly associated with the same large and long-lived clouds that dominate the total cloud cover. The mean number of precipitating regions (T_{IR} < 240K) also increases strongly with cloud lifetime (Fig. 5b). The longest living clouds typically contain 50 to 100 distinct regions of cold cloud within a single overcast deck at any one time. The probability that a cloud contains a precipitating region at some point during its lifecycle increases with cloud lifetime (solid line, Fig. 5c). Also, the fraction of that lifetime that the cloud precipitates reaches 1

for the longest living clouds (dotted line, Fig. 5c). While clouds at shorter temporal and smaller spatial scales may precipitate for only a fraction of their lifetime (or not at all), large semi-permanent clouds are always precipitating somewhere within their boundaries and typically contain many distinct regions of precipitation. Since such clouds are always precipitating, they never completely decay. Instead they tend to merge with another large cloud prior to fully dissipating.

4. CONCLUSIONS

Parameterization schemes for cloudiness in general circulation models are often based on the assumption that clouds are small relative to the size of the grid cell. Furthermore, cloud condensate, if predicted in a model, is rarely assigned a time constant such as a fall velocity. The observations presented here cast some doubt on these criteria, at least in the context of monsoonal convective clouds. Continuous overcast decks of cloud that are large enough to span numerous grid cells in global GCMs are demonstrated to persist for days to weeks.

The ability for parameterized subgrid-scale processes in the NCAR Community Climate Model to produce clouds with the spatial and temporal scales observed here will be tested in a subsequent study. Since clouds spanning several grid cells dominate the total cloud cover, the model should produce clouds whose boundaries can be detected and tracked in a fashion similar to those in the satellite images. The case studies and statistics presented here will serve as new tools for validating cloud parameterization schemes.

5. REFERENCES

Arkin, P. A., and B. N. Meisner, 1979: The relationship between large-scale convective rainfall and cold cloud over the western hemisphere during 1982-1984. *Mon. Wea. Rev.*, **115**, 51-74.

Mapes, B. E., and R. A. Houze, 1993: Cloud clusters and superclusters over the oceanic warm pool. *Mon. Wea. Rev.*, **121**, 1398-1415.

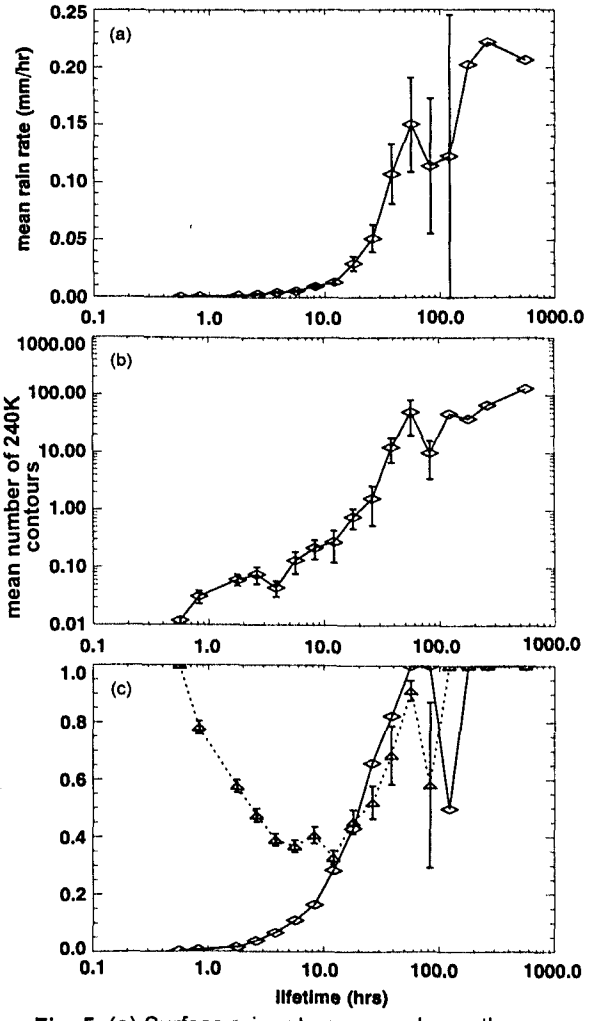

Fig. 5. (a) Surface rain rate averaged over the area and lifetime of the cloud. (b) Number of distinct regions of T_{IR}<240K. (c) Solid line: Fraction of clouds containing a region of T_{IR}<240K. Dotted line: Fraction of cloud's lifetime during which cloud colder than 240K is present (for those clouds containing a 240K contour at some point during their lifetime). Error bars are one standard deviation of the mean.

P2.25 VARIABILITY IN UTH AND WATER CYCLE DYNAMICS

John J. Bates*
NOAA Environmental Technology Laboratory, Boulder, Colorado

1. INTRODUCTION

There appears to be a disconnect between the mechanisms theoretically supposed to provide water vapor to the upper troposphere in the tropics and subtropics, and the mechanism that is most prominent in GCMs. In many GCMs, there is a strong cancellation between upper tropospheric moistening via the large-scale circulation, and drying due to compensatory subsidence from convection. A substantial net moistening effect arises from vertical transport of moisture by eddies, a mechanism that is completely ignored in most theoretical discussions

A key region showing variability in upper tropospheric humidity (UTH) during ENSO events is the subtropical region of the North Pacific. Although this is a region of time-mean descending air in the upper troposphere, analysis of atmospheric data shows that water vapor is supplied to the upper troposphere by vertical flux within transient eddies. The transient eddy activity in this region is in turn modulated by the interaction of the tropical circulation with the midlatitude circulation. Midlatitude interactions with the tropics are greatest during boreal winter and spring when transient eddy Rossby wave activity with periods between 5 and 30 days is at a peak. During most cold events, tropical convection is confined to the far western equatorial Pacific and westerly winds are found in the upper troposphere throughout the central and eastern equatorial Pacific. This allows the opening of a "westerly duct" in the eastern Pacific and supports anomalously high transient eddy activity in the subtropics. Conversely, during most warm events, deep convection and upper-tropospheric easterlies are found over the central and eastern equatorial Pacific. This closes the westerly duct, diminishes transient eddy activity in the subtropics, and creates extremely dry conditions. We have been able to relate the extremes in the tropical average (30N-30S) time series of upper tropospheric humidity (UTH) to variations in the westerly duct. We find that extremes in the UTH tropical time series over the last 20 years are twice as likely to occur in the boreal winter and spring, when the westerly duct is open, versus boreal summer and fall. This dynamical mechanism provides a negative feedback on interannual times scales.

*Corresponding author address: Dr. John Bates, NOAA ETL, 325 Broadway, Boulder, CO 80305; email: John.J.Bates@noaa.gov

2. TROPICAL TIME SERIES OF UPPER TROPOSPHERIC HUMIDITY

Figure 1 shows a time series of UTH interannual variability (Bates et al. 2001; bates et al., 1996) for the tropics (30N-30S) and the one-point correlation map of this time series.

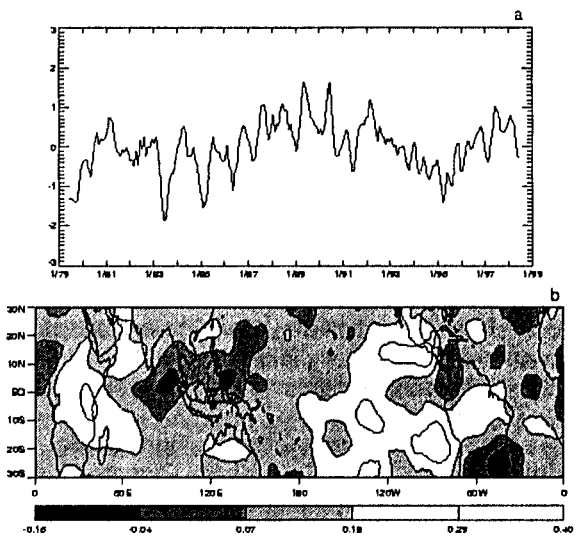

Figure 1. Interannual anomaly of UTH (a) and one-point correlation map (b).

Although the first three harmonics of the seasonal cycle have been removed to construct the anomaly time series, the time series still contains considerable high frequency variability and a suggestion of very low frequency variability in the second half of the record. Examining the timing of the extremes, we find that two thirds of the extremes occur in the boreal winter and spring. The largest extremes are found to coincide with the ENSO warm event of 1982-83 and the cold event of 1989-90. The largest areas of positive correlation in the spatial map are found in the subtropics of the eastern Pacific Ocean. This is a region where past studies have found large variability of extratropical Rossby wave propagation into the subtropics also related to seasonal and interannual variability.

3. PROPAGATION OF MID-LATITUDE ROSSBY WAVES INTO THE TROPICS AND THE ROLE OF THE WESTERLY DUCT

To examine the changes in transient eddy activity in this region during the large warm event of 1982-83

and the large cold event of 1989-90, we employed the dynamical analysis of 200 hPa winds as outlined in *Kiladis* [1998]. The horizontal E vector is a pseudo-vector constructed by calculating time-mean covariances between the perturbation zonal, u', and meridional, v', wind components:

$$\vec{E} = \left(\overline{v'^2 - u'^2}, -\overline{u'v'}\right) \quad (1)$$

The term $\overline{v'^2 - u'^2}$ is a measure of the mean anisotropy of Rossby waves. For example, if v'^2 is consistently larger than u'^2, the Rossby waves are preferentially elongated in the meridional direction and the E-vector points eastward. The term $-\overline{u'v'}$ is the negative of the time-mean northward flux of westerly momentum associated with perturbations. Together the two components approximate the preferred direction of the group velocity of the Rossby waves using suitable approximations, including the assumption of quasi-geostrophy. For this work, we use the NCEP re-analysis data and bandpass filter for 6-30 day transients.

Another useful diagnostic for representing the mean background state in which the transients are embedded is the stationary Rossby wavenumber:

$$K_s = \left(\frac{\beta_*}{\overline{U}}\right)^{1/2} \quad (2)$$

where $\beta_* = \beta - \frac{\partial^2 \overline{U}}{\partial y^2}$ (3)

is the meridional gradient of absolute vorticity associated with the basic flow, $\overline{U}$ is the monthly mean 200 hPa zonal wind, and $\beta = \frac{\partial f}{\partial y}$ is the meridional gradient of planetary vorticity. K_s is the total wavenumber at which a barotropic Rossby wave is stationary at a particular location in a given background zonal flow. Low values of the stationary Rossby wave number (below about 10) indicate regions of strong eddy activity and high values (above 15) indicate regions of weak eddy activity.

E-vectors and the stationary Rossby wavenumber were computed for all months and plots of the minima UTH (April 1983) and maxima UTH (February 1989) months are shown in Figure 2.

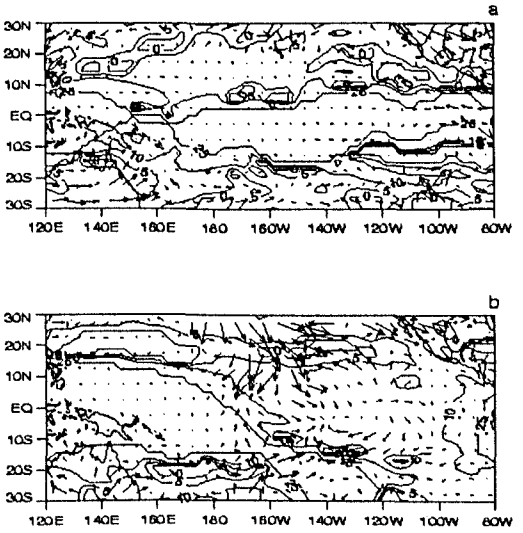

Figure 2. E-vectors and stationary Rossby wave numbers for February of 1983 (a) and January of 1989 (b).

In the northern hemisphere, mid-latitude interactions with the tropics are greatest in boreal winter and spring when transient Rossby wave activity with periods between 5 and 30 days is at a peak. During strong cold events, such as 1989 (Figure 2a), tropical convection occurs only over the far western Pacific Ocean since the western Pacific warm pool shrinks and moves to the west during cold events. In the tropical upper troposphere near the equator, this creates strong westerly winds in the outflow from this convection over the central and eastern Pacific. This allows the opening of a westerly duct in the eastern Pacific and supports propagation of Rossby waves deep into the subtropics [*Webster and Holton*, 1982]. This is evidenced in Figure 2a where values of stationary Rossby wave numbers less than 10 are found in the regions between the dateline and the west coast of South America. Large values of E-vectors pointing toward the equator near Hawaii are indicative of equatorially-propagating Rossby waves from the mid-latitudes into the subtropics. As shown by Kiladis [1998], the Rossby waves then propagate to the east and are associated with large plumes of moisture extending from near Hawaii to the U.S. west coast sometimes dubbed the 'pineapple express'.

Conversely, during the large warm event of 1982 (Figure 2b), deep convection extends far to the east in the equatorial Pacific Ocean. Upper tropospheric westerlies over the equator weaken dramatically or even reverse in the central and eastern Pacific. This is confirmed by calculations of the stationary Rossby wave number for these events. Large values of the stationary Rossby wave number are found over the eastern tropical Pacific, effectively

shutting down the westerly duct. Virtually no E-vectors pointing toward the equator are found in this month, indicating an almost complete absence of Rossby waves in the subtropical North Pacific.

We examined the statistical characteristics of the relationship between the UTH extremes and Rossby wave activity by computing the seasonal mean Rossby stationary wave number. We computed the mean of all months within the season for only those months within the season with tropical average UTH anomalies greater than 0.7% and UTH anomalies less than –0.7%. For the boreal spring season (Figure 3), we find low values of the stationary Rossby wave number extend further west versus the mean along the equator when UTH anomalies exceed 0.7% (Figure 3b) and are found further east when UTH anomalies are less than –0.7% (Figure 3c). The situation is similar for the boreal winter season. Thus, the westerly duct is larger when UTH anomalies exceed 0.7% and is much smaller when UTH anomalies are less than –0.7%.

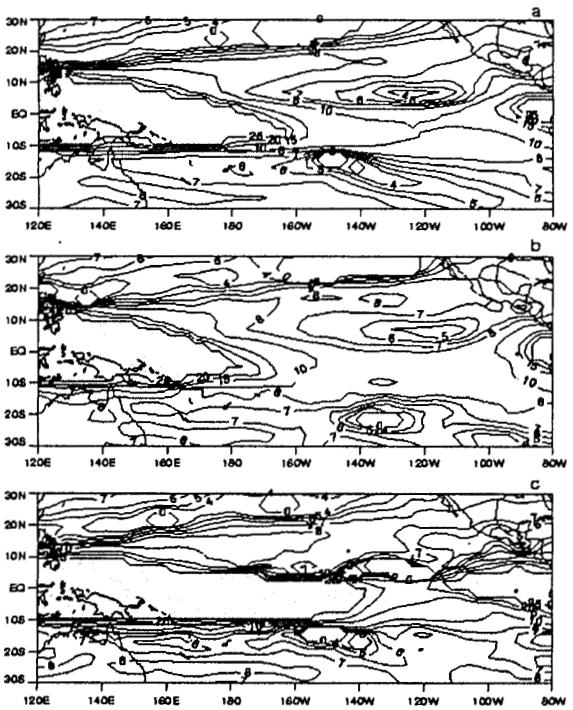

Figure 3. Stationary Rossby wave number corresponding to normal UTH (a), high extremes of UTH (b), and low extremes of UTH (c).

4. CONCLUSIONS

Atmospheric dynamical states, resulting from the interaction of the tropics with the mid-latitudes during boreal winter and spring, are responsible for most of the observed extremes in the tropical UTH time series. These states are referred to as the westerly duct in the eastern Pacific Ocean. The two extreme states of the westerly duct, and their influence on UTH, are illustrated schematically in figure 4.

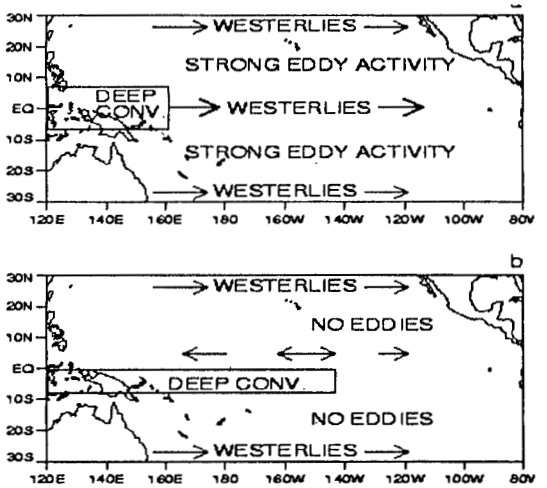

Figure 4. Schematic of tropical basic states for extremes of high UTH (a) and low UTH (b).

During extremes of high UTH (Figure 4a), strong westerlies flowing out from deep convection in the western equatorial Pacific create a long fetch of westerlies over the equatorial eastern Pacific. This opens the westerly duct and allows Rossby waves (strong eddy activity) to propagate into the subtropics and re-hydrate the subtropical upper troposphere. Conversely, when deep convection extends into the central and eastern Pacific (Figure 4b), westerly winds over the tropical eastern Pacific are weak and Rossby waves are blocked from propagating into the subtropics (no eddies).

5. REFERENCES

Bates, J.J., D.L. Jackson, F.-M. Breon, and Z.D. Bergen, Variability of upper tropospheric humidity 1979-1998, *Journal of Geophysical Research*, 2001.

Bates, J.J., X. Wu, and D.L. Jackson, Interannual variability of upper-tropospheric water vapor band brightness temperature, *Journal of Climate*, *9* (2), 427-438, 1996.

Kiladis, G.N., Observations of Rossby Waves Linked to Convection over the Eastern Tropical Pacific, *Journal of the atmospheric sciences.*, *55* (3), 321, 1998.

Webster, P.J., and J.R. Holton, Cross-equatorial response to middle-latitude forcing in a zonally varying basic state, *Journal of the*

Atmospheric Sciences, *39* (4), 722-733, 1982.

P2.27

DIURNAL VARIABILITY OF SATELLITE DERIVED PRECIPITABLE WATER IN THE AMAZON BASIN

Tracy L. DeLiberty* and John A. Callahan
University of Delaware, Newark, Delaware

1 INTRODUCTION

The Amazon Basin plays an important role in the tropical climate and hydrology. It contains one of the major convective centers that fuels the general circulation of the atmosphere and its abundant rainfall feeds the largest freshwater stream of the world. The tropical forests provide habitats for about half of the world's species and are an important natural sink of CO_2. Over the past decade, the Amazon Basin has received considerable attention from the scientific community as a result of the potential climatic and hydrologic impact of biomass burning and deforestation. Rates of deforestation in Brazilian Amazon have increased from 15,000 km^2yr^{-1} in the early 1990s to more than 18,000 km^2yr^{-1} in 1995 to 1998 (Laurance 2000).

Deforestation as a result of human activities is altering the conditions at the lower boundary of the atmosphere. Numerous modeling studies (e.g., Nobre et al. 1991, Costa and Foley 2000) have examined how the climate and hydrology of the basin may respond to deforestation. In order to evaluate possible anthropogenic impacts to the Amazon, we must improve our understanding of the "natural" climatic and hydrological processes operating within the basin. While long-term studies of the variability of precipitation (e.g., Paiva and Clarke 1995) and river discharge (e.g., Richey et al. 1989, Marengo 1995) have been examined, other components of the hydrologic cycle, such evapotranspiration and atmospheric water vapor have not received the same level of attention.

* Corresponding author address: University of Delaware, Center for Climatic Research, Newark, DE 19716;email:tracyd@udel.edu.

Water vapor is an important link connecting various components of the hydrologic cycle and a better understanding of its role requires long-term observations of both small- and large-scale water vapor features. Recent studies of atmospheric moisture and its transport have focused on its seasonal cycle and interannual variability using atmospheric reanalysis data (e.g., Curtis and Hastenrath 1999, Zeng 1999) at larger temporal and spatial scales. Remote sensing from satellites provides the opportunity to monitor atmospheric water vapor at higher spatial and temporal resolution than conventional sources, such as surface and radiosonde networks or model analyses. Geostationary satellites, in particular, provide excellent temporal sampling to supply the needed observations to characterize the diurnal variability of PW. This paper presents a picture of the meso-scale moisture patterns and diurnal variations of satellite derived estimates in June and October of 1988.

2 SATELLITE RETRIEVAL ALGORITHM

The satellite retrieval algorithm used in this study is a physical split-window (PSW) technique initially developed by Jedlovec (1987) and first applied to GOES imagery by Guillory et al.(1993). The PSW technique exploits the differential absorption of water vapor in the 11 and 12 μm channels. In this procedure, an initial estimate of the state of the atmosphere must first be supplied. Using a radiative transfer model, the expected atmospheric radiative emission received at the satellite sensor in the 11 and 12 μm bands is calculated. From the perturbations between the expected and observed radiation, we can calculate an appropriate offset between the estimated and actual integrated water vapor content

and retrieve PW. A detailed discussion of the mathematical formulation of PSW can be found in Guillory (1991) and a thorough evaluation of the performance is given in Suggs et al. (1999).

3 DATA AND METHODOLOGY

Observed radiances were retrieved from the GOES Visible Infrared Spin Scan Radiometer (VISSR) Atmospheric Sounder (VAS) for 1988. The NCEP/NCAR Reanalysis Project data provided the first guess atmospheric fields applied as input to the PSW. These fields included 17 levels of air temperature and 6 levels of humidity at 6-hourly intervals.

The area under investigation is the Amazon River Basin as shown in Figure 1. The box surrounding the basin represents the extent of the GOES imagery and therefore the derived PW fields. Also shown in figure 1 are seven 5x5 degree "zones" identified to concentrate our analysis.

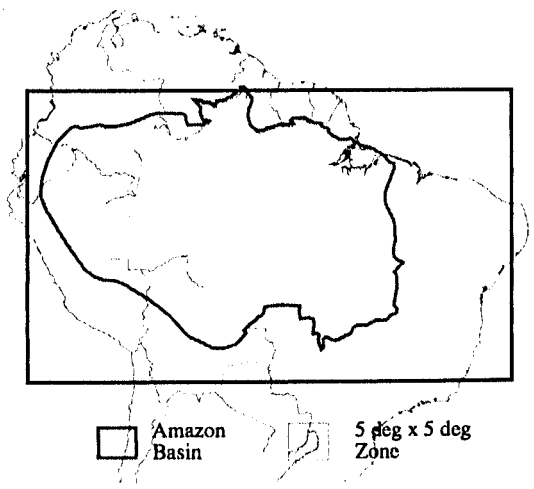

Figure 1: Study area encompasses the Amazon Basin and surrounding fringes. Box represents areal extent of geostationary imagery used in deriving PW with seven analysis zones outlined.

PW retrievals are made at a three-hourly time step during daylight hours for the months of June and October in 1988. Radiances are averaged using a 25 pixel neighborhood to minimize random noise in the sensor, thereby reducing the effective retrieval resolution to 40 km. Areas obscured by cloud cover are assigned the PW value of the first guess field from the Reanalysis data. Spatially continuous 0.5 degree fields are then generated 5 times daily at 12, 15, 18, 21 and 00Z, and then smoothed to reduce differences between PSW and the first guess values.

For each day, the maximum difference was computed among the 12Z, 15Z, 18Z, 21Z, and 00Z grids. A monthly average diurnal grid was then created and summarized by individual zones. The zones selected represent varying land surface and meteorological characteristics. When the PSW method is applied directly locations with radiosonde observations, PSW estimates PW reasonably well with MAE ranging from 3.0 to 9.0 mm and MAE/observed mean around 20%.

4 RESULTS

The geographic distribution of PW for June and October in 1988 is shown in Figure 2. A strong north-south gradient exists in June with a basin average of 38 mm. The highest PW values (over 55 mm) are found in the northwest, while the lowest (less than 25 mm) occur in the most southern and southeastern portions of the basin. In October the basin average is slightly higher at 41 mm, however, the spatial gradient is largely absent with higher PW throughout the area. More specifically, the monthly averages for zones 1 and 2 are between 45 and 50 mm, whereas zone 6 remains at 30 mm. The differences evident in June and October are largely due to changes in the large-scale circulation patterns and core centers of convection with the transition between the wet and dry seasons. In June, the ITCZ resides in the northern hemisphere causing surface winds to blow in an east-west direction into the mouth of the river. This draws in extremely moist air from the mid-Atlantic and allows periodic fronts to move up from the South Pacific High. In October, with the wet season just beginning, the ITCZ moves southward, pushing sur-

face winds in a more northeast-southwest direction. The subsidence of the South Pacific High and the increase of temperature produces a low pressure area over the basin, which increases precipitation and atmospheric water vapor.

The diurnal variations are among the most prominent modes of variability in the Amazon. The diurnal cycle exhibits marked regional variations, usually related to low-level, geographically tied circulations. The average diurnal range for June and October in 1988 is shown in Figure 3. Diurnal range of water vapor tends to increase as you move further south and east. June displays a north-south gradient of variation similar to the PW field, although with a negative correlation to PW. In October, many of the areas with large PW variations correspond to grasslands and non-forested areas (except for the southeast coast) and smaller variations correspond to areas with forested heavy precipitation areas, such as the northwest.

Figure 4 displays the daily diurnal range for three selected zones in both June and October. The y-axis represents the percent change from the daily mean (e.g., $100\frac{PW range}{PW mean}$). Zone 1 shows little diurnal variation and remains fairly consistent throughout both months. Zones 4 and 6 show a much larger variation, nearly 40% in some instances. The spikes in the graph most likely represent synoptic events (cold surges) moving northward.

PW peaks earlier in the day during October than in June. For all zones, except zone 2, the peak time for PW was 1 to 2 time-steps (3 - 6 hours) earlier in October than in June. This may be accounted for by land surface changes between June and October. For example, October is at the end of the dry season when foliage cover is less than at the end of the wet season. Also, the months prior to October are peak burning seasons for deforestation activities, leaving the land surface void of thick vegetation than existed in June.

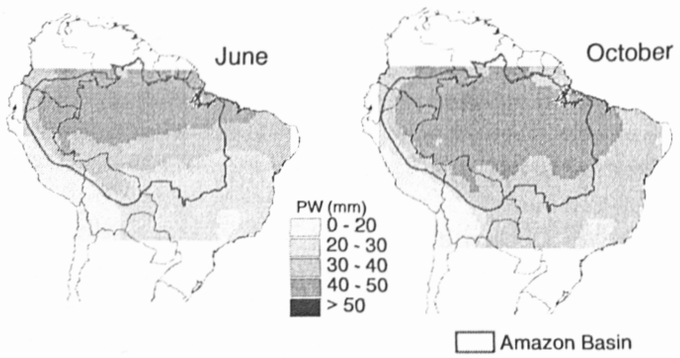

Figure 2: Average PSW-derived PW in 1988

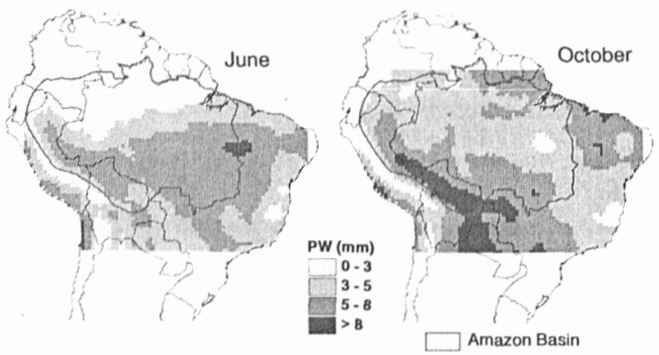

Figure 3: Average diurnal range of PSW-derived PW in 1988

5 SUMMARY

This paper examines the geographic distribution and diurnal variability of satellite derived precipitable water for June and October in 1988 across the Amazon Basin. The GOES estimates enables investigation of the moisture field at higher spatial and temporal scales than conventional radiosondes observations or model analyses. In addition, the PSW-derived estimates offers the opportunity to monitor the variability and trends over the region that may be evident as a result of biomass burning and deforestation.

6 ACKNOWLEDGMENTS

Special thanks is given to Dr. Paul Menzel and Ms. Elaine Prins in the early development of this

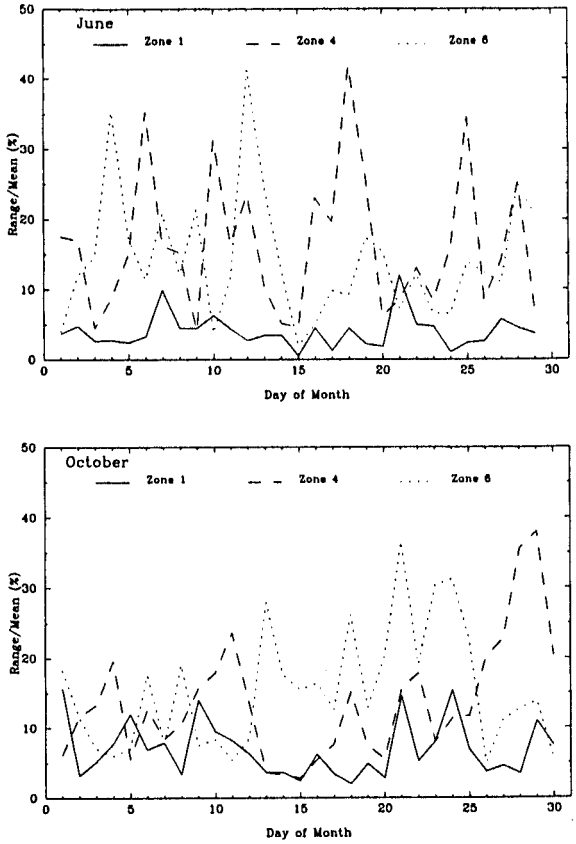

Figure 4: Diurnal range of PW in 1988 for Zone 1,4, and 6.

research and to Dr. Gary Jedlovec and Mr Anthony Guillory for assistance in using the PSW technique. Funding for this research was partially provided by the National Research Council's Associateships Program and the University of Delaware Research Foundation.

7 REFERENCES

Costa, M. H., and J. A. Foley, 2000: Combined effects of deforestation and doubled atmospheric CO_2 concentrations on the climate of Amazonia. *Journal of Climate*, 13(1), 18-34

Curtis, S. and S. Hastenrath, 1999: Trends of upper-air circulation and water vapor over equatorial South America and adjacent oceans. *International Journal of Climatology*, 19, 863-876.

Guillory, A. R., 1991: *A physical split window technique for deriving precipitable water utilizing VAS data.* M.S. Thesis, Florida State University, 70pp.

Guillory, A. R., G. J. Jedlovec, and H. E. Fuelberg, 1993: A technique for deriving column-integrated water content using VAS split-window data. *Journal of Applied Meteorology*, 32, 1226-1241.

Jedlovec, G. J., 1987: *Determination of atmospheric moisture structure from high resolution MAMS radiance data.* Ph.D. Dissertation, University of Wisconsin-Madison, 187pp.

Laurance, W. F., 2000: Mega-development trends in the Amazon: Implications for global change. *Environmental Monitoring and Assessment*, 61(1), 113-122.

Marengo, J. A., 1995: Variations and change in South American streamflow. *Climatic Change*, 31, 99-117.

Nobre, C., P. J. Sellers, and J. Shukla, 1991: Amazonia deforestation and regional climate change. *Journal of Climate*, 4, 957-988.

Paiva, E. M. C. D., and R. T. Clarke, 1995: Time trends in rainfall records in Amazonia. *Bulletin of the American Meteorology Society*, 76(11), 2203-2209.

Richey, J. E., C. A. Nobre, and C. Deser, 1989: Amazon River discharge and climate variability: 1903-1985. *Science*, 246, 101-103.

Suggs, R. J., G. J. Jedlovec, and A. R. Guillory, 1998: Retrieval of geophysical parameters from GOES: Evaluation of a split window technique. *Journal of Applied Meteorology*, 37, 1205-1277.

Zeng, N., 1999: Seasonal cycle and interannual variability in the Amazon hydrologic cycle.*Journal of Geophysical Research*, 104(D8), 9097-9106.

P2.28 TROPICAL PRECIPITABLE WATER CLIMATOLOGY FOR EQUATORIAL WAVES

Paul E. Roundy[1]
The Pennsylvania State University

1. Introduction

Theoretical and observational studies of the tropical atmosphere have led to in-depth analyses of waves and oscillations propagating parallel to the equator. These oscillations modulate tropical convection and rainfall and may frequently affect mid-latitude weather. Some of their forms were predicted analytically by Matsuno (1966) and by Lintzen (1967), who solved the governing shallow water equations in the equatorial beta plane. They found what have been labeled Mixed Rossby-Gravity (MRG), Inertial Gravity (IG, WIG—westward propagating, and EIG—eastward propagating), Kelvin, and Equatorial Rossby (ER) waves. These solutions depend on an equivalent depth parameter, h and a meridional mode number, n. The works of Matsuno and Lintzen invited the study of tropical observations to reveal the waves in nature.

Observations suggest the existence of several of the predicted waves. Lower modes have been discovered in the form of convectively coupled equatorial waves detected in Outgoing Longwave Radiation (OLR) data collected by near polar orbiting satellites (Takayabu 1994 and others). OLR has become the most commonly used wave tracer in observational digital data studies of equatorial waves, resulting in a wealth of information about convectively coupled equatorial waves. Other studies have used dynamical fields and station observations to identify the waves (Pires et al. 1996, Liebmann and Hendon 1990).

Precipitable water data (PW) may also provide useful information for tropical wave analysis. Use of PW is motivated by the strong signals it contains that appear to be forced by equatorial waves of various types. PW occasionally indicates waves that are not associated with deep convection which therefore do not produce a strong OLR signal.

PW for this study was provided by the NASA water vapor project (NVAP) (Randall et al.). NVAP contains total column PW estimates derived from rawinsande and satellite data including passive microwave and infrared sounders.

2. Spectral Analysis

Space-time spectral analysis was performed on the gridded PW using a manner similar to Wheeler and Kiladis (1999). Two-dimensional space-time spectral estimates were computed by means of a two-dimensional Fourier transform (Hayashi, 1982). Global wavenumber was computed zonally. The resulting spectra are the average of spectral quantities computed for 60 97-day time segments consecutively overlapping each other by 65 days. The temporal mean and linear trend were removed from each segment by a least-squares fit to eliminate signals with frequencies lower than or equal to 1/97 cycles per day. The ends of the segments were tapered in time with cosine bells to minimize spectral leakage. The 97-day segment length was sufficient to include most synoptic and planetary scale waves with inter-seasonal and shorter periods. The 65-day overlap recovers data lost by the tapering. Results are not sensitive to the length of this overlap. The resulting time-longitude segments were 97 days by 360 degrees longitude. The spectral power was then computed and averaged over all available segments and all applicable latitudes or latitude combinations according to the desired spectrum format.

Raw spectra were computed in four formats, symmetric, antisymmetric, northern hemisphere only, and southern hemisphere only. The northern hemisphere spectrum is the mean spectral estimate for all available latitudes from 1 to 15 degrees north latitude, and similarly, the southern hemisphere spectrum is limited to 1 to 15 degrees south latitude. The symmetric and antisymmetric spectra were computed using symmetric and antisymmetric data as done in Yanai and Murakami (1970).

2.2 Background spectra and normalization

Each of the spectra were systematically normalized point by point. A common background spectrum, an appropriate standard deviate, and an assumed Gaussian distribution of all segments about the background were needed to perform the normalizations. The Gaussian distribution assumption is acceptable for this case because there are over 500 degrees of freedom in the computation. The standard deviate for a given spectrum type is the root mean square difference between each segment included in the spectrum and the background. In other words, each of the six types has a unique standard deviate. The mean standard anomaly of each point of each spectrum was calculated (See Wilks 1995, p. 81 for an explanation of the statistics). The normalized value of the spectrum was then calculated by numerically integrating the standard Gaussian distribution from negative infinity to the mean standard anomaly for that point. This normalization technique accounts for the statistical stability of spectral peaks.

The background spectrum for the hemispheric

[1]Corresponding Author Address: 503 Walker Building
University Park, PA 16802

spectra (not shown) is defined to be the sum of the symmetric and antisymmetric spectra smoothed forty times with a 1-2-1 filter. The background used to normalize the symmetric and antisymmetric spectra is the same background divided by two, allowing the hemispheric and the symmetry spectra to be viewed on the same scale. An identical background may be calculated using the average of the hemispheric spectra. The 1-2-1 smoothing removes peaks produced by periodic signals, but conserves integrated spectral power. While these background spectra cannot be independent of periodic processes, they are analogous to the spectrum of random, non-periodic, and non-sinusoidal signals in the data.

In addition to the spectral analysis, two-dimensional Fourier Filtering was applied to isolate the behavior of specific wave types in time and space. Peak spectral regions similar to those used by Wheeler and Kiladis (1999) were selected. Fourier coefficients outside a selected region were set to zero, and the two-dimensional inverse Fourier transform was applied. Equatorial symmetry constraints were not applied, allowing asymmetries to appear in the filter products. Data were plotted for longitude-time and surface map diagrams to view wave events. Seasonal variance maps were also developed from the filtered data to isolate wave tracks and behavior as a function of season and location.

3. Discussion and conclusions

All spectra and filter products discussed here will be included in the poster. The PW background spectrum is similar to the OLR background spectrum in Figure 2 in Wheeler and Kiladis (1999), who note that the eastward and westward components of the OLR background have different amounts of integrated power, and that the background spectra are asymmetric about the zero wavenumber. They argue that advective processes may influence the shape, or that all systematic wave propagation was not removed by the smoothing. Like the OLR spectrum, the PW background is red, meaning that most of the power is confined to low frequencies and wavenumbers, with maximum power at the lowest frequency and zero wavenumber. The PW background is skewed more to the westward side than the OLR spectrum.

Most PW and OLR power occurs in the northern hemisphere except at the lowest frequencies. PW filter products are more stongly skewed toward the northern hemisphere than OLR filter products. Wheeler and Kiladis (1999) noted that select significant peaks in their normalized OLR spectra correspond to the patterns expected for convectively coupled equatorial waves with a given range of values of h. Their Figure 6 outlines these spectral regions. Spectra computed in the present work have more significant peaks in westward synoptic scales than those in Wheeler and Kiladis (1999). These peaks have little raw power, yet their statistical stability increases their normalized value. Statistics of these peaks correspond with those of tropical depression type disturbances and arguably single-hemisphere easterly waves. The only spectral region with more power in the southern hemisphere than in the northern hemisphere corresponds with the MJO. The northern hemisphere dominates the spectral ranges of all analytically modeled equatorial waves.

These results indicate that spectral analysis of tropical PW is enhanced by including single hemisphere information. Symmetric and antisymmetric spectra do not reveal the dominance of the northern hemisphere disturbances in the final spectra because they do not clarify the impact of asymmetries in waves. Traditional symmetric and antisymmetric decompositions are useful for studying waves that are described by the models of Matsuno and Lintzen, but asymmetric disturbances are a significant part of the tropical spectrum. Asymmetric waves may be enhanced by an asymmetric base state (eg. the tropical Pacific Ocean meridional sea surface temperature profile.) Enhanced parts of these waves are more common in the northern hemisphere than in the southern hemisphere.

Acknowledgements

This work was funded by a grant from the National Science Foundation, number ATM 0003351. Some assistance was provided by George Young and W.M. Frank of the Pennsylvania State University meteorology department.

Works Cited

Lindzen, R. S., 1967: Planetary waves on beta planes. *Mon. Wea. Rev.*, 95, 441-451.

------, 1974: Wave-CISK in the tropics. *J. Atmos. Sci.*, **31**, 156-179.

Madden, R., and P. Julian, 1994: Observations of the 40-50-day tropical oscillation--A review. *Mon. Wea. Rev.*, **122**, 814-837.

Matsuno, T., 1966: Quasi-geostrophic motions in the equatorial area. *J. Meteor. Soc. Japan*, **44**, 25-43.

Pires, P., J.-L. Redelsperger, and J.-P. Lafore, 1997: Equatorial atmospheric waves and their association to convection. *Mon. Wea. Rev.*, **125**, 1167-1184.

Takayabu, Y. N., 1994a: Large-scale cloud disturbances associated with equatorial waves. Part I: Spectral features of the cloud disturbances. *J. Meteor. Soc. Japan*, **72**, 433-448.

------, 1994b: Large-scale cloud disturbances associated with equatorial waves. Part II: Westward propagating inertial-gravity waves. *J. Meteor. Soc. Japan*, **72**, 451-465.

Wheeler, M., and G. N. Kiladis, 1977: Convectively coupled equatorial waves: Analysis of clouds and temperature in the wavenumber-frequency domain. *J. Atmos. Sci.*, **56**, 374:399.

Wilks, D.S., 1995: *Statistical Methods in the Atmospheric Sciences.* Academic Press, INC. p 79-82.

Yanai, M., and M. Murakami, 1970: Spectrum analysis of symmetric and antisymmetric equatorial waves. *J. Meteor. Soc. Japan.* **48**, 331-347.

P2.29 DIFFERENCES IN THE RESPONSE OF SATELLITE PRECIPITATION ESTIMATES TO ENSO

Wesley Berg* and Christian Kummerow
Colorado State University, Fort Collins, CO

1. INTRODUCTION

With the launch of the Tropical Rainfall Measuring Mission (TRMM) in November of 1997 and associated advances in techniques for the retrieval of tropical rainfall from the passive microwave and precipitation radar sensors on board TRMM, substantial progress has been made towards reconciling differences in zonal mean precipitation over the tropics. A number of significant issues remain, however, with regard to the effect of regional and temporal variability on the monitoring of climate variability in tropical precipitation. For example, regional changes in precipitation systems associated with El Niño-Southern Oscillation (ENSO) appear to result in sensor dependent biases in interannual tropical rainfall variability.

Current observations show that warming of tropical Sea Surface Temperatures (SSTs) associated with ENSO leads to a more vigorous hydrologic cycle (Soden, 2000). The magnitude of this increase is somewhat less certain, however. Soden (2000) investigated this issue by performing a comparison of tropical-mean oceanic rainfall derived from the Microwave Sounding Unit (Spencer, 1993) with that predicted by a number of global atmospheric climate models. The results of this comparison show that the magnitude of model predicted change in tropical-mean precipitation is roughly one quarter of that observed by the MSU observations. This discrepancy led Soden to conclude that "either (i) the sensitivity of the tropical hydrologic cycle to ENSO-driven changes in SST is substantially underpredicted in existing climate models or (ii) that current satellite observations are inadequate to accurately monitor ENSO-related changes in the tropical-mean precipitation.

2. TRMM OBSERVED ENSO VARIABILITY

Although the MSU precipitation product does not represent the state-of-the-art in satellite rainfall estimation techniques, recent observations from TRMM of variability in tropical-mean precipitation associated with the 1997/98 El Niño, shown in Figure 1, do nothing to resolve this issue. In fact, these results suggest that Soden's conclusion that current satellite observations may be inadequate to monitor ENSO-related changes in tropical rainfall is likely correct. As the figure shows, passive microwave rainfall estimates from the TRMM Microwave Imager (TMI) are in sharp disagreement with results from the TRMM Precipitation Radar with regard to the response of tropical-mean oceanic rainfall to the ENSO event. The TMI (2A12) results show a marked increase in tropical-mean precipitation associated with ENSO while the PR (2A25) results show no such increase.

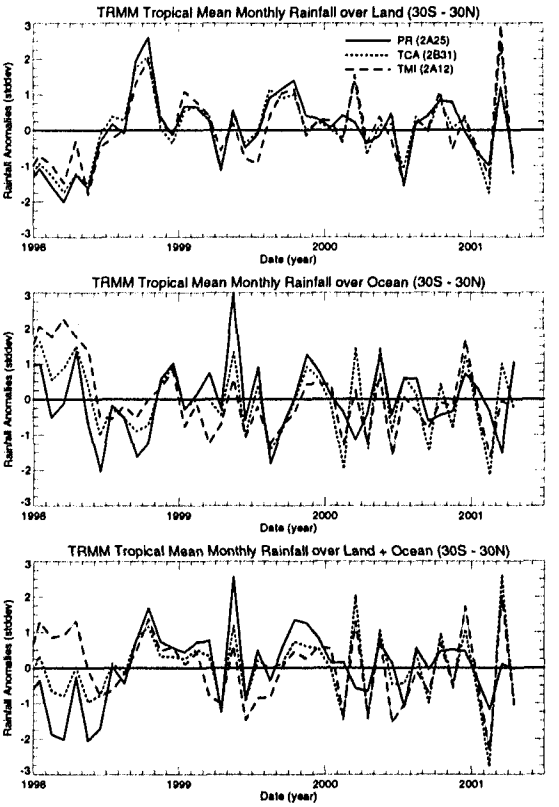

Figure 1: A comparison of the time series of monthly TRMM rainfall anomalies over a) land, b) ocean, and c) combined land+ocean. The algorithms shown include retrievals from TMI only (2A12), PR only (2A25), and combined TMI/PR (2B31) algorithms.

It is interesting to note that the satellite estimates agree very well over land, where passive microwave retrievals rely on more indirect methods relating scattering by ice particles to the surface rainfall rate. In contrast, emission-based techniques used over ocean depend on the more physically based relationship between liquid water content and surface rainfall rate. This suggests that the mechanisms producing rainfall over tropical land regions are relatively unaffected by changes due to ENSO, at least in the sense that there is little change in the resulting structure of rain systems. Over ocean, however, large-scale dynamics such as the Walker circulation appear to play a more significant role in determining the structure of rainfall systems.

* *Corresponding author address:* Wesley Berg, Colorado State Univ., Dept. of Atmospheric Science, Fort Collins, CO 80523-1371; e-mail: berg@atmos.colostate.edu

An EOF analysis of the difference between the TMI and PR rainfall estimates, shown in Figure 2, indicates that this disagreement is primarily due to differences in the response of the algorithms to changes over the tropical Pacific. As shown in this figure, the second EOF appears to capture most of the interannual variability of this difference, which is primarily located along the region of increased SSTs in the central and eastern Pacific. This indicates that ENSO induced changes in tropical Pacific rainfall are the key to understanding the differences in the interannual variability of TMI versus PR rainfall in the tropics.

3. EAST PACIFIC BIASES

As shown in Figure 3, rain systems in general are shallower and therefore have warmer cloud tops in the east Pacific, however, there is a prevalence of small shallow rain systems over the east Pacific ITCZ. Infrared-based rain retrieval techniques such as the Global Precipitation Index (Arkin and Meisner, 1987), relate the cloud-top temperature to rainfall. Such techniques will severely underestimate rainfall in the east Pacific, which has a larger proportion of shallow rain systems with warm cloud tops. During El Niño, however, warmer SSTs in the east Pacific lead to higher clouds. This reduces or even eliminates this east-west bias. As a result, IR techniques such as GPI will tend to overestimate the change in east Pacific rainfall associated with ENSO and thus overestimate interannual variability in tropical rainfall as well.

Conversely, precipitation estimates from the Microwave Sounding Unit (MSU) (Spencer, 1993) used in Soden's comparison (2000) will tend to overestimate rainfall in the east due to the fact that this algorithm neglects the effects of scattering by ice aloft. The brightness temperature/rain rate relationship of the 50.3 GHz channel used by the MSU algorithm is shown with and without the effects of ice scattering in Figure 4. The corresponding relationship for the 19.35 GHz channel used for emission-based rainfall retrievals from SSM/I and TMI is also shown in this figure. Because there is more ice in the taller west Pacific rain systems, and the MSU algorithm is calibrated there, the brightness temperature increase due to emission by liquid rain drops will dominate the decrease caused by ice scattering. This will result in an overestimate of rain in the east Pacific. During ENSO, conditions in the east Pacific are more like the west resulting in a reduction in this bias and a lower overall estimate of interannual variability in tropical rainfall. This suggests that the difference found by Soden (2000) should be even larger, however, other factors influencing the MSU estimates such as poor spatial resolution make it a poor choice for comparison with the models.

Although they suffer from a significantly shorter data record, the retrievals from TRMM, shown in Figure 1, provide much more physically direct measurements of rainfall over the ocean than IR or MSU techniques. An issue with emission-based passive microwave rainfall retrievals over the ocean such as the TMI 2A12

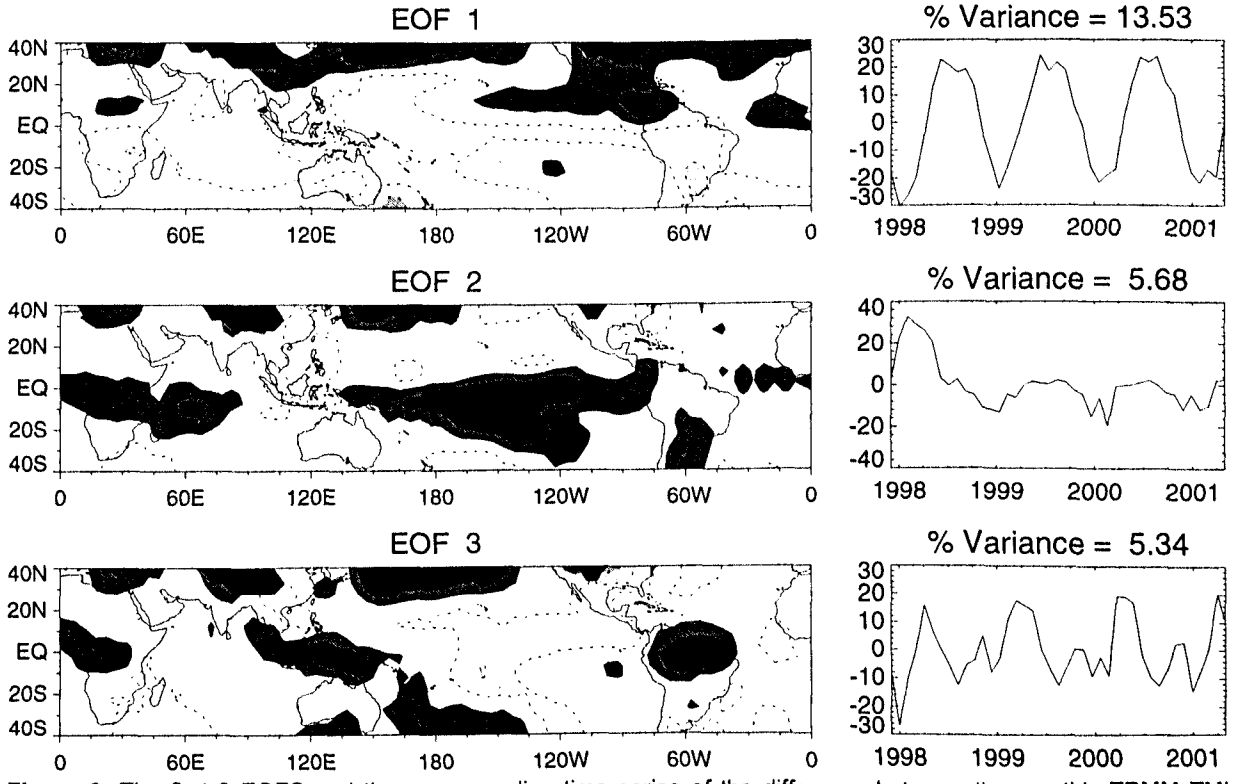

Figure 2: The first 3 EOFS and the corresponding time series of the difference between the monthly TRMM TMI (2A12) and the PR (2A25) rainfall retrievals.

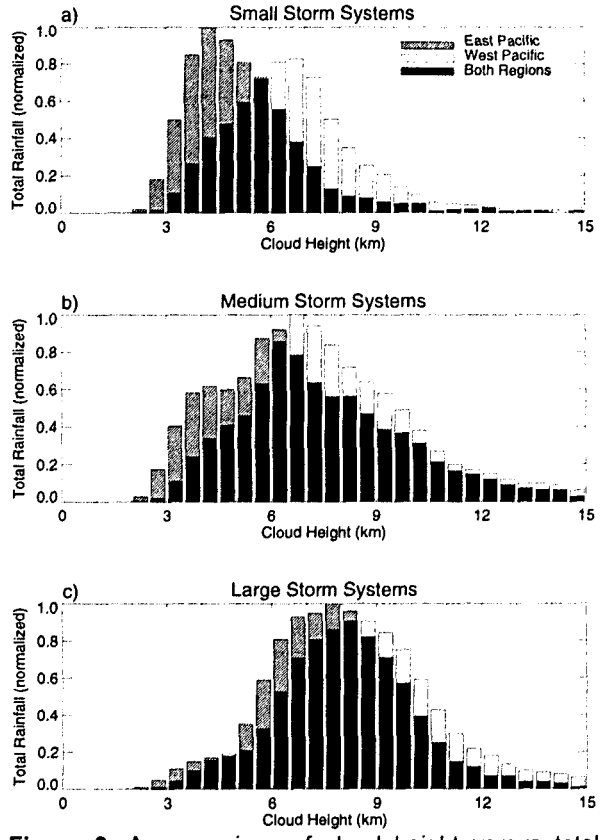

Figure 3: A comparison of cloud height versus total rainfall between the selected east and west Pacific regions for DJF 1999/2000. The results are broken into separate categories for a) small, b) medium, and c) large storms. Total rainfall within each 0.5 km cloud height category has been normalized so that the area under the curve is the same for both regions and the maximum is one.

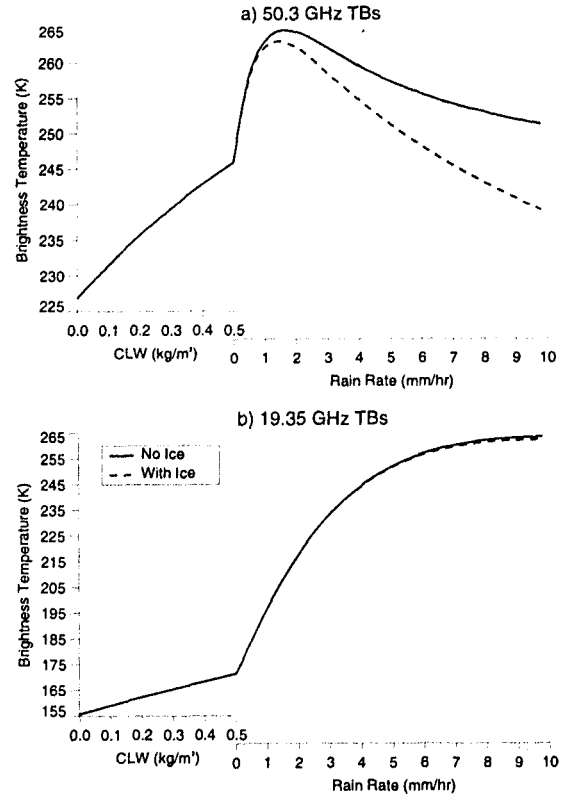

Figure 4: Simulated brightness temperatures vs. cloud liquid water and rainfall computed using an Eddington radiative transfer model (Kummerow, 1993) and a simple 6-layer cloud in the tropics. Results are shown for a) the 50.3 GHz MSU channel used for the MSU precipitation retrievals (Spencer, 1993) and b) the 19.35 GHz channel, which is the primary emission channel used for many SSM/I and TMI retrievals. The dashed line shows the scattering effect of adding ice to the cloud above the freezing level.

algorithm, however, is that the emission signal is related to the total amount of liquid water in the atmospheric column. In order to estimate the surface rain rate, therefore, it is necessary to estimate of the height of the column. This is generally based on the freezing level, which is a rough estimate of the height of the liquid water column. More accurate, however, is to use the mean height of the radar bright band, which is also a measure of the mean melting layer or the mean location of the top of the liquid water column.

Figure 5 shows a comparison of the freezing level height from several sources with the mean bright band height from the TRMM PR. Although there are significant differences in the freezing height estimates, all three sources indicate that the distance of the bright band below the freezing level is much larger in the east Pacific than in the west. Depending on the method used to estimate the freezing height or height of the water column, this difference can lead to a relative bias in the passive microwave retrievals by underestimating rainfall in the east Pacific and leading to an overestimate of the interannual variability associated with ENSO.

4. CONCLUSIONS

We have shown that rainfall estimates from GPI, MSU, and many SSM/I and TMI-based passive microwave retrieval techniques produce biased estimates of rainfall over the east Pacific ITCZ, which impact the magnitude of the observed interannual variability of tropical rainfall. Preliminary results comparing differences in drop-size distributions from the TRMM PR indicate that the PR retrievals may also suffer from biases in east Pacific rainfall. Clearly, a significant amount of work remains to be done in order to quantify and correct for these regional climate biases. This is especially difficult due to a lack of in-situ observations over regions such as the east Pacific. Until we manage to do this, however, Soden's conclusion that "current satellite observations are inadequate to accurately monitor ENSO-related changes in the tropical-mean precipitation" appears to

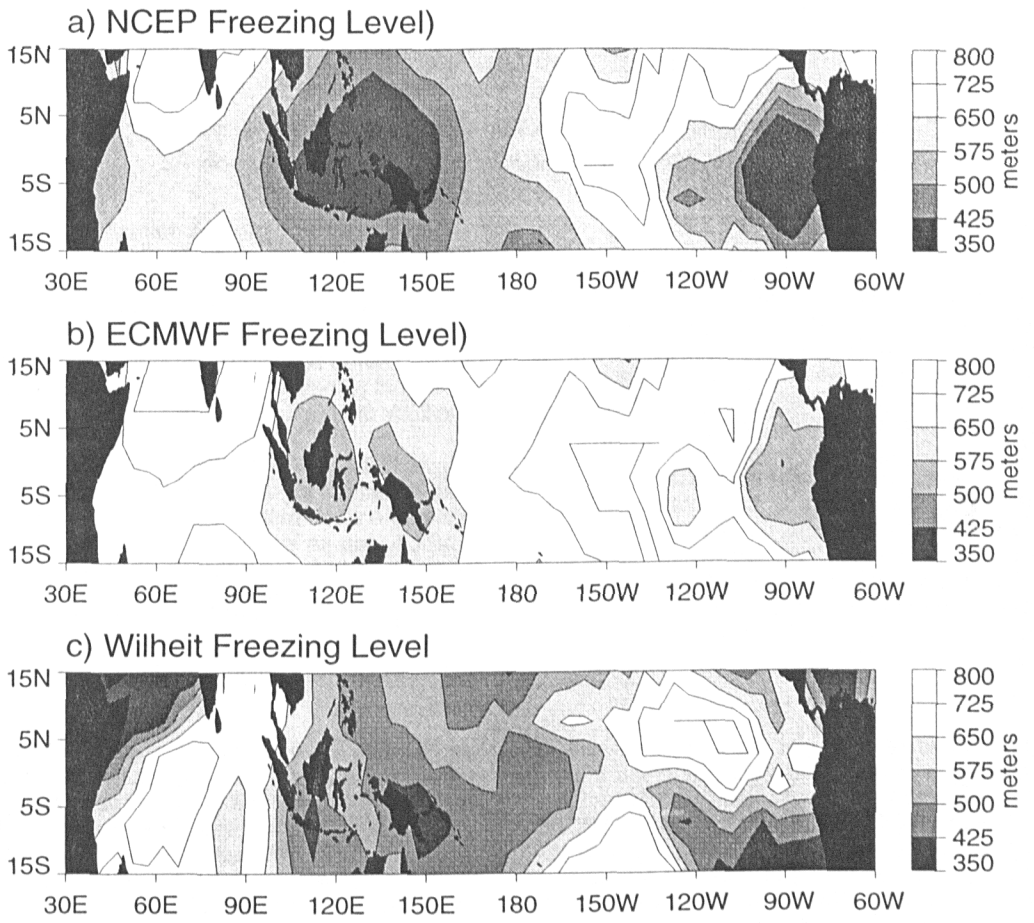

Figure 5: A comparison of the mean DJF 1999/2000 height of the freezing level, or zero degree isotherm minus the height of the bright band or melting layer height from the TRMM PR. The freezing level height is obtained from a) *NCEP reanalysis, b) ECMWF analysis, and c) a retrieval from* TRMM TMI using the technique by Wilheit et al. (1991).

be accurate even with respect to the latest retrievals being produced from TRMM.

5. REFERENCES

Arkin, P.A., and B. N. Meisner, 1987: The relationship between large-scale convective rainfall and cold cloud over the western hemisphere during 1982-84, *Mon. Wea. Rev.*, **115**, 297-316.

Kummerow, C. 1993: On the accuracy of the Eddington approximation for radiative transfer in the microwave frequencies, *J. Geophys. Res.*, **98**, 2757-2765.

Soden, B. J., 2000: The sensitivity of the tropical hydrologic cycle to ENSO, J. Climate, 13, 538-549.

Spencer, R. W., 1993: Global oceanic precipitation from the MSU during 1979-91 and comparisons to other climatologies, J. Climate, 6, 1301-1326.

Wilheit, T., A. Chang, and L. Chiu, 1991: Retrieval of monthly rainfall indices from microwave radiometric measurements using a probability distribution function, *J. Atmos. Ocean. Tech.*, **8**, 118-136.

P2.30 A TRMM-CALIBRATED INFRARED TECHNIQUE FOR CONVECTIVE AND STRATIFORM RAINFALL: ANALYSIS AND VALIDATION

Andrew J. Negri*[1], L. Xu[2] and R. F. Adler[1]

[1]Laboratory for Atmospheres, Goddard Space Flight Center, Greenbelt, MD
[2]Dept. of Hydrology and Water Resources, U. Arizona, Tucson, AZ

1. INTRODUCTION

In this paper, we present results from a combined satellite infrared (IR) and microwave (MW) technique for estimating rainfall over the Amazon Basin. Our objectives are to examine the diurnal variability of rainfall and to investigate the relative contributions from the convective and stratiform components. Anagnostou et al (1999) performed a similar analysis using SSM/I and GOES data. The current technique (designated CST/TMI) and described in Negri et al (2001), is based on the IR estimates from the Convective-Stratiform Technique (Adler and Negri, 1988) calibrated by coincident rain estimates from the TRMM Microwave Imager. This paper extends the results of Negri et al (2001) to examine the inter- and intra-annual variability of the diurnal cycle of rainfall for various periods in 1999-2001.

2. RESULTS

The diurnal cycle of rain over the Amazon Basin (0-10S, 75-50W) was constructed from 30-minute interval CST/TMI estimates. We examined six three-month periods: Jan-Mar, (JFM) 1999, 2000 and 2001 (for interannual variability) and well as Apr-Jun (AMJ), Jul-Sep (JAS) and Oct-Dec (OND) in 2000 for intra-annual variability. The first period coincided with the LBA experiment in Rondonia (southwestern Brazil). *In situ* radar data provided a comparison between the mean radar rain rates and convective/stratiform division with those estimated by the CST/TMI. The phase of the satellite estimates lagged the radar by one hour (Negri et al, 2001).

Buoyed by the success of the technique in an area with ground-truth, we examine the diurnal variation of rainfall in the entire Amazon basin. In such a large region, it is possible to utilize the TRMM PR data as ground truth, despite the limited sampling. In Figure 1, we display a time series of the estimated total, convective and stratiform rain rates (mm/h) for all of 2000 for both the CST/TMI (top) and TRMM PR (bottom). The IR estimates (total and convective) peak at 16 LT, with stratiform trailing 2-3 h later. Phase agreement with the PR is best for the convective portion. The IR estimates missed morning rainfall, which the PR identifies as mostly stratiform. The diurnal cycle of stratiform rain from the PR is essentially constant, unlike the CST/TMI cycle. In the mean, both methods find the convective rain to comprise ~ 60% of the rain volume. At the time of peak rainfall, the percentage is closer to 70% in both methods. Sampling is indicated by the number plotted across the bottom. We plot the number of TRMM orbits (by hour) in which the subpoint crossed the region of interest during 2000. We believe that the limited sampling contributes to the "noise" in the PR diurnal signal. There are obvious differences in the *amplitude* of the diurnal cycle.

Figure 2 shows the interannual variability of the diurnal cycle of rainfall for JFM 1999-2001. The CST estimates display the same pattern in all three periods, with a peak at 16 LT, and an indication of a smaller, early morning maximum at 4 LT. The PR data show a consistent spike between 6-8 LT, mostly stratiform rain, that the IR technique misses. For this period, the PR has the mean percent stratiform rain at ~ 50%, while the IR technique is closer to 66%, a result of underestimating the morning rainfall.

In Figure 3, we present seasonal (three-month) estimates for 2000. PR sampling in this 3-month period is about 16 overpasses at each hour. During the hours 0-10 LT, rainfall is not well represented in the CST/TMI estimates. The PR estimates show the onset of afternoon convection to be 1 h earlier than the IR, and the PR displays a broader afternoon maximum.

Future work will include an investigation of the morning stratiform rainfall missed by the IR technique, and a comparison with the diurnal cycle derived from the TMI retrievals. We hope to use the high-resolution, global IR dataset of Janowiak et al (2001) in conjunction with the PR data to produce global estimates at high spatial and temporal resolution.

3. REFERENCES

Adler, R.F. and A.J.Negri, 1988: A satellite infrared technique to estimate tropical convective and stratiform rainfall. *J. Appl. Meteor.*, **27**, pp. 30-51.

Anagnostou, E.N., A.J. Negri, and R.F. Adler, 1999: A satellite infrared technique for diurnal rainfall variability studies. *J. Geophys. Res.*,**104**, 31,477-31,488.

Janowiak, J.E, R.J. Joyce and Y. Yarosh, 2001: A real-time global half-hourly pixel-resolution infrared dataset and its application. *Bull. Amer. Meteor. Soc*, **82**, 205-217.

Negri, A.J. L. Xu, and R.F. Adler, 2001: A TRMM-calibrated infrared rainfall algorithm applied over Brazil, *J. Geophys. Res.*, (in press).

**Corresponding author address*: Andrew J. Negri, Code 912, NASA/GSFC, Greenbelt, MD 20771; e-mail: negri@agnes.gsfc.nasa.gov

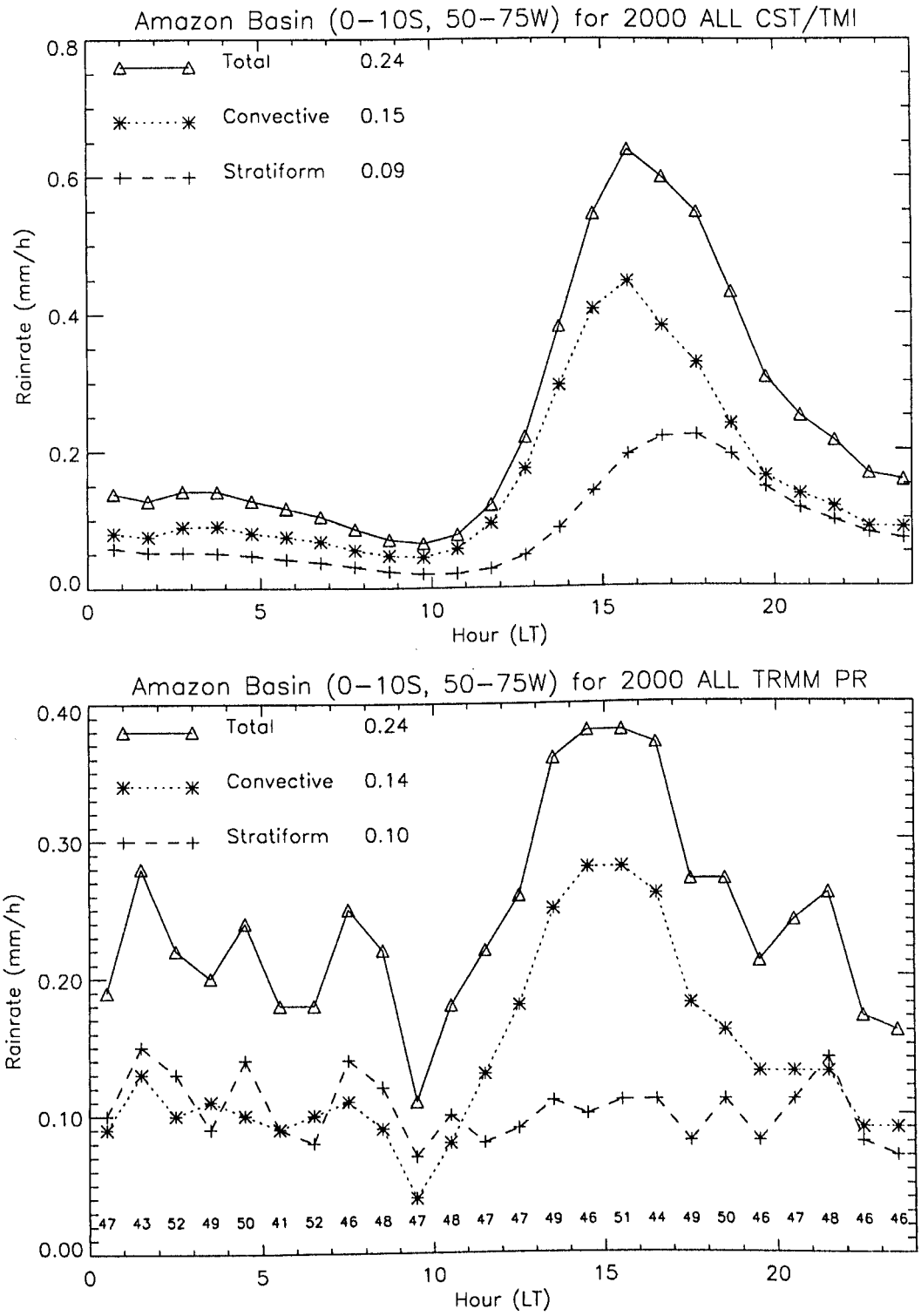

Figure 1. Diurnal cycle for the Amazon Basin estimated from the CST/TMI (top) and TRMM PR (bottom) for 2000. Total, convective and stratiform rain rates are plotted. Mean values for each are shown in the legend. Numbers along the bottom indicate the number of TRMM orbits in which the satellite subpoint intersected the region.

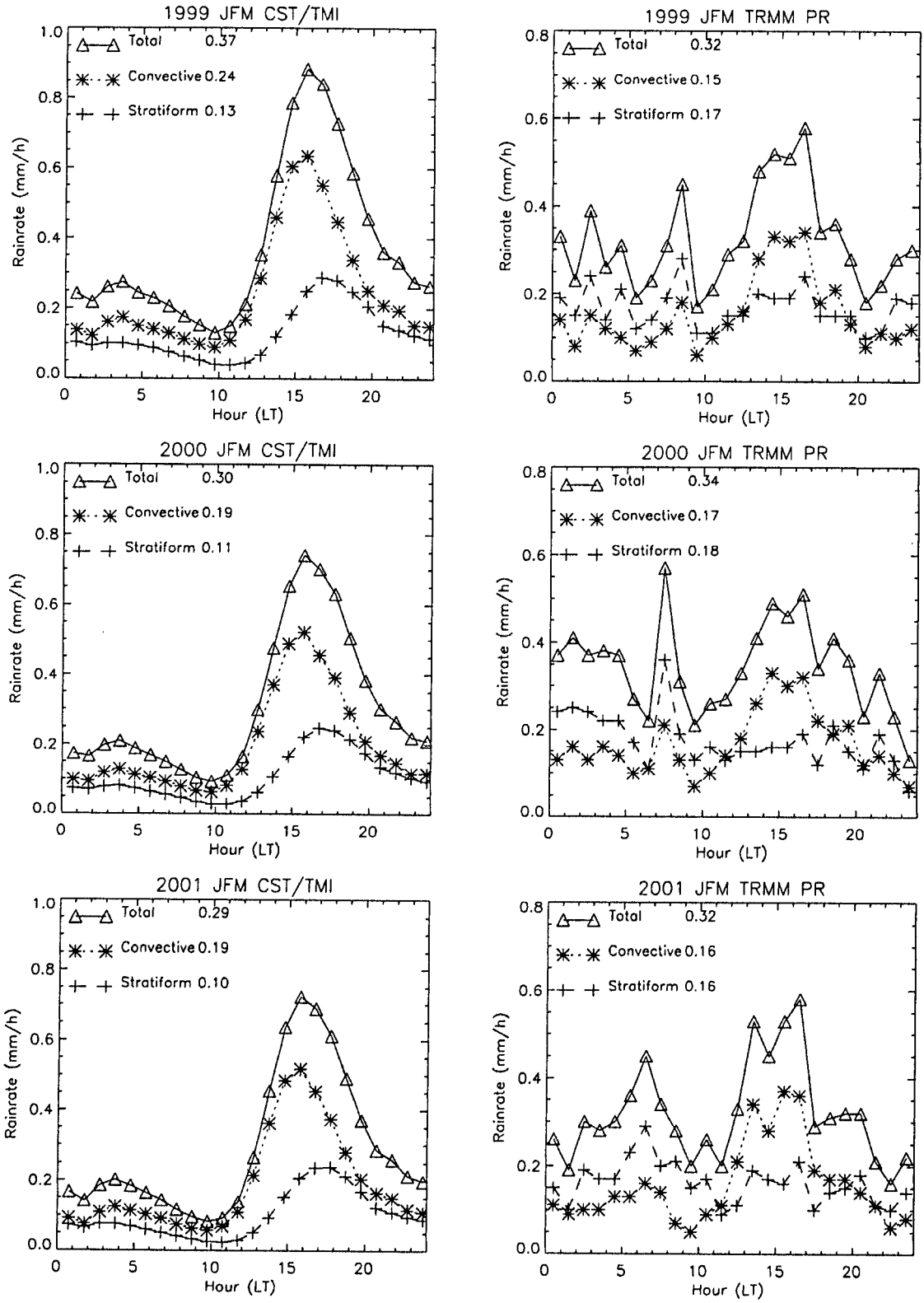

Figure 2. Same as Fig. 1 except for Jan-Mar 1999 (top), 2000 (middle) and 2001 (bottom). IR-based estimates are on the left, TRMM radar on the right.

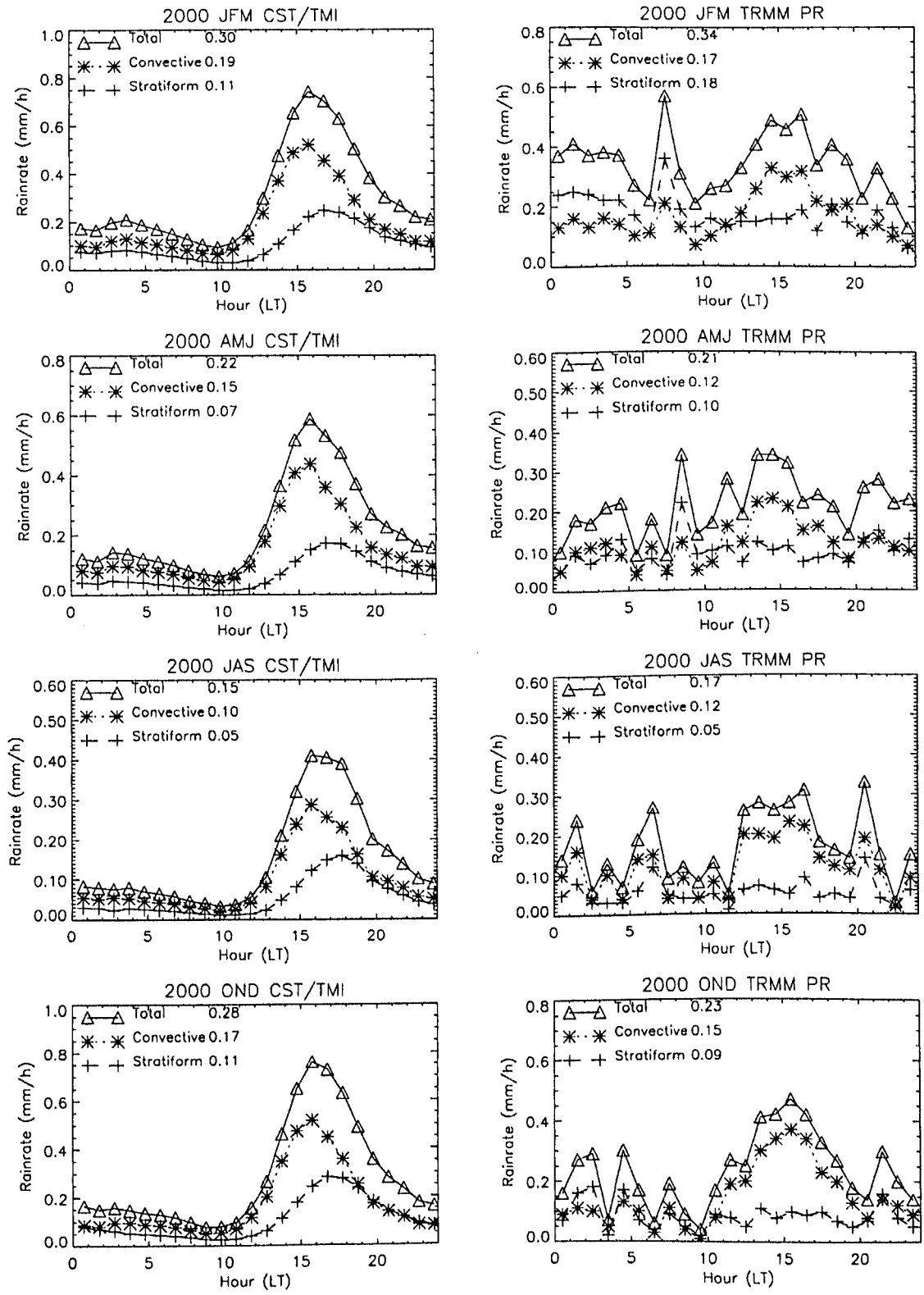

Figure 3. Same as Fig. 2 except for seasonal (three-month) periods in 2000.

P 2.32 STANDARD ERRORS OF THE ESTIMATED TREND IN CHANNEL 2 OF THE MICROWAVE SOUNDING UNIT

David S. Crosby* , Mitchell D. Goldberg, Tsan Mo, and Zhaohui Cheng (QSS)
NOAA/NESDIS/ORA, Camp Springs, MD 20746

1. INTRODUCTION

The Microwave Sounding Unit (MSU) on the NOAA polar-orbiting environmental satellites (POES) have been used to estimate trends in global temperatures (Christy et al. 2000). A new improved calibration algorithm for this instrument has been developed and tested. (Mo et al. 2000) and a data set using this calibration technique is now available for study. A question of primary interest is the standard error of the estimated slope of a trend line. In order to obtain an estimate of the standard error of the estimated trend and to simplify the analysis , a subset of the data will be studied. This subset is monthly global averages of the antenna temperatures over a 12 year period (November 1986 to October 1998) using the data from the NOAA-10 and NOAA-12 satellites. These satellites are both morning satellites and have little drift in their equator crossing time. We use only nadir and near nadir measurements and have a three month overlap period between the two satellites and a stable five year period of overlap between NOAA-10 and NOAA-12 with NOAA-11 for making a satellite to satellite adjustment. These features of the data set used in this study eliminate many of the difficulties which have complicated the analysis of the errors in the estimated trends.

The natural signals in the deseasonalized or anomaly time series from Volcanic , ENSO and solar forcing are partially removed by a multiple regression procedure. This is similar to the technique in Michaels and Knappenberger (2000). A simple analysis of the residuals from the multiple regression shows that the errors are not independent and the usual statistical tests and estimated standard errors are incorrect. The noise or errors in the time series is modeled using a first order autoregressive process (AR1) and the parameters are estimated using the Hildeth-Lu procedure (Neter et al.,1996) This procedure is used to estimate the trend and the standard error of the trend. The trend for this 12 year period is found to be .067 C per decade with a standard error of .062 C per decade. This gives an approximate 95 percent confidence interval for the trend to be (-.058,.+0.192) C per decade. The trend is not statistically significantly different from 0.0 at any reasonable level of significance. However, an analysis of the errors shows that if a 20 year time series of this quality were available a trend of the order of 0.1 C per decade should be detectable.

*Corresponding author address: David S. Crosby, NOAA/NESDIS, 5200 Auth Road, Room 810, Camp Springs, MD 20746, email:david.s.crosby@noaa.gov

2. THE DATA SET

For a general discussion of the time series see Christy et al (2000). For a detailed discussion of the MSU instrument see Mo (1995) and for the calibration techniques use for the data sets in this paper see Mo et al. (2000). For this study we use a specially constructed subset of the MSU time series. This subset consist of monthly global averages of antenna temperatures for the MSU channel 2 (53.74 Ghz). To simplify the analysis and avoid complications only MSU scan positions 5, 6 and 7 were used. Since these 3 positions are at nadir (position 6) or close to nadir (positions 5 and 7), the effect of the decrease in the orbit altitude should be minimal and it is not necessary to apply a limb adjustment procedure. The satellite does not uniformly sample the globe. Hence, some sort of adjustment is needed. For this data set the global monthly averages were constructed by binning the data by latitude (There were nine 20 degree latitudinal bins)and then this binned data was used to form a weighted average with weights proportional to the cosine of the mean latitude for each of the bins. The number of individual measurements per month was in all cases in excess of 2×10^5. To further simplify the analysis the data set for this study was limited to the MSU's on NOAA-10 and NOAA-12. These are morning satellites and there is much less drift in their equator crossing time than that in the afternoon satellites. In addition, there is a three month period (June, July and August of 1991) when there is overlap data from the two satellites. The differences between the two satellites (NOAA-12 - NOAA-10) using the new calibration coefficients for these three months are 0.51 C, 0.49 C and 0.49 C, respectively(Mo et al. (2000)). The small range of these differences gives us confidence that we can make a good adjustment for the intersatellite calibration effect using a constant offset. The constant offset was estimated by constructing a 60 month series of the differences of between the global averages of NOAA-10 and NOAA-11 and NOAA-12 and NOAA-11. The estimated offset was found to be 0.5335 C. Note that this was slightly larger than the average of the differences for the three month overlap period (0.497 C).

The data set consists of NOAA-10 values from December 1986 to August 1991 and adjusted NOAA-12 values from September 1991 until November 1998.

3. METHOD OF ANALYSIS AND RESULTS

The analysis is carried out on the original time series of global antenna temperatures. The parameter of primary interest is the standard error of the estimated

trend in this data. The data is modeled in the following way:

$$Y_t = X_t \beta + \epsilon_t$$

Here, Y_t is the temperature at time t, X_t is a vector of predictors at time t , and ϵ_t is the error in the model at time t. In this model X_t is a 16 dimensional vector. There are 15 predictor variables and the constant offset. They are time in months, 11 indicator variables for the 12 months , a lagged the multivariate ENSO index [Wolter and Timlin, 1993 and updates], lagged stratospheric aerosol optical depth measurements [Sato et al., 1993 and updates], and the F10.7 solar series. If we assume independent errors, then we find a trend of 0.0.095 C per decade with a estimated standard error of the trend of 0.036 C. These results have a p-value of less than 0.010, and would be determined to be significant. However, an analysis of the residuals from this model gives an estimated a lag one correlation of 0.40, which is significant at any reasonable level. Hence, the assumption of independent errors , in the above model, must be rejected.

This model will be fitted using the Hildeth-Lu technique (Neter et al. 1996) . In this procedure the noise is whitened by differencing . Using the Hildeth-Lu technique on the 12 year data set the estimated coefficient of time or trend term was 0.067 C per decade with a standard error of the trend of 0.062 C. This gives an approximate 95 percent confidence interval for the trend of (-0.058, 0.192). The residual standard error of the model was 0.12 C.

4. ESTIMATION OF STANDARD ERRORS FOR LONGER TIME SERIES

In a univariate time series with a trend, the standard error of the trend decreases approximately as $(1/n)^{3/2}$. The situation is more complicated in a multivariate situation but it is similar. Using this approximation it is possible to compute estimated standard errors for time series with different lengths. For example, a 20 year time series (n=240), an estimate of the standard error of the trend would be $0.029=0.062*(144/240)^{3/2}$.

This analysis shows that if there were a 20 year or longer time series of MSU type measurements from satellites with little orbital drift, good calibration , and with sufficient overlap periods it should be possible to detect trends of the order of 0.1 C per decade with almost absolute certainty. This is the case even if the errors due to the uncertainty of the merging procedure are included. The standard error of the adjustment from NOAA-10 to NOAA-12 is of the order of 0.015 C. If a longer overlap period was available this uncertainty in the adjustment would be considerably smaller.

5. SUMMARY

Using a new calibration procedure a 12 year subset of the MSU data was constructed. This set only uses nadir or near nadir measurements and NOAA-10 and NOAA-12 both morning satellites with overlap data. This subset avoids many of the difficulties associated with the full MSU data set, such as orbital drift and decreases in orbital height. This data was used to construct a global average temperature time series.

This time series was analyzed using a multivariate regression procedure which adjusted for seasonal effects, natural signals, and a trend. The multivariate procedure was modified to account for autoregressive error structure in the residuals from the model. Using this analysis, a trend of 0.067 C per decade with a standard error of 0.062 C was estimated. This trend was not significant.

If a 20 year or longer time series of MSU data of the quality of this 12 year time period, trends of the order of 0.1 C per decade would be detected with a high degree of reliability .

6. REFERENCES

Christy, J. R., R.W. Spencer, and W. D. Braswell, 2000: MSU Tropospheric Temperatures: Dataset Construction and Radiosonde Comparisons. *J. Atmospheric and Oceanic Technology*, **17**, 1153-1170.

Michaels, P. J. and P. C. Knappenberger, 2000: Natural Signals in the MSU Lower Tropospheric Temperature Record. *Geophysical Research Letters*, **27**, 2905-2908.

Mo, T. 1995: A study of the Microwave Sounding Unit on the NOAA-12 satellite, *IEEE Trans. Geosci. Remote Sens.*, **33**, 1141-1152.

Mo, T., M. D. Goldberg, D. S Crosby, Z. Cheng, 2001: Recalibration of the NOAA microwave sounding unit. *J. Geophysical Research*, **106**, 10,145-10,150.

Neter, J., M. H. Kutner, C. J. Nachtsheim and W. Wasserman ,1996: *Applied Linear Regression Models*. 3d ed. Irwin, 720 pp.

Sato, M. et al, Stratospheric Aerosol Optical Depths, 1850-1990, *J. Geophys. Res.*, **98**, 22,987-22,994, 1993. Updates available at Http://www.giss.nasa.gov/data/strataer.

Wolter, K. and M.S. Timlin, Monitoring ENSO in COADS with a seasonally adjusted principal component index. Proc. *Of the 17th Climate Diagnostic Workshop*, Normal OK, NOAA.N MC/CAC NSSL, Oklahoma Clim. Survey, CIMMS and the School of Meteor., University of Oklahoma, 52-57, 1993. Updates available at http://www.cdc.noaa.gov/~kew/MEI/mei.html.

P2.34 GLOBAL SATELLITE-BASED STUDY OF THE DIURNAL RANGE OF LAND SURFACE TEMPERATURE

Ivan Csiszar*[1] and Garik Gutman[2]
[1]CIRA/NOAA/NESDIS/ORA, Camp Springs, MD [2]NASA Headquarters, Washington, DC

1. INTRODUCTION

An earlier study with principal component analysis (Ignatov and Gutman 1999) showed that the diurnal cycle of land surface temperature can be approximated with root-mean-square accuracy of about 1-2°C by two empirical orthogonal functions, which characterize the mean temperature level and the diurnal temperature range (DTR), respectively. The current study focuses on DTR, whose properties on the global scale have not been sufficiently investigated. DTR is an important surface characteristic related to thermal inertia (Price, 1977). The advantage of considering DTR rather than the absolute values of temperatures is that some uncertainties, such as calibration errors or the effect of imperfect knowledge of surface emissivity in deriving surface skin temperature, are reduced.

On a global scale, DTR can be mapped and monitored only from space. In this work long-term time series of monthly mean DTR have been derived from climatological satellite-based data sets. The properties of multi-year means and inter-annual DTR variability have been investigated.

2. DATA

We used the "mean surface (skin) temperature (T_s) from clear sky composite" product from the ***ISCCP (International Satellite Cloud Climatology Project)*** Monthly Cloud Product D-2 data set from the 1984-1993 period. D-2 is a statistical summary of the original satellite observations presented as monthly means in eight 3-hour intervals, from 00 through 24 UTC, mapped globally in an equal-area (280 km)^2 projection (Rossow et al., 1996). T_s is derived from clear-sky infrared radiances corrected for water vapor absorption, assuming a surface emissivity of unity. Unfortunately, the ISCCP spatial coverage, produced by merging data from geostationary and polar orbiter operational environmental satellites by a certain hierarchy, is poor over Central Asia due to the lack of coverage from the geostationary Insat satellite (except for a 1-year period starting in April 1988). While some observations from polar satellites exist over this gap within ISCCP, for consistency reasons they were not used in creating the fully global, 15-year time series of DTR maps based on the AVHRR-based global data sets discussed below.

The ***NOAA/NESDIS Pathfinder Atmosphere (PATMOS)*** data set includes daytime and nighttime AVHRR-derived radiance products from 1981 through 2000 on a global 10000 km^2 equal-area grid. In the current analysis we used the following monthly mean products, re-projected onto 1°x1° global grid: daytime and nighttime, clear-sky, channel 4 and 5 brightness temperatures ($T4_d$, $T4_n$, $T5_d$, $T5_n$) derived from the corresponding longwave radiance products; absorbed all-sky and clear-sky solar radiation (ASR and ASR_0); all-sky and clear-sky outgoing longwave radiation (OLR and OLR_0); and fractional cloud amount (f_c). From the top-of-the atmosphere brightness temperatures daytime (T_{sd}) and nighttime (T_{sn}) skin temperatures were derived by the split-window equation from Becker and Li (1990).

The third generation of ***Global Vegetation Index (GVI)*** data set has been produced from AVHRR data operationally since April 1985 at NOAA/NESDIS (Gutman et al., 1995). The daily data are compressed into 7-day channel 2 – channel 1 maximum composite maps, from observations sampled and mapped daily into a latitude/longitude grid with 0.144° (nominally 0.15°) resolution. Weekly data are further processed into monthly means. In this study we used Normalized Difference Vegetation Index data derived from channel 2 (R2) and channel 1 (R1) reflectances: NDVI=(R2-R1)/(R2+R1), aggregated into (2.5°)^2 means.

Monthly precipitation amounts (PREC) within the ***CAMS-OPI blended global precipitation*** data set are produced from analysis of AVHRR-derived Outgoing Longwave Radiation (OLR) product (Gruber and Krueger 1984) and gauge observations for each (1°)^2 grid of the globe (Janowiak and Xie 1999).

For validation of satellite-derived DTR, we used a ***multi-year monthly climatology of DTR of in-situ temperatures at 124 stations in Russia*** (Groisman et al. 1996). It consists of temperatures of air at the shelter level in all-sky (T_{aa}) and clear-sky (T_{ac}) conditions, and of the ground surface (T_{ga} and T_{gc}, respectively). DTR values were calculated from the 1-hour diurnal cycles, which were obtained by cubic spline interpolation from the originally 3-hourly climatology.

• *Corresponding author address*: Ivan Csiszar, NOAA/NESDIS/ORA, WWB 712, Camp Springs, MD 20746-4304; e-mail: Ivan.Csiszar@noaa.gov

3. METHOD

An hourly ISCCP-based surface temperature database was constructed by converting the 3-hour GMT time slots into local times, and interpolating the surface temperatures with cubic splines into a regular 1-hour grid. This database was used to specify daily maximum (T_{max}) and minimum (T_{min}) temperatures. DTR was calculated as DTR= T_{max} - T_{min}.

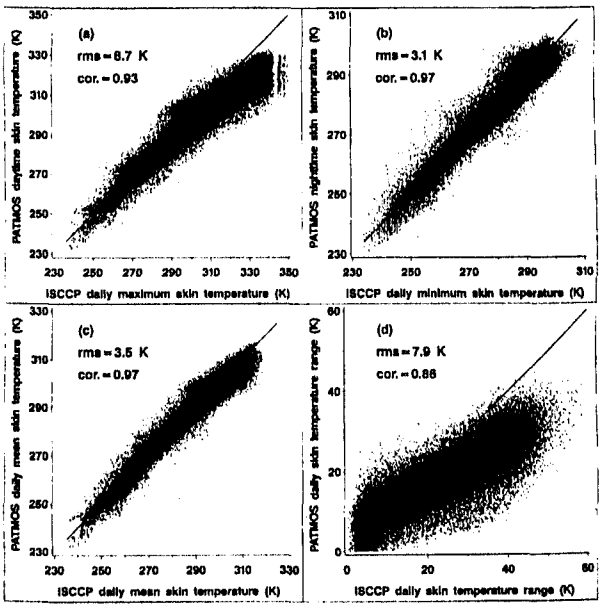

Fig. 1 Comparison of PATMOS daytime and nighttime surface skin temperatures with ISCPP daily maximum and minimum values

We can consider the daytime-nighttime AVHRR temperature difference as a first-order estimate of DTR and develop corrections to it. The error in the AVHRR-based estimate of DTR is mainly in the decrease of the afternoon temperature with the local time of observation and thus its deviation from the daily maximum. Fig. 1 shows the relationship between the PATMOS and ISCCP temperatures. The PATMOS daytime temperatures (Fig. 1a) deviate considerably from the daily maximum for high temperature values. This can be explained by the strong afternoon decrease of skin temperature in hot, mainly desert areas. The PATMOS nighttime temperatures (Fig. 1b), on the other hand, show good agreement with the daily minima, confirming the smaller change of temperature in the late night and early morning hours. The daily mean temperature from PATMOS ($[T_{sd}+T_{sn}]/2$) remains close to that derived from 24 hourly ISCCP values (Fig. 1c), but the daily temperature range (T_{sd}-T_{sn}; Fig. 1d) has a significant error for high values of DTR, driven by the high (T_{max}-T_{sd}) difference.

ISCCP data have been used as a training data set to derive relationships between daytime and nighttime PATMOS temperatures and DTR. A correlation analysis was performed between DTR and various potential predictors that were expected to characterize insolation and surface thermal inertia as well as atmospheric conditions. As expected, the PATMOS day-night skin temperature difference, (T_{sd}-T_{sn}) had highest correlation (0.86), followed by OLR (0.73), OLR_0 (0.70), $T5_d$ (0.69), $T4_d$ (0.65), f_c (-0.65), T_{sd} (0.55), NDVI (-0.53), PREC (-0.49) and ASR(0.39). Note that some of these variables are strongly inter-correlated (e.g. temperatures with longwave fluxes).

Using the above suite of predictors, multivariate regression analysis was performed. Before deriving the regression formulae, the predictors were standardized. This procedure allows the coefficients represent the relative weight of the particular predictor in the formula. The best fit was found by the following formula, where * denotes a standardized variable:

$$DTR=18.4 + 17.2xT4_d^* - 12.3xT4_n^* + 3.4xASR^* - 3.4xNDVI^* - 1.3x\,f_c^* - 0.9xPREC^* \quad (1)$$

In a global sense, this formula provides a good estimate of DTR (Fig.2). Some of scatter of the data is due to residual cloud effects inherent in both the ISCCP and PATMOS clear sky products.

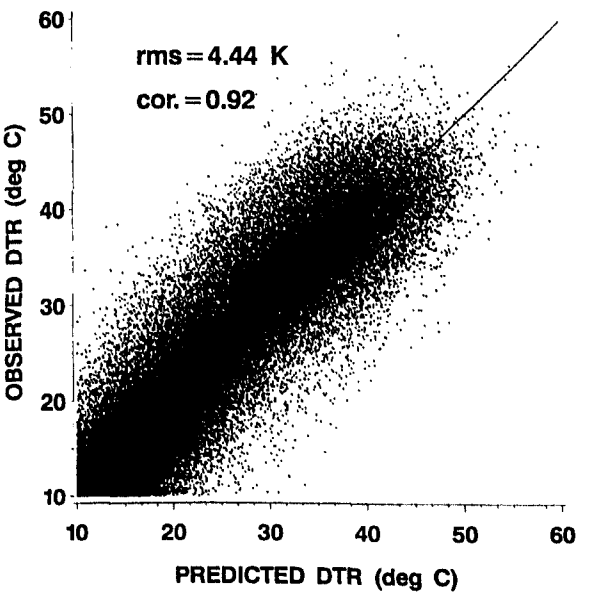

Fig. 2 Observed vs. predicted monthly mean DTR values over the 1984 -1993 period.

4. RESULTS

Eq. (1) was used to derive a monthly global data set of DTR for the 1981-2000 period, including the area of ISCCP data gap over Asia and the time period that is currently not covered by ISCCP D-2 data. A monthly

climatology of DTR was also derived for the 1984-1993 period, where ISCCP data were preferred whenever available, and the data gaps were filled with the regression estimates.

The multi-year monthly DTR climatology was compared to surface temperature measurements over Russia. The advantage of this data set is that it covers areas both outside and inside the Asian data gap in ISCCP, providing an opportunity to evaluate the accuracy of the regression model to estimate DTR. Fig. 3 shows a comparison of ISCCP-derived DTR outside the data gap. These plots confirm earlier findings (Ignatov and Gutman, 1998) that satellite-derived DTR best approximates the surface DTR derived from skin temperatures at all-sky conditions.

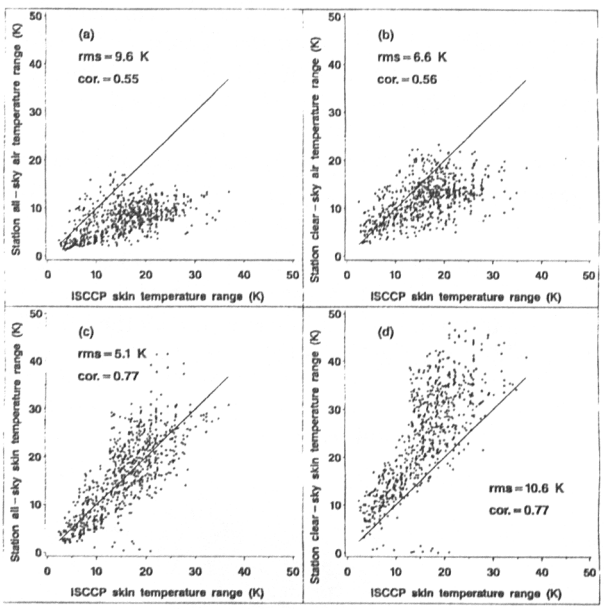

Fig. 3 Comparison of DTR with station temperature measurements in Asia, outside the Asian data gap in ISCCP.

Fig 4 shows DTR estimates inside the Asian data gap, i.e. over the area from where data were not used to derive Eq.1, thus representing a fully independent data sample. The regression-derived DTR estimates are in a good agreement with all-sky surface DTR. From this result we conclude that wherever ISCCP-derived DTR is not available, the regression estimates can be used for the further analysis of spatial patterns of DTR, at least in the case of climatological means.

Fig. 5 shows global maps of monthly DTR climatology. Apart from a few missing data points, there are no discontinuities in Asia between regression estimates of DTR and those directly derived from ISCCP. In general, arid areas exhibit the highest DTR values, with little annual cycle. In the mid-latitudes, variability is higher. DTR values are higher in the warm season. The maximum of DTR tends to occur during the spring after snow-melt but before the onset of intense evapotranspiration by vegetation.

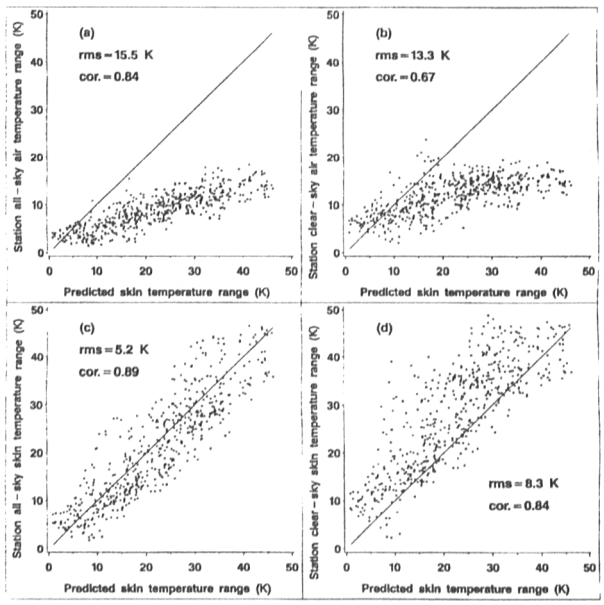

Fig. 4 Comparison of predicted temperature range with station measurements in Asia within the Asian data gap in ISCCP.

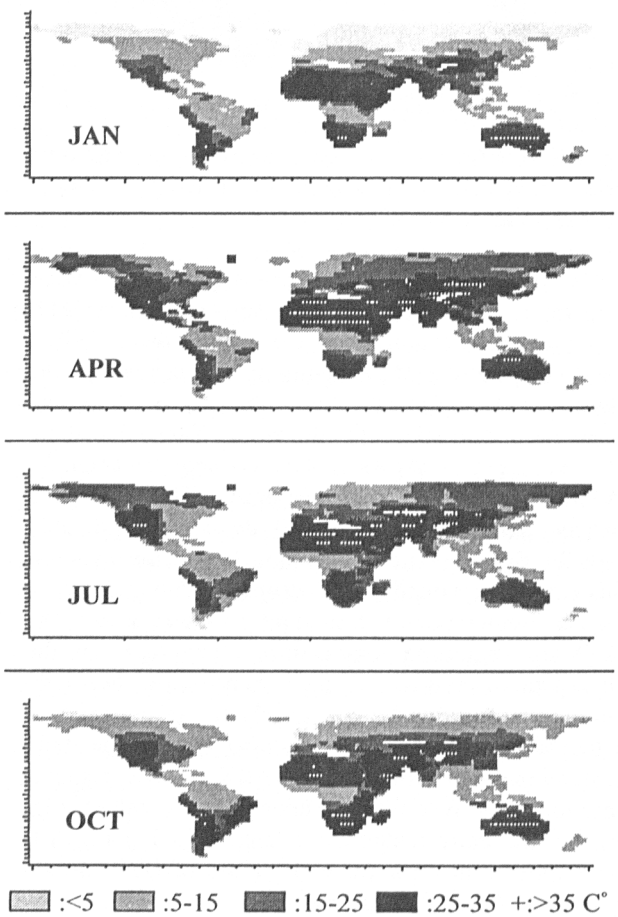

Fig. 5 Global maps of 10-year monthly mean DTR.

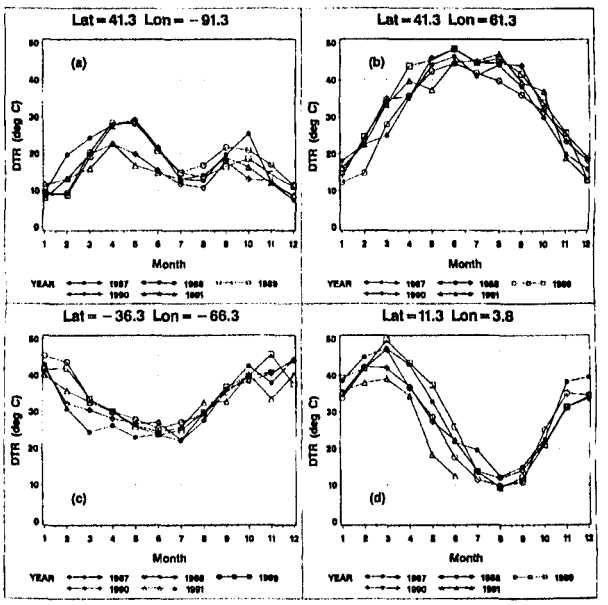

Fig. 6 Examples of the annual cycles and inter-annual variability of DTR

The annual course of DTR is shown for five separate years over four target areas in Fig. 6.In the agricultural areas such as Iowa (Fig. 6a) and Central Argentina (Fig. 6c) there is a distinct maximum in late spring. The Iowa target also shows a secondary maximum in fall after the harvest of crops when insolation is still strong. Note the significant inter-annual variability in spring, suggesting substantial differences in surface conditions.

The target in Central Asia (Fig, 6b) is within the Asian gap of ISCCP, and thus the annual curves shown are entirely from the regression estimates. The curves exhibit an annual cycle that is expected in that region. Most inter-annual differences occur during the spring green-up period. However, the inter-annual signal from these regression estimates should be analyzed with caution.

DTR in the Sahel target area follows (in anti-phase) the annual precipitation cycle. Large inter-annual differences occur in the dry season, whereas the wet season shows small variability.

5. CONCLUSIONS

Current and satellite-based climatological data sets allow the global, long-term study of DTR. Results confirm on a global scale the mid-latitude occurrence of a DTR maximum, but also a significant inter-annual variability, during the period between snow retreat and springtime green-up. Other climatic regions also show significant inter-annual signals, which need to be further analyzed.

Further research is needed to assess the capabilities of statistical estimates of DTR to detect inter-annual signals. Also, potential in the currently available data set can be further explored to achieve the best spatial and temporal coverage and resolution. In addition to DTR, a separate study of daytime and nighttime temperatures can provide further details of the thermal exchange processes at the surface.

The DTR monthly data sets derived will be useful for many other climate- and remote sensing related applications. Among them are validation of DTR produced by numerical climate models, monitoring of DTR in long-term climate change studies, and mapping thermal inertia on a global scale (Sobrino and Kharraz, 1999).

REFERENCES

Groisman, P., et al., 1996: Assessing surface-atmosphere interactions from Russian standard meteorological network data. Part 2: Cloud and snow cover effects. *J. Climate,* **10**, 2154-2183.

Gruber, A. and A.F. Krueger, 1984: The status of the NOAA Outgoing Longwave Radiation data set. *Bull. Amer. Met. Soc.*, **65**, 958-962.

Gutman, G., D. Tarpley, A. Ignatov, and S. Olson, 1995: The enhanced NOAA global land data set from the Advanced Very High Resolution Radiometer. *Bull. Amer. Met. Soc.*, **76**, 1141-1156.

Ignatov, A. and G. Gutman, 1999: Monthly mean diurnal cycles in surface temperatures over land for global climate studies. *J. Climate* **12**, 1900-1910.

Janowiak, J.E. and P.Xie, 1999: CAMS-OPI: A global satellite-raingauge merged product for real-time precipitation monitoring applications. *J. Climate*, **12**, 3335-3342.

Price, J.C., 1977: Thermal inertia mapping: a new view of the Earth. *J. Geophys. Res.* **18**, 2582-2590.

Rossow, W.B., A.W. Walker, D.E. Beuschel and M.D. Roiter, 1996: International Satellite Cloud Climatology Project (ISCCP). Documentation of new cloud data sets. World Meteorological Organization, World Climate Research Programme.

Sobrino, J.A.and M.H. Kharraz, 1999: Combining agternoon and morning NOAA satellites for thermal inertia estimation. 2. Methodology and application. *J. Geophys. Res.* **104**, 9455-9465.

Stowe, L.L., H. Jacobowitz, G. Ohring, K. Knapp and N.R. Nalli, 2001: The Advanced Very High Resolution Radiometer Pathfinder Atmosphere (PATMOS) Data Set. Submitted to Bull. Amer. Meteorol.Soc.

3.1 Weather Prediction Improvement Using Advanced Satellite Technology

L. Uccellini[†], F. Einaudi[*], J. Purdom[**], D. Rogers[††], R. Gelaro[*], J. Dodge[#], R. Atlas[*] and S. Lord[†]
* NASA/Data Assimilation Office, Goddard Space Flight Center, Greenbelt, MD USA
†NOAA/NWS/National Centers for Environmental Prediction, Camp Springs, MD USA
#NASA Headquarters, Washington D. C. USA
**NOAA/National Environmental Satellite Data and Information Service, Camp Springs, MD USA
††NOAA/Office of Oceanic and Atmospheric Research, Silver Spring, MD USA

I. INTRODUCTION

We discuss in this paper some of the problems that exist today in the full utilization of satellite data to improve weather forecasts and we propose specific recommendations to solve them. This discussion can be viewed as an aspect of the general debate on how best to organize the transition from research to operational satellites and how to evaluate the impact of a research instrument on numerical weather predictions. A method for providing this transition is offered by the National Polar-Orbiting Operational Environmental Satellite System (NPOESS) Preparatory Project (NPP). This mission will bridge the time between the present NOAA and Department of Defense (DOD) polar orbiting missions and the initiation of the converged NPOESS series and will evaluate some of the Earth Observing System (EOS) instruments as appropriate for operational missions. Thus, this mission can be viewed as an effort to meet the operational requirements of NOAA and DOD and the research requirements of NASA.

More generally, however, it can be said that the process of going from the conception of new, more advanced instruments to their operational implementation and full utilization by the weather forecast communities is not optimal. Instruments developed for research purposes may have insufficient funding to explore their potential operational capabilities. Furthermore, instrument development programs designed for operational satellites typically have insufficient funding for assimilation algorithms needed to transform the satellite observations into data that can be used by sophisticated global weather forecast models. As a result, years often go by before satellite data are efficiently used for operational forecasts.

NASA and NOAA each have unique expertise in the design of satellite instruments, their use for basic and applied research and their utilization in weather and climate research. At a time of limited resources, the two agencies must combine their efforts to work toward common goals of full utilization of satellite data. This is a challenge that requires the assimilation of myriad new data into increasingly sophisticated numerical forecast models that run on increasingly sophisticated computer systems.

In section II, we briefly outline the impact of satellite data on the quality of the National Centers for Environmental Prediction (NCEP) forecasts. In section III, we describe the present status of the utilization of satellite data in NCEP models and the challenges that lie ahead. In section IV, we propose solutions whose goals are summarized in section V.

II. STATUS OF SATELLITE DATA IN NCEP MODELS

Much progress has been made in the utilization of satellite data since the first meteorological satellite was launched in April 1960. This progress is related to improvement in the satellite instrumentation, continued increase in the computational power and related improvements in the numerical models and data assimilation techniques. During the 1960's and 1970's, a rapid advancement in satellite instruments preceded the computing capacity and sophisticated assimilation algorithms required to use these data effectively. Since that time, horizontal resolution of the models has increased from 381 km in 1960 to 55 km today. The vertical resolution has also increased markedly from 1 layer in 1960 to 42 layers today. The computer power, measured in floating point operations per second (flops), has increased from 20 Kflops in 1960 to over 30 Gflops today. During this period, the 36-hr mean sea level pressure forecasts over North America went from having no skill in 1960 (i.e., being no more useful than a forecast based on climatology), to being skillful 72% of the time in 1995 with the direct inclusion of TOVS radiances (starting in 1995) in concert with the use of more sophisticated models on more powerful computers.

A measure of the impact of satellite data on improving

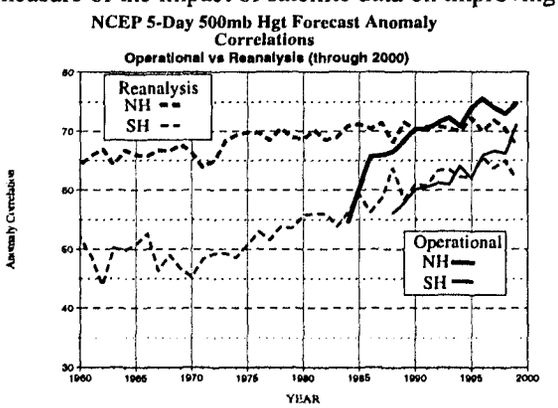

Fig. 1. Anomaly correlation coefficient (ACC) for 500mb height for the NCEP 5-day forecast as a function of time. Dashed (solid) lines refer to fixed (evolving) model and assimilation system. Bold (thin) lines refer to the Northern (Southern) Hemispehre.

operational numerical weather forecasts is given in Fig. 1, which shows the anomaly correlation coefficient (ACC) for 500mb height calculated for the NCEP 5-day forecast as a function of time. The correlation is between the observed and predicted deviations from the climatological 500mb height field. The dashed lines show the ACC calculated while reprocessing all the data with the model and data assimilation system kept fixed at the 1995 configuration. Results are shown for the Northern (bold) and Southern (thin) Hemispheres. Neglecting interannual variability, a steady improvement in the ACC is evident, with a larger rate of improvement for the Southern Hemisphere. The improvement must be due to new data, with the majority of new data coming from polar satellites. The larger rate of improvement for the Southern Hemisphere provides further evidence of the importance of satellite data, given the relative paucity of in-situ data there.

The solid lines in Fig. 1 show the ACC when the data are processed with an evolving operational system. The noticeably large improvements in 1996 and 1999 are due, in large part, to the introduction of direct assimilation of the radiances and inclusion of Advanced Microwave Sounding Unit (AMSU) data, respectively.

In addition to operational satellites, research instruments have also demonstrated positive impact in weather forecast models. An example of a research instrument that has shown tremendous potential operational impact is the scatterometer, which measures wind speed and direction over the global oceans. First flown on ERS-1 in 1991, this instrument presently flies on Quikscat, launched in 1999. The impact of Quikscat data was tested for several numerical forecasts of hurricanes over the Atlantic Ocean. For Hurricane Cindy in August 1999, the inclusion of Quickscat data reduced intensity errors by nearly 50%, and displacement errors by up to 80%, over a 72-hr forecast (Fig. 2). Improvements of this order are critical to reducing the uncertainty in hurricane track and intensity forecasts needed to allow emergency managers to make informed decisions.

III. THE NATURE OF THE PROBLEM

The transition from research and development (R&D) to operations is a complex topic that has been discussed in a number of reports. Reference [1] discusses this issue vividly and refers to the term "Crossing the Valley of Death" as being used in industry to describe a fundamental challenge for R&D programs. Moreover, [1] states that "For technology investments, the transitions from development to implementation are frequently difficult, and, if done improperly, these transitions often result in "skeletons in Death Valley." Successful transitions from R&D to operational implementation always require: (1) an understanding of the importance (and risks) of the transition, (2) development and maintenance of appropriate transition plans, (3) adequate resource provision, and (4) continuous

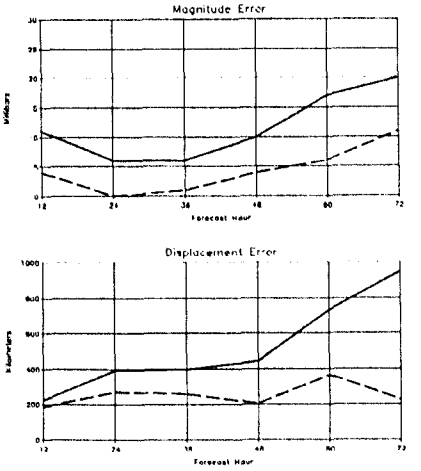

Fig. 2. Forecast errors in terms of (a) intensity and (b) position for Hurricane Cindy with (dashed) and without (solid) assimilation of Quickscat data. Units are mb in (a) and km in (b).

feedback (in both directions) between R&D and operational activities. In the case of atmospheric and climate sciences, inadequacies in transition planning and resource commitment can seriously inhibit the implementation of good research leading to useful societal benefits."

The situation is particularly serious for satellite data utilization. Although satellite data account for greater than 80% of the data assimilated in the NCEP models today, these data only correspond to roughly 14% of the available satellite data from operational lower-Earth orbiting systems. Most data are thinned upon receipt to minimize cross-correlation errors during ingestion. Furthermore, radiance data collected over land cannot be used directly because of the difficulties in modeling the varying emissivity and associated surface characteristics. The problem is compounded by the five-order magnitude increase in satellite data expected in the next ten years. Fig. 3 shows the number of individual daily upper air observations used by the NCEP operational models as a function of time, and an estimate of the data volume by 2010. Correspondingly, Fig. 4 shows a partial list of the new operational satellite instruments planned for launch over the next ten years that account for the five-order magnitude increase in available data. We are thus faced with a situation where current satellite data are under utilized operationally, and a new, more voluminous set of data will be available within ten years.

The present situation is the consequence of many factors:

- Insufficient funding for the operational assessment of instruments developed for research purposes.
- Insufficient funding for assimilation algorithms for instruments developed for operational satellites.
- Tendency of the operational community to be restrictive in the use of data from research satellites that may not be sustained as operational systems.
- Tendency of the operational community to be slow in the assessment and incorporation of new data.

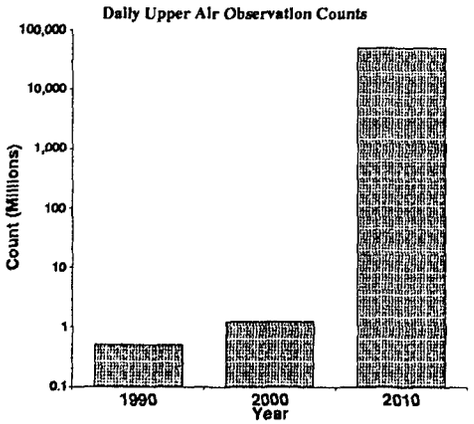

Fig. 3. Current and expected number (in millions) of daily upper air observations used by NCEP models as a function of time.

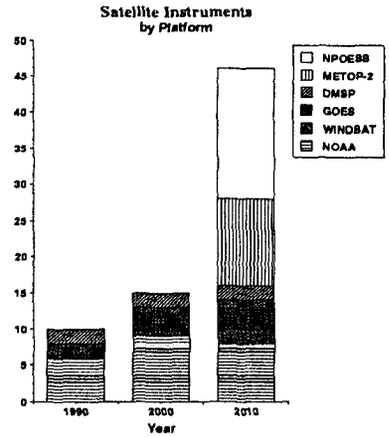

Fig. 4. Partial list of current and expected operational satellite instruments as a function of time.

- Underutilization of the full breadth of the weather research community in support of operational problems.

As a result, there often is a gap of many years before data are fully used operationally, as in the case of the radiance data from the GOES sounder. The situation has improved recently with the example of AMSU data being used by NCEP within 10 months of launch. However, we can and must do better to capitalize fully on the investment the U.S. makes on its satellite observing network.

To address these problems, NASA and NOAA scientists and managers should be involved in an end-to-end process, from defining an instrument, to characterizing that instrument's in flight performance, to developing algorithms and forward models for data assimilation, to integrating the data into NOAA operational products, to assessing its impact on the forecast.

To cover the entire process, the two agencies must work together and share costs for the *full spectrum* of these activities. Presently, this comprehensive approach is not taking place and areas of interaction involve only selected portions of the end-to-end process defined above. This need for comprehensive collaboration is the fundamental issue that the two agencies must address. Moreover, this collaboration is consistent with the strategic plans and vision statements of both agencies and should facilitate major advances in the analysis and prediction of weather, climate and hydrology. Accordingly, each agency would have its own role:

- NASA would apply scientific and technological capabilities that support NOAA's goals and operational forecast responsibilities.
- NOAA would apply operational model infrastructure and applied research capabilities that support NASA's research and technology-advancement objectives.

IV. SPECIFIC RECOMMENDATIONS

To achieve the goal of fully utilizing satellite data for both research and operations, we propose a collaborative effort where NASA and NOAA direct necessary resources to accomplish the following.

1. Support the goals of the U.S. Weather Research Program (USWRP) to:

a. increase understanding and prediction of Hurricanes at Landfall (HAL);
b. improve Quantitative Precipitation Forecasts (QPF);
c. extend accurate weather forecasts to 7 days and beyond.

2. Establish a NASA-NOAA Joint Center for Satellite Data Assimilation (JCSDA) to:

a. accelerate the use of data from advanced satellite sensors being launched into space by NOAA, NASA, DOD and international agencies;
b. develop and maintain a common model and data assimilation infrastructure for optimal use of satellite observations for research and operational applications;
c. develop and maintain a fast forward radiative transfer model for use of satellite microwave and infrared sounding data in data assimilation and product generation;
d. assess the use of satellite data within the common model and data assimilation infrastructure.

3. Develop an end-to-end process for the operational utilization of polar and geostationary observations.

This collaborative approach represents a commitment of NASA and NOAA to focus on research and operational issues related to improving the forecast of high impact weather events and extending accurate weather forecasts to seven days and beyond. Furthermore, these actions will accelerate the use of existing and new satellite data by the research and operational communities.

The USWRP addresses key issues related to the highest priority goals of the weather prediction component of the National Weather Service (NWS) strategic plan. NASA is interested in many components of the USWRP for several reasons: (1) NASA's Earth Sciences Enterprise program has

scientific and technological components relevant to forecasting extreme weather events and extending accurate weather forecasts to seven days and beyond, (2) USWRP provides an opportunity to integrate research data sets from instrumented aircraft within multi-agency field programs, (3) USWRP provides an excellent opportunity to assess the utility of various satellite observing systems in forecast models and (4) USWRP makes significant strides in establishing the credibility of global/climate models for predicting short range weather systems and thus assuring a physical consistency of these models. These consistencies will ease the transfer of physical parameterization schemes between global and mesoscale models.

The NASA-NOAA JCSDA would be a virtual center which will engage the Goddard Data Assimilation Office (DAO), the NESDIS Office of Research and Applications (ORA), the Office of Oceanic and Atmospheric Research (OAR) Forecast Systems Laboratory (FSL) and Environmental Technology Laboratory (ETL), and the NCEP Environmental Modeling Center (EMC) in a determined effort to ingest and use the large volume of data associated with planned satellite missions over the next 10 years. The advanced instruments from planned NASA and NOAA missions will provide data on atmospheric, oceanic and land surface conditions with accuracies and spatial resolutions never before achieved. Without the establishment of a NASA-NOAA JCSDA that focuses on satellite data assimilation, the nation's ability to utilize fully current and planned satellite observing systems will fall further behind over the next five to ten years as new generations of sensors are flown by NOAA, NASA, DOD and international agencies. Advances that might be realized from EOS, New Millennium Program (NMP), NPOESS NPP and NPOESS itself will not be realized by the NWS until well into the lifetimes of those programs, if ever. The establishment of a NASA-NOAA JCSDA must be recognized as a NASA and NOAA imperative to ensure that the nation realizes the maximum benefit from its investment in space as part of an advanced global observing system.

The JCSDA should be started from existing scientific interactions between NASA/DAO and NOAA/NCEP. These interactions have already produced a 13-point plan focused on testing existing and new satellite observations within the operational modeling framework, including data from AMSU, Quikscat, Tropical Rainfall Measurement Mission (TRMM), and GOES.

The JCSDA will have minimal bureaucratic infrastructure and will make a determined effort to engage the community at large. It is hoped that the National Science Foundation will support students and post-doctoral fellows who would perform their work at the Center.

V. GOALS AND EXPECTED DELIVERABLES

JCSDA activities will be divided into infrastructure activities and proposal-driven scientific projects. Initially, infrastructure activity will focus on the development and maintenance of a scientific backbone for the JCSDA composed of a community-based fast radiative transfer model, a community-based emissivity model and an infrastructure for performing assimilation experiments with real and simulated observations from new and future instruments. Proposal-driven scientific projects will be the primary mechanism used to accelerate the transition of research and technological advances in satellite data assimilation by incorporating new codes into NASA and NOAA operational data assimilation systems and by performing preliminary testing with these systems. Initial JCSDA projects will serve to solidify existing collaborations on AIRS, QuikSCAT, TRMM, and the NPOESS preparatory missions. Furthermore the JCSDA will facilitate new collaborations in areas deemed potentially important for improving climate and weather prediction, such as in the utilization of GIFTS, VIIRS and GPS radio-occultation data.

A primary goal of the JCSDA in the time frame 2001-2003 will be to lay the groundwork for establishing a common data assimilation infrastructure for assessing new satellite data and optimizing the utilization of these data in operational models. The first step is to establish, and make accessible to the community at large, parallel versions of the NCEP/EMC and NASA/DAO global data assimilation systems on JCSDA computer systems. This will include establishment of real-time communications to JCSDA computers and real-time data bases and observation handling algorithms for continued assessment of new instruments.

JCSDA deliverables by 2005 will include the development of a community-based forecast and data assimilation system for both global and regional scale applications. The system will be linked to the research community through the USWRP and will serve as the primary mechanism for infusing research and operational satellite data into NCEP operations.

The JCSDA thus provides 1) a bridge for NASA and NOAA to act on new satellite observing systems, 2) a basis for the evaluating experimental and operational satellite data in numerical prediction models, and 3) a way forward for achieving both agencies' vision of improving climate and weather prediction using advanced satellite technology.

ACKNOWLEDGMENT

The authors are grateful to R. Kistler and J. Terry for their efforts in preparing the figures for this paper and A. Stansbury for the manuscript preparation.

REFERENCES

[1] National Research Council, Board on Atmospheric Sciences and Climate, 2000: *From Research to Operations in Weather Satellites and Numerical Weather Prediction: Crossing the Valley of Death*. National Academy Press, 80 pp.

3.2 USES OF SATELLITE DATA IN AIR FORCE WEATHER

John V. Zapotocny*
Headquarters Air Force Weather Agency, Offutt AFB, Nebraska

1. INTRODUCTION

Environmental satellite data comprise a vital element of Air Force Weather (AFW) support to U.S. Department of Defense (DoD) and allied military operations. This paper provides an overview of the satellite data types, ingest and processing systems and operational methods used to generate products from satellite data for AFW customers worldwide. Operational applications using satellite data at AFW's strategic data processing centers, at regional weather squadrons, and by weather teams in the field will be discussed.

2. THE NEW AFW ORGANIZATION

The AFW Strategic Plan, approved by the Chief of Staff of the Air Force in August 1997, charted a course which systematically re-engineers AFW's products, processes, organizations, training, and technical tools consistent with the Aerospace Expeditionary Force concept and changes in the broader DoD mission. The end-state AFW structure is based upon a three-tiered concept replacing the legacy decentralized forecast structure at individual bases with a centralized regional forecasting structure. Realignment of weather functions has occurred at all levels (tactical, theater, and strategic).

The resulting operational AFW organization (Fig. 1) consists of Strategic Centers, Operational Weather Squadrons (OWS) and Combat Weather Teams (CWT). Three Strategic Centers accomplish data ingest, processing, and product distribution supporting national programs and global missions. Nine OWSs are aligned with numbered Air Forces and Air Force Major Commands to provide theater-scale forecasting and resource protection functions, and 162+ CWTs support Air Force and Army operators directly by tailoring OWS generated forecasts to meet specific mission needs. Satellite data are heavily employed at all levels in this "forecasting funnel." The following sections highlight some typical applications of satellite data across the spectrum of AFW operations.

3. STRATEGIC CENTER APPLICATIONS

AFW has three Strategic Centers; the primary data processing center is at Headquarters Air Force Weather Agency (AFWA), Offutt AFB, Nebraska; the Air Force Combat Climatology Center (AFCCC) in Asheville, North Carolina; and the Joint Typhoon Warning Center (JTWC) at Pearl Harbor, Hawaii.

* Corresponding author address: John V. Zapotocny, Headquarters Air Force Weather Agency, 106 Peacekeeper Drive, Offutt AFB, NE 68113-4039

AFWA and JTWC use satellite data as a primary data source for their strategic missions. Both of these centers ingest geosynchronous (GEO) satellite data directly and by retransmission from NESDIS or domestic communication satellite (DOMSAT) relay. AFWA is the primary DoD ingest site for Defense Meteorological Satellite Program (DMSP) data. These data are down linked from recorders on the DMSP satellites to Air Force Satellite Control Network ground stations. The data are relayed to AFWA via DOMSAT. AFWA also ingests National Oceanic and Atmospheric Administration (NOAA) polar orbiting environmental satellite (POES) data through DOMSAT relay. Satellite data paths into AFWA are shown in Fig. 2. JTWC has the ability to ingest DMSP and POES data in real-time using the Small Tactical Terminal (STT) and Mark IV field systems.

Although the AFCCC does not use satellite data directly in its operations, they do incorporate satellite soundings and derived analyses of global clouds and soil moisture into their comprehensive global climatological databases. These derived products are created at AFWA and transmitted to AFCCC.

3.1 Data Ingest, Processing and Distribution

AFWA is able to ingest six GEO and eight combined DMSP and POES data streams through its Satellite Data Handling System (SDHS) ingest subsystem. Fig. 3 shows ingest and processing data flows and operational applications that use satellite data at AFWA. During ingest, calibration and earth-curvature correction algorithms are applied as required and the satellite data are stored in the AFWA satellite databases as images and in "simple" format. Data are available to users from the satellite database via manual or automated retrievals within just a few minutes of ingest.

The Weather Product Management and Distribution System (WPMDS) at AFWA transmits Defense Meteorological Satellite Program (DMSP) data to the Fleet Numerical Meteorological and Oceanographic Center (FNMOC) and to the National Environmental Satellite Data and Information Service (NESDIS) for satellite sounding generation via high speed ATM connections. DMSP data are also provided to the National Geophysical Data Center (NGDC) for long-term archiving. AFWA ingests various research data streams in pseudo real-time via the WPMDS, including TRMM, QuickSCAT, and MODIS. These data flows are shown in the lower-left corner of Fig. 3.

Generation of automated products from satellite data consumes a major portion of AFWA's computing resources. Product lines include worldwide and target-scale cloud analyses and forecasts, user-tailored enhancement and animation of imagery, space weather analyses and forecasts, tropical cyclone intensity

estimates, troposphere wind estimates derived from GEO imagery feature tracking, and analyses and forecasts of volcanic ash plumes. Numerous environmental data records (EDRs) are also automatically generated using data from the DMSP Special Sensor Microwave/Imager (SSM/I). These include soil moisture, snow depth, surface temperatures, vertical temperature and moisture profiles, sea-surface wind speeds, and many more. The myriad AFWA processing applications and user outputs is shown on the right side of Fig 3.

3.2 *Human Interactive Analysis*

AFW Meteorologists rely heavily upon human interactive analysis of satellite imagery in their production processes. Such hands-on analysis is especially important to the tropical storm analysis, and forecasting functions at AFWA and JTWC, and AFWA's severe weather forecasting and cloud analysis bogus functions. Human interactive analysis at AFWA and JTWC is done primarily on Satellite Imagery Display and Analysis System (SIDAS). JTWC also uses the STT and Mark IV systems.

A screen shot of the SIDAS interface is shown in Fig. 4. The SIDAS can utilize any of the satellite data available in the AFWA satellite databases plus data from other satellites such as TRMM and QuickSCAT (McCrone, 2001). The SIDAS includes robust tools for image display, enhancement, animation, multi-channel mosaics, tropical cyclone intensity estimation, as well as plotting of observations and model output over satellite images, and plotting derived profiles. Holliday and Conner (2001) provide an in-depth description of existing SIDAS capabilities and planned enhancements.

3.3 *Modeling Applications*

Many operational modeling applications at AFWA use satellite data as primary inputs; most notably, the global cloud analyses and forecasts. Currently these are produced by the legacy Cloud Depiction and Forecasting System (CDFS) running on a Unisys mainframe. CDFS produces gridded cloud analyses at 25 n mi horizontal resolution with five vertical cloud layers. Input data to the legacy CDFS come only from DMSP and POES, which can introduce significant latency problems into the resultant analysis over portions of the globe. Cloud forecasts are done using an advective cloud model (ADVCLD) that produces forecasts out to 48 hours (McDonald, et. al., 2001).

By the end of 2001 a major upgrade to the CDFS, known simply as CDFS II, becomes operational. It will provide hourly global cloud analyses at 12 n mi horizontal resolution incorporating data from all GEO and POES in the AFWA satellite databases. Fig. 5 provides a functional view of the CDFS II. Through a series of complex processing steps incorporating advanced cloud analysis algorithms (Gustafson and Pesuzza, 2001), cloud gridded data records (GDRs) are produced for each class of satellite (DMSP, POES, GEO) and combined into an hourly worldwide merged cloud analysis. This product is manual quality controlled via the human interactive analysis tools described earlier Output products from CDFS II will support national programs, as well as mission planning and execution across the spectrum of military operations.

In the late 1990s AFWA developed a proof-of-concept target-scale cloud analysis and forecasting prototype to satisfy combat mission needs during operation "Allied Force" in Serbia. This system uses 3 n mi resolution DMSP "fine" imagery data as input to the CDFS II cloud analysis algorithms. The resultant high-resolution gridded cloud analysis is input to the ADVCLD model along with wind forecasts from AFWA's MM5 fine-scale model to generate target-scale cloud forecasts out to 30 hours (Fig. 6).

Satellite data provide critical input to several other AFWA analysis and forecast models. Derived soundings are assimilated into the MM5 fine-scale forecasting system using a multi-variant optimal interpolation scheme (Ritz, et. al., 2001). Special Sensor Microwave/Imager (SSM/I) data and worldwide GEO imagery are used in the Land Surface Model to specify precipitation rates, soil moisture content, vegetation conditions as well as snow depth and snow water content. Specially enhanced GEO, DMSP, and POES infrared imagery are used to establish initial plume conditions for driving the ash dispersion model "PUFF". Finally, data from the various DMSP and GEO space environment sensors feed AFW's space weather analysis and forecasting models.

3.4 Shared Data Processing

AFWA partners with other national processing centers through the Shared Processing Program (SPP) to help distribute its tremendous data processing volume. The SPP is comprised of AFWA, NESDIS, the National Centers for Environmental Prediction (NCEP), the Naval Oceanographic Office (NAVO), and FNMOC and is overseen by the Office of the Federal Coordinator for Meteorology. The SPP concept allows each center to focus effort, fiscal and computing resources toward generation of products for which it is identified as the lead center.

AFWA is the lead center for visible and infrared imagery, global cloud analysis, and land surface modeling. Under the SPP, AFWA provides DMSP data to NESDIS and FNMOC, and global cloud analyses along with land surface model output to NCEP. AFWA receives derived satellite soundings from NESDIS; satellite sea surface temperature analyses from NAVOCEANO; global model forecasts from FNMOC, and all NCEP global and regional forecast model data.

4. FIELD APPLICATIONS

AFW's nine OWSs provide theater level weather support. Fig. 7 shows where OWSs are located in the world and their parent Numbered Air Force or Major Command. The four continental U.S. (CONUS) OWSs also provide forecasts and resource protection warnings for their CONUS AORs. Specialized OWS-like forecasting centers are located at Vandenberg AFB, CA and Patrick AFB, FL to provide space launch support.

There are 162+ CWTs distributed worldwide providing tailored support to DoD at the tactical level. At the OWS and CWT primary operational applications of satellite data involves human interactive analysis similar to what is done at AFWA and JTWC. There is some limited automated production of satellite imagery visualizations for dissemination via web pages. Products generated by AFWA from satellite data (cloud analyses/forecasts, soundings, LSM output, etc.) are applied to theater level forecasting at the OWS and tailored for specific missions by the CWTs.

The human interactive analysis done at OWSs is accomplished on the OWS Production System (OPS). The OPS is based on a server-client architecture that incorporates the LEADS as it's primary forecaster interface. Fig. 8 depicts a typical OPS configuration. Data inputs/outputs to/from the OPS occur via the unclassified military Internet (NIPRNET) and classified counterpart (SIPRNET), Very Small Aperture Terminal (VSAT) satellite broadcasts, and various dedicated circuits. Satellite data are ingested at OWSs via an STT (Fig. 9) or Mark IV system (Fig. 10), either of which can be networked into the broader OPS system for data sharing and merged product creation.

At CWTs GEO, DMSP and POES satellite data are ingested directly with STTs. STTs are robust, fully deployable systems consisting of multiple fixed and tracking antennae, a primary processing computer and a data processing/display system. Experienced troops can establish a working STT configuration in the field in less than 30 minutes. The VSAT broadcasts from AFWA and OWSs also contain satellite imagery and satellite derived products and model output to support the CWT forecasting and product tailoring mission.

5. LOOKING TO THE FUTURE

AFW's mission will continue demanding real-time access to the ever-increasing suite of satellite data from U.S., foreign and commercial environmental satellites. In the near term, AFW is preparing to operationally integrate data from the new Special Sensor Microwave Imager/Sounder (SSMI/S) when DMSP Flight 16 becomes operational late this year. SSMI/S will provide data needed to generate more and higher quality EDRs for DoD mission support. See Kopp (2001) for an overview of SSMI/S processing at AFWA.

As a member of the tri-agency National Polar Orbiting Environmental Satellite System (NPOESS) program, AFW is actively involved in the ongoing NPOESS acquisition efforts. Incorporation of the NPOESS data into AFWA's production process will increase the amount of satellite data processed and disseminated by roughly three orders of magnitude. When added to other expected increases in GEO and non-traditional meteorological satellite data, AFWA is anticipating a satellite data growth of 10 orders of magnitude by 2010. In preparation for this "data deluge," AFWA has embarked on a major database, processing system, and communications infrastructure modernization and expansion effort known as the Re-engineered Enterprise Infrastructure Program.

On the deployed front, more effective field satellite data processing capability will result from the Joint MetSat Ingest and Support Terminal (JMIST). JMIST will merge and enhance the capabilities of the STT, Mark IV and SIDAS into an AFW standard satellite ingest, processing, and display system for use at all tiers within the AFW enterprise.

6. ACKNOWLEDGEMENTS

The author acknowledges the many contributions from AFWA's technical staff toward this paper and the accompanying presentation. Special thanks go to Mr. Francis Bieker, Dr. Charles Holliday, Capt. Scott Hausman, Dr. Thomas Kopp, Capt. Darryl Leon, Mr. Paul McCrone, Dr. David McDonald, Mr. Michael Moore, Mr. Joe Nolin, and Mr. Richard Ritz for their contributions.

7. REFERENCES

Gustafson, G. B. and D. C. Peduzza, 2001: Validation of a new global operational cloud analysis at AFWA. *11th Conference on Satellite Meteorology and Oceanography*, American Meteorological Society, P3.59.

Holliday, C. R. and M. D. Conner, 2001: The Satellite Imagery Display and Analysis System at Air Force Weather Agency. *11th Conference on Satellite Meteorology and Oceanography*, American Meteorological Society, P3.48.

Kopp, T. J., 2001: Air Force Weather Agency Special Sensor Microwave Imager/Sounder Processing. *11th Conference on Satellite Meteorology and Oceanography*, American Meteorological Society, P5.40.

McCrone, P. J., 2001: Analysis of subtropical cyclones using NASA QuickSCAT data. *11th Conference on Satellite Meteorology and Oceanography*, American Meteorological Society, P3.17.

McDonald, D.G., S. J. Storch and F. D. Bieker, 2001: Improvements to U.S. Air Force cloud forecast model, Advect Cloud (ADVCLD). *11th Conference on Satellite Meteorology and Oceanography*, American Meteorological Society, P3.16.

Ritz, R. L., M. D. McAtee and R. T. Swanson, Jr., 2001: Data assimilation at Air Force Weather Agency. *14th Conference on Numerical Weather Prediction*, American Meteorological Society.

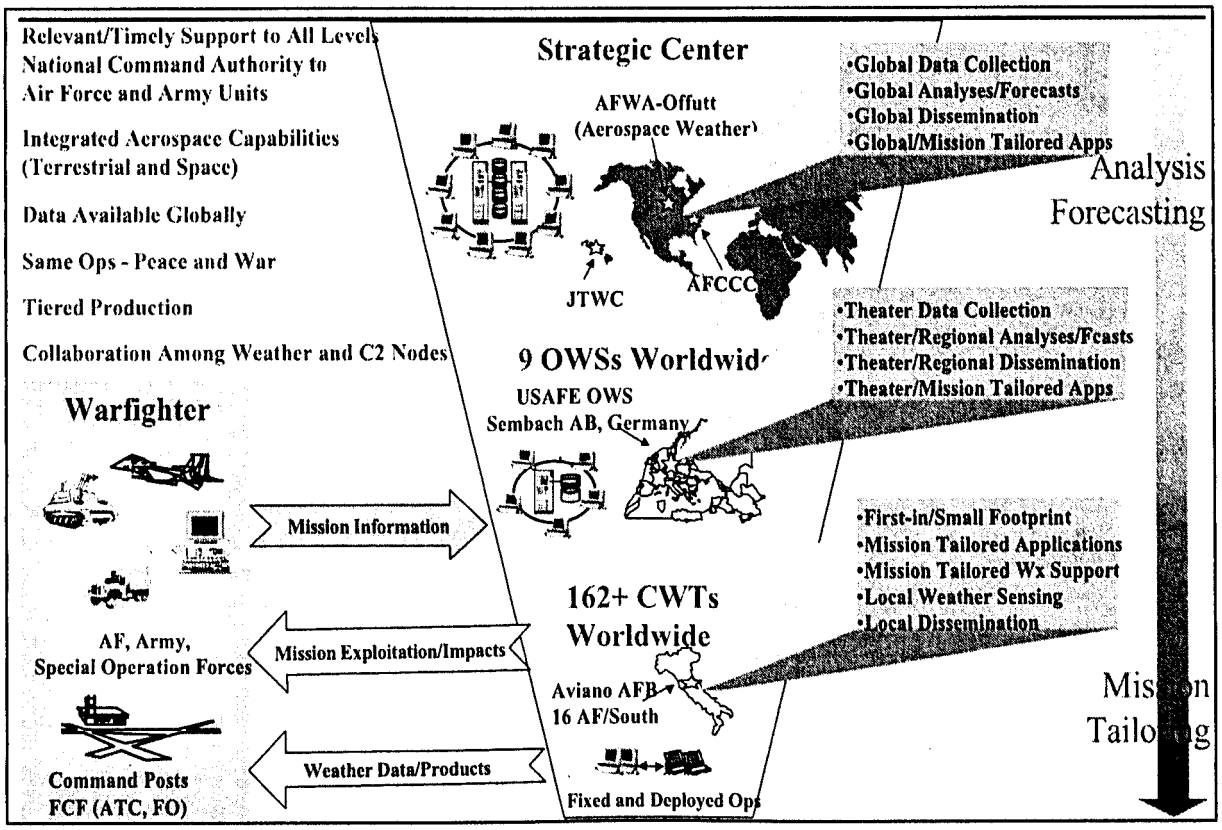

Figure 1. Air Force Weather organizational structure.

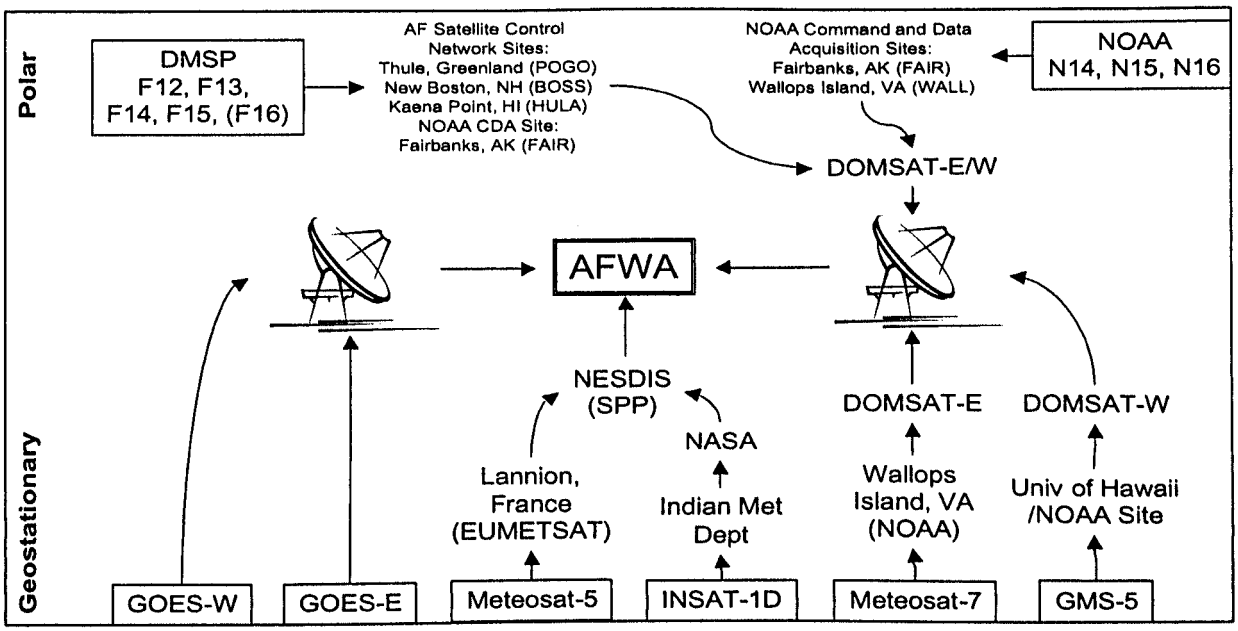

Figure 2. Satellite data ingest at HQ AFWA.

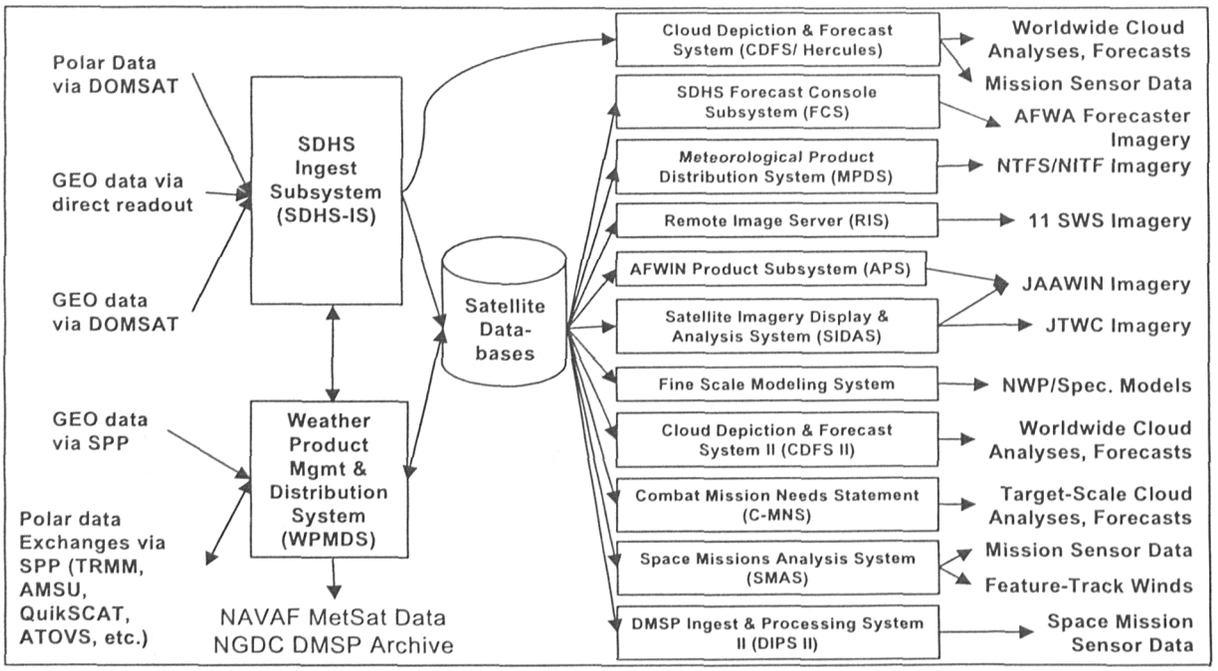

Figure 3. AFWA Strategic Center satellite data flow, processing applications, and product users.

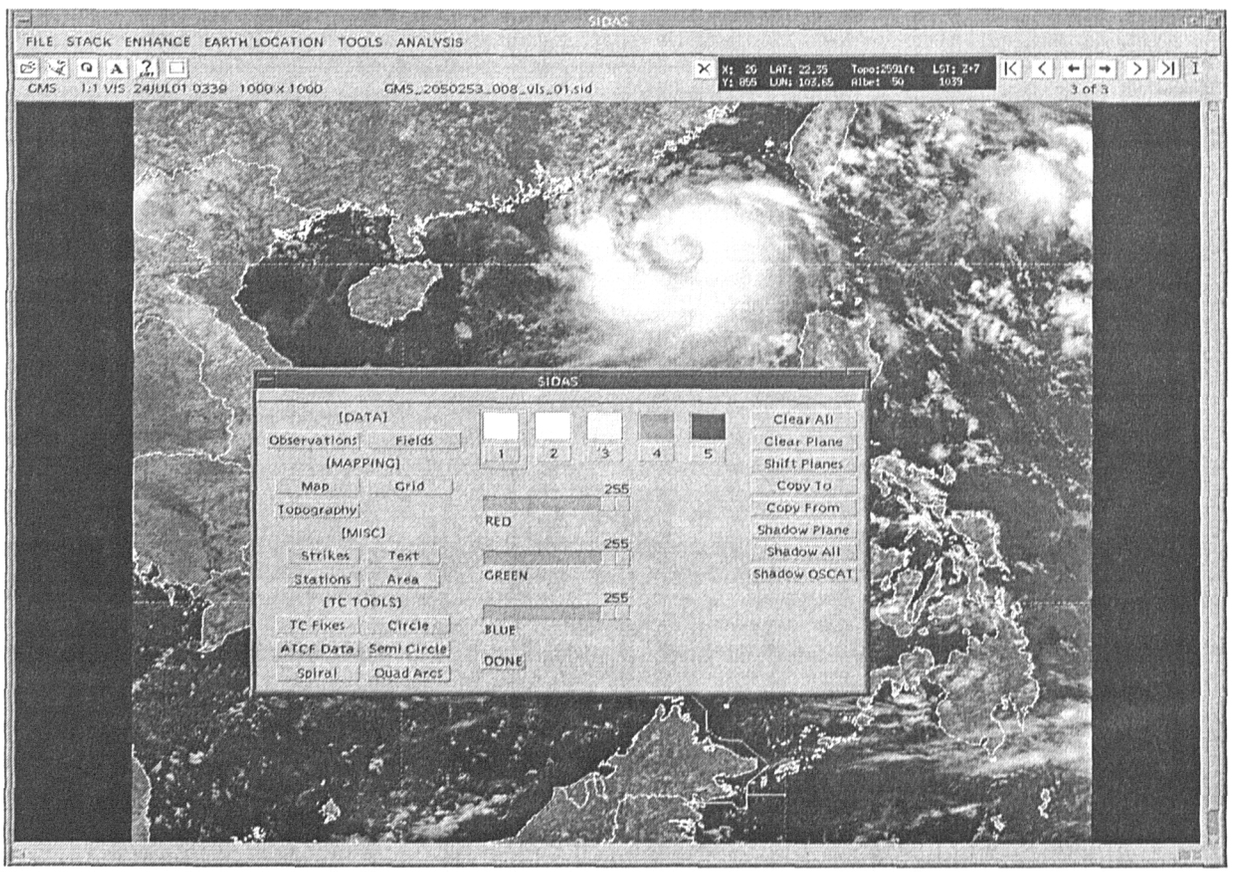

Figure 4. *Screen shot from the Satellite Imagery Display and Analysis System (SIDAS).*

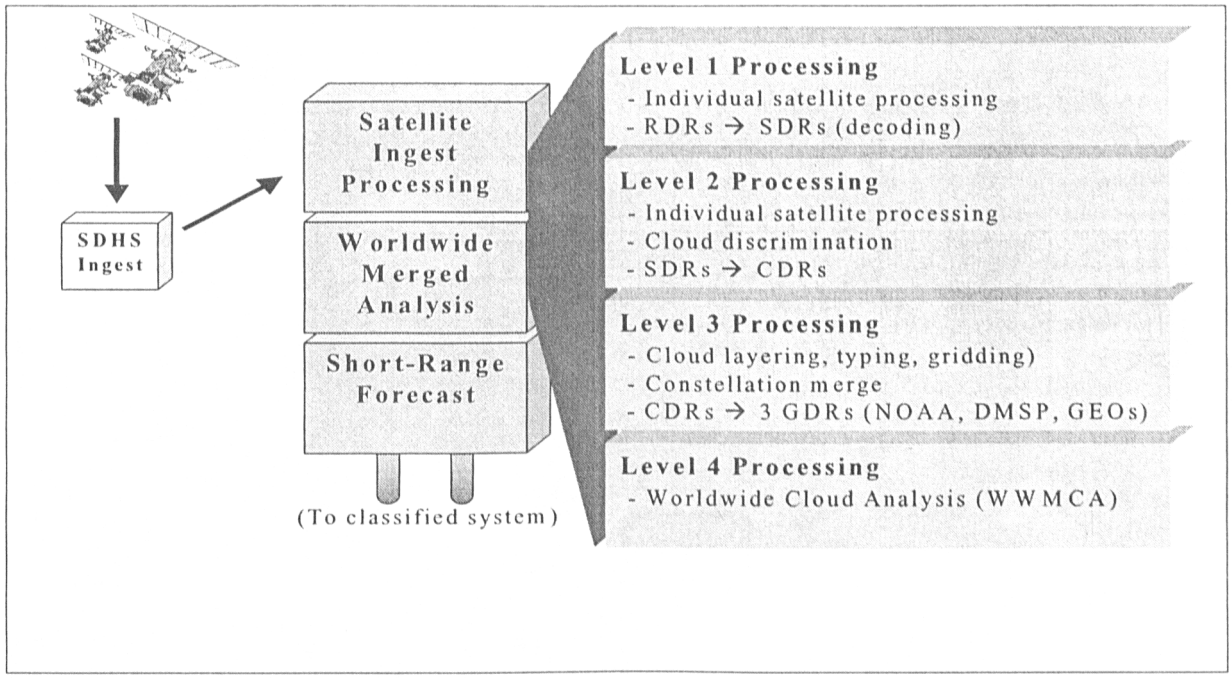

Figure 5. Cloud Depiction and Forecasting System (CDFS) II Functional Diagram.

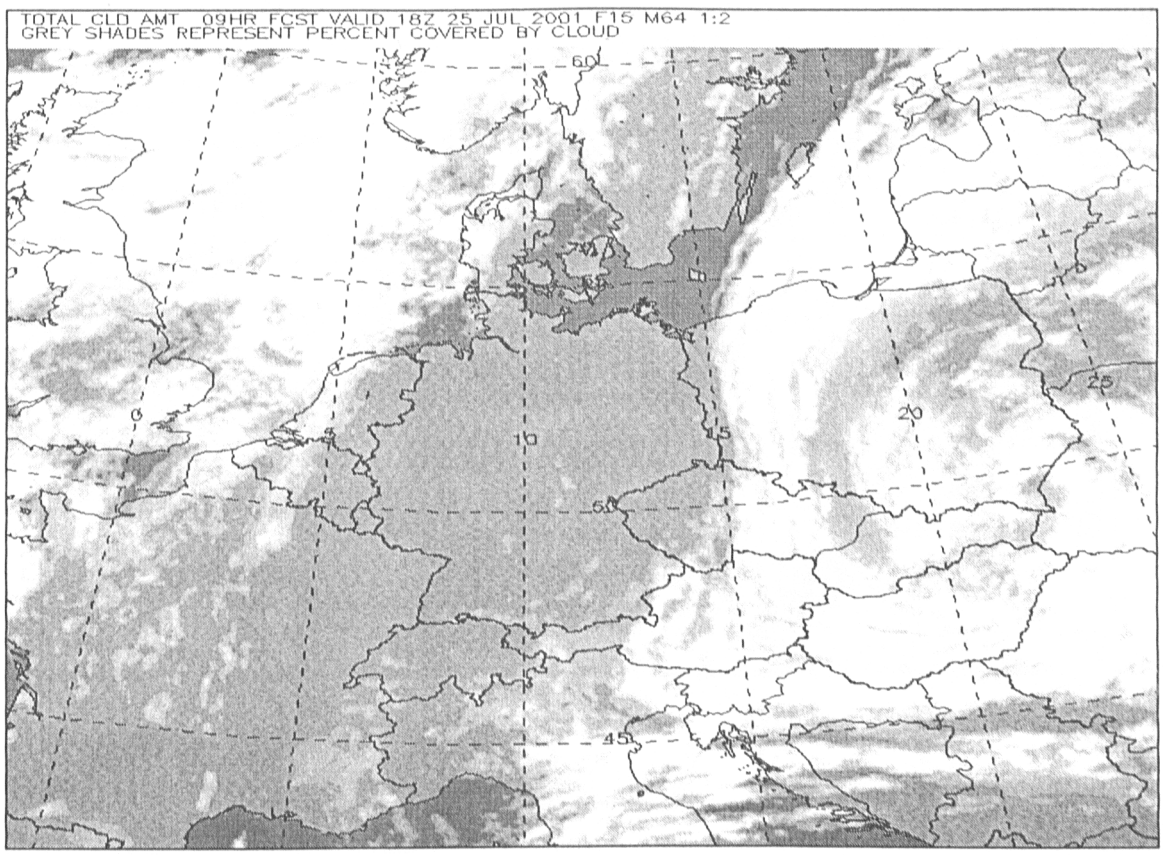

Figure 6. Nine-hour total cloud amount forecast based upon DMSP F-15 fine resolution imagery. Created using AFWA 64th-mesh (3 nautical mile) cloud analysis/forecasting prototype.

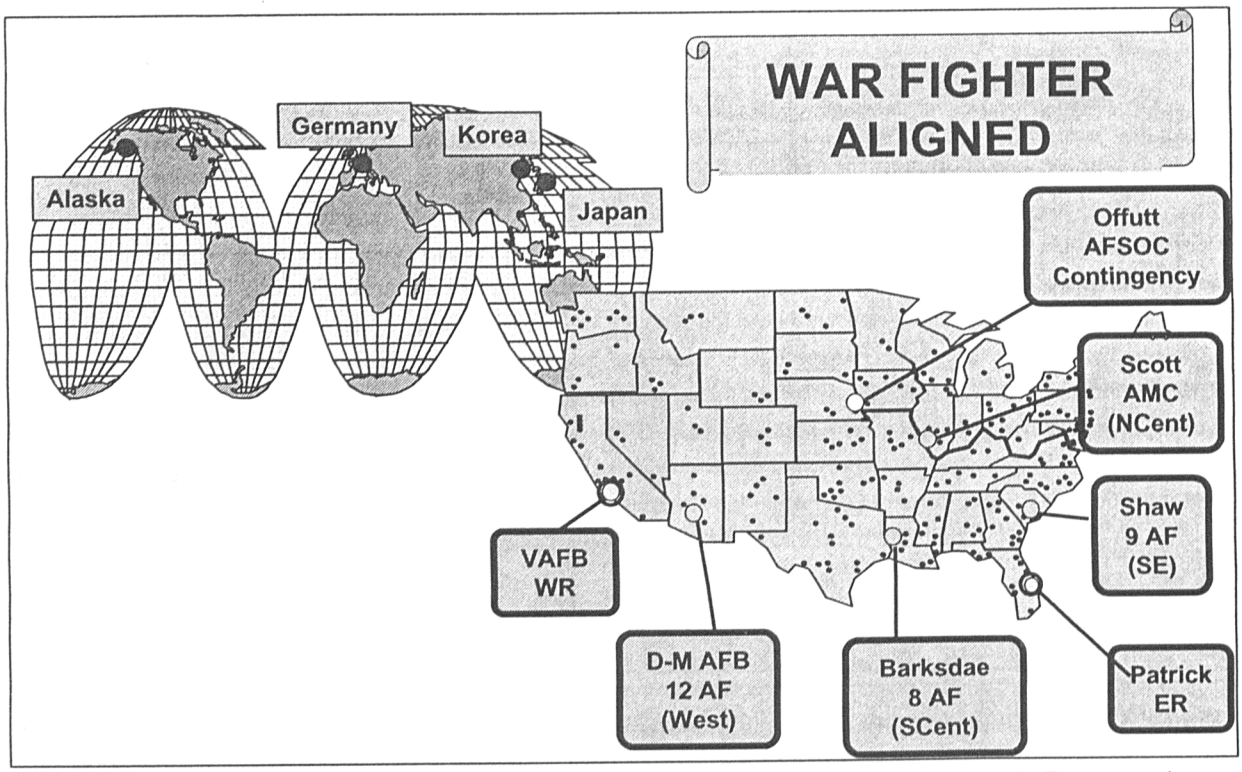

Figure 7. Worldwide Operational Weather Squadron (OWS) locations. Numbered Air Forces and Major Commands supported are indicated. For CONUS OWSs AORs are listed in parentheses.

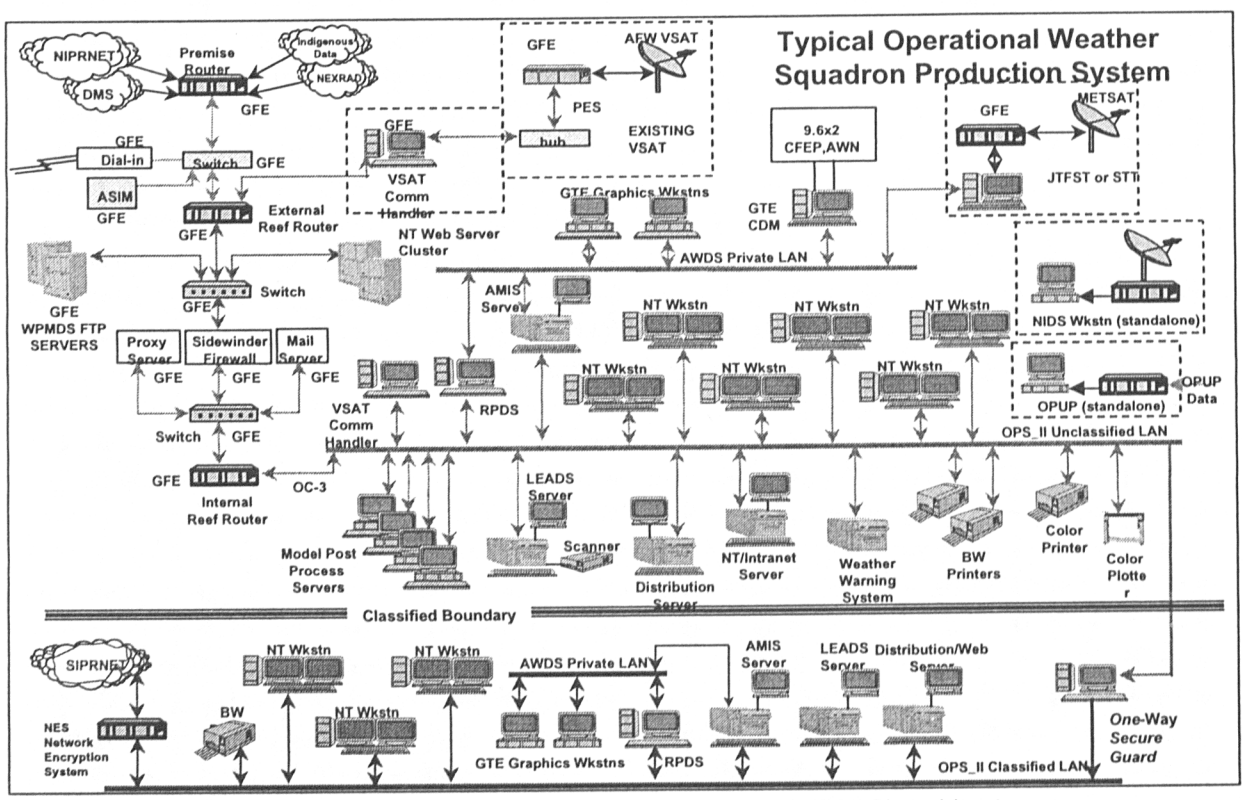

Figure 8. Typical Operation Weather Squadron Production System (OPS) architecture.

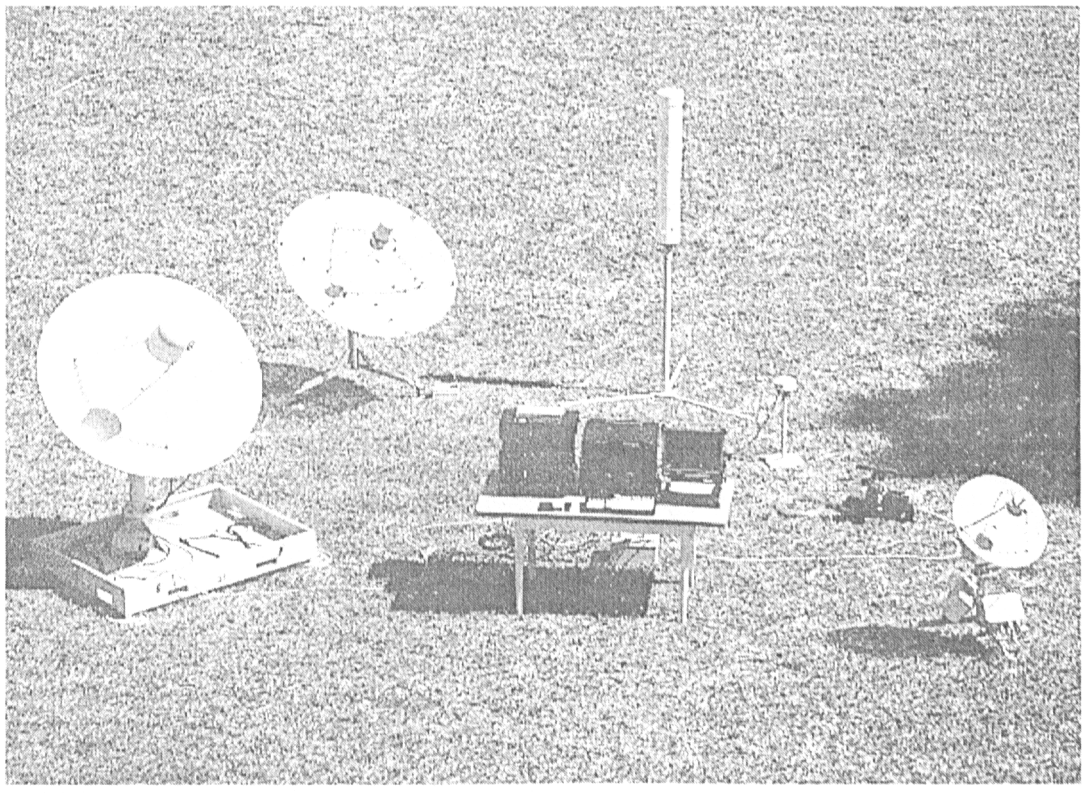

Figure 9. Enhanced Small Tactical Terminal (STT) system.

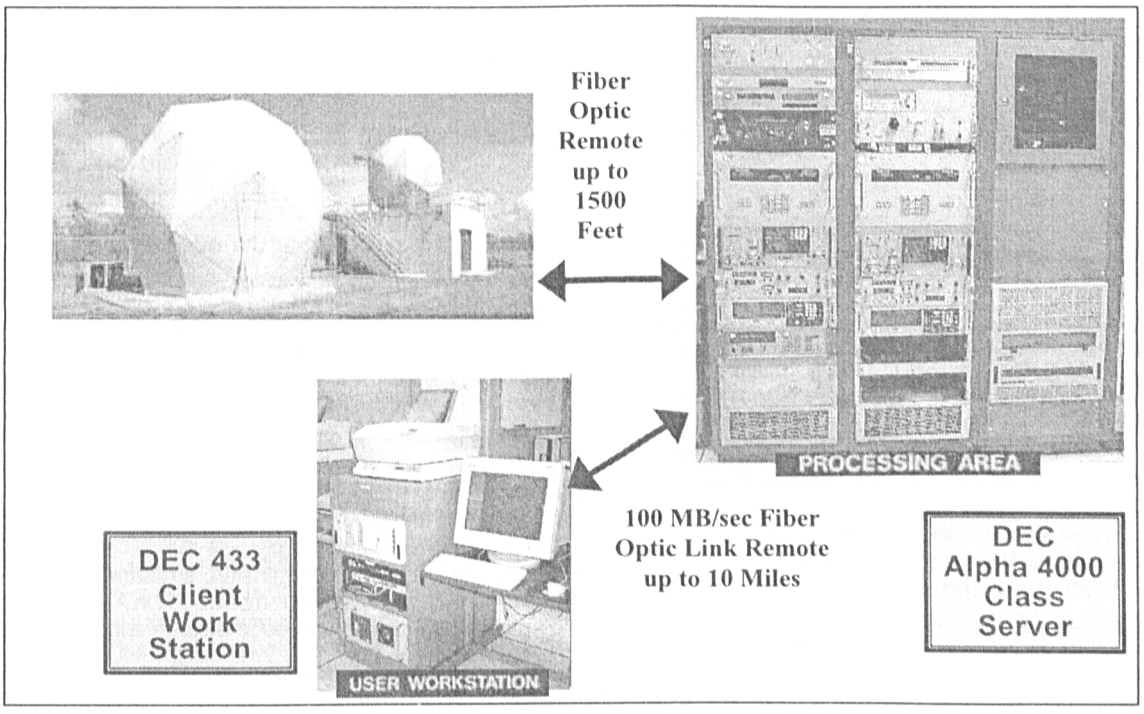

Figure 10. Mark IV system.

3.3 SATELLITE-BASED TROPICAL CYCLONE INTENSITY ESTIMATION USING THE NOAA-KLM SERIES ADVANCED MICROWAVE SOUNDING UNIT (AMSU):

Kurt F. Brueske[1]
And
Christopher S. Velden

University of Wisconsin – CIMSS, Madison, Wisconsin, USA

1. Introduction

The 2001 northern hemisphere hurricane season marks the third year of passive microwave warm core observations using the NOAA-KLM series Advanced Microwave Sounding Unit (AMSU). Over the past two decades, several authors (Kidder et al., 1978, Velden et al., 1991, Kidder et al., 2000) have documented the virtues of monitoring tropical cyclone (TC) intensity using satellite-borne passive microwave radiance data. In summary, 55GHz region microwave observations of TC upper tropospheric warm anomalies (UTWA) are linked to wind structure and minimum sea level pressure (MSLP) using thermodynamic and dynamic constraints on the TC scale (i.e., several hundred km).

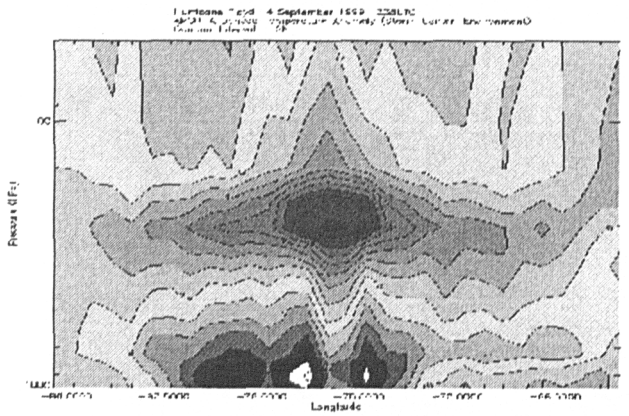

Figure 1. Hurricane Floyd 14 Sep 1999 1238UTC temperature anomaly derived from AMSU-A radiance data. An UTWA of approximately 18°C was observed at 250hPa. Aircraft reconnaissance reported a MSLP value of 924hPa at 1113UTC.

Recently, temperature profiles constructed using AMSU-A multi-spectral observations and the National Oceanic and Atmospheric Administration (NOAA) National Environmental Satellite Data Information Service (NESDIS) retrieval algorithm (Fig. 1) have produced TC warm core vertical cross sections strikingly similar to the classic profiles derived from composite aircraft and radiosonde observation data in the late 1960s (Koteswaram, 1967).

In a novel simulation study, Merrill (1995) introduced the concept of passive microwave radiometer observation "effective accuracy" and demonstrated that, for a variable horizontal resolution instrument like the NOAA-KLM AMSU-A, the TC UTWA resolving limit is a non-linear function of several time-variant parameters including:

- AMSU-A scan angle (ϕ)
- AMSU-A scan angle off-axis angle (θ)
- UTWA horizontal scale (R)
- Scattering by mixed-phase hydrometeors

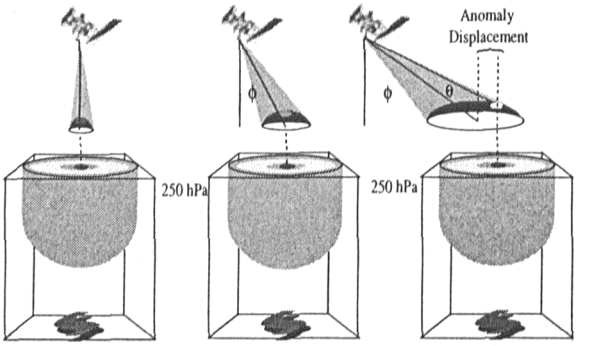

Figure 2. A schematic diagram illustrating AMSU-A horizontal resolution as a function of scan angle (ϕ) and off-axis angle (θ) for a mature TC. Note the difference in size between nadir and limb FOV.

Due to the ephemeral nature of TC position (ϕ,θ) and UTWA horizontal scale (R) between successive AMSU-A observations (Fig. 2), there exists a non-zero component of the UTWA temporal variability that is purely instrument related vs. change that reflects actual thermodynamic (and TC intensity) structure change. The end result is fictitious temporal UTWA variability and smoothing that can introduce error in schemes that

[1] *Corresponding author address: Kurt F. Brueske, Capt, USAF, PhD, United States Air Force Academy Department of Physics, Suite 2A211 Fairchild Hall USAF Academy CO 80840*

attempt to statistically relate 55GHz-region passive microwave UTWA observations with TC MSLP. The aforementioned effects are non-trivial and have limited past attempts to develop and implement satellite-based TC passive microwave intensity estimation techniques.

The remainder of this paper describes the development, test and evaluation of an algorithm designed to explicitly model and remove undesirable TC scale and AMSU-A instrument scan geometry effects according to the methodology prescribed by Merrill (1995). Section 2 describes the satellite data and in-situ observations used in this study followed by a description of the salient features of the maximum likelihood retrieval algorithm in Section 3. Section 4 describes the results of a fully automated, independent test in 2000 where TC MSLP was diagnosed using raw and scan geometry-corrected (hereafter referred to as retrieved) UTWA information derived from limb-corrected AMSU-A 54.94GHz brightness temperature data followed by a brief discussion of factors that limit AMSU TC intensity estimate accuracy. Section 5 provides a summary and briefly describes ongoing technology transition and future research activities. Acknowledgements and references are provided in Sections 6 and 7.

2. Data

Global AMSU-A/B earth observation radiance data is forwarded by NOAA/NESDIS to the University of Wisconsin-Madison (UW) Space Science and Engineering Center (SSEC) Cooperative Institute for Meteorological Satellite Studies (CIMSS) for near real-time processing and archival. Average time delays between AMSU TC observation and SSEC/CIMSS receipt range from 1-3 hours based on several factors including TC location, NOAA/NESDIS internal processing schedules, telecommunications network activity, etc. Only under extreme circumstances does the time delay exceed 3 hours.

Development of the 1999 dependent data set required the identification and manual retrieval of NOAA-15 AMSU-A/B orbits providing TC coverage. Visualization of orbit coverage (near-real time and post-event) and determination of precise TC overpass time (UTC) were made possible using the UW-SSEC Man-computer Interactive Data Access System (McIDAS). Relevant AMSU-A/B orbit files were then acquired from a local UW-CIMSS near real-time archive or restored from 8mm tape. The entire navigation/acquisition process was automated in support of the 2000 independent test, as well as for future research and development activities, and is discussed in more detail in Section 4. Radio frequency interference with NOAA-15 AMSU-A and AMSU-B instruments prohibited the consideration of TC data in 1998.

Atlantic and eastern Pacific basin TC reconnaissance observations from the United States Air Force Reserve 53rd Weather Reconnaissance Squadron and NOAA were used to (1) develop dependent test regression coefficients relating raw/retrieved AMSU-A UTWA magnitudes to aircraft reconnaissance estimates of MSLP and (2) validate independent test results. The selection of AMSU-A/aircraft reconnaissance "pairs", for both dependent and independent samples, were based on the time difference between aircraft reconnaissance and AMSU-A observations and environmental conditions. Only those observations that occurred within +/- 6 hrs of each other and for which the TC was not undergoing significant intensity change due to interaction with land, wind shear, etc. were considered.

3. Forward Model

As discussed in Section 1, AMSU-A horizontal resolution varies from approximately 48km near satellite nadir to over 100km near scan limb. The combined effects of subsidence and high inertial stability within the inner-eyewall region constrain the horizontal dimensions of peak TC UTWA warming to scales less than even the most optimal AMSU-A viewing conditions (i.e., $\phi = 0^{\circ}, \theta = 0^{\circ}$). As a result, the true magnitude of TC UTWAs will typically be sub-sampled for all but a small minority of TCs possessing large eyes (and corresponding UTWA horizontal scales) or average sized systems that happen to fall fortuitously near center of an AMSU-A FOV near satellite nadir. In reality, TCs are characterized by a wide variety of horizontal scales and are free to fall anywhere within the AMSU-A scan swath; therefore, knowledge of the effects of storm scale (R) and scan geometry (ϕ,θ) are vital steps towards TC UTWA optimization and MSLP estimate accuracy.

The approach used in this study is based on the methodology proposed by Merrill (1995) using previous generation Microwave Sounding Unit (MSU) data. Adopting Merrill's technique for use with AMSU-A, the observed 54.94GHz horizontal brightness temperature distribution $B^{obs}(x,y)$, from which the TC UTWA is estimated, is considered a convolution of the true upper tropospheric thermal distribution $B^{true}(x,y)$ and the antenna gain pattern $F(x,y,\nu)$ (Fig. 3).

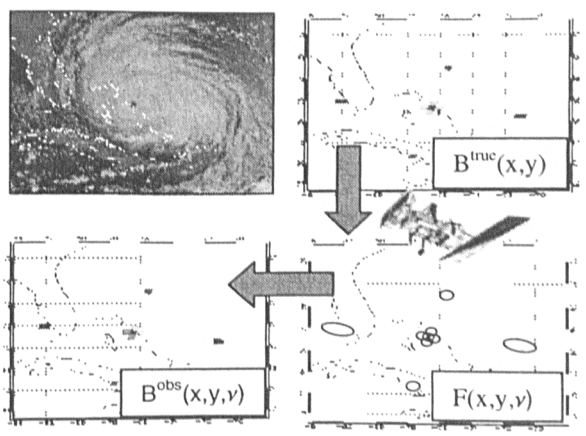

Figure 3. A schematic diagram illustrating the concept of true TC UTWA convolution with the AMSU-A antenna gain pattern for Hurricane Floyd 14 Sep 1999 1238UTC. *AVHRR multi-spectral image (inset) courtesy of Dave Santek, UW-SSEC.*

This can be represented mathematically as:

$$B^{obs}(x,y,\nu) = ??B^{true}(x,y)F(x,y,\nu)dA \qquad (1)$$

assuming that (1) the atmosphere is sufficiently opaque at ν = 54.94GHz such that the surface emission term can be neglected, (2) the frequency-dependent weighting function does not vary significantly over the depth of layer atmospheric layer characterized by the peak upper tropospheric warming, and (3) scattering by mixed-phase hydrometeors is negligible (see Section 4). The antenna gain pattern $F(x,y,\nu) \sim F(\phi,\theta,\nu)$ for off-nadir scan angle ϕ is uniquely prescribed based on the diffraction pattern of a uniformly illuminated circular aperture:

$$F(\phi,\theta,\nu) \sim 4\{J_1(\nu d\sin\theta)/\nu d\sin\theta\}^2 \qquad (2)$$

where J_1 is a Bessel function (first kind, order one), ν is the frequency of incident radiation (54.94GHz), d is the AMSU-A instrument bore sight aperture (m), and θ is the scan angle off-axis angle defined by the displacement of the TC LLCC from the center of the AMSU-A FOV containing the peak UTWA warming (Fig. 2). Finally, dA represents the area formed by the intersection of the AMSU-A antenna gain pattern with the earth's surface (see Fig. 3).

Assuming that the TC is in hydrostatic balance at the storm scale, the true upper tropospheric thermal distribution $B^{true}(x,y,\nu)$ is assumed to mirror the surface pressure distribution. As a result, the form of $B^{true}(x,y)$ is modeled after Holland (1980):

$$B^{true}(x,y) \sim B(x,y,\mathbf{X}) = B_{env} + delta_B\{1 - e[^{-(R/r)^{\gamma}}]\} + B_x(x-x_c)\,B_x(y-y_c) \qquad (3)$$

where B_{env} represents undisturbed environmental conditions, delta_B the UTWA magnitude for a mature TC, B_x and B_y the environmental derivatives (longitude and latitude), x and y the position relative to TC center (x_c,y_c), and $r = (|x - x_c|^2 + |y - y_c|^2)^{1/2}$. The term within curly brackets {} defines the shape of the radial distribution of the UTWA as a function of distance r from the TC center. R, which represents the UTWA horizontal scale, is a vital component of (3) and must be prescribed accurately in order to maximize the representativeness of $B^{true}(x,y)$ in the forward model. γ is a dimensionless shape factor that describes the eccentricity of the UTWA.

X represents a tunable TC UTWA horizontal structure function (column vector) consisting of 8 parameters

$$\mathbf{X} = [B_{env}, delta_B, R, \gamma, B_x, B_x, x_c, y_c]^T \qquad (4)$$

all of which, with the exception of R, x_c and y_c, are initially assigned constraint ($\mathbf{X}^{con}$) a-priori mean values and error variances based on satellite or aircraft reconnaissance-derived parameter climatologies (Merrill, 1995). In this study, the TC UTWA size parameter R is defined through the spatial analysis of AMSU-B 89.0GHz moisture sounder window channel radiance data (Fig. 4). AMSU-B 89.0GHz radiances are strongly attenuated by convection within the TC eye wall region (Kidder et al., 2000) and are therefore used as a proxy for eye size. An interpolating polynomial **F**(r) is fit to the radial distribution of AMSU-B 89.0GHz radiance data and R is assumed to occur at $|d^2\mathbf{F}(r)/dr^2| = 0$ (inflection point) coincident with reduced AMSU-B 89.0GHz brightness temperatures characteristic of convective hydrometeor scattering within the eye wall region. The final R value is found by averaging up to

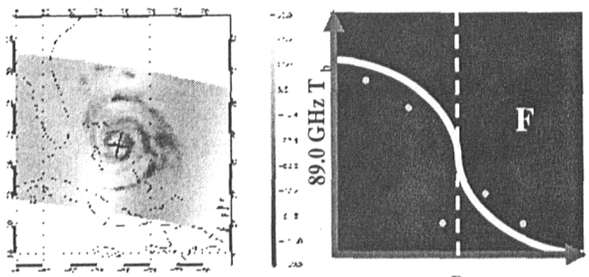

Figure 4. The retrieval algorithm horizontal size parameter (R) is determined through spatial analysis of AMSU-B 89.0GHz radiance data. In this example, TC position for Hurricane Floyd, 14 Sep 1999 1238UTC (left) is specified and an interpolating polynomial function F(r) is defined in each of four total directions (right) in image array line/element. Hydrometeor scattering within the eye wall region is used as an indicator of eye size itself a proxy for UTWA horizontal scale.

four separate R estimates from each radial direction in AMSU-B radiance array line/element space. For the development of the 1999 dependent sample, TC position (x_c, y_c) was determined using published forecast discussion bulletins generated by the National Hurricane Center (NHC) and Navy/Air Force Joint Typhoon Warning Center (JTWC) with fine scale adjustments based on the visual inspection of AMSU-B 89.0GHz data.

Once the constraint structure vector $\mathbf{X}^{con}$ (4) is specified, it is used by the forward model to estimate the expected radiance distribution $B_m^{fwd}(x,y,\mathbf{X}_m)$ where $\mathbf{X}_m$ is the m-th iterated storm structure vector. This process is repeated until the difference between the observed AMSU-A radiance distribution $B^{obs}(x,y,\nu)$ and $B_m^{fwd}(x,y,\mathbf{X}_m)_{m->\infty}$ are minimized. At each iterative step, $\mathbf{X}_m$ is perturbed according to the method proposed by Rodgers (1976):

$$\mathbf{X}_{m+1} = \mathbf{X}^{con} + \mathbf{S}^{con}\mathbf{K}_m^T(\mathbf{K}_m\mathbf{S}^{con}\mathbf{K}_m^T + \mathbf{S}_{yy})^{-1} x [\mathbf{Y}^{obs} - \mathbf{Y}_m - \mathbf{K}_m(\mathbf{X}^{con} - \mathbf{X}_m)] \qquad (5)$$

where $\mathbf{X}^{con}$ is the constraint (a priori) storm structure vector, $\mathbf{S}_{xx}^{con}$ the constraint structure error covariance, $\mathbf{K}_m$ the forward model sensitivity to changes in the

structure vector (i.e., $\partial B_m^{fwd}(x,y, \mathbf{X}_m)/\partial \mathbf{X}_m$), and $\mathbf{S}_{yy}$ the AMSU-A observation error covariance. Based on (5), the maximum likelihood solution for the storm structure function $\mathbf{X}^{ret}$ ($\mathbf{X}_m$, m→8), including the retrieved UTWA (delta_B^{ret}), occurs when the differences between the observed AMSU-A radiances B^{obs} and forward model radiances B_m^{fwd} and the forward model sensitivity-weighted difference between the constraint storm structure $\mathbf{X}^{con}$ and m-th iteration structure $\mathbf{X}_m$ are the same. Finally, the scan-geometry and diffraction-corrected UTWA (delta_B^{ret}) is retrieved through inversion of the solution structure function $\mathbf{X}^{ret}$

$$\text{delta_}B^{ret} = [\,\mathbf{X}^{ret}\,]^{-1} \qquad (6)$$

The ability of the retrieval algorithm (5) to resolve $\mathbf{X}^{ret}$, and therefore delta_B^{ret}, depends highly on the accuracy of the constraint storm structure $\mathbf{X}^{con}$. As noted by Merrill (1995), the solution storm structure $\mathbf{X}^{ret}$ will always fall between $\mathbf{X}^{con}$ and the value of $\mathbf{X}$ that best produces the AMSU-A observed radiance distribution B^{obs}. Whether the actual AMSU-A observation or constraint is favored depends upon the expected constraint structure error covariance $\mathbf{S}_{xx}^{con}$, the expected observation variance (noise) $\mathbf{S}_{yy}$, and the sensitivity of the forward model to changes in the storm structure $\mathbf{K}_m$. $\mathbf{S}_{xx}^{con}$ →0 implies that $\mathbf{X}^{con}$ is a good estimate of the storm structure and the solution will favor the constraint with zero variance. On the other hand, $\mathbf{S}_{xx}^{con}$ →8 implies $\mathbf{X}^{con}$ is a poor estimate of the storm structure and the solution tends toward the inversion of the forward model. $\mathbf{S}_{yy}$ and $\mathbf{K}_m$ are coupled in the sense that accurate AMSU-A observations (i.e., $\mathbf{S}_{yy}$ →0) or large forward model sensitivities $\mathbf{K}_m$ (i.e., favorable viewing geometry→satellite nadir, FOV centered) cause the solution to favor the solution of the forward model whereas $\mathbf{S}_{yy}$ →8 or small $\mathbf{K}_m$ (i.e., unfavorable view geometry → satellite limb, non FOV-centered) favor the constraint $\mathbf{X}^{con}$.

During 1999, 22 cases in the Atlantic/Eastern Pacific Basin satisfied the criteria specified in Section 2 and were used to develop the dependent sample. Three parallel tests were conducted using identical NOAA-15 AMSU-A and in-situ MSLP data sets (Fig. 5). The first test (red) related the raw AMSU-A 54.94GHz derived UTWA (delta_B) with in-situ MSLP estimates while the other two tests related the retrieved UTWA (delta_B^{ret}) with in-situ MSLP estimates after explicitly treating and removing the scan-geometry and diffraction effects. Of the two tests in which the retrieval algorithm was applied, one used a fixed climatological horizontal scale parameter (green) of 24km (Weatherford and Gray, 1988) while the other test (blue) used variable R values derived using AMSU-B 89.0GHz radiance data. The test results demonstrate that while a moderate degree of correlation (R^2 ~ 0.70) exists naturally between delta_B and MSLP, a significantly higher degree of correlation (R^2 ~ 0.90) between delta_B^{ret} and MSLP is possible using the retrieval and AMSU-B 89.0GHz radiance data. The relatively similar performance between delta_B^{ret} vs. MSLP (R fixed) and delta_B^{ret} vs. MSLP (R variable) likely reflects

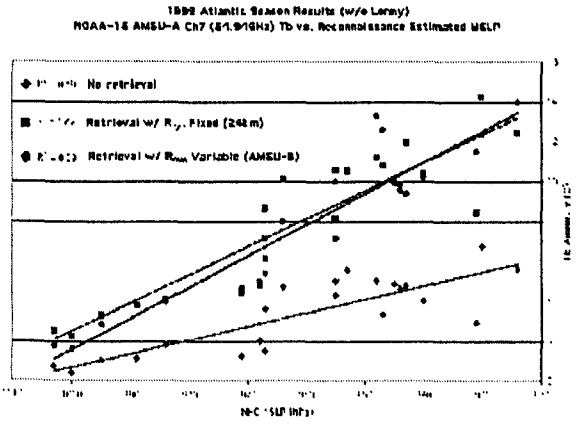

Figure 5. Results of the 1999 dependent test. Application of the retrieval increases the resolved UTWA and improves correlation with MSLP determined by aircraft.

the similarity in sizes between climatological R values and the average of those derived from AMSU-B 89.0GHz data ($R_{ave}^{89.0GHz}$=22.4km). In summary, the results of the dependent test – increased UTWA resolution and improved correlation with reconnaissance MSLP estimates – validate Merrill's earlier hypothesis on TC UTWA sub sampling and strongly support the need for application of the retrieval algorithm.

4. Independent Test

Based on the results of the dependent test in 1999, an automated processing scheme was devised (Fig. 6) to diagnose MSLP in 2000 using solely delta_B, delta_B^{ret} and regression coefficients derived

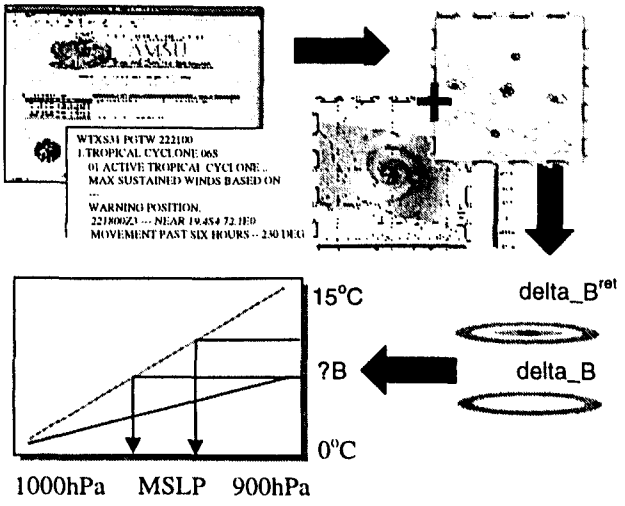

Figure 6. A schematic of the automated AMSU TC MSLP estimate processing routine executed during the independent test. Steps 1-4 are clock-wise starting in the upper left corner.

from the 1999 dependent sample. Processing was "event-driven" based on TC position estimates

published within NHC/JTWC forecast discussion bulletins (Step 1). Based on TC position, AMSU-A/B observation data was acquired, the size parameter R determined, and the forward model run using AMSU-A FOV scan angles (ϕ) and off-axis angles (θ) (Step 2) leading to estimates of the raw (delta_B) and retrieved (delta_B^{ret}) UTWA (Step 3). During the final step (Step 4), TC MSLP was diagnosed using the following dependent data set linear least squares regression equations:

$$MSLP_{ret} = (150.7 - delta_B^{ret}) / 0.15$$
$$MSLP_{raw} = (65.4 - delta_B) / 0.07 \quad (7)$$

Overall, the independent test in the Atlantic and eastern Pacific basins was a success and further reinforced the prior dependent test results. A total of 31 cases met the selection criterion discussed in Section 2. The retrieval yielded delta_B^{ret} values (green) more highly correlated with reconnaissance estimates of MSLP than did delta_B (red) (R^2=0.95 vs. 0.80) and AMSU-based MSLP estimate mean error and standard deviations were also smaller using the retrieval (6.2hPa +/- 8.0hPa vs. 7.5hPa +/- 9.9hPa). In addition, the independent test results performed admirably in a homogenous comparison with Dvorak (1975) intensity estimates (7.8hPa +/- 7.6hPa) generated by the NOAA Satellite Analysis Branch (SAB) and Air Force Weather Agency (AFWA). Fig. 7 illustrates the combined 1999/2000

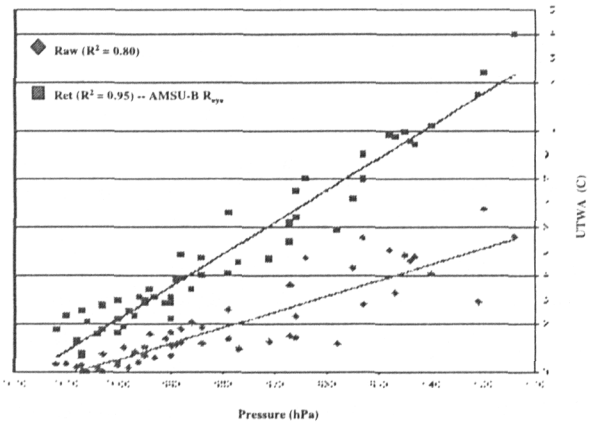

Figure 7. Combined 1999/2000 results. Year 2000 results reinforce earlier findings of the dependent test and further support the linear relationship between true UTWA strength and TC MSLP.

results (n=53). It is noteworthy that application of the retrieval algorithm further reinforces the linearity between satellite-borne 55GHz region passive microwave observations of TC UTWAs and MSLP.

After applying the AMSU TC MSLP retrieval algorithm over the past two years – the first year to train the algorithm followed by the independent test year -- several factors emerged that affect retrieval performance including (1) determination of TC position at the time of AMSU observation, (2) estimating eye size (radius) using AMSU-B 89.0GHz radiance data – particularly near the scan limb, and (3) hydrometeor scattering associated with deep convection in the inner eye wall region. Two years worth of AMSU-A TC observations suggests that the issue of 55GHz region scattering, assumed negligible in Eqn. 1 (Section 3), is occasionally violated particularly during periods when exceptionally deep convection (e.g. convective bursts) occurs close to the LLCC of a TC. Under these circumstances, AMSU-A 54.94GHz radiances can be attenuated (Fig. 8) and any attempt to determine the magnitude of the UTWA (now a cold anomaly) will lead to erroneous TC MSLP estimates.

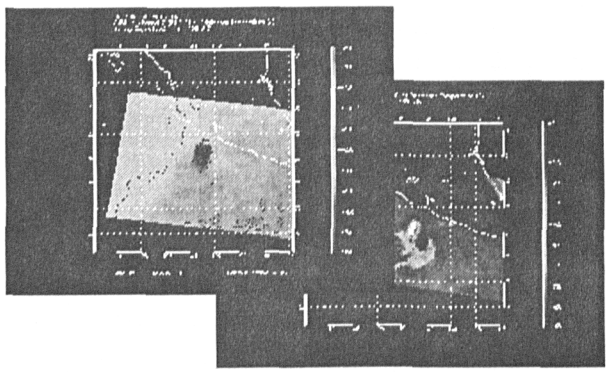

Figure 8. An example of the impact of a convective burst and hydrometeor scattering on AMSU-A 54.94GHz radiance data (left) for Tropical Storm Dalila 22 Jul 2001 1408UTC. The corresponding AMSU-B 89.0GHz image is provided (right).

Another leading factor that limited AMSU TC MSLP estimate accuracy during the independent test was the ability (or inability) of the algorithm to determine TC eye size (R) using AMSU-B 89.0GHz radiance data. As mentioned in Section 3, optimization of the constraint horizontal structure function $\mathbf{X}^{con}$ is absolutely critical to the retrieval algorithm performance. In its current form, R estimates require relatively precise TC position ing at the time of AMSU observation. Based on differences between published NHC/JTWC initial position and motion estimates and the time of AMSU observation, TC position is adjusted using linear extrapolation. In circumstances where TC extrapolated position is inaccurate, the quality of R estimates will be reduced and the performance of the retrieval and MSLP estimates will suffer accordingly. Any number of factors, often in combination, contribute to this problem including 1) poorly defined TCs (e.g., genesis stage, systems undergoing shear ing, etc.) where determination of position using visible/infrared satellite imagery is difficult, 2) TCs characterized by high uncertainty in short-term motion/track, and 3) cases with large time differences between forecasting center initial position estimates and AMSU TC observation.

5. Summary and Future Research

Passive microwave radiometers like the AMSU provide a unique opportunity to monitor and assess changes in TC intensity based on observed changes in UTWA structure. By implementing a maximum likelihood regression technique first proposed by Merrill (1995), the authors have successfully demonstrated that the adverse effects of variable sensor horizontal resolution, storm scan geometry, and diffraction effects can be explicitly modeled and removed. Furthermore, AMSU TC UTWA values produced by the retrieval yielded superior TC MSLP estimates compared to those generated using raw UTWA observations, reducing both mean MSLP estimate error and variance. Finally, the similarity in performance between AMSU and Dvorak (1975) intensity estimates Dvorak technique substantiates the value of the AMSU as a future TC intensity estimation tool.

In 2001, the UW-CIMSS, in cooperation with the USAF and Naval Research Laboratory-Monterey, is generating near real-time AMSU TC MSLP estimates using an automated, objective, web-based approached similar to the method exercised internally at UW-CIMSS in 2000. The software suite, in its current form, is capable of supporting up to 5 simultaneous TCs in 4 geographically separate basins (Atlantic, Eastern Pacific, Western Pacific (Northern and Southern Hemisphere), and Indian Ocean (Northern and Southern Hemisphere)) with minimal human intervention. Near real-time AMSU TC imagery products are available to a global audience via the world-wide-web at http://amsu.ssec.wisc.edu. AMSU TC MSLP estimates are also being forwarded to NHC, JTWC, NOAA/SAB and AFWA for evaluation and feedback.

Several initiatives and enhancements are undergoing immediate development or are in the process of being planned in the near future. These include:

- A multiple channel regression approach using multiple AMSU-A tropospheric channels
- A web-based manual retrieval interface that allows client specification of TC position and R
- AMSU 'INVEST' processing coupled with NRL-MRY and ATCF
- Extension of the retrieval algorithm for use with DMSP SSMIS
- AMSU-A based hydrostatic eye sounding corrected for precipitation (scattering) effects

all of which will improve our ability to monitor and assess TC intensification and environmental interaction.

6. Acknowledgements

We gratefully acknowledge the support of our research sponsors, the Office of Naval Research, Program Element (PE-060223N), the Space and Naval Warfare Systems Command, PMW-155 (PE-0603207N), the Naval Research Laboratory (Jeff Hawkins), and the United States Air Force Academy Department of Physics (USAFA/DFP). The authors would also like to recognize Dr. Robert T. Merrill (formerly of UW-CIMSS) for his pioneering contributions towards the development of the original XTCR algorithm upon which this research is based. Finally, the authors would like to thank the USAF 53rd WRS, NOAA/NESDIS, USAF Weather Agency, and the Australian Bureau of Meteorology for making available timely TC in situ observation data in near real-time.

7. References

Dvorak, V. F., 1975: Tropical cyclone intensity analysis and forecasting from satellite imagery. *Mon. Wea. Rev.*, 103, 420-430.

Holland, G. J., 1980: An analytic model of the wind and pressure profiles in hurricanes. *Mon. Wea. Rev.*, **108**, 1212-1218.

Kidder, S. Q., Gray, W. M., and T.H. Vonder Haar, 1978: Estimating Tropical Cyclone Central Pressure And Outer Winds From Satellite Microwave Sounder Data. *Mon. Wea. Rev.*, **108**, 1458-1464.

Kidder, S.Q., M.D. Goldberg, R.M. Zehr, M. DeMaria, J.F.W. Purdom, C.S. Velden, N.C. Grody, and S.J. Kusselson, 2000: *Bull. Amer. Meteor. Soc.*, 81, 1241-1259.

Koteswaram, P., 1967: On The Structure Of Hurricanes In The Upper Troposphere And Lower Stratosphere. *Mon. Wea. Rev.*, 95, 541-564.

Merrill, R.T., 1995: Simulations of Physical Retrieval of Tropical Cyclone Thermal Structure Using 55 GHz-Band Passive Microwave Observations from Polar-Orbiting Satellites. *J. App. Meteor.*, **34**, 774-787.

Rodgers, C. A., 1976: Retrieval of atmospheric temperature and composition from remote measurements of thermal radiation. *Rev. Geophys. Space Phys.*, 14, 609-624.

Simpson, J., 2000: Personal communication.

Velden, C. S., Goodman, B. M., and R. T. Merrill, 1991: Western North Pacific Tropical Cyclone Intensity Estimation from NOAA Polar-Orbiting Satellite Microwave Data. *Mon. Wea. Rev.*, **119**, 159-168.

Weatherford, C. L., and W. M. Gray, 1988: Typhoon structure as revealed by aircraft reconnaissance. Part I: Data analysis and climatology. *Mon. Wea. Rev.*, 116, 1032-1043.

3.5

SATELLITE DATA UTILIZATION BY U.S. NAVY METEOROLOGY AND OCEANOGRAPHY

Don T. Conlee and Richard L. Crout*

Naval Meteorology and Oceanography Command
Stennis Space Center, MS 39529

1. INTRODUCTION

Meteorology and Oceanography (METOC) professionals of the U.S. Navy and Marine Corps face a daunting task: characterize the operating environment globally, and more specifically, in the vast oceans and littoral regions, to enhance the safety and efficacy of forces. However, this operating environment is typically the very definition of "data sparse". Remote Sensing from satellites has become an integral part of Naval operational analysis and forecasting. This has been accomplished though extensive and focused research and operational transition efforts, both Navy-sponsored and leveraged from the scientific community at large.

This paper offers an overview of current satellite usage and those research areas which hold the promise of transition to operations in the near term. Technologies include passive microwave, visual and infrared imaging applications, multispectral applications, scatterometry, altimetry, SAR and feature analysis from high-resolution commercial imagery. Applications of these technologies to real-world Naval operations are detailed.

2. VIS/IR APPLICATIONS

Like all of those charged with operational meteorology, visible and infrared imagery remain primary tools in weather analysis and forecasting. We therefore share the common requirements of increased spatial resolution and refresh for this type of data from both geostationary and polar-orbiting platforms.

The VIS/IR data are also used extensively in more quantitative ways. The Naval Oceanographic Office (NAVO) produces Sea Surface Temperature analyses from multi-channel IR sensors using the 11-12 micron split-window technique for operational Navy usage and for general use under the auspices of the Shared Processing Program (SPP) (Rigney et al., 1997).

Geostationary VIS/IR and water vapor channels are used to derive high-density feature-tracked winds for use in Numerical Weather Prediction (NWP) models run at Fleet Numerical Meteorology and Oceanography Center (FNMOC) in Monterey, CA (Figure 1). This operational capability is the culmination of a collaborative research effort between the Naval Research Laboratory (NRL) Monterey and U. of Wisconsin/CIMMS (Velden et al., 1997). Expansion of this program is underway to include data from the Japan Meteorological Agency GMS and EUMETSAT Meteosat processed by another SPP partner, the Air Force Weather Agency (AFWA) in Omaha, NE with FNMOC background fields.

Data from IR Sounders are also important inputs to NWP efforts. Through SPP, the Navy leverages NESDIS expertise in soundings, using the NESDIS-supplied POES soundings delivered via SPP communications operationally. In addition, research is progressing on direct radiance assimilation into Navy numerical models.

Recent transitions into operational usage include a low cloud product using a bispectral IR technique, which gives forecasters a nighttime capability for fog/stratus determination. A new capability to stitch together multiple geostationary data has also been developed, offering military planners with global purview (and the METOC professionals supporting them) a virtually seamless global satellite depiction. These capabilities were part of a Cooperative Research and Development Agreement (CRADA) between NRL Monterey and SeaSpace, Inc. described in Hawkins, et al., 2000.

Corresponding author address: Dr. Richard L. Crout, N543, COMNAVMETOCCOM, 1100 Balch Blvd., Stennis Space Center, MS 29529-5005;
email: croutr@cnmoc.navy.mil
Online paper link: https://www.cnmoc.navy.mil/nmosw/handbk.htm#articles

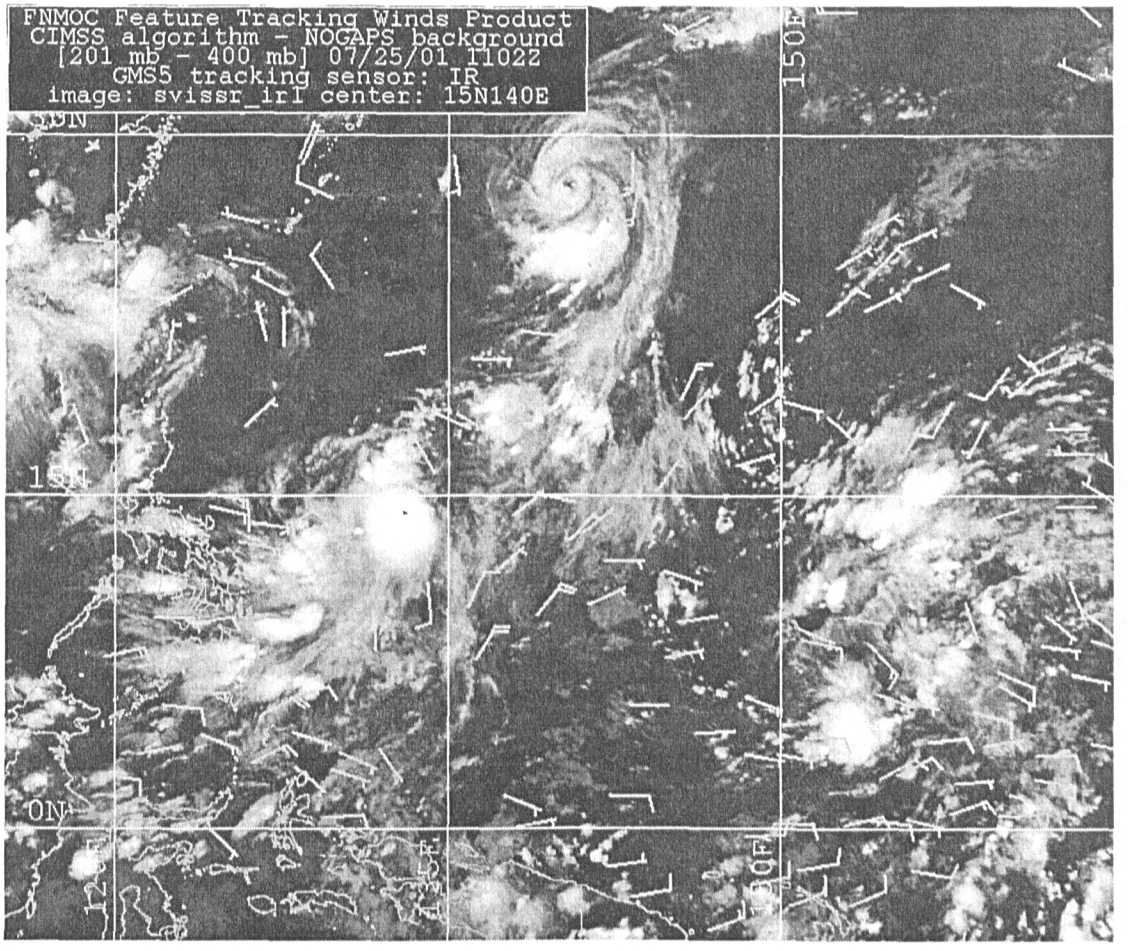

FIG. 1. High density feature tracked winds product. The typhoon near 28N, 140E is Kong-Rey (9W).

3. PASSIVE MICROWAVE

Exploitation of passive microwave imagery, particularly that from the Special Sensor Microwave Imager (SSM/I), has long been a primary emphasis of Navy remote sensing. The passive microwave ability to sense surface wind speed over the vast data-sparse oceans is fundamental to Navy METOC efforts to assess and predict high winds and seas. FNMOC is the SPP Core Processing Center (CPC) for passive microwave imagery, providing the parameters of wind speed, rain rate, integrated water vapor, cloud water content, soil moisture and ice concentration for SPP and operational Navy usage (Cornelius, et al., 2000). The algorithms for these parameters are those approved by the SPP Algorithm Research Panel (ARP) process, co-chaired by FNMOC and the Naval Research Laboratory (Colton and Poe, 1994). FNMOC also partners with NRL as lead agents for Calibration/Validation of newly-flown passive microwave sensors.

A less quantitative but operationally useful technique of using microwave imagery is that of using SSM/I 85 GHz imagery to locate tropical cyclone centers and convective structure. This is used extensively at centers such as the Joint Typhoon Warning Center in Pearl Harbor, Hawaii which obtains the data from the Navy's Tropical Cyclone Web Page, currently in transition from NRL Monterey to FNMOC (Hawkins et al., 2001). Figure 2 is an example of SSM/I 85 GHz imagery of TC Bilis and shows how clearly passive microwave can locate a circulation center via the convective organization. The most valuable application of this is in cases when no clear eye is apparent in traditional VIS/IR imagery.

Partnering with the NPOESS Integrated Program Office and the Space Test Program, NRL is developing the WindSat instrument (St. Germain and Gaiser, 2000). This effort is designed to demonstrate the ability of polarimetric methods to

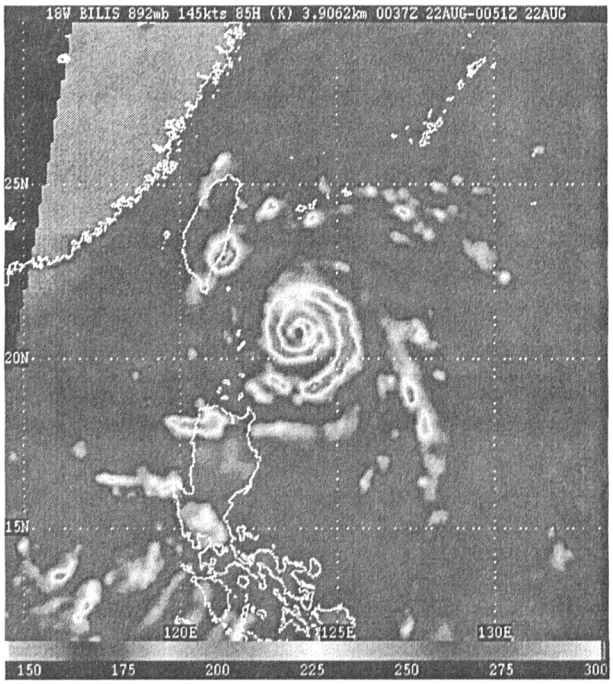

FIG. 2 85 GHz (Horiz. Pol.) imagery from FNMOC.

retrieve wind direction as well as speed from a passive microwave instrument. FNMOC will be the Payload Operations Center (POC) for WindSat. The Navy also makes use of other R&D passive sensors such as the TRMM TMI in much the same fashion as SSM/I.

As in the case of IR sounders, microwave sounders play an important role in NWP. Again leveraging SPP partnerships, NESDIS SSM/T-1 and T-2 soundings are used operationally in Navy models. The integrated microwave imager and sounder, SSMIS, to be launched on the next DMSP satellite, will be exploited similarly to SSM/I and SSM/T-1/2, with some improvements likely to be derived from the co-located conically scanning configuration.

4. SCATTEROMETRY

The scatterometer provides an important supplement to passive microwave methods for retrieval of ocean surface wind in providing wind direction and supplementing coverage. At FNMOC, Navy model data is applied to the backscatter from the QuikSCAT and ERS-2 scatterometers to remove directional ambiguity in a product-line consistent fashion. Figure 3 is an example of a web-based, interactive surface wind speed product that combines both scatterometry and passive microwave.

5. ALTIMETRY

The radar altimeter provides a function for the ocean similar to that of a barometer for the atmosphere. The sea surface height, determined by processing the altimeter range measurement with a full set of corrections, is a function of the density of the water mass beneath it. Cold (dense) and warm (less dense) water masses are represented by differences in the sea surface height of the column of water. Narrow geostrophic currents generated at the boundaries of water masses are represented by rapid (10 to 100 centimeters) changes in sea surfaces over a relatively short spatial scale (50 to 100 kilometers). These features are revealed in the sea surface heights generated by the radar altimeter (Figure 4). Mesoscale features are gleaned from a combination of altimeter sea surface height and sea surface temperature measurements.

NRL Stennis Space Center devised a method to assimilate sea surface height and sea surface temperature measurements to resolve a three-dimensional cube of the temperature, salinity, and density of the water column. The Modular Ocean Data Assimilation System (MODAS) was developed and transitioned to NAVO to assimilate GEOSAT Follow-On (GFO), Topex/Poseidon, and ERS-2 altimeter data at the Altimeter Data Fusion Center. In a majority of ocean areas MODAS provides information that is superior to climatology or climatology plus sea surface temperature measurements alone. The Navy Layered Ocean Model (NLOM) is a global/regional ocean model capable of assimilating sea surface heights. Model evaluations indicate that in order to properly represent the mesoscale oceanic variability, an altimeter in a 17- or 35-day exact repeat orbit is adequate, although model improvements continue with additional satellites up to a maximum of three altimeters (Hurlburt, 2000). An altimeter ARP is being formed under the SPP to continue investigating improvements in altimeter research and transitioning those efforts to operations.

6. SYNTHETIC APERATURE RADAR

Synthetic Aperture Radar (SAR) technology takes advantage of the forward motion of the spacecraft carrying the active microwave radar to synthetically increase the antenna size and acquire more information from the signal, thus allowing a higher spatial resolution to be extracted from the signal. The U.S. National/Naval Ice Center (NIC) has the responsibility of mapping sea ice

conditions over all ocean regions of the world. In addition to visible and infrared imagery and ice imagery from the Special Sensor Microwave Imager on the DMSP satellite, the Navy uses SAR data from the Canadian RADARSAT-1. The synthetic aperture radar (SAR) imagery is extensively used in the production of sea ice analyses in U.S. waters and the Arctic. SAR data allow an all-weather, day/night capability that determines ice edge, ice coverage, and ice concentration.

Much of the analysis of the SAR data is manual, but Navy and NOAA funded research is underway to automate the processes to distinguish between first year and multiyear ice. Gineris et al. (2000) describe an operational evaluation of ARKTOS, a knowledge-based sea ice classification system. ARKTOS is in use at NIC to aid in the mapping of ice covered oceans.

7. SPECTRAL APPLICATIONS

The utilization of multi-spectral data is increasing in Naval METOC. Although the utility of satellite-sensed ocean color data for Naval operations has been known for some time, the availability of real-time data has been the limiting factor. The SeaWiFS sensor on Orbview-2 has provided the consistent data to implement ocean color into operations. Recently transitioned from R&D by NRL Stennis Space Center to NAVO, Figure 5 shows a chlorophyll product, which along with water clarity/visibility is now available for METOC support of Naval expeditionary, special, and mine warfare operations.

SeaWiFS is also showing promise in Meteorology in detecting sand/dust/aerosols. In regions prone to major sand/dust events, the impact on Naval operations is severe, and forecasting is challenging. Although the once per day frequency is insufficient, the clarity with which multi-spectral data depicts these events makes it a useful supplement to other analytical and forecasting tools. The cover of this volume depicts a sand/dust event which is about to accompany frontal passage on the Iberian peninsula. The sand/dust was entrained into the mid-latitude system beginning with easterly surface winds off of North Africa.

8. COMMERCIAL/HIGH-RES APPLICATIONS

The arrival of commercial high-resolution imagery has brought new capability to efforts by NAVO's Warfighting Support Center (WSC) to support DoD customers in describing the ocean environment, particularly in the littorals. The latest generation of commercial satellites with a resolution of 1 m add to the existing usage of sensors such as Landsat. Figure 6 is a product of the WSC which uses imagery as an "anchor" for providing littoral oceanographic data pertinent to Navy and USMC operations.

9. SUMMARY

The Navy and Marine Corps extensively use satellite data in operational METOC analysis and forecasting efforts, and are increasingly reliant upon satellites for gains in forecasting accuracy and quality of METOC support. We are engaged in strong partnerships, leveraging the expertise areas of our SPP partners, acedemia and industry.

Although the Navy maintains a focused R&D capability in critical areas of remote sensing, opportunities do exist for other researchers to contribute and participate in areas which can eventually lead to operational usage. Collaboration by other government, academic and commercial scientists with Navy labs such as NRL Monterey and with the Naval Postgraduate School have lead to many of the recent advancements in operational remote sensing. NRL's sponsor, the Office of Naval Research, solicits proposals from the research community in specific areas of interest, information available from the ONR homepage at http://www.onr.navy.mil. The CRADA process provides a path for commercial developers and vendors to partner with Navy. Finally, the Shared Processing Program maintains Algorithm Research Panels (ARP) in Passive Microwave, Altimetry, Satellite Soundings and Multi-Channel Sea Surface Temperature. Proposed algorithms or improvements in these areas may be submitted to the appropriate ARP chair.

10. REFERENCES

Colton, M.C. and G.A. Poe, 1994: Shared Processing Program, Defense Meteorological Satellite Program, Special Sensor Microwave /Imager Algorithm Symposium, June 8-10, 1993. *Bull. Amer. Meteor. Soc.* **75**, 1663-1669.

Cornelius, C.J., J.L Haferman, and C.E. Skupniewicz, 2000: Operational Satellite Data Processing at Fleet Numerical Meteorology and Oceanography Center. *Tenth Conference on*

Satellite Meteorology and Oceanography, 9-14 January, Long Beach, CA, 40-43.

Gineris, D., C. Bertoia, M.R. Keller, L.K. Soh and C. Tsatsoulis, 2000: Operational Evaluation of a Knowledge-Based Sea Ice Classification System, *Proceedings of a Workshop on Mapping and Archiving of Sea Ice Data – The Expanded role of Radar*, Ottawa, Canada, May 2-4, 2000, World Meteorological Organization/TD No. 1027, 173-178.

Hawkins, J.D., T.F. Lee, J. Turk and K. Richardson, 2000: U.S. Navy Satellite Meterology Applications – R&D to Applications. *Tenth Conference on Satellite Meteorology and Oceanography*, 9-14 January, Long Beach, CA, 4-7.

____, ____, ____, C. Sampson, J. Dent, and K. Richardson, 2001: Real-Time Internet Distribution of Satellite Products for Tropical Cyclone Reconnaissance. *Bull. Amer. Meteor. Soc.* **82**, 567-578.

Hurlburt, H.E., R.C. Rhodes, C.N. Barron, E.J. Metzger, O.M. Smedstad, and J-F. Cayula, 2000: A Feasibility Demonstration of Ocean Model Eddy-Resolving Nowcast/Forecast Skill Using Satellite Altimter Data. Naval Research Laboratory MR/7320-00-8235, 23 pp. [Available from the Naval Research Laboratory Detachment, Stennis Space Center, MS 39522].

Rigney, J.P, R. Bouchard, C. Diamond, D. Bershire, D. L'Heureux, D. T. Conlee, M. C. Colton, and R.L. Crout, 1997: Oceanography from Space in Support of Naval Operations. *Marine Tech. Soc. Journal*, **31**, 31-40.

St. Germain, K.M. and P.W. Gaiser, 2000: Space Borne Polarimetric Microwave Radiometry And The Coriolis WindSat System, *IEEE Aerospace Conference Proceedings*, **5**,159-164.

Velden, S.C., C.M Hayden, S. J. Nieman, W.P. Menzel, S. Wanzong, and J.S. Goerss, 1997: Upper-Tropospheric Winds Derived from Geostationary Satellite Water Vapor Observations. *Bull. Amer. Meteor. Soc.* **78**, 173-194.

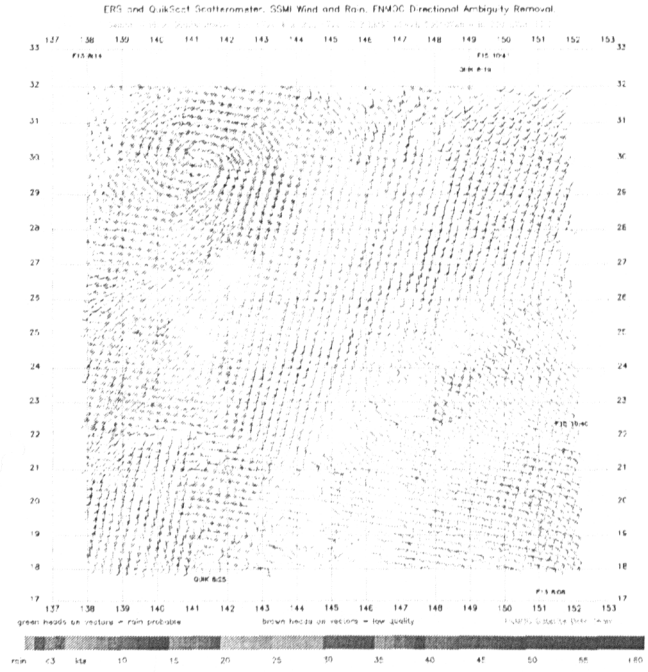

FIG. 3. Web-based, interactive surface wind product from FNMOC, zoomed to reveal full resolution data.

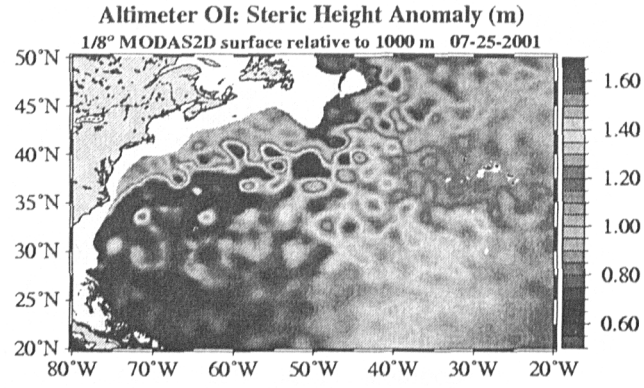

FIG. 4. MODAS Sea Surface Height (SSH) residuals product derived from altimetry.

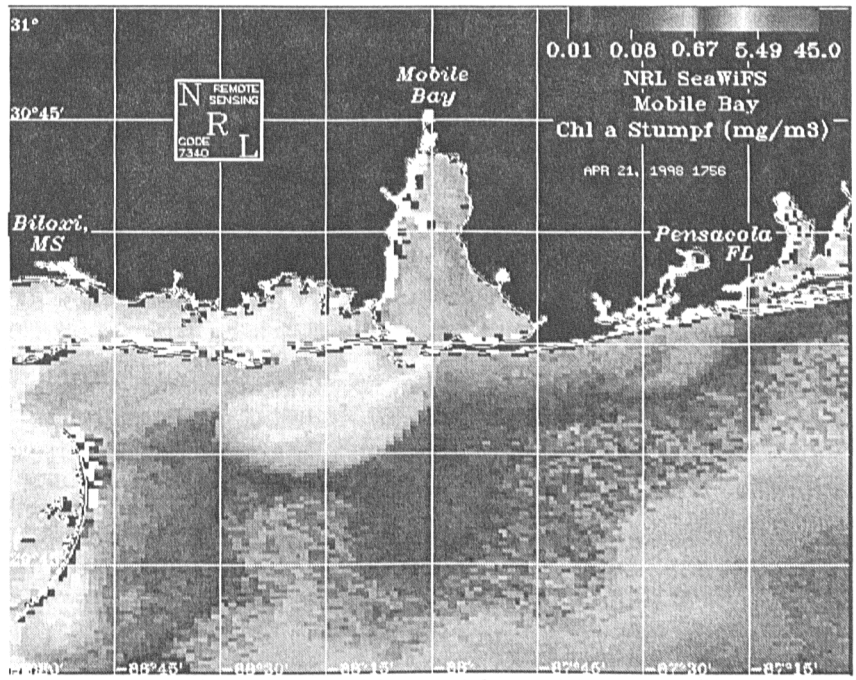

FIG. 5. SeaWiFS-derived Chlorophyll Concentration product from NRL/NAVO. SeaWiFS data used with permission of ORBIMAGE.

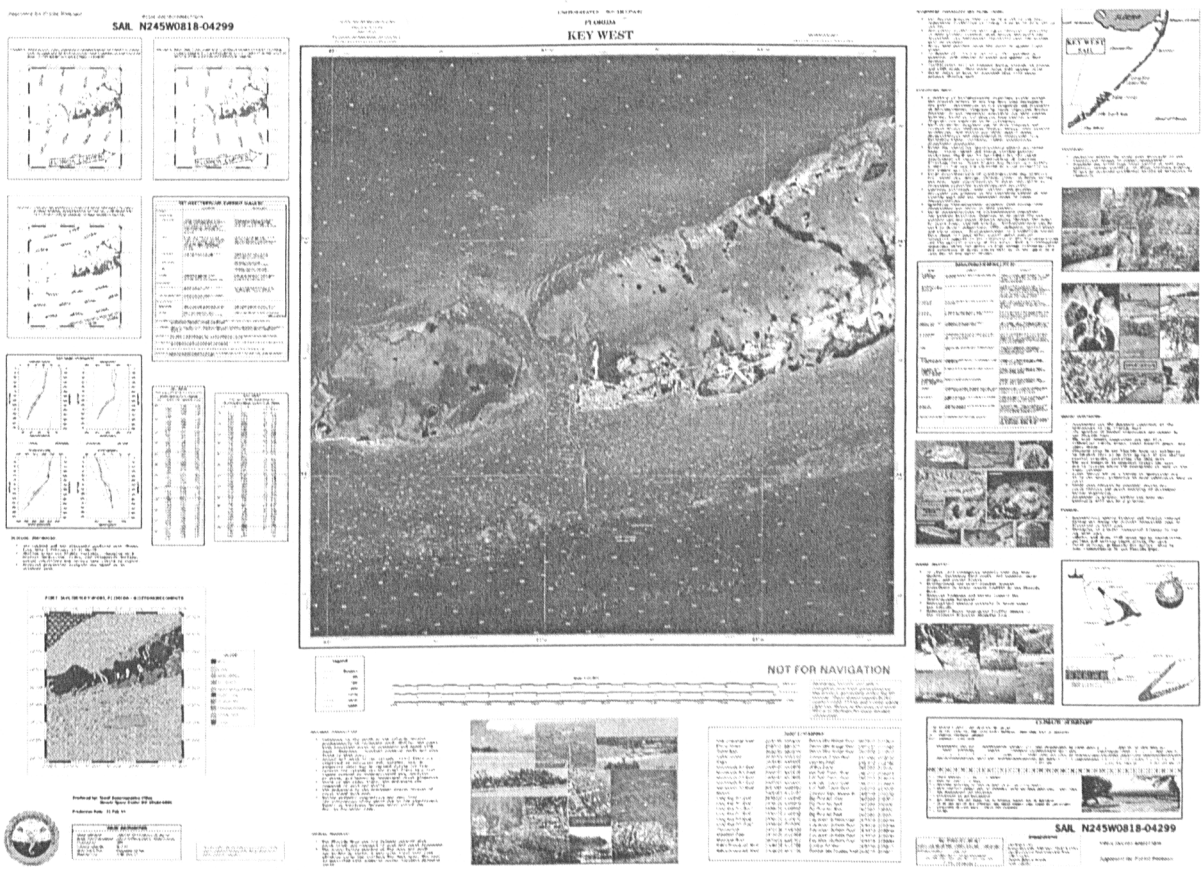

FIG. 6. NAVO High Resolution Commercial Imagery Product: Special Analyzed Image Littoral (SAIL)

3.6 Some New Operational Applications of MetSat Observations

By
Tom Vonder Haar
University Distinguished Professor of Atmospheric Science
Colorado State University and the Cooperative Institute for Research in the Atmosphere

Abstract

This paper will discuss a number of new satellite products recently available to forecasters and weather forecast centers as well as some presently in a testing mode. Advent of increased operational satellite microwave sounding capabilities has been a key factor in some of the new products. Web access to near real-time products from research satellites also has opened a new segment of satellite data applications.

The new satellite application products mentioned will include: Precipitation Estimates including Tropical Rainfall Potential; Total Column Water Vapor; Fog and Day/Night Albedo Products; Severe Weather Indices; Asynchronous Stereo Cloud Drift Winds; Surface Wind Vectors over the ocean; and others. In addition, development and test of a new suite of satellite data assimilation products will be mentioned.

Presentation

The oral presentation of this paper will highlight several examples of new operational applications drawn from the poster presentations of this Session of the Conference to foster additional discussion. In addition, we will recognize recent recipients of the David Johnson Award for Innovative Use of Earth Observation Satellite Data and briefly note the satellite applications they have developed.

P3.1 UW-CIMSS SATELLITE WINDS ALGORITHM

Gail A. Dengel*, C.S. Velden, T.L. Olander, D.A. Santek, and D.R. Stettner
CIMSS/Univ. of Wisconsin, Madison, WI 53706.

1. INTRODUCTION

Tracking cloud motions from geostationary meteorological satellites has become an important source of global tropospheric wind information. UW-CIMSS (University of Wisconsin-Madison, Cooperative Institute for Meteorological Satellite Studies) has pioneered the development of cloud and water vapor tracking algorithms, which have evolved from subjective, labor-intensive processes into a fully automated system. Today, winds from this system are produced operationally by NOAA NESDIS (National Environmental Satellite, Data, and Information Service) and the U.S. Air Force from GOES, GMS and Meteosat satellites (Velden et al. 1997, 1998; Nieman et al. 1997). This flexible software package can be used in applications and environments ranging from small research projects to large operational facilities, and algorithm derivatives are employed at operational and research satellite data centers around the world. Future development will be directed toward independence of the processing platform (computer host and operating system) and user-friendly interfaces, with a long range goal of standardizing international satellite feature-tracked winds production.

2. CURRENT STATUS

The UW-CIMSS winds algorithm currently exists in two forms; a mature 'operational' version written in Fortran, and a research and development version written in the C programming language. Both run under the Unix operating system. The C version is undergoing a rigorous testing and verification procedure, and it will eventually supplant the Fortran version (Olander, 2001).

Processing cloud and water vapor motions from successive satellite images into wind vectors is divided into modules. These include automated satellite image registration, initial target identification, calculation of target displacement vectors, wind vector production, quality control and editing.

*Corresponding author address: Gail Dengel, UW-CIMSS, 1225 West Dayton St., Madison, WI 53706; email: gaild@ssec.wisc.edu

Registration is performed using an automated routine that employs cross correlation and minimum lag coefficient analysis at selected landmark points in the imagery to ensure proper alignment. In the targeting step, water vapor gradients or cloud edges are identified and assigned initial pressure heights. The vector derivation step computes direction and speed of target displacements between image pairs, which are then used to calculate time-averaged wind vectors. Three-dimensional postprocessing and quality assessment is performed on a data set containing vectors from all vertical levels. A series of checks are applied to identify misanalyzed vectors, adjust height assignments and flag anomalies. Remaining vectors are tagged with quality indicators based on their fit to the rest of the vector field. Recursive filter analysis is applied in the final editing step.

Input data requirements include a time series of three to five sequential satellite images for target tracking, images used for height assignment, and temperature, pressure and wind fields from numerical model grids. Images must be in McIDAS (Man computer Interactive Data Access System) Area format and the model data in GRIB format. The algorithm currently handles data from GOES, Meteosat and GMS, from visible, infrared, and water vapor sensors. Additional satellites and sensors can be incorporated when suitable geolocation (image line/element to earth latitude/longitude conversions) and calibration (raw count to brightness temperature conversion) modules are produced. Currently, the derived wind vector fields can be output in three file formats: McIDAS MD, ASCII text, and BUFR.

The Fortran version is currently in use at UW-CIMSS and NESDIS. Real-time wind sets are produced routinely from GOES-8 and -10, GMS, and Meteosat-5 and -7, incorporating data from visible, infrared, and water vapor bands. An example of a global composite upper tropospheric wind set comprising vectors from all five satellites is shown below.

In collaboration with the U.S. Navy and Air Force, the C version is being transitioned into operational use, and an additional cooperative effort is in progress with the Australian Bureau of Meteorology.

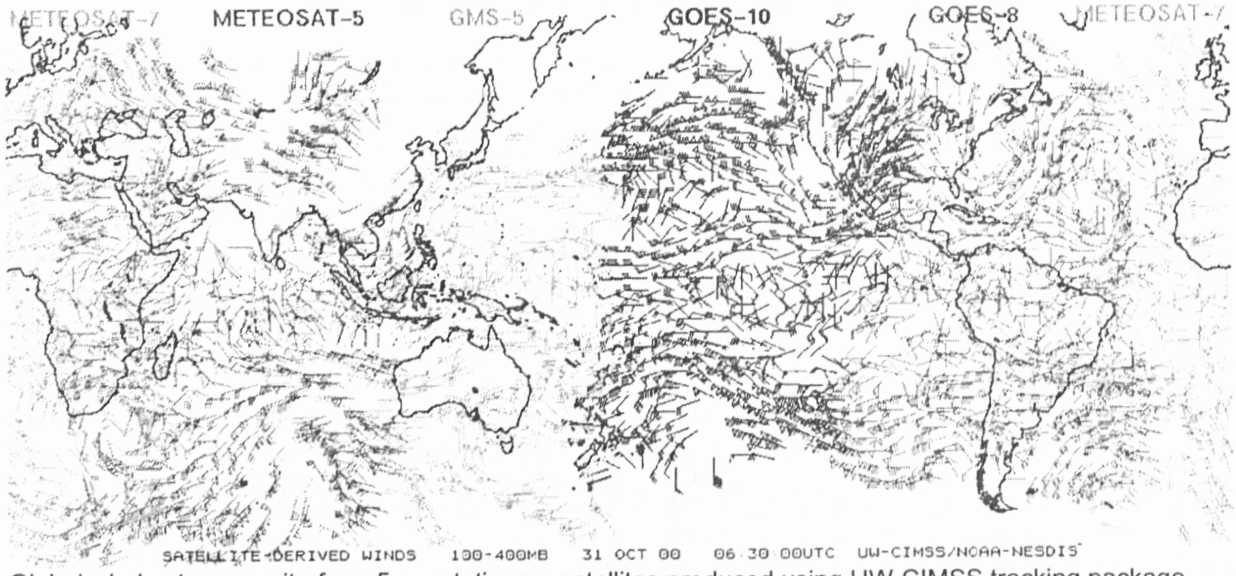

Global wind set composite from 5 geostationary satellites produced using UW-CIMSS tracking package.

Real-time field experiments provide excellent opportunities for testing the limits of the algorithm's capabilities. Most recently, this system played an important role in providing high-resolution winds from GOES rapid-scan imagery in support of *GWINDEX* (*G*OES rapid scan *WIND*s *EX*periment) and *CAMEX*-4 (*C*onvection *A*nd *M*oisture *EX*periment) (See paper by Velden et al., this volume). The following image is from the GOES-10 GWINDEX data set for 1800 UTC, 25 February 2001.

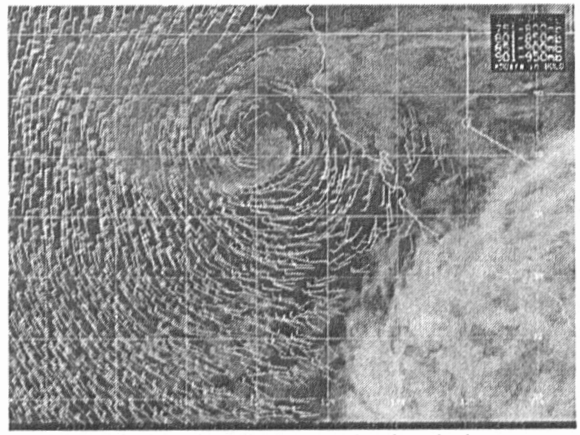
High-resolution, lower-tropospheric winds.

In addition to field experiments, the UW-CIMSS algorithm supports developing research projects and quasi-operational application demonstrations. For example, datasets are routinely derived at UW-CIMSS over tropical regions in support of tropical cyclone analysis at the National Hurricane Center and the Joint Typhoon Warning Center. An example of winds derived from GOES-8 during Hurricane Floyd in 1999 is shown below.

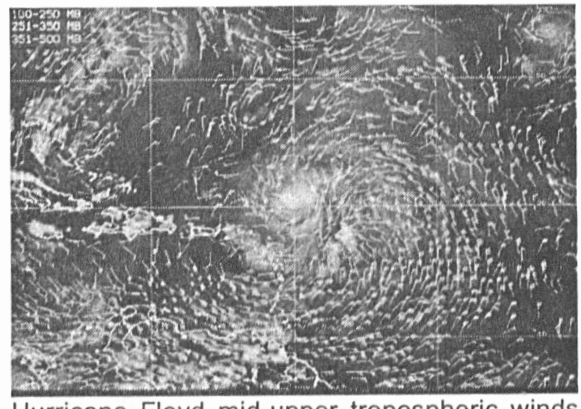

Hurricane Floyd mid-upper tropospheric winds derived from GOES-8 at 2100 UTC, 10 September 1999.

3. FUTURE OUTLOOK

Our vision is to create a user-friendly, state-of-the-art winds derivation system that can be universally used on different platforms and with any available satellite imagery. UW-CIMSS scientists play a prominent role in the WMO International Satellite Winds Working Group. It is a goal of this group to advance and standardize satellite feature-tracked winds production from all global satellite data centers. It is with this goal in mind that we plan to focus our future efforts, which include three primary themes.

The first is a continuation of research and development of the C version for major data production, with emphasis on operating platform/environment independence. Algorithm upgrades will be an ongoing process, and increased efficiency will reduce system requirements and processing time. Modular design enhancement will better facilitate the addition of new satellites and sensors, and generic data input and output formats will reduce dependency on McIDAS data structures. It is our intention to make the code available to the global user community.

The second development thread will be an optional winds algorithm add-on to McIDAS. This version will be more suitable for small-scale winds production or individual users. It will be available through the McIDAS User's Group (http://www.ssec.wisc.edu/mug/mug.html). A graphical user interface consistent with the McIDAS operating environment will be provided.

The third development path comprises research efforts aimed at taking feature-tracked winds production into new areas. These include deriving winds from new instruments currently in flight and planned in the near future. For example, preliminary experiments with successive-pass imagery over the polar regions from the MODIS instrument onboard the EOS (Earth Observing System) Terra polar-orbiting satellite are providing encouraging results (see paper by Key et al., this volume). Hyperspectral imaging from space-borne geostationary interferometers is just around the corner. The GIFTS (Geostationary Imaging Fourier Transform Spectrometer) instrument will provide hyperspectral images, multi-channel averaged 'superchannels' and moisture product retrievals. To be ready for these data, the UW-CIMSS algorithm is being adapted to run on simulated GIFTS datasets as part of a funded effort by NASA

4. REFERENCES

Nieman, S.J., J. Schmetz, and W.P. Menzel, D. Gray, S. Wanzong, C.S. Velden, and J. Daniels, 1997: Fully automated cloud-drift winds in NESDIS operations. Bull. Amer. Meteor. Soc., 78, 1121 1134.

Olander, T.L., 2001: UW-CIMSS satellite-derived wind algorithm user's guide. 83 pp. [Available from The Cooperative Institute for Meteorological Satellite Studies, Space Science and Engineering Center, University of Wisconsin-Madison, 1225 West Dayton St., Madison, WI 53706]

Velden, C.S., C.M. Hayden, S.J. Nieman, W.P. Menzel, S. Wanzong, and J.S. Goerss, 1997: Upper-tropospheric winds derived from geostationary satellite water vapor observations. Bull. Amer. Meteor. Soc., 78, 173-195.

Velden, C.S., T.L. Olander, and S. Wanzong, 1998: The impact of multispectral GOES-8 wind information on Atlantic tropical cyclone track forecasts in 1995. Part I: Dataset methodology, description, and case analysis. Mon. Wea. Rev., 5, 1202-1218.

5. ACKNOWLEDGMENTS

The authors wish to acknowledge the many UW-SSEC and CIMSS programmers/developers whom contributed to this state-of-the-art algorithm over the 20+ years of the effort. Jaime Daniels, Wayne Bresky and Ricky Irving contributed to the operational version at NOAA/NESDIS. Recent collaborations with Jeff Hawkins of NRL-MRY, Chuck Skupniewicz of FNMOC and Ken Holmlund of EUMETSAT have led to many advancements and proliferation of the code into the user community. Financial aid from NOAA/NESDIS (Grant NA07EC0676) and NRL (Grants N00173-98-C-6011 and N00173-01-C-2024) is responsible for supporting the research advances, and transition to operations.

P3.2 GWINDEX - GOES RAPID-SCAN *WINDS EX*PERIMENT: APPLICATIONS FOR WEST COAST FORECASTING

Chris Velden* and Dave Stettner
UW-CIMSS, Madison, Wisconsin

Jaime Daniels and Wayne Bresky
NOAA/NESDIS

1. INTRODUCTION

GWINDEX was carried out in January through March of 2001. It was designed to demonstrate the improvement that could be gained in both the quantity and quality of satellite-derived cloud-motion winds using 7.5 minute interval rapid-scan visible (0.65 μm channel, VIS) and infrared (10.7 μm channel, IR) imagery from GOES-10. The primary goal of this experiment was to provide improved wind information over the data sparse northeast Pacific Ocean. Data and mission planning support was also provided to the coincident Pacific Landfalling Jets Experiment (PACJET).

The datasets were evaluated in real time by NWS forecasters, and assessed through impact studies on the Rapid Update Cycle (RUC) model short-term forecasts. A brief review of the satellite wind derivation process used is presented in section 2. Details of the experimental set-up can be found in section 3. A preliminary assessment of the impacts made by the satellite wind products is presented in section 4.

2. BACKGROUND

Automated wind extraction algorithms developed at the Cooperative Institute for Meteorological Satellite Studies (CIMSS) employ a series of sequential geostationary satellite images to generate three dimensional wind products (Nieman et al. 1996; Velden et al. 1998). Cloud-motion vectors calculated from IR imagery can be produced in cloud covered regions at any time of the day. During daylight hours, cloud elements can be tracked in high resolution VIS images. The water vapor sensitive 6.7 μm channel (WV) images can be used to produce motion vectors at upper levels in both cloud and clear scenes (Velden et al. 1997).

2.1 Basic Wind Vector Processing

Cloud or water vapor features are tracked across three consecutive satellite images. Traditionally, these images are 15 to 30 minutes apart. The process begins by subjecting the image triplet to a careful registration check. Registration is a measure of navigation consistency from image to image. Images with inconsistent navigation would result in artificial tracking errors.

Next, the middle image is used for the selection of tracking targets. These targets are identified by bidirectional brightness temperature gradients calculated around each pixel. Targets are selected if they exceed minimum threshold values and pass a filtering process.

Once targets are identified, initial height assignments are made. Each target is assigned to a pressure level using one of several techniques (Nieman et al. 1993). The initial assignment method used depends on the image channel.

Displacement vectors can then be calculated from the target (middle) image; one forward to the final image and one backward to the initial image. Coherent pattern matches are sought in the non-targeted images and correlated with the target. The two resulting vectors must meet empirically determined consistency thresholds to eliminate excessive accelerations. If they pass, the two vectors are averaged to create a final vector. The trackability of cloud features is highly dependent on the tracking interval. It has been shown that more frequent imaging enhances the reliability of the automated correlation tracking techniques.

At this point the wind vector field is run through automated quality control procedures designed to reassess vector height assignments, edit out vectors that are in obvious error, and provide end users with discretionary vector quality flags (Velden et al. 1997; Holmlund et al. 2001).

* Corresponding author: Chris Velden, UW-CIMSS, 1225 West Dayton St., Madison, Wis., 53706. Chrisv@ssec.wisc.edu

2.2 Impacts of Satellite-Derived Winds

High-density satellite-derived winds from multispectral imagery are produced at operational weather centers around the globe. NOAA/NESDIS derives datasets from two operational GOES satellites on a 3-hourly basis. These winds cover much of the Western Hemisphere, and are ingested into NCEP and US Navy operational models on a routine basis. It has been shown these data can have a significant impact on numerical weather prediction (Velden et al. 1997, 1998; Goerss et al. 1998; Soden and Velden 2001; Holmlund et al. 2001; Xiao et al. 2001).

3. GWINDEX

3.1 Experiment Description

Beginning in January 2001, NOAA implemented a special (and temporary) scanning schedule for GOES-10 that allowed one extra image each hour over the eastern North Pacific region (Fig. 1). This extra image resulted in a set of three successive images approximately 7.5 minutes apart encompassing the same geographic area (with daily exceptions for routine satellite maintenance at 0400, 1600, and 2200 UTC). This extra Pacific Ocean sector image was delivered through March 2001. Special GWINDEX wind fields were limited to the region displayed in Fig. 1, but only north to 60 degrees latitude and from 115 to 175 degrees west longitude.

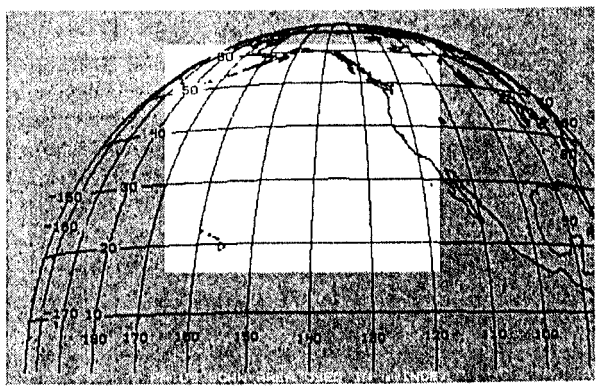

Figure1: GWINDEX coverage (unshaded region).

During the GWINDEX period, satellite derived wind sets were generated by CIMSS on an hourly basis using the 7.5 minute interval VIS and IR image triplets. The VIS winds were created only from 1500 UTC through 0300 UTC, IR winds could be run throughout the day. A combined data set in ASCII text format was made available for RUC model runs and forecaster use within an hour of the nominal time. WV winds were produced at NOAA/NESDIS using one-hour interval image triplets. The WV product spatial coverage was coincident with the VIS and IR products.

Within two hours of each processing time, the GWINDEX products were available for use by forecasters on a CIMSS web site. Very high-density vector plots each hour were focused on California and on Washington/Oregon providing close-ups on landfalling systems for the PACJET users. Three-hourly lower resolution plots provided synoptic scale perspectives for the entire northeastern Pacific Ocean region.

During GWINDEX, the most recent day's worth of products was displayed, with previous datasets stored in an accessible on-line archive. Currently, all plots generated during GWINDEX are available from this archive at http://gale.ssec.wisc.edu/.

3.2 GWINDEX Product Examples

An example of the PACJET regional upper tropospheric winds plot from 2300 UTC on 18 March, 2001 is depicted in Fig. 2. Winds included in this plot are derived from both GWINDEX rapid-scan IR and one-hour interval WV. The plotted wind field has been decluttered (vector filtering was used) to allow better interpretation of the data.

The lower tropospheric winds for the same location and time are shown in Fig. 3. Since this time period was during daylight hours, most of the winds shown were derived from rapid-scan VIS images. Some rapid-scan IR winds are also included.

4. SUMMARY AND PRELIMINARY ASSESSMENT

Initial feedback on the impact of the GWINDEX datasets has been positive. The PACJET community used the data to help in mission planning and will evaluate the data with in situ observations taken during the experiment. An initial assessment on the impact of the datasets on RUC forecasts has been done (Weygandt et al. 2001). Further data assimilation experiments are underway or planned (Mecikalski et al. 2001). A statistical analysis is being performed, but qualitative indications are that the rapid-scan data are coherent and the quantities produced vastly exceed those produced routinely using traditional image intervals.

A second experiment was run in the summer/fall of 2001. This exercise employed GOES-8 rapid-.

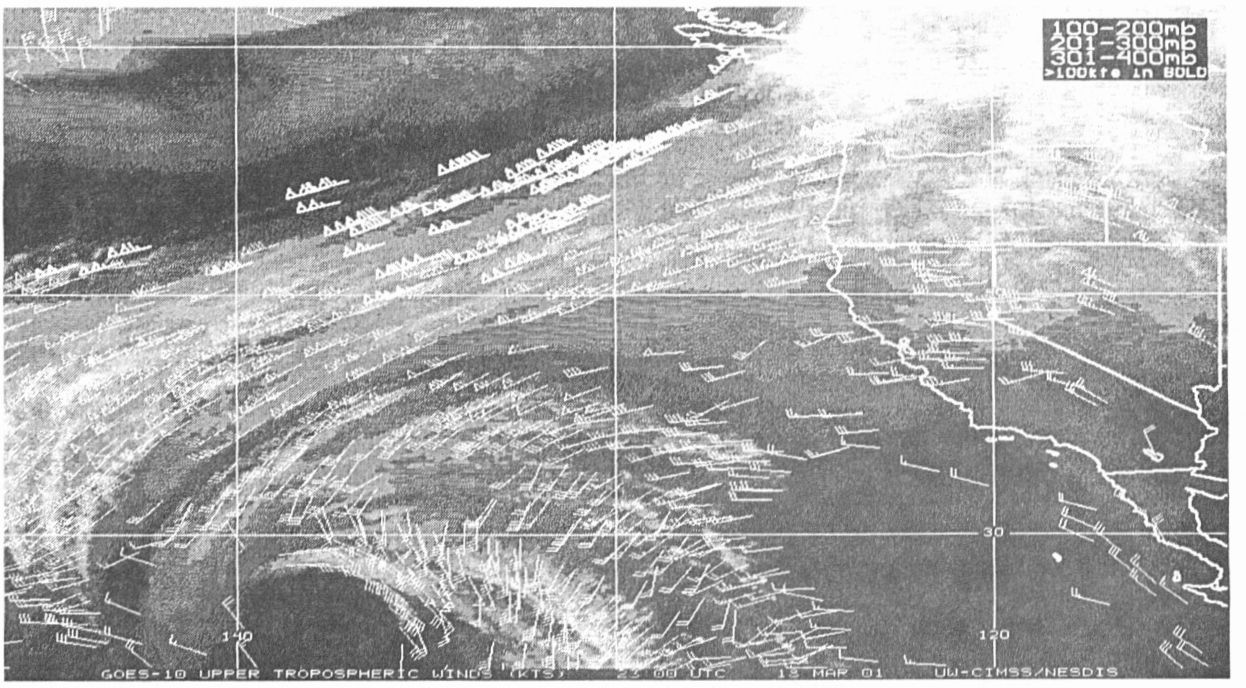

Figure 2: Upper-tropospheric wind plot over the GWINDEX region at 2300 UTC on 18 March, 2001. Vectors have been filtered for plotting purposes.

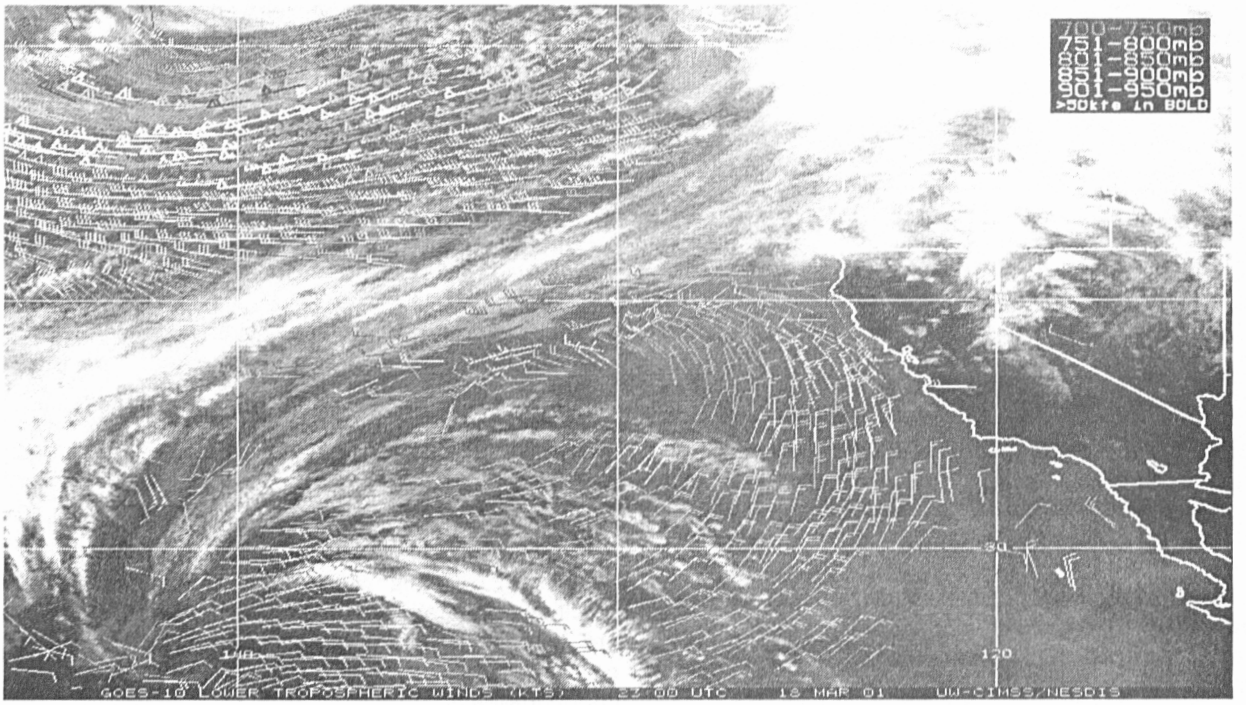

Figure 3: Same as Fig. 2, except for lower-troposphere.

scan schedules to observe Atlantic hurricane activity. It is hoped that these rapid scan demonstrations will lead to permanent operational 7.5 minute rapid scan schedules for GOES.

5. REFERENCES

Goerss, J., C.S. Velden and J. Hawkins, 1998: The impact of multispectral GOES-8 wind information on Atlantic tropical cyclone track forecasts in 1995. Part 2: NOGAPS forecasts. Mon. Wea. Rev, 126, 1219-1227.

Holmlund, K., C.S. Velden and M. Rohn, 2001: Enhanced quality control applied to high-density satellite-derived winds. Accepted in Mon. Wea. Rev.

Mecikalski, J., C. Velden, M. Morgan, D. Kleist, D. Stettner, K. Goodstein and B. Baum: Assimilating satellite wind, moisture and temperature for numerical forecast improvements during the PACJET experiment. 14th Conf. On Numerical Weather Prediction, Ft. Lauderdale, FL, Aug., 2001.

Nieman, S., W.P. Menzel, C.M. Hayden, S. Wanzong and C.S. Velden: Upgrades to the NOAA/NESDIS automated satellite-motion winds system. 8th Conf. on Satellite Meteorology, Atlanta, GA, Feb., 1996.

Soden, B., C.S. Velden and B. Tuleya, 2001: Impact of satellite winds on experimental GFDL hurricane forecasts. Accepted in Mon. Wea. Rev.

Velden, C.S., C.M. Hayden, S. Nieman, W.P. Menzel, S. Wanzong and J. Goerss, 1997: Upper-tropospheric winds derived from geostationary satellite water vapor observations. Bull. Amer. Meteor. Soc., 78, 173-195.

Velden, C.S., T.L. Olander and S. Wanzong, 1998: The impact of multispectral GOES-8 wind information on Atlantic tropical cyclone track forecasts in 1995. Part 1: Dataset methodology, description and case analysis. Mon. Wea. Rev., 126, 1202-1218.

Weygandt, S., S. Benjamin and C. Velden: Assimilation of rapid-scan satellite cloud motion vectors into the RUC model in support of the PACJET experiment. 14th Conf. On Numerical Weather Prediction, Ft. Lauderdale, FL, Aug., 2001.

Xiao, Q., X. Zou, M. Pondeca, M. Shapiro and C.S. Velden, 2001: Impact of GMS-5 and GOES-9 satellite-derived winds on the prediction of a mid-Pacific-Ocean Cyclone. Submitted to Mon. Wea. Rev.

Acknowledgements

The authors would like to express gratitude to NOAA/NESDIS for promoting the research on rapid-scan winds by allowing flexible scheduling of GOES imagery during the GWINDEX period. Special thanks go to Tom Renkevens, Jaime Daniels and James Heil. We also want to acknowledge Marty Ralph of NOAA/ETL for his enthusiasm on GWINDEX in support of PACJET. Financial support for this effort: NOAA grant NA67EC0100.

P3.3 **VALIDATION OF GOES CLEAR-AIR WATER VAPOR WINDS**

[1]Jaime Daniels* and [2]Wayne Bresky

[1]NOAA/NESDIS/Office of Research & Applications/Atmospheric Research & Applications Division
Camp Springs, Maryland

[2]Raytheon Information Technology and Services Company
Lanham, Maryland

1. Introduction

Wind vector fields, derived from consecutive water vapor (WV) imagery, are now considered one of the core operational satellite products at the National Oceanic and Atmospheric Administration (NOAA)/National Environmental Satellite Data and Information Service (NESDIS). NOAA/NESDIS has been deriving WV motion winds from the 6.7um channel of the GOES-I/M series of satellites in an automated way since 1995. The strength of the WV wind product lies in the fact that it provides coverage in both cloudy and cloud-free environments. The ability to track pure WV structures in clear air provides satellite wind estimates over large areas where conventional cloud-drift winds do not. Furthermore, these clear-air WV winds can provide significantly improved coverage in the middle troposphere where cloud tracers are scarce and often times difficult to track.

The major users of the WV wind products range from the operational analysts and forecasters, who utilize them in a qualitative way during the forecast process, to the Numerical Weather Prediction (NWP) community who make quantitative use of them in the data assimilation process. Their use in NWP is vital, particularly over oceanic areas, for defining the initial state of the atmosphere. Numerous improvements in NWP have been documented as a result of simulating the GOES WV winds. Goerss et al., 1998 and Velden, et al, 1998b, for example, have demonstrated modest improvements in Atlantic tropical cyclone track forecasts during 1995 when GOES cloud-drift and water vapor winds were introduced into the Navy Operational Global Atmospheric Prediction System (NOGAPS).

The GOES cloud-top WV winds are currently being assimilated into the operational regional and global NWP models at the National Centers for Environmental Prediction (NCEP)/Environmental Modeling Center (EMC). The clear-sky water vapor winds are not, however. A major obstacle impeding the use of these winds in data assimilation is the confidence in the heights assigned to these pure WV structures and determining what this motion represents. What are the error characteristics of the height assignments of these pure WV structures? Is the measured motion of these pure WV structures representative of motion at a single level or a layer? Since the radiometric information measured in these cases is emanating from a finite layer, the motion being tracked is almost certainly representative over a layer. But how deep of a layer? How well can these features be tracked in time? Will the answers to these questions explain the characteristic slow speed bias observed in the clear air WV winds, particularly at middle levels of the atmosphere?

The goal of this study is to answer these questions and test new approaches which will, ultimately, improve the quality of the GOES WV winds, particularly under clear sky conditions. Two items which are focused on include feature tracking and height assignment, since these two items can be large contributors to errors introduced to the WV wind product. The errors associated with each of these items will be discussed and characterized in this paper. New approaches aimed at minimizing both of these errors will be presented. In Section 2 we summarize the relevant characteristics of the GOES 6.7um WV channel. In Section 3, we address the feature tracking technique used at NOAA/NESDIS for estimating motion from WV features and present results which demonstrate the optimal image time interval to use when tracking pure WV structures. In Section 4, we address the height assignment problem for clear-sky WV targets. A new height assignment algorithm, which makes use of the local 6.7um contribution weighting function (CWF), is tested and validated. Results are presented which characterize the height assignment errors associated with this new height assignment algorithm as well as those currently being used operationally at NOAA/NESDIS. This information should prove useful to the NWP community for assimilating clear-air WV winds into their data assimilation systems.

2. GOES 6.7um Channel Characteristics

The GOES 6.7μm channel, which has a resolution of 2.3km (E/W) x 8km (N/S), responds to mid- and upper-level WV and clouds. Because organized atmospheric disturbances usually have large regions of upward (or downward) motion and consequent moistening (or drying), the water vapor data can often be used to locate and define synoptic features such as shortwave troughs, ridges, and jet streams. When animated, this imagery shows atmospheric circulation not always observed in the visible or infrared imagery. This is especially true in areas which are void of clouds where moist and dry air masses can be clearly identified.

In cloud-free regimes, gradients observed in this imagery are indicative of moisture gradients present in the mid to

*Corresponding author address:
Jaime Daniels, E/RA2
NOAA/NESDIS/Office of Research & Applications
5200 Auth Road, Room 601
Camp Springs, MD 20746

upper troposphere. These moisture gradients, or pure WV structures, are often conserved through time. This behavior allows for these features to be tracked in time in order to arrive at an estimate of wind motion.

It is clear that a significant amount of information regarding atmospheric motion can be extracted from the 6.7um imagery. However, the additional piece of information which is needed to further enhance the utility of these data is the height associated with the phenomena being observed. The CWF for the WV channel, using Standard Atmosphere temperature and moisture profiles, is shown in Figure 1. This figure shows that the radiance measured by the 6.7um channel arises primarily from an atmospheric layer between 200mb and 600mb. Where the peak of the CWF occurs will depend on several factors which include: the presence of clouds, the vertical distribution of temperature and moisture, and the viewing angle of the instrument.

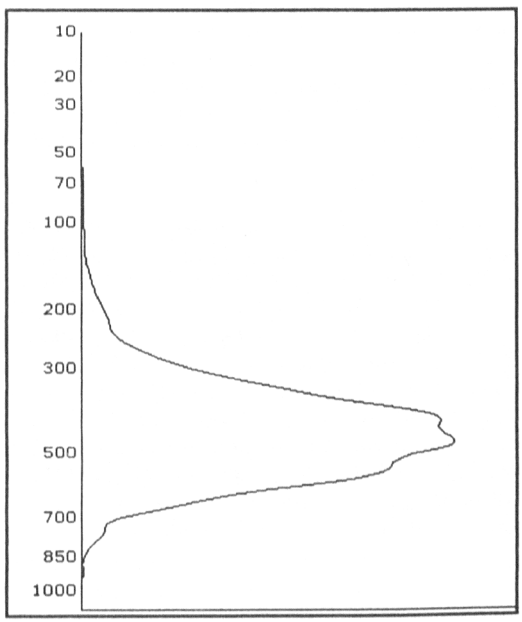

Figure 1. Contribution weight function for GOES-8 water vapor channel for the standard atmosphere.

Further discussion of the CWF, its use in defining the heights of pure WV structures, and the impact it has on the quality of the clear-air WV winds is presented in Section 4.

3. Water Vapor Feature Tracking: Selecting the Appropriate Image Time Interval

In the operational NESDIS winds processing system, feature identification and tracking are performed via automated techniques (Nieman et al, 1997, Velden et al, 1997). WV targets are selected, from the middle image of an image triplet, by evaluating bidirectional gradients surrounding each pixel in the 15x15 pixel target array and selecting the maximum value. Once selected, heights of the targets are computed. Further discussion on how these heights are assigned will be discussed in the following section. Once the height is assigned, the feature is tracked in the previous image (backward in time) and the subsequent image (forward in time). Feature tracking is achieved by searching for the minimum in the sum of squares of the radiance differences between the target scene and search scenes.

Several factors contribute to tracking errors. These include: resolution of imagery, navigation and registration, low contrast or lack of fine structure in the imagery, and the limited stability of tracers due to non-advective processes. Image resolution and the temporal separation of images used in the feature tracking step are important considerations for deriving high quality wind estimates. The need to have the proper mix of these two variables is well known and documented in previous studies (Jedlovek, 1998).

For the current operational NESDIS WV wind product, the temporal resolution of the images used is 30 minutes. The question is: Is this the optimal time interval to use for clear air WV winds? The coarse resolution (8km) of the water vapor imagery suggests a longer time interval should be used. A longer time interval can be used since the shape of pure WV structures is often more conservative than clouds. Longer time intervals also tend to minimize navigation and registration errors . Several experiments were run where WV winds were generated and validated using 30-minute and 60-minute interval imagery in order to answer the original question.

Figures 2 and 3 show 30-minute and 60-minute GOES-8 clear air WV winds, respectively, over the continental United States on September 26, 2000. A dramatic increase in coverage is observed. Although not shown in these figures, the most dramatic increase is observed at middle levels (400-700mb) of the troposphere where current satellite wind coverage is lacking. Inspection of clear-air WV wind fields (not shown) prior to the final

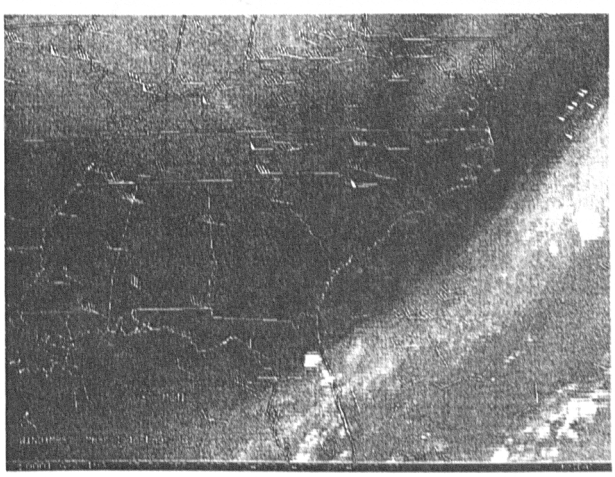

Figure 2. GOES-8 Clear air water vapor winds using ***30-minute*** interval water vapor imagery.

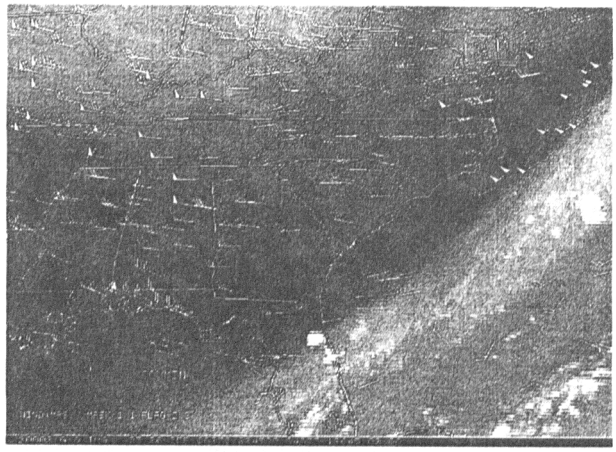

Figure 3. GOES-8 Clear air water vapor winds using ***60-minute*** interval water vapor imagery

quality control step reveals that the resulting wind fields are more coherent when using 60-minute imagery.

Side-by-side (one using 30-minute interval imagery, the other 60-minute) runs of clear-air WV winds were generated over a period of time and compared to radiosonde winds in order quantify the impact of using different time intervals on the quality of the satellite winds. Table 1 shows GOES-8 collocation statistics for the 30-minute and 60-minute clear-air WV winds (before final quality control) for the period March 27 - April 14, 2000. Note the dramatic reduction in the mean vector difference, speed bias, and directional difference. These statistics, together with the increase observed in coverage at middle levels of the troposphere, clearly demonstrate that the clear-air WV wind product can be improved if a 60-minute time interval is used. Use of the 60-minute interval imagery, however, results in about a 30% reduction in the number of cloud-top WV winds generated. This was not deemed as detrimental since coverage in the more cloudy regimes is taken care of by the infrared cloud drift winds.

Statistic	30-minute	60-minute
RMS Difference (m/s)	13.61	10.33
Mean Vector Difference (m/s)	11.27	8.78
St. Deviation (m/s)	7.63	5.44
Speed Bias (m/s)	-3.05	-2.15
|Directional Diff| (deg)	25.62	20.15
Speed (m/s)	20.06	20.55
Sample Size	8816	8816

Table 1. Collocation statistics for pre-quality controlled 30-minute and 60-minute GOES-8 water vapor winds for the period 3/27-4/14/2000. Radiosondes serve as ground truth.

4. Clear-Air Water Vapor Height Assignment: An Error Assessment

Errors in the height assignment can render a perfectly tracked feature useless to the numerical weather prediction (NWP) community. Furthermore, the representativeness of clear-air WV winds at a single level can be questioned since the radiation sensed by the satellite instrument is emitted from a finite layer. This causes problems for the NWP community when attempts are made to assimilate the data and treat it as a single-level value.

In the current NESDIS winds processing system, measured WV radiances from 5x5 fields of view centered about the clear-air feature being tracked are averaged and compared to a collocated model profile. The height of the feature is then assigned where the satellite and model profile temperatures are equivalent. In this study, a new height assignment scheme which assigns tracer height based upon the CWF is developed and validated. For this height assignment method, model temperature and moisture profiles are used to compute the localized CWF. The height is assigned where the normalized CWF equals 0.75. Characterization of vertical errors for this height assignment method, and the current operational method, are shown below.

To characterize the height assignment errors associated with the clear-air WV winds, root mean square error (RMSE) statistics were generated to include comparisons of the clear air WV winds against all levels of collocated radiosondes. One example of this is shown in Figure 4 which illustrates the accuracy of the satellite winds assigned at 412mb using the operational height assignment algorithm. Figure 5 shows the same thing, but for satellite winds assigned to 412mb using the CWF height assignment. In these figures, the RMSE and speed bias (sat-raob) profiles are shown for a sample of collocations from April-September, 2000.

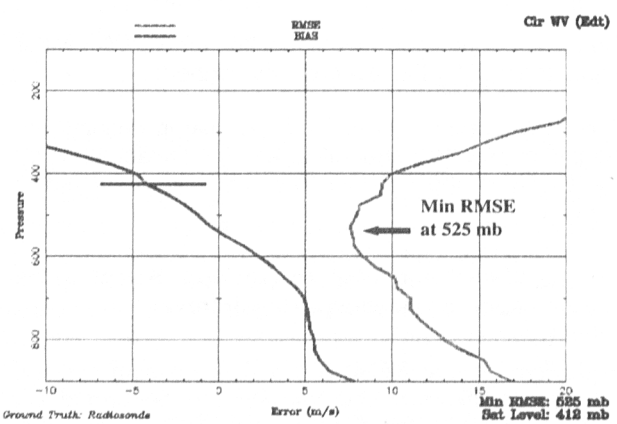

Figure 4. RMSE (m/s) and bias (m/s) for GOES-8 clear air water vapor winds (assigned at 412mb using operational height algorithm) against collocated radiosonde profiles. Bias is satellite - radiosonde.

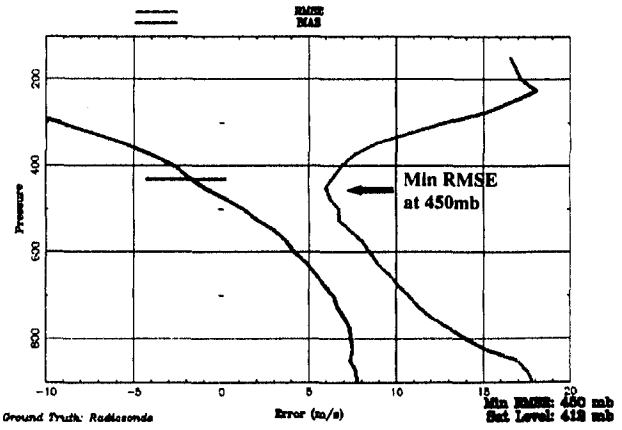

Figure 5. RMSE (m/s) and bias (m/s) for GOES-8 clear air water vapor winds (assigned at 412mb using CWF height algorithm) against collocated radiosonde profiles. Bias is satellite - radiosonde.

Figure 4 illustrates that the clear-air WV winds (those assigned to 412mb in this case) are assigned heights that are too high as the minimum RMSE occurs at 525mb. Note that the magnitude of the RMSE and bias for the water vapor winds at 412mb are about 9m/s and -4 m/s, respectively. Figure 5 shows much better agreement between the assigned CWF heights (again, those assigned to 412mb) and the pressure (450mb) where the minimum RMSE occurs. Note the improved RMSE and bias for the WV winds at 412mb which are about 7m/s and -2m/s, respectively. This kind of analysis was done for WV winds whose height assignments were at other pressures. The statistics for the 412mb WV winds case presented here are somewhat more extreme than the statistics at other pressure levels, but was presented to highlight the potential magnitude of the problem. Table 2 shows the bias (tracer height assignment - pressure where minimum RMSE occurs). Note the reduction in the height assignment bias when heights are assigned via the CWF height assignment method.

Assigned Pressure	Bias (mb) (Opr heights - height of min RMSE)	Bias (mb) (CWF heights - height of min RMSE)
350	-70	-30
375	-55	-5
400-	-60	-20
425	-65	+5
450	-40	+30

Table 2. Height assignment bias (tracer height - pressure where minimum RMSE occurs) for operational heights versus CWF heights.

Improved height assignments will improve the quality and utility of the satellite winds. Table 3 shows collocation statistics for mid-level (400-700mb) clear-air WV winds (9/20-10/3/2000) using the current operational height assignment algorithm and the local CWF height assignment algorithm. Note the significant reduction in RMSE and speed bias when heights are assigned using the CWF. In addition, a significant increase in the sample size at mid-levels is observed as the heights of many clear-air tracers are correctly assigned lower in the atmosphere.

Statistic	Opr Heights	CWF Heights
RMS Difference (m/s)	8.10	6.41
Mean Vector Difference (m/s)	6.77	5.41
St. Deviation (m/s)	4.45	3.43
Speed Bias (m/s)	-4.38	-1.23
IDirectional Diffl (deg)	12.00	11.96
Speed (m/s)	16.53	17.42
Sample Size	493	1051

Table 3. Collocation statistics for GOES-8 clear-air water vapor winds generated using the operational height assignment algorithm and the CWF height algorithm for the period 3/27-4/14/2000. Radiosondes serve as ground truth.

5. Summary

Satellite-derived clear-air WV winds represent a potentially useful source of information for NWP regarding winds in the middle troposphere. At present, they are currently not being assimilated at the major NWP centers. Results have been presented which indicate that significant improvements in these winds can be realized by improving the tracking and height assignment of WV features. Use of WV images separated by 60-minutes improves the overall tracking. Use of the local CWF improves the heights assigned to these pure WV features. Together, an improved product is realized.

6. References

Nieman, S., W.P. Menzel, C. Hayden, D.Gray, S. Wanzong, C. Velden, and J. Daniels, 1997: Fully automated cloud-drift winds in NESDIS operations.*Bull.Amer. Meteor. Soc.*,**78**, 1121-1133.

Velden, C., C. Hayden, S. Nieman, W.P. Menzel, S. Wanzong, and J. Goerss, 1997: Upper-tropospheric winds derived from geostationary satellite water vapor observations. *Bull. Amer. Meteor. Soc.*, **78**, 173-195.

Jedlovek, G. and R. Atkinson, 1998: The Marshall automated wind algorithm: error analysis, quality control, and climate applications. *Proceedings of the Fourth International Winds Workshop*, Saanenmoser, Switzerland, 20-23, October 1998. EUM P 24, Published by EUMETSAT, 247-254.

P3.4 WATER VAPOR WINDS IN VICINITY OF CONVECTION AND WINTER STORMS

Robert M. Rabin[1,2], Jason Brunner[2], Carl Hane[1], John Haynes[3]

NOAA/National Severe Storms Laboratory (NSSL), Norman, OK[1]
Cooperative Institute of Meteorological Satellite Studies (CIMSS), Madison, WI[2]
Cooperative Institute of Mesoscale Meteorological Studies (CIMMS), Norman, OK[3]

1. INTRODUCTION

Forecast applications of water vapor imagery have relied on the subjective interpretation of upper-level features from imagery (Weldon and Holmes, 1991) and comparison with their location and intensity in forecast models. Winds obtained from tracking features in the imagery have been used to improve analyses and forecasts over ocean areas. In order to explore the use of target-tracked winds in nowcasting over land, the water vapor wind tracking algorithm developed at CIMSS (Velden et al., 1997) has been applied to GOES-8 data on an experimental basis at 30-minute intervals in near real-time over much of the U.S. This is about 6 times more frequent than the operational water vapor wind products, which are produced at 3-hourly intervals. More importantly, the amount of wind vector editing has been greatly reduced in order to include larger deviations from the model 'guess' fields. This allows the detection of perturbed flow aloft due to convection and other mesoscale features not correctly captured by models.

This paper examines the upper level wind fields deduced from water vapor imagery for a variety of winter storms and summertime convective events. The analysis technique is briefly described in Section 2. Results are presented in Section 3. The study is summarized in Section 4.

2. METHOD

The first wind tracking techniques required manual interaction with the computer to identify common cloud features in successive satellite images. Wind vectors were then estimated from the displacement of features and the time interval between images. The height of each wind vector was estimated from cloud top temperature (from the window channel radiance) and vertical soundings of temperature. More recently, the process has been automated and expanded to track features in water vapor imagery. The automated technique is described in Veldon et al. (1997). It consists of target identification, height assignment, wind calculation, and editing. The automated technique relies on a background wind field to facilitate the location of common features between successive images. The Navy Operational Global Atmospheric Prediction System (NOGAPS) model (Rosmond, 1992) is used as the background field. By employing a lower resolution model such as the NOGAPS, the addition of higher resolution winds from the satellite is more clearly identifiable. For most of the cases presented in this paper, the background wind field was updated only every 6 hours. Current implementation utilizes time interpolation to provide hourly updates of the background wind field between forecast output times. It is important to note that the winds from features tracked from water vapor imagery (other than clouds) are not associated with a single altitude. Rather, these winds are representative of layers, weighted in the vertical in accordance with the weighting function of the 6.7 micron GOES image channel. Typically, most of the weight comes from a layer 200-300 hPa deep. The altitude of the weighting functions varies directly with upper level moisture. Typically, mean layer heights vary from 400 hPa in dry areas to 200 hPa where upper level moisture is high. Wind vectors directly associated with thick high clouds, such as anvil tops, are from a single level near cloud top.

Since the mean height of wind vectors vary over a given region, it is necessary to interpolate the values to a constant altitude before evaluation of horizontal gradients required in the computation of kinematic parameters such as vorticity and divergence. For this purpose, an objective analysis is used which combines available wind vectors with the background wind field at constant pressure levels from the NOGAPS forecast model. For purposes of this study, analyses centered at 300 hPa are used for evaluation of divergence, absolute and relative vorticity, and wind speed. This layer includes the anvil region of deep convection where upper level divergence can be strong and related to the mesoscale upward air motion. Because of the vertical weighting of the water vapor winds, the derived quantities such as divergence and vorticity represent vertical averages centered near 300 hPa. Caution should be observed in interpreting the kinematic properties near dry areas where no satellite winds may be available near 300 hPa. The objective analysis will be based mainly on the background wind field in such areas. A map of wind vectors should be examined to ensure adequate coverage.

3. ANALYSES

Analyses from the wind fields include the display of wind vectors and objectively analyzed divergence, absolute and relative vorticity, and isotachs at 300 hPa. The output of these products are available in real time on the Web and includes interactive displays (http://zonda.ssec.wisc.edu/~rabin/real.html). Comparisons are also available between the analyzed fields of divergence, vorticity, and isotachs and those

*Corresponding author address: Robert M. Rabin, NOAA/NSSL, 1313 Halley Circle, Norman, OK 73069; e-mail: rabin@ssec.wisc.edu

from the NOGAPS and Rapid Update Cycle (RUC-2) model (Benjamin et al., 1998).

3.1 *Winter Storms*

On 26 January 2000, a widespread area of snow developed across central Oklahoma producing 10-15 cm of accumulation (~12-23 UTC). The snowfall appeared to be related to isentropic lift associated with warm air advection. This snow event was not well predicted. It occurred well downstream of an upper level trough which moved across the region on 27 January. Snow had been forecasted to begin after 00 UTC on the 27th. This upper system produced convective precipitation further east on the 27th. Freezing rain and ice pellets effected north Texas & the heaviest snow fell over parts of eastern Oklahoma with as much as 17" reported in Eufaula, Oklahoma.

In general, the RUC-2 wind fields contain more structure than the satellite winds because of the model's high resolution. The RUC-2's upper level divergence field seems to match the location of the snow band on 26 January more consistently than the satellite analysis. The divergence visible from satellite may have been limited due to the shallow nature of the upward motion during the warm air advection phase of the storm.

A strong divergence couplet develops with the upper low as it tracks across Oklahoma by 16 UTC on 27 January (Fig. 1). The most intense divergence is located over the convective cloud region centered near the southeast tip of Oklahoma. Strong convergence is located to the west near the leading edge of a dry band aloft. The RUC-2 and the background NOGAPS fields indicate the divergence further west in western Oklahoma. The background field was 3 hours old at the time of the analysis. Despite this, the satellite analysis captured the eastward movement and evolution of intensity.

Two significant snowstorms effected the upper Midwest on 11 and 18 December 2000. The early stages of these storms appear to have similarities from satellite imagery. Maximum divergence developed in the central Plains ahead of an upper level trough, convergence behind it in the Great Basin. As the storms moved east, upper level divergence was elongated from southern Minnesota to Michigan. In the case of 18 December, a double maximum occured: a western one just ahead of the upper trough and an eastern one near a speed gradient well north of the surface system. Both systems also exhibited an area of upper level convergence and drying to the southwest. On the 11th, the divergence was to the north of an east-west band of maximum vorticity. A jet maximum was approximately 700 km to the south of the divergence maximum. Radar echoes were widespread through the area of divergence, although only the backside appeared to be convective from the satellite imagery. On both days, the highest radar reflectivities were south of the area with maximum divergence, although heaviest snowfall was in vicinity of the divergence. The high reflectivities to the south may have been due to mixed precipitation in these areas. In addition, displacement of the divergence pattern to the north due to a slope of upward air motion with height was a likely factor.

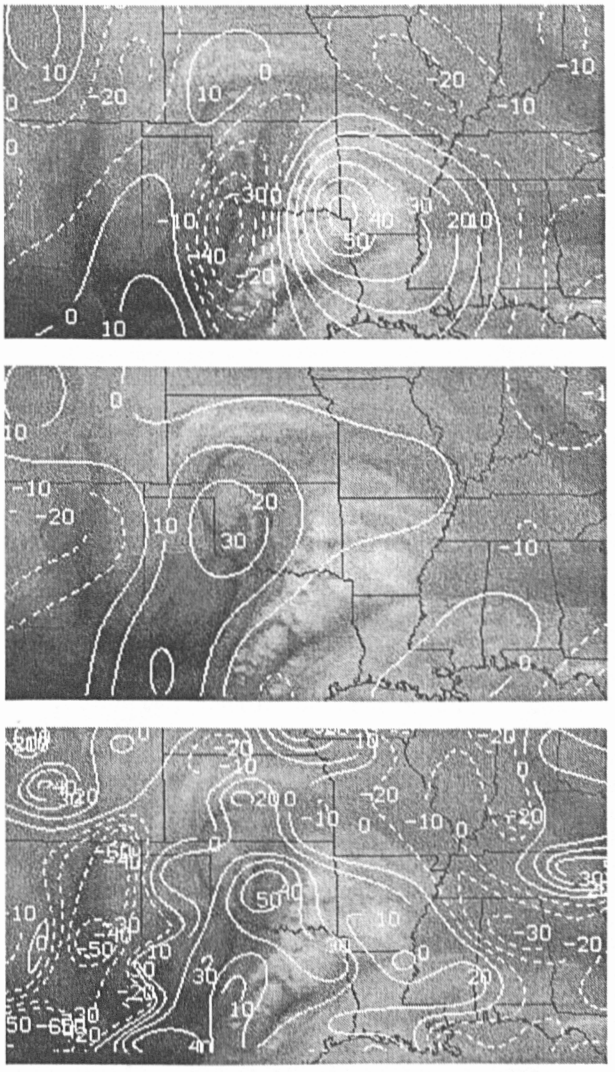

Fig.1 Water vapor image and divergence at 300 hPa ($10^{-6}s^{-1}$) at 16 UTC, 27 January 2000 from water vapor winds (top), background wind field (middle) and RUC-2 (lower).

A severe ice storm effected parts of Oklahoma and Arkansas on 25-26 December 2000. On the 25th at 1845 UTC, a strong upper level system was located in Arizona. Far to the east, convective precipitation commenced from northeast Texas to western Arkansas. Vorticity gradients were weak in this area, yet a strong divergence signature had developed above the convection. From the isotach field, the divergence appeared to result from a considerable speed gradient near the top of a ridge aloft. By the 26th at 0345 UTC, the upper low dropped slightly to the southeast as convection and strong divergence aloft developed to its east in New Mexico. Convection and divergence

continued to form in northeast Texas in an area of strong warm air advection under the upper level ridge. The speed gradient appeared to be weak by this time. A third band of convection developed between the two other bands. Initially, upper level divergence was weak over this area. By 0945 UTC, this band expanded eastward and had large divergence associated with it. In this case, the divergence resulted from a considerable speed gradient ahead of the upper level low as it moved eastward. Over the next several hours, the upper level circulation moved east and developed a couplet of divergence, with the divergence and heavy precipitation in Arkansas. By this time, parts of Oklahoma and Arkansas had experienced significant upper level lifting for as much as 36 hrs. Given subfreezing surface temperatures and plentiful moisture, ice accumulations of several inches resulted in considerable tree and power line damage in many locations.

3.2 *Warm Season Convection*

An example of strong mesocale forcing occurred in Oklahoma and Kansas on 3-4 May 1999. Multiple supercell thunderstorms produced over 70 tornadoes after 2100 UTC on 3 May. Of interest was a wind maximum near the Oklahoma and Texas panhandles about 500 km to the west-northwest of the convection at the time of early development (2145 UTC). An upper level trough was centered to the west in New Mexico and Colorado. The trough and wind maximum had moved from south central Arizona and southwest New Mexico respectively at 1200 UTC. The convection formed on the anticyclonic side of the wind maximum near a minimum in relative vorticity ($-2x10^{-5}s^{-1}$). Peaks in divergence developed over the convection and ahead of the main trough in eastern New Mexico, however the intensity was not unusually strong as compared to other convective events. By 4 May 0045 UTC, the wind maximum had shifted east and was near the western edge of the active convection. Also, the convection was centered between a couplet of cyclonic-anticyclonic vorticity. Comparisons of upper level fields were made with the operational ETA (Black, 1994) and RUC-2 models. The models did well in depicting the divergence above the convection and the vorticity couplet at 00 and 06 UTC on 04 May. Earlier, there are differences between the satellite, RUC-2 and ETA fields.

Mesoscale Convective Systems (MCS) often develop under weak upper forcing during the summer months in the U.S. Fueled by moisture and warm air advection in the low levels, they typically occur in vicinity of upper level ridges. Blanchard et al. (1998) proposed a role of inertial instability in the growth of MCSs by enhancement of upper level divergence. Using upper wind analyses from rawinsonde data, the occurrence of negative absolute vorticity, a necessary condition for inertial instability, accompanied the onset of large systems. The absolute vorticity was examined here using the satellite wind analyses for events with weak forcing.

The time series of maximum divergence was examined for a large MCS lasting 14 hours on 20 July 1995. This system was associated with a frontal boundary and had an elongated shape rather than the more circular pattern typical of Mesoscale Convective Complexes (MCC). In this case, the time trend of maximum divergence appeared related to the evolution of the MCS as observed from the coverage of the cold cloud shield in the infrared satellite imagery. The strongest divergence was near the end of the mature phase (2-5 UTC). There was a rapid decline after 0530 UTC, near the onset of decay. However, the decline in divergence did not continue during the decay phase (5-8 UTC) when values remained nearly constant at $6x10^{-5}s^{-1}$. During the early stages of development (23-03 UTC), the minimum absolute vorticity was just southeast of the convection. Perhaps this was a factor in the observed expansion of the cloud shield to the southeast. During the mature phase, the minimum absolute vorticity was aligned roughly with the convection, however the minimum was located downwind (northeast) from the most active area. In these areas, the absolute vorticity became negative. During the decay phase, the minimum remained aligned with the convective cloud, but was slightly positive.

Another smaller, long-lived MCS formed on 15 July 2001. The first individual convective cells formed to the west of the upper ridge axis at 21:45 UTC. Weak divergence was first detected at 22:15 UTC over an individual storm in the Texas panhandle. As a speed max spread northeast into Colorado, the speed shear increased and a minimum in absolute vorticity ($6\text{-}8x10^{-5}s^{-1}$) approached the storms from southwest. By 01:15 UTC on 16 July, the system was comprised of a cluster of individual cells with strong divergence at times, and absolute vorticity near $6x10^{-5}s^{-1}$. During the period 02:45-08:15 UTC, as the cluster expanded in coverage, the divergence was moderately high. The MCS was located near a minimum in absolute vorticity ($2\text{-}4x10^{-5}s^{-1}$) in southwesterly flow. This was on the anticyclonic side of a speed maximum where the speed shear was highest. There was a vorticity maximum embedded in the ridge further to the south, but that region was void of convective development. The MCS moved eastward over the ridge axis during 08:45-11:15 UTC. During this period, the divergence was steady ($3x10^{-5}s^{-1}$). Also, the southern end moved away from minimum absolute vorticity and weakened. The remaining portion weakened during 11:45-14:15 UTC except for regeneration of cells near the southeast end, along the southern edge of the speed shear. During 14:45-17:15 UTC, dissipation into cirrus occurred. Divergence was weak during this period.

The upper air features from a long-lived MCS on 20 July 2000 tracked south of the westerlies and appeared to be associated with new convective development after its demise. The first system formed at 00:45 UTC and propagated along a ribbon of uniform gradient of absolute vorticity. This was near the northern edge of the maximum speed shear. Impressive divergence was first detected at 10:45 UTC. Convergence developed ahead of the convection and the divergence couplet persisted for several hours. After dissipation of the MCS (14:45 UTC), remaining cirrus tracked southeast where new convection developed from 18:45-22:45 UTC. This convection exhibited strong

divergence at times and was accompanied by a minimum in absolute vorticity ($2x10^{-5}s^{-1}$).

An example of an MCS associated with a weak vorticity maximum occurred on 19 July 2000. The first isolated convection formed in northeast Colorado at 00:45 UTC and was accompanied by localized divergence. The speed maximum was located just east of this location. As the MCS reached a mature stage by 07:45 UTC, the wind speed maximum moved further east leaving a weak speed gradient near the convection. The convection occurred within a region of relatively high absolute vorticity with a weak vorticity maximum nearby. The MCS decayed between 08:45-10:45 UTC in Kansas. Divergence appeared to be quite variable during the lifecycle of this MCS.

A set of shorter-lived MCSs was also examined. These all occurred near the periphery of an upper level ridge centered near the high plains.

On 3 July 2000, an MCS formed at about 03:45 UTC near the top of the ridge. It rapidly intensified an hour later and dissipated by 08:45. The absolute vorticity became negative near the time of intensification. Moving southeastward, the convection was on the anticyclonic side of a wind maximum (right entrance region of the jet), located on the east side of the upper ridge. After the demise of the convection, cirrus debris persisted at least another 13 hours. The cirrus remained centered on the location of minimum vorticity as it propagated southeast. Scattered new convection formed underneath this area by afternoon (21:45 UTC).

Another short-lived event developed near the top of the ridge on 11 July 2000. Convection initiated in southern Colorado at about 20 UTC and dissipated by 03 UTC the following day. The area of formation was collocated with a minimum in absolute vorticity ($<4x10^{-5}$) in a region of broad speed shear. However, that feature moved east of the convection and was replaced with increasing values ($>8x10^{-5}$) by dissipation time. There was no local wind maximum present in this case.

4. SUMMARY AND CONCLUSIONS

The CIMSS water vapor wind tracking algorithm has been implemented to allow the detection of perturbed flow aloft due to convection and other mesoscale features. The horizontal resolution of wind fields is limited by the density of targets identified by the automated technique, and the resolution of the objective analysis. For example, the fields of divergence and vorticity do not contain as much detail as RUC-2 analyses.

Examination of winter storm cases usually revealed a consistent relation between divergence aloft and precipitation evolution, especially near convective cloud tops. In some cases, the divergence can be displaced downwind due to shear. Areas where air ascent is limited to shallow layers may not be detectable.

Investigation of several MCS's confirm the lack of significant vorticity or divergence perturbations aloft before convective development. With areal growth of these systems, divergence and vorticity signatures emerge and occasionally persist after the demise of the active convection. Given the presence of divergence aloft on a scale of at least 200-300 km, the thunderstorm clusters usually persist for several hours over similar horizontal scales. In contrast, isolated thunderstorms are often too small to be resolved by the satellite wind analysis and appear to develop in areas with no preferred sign of divergence. However, the rapid intensification of divergence is observed occasionally with the explosive growth of a single storm.

The absolute vorticity was examined using the satellite wind analyses for events with weak forcing. In many cases, convective systems developed in the vicinity of upper ridges near minima in absolute vorticity (with values $< 4x10^{-5}s^{-1}$). These values were only slightly above the threshold for inertial stability, suggesting a possible role of this mechanism in MCS growth. However, it is important to note that inertial instability can be ruled out in other cases where absolute vorticity was relatively high.

Derived wind fields have been made available to the NOAA Storm Prediction Center (SPC) on an experimental basis. The operational value of these products in forecasting storm evolution remains to be determined. The principal limitations of the water vapor wind analysis are the variable nature of the target heights and lack of vertical profiling. The future implementation of the Geostationary Imaging Fourier Transform Spectrometer (GIFTS) by NASA has the potential to provide analysis of water vapor winds at multiple levels.

4. REFERENCES

Benjamin, S.G., J.M. Brown, K.J. Brundage, B.E. Schwartz, T.G. Smirnova, and T.L. Smith, 1998: The operational RUC-2. Preprints, 16th Conference on Weather Analysis and Forecasting, AMS, Phoenix, 249-252.

Black, T.L., 1994: The new NMC mesoscale Eta model: Description and forecast examples. *Wea. Forecasting*, **9**, 265-278.

Blanchard, D.O., W.R. Cotton, and J.M. Brown, 1998: Mesoscale circulation growth under conditions of weak inertial instability. *Mon. Wea. Rev.*, **126**, 118-140.

Rosmond, T.E., 1992: The design and testing of the Navy Operational Global Atmospheric Prediction System. *Wea. Forecasting*, **7**, 262-272.

Velden, C.S., C.M. Hayden, S. Nieman, W.P. Menzel, S. Wanzong and J. Goerss, 1997: Upper-tropospheric winds derived from geostationary satellite water vapor observations. *Bull. Amer. Meteor. Soc.*, **78**, 173-195.

Weldon, R.B., and S.J. Holmes, 1991: Water vapor imagery: Interpretation and applications to weather analysis and forecasting. NOAA Tech. Rep. NESDIS 67, 213 pp.

P3.6 Evaluating the potential impact of the assimilation of satellite derived products on a mesoscale forecast of PACific landfalling JETs experiment (PACJET) IOP 10

Michael C. Morgan[1], Katherine La Casse[1,2], Daryl T. Kleist[1], Hyun Mee Kim[1], Justin McLay[1], Derek J. Posselt[2], John R. Mecikalski[2], Christopher Velden[2], and Dave Stettner[2]
Department of Atmospheric and Oceanic Sciences, Univ. of Wisconsin - Madison[1]
Cooperative Institute for Meteorological Satellite Studies, UW-Madison[2]

1. INTRODUCTION

As part of the PACific landfalling JETs experiment (PACJET), the GOES rapid scan WINDs EXperiment (GWINDEX) was conducted with the objective of demonstrating improved quantity and quality of cloud-motion winds using 7.5 minute rapid-scan visible and infrared imagery from the GOES-10 satellite. The goals of PACJET are to develop and test methods to improve short-term (0-24 h) forecasts of damaging weather on the U. S. West Coast in landfalling winter storms emerging from the data sparse Pacific Ocean. The goals of the GWINDEX component of PACJET are to provide improved remotely-sensed data over the Eastern Pacific (EPAC) domain for National Weather Service (NWS) forecasters, support PACJET and THORPEX initiatives, and assess data impact on the RUC model short-term forecasts. PACJET was designed to test new ways to observe approaching storms, develop better ways to use existing data, improve our understanding of key physical processes, explore the linkages between climate variability and extreme weather, and work with forecasters to develop new forecasting tools.

GWINDEX, conducted during PACJET, took place from 10 January through 31 March 2001 over the EPAC and west coast of North America, and brought together participants within NOAA/NESDIS/ORA and FPDT, the University of Wisconsin-CIMSS, the NWS, NOAA/FSL/NSSL, and the U.S. NAVY. Data collected during PACJET/GWINDEX included, in addition to GOES-10 data, special dropsonde soundings, ocean surface flux measurements, and wind profiles on the U.S. west coast.

This study, using data collected during February 2001, intends to assess how well these special satellite and sounding observations may be used to improve forecasts of landfalling winter storms. We focus on improving how the assimilation of these data into the Pennsylvania State University-National Center for Atmospheric Research (PSU-NCAR) non-hydrostatic mesoscale model (MM5) may improve forecasts made with a numerical weather prediction model, one main focus of PACJET/GWINDEX.

The four-dimensional variational (4DVAR) assimilation system to be used in this study is developed from the MM5 Adjoint Modeling system based on the PSU-NCAR MM5 version 1 (Zou et al., 1997) and used in a set of assimilation experiments including Guo et al. (2000). As the first part of this study, we diagnose the sensitivity of the forecast (error) to changes in the initial conditions using the MM5 adjoint model. This will provide insight into where assimilation of observations may have the largest effect in improving the MM5 forecast and will serve as a basis for the study of the impact of the analysis increment attributed to the assimilation of wind and temperature on particular aspects of the model forecast.

In the presentation to follow, we briefly describe the synoptic characteristics of the case to be studied and provide a description of the model errors and the sensitivity of the forecast error to the initial conditions. We conclude with an outline of the proposed experimental design.

2. SYNOPTIC OVERVIEW

For this study, we focus on a cyclogenesis event that occurred between 0000 and 1200 UTC 13 February 2001 southwest of Los Angeles, CA. This event occurred during intensive observing period 10 (IOP 10) of the PACJET experiment. The precursor to the event was a vigorous upper tropospheric trough that was located west of the Oregon coast 0000 UTC 12 February (Fig. 1a). During the next 24 h, the vorticity maximum associated with this trough moved southward around a nearly stationary geopotential height minimum situated just offshore the northern and central California coasts. Following 0000 UTC 13 February the vorticity maximum moved eastward to a position just west of the northern Baja Peninsula of Mexico (Fig. 1b) by 1200 UTC 13 February.

During this 12 hour period a surface cyclone developed west-southwest of 32N 119W and moved east-northeast, making landfall east of Santa Barbara, CA after 1500 UTC 13 February. In the 6 h period ending at 1200 UTC 13 February, the cyclone deepened nearly 10 hPa to 992 hPa (Fig. 2a, close scrutiny of the surface observations reveals a cyclone deeper than analyzed). 12 hour pressure changes offshore of the bight of south-

* Corresponding author address: Michael C. Morgan, Department of Atmospheric and Oceanic Sciences, 1225 W. Dayton Street, Madison, Wisconsin 53706
email: morgan@aurora.aos.wisc.edu

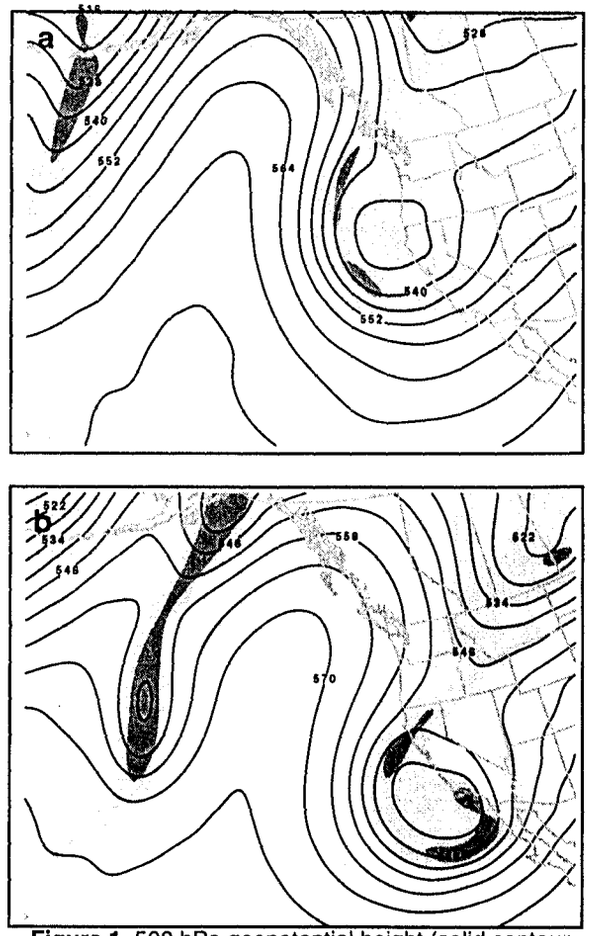

Figure 1. 500 hPa geopotential height (solid contour, interval 6 dam) and absolute vorticity (shaded above 12 x $10^{-5}s^{-1}$, interval 6 x $10^{-5}s^{-1}$) analyses for (a) 0000 UTC 12 February and (b) 1200 UTC 13 February.

ern California were as much as 17 hPa ending at 1200 UTC 13 February. This cyclone was accompanied by heavy precipitation (rain in the coastal areas and snow in the mountains) and wind.

3. MODEL FORECAST ERROR

A 36 h MM5 simulation of the event was performed. The model, initialized with National Center for Environmental Prediction (NCEP) 'final analyses', was run with 16 vertical levels, on a 68x85 60 km grid. The model physics included a bulk planetary boundary layer scheme, Kuo cumulus parameterization, and simple iced physics. The rather crude physics and resolution were chosen to make the run compatitble with the physics available for the MM5 Adjoint Modeling System. The 36 h MM5 forecast of this event was associated with an underforecast of the cyclone intensity and also a cyclone position error (compare Fig. 2b with Fig. 2a). In addition, the lower tropospheric wind field was poorly forecast. The poor forecast of the wind in regions of significant orography can lead to poor precipitation forecasts.

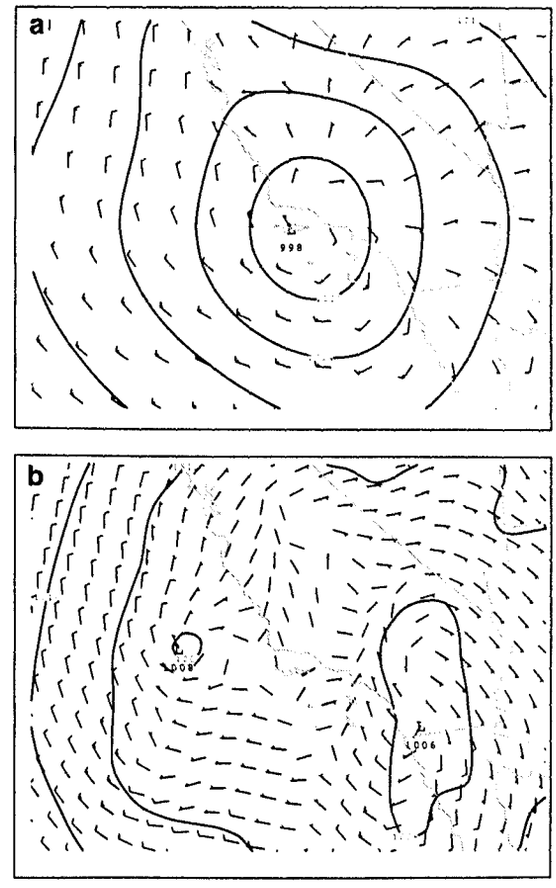

Figure 2. Mean seal level pressure (contour interval 4 hPa) and wind (ms^{-1}) from (a) NCEP final analysis and (b) 36 h MM5 forecast valid 1200 UTC 13 February. The box in (a) denotes the domain in which the area weighted vorticity was calculated.

4. FORECAST SENSITIVITY

For the purposes of assessing the potential impact of assimilation of the GOES-10 derived winds on the forecast of the PACJET 1OP 10 event, we conduct an adjoint sensitivity study. The response function chosen is the "energy-weighted forecast error" (e.g., Rabier 1996 and Gelaro et al. 1998) in a 10 degree latitude by 10 degree longitude box centered on the analyzed position of the surface cyclo ne. We define the forecast error as the difference between the 36 h forecast of the model state and the NCEP 'final analysis' interpolated to the model grid at the same time (1200 UTC 13 February 2001).

An examination of vertical and horizontal cross sections along the vertical and horizontal shear (not shown) reveals that the sensitivity fields show considerable barotropic and baroclinic upshear tilt. In the upper troposphere, the sensitivity fields appear to be maximized in the vicinity of the precursor upper tropospheric vorticity maximum. Fig. 3a shows the sensitivity of the response function with respect to the initial distribution of the meridional component of the wind at 500 hPa. Regions

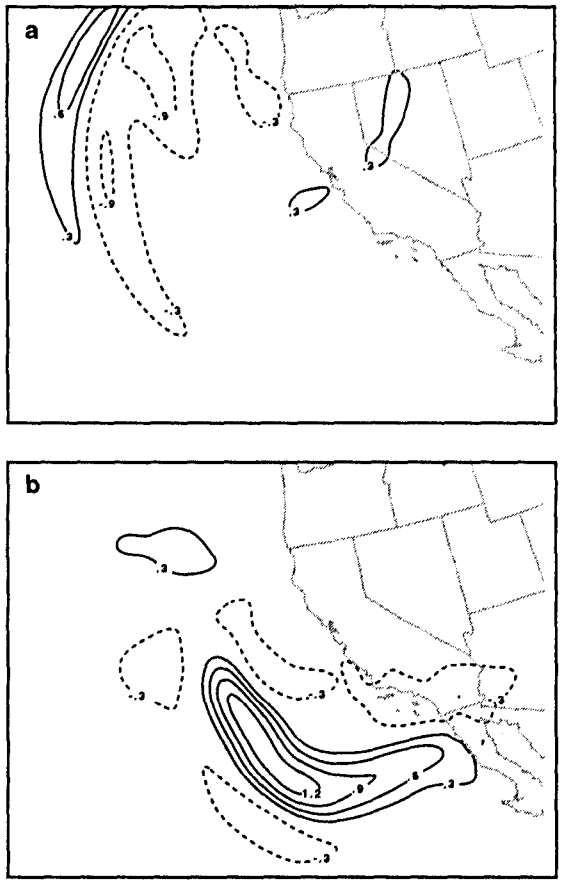

Figure 3. Gradient of response function (defined in text) with respect to initial model distribution of (a) meridional wind at 500 hPa and (b) zonal wind at 850 hPa on 0000 UTC 12 February 2001.

in which the sensitivity is positive correspond to regions in which a positive meridionalperturbation to the wind in the initial analysis will lead to an increase in the weighted forecast error at 36 h. The larger the sensitivity, the larger the change in the response function. Regions of low sensitivity correspond to regions where changes in the analysis will have a small effect on the response function at 36h. Fig. 3b shows the gradient of the response function at 850 hPa with respect to the initial zonal component of the wind. Note that the maximum sensitivity at this level is further to the southeast of the maximum at 500 hPa. A response function defined as the circulation about the same box defined for the energy-weighted forecast error is associated with sensitivity fields which would yield a consistent interpretation.

A comparison of the distribution of GOES wind data available from GWINDEX at 0000 UTC 12 February (Fig. 4) with the sensitivity fields in Fig. 3 reveals that the 850 hPa winds best overlap the sensitivity fields at 850 hPa. This overlap suggests that the analysis increments associated with assimilating these winds will have an impact on the forecast of area weighted vorticity in the box shown. A calculation of the observational increments determined by interpolating the model analysis to the satellite wind vector locations, (not shown) suggests that

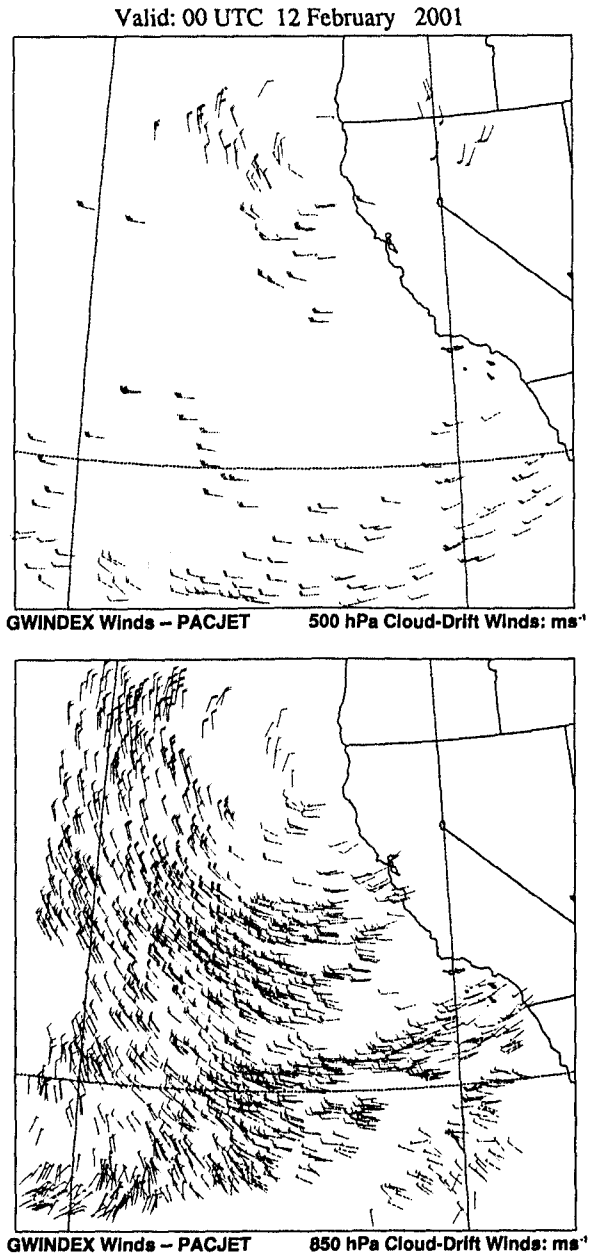

Figure 4. Distribution of GWINDEX winds (ms^{-1}) at 0000 UTC 12 February 2001 in a 35 hPa layer centered about 500 hPa (top) and 850 hPa (bottom).

the implied *analysis increments* for both the zonal (u) and meridional (v) components of the wind associated with these additional observations are of a sign which would lead to an *increase* in forecast error. Thus assimilation of these winds would be detrimental to the forecast.

In addition we note that a comparison of the distribution of the satellite derived winds as a function of height with the sensitivities of forecast errors with respect to u and v as a function of height (Fig. 5) reveals that the satellite data is most plentiful in regions for which the sensitivities of the forecast error with respect to the initial

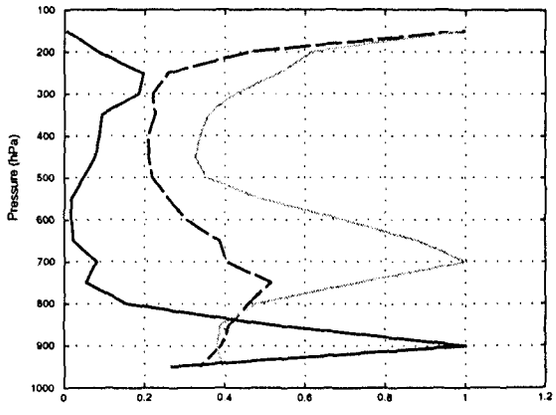

Figure 5. Vertical distribution of normalized area averaged forecast sensitivities with respect to initial *u* (grey) and *v* (dashed) components of the wind. Also shown is the normalized number of satellite derived wind vectors as a function of pressure (solid). The count of wind vectors is normalized by the maximum count of 3020 at 900 hPa. Note that the level of the largest number of satellite derived winds does not coincide with the level at which the sensitivities are maximized.

conditions are relatively small.

5. SUMMARY AND FUTURE WORK

The initial results of the study thus far suggest that the impact of the satellite data on the forecast of the PACJET IOP 10 cyclone would be detrimental (as measured by the energy-weighted forecast error). We further observe that, for this case, the satellite winds are not found in regions that would have the largest impact on the forecast error - though we note that assimilation of these winds may result in a 'spreading' of the observational information to these sensitive regions.

While our longer term goal is to assimilate the GOES-10 winds into the MM5, our more immediate objectives are to understand from an observational and dynamical perspective the relationship between the forecast sensitivities and the synoptic precursor, and to determine an "optimal" initial condition which would yield a reduced forecast error. This improved initial condition may be viewed as the upper limit of any improvements in the initial analysis which could be obtained from four-dimensional data assimilation.

We will use the MM5 adjoint modeling system to conduct a 4DVAR assimilation of the GWINDEX winds. 4DVAR assimilation over a time window (τ) involves the minimization of a cost function, J

$$J = J_b + J_o + J_p$$

where J_b measures the degree of misfit of a background (or first guess) analysis with the desired analysis, J_o measures the misfit of the observations to be assimilated distributed in time and interpolated to the model grid with the model forecast initialized with that analysis, and J_p (a penalty term) is a measure of the degree of dynamical imbalance the analysis possesses. Each of the 'misfits' is weighted by the corresponding uncertainties in the background field or the observations. The weightings are in fact the inverses of error covariances of the background and the observational error. Thus in order to assimilate the GOES winds, we must specify the length of the assimilation window and the background and observational error covariances. In addition, we must develop an interpolation operator to interpolate the observations to the model grid. Finally, if we seek a balanced initial state, we need to determine a proper formulation for the penalty term J_p.

We will assimilate the observations over 3 and 6 hour time windows beginning at 0000 UTC 12 February 2001. In order to calculate the background error covariances, we will accumulate the 6 h error statistics of MM5 forecasts during GWINDEX and employ the technique of Parrish and Derber (1992) to determine the diagonal elements of the background covariance matrix.

Having assimilated the GWINDEX winds, we will diagnose the changes to the 36 h forecasts by re-running the model, and by examining the analysis increments and their relationship to measures of forecast error sensitivity to initial condition perturbations.

6. REFERENCES

Gelaro, R., R. Buizza, T. Palmer, and E. Klinker, 1998: Sensitivity analysis of forecast errors and the construction of optimal perturbations using singular vectors. *J. Atmos. Sci.*, **55**,1012-1035

Guo, Y.-R., Y.-H. Kuo, J. Dudhia, and D. Parsons, 2000: Four-dimensional variational data assimilation of heterogeneous mesoscale observations for a strong convective case. *Mon. Wea. Rev.*, **128**, 619 - 643.

Parrish, D., and J. Derber, 1992: The National Meteorological Center's Spectral Statistical Interpolation Analysis System. *Mon. Wea. Rev.*, **120**, 1747 - 1763.

Rabier, F., E. Klinker, P. Courtier, and A. Hollingsworth, 1996: Sensitivity of forecast errors to initial conditions. *Quart. J. Roy. Meteor. Soc.*, **122**, 121-150.

Zou, X., F. Vandenberghe, M. Pondeca, and Y.-H. Kuo, 1997: Introduction to adjoint techniques and the MM5 adjoint modeling system. *NCAR Technical Note*, NCAR/TN-435+STR, 117 pp.

Acknowledgments

This work was supported by National Science Foundation grant ATM-9810916 and National Oceanic and Atmospheric Administration grant NA67EC0100.

P3.7 ASSIMILATION OF GOES RAPID-SCAN WINDS INTO AN EXPERIMENTAL ETA MODEL DURING HURRICANE KEITH

Howard I. Berger* and Chris Velden
University of Wisconsin-CIMSS

1. Introduction:

The lack of in-situ data in the tropics makes it difficult to properly initialize tropical cyclones in Numerical Weather Prediction (NWP) models. Remotely sensed data from satellites offer an alternative source of information for this initialization problem.

To examine this problem, experiments are performed that are designed to optimize the assimilation of winds derived from GOES rapid-scan data into the National Centers for Environmental Prediction's (NCEP) Eta model. The wind data are assimilated into the 48 km Eta model through the Eta Data Assimilation System (EDAS). The case study evaluated in this paper is Atlantic Hurricane Keith (Sept/Oct 2000). The satellite-derived winds will more accurately describe the initial upper-level environment over Keith. Various assimilation strategies will be explored in order to optimize the influence of these wind data on the model initialization and resulting analyses. Model forecasts of track and intensity will be used to evaluate the various imposed assimilation strategies.

2. Methodology, Data and Case study

2.1 Eta Model

The Eta model version used in this study has 48 km resolution and 45 vertical levels. The model is being run on a Silicon Graphics Origin workstation at the University of Wisconsin-CIMSS. The Eta was chosen for this experiment because it is one of NCEP's primary operational regional models and it has a well-established assimilation system.

This assimilation system, the EDAS, uses a regional 3-d variational analysis (Rogers 1996). The EDAS creates its analysis by minimizing a cost function at observation locations. It is designed to use high-resolution mesoscale data types, making it an ideal system to test assimilating rapid scan winds (Rogers 1996). Experiments were performed on the 00Z Oct 02, 2000 Eta run. The operational run is used as the control run for this study.

* Corresponding author address: Howard Ian Berger
1225 West Dayton St. Madison, WI 53706
Email: howardb@ssec.wisc.edu

2.2 Rapid-scan (RS) winds from GOES

During selected hurricane events in 2000, the GOES-8 satellite was operated in a special scanning mode that allowed multi-spectral images of the storm at 1-minute intervals over several hour periods. Winds are derived from successive images using automated feature (cloud) tracking techniques developed at CIMSS (Velden et al. 1998). It has been shown that the quantity and quality of cloud-motion winds can be greatly enhanced by more frequent sampling strategies. The normal operational sampling interval for GOES wind determinations is 15-30 minutes.

In this study, the GOES RS data set was sub-sampled so that the winds were derived from successive 3-5 minute scans (to minimize the effects of image-to-image registration errors). Winds were produced from both visible and IR imagery. An example of the coverage obtainable over the cloud canopy of Hurricane Keith is shown in Figure 1.

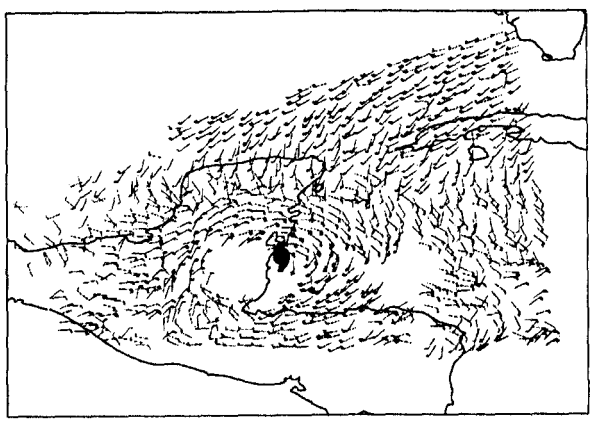

Fig. 1: Plot of GOES RS winds over the 100-400 hPa range during Hurricane Keith on 02 October 2000. The hurricane symbol represents the storm's center at the time the winds are valid.

2.3 Hurricane Keith

Keith was an intense tropical cyclone in the Northwest Caribbean Sea and the Gulf of Mexico during the fall of 2000. It was a Category 3 hurricane when it made landfall over Belize with maximum winds near 120 kts (Beven 2001).

The official National Hurricane Center (NHC) forecasts for Keith as a whole were worse than CLIPER (Climate-Persistence model) at the 12 and 24 hour

forecast periods, and worse than the 10-year average at longer forecast intervals (Beven 2001). The NCEP Aviation (AVN) model in particular had a difficult job of predicting Keith's westward motion as well as being biased too far to the north. For the 12 UTC forecast on Oct. 02, the actual track that verified was outside of the entire envelope of numerical guidance. Thus, the models had significant problems forecasting the track of this storm.

The intensity forecasting was also difficult, being significantly worse than the ten-year average. This intensity error was tied both to the track forecast uncertainty (the storm remaining over water when it was predicted to go over land), and a lack of understanding about the storm's structural changes as it passed over changing surface types (Beven 2001).

3. Model Initialization Impact

Initially, traditional operational values for visible and infrared cloud-drift winds were used in the observation weighting. The winds were assimilated into the 00 UTC initialization of the Eta model on 02 Oct., which was close to the time of the rapid scan wind set.

Figure 2 is a plot of wind differences between the experimental and control run at 300 hPa. Although the wind impact is not dramatic, one can see that the experimental winds are adding a counterclockwise rotation around the center of the storm. The rapid scan winds are capturing an upper level cyclonic circulation that the operational model analyses did not resolve.

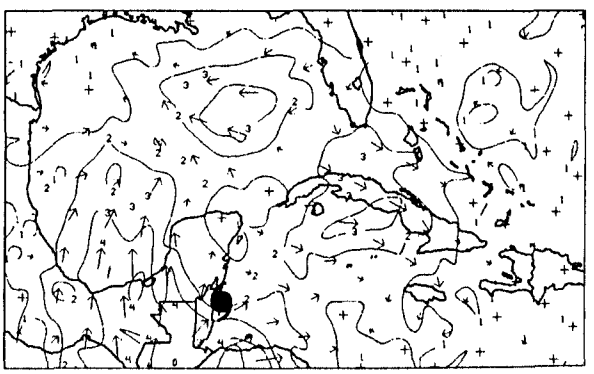

Fig. 2: 300 hPa wind differences between the experimental and control Eta analyses. The barbs show direction, while the isotachs show wind speed differences in ms^{-1}. The hurricane symbol represents the location of the storm's center at this time.

4. Future Work

This project will continue to explore ways to optimally assimilate the GOES RS wind observations in hurricane events to improve the initialization of the storm structure that should improve forecasts.

Two directions for future study are envisioned. The first involves the implementation of a vortex relocation algorithm within the Eta model. A similar relocation algorithm showed improvement during some tests in NCEP's Aviation model during the 1999 hurricane season (Liu, 2000). The algorithm, similar to that used in the GFDL hurricane model, involves relocating the model's initial vortex to the location determined by the NHC. It is hoped that by improving the initial vortex position, adding the satellite winds will be even more effective because the winds will be assimilated to a properly initialized storm center.

The second direction involves modifying the observation weights and correlation lengths in the assimilation system. Using the operational weights showed only minor impact. It is hoped that an optimal configuration will have a greater impact on the initial analyses and result in an improved forecast track and intensity. The results from these experiments will be presented.

5. References

Beven, J. 2001: Tropical Cyclone Report Hurricane Keith. Preliminary Report

Liu, Q.,T. Marchok, H. Pan, M. Bender, and S. Lord, 2000:Improvements in Hurricane Initialization and Forecasting at NCEP with Global and Regional (GFDL) Models, NOAA Technical Procedures Bulletin 472.

Rogers, E., D. Parrish, Y. Lin, and G.J. DiMego, 1996: The NCEP Eta Data Assimilation System: Test with a Regional 3-D Variational Analysis and Continuous Cycling. Preprints, 11th AMS Conference on Numerical Weather Prediction, 19-23 August 1996, Norfolk Virginia.

_____, D. Parrish, G.J. DiMego, 1996: Data Assimilation Experiments with the Regional 3-D Variational Analysis at the National Centers for Environmental Prediction

Velden et al. 1998 The Impact of Multispectral GOES-8 Wind Information on Atlantic Tropical Cyclone Track Forecasts in 1995. Part I: Dataset Methodology, Description and Case Analysis. *Mon. Wea. Rev*, **126**,1202-1218

Acknowledgements. Thanks go to CIMSS scientists Dave Stettner and Tom Zapotocny for assistance with the GOES winds data and Eta set-up, respectively. Thanks to Jim Jung for additional Eta/EDAS support. The first author benefited greatly from a visit to NCEP EMC. He would also like to thank the AMS and Lockheed Martin Missiles and Space who supported his first year of graduate work. This study was supported by NOAA grant NA67EC0100.

P3.9 AN IMPACT STUDY OF FIVE REMOTELY SENSED AND FIVE IN-SITU DATA TYPES IN THE ETA DATA ASSIMILATION SYSTEM

Tom H. Zapotocny*, W. Paul Menzel, James P. Nelson III and James A. Jung
Cooperative Institute for Meteorological Satellite Studies
University of Wisconsin-Madison

1. INTRODUCTION

The primary role of geostationary and polar orbiting satellites in the atmospheric sciences is to provide frequent observations over a large geographical extent. In otherwise data sparse maritime regions, satellite observations have become the primary source of information. Currently the National Environmental Satellite, Data, and Information Service (NESDIS) produces hourly Geostationary Operational Environmental Satellite (GOES) temperature and moisture retrievals, as well as temperature profiles down to cloud top from the TIROS Operational Vertical Sounder (TOVS) and vertically integrated precipitable water from the Special Sensor Microwave/Imager (SSM/I). These three satellite systems provide a wealth of nearly continuous remotely sensed data, which generously supplements in-situ data.

In order to assess the quality of such satellite data, the Cooperative Institute for Meteorological Satellite Studies (CIMSS) acquired the complete Eta Data Assimilation/Forecast System (EDAS) (Black 1994) from the National Centers for Environmental Prediction (NCEP). A primary goal of the CIMSS EDAS effort is to maintain a system that, except for horizontal and vertical resolution, is consistent with the operational EDAS. The CIMSS EDAS is used in coordination with NCEP personnel for investigating the impact of current and planned satellite data sources on NWP forecasts.

This paper describes the results of an experiment utilizing the EDAS to study the 24-hr forecast impact of five remotely sensed and five in-situ data types during 11-day periods for three seasons and is a follow-on to Zapotocny et al. (2000). The three 11-day periods are 13-23 December 1998, 10-20 April 1999, and 13-23 July 1999.

This extended length study involves running the EDAS repeatedly on the same cases with varied sets of input data. A control run utilizes all EDAS data types. Separate experiments, with one of the ten data types denied in each, were then run. Summing the difference between the control and experimental runs for the multiple time periods yields a measure of the forecast impact from each data type.

2. EXPERIMENTAL DESIGN

The five remotely sensed data types studied are SSM/I vertically integrated precipitable water (SSM/I), TOVS temperature profiles down to cloud top (TOVCD), GOES Sounder three layer clear air precipitable water (GOESPW), GOES Imager infrared cloud drift winds (GOESCD), and GOES Imager cloud top water vapor winds (GOESWV). All five of these data types are used only within a marine environment within the EDAS. The five in-situ data types analyzed are rawinsonde temperature and moisture observations (RAOBM), Aircraft Communications Addressing and Reporting System (ACARS) temperature data (ACARM), rawinsonde wind observations (RAOBW), ACARS wind observations (ACARW), and surface land observations of pressure, temperature and moisture (SFCLM).

For this three season experiment, a total of 726 separate EDAS runs were required to isolate the contributions from all data types examined (10 denials plus a control run for 66 time periods). The operational EDAS was executing at a resolution of 32 km during all three 11-day time periods studied. However, initial model conditions in the experiments reported here were obtained from an 80 km horizontal resolution, 38 level vertical resolution EDAS which was also being executed at NCEP twice-daily "parallel" to the 32 km operational EDAS. All 726 EDAS runs performed herein were also run with a 80 km, 38 level EDAS. Furthermore, while the experiments were run on the native 80 km Eta grid, all results were interpolated to, diagnosed and displayed on the 80 km NGM Super C grid. Horizontal and vertical interpolations of the Eta model variables to isobaric surfaces and the C grid were performed within the Eta post-processor (Treadon 1993). Presenting results on isobaric surfaces should be more amenable to most readers, and removes the horizontal staggering of variables on the Eta model E grid. Finally, it is important to note that the 80 km results presented here may not be applicable to higher operational resolutions.

The RMS forecast impact (FI) of an individual data type is evaluated as the RMS error of the denied forecast minus the RMS error of the control forecast. Dividing this difference by the RMS error of the control forecast and multiplying by 100 normalizes the results and provides a percent improvement with respect to RMS FI. A positive FI means the forecast is better with the data type included than with it denied. The time-averaged 24-hr FI diagnostics exclude the first day of each 11-day period, removing more impact of the denied data type from the first guess.

All three 11-day periods used in this study were run with the EDAS operating in "full-cycling" mode.

* Corresponding author address: Tom H. Zapotocny, Univ. of Wisconsin-Madison, 1225 W. Dayton St. Madison, WI 53706; email: tomz@ssec.wisc.edu.

This involves denying the particular data type for 11 consecutive days and carrying the results of each 12-hr assimilation cycle forward to the starting point for the next 12-hr assimilation. This mode of operation was chosen to duplicates the NCEP twice-daily run cycle.

For completeness, diagnostic evaluations use both the entire horizontal model domain as represented by the 104 grid and a subsection closely outlining CONUS The entire domain diagnostics show data effects over large geographical distributions, while the CONUS subsection reduces the impact lateral boundary conditions play as the forecast proceeds and avoids possible problems with temporally-correlated observation errors from remotely sensed data.

3. RESULTS

In these experiments data were assimilated via 3DVAR at T-12, T-9, T-6, T-3, and T-0, using 3-hour Eta model forecasts between each assimilation step. Differences between the various time-averaged forecast runs and the control forecast run provide a measure of the FI of the EDAS to each data type. In the bar charts that follow, the five isobaric levels for each data type proceed from 300 hPa on the left to 1000 hPa on the right. Moreover, grid points on isobaric surfaces underground are not used in the diagnostics.

3.1. The 24-hr domain wide RMS FI statistics

Figure 1 presents a three season summary of the three 11 day time periods and indicates that nearly all data types provide a positive FI. In fact, only the 300 hPa u-component FI from SSM/I is negative for the 60 time period summation. Except for the u-component, RAOBM provides the largest positive FI by level and field on a fairly regular basis. However, because of their large July values, the precipitable water data types of SSM/I and GOESPW provide relatively large cumulative positive contributions to relative humidity at and above 850 hPa. GOESCD and RAOBW contributions, which are fairly uniform from season to season (not shown), also make relatively large positive FIs to all three fields. Of these ten data types, GOESWV and ACARM regularly provide the smallest overall FI for each of the three fields; however, even their contributions are slightly positive when summed over the three periods.

In general, it was found that the cumulative impact of most in-situ data types decreased in summer relative to winter. The opposite was true for the remotely sensed data types (not shown).

The only data type to have its largest three time period positive FI at 1000 hPa is the SFCLM temperature data type. The generally small 1000 hPa FI results are not surprising. Levels that close to the earth's surface are dominated by the physical parameterizations of sensible and latent heat addition, skin friction, and stronger PBL effects, all of which will tend to quickly drive the state fields to the same general solution, no matter what data type has been denied.

3.2. The 24-hr CONUS RMS FI statistics

This subsection examines the 24-hr FI results within a subsection closely outlining CONUS and a small percentage of adjacent coastal waters. CONUS subsection results are presented for two reasons. First, since the COUNUS subsection is far removed from the EDAS domain boundaries, the impact of the lateral boundary conditions is reduced as the forecast proceeds. Second, use of the CONUS subsection reduces the problem of temporally-correlated observation errors with remotely sensed data. The subsection used is approximately 84% land covered, compared with the entire domain being approximately 70% water covered. Finally, note that the CONUS bar charts use the same y-axis scales as the entire domain results of Fig. 1.

With respect to temperature impact (Fig. 2A), the two upper levels of RAOBM are the largest positive contributors, with impacts of 6 to 10%. Interestingly, one of the largest negative contributors to temperature forecast impact exists for RAOBM at 1000 hPa. RAOBW is the second largest overall contributor with GOESCD, ACARW and GOESPW the next largest contributors. The remaining five data types (SSM/I, TOVCD, GOESWV, ACARM, and SFCLM) cumulatively all have small positive or negative FI contributions to the temperature forecast.

For the five levels displayed, RAOBW cumulatively has the largest positive contribution to the u-component (Fig. 2B), with its most positive contributions at and above 700 hPa. The next three largest contributors cumulatively are RAOBM, GOESCD and ACARW. The GOESCD contributions are fairly uniform at each of the five levels, in contrast to RAOBW, RAOBM and ACARW. The six remaining data types (SSM/I, GOESPW, TOVCD, GOESWV, ACARM, and SFCLM) all show small positive or negative FI contributions in the CONUS subsection.

RAOBM provides the largest cumulative positive FI for relative humidity (Fig. 2C). GOESCD, RAOBW and GOESPW are the next largest contributors. The remaining six data types provide very small contributions either way.

A comparison of the in-situ domain wide results (Fig. 1) and the CONUS subsection results (Fig. 2) reveals that the positive contribution from RAOBW is similar in a cumulative sense over both diagnostic domains. However, all other data types provide smaller FI in the subsection than over the entire domain. There are also more negative FIs in the subsection than in the entire domain.

Finally, from a remotely sensed perspective, it is interesting to note that in both the subsection and entire domain the GOESWV impacts are less than the GOESCD impacts, even though they use identical observational error weights and are somewhat

redundant spatially. A long-standing concern, which could help explain the different impacts, revolves around the different height assignment methods used for infrared cloud drift winds and water vapor cloud top winds. Velden et al. (1998) and Rao et al. (2000) provide detailed descriptions of the error characteristics and on how the height assignment is made for both of these remotely sensed data sets. The vertical distribution of these data types is also a key contributor. GOESCD infrared data tends to span the troposphere, with relative density maxima at cirrus level and stratus level. However, GOESWV data is predominately located between 350 and 200 hPa (Velden et al. 1997). As such, since GOESCD samples low level information, it tends to capture trade wind easterlies and open celled cumulus that GOESWV cannot. A final factor is the amount of data. GOESCD typically has more observations than GOESWV for most time periods.

4. SUMMARY

This paper summarizes the 24-hr forecast impacts (FIs) of five remotely sensed satellite data types and five in-situ data types in the Eta Data Assimilation System during 11-day periods in a winter, summer and transition season. The five satellite data types are used only in a marine environment and are SSM/I vertically integrated precipitable water (SSM/I), GOES sounder three layer clear air precipitable water (GOESPW), TOVS temperature profiles down to cloud top (TOVCD), GOES imager infrared cloud drift winds (GOESCD), and GOES imager cloud top water vapor winds (GOESWV). The five in-situ data types are rawinsonde temperature and moisture (RAOBM), rawinsonde winds (RAOBW), aircraft temperatures (ACARM), aircraft winds (ACARW) and surface land observations (SFCLM). The three 11-day periods are 13-23 December 1998, 10-20 April 1999, and 13-23 July 1999. FI statistics are presented for three standard meteorological fields, at each of five isobaric levels over both the entire domain and CONUS. The fields consist of temperature, u-component of the wind and relative humidity. While only the u-component statistics are presented, the v-component FI statistics were found to be very similar.

The domain wide 24-hr FI results (Fig. 1) indicate that all of the data types provided some positive impact. RAOBM cumulatively had the largest positive contribution, with GOESCD another consistent contributor throughout. The precipitable water data types of SSM/I and GOESPW had the most positive FI during summer in terms of relative humidity, but their importance was reduced during winter (not shown). GOESWV and ACARM had the smallest cumulative impact of all ten data types, with their overall contribution being just slightly positive.

While the positive FIs are termed modest for all data types, it is important to note that very few negative FIs were observed in the domain wide diagnostics, even when examining individual time periods (not shown). Finally, also while not shown, it is important to note that the cumulative impact of most in-situ data types decreased in summer relative to winter, while the opposite was true for the remotely sensed data.

In the CONUS subsection (Fig. 2), the overall importance of in-situ data were larger than the remotely sensed data for most data types. RAOBW provided the most consistently positive FI from season to season, while the importance of RAOBM dropped dramatically from winter to summer (not shown). The most consistently positive FI from the remotely sensed data season to season was from GOESCD; however, GOESPW had some of the largest positive impacts in July of any data type for relative humidity (not shown). Overall, the number of negative FIs was found to be larger in the CONUS subsection than the entire domain for both the in-situ and remotely sensed data.

Several future studies could prove to be very beneficial. First, would a similar study of data in global models reveal the same results? Second, what is the impact of using radiances versus retrievals in operational models? In any event, a more complete understanding of how to utilize existing and future data types is required if modeling improvements related to the available data are to be realized.

5. REFERENCES

Black, T. L., 1994: The new NMC mesoscale Eta model: Description and forecast examples. *Wea. Forecasting*, **9**, 265-278.

Rao, P. A., Z.-X. Pu, S. A. Braun, and C. S. Velden, 2000: Error characteristics of satellite derived water vapor winds as compared to ECMWF model analyses. Preprints, *10th Conf. on Satellite Meteorology and Oceanography*, Long Beach, CA, Amer. Meteor. Soc., 16-19.

Treadon, R., 1993: The NMC Eta model post processor: A documentation. Office Note 394, National Oceanic and Atmospheric Administration, 42 pp. [Available from NASA Goddard Space Flight Center, Wallops Flight Facility, Wallops Island, VA 23337.]

Velden, C. S., S. J. Nieman, W. P. Menzel, and S. T. Wanzong, 1997: Upper-tropospheric winds derived from geostationary satellite water vapor observations. *Bull. Amer. Meteor. Soc.*, **78**, 173-195.

Velden, C. S., T. L. Olander, and S. T. Wanzong, 1998: The impact of multispectral GOES-8 wind information on Atlantic tropical cyclone track forecasts in 1995. Part I: Dataset methodology, description and case analysis. *Mon. Wea. Rev.*, **126**, 1202-1218.

Zapotocny, T. H., and Coauthors, 2000: A case study of the sensitivity of the Eta data assimilation system. *Wea. Forecasting*, **15**, 603-621.

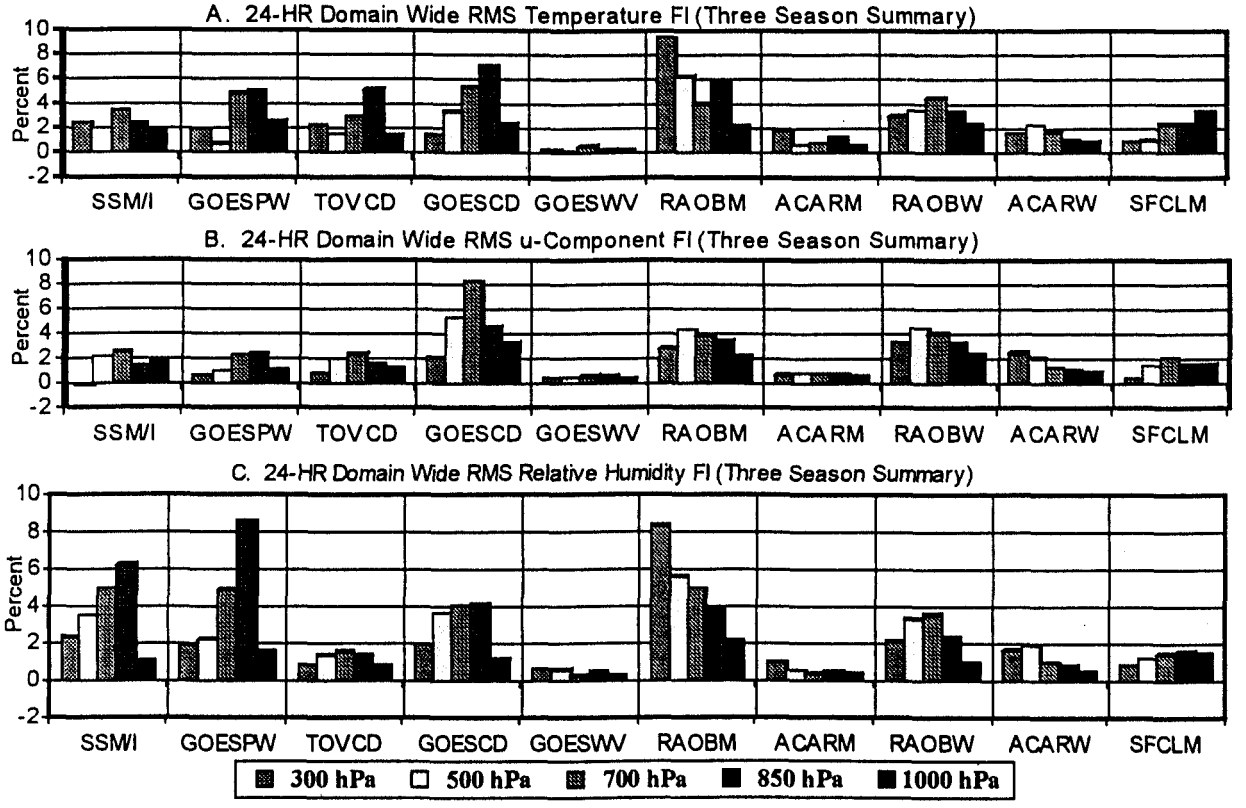

Fig. 1. Entire domain FI (%) of the ten data types after 24-hrs of ETA model integration.

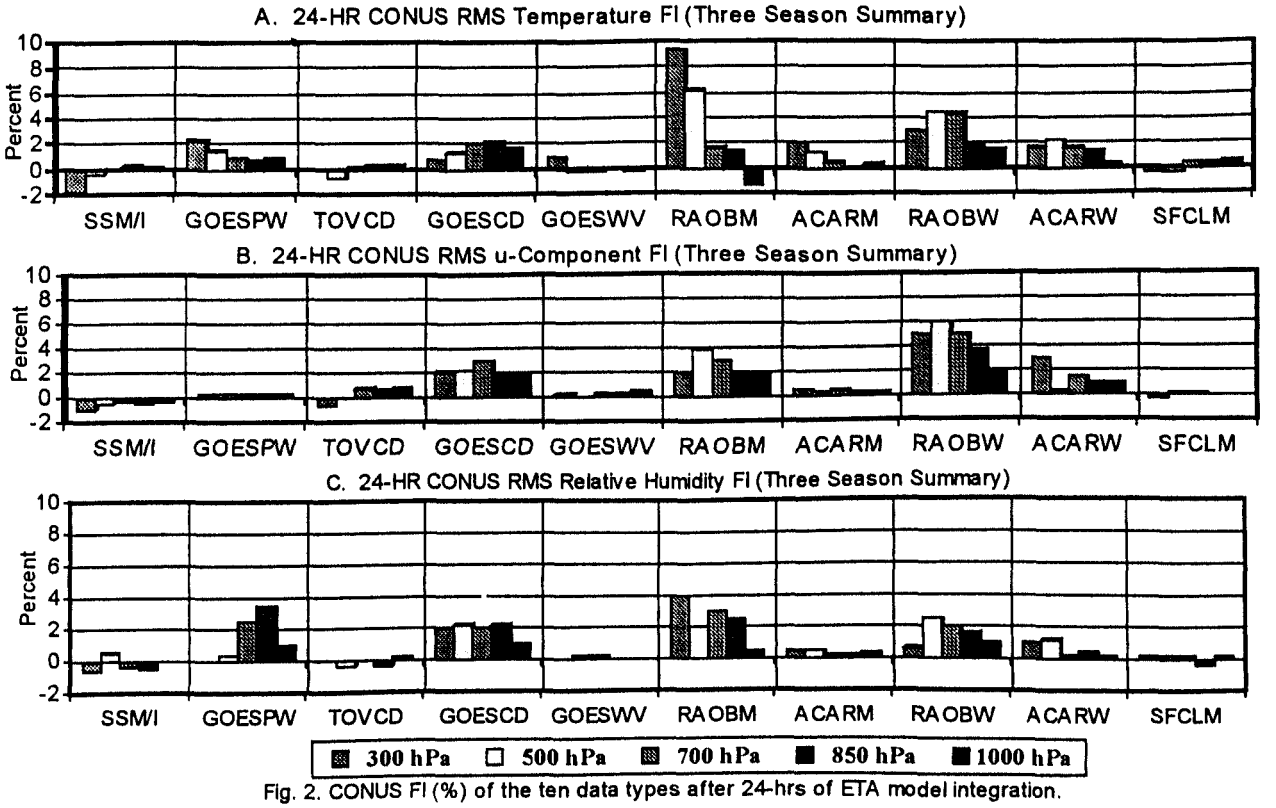

Fig. 2. CONUS FI (%) of the ten data types after 24-hrs of ETA model integration.

P3.10

ASSIMILATION OF GOES SOUNDER CLOUD TOP PRESSURE IN NCEP'S 48KM ETA MESOSCALE MODEL

James A. Jung
Cooperative Institute for Meteorological Satellite Studies (CIMSS)
University of Wisconsin-Madison

Robert M. Aune
NOAA/NESDIS, Office of Research and Applications, Advanced Satellite Products Team (ASPT)

Timothy J. Schmit
NOAA/NESDIS, Office of Research and Applications, Advanced Satellite Products Team (ASPT)

Tom H. Zapotocny
Cooperative Institute for Meteorological Satellite Studies (CIMSS)
University of Wisconsin-Madison

Madison, WI

1. INTRODUCTION

As numerical models move to higher resolution and become more sophisticated a greater emphasis will be put on cloud prediction schemes. In the past modelers have used a wide spectrum of cloud prediction algorithms. Zivkovic and Louis (1992) and Arakawa and Schubert (1974) used diagnostic relationships of model dependent moisture variables. Lin et al. (1983) used bulk parameterizations of condensation and precipitation. Cotton et al. (1982) used comprehensive physical cloud algorithms that incorporated predictive equations for numerous particle shapes, size distributions and growth rates.

More mesoscale models are incorporating cloud prediction schemes that represent cloud water explicitly. Zhao and Carr (1997) developed the cloud prediction scheme for the Eta Model (Rogers et al. 1996), Brown et al. (1998) developed the cloud prediction scheme presently used in the Rapid Update Cycle (Benjamin et al. 1998). These cloud schemes are playing an ever increasing role in the models through their interactions with radiation, moisture transport and precipitation forecasts.

Corresponding author address: James A. Jung, NOAA Science Center, 5200 Auth Road, Camp Springs, MD, 20746;
email: Jim.Jung@noaa.gov.

Attempts have been made to initialize moisture and clouds in models using various types of satellite observations. Various degrees of success, using different methods, have been obtained by Wright and Hand (1994), Aune (2000), Kim and Benjamin (2000), and Bayler et al. (2000). In this paper we describe our initial attempt to modify or nudge the Eta cloud water mass field toward current satellite cloud observations. Our goal is to produce an improved cloud and moisture field for the analysis and subsequent forecast.

2. CLOUD OBSERVATIONS

The cloud top pressure product used is derived from the Geostationary Operational Environmental Satellites (GOES) infrared sounder (Menzel et al. 1998). The sounder covers about half of the operational Eta domain (using both GOES-east and GOES-west) with a pixel resolution of about 10km. The cloud top pressure is determined by the CO_2 absorption and a "split window" technique (Menzel et al. 1992). These data are produced hourly by NOAA/NESDIS and are available to NCEP.

3. MODEL BACKGROUND

For this experiment we used the November 1999 version of NCEP's operational Eta Data Assimilation/ Forecast

System (EDAS) (Black 1994; Rogers et al. 1996). Our experiment was conducted at 48km resolution with 45 vertical layers and is the same size as the operational Eta. The observations, including radiances, used during the 12-hour data assimilation cycle were obtained from NCEP and are equivalent to the operational Eta.

4. TECHNIQUE DESCRIPTION

The latitude/longitude of each cloud observation is mapped onto the corresponding Eta line/element. In the case of the 48km Eta, it is possible to have more than one observation at a grid point. Where more than one cloud observation is present the lowest pressure (highest cloud) observation is used. The cloud top pressure is then converted to the corresponding model layer. In an attempt to reduce some of the temporal variability, the relative humidity is checked one layer above and below the observation and is adjusted to that layer with the highest relative humidity.

Starting from the top of the model downward, cloud water mass is set to the minimum model threshold down to the cloud layer. If the cloud water mass is greater than the model's minimum threshold at the cloud layer, the cloud water mass is not changed. If the cloud water mass is equal to the model's minimum threshold, cloud water mass is added. The amount of cloud water mass added varies with respect to the model's threshold to initiate precipitation. Presently one-fourth of the precipitation threshold is added. Cloud water mass is not adjusted below this point. If no cloud is detected in the model grid box, cloud water mass is set to the minimum threshold down to the surface of the model.

The cloud water mass is adjusted after each cloud physics timestep (every 4th model timestep or 480 seconds) with the cloud top pressure data valid during that hour. The cloud nudging technique is done during the entire 12 hour data assimilation cycle with the T-0 analysis being used for the forecast and the next data assimilation cycle.

5. RESULTS

The impact of initializing the cloud water field is determined by comparing forecasts with the initialized clouds to a parallel control forecast which is as close as possible to the operational Eta model. The control forecast typically has an excess of high cirrus clouds. Most of the adjustment the cloud nudging does during the 12 hour EDAS is to remove cirrus. A comparison of a cloud-adjusted analysis with the control analysis is shown in Fig.1. Once the forecast cycle starts the Eta model begins to generate excess cirrus. There is generally good agreement out to about 6 hours at which time the cirrus becomes excessive as shown in Fig. 2.

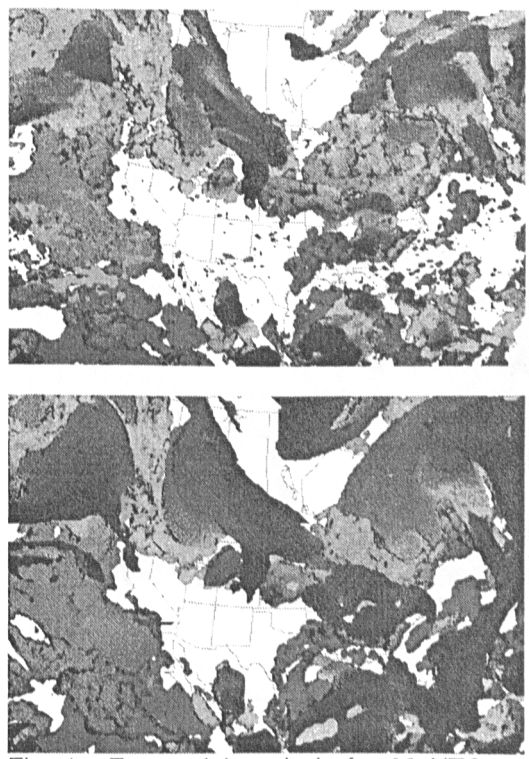

Fig. 1. Eta model analysis for 00 UTC on June 4, 2001. (top) Cloud field adjusted with GOES Sounder clouds. (bottom) Cloud field from control analysis.

The authors have looked at other statistics to determine impact of the cloud adjustment. We have presently completed winter and spring cases. The relative humidity shows a small improvement in the upper level wet bias associated with the

removal of the excess cirrus. The precipitation threat scores showed small mixed results. This result was expected since the cloud adjustment only has an impact out to about 6 hours where the threat scores are for a 24-hour time period. Results that were not expected are the lack of impact on the temperature. No differences were found in the temperature comparisons between the cloud adjusted and control forecasts. It has since been found that the radiation physics do not take into account changes in the grid scale cloud water mass.

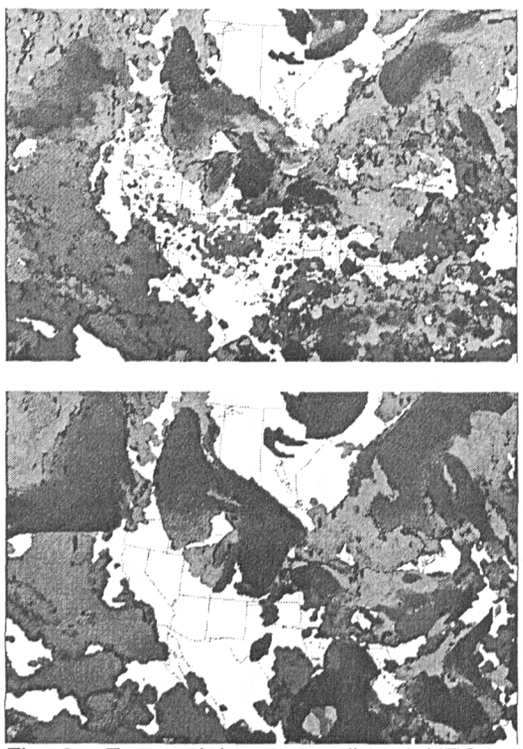

Fig. 2. Eta model output valid 06 UTC on June 4, 2001. (top) Analysis of the cloud field adjusted with GOES Sounder clouds. (bottom) Cloud field from 6 hour forecast using the 00 UTC cloud adjusted analysis.

Some problems were also found in the cloud product. At times there can be considerable temporal variability in the assigned cloud top pressure. To remove some of this, the layers above and below the assigned layer are checked for the highest relative humidity. If one of these layers has a higher relative humidity, the cloud top is reassigned to that layer.

6. REMARKS

The scheme described above will be tested during the summer and fall to get a more complete picture of the cloud assimilation effects. Efforts are presently underway at NCEP and NESDIS to address some of the deficiencies identified in the cloud product and the Eta's cloud physics.

7. REFERENCES

Arakawa A., and W.H. Schubert, 1974: Interaction of a cumulus cloud ensemble with the large-scale environment. Part I, *J. Atmos. Sci.* **31**, 674-701.

Aune, Robert M., 1996: Initializing cloud predictions using the GOES-8 sounder. 8th Conf. On Satellite Meteorology and Oceanography, Atlanta, GA, Amer. Meteor. Soc., 408-412.

Bayler, G.M., R.M. Aune, and W.H. Raymond, 2000: NWP cloud initialization Using GOES sounder data and improved modeling of nonprecipiataing clouds. *Mon. Wea. Rev.*, **128**, 3911-3920.

Benjamin, S.G., J.M. Brown, K.J. Brundage, B.E. Schwartz, T.G. Smirnova, T.L. Smith, L.L. Morone, and G.J. DiMego, 1998: The operational RUC-2. 16th Conference on Weather Analysis and Forecasting, Phoenix, AZ, Amer. Meteor. Soc., 249-252.

Black, T.L., 1994: The new NMC mesoscale Eta model: Description and forecast examples. *Wea. Forecasting*, **9**, 265-278.

Brown, J.M., T.G. Smirnova, and S.G. Benjamin, 1998: Introduction to MM5 level-4 microphysics into the RUC-2. Preprints, 12th Conf. On Numerical Weather Prediction, Phoenix, AZ, Amer. Meteor. Soc., 113-115.

Cotton W. R., M.A. Stephens, and G.J. Tripoli 1982: The Colorado State University three-dimensional cloud/mesoscale model – 1981. Part II: An ice phase parameterization. *J. Rech. Atmos.*, **16**, 295-320.

Kim, D., S.G. Benjamin, 2000: Assimilation of cloud-top pressure derived from GOES sounder. Preprints, 10th Conf. On Satellite Meteorology and Oceanography, Long Beach, CA. Amer. Meteor. Soc., 110-113.

Lin, Y-L., R.D. Farley, and H.D. Orville, 1983: Bulk Parameterization of the snow field in a cloud model. *J. Clim. Appl. Meteor.*, **22**, 1065-1092.

Menzel, W.P., F.C. Holt, T.J. Schmit, R.M.Aune, A.J. Schreiner, G.S. Wade, and D.G. Gray, 1998: Application of GOES-8/9 soundings to weather forecasting and nowcasting. *Bull. Amer. Meteor. Soc.*, **79**, 2059-2077.

Menzel, W.P. D.P. Wylie and K.I. Strabala, 1992: Seasonal and diurnal changes in cirrus clouds as seen in four years of observations with the VAS. *J. Appl. Meteor.*, **31**, 370-385.

Rogers, E., T.L. Black, D.G. Deaven, G.J. DiMego, Q. Zhao, M. Baldwin, N.W. Junker, and Y. Lin, 1996: Changes to the operational "early" Eta analysis/forecast system at the National Centers for Environmental Prediction. *Wea. Forecasting*, **11**, 391-413.

Wright, B.J., and W. Hand, 1994: An operational cloud analysis for the UK Met Office mesoscale model. Preprints, 10th Conf. On Numerical Weather Prediction, Portland, Amer. Meteor. Soc., 321-323.

Zhao, Q., and F.H. Carr 1997: A prognostic cloud scheme for operational NWP models. *Mon. Wea. Rev.*, **125**, 1931-1953.

Zivkovic, M. and J-F. Louis, 1992: A new method for developing cloud specification schemes in a general circulation model. *Mon. Wea. Rev.*, **120**, 2928-2941.

P3.11

GPS-DERIVED INTEGRATED PRECIPITABLE WATER COMPARED WITH AFWA MM5 MODEL OUTPUT

Patricia A. Vollmer
Gary R. Huffines
Department of Engineering Physics
Air Force Institute of Technology, Wright-Patterson AFB, OH*

1. INTRODUCTION

GPS-derived precipitable water is a tool that provides unprecedented spatial and temporal resolution of water vapor, a highly variable parameter that is currently very difficult to accurately initialize. By measuring the "wet delay" of a transmission to a GPS receiver, where the delay is proportional to the integrated water vapor, it is possible to remotely sense a line-of-sight precipitable water amount for a given transmission time and receiver location. This parameter can be normalized into an estimate of a vertically integrated precipitable water value. In order to produce the most accurate water vapor measurement, the GPS receiver must have a means to measure temperature and sea level pressure concurrently.

The goal of this research is to perform statistical comparisons of raw precipitable water measurements from existing GPS-Meteorology sensor networks (networks of sensors with temperatures and SLP measurement devices in place) in five regions worldwide. This data will be compared with Air Force Weather Agency Mesoscale Model 5 (AFWA MM5) moisture output. This information will be presented to AFWA as evidence regarding future integration of GPS precipitable water measurements into their model initialization schemes.

2. BACKGROUND

2.1. *Delays in the GPS Signal*

The Global Positioning System was established by the U.S. government in the early 1980s as a crucial element in navigation and relative positioning. Today, GPS includes a constellation of 24 low-earth-orbit (LEO) satellite vehicles that transmit signals in the L-band (1.2 and 1.6 GHz) to terrestrial users equipped with receivers. These signals are converted into information to aid in navigation, timing, and positioning, not only for military assets, but also for many civilian uses (Trimble 1996).

Due to the requirement for highly accurate GPS readouts in every transmission, post-processing has been developed to write out signal delays from each of these transmissions. These delays are excess path lengths due to the phase shifting between the standing signal and the transmission signal. They are calculated out of the signal through post-processing at the receiver end of the transmission. There are two major components of the GPS signal delay, the hydrostatic delay and the wet delay.

Hydrostatic delay arises from the induced dipole moment of the atmosphere. This part of the delay factors in all constituents of the neutral atmosphere (to include nitrogen, oxygen, argon, and other trace gases) *except* water vapor. These constituents have relatively uniform composition in the troposphere. Using a surface pressure measurement, the hydrostatic delay is calculated:

$$ZHD = \frac{(2.2779 + 0.0024) P_s}{f(\phi, H)}$$

Ps is the surface pressure, and f is the variation of the gravitational constant with latitude and height (Borbas 1997). With surface pressure measurements, the hydrostatic delay can be measured to better than 1mm. (Businger 1996).

The wet delay arises from the refractivity of the water vapor in the neutral atmosphere. Due to the variability of water vapor in the tropopause, the wet delay can vary from 10mm in desert regions to more than 400mm in more humid regions. Not only is there a significant spatial variability in wet delay, but there also exists a significant temporal variability. When the wet delay is measured in the zenith direction, an amazingly simple relationship exists:

$$PW := \Pi \cdot ZWD$$

PW is precipitable water in a vertical column, and ZWD stands for zenith wet delay, which is typically a slant-wise wet delay measurement that has been normalized with a basic mapping function: ZWD = WD*(sin θ), where θ is the elevation angle.

* *Corresponding author address*: Gary R. Huffines, Air Force Institute of Technology AFIT/ENP, 2950 P. St. WPAFB, OH 45433, USA, E-mail: gary.huffines@afit.edu

$$\Pi = \frac{10^6}{\rho \cdot R_v \cdot \left[\left(\frac{k_3}{T_m}\right) + k_2\right]}$$

R_v is the gas constant for water vapor, ρ is the density of liquid water, T_m is the mean temperature through a vertical layer, and k_2 and k_3 are constants related to the refractivity of water (Bevis 1994).

2.2. *Research Efforts in GPS Meteorology*

Exploiting the GPS signal delay for meteorological applications is a relatively young endeavor. The GPS network has only been operational since the mid-1980s. GPS meteorology shows considerable promise for both short- and long-term forecasting, including climatology. In addition, research is ongoing for the assimilation of GPS water vapor data into larger-scale forecast models, the mapping of global water vapor patterns in a manner similar to computerized axial tomography (CAT scanning), and the measurements of atmospheric refractivity soundings via radio occultation to gather information about temperature, humidity and ionospheric structures (Ware 2000).

2.3. *Precipitable Water in the AFWA MM5*

The MM5 is a three-dimensional, non-hydrostatic, primitive-equation, nest-grid model with a terrain following vertical coordinate system (σ) (Grell 1995). It is the Air Force Weather Agency's (AFWA's) weather forecast model of choice. As of this writing, AFWA runs MM5 windows over 29 worldwide mission critical theaters of operations. AFWA maintains 18 parent domains, from which 11 inner nest windows are derived (Applequist 2001, personal correspondence).

Kuo (1993) has already shown that precipitable water, although a two-dimensional variable can be aptly assimilated into the MM5. Therefore, it is plausible that with its exceptional temporal and spatial resolution, the GPS-derived precipitable water can be a valuable input for modeling the tenuous water vapor variables.

Gutman (2001) has offered theories on how GPS PWV can be integrated into mesoscale models by using a vertical aliasing technique, similar to the one mentioned by Kuo (1993). Gutman shows a case study in which GPS PWV was assimilated into the National Center for Environmental Prediction's (NCEP's) Rapid Update Cycle 2 (RUC-2) mesoscale forecast model. In addition, he cites previous studies in which it has been shown that the most vertical variability in the integrated vertical moisture profile is in the lower 4000m.

Currently, data is assimilated into AFWA's MM5 for analysis using the Multivariate Optimal Interpolation (MVOI) scheme. MVOI uses point analyses in the vertical to derive vertical profiles of temperature, winds, and moisture. GPS-derived moisture products are currently not assimilated into the MM5 (partly due to the form of assimilation technique). By summer 2002, AFWA's analysis scheme will transition from MVOI to the 3-Dimensional Variational Analysis (3DVAR) system. This method is designed to employ more data sources along with parallelization techniques to compile more information in a comparable amount of time (Ritz, et. al. 2001). This future transition provides more validity to my research, for 3DVAR may be able to ingest the GPS-derived products for initialization.

3. METHODOLOGY

Five locations have been selected and each met the following criteria: (1) the region has an existing GPS Meteorology network whose resolution is better than the existing rawinsonde network and (2) AFWA must have an existing MM5 grid in place and operating daily. For each location, a period of time will be selected to study the location in a significant weather event. Ten days should be enough time to gather a variety of weather conditions. Barring an anomalous long-term weather pattern (such as an Omega block), a significant synoptic scale system should impact each area, giving the network a chance to gather potentially significant precipitable water data.

NOAA's Forecast Systems Laboratory is providing the CONUS GPS meteorology data for this research. In addition, representatives in the GPS meteorology office have been coordinating through international channels the use of some of the international GPS meteorology networks. For research with the most Air Force applicability, access to the international locations would develop a well-rounded data set, this way we can get an idea of how this information will fare in more significant warfighting locations.

For each area, the following tasks will be accomplished to prepare the data for analysis:

- Gather GPS readings from the network sites every 3 hours and process the data into precipitable water values.
- At each data time, place the precipitable water values onto the corresponding MM5 grid, using a gridded interpolation technique.
- Perform analysis runs for the MM5 at 12-hour intervals. Each of these runs will have an analysis and 3 hour forecasts for 12 hours.

Having performed the analysis preparation, various statistical measurements will be taken to

compare the GPS-derived moisture profiles with MM5 analysis and forecast data. While the statistical measures that will need to be performed have not been finalized, bias, skill score, and correlations would be among the those measured. These parameters would be calculated for each location, and then compared among the locations – both with the MM5 output and with each other. Output will include both tabular and graphical methods.

4. EXPECTED RESULTS

This project is expected to further verify what Powers and Gao (2000) and Spangenberg (1997) have shown in related studies involving MM5 moisture: significant shortcomings exist in the MM5 moisture prognoses. In fact, Powers demonstrated that assimilating DMSP precipitable water data into the MM5 could reduce errors by more than 30%! If a significant difference between the GPS moisture plots and MM5's precipitable water plots can be shown, perhaps AFWA can allow this research to continue by testing true incorporation of GPS-derived precipitable water into the model.

5. ACKNOWLEDGEMENTS

The views expressed in this article are those of the authors and do not necessarily reflect the official policy or position of the Air Force, the Department of Defense or the U.S. Government.

6. REFERENCES

Bevis, Michael, "GPS Meteorology: Mapping zenith wet delays onto precipitable water," *Journal of Applied Meteorology*, **33**, 379-386, 1994.

Bevis, Michael, "GPS Meteorology: Remote Sensing of Atmospheric Water Vapor Using the Global Positioning System," *Journal of Geophysical Research*, **97**, No D14, 15,787-15,801, 1992.

Businger, Steven, "The Promise of GPS in Atmospheric Monitoring," *Bulletin of the American Meteorological Society*, **77**, 5-18, 1996.

Grell, G.A., *A Description of the Fifth Generation Penn State/NCAR Mesoscale Model (MM5)*, NCAR Tech. Note TN-398+STR, 122 pp., 1995.

Gutman, Seth I., "The Role of Ground-Based GPS Meteorological Observation in Numerical Weather Prediction," *GPS Solutions*, **4**, 2001.

Kuo, Ying-Hwa, "Assimilation of Precipitable Water Measurements into a Mesoscale Numerical Model," *Monthly Weather Review*, **121**, 1215-1238, 1993.

Powers, Jordan G. and Kun Gao, "Assimilation of DMSP and TOVS Satellite Soundings in a Mesoscale Model", *Journal of Applied Meteorology*, **39**, 1727-1741, 2000.

Ritz, Richard L., Michael D. McAtee, Robert T. Swanson, Jr., "Data assimilation at the Air Force Weather Agency," in press for preprint, 2001.

Spangenberg, Douglas A., "Evaluation of model-simulated upper troposphere humidity using 6.7 mm satellite observations," *Journal of Geophysical Research*, **102**, 25,737-25,749, 1997.

Trimble Navigation Inc., *How GPS Works*, Online Tutorial, Trimble Navigation Inc., 1996.

Ware, Randolph H, "SuomiNet: A Real-Time National GPS Network for Atmospheric Research and Education," *Bulletin of the American Meteorological Society*, **81**, 677-693, 2000.

P3.13 UTILIZING VARIATIONAL METHODS TO INCORPORATE A VARIETY OF SATELLITE DATA IN THE LAPS MOISTURE ANALYSIS

Daniel Birkenheuer*
NOAA Research - Forecast Systems Laboratory, Boulder, Colorado

1. INTRODUCTION

The Local Analysis and Prediction System (LAPS) analyzes three-dimensional moisture and other state variables hourly (or more frequently) over a high-resolution relocatable domain. LAPS analyses have been routinely used to initialize local-scale, high-resolution models such as the Colorado State University's Regional Atmospheric Modeling System (RAMS) model and the National Center for Atmospheric Research's MM5 (mesoscale model, version 5) as a means to utilize local data in the forecast model. LAPS has been integrated into the Advanced Weather Information Processing System (AWIPS) as part of the National Weather Service (NWS) modernization. Research to expand LAPS capabilities is one avenue toward providing advanced technologies and new innovations to the operational forecaster.

This paper describes progress toward advancing the variational technique in the LAPS moisture analysis. To date, the variational step has been used only with GOES sounder radiances. Other moisture variables were analyzed separately and either merged with that variational result or with the background field prior to the variational step (Birkenheuer 2000, 1999). This change will enable the use of more data in the variational framework. The solution strategy allows different data sources to be represented by different terms in the minimized functional. The functional can automatically adjust to match the datasets present. More important, this approach accommodates nonlinear functionals.

1.1 *Brief History of LAPS*

During the 1980s, FSL conducted forecast exercises to test its workstation prototypes. Forecasters were burdened with the impossible task of reviewing all the incoming data made possible through new technologies, while producing timely forecasts. It became obvious that local data needed to be objectively analyzed in conjunction with nationally disseminated data. Conceived as a resolution to this challenge, LAPS was designed to analyze available local data in real time on affordable computer workstations and utilize the analyses to initialize local-scale forecast models. So far LAPS has been interfaced with RAMS and MM5, but in principle it can function with any weather prediction model. Such models can address specific problems of a small forecast domain with greater detail than can be achieved with nationally disseminated model guidance (Snook et al. 1998). A more detailed review of LAPS is available in McGinley et al. (1991).

The LAPS system is routinely tested with new data sources and innovative improvements, using more "conventional" data, which typically are nationally disseminated. Advanced data include Doppler reflectivity and velocity fields, satellite observations including GOES infrared (IR) sounder data, wind profiler data, automated aircraft reports, and dual-channel ground-based radiometer data. New data sources included here are GOES-derived layer precipitable water data (GVAP), and Global Positioning System (GPS) data.

2. DATA SOURCES SPECIFIC TO THIS UPGRADE

2.1 *GOES-Derived Layer Precipitable Water Data*

GVAP data were obtained from the University of Wisconsin - Madison in real time on a daily basis (Menzel et al. 1998). The new variational scheme scales the appropriate parts of the LAPS moisture column to fit each of the three layers provided by GVAP data. The prior LAPS system only utilized total column GVAP water vapor data. The GVAP layers (defined as surface to 0.9 sigma, 0.9 to 0.7 sigma, and 0.7 to 0.3 sigma) are converted to a pressure coordinate system as part of the GVAP preanalysis. Also as part of this step, data are distributed on an analysis grid with a radial influence corresponding to the field of view. In this case, 30 km GVAP data have a nominal latency of 2 h at the current time.

2.2 *Global Positioning System Vapor Delay Data*

GPS data refer to derived total column water vapor (zenith) from GPS signal delay (Wolfe et al., 2000). These data are obtained in real time with a characteristic latency of 20 min. GPS data are immune from cloud effects, and therefore can be used where clouds are present. A horizontal influence of 12 km was applied to the GPS data. Similar to the GVAP data

* *Corresponding author address*: Daniel Birkenheuer, NOAA FSL, R/FS1, 325 Broadway, Boulder, Colorado 80305; e-mail birk@fsl.noaa.gov

treatment, these data are distributed on an analysis grid.

2.3 *Cloud Data*

Gridded cloud data are obtained from the LAPS cloud analysis, which relies on satellite image data in addition to Doppler radar, ACARS, surface-based observations of sky conditions, and pilot reports. These data define clear fields of view for utilizing satellite radiance data and help identify regions that require saturation due to complete cloudiness. In partly cloudy regions, the scheme relates cloud fraction to RH and influences the variational result. The partial cloud enhancement starts at 0.6 cloud fraction assigning a 60% RH at that point, and ramps linearly to saturation at total cloud cover.

3. LAPS MOISTURE ANALYSIS

The specific humidity (SH) module is one of 17 LAPS algorithms that span everything from data preparation and quality control (QC) to actual analysis. In addition to state variables, LAPS also produces highly specific analyses of special interest, such as aircraft icing threat and relative humidity with respect to both mixed and liquid phases. The SH module is one of the last analyses run, prior to the new mass balance scheme. It incorporates many fields that have already been processed such as clouds and surface moisture.

3.1 *Background Setup*

Like most analysis systems, LAPS requires a starting field, which it later modifies by adding information from other datasets. This background, or first-guess field for the test discussed here, is FSL's Mesoscale Analysis and Prediction System (MAPS) analysis. Updated each hour, MAPS is the development model of the operational Rapid Update Cycle (RUC-2) at the National Centers for Environmental Prediction (NCEP). The background model moisture data are interpolated to the denser LAPS grid and reconciled with the LAPS temperature analysis to avoid supersaturation.

Additionally, LAPS can also use a previous short-range forecast (i.e., MM5 1-h forecast initialized with LAPS) and uses this as the background for the next analysis in the cycle. This four-dimensional data assimilation (4DDA) scheme is currently being tested using an hourly update cycle.

3.2 *Boundary Layer Moisture*

Since the surface analysis uses hourly observations, its representation of surface moisture is possibly the most up-to-date moisture field attainable using conventional data sources, and is key to tracking moisture changes in the boundary layer. The boundary layer moisture module mixes surface humidity into the calculated boundary layer by adjusting the moisture in the low levels of the 3-D grid.

3.3 *GVAP and GPS Pre-analysis*

The GVAP and GPS fields are individually preanalyzed prior to the variational step. This is done to specify data at all grid points and assure they have a spatial influence related to instrument characteristics. The preanalysis consists of a simple nearest gridpoint assignment of the observation, and a smoothed interpolated field between observation locations. In addition to the three GVAP fields (one for each sigma layer) and the one GPS field, each field has a corresponding weighting function. The spatial weight controls the horizontal influence of the data field at grid points surrounding those that represent the observation. This includes the spatial influence of observations and other error factors (i.e., limb effects for microwave data, a possible future consideration). In addition, data latency (temporal considerations) can be set up to modify data source influence in the variational step in this same function.

3.4 *The Expanded Variational Adjustment*

The variational adjustment using GOES radiances (Birkenheuer 1999) is being expanded to include GVAP layer precipitable water (over the column water previously analyzed), GPS total column water, and cloud information in one step. The cloud information is made available from the LAPS cloud analysis (Albers et al. 1996). In this newly revised variational approach, cloud fraction is included in the moisture solution.

3.5 *Cloud Saturation*

As a safeguard to assure consistency, a final check is made to the field to make sure that moisture is saturated in 100% cloudy areas with respect to the applicable water phase. With the variational step now including cloud influence, this adjustment is invoked less often.

3.6 *Quality Control*

The final step in the SH algorithm is quality control. Each moisture value is compared to the LAPS analyzed temperature, and if supersaturated, it is reported and reduced to saturation. Typically, supersaturation rarely occurs.

4. VARIATIONAL FORMALISM

The mathematical formalism of the variational procedure is presented in equation 1. The advantage of this approach is that it offers a robust method for operational application and can accommodate nonlinear terms.

$$J = S_{SAT}\sum_{k=1}^{7}\frac{GT(g_i)[R(t,cq,o_3)_i - R_i^o]^2}{E_{SAT}^2 L_{SAT}} + \sum_{i=1}^{N}\frac{(1-c_i)^2}{E_{BACK}^2}$$
$$+ S_{GPS}\frac{(\sum_{i=1}^{N} c_i q_i - Q^{GPS})^2}{E_{GPS}^2 L_{GPS}} \qquad (1)$$
$$+ S_{GVAP}\sum_{j=1}^{3}\frac{G(g)(\sum_{i=1}^{N} P_{ji}(c_i q_i) + Q_j^{GVAP})^2}{E_{GVAP_j}^2 L_{GVAP}} + S_{CLD}\sum_{i=1}^{N}\frac{g_i[c_i q_i - q_s(t_i)]^2}{E_{CLD}^2 L_{CLD}}$$

Each term in (1) is modified by the variable *S*, which is a switch (with the exception of the background term which is always on). Thereby, the terms can be used or ignored depending on whether or not data are available or if clouds are present. Furthermore, a user can easily add terms for new datasets by simply creating a new term. The variables are as follows:

- C_i the coefficient vector applied to *q* to adjust the moisture field. Ideally this would have the same dimensions as *q* has levels, but may be reduced depending on computer horsepower. Adjustment of this parameter is in essence the variational fit to the solution, i.e., $c_i q$ becomes the adjusted *q* field. The adjustment coefficient is a scalar with a lower limit of 0 (never negative). A value of 1 indicates no change to the background. Because of this, the system will only work with a quantity such as temperature or humidity that uses absolute units. For example, using this approach to analyze temperature in degrees F will fail.
- *q* the specific humidity profile at one LAPS grid point
- *R* the forward-modeled radiance or radiance observation with the superscript *o*.
- *i* index for the LAPS vertical (vector dimension of *q*), with a current maximum of 40 (accommodating the climatological stratospheric layers needed for the forward radiance model).
- *k* the index indicating the satellite sounder or imager channel used.
- Q^{GPS} the total precipitable water measurement from GPS.
- *E* the error function (squared quantity) that describes the observation or background error, subscripted by observation type.
- *L* spatial weighting term subscripted by observation type. This weights the smoothed (preanalyzed) field value by its proximity to the observation and reflects the horizontal influences of the measurement. Each data source has an associated gridded field of spatial-weighting terms characterizing its proximity to the observation and its spatial representation.
- *P* the function to convert from pressure to sigma coordinates
- Q^{GVAP} the GOES vapor total precipitable water layer data. The layers are defined in sigma coordinates and vary grid point to grid point.
- *j* the index of the GVAP layer, with a current maximum of 3 (1 is lowest, 3 is highest).
- *Cld* cloud function designating cloudy regions in the vertical, with dimensions of *q*.
- *J* the functional to be minimized.
- *t* is the temperature profile (LAPS) at the same location as *q*.
- *S* logical switch for the observation type to be present or not. Each term in the functional can be easily included or excluded depending on the presence of the data source. Also new data sources can be added by including new terms.
- $q_s(t)$ saturated *q* as a function of temperature.
- *g* cloud fraction indicator as a function of level.
- *G* a function of *g* such that it indicates cloud in the column. For radiance measurements, this has the advantage of disabling IR terms including GVAP. Finally, the GPS term would be unaffected by clouds in principle since the data source can deliver data in cloudy areas. However, the analysis needs to probably give more credence to the cloud field, since it is vital the cloud field complements the moisture field. *G* can be a linear function of cloud such that it might serve to help define partly cloudy regions by allowing a smooth gradient from total through partly cloudy to clear air.
- *GT* is a similar function to *G*, but it may be nonlinear and can match the satellite radiometer's field of view.

5. SOLUTION METHODOLOGY

The minimization of (1) is accomplished using the same methods as the prior moisture analysis. The Powell method (Brent 1973) employs a multidirectional search to seek out a solution. Typically, two to five calls of the algorithm are required to find a solution. Each call to the numeric method involves approximately 25 calls to the functional. Although more efficient methods are available, this technique has worked reliably to date. Model adjoints are not required for this technique.

6. EXAMPLE

The very deep and premature monsoon flow over the regional observation cooperative (ROC) domain in early July 2001 provided a very good signal for moisture study. Figures 1 and 2 contrast the old and new analysis schemes. Both figures depict a cross section of relative humidity from west to east through Boulder, Colorado.

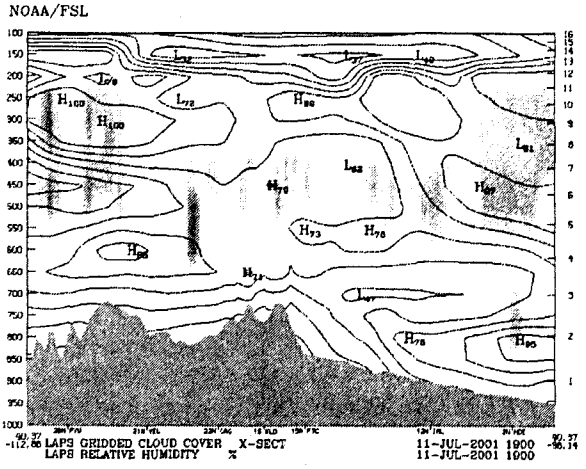

Fig. 1. Cross section through 40° N latitude showing relative humidity and cloud fraction through the ROC domain.

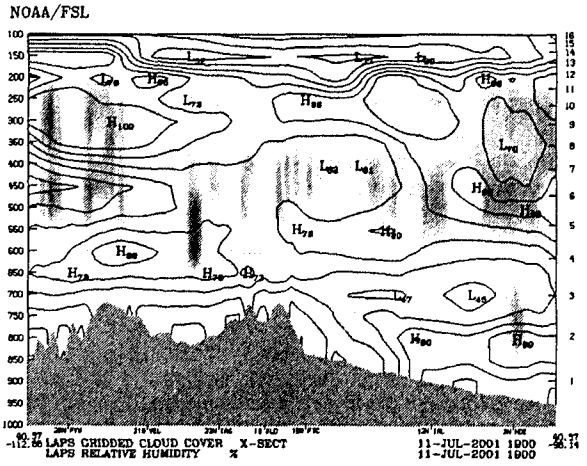

Fig. 2. Same as Fig. 1 except using the newer variational analysis.

For the most part, the two analyses are very similar with the newer scheme possibly showing more detail. The cloud field is the same in both sets and is depicted by shaded features. The lighter shades indicate low cloud fraction while black would show 100% cloud. It is apparent that very low cloud fractions existed; therefore, clouds had minor impact on the RH adjustment. Even so, the analysis shows higher RH values in partly cloudy areas. A quantitative evaluation of the scheme is currently being performed.

7. SUMMARY

The new functional solution is now being tested with broader focus on the run times and feasibility of real-time operation. These aspects of the algorithm look promising, even for AWIPS-type resources. Error functions are currently approximated and will require refinement.

When running the system in 4DDA mode, it quickly becomes apparent that model and analysis moisture components must be compatible. For example, the model may base RH computations on the liquid phase for all temperatures while the analysis may use ice as a reference below some threshold temperature. Such discrepancies can lead to artificial "generation" of water or chronic drying of the atmosphere as these discrepancies are compounded in the 4DDA cycle. The new variational scheme has demonstrated a resistance to this effect during ongoing 4DDA tests.

8. REFERENCES

Albers, S., J. McGinley, D. Birkenheuer, and J. Smart 1996: The Local Analysis and Prediction System (LAPS): Analyses of clouds, precipitation, and temperature. *Wea. Forecasting*, **11**, 273-287.

Birkenheuer, D., 2000: Progress in applying GOES-derived data in local data assimilation, *10th Conf. on Satellite Meteorology and Oceanography*, Amer. Meteor. Soc., Long Beach, CA, 70-73.

_____, 1999: The effect of using digital satellite imagery in the LAPS Moisture Analysis. *Wea. Forecasting*, **14**, 782-788.

Brent, R.P., 1973: *Algorithms for minimization without derivatives.* Prentice-Hall, Chapter 7.

McGinley, J. A., S. Albers, and P. Stamus, 1991: Validation of a composite convective index as defined by a real-time local analysis system. *Wea. Forecasting*, **6**, 337-356.

Menzel, W. P., F. C. Holt, T. J. Schmit, R. M. Aune, A. J. Schreiner, G. S. Wade, and D. G. Gray, 1998: Application of GOES-8/9 Soundings to weather forecasting and nowcasting. *Bull. Amer. Meteor. Soc.*, **79**, 2059-2077.

Snook J. S., P. A. Stamus, J. Edwards, Z. Christidis, and J. A. McGinley, 1998: Local-domain mesoscale analysis and forecast model support for the 1996 Summer Olympic Games. *Wea. Forecasting*, **13**, 138-150.

Wolfe, Daniel E., Seth I. Gutman, 2000: Developing an operational, surface-based GPS water vapor observing system for NOAA: Network design and results. *J. Atmos. Oceanic Technol.*, **17**, 426–440.

P3.14 ONE DIMENSIONAL VARIATIONAL ASSIMILATION EXPERIMENTS COMBINING GOES SOUNDER AND IMAGER RADIANCE DATA

Dongsoo Kim and Dezso Devenyi

Cooperative Institute for Research in Environmental Sciences (CIRES)

University of Colorado/NOAA Research-Forecast Systems Laboratory, Boulder, Colorado

1. INTRODUCTION

Sounder and imager data from the GOES platform offer an opportunity to enhance the quality of the initial conditions for numerical weather prediction, as is done in the Rapid Update Cycle (RUC, Benjamin et al., 2001). The most important strength of sounder data over imager data is that their multichannels are designed for retrieving vertical distribution of temperature and moisture. The relative advantages of GOES imager data over sounder data includes better spatial coverage in the RUC domain, higher ingest frequency (15 min vs 1 hour), and higher resolution (4 km vs 10 km). The higher ingest frequency helps in reducing temporal sampling error, and higher spatial resolution refines the spatial variability of clouds. Therefore, imager data are used to enhance the subgrid variation of clouds, namely, multilevel fractional clouds. We formulate the fractional cloud coverage derived by imager data as a weak contraint in one dimensional variational formulation to generalize current cloud analysis employed in the 20-km RUC.

2. 20-KM RUC CLOUD ANALYSIS

The 20-km version of RUC uses the bulk mixed-phase cloud microphysics scheme from the NCAR/Penn State MM5 model, with five hydrometeor types explicitly forecast. The RUC 1-h predicted hydrometeor mixing ratios provide background fields to be modified using the single field-of-view (FOV) GOES sounder-based cloud-top pressure data. A threshold value (10^{-5} g Kg^{-1}) of the hydrometeor mixing ratio determines predicted cloud-top pressures at each grid point. Then, the GOES cloud-top data are used to determine whether hydrometeors have to be added or cleared. Since the cloud-top pressure does not include cloud thickness, a conservative cloud thickness of 50 hPa is used for cloud building. For cloud clearing, hydrometeor mixing ratios are set to zero, and the water vapor profile is adjusted such that it does not exceed 50% in relative humidity in the cleared part of the column. Detailed description is given in Kim and Benjamin (2001). Figure 1 shows the single FOV GOES sounder-based cloud-top pressure data used in a RUC cloud analysis. Figure 2 shows GOES imager data based on cloud-top pressure processed on the same domain. While the GOES imager-based cloud uses the window channel method with 1-h forecast profiles as background, a strong resemblance is seen between the two products, providing justification for the combined use of the products for initializing clouds in the RUC model.

Corresponding author address: Dongsoo Kim, NOAA/FSL R/FS1, 325 Broadway, Boulder, CO 80305, dkim@fsl.noaa.gov

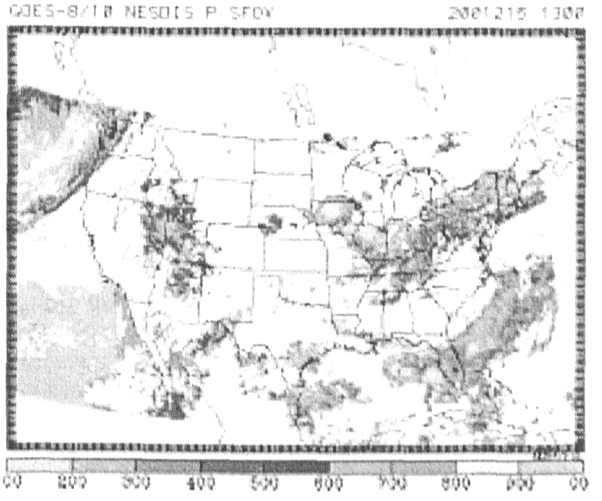

Figure 1. NESDIS single field-of-view cloud-top pressure data valid at 1300 UTC 3 August 2001. The median values of the samples in 20-km RUC are selected.

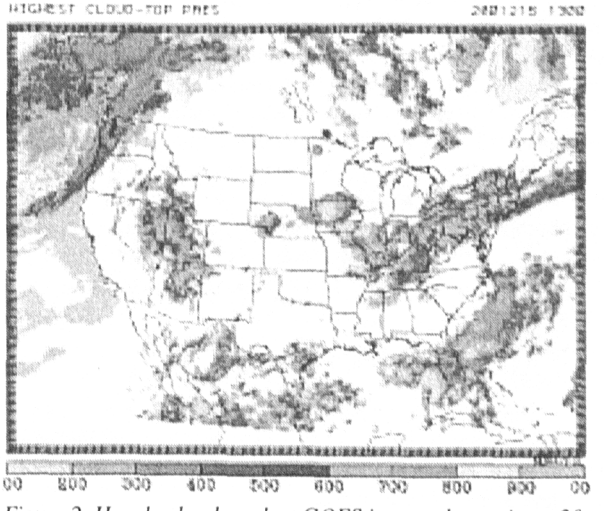

Figure 2. Hourly cloud product GOES imager data using a 20-km RUC 1-h forecast as background. The highest cloud-top pressure is plotted in the case of multilevel clouds.

3. DESIGN OF 1DVAR

In an earlier experiment, we have shown an example combining TIROS HIRS radiances with AVHRR radiances using the constrained least squares method, and results were compared with cloud profiling radar (Kim et al., 1997). In a new design of one-dimensional (1DVAR) assimilation of GOES sounder radiance data, we start with the familiar functional (for example Eyre et al., 1993)

$$2J(x) = (x - x_b)^T B^{-1}(x - x_b) + (y_o - H(x))^T R^{-1}(y_o - H(x)) + J_c + J_{op}$$

where B and R represent background error and the sum of observation and representativeness error covariances, respectively. In the first version of 1DVAR both of them are approximated by continuous functions. In a later version digital filters will be used according to the present RUC 3DVAR scheme (Devenyi et al., 2001). The nonlinear operator H is for the radiance forward model. The state vector x represents the vertical profile of temperature, water vapor, and cloud water mixing ratios. The first constraint term (J_c) is a restriction of the moisture profile to stay below saturation. The second term (J_{op}) constrains the cloud water profile by multilevel fractional cloud coverage information derived from the GOES imager. A quasi-Newton minimization method will be used in finding the optimal value of x.

4. RESULTS

We are currently evaluating two community forward/adjoint radiative transfer models, RTTOV (Saunders et al., 1999) and OPTRAN(McMillin and Kleespies, 2000) using identical background profiles and surface information (temperature, water vapor, skin temperature) at the Atmospheric Radiation Measurement (ARM) Cloud and Radiation Testbed (CART) site in Oklahoma in order to characterize bias and covariance errors in the forward model. The background profiles are 1-, 3-, 6-, 9-, and 12-h forecasts of height, temperature, water vapor, and winds as well as five hydrometeors (cloud water, rain water, ice, snow, graupel mixing ratios) from the RUC. Also, surface information is from the RUC forecasts. Both models are being used for GOES-8/10 sounder and imager radiance data, which are sampled hourly within an approximately 40-km x 40-km grid box. The sounder radiances are selected as a nearest neighborhood to the grid point, and all imager radiances are adaptively classified to obtain fractional coverages and their respective cloud-top heights. The results will be shown at the conference.

5. ACKNOWLEDGMENTS

This research is partially supported by the NASA/NOAA GCIP and NASA/NOAA Joint Center for Satellite Data Assimilation. Authors thank Nita Fullerton, Tanya Smirnova and Steve Koch for their review.

REFERENCES

Benjamin, S. G., G. A. Grell, S. S. Weygandt, T. L. Smith, T. G. Smirnova, B. E. Schwartz, D. Kim, D. Devenyi, K. J. Brundage, J. M. Brown, and G. S. Manikin, 2001:The 20-km version of the RUC. *Preprints, 14th Conf. on Numerical Weather Prediction,* Ft. Lauderdale, FL., Amer. Meteor. Soc. J75-79

Devenyi, D., S. G. Benjamin and S. S. Weygandt, 2001: 3DVAR analysis in the Rapid Update Cycle. *Preprints, 14th Conf. on Numerical Weather Prediction,* Ft. Lauderdale, FL., Amer. Meteor. Soc. J103-107

Eyre, J. R., G. A. Kelly, A. P. McNally, E. Andersson, and A. Persson, 1993: Assimilation of TOVS radiances through one dimensional variational analysis. *Quart. J. Roy. Meteor. Soc.*, 119, 1427-1463

Kim, D., B. Stankov, and K. P. Moran, 1997: Evaluation of multilevel cloud parameters with cloud profiling radar. *Preprints, 9th International TOVS Study Conf.,* Igls, Austria.

Kim, D. and S. G. Benjamin, 2001: Cloud/hydrometeor initialization for the 20-km RUC using satellite and radar data. *Preprints, 14th Conf. on Numerical Weather Prediction, Ft. Lauderdale,* FL., Amer. Meteor. Soc. J113-115

McMillin, L. M. and T. Kleespies, 2000: A rapid transmittance procedure for use in numerical models, *Preprints, 10th Conf. on Satellite Meteorology and Oceanography,* Long Beach CA, Amer. Meteor. Soc. 48-50.

Saunders, R., M. Matricardi, and P. Brunel, 1999: An improved fast radiative transfer model for assimilation of satellite radiance observations. *Quart. J. Roy. Meteor. Soc.*, 125, 1407-1425.

P3.15 **The Assimilation of Satellite Observations with the NRL Atmospheric Variational Data Assimilation System (NAVDAS)**

Nancy L. Baker*, Roger Daley, Steve Swadley, Jim Clark, Ed Barker, Jim Goerss, Keith Sashegyi
Naval Research Laboratory, Monterey CA

1. INTRODUCTION

Scientists at the Marine Meteorology Division of the Naval Research Laboratory have recently developed a new three-dimensional variational system NAVAS (Navy Atmospheric Variational Analysis System). NAVDAS is designed to replace the operational multivariate optimum interpolation analysis system (Barker (1992); Goerss and Phoebus (1992)), and to satisfy both the global and regional atmospheric data assimilation requirements of Fleet Numerical Meteorology and Oceanography Center.

NAVDAS is designed to assimilate a variety of satellite observations, including visible and infrared cloud-tracked and water vapor winds, scatterometer winds, radiances or retrievals for polar orbiting sounders, and the Special Sensor Microwave Imager (SSM/I) surface wind speed and total precipitable water. This paper highlights some of the more innovative features of NAVDAS satellite observation assimilation. Additional details may be found in Daley and Barker (2000) or Daley and Barker (2001).

2. ANALYSIS ALGORITHM

The most probable (maximum likelihood) analysis state vector $\mathbf{x}_a$ may be obtained by minimizing the scalar cost function J with respect to $\mathbf{x}_a$, where

$$J = 0.5[\mathbf{y} - H(\mathbf{x}_a)]^T \mathbf{R}^{-1}[\mathbf{y} - H(\mathbf{x}_a)] + 0.5[\mathbf{x}_b - \mathbf{x}_a]^T \mathbf{P}_b^{-1}[\mathbf{x}_b - \mathbf{x}_a], \quad (1)$$

where $\mathbf{x}_b$ is the background state vector, $\mathbf{y}$ is the vector of observations, $\mathbf{R}$ is the positive-definite symmetric observation error covariance matrix, and $\mathbf{P}_b$ is the square, symmetric positive definite background error covariance matrix. In general, the application of the forward operator H represents any necessary spatial and temporal interpolations from the forecast model background to the observation location and time. If the observed quantity is not directly related to the model state variables, H also represents the transformation from the forecast values to the observation quantity. For satellite radiances, $H\{\mathbf{x}_a\}$ represents the forward radiative transfer model applied to $\mathbf{x}_a$ and computes the analyzed radiances. The forward operator H is nonlinear for some observations (such as SSM/I windspeed and TOVS radiances when moisture is considered).

The cost function J (for the linearized analysis problem) is minimized when

$$\mathbf{x}_a - \mathbf{x}_b = \mathbf{P}_b\mathbf{H}^T\left[\mathbf{H}\mathbf{P}_b\mathbf{H}^T + \mathbf{R}\right]^{-1}\left[\mathbf{y} - H(\mathbf{x}_b)\right], \quad (2)$$

where the Jacobian matrix $\mathbf{H}$ corresponds to the forward operator H linearized about the background $\mathbf{x}_b$. The order of this equation is equivalent to the number of observations used in the analysis, and is typically between 200,000 and 300,000.

2.1 *Clustering of High Density Observations*

Since NAVDAS is an observation space algorithm, it is computationally efficient when the observation density is lower than the grid density. When the horizontal density of the observations exceeds the grid density, the algorithm becomes less efficient (see Section 4.3.3 of Daley and Barker (2000) for the discussion of high vertical density observations). Satellite observations in particular may have very high spatial density. Conventional solutions include thinning the observations, or creating super-observations. NAVDAS utilizes both of those approaches, but can also cluster the observations when the horizontal density exceeds the grid density. Effectively, this means that the background error covariance term $\mathbf{H}\mathbf{P}_b\mathbf{H}^T$ in (2) is computed between analysis gridpoints (rather than observation locations), and then projected into observation space.

3. ASSIMILATION OF SATELLITE SOUNDER OBSERVATIONS

For polar-orbiting sounders such as NOAA/ATOVS, NAVDAS is designed to assimilate radiances, but can also assimilate retrievals provided by either outside agencies (e.g., National Environmental Satellite, Data, And Information Service or NESDIS), or in-house one-dimensional variational algorithms. In the present configuration, radiances are treated as a variant of profile (e.g., several collocated radiances) instead of a variant of a single level observation. Both the retrievals and collocated radiances are projected onto the eigenvectors of the background error correlation matrix. However, for profiles, we assume that the observations project onto all the vertical modes, while for soundings we project onto the ten gravest vertical models. This eigenvector projection provides an efficient data compression technique for retrievals, and

* Corresponding author address: Nancy L. Baker, Naval Research Laboratory, Monterey, CA 93943-5506; e-mail: baker@nrlmry.navy.mil.

the number of vertical modes can be easily changed to accommodate varying numbers of independent pieces of information for different satellite sensors.

In the present NAVDAS configuration, the radiance assimilation is performed linearly so that the radiances are allowed to affect only the temperatures. Neglecting the contributions (through the Jacobian matrix) from certain satellite channels on the moisture, ozone, skin temperature and other surface variables, and clouds poses several problems because the background error covariances in radiance space or $\mathbf{HP}_b\mathbf{H}^T$ in (1) should properly be computed using the Jacobian matrix corresponding to the full state vector. There are several possible solutions. During the radiance pre-processing step, it is possible to compute $\mathbf{HP}_b\mathbf{H}^T$ corresponding to the neglected portion of the state vector and add these variances (that are in radiance space) to $\mathbf{R}$, effectively increasing the representativeness error. The modified observation error variances may then be passed to NAVDAS. A second option would be to include the full state vector and Jacobian matrix in the computation of $\mathbf{HP}_b\mathbf{H}^T$, but restrict the post-multiplier to include only the contributions to the temperature. This option would require carrying significantly more information for each profile. Other options include including a skin temperature analysis in NAVDAS, assimilating fewer channels, or performing a nonlinear iteration for satellite radiances. These options will be explored using NAVDAS.

4. DMSP SSM/I WINDSPEED AND TOTAL PRECIPITABLE WATER ASSIMILATION

SSM/I wind speeds may be assimilated using either a nonlinear or linearized forward operator. In either case, the wind speed alone is assimilated, as opposed to the method used in the operational MVOI where the wind direction is assigned from the background field. For the linearized SSM/I windspeed assimilation, the analyzed windspeed is a linear combination of the observed SSM/I windspeed and the background windspeed, and the analyzed wind direction is equal to the background wind direction (see Daley and Barker, 2000). Nonlinear SSM/I windspeed assimilation requires an outer iteration around the linearized NAVDAS algorithm. For each outer iteration, the SSM/I forward operator is relinearized around the best estimate of the atmospheric state. In the present NAVDAS configuration, only the SSM/I windspeed observations may be assimilated nonlinearly. Since these observations represent only a small proportion of the total observations, the outer iteration process can be substantially sped up if only the SSM/I windspeed observations are handled nonlinearly. This approach, which is described in Daley and Barker (2000), has been implemented in NAVDAS.

The SSM/I total precipitable water (TPW) retrievals represent the vertically integrated amount of water vapor in the atmosphere, while the NAVDAS state variables are vertical profiles of the natural log of specific humidity. In this case, the linearized forward operator $\mathbf{H}$ transforms vertical profiles of log specific humidity to TPW, while $\mathbf{H}^T$ performs the opposite transformation back to log specific humidity. The SSM/I TPW observations are assimilated by projecting the TPW innovations onto the 5 gravest eigenvectors or vertical modes of the background log specific humidity error covariances. This effectively spreads the TPW innovation out in the vertical, with the maximum effect in the lower troposphere.

5. THE NAVDAS ADJOINT

The adjoint of the NAVDAS assimilation system has also been developed. The adjoint of NAVDAS is used to compute the sensitivity of a specified forecast aspect J (such as forecast error) to the observations and background (see Baker (2000)). The sensitivity of J to the observations is derived from (2), and may be expressed as

$$\frac{\partial J}{\partial \mathbf{y}} = \left[\mathbf{HP}_b\mathbf{H}^T + \mathbf{R}\right]^{-1} \mathbf{HP}_b \frac{\partial J}{\partial \mathbf{x}_a}, \qquad (3)$$

where $\partial J/\partial \mathbf{x}_a$ represents the sensitivity of the forecast aspect J to the initial conditions (e.g., initial temperature and wind fields). Baker (2000) demonstrated that the sensitivity to an observation is largest when (1) the observation is relatively isolated or an abrupt change in observation density occurs, (2) the observation is assumed to be accurate relative to the background, and (3) the observation is located in a region with strong sensitivity of J to the initial temperature and wind fields. The sensitivities to the observations are also maximized when the spatial scales of $\partial J/\partial \mathbf{x}_a$ are similar to the spatial scales of the background error covariances. Since NAVDAS assumes that the background error correlation spectrum is red (i.e., large-scale), the sensitivity to the observations is largest when $\partial J/\partial \mathbf{x}_a$ is also large in spatial scale.

The magnitudes of the sensitivities of J to the TOVS Microwave Sounding Unit (MSU) channel 2 brightness temperatures, which have a broad vertical weighting function that peaks near 700 hPa (Smith *et al.* 1979), are shown in Fig. 1. The maximum observation sensitivities occur where large-scale $\partial J/\partial \mathbf{x}_a$ (amplitude and scale; not shown) coincide either with an abrupt discontinuity in the observation density, or with a relatively isolated observation. Observation discontinuities frequently occur with TOVS brightness temperatures for a variety of reasons. For example, polar-orbiting satellite instruments such as TOVS observe the atmosphere continuously, and the observations are selected or rejected according to the time difference between the observations and analysis. Two instances of time-window data discontinuities occur in Fig. 1 near 30°N, 155°W and 45°N, 175°E. The data discontinuity near 45°N, 175°E occurs in the middle of a large-scale sensitivity to the initial 700-hPa temperature

field (not shown), and is associated with large observation sensitivities.

Other discontinuities in the TOVS brightness temperatures are associated with larger observation errors, and these have important implications for data assimilation systems. For example, the TOVS brightness temperatures over land and ice are more difficult to assimilate properly and are eliminated in the present NAVDAS configuration, which creates a discontinuity in the brightness temperature observation density along the coastlines and ice-edge boundaries. The brightness temperatures along these boundaries contain contributions from the different surface types and have larger representativeness errors than the brightness temperatures over the open oceans. Abrupt changes in the data density also occur for the less accurate observations along the edges of the satellite scan (*cf.*, Chapter III.F.3.d). If the MSU observation errors are incorrectly assumed to be spatially homogeneous, and the data discontinuities coincide with large-scale analysis sensitivity gradients, the sensitivity to the relatively inaccurate observations along the data discontinuity will be larger than the sensitivity to the more accurate (data dense) observations. This implies that the less accurate observations have greater potential to change the forecast aspect J, and influence the analysis. As demonstrated in Chapter III.C.4.b and Chapter III.E.3.c, increasing the assumed observation error variance decreases both the observation sensitivity and the influence of the observation on the analysis. These results, which illustrate a non-targeting application of the data assimilation adjoint theory, highlight the importance of properly specifying the observation errors.

6. SUMMARY

NAVDAS will provide the U.S. Navy with a powerful and flexible system for assimilating observations and producing the initial conditions for the global and mesoscale numerical weather forecasts. One of the most important advantages of NAVDAS over the operational MVOI is the ability to directly assimilate satellite radiances and indirect observations such as SSM/I windspeed and total precipitable water. Preliminary results (using NESDIS retrievals) indicate an increase in the 120-hr global forecast skill of nearly 12 hours.

7. ACKNOWLEDGEMENT

The support of the Naval Research Laboratory and the Office of Naval Research, Marine Meteorology and Atmospheric Effects, through program element 0602435N, is gratefully acknowledged. We are also grateful for the support of Space and Naval Warfare System Command through program element 0609207N.

8. REFERENCES

Baker, N.L., 2000: Observation adjoint sensitivity and the adaptive observation-targeting problem. Ph.D. dissertation, Naval Postgraduate School, 265 pp. [Available from the Naval Research Laboratory, 7 Grace Hopper Ave., Monterey, CA 93943.]

Barker, Edward H., 1992: Design of the Navy's Multivariate Optimum Interpolation Analysis System. Wea. Forecasting, 7, 220-231.

Daley, R. and E. Barker, 2000: The NAVDAS Sourcebook. Naval Research Laboratory NRL/PU/7530-00-418, 151 pp.

Daley, R. and E. Barker, 2001: NAVDAS: Formulation and Diagnostics. Mon. Wea. Rev., 129, 869-883.

Goerss, J. and P. Phoebus, 1992: The navy's operational atmospheric analysis. Wea. Forecasting, 7, 232-249.

Smith, W.L., H.M. Woolf, C.M. Hayden, D.Q. Wark, and L.M. McMillin, 1979: The TIROS-N operational vertical sounder. *Bull. Amer. Meteor. Soc.*, 60, 1177-1187.

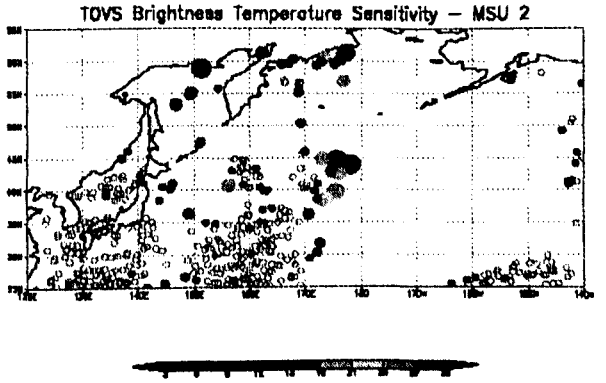

Figure 1. Magnitude of the sensitivity of the forecast aspect J to the TOVS MSU Channel 2 brightness temperatures valid at 00 UTC 7 February 1999. The open circles correspond to magnitudes less than 3.0. The magnitudes of the sensitivity are proportional to the size of the circles.

P3.16 IMPROVEMENTS TO U.S. AIR FORCE CLOUD FORECAST MODEL, ADVECT CLOUD

Steven J. Storch
and
David G. McDonald*
Air Force Weather Agency
Offutt Air Force Base, Nebraska

1. INTRODUCTION

Advect Cloud is an Air Force model that predicts the short-range movement of cloud cover. The model initialization is based on polar orbiting satellite imagery and has a long history at the Air Force Weather Agency (AFWA). The first numerical cloud forecast model was designed by Jensen during the early 1960s (Collins, 1970). This model was used operationally at the then Strategic Air Command Global Weather Central, from 1962-1964, and showed skill over persistence in forecasting macro-scale cloudiness. In 1964, the model was replaced by a condensation pressure spread (CPS) and trajectory model (Collins, 1970). CPS is defined as the number of hectopascals an air parcel must be lifted to become saturated. This model is the basis of the present Advect Cloud.

The initial cloud field is developed using AFWA's Real-Time Nephanalysis Model (RTNEPH) (Hamill, 1992). The RTNEPH combines DMSP and NOAA satellite data, rawinsonde data, conventional surface observations, and aircraft reports to provide an automated cloud analysis on a 25 nm horizontal resolution, bi-hemispheric grid (Kiess and Cox, 1988). Figure 1 shows the grid for the Northern Hemisphere. Each grid point is assigned a percent cloudiness at up to four levels. Since 1999, AFWA has produced developmental 12.5 nm hemispheric and 3 nm limited area cloud forecasts (Bieker, 2001).

Advect Cloud forecasts percent cloudiness for five fixed levels: 300, 500, 700, 850 hPa, and 60 hPa above the surface (defined as the gradient level). In addition, the total cloud in the column is forecast.

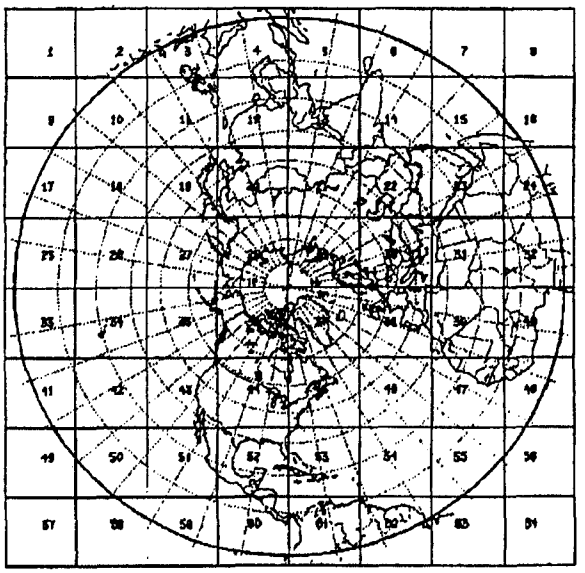

Figure 1. Advect Cloud uses a bi-hemispheric grid system. The Northern and Southern Hemispheres are run independently. Points off the hemisphere traditionally have been unused. This has caused continuity problems near the equator.

The first step in Advect Cloud is to convert the cloud analysis to a moisture amount. This is done through a cloud amount to CPS conversion table. Figure 2 shows the empirically derived relationship between CPS and cloudiness (Edson, 1965). In cloud-free areas, AVN or NOGAPS are used to initialize the model's moisture.

The next step is to develop trajectories to advect the moisture field. Advect Cloud uses a quasi-Lagrangian technique in its trajectory development (Crum, 1987). At the end of each one hour time step, the parcels are assumed to have advected to each grid point. This is accomplished by calculating trajectories (u, v, ω) that pass through each grid point at the end of the hour (McDonald, 1993). The advected parcel is initialized with the properties of the nearest grid point to the beginning of the trajectory.

* *Corresponding author address:* Dr. David McDonald, Air Force Weather Agency, DNXM, Offutt AFB NE, 68113-4049; email: david.mcdonald@afwa.af.mil.

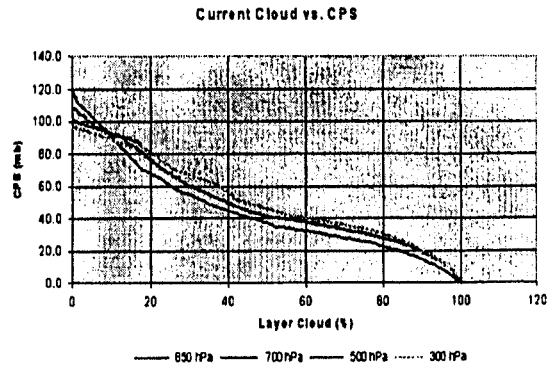

Figure 2. Advect Cloud uses empirically derived CPS to cloud amount values for 850, 700, 500, and 300 hPa. This has limited Advect Cloud to those layers

Finally, the moisture fields are advected with the trajectories and the CPS values are updated due to vertical displacement. CPS values are reconverted to cloud amount.

Several problems have been identified in Advect Cloud over the years. 1) The zero-hour forecast initializes with incomplete or old satellite data. 2) The conversion between moisture and cloud is based upon an old limited study and the results are for only four fixed levels. 3) Bi-hemispheric grids have caused a discontinuity at the equator. 4) Clouds develop excessive smoothing and linear artifacts later in the forecast.

2. IMPROVEMENTS TO ADVECT CLOUD

Since 1999, AFWA has applied the Advect Cloud model to 12.5 and 3 nm horizontal resolution cloud analyses. The increased resolution magnified the shortcomings of the original Advect Cloud model and indicated a need for greater vertical resolution. In 2000, we began a rewrite of Advect Cloud to address these problems.

2.1 FIRST GUESS FIELD

The cloud analyses contain areas of aged or incomplete satellite data that are assumed to be current. These areas are mitigated by initializing Advect Cloud with the previous forecast in areas where satellite data are more than 30 minutes old. The one hour forecast moisture field is advected, over time, to the target analysis time. At each time step during this advection process, any timely (± ½ time step) analyzed cloud is assigned to one of the five layers, converted to moisture, and overwrites the forecast moisture at those points (figure 3). The end result is an updated moisture field, representing the best guess of conditions at the analysis time.

An advantage of this technique is it provides a method to estimate model performance. Each time new moisture amounts derived from current satellite data are written over the first-guess forecast field, the two are compared and error statistics are computed.

2.2 Moisture Conversion

The moisture conversion method represents two problems: 1) the validity of the actual conversion and 2) the lack of flexibility to apply the conversion at an arbitrary level. The solution presented corrects the flexibility issue and lays the ground work to address the validity issue.

To correct the flexibility issue and begin to address the validity problem, the current cloud to moisture tables were fitted to a nonlinear function

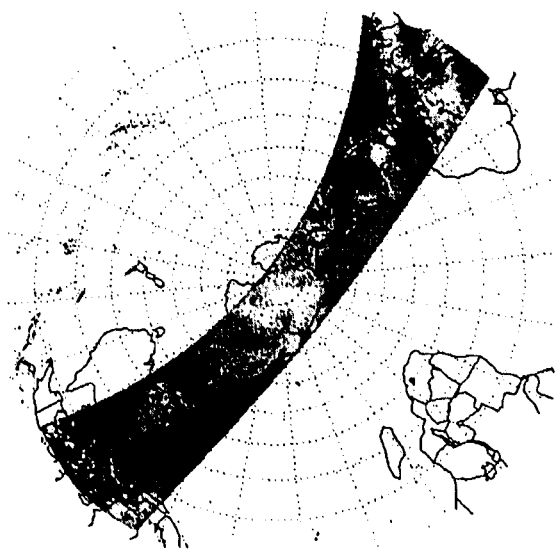

Figure 3. The improved Advect Cloud model uses the previous forecast (indicated by the white area) instead of old satellite data as the first guess. It overlays new satellite data where available. In practice, data from several satellites are available.

relating cloud amount to relative humidity:

$$Ln\left(-Ln\left(r\cdot\frac{RH}{100}\right)\right)=\beta_0(T)+\beta_1(T)\cdot Ln\left(-Ln\left(\frac{Cloud-C_L}{C_U-C_L}\right)\right).$$

The values C_L and C_U are offset and scaling factors allowing the function to be evaluated under the conditions of 0% and 100% cloud. The value r is a scaling factor that allows evaluation for 100% relative humidity.

Based on the fitted equation, new moisture – cloud conversion tables were created. The tables relate the cloud amount with *standardized* CPS (the ratio of CPS over pressure); temperature is used as the second variable. See figure 4 for an example.

The advantage of fitting a generalized function to the empirical CPS values is it enables us to increase the number of levels in Advect Cloud in the future.

2.3 CROSS-EQUATORIAL FLOW

In the current version of Advect Cloud, the equator is a boundary and cross-equatorial flow is not allowed. This was a natural outgrowth of the

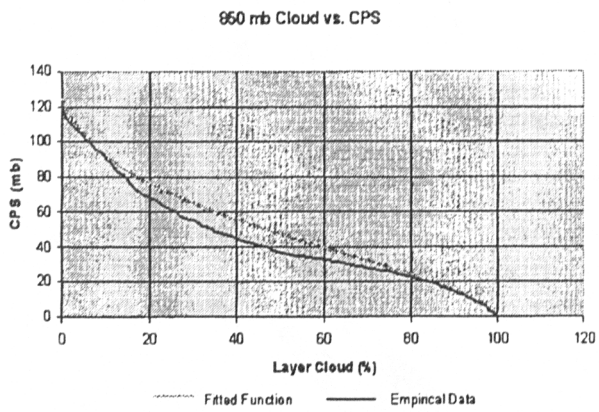

Figure 4. Comparison of the empirical and fitted CPS – Cloud conversion curve for 850 hPa in a standard atmosphere.

Figure 5. Clouds are held constant within one degree of the equator. This causes streamers from the equator, seen here on the 850 hPa level over the Northwestern Pacific.

forecasts originally being made on an extra-tropic polar-stereographic grid. When the model was last rewritten, the forecast area was extended to the equator, but Northern and Southern hemisphere forecasts remained independent. To avoid boundary problems, moisture (*i.e. clouds)* was held constant within one degree of the equator; this constraint caused streamers of clouds to be advected from the equator. Figure 5 is an example of the equatorial discontinuities at 850 hPa.

We solved the equatorial discontinuity by linking the Northern Hemisphere and Southern Hemispheres. The hemispheres are linked, *each time step*, by mapping opposite hemisphere points to the off-hemisphere grid points of the polar stereographic grid. Filling the off-hemisphere points (see figure 1) with moisture amounts provides a source for the quasi-lagrangian advection. Thus, the two hemispheric polar-stereographic grids are linked and cross-equatorial flow is possible. The result is a continuous forecast across the equator. Figure 5 shows a comparison between the current and improved model near the equator.

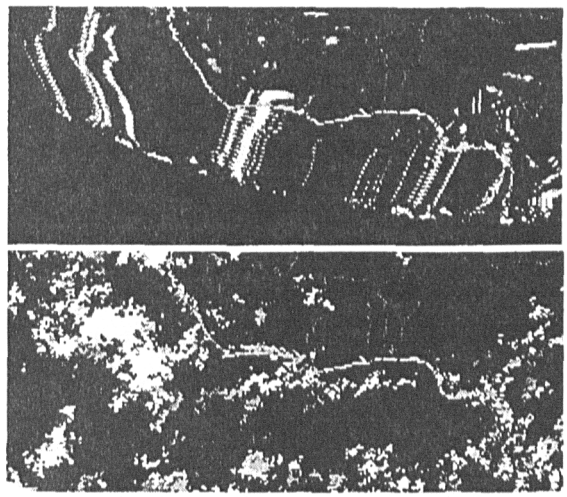

Figure 6. The standard model 30 hour 850 hPa forecast on the top shows streamers near the equator. The improved model on the bottom fills off-hemisphere points with cloud data from the opposite hemisphere. The resulting 30 hour forecast appears more meteorologically realistic.

2.4 ASSIGNMENT OF CPS TO START POINTS

The current Advect Cloud model assigns the trajectory start point CPS to equal the nearest gridded CPS. Tests showed *any* interpolation of CPS, either in the vertical or horizontal, resulted in excessively smooth forecast clouds.

In low-wind areas, assigning the nearest-grid moisture to the trajectory start resulted in repeated use of the same moisture value; this caused straight line and right angle artifacts in the clouds.

To eliminate excessive smoothing and correct the linear cloud artifacts, we use a probabilistic approach based upon the idea that moisture values of the points surrounding the trajectory starting point represent a *sample of area moisture values*. The probability that the starting point moisture equals the moisture at a given grid point is inversely proportional to the squared distance from the grid point. The technique gives more granularity to the cloud forecasts (see figure 6).

3. CONCLUSIONS

Improvements to the AFWA's Advect Cloud model address the model's weaknesses due to aged satellite data, limited cloud-to-moisture conversions, equatorial boundaries, and grid limitations. The improvements produce forecasts that appear more meteorologically reasonable than the current version of the model. Error comparisons between the two versions are still unavailable; however, these improvements bring us closer to our goal of producing an accurate, three-dimensional forecast of global cloud cover.

We are prepared to increase the vertical resolution and re-evaluate the cloud to CPS conversion process.

4. FUTURE DEVELOPMENT

AFWA expects further improvements to Advect Cloud with the next cloud analysis system. This system will use data from both geosynchronous and polar orbiting satellites to improve timeliness of the cloud analysis.

5. REFERENCES

Bieker, F. D., personal interview, July 2001.

Collins, R. W., 1970,: AFGWC multilevel cloud model. AFGWC Tech Memo 70-10, Air Force Global Weather Central, Offutt AFB, NE, 35 pp.

Crum, T. D., 1987, AFGWC cloud forecast models. AFGWC Tech. Note 87/001, Air Force Global Weather Central, Offutt AFB, NE, 66 pp.

Edson, H., 1965, Numerical cloud and icing forecasts. Scientific Services Tech. Note 13, 3rd Weather Wing, Air Weather Service (MAC), Offutt AFB, NE, 61 pp.

Hamill, T. M., 1992, A description of the air force real-time nephanalysis model. Weather and Forecasting, **7**, 288-306.

Kiess, R. B., and W. Cox, 1988, The AFGWC automated real-time cloud analysis model. AFGWC Tech. Note 88/001, Air Force Global Weather Central, Offutt AFB, NE, 82 pp.

McDonald, D. G., 1993, Proposed modifications to the calculation of quasi-lagrangian trajectories. Unpublished report, Air Force Global Weather Central, Offutt AFB, NE, 20 pp.

P3.17 ANALYSIS OF SUBTROPICAL CYCLONES USING NASA QUIKSCAT DATA

Paul J. McCrone
Meteorological Satellite Applications Branch
Air Force Weather Agency (AFWA)
Offutt AFB, NE

1. Introduction

Between 04-07 February 2001, a Kona low (a Hawaiian name for subtropical cyclones) developed approximately 500nm northeast of the Hawaiian Islands. This system was tracked by the Air Force Weather Agency (AFWA) Meteorological Satellite (METSAT) Applications Branch using the Hebert / Poteat (H/P) Analysis Method (Hebert/Poteat 1975). Surface wind data from the NASA QuikSCAT satellite was employed operationally to further fine-tune AFWA's manually produced analyses. This presentation will demonstrate the practical utility of NASA QuikSCAT data fields, including examples of subtropical cyclones for other ocean basins. Cross-comparisons will be made between the NASA QuikSCAT wind field and similar data sets from the Defense Meteorological Satellite Program (DMSP) Special Sensor Microwave Imager.

In figure 1, the Kona low is shown. The image is a 1600 UTC infrared shot from the DMSP F13 Satellite Operational Linescan System (OLS). QuikSCAT observations from the 1400 UTC pass (two hours earlier than the DMSP imagery) clearly show the surface circulation. This image served as the primary motivation behind this study, which intends to describe how well the QuikSCAT winds handle the overall structural features of a subtropical cyclone. Because of the characteristic lack of convection near the surface circulation center of subtropical lows, the NASA QuikSCAT SeaWinds sensor has the ability to measure near surface winds with greater accuracy than over the center of tropical cyclones, where convection can cause a degradation in the accuracy of these winds. This study has several goals: (1) it hopes to provide an assessment of the QuikSCAT winds in a nearly ideal situation for the sensor, (2) it provides an easily displayed comparison of cloud and surface features from multiple satellite sensors, and (3) it provides a starting point in

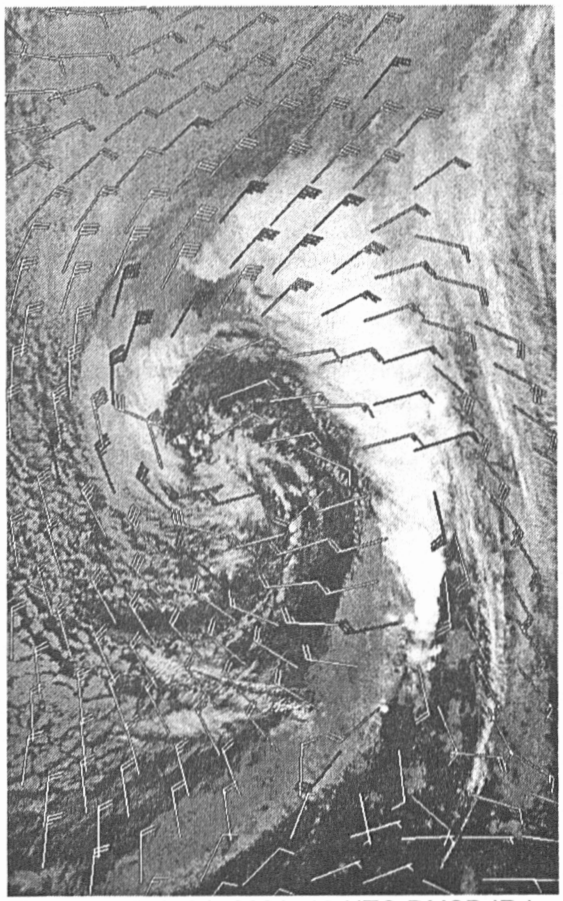

Figure 1. Feb 04, 2001, 16 UTC DMSP IR image with 1400 UTC QuikSCAT winds overlaid.

* *Corresponding author address:*
Paul J. McCrone, Air Force Weather Agency (Office code XOGM), 106 Peacekeeper Dr. STE 2N3 Offutt AFB NE 68113-4039;
email: Paul.McCrone@afwa.af.mil

further use of QuikSCAT winds in the analysis of both subtropical and tropical cyclones.

2. Data and Methodology

DMSP imagery, including data from the Special Sensor Microwave Imager (SSM/I), was obtained from the Satellite Data Handling System (SDHS) of the Air Force Weather Agency (AFWA). Visible, Infrared, and Microwave imagery (SSM/I) was retrieved and analyzed for examining details of the subtropical vortex because of its ability to determine scalar Ocean Surface Wind (OSW) speeds.

From the SSM/I, the 19, 22 and 37 GHz channels are used for determining surface wind speed. The Goodberlet, Swift and Wilkerson algorithm (1989) was used to calculate the SSM/I OSW product. SSM/I data provides surface wind estimates with 50km (25nm) resolution up to gale force and beyond. Erroneous wind speeds can be produced by convective rainfall that can lead to high wind speeds, similar to the QuikSCAT. Due to the lack of surface observations over open ocean areas, SSM/I provides a useful cross-correlation data source for the QuikSCAT winds. In the case of the OSW product at AFWA, the rain contaminated data is rendered black in color on the display.

The wind barbs from the SeaWinds sensor are actually a visualization of the 'Near-Real-Time' (NRT) data being calculated by Dr. Paul Chang of NOAA NESDIS. NESDIS ships a portion of this data set (called NRT 'lite' files) to AFWA for operational forecast use. The rain flagged winds are depicted in a dark purple color in this display. Note: this preprint depicts the near gale winds in dark grey. Also, all scalar winds/wind barbs in the graphics are depicted in knots.

The QuikSCAT wind barbs were overlaid on top of both types of DMSP data (OLS and SSM/I Ocean Surface Winds). The SSM/I OSW product is color coded to a consistent scale – Dark blue is 0-10 knots, Aqua-Green is 10-20 knots, Yellow is 20-25, Orange ranges from 25-30, and all winds over 30 knots are depicted in shades of red. The QuikSCAT winds follow an approximately similar scale. The analyses were performed using the Satellite Image Display and Analysis System (SIDAS), a satellite image manipulation interface. Numerous examples from 2001 were studied - only a small sample will be discussed. The direct display of QuikSCAT wind barbs on the SSM/I OSW data makes it simple to determine the degree to which the SSM/I and QuikSCAT agree on wind speed measurement.

3. Results and Discussion

The DMSP SSM/I data easily depicts the subtropical vortex wind speed distribution (Fig.2). This image comes from February 05, 2001, at 0300 UTC. The feature is synoptic scale in size, with numerous interesting mesoscale features. Figure 3 shows the QuikSCAT data, from approximately the same time, imaged over the DMSP OLS IR data. An isotach analysis of both figures 2 and 3 reveal a strong similarity between the wind fields of both. The regions of near gale force winds (30 knots and over) are very closely aligned. The winds found outside this area (15-25 knots) seem to show slightly stronger winds on the QuikSCAT (by approximately 5 knots) as opposed to the SSM/I OSW.

This analysis technique can then be augmented by directly overlaying the QuikSCAT winds on the SSM/I OSW product directly. Figure 4 shows an example of this from another subtropical system on 23 March, 2001, at 0700 UTC. Both the QuikSCAT and DMSP were very close to each other in time. Notice that similar conclusions can be drawn more readily in this display: the near gale winds are well correlated, but there is a slightly stronger depiction of surface winds in the QuikSCAT over the SSM/I OSW product in the 15-25 knot wind range – the QuikSCAT tends to be about 5 knots higher than the SSM/I winds. Because there are very few surface reports available for inter-comparison, it is difficult to say which is the "right" wind speed. Hebert / Poteat (1975) tends to show a more broad distribution of wind speeds in the 'typical' subtropical cyclone, which would suggest that the QuikSCAT gives the more realistic solution. This 5 knot 'bias' is minor in comparison to the accuracy of the near gale winds, however, and leads the author to suggest that the QuikSCAT data can provide a good estimate of near gale force wind speed distribution in cyclones that do not exhibit excessive rain contamination.

An additional observation is also in order. In connection with rain bands in tropical cyclones, Anthes (1982) indicates that rain bands are associated with "...a mesoscale trough of low pressure (which) occurs along the leading edge of the band...this pressure trough is in advance of the heaviest rainfall by one quarter wavelength, where the width of the band is taken as one-half the wavelength." Further, Anthes states that "...the mean low level winds in the vicinity of [rain] bands show convergence into the mesoscale pressure trough...". The imagery in figures 1 and

3 strongly suggests that the same is happening in subtropical cyclones. Consider figure 5 (an expansion of figure 1). In the area located southeast of the cyclone center, there is a well-defined convergence line, associated with a convective rainband. This situation is strikingly similar to the description of rainbands in tropical

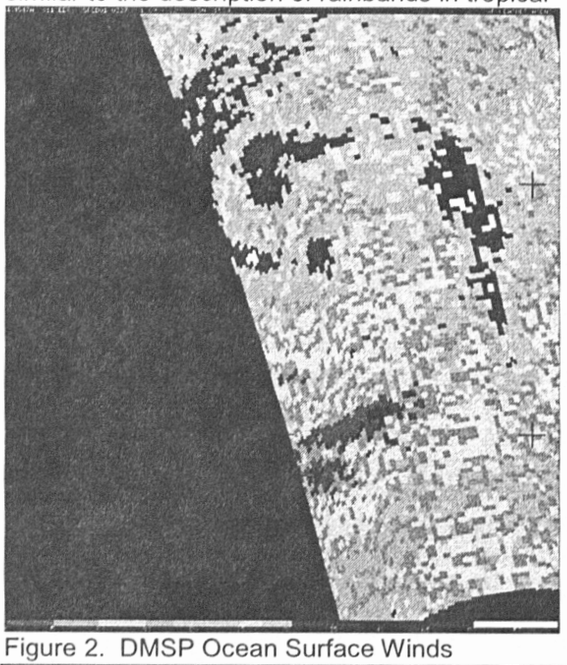

Figure 2. DMSP Ocean Surface Winds

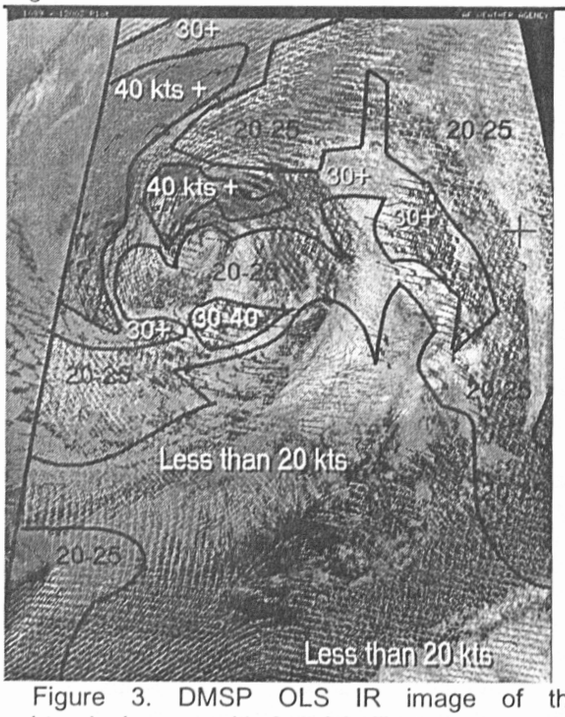

Figure 3. DMSP OLS IR image of the subtropical vortex with QuikSCAT winds overlaid

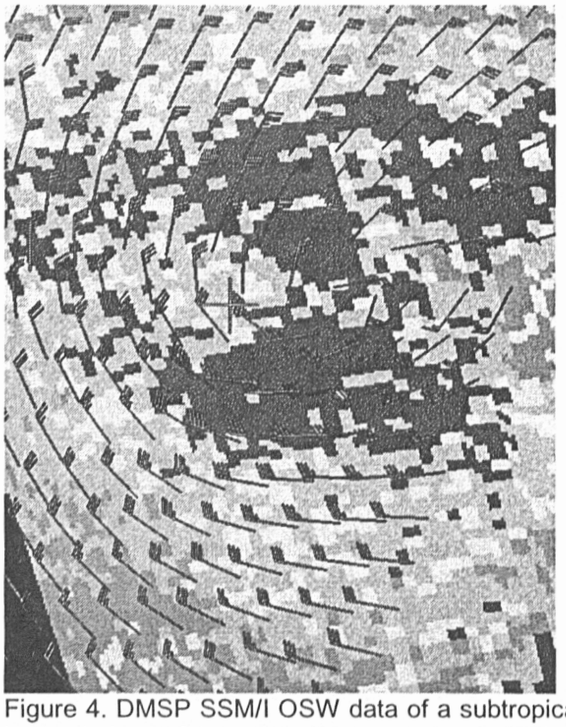

Figure 4. DMSP SSM/I OSW data of a subtropical low with QuikSCAT winds (23 March 2001, 07Z)

cyclones. This similarity gives some hope that this capability can be exploited when QuikSCAT data is used to analyse tropical cyclones. The potential benefit includes the capability to more accurately forecast tropical cyclone motion, in addition to rainfall in the rainband itself (the possibility exists to calculate divergence values and thence more accurately forecast the development of convection).

An additional benefit from this study: the QuikSCAT, with its ability to detect high winds in low cloud cover scenarios, may be used to add more objectivity in the analysis process of estimating subtropical cyclone intensity using the Hebert/Poteat technique. H/P is hampered by a strong reliance on subjective, manual analysis. QuikSCAT could easily handle this situation.

4. Conclusion:

QuikSCAT data was considered over subtropical cyclones and compared to DMSP SSMI data. Overall, the two compared favorably, with the QuikSCAT estimating slightly high wind estimates in the 15-25 knot range, but otherwise performed well in the gale force wind regime. A number of mesoscale features were observed, giving the forecaster a potentially valuable aid when dealing

with both subtropical and (potentially) tropical cyclones. There may be some similarity in the nature of the rainbands of subtropical cyclones, as compared to those found in tropical cyclones.

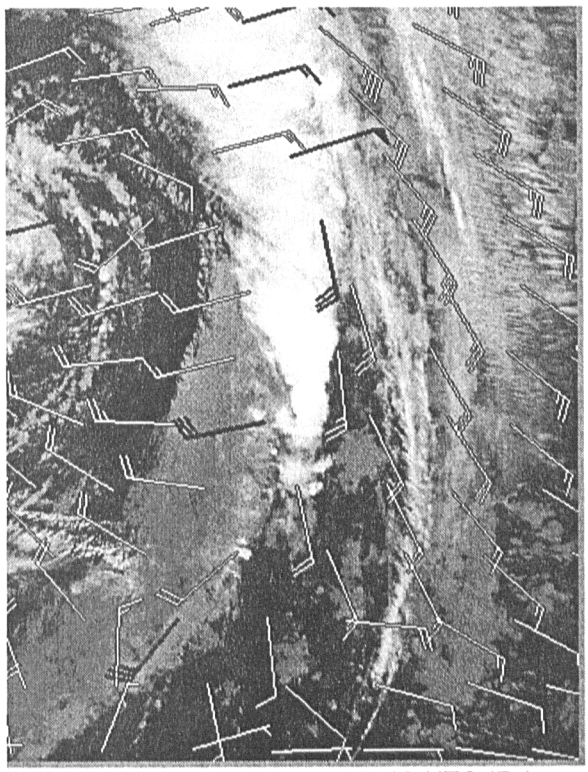

Figure 5. DMSP Feb 04, 2001, 16 UTC IR image with 1400 UTC QuikSCAT winds overlaid. The imagery has been zoomed in to focus on the region of surface convergence to the southeast of the cyclone center

5. Acknowledgements:

The author would like to thank Dr. Paul Chang of NOAA NESDIS for the use of the NASA QuikSCAT lite data and for technical advice.

6. References

Anthes, R.A., 1982: Tropical Cyclones: Their Structure and Evolution, AMS Meteorological Monographs, Volume 19, February 1982, Number 41, American Meteorological Society, 45 Beacon St. Boston MA 02108, pp. 39-41

Goodberlet, M.A., C.T. Swift and J.C. Wilkerson, 1989: Remote sensing of ocean surface winds with the Special Sensor Microwave/Imager. J. of Geophys. Res., 94, 14547-14555

Hebert, P.H., K.O. and Poteat, 1975: A satellite classification technique for subtropical cyclones. NOAA Technical Memorandum NWS SR-83, Scientific Services Division, Southern Region, NOAA/NWS, Fort Worth Texas, July 1975

P3.18 STATUS OF THE UW-CIMSS OBJECTIVE DVORAK TECHNIQUE (ODT)

Timothy L. Olander and Christopher S. Velden
University of Wisconsin - CIMSS, Madison, Wisconsin

1. INTRODUCTION

An algorithm has been developed at the University of Wisconsin-Madison, Cooperative Institute for Meteorological Satellite Studies (UW-CIMSS) to objectively determine tropical cyclone intensity utilizing geostationary infrared satellite data (Velden et. al., 1998). This algorithm is based upon the original subjective Dvorak Technique, utilizing many of the same rules and procedures outlined by this methodology (Dvorak, 1984) for determination of the current intensity estimate. The ODT is currently being used experimentally and operationally at many tropical cyclone forecast centers worldwide, with significant improvements in intensity estimations being realized at these locations.

2. BACKGROUND

ODT intensity estimations are based upon two temperature values (an eye and surrounding cloud temperatures) and recognition of the storm cloud pattern type. Cloud pattern types are determined utilizing Fourier Transform and histogram analyses of the cloud region within 136km of the center. The four valid cloud pattern types are eye, embedded center, central dense overcast (CDO), and shear. Adjustments to the intensity estimate for the eye pattern are dependent upon the temperature and clarity of the eye, as defined in the original subjective Dvorak rules (Dvorak, 1984).

A time averaged intensity estimate value (Final T-No.) is calculated utilizing a 12-hour, linearly-weighted averaging scheme, giving the most recent intensity estimates the most weight. A final current intensity value (CI number) is determined after implementation of a specific subjective Dvorak rule for weakening storms. This rule increases the final, time-averaged intensity estimate by a set value during the weakening stage of a storm life cycle until dissipation or restrengthening occurs.

3. RESULTS

Statistical comparisons between the ODT estimates, those obtained from operational center subjective techniques, and a previous objective Dvorak algorithm are presented in Tables 1 and 2.

Table 1 displays results from the developmental (dependent) test data set for 12 storms during the 1995-1997 Atlantic storm seasons. Table 2 shows results from an independent data set from the 1998 and 1999 Atlantic storm seasons. As can be seen, the ODT compares very favorably with the Tropical Analysis Centers (TAC) average bias and RMS error, displaying an overall reduction in the RMS error for the storms investigated. The ODT displays a marked improvement over a previous objective Dvorak algorithm (DD), reducing the RMS error by almost half.

MSLP estimate	Bias	RMSE	Matches
ODT	+1.69	7.34	407
ODT(Auto)	+2.84	8.59	407
DD	+3.63	14.33	407
TAC (any of 3)	+4.31	10.35	407

Table 1. Comparison of the ODT and DD estimates of 1995-1997 Atlantic TC intensities (MSLP) with operational estimates obtained from three Tropical Analysis Centers (TAC) which employed the standard Dvorak method (the Tropical Analysis and Forecast Branch of the Tropical Prediction Center, the Synoptic Analysis Branch of NOAA/NESDIS, and the Air Force Weather Agency). A match is considered whenever a ODT/DD estimate and any of the three TAC estimates were available with a coincident (within one hour) aircraft reconnaissance report of MSLP. Bias and RMSE are in hPa.

MSLP estimate	Bias	RMSE	Matches
ODT	-0.72	7.97	397
TAC (any of 3)	-0.05	10.38	397

Table 2. Same as Table 1, except only comparing the ODT with operational estimates from three TAC for Atlantic TC during 1998 and 1999 (MSLP). Bias and RMSE are in hPa.

4. ALGORITHM FUNCTIONALITY IMPROVEMENTS

During the past few years, modifications and additions have been implemented within the ODT algorithm at the request of the tropical cyclone forecast centers utilizing the ODT. These improvements have added functionality to the algorithm, allowing for a greater degree of objectivity and/or more control over the operation of the ODT.

A fully-automated, objective center finding routine has been developed to remove the final subjective element within the ODT algorithm, the storm center location determination. The routine relies on interpolation of tropical cyclone forecast positions, a 10° log spiral approximation scheme, and a Laplacian analysis scheme to automatically determine the storm center location. Comparisons with user selected storm center intensity estimate statistics are presented in Table 1 as ODT(Auto). A slight increase in bias and RMS error of the intensity estimates are noted over the user selected values for the same data set, however the

* *Corresponding author address:* Timothy Olander, Univ. of Wisconsin - CIMSS, 1225 West Dayton St., Madison, WI 53706; Email: timo@ssec.wisc.edu.

results are still comparable to TAC subjective estimate statistics for the dependent data set.

The second major addition allows the user to change the ODT automatic scene identification result if it is felt it has misidentified the scene type. The addition of this functionality introduces a further subjective element to the ODT analysis, however if the operator is experienced with the ODT and the Dvorak Analysis schemes, statistical improvement can be achieved. Table 3 demonstrates the impact observed at the Satellite Analysis Branch of NOAA/NESDIS (SAB), between the 1998 and 1999 Atlantic hurricane seasons. The scene type override was implemented approximately 10% of the time in 1999 for the storms in this case study, with scene type modifications focusing on the embedded center and eye categories.

Year	No Difference	Within 1/2 T-No.	Matches
1998	19.4	75.6	160
1999	35.6	82.8	163

Table 3. Comparison between Synoptic Analysis Branch of NOAA/NESDIS ODT intensity estimates versus aircraft reconnaissance intensity values (pressure values converted from hPa to T-No.) for selected 1998 and 1999 Atlantic TC events. Values are given in percentages.

5. SUMMARY AND FUTURE DIRECTIONS

Numerous tropical cyclone forecasting centers have utilized the ODT operationally or experimentally since 1998. Operational users include the SAB, the NOAA Tropical Prediction Center/National Hurricane Center (TPC/NHC) in Miami, FL, the Joint Typhoon Warning Center (JTWC) at Pearl Harbor, HI, the Australian Bureau of Meteorology (Brisbane)-Severe Weather Section, and the Western Australian Regional Forecasting Center (Perth).

The original ODT algorithm was developed within the McIDAS architecture, however the code has recently been modified to allow for easier transition to site-specific satellite display and analysis systems. The JTWC is currently using this version operationally, while the Air Force Weather Agency (AFWA) at Offutt AFB, and will utilize this code in an experimental mode during the 2001 tropical cyclone season. A version has also been provided to NOAA for transition into AWIPS via TPC/NHC. An X-Windows based version of the ODT is currently being developed for other interested users. This version will be self-contained, requiring no existing satellite navigation/ calibration libraries or image display platforms, but use of the algorithm will require conversion of satellite imagery into McIDAS format.

Continued feedback from the tropical cyclone forecasting sites utilizing the ODT will be necessary to further tune the algorithm, especially in tropical cyclone basins outside of the North Atlantic Ocean and Caribbean Sea. The ODT was developed and tuned based primarily on Atlantic basin aircraft/ reconnaissance data. Tuning of the ODT for other regions will rely primarily on the significant experience of the tropical cyclone forecasters within these regions to help identify the strengths and weaknesses of the ODT.

Future research regarding the ODT will focus on the utilization of additional satellite information from geostationary and polar orbiting satellites, as well as the addition of new numerical techniques to analyze the current and future satellite data available. The use of a deep convection parameter (Velden and Olander, 1998), involving the differencing of collocated IRW and WV pixel values, has shown promise for the GOES geostationary satellites. The use of visible and other IR channels will also be explored for the GOES satellites. Microwave data from polar orbiting satellites will also be investigated, focusing on the analysis of convection patterns and the thermal structure of the tropical cyclones using SSM/I and AMSU instruments, respectively. Experimental quantitative analysis of the storm structure will be conducted using both geostationary and polar orbiting satellite data, focusing on the symmetry and extent of the convective regions as well as the structure of the eye/storm center region. Principle component analysis, empirical orthogonal functions, and/or neural networks will be explored.

6. ACKNOWLEDGMENTS

This study was coordinated with Jeff Hawkins of the satellite meteorology applications section of NRL-MRY. Funding through Space and Naval Warfare Systems Commands (PMW-185) under PE 0603207N.

7. REFERENCES

Dvorak, V., 1984: Tropical cyclone intensity analysis using satellite data. NOAA Tech. Rep. NESDIS11, 47pp. [Available from NOAA/NESDIS, 5200 Auth Rd., Washington, DC 20233.]

Velden, C.S., T.L. Olander, and R.M. Zehr, 1998: Development of an objective scheme to estimate tropical cyclone intensity from digital geostationary satellite infrared imagery. *Wea. and Forecasting*, **13**, 172-186.

Velden, C.S. and T.L. Olander, 1998: Bispectral satellite technique for delineating intense convection: Applications to tropical cyclones. *Extended Abstracts, Ninth Conf. on Satellite Meteorology and Oceanography*, Paris, France, Amer. Meteor. Soc., 458-461.

P3.19 PRELIMINARY OBJECTIVE ANALYSES USING THE NESDIS/CIRA TROPICAL CYCLONE INFRARED IMAGERY PART I: HURRICANE HARMONICS

James P. Kossin*

Cooperative Institute for Research in the Atmosphere (CIRA)
Colorado State University, Fort Collins, Colorado

1. INTRODUCTION

The NESDIS/CIRA tropical cyclone infrared (IR) imagery archive contains half-hourly, 4 km horizontal resolution, geostationary IR images of tropical cyclones that occured since the onset of the 1995 hurricane season (Zehr 2000). The present abstract introduces some preliminary results of analyses of this largely unexplored data set. By combining the IR data with information regarding storm position and track, a coherent depiction of the spatial and temporal structure of hurricane cloudiness can be demonstrated. Spatially dependent periodic oscillations are revealed, and new insights into the respective roles of the diurnal and semidiurnal oscillations are uncovered. Although the present results are preliminary, a controversial hypothesis, namely that the diurnal cycle may force only the hurricane cirrus canopy, and not the convection in the eyewall, is suggested.

2. DAILY VARIATIONS

By combining the half-hourly IR hurricane images with best track storm center fixes interpolated to the times of the images, azimuthal averages of equivalent blackbody cloud-top temperature (T_{BB}) can be calculated, and Hovmöller type diagrams (radius versus time) can be created (Fig. 1). Casual scrutiny of these diagrams immediately reveals periodic oscillations on a diurnal timescale, while closer inspection often reveals semidiurnal oscillations.

The diurnal oscillations are most obvious at larger distances from the storm center ($r > 200$ km) and are largely induced by the horizontal expansion and contraction of the cirrus canopy. The behavior of tropical cyclone cirrus canopies has been well documented (e.g., Browner et al. 1977, Muramatsu 1983, Lajoie and Butterworth 1984, Steranka et al. 1984), but the examples shown in Fig. 1 greatly facilitate the interpretation of these previous studies by *succinctly* capturing many of their results, including:

1)The areal extent of the cirrus canopy horizontally expands and contracts on a diurnal cycle.

2) The maximum area of the canopy typically occurs around 1600-1800 Local Mean Solar Time (LMST) in the Atlantic and Eastern Pacific basins. This agrees well with Browner et al. (1977).

3) The amplitude and radial extent of the canopy area oscillation often decrease as eye formation occurs. This result may extend the findings of Steranka et al. (1984) where the amplitude was found to decrease in multiple-storm composites of hurricanes versus composites in tropical storms.

4) Since canopy area oscillates diurnally, the phase of the diurnal cycle is systematically dependent on radial distance from storm center. Furthermore, it is clear from Fig. 1 that the phase is systematically dependent on choice of T_{BB} threshold. This may illuminate the reason that Reed (1983) found that in ordinary Pacific ocean convection, the time of maximum area of cloud top colder than -55°C was significantly out of phase with the time of maximum area of cloud top colder than -20°C.

5) The apparent speed of radial propagation of the T_{BB} features of the canopy can be explicitly calculated from Fig. 1 and is typically near ~ 10 m s^{-1}, in good agreement with Wexler and Merritt (1967), whose calculations based on limited data necessarily required numerous assumptions. It should be noted here that this expansion rate is not necessarily a direct measure of upper level outflow rates, just as the canopy contraction is not a measure of upper level inflow.

Each panel in Figure 1 essentially comprises a set of individual time series in 4 km radial increments. Objective time series analyses can then be performed at each radius. The results of such analyses for the 3 hurricanes in Fig. 1 are shown in Fig. 2, which displays the most significant harmonics at each radius. As expected from the subjective

*Corresponding author address: James P. Kossin, Cooperative Institute for Research in the Atmosphere, Colorado State University, Fort Collins, CO 80523-1375; e-mail: Kossin@CIRA.colostate.edu

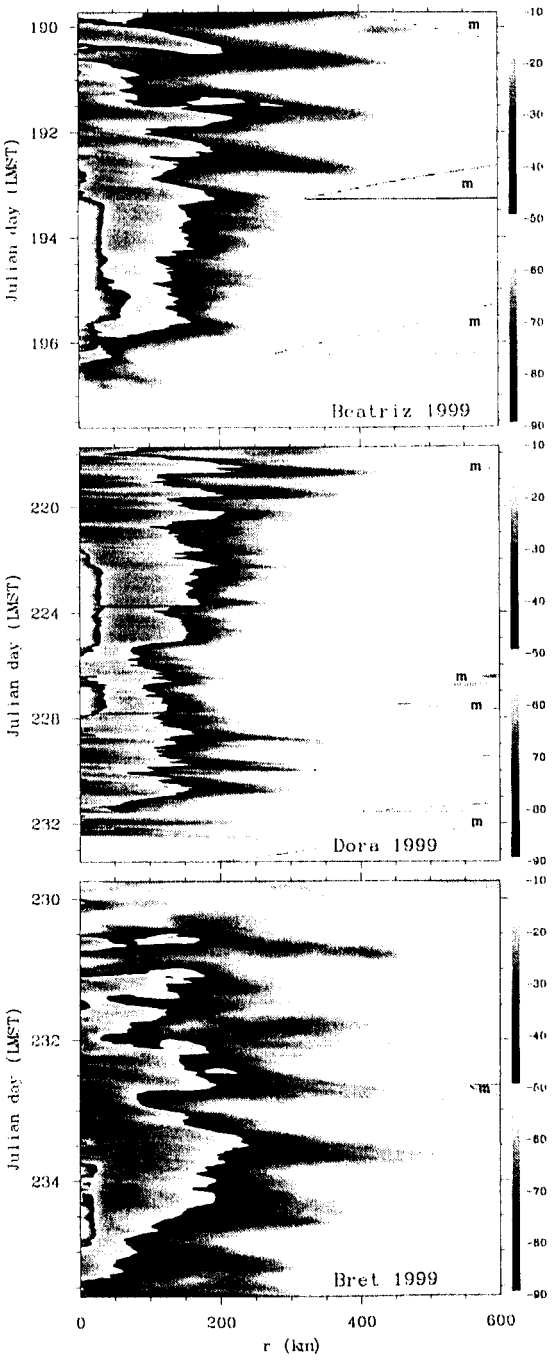

Figure 1: Hovmöller (radius versus LMST) diagrams of azimuthally averaged T_{BB} in eastern Pacific hurricanes Beatriz 1999 and Dora 1999, and Atlantic hurricane Bret 1999. Averages are with respect to interpolated best track center. The small "m" denotes missing values. Values along the label bars are in degrees Celsius.

scrutiny of Fig. 1, T_{BB} evolution at outer radii away from the eyewall ($r > 200$ km) is generally dominated in all three storms by the diurnal harmonic. However, closer to the convection near $r = 100$ km, *the diurnal harmonic becomes insignificant* and T_{BB} variation in Hurricanes Beatriz and Bret is *dominated by a semidiurnal harmonic*. No significant periodic oscillations are evident at inner radii in Hurricane Dora.

Figures 3 and 4 show T_{BB} time series at $r = 100$ km in Beatriz and $r = 40$ km in Bret. The phase of the planetary pressure tide S_2 is shown on each figure and is aligned with T_{BB} evolution, that is, colder cloud tops occur when the local pressure is lower (S_2 is minimum). The phase of the semidiurnal oscillations in Beatriz and Bret exhibit little dependence on radial distance from the storm center. This is physically consistent with the local effects of S_2.

At this point, it has been shown that T_{BB} away from the hurricane eyewall oscillates diurnally, while T_{BB} in the convective region near the eyewall can exhibit a dominant semidiurnal cycle. What might be driving this convective cycle? Aircraft data from Hurricane Elena 1985 (chosen because of relatively good temporal sampling) shows that θ_e in the eye and eyewall can oscillate semidiurnally (Fig. 5). The amplitude of the semidiurnal harmonic is about 1 K in the eyewall on the 850 hPa flight-level surface. The phase is physically consistent with S_2, that is, higher θ_e occurs when the pressure is lower. If the amplitude of the θ_e oscillation depends on height, then the passing of the S_2 pressure wave may cause small lapse rate changes. In an eyewall that is moist-neutral (angular momentum and θ_e surfaces are approximately parallel), a small change in static stability might effect large changes in the convection.

The notion that hurricane convection is not diurnally forced is speculative and controversial, and requires further work to confirm or deny. It may be that a diurnal cycle of low level convergence is too small in amplitude to measurably affect the strongly convergent hurricane low level circulation. It is not yet clear whether the diurnal cycle of cloud top cooling and associated lapse rate variability plays any role in the present results. Spectral analyses of large composites of the irregularly sampled flight-level data in the lower and middle levels are currently underway, and will hopefully be illuminating in questions of semidiurnal lapse rate changes. The robustness of results using the satellite imagery archive is currently being thoroughly tested using data from additional hurricanes.

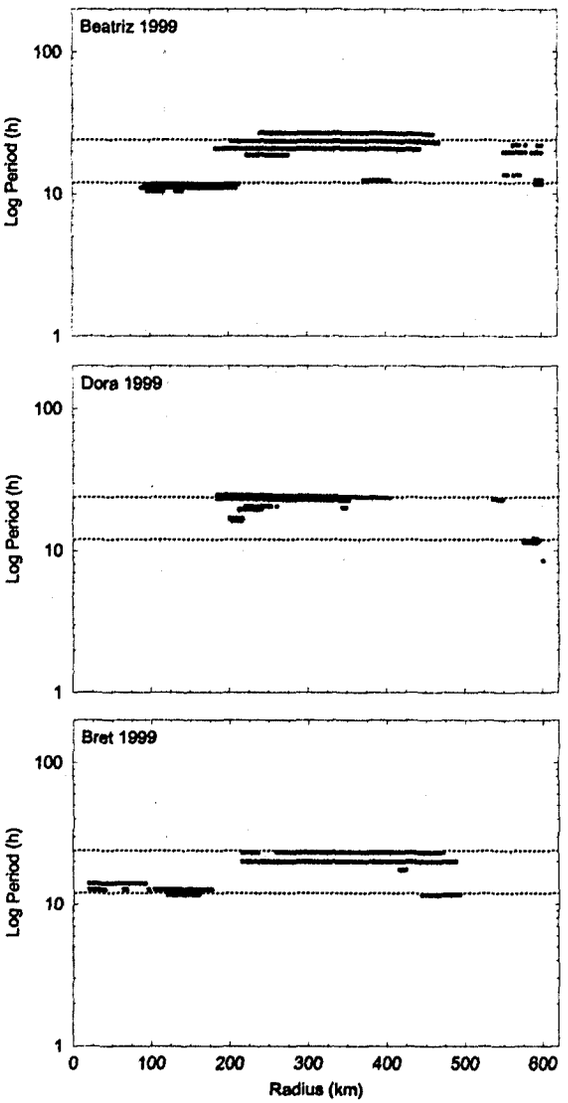

Figure 2: Results of spectral analyses of T_{BB} time series at each radius (from storm center) in Hurricanes Beatriz, Dora, and Bret 1999. Points represent the most significant harmonics. The dashed lines denote periods of 12 and 24 h.

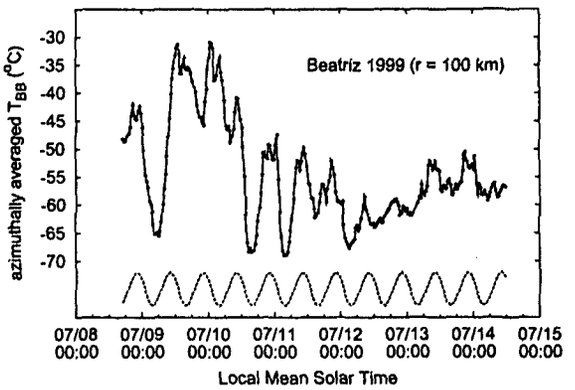

Figure 3: Time series of azimuthally averaged T_{BB} in Beatriz at $r = 100$ km. The lower sinusoidal curve (dashed) shows the phase of the semidiurnal pressure tide (S_2).

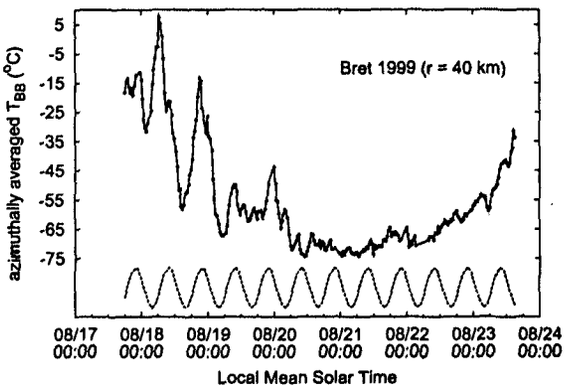

Figure 4: Time series of azimuthally averaged T_{BB} in Bret at $r = 40$ km, and the phase of S_2 (dashed).

3. CONCLUDING REMARKS

1) Consistent with previous studies, application of the NESDIS/CIRA tropical cyclone infrared imagery archive to T_{BB} time series shows a distinct diurnal cycle in the cold cloud of the hurricane environment.

2) The diurnal oscillation in cold cloud appears to be largely due to the evolution of the hurricane's cirrus canopy which oscillates in areal extent as it is affected by diurnal radiative and subsidence processes. Since the canopy's size oscillates diurnally, the phase of the diurnal cycle is systematically dependent on radial distance from storm center.

3) The amplitude of the diurnal signal also has a strong dependence on radial distance from storm center, and can become insignificant near the convective region (eyewall). *This may indicate that hurricane convection is not necessarily diurnally forced*, as suggested in previous studies.

4) Near the eyewall, a semidiurnal oscillation can dominate the power spectrum of the T_{BB} time series. The phase is aligned with the planetary pressure tide S_2, that is, the minimum T_{BB} occurs nearly simultaneously with the minimum perturbation surface pressure.

5) Time series of 850 hPa flight-level data in the eye and eyewall of Hurricane Elena 1985 show significant semidiurnal oscillations of θ_e, consistent

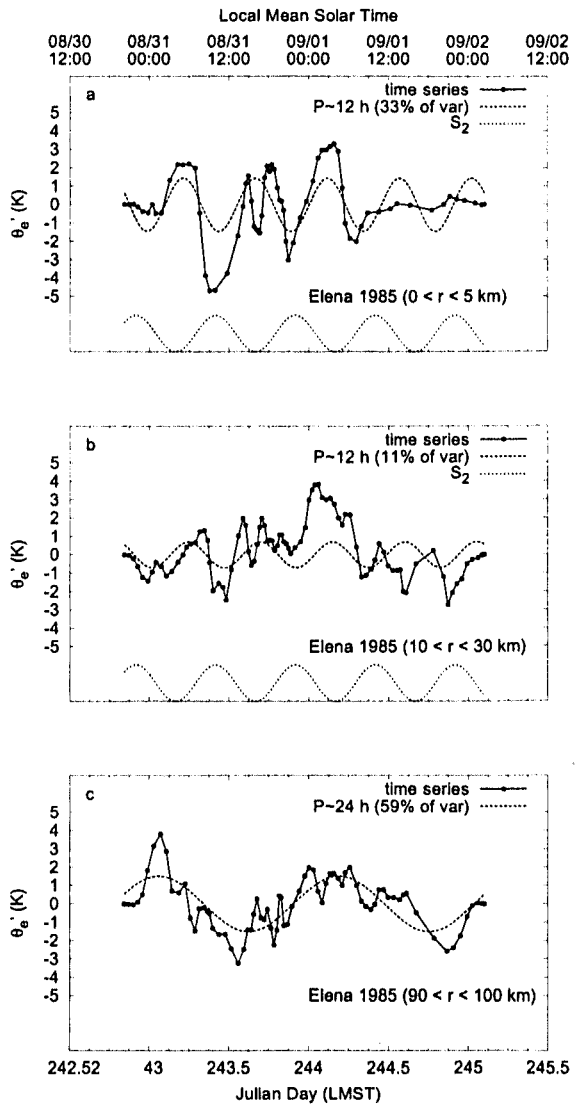

Figure 5: Time series analyses of perturbation θ_e, with respect to LMST, measured by aircraft at 850 hPa flight level in Hurricane Elena 1985. a) Average θ'_ein the eye ($0 \leq r \leq 5$ km) (solid), and the most significant harmonic ($\sim$ 12 h period) (long dash). The lower sinusoidal curve (short dash) shows the phase of the semidiurnal pressure tide (S_2). b) Same as a), but for average θ'_ein an annulus representing the eyewall region. c) Average θ'_e near the outer limit of the flight level radial leg data. Here, the most significant harmonic is diurnal ($\sim$ 24 h period).

with the satellite derived T_{BB} oscillations in Hurricanes Beatriz and Bret. The low-level θ_e is maximum when T_{BB} (and perturbed surface pressure) is minimum. It is hypothesized that the local pressure oscillation caused by S_2 might change local lapse rates by affecting θ_e differently at different heights. Such systematic lapse rate changes might explain the semidiurnal oscillation noted in T_{BB} in the convective regions of some hurricanes.

ACKNOWLEDGMENT: Many thanks to John Knaff, Mark DeMaria, Paul Ciesielski, Ray Zehr, Tom Vonder Haar, Rick Taft, and Dick Johnson for numerous illuminating discussions. This work was supported by NOAA Grant NA67RJ0152.

4. REFERENCES

Browner, S. P., W. L. Woodley, and C. G. Griffith, 1977: Diurnal oscillation of the area of cloudiness associated with tropical storms. *Mon. Wea. Rev.*, **105**, 856–864.

Gentry, R. C., E. B. Rodgers, J. Steranka, and W. E. Shenk, 1980: Predicting tropical cyclone intensity using satellite-measured equivalent blackbody temperatures of cloud tops. *Mon. Wea. Rev.*, **108**, 445–455.

Hobgood, J. S., 1986: A possible mechanism for the diurnal oscillation of tropical cyclones. *J. Atmos. Sci.*, **43**, 2901–2922.

Lajoie, F. A., and I. J. Butterworth, 1984: Oscillation of high-level cirrus and heavy precipitation around Australian region tropical cyclones. *Mon. Wea. Rev.*, **112**, 535–544.

Merritt, E. S., and R. Wexler, 1967: Cirrus canopies in tropical storms. *Mon. Wea. Rev.*, **95**, 111–120.

Muramatsu, T., 1983: Diurnal variations of satellite-measured T_{BB} areal distribution and eye diameter of mature typhoons. *J. Meteor. Soc. Japan*, **61**, 77–89.

Reed, R. J., 1983: The diurnal variation of precipitation in the tropics. *Proceedings of the 1st International Conference on Southern Hemisphere Meteorology. Amer. Meteor. Soc.* 312–319.

Steranka, J., E. B. Rodgers, and R. C. Gentry, 1984: The diurnal variation of Atlantic Ocean tropical cyclone cloud distribution inferred from geostationary satellite infrared measurements. *Mon. Wea. Rev.*, **112**, 2338–2344.

Zehr, R. M., 2000: Tropical cyclone research using large infrared image data sets. *Proceedings of the 24th Conference on Hurricanes and Tropical Meteorology. Amer. Meteor. Soc.* 486–487.

P3.20

TROPICAL CYCLONE SURFACE WIND ANALYSIS USING SATELLITE SENSORS

Raymond M. Zehr*
NOAA/NESDIS/ORA/RAMMT/CIRA
Fort Collins, CO 80523

1. INTRODUCTION

Hurricane forecasts are primarily disseminated as a track of the hurricane center and an intensity. The intensity is the maximum surface wind speed located somewhere near the center. The forecasts also include additional information on the radial extent of the hurricane force and tropical storm force winds in geographical quadrants (i.e. NW, SW, SE, and NE) or semicircles. A more detailed real-time analysis of hurricane surface winds has been produced by NOAA/AOML's Hurricane Research Division (HRD) since 1994 on an experimental basis (Powell and Houston, 1998). The detailed isotachs and streamlines in the HRD analyses pinpoint the location of the strongest winds and give an improved depiction of the surface wind distribution compared with the advisories and forecasts. Users would likely benefit from having reliable analyses and forecasts in this format.

Routine dissemination of such analyses to users of tropical cyclone forecasts around the world has been very limited or non-existent. Undoubtedly, this is because the data required to produce reliable analyses have not been routinely available. The HRD Surface Wind Analysis System originated primarily to optimize the use of aircraft observations for hurricane forecasting. From the global viewpoint, only a small percentage of tropical cyclones have aircraft reconnaissance observations. This number declined in the late 1980s with termination of routine reconnaissance flights in the western North Pacific. However, in recent years, tropical cyclone reconnaissance capabilities with satellites have improved. Data on hurricane surface winds are now available in real time from a variety of satellite sensors. Objective IR intensity algorithms, scatterometer winds, microwave sounders, microwave imagers, and low-level satellite cloud motion vectors are the primary data sets. More specifically, they provide estimates of maximum winds or wind observations at various locations, obtained from an algorithm based on the satellite measurements.

There is a need to address the logistical problem of combining information from a wide variety of data sources to systematically produce a real time analysis of the entire hurricane surface wind field. The value of remotely sensed data to the tropical cyclone warning process depends on validation, interpretation, training, technique development, and a unified method for their application (Finta, 2000). Since advisories and warnings are typically issued at 6-hour intervals, and specific remote sensing data types are only available at less frequent intervals, there is also a need to address reliability, dependent on data types and timeliness.

The purpose of this paper is to provide an overview of available data sets and discuss possible approaches to systematic surface wind analyses obtained primarily from satellite data. A brief assessment of each data type and review of recent research is presented. Aircraft observations, and the HRD Surface Wind Analysis, are viewed as vitally important validation and comparison data sets for refinement of analysis methods. The poster at the conference will show examples of the various satellite data sets and highlight their strengths and weaknesses. Preliminary technique development results will be shown.

2. DATA TYPES

A list of data types that have been shown to have the capability to contribute to a hurricane surface wind analysis follows:

GROUP 1:

1) Intensity estimate using the Dvorak technique (Dvorak, 1984) and Objective Dvorak Technique (ODT) (Velden, et al, 1998)
2) Quantitative IR cloud area analysis (e.g "Holland-Martin" Wind Radii Algorithm) (Guard, 1992)

GROUP 2:

3) Surface / Radiosonde / Ship / Buoy observations
4) Satellite derived low-level cloud vectors (Velden, et al, 1998)

GROUP 3:

5) Scatterometer derived surface winds (Edson and Hawkins, 2000)
6) Microwave imager surface wind estimates (SSMI / TRMM) (Hollinger, et al 1987)
7) SSMI / TRMM Dvorak-type intensity assignment (Edson, 2000)
8) Microwave sounder (AMSU) analysis of surface pressure/wind (Kidder, et al, 2000)

*Corresponding author address: Ray Zehr, NOAA, CIRA Bldg., W. LaPorte Ave., Colorado State University, Fort Collins, CO 80523; Email: zehr@cira.colostate.edu

GROUP 4:

9) Aircraft observations of flight level wind and sea-level pressure
10) GPS Dropwindsonde observations of surface wind (Hock and Franklin, 1999)
11) Stepped Frequency Microwave Radiometer (SFMR) surface wind estimates (Black et al, 2000)

GROUP 5:

12) Doppler radar and profiler velocities (Lee and Marks, 2000; Dodge, et al, 2000; Knupp, et al, 2000)
13) Other satellite sensors (Moderate-resolution Imaging Spectroradiometer (MODIS) on NASA's EOS satellites, spaceborne Synthetic Aperture Radar (SAR))

This is indeed an impressive list of observations. Providing details on each data type is beyond the scope of this paper. Some of them are operational and have been in use for many years (i.e Dvorak intensity, flight level aircraft winds). Some of them (i.e SFMR, MODIS) are experimental and very new. They are grouped here roughly according to availability and time interval of observation. Interestingly, the inverse of that grouping may be by order of accuracy and reliability. Once again, that assessment is well beyond the scope of this paper.

Group 1 data types have global coverage with high temporal frequency, and are always available. Group 2 data are less timely, nearly always available, but may not provide optimum spatial coverage. Group 3 includes routine polar orbiting satellite observations. They are somewhat limited in temporal frequency and coverage, but nevertheless nearly always provide more than one good observation per day of a particular tropical cyclone. Group 4 data types are produced by the US operational and research aircraft reconnaissance programs that provide excellent data with tropical cyclones approaching US coastlines. Group 5 data types are very limited in coverage but provide unprecedented detailed measurements of tropical cyclone structure.

3. Discussion – Group 1 Data Types

Tropical cyclone size as given by the radial extent of gale force (greater than 17 m/s) winds, is highly variable for a given intensity (Weatherford and Gray, 1988). For example, Hurricane Bret's average radius of gale force winds was estimated to be 68 n. mi. (126 km) with an intensity of 125 kt at 06 UTC 22 August 1999. In contrast, just about a week later, Hurricane Cindy, at its maximum intensity of 120 kt, had associated average radius of 34-kt (17 m/s) winds of 231 n. mi. (427 km).

Such observed tropical cyclone size differences along with the practical impacts of winds exceeding gale force, make it clear that detailed hurricane wind analyses are vitally important and simply providing an intensity analysis may be inadequate. Cocks and Gray (2001) provide additional information on recent technique development work with outer wind analysis and forecasting.

Holland (1980) gives a quantitative basis for computing radial profiles of tropical cyclone winds and shows how intensity, radius of maximum winds, and size are related. It has also been shown that the size of the IR defined cloud canopy is related to tropical cyclone size (Zehr, 1989). An operational technique (the "Holland-Martin" algorithm) uses a Dvorak intensity estimate, along with IR cloud area measurements, tropical cyclone motion vector, and the Holland (1980) radial profile equation to specify outer wind radii. Extension and refinement of that approach provides an objective analysis of the tropical cyclone's entire surface wind field, derived from Group 1 Data Types alone.

Such an analysis may be somewhat crude, and less reliable compared with HRD surface wind analyses that incorporate aircraft observations. However, surface wind analyses derived from Group 1 Data Types (Section 2) are useful for several reasons.

1) They provide a "first guess" field for a satellite based real time surface wind analysis.

2) They can be provided routinely with uniform global coverage of tropical cyclones.

3) They can be produced at frequent intervals and capture rapid changes that cannot be reliably diagnosed by other data types.

4) They can readily be validated and compared with HRD Surface Wind Analyses.

5) They can be used as a "benchmark" measure of the impact and information content of other data types.

4. Discussion – Group 2 Data Types

In situ measurements of surface wind from conventional observations, radiosondes, buoys, and ships are vitally important for validation and incorporation into hurricane surface wind analyses.

Low-level geostationary satellite derived cloud motion vectors have been analyzed with hurricanes for many years. Their contribution to surface wind analyses have been limited due to their lack of coverage because of extensive high cloud obscuration. However, with improved technology and analysis techniques, it has been shown that they provide important information in defining outer wind radii estimates (Dunion, et al, 2000).

5. Discussion – Group 3 Data Types

Active microwave scatterometers measure backscatter of centimeter scale capillary waves. This allows retrieval of ocean surface wind speed and direction, with some ambiguity. The SeaWinds instrument on board NASA's QuikScat satellite complements the ERS-2 scatterometer data to provide near real time data to forecasters. Despite some shortfalls in observing capability such as rainfall contamination and direction assignment ambiguity, the high resolution and improved coverage of scatterometer data have greatly enhanced the forecaster's ability to evaluate tropical cyclone surface winds in the data poor regions of the tropics (Edson and Hawkins, 2000).

Surface wind speed estimates from the SSMI have been available for many years, and the improved views of tropical cyclone structure from the microwave imager are well documented (Velden, et al 1989). With the recent higher resolution views provided by TRMM, new opportunities and technique development work show promise of providing improved information on surface wind distribution from the microwave imager. (Hawkins, et al 2000; Edson, 2000)

The capability of microwave sounders to detect and measure the upper tropospheric warm cores of tropical cyclones has been known for many years. (Kidder, et al, 1978) With the advent of the higher resolution AMSU on NOAA's new series of polar orbiters, there has been a great deal of renewed interest and research. (Kidder, et al 2000; DeMuth, et al 2000; Brueske and Velden, 2000). DeMaria et al, (2000) have shown that tropical cyclone surface wind and pressure analyses can be retrieved from AMSU data alone using a simple hydrostatic model with compensation for the rainfall attenuation influences. Although the resolution is improved (48 km), AMSU-A still is inadequate for reliably measuring eye size and radius of maximum wind in most tropical cyclones.

6. Discussion – Group 4 Data Types

Aircraft observations of flight level winds have been used for many years for tropical cyclone intensity analysis. Even though there has been uncertainty in converting flight level winds to surface wind estimates, the data has been invaluable for surface wind analyses (Powell and Houston, 1998). Greatly improved surface wind estimates are now available from the new aircraft observations – GPS Dropwindsondes and SFMR surface wind estimates (Black et al, 2000; Powell, et al 2000; Franklin, et al, 2000). These data sets will improve our understanding of the details of the hurricane's boundary layer wind field. They are also essential to validation and development of reliable satellite remote sensing derived analyses of tropical cyclone surface winds.

7. Concluding Remarks

Preliminary work is underway at NESDIS RAMM / CIRA to improve real-time analysis of tropical cyclone surface winds, exploiting the capabilities of all available data types. The ultimate goal is to have real-time analyses with accuracy and reliability as good as possible for all tropical cyclone regions. This of course is aimed at improved forecasts and mitigation of damage to lives and property. With this in mind, it is important to recognize the improved capability of operational models in analysis and forecasting of the surface wind field (Tuleya and Bender, 2000). Operational model analysis and forecasts surface wind fields need to be incorporated into the overall validation and technique development goal of improved tropical cyclone surface wind analysis.

8. Acknowledgements

This work is supported by NOAA Grants NA90RAH00077 and NA17RJ1228.

9. Acronyms

AMSU: Advanced Microwave Sounding Unit
AOML: Atlantic Oceanographic and Meteorological Laboratory
CIRA: Cooperative Institute for Research in the Atmosphere
ERS: European Space Agency Research Satellite
EOS: Earth Observing System
RAMM: Regional and Mesoscale Meteorology
SSM/I: Special Sensor Microwave / Imager
TRMM: Tropical Rainfall Measurement Mission

10. References

Black, P.G., E. Uhlhorn, M. Powell, and J. Carswell, 2000: A new era in hurricane reconnaissance: Real-time measurement of surface wind structure and intensity via microwave remote sensing. *Preprints, 24th Conf. Hurr. Trop. Meteor.*, Fort Lauderdale, FL, Amer. Meteor. Soc., 199-200.

Brueske, K.F., and C.S. Velden, 2000: Tropical cyclone intensity estimation using the NOAA-KLM series AMSU: Preliminary results and future prospects. *Preprints, 24th Conf. Hurr. Trop. Meteor.*, Fort Lauderdale, FL, Amer. Meteor. Soc., 258-259.

Cocks, S.B., and W.M. Gray, 2001: Variability of the outer wind profiles of western North pacific typhoons: Classifications and techniques for analysis and forecasting. Submitted to *Mon Wea. Rev.*

DeMaria, M., J.A. Knaff, S.Q.Kidder, M.D. Goldberg, 2000: Tropical cyclone wind retrievals using AMSU-A Data from NOAA-15. *Preprint, AMS 10th Conf Sat Met.*

DeMuth, J. D., M. DeMaria, J. Knaff, and T.H. VonderHaar, 2000: An objective method for estimating tropical cyclone intensity and structure from NOAA-15 AMSU data. *Preprints, 24th Conf. Hurr. Trop. Meteor.*, Fort Lauderdale, FL, Amer. Meteor. Soc., 484-485.

Dodge, P. et al, 2000: Dual Doppler analyses of mesovorticies in a hurricane rainband. *Preprints, 24th Conf. Hurr. Trop. Meteor.*, Fort Lauderdale, FL, Amer. Meteor. Soc., 302-303.

Dunion, J.P., S. Houston, C. Velden, M. Powell, P. Black, 2000: Using surface adjusted GOES low-level cloud drift winds to improve the estimation of tropical cyclone outer wind radii. *Preprints, 24th Conf. Hurr. Trop. Meteor.*, Fort Lauderdale, FL, Amer. Meteor. Soc., 488-489.

Dvorak, V.F., 1984: Tropical cyclone intensity analysis using satellite data. NOAA Tech. Report NESDIS 11, U.S. Department of Commerce, Washington.

Edson, R.T., 2000: Evaluation of TRMM and SSM/I imagery in early development of tropical cyclones. *Preprints, 24th Conf. Hurr. Trop. Meteor.*, Fort Lauderdale, FL, Amer. Meteor. Soc., 254-255.

Edson, R. T, and J.D. Hawkins, 2000: A comparison of scatterometer derived wind data over tropical cyclones as determined from ERS-2 and QuikScat data. *Preprints, 24th Conf. Hurr. Trop. Meteor.*, Fort Lauderdale, FL, Amer. Meteor. Soc., 195-196.

Finta, C.A., 2000: JTWC integration of remote sensing data into the TC warning process. *Preprints, 24th Conf. Hurr. Trop. Meteor.*, Fort Lauderdale, FL, Amer. Meteor. Soc., 122-123.

Franklin, J.L., M.L. Black, and K. Valde, 2000: Eyewall wind profiles in hurricanes determined by GPS dropwindsondes. *Preprints, 24th Conf. Hurr. Trop. Meteor.*, Fort Lauderdale, FL, Amer. Meteor. Soc., 446-447.

Guard, C.P., et al, 1992: Joint Typhoon Warning Center and the challenges of multibasin tropical cyclone forecasting. Weather and Forecasting, 7, 328-352.

Hawkins, J. D., et al, 2000: Multi-satellite tropical cyclone structure (SSM/I and TRMM Microwave Imager). *Preprints, 24th Conf. Hurr. Trop. Meteor.*, Fort Lauderdale, FL, Amer. Meteor. Soc., 482-483.

Hock, T.F., and J.L. Franklin, 1999: The NCAR GPS Dropwindsonde. *Bull. Amer. Meteor. Soc.*, 80, 407-420.

Holland, G.J., 1980: An analytical model of the wind and pressure profiles in hurricanes. *Mon. Wea. Rev., 108,* 1212-1218.

Hollinger, J., Lo, R., Poe, G., Savage, R. and Pierce, 1987: *Special Sensor Microwave / Imager User's Guide,* Naval Research Laboratory, Washington, D.C., 179 pp.

Kidder, S. Q., W.M. Gray, and T.H. VonderHaar, 1978: Estimating tropical cyclone central pressure and outer winds from satellite microwave data. *Mon. Wea. Rev.*, 106, 1458-1464.

Kidder, S. Q., M. D. Goldberg, R. M. Zehr, M. DeMaria, J.F.W. Purdom, C. S. Velden, N. C. Grody, and S. J. Kusselson, 2000: Satellite analysis of tropical cyclones using the Advanced Microwave Sounding Unit (AMSU). *Bull. Amer. Meteor. Soc.*, 81, 1241-1259.

Knupp, K.R., J. Walters, and E.W. McCaul, 2000: Doppler Profiler observations of the boundary layer within the eyewall of Hurricane Georges during landfall. *Preprints, 24th Conf. Hurr. Trop. Meteor.*, Fort Lauderdale, FL, Amer. Meteor. Soc., 590-591.

Lee, W. and F. Marks, 2000: An objective method to determine tropical cyclone center near landfall with WSR-88D data – the GBTVD-simplex algorithm. *Preprints, 24th Conf. Hurr. Trop. Meteor.*, Fort Lauderdale, FL, Amer. Meteor. Soc., 310-311.

Powell, M. D., and S. H. Houston, 1998: Surface wind fields of 1995 Hurricanes Erin, Opal, Luis, Marilyn, and Roxanne at landfall. *Mon Wea. Rev.*, 126, 1259-1273.

Powell, M.D., T.Reinhold, and R. Marshall, 2000: Tropical cyclone boundary layer wind variability. *Preprints, 24th Conf. Hurr. Trop. Meteor.*, Fort Lauderdale, FL, Amer. Meteor. Soc., J57-58.

Tuleya, R.E., and M.A. Bender, 2000: Improvements to the GFDL Hurricane Forecast System. *Preprints, 24th Conf. Hurr. Trop. Meteor.*, Fort Lauderdale, FL, Amer. Meteor. Soc., 238-239.

Velden, C.S., Olson W.S, and Roth, B.A, 1989: Tropical cyclone center fixing using DMSP SSMI/I data. *Preprints, 4th AMS Conf. On Satellite Meteorology and Oceanography. 16-19 May 1989. San Diego, CA., Amer. Meteor. Soc, Boston, MA, 136-138.*

Velden, C.S., T. Olander, and R. Zehr, 1998: Evaluation of an objective scheme to estimate tropical cyclone intensity from digital geostationary satellite infrared imagery. *Wea. and Forecasting, 13,* 172-186.

Velden, C.S., T. Olander, and S. Wanzong, 1998: The impact of multispectral GOES-8 wind information on Atlantic tropical cyclone track forecasts in 1995. Part I: Dataset methodology, description, and case analysis. *Mon Wea. Rev.*, 126, 1202-1218.

Weatherford, C.L. and W.M. Gray, 1988: Typhoon structure as revealed by aircraft reconnaissance: Part II, Structural variability. *Mon. Wea. Rev., 116,* 1044-1056.

Zehr, R.M., 1989: Improving objective satellite estimates of tropical cyclone intensity. 18th Conf. on Hurricanes and Tropical Meteorology, San Diego, CA, Amer. Meteor. Soc., Boston, MA.

P3.21 VALIDATION OF AN ADVANCED MICROWAVE SOUNDER UNIT (AMSU) TROPICAL CYCLONE INTENSITY AND SIZE ESTIMATION ALGORITHM

Mark DeMaria*
NOAA/NESDIS, Fort Collins, Colorado

Julie L. Demuth
Colorado State University, Fort Collins, Colorado

John A. Knaff
Cooperative Institute for Research in the Atmosphere, Fort Collins, Colorado

1. INTRODUCTION

The Advanced Microwave Sounder Unit (AMSU) that was included on the NOAA-15 satellite has an increased number of channels (15 on AMSU-A and 5 on AMSU-B), and increased horizontal resolution (48 km and 15 km at nadir for AMSU-A and –B, respectively) relative to the previous generation Microwave Sounder Unit (MSU). Kidder et al (2000) have shown that the AMSU-A instrument, which was designed for temperature sounding, can observe the upper-level warm core of tropical cyclones. A number of algorithms have been developed that provide quantitative estimates of tropical cyclone intensity based upon the upper-level temperature structure as observed by AMSU (Spenser and Braswell 2001; Brueske and Velden 2000; Demuth et al 2000). The algorithm described by Demuth et al 2000 (hereafter the DDK algorithm) also provides estimates of the azimuthally averaged radii of 34, 50 and 64 kt winds. In this study the DDK algorithm will be generalized to predict the wind radii in four quadrants relative to the storm center, as required by the National Hurricane Center (NHC), and will be evaluated using cases from the 2001 Atlantic hurricane season.

2. WIND ESTIMATION ALGORITHM

The DDK algorithm uses a physical retrieval based upon hydrostatic balance in the vertical and a dynamical balance in the horizontal. This method is described in Kidder et al (2000), and only a brief summary is presented here. A statistical algorithm is used to determine the temperature as a function of pressure (40 pressure levels from 1000 to 0.1 hPa) from the AMSU-A radiances at all of the satellite footprint locations. A single-pass Barnes analysis (with an e-folding radius of 100 km) is applied to interpolate the temperature profiles to an evenly spaced 20 km horizontal grid. The hydrostatic equation is then used to determine the geopotential height field as a function of pressure, where virtual temperature effects are neglected. NCEP global model analyses are used as a lower boundary condition for the hydrostatic equation on the outer edge of the analysis domain, which is integrated upwards to 50 hPa. A smoothness condition is applied to obtain the entire height field at 50 hPa in the interior of the domain from the boundary values. The hydrostatic equation is then integrated downward to the surface at all grid points within the analysis domain. Prior to the hydrostatic integration, an empirical correction is applied to the temperature profiles to adjust for attenuation of the AMSU radiances by liquid water and scattering by ice.

Once the height field is determined as a function of pressure, the wind field is calculated assuming gradient balance. The height field is azimuthally averaged relative to the storm center for this purpose. This method can be generalized to provide the horizontal wind as a function of latitude, longitude and pressure by replacing the gradient wind equation with the nonlinear balance equation. However, only the gradient wind results are currently used.

Figure 1 shows an example of the retrieved gradient wind as a function of radius and height for Hurricane Floyd at 0000 UTC on 12 September 1999. The retrieved wind field shows a cyclonic circulation through a deep layer, and an anticyclonic circulation at upper levels. Although the tangential wind field is qualitatively reasonable, the maximum retrieved wind in the low levels is only about 42 kt at a radius of about 200 km. At the time of this analysis, the maximum winds were estimated by NHC to be 85 kt at a radius of about 45 km. Thus, the AMSU-A data does not have adequate resolution to fully sample the inner core structure of intense tropical cyclones.

*Corresponding author address: Mark DeMaria, NOAA/NESDIS/RAMMT, CSU, West Laporte Ave, Fort Collins, CO 80523

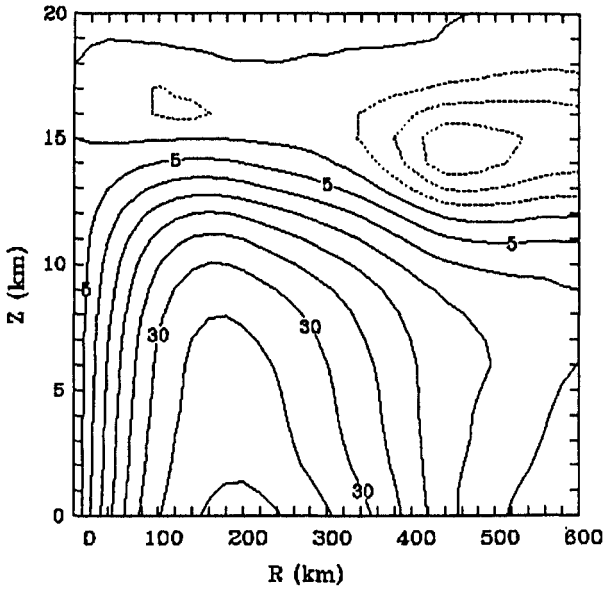

Figure 1. Radial-height cross-section of the AMSU retrieved tangential wind (kt) for Hurricane Floyd at 0000 UTC on September 12, 1999.

To correct for the lack of resolution, a statistical method is used to estimate the maximum winds and the azimuthally averaged radii of 34, 50 and 64 kt winds from parameters obtained from the AMSU analyses. The inputs include the surface pressure drop from 600 to 0 km radius, the maximum retrieved gradient wind at the surface and 3 km, the maximum temperature perturbation, the height of the maximum temperature perturbation, and the average cloud liquid water near the storm center (determined from AMSU-A). The outputs are estimates of the maximum wind and average wind radii. This algorithm was developed using cases from the 1999 and 2000 east Pacific and Atlantic hurricane seasons.

Although the DDK algorithm predicts the average wind radii, NHC is required to estimate the wind radii in four quadrants relative to the storm center (NE, SE, SW, SE). To determine the wind radii in each quadrant, given the maximum wind and the average radii, the surface wind speed (V) outside of the radius of maximum wind is assumed to be given by a simple model defined by

$$V(r,\theta) = (V_m - a)(\frac{r_m}{r})^x + a\cos(\theta) \qquad (1)$$

where r is the radius from the storm center, θ is the angle measured counterclockwise starting from a direction 90° to the right of storm motion vector, V is the wind speed, V_m is the maximum wind speed, r_m is the radius of maximum wind, a is the asymmetry factor due to the storm translation, and x is a parameter that determines the rate at which the wind speed decays with radius. The asymmetry factor is a fraction of the storm translation speed, given by the empirical formula described by Schwerdt et al (1979).

Equation (1) contains two free parameters (r_m and x), which could be found by solving (1) for r, and then applying an azimuthal average to give

$$\bar{r} = \frac{r_m}{2\pi}\int_0^{2\pi}[\frac{V_m - a}{V - a\cos(\theta)}]^{1/x} d\theta \qquad (2)$$

For the case where the maximum wind is 50 kt or greater, but less than 64 kt, the DDK algorithm provides estimates of the average 34 and 50 kt wind radii. The values of x and r_m could then be adjusted so that (2) passes through the two predicted wind radii. Given these values of x and r_m, (1) could then be used to determine V at any radius and azimuth, and the wind radii in each quadrant could be estimated. A difficulty with this approach is that when the maximum wind is less than 50 kt, the DDK algorithm only provides one average wind radius (34 kt), and when the wind is 64 kt or greater, three wind radii are provided. To overcome these problems, the parameters x and r_m are determined by minimizing a "cost function" C given by

$$C = \frac{(r_{34} - R_{34})^2}{\sigma_{34}^2} + \frac{(r_{50} - R_{50})^2}{\sigma_{50}^2} + \frac{(r_{64} - R_{64})^2}{\sigma_{64}^2} \qquad (3)$$
$$+ \lambda_x \frac{(x - x_c)^2}{\sigma_x^2} + \lambda_{rm} \frac{(r_m - r_{mc})^2}{\sigma_{rm}^2}$$

where r_{34} is the average 34 kt wind radius determined from (2), R_{34} is the average 34 kt wind radius from the DDK algorithm, σ_{34} is the standard deviation of a sample of mean 34 kt wind radii, (and similarly for the 50 and 64 kt wind radii), x_c is the climatological value of x, r_{mc} is the climatological value of r_m, and σ_x and σ_{rm} are the sample standard deviations of x and r_m, respectively. The values of the climatological variables and standard deviations were determined from NHC operational estimates of wind radii for all storms from 1988-2000 that were west of 50°W longitude. The wind radii for this time period were available from an "Extended Best Track" data file, which combines the standard NHC best track data with the

operational wind radii and other storm parameters. The sample used to determine the statistical parameters was restricted by longitude because most of the storms in the western part of the Atlantic basin had aircraft reconnaissance data available to more accurately estimate the wind radii.

The last two terms on the right side of (3) are "penalty terms" that keep the values of x and r_m from deviating too far the climatological values. The parameters λ_x and λ_{rm} determine how far x and r_m can deviate from climatology. Research is still being performed to determine the best choices for λ_x and λ_{rm} . In the example presented below, a value of 0.1 was used for both. The penalty terms provide a solution for the case where only one wind radius estimate is available. The penalty terms also help provide a reasonable solution for the case when the wind model (1) can not fit the average wind radii from the DDK algorithm. This problem occurs when the wind threshold for a given radius is very close to the maximum wind and the asymmetry factor is large (fast moving storms). In these cases, the wind radii are zero for some quadrants. For example, if the maximum wind was 55 kt for a storm moving at 15 kt, there would only be a small arc to the right of the storm center where the wind exceeded 50 kt. The radius of 50 kt winds would be zero for azimuths outside of this small arc, and the average 50 kt wind radius would be quite small. Although these cases were included in the development of the DDK algorithm, this problem only occurred for a small number of cases. Thus, the algorithm tends to over-estimate with mean wind radius for these cases. When the wind model (2) is fitted for this type of case, the radius of maximum wind becomes unrealistically large. The penalty term prevents this from occurring, and the fit is becomes based on climatology and the other mean wind radii information (the 34 kt wind radius in the above example).

3. RESULTS

The goal of this study is to evaluate the AMSU maximum wind and wind radii algorithm using independent cases from the 2001 hurricane season. The evaluation will be restricted to storms with aircraft reconnaissance data available, so that the "observed" wind radii will be relatively accurate. As of this writing, only one named tropical cyclone (Allison) has occurred in the Atlantic basin. Since Allison was only over the water for a short amount of time, no cases are available.

To illustrate the wind radii algorithm, an example from hurricane Floyd at 0000 UTC on 12 September, 1999 is presented. This case was chosen since the maximum wind prediction was fairly accurate, and the storm had recently been sampled by reconnaissance aircraft. The radial-height cross-section of the AMSU retrieved tangential wind for this case is shown in Fig. 1. Using the DDK algorithm, the maximum surface winds were estimated to be 86 kt, compared with 85 kt in the NHC best track. The DDK algorithm predicted the average radii of 34, 50 and 64 kt winds to be 144, 81 and 48 nm, compared with 119, 75, and 53 nm estimated by NHC. The minimization of (3) with the DDK wind radii input and the observed storm motion (heading of 280° at 10 kt) resulted in an x value of 0.61 and an r_m value of 29 nm.

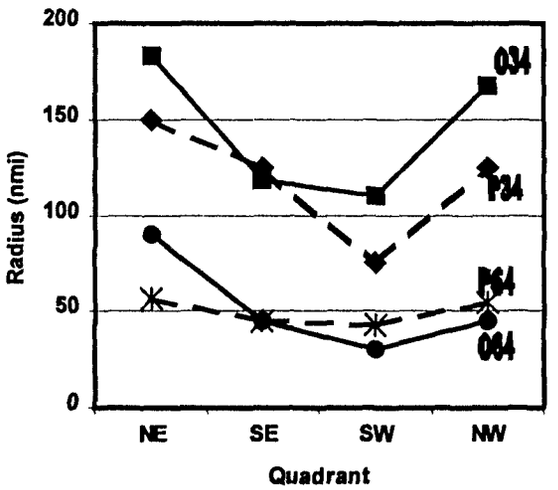

Figure 2. The predicted and observed radii of 34 kt (P34 and O34) and 64 kt (P64 and O64) winds for four quadrants relative to the storm center for Hurricane Floyd at 0000 UTC on 12 September 1999.

Figure 2 shows the predicted and observed 34 and 64 kt wind radii for this case (similar results were obtained for the 50 kt radii). This figure shows that both the predicted and observed radii were a maximum in the NE quadrant and a minimum in the SW quadrant, although the AMSU algorithm under-predicted the amplitude (NE radius-SW radius) of the asymmetric component of the 64 kt wind radii. The amplitude of the predicted asymmetric component of the 34 kt wind radius was similar to the observations. A more complete evaluation of

the algorithm will be performed at the end of 2001 hurricane season.

4. CONCLUDING REMARKS

A method was presented where the maximum wind and the radii of 34, 50 and 64 kt winds in four quadrants relative to the tropical cyclone center (NE, SE, SW, NW) can be estimated from AMSU-A data on the NOAA-15 and –16 satellites. Based upon results from the 1999 and 2000 hurricane seasons, it is estimated that at least one pass per day (and possibly as many as four passes per day) would be available for any tropical cyclone. A more complete evaluation of the algorithm will be performed at the end of the 2001 hurricane season using cases where aircraft reconnaissance data are available for ground truth. The algorithm assumes an idealized radial and azimuth structure of the surface wind field to obtain the wind radii in each quadrant, given the predicted maximum wind and azimuthally averaged wind radii. In principle, this wind field could be combined with QuikScat surface winds and low-level cloud drift winds reduced to the surface, to provide the best possible satellite surface wind field estimate.

REFERENCES

Brueske, K.F., and C.S. Velden, 2000: Tropical cyclone intensity estimation using the NOAA-KLM series Advanced Microwave Sounder Unit (AMSU): Preliminary results and future prospects. *Preprints, 24th Conference on Hurricanes and Tropical Meteorology*, 29 May-2 June 2000, Fort Lauderdale, FL, AMS, 258-259.

Demuth. J.L., M. DeMaria, J.A. Knaff, and T.H. Vonder Haar, 2000: An objective method for estimating tropical cyclone intensity and structure from NOAA-15 Advanced Microwave Sounder Unit (AMSU) data. *Preprints, 24th Conference on Hurricanes and Tropical Meteorology*, 29 May-2 June 2000, Fort Lauderdale, FL, AMS, 484-485.

Kidder, S., M. Goldberg, R. Zehr, M. DeMaria, J.F.W Purdom, C.S. Velden, N.C. Grody, and S.J. Kusselson, 2000: Satellite analysis of tropical cyclones using the Advanced Microwave Sounding Unit (AMSU). *Bull. Amer. Meteor. Soc.*, **81**, 1241-1259.

Spencer, R.W., and W.D. Braswell, 2001: Atlantic tropical cyclone monitoring with AMSU-A: Estimation of maximum sustained wind speeds. *Mon. Wea. Rev.*, **129**, 1518-1532.

Schwerdt, R.W., F.P. Ho, and R.R. Watkins, 1979: Meteorological criteria for standard project hurricane and probable maximum hurricane wind fields, Gulf and East Coasts of the United States. NOAA Tech. Rep. NWS 23, NWS NOAA, U.S Dept. of Commerce, Silver Spring, MD, 317 pp.

P3.22 TRMM TMI VIEWS OF TROPICAL CYCLONES FOR TACTICAL RECONNAISSANCE

Thomas F. Lee*, NRL, Monterey, CA; and F. J. Turk,
J. D. Hawkins, and R. T. Edson

Naval Research Laboratory, Monterey, CA

1. INTRODUCTION

In late 1997, operationally useful imagery became available from the Tropical Rainfall Measuring Mission (TRMM) Microwave Imager (TMI). See Simpson et al. 1998 (cover) for an example. The primary purpose of the TRMM satellite is to provide detailed precipitation estimates over the tropics to support climate research. However, since real-time data have become available in 1998 to the Joint Typhoon Warning Center (JTWC) in Pearl Harbor, TRMM TMI images have become a mainstay of satellite analysis. They are also used operationally by the National Hurricane Center (NHC) and other tropical cyclone forecast agencies, as provided by the Naval Research Laboratory (NRL), marine meteorology division.

The images are based on the superior spatial resolution footprints of the TMI, which enables forecasters to use two imaging channels (i.e., 37 and 85 GHz) compared to just one from the lower resolution DMSP Special Sensor Microwave Imager (SSM/I) sensor (85 GHz only). This paper presents a case study of one storm for which TMI images were available.

The SSM/I instrument is a passive microwave radiometer that collects radiation naturally emitted by the surface of the Earth and the intervening atmosphere (Table 1). Its swath width is 1400 km and has an orbital period of 102 minutes. In the tropics, large gaps appear between successive swaths of the SSM/I. However, in recent years there have been at least two SSM/I instruments in orbit at any given time, increasing the frequency of coverage and reducing the gaps (Hawkins et al. 2001). Thus, most storms have been covered several times a day in near-real time (Lee et al. 1999).

Corresponding Author Address: Thomas F. Lee, NRL, 7 Grace Hopper Avenue, Monterey CA, 99943-5502, lee@nrlmry.navy.mil

Table 1 Characteristics of DMSP SSM/I and TRMM TMI.

SSM/I	
Center Frequency (GHz)	EFOV (km x km)
19.35 V, H	70 x 45
22.235 V	60x40
37.0 V, H	38x40
85.5 V, H	16x14

V refers to Vertical Polarization; H refers to Horizontal Polarization. EFOV refers to the Effective Field of View.

TMI	
Center Frequency (GHz)	EFOV (km x km)
10.65 V, H	63x37
19.35 V, H	30x18
21.3 V	23x18
37.0 V, H	16x9
85.5 V, H	7x5

The TRMM TMI sensor (Table 1) is similar to the SSM/I, but there are several fundamental differences (Kummerow et al. 1998). Flying at approximately half the altitude, the TMI has significantly superior spatial resolution and yields one additional frequency (10.65 GHz). While the large footprint of this additional channel does not support images which are operationally useful to observe tropical cyclone structure directly, this channel does improve retrieval of surface winds in regions of heavy cloudiness and light precipitation (Conner and Chang 2000). Unlike the sun-synchronous SSM/I, which was launched into morning and evening orbits (no coverage in the middle of the day and night) the TMI collects data at all times of day and night. Its unique orbit covers mainly the tropics (from about 38 S to 38 N), suiting it well to the mission of observing tropical cyclones.

More recently, 89 and 150 GHz images from the Advanced Microwave Sounding Unit (AMSU-B) aboard the NOAA polar-orbiting satellites have become available to forecasters (Kidder et al.

2000). Interpretation of these images is similar to SSM/I 85 GHz.

2. FERNANDA, EASTERN PACIFIC, 20 AUGUST 1999

Tropical Storm Fernanda was moving into cooler waters and had weakened to an intensity of about 40 knots at the time the TMI and SSM/I sensors imaged it Figs. 1b-d (final page of preprint, past references). The GOES infrared image (Fig. 1a) shows the top of the cirrus canopy displaced significantly to the west of the clouds comprising the low-level center. In such situations, forecasters periodically have difficulty estimating a storm center position from infrared images out of confusion about which cloud level to observe. Furthermore, the warm tops of the low-level cloud circulation are difficult to distinguish from the sea surface, causing further confusion (Lee 2000). (This problem can be much worse than illustrated in Fig. 1a, since this figure has been enhanced to shows the low clouds distinctly).

The TMI 85 GHz image shows a small area of depressed Tb (dark gray shades) on the left (western) side of the image, indicating ice-phase precipitation aloft (Fig. 1b). Away from the convection, exposed bands of cloud/rain water create a cyclonic circulation pattern, but there is little evidence of a cloud-free center. At 37 GHz, on the other hand (Fig. 1c), the storm eye stands out distinctly, enclosed within a ring of cloud/rain water. The discrepancy between the two is a function of the difference in sensitivity to cloud/rain water in 37 vs. 85 GHz. At 37 GHz there is enhanced sensitivity for liquid water paths in the range from about 0 to 0.5 mm. This range is represented often in the water-laden core regions of tropical cyclones (Weng and Grody 1994). However, the 85 GHz channel saturates in amounts greater than about 0.3 mm, eliminating spatial detail on images. The 85 GHz channel has some sensitivity to smaller amounts (Spencer et al. 1989), explaining the suggestion of Weng and Grody (1994) to use the 85 GHz channel to retrieve smaller liquid water amounts in stratus clouds which contain minimal cloud water. However, for tropical cyclones this channel has only limited ability to show variations in cloud water well. Thus, 37 GHz is often the preferred channel to resolve low-level eye structure in the absence of deep convection. Even lower frequency channels might even be better suited to this purpose, but their relatively poor spatial resolution limits their effectiveness.

For comparison, the SSM/I 37 GHz image is shown for a nearly coincident time (Fig. 1D). The ability to detect the storm eye is severely compromised compared to Fig. 1C, the TMI image of the same frequency. Thus, most forecasters have preferred 85 GHz images. Up until the time that TMI images became available, images of the lower frequencies simply did not have the spatial resolution sufficient for tropical cyclone analysis.

3. DISCUSSION

Over the core of tropical cyclones tropical cyclones, the TMI 37 GHz channel generally has much greater sensitivity to variations in cloud/rain water than the 85 GHz channel. The advantage at 37 GHz appears in images where convection is absent and stratiform water/rain clouds are exposed. Images of 37 GHz provide particularly effective images of low-level storm circulations, where convection is absent at upper levels. In particular, 37 GHz images can detect eyes and low-level bands unseen at 85 GHz.

The 37 GHz channel has two main disadvantages that limit its usefulness in discerning the convection-free eyes. Infrequently, eyes are simply too small to be seen in TRMM 37 GHz images, owing to its relatively coarse footprint size. This limitation arises occasionally over very small storms. Second, scattering from intense convection over the central eye wall region of a storm can be mistaken as a large eye on uncorrected 37 GHz images. At other times, the center position can be misdiagnosed because nearby convection distorts the eye appearance. The poster shown at the conference will address ways to correct for these ambiguities.

4. ACKNOWLEDGEMENTS

The support of the research sponsor, the Oceanographer of the Navy through the program office Space and Naval Warfare Systems Command, under program element 0603207N is gratefully acknowledged. The authors thank the NASA TRMM Science Data and Information System team, including Erich Stocker, for providing TRMM TMI data. Dr. Steve Miller of NRL Monterey offered invaluable suggestions.

5. REFERENCES

Connor, L.N., and P.S. Chang, 2000: Ocean Surface Wind Retrievals using the TRMM Microwave Imager, *IEEE Trans. Geosci. Remote Sensing*, 38, 2009-2016.

Hawkins, Jeffrey D, Thomas F. Lee, Joseph Turk, Charles Sampson, John Kent, and Kim Richardson, 2001: Real-Time Internet Distribution of Satellite Products for Tropical Cyclone Reconnaissance, *Bull. Amer. Meteor. Soc.*, 82, 4, 567-578.

Kidder, S.Q., M.D. Goldberg, R.M. Zehr, M. DeMaria, J.F.W. Purdom, C.S. Velden, N.C. Grody, and S.J. Kusselson, 2000: Satellite Analysis of Tropical Cyclones using the Advanced Microwave Sounding Unit (AMSU), *Bull. Amer. Meteor. Soc.*, 6, 1241-1259.

Kummerow, C., W. Barnes, T. Kozu, J. Shiue, and J. Simpson, 1998: The Tropical Cyclone Rainfall Measuring Mission (TRMM) sensor package. *J. Atmos. Ocean. Technol.*, 15, 809-817.

Lee, T.F., and J.D. Hawkins, F.J. Turk, K. Richardson, C. Sampson, and J. Kent, 1999: Tropical Cyclone Images now can be viewed "live" on the web, *EOS*, 50, 612, 164.

Lee, Thomas F., 2000: Nighttime Observation of Sheared Tropical Cyclones Using GOES 3.9-m Data. *Wea. Forecasting*, 15, 6, 759–766.

Simpson, J., Halverston, H. Pierce, C. Morales, and T. Iguchi, 1998: Eyeing the eye: Exciting early stage science results from TRMM, *Bull. Amer. Meteor. Soc.*, 79, 1711.

Spencer, R.W., H.M. Goodman, and R.E. Hood, 1989: Precipitation retrieval over land and ocean with SSM/I: Identification and characteristics of the scattering signal. *J. Amos. Oceanic Technol.*, 6, 254-273.

Weng, F. and N. Grody, 1994: Retrieval of cloud liquid water using the Special Sensor Microwave Imager (SSM/I). *J. Geophys. Res.*, 99, 25 535-25 551.

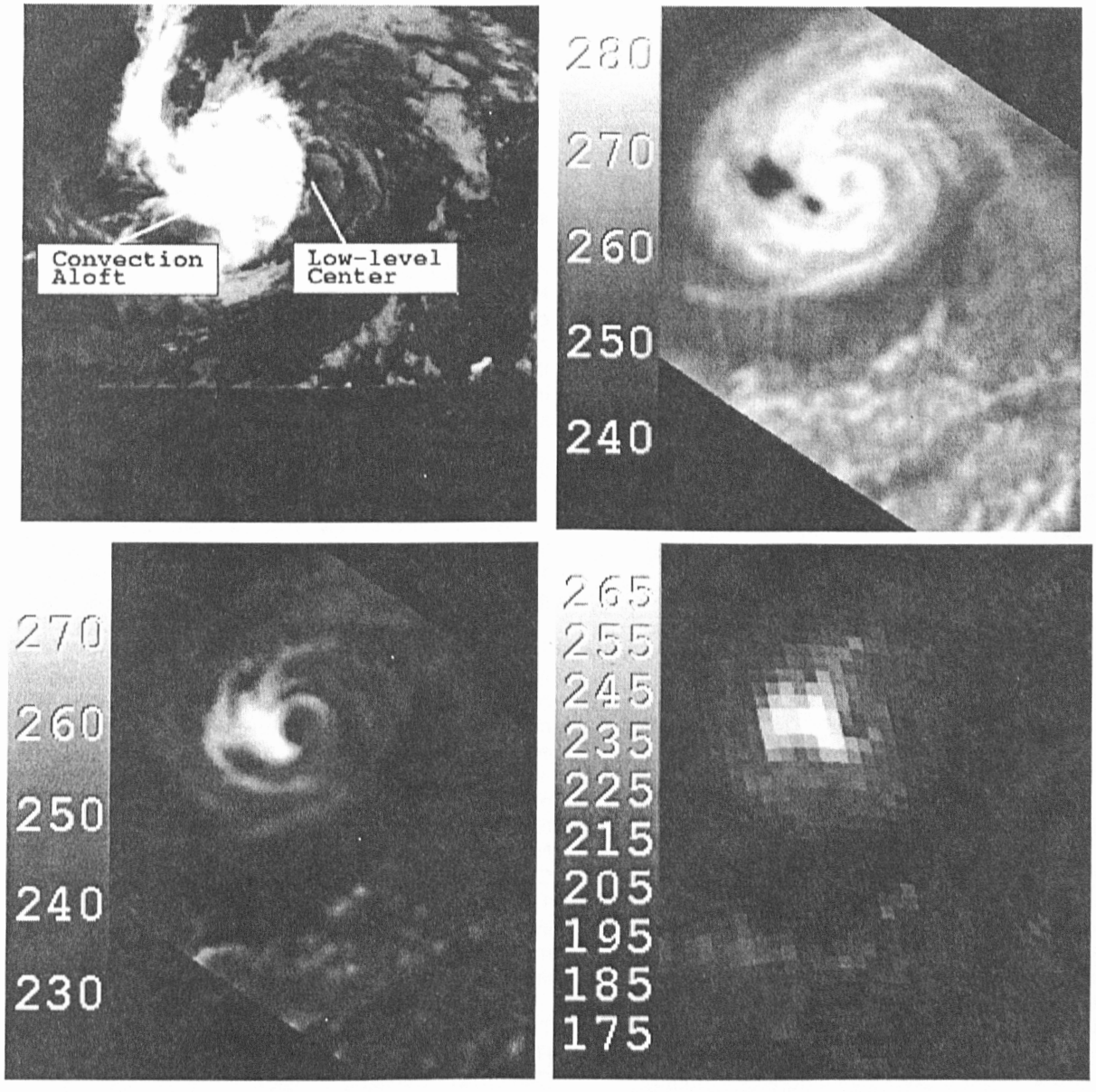

Figure 1 Northeastern Pacific images for Tropical Storm Fernanda, 20 August 1999: upper left) GOES-10 IR image 0215 UTC; upper right) TMI 85 GHz Image, 0209 UTC; lower left) TMI 37 GHz Image, 0209 UTC; lower right) SSM/I 37 GHz Image, 0242 UTC.

P3.23 MAPPING TROPICAL CYCLONE CHARACTERISTICS VIA PASSIVE MICROWAVE REMOTE SENSING

Jeffrey D. Hawkins[1], Tom F. Lee[1], F. J. Turk[1], Kim L. Richardson[1], Charles Sampson[1], and John Kent[2]

[1]Naval Research Laboratory, Marine Meteorology Division, Monterey, CA 93943
[2]Science Applications International, Inc., Monterey, CA

1. INTRODUCTION

The Naval Research Laboratory's Marine Meteorology Division in Monterey, CA (NRL-MRY) has demonstrated the potential utility of passive microwave imagery and products for global tropical cyclone (TC) monitoring by developing a near real-time web page (Hawkins et. al., 2001). The web page contains a suite of passive microwave images and products that assist the user in seeing through cirrus clouds. The upper-level cirrus clouds often obscure the satellite analyst's ability to extract storm positions and/or rain organization needed to estimate real-time intensity values. Thus, the rapid refresh afforded by geostationary visible and infrared (vis/IR) satellite imagery is thus partially mitigated by the inability to observe the full two-dimensional structure of the spiral rainbands, eyewall and eye features. The passive microwave data can thus play an important role in supplementing the vis/IR data sets that provide the backbone support to the TC satellite reconnaissance mission.

The Special Sensor Microwave/Imager (SSM/I) served as the first major data set for the TC web page. The SSM/I is a seven-channel instrument that includes important TC-related information in the 85 GHz frequency. Intense convection associated with TC rainbands and eyewall features can be readily viewed by the dramatically lowered brightness temperatures resulting from scattering due to frozen hydrometeors. Thus, although small ice crystals in cirrus clouds will not scatter much energy at 85 GHz, the larger frozen hydrometeors (graupel and hail) created within thunderstorms easily leave their mark in 85 GHz channel imagery. The 85 GHz data is also used since it has the best spatial resolution among the seven channels.

Similar frequencies on the Tropical Rainfall Measuring Mission (TRMM) Microwave Imager (TMI) have complemented the SSM/I coverage on the tropical cyclone web page since its launch in 1997. The high-resolution TRMM data has become a key addition to the passive microwave sensing of TCs globally.

Section 2 will describe the global microwave and geostationary data sets and their use at NRL-MRY. Section 3 will outline how the user can extract TC characteristics from the passive microwave products. Section 4 will summarize the potential that exists in the near term for improved TC reconnaissance, as additional satellite sensors become available.

Corresponding author address: Jeffrey D. Hawkins, Naval Research Laboratory, 7 Grace Hopper Ave, Monterey, CA, 93943; e-mail: hawkins@nrlmry.navy.mil

2. Data Sets

NRL-MRY routinely ingests data from the three current operational SSM/I sensors (F-13, 14 and 15). F-14 and F-15 are in similar orbits and thus frequently provide rapid coverage of a storm within one hour of one another. The 1400-km SSM/I swath is approximately 50% that of typical polar orbiter vis/IR sensors, but does a reasonable job covering TCs even away from the center swath (nadir). The conical scan helps use edge of swath data, since the user experiences no loss of spatial resolution as encountered on more conventional cross track scanners. The SSM/I stored digital data is provided via the Fleet Numerical Meteorology and Oceanography Center (FNMOC). The data is typically available 1-3 hours after sensor acquisition, worldwide. All images and products are produced within minutes and posted to the web page immediately.

The TRMM data is sent to NRL-MRY via the TRMM Science and Data Information System (TSDIS) located at the Goddard Space Flight Center in Maryland. Global digital data is available within timeframes comparable to the SSM/I data set. The 350-km TRMM spacecraft altitude enables the TMI sensor to provide 5-km resolution 85 GHz imagery. The superior spatial resolution removes some uncertainties in the 13-15 km SSM/I data and also brings the 37 GHz into play. 37 GHz data has a resolution of 13-km and is now sufficient to resolve many TC features. The 37 GHz data responds less to ice scattering and more to emissions from heavy rain. Thus, the channel effectively maps out storm characteristics that are lower in the atmosphere, since the large ice scattering impacting 85 GHz data is typically at a higher altitude.

Advanced Microwave Sounder Unit (AMSU-B) data has been recently incorporated into the NRL-MRY TC processing system. The passive microwave sounder carries an 89 GHz channel that responds similarly to the 85 GHz channels on the SSM/I and TMI. However, the sounder version has spatial resolutions near 16-km and thus limits the ability to resolve many smaller tropical cyclone features.

In-house tests have demonstrated the potential utility of the sensor since it has the following advantages; a) increases temporal refresh since it flys in a different orbital plane, and b) has enough resolution to observe many TC characteristics, especially for larger systems. These attributes can be quite positive when one considers that routine aircraft reconnaissance only occurs within the Atlantic Ocean basin. The AMSU-B data is provided in near real-time via collaborative efforts with the National Oceanic and Atmospheric Administration's (NOAA) National Environmental Satellite Data and Information Service (NESDIS).

The three sets of passive microwave sensors are complemented by the active microwave SeaWinds scatterometer onboard the QuikSCAT spacecraft. The June 1999 launch provided a large swath (1800-km) scatterometer to the potential tools available for tropical cyclone analysts and forecasters. The scatterometer retrieves surface wind vectors, wind speed and direction, whereas the SSM/I and TMI can only provide the scalar quantity wind speed. Information on closing off the low-level wind circulation, the radius of gale force winds and mapping the wind field asymmetries are important information for both warnings and potentially for assimilation into forecast models.

The NRL-MRY TC web page is unique in its combination of passive and active microwave products for near real-time tropical cyclone applications. The web page includes a suite of vis/IR products that are storm centered and thus able to focus on the finer details relating to rainband and storm formation and evolution. Data from five geostationary satellite (GOES-8/10, GMS-5 and Meteosat 5-7 provide true worldwide coverage).

The page also includes 72-hour track forecast graphics that incorporate the official warnings from the appropriate tropical cyclone operational center via the Automated Tropical Cyclone Forecasting (ATCF) system (Sampson and Schrader 2000). Official forecasts from the National Hurricane Center (NHC) in Miami, FL and the Joint Typhoon Warning Center (JTWC) in Pearl Harbor, HI enable the web page to cover storms anywhere on the globe.

The web page is driven entirely by the operational warning centers via software that permits the start, update and stop of a system anywhere within their area of responsibility. The popularity of the near real-time products and successful automation is leading to the operational transition of the TC web page to FNMOC. The NRL-MRY demonstration web page is located at:

http://kauai.nrlmry.navy.mil/sat-bin/tc_home

The near real-time aspects of this demonstration can not be overstated. The warning centers were willing to evaluate the products due to the 1-3 hour delay for the passive microwave imagery and products. The updates were thus within the data window used operationally to assess the current state of each tropical system. Trying to figure out the utility of this data suite after the fact would have been cumbersome and speculative. The near real-time nature and distribution via the web with an easy user interface were key factors in feedback and acceptance by a wide-ranging user group.

2. Data Interpretation

Passive microwave data images and products have the ability to see TC rainbands and eyewall features that simply can not be viewed when vis/IR images include upper-level cirrus clouds. Several prior publications by NRL-MRY have demonstrated the utility by using coincident vis/IR examples matched up with both SSM/I and TMI data (Hawkins et. al 1996, 1998, 2001, Lee et. al 1999, Barrett 1999). The full extent of this capability can only be gleaned by examining color figures, thus the 2001 and 1999 references are the best for this purpose. We have included below several black/white examples to illustrate the general capabilities and briefly discuss the overall database.

Passive microwave data has shown the ability to identify the early stages of eyewall development; a key feature when trying to anticipate which system will intensify into a hurricane or typhoon. In addition, passive microwave data has been very useful for fully developed systems to better understand the internal 2-D structure of the eyewall and associated rainbands. Figure 1 below is an example for typhoon Toraji while near peak strength southeast of Taiwan.

Figure 1 is a product of combining the horizontal and vertical polarized channels at 85 GHz and the polarization correct temperature (PCT) created by taking a difference of these two channels (Spencer et. al 1989). The 5-km TMI spatial resolution clearly reveals the eye and eyewall features as well as the rainbands to the south and west. The rainbands are not readily discernable in the IR image shown in Figure 2.

Figure 2 is an IR BD curve enhanced image used to extract intensity estimates using the subjective Dvorak technique (Dvorak 1984). Other false color enhancements can detect more subtle temperature structure, but still do not map

the rainbands to the extent seen in the passive microwave products.

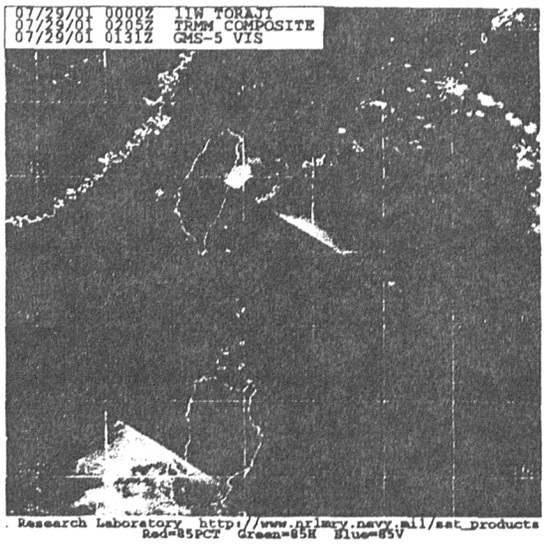

Figure 1. TRMM 85 GHz color product on July 29, 2001 at 0205 GMT for typhoon Toraji near Taiwan. Coincident GMS-5 visible data fills in the domain outside of the TRMM swath. Grid lines are 2x2 degrees.

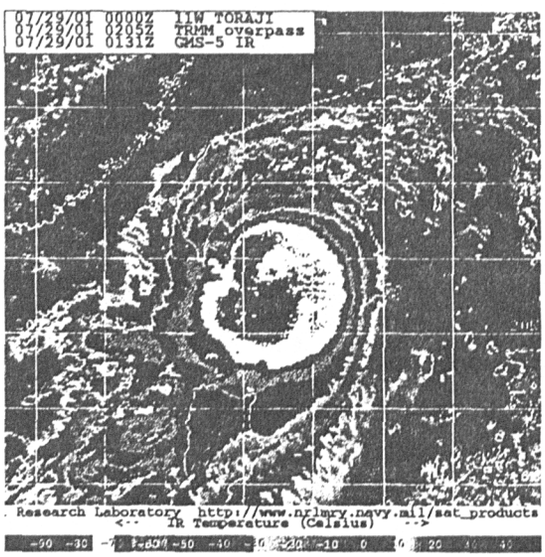

Figure 2. GMS-5 infrared BD curve enhancement (used to highlight cold high clouds) for July 29, 2001 at 0131 GMT. Eye is visible, but rainband structure difficult to discern. Grid lines are 2x2 degrees.

The TRMM data has proven valuable, partially due to the 35-degree inclination orbit purposely designed to spend all its time in the tropics. The TRMM overflights are not at the same times as the SSM/I data and change revisit times daily. This complementary aspect for temporal refresh is highly beneficial. More frequent visits are also provided when the AMSU-B 89 GHz data is added to the dataset.

The AMSU sounder data provides additional passive microwave data that is now being used to derive storm intensities via the warm core upper-level temperature anomalies (Brueske and Velden 2000). The technique uses temperature data from the AMSU-A portion of the sounder and the 89 GHz data from the AMSU-B. The 89 GHz sounder data can be mapped into an image similar to that for both SSM/I and TMI. The 16-km spatial resolution then enables the analyst to incorporate a third passive microwave sensor into the mix of TC monitoring sensors.

Figure 3 is an example of the 89 GHz AMSU-B data for typhoon Toraji on July 28, 2001 at 2337 GMT. The well-formed eye and eyewall is clearly evident. In addition, the convective strength in the southern semicircle is well mapped as seen also in Figure 1 and the TMI data product (it is easier to see the finer details with the original false colored product). Additional products incorporating 89 and 150 GHz channels are in development.

The 2200-km AMSU swath greatly assists in ensuring a passive microwave sensor overflys TCs in a more timely manner. The biggest drawback to applications has been the temporal refresh inherent with limited-swath polar orbiter data sets. The SSM/I and TMI are conical scanners and thus maintain the same spatial resolution across the entire swath. Cross track scanners such as AMSU have the best resolution at nadir and poorer footprints at swath edges. AMSU-B data is a welcome addition to the overall database due to the temporal updates.

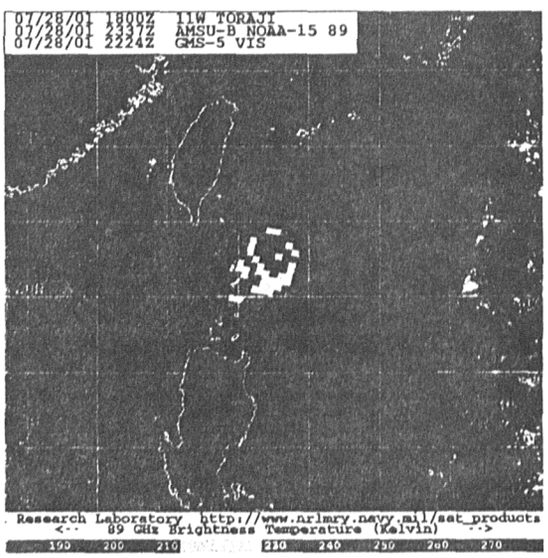

Figure 3. AMSU-B 89 GHz imagery product on July 28, 2001 at 2337 GMT. Grid lines are 2x2 degrees.

3. Summary and Future Potential

The NRL-MRY tropical cyclone web page will continue to evolve as new sensors enable enhanced capabilities. We have recently added F-15's SSM/I data set to the web page's routine processing and this sensor is complimenting an existing sensor on F-14. Four operational SSM/Is increase the temporal sampling sorely needed for TC recon efforts.

The SSM/IS (Special Sensor Microwave Imager and Sounder), that combines the SSM/I with the T1/T2 sounder is slated for launch in late 2001. The SSM/IS has major implications for enhanced geophysical algorithms with collocated imager and sounder data sets. In addition, the Navy will launch a passive polarimetric sensor (Windsat) next summer to retrieve ocean surface wind vectors. Remote sensing of surface wind vectors has direct applications to TC monitoring.

The Advanced Microwave Scanning Radiometer (AMSR) and the upcoming Aqua spacecraft will provide an additional high-resolution passive microwave radiometer. The large antenna will permit 89 GHz data at 5-km and 36.5 GHz data at 10-km over its 1445-km wide swath. The AMSR data has significant potential to advance the TC reconnaissance effort globally.

Acknowledgments. Special thanks are given to Erich Stocker at the TRMM Science Data and Information System (TSDIS) who assisted in near real-time access to the TRMM data and the Fleet Numerical Meteorology and Oceanography Center (FNMOC) for access to SSM/I global data sets. We gratefully acknowledge the support of our research sponsors, the Office of Naval Research, Program Element (PE-060243N) and the Oceanographer of the Navy through the program office at the Space and Naval Warfare Systems Command, PMW-185 (PE-0603207N).

4. REFERENCES

Barrett, E. C., 1999: Estimating the amount of rainfall associated with tropical cyclones using satellite techniques, WMO Report No. TCP-42.

Brueske, K. F. and C. S. Velden, 2000: Tropical cyclone intensity estimation using the NOAA-KLM series Advanced Microwave Sounding Unit (AMSU): Preliminary results and future prospects, AMS 24th Conf. on Hurricanes and Tropical Meteorology, pp. 258-259.

Dvorak, V. F., 1984: Tropical cyclone intensity analysis using satellite data. NOAA Tech. Rep. NESDIS 11, 47 pp.

Hawkins, J. D., J. Sandidge, R. Holyer, D. A. May, G. Poe, 1996: Tropical cyclone characterization via satellite remotely sensed techniques, Preprints, AMS 8th Conf. on Satellite Meteorology and Oceanography, pp. 200-203.

Hawkins, J. D., D. A. May, J. Sandidge, R. Holyer, and M. J. Helveston, 1998: Satellite tools for monitoring tropical cyclone intensity change, AMS Symposium on Tropical Cyclone Intensity Change, 51-55.

Hawkins, J. D., T. F. Lee, K. Richardson, C. Sampson, F. J. Turk, and J. E. Kent, 2001: Satellite multi-sensor tropical cyclone structure monitoring, *Bull. Amer. Meteor. Soc.*, **82**, 4, 567-578.

Lee, T. F., J. D. Hawkins, F. J. Turk, K. Richardson, C. Sampson, and J. Kent, 1999: Tropical cyclone images now can be viewed "Live" on the web, EOS, *Trans. Amer. Geophys. Union*, **80**, 50, 612-614.

Sampson, R. C., and A. J. Schrader, 2000: The Automated Tropical Cyclone Forecasting system, version 3.2. *Bull. Amer. Meteor. Soc.*, **81**, 1231-1240.

Spencer, R. W., H. M. Goodman, R.E. Hood, 1989: Precipitation retrieval over land and ocean with SSM/I: Identification and characteristics of the scattering signal. *J. Atmos. Ocean. Technol.*, **6**, 254-273.

P3.24

THE REALTIME VALUE OF COMBINED UPPER TROPOSPHERIC INERTIAL STABILITY MEASUREMENTS AND SATELLITE-DERIVED WINDS ON TROPICAL CYCLONE AND CONVECTION FORECASTING

John R. Mecikalski[1] and Christopher S. Velden

Department of Atmospheric and Oceanic Sciences
Space Science and Engineering Center
University of Wisconsin - Madison

1 MOTIVATION

The purpose of this note (complemented by the accompanying poster) is to introduce derived products which combine geostationary (infrared and water vapor) satellite data and derived "cloud drift" wind vectors (Velden et al. 1998), upper tropospheric potential vorticity (PV), and quantities that diagnose the lateral outflow potential from the anvils of deep convection (Mecikalski and Tripoli 1998; Sui and Yanai 1986). Isentropic levels between 340 and 365 K are analyzed using products designed for the purpose of evaluating the correlations between cloud motion-derived winds, low inertial stability and intensity changes of tropical convection and tropical cyclones.

Low upper-tropospheric inertial stability has been shown to be important for determining the intensity of convective systems (Molinari et al. 1997; Dickinson and Molinari 2000). Issues of the influence inertial stability has on the behavior of deep convection are examined theoretically by Emanuel (1979), demonstrating that convection should grow most readily into regions of lowest inertial (or symmetric) stability. In addition, the observational and numerical modeling work by Blanchard et al. (1998) positively correlates regions of weak inertial stability with mesoscale convective complex development over the central US.

In the upper troposphere, surrounding deep convection, low inertial stability would result in a tendency for air parcels, exiting the top of the convective clouds, to spread outward from the updraft (at the parcel's equilibrium level) with relative ease. In contrast, should air parcels exiting deep convection encounter high inertial stability, the rate of horizontal mass transport away from storm top may be significantly limited. This would result in either forced, dry subsidence immediately surrounding the convection, or a weakening of the convection's vertical mass transport, or both. Given two deep convective clouds in similar vertical shear and convective available potential energy (CAPE) environments, the one extending into the less inertially stable upper troposphere would perform less work on its environment and thus should persist longer and achieve greater intensity compared to the convection encountering high inertial stability aloft.

Although the work of Blanchard et al. (1998) demonstrated that deep convection preferentially forms in conditions of low upper tropospheric (above about 30.0 kPa) PV (inertial stability), one unanswered question is how self-serving is low PV to enhancing the convection that may generate it? In other words, and in addition, given that low upper tropospheric PV is a known prerequisite to the development (or invigoration) of deep convection, how does the production and re-distribution of this low PV influence the long-term behavior of mesoscale convection? Can "outflow corridors" be established via the perpetual generation of low PV aloft, or must low upper tropospheric PV be present prior to the establishment of such an outflow pathway?

These questions may best be answered by combining the above data sets. In particular, cloud motion vectors can provide information about the inherently un-(geostrophically) balanced flows exiting the anvils of thunderstorms, tropospheric levels that are in fact well sampled by cloud motion vectors. By combining the PV-related products, computed from routinely available global analyses, with the cloud drift wind data, realtime diagnostics and short-range (0-6 h) forecasts are provided. Three to twelve hour convection-intensity forecasts can be made using the PV-derived products alone. Diagnostic products are computed for three oceanic basins: the Eastern Pacific, the Western Atlantic and the Eastern Atlantic to the African coast. The intention is to have these products available in realtime via the internet (http://cras.ssec.wisc.edu:8080/~jrm/trmm_istc.html) throughout the 2001 and beyond North American tropical cyclone season (roughly July into October). These product are being developed in collaboration with the Tropical Cyclone Research Team (headed by C. Velden of CIMSS).

As of spring 2001, only a few products are available in realtime. In this note the products being created will

[1] *Corresponding author*: John R. Mecikalski, Cooperative Institute for Meteorological Satellite Studies, University of Wisconsin - Madison, 1225 West Dayton Street, Madison, WI 53706. email: *johnm@ssec.wisc.edu*

be described, with a few examples presented. Interested parties are encourages to visit the CIMSS Tropical Cyclones homepage, as well as the URL above. Research results, incorporating data from the Tropical Rainfall Measuring Mission (TRMM) Visible and Infrared Scanner (VIRS) and Precipitation Radar (PR), highlighting these products' value will be reported on in a later AMS conference, as well in the refereed literature.

2 DERIVED CONVECTION-INTENSITY DIAGNOSTICS

The following products will be developed during 2001:

- Combined enhanced-satellite (identifying the most active, growing thunderstorms and tropical cyclones), inertial available kinetic energy (IAKE; Mecikalski and Tripoli 1998) and cloud drift winds to diagnose low-PV—convective outflow correlations. IAKE is in effect the horizontal (along-line) integration of PV in units of energy (m^2s^{-2});
- Vector differences between measured cloud drift winds and IAKE vectors across isentropic convective outflow layers, used to determined whether convection, in fact, seeks the path of least horizontal resistance for its outflow;
- Combined IAKE, PV and cloud drift winds to determine whether pre-existing low upper-tropospheric PV causes convective enhancements, and the role convectively-generated low upper-tropospheric PV plays in invigorating new or existing convection;
- Combined IAKE and cloud drift winds to analyze the acceleration (or deceleration) of flow from the tops of tropical storm systems. Products like this will be used to assess intensity changes.

Figure 1 (top) shows a product that combines enhanced GOES-10 imagery, contoured IAKE and cloud drift winds. Note the correspondence between active convection (shading) within the intertropical convergence zone, centered on about 8-10° N and positive IAKE (low inertial stability). Figure 1 (bottom) presents tropical storm Adolph (near 15° N 101° W). For this storm, this derived product highlights the co-location of low inertial stability (solid contours) and an upper tropospheric outflow "stream" extending southeastward from the storm, which is highlighted well by the satellite-derived winds. This relationship suggests that the convection in this region is ventilating its anvil-level outflow easily, and will persist longer and reach greater intensity than otherwise.

Diagnostics for selected convective events, statistical results and more complete derived product examples will be presented during the conference.

This research is supported by NASA TRMM Grant NAG5-9673.

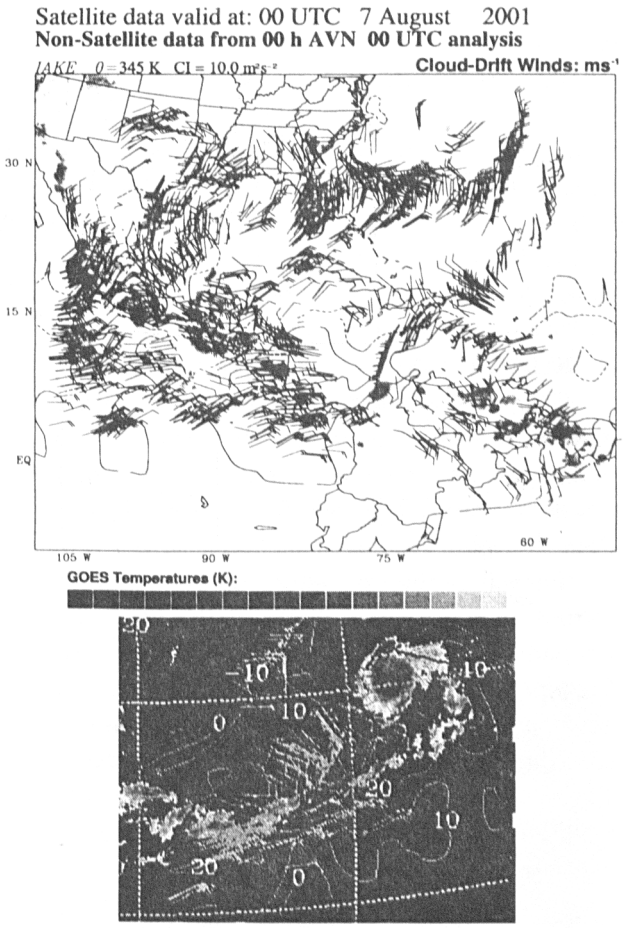

Figure 1: (Top) A composite of contoured IAKE (no vectors), enhanced GOES-10 data (shading with accompanying scale on bottom denoting cloud temperatures, K), and infrared GOES-10 satellite-derived cloud motion vectors for 00 UTC 7 August 2001. (Bottom) A derived product showing tropical storm Adolph off the Mexican coast at 00 UTC 31 May 2001.

3 BIBLIOGRAPHY

Blanchard, D. O., W. R. Cotton and J. M. Brown 1998: Mesoscale circulation growth under conditions of weak inertial instability. *Mon. Wea. Rev.*, **126**, 118–140.

Dickinson, M., and J. Molinari, 2000: Climatology of sign reversals of the meridional potential vorticity gradient over Africa and Australia. *Mon. Wea. Rev.*, **128**, 3890–3900.

Emanuel, K. A. 1979: Inertial instability and mesoscale convective systems. Part I: Linear theory of inertial instability in rotating viscous fluids. *J. Atmos. Sci.*, **36**, 2425–2449.

Molinari, J., D. Knight, M. Dickinson, D. Vollaro, and S. Skubis, 1997: Potential vorticity, easterly waves, and Eastern Pacific tropical cyclogensis. *Mon. Wea. Rev.*, **125**, 2699–2708.

Mecikalski, J. R. and G. J. Tripoli 1998: Inertial available kinetic energy and the dynamics of tropical plume formation. *Mon. Wea. Rev.*, **126**, 2200–2216.

P3.25

SATELLITE APPLICATIONS FOR TROPICAL WAVE/TROPICAL CYCLONE TRACKING

Jason P. Dunion[1], and Christopher S. Velden[2]
1 NOAA/AOML/Hurricane Research Division
2 UW/CIMSS

1. INTRODUCTION

The accurate detection and analysis of tropical waves and tropical cyclones pose a challenge to operational forecasters. It is therefore necessary to develop analysis tools that aid in locating and describing these features.

Recent collaborative efforts between NOAA's Hurricane Research Division (HRD) and the Cooperative Institute for Meteorological Satellite Studies (UW-CIMSS) have resulted in the development of several new satellite-derived products designed for tropical cyclone applications. These products utilize geostationary satellite winds produced at UW-CIMSS and are made available in real-time.

Low-level (600-925 hPa) cloud-drift winds are generated in the tropical cyclone environment using the visible channels on the GOES-8, GOES-10, and GMS-5 satellites. These wind data are surface adjusted using a planetary boundary layer program developed at HRD and are made available to forecasters during real-time storm events (Dunion et al. 2001). Recent efforts have also resulted in the development of techniques for generating cloud-drift winds using the 3.9 μm shortwave infrared (SWIR) channel available on the GOES satellites. These near infrared winds show promise for providing substantial nighttime low-level wind information in the tropical cyclone environment in the northwest Atlantic and northeast Pacific basins.

A new product that uses the 10.7 and 12 μm channels on GOES –8 is being developed to track the advance of the Saharan Air Layer (SAL) across the north Atlantic basin. The SAL can be associated with tropical cyclone development, but can also negatively impact tropical systems.

*Corresponding author address: Jason P. Dunion, NOAA/AOML/HRD, 4301 Rickenbacker Causeway, Miami, FL 33149; e-mail: dunion@aoml.noaa.gov

2. SURFACE ADJUSTED GOES CLOUD-DRIFT WINDS

Using a sequence of three 15 min. interval images, low-level cloud-drift winds are produced from the high-resolution visible channel on the GOES-8/10 and GMS-5 satellites. In recent years, UW-CIMSS has fully automated its wind extraction algorithm. Tracer selection and derivation procedures include enhanced filtering capability to screen out undesirable cloud features as well as the implementation of an objective quality control module (Velden et al. 1998). Targets are height assigned using a cloud base height assignment technique that utilizes an IR histogram to estimate the base temperature of tracked low-level cloud features. These low-level cloud-drift winds (700-925 hPa) are adjusted to the surface (10 m) using a combination of HRD's planetary boundary layer model and empirical optimizations derived from comparisons with in situ data in tropical cyclone environments. This data allow for the analyses of both low-level and surface wind fields near and peripheral to the circulation center.

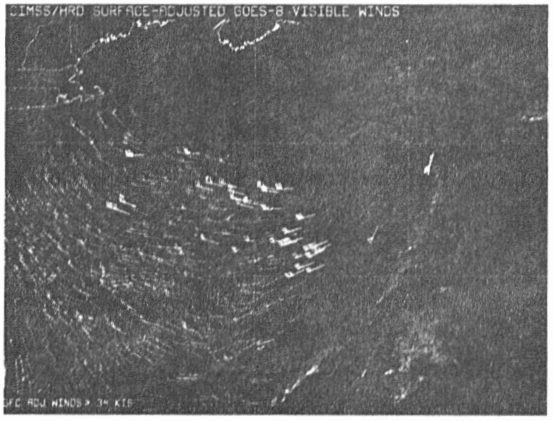

Figure 1: Surface adjusted GOES low-level cloud-drift winds in the environment of Hurricane Michael on 19

October 2000 at 1245 UTC. Winds are valid for 10 m, maximum 1-min. sustained winds with marine exposure.

Figure 1 shows an example of surface adjusted GOES low-level visible winds associated with Hurricane Michael on 19 October 2000.

3. SHORTWAVE INFRARED CLOUD-DRIFT WINDS

Using the 3.9μm channel on the GOES-8/10 satellites, SWIR cloud-drift winds are currently being developed to provide nighttime coverage in the tropical cyclone environment (Velden and Dunion 2001). The SWIR channel is a slightly cleaner window channel than the 10.7 μm longwave infrared (LWIR) channel also available on GOES. This allows for a higher detectability of low-level (600-925 hPa) cloud tracers in the SWIR channel. However, in order to effectively track these features, this channel must be limited to nighttime use. The SWIR channel is sensitive to solar reflection by cirrus and especially low-level cumulus clouds. This can affect the brightness temperature that is retrieved by the GOES instrumentation and can adversely impact the ability of the UW-CIMSS wind algorithms to detect wind vectors (see Fig. 3).

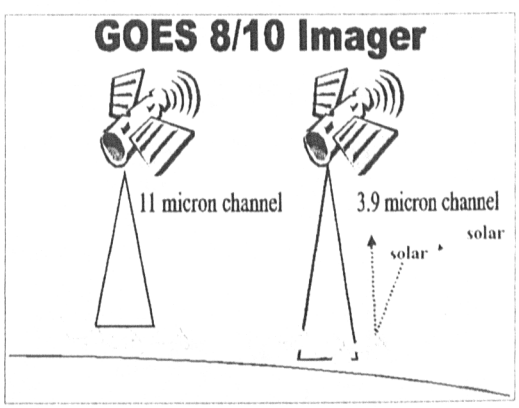

Figure 2: Graphical representation of the superior ability of the 3.9 μm SWIR channel over the LWIR channel at detecting low-level cumulus features. Susceptibility to solar reflectance by the SWIR channel is also indicated.

To avoid the problem of solar contamination in the SWIR channel, an algorithm was developed to track the position of targeted wind vectors relative to the geographical position of the solar terminator. Any targets located in sunlit conditions or that are positioned within 30 min. of local sunset (when utilizing 15 min. imagery) are excluded from being processed. This ensures that no solar contamination affects the generation of SWIR winds.

Another issue that was addressed to maximize SWIR wind generation related to the flat gradients of brightness temperature characteristic of this channel on GOES-8/10. This factor limits the ability of the UW-CIMSS wind tracking algorithms to detect a substantial number of winds in the tropical cyclone environment. New techniques were developed to enhance the low-level gradients in the SWIR channel prior to their being input into the UW-CIMSS winds package. Figure 3 shows that this enhancement improves the appearance of low-level features relative to an identical unenhanced SWIR image around Tropical Storm Florence.

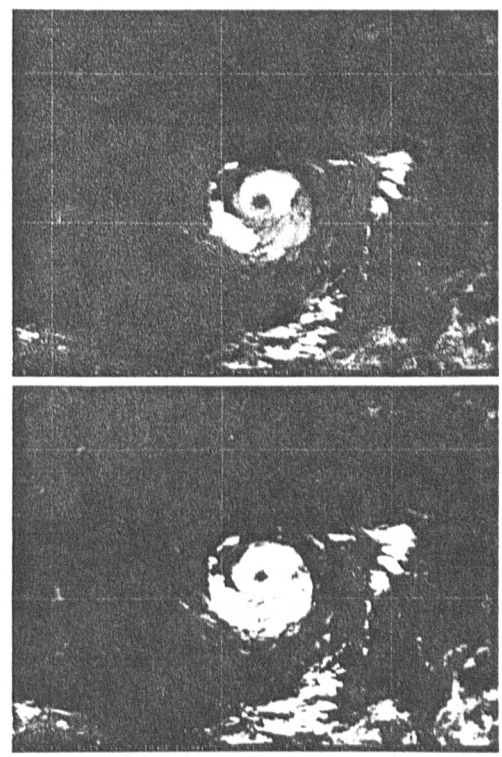

Figure 3: Comparison of normal GOES-8 SWIR 3.9 μm imagery (top panel) vs, enhanced imagery (bottom panel) designed to improve low-level cloud detection.

Recent tests have shown that this enhancement technique results in a 40-50% increase in the number of low-level cloud-drift winds tracked around tropical cyclones by the UW-CIMSS wind tracking algorithms. (Fig. 4).

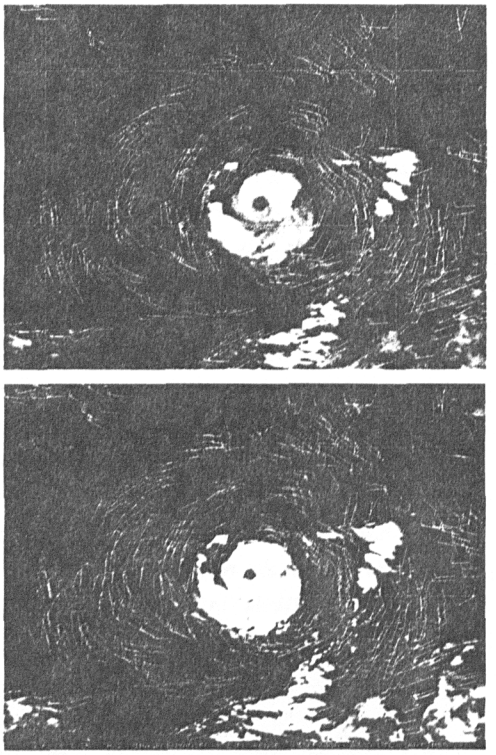

Figure 4: Comparison of wind vectors generated using normal GOES-8 SWIR 3.9 μm imagery (top panel) vs. those detected using enhanced imagery (bottom panel). The image enhancement technique resulted in a 50% increase in wind coverage for this case.

Improvements were also made to the wind tracking algorithms to further optimize the SWIR wind production. These improvements produce low-level wind coverage that rivals that obtained using the visible channel during daylight hours. The SWIR satellite winds will compliment the visible cloud-drift winds currently being generated in the northwest Atlantic and northeastern Pacific basins by providing more continuous temporal coverage in tropical cyclone environments. Plans include the application of the HRD surface adjustment algorithms on these nighttime SWIR winds.

3. SAHARAN AIR LAYER TRACKING

The Saharan Air Layer (SAL) is often associated with a low-level easterly surge centered at about 700 hPa that originates over the northwest African continent. This westward advancing surge is detectable using two methods that utilize GOES-8 satellite imagery. First, a marked increase in low-level wind speeds can be detected behind the advancing SAL. Low-level winds associated with this surge are typically on the order of 25-35 kt. Using a combination of visible and SWIR imagery and special relaxed settings in the UW-CIMSS winds package, low-level cloud-drift winds that can easily detect the low-level wind surge can be generated.

A second method that can be used to track the SAL utilizes 10.7 and 12 μm channels on GOES-8 to track suspended dust silicates that usually get caught up in the SAL. Under normal atmospheric conditions, the 10.7 μm channel (Ch. 4) represents a cleaner window channel than the 12 μm channel (Ch. 5), which is slightly more susceptible to the effects of low-level atmospheric water vapor. Therefore, the 10.7 μm channel usually appears slightly warmer than the 12 μm channel. Suspended dust silicates both reflect and absorb a portion of the incident solar radiation that is incident on the SAL. This energy is then released by the silicates as LWIR radiation. These dust silicates more effectively emit LWIR radiation at 12 μm than at 10.7 μm (Fig. 5).

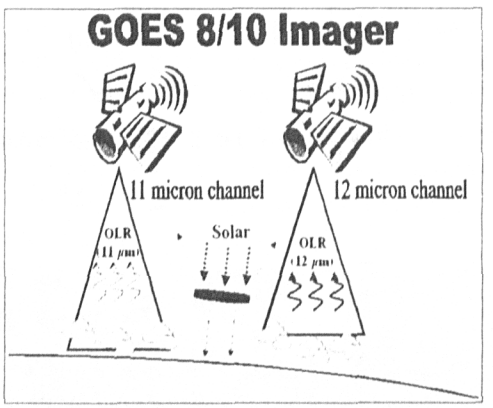

Figure 5: Graphical representation of the ability for the 10.7 μm channel on GOES to detect warmer, lower level surface features than the 12 μm channel. Suspended dust silicates absorb incident solar radiation and re-emit LWIR radiation more effectively at 12 μm than at 10.7 μm. This creates an anomalous situation where the 12 μm channel appears warmer than the 10.7 μm channel. This condition indicates the presence of dust silicates in the atmosphere.

Therefore, in the presence of dust silicates, the 12 μm channel on GOES appears anomalously warmer than the 10.7 μm channel. Enhancements were developed to take advantage of this anomaly to track the dust silicates that are suspended in the SAL. Figure 6 shows an example of a product that utilizes both special visible wind vectors and the 10.7/12 μm channel anomalies and clearly shows the presence of the SAL surge. This image shows Hurricanes Isaac (26 N 54 W) and Joyce (12 N 43 W) and the advancing SAL (light shading in the northeast portion of the image) at 1445 UTC 28 Sep 2000. Joyce was a minimal category 1 hurricane at this time and contrary to model predictions, was a minimal tropical storm 48 hours later. Joyce's demise was likely related to the increased shear induced by the strong low-level easterlies associated with the SAL, as well as the entrainment of dry stable SAL air that was encroaching on the system.

Figure 6: Image generated by differencing the 10.7 and 12 μm channels on GOES-8. The light shading indicate the presence of suspended dust silicates associated with the SAL and low-level wind vectors >25 kt are plotted to track the coincident extent of the low-level wind surge. The triangles show the geographical position and advance of the SAL. Hurricanes Isaac and Joyce can be seen in the NW and south central extents of the image respectively.

4. CONCLUSIONS

Satellite derived wind products such as surface adjusted low-level visible and SWIR cloud-drift offer forecasters an additional means of effectively determining the outer wind radii for tropical cyclones in the northwest Atlantic and northeast Pacific basins. A new product that tracks the position of dust silicates suspended within the Saharan Air Layer also has potential applications for forecasting tropical cyclone formation and intensity change.

5. REFERENCES

Velden, C.S., and J.P. Dunion, 2001: New satellite derived wind products and their applications to tropical cyclone/tropical wave forecasting. Minutes of the 55th Interdepartmental Conf., Orlando, FL, Office of Fed. Coord. For Meteor. Services and Supporting Research, NOAA, In Print.

Dunion, J.P., C.S. Velden, S.H. Houston, and M.D. Powell, 2001: Application of surface adjusted GOES low-level cloud-drift winds in the environment of Atlantic tropical cyclones: Part II: Integration into surface wind analyses. Mon. Wea. Rev. (submitted).

Velden, C.S., T.L. Olander, and S. Wanzong,1998: The impact of multispectral GOES-8 wind information on Atlantic tropical cyclone track forecasts in 1995: Part I: Dataset, methodology, description, and case analysis. Mon. Wea. Rev., **126**,1202-1218.

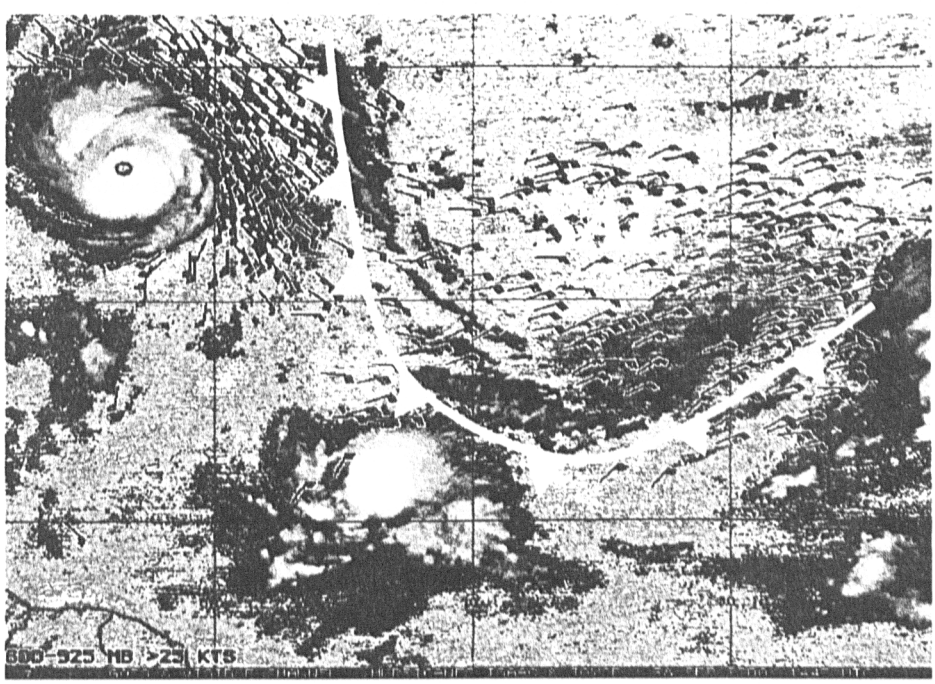

P3.28 ANTARCTIC METEOROLOGY: SATELLITES AND WEATHER FORECASTING

Matthew A. Lazzara*, Linda M. Keller, Charles R. Stearns, Jonathan E. Thom, and George A. Weidner
University of Wisconsin, Madison, Wisconsin

1. INTRODUCTION

Applications of satellite imagery during the early days of the polar orbiting weather satellites (Television Infrared Observing Satellite (TIROS) and Nimbus) were few for the Antarctic. The high altitude and coarse resolution made it difficult to resolve many surface features. With the advent of the Environmental Science Services Administration (*ESSA-1*) satellite, operational products for the Antarctic were processed from the digitized video data. Streten (1968) and Troup and Streten (1972) used the archived imagery to study the large-scale circulation and to compare the cloud vortices with conventional observations of positions. This began the evolution of using satellite data and imagery for Antarctic forecasting.

2. SCIENCE AND FORECASTING

In January 1980, the United States Antarctic Program (USAP) installed a high resolution picture transmission (HRPT) system to receive the National Oceanic and Atmospheric Administration (*NOAA-6*) and *TIROS-N* series of satellites (Wiesnet et al. 1980). Science was able to utilize the output for a variety of applications. The new system was primarily used for operational weather forecasting, especially in support of aviation operations (Wiesnet et al. 1980 and Foster 1982). HRPT data are now received at most of the manned Antarctic stations.

2.1 Mesoscale Features

With the availability of science quality polar orbiting imagery, mesoscale features that affect operations could be investigated. Mesoscale vortices, with their small size and intense winds, were especially troublesome not only for aviation but also oceanographic vessels and research projects. Satellite imagery allowed investigators to pinpoint favored regions of development as well as synoptic conditions that enhanced the possibility of their occurrence. In addition, katabatic winds also caused problems at many of the manned stations. Satellite infrared imagery allowed detection of the characteristic thermal signature of the adiabatically warmed air (e.g., Bromwich 1989; Bromwich et al. 1992). Today all Antarctic weather forecasting benefits from this work and include katabatic wind and polar low effects in the forecasts.

2.2 Composite Imagery

Bristor et al. (1966) were among the first to generate a full resolution polar stereographic mosaic of a section of the Southern Hemisphere using *ESSA-1* weather satellite data (Wiesnet et al. 1980). In addition, one of the first research uses was the development of an Antarctic mosaic for a joint NOAA and United States Geological Survey (USGS) program funded by the National Science Foundation (NSF) (Wiesnet et al. 1980). In late 1992, with support from NSF, the University of Wisconsin began routine generation of composite satellite images over the Southern Ocean and Antarctic continent (Stearns et al. 1999). These composites combined the available geostationary and polar orbiting satellite imagery which were remapped into a polar stereographic projection. This product is useful to researchers for the depiction of the atmospheric circulation from a hemispheric view. It is even more popular with forecasters who are able to determine long-wave patterns and monitor regions up stream and beyond the area covered by typical HRPT and other polar orbiting satellites local/regional view.

2.3 Forecasting Research and Procedures

In 1994 and 1995, the First Regional Observing Study of the Troposphere (FROST) project, organized by the Physics and Chemistry of the Atmosphere Group of the Scientific Committee on Antarctic Research (SCAR), took place. The main objective was to focus on "the meteorology of the Antarctic, determine the strengths and weaknesses of operational analyses and forecasts ... and to assess the value of new forms of satellite data that are becoming available" (Turner et al. 1996). In a study of Southern Hemisphere analyses during this time (Turner et al. 1999), reanalyzed surface charts were created using data from satellite sources. The satellite data was important and in some cases critical in improving most of the analyses.

The outcome of Project FROST led to the development of the International Antarctic Weather Forecasting Handbook (Turner and Pendlebury 2000). Previously, few manuals existed that were widely available that documented Antarctic weather forecasting procedures (e.g., the Naval Support Force Antarctica (NSFA) Forecaster's Handbook). The new handbook

* *Corresponding author address:* Matthew A. Lazzara, Univ. of Wisconsin, Space Science and Engineering Center, 1225 W. Dayton St., Madison, WI 53706; *email:* mattl@ssec.wisc.edu.

has a comprehensive examination of the climatology and topography of each station along with specific guidelines for forecasting. In a substantial section on satellite data, each of the instruments or sensors is discussed along with ways to use them singly or in combination as forecasting tools. The process of deriving vertical profiles of temperature and water vapor (TOVS and Advanced TOVS (ATOVS)) is explained in detail. The problems encountered when processing retrievals near and over Antarctica are discussed. Several studies are cited which have developed techniques to compensate for the peculiar properties in the atmosphere over Antarctica.

2.4 New Generation of Satellite Sensors

Over the years, satellites have grown dramatically in number and ability. The latest set of satellites launched contains improved sensor capabilities. *NOAA-16* carries the ATOVS while the DMSP satellite uses the special sensor for microwave imaging and sounding (SSMIS). The National Aeronautics and Space Administration (NASA) has launched its Earth Observing System (EOS) *Terra* satellite, and the EOS *Aqua* will be launched in late 2001. Both *Terra* and *Aqua* transmit data at X-Band (18 Ghz) with much higher data rates than NOAA or DMSP satellites, and both carry the Moderate Resolution Imaging Spectroradiometer (MODIS) sensor with 36 channels and increased spatial resolution (Bernstein 2000). MODIS offers the multispectral capability to retrieve a large number of atmospheric properties that are useful for forecasting and numerical modeling simulations (Bromwich and Cassano 2000). *Aqua* and the Japanese Advanced Earth Observation Satellite (*ADEOS-2*) will carry the Advanced Microwave Scanning Radiometer (AMSR) that greatly improves upon the capabilities of SSM/I for detecting cloud liquid water and precipitation rate over the ocean. The challenge for both the Antarctic forecaster and researcher will be in developing means to exploit these data for better forecasts.

3. SUMMARY

Antarctic weather forecasting has evolved since the advent of the weather satellite. Advances in detection and monitoring of mesoscale features; generation and use of composite imagery; improved forecasting procedures and scientific research; and continuous updating of weather satellite sensors has brought Antarctic weather forecasting into the modern age. New satellite technologies are planned, so the potential for improved Antarctic weather forecasts is promising.

ACKNOWLEDGMENTS. This work was supported by the NSF-OPP, Ocean and Climate Program Grant OPP-9908842.

4. REFERENCES

Bernstein, R.L., 2000: Availability and visualization of satellite data in the Antarctic. Preprints, Antarctic Forecasting Workshop, BPRC Miscellaneous Series M-419, Byrd Polar Research Center, The Ohio State University, Columbus, OH, 24-25.

Bristor, C.L., W.M. Callicott, and R.E. Bradford, 1966: Operational processing of satellite cloud pictures by computer. *Mon. Wea. Rev.*, **94**, 515-527.

Bromwich, D.H., 1989: Satellite analyses of Antarctic katabatic wind behavior. *Bull. Amer. Meteor. Soc.*, **70**, 738-749.

_____, and J.J. Cassano, Eds., 2000: Recommendations to the National Science Foundation from the Antarctic Weather Forecasting Workshop, BPRC Miscellaneous Series M-420, Byrd Polar Research Center, The Ohio State University, Columbus, OH, 48 pp.

_____, J.F. Carrasco, and C.R. Stearns, 1992: Satellite observations of katabatic wind propagation for great distances across the Ross Ice Shelf. *Mon. Wea. Rev.*, **120**, 1940-1949.

Foster, M.S., 1982: Aviation forecasting for the U.S. Antarctic program. *Antarctic J. of the U.S.*, **17**, 265-266.

Stearns, C.R., B. Sinkula, R. Holmes, M.A. Lazzara, and J.T. Young, 1999: Six years of composite infrared images south of Forty South at three hourly intervals. IUGG99 Conference, Birmingham, UK, p. B119.

Streten, N.A., 1968: Some aspects of high latitude Southern Hemisphere summer circulation as viewed by ESSA 3. *J. Appl. Meteor.*, **7**, 324-332.

Troup, A.J., and N.A. Streten, 1972: Satellite-observed Southern Hemisphere cloud vortices in relation to conventional observations. *J. Appl. Meteor.*, **11**, 909-917.

Turner, J., and S. Pendlebury, Eds., 2000: The International Antarctic Weather Forecasting Handbook, Vol. 1.1, 691 pp. [Available via FTP from the BAS Web site where details are available at http://www.nerc-bas.ac.uk/public/icd/jtu/ftpinst.html.]

_____, and Coauthors, 1996: The Antarctic First Regional Observing Study of the Troposphere (FROST) project. *Bull. Amer. Meteor. Soc.*, **77**, 2007-2032.

_____, S. Leonard, G.J. Marshall, M. Pook, L. Cowled, R. Jardine, S. Pendlebury, and N. Adams, 1999: An Assessment of Operational Antarctic Analyses based on data from the FROST Project. *Wea. Forecasting*, **14**, 817-834.

Wiesnet, D.R., C.P. Berg, and G.C. Rosenberger, 1980: High-resolution picture transmission satellite receiver at McMurdo Station aids Antarctic mosaic project. *Antarctic J. of the U. S.*, **15**, 190-193.

P3.29 CLOUD-DRIFT AND WATER VAPOR WINDS IN THE POLAR REGIONS FROM MODIS

Jeffrey R. Key[1*], David Santek[2], Christopher S. Velden[2], and W. Paul Menzel[1]
[1]Office of Research and Applications, National Environmental Satellite, Data, and Information Service, NOAA
1225 West Dayton Street, Madison, WI, 53706
[2]Cooperative Institute for Meteorological Satellite Studies, University of Wisconsin-Madison
1225 West Dayton Street, Madison, WI, 53706

1. INTRODUCTION

In the early 1960s Tetsuya Fujita developed analysis techniques to use cloud pictures from the first TIROS polar orbiting satellite for estimating the velocity of tropospheric winds (Menzel, 2001). Throughout the 1970s and early 1980s cloud motion winds were produced from satellite data using a combination of automated and manual techniques. In 1992, the National Oceanic and Atmospheric Administration (NOAA) began using an automated winds software package that made it possible to produce a full-disk wind set without manual intervention. The carbon dioxide (CO_2) slicing algorithm (Menzel et al., 1983) made it possible to assign accurate cloud heights to the motion vectors. Fully automated cloud-drift wind production from the Geostationary Operational Environmental Satellites (GOES) became operational in 1996, and now wind vectors are routinely used in operational numerical models of the National Centers for Environmental Prediction (NCEP).

Satellite-derived wind fields are most valuable for the oceanic regions where few observations exist and numerical weather prediction model forecasts are less accurate as a result. Like the oceans at lower latitudes, the polar regions also suffer from a lack of observational data. While there are land-based meteorological stations in the Arctic, and a small number of stations around the coast of Antarctica, there are no routine observations of winds over the Arctic Ocean and most of the Antarctic continent. Unfortunately, geostationary satellites are of little use at high latitudes due to the large view angles and poor spatial resolution, resulting in large uncertainties in the derived wind vectors.

Can polar-orbiting satellites be used to obtain wind information at high latitudes? Difficulties arise from the irregular temporal sampling and viewing geometry, but the idea has been explored before with promising results. The Advanced Very High Resolution Radiometer (AVHRR) was used by Herman (1993) to estimate cloud-drift winds for a few Arctic scenes. When compared to rawinsonde winds, the AVHRR winds were found to have a root-mean-square error of 6 m s^{-1}. Herman and Nagle (1994) compared cloud-drift winds from the AVHRR using two different methods of obtaining cloud height to gradient winds computed with the HIRS sounder. The AVHRR cloud-drift winds that incorporated the CO_2 slicing method (using HIRS channels) were found to be comparable to the HIRS gradient winds, with root-mean-square errors less than 5 m s^{-1}. Turner and Warren (1989) obtained useful cloud track wind information from AVHRR Global Area Coverage (GAC) data in the Weddell Sea, Antarctica.

In this paper we discuss a new effort to obtain estimates of high-latitude tropospheric winds using the MODerate Resolution Imaging Spectroradiometer (MODIS) on-board the National Aeronautics and Space Administration's (NASA) polar orbiting Terra satellite. Sampling issues are discussed, and results from a case study are presented.

2. TEMPORAL SAMPLING

Statistical analyses of visible, infrared, and water vapor wind data sets from geostationary satellites versus rawinsonde verification data have shown that the optimal processing intervals are 5 minutes for visible imagery of 1 km resolution, 10 minutes for infrared imagery of 4 km resolution, and 30 minutes for water vapor imagery of 8 km resolution. How often can we obtain wind vectors from a polar-orbiting satellite? Not surprisingly, the answer depends on the latitude and the number of satellites. Figure 1a shows the frequency of time differences between successive overpasses at a given latitude-longitude point on a single day with only one satellite. At 60° latitude there are two overpasses separated by about 10 hours. Obviously, no useful wind information can be obtained at this latitude with only a single satellite. At 80° there are many views separated by 100 minutes (the orbital period), but there is still a 13 hour gap each day. Even with large gaps at a single location, however, wind vectors can be obtained during part of every day for the entire Arctic and Antarctic regions.

Figure 1b shows the coverage with multiple satellites: the current NOAA-15, NOAA-16, Terra, and Chinese FY-1C satellites and NASA's future Aqua platform. Orbital characteristics based on current plans for Aqua were used in the simulation. Temporal gaps of a few hours still exist at the lower latitudes of the polar regions but at the higher latitudes the temporal coverage is very good. Given that geostationary satellites provide wind information equatorward of about 60 degrees latitude, global coverage can be obtained by using polar-orbiting satel-

* *Corresponding author address:* Jeff Key, NOAA/NESDIS, 1225 West Dayton Street, Madison, WI 53706; e-mail: jkey@ssec.wisc.edu.

lites for the high-latitudes, though two or more will be required to satisfy temporal sampling requirements.

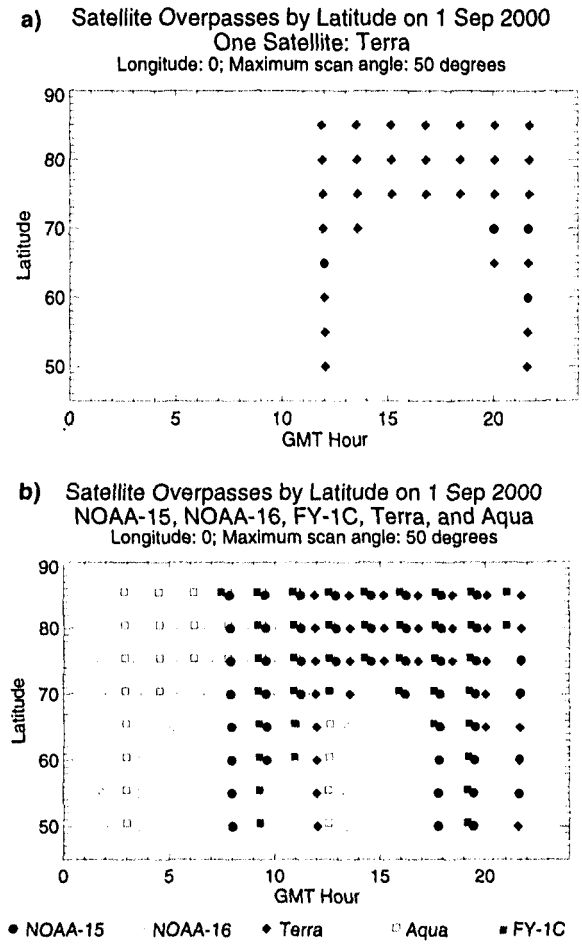

Fig. 1. (a) Time differences between successive overpasses of a single satellite (Terra) as a function of latitude over the course of a day at the Prime Meridian. Only overpasses with view angles less than 50 degrees are considered. (b) Time differences between successive overpasses of five satellites.

3. METHODS

Cloud and water vapor tracking with MODIS data is based on the established procedure used for GOES, which is essentially that described in Merrill (1989), Nieman et al. (1997), and Velden et al. (1997). With MODIS, cloud features are tracked in the infrared window band at 11 μm; water vapor features are tracked in the 6.7 μm band.

After remapping the orbital data to a polar stereographic projection, potential tracking features are identified. The lowest brightness temperature in the infrared window band (generally indicating cloud) within a target box is isolated and local gradients are computed. The size of the target area controls the density of derived vectors. Gradients that exceed a specified threshold are classified as targets for tracking. For water vapor target selection, local gradients are computed for the area surrounding every pixel rather than the single pixel with the minimum brightness temperature in a box. Water vapor targets are selected in both cloudy and cloud-free regions.

The tracking method employs a simple search for the minimum of the sum of squared radiance differences between the target and the search boxes in two subsequent images. A model forecast of the upper level wind is used to choose the appropriate search areas. Displacement vectors are derived for each of the two subsequent images. They are then subject to consistency checks to eliminate accelerations that exceed empirically determined tolerances. A final step in the tracking process is an adjustment to the vector speed for a well-documented slow bias in the upper-tropospheric cloud-tracked winds.

Height assignments can made with any of three methods. The infrared window method assumes that the mean of the coldest values in a sample is the temperature at the cloud top. The temperature is compared to a numerical forecast of the vertical temperature profile to determine the cloud height. This method is reasonably accurate for opaque clouds, but inaccurate for semi-transparent clouds.

The CO_2 slicing method works well for both opaque and semitransparent clouds. Cloudy and clear radiance differences in the CO_2 (13.3 μm) and infrared window bands are ratioed and compared to the theoretical ratio of the same quantities, calculated for a range of cloud pressures. The cloud pressure that gives the best match between the observed and theoretical ratios is chosen (Menzel et al., 1983; Frey et al., 1999).

The H_2O-intercept method of height determination can be used as an additional metric or, in the case of some other polar-orbiting imagers, in the absence of a CO_2 band. This method examines the linear trend between clusters of clear and cloudy pixel values in water vapor-infrared window brightness temperature space, predicated on the fact that radiances from a single cloud deck for two spectral bands vary linearly with cloud amount. The line connecting the clusters is compared to theoretical calculations of the radiances for different cloud pressures. The intersection of the two gives the cloud height (Schmetz et al., 1993).

We are investigating cloud height assignment where the results of the MODIS cloud product algorithm (Menzel and Strabala, 1997) are incorporated into the processing stream. Cloud top pressure is derived from a multi-channel CO_2 slicing technique and the cloud mask.

After wind vectors are determined and heights are assigned, the resulting data set is subject to a postprocessing, quality-control step. The purposes of this step are to determine the tropospheric level that best represents the motion vector being traced, to edit out vectors

that are in obvious error, and to provide end users with vector quality information (Velden et al., 1998).

4. APPLICATION

Figure 2 illustrates the application of the method to MODIS data. The figure shows wind vectors derived from both cloud and water vapor tracking in three consecutive overpasses on 6 September 2000 over the western Arctic Ocean. Portions of the underlying infrared image are devoid of wind vectors because those areas were not observed in subsequent overpasses. The three overpasses were separated by approximately 100 minutes for a total time span of 3.3 hours.

Vector heights, which represent the height of the cloud or water vapor feature that was tracked, are given in three broad categories: low (white), middle (grey), and high (black). Lower tropospheric wind estimates occur within the cyclonic system north of Siberia and also just east of 120 E longitude; mid-level, high velocity winds were measured in and around the frontal structure extending from the lower center portion of the image through the New Siberian Islands and also northeast of Wrangel Island in the bottom left portion of the image. Vectors for upper-level winds, primarily from the water vapor band, occur throughout the field.

5. CONCLUSIONS

This study has demonstrated the feasibility of deriving tropospheric wind information at high latitudes from polar-orbiting satellites. The methodology employed is based on the algorithms currently used with geostationary satellites, modified for use with the polar-orbiting MODIS instrument.

The project presents some unique challenges, including the irregularity of temporal sampling, different viewing geometries from one image to the next, large uncertainties in the model forecast profiles used in height assignment and quality control, and the complexity of surface features, including their motion. These and other issues will be investigated in the future, as part of an extensive processing and validation campaign. Model impact studies are also planned.

Acknowledgments. This work was supported by NOAA contract NA07EC0676.

6. REFERENCES

Frey, R., B. A. Baum, W. P. Menzel, S.A. Ackerman, C.C. Moeller, and J. D. Spinhirne, 1999: A comparison of cloud top heights computed from airborne LIDAR and MAS radiance data using CO2-slicing. *J. Geophys. Res.,* 104(D20), 24,547-24,555.

Herman, L.D., 1993: High frequency satellite cloud motion at high latitudes. *Proceedings of the 8th Symposium on Meteorological Observations and Instrumentation,* Amer. Meteorol. Soc., Anaheim, CA, 17-22 January, 465-468.

Herman, L.D. And F.W. Nagle, 1994: A comparison of POES satellite derived winds techniques in the Arctic at CIMSS. *Proceedings of the 7th Conference on Satellite Meteorology and Oceanography,* Amer. Meteorol. Soc., Monterey, CA, June 6-10, 444-447.

Menzel, W.P., 2001: Cloud tracking with satellite imagery: From the pioneering work of Ted Fujita to the present. *Bull. Amer. Meteorol. Soc.*, 82(1), 33-47.

Menzel, W.P. and K. Strabala, 1997: Cloud top properties and cloud phase algorithm theoretical basis document. Unpublished report, Cooperative Institute for Meteorological Satellite Studies, University of Wisconsin, 1225 W. Dayton Street, Madison, WI, 53706, 55 pp.

Menzel, W.P., W.L. Smith, and T.R. Stewart, 1983: Improved cloud motion vector and altitude assignment using VAS. *J. Climate Appl. Meteorol.*, 22, 377-384.

Merrill, R., 1989: Advances in the automated production of wind estimates from geostationary satellite imageing. *Proc. Fourth Conf. Satellite Meteorol.*, San Diego, CA, Amer. Meteorol. Soc., 246-249.

Nieman, S.J., W.P. Menzel, C.M. Hayden, D. Gray, S.T. Wanzong, C.S. Velden, and J. Daniels, 1997: Fully automated cloud-drift winds in NESDIS operations. *Bull. Amer. Meteorol. Soc.*, 78(6), 1121-1133.

Schmetz, J., K. Holmlund, J. Hoffman, B. Strauss, B. Mason, V. Gaertner, A. Koch, and L. van de Berg, 1993: Operational cloud motion winds from METEOSAT infrared images. *J. Appl. Meteorol.*, 32, 1206-1225.

Turner, J. and D.E. Warren, 1989: Cloud track winds in the polar regions from sequences of AVHRR images. *Int. J. Remote Sensing,* 10(4), 695-703.

Velden, C.S., C.M. Hayden, S.J. Nieman, W.P. Menzel, S. Wanzong, and J.S. Goerss, 1997: Upper-tropospheric winds derived from geostationary satellite water vapor observations. *Bull. Amer. Meteorol. Soc.*, 78(2), 173-196.

Velden, C.S., T.L. Olander and S. Wanzong, 1998: The impact of multispectral GOES-8 wind information on Atlantic tropical cyclone track forecasts in 1995. Part 1: Dataset methodology, description and case analysis. *Mon. Wea. Rev.*, 126, 1202-1218.

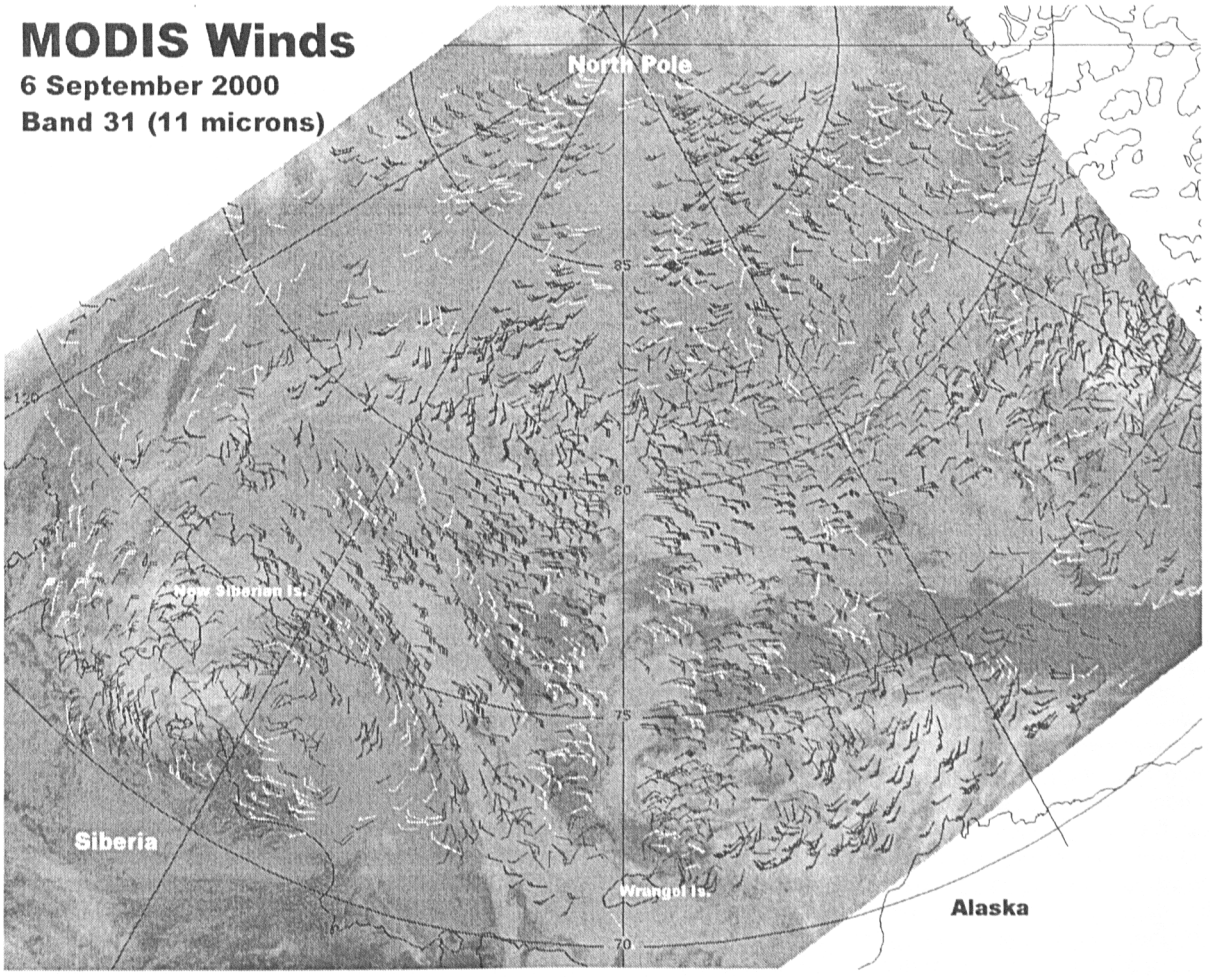

Fig. 2. Wind vectors determined with the automated cloud and water vapor tracking algorithm for 6 September 2000. Vectors are plotted on a MODIS 11 μm image, the first in the sequence of three overpasses spanning a time period of approximately 4.5 hours. Vector heights are given in three broad categories: low (white), middle (grey), and high (black).

P3.30 VIRTUAL LABORATORY FOR TRAINING IN SATELLITE METEOROLOGY

James Purdom
Cooperative Program for Research in the Atmosphere (CIRA)
Ft. Collins, Colorado

Anthony Mostek*
National Weather Service - Office of Climate, Water, and Weather Services
Boulder, Colorado

1.0 BACKGROUND

Operational meteorological satellites provide essential data for meteorological, climate, oceanographic and hydrological services to World Meteorological Organization (WMO) Members across the globe. New instruments on research satellites are providing insights into future satellite systems, such that a variety of new environmental applications are growing vigorously. We should expect great strides forward during the next decade with planned improvements to the space based component of the global observing system, and we must strive for full exploitation of that component. Updated and improved methods must be developed for preparing products for distribution to an increasingly sophisticated and diverse user community to accommodate the rapid-paced development cycle that informed users will demand. Maximum utilization of satellite data for environmental applications requires a strong training component. Meeting the demands of this challenge is becoming possible because of the combined efforts of the WMO and the world's producers of operational meteorological satellite data. This combined effort is taking shape through the Coordination Group for Meteorological Satellites (CGMS) with the formation of the Virtual Laboratory for Satellite Data Utilization.

The Virtual Laboratory for Satellite Meteorology (VL) is a collaborative effort joining the major satellite operators across the globe with WMO "centers of excellence" in satellite meteorology. Those "centers of excellence" serve as the satellite-focused training resource for WMO Members across the globe. A schematic of the VL is shown in Figure 1a. The "centers of excellence" are five WMO Regional Meteorological Training Centers (RMTCs) and the Australian Bureau of Meteorology, while the four satellite operators are the USA (NESDIS), Europe (EUMETSAT), China (NSMC), and Japan (JMA). The various centers of excellence are sponsored by one of the major satellite operators (see the circles touching the boxes in figure 1a).

The Virtual Laboratory for Satellite Meteorology traces it origins back to work done by CIRA, the Cooperative Institute for Research in the Atmosphere, at Colorado State University.

*Corresponding author address: Anthony Mostek, NCAR/COMET, P.O. Box 3000, Boulder, CO 80307; email: mostek@comet.ucar.edu

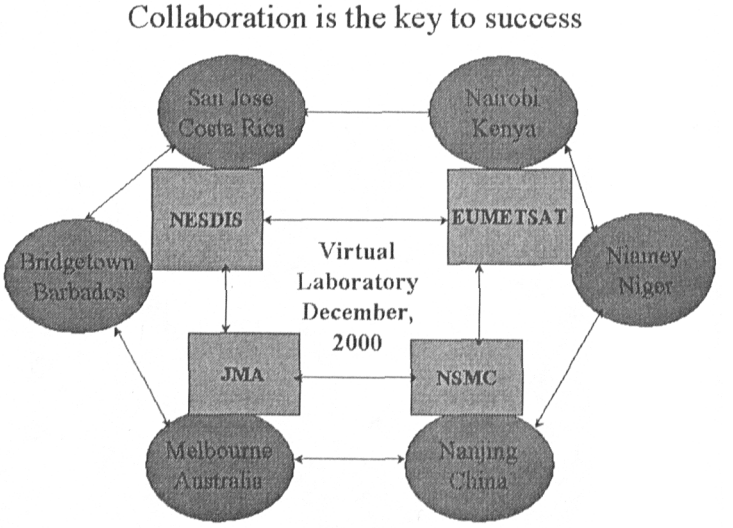

Figure 1a. Schematic illustration of Virtual Laboratory for Satellite Meteorology.

Initially aimed at providing online case study data for training US National Weather Service (NWS) offices staff to fully utilize GOES data, CIRA soon expanded to providing case study and near real time data to the WMO RMTCs in Barbados and Costa Rica. As with the NWS training effort, RAMSDIS software and data were provided to those RMTCs. Using common software and hardware allows work done on algorithm research at CIRA and other institutes to be used by RMTC and National Meteorological Service (NMS) staff in Barbados and Costa Rica on real-time satellite data and imagery. This cooperative arrangement has benefited the two countries and the researchers through new products, real time ground truth and increased use of existing satellite resources. For detailed discussion of the use of the RAMSDIS system and RAMSDIS Online see the Report on *ETM on Satellite Systems Utilization and Products, Second Session, Melbourne,* October 1999 available at http://www.wmo.ch/hinsman/Publications.html. Thus, much of the functionality of what is proposed for the Virtual Laboratory for Satellite Meteorology (training in basic and advanced topics, access to software, research and access to expertise) builds upon the work done by CIRA.

Recognizing the importance for a coordinated, world-wide approach to improving satellite data utilization, the WMO's Commission on Basic Systems (CBS) Open Programme Area Group on Integrated Observing Systems (OPAG IOS) Expert Team (ET) on Satellite Systems Utilization and Products has discussed the Virtual Laboratory concept at each of its three meetings to date. Initial discussions began in Locarno (Switzerland) in June 1999. The next meeting of the group, held in Melbourne, noted that satellite training institutions and their sponsoring satellite agencies must utilize modern technology to provide a range of training opportunities and materials to WMO Members. The meeting noted that a key ingredient of the Virtual Laboratory would be to build strong links with science groups. The most recent meeting of the ET, in Lannion (France) in July 2000, identified the need for two streams of learning skills (basic and specialist) and a virtual resource library within the VL. A schematic representation of the relationships between the various components of the Virtual Laboratory is shown in Figure 1b.

The concept of the VL was brought before CGMS in October 2000. CGMS and WMO agreed to establish a focus group on satellite data utilization and training within the Virtual Laboratory Framework and report back to CGMS and the WMO OPAG IOS on its findings A major function of the focus group is to help foster the VL to realize the challenges set forth by the WMO Executive Council Panel on Education and Training and in support of the WMO Strategy for Education and Training in Satellite Matters. The meeting of the focus group occurred during mid-May, 2001, and defined the various roles and responsibilities of participants, as well as the relationships between various components of the VL, as shown in Figure 1b. (This figure, and parts of the text from the latter portion of this abstract, was taken from materials provided by Jeff Wilson, Australia Bureau of Meteorology, at the May 2001 VL focus group meeting.) This article provides the current status of the VL and how it plans to move into the future.

2.0 INTRODUCTION TO VL

The first session of the CGMS/WMO Virtual Laboratory Focus Group to discuss coordination and oversight requirements for the Virtual Laboratory (VL) for Education and Training in Satellite Matters was held at the EUMETSAT Headquarters at Darmstadt, Germany, 16-18 May 2001. This first meeting of the focus group led to several important and far-reaching accomplishments. The focus group agreed upon: 1) a Management structure; 2) Immediate and Strategic Goals; 3) Goals relating to implementation which included Connectivity, a Virtual Resource Library (VRL), and Utilization and evaluation of the VL; and, 4) specific action items and time tables for 0 to 1 year, and 2 to 5 years.

2.1 Management Structure

Management of the VL is the responsibility of the VL Focus Group, which is co-chaired by one satellite operator and one representative from the "centers of excellence," with the WMO Satellite Activities Office serving as the Secretariat. The two co-chairs have the responsibility for day-to-day management, and report to the VL focus group that provides overall guidance for the VL. Membership on the VL focus group includes: 1) a permanent core composed of the two co-chairs and representatives from each of the remaining satellite operators and centers of excellence (see figure 1a); 2) representatives of science teams as appropriate (see figure 1b); and, 3) other interested parties as appropriate. With regard to management, the VL management group will review progress, assimilate inputs/feedback and assign actions. There will be regular and extensive use of teleconferencing for coordination of the various activities underway within the VL, and to review progress with respect to action items and time tables, and to discuss other matters of relevance to the VL.

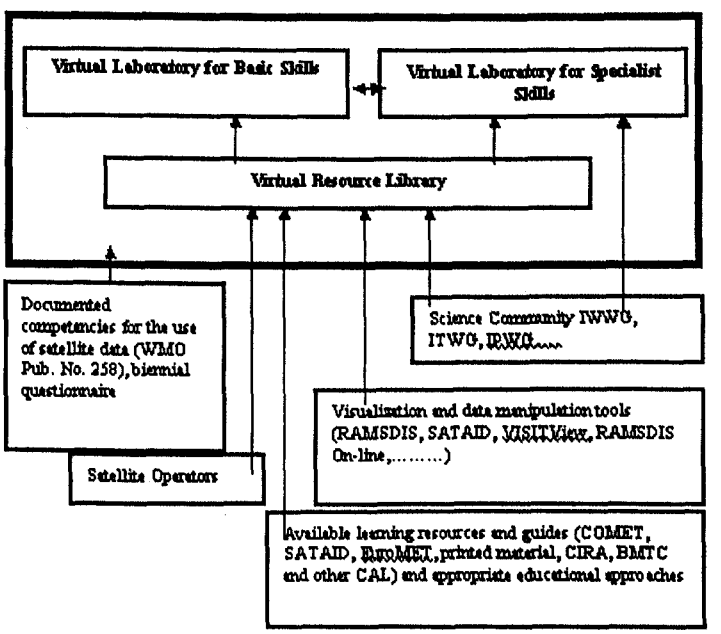

Figure 1b. Schematic of the Virtual Laboratory

2.2 Immediate and Strategic Goals

The immediate goal set by the focus group was to implement a baseline VL and to foster its logical growth. Challenges that will be met in implementing this immediate goal are set forth in the section below that addresses year one actions. Strategically, the focus group emphasized the need to provide high quality and up-to-date training resources on current and future meteorological and other environmental satellite systems, data, products and applications to improve utilization among Members; and, to enable the "centers

of excellence" to facilitate and foster research and the development of socio-economic applications at the local level by the NMS through the provision of effective training and links to relevant science groups. A component of immense strategic importance to the VL will be a virtual resource library, addressed in a separate section below. The virtual resource library supports all three cornerstones of the WMO strategy to improve satellite system utilization: 1) providing access to training and educational material; 2) providing software and expertise on how to the utilize data; and, 3) providing case study and near real time data. Baseline activity toward the establishment of the virtual resource library includes web servers by EUMETSAT at their Darmstadt facility as an initial site for training resources and materials (end of September 2001) and by NESDIS at CIRA for an initial set near real time data and products (end of November 2001). To facilitate this, each member of the focus group agreed to prepare an inventory of training resources and materials that are presently available for the core virtual resource library. Each satellite operator will identify what data and products could be linked into the core virtual resource library. In the initial implementation, the servers will be at only selected locations, the final goal is to have servers located at all nodes.

2.3 GOALS FOR IMPLEMENTATION

2.3.1 Connectivity

The components of the virtual laboratory must be able to communicate with one another from their home facility. In addition, each component must have access to resources available within the virtual laboratory. To address those issues, a near term goal is to establish Internet links at the six "centers of excellence" and supporting satellite operators. The main purpose of those links is to support communications (email, voice) as well as the exchange of software and selected image data sets. Those selected image data sets will include both case studies and some near real-time data sets. Data is of fundamental importance to the centers of excellence, and a preferred method for receipt of data, in the short-term, is the direct ingest of data from a ground receiving station at each site for possible insertion into their Virtual Laboratory servers. To enhance the exchange of training materials, including real-time lectures and classroom participation between nodes of the VL, the "centers of excellence" will consider means to increase communications capacity within 5 years.

2.3.2 Virtual Resource Library (VRL)

A strategic goal is to have servers located at all nodes of the VL. Those servers are at the heart of the Virtual Resource Library (VRL). The VRL will have two components: a core of baseline information to be exchanged (mirrored as appropriate) to all "centers of excellence", and a repository of data and specialized information for local use. Local use distribution will be the responsibility of the data provider, and could range from complete distribution to all "centers of excellence," to restricted distribution to only the local "center of excellence." Included within the baseline information at the VRL (refer to figure 1b) will be a suite of standard software packages and applications for use with those software packages. Used in combination with the case study data, it will provide capabilities for adapting algorithms and software to those data in a variety of standard formats. The data will be linked to training sessions, and may be used independently for activities such as application development and testing. Visualization and data manipulation tools such as RAMSDIS, SATAID, VISITview, and RAMSDIS On-line will be important components of the VRL core, as will learning resources and guides. A number of important issues are being addressed by the focus group: 1) establishing a list of usable training resources (includes image data sets, s/w, tools); 2) implementing a structure for the depository of training resources which will allow easy access by the "centers of excellence" trainers; and, 3) populating this structure with a core set of material from the training resources list. To assure scientific integrity, the VL will have strong links to specialized science groups such as the International TOVS working group (ITWG) and the International Wind Workshops (IWW).

Remote training will become an important part of the VL in the years to come. The VISITview program, in which an instructor in a remote location utilizes modern computer and communications technology to train forecasters at different locations, is expected to be an important resource within the core VRL. VISITview <http://www.ssec.wisc.edu/visitview/> is a platform-independent distance learning and collaboration software program. It allows multiple users located in different offices across a wide geographic region to view the same series of images containing graphics and text. VISITview provides a large number of features, including annotation, color enhancements, zooming, animations, multi-panel displays, image fading, quiz questions, etc. To avoid problems with limited Internet bandwidth, files used for the real-time presentations are acquired by the offices in advance. The files for each training session contain all the information needed for the training. This allows each training office the opportunity to use the session to conduct on-station training. Standard voice phones are used during the session. However, for those remote offices with limited phone access, Internet voice software can be used.

2.3.3 Utilization: User Requirements and VL assessment

Addressing user needs, and assuring that those needs are being met were important items of discussion by the focus group. Effective use of WMO Publication 258 and the biennial satellite data utilization questionnaire are central to the success of the VL. To assess how well user requirements were being met, the focus group noted the important linkage between WMO Publication 258 and the biennial satellite data utilization

questionnaire. The analysis of user responses focused on education and training, taken from the biennial questionnaire, would be carried out by the relevant "center of excellence." From their analyses, results would be reported to the VL focus group. This analysis and reporting serves a number of important purposes, such as identifying areas of common training needs and areas where development activities are required to address unmet user requirements. Thus, establishment of a VL user tracking and feedback mechanism was recognized as an important activity. Another matter discussed with respect to training was the use of real-time data. For a number of applications (such as nowcasting), training meteorological students to an operational level of expertise using near real-time data and products is a strong requirement. Near real-time data are needed to train forecasters on the effective use of new satellite reception and processing systems. This need will be one of the items addressed during the VL's evolution over the next five years.

2.3.4 Activities Conducted As VL Develops

The focus group discussed a number of generic activities that would be undertaken as the VL takes shape, as well as specific actions that must be undertaken during the next five years. The generic activities are given immediately below. These are followed by specific actions for the next five years.

- Consolidate documentation of the range of skills/competencies for operational meteorologists and specialists;
- Examine which Web-based learning, computer aided learning, CDs and hard copy learning materials are currently available for use in the virtual laboratory;
- Negotiate with copyright holders of training material rights to either link to their material and/or to acquire the rights to use their material at the designated centers of satellite training expertise;
- Work with expert training groups to design and test possible user interfaces, educational approaches for delivering the material, and examine methods for online tracking of student participation;
- Evaluate, on a trial basis, the proposed virtual laboratory material in conjunction with one of the WMO satellite training workshops for more user feedback;
- Incorporate user feedback into the educational approach and review the content of the virtual laboratory;
- Move to a wider implementation of the material;
- Undertake a periodic review of the virtual laboratory sites in conjunction with reviews of the skills and competencies of the operational meteorologists and specialists;
- Prepare sample data sets for the various data streams now being provided or planned for in the near future. The data sets would be used within the VL concept;
- Provide for continuous monitoring of user requirements for education and training as well as the effectiveness of the virtual laboratory.

The implementation schedule for the VL with corresponding action items is as follows:

First year (2001):

- During the next 6 months, all "centers of excellence" to evaluate content, and how and what can be maintained on a server at the "center";
- Train satellite operators and "centers of excellence" on the use of RAMSDIS using VISITview;
- Increase training event effectiveness through the use of VISITview;
- Add the SATAID training resource to the VRL and utilize VISITview.

Second year and beyond (2002-2005):

- Within 1½ years, all satellite operators to strive to have a server online and connected to the VL;
- Each "center of excellence" will strive to have a server online and connected to the VL;
- To establish a voice channel capability within VISITview;
- To evaluate and to improve the VRL;
- To evaluate the quality of submitted materials by the "centers of excellence", completeness (e.g., speaker notes), appropriate deletion dates, compatibility issues, and virus protection.
- After 5 years, conduct comprehensive review.

No doubt some actions will change as the VL becomes a reality, but the basic goal of improving satellite data utilization will remain unchanged.

3.0 SUMMARY

A very successful first session of the CGMS/WMO Virtual Laboratory Focus Group to discuss coordination and oversight requirements for the Virtual Laboratory for Education and Training in Satellite Matters (VL) was held at the EUMETSAT Headquarters at Darmstadt, Germany, 16-18 May 2001. Several important and far-reaching accomplishments were realized: 1) a Management Structure was established; 2) Immediate and Strategic Goals were defined; 3) Goals relating to implementation which included Connectivity, a Virtual Resource Library (VRL), and Utilization and evaluation of the VL were established; and, 4) specific action items and time tables for 2001 to 2005 which will lead to the successful implementation of the Virtual Laboratory for Satellite Data Utilization were agreed upon.

The VL represents a vehicle through which the WMO and CGMS will work to improve the utilization of satellite data worldwide. Effective Member interaction with their respective "center of excellence" is required for Members to fully realize this benefit. Exciting times, with great opportunities await us!

4. ACKNOWLEDGEMENTS

We thank the members of the WMO VL Focus Group (Don Hinsman, Jeff Wilson, and others) for their assistance in preparing this article and the plans for the Virtual Laboratory for Satellite Meteorology.

P3.31 VIRTUAL INSTITUTE FOR SATELLITE INTEGRATION TRAINING BRINGING TRAINING TO THE FORECASTERS USING VISITVIEW

Anthony Mostek*
National Weather Service - Office of Climate, Water, and Weather Services
Boulder, Colorado 80307

Scott Bachmeier and Tom Whittaker
Cooperative Institute for Meteorological Satellite Studies
Madison, Wisconsin

Dan Bikos, Brian Motta and Bard Zajac
Cooperative Institute for Research in the Atmosphere
Ft. Collins, Colorado
John Weaver
National Environmental Satellite Data and Information Service
Ft. Collins, Co

Kevin Schrab
National Weather Service – Western Region
Salt Lake City, Utah

Brad Grant and Jim LaDue
National Weather Service – Warning Decision Training Branch
Norman, Oklahoma

1. INTRODUCTION

The results of the first 2 1/2 years of teletraining by IST PDS and VISIT programs are:

- **298 sessions conducted**
- **More than 1500 offices trained**
- **Over 5500 certificates issued**
- **Over 1400 evaluations received**

This article describes the rapid rise in the use of teletraining by the National Weather Service (NWS) training program. The teletraining activity is conducted by the Integrated Sensor Training (IST) program professional development series (PDS) (Lamos 1998) and the Virtual Institute for Satellite Integration Training (VISIT). VISIT is comprised of staff from the Cooperative Institute for Meteorological Satellite Studies (CIMSS), the Cooperative Institute for Research in the Atmosphere (CIRA), and NWS training centers.

*Corresponding author address: Anthony Mostek, NCAR/COMET, P.O. Box 3000, Boulder, CO 80307; email: mostek@comet.ucar.edu

The VISIT and the Integrated Sensor Training programs bring together diverse training activities that have traditionally focused on individual sensors such as radar, satellite, and other observing systems. Information on the VISIT program can be accessed at www.cira.colostate.edu/ramm/visit/visithome.asp.

To support the rapidly changing training needs of the operational forecaster, the IST PDS program is developing a set of instructional components that utilize various tools. Training sessions and modules are developed using both Web-based and teletraining approaches.

An interactive training tool called VISITview (Whittaker 1999) was developed by the VISIT program. The VISIT program is supported by the NWS and the National Environmental Satellite, Data, and Information Service (NESDIS). VISITview is a platform- independent distance learning and collaboration software program that allows multiple users to view and manipulate the same series of pages containing images, animations, graphics and text.

Based on the extensive feedback received from the various NWS offices, the strength of the

VISITview teletraining instructional approach is the ability to bring the instructor directly into the office and put them in touch with the students. The direct interaction between instructor and students establishes an active link with the students that is difficult to achieve other than with face-to-face instruction. The benefits of this direct interaction are well worth the effort involved with the teletraining approach.

2. VISITVIEW – A FLEXIBLE TELETRAINING TOOL

The VISITview teletraining software (www.ssec.wisc.edu/visitview/) is designed to provide instructors and students with a set of easy to use tools for creating, conducting and taking teletraining sessions. VISITview is Web-based, and can be used in two modes: with the data files located remotely on a central server or with these files residing on a local disk drive. In the latter case (where the files are available locally), only the VISITview commands are sent over the Web.

Most NWS offices have reliable bandwidth connections but they usually are congested moving large data files. The high volume of data restricts the amount of information that can be transmitted in real-time to support live teletraining sessions. To avoid this limitation, the files used for the sessions are put into a compressed file and distributed via FTP to the training sites. These files can be large (over 60 MB for some sessions). Once at the training site, the compressed file is expanded into a local disk drive. Then, the session can be previewed at the convenience of the office staff to ensure that the session runs properly. The students can view the session at any time after the live interactive session to review the materials or for local training. There is a student guide available on the Web for each session (see www.cira.colostate.edu/ramm/visit/newrso.html).

Because of the potential for network fluctuations or losing connectivity, the training sessions include batch files that make it easy to switch to a backup server machine (typically, one at CIRA and one at CIMSS are used).

The VISITview teletraining program (see example of display in Figure 1) provides the following functions:

- A complete set of animation controls
- Multiple panel displays with animation
- Drawing tool with various color choices
- Erase previous drawing
- Add text
- Change enhancement or colorization of images
- Add/remove overlays
- Chat window
- Quiz questions with feedback
- View status of all session participants
- Recorded audio/video for future playback

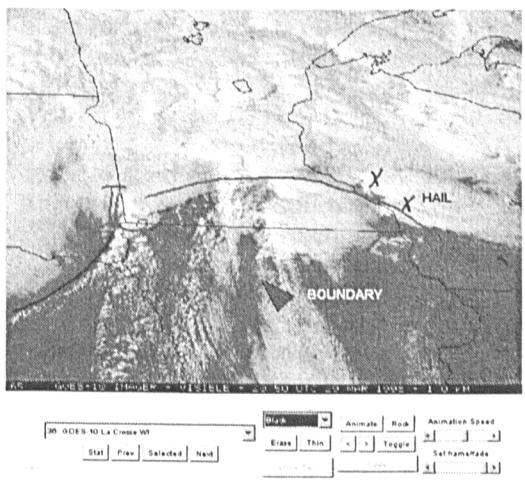

Figure 1 - VISITview panel from GOES Rapid Scan Operations training session showing instructor's annotations on a 640x480 pixel image with the control menu at the bottom.

While developing a fully functional teletraining program, the following criteria were employed:

- Platform independence - Java run time environment (JRE) selected to support this
- Minimal user interface knobs and widgets provide a clean and easy to use environment
- For audio, reliance on conference calls via conventional phones
- A display size (800x600 and larger) that supports computer projectors found in most forecast offices

An interactive Lesson Builder was developed to assist instructors in organizing materials for teletraining lessons. Each page of a lesson consists of one or more frames. Usually, multiple frames are employed to show animations, portals, or overlays. The Lesson Builder gives instructors a tool to create a lesson and then automatically creates the zip archive file that may be distributed.

A key aspect of VISITview teletraining sessions is that they can be run locally or remotely. The datasets are preloaded to students' workstations in advance of the session. Preloading the files avoids the delays caused by limited bandwidth when loading over the Web. The sessions can be controlled either locally or remotely, so they are suitable for both distance- and on-site-learning applications. The VISITview tool provides instructors with a complete set of drawing and animation tools including image combination, enhancements, fading, and multiple panel displays. Several of the VISITview functions were developed to emulate some key AWIPS functions.

As the VISITview program evolves, additional techniques for distance learning are included. For example, one VISITview "session" was created and is available on-line at CIRA (http://visit.cira.colostate.edu/vview/vmeast.html) that uses the RAMSDIS on-line database of real-time data. This approach encourages experimentation with distance collaboration, facilitates discussions of real-time weather events, and supports coordination among various offices. Also, the incorporation of a recorded speech option allows the lessons to be "played back" in virtual real time right along with the voice and annotations of the instructor.

Ten to twenty teletraining sessions are given per month. These sessions cover a wide range of topics such as: Using GOES Rapid Scan Operations in AWIPS, Detecting Boundaries with AWIPS, QuickSCAT Winds, Using AWIPS to Evaluate Model Initializations, GOES Sounder Data and Products, GOES High-Density Winds, Mesoscale Analysis of Convective Weather Using GOES RSO Imagery, and Forecasting Mesoscale Convective Systems. The procedures for signing up and taking a teletraining lesson are listed on the VISIT Web site. More information on all the teletraining sessions (Motta et al 2000) is also available at the VISIT Web site (www.cira.colostate/ramm/visit/visithome.asp).

3. TELETRAINING SESSIONS - RESULTS

From April 1999 to July 2001, the training provided by the IST PDS and VISIT has resulted in the following:

- **298 sessions conducted**
- **More than 1500 offices trained**
- **Over 5500 certificates issued**
- **Over 1400 evaluations received**

Many offices have participated in more than one session. Most of these are NWS offices with a few other organizations (Navy, NESDIS and Canada) also participating. Beginning in late 2000, the VISIT teletraining program has seen a rapid rise in the number of sessions offered and the number of certificates issued (see Figure 2).

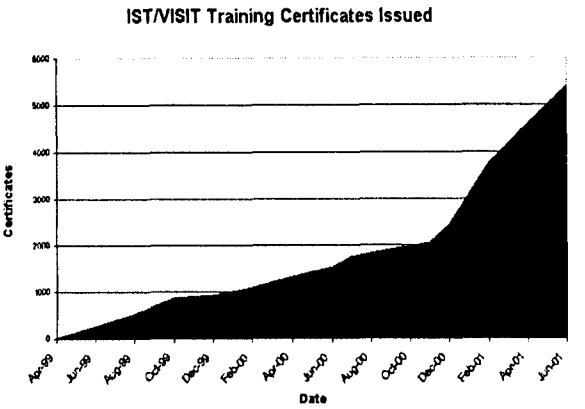

Figure 2 – Cumulative number of IST/VISIT training certificates issued from April 1999 to June 2001.

Evaluations for the teletraining sessions are sent via e-mail to all offices upon completion of the session. The evaluation form consists of 9 questions requesting feedback on a scale of 1 (strongly disagree) to 5 (strongly agree) plus 6 questions requesting for additional feedback. The large number of evaluations received (over 1500) is the result of an incentive. Upon receipt of the evaluation, training certificates are sent to all students that participated in the session. The linkage of the evaluation to the certificates helps to explain the large number of evaluations received and the large number (over 5500) of certificates. The evaluations provide some useful insights into the teletraining program:

- High quality graphics are a big plus
- Interactions between instructors and students are great
- Animations are very useful
- VISITview is easy to install and use
- Make sure the training materials are at appropriate level of difficulty
- Scheduling is a challenge with 24/7 operations in several time zones but it can be done
- Using phone conference call for audio works but the audio quality and volume need to be monitored
- Overall, most agree that VISITview is an effective tool and teletraining works

Student feedback also is provided with the open-ended questions. This feedback has helped to improve the teletraining approach, the scheduling, the content and the delivery of the teletraining sessions.

Beginning in fiscal year 2001, the Warning Decision Training Branch (WDTB) converted the teletraining portion of the Distance Learning Operations Course (DLOC) to use VISITview. DLOC teletraining sessions incorporate more extensive use of prepared questions.

In the near future, the NWS training program will incorporate a Learning Management System (LMS). The LMS selected will help with the teletraining efforts by establishing set procedures for the scheduling, evaluation and certificates across all parts of the training program.

4. SUMMARY

The National Weather Service training program has moved from the traditional classroom setting to an integrated distance learning approach to provide cost-effective training. Some of the training materials require an active component to allow the student to interact directly with an instructor. To meet this need, the IST PDS and VISIT programs have developed VISITview, a new teletraining tool that is flexible, platform independent, and extensible. VISITview allows for the expansion of teletraining functionality needed in today's environment of rapidly evolving technology.

The results of the first 2 1/2 years of teletraining by IST PDS and VISIT programs are:

- **298 sessions conducted**
- **More than 1500 offices trained**
- **Over 5500 certificates issued**
- **Over 1400 evaluations received**

Information on the VISIT program is available at: www.cira.colostate.edu/ramm/visit/visithome.asp.

5. ACKNOWLEDGEMENTS

We thank the many individuals involved at the NOAA cooperative institutes, NESDIS, and COMET that have provided valuable support to the IST PDS and VISIT programs.

6. REFERENCES

Lamos, J., cited 1998: Operational Forecasters' Professional Development Series Training Program. [Available online from http://www.comet.ucar.edu/pds/PDS_V3.htm]

Motta, B., D. Bikos, B. Zajac, S. Bachmeier, T. Whittaker and A. Mostek, 2000: Integrated sensor training in the national weather service AWIPS era. Preprints, *10th Conference on Satellite Meteorology and Oceanography*, Long Beach, CA, AMS.

Whittaker, T. M., 1999: VISITVIEW- A Collaborative Distance Learning Tool for the Virtual Institute for Satellite Integration Training (VISIT). Preprints *15th International Conference on Interactive Information and Processing Systems for Meteorology, Oceanography, and Hydrology*, Dallas, Texas, AMS.

P3.32 Recent Training From the Virtual Institute for Satellite Integration Training

Brian Motta*, Dan Bikos, and Bard Zajac
Colorado State University (CSU)/Cooperative Institute for Research in the Atmosphere (CIRA)
Regional And Mesoscale Meteorology Team (RAMM)/Virtual Institute for Satellite Integration Training (VISIT)
Fort Collins, Colorado

Scott Bachmeier and Tom Whittaker
University of Wisconsin/Cooperative Institute for Meteorological Satellite Studies/VISIT
Madison, Wisconsin

Brad Grant and James LaDue
National Weather Service (NWS)/ Warning Decision Training Branch
Norman, Oklahoma

Stephen Jascourt and William Bua
COMET / NWS National Centers for Environmental Prediction (NCEP)
Camp Springs, MD

Kevin Schrab
NWS Western Region Headquarters
Salt Lake City, UT

Mike Schichtel and Steve Flood
NWS NCEP/Hydrometeorological Prediction Center (HPC)
Camp Springs, MD

Dan Baumgardt
National Weather Service - Warning and Forecast Office
La Crosse, WI

Richard Grumm
National Weather Service - Warning and Forecast Office
State College, PA

Peter Wolf
National Weather Service - Warning and Forecast Office
Wichita, Kansas

John Weaver and Raymond Zehr
NOAA/NESDIS RAMM Team
Fort Collins, CO

1. INTRODUCTION

This paper describes the training efforts of the Virtual Institute for Satellite Integration Training (VISIT) developed for the National Weather Service (NWS), focusing on the recent VISIT teletraining sessions. The

*Corresponding author address: Brian Motta, CSU/CIRA, Fort Collins, CO 80523-1375, motta@cira.colostate.edu

VISIT project -- with its emphasis on distance learning -- was developed to provide cost-effective training to the operational weather forecaster in the Advanced Weather Interactive Processing System (AWIPS) era.

The NWS has undergone many changes as new remote sensing systems and analysis workstations have been deployed. One of the most dramatic changes has been the satellite data utilization and new satellite products. To address the resulting training need, the National Environmental Satellite, Data, and Information Service (NESDIS) and the NWS have established the VISIT. The VISIT has produced computer-based learning modules to highlight imagery and products from the Geostationary Operational Environmental Satellites (GOES). In addition, interactive teletraining materials addressing the integrated use of data sources in the NWS Warning and Forecast Office (WFO) environment have been developed. The content from VISIT has been integrated into the overall NWS Professional Development Series (PDS) training structure. In general, PDS efforts are directed at job-specific performance objectives and organized under one "umbrella" (Lamos, 1997). The Integrated Sensor Training PDS is directed at the efforts to combine information useful to forecasters throughout the range of space and time scales. This paper summarizes the current teletraining sessions to date as examples of the success that VISIT has demonstrated with interactive distance learning technologies.

2. SPECIALIZED SOFTWARE FOR DATA INTEGRATION TRAINING AND STUDIES

VISIT learning materials have been developed on Internet web sites to allow ready access to these training materials. In an effort to provide improved functionality for interactive learning sessions, many of the current capabilities have been collected into an Internet-based distance learning application called VISITview (Whittaker, 1999).

3. RECENT TRAINING

A number of training sessions continue to be offered using the VISITview interactive training software. A complete list of training sessions, including web-based versions and talking points, can be found on the VISIT homepage at http://visit.cira.colostate.edu

Training sessions which continued during 2001 included 1) Diagnosing the Potential for Surface Boundaries to Initiate Convection, 2) QuickScat Winds, 3) Lake Effect Snow, 4) Using AWIPS to Evaluate Model Initializations, 5) An Ingredients-based Approach to Forecasting Winter Season Precipitation, 6) Lightning Meteorology I , 7) Precipitation Type Forecasting, 8) Hydrometeorological Prediction Center Medium Range Forecasting, 9) Using Near-storm Environment Data in the Warning Decision Making Process, 10) Top Ten Misconceptions About NWP Models, 11) GOES Sounder Data and Products, 12) GOES High Density Winds, and 13) Mesoscale Analysis of Convective Weather Using GOES Rapid Scan Imagery. The following sections will briefly summarize these training sessions.

4. DIAGNOSING THE POTENTIAL FOR SURFACE BOUNDARIES TO INITIATE CONVECTION

The goal of this session is to acquaint forecasters with AWIPS tools which can be used to objectively analyze and assess the most relevant boundary characteristics which are presently considered influential in initiating deep moist convection. The forcing in and near boundaries is shown to be related to the potential for convective initiation in, along and near the boundaries. Advanced topics in boundary analysis are examined with a goal of producing a better short-term convective forecast. Forecasters are shown a variety of examples from across the United States and are asked to determine 1) which boundaries (or parts of boundaries) are important, 2) the effects of boundary-relative flow, and 3) where new convection will form.

5. QUIKSCAT

The goal of this teletraining session is to review the availability and use of QuikScat wind data in (and out of) the AWIPS environment. The training covers basic satellite and sensor characteristics as well as the usage of the wind retrievals. The QuickScat data are also compared with model and observed data to show differences. Factors which may affect the wind retrievals (such as heavy rain) are also discussed.

6. LAKE EFFECT SNOW

The goal of this session is to present a comprehensive introductory treatment of Lake Effect Snow (LES) events. Case studies from the eastern and western Great lakes are used to demonstrate the theoretical and practical LES forecasting issues. Synoptic, mesoscale and microphysical aspects of LES events are discussed.

Operationally-available data and imagery show the various types of LES bands using both Geostationary operational Environmental Satellite (GOES), Polar Operational Environmental Satellite (POES) imagery, and Doppler radar. Lake surface temperatures and the role of the coastline are among other aspects covered in this training.

7. USING AWIPS TO EVALUATE MODEL INITIALIZATIONS

The goal of this session is to review the current use of satellite and other data in the critical model initialization evaluation step of the forecast process. This highly-interactive training session leads forecasters to critically examine what they do to evaluate model output/guidance. Because of the time lag after data cutoffs in availability of new numerical model output, using new data and updating forecasts in the intervening period can be very important when trying to meet operational forecasting deadlines. Winter snowstorm data are used to show the importance of identifying model errors and tracking them with time. Important findings in recent literature, research being done at NCEP, and the NESDIS Advanced Satellite Products Team showed the impact that GOES sounder data can have on such events. The sensitivity of operational data assimilation systems to different data sources is also shown and discussed. The use of satellite imagery interpretation, NCEP products, and newly-available GOES sounder multi-channel water-vapor imagery are used to show continuing model errors in the day previous to the actual snowstorm event. Successfully diagnosing these errors in the model guidance were the key to forecasters being able to successfully forecast this high-impact weather event.

8. AN INGREDIENTS-BASED APPROACH TO FORECASTING WINTER SEASON PRECIPITATION

The goal of this session is to review the basic ingredients involved in winter season precipitation events. The ingredients include forcing, instability, moisture, precipitation efficiency, and temperatures. The diagnostics which have been found useful in revealing these ingredients are shown. Analysis scripts are employed in the GEMPAK and AWIPS environments for a variety of winter precipitation events. Differences between GEMPAK and AWIPS diagnostic capabilities are also presented and discussed.

9. LIGHTNING METEOROLOGY I

This session examines thunderstorm electrification and cloud-to-ground lightning activity in isolated thunderstorms and mesoscale convective systems. Cloud-to-ground lightning is shown to be useful in monitoring the thunderstorm lifecycle and inferring rainfall location and intensity (both convective and stratiform). Basic understanding of the ice-ice charging mechanism, identifying minimum thresholds in vertical reflectivity structure and cloud-top temperature associated with CG lightning, use of lightning polarity, and integration with other data sets are all covered.

10. PRECIPITATION TYPE FORECASTING

This session examines the use of operationally-available data sets for use in determining current and forecasted precipitation types. A review of microphysics and operationally-useful techniques are covered. Participants responded with very favorable reviews and requests for encore presentations. This very popular training was unanimously-rated as excellent and the most-operationally-relevant to forecasters. Participants are tested at the end with a graphical exercise to reinforce the theoretical and practical concepts covered in the training.

11. HPC MEDIUM RANGE FORECASTING

This session arose from an interaction with the HPC and the new responsibility of local NWS offices to provide extended-range forecasts. HPC experts in extended-range forecasting were the instructors. Issues such as model availability, model configuration changes, mean and climatological patterns for establishing storm tracks, comparing initial and model forecast fields with observed data, contrasting medium range model runs for plausibility and particular forecast problems, model run-to-run continuity and trends, ensemble forecasting techniques, assessment of forecast confidence and uncertainty, and the importance of verification were presented and discussed.

12. AN APPLICATION OF PATTERN RECOGNITION TO MEDIUM RANGE FORECASTING

This session was presented to increase the understanding of medium range forecasting at the NWS field offices. The reliability of mean charts as predictors were reviewed. Given the proper identification of mean patterns, forecasters are shown how to identify and

investigate model errors. That analysis is useful in understanding how a changing mean pattern leads to changes in the character of model errors such as time lag. An important aspect of medium range forecasting is being able to understand how diagnosis of model bias provides a beneficial tool in helping to anticipate forecast errors.

13. USING NEAR-STORM ENVIRONMENT DATA IN THE WARNING DECISION MAKING PROCESS

This session covers the increasing array of graphical data sets to analyze the mesoscale environment with AWIPS. Issues such as determining which fields or parameters are most important, the possibility of becoming radar-centric in perspective, and the use of the Local Analysis and Prediction System (LAPS) are among the topics covered. Analyzing mesoscale data with systems such as LAPS can help reduce false alarms by enabling the warning forecaster to distinguish between favorable and unfavorable environments for severe storms.

14. TOP TEN MISCONCEPTONS ABOUT NWP

This session examines the process by which forecast models assimilate and initialize data sets with observations and then change from run-to-run. Many of the misconceptions were common to operational forecasters until this training. Issues examined included the usefulness of resolution and appearance of weather systems in differing spatial and temporal scales of model output/guidance. This teletraining was an active presentation of information which is also located at the Numerical Weather Prediction Professional Development Series web site.

15. GOES SOUNDER DATA AND PRODUCTS

This session covers an introduction to the GOES Sounder instrument, data, and products. Derived Product Imagery (DPI) have recently become available to the NWS in AWIPS. The product generation and applications to operational forecasting are shown. While this material has been covered in classroom training in the past, there have been several changes since earlier versions of the product and related training.

16. GOES HIGH-DENSITY WINDS

This session covers the basic techniques used to generate the GOES High-Density Winds. Some NWS offices currently ingest the GOES winds into their AWIPS systems. Other aspects of the data including the target selections, height assignments, quality control, and sources of error are covered. The display of the winds on AWIPS is also explained so that they may be used correctly with other types of observations or model output.

17. MESOSCALE ANALYSIS OF CONVECTIVE WEATHER USING GOES RSO IMAGERY

This session continues where previous training ended. It focuses on the use of GOES visible imagery and other data sets in the short-range forecast, nowcast, and warning decision-making processes. Among the topics covered are the complementary use of radar and satellite imagery, identification of boundaries in the pre-storm environment, importance of RSO for convective initiation, and satellite interpretation for severe convection.

18. CONCLUDING REMARKS

Significant interaction with NWS WFOs takes place during the development of training and the actual training sessions. We look forward to continuing those interactions. The Integrated Sensor Training/VISIT team also plans to help coordinate training developed at WFOs and assist in the expansion of distance learning efforts. The software used for the teletraining version of these presentations is evolving to meet the needs of the integrated sensor training environment.

19. ACKNOWLEDGEMENTS

Portions of the research described in this paper were performed under NOAA Grant #NA37RJ0202. The authors would like to thank Tony Mostek of the NWS for his contributions to the VISIT project.

20. REFERENCES

Lamos, J., 1997: Operational Forecasters' Professional Development Series. Cooperative program for Operational Meteorological Education and Training Process Definition Committee. Boulder, CO. http://www.comet.ucar.edu/pds/PDS_V3.htm

Whittaker, Thomas M., 1999: VISITVIEW- A Collaborative Distance Learning Tool for the Virtual Institute for Satellite Integration Training (VISIT). Preprints 15th IIPS, Dallas, Texas, AMS.

P3.33

ATMOSPHERIC INSTABILITY PARAMETERS DERIVED FROM MSG SEVIRI OBSERVATIONS

Marianne König*, Stephen Tjemkes, Jochen Kerkmann
EUMETSAT, Darmstadt, Germany

1. INTRODUCTION

Convective systems can develop in a thermodynamically unstable atmosphere. Such systems may quickly reach high altitudes and can cause severe storms. Meteorologists are thus especially interested to identify such storm potentials when the respective system is still in a preconvective state. A number of instability indices have been defined to describe such situations. Traditionally, these indices are taken from temperature and humidity soundings by radiosondes. As radiosondes are only of very limited temporal and spatial resolution there is a demand for satellite-derived indices. The Meteorological Product Extraction Facility (MPEF) for the new European Meteosat Second Generation (MSG) satellite envisages the operational derivation of a number of instability indices from the brightness temperatures measured by certain SEVIRI channels (Spinning Enhanced Visible and Infrared Imager, the radiometer onboard MSG). The traditional physical approach to this kind of retrieval problem is to infer the atmospheric profile via a constrained inversion and compute the indices then directly from the obtained profile. As this algorithm would impose a too high computer load on the MPEF system, the operational MPEF will use a statistical approach: The measured brightness temperatures together with further predictors are used to derive each instability index, where the statistical relations between these parameters are gained from a neural network and appropriate training data. Both methods are currently installed in the Eumetsat MPEF prototype environment and are tested on GOES sounder data. This paper shortly describes the two methods and shows a detailed comparison between the two methods and to independent radiosonde data. It should be noted that both methods only allow the derivation of instability indices over cloudfree areas.

2. DEFINITION OF INSTABILITY INDICES

Various studies have been performed to relate certain instability measures taken from radio soundings to the occurrence of severe weather. It became soon clear that there is no unique index for all synoptic situations and for all locations. This paper focuses on 4 different parameters, three classical instability indices:

K-Index:
$(T^{obs(850)} - T^{obs(500)}) + TD^{obs(850)} - (T^{obs(700)} - TD^{obs(700)})$

Lifted Index:
$T^{obs} - T^{lifted\ from\ surface}$ at 500 hPa

Maximum buoyancy:
$\Theta_e^{obs(max\ betw.\ surface\ and\ 850)} - \Theta_e^{obs(min\ betw.\ 700\ and\ 300)}$

(T is temperature, TD is dewpoint temperature, and Θ_e is equivalent potential temperature, numbers 850, 700, 300 indicate respective hPa level in the atmosphere)

and the precipitable water content as additionally derived parameter.

3. DESCRIPTION OF ALGORITHMS

3.1 The Physical Retrieval

An iterative solution to the inversion equation (e.g. Ma et al. (1999)) tries to infer the temperature and humidity profile from the measured brightness temperatures, the back-ground atmospheric profile (usually referred to as first guess) and the associated error/noise matrices. In each iteration step, the inversion needs knowledge about the change of brightness temperature with the change of the atmosphere in each level, which is described by the Jacobians of a radiation model. It is the computation of these Jacobians together with the inversion of large matrices which make this method very CPU intensive. This method was chosen for the current operational retrieval of lifted index and precipitable water a for the GOES sounder at CIMSS (Menzel et al., 1998), and the Eumetsat prototype only differs from the CIMSS approach by using RTTOV as the radiation model (Saunders et al., 1999). RTTOV has the advantage of a much faster computation of the Jacobians. In application to the GOES sounder, the algorithm uses the sounder channels 5, 7, 8, 10, 11, and 12, which are at about 13.4 μm, 12.0 μm, 10.8 μm, 7.3 μm, 6.5 μm, and 6.2 μm wavelength, resp.. In a possible future application to SEVIRI, the method will also use 6 channels, and as SEVIRI will not have a 6.5 μm channel, the 8.7 μm channel will be used instead. This channel selection ensures that sufficient information concerning the atmospheric state is passed to the retrieval algorithm, e.g. surface skin temperature and low level moisture via the two window channels, higher level humidity via the water vapour channels, and the higher level temperature information via the 13.4 μm channel.

* *Corresponding author's address:* Marianne König, EUMETSAT, Postfach 100555, 64205 Darmstadt, Germany, phone (49) 6151 807344, email: koenig@eumetsat.de

Over clouds, the algorithm cannot find a solution, i.e. the iteration scheme does not converge in these cases. Over clear skies, convergence is usually achieved after one or two iterations, and each instability index can then easily be derived from the atmospheric profile.

Tests show that the physical retrieval substantially improves the first guess data concerning the resulting instability indices, where the improvements are clearly related to the better detection of the unstable cases.

Closer inspection of the retrieved actual profiles demonstrates that the retrieval scheme mostly changes the surface skin temperature and the low level humidity profile, while it leaves the temperature profile very near to the first guess values.

For the MSG MPEF prototyping, the results of the physical method are used as a kind of reference to assess the results of the statistical approach.

3.2 The Statistical Method

This method is based on a neural network approach: The neural net is used to identify linear and non-linear relationships between a number of input values – the predictors – and one output value – the respective instability index. In general, a neural network is a computer model of individual elements commonly referred to as neurons. The input parameters to the model make up the input neurons, the output value is then the output neuron. There can be intermediate layers which are called hidden layers of any number of neurons. The neurons of the individual layers are connected by links, where each link is given a certain weight. The inputs are processed by a weighted summation and the transfer function passes the result to the neurons of the next layer, until the output is produced. During a training phase of the neural net, the weights are optimised to fit the wanted output. A neural network must thus be trained with input / output pairs, i.e. with some independent data.

In our case, we use a simple three-layer backpropagation neural network (e.g. Chauvin and Rumelhart, 1995) with 15 input neurons and one hidden layer with 20 neurons. The transfer function is the hyperbolic tangent $f(x) = \tanh(x)$.

A backpropagation network is trained by learning with clearly defined pairs of inputs and outputs. With these 'wanted' outputs, the neural net successively adjusts its weights in every learning cycle to minimise the error between the 'wanted' output and the output produced with the weights and the transfer function from the given inputs. This training cycle is repeated for a large number of input / output patterns until a minimum error is achieved. The criterion of a minimum error is also used to determine the characteristics of the input values and the number of the hidden neurons. Obvious input values are of course the six brightness temperatures in the six channels (see section 3.1) and the satellite viewing angle. Eight further parameters, which give some seasonal and diurnal time information and knowledge about the geographical location, slightly improved the performance of the net.

The real problem concerned with the neural net is to have a good training dataset: This dataset must contain a wide range of possible observations of the predictors and the output value. Otherwise the net will perform badly if it is faced with real data which were not properly reflected in the training dataset. This problem is quite evident if radiosonde data are used for training: Although the input values can be obtained from the sounding rather easily – the brightness temperatures can be calculated with a forward model – and the instability index is directly inferred from the sounding, the radiosondes still give a very poor training dataset. Due to the only twice daily (00 and 12 UTC) soundings, the diurnal cycle is not resolved, and also spatial coverage is very poor. Locations are only a fixed set of certain values, and the ocean areas are practically not covered at all. It was thus decided to use the results of the physical retrieval (taken from historical data) as training data for the neural net. This provides data for every possible location within the satellite's field of view with good diurnal coverage. Initial results with training based on several months of GOES data showed very good agreement between the two methods.

For this training phase, data were collected of satellite measured brightness temperatures, of the pixel locations and scan times and of the respective instability index as provided by the physical method. This large dataset (about 70,000 entries of heavily sampled GOES sounder data over several months) was randomly split into three categories: One third of the data was used for the neural network training, one third was used as the so-called generalisation data within the network training, and the third section was used as an independent dataset to test the network's performance for data unknown to the net during its learning phase. Figure 1 shows an example of this initial network test for the precipitable water content. For the other indices, there is slightly more scatter with correlation coefficients between 0.85 and 0.90.

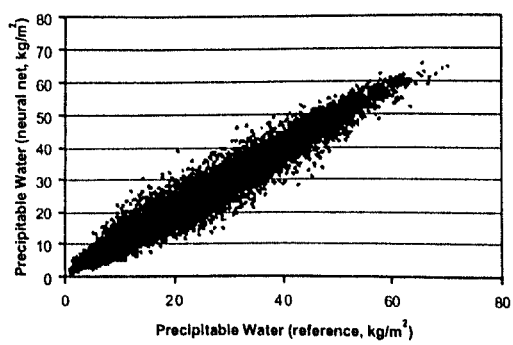

Figure 1: Scatter plot of neural network derived precipitable water compared to independent reference data from the physical method (correlation coefficient 0.97)

4. RESULTS

The two methods were applied to several GOES-8 sounder images during the months of May and June 2001. In general, good agreement was achieved between the statistical results and the results of the physical method, especially regarding the temporal evolution of unstable regions. 25 hourly images collected between 0800 UTC on 24 May 2001 and 0800 UTC 25 May 2001 comprise a sample case. During this day, a large region of highly unstable air developed over southern Texas along the coast, and an extended convective system developed in the same region in the morning hours of the 25th. Colour plots of the spatial distribution of various instability indices derived by the two methods and corresponding time loops are shown in http://www.eumetsat.de/GII.

To demonstrate the rather good performance of the statistical method with respect to the physical retrieval, Figure 2 shows the lifted index difference between the two methods as a mean over the entire GOES-8 field of view and as a mean over the region of instability.

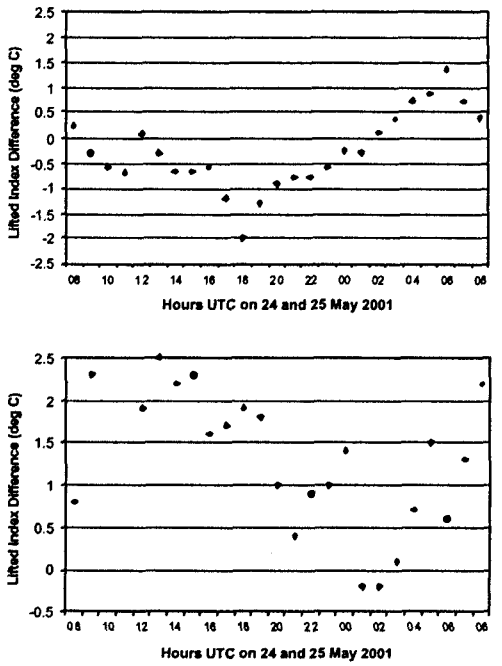

Figure 2: Difference of the lifted index between the physical and the statistical approach for the entire GOES-8 sounder fov (top) and over the region of instability over Texas and the adjacent Gulf (bottom)

Potentially unstable air is described by a negative lifted index. The positive lifted index difference shown in the bottom section of Figure 2 thus means that the statistical method indicates a slightly higher degree of instability than the physical method. This is a general behaviour of the statistical approach that is found in many examples. As the instability measure, however, is meant to be a warning against severe weather, this slight exaggeration is probably a good feature.

Comparisons with the 00 UTC radiosondes on the 25th show good overall agreement to the results of both methods. These comparisons can also be seen in http://www.eumetsat.de/GII.

In the future application to MSG, the intention is to disseminate the instability results as area averages over n*n image pixels, where n will be typically of the order of 10. There are several possibilities of how to average:

(a) a simple arithmetic mean over the pixels
(b) provide the value of the most unstable pixel
(c) average only over the unstable pixels, take the simple average over all pixels if there are no unstable ones
(d) average over the unstable pixels if their number exceeds a certain threshold, else average over all pixels

For the precipitable water content, clearly option (a) would be applicable, while for the actual instability indices option (d) would be more preferrable. Again, http://www.eumetsat.de/GII shows examples of the different averaging methods.

5. CONCLUSIONS

It can be shown that a statistical approach to the general retrieval problem of instability indices is possible and gives good results if the regression coefficients are obtained from a representative dataset. In the application within the MSG/MPEF, this method will be used as it is computationally fast and thus easily applicable on a pixel basis to each of the MSG images, which will be recorded at 15-minute intervals. The operational results of the MPEF scenes analysis will provide the cloud information so that clouds can be screened from the processing.

As a good training dataset can probably only be collected from selected runs of the physical method on actual MSG image data, the quality of the MPEF instability product is expected to increase with time as more training data becomes available which will lead to a successive improvement of the regression data.

6. REFERENCES

Chauvin, Y. and D.E. Rumelhart, 1995: Backpropagation: Theory, Architectures, and Applications. Lawrence Erlbaum Associates, 561 pp.

Ma, X.L., T.J.Schmit, and W.L.Smith, 1999: A Nonlinear Physical Retrieval Algorithm – Its Application to the GOES-8/9 Sounder. *J. Appl. Meteor.*, **38**, 501-513.

Menzel, W.P., F.C. Holt, T.J.Schmit, R.M. Aune, A.J. Schreiner, G.S. Wade, and D.G. Gray, 1998: Application of GOES-8/9 Soundings to Weather Forecasting and Nowcasting. *Bull. Amer. Meteor. Soc.*, **79**, 2059 – 2077.

Saunders, R., M. Matricardi, and P. Brunel, 1999: An improved Fast Radiative Transfer Model for Assimilation of Satellite Radiance Observations. *Q. J. R. Meteorol. Soc.*, **125**, 1407-1425

P3.34 ASSESSING THE QUALITY AND UTILITY OF HIGHER RESOLUTION GOES SOUNDER RETRIEVALS

[1]Gary E. Gray* and [2]Jaime Daniels

[1]Raytheon Information Technology and Services Company
Lanham, Maryland

[2]NOAA/NESDIS/Office of Research & Applications/Atmospheric Research & Applications Division
Camp Springs, Maryland

INTRODUCTION: The purpose of this study is to show the utility and the advantage of producing GOES atmospheric soundings at every field of view (roughly, 10km resolution). Historically, in order to reduce the impact of noise, several fields of view have been averaged. Currently, the NESDIS operations is producing soundings at a resolution of five pixels by five pixels, averaging out 25 fields of view. Production at the Cooperative Institute for Meteorological Satellite Studies has long been at 3x3 resolution, averaging nine pixels. Since early in the year 2000, however, the Forecast Products Development Team (FPDT) has been generating GOES soundings at every field of view. Some results from this production are presented herein.

PRODUCT QUALITY ASSESSMENT: The first issue raised in single field of view production is product quality. There was valid reason behind the desire to average a number of fields of view and, thus, produce soundings on a 5x5 or 3x3 basis. The predominant concern was that a lack of averaging, thereby not reducing the impact of noise, could result in cloud contamination.

An analysis of the cloud detection algorithm found that there were several cloud detection tests that were rather "loose" in their cloud/no-cloud determination. As a result, it was speculated that if these checks were made more stringent single field of view soundings could be made without significant cloud contamination. The following table shows the results of radiosonde match statistics taken over a six month period during 2001. It compares the two extreme ends of the spectrum, the single field of view and the operational 5x5 soundings.

*Corresponding author address:
Gary E. Gray
Raytheon/ITSS
4400 Forbes Blvd.
Lanham, MD 20706

	TPW AAE	TPW Bias	Sample
5x5	2.54mm	-0.61mm	17635
1x1	2.44mm	+0.40mm	24595

AAE = Average Absolute Error
TPW = Total Precipitable Water

Clearly, these numbers show no degradation in going to the single field of view production. In fact, the error reduces slightly. The bias is also closer to zero. The reason for the bias being in the opposite direction is not obvious. There could be any number of factors at work here. The most obvious would be that the single field of view soundings will get a lot more soundings near cloud edges (the 5x5 and 3x3 production require a minimum number of clear fields of view before a sounding will be made). This tends to be an area of high moisture gradient. As such, depending on the radiosonde match distance, the radiosonde may have gone through much drier air. As such, the single field of view bias increases relative to the 5x5 production.

The product quality is clearly maintained in single field of view production. Moreover, a simple overall statistic does not paint the entire picture. Take, for example, a user utilizing the GOES soundings for convective forecasting. In these cases it is the lower levels of the sounding that are most critical, as these define the parcel, thereby greatly impacting the convective parameters (Lifted Index, CAPE, etc.). The following table shows the radiosonde match statistics for precipitable water in layer one (PW1, from the surface to 0.9 sigma).

	PW1 AAE	PW1 Bias	Sample
5x5	1.40mm	-0.75mm	17635
1x1	1.22mm	-0.57mm	24595

AAE = Average Absolute Error
PW1 = Layer-1 (sfc to 0.9 sigma) Precip. Water

This table shows that the single field of view soundings have even more success over the 5x5 production in this low layer. There is greater error reduction and the bias is, again, closer to zero.

Still, this tells only half the story. As it turns out, the success of the 1x1 soundings is focused in areas of higher moisture. These are, of course, areas more critical to those concerned with the prediction of convective events, excessive rainfall, etc. The following two graphs show the PW1 average absolute error and bias, respectively, with respect to increasing radiosonde precipitable water.

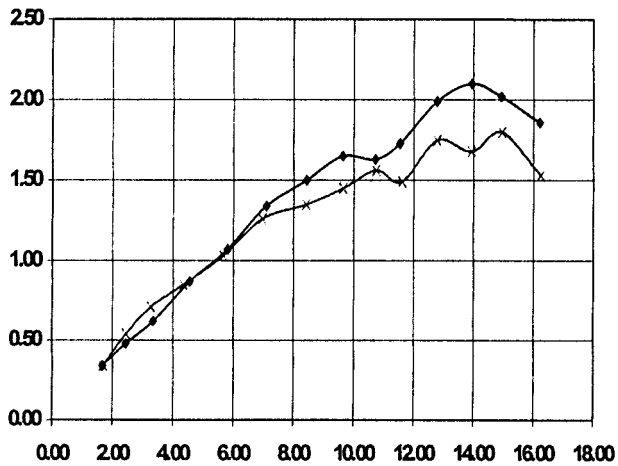

The above chart of PW1 absolute error shows the error (Y-axis) with respect to PW1 amount (X-axis) in millimeters. Note the divergence of the two lines beyond roughly 6mm. The line with the higher error represents the 5x5 GOES soundings production from GOES-8; the lesser error is from the 1x1 GOES-8 soundings production.

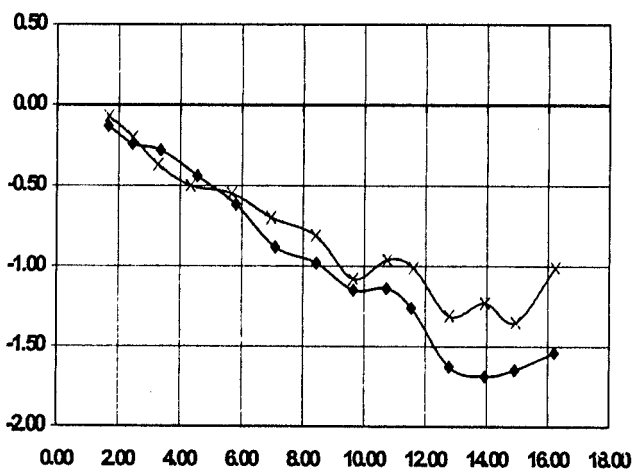

The preceding chart of PW1 bias shows the bias (Y-axis) with respect to PW1 amount (X-axis) in millimeters. Note the divergence of the two lines beyond roughly 6mm. The line with the more extreme negative bias represents the 5x5 GOES soundings production from GOES-8; the closer to zero bias is from the 1x1 GOES-8 soundings production.

These charts leave no doubt that 1x1 soundings are not only no worse, but are, in fact, superior in quality to their lower resolution counterparts.

PRODUCT UTILITY ASSESSMENT: Raw data quality is not the only measure of the usefulness of the single field of view data. There are also other beneficial aspects of the single field of view data.

The most obvious advantage in data utility is the higher resolution of the product. However, more data is not only the result of increased resolution. As mentioned earlier, the 5x5 and 3x3 productions require a minimum number of clear fields of view before the sounding is output. Obviously, by its nature, 1x1 production has no such requirement. As a result, if a sounding is attempting to be retrieved near a cloud the 5x5 box may, for example, only identify four clear fields of view, while the 3x3 identifies two. Neither system will output any product data for this location. However, the 1x1 production will output all available clear fields of view. The only reduction in product output could come from the more stringent cloud detection tests, as noted earlier. However, the data most likely to be discarded by this effect is potentially cloud contaminated. So, this data loss is of small quantity and is data whose loss is actually of benefit to the product.

Also, this increased resolution is not simply a greater amount of data. The lack of averaging also allows for improved display of gradients. Consider that a 5x5 soundings box is, roughly, 50km X 50km. While variations over that distance may tend to be small, they can occasionally be significant in the moisture field. For example, if a pocket of increased moisture exists (which could eventually be the focus for convection) the pixels on the left side of a 5x5 box may represent an atmosphere containing 30mm of total precipitable water (TPW). Meanwhile, on the right side the pixels could represent the pocket of moisture with, say, 35 to 40mm of TPW. The 5x5 box to the right of this may have the mirror image as one exits the moisture pocket. As a result, both 5x5 retrievals may end up with a smoothed TPW of roughly 35mm. Single field of view soundings, however, will represent each pixel individually. As such, so

long as the moisture pocket exceeds a 10km by 10km size, the gradient will be fully represented.

The following three images show the Lifted Index from the GOES Soundings over the central United States from the 5x5 production, 3x3 production, and 1x1 production, respectively.

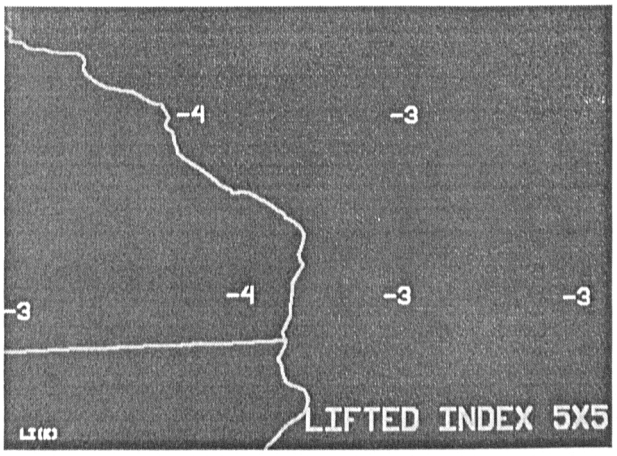

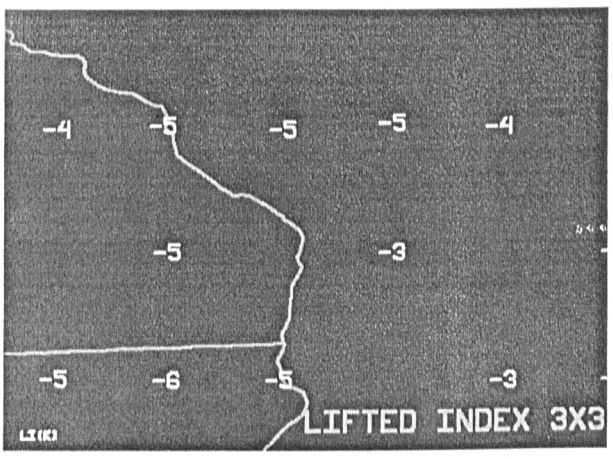

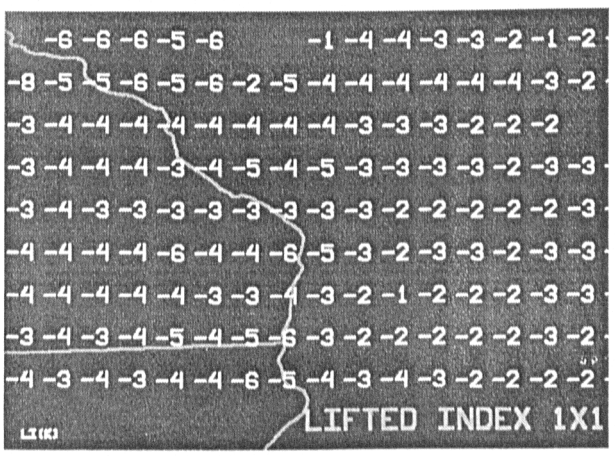

It is obvious that the 1x1 production provides a much higher resolution, much more detailed product. However, also notice near the missing data regions on the 5x5 and 3x3 fields (determined to be cloudy, although little is evident in this imagery); in some regions it is not simply a matter of there being *more* data in the single field of view production. Rather, there is data where the 5x5 and 3x3 production had *none*. This is most notable in the northeastern part of these images. Notice that the 5x5 has no sounding east of the –3 L.I. value in the top row of data. In the same general region, the 3x3 field has no sounding either east or south of the –4 value at the eastern end of the top row of data. This is because these attempted soundings locations failed to meet the minimum clear field of view requirements. The 1x1 data, however, will make a sounding at every possible location. Notice that it has only a tiny data gap in that area.

Along with the increased amount of data, as discussed in general terms earlier, these images provide a good example of the improved gradient depiction. The smoothing of the fields on the 5x5 provides virtually no gradient in this Lifted Index field. In the 3x3 display the gradients become more evident, with –3 values in the southeast part of the image and –4s and –5s (even one –6) in the west. Still, it is somewhat of a washed out gradient. The single field of view product, however, shows the gradient well. This is especially true up into the northwest part of the image where Lifted Index values drop to –6.

More specifically, in this example provided the region displayed is west-central Wisconsin and extreme east-central Minnesota. The time of the plot is during the overnight hours (04Z). Rather strong thunderstorms moved into the region in the morning, especially around Eau Claire, WI and heading towards La Crosse, WI. Focusing in on that area is virtually impossible with the 5x5 retrievals. The Lifted Index values are a touch lower in the general region around Eau Claire and La Crosse, but not significantly. The 3x3 soundings are better, but are still rather broad-brushed, making for a difficult analysis. The high-resolution 1x1 field, however, clearly shows a patch of L.I. values of –5 to –6 roughly from Rochester, MN to Eau Claire, WI. Other scattered –5 to –6 values continue southward near the WI-MN border, including near La Crosse. Meanwhile, the entire remaining regions of Minnesota and Wisconsin have Lifted Index values between –1 and –4. In short, the single field of view

production provides a distinct focus to the convective activity, which proved to be correct, that the 3x3 and 5x5 were marginal, at best, in depicting.

The higher resolution is not just an advantage for those using the data in real-time for situational analysis. It is also an advantage from an NWP standpoint. Note that data from the GOES soundings is being ingested into the ETA model. Current plans for the ETA model have it going to 12km resolution before the end of the year 2001. Having GOES soundings at almost the exact same resolution could make the assimilation of the data an easier task. Easier or not, it certainly makes the assimilation more accurate as the soundings data more precisely represents the related grid cell in the model field. Assimilation of the current operational data into such a high resolution model would mean that 2500km^2 GOES soundings (50km X 50km) would be used to influence model grids an order of magnitude smaller in coverage (12km X 12km = 144km^2).

CONCLUSION: The single field-of-view GOES soundings are clearly the most desired and optimal production level. The data presented herein shows the quality of the single field-of-view data to be slightly superior to that of the 5x5 production. Comparison statistics were not readily available for the 3x3 production. However, past studies including the 3x3 data yielded similar results. Also, the cloud detection modifications made for 1x1 production were exclusive to the 1x1; *in other words, 3x3 production is more similar* to 5x5 production than 1x1. Note also that all data presented herein is from GOES-8. This satellite suffers from worse noise than GOES-10, and should be worse than GOES-11 or GOES-M as well. Recall that a primary argument for *not* producing single field-of-view soundings is the noise. If quality improvements can be shown in 1x1 production with GOES-8, it is almost a foregone conclusion that the other GOES satellites will also benefit. Statistics have been run for GOES-10 with very similar results as GOES-8. The overall GOES-10 statistics show a smaller, almost negligible improvement in the 1x1 soundings over the 5x5 soundings. However, this is due to the drier atmosphere typically sampled by GOES-10. The high-PW soundings from GOES-10 yield similar improvements in the 1x1 over the 5x5.

Moreover, the quality improvements were most distinct in the lowest layer. This layer has the greatest impact on many ancillary fields used by forecasters and others. This further enhances the quality improvements seen in the 1x1 production.

Besides the quality improvements, the 1x1 fields also yield a coverage improvement. The coverage improvement is two-fold; where the 5x5 or 3x3 retrieve one sounding, the 1x1 will retrieve as many as 25 or 9, respectively; secondly, where the 5x5 or 3x3 retrieve no sounding, the 1x1 *may* still retrieve a few soundings in that region. This improved coverage provides not only higher resolution product, but also yields superior depiction of gradients.

With improvements in quality and coverage single field-of-view soundings should prove beneficial to several entities within the meteorological community. These soundings are better suited for analysis by forecasters than are the lower resolution options. Also, these soundings are more in line with what will be useful to the NWP community. With better quality and coverage, the single field-of-view GOES soundings are simply a better product than the current operationally available 5x5 GOES soundings or the 3x3 GOES soundings.

REFERENCES:

Ma, Xia, L., T. J. Schmit, and W. L. Smith, 1999: A non-linear physical retrieval algorithm – its application to the GOES-8/9 sounder. Journal of Applied Meteorology, 38, No. 5, 501-513.

P3.35 AN ASSESSMENT OF THE TEMPORAL VALUE OF RETRIEVED PARAMETERS FROM THE GOES SOUNDER

Robert M. Aune*
NOAA/NESDIS
Office of Research and Applications
Madison, Wisconsin

Ralph Petersen
NOAA/NWS
Environmental Modeling Center
Camp Springs, Maryland

1. INTRODUCTION

Today's modern data assimilation systems do an amazing job of using sparsely distributed observations from a scientifically diverse collection of observing systems, to generate initial conditions for numerical weather prediction (NWP) models. They, however, do not necessarily produce accurate analyses of atmospheric parameters in the absolute sense. Most operational NWP centers use optimal statistical approaches to extract information from observations by fitting the model variables to the observations in a least-squared sense across three space dimensions over a discrete time intervals (Daily, 1991). Absolute accuracy is sacrificed to achieve the best overall spatial fit that satisfies the model numerics. Some of the information introduced in previous assimilation cycles (especially maxima and minima) is lost due to imperfections in the analysis and the prediction model: numerics, truncation, smoothing, interpolation, etc. Physical and dynamical constraints, imposed during the analysis phase, required to maintain numerical stability, also reduce the influence of perfectly good observations. Consequently, initial model fields frequently contains unrepresentative gradients and reduced maxima and minima.

One obvious method for improving the absolute accuracy of gridded analyses is to increase the volume of observations available to the assimilation system within the assimilation window. The National Centers for Environmental Prediction's (NCEP) Eta Data Assimilation System (EDAS) currently performs an analysis update using a 3-D variational system at three-hour intervals, with a time window of +/- 90 minutes (Rogers, et. al. 1996). Allowing off-time observations in the analysis is one method for increasing spatial coverage. If the time window is short time-space corrections are not necessary. One assimilation method that allows observations to influence the analysis over a wider time window is the 4-D variational approach like that used by the European Center for Medium Range Prediction (ECMWF). This system iterates toward a forecast model trajectory that best fits the model background and observations for a given time interval, typically 6 to 24 hours in length (Rabier et. al., 1998). 4-D variational systems are also bound to the same physical and dynamical constraints that are required for model initialization, are complicated to maintain, and require extensive computer resources.

It is our intent to design an objective analysis system that does not rely on a forecast model to fill in no-data areas. We propose to use non-perishable observations from previous valid times, projected along forward trajectories, to augment spatial and temporal coverage and keep absolute errors in check. Maxima and minima in the analyzed fields would be preserved. Such a system would be useful for nowcasting and for short range forecasting of extreme events.

2. OBSERVATION BASED OBJECTIVE ANALYSIS

In theory, if the spatial coverage and density of observations are greater than the analysis grid, a model generated background field has less influence on the analysis and in the extreme may not be required. One observing system that comes close to having the ability to provide observations of atmospheric parameters at excellent spatial (at least horizontal) and temporal resolutions is the sounder onboard the Geostationary Operational Environmental Satellite (GOES) (See Menzel et. al., 1998). The sounder measures the atmosphere at 18 spectral bands in real time with a 10 km footprint, at one-hour intervals. Retrieved temperature and moisture

*Robert M. Aune
1225 W. Dayton St.; Madison, Wisconsin 53706
Email: Robert.Aune@noaa.gov

profiles are currently processed in real time at hourly intervals using 3 by 3 fields of view (FOV), yielding a horizontal resolution of 30 km. Clear FOVs are required for the proper conversion of measured radiances to standard meteorological parameters. The question becomes one of whether information from the sounder can be used in an observation-dominated analysis system that relies on spatial coverage and high temporal availability to keep absolute errors in check? Such an analysis system would be useful for nowcasting and near-casting of extreme weather events.

3. A SIMPLE EXPERIMENT

An initial experiment was designed to assess the temporal and spatial characteristics of retrievals from the GOES-8 sounder. An analysis system based on a recursive filter (Hayden and Purser, 1995) was used to filter retrieved equivalent potential temperatures (thetae) onto an analysis grid (AWIPS 212 subset). Retrieved values of thetae from GOES-8 were obtained for 30 August 2000, at hourly intervals starting at 12 UTC. The initial retrieval data set was then projected forward at one hour intervals using trajectories computed from winds obtained from the NCEP Rapid Update Cycle (RUC), producing pseudo-trajectory (PT) observation data sets at each of the hourly observation times. Figure 1a is a plot of the observation counts for the PT observations and the successive hourly thetae retrievals from GOES-8. Although the PT observations decrease slightly with time as some of them move off the test domain, the GOES-8 retrievals decrease more rapidly in time due to increasing cloud cover. Since the GOES-8 retrievals are available in clear are, it is hypothesized that the thetae values will remain unchanged as long as the atmosphere remains adiabatic. If this holds true, the total number of observations available to the analysis would grow with each hour as PT observations from previous hours would be joined by new retrievals. The accuracy of the PT observations was assessed by statistically comparing them to the analyzed thetae retrievals for each hour. Root mean square (rms) differences (Figure 1b) remain reasonable for the first four hours. Rms values at 850 hPa degrade faster because of diurnal boundary layer effects, which would be maximized in the morning hours. These boundary layer effects are evident in the negative biases (Figure 1c) which grow throughout the period for the 850 hPa and the 700 hPa PT observations. The bias remains small at 500 hPa because the thetae field is relatively flat and disconnected from the surface.

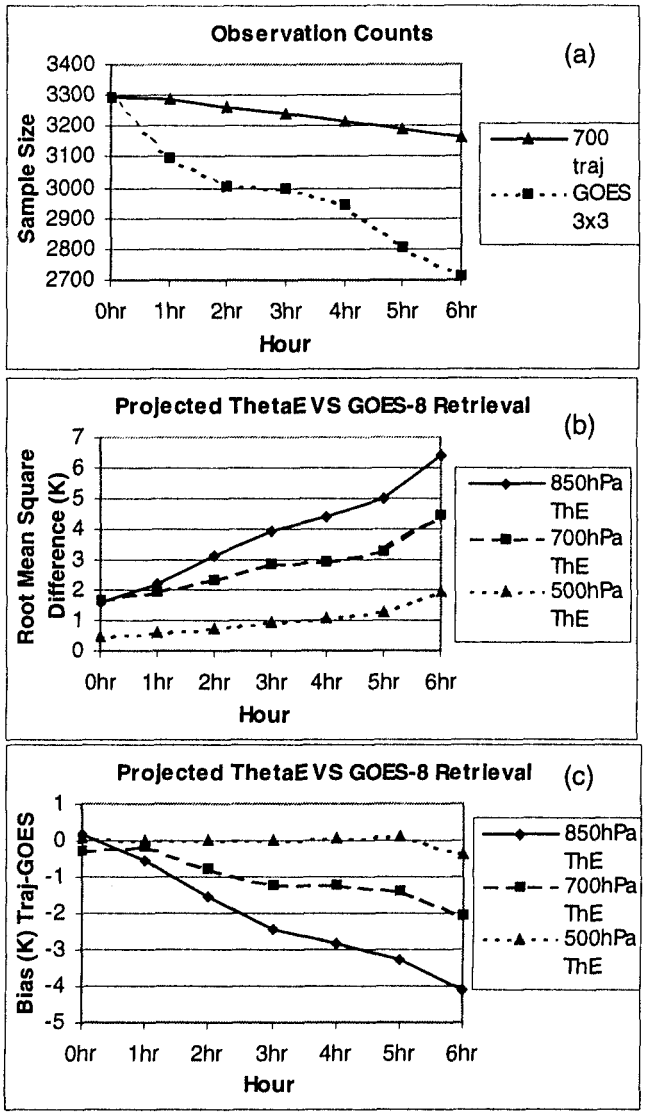

Fig 1. Statistics comparing pseudo trajectory observations from the 12UTC GOES-8 retrieved thetae to the actual hourly GOES-8 thetae retrievals. Observation counts (a), rms differences (b) and bias (c) are shown.

and disconnected from the surface. Figure 2 shows the scatter of the PT observations (y-axis) against an analysis of the GOES-8 thetae retrievals (x-axis) for 850 hPa at 12 UTC (a), and 16 UTC (b), and for 500 hPa at 16UTC. The initial scatter (not shown for the 500 hPa level) shows a reasonable fit of the data by the analysis. A bias appears after a four-hour trajectory (16UTC) at 850 hPa but not at 500 hPa. Again this is due to the influences of surface processes. It remains to be determined how much of this change is due to the reduction in accuracy of the PT observations or to the reduced number of GOES-8 retrievals

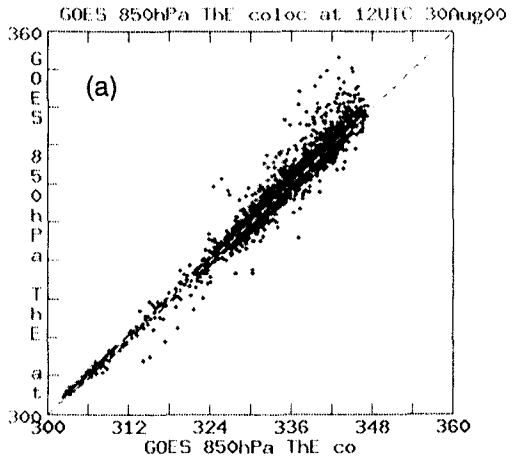

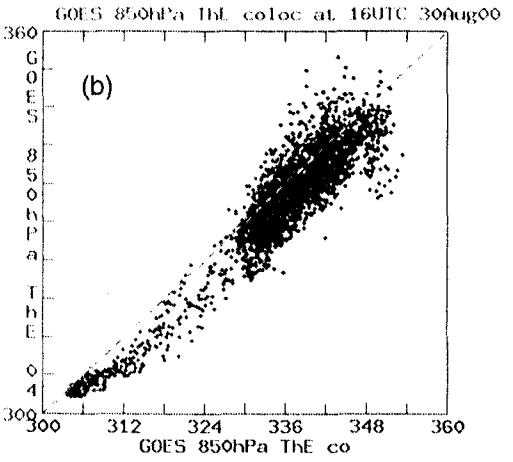

Fig. 2. Plots comparing pseudo trajectory observations against actual GOES-8 thetae retrievals at the initial time (a) and four hours later (16UTC) at levels 850 hPa and 500 hPa.

as a result of increased cloud cover.

4. DIRECTIONS

Ultimately we want to configure an analysis system that incorporates current and PT observations. GOES retrievals from previous hours could be projected forward in time along isentropic trajectories to new locations since they exist where the atmosphere is adiabatic. The quality of the projected retrievals could be assessed dynamically and down-weighted, as their validity becomes questionable. The resulting four-fold increase in the number of contributing observations every 4 hours would result in better spatial coverage and a better chance at retaining horizontal gradients and field extremes.

The amount of information defining the physical and dynamical state of our atmosphere, collected in near real time, is rapidly becoming unmanageable. The vast majority of these observations are coming from space-based platforms. An observation-based analysis system could serve as an intelligent data compression tool, especially when considering the needs for immediate forecaster use.

5. REFERENCES

Daley, R., 1991: *Atmospheric data analysis.* Cambridge Atmospheric and Space Science Series. Cambridge University Press, 457pp.

Hayden, C. and J. Purser, 1995: Recursive filter objective analysis of meteorological fields:

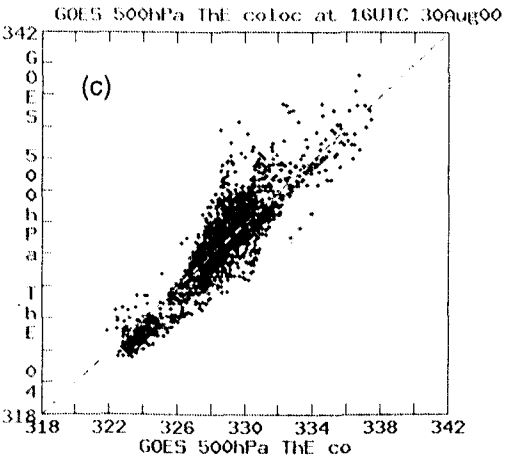

Applications to NESDIS operational processing. *J. Appl. Meteor.*, 34, 3-15.

Menzel, W. P., F. Holt, T. Schmit, R. Aune, A. Schreiner, G. Wade, and D. Gray, 1998: Application of GOES-8/9 soundings to weather forecasting and nowcasting. *Bull. Amer. Meteor. Soc.*, 79, 2059-2077.

Rabier, F., J-N.Thepaut, and P. Courtier, 1998: Extended assimilation and forecast experiments with a four-dimensonal variational assimilation system. *Quart. J. Roy. Meteor. Soc.*, **124**, 1861-1887.

Rogers, E., D. Parrish, Y. Lin, and G. DiMego, 1996: The NCEP Eta data assimilation system: Tests with regional 3-D variational analysis and cycling. Preprints, *11th Conf. on Numerical Weather Prediction*, Norfolk, VA, Amer. Meteor. Soc., 105-106.

P3.36

CASE STUDIES USING HOURLY REAL-TIME GOES SOUNDER OZONE ESTIMATES

Christopher C. Schmidt, Jun Li
Cooperative Institute for Meteorological Satellite Studies, University of Wisconsin-Madison

Anthony J. Wimmers
Department of Environmental Sciences, University of Virginia-Charlottesville

1. INTRODUCTION

For over three years data from the Geostationary Operational Environmental Satellite (GOES) Sounder has been used to estimate total column ozone (TCO) hourly at 30 km by 30 km resolution in real-time. Colocated, instantaneous ozone estimates from the Total Ozone Mapping Spectrometer (TOMS) and the GOES Sounder compare to within 4-7% (Li 2001). Gradients in the GOES Sounder total column ozone field depict ozone features in the atmosphere (Schmidt 2000). TOMS observations, water vapor imagery, and potential vorticity fields are used to confirm these observations. Many atmospheric features, including tropopause folds, breaking synoptic waves, cut-off lows, upper-air troughs, and jet streams, can be identified in real-time from GOES Sounder TCO imagery. Hourly GOES Sounder TCO estimates provide the first real-time glimpse of ozone dynamics over a large region at high spatial and temporal resolutions.

2. TOTAL COLUMN OZONE ESTIMATION METHOD AND ACCURACY

GOES Sounder TCO estimates are made by linear regression against cloud-free and partly cloudy brightness temperatures from the GOES Sounder, latitude, month, and surface pressure. The regression coefficients are derived from the NOAA88b atmospheric temperature, moisture, and ozone profile set provided by the National Oceanic and Atmospheric Administration (NOAA). Regression is the preferred method since physical retrievals fail to improve upon the accuracy of the regression results, and in many cases perform worse than the regression based ozone estimate (Li 2001).

Variations of GOES Sounder ozone estimates relative to TOMS and surface-based observations are small. The relatively small size of the NOAA88b profile training set (2631 profiles) introduces biases into the estimates. Dry atmospheres and hot surface temperatures correlate to the most notable variances between TOMS ozone measurements and GOES ozone estimates. The GOES Sounder has reduced sensitivity to ozone changes outside of the lower stratosphere and upper troposphere, though with little effect on TCO due to the low ozone densities at those levels. Uncertainties regarding surface type, elevation, and thin cloud cover also introduce variances into the GOES TCO field (Li 2001).

Corresponding author address: Christopher C. Schmidt, Cooperative Institute for Meteorological Satellite Studies, University of Wisconsin-Madison, 1225 W. Dayton St., Madison, WI 53706; e-mail:chris.schmidt@ssec.wisc.edu.

3. CASE STUDY: TOTAL COLUMN OZONE AND ATMOSPHERIC VARIABLES

GOES Sounder TCO estimates provide hourly, real-time tracking of ozone features in the upper troposphere and lower stratosphere. Ozone reflects the dynamics of those atmospheric levels through its relationship to potential vorticity and thereby allows for a preliminary diagnosis of atmospheric features that result in or are the result of the deformation of the tropopause (Shapiro 1981; Steinbrecht 1998). Such features include tropopause folds, breaking synoptic waves, cut-off lows, upper-air troughs, and jet streams.

Fig. 1 includes an example of how GOES Sounder TCO relates to potential vorticity and the altered water vapor (AWV) product (Moody 1999). Potential vorticity was calculated from the ETA model 12 UTC analysis and the AWV product was generated from the GOES-8 water vapor channel (6.8 μm) image and ETA model 12 UTC analysis for September 29, 1999. Fig. 1b, the AWV product, shows a dry (dark) region over Minnesota, Wisconsin, and Iowa that corresponds very well with the enhanced ozone region in Fig. 1a. Fig. 1c illustrates the potential vorticity at 200 hPa, and a clearly defined lobe is visible, collocating well with the ozone feature in Fig. 1a. Fig. 1d depicts the cross section of the potential vorticity field. The shape of the contours are reminiscent of the potential vorticity structure along a jet stream axis (Shapiro 1981). The gradients and features observed in the ozone field commonly reflect similar potential vorticity, and therefore lower stratospheric and upper tropospheric, structures (Schmidt 2000). The hourly ozone product resolves these structures with temporal and spatial resolutions that is lacking from most models and traditional sources of ozone data.

4. SUMMARY

The fields depicted by the GOES Sounder total column ozone estimates reflect structures in the lower stratosphere and upper troposphere. Model-derived potential vorticity, water vapor imagery, and other data indicate that the features in those ozone fields represent atmospheric structures that involve deforming the tropopause through raising, lowering, or folding. With

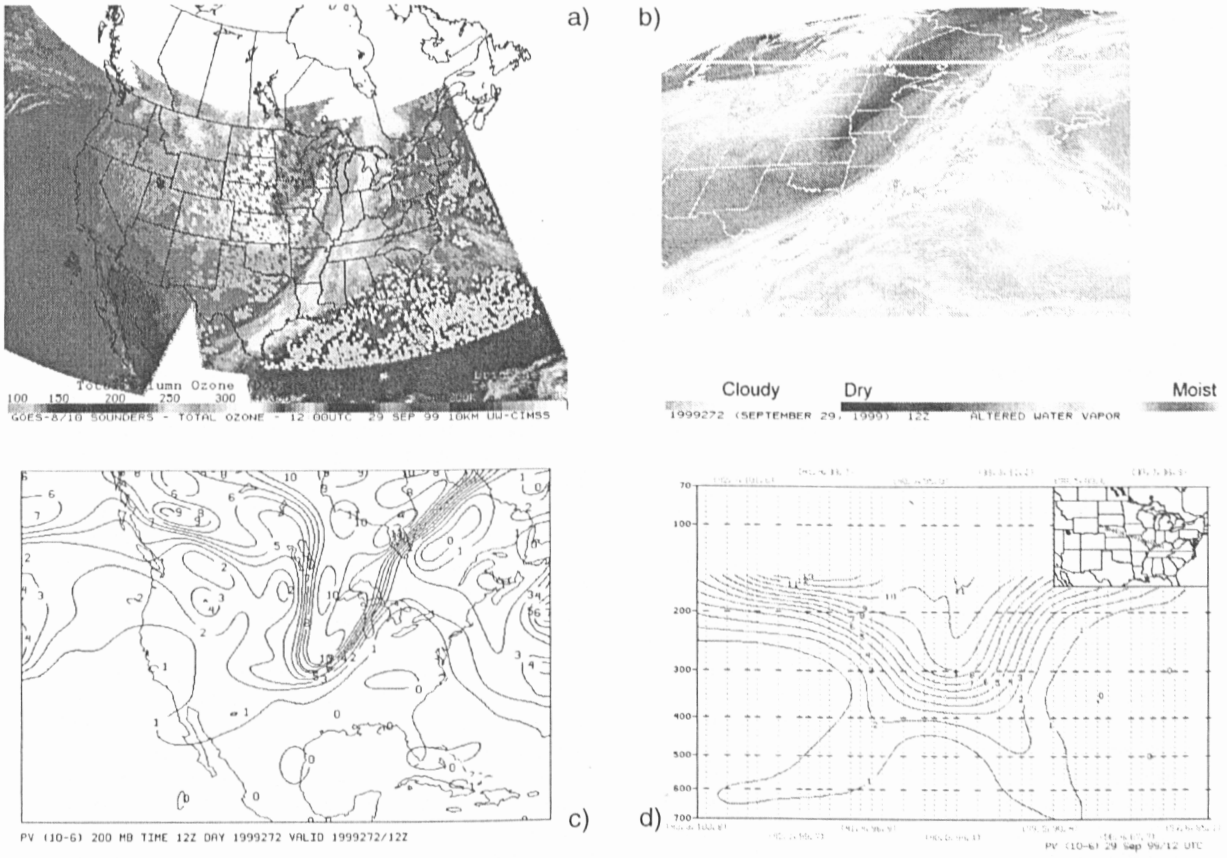

Fig. 1. GOES Sounder total column ozone (TCO), altered water vapor (AWV), and potential vorticity on September 29, 1999 (1999272) at 12 UTC. The AWV and potential vorticity fields confirm that the ozone field represents real atmospheric features. The dark ozone feature in (a) located over Minnesota, Wisconsin, and Iowa correlates well with the features in the AVW (b) and potential vorticity at 200 hPa (c). (d) is a potential vorticity cross-section.

high spatial and temporal resolutions, GOES Sounder TCO estimates allow tracking the life cycles of such features at a level of detail that was previously impossible to achieve. Furthermore, the GOES Sounder TCO fields provide insight into the upper atmosphere in data poor regions as well as opportunities to observe phenomenon, such as clear air turbulence, that exist on too small a scale or for too short a time to be observed with more traditional ozone measurement methods.

Further examples of ozone features observed in the GOES Sounder TCO fields, as well as corroborating information and animations, may be found at: http://cimss.ssec.wisc.edu/goes/amssatconf2001/ozone_p3.36.html

5. REFERENCES

Li, Jun, C. C. Schmidt, J. P. Nelson III, T. J. Schmit, and W. P. Menzel, 2001: Estimation of total atmospheric ozone from GOES Sounder radiances with high temporal resolution. *J. Atmos. Oceanic Tech.*, **18**, 157-168.

Moody, J. L., A. J. Wimmers, J. C. Davenport, 1999: Remotely sensed specific humidity: Development of a derived product from the GOES Imager Channel 3. *Geophys. Res. Letters*, **26**, No. 1, 59-62.

Schmidt, C. C., 2000: Hourly ozone estimates utilizing the GOES I-M sounders. M.S. thesis, Department of Atmospheric and Oceanic Sciences, University of Wisconsin-Madison, 133 pp. [Available from Schwerdtfeger Library, 1225 W. Dayton St., Madison, WI 53706.]

Shapiro, M. A., 1981: Frontogenesis and geostrophically forced secondary circulations in the vicinity of jet stream-frontal zone systems. *J. Atmos. Sci.*, **38**, 954-973.

Steinbrecht, W., H. Claude, U. Köhler, K. P. Hoinka, 1998: Correlations between tropopause height and total ozone: Implications for long-term changes. *J. Geophys. Res.*, **103**, No. D15, 19,183-19,192.

P3.37

A Validation Study of the GOES Sounder Cloud Top Pressure Product

James A Hawkinson*, Wayne Feltz, Timothy J. Schmit#, Anthony J. Schreiner, Steven A. Ackerman

Cooperative Institute for Meteorological Satellite Studies (CIMSS)
Space Science and Engineering Center UW-Madison
Madison, Wisconsin

NOAA/NESDIS/ORA Advanced Satellite Products Team

1. INTRODUCTION

One of the derived operational products from the Geostationary Operational Environmental Satellite (GOES-8) Sounder is the Cloud Top Pressure measurement. This product is available for the GOES-8 domain in real-time at hourly time resolution. The sounder outputs the average cloud top pressure reading from a 3X3 (nine pixels approximately 35x45 km) Field of View (FOV), and the single FOV, as well as the maximum and minimum values from the 3X3 FOV. The data used for validation purposes comes from the March 2000 Intensive Operational Period (IOP) from the Department of Energy's (DOE) Atmospheric Radiation Measurement (ARM) program Cloud and Radiation Testbed (CART) site near Lamont, OK. This includes cloud top height derived from a ground-based combination Micropulse Lidar/Millimeter Cloud Radar (MPL/MMCR), which uses an algorithm developed by Eugene Clothaiux (Clothiaux et al. 2000). MPL/MMCR output is every ten seconds during the IOP. GOES cloud top data range from 7 March 2000 to 31 March 2000, giving 600 possible observation times. Data were filtered to give only observation times that contain one cloud layer to provide an accurate comparison between the ground-based and space-based observation locations.

2. Method

In order to prepare the two data sets for an objective comparison, the GOES cloud top pressure observations were converted into altitude in meters. This was achieved by using radiosonde data from the CART site. A pressure-height profile was constructed from the closest radiosonde to the time of observation. Radiosondes were launched every six hours during the IOP from the CART site. Once this conversion was done, the two data sets could be compared using a time series plot (Fig. 1).

* Corresponding author address: James Hawkinson, 1225 West Dayton Street Room 238, Madison, WI, 53706; e-mail: jahawkin@students.wisc.edu.

Since the MPL/MMCR is subject to attenuation effects and local cloud top height deviations at the single observation point over the CART site, the data needed to be desensitized. This was achieved by using a range binning process which entailed placing every MPL/MMCR observation surrounding the GOES sounder observation time (five minutes before and after the GOES observation time was used) into a range bins of 250m. Each range bin must have a given amount of observations in it to be considered valid (a threshold of observation). Those range bins that do not meet the threshold value are discarded, while the temporal average cloud top height is used from the valid range bins. Noticeable improvement in the results was seen after this range binning tool place. This is demonstrated in scatter plots within figures 2 and 3. Notice the considerable improvement in agreement when the binning methodology is used.

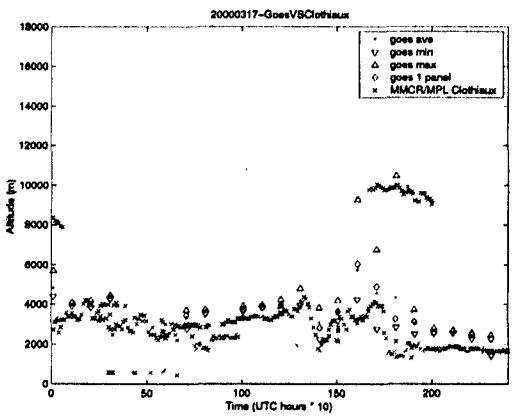

Figure 1: An example of GOES and MPL/MMCR cloud top height time series. This is for 17 Mar 2000.

To further filter the data for a direct comparison, measures were taken to eliminate observation times where multiple cloud layers were present. Although the GOES sounder product cannot explicitly detect multiple cloud layers, use of the 3X3 FOV maximum and minimum cloud top height values can give a reasonable estimate of the existence of multiple cloud layers. The

determination of multiple cloud layers was done by specifying a maximum variance in the 3X3 FOV maximum and minimum cloud top height. Any observation time that had a variance greater than 2000 meters would be deemed to be a multiple cloud layer situation. Through the use of two different methods of filtering, the ground-based data was desensitized and multiple cloud layers were eliminated, allowing for an objective comparison between the two independent observations.

3. Results

The first direct comparison made between the GOES and MPL/MMPL was detection of clouds. This is a yes/no comparison, either the instrument is reporting a cloud top height or it is not. For this comparison, the temporal threshold for the MPL/MMCR data set was set to a very low value 16% of observations needed for a valid cloud. The value was set so low in order to minimize attenuation effects of the instruments. The GOES sounder and MPL/MMCR agree on the existence or lack there of a cloud 75% of the time (345/460). It should be noted that for 140 of 600 possible observation times, the sounder was in eclipse mode.

To further compare the two measurements, scatter plots with both GOES sounder and MPL/MMCR cloud top height values were produced. To demonstrate the importance of data filtering, the progression of filtering techniques is shown with their respective scatter plots.

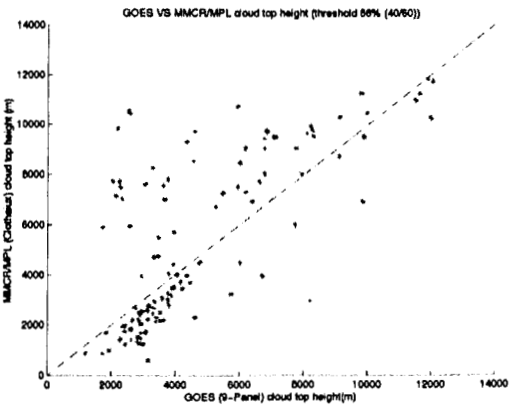

Figure 2: A scatter plot comparing GOES and MPL/MMCR cloud top height with no data filtering. Little correlation is seen.

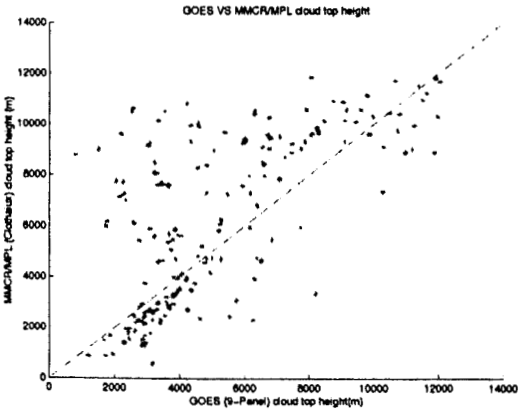

Figure 3: Scatter plot using binning process for MPL/MMCR.

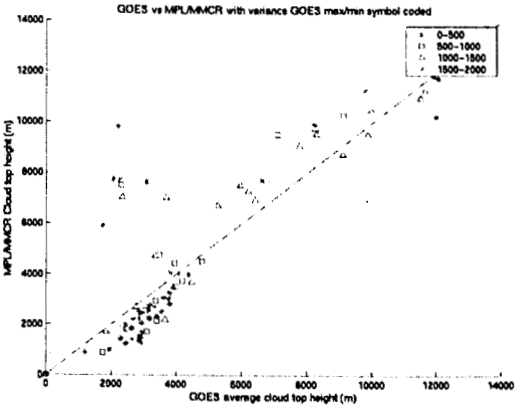

Figure 4: Scatter plot using binning process for MPL/MMCR and filtering out multiple cloud layers. Amount of variance between sounder 3X3 FOV maximum and minimum cloud top height is symbol coded.

At this point after using the two different filtering techniques, significant correlation was seen in the scatter plot. But there still were eight outliers (seen in a cluster in Figure 4 in the upper-left corner) where the GOES sounder were placing the cloud top height around 2000 meters, and the MPL/MMCR cloud top height around 6000 meters-10000 meters. This group of outliers can be seen in Figure 4. Such large variance between the two sources is alarming, so each individual outlier was examined to determine why the discrepancy exists. Six of the eight outliers could be explained by examining the data close up. This was done by going back to the time series plots as seen in Figure 1.

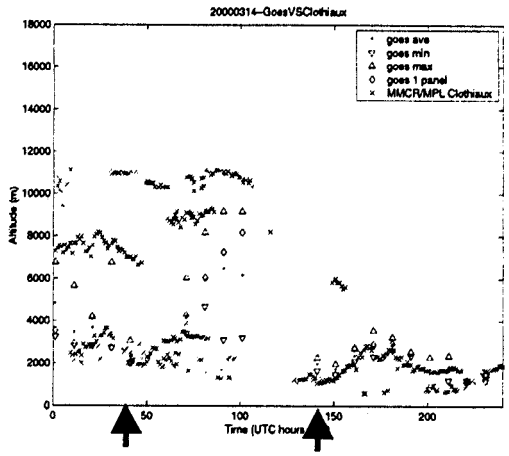

Figure 5: Two instances of outliers that can be explained by examining the time series. Attenuation effects and multiple cloud layers led to the outliers.

After six of the eight outliers were accounted for, they were discarded from the scatter plot. Eliminating these outliers led to an increase in correlation as seen in Figure 6. Of the two remaining outliers that could not be accounted for by manual inspection, both were found to be high cirrus cloud tops.

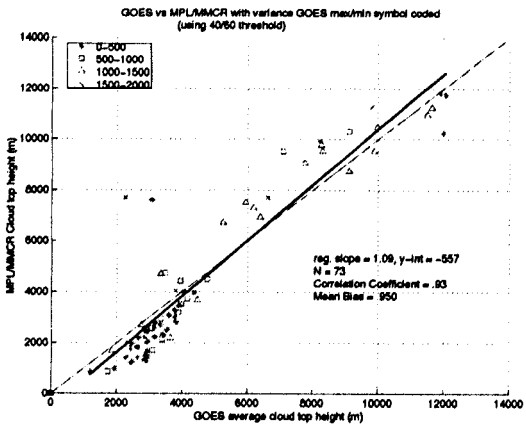

Figure 6: A correlation coefficient of .93 and a mean bias of 950m is seen after application of filtering techniques and removal of outliers.

4. Conclusions

In order to ensure a direct comparison between GOES sounder cloud top height and ground-based MPL/MMCR cloud top height, measures were taken filter out instances of multiple cloud layers. Once this was achieved, high correlation was seen between the two sets of observations. With a mean bias of 950m between the two data sets, the GOES sounder cloud top pressure product can be seen as an accurate instrument. Both of the instances where the GOES sounder had significant error (> 2500m), cirrus clouds were present. The error in the GOES sounder measurement can be attributed to the low optical depth and emmitance of the clouds. This exposes the limits of the current GOES sounder instrument, and demonstrates the need for development of a higher resolution sounder instrumentation.

2. ACKNOWLEDGEMENTS

This research was supported by the Department of Energy Atmospheric Radiation Measurement Program Grant DE-FG-02-92ER61365 and NOAA Grant NA67EC0100.

6. REFERENCES

Clothiaux, E. E., T. P. Ackerman, G. G. Mace, K. P. Moran, R. T. Marchand, M. A. Miller, B. E. Martner, 2000: Objective Determination of Cloud Heights and Radar Reflectivities Using a Combination of Active Remote Sensors at the ARM CART Sites. J. Appl. Meteor: 39, No. 5, pp. 645-665.

McClesse, D. J. and L. S. Wilson, 1976: Cloud top heights from temperature sounding instruments. Quart. J. Royal Meteor. Soc., 102, 781-790.

Ma, Xia L., T. J. Schmit, W. L. Smith, 1999: A nonlinear physical retrieval algorithm'its application to the GOES-8/9 sounder. J. Appl. Meteor. 38, No. 5, 501-513.

Menzel, W. P., F. C. Holt, T. J. Schmit, R. M. Aune, G. S. Wade, D. G. Gray, A. J. Schreiner, 1998: Application of GOES- 8/9 Soundings to weather forecasting and nowcasting. Bull. Amer. Meteor. Soc. 79, 2059R 2078.

Schreiner, A. J., T. J. Schmit, and W. P. Menzel, 2001: Observations and Trends of Clouds Based on GOES Sounder Data. J. Geophys. Res. Accepted for publication 2001.

P3.38 IS THE RESOLUTION OF GOES SOUNDER DATA SUFFICIENT TO SUPPORT SINGLE FIELD OF VIEW RETRIEVALS AND DERIVED PRODUCTS?

Gail M. Bayler*, Suzanne Wetzel Seemann, Jun Li and Timothy J. Schmit**
Cooperative Institute for Meteorological Satellite Studies, University of Wisconsin-Madison
**NOAA/NESDIS/ORA/ARAD/ASPT
Madison, Wisconsin

1. INTRODUCTION

Atmospheric profiles of temperature and moisture, and subsequent derived product imagery of precipitable water, lifted index and skin temperature, are calculated from Geostationary Operational Environmental Satellite (GOES) sounder radiances (Ma et al., 1999) in clear-sky Fields of View (FOV). In cloudy areas, cloud-top parameters are generated from sounder radiances. The sounder instrument FOV varies from approximately a 10 km by 10 km square at nadir to about a 11 km (east-west) by 16 km (north-south) rectangle in the mid-latitudes. Operationally, the data are spatially averaged over a field of regard (FOR) of 5x5 pixels. Hence temperature and moisture retrievals (at 40 pressure levels) have a spatial resolution of, at best, about 50 km. The signal-to-noise ratio of the GOES-9 sounder (launched in May 1995) improved from that of GOES-8 (launched in April 1993) (Menzel et al., 1998) and the trend has continued through GOES-11 (launched in May 2000), Daniels and Schmit, 2001.

At the Cooperative Institute for Meteorological Satellite Studies (CIMSS), retrievals and derived product images (DPI) are produced routinely with a 3x3 FOR. Sounder DPI consist of 3-layer precipitable water (PW1, PW2, PW3), total precipitable water (TPW), lifted index (LI), and skin temperature (SKN T). TPW (surface to 300 hPa) is the product considered in this paper since it is an integrated value.

The improved spatial resolution of approximately 30 km from 50 km allows more precise depiction of cloudy/clear regions, profiles of temperature and dew point temperature, and DPI. Since FOV averaging is done to reduce instrument noise and the signal-to-noise ratios have improved, the question then arises whether single FOV (SFOV), i.e. each individual pixel (1x1) retrievals and DPI depict true meteorological signal or whether the instrument noise remains too large. Ferraro and Daniels, 2001, found the similarity between GOES-8 and –10 and AMSU TPW retrievals to decrease for SFOV. Comparisons of 5x5, 3x3 and 1x1 TPW are presented. MODIS (MODerate resolution Imaging Spectroradiometer) data (Ackerman et al. 1998) are used as a source of validation.

* *Corresponding author address:* Gail M. Bayler, Cooperative Institute for Meteorological Satellite Studies, University of Wisconsin-Madison, 1225 W. Dayton St., Madison, WI 53706; e-mail: gail.bayler@ssec.wisc.edu.

2. GOES SOUNDER RETRIEVAL AND DERIVED PRODUCT IMAGERY ALGORITHM

Retrievals and DPI may be produced only in clear skies; therefore, the first step in the retrieval process determines the location of cloud (Schreiner et al. 2001), sometimes referred to as the cloud mask. For each FOV, a flag is set that indicates clear, cloudy, or unknown conditions.

To produce 5x5 or 3x3 FOR retrievals and DPI, there must be a minimum number of clear FOVs. For example, a 3x3 FOR is flagged cloudy if 5 or more FOV are cloudy and a 5x5 FOR is flagged cloudy for 9 or more cloudy FOV. Retrievals that otherwise might have been made in the clear SFOV are not made (a drawback of spatial averaging). Next, the algorithm attempts to achieve convergence for the retrieval within three iterations. If convergence is not reached, the retrieval is abandoned and the next 3x3 FOR is

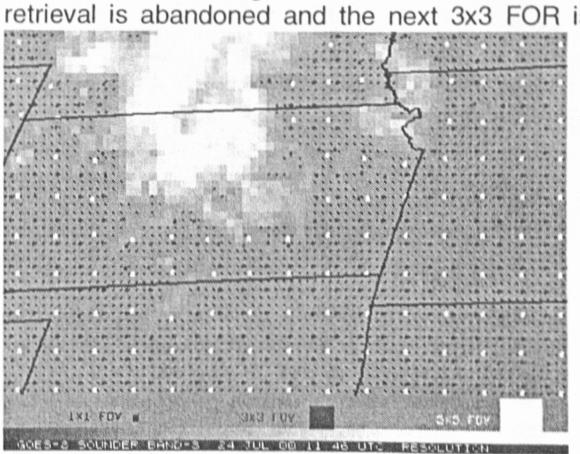

Fig. 1. Grid resolution for single field of view (SFOV), 3x3 field of regard (FOR) and 5x5 FOR. Image shown is 12:00 UTC on 24 Jul 2000 centered on Kansas. The three boxes at the bottom show spatial coverage for 1x1, 3x3 and 5x5 FOR, respectively.

examined. DPI are calculated from the temperature/moisture retrievals. Everywhere that 3x3 FOR retrievals are made, DPI are calculated for the clear-flagged SFOV within the 3x3 FOR. If a 3x3 retrieval is not made, SFOV DPI are not attempted since it was not possible to update the model guess.

SFOV retrievals and DPI do not use a 3x3 FOR guess and so both are made at each clear-flagged FOV.

3. COMPARISON OF SPATIAL AVERAGING

A case study is presented for 24 July 2000 with data from both GOES-8 and GOES-11. Figure 1 illustrates the retrieval locations of the three spatial resolutions considered. GOES-8 TPW calculated as SFOVs exhibit some striping compared to 3x3 FOR and 5x5 FOR. In Fig. 2a, this striping, variation in TPW values in rows of pixels, is exhibited in central Oklahoma parallel to the axis of instability in the 20-30 mm range. Most likely, this is an artifact of the instrument since atmospheric TPW variations are typically more continuous and because averaging into 3x3 or 5x5 FOR generally removes striping, Fig. 2b. Detail is lost with 3x3 processing, however, as Fig. 2b depicts a less continuous axis of instability.

a)

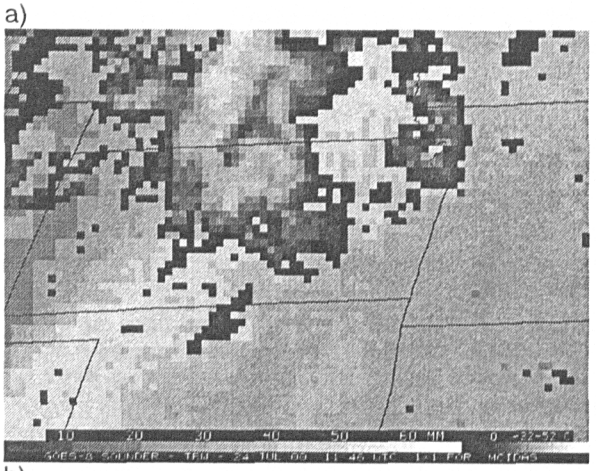

b)

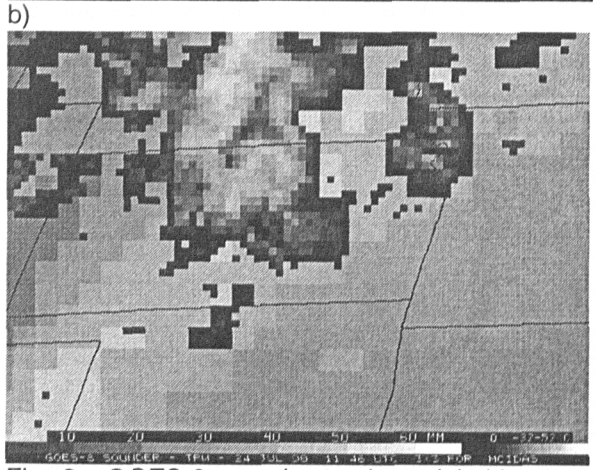

Fig. 2. GOES-8 sounder total precipitable water (mm) at 11:46 UTC on 24 Jul 2000. Cloud edges are black. a) single field of view (1x1) with evidence of striping over central Oklahoma. b) 3x3 field of regard. where spatial averaging minimizes striping.

a)

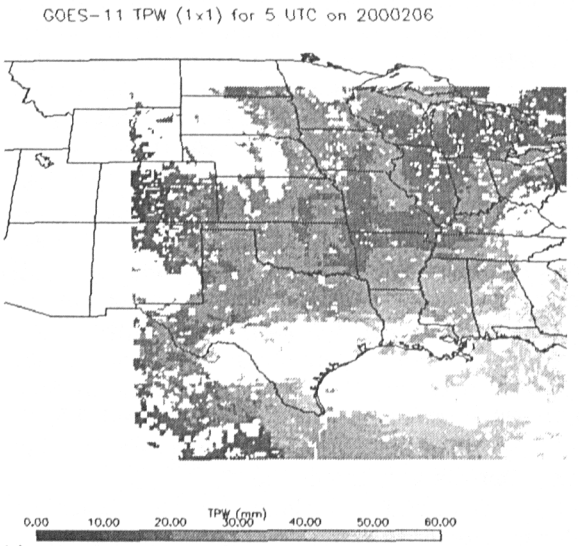

b)

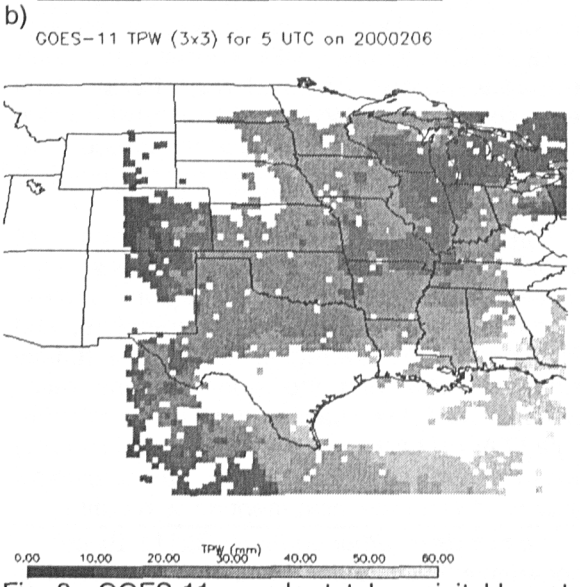

Fig. 3. GOES-11 sounder total precipitable water (mm) at 05:00 UTC on 24 Jul 2000 for a) single field of view (1x1) and b) 3x3 field of regard.

Figures 3a and 3b depict GOES-11 1x1 and 3x3 FOR respectively, at 05:00 UTC for the same day. The GOES-11 data came from the 6-week NOAA science test during the satellite check-out phase. Striping is not manifested in Fig. 3a. Thus instrument improvements may mean SFOV DPI are feasible.

GOES-8 TPW is verified against radiosonde data at 12:00 UTC for 24 Jul 2000 (Table 1). For each spatial resolution, retrievals within 55 km (half a degree) of the radiosonde were verified. Differing resolution retrievals within 5 km of each other were then extracted for final statistics. This colocation was done so comparisons were between spatially close retrievals and the compared retrievals were verified with the same radiosonde data. Although the sample size is small, the statistics indicate that both 3x3 and 5x5 spatial averaging for GOES-8 produce retrievals that more closely agree with radiosonde TPW.

Table 1. Radiosonde verification of GOES-8 sounder total precipitable water at 12:00 UTC on 24 Jul 2000.

RAOB vs. Retrieval	1x1 vs. 3x3	1x1 vs. 5x5
Bias*	2.75/2.04	2.92/2.30
standard deviation	3.22/2.26	2.60/2.27
RMSE**	4.24/3.04	3.91/3.23
Number of matches	23	13
Max. match distance between retrievals	5 km	5 km
Avg. match distance between RAOB and retrievals	34/34 km	39/38 km

*Bias=RAOB-retrieval

**RMSE=SQRT((bias)^2+(standard deviation)^2)

High spatial resolution MODIS TPW data, an independent source of verification, is shown in Fig. 4. MODIS data are collected in 5 minute granules; therefore, this is a two granule image, from 04:50 and 04:55 UTC. The southern Gulf States exhibit TPW values (mm) in the high 20s, with the tip of Texas and southward in the 30s. The large, dark area in the northwest corner represents TPW values of 15 mm. The MODIS and GOES-11 TPW data qualitatively agree.

4. SUMMARY

Improvements in sounder technology over the succession of the GOES-8-11 have yielded improved signal-to-noise ratios. To minimize striping, spatial averaging (3x3 or 5x5 FOR) was a necessity for GOES-8. The striping is not seen with a case comparing GOES-11 sounder total precipitable water data. Additionally, values compare well with higher resolution MODIS data. Thus for this case, single field of view TPW DPI are feasible with GOES-11 sounder data. New case studies will be examined and further radiosonde comparisons will be made.

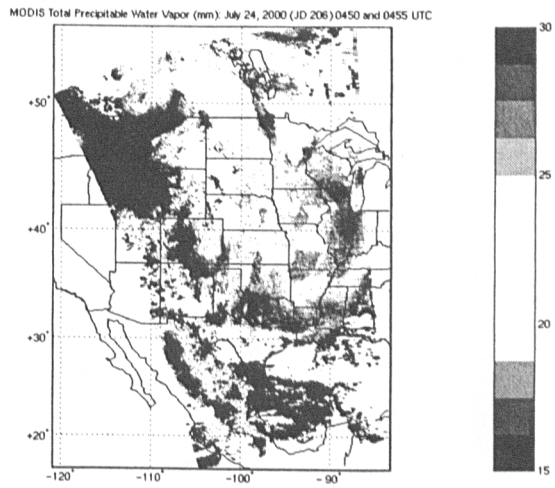

Fig. 4. MODIS total precipitable water (mm) at 4:50 and 4:55 UTC on 24 Jul 2000.

5. REFERENCES

Ackerman, S. A., K. I. Strabala, W. P. Menzel, R. A. Frey, C. C. Moeller, and L. E. Gumley, 1998: Discriminating clear sky from clouds with MODIS. J. Geophys. Res., **103**, 32141-32157.

Daniels, J. M. and T. J. Schmit, 2001: GOES-11 Imager and Sounder Radiance and Product Validations. NOAA Tech. Memo., in press.

Ferraro, R. and J. Daniels, 2001: A comparison of GOES and AMSU based total precipitable water retrievals. Preprints, *Fifth Symposium on Integrated Observing Systems*, Albuquerque, NM, Amer. Meteor. Soc., 130-131.

Ma, X. L., T. J. Schmit, and W. L. Smith, 1999: A nonlinear physical retrieval algorithm-Its application to the GOES-8/9 sounder. J. Appl. Meteor., **38**, 501-513.

Menzel, W. P., F.C. Holt, T.J. Schmit, R.M. Aune, A.J. Schreiner, G. S. Wade, and D. G. Gray, 1998: Application of *GOES8/9* soundings to weather forecasting and nowcasting. *Bull. Amer. Meteor. Soc.*, **79**, 2059-2077.

Menzel, W. P., and J. F. W. Purdom, 1994. Introducing GOES-I: The first of a new generation of geostationary operational environmental satellites, *Bull. Amer. Meteor. Soc.*, **75**, 757-781.

Schreiner, A. J., T. J. Schmit, and W. P. Menzel, 2001: Trends and observations of clouds based on GOES sounder data. *J. Geophysical Rev.*, in press.

P3.39 AN ANALYSIS OF PRE-TORNADIC LOW-LEVEL MOISTURE-FLUX CONVERGENCE AND THE UTILITY OF GOES AND GIFTS SOUNDER DATA

Ralph A. Petersen, NCEP, Camp Springs, MD
Wayne F. Feltz, UW/CIMSS, Madison, WI
Hung-Lung Huang, UW/CIMSS

1. INTRODUCTION

The availability of high time resolution boundary-layer wind, temperature and moisture around the tornadic thunderstorms which developed in central Oklahoma on 3 May 1999 offers an unprecedented opportunity to study the evolution of the lower-level moisture flux convergence fields needed to support the development and continued growth of convection. In addition to the continuous Wind Profiler reports available from four stations in the inner core of the demonstration network, data from co-located Atmospheric Emitted Radiance Interferometer (AERI) instruments provided detailed temperature and moisture data at each of these sites (See Figure 1). The AERI data, which were available for the lowest three kilometers of atmosphere at ten-minute resolution in clear sky, were supplemented aloft by short-range NWP forecast data..

Although data from the AERI alone can be used to monitor the evolution of the pre-convective environment at each of the instrument locations, the combination of AERI moisture and temperature information with Profiler wind data provides a detailed picture of the dynamical processes which modify the pre-convective environment and focus the energy convective instability needed to support the subsequent convection in the local

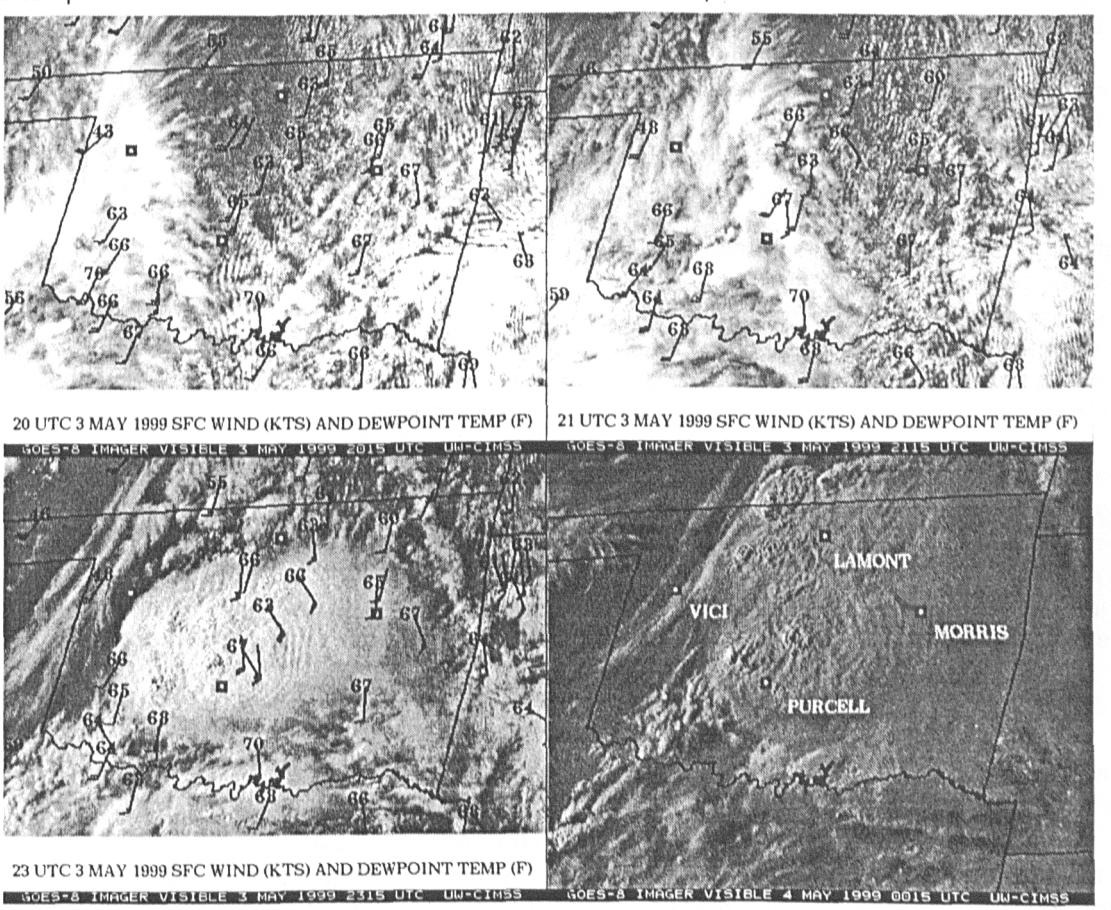

Figure 1. Visible GOES imagery for 2000, 2100, 2300UTC 3 May and 0000UTC 4 May 1999. Locations of co-located Wind Profiler and AERI sites shown. Data from Morris were unavailable for this period and not used.

*Corresponding author's address: Dr. Ralph A. Petersen, NOAA National Centers for Environmental Prediction, 5200 Auth Road, Room 207, Camp Springs, MD 20746, email: Ralph.Petersen@NOAA.GOV

area Diagnostic results of Petersen et al., 2000 showed that both wind and moisture observations can be equally important in modifying the pre-convective environment. In fact, less than ½ of the total moisture flux convergence observed in the period immediately prior to convection was due to wind divergence, with the remainder being the result of moisture advection in the area. This result pointed to the need to continuously update not only wind data but also information of horizontal and vertical moisture gradients both for use in subjective forecasting and future NWP and nowcasting systems.

In this paper, the AERI data are used to emulate frequent moisture and temperature retrievals typical of those available from the current GOES sounders and from future systems such as the Geostationary Imaging Fourier Transform Spectrometer (GIFTS, see Smith et al. also in this volume.). These data are then compared both with the original observations and combined with Wind Profiler data to derive kinematic parameters to assess the potential utility of current and future geostationary sounders in integrated mesoscale observing systems.

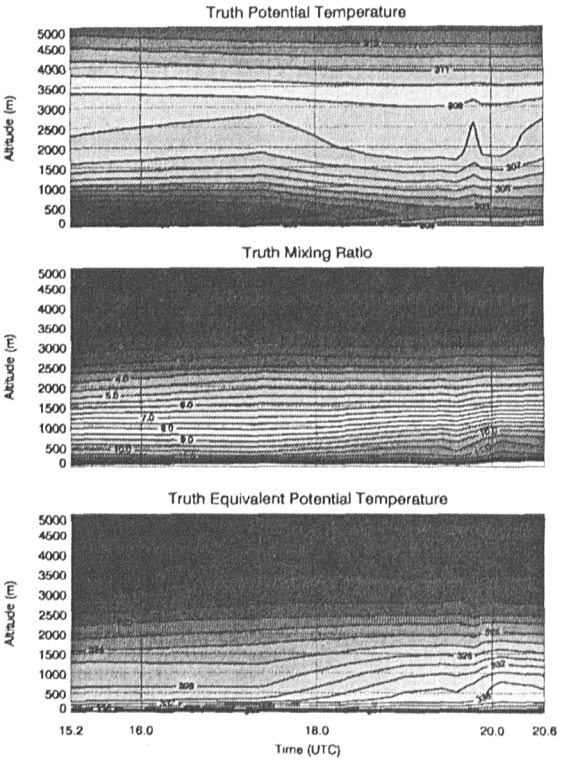

Figure 2. Vertical time series of areal average AERI Potential Temperature (top), Mixing Ratio (middle) and Equivalent Potential Temperature (bottom) from surface to 5 km and from 1510 to 2036UTC

2. METHODOLOGY AND RESULTS

Co-located wind, temperature and moisture profiles were available during the 5 hour period prior to convection from 3 Wind Profiler sites located south-west of Oklahoma. The northeast-most site was Lamont, with the other two sites at Vici and Purcell.

The time series in Figure 2 show not only a warming and moistening of the bottom-most 1.5km throughout the day, but also a deepening of the moist layer (especially after 1800UTC) and a strengthening of the convective instability (indicated by increases in low-level values of and vertical gradient of equivalent potential temperature) in the two hours prior to convection.

The combined Wind Profile and full resolution AERI data were then used to derive vertical time series of derived kinematic quantities, including. velocity divergence and moisture flux divergence. The divergence data showed a rapid transition from a pattern of near 3km overlaying lower level divergence to one with stronger low-level convergence and increasing divergence above 4 km after 1800UTC. The initial pattern of low-level subsidence helped to maintain the inhibiting lid before 1900UTC, while the later configuration provided some lifting (3-4 cm s^{-1}) thereafter.

The moisture flux divergence showed a generally similar evolution but with continued increases in low-level moisture flux convergence throughout the period, even after the velocity convergence maxima has shifted away from the surface after 1900UTC. Although the initial increase of moisture flux convergence at 1900UTC was forced by the velocity convergence, more than half of the moisture flux convergence in the 1½-hour prior to convection was due to moisture advection.

In order to assess the role of current and future geostationary sounders in our future integrated mesoscale observing systems, the full resolution, upward-pointing AERI data and mid-/upper-level NWP data were transformed to emulate downward-looking radiances (and corresponding temperature and moisture profiles) from both broad-band radiometers currently available on GOES and planned for the high spectral resolution interferometer on GIFTS. These data were then

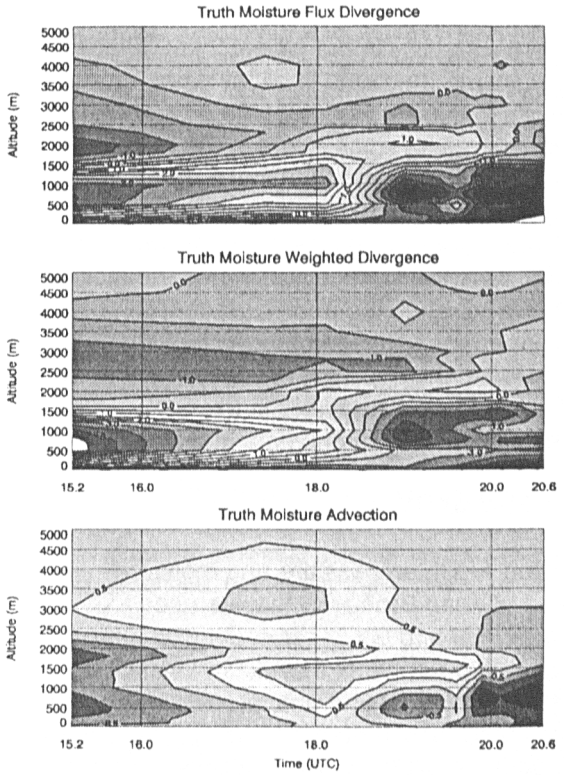

Figure 3. Vertical time series of areal average Moisture Flux Divergence (top), Moisture Weighted Velocity Divergence (middle), and Moisture Advection (bottom) from surface to 5 km and from 1510 to 2036UTC.

combined with the Wind Profiler observatons in identical diagnostic calculations.

Comparison of individual station data shows errors in the GOES temperature and moisture data were 3 to 6 time larger for GOES than GIFTS, with the GOES data having large near-surface warm and dry biases. In addition, the GOES data were not able to capture the strong vertical stability and moisture gradients as well as AERI, while GIFTS data performed much better.

Comparison of areal mean data shows similar patterns, with superadiabatic layers extending through nearly 1 km in the synthetic GOES data. Correspondingly, the low-level GOES moisture field were biased dry. This is consistent with the expected effects of the broad weighting function of the GOES radiometers. The GIFTS data showed much smaller overall biases, but with some small vertical couplets of compensating biases in areas of strong vertical moisture gradients.

The net effects of GOES biases are also evident in the derived equivalent potential temperature fields in Fig.4. It should be noted that the net impact of the errors is reduced in this parameter due to the negative correlation between the individual temperature and moisture biases. However, the GOES data still exaggerate near-surface values and misrepresent vertical gradients and convective instability after 1800UTC.

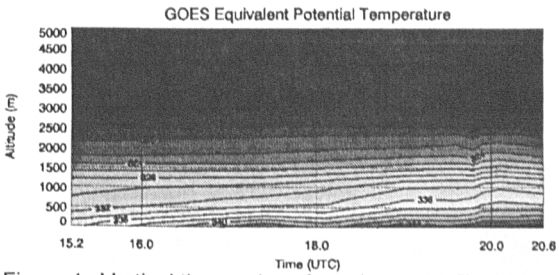

Figure 4. Vertical time series of areal average Equivalent Potential Temperature using emulated GOES data from surface to 5 km and from 1510 to 2036UTC.

The next question to be addressed is whether the increased vertical resolving capabilities of GIFTS will be adequate to monitor important and rapid changes occurring in pre-convective environments. To accomplish this, the aforementioned kinematic studies were repeated using both the emulated GOES and emulated GIFTS data.

The results in Fig. 5 show that the overall patterns and trends of moisture flux convergence detected in the AERI/Profiler study are retained using the emulated GIFTS data. The largest differences are noted below 1 km before 1800UTC, when the GIFTS data were unable to resolve the strength of the vertical gradients seen in the original observations. The GIFTS errors, however, were substantially less than those using the GOES data, in which case the errors extended upward to 3 km and persisted throughout the entire period.

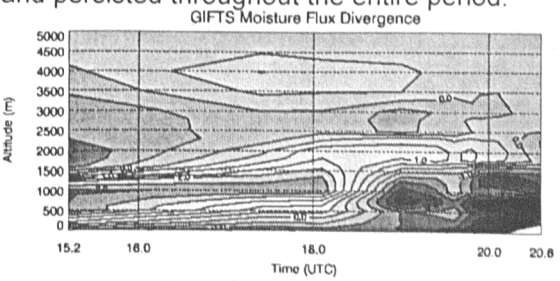

Figure 5. Vertical time series of areal average Moisture Flux Divergence using emulated GIFTS data from surface to 5 km and from 1510 to 2036UTC.

When the moisture flux divergence is broken into its two components (moisture weighted divergence and moisture advection), the impact of the bias in the GOES moisture errors becomes apparent.

Because the low-level GOES mixing ratios are underestimated by 10-15% below 1 km and overestimated by 10-20% from 1-3 km, the impact of the divergence component of the moisture flux divergence (Fig. 6). was underestimated during the earlier period when it dominated. By contrast, the reduced biases in the GIFTS data produced patterns that were within a few percent of the true values throughout the entire period.

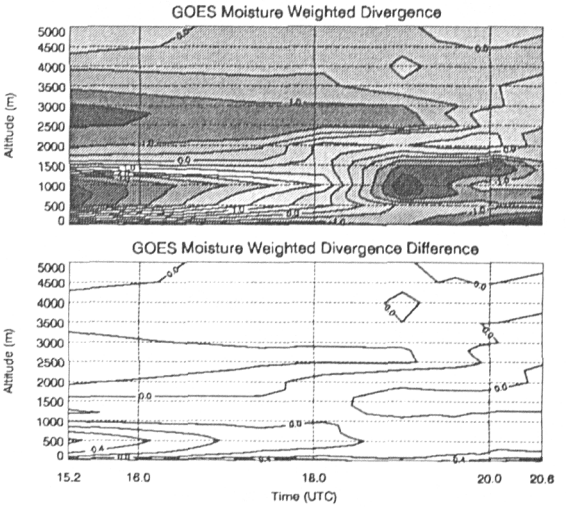

Figure 6. Vertical time series of areal average Moisture Weighted Divergence (top) and Errors (bottom) using emulated GOES data from surface to 5 km and from 1510 to 2036UTC.

The advective term using the GIFTS data (Fig. 7) also matches the observed time series better than when using synthetic GOES data (Fig. 8), most notably during the latter half of the period, at which time the configuration of moistening near the surface overlain by drying aloft was increasing the convective instability in the lowest 2 km. Since the wind fields were the same in all tests, the small differences in the magnitude of the advective components reflect small errors in the horizontal moisture gradients using the GIFTS data. This is especially noticed during the period immediately prior to the convective development when advection near the surface dominated the moisture supply. By contrast, the near-surface GOES data show oscillations between underestimating and overestimating the moisture advection, reflecting large fluctuations in the errors in the GOES data between sites and from one time to the next.

3. SUMMARY

Co-located AERI temperature and moisture profiles and Wind Profiler data were used to emulate GOES and GIFTS soundings in a pre-convective environment. Results of kinematic studies using original and emulated data showed that GIFTS not only reduces biases present in the GOES data, but also provides sufficient vertical and horizontal consistency to correctly diagnose the develop of convective instability and low-level moistening needed to support storm growth.

4. REFERENCES

Petersen, R. A., W. F. Feltz, J. Schaefer and R. Schneider, 2000: An Analysis of Low-level Moisture-Flux Convergence Prior to the 3 May 1999 Oklahoma City Tornadoes. Preprints, AMS Conference on Severe Local Storms Conference

Smith, W.E., et al., 2001: The Geostational Imaging Fourier Transform Spectrometer (GIFTS). Preprints, AMS Conference on Satellite Meteorology and Oceanography

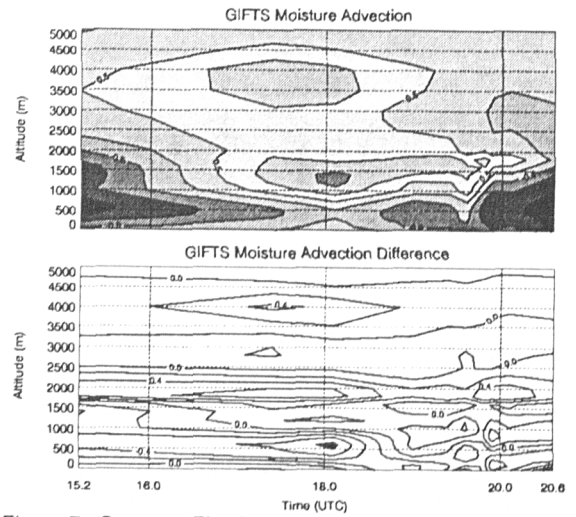

Figure 7. Same as Fig. 6, except Moisture Advection (top) and Errors (bottom) using emulated GIFTS data.

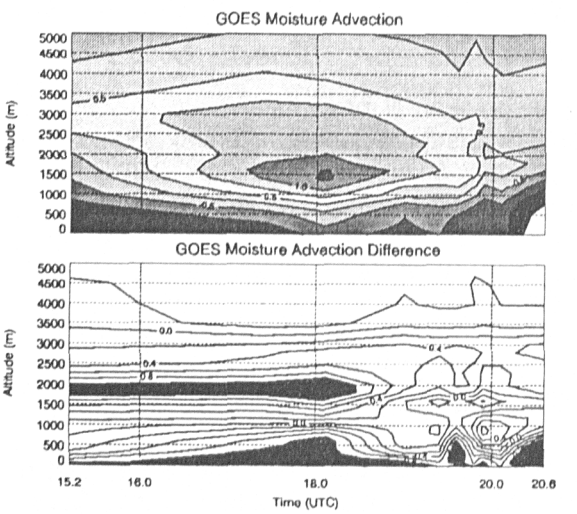

Figure 7. Same as Fig. 7, except using emulated GOES data.

P3.40 AN EVALUATION OF SEVERAL YEARS OF CIMSS AND NESDIS GOES SOUNDER DATA

James P. Nelson III *[,1], Timothy J. Schmit,[2] and W. Paul Menzel [2]

[1] Cooperative Institute for Meteorological Satellite Studies (CIMSS)
University of Wisconsin-Madison, Madison, WI

[2] NOAA/NESDIS/ORA
Advanced Satellites Products Team (ASPT)
Madison, WI

1. INTRODUCTION

At The Cooperative Institute for Meteorological Satellite Studies (CIMSS), vertical temperature and moisture profiles retrieved from GOES Sounder radiances (retrievals) have been produced and compared to radiosondes since 1995. In addition, National Environmental Satellite, Data, and Information Service (NESDIS) operational retrievals have also been compared with radiosondes. Comparision of these two rich datasets allows for extensive evaluation of past performance, and could lead to ideas for future retrieval improvements.

The main focus of this paper is to compare these two sets of retrievals with collocated, verifying radiosonde data. Due to space limitations, only Total Precipitable Water (TPW) will be examined; however, several temperature and moisture parameters will be examined at the conference. The data will be analyzed by month and season, by time (00UTC vs. 12UTC), by region (north vs. south, etc.), and by sensor (GOES-E vs. GOES-W). Moreover, an evaluation of one of the more important components of the retrieval process, the bias adjustment of the measured GOES radiances, will also be undertaken. The differences between the adjustments used in the CIMSS and NESDIS retrievals will be outlined and compared explicitly for Sounder band 5 (13.4μm) here, but will be expanded to include numerous Sounder bands at the conference.

2. GOES RETRIEVALS OF TEMPERATURE AND MOISTURE

Radiance data from the Sounder instruments aboard the GOES-I/M series of spacecraft have been available since mid-1994 (Menzel and Purdom 1994). This information can be used in a number of different ways; one of its uses is as a major component in deriving vertical profiles of temperature and moisture (satellite retrievals). For the last several years, GOES retrievals at both CIMSS and NESDIS (designated as OPS) have been produced using a nonlinear physical retrieval algorithm (Ma et al. 1999). Briefly, this algorithm uses GOES Sounder cloud-free radiances in a number of spectral bands that have been averaged over 1-N Fields of View (FOV) to adjust initial guess vertical profiles of temperature and moisture. At CIMSS, the averaging is done within a 3 X 3 matrix of FOVs (N<=9), while the NESDIS operational retrievals are produced using a 5 X 5 FOV matrix (N<=25). Since the nominal horizontal resolution of a GOES Sounder FOV is approximately 10km at the sub-satellite point (Menzel and Purdom 1994), the nominal dimensions of the CIMSS and NESDIS retrievals are approximately 30 X 30 and 50 X 50 km, respectively.

As part of the physical retrieval process, an adjustment to the input radiances is necessary to account for errors in both the radiative transfer model and instrument calibration (Ma et al. 1999). This correction is known as the radiance bias adjustment. The adjustment is computed differently for the OPS and CIMSS retrievals. The OPS retrievals use a method known as "shrinkage estimation" (Schmit 1996), a regression approach that involves using 26 predictors to determine an hourly bias adjustment to apply in each Sounder channel.

On the other hand, retrievals produced at CIMSS now employ a somewhat simpler approach to bias adjustment. Not only are the number of predictors reduced from 26 to 5, the regression coefficients need only be computed once every several months. The simpler approach has been made possible because of expanded GOES radiance ground processing that resulted in more accurate calibration of radiance data (Weinreb 1997).

*Corresponding author address: James P. Nelson III, Univ. of Wisconsin-Madison, 1225 W. Dayton St. Madison, WI 53706; email: jimn@ssec.wisc.edu.

3. RETRIEVAL AND BIAS CORRECTION RESULTS

In this work, several years of GOES retrieval results from both CIMSS and NESDIS are examined. The examinations are conducted using two approaches: 1) comparisons of retrieval parameters, such as precipitable water and temperature, with the same from verifying radiosonde data, and 2) comparisons of the radiance bias adjustments made at CIMSS and NESDIS. The overall period of study for GOES-8 ranges from January 1998 through June 2001, while the same for GOES-10 ranges from January 1999 through June 2001. In the interest of brevity, our discussion will focus on comparing retrieval Total Precipitable Water vapor (TPW) with collocated radiosonde data. Previous work has shown that the nonlinear retrieval algorithm makes a larger adjustment to the guess moisture profile than the guess temperature profile (Ma et al. 1999).

3.1. Comparisons of retrieval parameters with radiosondes

Table 1 shows retrieval versus radiosonde bulk statistics for both the CIMSS and OPS retrievals, further subdivided by guess and retrieval, as well as retrieval time. These datasets have been constructed by requiring that each retrieval be collocated within approximately 0.1 degrees latitude/longitude (L/L) with a nearby radiosonde. The number of collocation matches (N) is larger for the CIMSS retrievals than the OPS retrievals because of the different retrieval processing box sizes. Looking first at the GOES-8 bulk statistics, one can see that the bias (GOES minus RAOB) is always negative. Furthermore, the standard deviation (SD) is reduced for all 4 sets of GOES-8 retrievals (00Z CIMSS, 12Z CIMSS, 00Z OPS, 12Z OPS) compared to their respective guesses. The 12Z retrieval SD values tend to be larger than their 00Z counterparts (3.22 versus 3.04 for CIMSS retrieval TPW, 3.29 versus 3.05 for OPS retrieval TPW). Looking at the average TPW data, there is a tendency for the CIMSS guesses and retrievals to contain less moisture than the OPS guesses and retrievals. Perhaps this is related to the different retrieval box sizes.

Turning our attention now to the GOES-10 bulk statistics, note that the number of radiosonde matches is approximately one-quarter of those from GOES-8. This is because less of the GOES-10 data is over CONUS. Also note how both the bias and SD values are reduced compared to the GOES-8 data. This is probably not too surprising, considering the average TPW values for GOES-10 are significantly smaller than the GOES-8 data. However, it is also interesting to note that the change in TPW bias when comparing the guess and retrieval data more often has the proper sign (i.e., the retrieved TPW is closer to the collocated radiosonde TPW than the guess) for GOES-10 when compared to GOES-8.

Table 1. Retrieval versus radiosonde bulk statistics. Collocation distance is approximately 0.1 degrees latitude/longitude. Minimum clear FOVs is 4. BIAS, SD and AVG values are in mm.

DATASET	PERIOD	BIAS	SD	AVG GUESS / RET TPW	AVG RAOB TPW	CC	N
00Z CIMSS G-8 TPW guess	1/98-6/01	-0.62	3.15	16.25	16.88	0.959	2260
00Z CIMSS G-8 TPW retrieval	1/98-6/01	-0.64	3.04	16.23	16.88	0.961	2260
12Z CIMSS G-8 TPW guess	1/98-6/01	-1.10	3.39	16.51	17.61	0.957	1870
12Z CIMSS G-8 TPW retrieval	1/98-6/01	-0.89	3.22	16.72	17.61	0.961	1870
00Z OPS G-8 TPW guess	1/98-6/01	-0.23	3.33	17.68	17.91	0.956	750
00Z OPS G-8 TPW retrieval	1/98-6/01	-0.62	3.05	17.29	17.91	0.963	750
12Z OPS G-8 TPW guess	1/98-6/01	-0.61	3.38	17.65	18.26	0.963	679
12Z OPS G-8 TPW retrieval	1/98-6/01	-1.11	3.29	17.15	18.26	0.965	679
00Z CIMSS G-10 TPW guess	1/99-6/01	-0.40	2.62	10.00	10.40	0.906	630
00Z CIMSS G-10 TPW retrieval	1/99-6/01	-0.35	2.05	10.05	10.40	0.944	630
12Z CIMSS G-10 TPW guess	1/99-6/01	-0.86	2.73	11.06	11.92	0.925	442
12Z CIMSS G-10 TPW retrieval	1/99-6/01	-0.41	2.56	11.51	11.92	0.936	442
00Z OPS G-10 TPW guess	1/99-6/01	-0.11	2.59	12.17	12.29	0.928	143
00Z OPS G-10 TPW retrieval	1/99-6/01	0.12	2.46	12.41	12.29	0.935	143
12Z OPS G-10 TPW guess	1/99-6/01	-0.76	2.66	10.72	11.48	0.900	170
12Z OPS G-10 TPW retrieval	1/99-6/01	-0.49	2.46	10.99	11.48	0.914	170

Finally, the correlation coefficients (CC) are also smaller for GOES-10 than for GOES-8, perhaps showing that the GOES-10 averaged radiances tend to show a little less sensitivity to the first guess than the GOES-8 radiances.

In all subsequent results, the input data to the statistics computations are filtered twice. First, retrievals are only used in the computations if they

are collocated within approximately 0.5 degrees L/L of a nearby radiosonde. This initial filtering procedure produces CIMSS/RAOB and OPS/RAOB collocation files. Then, the CIMSS/RAOB and OPS/RAOB matches are themselves subjected to the same 0.5 degrees L/L collocation procedure, as well as a 1 hour time collocation threshold. This results in one final file of matches, with all retrieval/RAOB matches being collocated within 0.5 degrees L/L, and the CIMSS and OPS retrievals themselves also being collocated within 0.5 degrees L/L. The intent is to compare CIMSS and OPS retrievals at very similar locations, while still maintaining a reasonably large dataset for the statistics.

Figure 1 shows a time series of GOES-8 00UTC and 12UTC combined TPW retrieval versus radiosonde bias for the CIMSS and OPS retrievals. Note the overwhelming tendency for negative biases, in agreement with Table 1 above. This may be demonstrating a weakness of coarse spectral resolution radiometers to detect low-level moisture. Also, the biases for both the CIMSS and OPS retrievals are maximized, in terms of largest dry bias versus the radiosondes, during the warmest and most moist summer months, and minimized during the cooler/dryer months. The same warm/moist and cool/dry seasonal tendencies also exist for GOES-10 (not shown). Furthermore, comparing the CIMSS and OPS biases to each other, one can see an interesting shift that occurred about July 2000. Prior to that time, the CIMSS biases tended to be closer to zero than the OPS retrievals, while after that point the OPS retrieval biases were closer to 0. This may be an indication of needing to update the CIMSS radiance adjustment database.

Figure 2 depicts a geographical distribution of CIMSS GOES-8 and GOES-10 combined 00UTC and 12UTC TPW bias at radiosonde locations. As one might expect, there are more negative than positive bias values. No clear regional bias tendencies are apparent, although pockets of positive bias exist in the Upper Midwest, along the eastern seaboard, along the Gulf coast, and over Mexico. Note also the large (in magnitude) negative biases in southern Texas. Similar distributions of bias are seen in Fig. 3 for the OPS retrievals, with an additional region of positive bias in the Pacific Northwest, and even larger negative biases in southern Texas (-4.45 mm versus -3.46 mm). More detailed study is required to determine the source of these large negative biases.

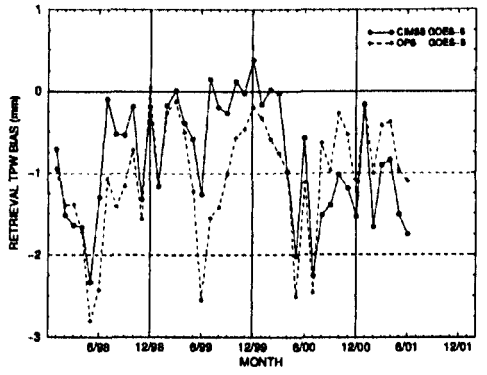

Fig. 1. GOES-8 CIMSS and OPS monthly, combined 00UTC and 12UTC TPW bias. Period is from January 1998 through June 2001.

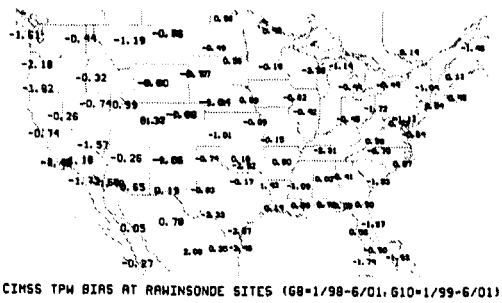

Fig. 2. CIMSS combined 00UTC and 12UTC retrieval TPW bias at radiosonde locations for GOES-8 (January 1998 – June 2001) and GOES-10 (January 1999 – June 2001). The larger numeric fonts (western portion) represent GOES-10 data.

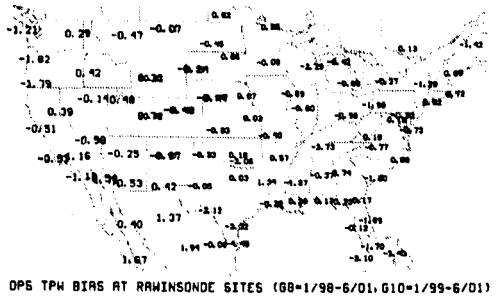

Fig. 3. As in Fig. 2 but for OPS retrievals.

3.2. Comparisons of bias-corrected radiances with radiosondes

As mentioned above, a GOES Sounder radiance bias adjustment in each channel is vital for producing satellite retrievals of temperature and moisture via a physical retrieval algorithm (Ma et al. 1999). To examine the results of the bias adjustment procedures used in the last several years at CIMSS and NESDIS, we have selected band 5 (13.4μm), a channel used in the retrieval of both temperature and moisture. Radiation in this band eminates mainly from the lower troposphere and surface (Menzel et al. 1998).

Figure 4 shows a time series of CIMSS monthly-averaged band 5 retrieval brightness temperatures for the period January 1998 – June

2001. The most obvious feature is the seasonal cycle. In the chart, the lowest average brightness temperatures are always the cloud-cleared, 3 X 3 FOV- averaged values, with the bias-corrected values being slightly warmer. The collocated radiosonde data are the warmest values. It can be seen that the bias adjustment is always towards the collocated radiosonde data. Note that these radiosondes are only shown for comparison and are not the same historical set of radiosondes used in calculating the CIMSS bias adjustment regression coefficients.

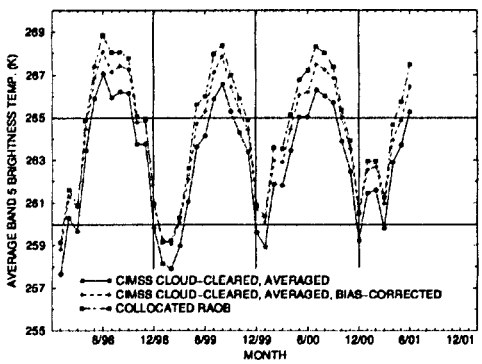

Fig. 4. CIMSS 12UTC GOES-8 monthly, averaged band 5 (13.4μm) retrieval brightness temperatures (measured and bias-corrected), along with average band 5 brightness temperatures computed for collocated radiosondes. Period is from January 1998 through June 2001.

The corresponding time series of OPS retrieval monthly-averaged band 5 brightness temperatures for the same period (not shown) is very similar, although the OPS average values are usually a fraction of a degree warmer than their CIMSS counterparts. Furthermore, and perhaps more significantly, the OPS bias-corrected brightness temperatures tend to be closer to the collocated radiosonde data than the CIMSS bias-corrected brightness temperatures. This may be a reflection of the more frequent updates of the OPS bias adjustment regression coefficients. The CIMSS bias adjustment regression coefficient database is likely in need of an update.

4. SUMMARY AND FUTURE WORK

This paper presents comparisons of satellite retrievals of temperature and moisture produced at CIMSS and NESDIS over the last several years, focussing on the derived product TPW. In terms of bulk statistics, both the CIMSS and NESDIS retrieved TPW exhibit a reduced SD when compared to its guess when compared to collocated radiosondes. In addition, the GOES-10 biases are usually smaller than GOES-8, and the GOES-10 SD values are always smaller than GOES-8.

Both the CIMSS and OPS GOES-8 and GOES-10 retrieval TPW biases tend to be more negative (retrieval drier than collocated radiosonde) in the warmer, more moist months. In terms of regional distributions of TPW bias, negative biases predominate for both the CIMSS and OPS retrievals, although pockets of positive biases also exist.

The radiance bias adjustment in Sounder band 5 (13.4μm) for both the CIMSS and OPS retrievals is such that the final bias-corrected brightness temperatures used in the physical retrieval algorithm agree more closely with nearby collocated radiosonde data than the uncorrected radiances.

By necessity due to space limitations, only retrieved TPW and band 5 bias adjustment data have been explicitly examined in this paper. At the conference, the comparisons will be expanded to include other retrieval parameters and Sounder bands. In particular, the radiance bias adjustment used at CIMSS and NESDIS will be examined more closely in an attempt to determine which is the better approach.

5. REFERENCES

Ma, X. L., T. J. Schmit, and W. L. Smith, 1999: A nonlinear physical retrieval algorithm—its application to the GOES-8/9 Sounder. *J. Appl. Meteor.*, **38**, 501-513.

Menzel, W. P., and J. F. W. Purdom, 1994: Introducing GOES-I: The first of a new generation of geostationary operational environmental satellites. *Bull. Amer. Meteor. Soc.*, **75**, 757-781.

Menzel, W. P., F. C. Holt, T. J. Schmit, R. M. Aune, A. J. Schreiner, G. S. Wade, and D. G. Gray, 1998: Application of GOES-8/9 soundings to weather forecasting and nowcasting. *Bull. Amer. Meteor. Soc.*, **79**, 2059-2077.

Schmit, T. J., 1996: Sounder bias correction of the east-west radiance gradient. *Proc. SPIE*, **2812**, Denver, CO, 630-637.

Weinreb, M. P., M. Jamieson, N. Fulton, Y. Chen, J. X. Johnson, J. Bremer, C. Smith, and J. Baucom, 1997: Operational calibration of Geostationary Operational Environmental Satellite-8 and –9 imagers and sounders. *Appl. Opt.*, **36**, 6895-6904.

P3.41 A SUMMARY OF SATELLITE DATA USAGE IN THE NWS WESTERN REGION

Kevin J. Schrab*
NOAA, National Weather Service, Western Region Scientific Services Division
Salt Lake City, UT

1. INTRODUCTION

The Western Region (WR) of the National Weather Service (NWS) has been very active in the usage of digital satellite data for over 6 years. Digital data was first introduced in 1995 through the use of RAMSDIS, which was developed at the Cooperative Institute for Research in the Atmosphere (CIRA). Initially, digital data from the GOES-8 imager was sent to all 24 WR Weather Forecast Offices (WFOs). Once GOES-9 became operational as GOES-West, data from that satellite was sent to all WR WFOs for display on RAMSDIS. Additional data sets sent to the WR WFOs included: SSM/I products (ocean surface wind speed, total precipitable water, rain rate), GOES derived product imagery (total precipitable water, lifted index, cloud top pressure) and GOES high density winds. The data proved to be very useful to forecasters in both the convective warning program and in the normal day-to-day forecasting program.

In 1997 AWIPS began to be deployed to all NWS WFOs, all WR WFOs had AWIPS by 1999. AWIPS allowed for the ingest and display of digital satellite data. However, the early versions of AWIPS were only supplied with basic image data from GOES (VIS, IR, WV). At the present time only GOES derived product imagery (DPI) has been added to the delivery of satellite data to AWIPS.

To alleviate this problem, WR developed a method to easily ingest digital satellite data from various sources into AWIPS. The data is retrieved from various sources, reformatted to be compatible with AWIPS, and then sent to all 24 WR WFOs using LDM and the Local Data Acquisition and Dissemination (LDAD) system. AWIPS was modified to store this data and menus were modified to make the data displayable.

Several examples of the supplemental data that are being ingested and displayed on AWIPS will be presented. It will also be shown how these new GOES/POES images and products can be combined with other AWIPS data to aid in the forecast process in a WFO.

2. REQUIREMENTS FOR SATELLITE DATA

To aid the development of the ingest and display process for the supplemental satellite products a simple set of requirements were formulated. The requirements for these supplemental (non-AWIPS SBN) data sets are:

1) Conversion of data into AWIPS compatible format (netCDF)
2) Automatic ingest of data into the AWIPS database via LDAD
3) Ability to display these data in a meaningful way, this means:
   - 3a) Allow "hot cursor" readout of digital data
   - 3b) Allow integration of these data with other data available in AWIPS
   - 3c) Allow display of data on appropriate map backgrounds

3. SATELLITE DATA TRANSFER TECHNIQUE

The data flow presented here is that currently used in the NWS Western Region (WR). Some of the satellite data is being transferred to other NWS Regions for delivery to other WFOs around the United States. The data flow from originating source to the AWIPS database follows these steps:

1) The ingest of data from originating source (NESDIS, NWS/NCEP/AWC, WR direct GOES readout system, NESDIS-RAMMT/CIRA) is accomplished using a McIDAS-X server (this machine is the WR AWIPS satellite server).
2) Individual data products are converted into AWIPS compatible netCDF files using a java-based conversion program. This conversion to netCDF generally takes less than one minute (dependent on file size and system load).
3) Data products are transferred from the WR AWIPS satellite server to an individual AWIPS site's LDAD server using LDM. As soon as a data product is converted into netCDF it is placed in the LDM queue for retrieval by the LDM running on each AWIPS sites' LDAD server.
4) Data is transferred from the LDAD server to the AWIPS database on the AWIPS data server using the LDAD software. A special script was written that places the satellite data products into specific locations in the database.

The total amount of data transferred from the WR AWIPS satellite server into AWIPS is about 15 MB/hr.

4. SUPPLEMENTAL SATELLITE DATA AVAILABLE ON WR WFO AWIPS

Numerous satellite products are being sent to WFOs in WR. Table 1 lists the products that are available for display on AWIPS in WR.

* *Corresponding author address*: Kevin J. Schrab, NOAA/National Weather Service, Western Region Headquarters, 125 S. State St, Salt Lake City, UT 84138; e-mail: kevin.schrab@noaa.gov

Table 1. Supplemental satellite products available on AWIPS via LDAD.

Product	Source
GOES fog/reflectivity product	WR
GOES TPW	CIMSS
GOES low-level PW	CIMSS
GOES mid-level PW	CIMSS
GOES high-level PW	CIMSS
GOES 24hr TPW difference	WR and CIMSS
GOES CAPE	CIMSS
GOES LI	CIMSS
GOES cloud top pressure	CIMSS
SSM/I TPW	NESDIS
SSM/I rain rate	NESDIS
SSM/I ocean surface wind speed	NESDIS
NOAA-15/AMSU TPW	CIRA and NESDIS
NOAA-15/AMSU rain rate	CIRA and NESDIS
NOAA-15/AMSU 89 GHz	CIRA and NESDIS
NOAA-15/AMSU cloud liquid water	CIRA and NESDIS
NOAA-15/AMSU snow cover	CIRA and NESDIS
GMS/GOES/Meteosat WV comp.	NWS/NCEP/AWC
GMS/GOES/Meteosat IR comp.	NWS/NCEP/AWC
GOES VIS/fog product	NWS/NCEP/AWC
GOES sounder channel 8	CIMSS
GOES sounder channel 10	CIMSS
GOES sounder channel 11	CIMSS
GOES sounder channel 12	CIMSS
GOES Pacific NW VIS	WR
GOES Pacific NW IR	WR
QuikSCAT winds	NESDIS
GOES High Density Winds	NESDIS

Examples of some products are seen in Figures 1-5.

Note that in each image there is a hot cursor readout that gives digital values in the units appropriate for each product. Examples of the other products listed in Table 1 will be available on the poster and on a webpage (URL will be available during poster viewing).

5. EXAMPLES OF IMPACTS AT WR WFOs

The supplemental data sent to WR WFOs has proven to be very useful in forecast operations. The GOES DPI are used extensively during the summer convection season to track moisture and instability. The frequent updates (hourly) compared to RAOB data, allow forecasters to track moisture movement and the development of instability. Figure 6 shows how the GOES TPW gives better spatial coverage of moisture distribution that can help forecasters better predict convection. In this case the forecaster indicated the following in the Area Forecast Discussion:

"12Z KTUS sounding and GOES total precipitable water imagery both indicate lots of moisture to work with across southern Arizona."

The AMSU and SSM/I TPW are used extensively during the winter season to track moisture surges associated with strong storm systems that affect the west coast of the United States. Forecast offices frequently refer to these products in their Area Forecast Discussions and in developing their forecasts. Figure 7 shows how the AMSU TPW can show moisture plumes over the Pacific Ocean.

6. COMBINING SUPPLEMENTAL SATELLITE DATA WITH OTHER AWIPS DATA

A few examples will now be shown to highlight how these satellite products can be combined with other data that are available on AWIPS.

Figure 8 shows how the GOES TPW product can be used with numerical model guidance. In this example, GOES TPW at 12Z on 1 Aug 2001 is plotted with the 0 hour forecast of TPW from the ETA model. It is apparent from this comparison that the general distribution of moisture represented in the ETA matches what the GOES TPW very well. The ETA may be slightly under-predicting the TPW in the lower Colorado River valley area. This also shows that the GOES TPW has a finer spatial resolution that the ETA TPW.

Figure 9 shows how GOES high density winds can be compared to AVN model output. High density winds are available at every mandatory level and can be compared to any model output or conventional data on AWIPS. This is a very useful way for a forecaster to evaluate the wind field over the data sparse Pacific Ocean.

7. SUMMARY

AWIPS is a very useful tool for integrating supplemental satellite data and products with conventional weather data. This integration of data has proven to be very useful to the forecasters at Weather Forecast Offices in the Western Region of the National Weather Service.

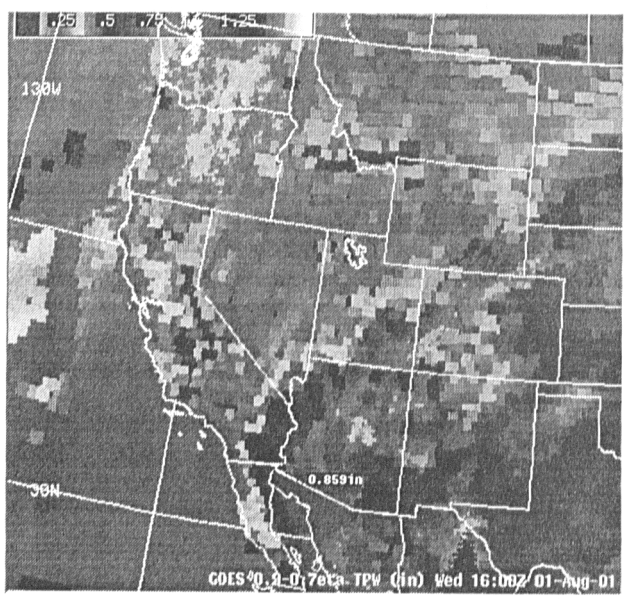

Figure 1. GOES 0.9-0.7eta precipitable water.

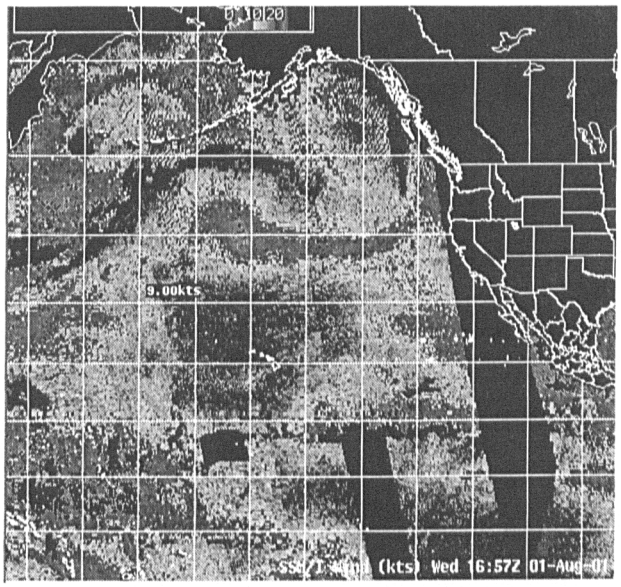

Figure 2. SSM/I ocean surface wind speed.

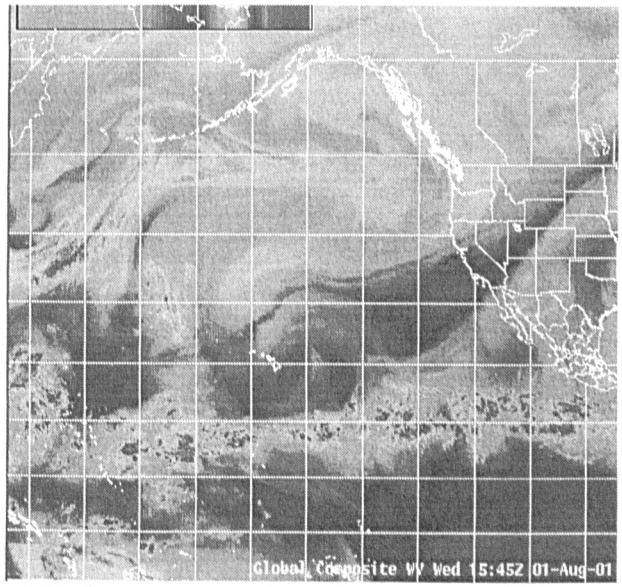

Figure 4. GMS/GOES/Meteosat WV composite image.

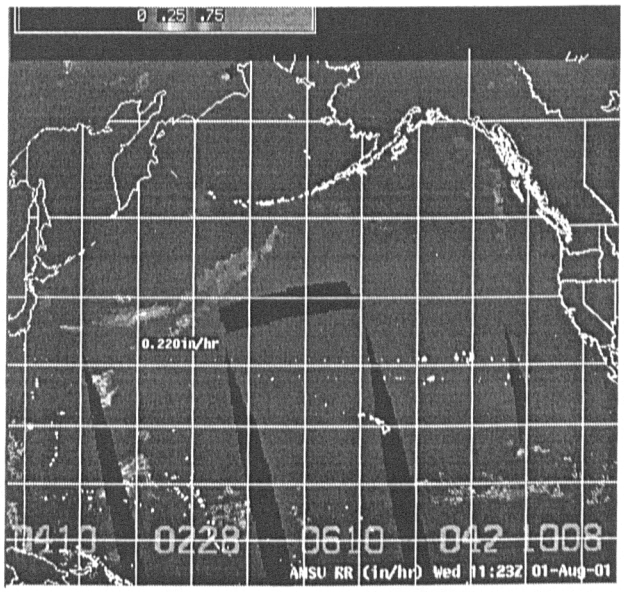

Figure 3. NOAA-15/AMSU rain rate product.

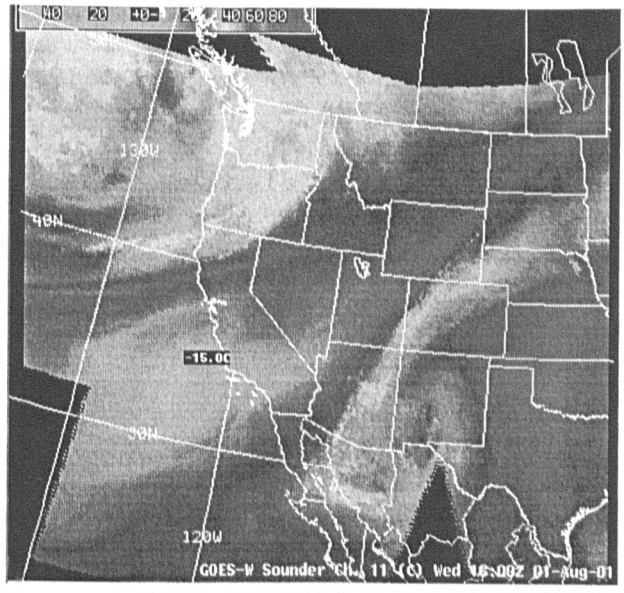

Figure 5. GOES-10 sounder channel 10 image.

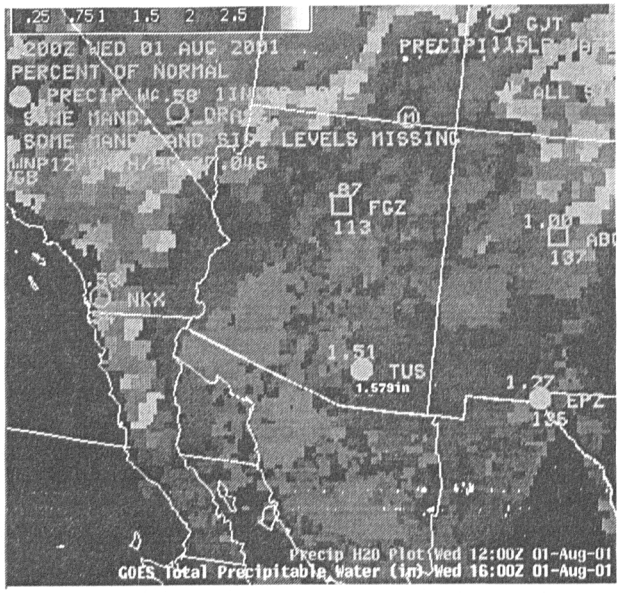

Figure 6. GOES TPW with RAOB Pws overlain.

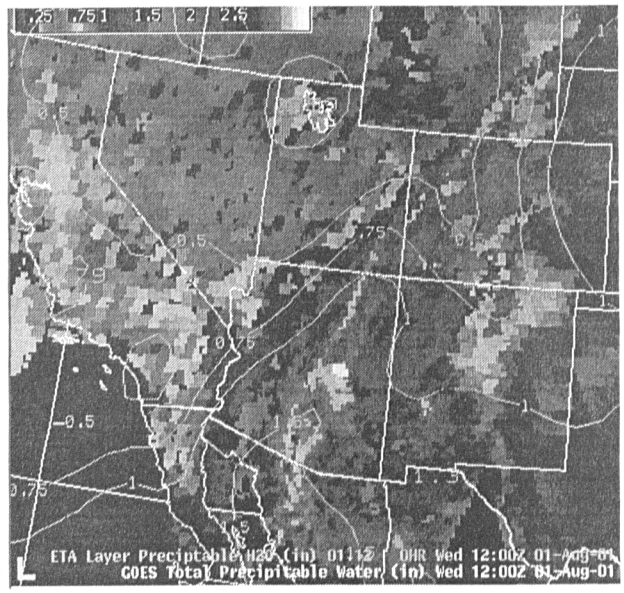

Figure 8. GOES TPW with ETA PW overlain.

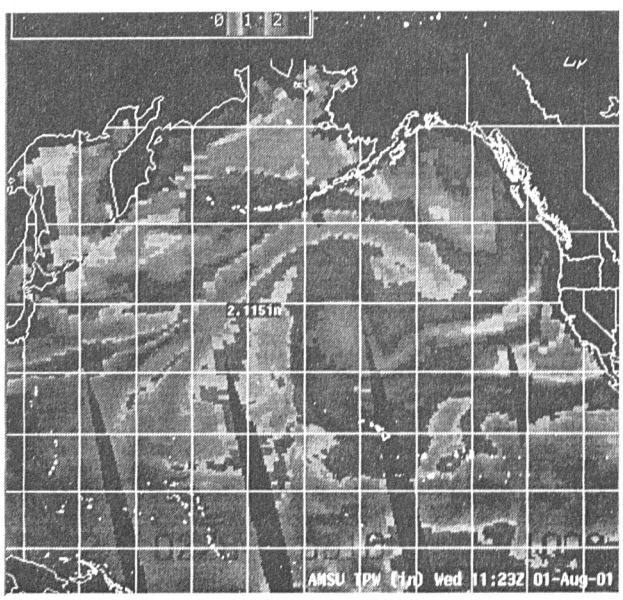

Figure 7. NOAA-15/AMSU TPW showing high PW plume entering the Gulf of Alaska.

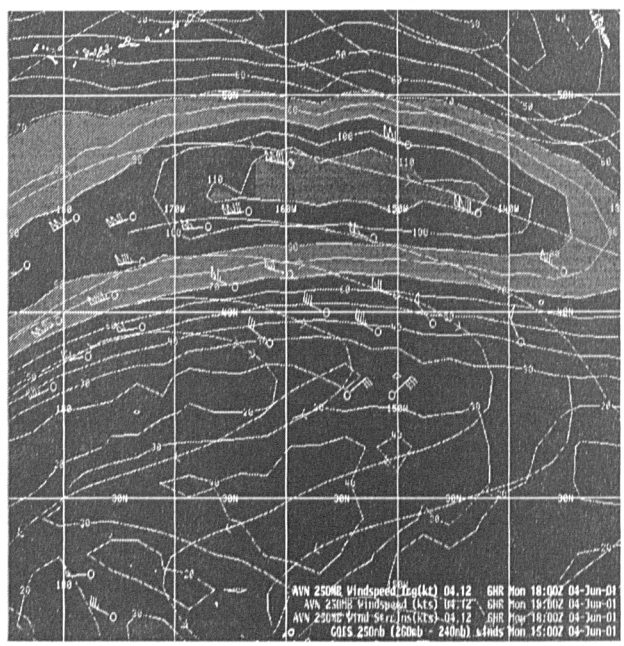

Figure 9. GOES high density winds overlain on AVN analysis, valid at 250mb.

P3.42 USE OF ATOVS AND SSMI OBSERVATIONS AT MÉTÉO-FRANCE

Florence Rabier *, Élisabeth Gérard
Météo-France, Toulouse, France
Zahra Sahlaoui, Mohamed Dahoui
Maroc-Météo,Casablanca, Morocco
Roger Randriamampianina
Hungarian Meteorological Service, Budapest, Hungary

1 INTRODUCTION

Preprocessed NOAA-15 radiances from NESDIS are currently being used in the four-dimensional variational (4DVar) assimilation system of ARPEGE, the global numerical weather prediction model operational at Météo-France. The current analysis scheme consists of applying a one-dimensional variational (1DVar) assimilation system to the pre-processed radiances to obtain quality control flags, vertical profiles of temperature and humidity and surface temperature. The radiances are then injected into 4DVar together with the surface temperature and the retrieved profiles above the top of the model (5 hPa). More details are to be found in Rabier *et al.* (2001). As a first illustration of the use of ATOVS data at Météo-France, the impacts on analysis and forecast of additionally using NOAA-16 data will first be presented (Section 2). Then the potential benefit of using locally received ATOVS data for mesoscale applications will pe pointed out in Section 3. NESDIS preprocessed data undergo a number of significant preprocessing steps,i.e. limb correction, emissivity adjustement, instrument collocation. Some of these steps introduce complicated random and systematic errors in the data that are not present in the raw radiances. With the advanced data assimilation schemes such as 4DVar many of the preprocessing steps can be bypassed and consequently more information is expected to be extracted from the data. The assimilation of ATOVS raw radiances at Météo-France is under investigation; the first results are presented in Section 4. Another development at Météo-France concerns the experimental assimilation of total column water vapour and surface wind speed over the ocean derived from the SSM/I one-dimensional variational (1DVar) scheme developed at ECMWF. The model fit to other observations and the impacts of both retrieved products on analysis and forecast will be presented in Section 5. All experimental assimilations are performed using a model with a quadratic troncature of 199 wavenumbers, 31 hybrid coordinate vertical levels from the surface up to about 5 hPa and a spherical geometry with France as the pole (stretching factor of 3.5), i.e. 19 km horizontal resolution over France and 234 km at the Antipodes.

* Corresponding author address : CNRM/GMAP, Météo France, 42 av. G. Coriolis, F-31057 Toulouse Cedex, email=Florence.Rabier@meteo.fr

2 ADDITION OF NESDIS NOAA-16 DATA

Since 21 May 2001 NOAA-16 data are operationally processed at NESDIS and received at Météo-France. An experimental assimilation and forecast suite has been run from the operational configuration to assess to which extent these new data are beneficial to the model. Bias correction coefficients for NOAA-16 data have been computed following the method developed in Harris and Kelly (2001) which contains a dual bias correction with respect to the scan position as well as to the air-mass similarly to what is done for NOAA-15 data. The assimilation of NOAA-16 data on top of NOAA-15 data was found to behave better than the assimilation of NOAA-15 data only on a 19-day period in July 2001, especially in the medium-range as illustrated by the difference in 300 hPa geopotential height performance at day 4 in Figure 1.

3 USE OF ATOVS LOCALLY RECEIVED DATA

The Spatial Meteorological Centre (CMS) of Météo-France in Lannion (France) produces pre-

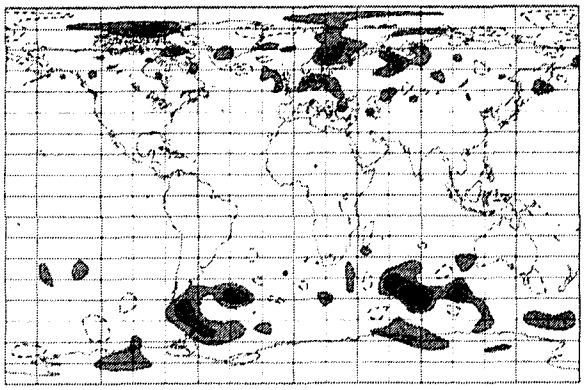

Figure 1: 300 hPa geopotential height difference between the 96-hour forecast root-mean-square error from the experiment with only NOAA-15 ATOVS data and from the experiment with NOAA-15 and NOAA 16 ATOVS data, averaged over 19 days of assimilation (1-19 July 2001). Contour interval is 10 m. Shaded surfaces represent positive differences greater than 10 m, showing a significant improvement brought by NOAA-16 data.

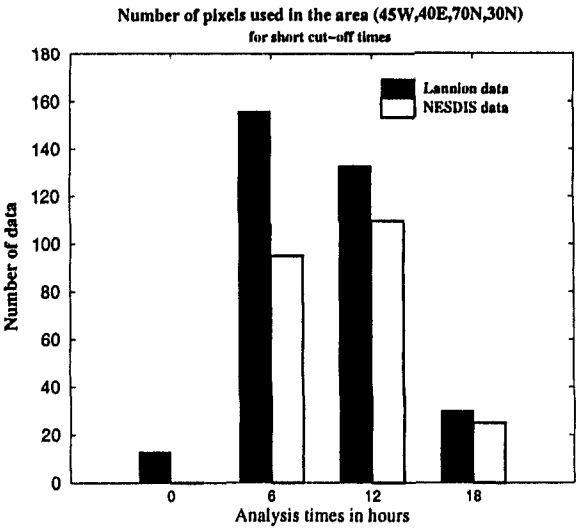

Figure 2: Comparison of the number of AMSU-A data used in the "Lannion" area for short analysis cut-off times, received from NESDIS and Lannion, as a function of the analysis time. This number of data is averaged over six days in May 2001.

processed ATOVS radiances on the West-European area (45°W,30°N,40°E,70°N) from HRPT data, encodes them and transmits them in real-time to Toulouse. Thus, these data are available with a short time-delay. An illustration of the number of data potentially used in our system compared to NESDIS preprocessed radiances in the same area is provided in Figure 2 for the four analysis times. Cut-off times are as short as 1h50 after the analysis times at 0 and 12 UTC, as opposed to 3h at 6 and 18 UTC. Preliminary assimilation experiments show a slight positive improvement in forecast performance over the European area in the short-range.

4 USE OF ATOVS RAW RADIANCES

The assimilation of ATOVS raw radiances without collocation and 1DVar inversion is currently under investigation. Major developments in that respect concern the extrapolation of model fields above the top of the model as an input to the radiative transfer model, the radiance bias correction, the optimal density of observations and the quality control.

The radiative transfer code currently being used (RTTOV, Saunders *et al.* 1998) requires the vertical temperature on 43 pressure levels. Under the top of the model, profiles are interpolated to RTTOV pressures levels. Above the top of the model (about 5 hPa) an extrapolation of the profiles using a regression algorithm (Clément Chouinard, personal communication) which extrapolates the departure from a reference profile (see Figure 3) has been tested. Regression coefficients are obtained using statistics over a dataset based on rockets, satellite and perfect gas theory.

An horizontal thinning is performed to ensure a minimum distance of about 200 km between observations. Cloud and precipitation detection is necessary as in the first case temperature and humidity information cannot be extracted from the cloud contaminated infrared HIRS measurements and in the second case lower microwave channels are too sensitive to rain to be used in presence of precipitation in the field of view. The detection is done by comparing the observed to the background radiances in HIRS window channel 8 and channel 12 for cloud detection and in AMSUA-4 window channel radiance. Bias correction coefficients have been computed following the method developed in Harris and Kelly (2001).

The assimilation of raw radiances was found to behave better than the assimilation of preprocessed radiances on a 11-day period in April 2001, especially in the medium-range as illustrated by the difference in

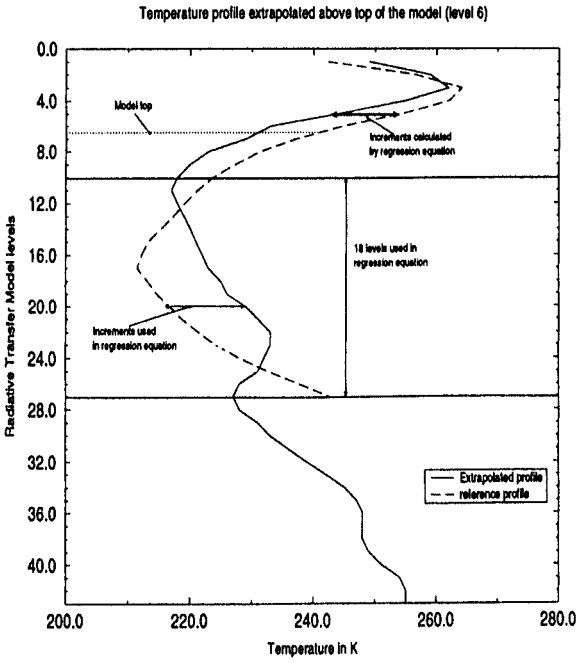

Figure 3: Extrapolation of the the temperature profile above the top of the model.

300 hPa geopotential height performance at day 4 in Figure 4. On a global scale raw radiances enable the 300 hPa geopotential height forecast rms error to be reduced by about 3.3% (1.9 m absolute difference). In this experiment only AMSUA from NOAA15 have been used, as HIRS instrument on board the same platform encountered some technical problems. Further experiments will be performed with both instruments and both available satellites (NOAA-15 and NOAA-16).

5 USE OF SSM/I DATA

Experimental assimilation of total column water vapour (TCWV) and surface wind speed (SSWS) over the ocean, derived from the 1DVar inversion (see Phalippou (1996) for description of the method developed at ECMWF and Gérard and Saunders (1999) for assimilation of TCWV at ECMWF) has been investigated at Météo-France. An horizontal thinning of the 1DVar products has been performed, i.e. 250 km for TCWV and 125 km for SSWS. The observation errors are derived from the 1DVar error covariance matrix and are such that an equivalent global weight is given to both model and observations between extreme values, whereas the TCWV observation errors are higher than the model errors below 10 kg m^{-2} and above 60 kg m^{-2} and the weight given to SSWS observations is weaker for SSWS lower than 6 m s^{-1} and higher for values above 12 m s^{-1}.

Assimilation experiments of these data over a two week period (1-15 January 2000) have been performed together with a control run where no SSM/I data is used. These experiments show a global moistening of the model analysis in the Northern Hemisphere (1.5% increase), in the Southern Hemisphere (2.2% increase) and in the Tropics (0.9% increase), as shown in Figure 5.a. However a drying is to be noticed in the dry tongues located off the western coasts of subtropical continents. Moreover a better coherence between first guess and analysis is noticeable as these data help to reduce the global difference between first guess and analysis. As for the assimilation of SSWS, it tends to strenghten the analysis surface wind speed in the Tropics (1.4% increase), in the Southern Hemisphere (1.2% increase) and in the Northern Hemisphere (1.1% increase), as shown in Figure 5.b. Moreover, the SSM/I data seem to be beneficial to the reproduction of cyclone intensity and position. Even though the effect of assimilating SSM/I TCWV and SSWS remains in the forecasts for up to 96 hours, no significant impact is seen in the mean forecast performance.

6 SUMMARY AND PERSPECTIVES

Several experiments were performed investigating the impact of satellite data in the French global model. NOAA-16 preprocessed radiances from NESDIS were found to have a positive impact on forecast performance on top of NOAA-15 data. ATOVS raw radiance assimilation experiments also showed some improvements in the quality of the subsequent forecasts. To improve the analysis scheme, some tunings are necessary, especially for observation error, surface skin temperature error and thresholds used for cloud and precipitation detection. It is also more appropriate to calculate regression coefficients used in extrapolation for different latitudes. Work will be continuing in this area, until operational implementation. Other topics of interest are the assimilation of locally received ATOVS radiances and of SSM/I data.

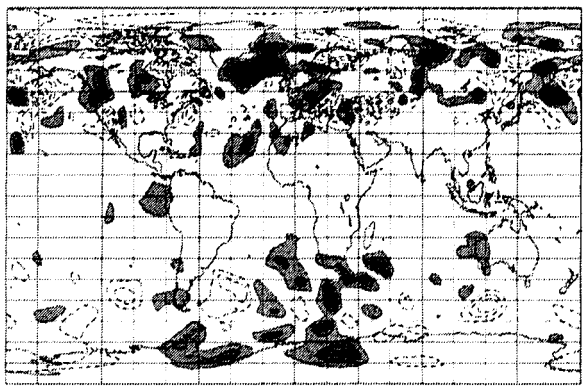

Figure 4: 300 hPa geopotential height difference between the 96-hour forecast root-mean-square error from the experiment with ATOVS preprocessed data and from the experiment with ATOVS raw radiances, averaged over 11 days of assimilation. Contour interval is 10 m. Shaded surfaces represent positive differences greater than 10 m, showing a significant improvement brought by the raw radiances.

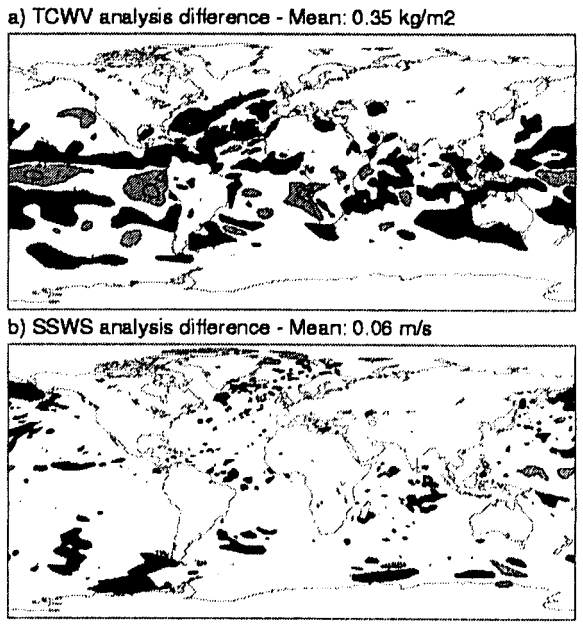

Figure 5: (a) TCWV and (b) SSWS analysis differences between the experiment with SSM/I data and the experiment without. Units are in (a) kg m^{-2} and (b) m s^{-1} and mean difference values are indicated at the top of each panel. Contour lists are -3/-1/1/3 kg m^{-2} for TCWV (a) and -0.8/-0.4/0.4/0.8 m s^{-1} for SSWS (b). Dark shaded surfaces represent positive differences, light shaded surface represent negative differences.

REFERENCES

Gérard, E. and Saunders, R., 1999 : Four-dimensional variational assimilation of Special Sensor Microwave/Imager total column water vapour in the ECMWF model, *Q. J. R. Meteorol. Soc.*,**125**, 3077–3101

Harris, B.A. and Kelly, G., 2001 : Satellite radiance bias correction scheme for radiance assimilation, *Q. J. R. Meteorol. Soc.*,**127**, 1453–1468

Phalippou, L., 1996 : Variational retrieval of humidity profile, wind speed and cloud liquid water path with the SSM/I: Potential for numerical weather prediction, *Q. J. R. Meteorol. Soc.*,**122**, 327–355

Rabier, F., Puech, D. and Benichou, H., 2001 : Monitoring and assimilation of ATOVS data at Meteo-France. Proceedings of the Eleventh International TOVS Study Conference, Budapest, Hungary. 20th-26th September 2000. Ed. J. Le Marshall, Bureau of Meteorology, Melbourne, Australia

Saunders, R.W., Matricardi, M. and Brunel, P., 1999 : An improved fast radiative transfer model for assimilation of satellite radiance observations, *Q. J. R. Meteorol. Soc.*,**125**, 1407–1426

P3.44 A PHYSICALLY-BASED ALGORITHM TO DERIVE SURFACE RAINFALL RATE USING ADVANCED MICROWAVE SOUNDING UNIT-B (AMSU-B) MEASUREMENTS

Limin Zhao [*1, 2], Fuzhong Weng[1] and Ralph Ferraro[1]

[1]*NOAA/NESDIS/ORA/Office of Research & Applications, Camp Springs, MD*

[2]*QSS Group, Inc, Lanham, MD*

1. INTRODUCTION

Many satellite precipitation algorithms utilize scattering signatures from cloud ice to retrieve rainfall rate (e.g., Adler et al., 1993; Petty, 1994; Grody, 1991). The scattering index (*SI*) is a measure of temperature depression due to the presence of ice particles in clouds. The scattering index ~ rain rate relationship is usually obtained by calibrating the *SI* with surface radar data under certain conditions (Ferraro and Marks, 1995). The *SI* ~ rain rate relationship, therefore, is sensitive to the ground truth data used and the sensitivity of scattering index to precipitation intensity varies within a broad range for different types of precipitation events (Bennartz and Petty, 2000). In addition, the retrieval accuracy is also affected by the temporal and spatial mismatch between the two data fields.

Due to its sensitivity to light rain and high spatial resolution, the AMSU-B 150 GHz on board both the NOAA-15 and NOAA-16 provides a dramatic ability to detect surface rainfall, especially for light rain (Ferraro et al., 2000). Zhao and Weng (2001) developed an algorithm to simultaneously derive cloud ice water path (*IWP*) and ice particle effective diameters (D_e) using AMSU-B measurements at 89 and 150 GHz. It was found that the AMSU-B derived *IWP* and D_e strongly correlated with the features of surface rainfall in many storm cases.

In this study, an attempt is made to derive the surface rainfall rate based on the retrieved *IWP* and D_e. Cloud model simulations (from MM5 and NASA GPROF database) are used to provide guidance to derive physically meaningful *IWP* ~ surface rainfall relationships. More detailed studies are ongoing to explore various relationships between the ice water path and the surface rain rate with an ice particle size as a parameter.

2. Methodology

2.1 *IWP and D_e Retrievals*

The ice cloud scattering parameter, Ω, is defined as

$$\Omega(\mu) = \frac{\kappa\tau}{2a} = \frac{1}{2\mu}(1-\omega g)\tau \qquad (1)$$

with a two-stream approximation. Here, τ is the ice cloud optical thickness, κ the eigenvalue, a the similarity parameter, μ the cosine of the zenith angle (Weng and Grody, 2000). When the brightness temperature emanating from the ice cloud top, $T_B(z_t, \mu)$, and that at the cloud base, $T_B(z_b, \mu)$ are known, the ice scattering parameter can further be estimated with,

$$\Omega(\mu) = \frac{T_B(z_b,\mu) - T_B(z_t,\mu)}{T_B(z_t,\mu)}. \qquad (2)$$

where z_t and z_b are the heights of the cloud top and base, respectively. The brightness temperature in Eq. (2) decreases as the scattering parameter, Ω, increases. Variation of the scattering parameter results from changes in the cloud ice water path and particle size. The ice water path, therefore, can be related to Ω through the following equation,

$$IWP = \mu\bar{\rho}_i D_e \frac{\Omega}{\Omega_N}, \qquad (3)$$

where D_e is the ice particle effective diameter; $\overline{\rho_i}$ is the ice particle bulk volume density averaged for ice cloud particles with the size distribution. Note that both *IWP* and D_e are related to the ice particle scattering parameters, which can be determined from the AMSU 89 and 150 GHz measurements. The ratio of the scattering parameters measured at two frequencies provides a direct estimate of D_e. Then, the *IWP* is proportional to D_e and ice particle scattering parameters with a given ice particle bulk volume density.

Assuming a modified Gamma size distribution (Ulbrich 1983) and a constant ice particle bulk volume density, we derived two relationships of D_e ~ r and Ω_N ~ D_e as follows,

$$D_e = a_0 + a_1 r + a_2 r^2 + a_3 r^3, \qquad (4)$$

$$\Omega_N = exp\,(b_0 + b_1\, ln(D_e) + b_2\, (ln(D_e))^2), \qquad (5)$$

where $r = \Omega_{89}/\Omega_{150}$ is the scattering parameter ratio; a_i (i=0,1,2,3) and b_i (i=0,1,2) are the regression coefficients that are dependent on the ice particle bulk density and size distribution. Given the ice particle bulk volume density, *IWP* and D_e can be uniquely determined from Eqs. (1), (3), (4) and (5) with satellite measurements from two frequencies (Zhao and Weng).

2.2 *IWP ~ Rain Rate Relationship from Cloud Model Simulations*

* *Corresponding author address*: Limin Zhao, NOAA/NESDIS, WWB 703F, 5200 Auth Road, Comp Springs, MD 20746. e-mail: Limin.Zhao@noaa.gov.

In most precipitation systems, the rain layer extends above the freezing level, and contains a mixture of water and ice particles. Large scattering signatures due to precipitating ice particles have been observed from satellite at frequencies as low as 37 GHz (e.g., Spencer et al. 1983). Depending upon the cloud microphysics and vertical velocities, the size and density of these ice particles will vary. Ice water generated by deep convection usually reflects the strength of the convection and the stage in the life cycle of the convective cloud.

The AMSU-B 89 and 150 GHz channels respond primarily to ice-phase hydrometers. They saturate very quickly with liquid water in the column and then tend to decrease as ice concentration increases. If we assume that the high variability of rainfall on the ground is related to the high variability of ice content, the 89 and 150 GHz channels are expected to have the ability to measure this variability and provide a good rainfall estimate.

Cloud model simulations (from both MM5 and NASA GPROF database) are studied and used to derive *IWP* ~ surface rainfall relationships. Fig.1 shows the *IWP* ~ rain rate relationship derived based on the MM5 cloud model, which serves as the first step toward the development of a useful *IWP* ~ rain rate algorithm.

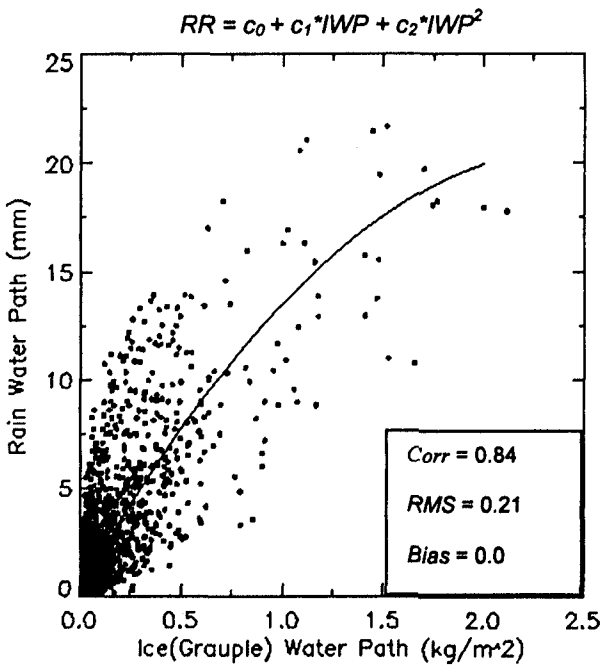

Figure 1. The IWP ~ rain rate relation based on MM5 cloud model simulations.

The scattering signatures resulting from desert sand, sea ice and surface snow particles at higher microwave frequencies are quite similar to that of the ice particles because the dielectric constants among these scatterers are almost the same. For global applications, the algorithms must be able to distinguish an individual scattering feature among a wider range of surface and precipitation conditions.

Due to the difficulties to distinguish the ice clouds from the surfaces, no retrievals are conducted over surfaces covered by snow and sea ice. AMSU-A snow cover and sea ice concentration products are used to indicate the presence of snow and sea ice. Furthermore, there is no retrieval over high terrains such as Tibetan plateau where the surface temperatures usually are colder than 273 °K. A detailed screening method has been discussed in Zhao and Weng (2001). In addition, the method to remove the non-precipitating ice clouds is essential for a useful *IWP* ~ rain rate relationship. The AMSU-B rain rate algorithm, including the screening procedure, is summarized in Fig. 2.

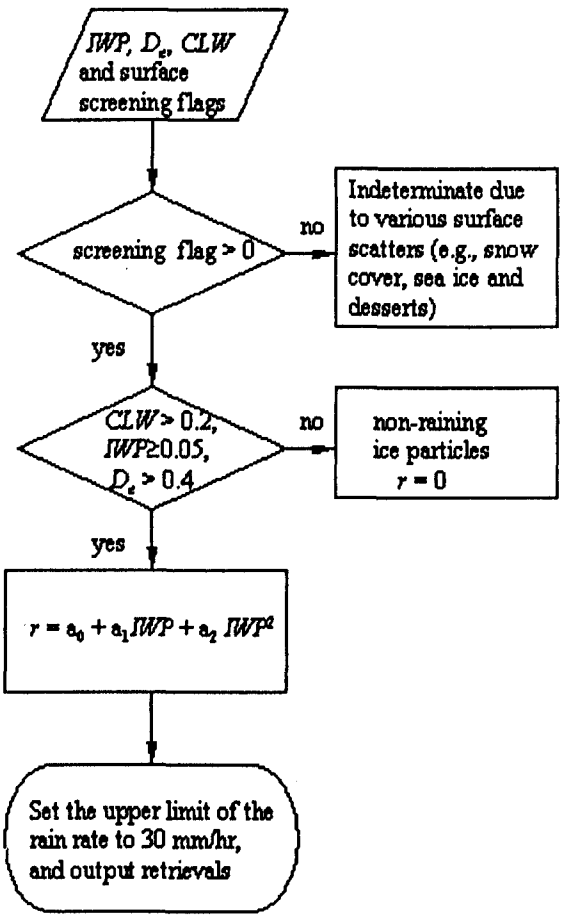

Figure 2. The Flow Diagram of the AMSU-B rain rate algorithm.

3. VALIDATION

3.1 Data Source

To validate the AMSU-B instantaneous rainfall rate, the NCEP multi-sensor hourly rainfall estimates (NEXRAD and rain gauge composite products), is used for ground truth over land (Seo, 1998).

The AMSU-B rain rate data are projected into the NCEP hourly precipitation analysis domain (~15km) with the same set of map projection parameters. Considering that each satellite sampling point represents a mean value of its FOV, a simulated FOV is used and the AMSU-B rain rate estimate at each corresponding beam position is used to fill the area of the FOV projected in the map plane. Then the NCEP multi-sensor hourly rainfall data that are the closest to AMSU-B observation time are selected. By doing so, a grid-to-grid match-up between NCEP multi-sensor hourly rainfall data and AMSU-B rainfall estimates is generated. Various statistics are computed between the AMSU-B rainfall estimates and that of the NCEP Stage-IV hourly rainfall estimates.

SSM/I and rain gauge monthly mean are also used to validate the corresponding AMSU-B monthly mean, and to check out its global features.

3.2 Instantaneous Rainfall Rate

Figure 3 shows the AMSU-B rainfall estimates validated against with the NCEP multi-sensor hourly rainfall in April 24, 2001. Note that the AMSU-B algorithm shows a great ability to delineate the raining area. The rainfall intensity structure of the squall line is well retrieved; although the location of the maximum of AMSU-B retrieved rainfall rate does not correspond exactly to that of the NCEP rainfall. This dislocation may be caused by the time difference between the satellite measurements and NCEP rainfall data. In particular, the retrieved *IWP* represents an instantaneous observation whereas NCEP rainfall data is a cumulative estimate during an hour period.

The AMSU-B derived rainfall rate is generally higher than that of radar estimates. A likely explanation is that the radar rain rates may be underestimated due to inaccuracies in the Z-R relationships; to attenuation effects; or to the difficulties in precipitation at large distances. It is worthwhile to mentioning that the WSR-88D radar also has difficulty detecting precipitation when rain drops are very small or when the precipitation is in the form of snow. Under these conditions radar precipitation rate may be underestimated. Large hail within a storm also can cause the radar to overestimate precipitation amounts. Hence, we feel that the uncertainties in the radar estimates are comparable to that of the satellite.

Based on the comparison of the distribution of zonal and longitudinal mean, and the rain frequency in latitudinal and longitudinal bands, we found that although there are some differences in the two observations, AMSU-B rainfall estimates agree very well with its NCEP Stage-IV counterpart. An intensive validation study of the AMSU-B rain rate algorithm over land is going.

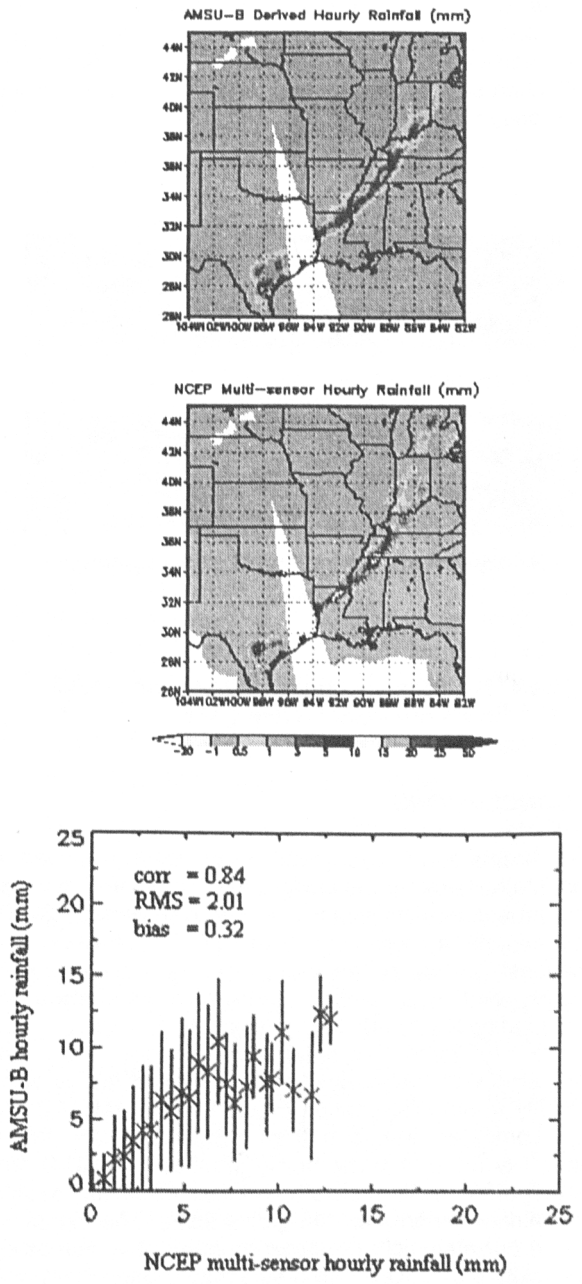

Figure 3. The AMSU-B rainfall estimates validated With NCEP Stage-IV hourly rainfall estimate In April 24, 2001.

3.3 Monthly Rain Rate

The monthly mean rainfall comparisons are also performed between AMSU-B and SSM/I and rain gauge data. The data were binned in 2.5 by 2.5 degree longitude-latitude grid boxes for the latitudinal band between 50S and 50N. Figure 4 shows the comparison of monthly mean rainfall between AMSU-B and SSM/I. Generally, AMSU-B rain rate algorithm provides a larger raining area and higher rainfall intensity compared to

SSM/I, which might be due to the increasing sensitivity of AMSU-B 150 GHz scattering to small ice particles, and therefore high capability to detect light rain. More validation studies are needed to confirm this, especially over ocean.

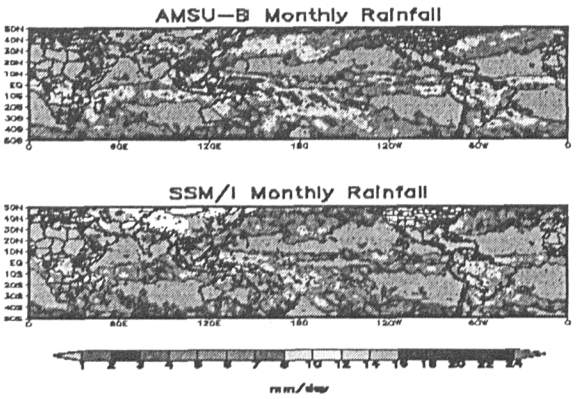

Figure 4. The comparison of monthly mean rainfall between AMSU-B and SSM/I.

4. CONCLUSIONS

In this study, a physical approach is proposed to quantitatively relate the surface rainfall rate to ice water amount and particle size that are derived from AMSU-B. The algorithm consists of an *IWP* ~ rainfall rate relationship that is derived based on cloud model results, and a screening method to separate non-precipitating ice clouds from precipitating ones.

The retrieved instantaneous rainfall rate are compared with that derived from radar and gauge data. Monthly mean precipitation products from AMSU-B are also compared with that from SSM/I and rain gauge data. It is found that the newly proposed AMSU-B rain rate algorithm well depicts both localized rainfall events and rainfall patterns on the global scale. The algorithm is able to detect light precipitation due to the increasing sensitivity of AMSU-B 150 GHz scattering to smaller ice particle sizes in the rain layer.

For a more accurate retrieval of rain rate, it might be better to group ice clouds into several classes so that separated *IWP* ~ rain rate relationships can be derived and used for different type of rain scenarios, such as, stratiform and convective type. Further improvement of the algorithm is ongoing toward this direction.

Acknowledgments. We sincerely thank Sheldon Kusselson at NESIDS/SAB for his efforts on evaluating the early algorithm and providing us invaluable inputs that leads to remarkable improvements on the algorithm. Thanks also go to Huan Meng for her help on implementing and testing the algorithm on the MSPPS system.

Reference

Adler, R. F., A. J., Negri, P. R. Keehn, and I. M., Hakkarinen, 1993: Estimation of monthly rainfall over Japan and surrounding waters from a combination of low-orbit microwave and geosynchronous IR data. *J. Appl. Meteor.*, **32**, 335-356.

Bennartz, R. and G. W. Petty, 2001: The sensitivity of microwave remote sensing observations of precipitation to ice particle size distributions. *J. Appl. Meteor.*,**40**, *345-364.*

Ferraro, R. R. and G. F. Marks, 1995: The development of SSm/I rain-rate retrieval algorithms using ground-based radar measurements. *J. of Atmos. and Ocean Tech.*, **12**, 755-770.

Grody, N. C., 1991: Classification of snow cover and precipitation using the Special Sensor Microwave/Imager (SSM/I). *J. Geophys. Res.*, **96**, 7423-7435.

Seo, D.J., 1998: Optimal estimation of rainfall fields using radar rainfall and rain gauge data. *Journal of Hydrology.* **208**, 37-52.

Ferraro, R.R, F. Weng, N.C. Grody and L. Zhao, 2000: Precipitation characteristics over land from the NOAA-15 AMSU Sensor. *Geophysical Research Letters*, **27, No. 17**, 2669-2672.

Petty, G. W., 1994: Physical retrieval of over-ocean rain rate from multichannel microwave imagery. Part 2: Algorithm implementation. *Meteor. Atmos. Physi.*, **54**, 101-121.

Spencer, R. W., S. Olson, W. Rongzhong, D. W. Martin, J. A. Weinman, and D. A. Santek, 1983: Heavy thunderstorms observed over land by the Nimbus-7 Scanning Multichannel Microwave Radiometer, *J. Appl. Meteor.*, **22**, 1041-1046.

Ulbrich, C. W., 1983: Natural variations in the analytical form of the raindrop size distribution. *J. Climate Appl. Meteor.*, **22**, 1764-1775.

Weng, F. and N. Grody, 2000: Retrieval of ice cloud parameters using a microwave imaging radiometer. *J. Atmos. Sci.*, **57**, 1069-1081.

Zhao, L. and F. Weng, 2001: Retrieval of ice cloud parameters using the Advanced Microwave Sounding Unit (AMSU). Submitted to *J. Appl. Meteor.*

P3.45 IMPROVEMENTS TO THE EXPERIMENTAL TROPICAL RAINFALL POTENTIAL (TRaP) TECHNIQUE

Stanley Q. Kidder*[,1], Sheldon J. Kusselson[2], John A. Knaff[1], and Robert J. Kuligowski[3]

[1]CIRA/Colorado State University, Fort Collins, Colorado
[2]NOAA/NESDIS/Satellite Services Division, Camp Springs, Maryland
[3]NOAA/NESDIS/ORA, Camp Springs, Maryland

1. INTRODUCTION

As discussed by Kidder et al. (2001), heavy rainfall from landfalling tropical cyclones is a major threat to life and property. Rappaport (2000) found that in the contiguous United States during the period 1970–1999, freshwater floods accounted for more than half of the 600 deaths directly associated with tropical cyclones.

Forecasting rainfall from landfalling tropical cyclones is a difficult task. While the storm is offshore, few rainfall observations are possible, and initializing NWP models with sufficient details of the storm so that accurate rainfall forecasts can be made is extremely difficult. Radar observations of storm rain rate and rain area are valuable, but only when the storm is within radar range of the coast.

Since 1992, the Satellite Services Division (SSD) of the National Environmental Satellite, Data and Information Service (NESDIS) has experimentally used the operational Defense Meteorological Satellite Program (DMSP) Special Sensor Microwave Imager (SSM/I) rain rate product (Ferraro 1997) to produce a rainfall potential for tropical disturbances expected to make landfall within 24 hours. The launch in 1998 of the first Advanced Microwave Sounding Unit (AMSU) on the NOAA-15 satellite provided an additional rainfall data source.

The NESDIS/SSD technique (Kidder et al. 2000) was performed manually by an analyst and resulted in a single number called the tropical rainfall potential, defined as

$$\mathrm{TRaP} = R_{av} D V^{1}, \qquad (1)$$

where R_{av} is the average rainfall rate of the storm, D is the diameter of the storm, and V is the speed of the storm. Kidder et al. (2001) attempted to improve the technique by automating it and by calculating the rainfall at every point in an image, so that the location as well as the amount of the precipitation could be estimated. A similar but not identical method is now initiated by NESDIS/SSD analysts to calculate TRaP images.

The TRaP technique of Kidder et al. (2001) is described in Section 2. For the 2001 western hemisphere hurricane season, the TRaP technique has been further improved. These improvements are described in Section 3. The results of the improved technique for the one case which has occurred as of this writing (Tropical Storm Allison) are presented in Section 4. Conclusions are the subject of Section 5.

2. 2000-SEASON TRaP TECHNIQUE

The TRaP technique starts with a satellite-based observation of rain rate. The Cooperative Institute for Research in the Atmosphere (CIRA) uses rain rates from the AMSU instrument produced by the NESDIS Atmospheric Research and Applications Division Hydrology Team (Ferraro et al. 2000). SSD also uses the technique with rain rates from the DMSP SSM/I and the operational NESDIS Auto-Estimator (Vicente et al. 1998).

To make the technique work properly, the time of observation of the storm must be known. CIRA uses the Tropical Prediction Center (TPC) track forecast, together with the observed storm positions and the satellite ephemeris calculated from the orbital elements, to precisely calculate the time when the satellite observed the center of the storm. Next, a cubic spline interpolation of the position of the storm center every 15 min throughout the 6-h or 24-h forecast period is calculated as well as the cubic spline position of the storm at the time of the satellite observation. At every point in the output image, the rainfall is calculated as

$$\text{accumulated rainfall} = \int_{t_1}^{t_2} R(t)\,dt \qquad (2)$$

It is assumed (1) that everything in the rain rate image is accurate, invariant in time and moves with the storm center and (2) that the forecast track does a reasonably good job of depicting the

*Corresponding author address: Stanley Q. Kidder, CIRA, Colorado State University, Fort Collins, CO 80523-1375; (970) 491-8367; kidder@cira.colostate.edu.

future track of the cyclone. $R(t)$ is calculated by picking out in the rain rate image the point which will be over the station at time t. All calculations are performed on a Mercator map grid with 8 km resolution at the equator. Since everything moves with the storm, the calculation simplifies to applying a set of x-y offsets for each 15 min time period.

The TRaP calculation has been entirely automated at CIRA. Triggered by receipt of a track forecast fom TPC's Automated Tropical Forecasting System (ATCF; Sampson and Schrader 2000), the AMSU rain rate data are accessed, and the TRaP forecasts are made.

As reported by Kidder et al. (2001) the automated TRaP technique appeared promising.

3. 2001-SEASON IMPROVEMENTS

The TRaP technique has been improved in three important ways. First, a second satellite (NOAA-16) carrying the AMSU instruments has been launched. This approximately doubles the number of observations of a particular storm.

Second, the AMSU-B rain rates have been substituted for the AMSU-A rain rates used last year. Since the spatial resolution of the AMSU-B is three times as fine as that of the AMSU-A (16 vs. 48 km) and the same rain rate algorithm is used over land and ocean, TRaPs generated this year have better spatial information.

Third, we are attempting to receive track forecasts from all the world's oceans by accessing both the TPC and the Navy version of the ATCF so that more storms can be studied.

4. RESULTS

As of this writing, one landfalling tropical cyclone has occurred in the western hemisphere during the 2001 season: Allison, the most costly tropical storm in United States history (Fig. 1). Figure 2 shows the NOAA-16 AMSU-B rain rates at 0812 UTC on 5 June 2001 while the storm was in the western Gulf of Mexico. The storm was traveling toward the north-northwest at 8 kt. Figure 3 shows the results of the TRaP calculation for the 24-h period ending at 1200 UTC 6 June 2001.

The TRaP rainfall amounts were validated against Stage III raingauge-adjusted radar data (Fulton et al. 1998) that are produced operationally by the River Forecast Centers (RFCs), in particular, the West Gulf RFC and the Lower Mississippi RFC. The 24-h estimates corresponding to Fig.3 are shown in Fig. 4.

A comparison of Figs. 3 and 4 shows that even though the TRaP technique misplaced the location of the maximum rainfall, it did a credible job both of indicating the general location of the heavy rain threat area and of estimating the peak rainfall amount. (Note that CNN reported on 6 June 2001 that "a National Weather Service employee recorded 12 inches (30 centimeters) of rainfall in about six hours at his home in the western Galveston County city of Santa Fe," Texas.) As Allison came ashore, rain developed to the east of the storm, which accounts for the heavy rain that fell in southeast Louisiana.

5. CONCLUSIONS

The experimental TRaP estimates for Allison were transmitted by NESDIS/SSD to the National Weather Service's River Forecast Center at Fort Worth and the National Center for Environmental Prediction's Hydrometeorological Prediction Center and Tropical Prediction Center hours before the storm's landfall. We conclude that the improved TRaP technique could be of significant value to forecasters concerned with landfalling tropical cyclones. We continue to collect cases, and we will have further results at the conference in October.

Acknowledgments

The support of the National Oceanic and Atmospheric Administration through Contract No. NA67RJ0152 is gratefully acknowledged.

References

Ferraro, R. R., 1997: SSM/I derived global rainfall estimates for climatological applications. *J. Geophys. Res.*, **102**, 16,715–16,735.

Ferraro, R. R., F. Weng, N. C. Grody, and L. Zhao, 2000: Precipitation characteristics over land from the NOAA-15 AMSU sensor. *Geophys. Res. Lett.*, **27**, 2669-2672.

Fulton, R. A, J. P. Breidenbach, D. J. Seo, and D. A. Miller, 1998: The WSR-88D rainfall algorithm. *Wea. Forecasting*, **13**, 377-395.

Kidder, S. Q., M. D. Goldberg, R. M. Zehr, M. DeGrody, and S. J. Kusselson, 2000: Satellite analysis of tropical cyclones using the Advanced Microwave Sounding Unit (AMSU). *Bull. Amer. Meteor. Soc.*, **81**, 1241-1259.

Kidder, S. Q., J. A. Knaff, and S. J. Kusselson, 2001: Using AMSU data to forecast precipitation from landfalling hurricanes. *Symposium on Precipitation Extremes: Prediction, Impacts, and Responses.* American Meteorological Society, Boston, 344–347.

Rappaport, E. N., 2000: Loss of life in the United States associated with recent Atlantic tropical cyclones. *Bull. Amer. Meteor. Soc.*, **81**, 2065–2073.

Sampson, C. R., and A. J. Schrader, 2000: The automated tropical cyclone forecasting system (version 3.2). *Bull. Amer. Meteor. Soc.*, **81**, 1231-1240.

Vicente, G. A., R. A. Scofield, and W. P. Menzel, 1998: The operational GOES infrared rainfall estimation technique. *Bull. Amer. Meteor. Soc.*, **79**, 1983–1998.

Figure 1. The Interstate 45/Interstate 10 interchange north of downtown Houston on Saturday, 9 June 2001, after Tropical Storm Allison. [Courtesy of DallasNews.com.]

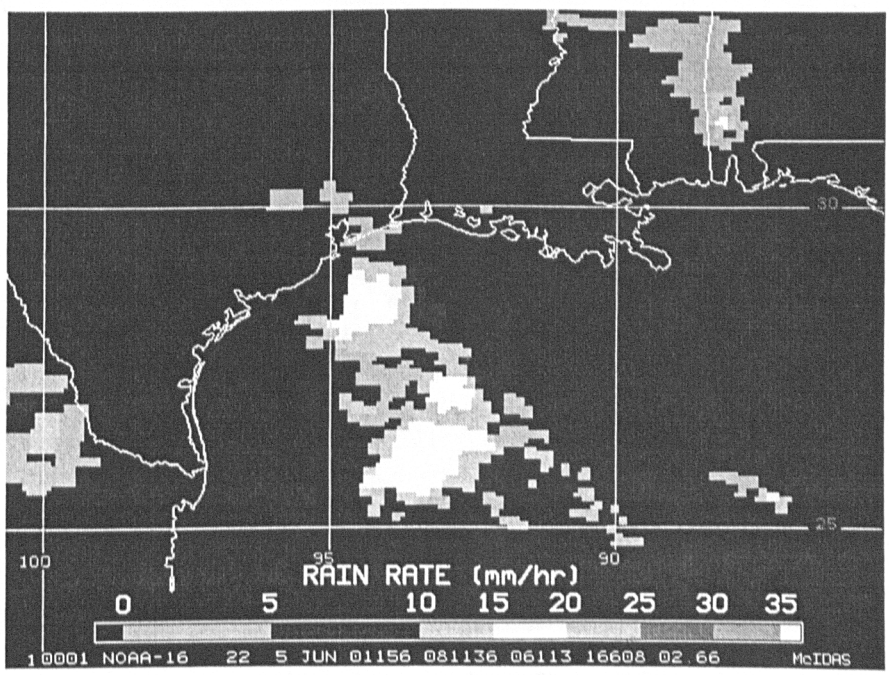

Figure 2. NOAA-16 AMSU-B rain rates for Tropical Storm Allison at 0812 UTC on 5 June 2001.

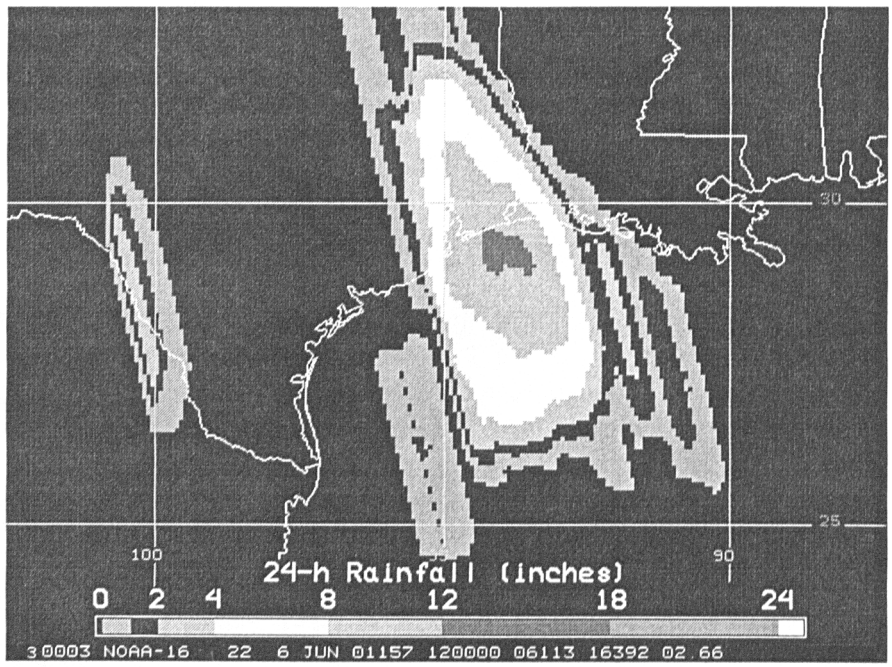

Figure 3. The 24-h TRaP for the period ending 1200 UTC on 6 June 2001. This image was created using the rain rates in Fig. 2. The peak 24-h rain amount is 12+ inches.

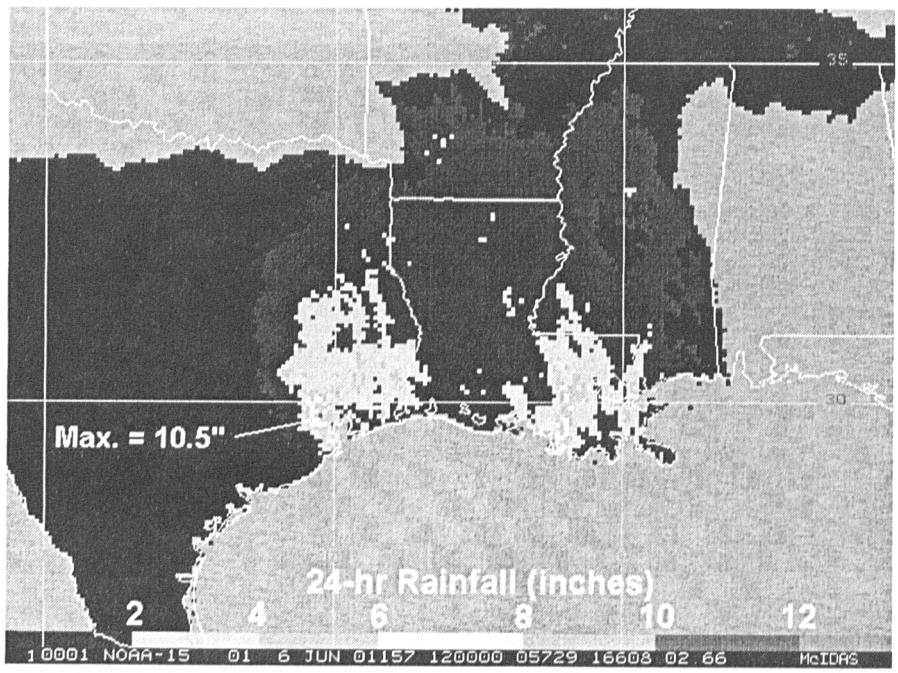

Figure 4. Stage III raingauge-adjusted radar rainfall estimates for the 24-h period corresponding to Fig. 3. Note that a NWS employee measured 12 inches at his home in Galveston County, Texas.

P3.46 VALIDATION OF GOES PRECIPITATION ESTIMATES OVER CENTRAL AMERICA

Rosario Alfaro *
NOAA/NESDIS/ORA/Hydrology Team
Camp Spring, Maryland 20746

Roderick A. Scofield
NOAA/NESDIS/ORA/Hydrology Team
Camp Spring, Maryland 20746

1. INTRODUCTION

According to a report of the National Meteorological Institute from Costa Rica (Alvarado 2001), 29 hurricanes have caused major disasters over the area during the past 30 years. The most recent, hurricane Keith, occurred by the end of September and the beginning of October, 2000. In addition, tropical waves and low pressure systems in the Caribbean basin near Central America, can also cause serious flooding comparable with that observed from hurricanes.

Central America's rain gauge network has been decreasing over the years and radar data is not available over the area. Therefore, GOES satellite data represent a valuable tool for warning purposes due to the high frequency and spatial resolution of the measurements.

This study is part of a regional effort to validate some satellite rainfall algorithms in order to use them to estimate precipitation over the region. Three precipitation algorithms have been used to estimates rainfall precipitation for hurricane Keith. The first one is the Auto-Estimator (AE), the second one is a modified version of it called the Hydro-Estimator (H-E) and the third is the GOES Multispectral Rainfall Algorithm (GMSRA).

The methodology and the data used in this study will be described in the next two sections. The results and a summary and discussion are addressed in sections 4 and 5.

2. METHODOLOGY

Hurricane Keith has been used in this study to validate the performance of three precipitation algorithms over the Central American region.

2.1. Auto-Estimator (AE)

Developed by Vicente et al (1998), this algorithm uses GOES channel 4 (10.7 um) brightness temperatures to generate precipitation estimates based on an empirical power-law regression function. Fields of precipitable water (PW) and relative humidity (RH) from the National Centers for Environmental Prediction (NCEP) Eta Model are used to determine a moisture correction factor (PWRH) suggested by Scofield (1987) in order to account for the effects of subcloud conditions on rainfall rates. The evolution of the cloud systems are considered in the cloud growth rate correction factor (when successive images are available) or the cloud-top temperature gradient correction factor (when successive images are not available). This latter factor is particularly useful during satellite eclipse periods. This algorithm also include an orographic correction (Vicente et al., 2001) and an Equilibrium Level (EQL) correction factor to take into account convection with warm tops (warmer than -58 °C) (Scofield 1987).

2.2. The Hydro-Estimator technique

This tecnique is a variant of the original AE (a manuscript is being completed regarding this technique). The cloud growth rate correction factor from the AE is not used in this algorithm. It uses a greatly expanded temperature gradient correction in order to screen out non-raining pixels, and considers the average brightness temperature and the standard deviation for a region centered on each pixel whose area depends on the precipitable water (PW) field. In this algorithm, the relative humidity is used as a separate factor. The orographic factor is the same as that used in the AE.

2.3. The GMSRA

This technique combines multispectral measurements of the GOES satellites to estimate rainfall (Ba and Gruber 2001). It uses different filters for rain-no rain screening. The visible imagery is used in the albedo filter, channel 4 (10.7 um) and the water vapor channel (6.7 um) are used to determine overshooting tops. IR channels 4 and 5 (12.0 um) and the 3.9 um channel are used to determine the effective radius of cloud particles. A threshold of 15 um is used as a low boundary to separate rain from non-raining pixels in warm cloud conditions. A PWRH and a growth correction factors similar to the AE's are applied to the rainfall fields.

2.4. Correction factors not applied for Keith

Due to lack of numerical model data and the region analyzed in this study, some correction factors could not be applied in the precipitation estimates over Central

* Corresponding author address: Rosario Alfaro, 5200 Auth Rd. WWB/601, Camp Springs, MD 20746; e-mail: Rosario.Alfaro@noaa.gov

America. Suitable numerical model grid data for the EQL and PWRH corrections were not available.

2.5. Comparisons

The validation of the satellite precipitation techniques for hurricane Keith were done based on comparisons of the satellite estimates with the only available "ground truth" data over the region: daily rain gauge measurements.
Comparisons between satellite and rain gauge data were done in two different ways in order to take into account the relatively large instrument footprints, navigation errors and errors in the rain gauge location. First, a rain gauge image was produced by assigning a rain gauge value in a radius of 1 pixel surrounding the rain gauges according to a weighted averaging in each pixel based on a cubic inverse distance as an interpolation method. Then, the first comparisons were done pixel by pixel between the rain gauge and the satellite images. The second comparisons were done by comparing each pixel of the rain gauge image with the 9 pixels surrounding it and centered in the rain gauge location. These comparisons were done between the Best Estimated Value (BEV) of the nine pixels surrounding the pixel being considered and the pixel itself (Vila et al. 2001).
Validation of the 2001 rainy season over the area is underway and uses daily and 6-hour precipitation totals. Results for year 2001 are not included in this paper.
The false alarm ratio (FAR) and the SKIL are slightly different from the standard definitions. They are defined by:

$$FAR = \frac{q_2}{q_3 + q_4} \qquad (1)$$

$$SKIL = 1 - \frac{1}{N}\sum \frac{|G_i - S_i|}{G_i + S_i} \qquad (2)$$

where G_i = rain gauge measurement, S_i = satellite estimate, q_2 = cases in which $G_i < 0$ and $S_i > 0$, q_3 = cases in which $G_i > 0$ and $S_i < 0$ and q_4 = cases in which both G_i and $S_i > 0$.

3. DATA SET

In this study, GOES-8 imagery from the all 5 image channels were used to calculate the GMSRA, the AE and the H-E estimates from September 30 to October 2nd, 2000, for Hurricane Keith. An orographic file of 10x10-km resolution with AVN model GRID files to obtain u and v wind components at 850 hPa were used to calculate the orographic correction factor used by the AE and the H-E algorithms.
Daily precipitation estimates were obtained using satellite images at 15 and 45 minutes of every hour between 13:15 UTC of one day to 12:45 UTC of the next day, beginning at 13:15 UTC, September 30. Missing images are due to satellite eclipse periods and correspond to images between 3:45 and 6:15 UTC of each day. In total, 42 images per day were used in the daily precipitation estimates.
Daily rain gauge data over Central America were the only "ground truth" reliable for validating the remotely sensed measurements of rainfall for this hurricane; the hourly precipitation network is too scarce to make reliable comparisons.
The validation data set corresponds to daily rain gauge data over Central America. The number of rain gauges used per country and day in this study are shown in Table 1. The approximate area of each country in square kilometers is also shown in the table.

Country	Area (km^2)	Sept 30	Oct 1	Oct 2
Belize	23000	22	21	21
Guatemala	110000	7	11	11
Nicaragua	128000	14	16	16
Costa Rica	51000	86	41	42
Panama	87000	11	12	12
TOTAL	339000	140	101	102

Table 1: Rain gauge data used in this study. Data are shown by country and day. The area of each country in square kilometers is shown in column 2.

4. RESULTS

Heavy rains produced significant damages and numerous deaths in Belize, Nicaragua, Honduras and Guatemala during hurricane Keith between 30 September and 2 October. The heaviest rains in Costa Rica were observed when the storm had not reached hurricane strength.
The validation of the three precipitation algorithms described previously are shown in the summary statistics within the following tables. Tables a) refer to a pixel-by-pixel comparison for each day and tables b) refer to comparisons done using the BEV, both mentioned in section 2.

Alg.	NUM	RMSE	BIAS	CC	POD	FAR	SKIL
AE	3292	90.51	53.42	0.15	0.49	2.04	0.33
GMSRA	3843	76.17	52.64	0.17	0.75	2.44	0.40
H-E	2668	33.48	6.87	0.25	0.42	0.84	0.39

Table 2a): Summary statistics for hurricane Keith. Results shown correspond to a weighted average for the whole event on September 30, 2000. Pixel by pixel comparisons are produced between the rain gauge image and its corresponding satellite estimate image.

Alg.	NUM	RMSE	BIAS	CC	POD	FAR	SKIL
AE	3034	76.74	45.3	0.16	0.68	1.71	0.41
GMSRA	3504	69.48	48.14	0.20	0.85	2.25	0.47
H-E	2321	27.34	0.99	0.29	0.55	0.45	0.50

Table 2b): Same as Table 2a). Comparisons between rain gauge image and BEV of the satellite estimate image.

Alg.	NUM	RMSE	BIAS	CC	POD	FAR	SKIL
AE	2849	144.23	100.5	0.51	0.85	0.72	0.42
GMSRA	3128	86.38	61.85	0.53	0.91	0.89	0.48
H-E	2404	53.15	24.09	0.51	0.77	0.38	0.55

Table 3a): Same as Table 2a), for October 1, 2000

Alg.	NUM	RMSE	BIAS	CC	POD	FAR	SKIL
AE	2678	120.64	84.67	0.5	0.88	0.63	0.51
GMSRA	2842	77.52	55.04	0.53	0.96	0.74	0.56
H-E	2224	44.95	18.16	0.59	0.80	0.28	0.64

Table 3b): Same as Table 2b), for October 1, 2000

Alg.	NUM	RMSE	BIAS	CC	POD	FAR	SKIL
AE	2341	126.12	64.16	0.39	0.69	0.46	0.36
GMSRA	2712	74.67	30.02	0.46	0.87	0.72	0.48
H-E	1969	66.60	-17.36	0.55	0.65	0.24	0.49

Table 4a): Same as Table 2a), for October 2, 2000

Alg.	NUM	RMSE	BIAS	CC	POD	FAR	SKIL
AE	2197	100.44	51.34	0.53	0.74	0.38	0.46
GMSRA	2469	65.76	23.51	0.59	0.92	0.56	0.58
H-E	1869	60.88	-20.47	0.70	0.70	0.17	0.58

Table 4b): Same asTable 2b), for October 2, 2000

Statistical summaries for this event show that all three algorithms overestimate the amount of rainfall with the exception of the Hydro-Est algorithm for 2 October when the highest rain gauge values were observed and underestimation occurred with this technique. The highest RMSE values were obtained with the AE and most were higher than 100.0 mm. The lowest RMSE values were obtained with the Hydro-Est algorithm in all cases. The highest correlation coefficients are also observed for the Hydro-Est and they are not as high as those results obtained by Vila et al. (2001), but are similar to results for Tropical Storm Allison (2001) which are part of the NESDIS Satellite QPE verification program which is underway in the Office of Research and Applications (Kuligowski 2001).

The POD measurements, show that the H-E algorithm have the highest detections problems related with the lower wet bias compared with the other algorithms in all cases. The lowest false alarm values (FAR column) and the highest SKILL scores are obtained with the H-E algorithm. In all cases, the results improve when comparisons are done with the BEV of the satellite estimates.

It is important to mention that 6 satellite images were missing in the estimation process due to the satellite eclipse. Therefore, satellite estimates could be higher than the results obtained.

One factor that may influence the results obtained is that satellite estimate patterns seems to be displaced because of the strong winds associated with hurricanes. Since the comparisons with the BEV give better results, a similar procedure could be used to correct the precipitation field on a basin using rain gauge measurements over the region. So far, hydrological models used in the area have based their precipitation estimates on some less realistic interpolation methods.

The use of the PWRH correction in this validation study would not have had a significant impact on the results obtained since the purpose of this correction factor is to decrease the rainfall rates in dry environments; most hurricanes occur in very moist environments.

The EQL correction factor for warm tops is not applied when $T_{10.7}$ or the Equilibrium Level temperature is less than 210 K which is mostly observed where the heaviest precipitation estimates where obtained with the algorithms in this case.

5. FUTURE WORK

The impact of the correction factors mentioned above could be investigated in more detail in the future along with an adjusted power-law regression curve that can be obtained based on more case studies over the region.

A more detailed orographic map could also be included in the orographic correction factor over the area due to the complex mountain terrain in this narrow part of the Americas. The use of Geographical Information Systems (GIS) can be a helpful tool at this respect.

A pattern recognition for convective systems (Vila and Toledo 2001) can be included in a future work

Overestimations could decrease due to the influence that this application have in the calculation of the mean average and the standard deviation procedure used by the H-E algorithm.

Table 1 shows that the highest density of rain gauges used in this validation study is 140 stations over a total area of 339000 Km^2. Most of the past hydrological, climatological and agricultural studies over the area have been done based on a similar network density and human subjectivity. Therefore, the use of satellite data in this kind of studies represents for this region a new and more objective tool that could provide new information on rainfall.

Hourly estimates could be used in the future to validate estimates for shorter periods of time if the countries make an extra effort to support and provide the necessary information. These magnitudes and patterns need to be validated for hourly measurements in order to use them in future flash flood warning systems over the area.

The availability of satellite data in Central America marks the beginning of a more cooperative work between the satellite community and the national weather services of these countries. Such interaction will undoubtedly benefit all Central American countries and improve understanding of meteorology over these areas.

6. ACKNOWLEDGMENTS

The authors offer thanks to CIRA and the NOAA/NESDIS Hydrology Team. In particular, we appreciate Clay Davenport and Bob Kuligowski for their invaluable help with the source code of the algorithms and their untiring dedication to answer questions continuously. Special thanks to Daniel Vila for his

comments and suggestions. Finally, the support obtained from the Central American Weather Services regarding rain gauge measurements was essential to accomplish this study.

7- REFERENCES

Alvarado, L., 2001. Climatologia de los Ciclones Tropicales que afectaron a Costa Rica en el Siglo XX. Boletin Meteorologico Mensual. Instituto Meteorologico Nacional, MINAE, in press.

Ba, M., and A. Gruber, 2001: GOES Multispectral Rainfall Algorithm (GMSRA). *J. Appl. Meteor.*, in press.

Kuligowski, R., 2001: The NESDIS Satellite QPE verification program. Proceedings 11th Conference on Satellite Meteorology and Oceanography of the Amer. Meteorological Soc., 15-18 Oct. 2001, Paper #P3.47

Scofield, R., 1987: The NESDIS Operational Convective Precipitation Estimation Technique. *Mon. Wea. Rev.*, **115**, 1773-1792.

Vicente G., Scofield, R., Menzel W., 1998: The Operational GOES Infrared Technique, *Bull. Ame. Met. Soc.*, **79**, 1883-1898

----, Davenport, C., Scofield R., 2001: The Role of Orographic and Parallax Corrections on Real time High Resolution Satellite Rainfall Distribution, submitted to *Int. J. Remote Sensing*, in press.

Vila, D., Scofield, R. and C. Davenport, 2001: Satellite Rainfall Estimation Over South America: Evaluation of Two Major Events, submitted to *11th Conference on Satellite Meteorology and Oceanography, Madison*, Wi., Amer. Meteor.Soc.

Vila, D. and L. A. Toledo, 2001: Pattern Recognition Applied to Convective Systems, submitted to the *International Journal of Remote Sensing*.

P3.47 THE NESDIS SATELLITE QPE VERIFICATION PROGRAM

Robert J. Kuligowski[1]*, Shuang Qiu[2], Roderick Scofield[1], and Arnold Gruber[1]
[1]Office of Research and Applications, NOAA/NESDIS, Camp Springs, MD
[2]QSS Corporation, Lanham, MD

1. INTRODUCTION

Numerous algorithms for quantitative precipitation estimates (QPE) from satellites have been developed or are under development. Systematic validation of these algorithms is crucially important (a) in order to communicate the relative merits and weaknesses of these algorithms to potential users; and (b) to determine which algorithms present the most promising avenues for further development. However, algorithm intercomparison data for short-range applications (i.e. hours to days) is lacking.

In response, on 1 April 2001 personnel at the Office of Research and Applications (ORA) of the National Environmental Satellite, Data, and Information Service (NESDIS) initiated real-time evaluation of several satellite QPE algorithms over portions of the continental United States. The specifics of this evaluation are described in section 2, followed by a brief presentation of results in section 3 and future plans in section 4.

2. VALIDATION PROGRAM SPECIFICS

2.1. Algorithms

Six variations of four satellite rainfall algorithms are being tested. These include the operational Auto-Estimator (AE) (Vicente et al. 1998, 2001) and a variant dubbed the "Hydro-Estimator". The latter adjusts the rain-rate curve according to the difference in brightness temperature between the pixel of interest and its neighbors; it also treats the precipitable water and relative humidity adjustments separately. Versions of the "Hydro-Estimator" with and without the radar-based rain-no rain screen of the operational AE are being tested.

In addition to these three algorithms, two versions of the GOES Multi-Spectral Rainfall Algorithm (GMSRA) (Ba and Gruber 2001) are being tested: the standard version and a version that uses the difference between the 6.9-μm and 10.7-μm brightness temperature to differentiate between raining and nonraining areas at night.

The sixth algorithm being tested is a GOES-microwave blended product (Turk et al. 1998) that uses the AE screens and adjustments but updates the rain rate curves by matching the cumulative distribution functions of microwave rain rate estimates from the Special Sensor Microwave/Imager (Ferraro 1997), the Advanced Microwave Sounding Unit (AMSU) (Ferraro et al. 2000), and the Tropical Rainfall Measuring Mission (TRMM) Microwave Imager (TMI).

2.2. Validation Data and Event Classification

Validation is performed against two data sets. Daily estimates of precipitation from the satellite algorithms are evaluated against raingauges from the cooperative observer network. For shorter time periods, 6-h totals of satellite-estimated precipitation are evaluated against the Stage III radar-raingauge rainfall estimates (Fulton et al. 1998) produced operationally by the River Forecast Centers (RFC's).

At this time validation is being performed over a limited area. During this past spring season (April-May 2001), evaluation was performed in two regions. The first was the West Coast, consisting of the areas of responsibility of the Northwest RFC (NWRFC), and the California-Nevada RFC (CNRFC). The second area was the southern Plains, comprising the areas of the Arkansas-Red Basin RFC (ABRFC), the West Gulf RFC (WGRFC), and the Lower Mississippi RFC (LMRFC). These regions are indicated in Fig. 1. For the summer season (June-August 2001), the Colorado Basin RFC (CBRFC) was substituted for the NWRFC in order to capture the effects of the summertime monsoon in the Southwest.

To facilitate the evaluation of algorithm performance for specific events, the precipitation events were divided into four categories: stratiform, "cold-top" convective

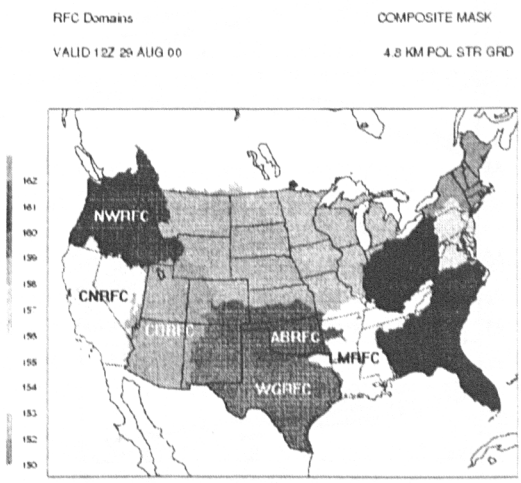

FIGURE 1. River Forecast Center (RFC) areas used in this study. [Figure courtesy of NCEP.]

* *Corresponding author address*: Robert J. Kuligowski, 5200 Auth Rd. WWB/601, Camp Springs, MD 20746; e-mail: Bob.Kuligowski@noaa.gov.

(coldest tops below -58°C), "warm-top" convective (no tops colder than -58°C), and tropical.

2.3. Statistics

Algorithm performance is evaluated using the root-mean-squared error (RMSE), the bias ratio (total estimated amount / total observed amount), and the correlation coefficient (CC). The performance of the algorithms is also evaluated as a function of observed rainfall amount using the probability of detection (POD), false alarm rate (FAR), bias ratio, and Heidke Skill Score (HSS).

3. RESULTS

Sample statistics for cold-top convective events are given in Table 1, while Fig. 1 contains a sample plot of the POD, FAR, bias, and HSS as a function of observed 6-h precipitation amount.

TABLE 1. Summary statistics for April-June 2001 cold-top events in the ABRFC, LMRFC, and WGRFC regions.

Algorithm	RMSE (mm)	Bias Ratio	CC
Operational AE	5.3	1.20	0.64
"Hydro-Estimator"	5.1	1.05	0.56
"Hydro-Est." (radar screen)	4.8	0.89	0.59
GMSRA	6.3	1.66	0.47
GMSRA (nighttime screen)	6.5	1.73	0.48
GOES/Microwave blend	6.0	1.15	0.56

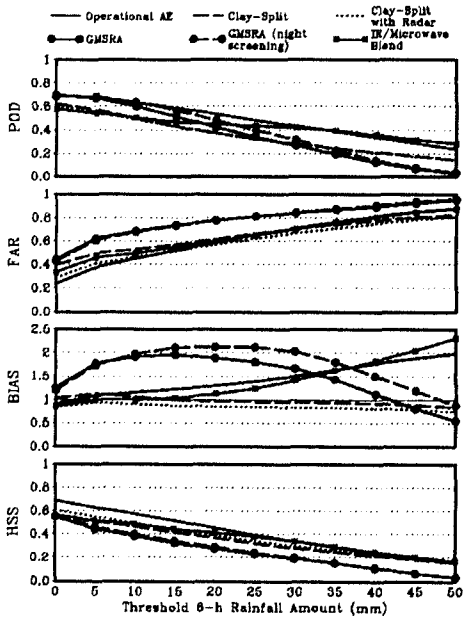

FIGURE 2. POD, FAR, bias, and HSS as a function of observed 6-h precipitation amount for the same data as in Table 1.

During April-June 2001, the operational AE exhibited the best overall correlation between estimates and observations. However, the "Hydro-Estimator" estimates were less biased than the AE and significantly outperformed the AE in some instances, such as for heavy precipitation from warm-top convection (not shown). The radar-based rain/no rain screen had a small effect on the performance of the "Hydro-Estimator", especially compared to the considerable difference (not shown) between the AE with and without the screen. The GOES/Microwave blend performed similarly to the AE; significant improvement in the rain-rate curves was achieved only for heavy warm-top convective events. The GMSRA exhibited the poorest overall performance.

4. FUTURE WORK

In addition to eventually expanding the validation to the entire continental U.S., additional algorithms will be evaluated These include the Microwave-Infrared Rain Rate Algorithm (MIRRA) (Miller et al. 2001), Precipitation Estimation from Remotely Sensed Information using Artificial Neural Networks (PERSIANN) (Sorooshian et al. 2000), and the Self-Calibrating Multivariate Precipitation Retrieval (ScaMPR) algorithm (Kuligowski 2001).

5. REFERENCES

Ba, M., and A. Gruber, 2001: GOES Multispectral Rainfall Algorithm (GMSRA). *J. of Appl. Meteor.*, in press.

Ferraro, R. R., 1997: SSM/I derived global rainfall estimates for climatological applications. *J. Geophys. Res.*, **102**, 16,715-16,735.

-----, F. Weng, N. C. Grody, and L. Zhao, 2000: Precipitation characteristics over land from the NOAA-15 AMSU sensor. *Geophys. Res. Lett.*, **27**, 2669-2672.

Fulton, R. A., J. P. Breidenbach, D. J. Seo, and D. A. Miller, 1998: The WSR-88D rainfall algorithm. *Wea. Forecasting*, **13**, 377-395.

Kuligowski, R. J., 2001: A self-calibrating real-time GOES rainfall algorithm for short-term rainfall estimates. Submitted to *J. Hydrometeor.*

Miller, S. W., P. A. Arkin, and R. Joyce, 2001: A combined microwave/infrared rain rate algorithm. *Int. J. Remote Sens.*, in press.

Sorooshian, S., K.-L. Hsu, X. Gao, H. V. Gupta, B. Imam, and D. Braithwaite, 2000: Evaluation of PERSIANN system satellite-based estimates of tropical rainfall. *Bull. Amer. Meteor. Soc.*, **81**, 2035-2046.

Turk, F. J., F. S. Marzano, and E. A. Smith, 1998: Combining geostationary and SSM/I data for rapid rain rate estimation and accumulation. Preprints, *9th Conf. on Satellite Meteorology and Oceanography*, Paris, Amer. Meteor. Soc., 462-465.

Vicente, G. A., R. Scofield, and W. P. Menzel, 1998: The operational GOES infrared rainfall estimation technique. *Bull. Amer. Meteor. Soc.*, **79**, 1883-1898.

-----, J. C. Davenport, and R. A. Scofield, 2001: The role of orographic and parallax corrections on real time high resolution satellite rain rate distribution. *Int. J. Remote Sens.*, in press.

P3.48 THE SATELLITE IMAGERY DISPLAY AND ANALYSIS SYSTEM AT AIR FORCE WEATHER AGENCY

Charles R. Holliday *
Air Force Weather Agency, Offutt AFB, Nebraska

Mark D. Conner
Atmospheric and Environmental Research, Inc., Offutt AFB, Nebraska

1. INTRODUCTION

The Satellite Imagery Display and Analysis System (SIDAS) software package at Air Force Weather Agency (AFWA) is a powerful and flexible system designed to allow analysts to view and interact with the wide selection of meteorological satellite imagery available at the agency. The software was built using a fourth-generation language, which permits rapid prototyping of new visualization techniques and incorporation of new datasets. Image processing and enhancement methods are used to bring out features of interest. Data fusion techniques allow the analyst to overlay observations, gridded numerical model fields, and other data types to enhance understanding of the meteorological situation. A complementary automated process prepares images for viewing and places them on the agency's Web server for remote customers.

2. HISTORY

During Operation DESERT SHIELD/DESERT STORM in 1990-1991, it became apparent that a means to rapidly prototype new methods of displaying and analyzing meteorological satellite (METSAT) data was needed at what was then Air Force Global Weather Central (AFGWC, now part of AFWA). The SIDAS software grew out of that effort, with an initial capability to display data from the Air Force's Defense Meteorological Satellite Program (DMSP) satellites. Subsequent development led to the inclusion of data from the polar-orbiting satellites operated by the National Oceanic and Atmospheric Administration (NOAA), followed by data from operational geostationary satellites (both US and foreign) and the NASA Tropical Rainfall Measuring Mission (TRMM) satellite.

The software's initial purpose was to allow a small team of satellite meteorologists a means to prototype new display and analysis methods. As capabilities were added, operational forecasters were allowed to use the software to provide feedback on its operational utility. This feedback has been invaluable for refining the software and for prioritizing and implementing new display and analysis capabilities.

3. DESIGN

There are two major components to SIDAS: (1) an automated component that preprocesses the incoming data, and (2) a user interface which the analysts use to view, analyze, and interpret the data.

The automated component is a combination of clock-driven and event-driven software that takes the incoming data and performs the necessary preprocessing. Standard operations include brightness temperature calibration, image warping to standard map projections, database retrievals, and so forth. The automated software also prepares satellite images for the AFWA web server and users worldwide access these images over 750,000 times per month. This software is tailored for the operational needs and data formats at AFWA.

The user interface component is the visible portion of SIDAS. It consists of a retrieval interface for the preprocessed files, image manipulation controls, overlay selections, and analysis functions. Options are provided for the user to save modified files in the native format, or to save the resulting bitmaps into standard graphics files for display on a web server. Currently, the interactive software is run on desktop UNIX workstations with modest requirements for memory and processor speed.

* *Corresponding author address:* Charles R. Holliday, HQ AFWA/XOGM, 106 Peacekeeper Dr STE 2N3, Offutt AFB, NE 68113-4039; e-mail charles.holliday@afwa.af.mil

4. CAPABILITIES

SIDAS provides the forecaster or satellite analyst a wide variety of functions. The imagery is presented in scales ranging from the hemispheric mosaics for strategic-level users down to 500 meters per pixel for mission-tailored operations forecasts. Images are kept on-line for three to five days to provide continuity for the analyses.

Because SIDAS was designed as a METSAT analysis software package, the emphasis is placed on the imagery and on the observational data that can be used to support the image analysis. Below is a selection of the more commonly used SIDAS capabilities.

4.1 *Image manipulation*

Adjust brightness, contrast, and ramping of images. Load standard enhancement curves for infrared images. Apply channels to red, green, or blue color guns for multispectral presentation. Perform a brightness correction on visible images to remove the effects of solar elevation changes. Animate a time series of images.

4.2 *Observational data overlays*

Add surface, upper-air, aircraft, geostationary-derived wind, or QuickSCAT observations. Select the components of the observations to be displayed (e.g., winds only, winds and temperatures, etc.). Add observations automatically when loading an image time series for animations. Provide contouring of standard parameters.

4.3 *Gridded data overlays*

Overlay contours of model field analyses and derived parameters.

4.4 *Geopolitical data overlays*

Add political and geographic boundaries. Add customized geographic reference points. Overlay topographic contours.

4.5 *Text and symbology overlays*

Add fronts, weather symbols, and text. Save the overlay separately for continuity for a future analysis.

4.6 *Analysis functions*

Provide rainfall estimates based on infrared images. Provide Dvorak eye intensity estimates for tropical cyclones. Provide cloud height estimates from cloud shadow length. Compute an average pixel brightness for a time series of images. Compute ocean surface winds speeds, snow depth, rain rate, etc., from microwave imager data. Overlay tropical cyclone position fixes, forecast positions, and model guidance for forecast center locations.

5. FUTURE WORK

AFWA has contracted for a redesign effort for SIDAS to make significant improvements. The upgrade will allow for even more flexibility for viewing data from both meteorological and research satellites, giving the agency the ability to evaluate new data types in an operational setting. Object-oriented software design principles will permit re-use of common techniques and toolsets in other applications and provide improved code maintenance. The software will be portable to UNIX or Windows® computers and file systems. It is expected that these efforts will allow the agency to move towards its goal of a common suite of satellite analysis tools for all of Air Force Weather.

P3.50

FINDINGS FROM THE PRE-ASSIMILATION OF GOES IMAGER CHANNELS

Louis Garand and Nicolas Wagneur
Meteorological Service of Canada, Dorval, P. Quebec, Canada

1. INTRODUCTION

An important advantage of geostationary satellites is the availability of full disk observations at high temporal resolution. Another advantage is the high horizontal resolution of imaging channels. At the MSC, an effort has been undertaken to directly assimilate the GOES imager channels and at the same time pave the way for the assimilation of infrared data from upcoming satellites such as AIRS, IASI and GIFTS.

In preparation for the assimilation of GOES radiances every six hours, statistics of observed (O) minus calculated (P, for predicted) model 6-h equivalent radiances were computed at that temporal scale. This paper shows the strong diurnal cycle in the (O-P) statistics for the surface channels (4 and 5) for the entire month of March 2001. This is attributed to the diurnal cycle of sea surface temperature (T_s). The amplitude of this cycle is studied from a retrieval of T_s. Surprisingly, there is also a diurnal cycle in Imager 3, a channel which does not see the surface. This is attributed to the MSC forecast model in which upper tropospheric humidity tends to be higher in daytime than at nighttime.

2. RADIANCE STATISTICS

Model equivalent radiances are computed using a radiative transfer model named MSCFAST (Garand et al.,1999). This model proved to be very accurate in a recent intercomparison of radiative transfer models (Garand et al., 2001). Statistics of (O-P) were computed from GOES-08 and GOES-10 imager channels 2-5. In the case of Imager-2, affected by the sun, only nighttime data were compiled. The GOES processing is done on 1 X 1 degree boxes since data are to be assimilated at that scale. Within each box, the processing software finds the most likely clear area using criteria such as the local variance (the original GOES pixels at ~4 km resolution were sampled at ~13 km resolution and re-mapped to 1 X 1 degree: each box contains about 8 X 8 pixels). Various tests are made to decide if the pixel is to be assimilated or rejected as cloudy. Surface emissivity was modeled as a function of wavelength and surface wind speed over oceans. Over land, it depends only on the surface type (maps available on the same 13 km grid as the re-mapped GOES images). The (O-P) statistics revealed some biases of the order of 0.5 K in surface channels and 1.5 K in the water vapor channel 3. Assuming that the model over a large number of cases has no bias, the satellite observation bias is removed using the simple relation: bias = a BT+ b where BT is the observed brightness temperature. For example, for March 2001 and GOES-08 imager 4, the bias is -0.49 K and it is removed using a =-0.00657 and b = -2.406 K. Using additional parameters such as the viewing angle or atmospheric predictors from the model first guess was judged undesirable.

Fig. 1 shows the statistics for GOES-08 and GOES-10. The plot indicates the number of cases, the bias and the standard deviation. The number of cases is larger for Imager-3 as the system accepts the observations when clouds are below the level where the humidity and temperature Jacobians become negligible (low clouds do not affect the outgoing radiance). The bias is negligible after bias correction. The peak-to-peak amplitude of the diurnal cycle is of the order of 0.6 K and is quite regular. There is a sharp minimum for 06 UTC data. This is due to the sea surface temperature cycle. A retrieval of

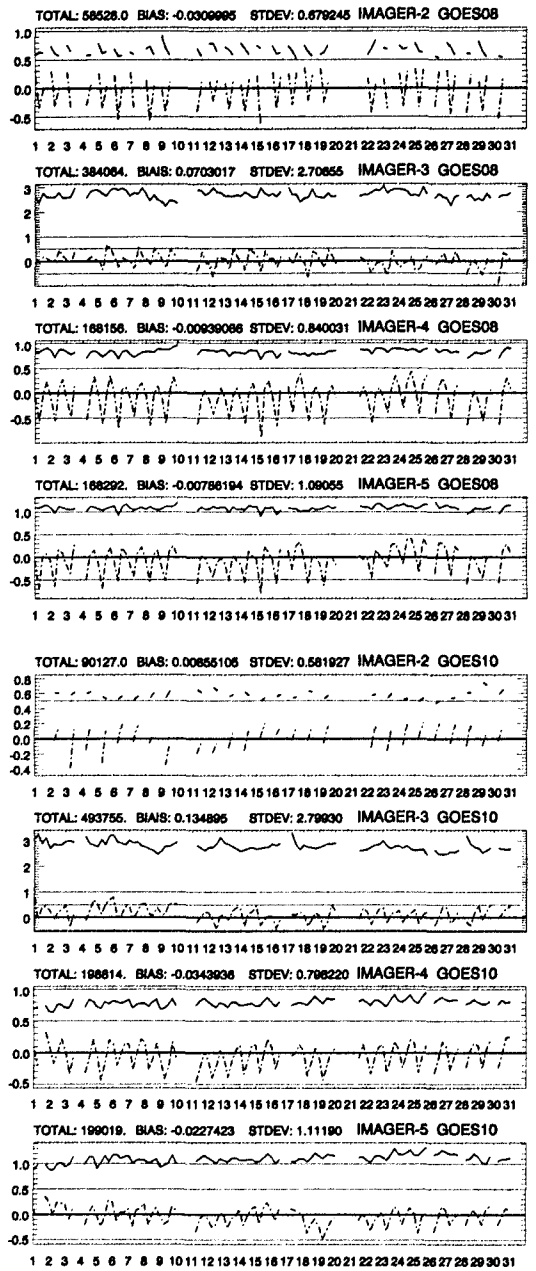

Fig. 1 Statistics of observed minus 6-h forecast calculated BT for imager channels of GOES-08 and 10 in March 2001 every six hours. Upper line is standard deviation; the mean is centered around zero. A bias correction was applied to the observations (see text). Only daytime date used for Imager 2. Number of cases, overall bias and standard deviation indicated. Data taken over oceans in clear areas for surface channels.

T_s is presented in the next section along with an evaluation of the amplitude of the T_s cycle..

3. DIURNAL CYCLE OF THE SURFACE TEMPERATURE

For surface channels, the Jacobian routine accompanying the radiative transfer model reveals that the surface temperature Jacobian dBT/dTs is of the order of 0.7 K/K (it varies from about 0.4 to 0.9 K/K). Thus, if the amplitude of the BT cycle is 0.6 K (Fig. 1), the amplitude of the T_s cycle should be about 0.85 K. T_s has been one of the first quantitative products obtained from satellite. Yet, it is only recently that attempts have been made to evaluate the T_s diurnal cycle. Most algorithms use a "split window" technique consisting in a regression using BT4 and BT5 (from imager channels 4 and 5). Yu et al (1999) estimated that over calm seas, the diurnal variation of T_s may reach 4 K. The split-window technique is very fast, but ignores or does not consider explicitly nonlinear aspects of the problem (such as the dependency on emissivity or viewing angle), which may introduce significant errors.

Here T_s is determined by a variational technique (see e.g. Garand, 2000). Such a physical method allows the determination of the surface temperature over land as well. The formulation has been presented many times: it minimizes the objective function J(X):

$$J(X) = 0.5(X-X_b)\mathbf{B}^{-1}(X-X_b)^T + 0.5(H(X)-y)^T\mathbf{O}^{-1}(H(X)-y)$$

where X is the analyzed state of the atmosphere, X_b its first guess, **B** and **O** the background and observation error covariance matrix, respectively, and T denotes the transpose. H(X) represents the radiative transfer model which computes BT from X and the y represent the BT observations. An iterative procedure finds the solution X, which requires the Jacobian H'(X). If we

limit X to T_s and the BTs to channels 4 and 5, and if in addition the solution is calculated for the sum of J(X) over an ensemble of locations (instead of each location one by one), then we can obtain T_s over a full disk in less than 30 s on a large computer (SX4). If on the other hand, we let profiles of temperature and humidity vary (28 levels at MSC), the processing requires about 1100 s due to slower convergence of the Gauss-Newton iterative procedure. The solution for T_s is then in principle more optimal and differences of a few tenths of a degree from the one based on T_s alone are noted locally. For the evaluation of the diurnal cycle, we used the simpler method. Obviously, the fact that we blend information from observations sensible to the diurnal cycle with the first guess of T_s which does not resolve that cycle implies that the solution will lead to a somewhat reduced diurnal cycle compared to the one obtained from observations alone (such as from a split-window retrieval). The error associated to the background T_s was set to 1 K; that associated to BT4 was set to 0.38 K and that associated to BT5 to 0.49 K (i.e. 20 % of the total variance noted in Fig. 1). This means that the effective BT4 error associated to the background is about 0.70 K. For the month of March 2001, 62,565 cases of T_s differences (18-06 UTC) were obtained. The average difference was 0.50 K, slightly less than the expected 0.85 K difference. A map of differences was obtained. For 1 X 1 degree boxes with more than 10 cases, maxima as high as 1.5 K were noted. Another estimate of T_s was obtained by using BT4 only: inverting the radiative transfer equation, assuming the first guess temperature and humidity profile as perfect. For the same cases, an amplitude of 0.68 K was obtained. The diurnal cycle of T_s was also obtained over land. Its amplitude exceeds 30 K over regions such as the Sierra Madre (Mexico). These observations are very useful to validate the model's diurnal cycle, but such a study is beyond the scope of this paper.

4. DIURNAL CYCLE OF HUMIDITY

It is rather surprising to note a diurnal cycle for Imager 3 in Fig. 1, since this channel does not see the surface. The amplitude of the cycle is about 0.45 K. In order to evaluate if this signal is due to the model or is indeed present in the observations, we computed separately the observed and modeled BT difference (18 UTC- 06 UTC) and (12 UTC -. 06 UTC) for GOES-10 over the month of March. Only cases not affected my modeled or observed clouds were retained. In addition, the corresponding modeled total (TPW) and high precipitable water (HPW, 400 hPa to top) were calculated (more than 135,0000 cases). Results are shown in table 1.

Table 1. Mean Imager 3 BT differences for GOES-10 in March 2001 between various synoptic times. Corresponding model 6-h forecast TPW and HPW differences shown. For each day, data for both times had to be available.

BT3 difference (K)

	Model	Observed
(12-06 UTC)	-0.362	-0.018
(18-06 UTC)	-0.482	0.012

Model PW difference (%)

	TPW	HPW
(12-06 UTC)	0.76	1.81
(18-06 UTC)	1.93	3.06

It can be concluded from Table 1 that there is no diurnal cycle of BT3 in the observations. The magnitude of the diurnal cycle seen in the model approaches 0.5 K and corresponds to an increase in daytime HPW of about 3 % (the mean HPW is ~0.7 mm). Model TPW (mean of ~25 mm) also increases in daytime by 1-2 %. Further analysis is required to see if this cycle is an artefact of the assimilation cycle or is really a characteristic of the model. This will be determined by verifying if the noted cycle exists in medium range forecasts (beyond day 3).

5. CONCLUSION

It is argued that time has come to produce global T_s maps at fixed hours instead of limiting ourselves to a daily product which eliminates the diurnal cycle. On average, the amplitude of this cycle approaches 1 K. Statistics of observed minus calculated radiances at high temporal resolution also reveal an amplitude of the order of 2-3 % in the model upper tropospheric humidity which does not seem to be confirmed by the satellite observations. It was also shown that a variational estimate of T_s can be obtained at a relatively modest cost, allowing studies of the large diurnal cycle over land as well.

6. REFERENCES

Garand, L., D. S. Turner, C. Chouinard, and J. Halle, 1999: A physical formulation of atmospheric transmittances for the massive assimilation of satellite infrared radiances. J. Appl. Meteor.,38, 541-554.

Garand, L., 2000: Sensitivity of retrieved atmospheric profiles from infrared radiances to physical and statistical parameters of the data assimilation system. Atmosphere-Ocean, 38, 431-455.

Garand, L., and coauthors, 2001: Radiance and Jacobian intercomparison of radiative transfer models applied to HIRS and AMSU channels, to appear in J. Geophys. Res.

Wu, X., W. P. Menzel, and G. S. Wade, 1999: Estimation of sea surface temperatures using GOES-8/9 radiance measurements, Bull. Amer. Meteor. Soc., 80, 1127-1138.

P3.51

Validation of GOES-11 Data

Xiangqian Wu*
Cooperative Institute for Meteorological Satellite Studies
University of Wisconsin, Madison, WI

Timothy J. Schmit
NOAA/NESDIS, Office of Research and Applications (ORA),
Advanced Satellite Products Team (ASPT), Madison, WI

1. Introduction

After successful launch of the 11'th Geostationary Operational Environmental Satellite (GOES-11, Menzel and Purdom, 1994) and the engineering check-out period, the National Oceanic and Atmospheric Administration (NOAA) National Environmental Satellite, Data, and Information Service (NESDIS) conducted a GOES-11 Science Test from June 30 to August 13, 2000. At the Cooperative Institute for Meteorological Satellite Studies (CIMSS) and Advanced Satellite Products Team (ASPT), there were two goals for the GOES-11 science test. One was to investigate the quality of the GOES-11 data, the results of which are summarized in this poster. The other was to generate GOES-11 products (temperature and moisture profiles, total precipitable water, lifted index, cloud-top pressure, satellite-derived winds, sea surface temperature, and biomass burning) and compare these products to those from other satellites. These results, as well as more details of the first goal, are reported by Daniels and Schmit (2001).

2. Instrument Noise

2.1. Sounder

Special GOES-11 Sounder scans of space allowed the determination of noise values by calculating the scatter of radiance when looking at uniform space. Results for all 18 infrared bands of GOES-11 Sounder, taken at 23:46 UTC of July 8, 2000, is presented in Fig. 1. The noise values are generally within specification and lower than those from GOES-8. These noise values have also been monitored for a 24-hour period (between July 7-8, 2000) to confirm that the noise has little diurnal change.

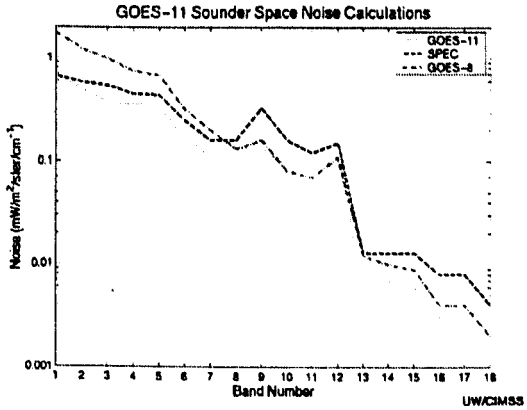

Figure. 1: The noise values of 18 infrared bands of GOES-11 Sounder.

2.2. Imager

Imager noise has been determined in the same way and reported in Table 1. These noise values were once monitored every 15 minutes for a period of 3 hours and were found to vary less than 0.01 to 0.02K. Additionally, they were found to be well within specification and comparable to previous GOES (personal communication, Donald W. Hillger).

Table 1: The noise values of the infrared channels of GOES-11 Imager in terms of brightness temperatures (K). The counterpart values from previous GOES and the specified NEdT values (SPEC) are also listed. The reference temperature is 230K for Band 3 and 300K for other bands.

Band	SPEC	G11	G10	G09	G08
2 (3.9μm)	1.40	0.13	0.17	0.08	0.16
3 (6.7μm)	1.00	0.21	0.09	0.15	0.27
4 (11μm)	0.35	0.07	0.20	0.07	0.12
5 (12μm)	0.35	0.18	0.24	0.14	0.20

* *Corresponding author*: Xiangqian Wu, CIMSS, 1225 W. Dayton St., Madison, WI 53706. fredw@ssec.wisc.edu

3. Imager-to-Imager Comparison

Imager-related comparisons are primarily based on GOES-11 Imager data collected every half hour between 20N-40N, from 00 UTC July 21 to 19 UTC July 24, 2000. The latitude range was chosen to cover both land and sea. To minimize the difference due to view angle, the longitude was limited to 88W-92W and 118W-122W. Corresponding GOES-11 Sounder and GOES-8/10 Imager data were also collected. Weinreb et al. 1997 discusses the calibration methods.

3.1. Visible

Due to the lack of a visible on-board calibration source, visible channels are not absolutely calibrated after launch, hence measurements in these channels are expected to be different. Figure 2 suggests that the sensitivity of GOES-8 (10) visible channel is about 60% (83%) of that of GOES-11.

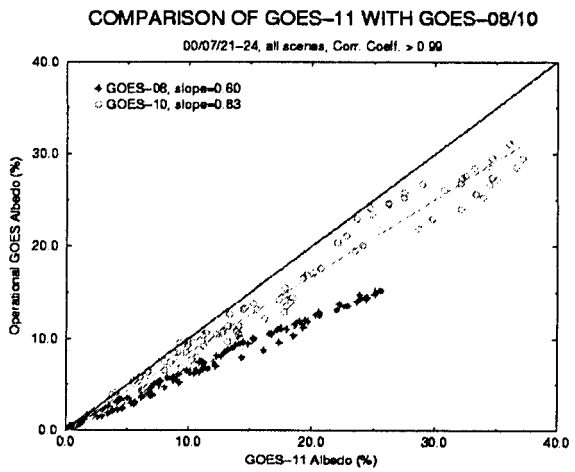

Figure 2: Scatter plot of GOES-8 (*) and GOES-10 (°) albedo as a function of GOES-11 albedo. Albedo is the arithmetic mean of individual pixel albedo within the area of comparison. A diagonal line is shown for reference. The lines of least-squares regression are also shown, whose slopes indicate the sensitivity of the operational GOES relative to GOES-11.

Fig. 2 offers an opportunity to assess the degradation rate of the visible channels of GOES-8/10. In April 1998, a similar comparison revealed that the sensitivity of GOES-8 was about 70% of that of GOES-10 (GOES-K Report). In July 2000, the sensitivity of GOES-8 was about 0.60/0.83=72% of that of GOES-10. This indicates that, in the past two years, the rate of degradation for the two operational satellites have been similar (GOES-10 slightly faster). However, had the degradation rate been constant for each satellite since their launch times, the degradation rate for GOES-8 would be larger:

G08 (6.3 yrs in space): 6.3x=(1-60%) => x=6.3%/yr
G10 (3.3 yrs in space): 3.3x=(1-83%) => x=5.2%/yr

Typically, though, the sensitivity of visible channels experiences a rapid drop shortly after launch, followed by relatively constant degradation. Also note that GOES-10 was in a stowed position for more than a year in space, during which time there probably was little degradation. Taking these into consideration, the rate of degradation can be estimated as following:

G08 (6.3 years in service): x + 6.3y = (1-60%)
G10 (2.1 years in service): x + 2.1y = (1-83%)

which leads to a one-time post-launch drop of x=5.5% and annual degradation of y=5.5%/yr. According to these results, GOES-10 in the past 2.3 years should have lost 5.5+2.1*5.5=17% of its sensitivity (two months in stowed position), whereas GOES-8 should have lost only 2.3*5.5=12.7% of its sensitivity during the same period. This agrees with early observation that GOES-10 has been degrading faster than GOES-8 since April 1998. Also, the sensitivity of GOES-8 in July 2000 would be 70%*(1-12.7%)=61%, close to the 60% obtained by direct comparison.

Knapp and Vonder Haar (2000, referred to as KH hereafter) recently found a 7.6% one-time post-launch drop followed by a 5.6% annual degradation for the visible band of GOES-8 Imager. These results are in reasonable agreement with other studies including ours. Such agreement is remarkable for several reasons. First, their approach of using a radiative transfer model is theoretical in nature, whereas our approach is largely empirical. The consistency of the results from these two very different approaches lends credit to both.

Second, KH restricted their study to the dark ocean scene at local noon. Other studies, for example Greenwald et al (1997), focused on highly reflecting surfaces such as clouds. In our case, scenes for a wide range of illuminations and albedo were examined. Despite of these differences in target selection, the results are similar. In particular, Fig. 2 shows that a linear least-squares regression is a good fit for comparisons of dark and bright scenes. These reconfirm a conclusion by KH that the degradation is relatively uniform throughout the dynamic range of instrument response.

Finally, KH were focused on GOES-8 only, whereas we studied the degradation of both GOES-8/10. Our approach has implicitly assumed that: (1) the sensitivity of the visible channel of GOES-8/10/11 Imagers are the same when first operated on orbit; and (2) the degradation pattern are the same for both GOES-8/10, i.e., a post-launch drop and annual degradation at the same rate. The agreement between the two studies suggests that these assumptions may be valid.

3.2. Infrared

The differences in brightness temperature between GOES-11 and GOES-8/10 for the Imager infrared bands are summarized in Table 2. The infrared bands are expected to be well calibrated without systematic bias among the Imagers, although an absolute calibration difference of 1K is allowed. Table 2 shows that the brightness temperature measured by GOES-11 is about 1K cooler (0.8K warmer) than that by GOES-8/10 for the 3.9 μm (6.7 μm) band. These differences are larger and more persistent than expected. For the split-window bands (11 and 12 μm), the differences are smaller and more variable.

Table 2: Mean difference (K) between GOES-11 Imager and GOES-8/10 Imagers and GOES-11 Sounder for the IR bands.

Band	G11-G08	G11-G10	Img-Snd
2 (3.9μm)	-0.98	-1.43	-1.67
3 (6.7μm)	+0.80	+0.75	+1.33
4 (11μm)	+0.75	+0.45	+0.71
5 (12μm)	-0.01	-0.70	-0.44

In addition to the mean difference, the standard deviations of the differences were analyzed but no significant patterns emerged. The area has also been divided into land and ocean, again the differences are similar to those of the whole. To examine whether the overall difference is caused by a few isolated events, the time series of the differences is studied, which concluded that the differences are fairly steady throughout the 5-day period. The differences do exhibit some diurnal variations, though, which are believed to be caused by a combination of differential heating and viewing geometry of the target and GOES-11 calibration. Finally, to investigate whether the differences are caused by a poor calibration at certain temperatures, for example the very cold/hot scenes, histograms of the differences are examined, which showed that the differences are persistent throughout the range of temperature.

4. Sounder-to-Sounder Comparison

4.1. Visible

On Friday 30 June (14:42 UTC), GOES-11 Sounder normalization software was installed by SOCC, leading to less striping in the Sounder visible imagery (Fig. 3).

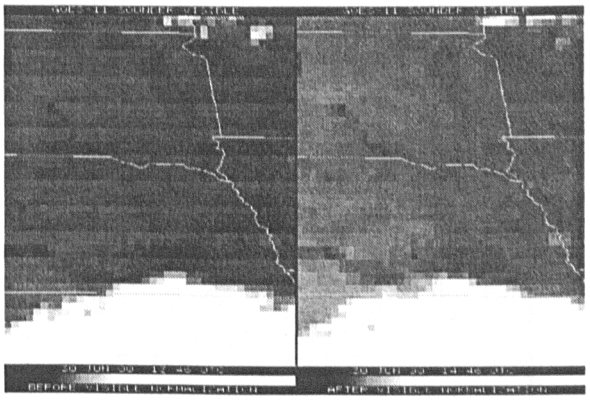

Figure 3: Before (left) and after (right) the application of GOES-11 Sounder visible normalization.

4.2. Infrared

Fig. 4 shows the Sounder brightness temperature differences for all 18 infrared bands between GOES-11 and GOES-8/10 during a nighttime period. Only measurements of similar view angles were compared. The GOES-11 Sounder brightness temperatures are in better agreement with those from GOES-10 than from GOES-8. The operational spectral response functions for both GOES-8 and GOES-10 Sounders were used. The largest differences are for Sounder bands on the edges of absorption features (e.g. 3, 13 and 15).

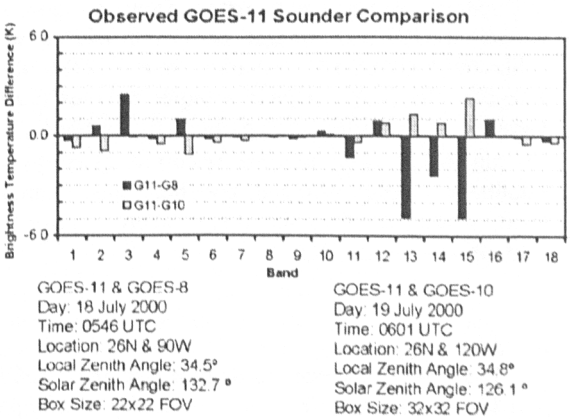

Figure 4: Sounder brightness Temperature differences between GOES-11 and GOES-8/10.

5. Imager-to-Sounder Comparison

Fig. 5 is a comparison of GOES-11 Imager with Sounder. The Imager Band 1 is compared with Sounder band 19; Imager band 4 is compared with Sounder band 8; and Imager band 5 is compared with Sounder band 7. Since there is no Sounder band corresponding closely to the other two Imager bands, Imager band 2 is compared with the mean of Sounder bands 17 and 18 and Imager band 3 is compared with the mean of Sounder bands 11 and 12.

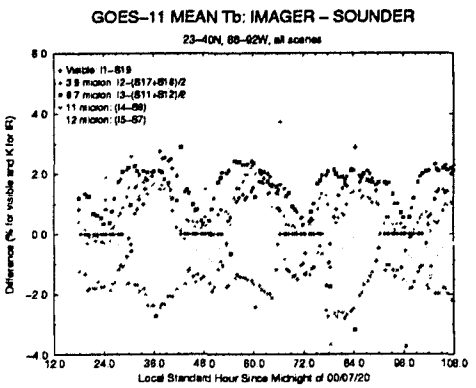

Figure 5: Differences of GOES-11 Imager and Sounder brightness temperatures plotted as a function of time.

The mean differences of Imager-Sounder during this 4-day period have been reported earlier in Table 2. The overall differences for the first three bands could be due to spectral response differences, and the differences for the last two bands are reasonably small. It is interesting, however, that the Imager-Sounder differences are quite similar to the Imager-Imager differences, which could result from a less well calibrated GOES-11 Imager compared with a well-calibrated GOES-11 Sounder and GOES-08/10 Imagers. Fig. 5 also depicts a rather obvious diurnal variation of the differences, particularly for the 6.7 and 11 μm bands. The minima occurred close to the satellite midnight, which is one hour later than the local midnight. This is more likely caused by calibration uncertainties.

6. Summary

The NOAA Science checkout phase of the GOES post-launch testing offers an opportunity to compare various satellite radiances and products. GOES-11 imager and sounder data were taken during the six-week NOAA science test, when the satellite was stationed at 105W. The imager-to-imager radiance comparisons show fair agreement, although the GOES-11 imager shows the greatest differences. The visible sensors of GOES-8/10 were shown to degrade 5.5% shortly after launch, followed by a steady annual rate of degradation of 5.5%. These results are in close agreement with previous studies. Overall, the sounder data from GOES-11 are slightly better than those from GOES-8. The GOES-11 data exhibited less noise and less striping.

7. References

Daniels, J. M., T. J. Schmit, 2001: GOES-11 Science Test: GOES-11 Imager and Sounder Radiance and Product Validations. *NOAA Tech. Rep.* (in press).

Greenwald, T. J., S. A. Christopher, and J. Chou, 1997: Cloud liquid water path comparisons from passive microwave and solar reflectance satellite measurements: Assessment of sub-field-of-view cloud effects in microwave retrievals. *J. Geophys. Res.*,**10 2**, 19,585-19,596.

Knapp, K. R., T. H. Vonder Haar, 2000: Calibration of the Eighth Geostationary Observational Environmental Satellite (GOES-8) Imager Visible Sensor. *J. Atmos. Oceanic Tech.* **17**, 1,639–1,644.

Menzel, W. P., and J. F. W. Purdom, 1994: Introducing GOES-I: The first of a new generation of Geostationary Operational Environmental Satellites. *Bull. Amer. Meteor. Soc.*,**75** , 757-780.

Weinreb, M. P., M. Jamison, N. Fulton, Y. Chen, J. X. Johnson, J. Bremer, C. Smith, and J. Baucom, 1997: Operational calibration of Geostationary Operational Environmental Satellite-8 and -9 imagers and sounders. *App. Optics*, **36**, 6,895-6,904.

P3.52 LIFE CYCLE OF CONVECTIVE ACTIVITY IN TERMS OF CLOUD TYPE OBSERVED BY SPLIT WINDOW

Toshiro Inoue, Xiangqiuan Wu* and Kotaro Bessho
Meteorological Research Institute / JMA, Tsukuba, Ibaraki, Japan
*CIMSS/SSEC University of Wisconsin, Madison, Wisconsin

1. Introduction

Mesoscale deep convective system (hereafter called DC) is a significant meteorological phenomenon. The structure and evolution of DC have been studied by many authors using rain radar, wind profilers and satellite observations. These studies have revealed the substantial variety and complexity of convective processes and structures in DC.

Satellite observations from geostationary orbit are effective in studying the evolution of DC in terms of cloud, considering high temporal observations and wide range of coverage. A large number of studies have been conducted using the infrared and/or visible radiance images from geostationary weather satellites (eg. Machado et. al.). The previous study mostly used single infrared data to delineate DC using the threshold of brightness temperature of the infrared channel (TBB). Depending on the value of the TBB threshold, we might discard both the beginning and ending stages of the DC life cycle.

In this study, we aim to see how effectively we can delineate the life cycle of DC over the eastern tropical Pacific by using split window cloud type information, and some preliminary results for case studies are reported.

2. Data

The split window (11 and 12 μm) data of GOES-West/East data over the area of180-60W and 30S-30N are used to study the life cycle of deep convective activity. The three infrared data of 6.7, 11 and 12 μm are gridded on 0.1 latitude/longitude within the area. We are collecting hourly data, but so far we have used only three hourly data as a preliminary survey.

3. Cloud Type Classification by Split Window

Inoue (1985) showed the feasibility of cirrus cloud detection using the split window data. Furthermore, he developed a method to classify several cloud types based on a threshold technique in the two-dimensional diagrams of brightness temperature of 11 μm (TBB) and brightness temperature difference between the split window (BTD) (Inoue,1987). The BTD is used to classify optically thin cloud and the TBB is used to classify the level of cloud.

Corresponding author address: Toshiro Inoue, Meteorological Research Institute, Dept. of Climate Research, 1-1 Nagamine, Tsukuba Ibaraki 305-0052, *Japan*; *e-mail: tinoue@mri-jma.go.jp*

Optically thin cirrus cloud shows the larger BTD due to the differential absorption characteristics between the split window, while optically thick cumulus type cloud shows the smaller BTD due to the black-body characteristics. In this study, we use the TBB threshold of 210K, 253K and 288K to classify very cold cloud, high-level cloud and cloud free. As the BTD threshold, we used 1K and 2.5K to classify optically thick cloud and optically thin cloud. Seven cloud types of very cold cloud colder than 210K, cumulonimbus-type (CB), dense cirrus-type, cirrus-type, thin cirrus-type (CI), low-level cumulus/stratocumulus-type (CU) and non-classified cloud are classified in this study. Hereafter we combine dense cirrus-type cloud and cirrus-type cloud, and call it as DCI.

4. Identification of DC

Inoue and Aonashi (2000) studied the relationship between cloud information from VIRS (Visible Infrared Scanner) and precipitation information from PR (Precipitation Radar) on board TRMM. They found that the clouds colder than 260K in TBB with smaller BTD correspond well to the rain observed by PR from the dataset for rain events during June, 1998 over the frontal zone in east Asia. The clouds colder than 210K in TBB indicate a higher possibility of convective rainfall by PR. Therefore, CB classified by the split window is considered as a good indicator of DC in this study. Further, the anvil cloud associated with the DC is considered to correspond to cirrus-type cloud.

5. Case Study 1

Fig.1. shows the 6 hourly temporal variation of cloud type distribution over the area of EQ-5N and 170W-160W during May 14 06Z – May 15 00Z, 2001. The darker area corresponds to CB and the brighter area corresponds to CI. We can see the evolution of the DC in the Figure. At the developing stage CU and CB cloud are dominant then DCI increases. Then the cloud amount of CI becomes very large at the decaying stage.

Fig.2. shows the temporal variation of cloud amount for each cloud type in the area. The CB first shows a peak, then DCI shows a peak and finally CI shows a peak. This delineates the characteristics of the DC life cycle. From the temporal change of CB cloud amount we can classify the DC stages as developing, mature and decaying.

Here, we introduce the cloud amount ratio of DCI/CB and CI/CB. Figure 3. shows the temporal variation of CB cloud amount and the ratio for the above case. The value of DCI/CB ratio is small at the developing/mature stage, while the value of

CI/CB becomes very large at the decaying stage.

6. Case Study 2

Figure 4. shows another example of the evolution of DC over the area of 5N-15N and 180-170W. The figure shows rather from mature stage to decaying stage. We can clearly see that CI is dominant at the decaying stage. A similar characteristics of temporal variation of each cloud type can be seen. First, CB peak appears and followed by a peak of DCI and CI.

7. Summary

With the use of cloud type information classified by the split window, we can delineate the life cycle of deep convection. Contrary to the previous studies which use the TBB threshold to identify DC, we may track from the beginning to the end of the DC since the split window can classify cumulus-type (mostly appears at developing stage), cumulonimbus-type (mature stage) and cirrus-type cloud (decaying stage). In the developing stage the DCI/CB ratio is smaller, and in the decaying stage the CI/CB ratio becomes larger. These ratios could be used to identify the stage of DC from a single snap shot by satellite.

Acknowledgment

This study is partly supported by the NASDA TRMM program.

References

Inoue, T., 1985, J. Met. Soc. Jpn., 63, 88-99

Inoue, T., 1987, J. Geophys. Res., 92, 3991-4000

Inoue, T and K. Aonashi, 2000, J. Appl. Meteor., 39, 2292-2301

Machado, L. et al., 1998, Mon. Wea. Rev., 126, 1630-1654

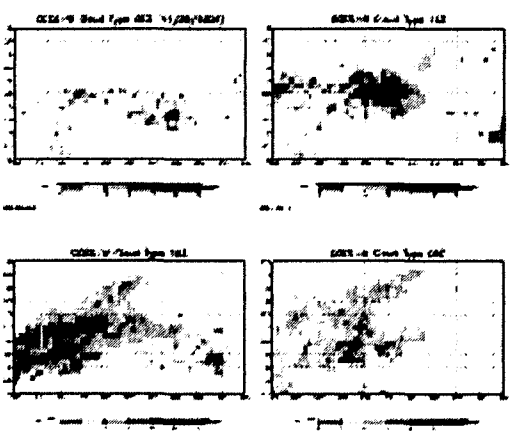

Fig. 1. Six hourly cloud type map for the deep convective activity. The darker area corresponds to cumulonimbus-type cloud, while the brighter area corresponds to cirrus-type cloud.

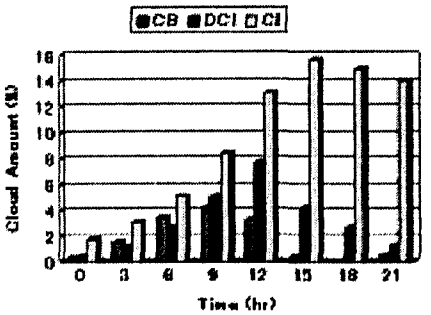

Fig. 2. Temporal variation of cloud amount within the area for Cumulonimbus-type cloud (CB), dense cirrus-type cloud (DCI) and thin cirrus-type cloud (CI).

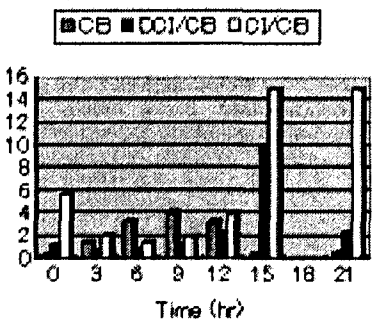

Fig.3. Temporal variation of CB cloud amount and the cloud amount ratio of DCI/CB and CI/CB. In the figure, ratio has ceiling at value of 15.

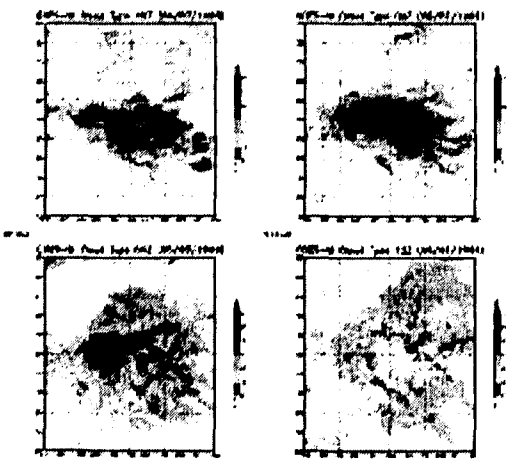

Fig. 4. Six hourly cloud type map for another case of deep convective activity.

P3.53

Observations of a Severe Supercell Thunderstorm on 24 July 2000 using GOES-11 Sounder and Imagery

by

John F. Weaver (NOAA/NESDIS/RAMMt)[1]
John A. Knaff, Dan Bikos (CIRA/CSU)
Jaime M. Daniels (NOAA/NESDIS/ORA)
Gary S. Wade (NOAA/NESDIS/CIMSS)

1. Introduction.

On 27 April 1994, the fourth in a series of new NOAA geostationary satellites, GOES-11, was launched. As with the other satellites in this series, it is fitted with instruments that provide frequent scans of the western hemisphere in 5 imaging channels, and 19 sounder channels.

Following the launch and orbit stabilization, a six week science test was conducted (from 30 June - 13 August 2000). The first half of the test was devoted to instrument optimization, the latter half focused on capturing real-time weather events. During the second half of the experiment, the default programming called for the imager to routinely collect 5-minute interval imagery over the continental United States. The sounder was set to collect routine 30-min interval data. Science-test coordinators also had the option of increasing the scan frequency of the imager to a one-minute interval (a scheduling strategy commonly referred to as super-rapid scan operations, or SRSO), over a limited area to capture significant mesoscale weather events.

On 24 July 2000, NOAA's Storm Prediction Center issued a moderate risk for severe thunderstorms over the central Plains of the United States, and GOES-11 project forecasters requested that the satellite be placed into its SRSO scan mode. At approximately 21:00 UTC a storm formed in south-central South Dakota. Shortly thereafter, the storm appeared to split. The left–moving component propagated to the east, while the right-mover traveled due south across central Nebraska. During a 10-hour period, the right-moving storm produced hail exceeding 2 inches in diameter, and 3 confirmed tornado sightings – all of which were in rural areas.

This paper presents an overview of the pre-storm environment, a general synopsis of the evolution of the sub-synoptic environment throughout the day, and a brief overview of the thunderstorm's formation and unique behavior. GOES-11 sounder products are presented that illustrate the added value of having frequent interval sounder data available to forecasters.

[1] NOAA – National Oceanic & Atmospheric Administration, NESDIS – National Environ-mental Satellite Data & Information Service, RAMMt – Regional & Mesoscale Meteorological team, CIRA – Cooperative Institute for Research in the Atmosphere, CSU – Colorado State University, ORA – Office of Research and Applications, CIMSS – Cooperative Institute for Mesoscale Meteorology Studies.

2. Data Sets.

a. Satellite data. The standard five imaging channels on the current GOES instruments include a visible channel (responding from 0.52 – 0.72 μm), as well as four infrared channels with central wavelengths at 3.9 μm, 6.7 μm, 10.7 μm and 12.0 μm.

The GOES sounder has instrumentation to measure emitted radiation in 1 visible wavelength band as well as in 18 thermal infrared bands sensitive to temperature, moisture, or ozone. The "footprint" or spatial sampling resolution at satellite sub-point is 8 km, with 13-bit data transmitted to the GOES receiving facilities.

In this study, plotted horizontal fields of lifted index (representing air mass instability) and precipitable water are utilized. For more information on the characteristics and capabilities of both the imager and sounder channels refer to Menzel and Purdom (1994).

b. Other data. Radar data used in this study are from the National Weather Service (NWS) Weather Surveillance Radar – 1988 Doppler (WSR-88D) located at North Platte, Nebraska. Conventional data include standard NWS surface and upper air observations, along with model output from the National Center for Environmental Prediction (NCEP).

3. 24 July 2000 case study.

Synoptic data from 12:00 UTC on the morning of 24 July, found the north-central Plains under northwesterly flow aloft (Figure 1). A shortwave trough over South Dakota (SD) and Nebraska (NE) was exiting the region, a second was expected to arrive in the area by mid-afternoon (Figures 1, 2a, and 2b). This second disturbance would trigger deep convection – lapse rates in the area were nearly dry adiabatic in a very unstable air mass (Figure 3).

The Convective Available Potential Energy (CAPE), using an assumed mixed dewpoint of 63°F with the morning sounding

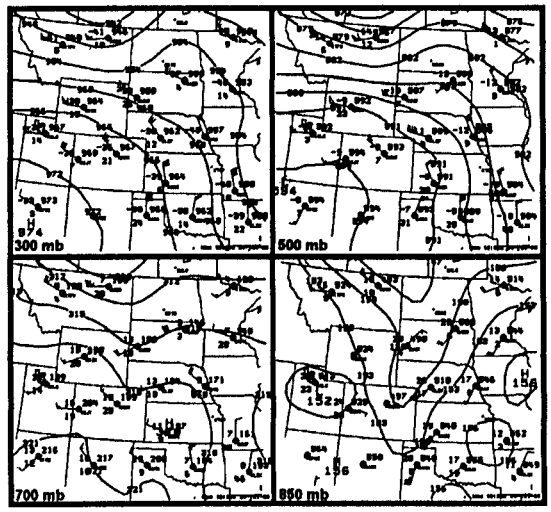

Figure 1. Synoptic analyses from 12:00 UTC on 24 July 2000. Station plots are standard U.S. Heights in dm. The four panel includes analyses at 300 mb, 500 mb 700 mb and 850 mb.

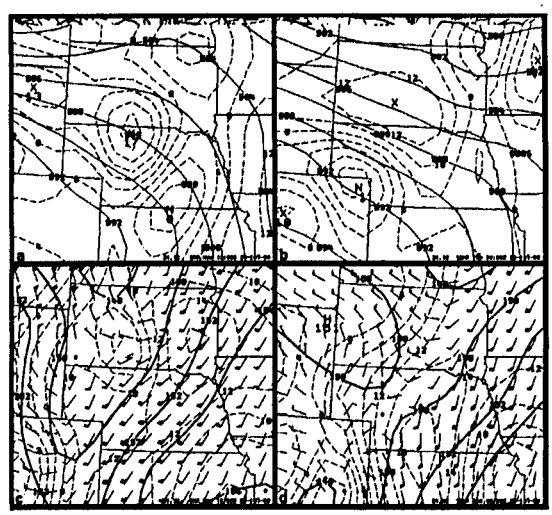

Figure 2. Top: ETA model 500 mb heights and vorticity valid at a) 12:00 UTC on 24 July 2000 (initial analysis), and b) 00:00 UTC on 25 July 2000 (12-hr forecast). Bottom: ETA model 850 mb heights and dewpoints with standard wind barbs valid at a) 12:00 UTC on 24 July 2000, and d) 00:00 UTC on 25 July 2000.

at North Platte, NE was estimated at over 4,000 J/Kg. This estimate was realistic, given that low-level moisture advection into central NE and south-central SD was anticipated (Figure 2c, 2d). Synoptic analysis also revealed a surface low in western NE at 12:00 UTC (not shown). This low was forecast to move into central

NE by late afternoon, bringing with it a dryline/trough to its south.

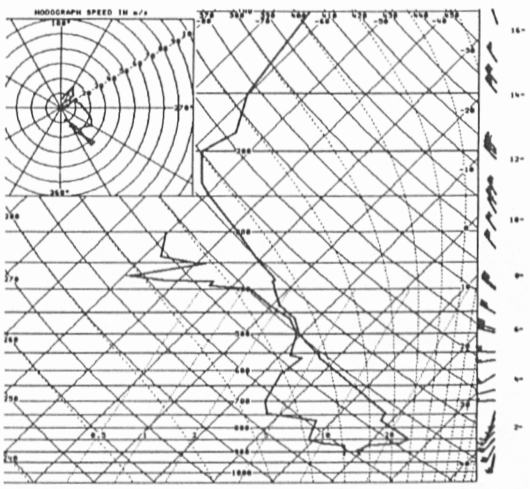

Figure 3. Radiosonde data from North Platte, NE at 12:00 UTC on 24 July 2000 plotted on a Skew-T/Log-P diagram. Winds are in knots.

The morning run of the ETA model suggested that Lifted Indices (LIs) less than (–7) would develop by noon in the area of interest. The output also predicted that a narrow axis of maximum instability would stretch from north-eastern SD into southwest NE. This is approximately what occurred. However, a mesoscale convective system (MCS) – one that did not appear in the model run – crossed SD during the morning hours. This morning system altered the picture somewhat.

Figure 4 presents a direct comparison between the model forecast LIs and those computed from the satellite sounder data. The background image is an LI product from GOES-11. It is overlaid with the ETA-model, 6-h forecast fields. As noted, the model forecast finds a tongue of maximum instability (LI = -7) stretching southwest, from northeastern SD into southwest NE. However, note some important differences. The remnants of the MCS can be seen in eastern SD/NE. Southwest of there, a cloud line along a low-level thunderstorm outflow (LTO) boundary is seen in central NE. The tongue of maximum instability is actually oriented more north-south, and is located in western portions of both states. It intersects the LTO boundary in south-central SD. However, notice that sounder-based values are roughly the same magnitude (-8, -9) as those forecast by the ETA.

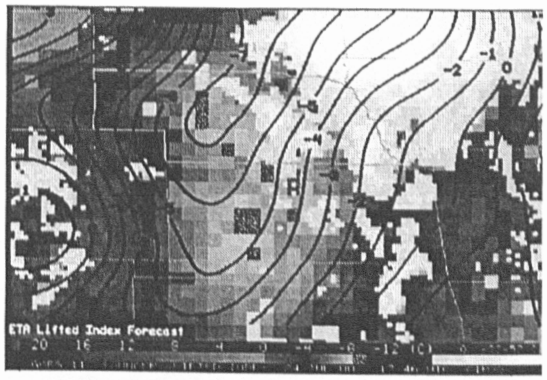

Figure 4. Surface-based lifted index image computed from GOES-11 sounder data overlaid with the ETA-model, 6-h forecast LI fields. Beginning scan time is 17:46 UTC. Model forecast valid at 18:00 UTC. Central column of states (from top to bottom) are South Dakota Nebraska, Kansas, and Oklahoma.

SRSO began on schedule at 19:15 UTC, and at approximately 21:00 UTC a thunderstorm formed near the intersection of the LTO boundary with the ridge of maximum, low-level instability. The genesis region was just northeast of the surface low noted above, and the timing also coincided with the arrival of the shortwave trough from the west. It is not known whether any one of these factors played a dominant role in storm formation.

Within an hour of formation, the storm appeared to develop a right- and left-moving component. However, satellite imagery reveals that the process was not a "classical" storm split, i.e. one in which shear-induced pressure gradients on the flanks of the original updraft enhance lift, and produce two new updrafts (e.g., Rotunno and Klemp 1982, 1985). Figure 5, along with sequential imagery, shows that the left-moving storm in this case formed along an LTO boundary on the north side of the storm. Furthermore, the hodograph was curved cyclonically in this case. Were this a classical split, one

might expect a region of high pressure to develop above the low pressure area on the left flank, and the left-moving updraft to quickly dissipate (Wilhelmson and Klemp 1981). This storm did not dissipate, but continued east for nearly three hours and produced severe weather all along its path.

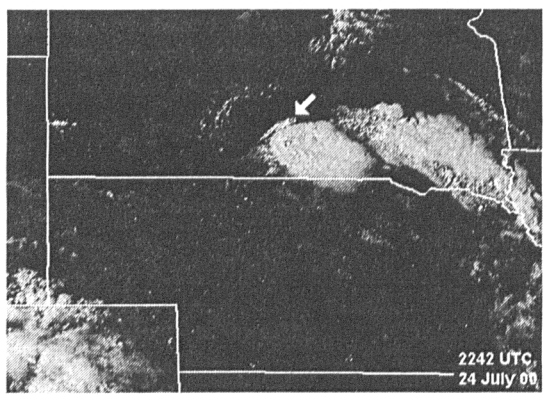

Figure 5. GOES-11 visible image from 22:42 UTC on 24 July 2000. Arrow points to an LTO boundary formed by the large storm in south-central South Dakota. There is a new storm forming on the boundary that will move left of the mean flow and produce severe weather.

Animated sounder imagery reveals that the right-moving component traveled along the western side of the tongue of high values of surface-based CAPE. Figure 6 shows an example of the surface-based CAPE derived from GOES-11 sounder data. The arrow points along the path that the storm will take over the next 8-hr. This path also coincides with the eroding edge of the Convective Inhibition (CIN) as computed from half-hourly sounder data (not shown). Thus, the right-mover's motion can readily be explained by factors other than shear-induced pressures.

4. Concluding Remarks.

Before successfully creating an accurate meteorological prediction, it is necessary to understand the current state of the atmosphere, and to identify those conditions that are present which might alter the current state. In this sense, more data is better than less. Without sufficient information, one might assume that one process is occurring (in this case, a classical storm-split), when something else entirely is actually taking place (in this case a new storm formed and propagated along an LTO boundary, while the original cell traveled along a pre-existing tongue of extreme instability).

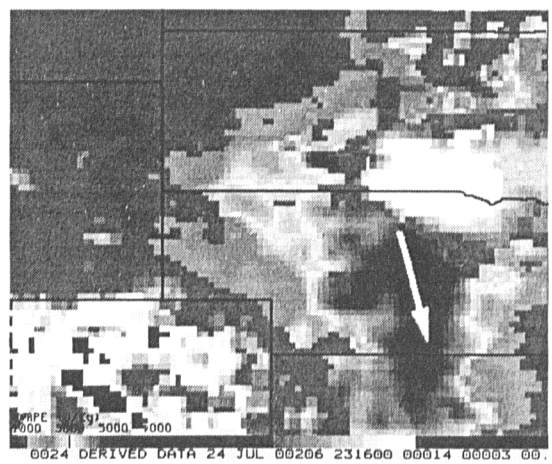

Figure 6. Surface-based CAPE derived from GOES-11 sounder data valid at 23:16 UTC on 24 July 2000. Arrow portrays path of the storm from about 00:00 - 08:00 UTC on 25 July 2000. CAPE values along the dark ridge-line are in the range of 5,000 - 6,000 J/Kg.

The example presented in this paper illustrates how frequent interval satellite data can supply information to 'fill the gap' between other data sources. The LTO boundary was seen only on satellite imagery – the tongue of instability, only on sounder imagery. Without this information, the forecaster might have expected the northern component to dissipate quickly. Instead it intensified and produced severe weather for more than two hours. The right-mover produced severe weather for more than ten hours as it traveled the length of the instability tongue – from South Dakota, all the way into central Kansas.

5. Acknowledgements.

A portion of the research presented in this study was performed under NOAA Grant #NA67RJ0152.

6. References

Menzel, W.P., and J.F.W. Purdom, 1994: Introducing GOES-I: The first of a new generation of geostationary operational environmental satellites. *Bull. Amer. Meteor. Soc.*, 75(5), 757-781.

Rotunno, R., and J.B. Klemp, 1982: The influence of the shear-induced pressure gradient on thunderstorm motion. *Mon. Wea. Rev.*, **110**, 136-151.

Rotunno, R., and J.B. Klemp, 1985: On the rotation and propagation of simulated supercell thunderstorms. *J. Atmos. Sci.*, **42**, 271-292.

Wilhelmson, R.B., and J.B. Klemp, 1981: A three dimensional numerical simulation of splitting severe storms on 3 April 1964. *J. Atmos. Sci.*, **38**, 1581-1600.

P3.54 A CLOUD MODEL INTERPRETATION OF THE ENHANCED V AND OTHER SIGNATURES ATOP SEVERE THUNDERSTORMS

Pao K. Wang[1*], Hsin-mu Lin[1], Stefano Natali[1], Scott Bachmeier[2], and Robert Rabin[3]
[1]Deaprtment of Atmospheric and Oceanic Sciences, University of Wisconsin-Madison, Madison, WI
[2]Space Science and Engineering Center, University of Wisconsin-Madison, Madison, WI
[3]National Severe Storm Laboratory, NOAA, Norman, OK

1. INTRODUCTION

Satellite observations have become an indispensable tool for the forecasting and study of severe thunderstorms, especially in places where conventional data are either sparse or unavailable. Over the years, important cloud top characteristics of severe thunderstorms have been studied and classified using satellite visible and infrared images, and utilized for the above-said purposes.

One of the peculiar characteristics has been defined as enanced-V and svereal studies were performed to correlate this feature with severe storms (e.g., Negri, 1982; McCann 1983; Heymsfield et al. 1983ab; Heymsfield and Blackmer 1988; Adler and Mack 1986). For example, McCann (1983) accumulated V statistics from half-hourly enhanced IR data from April to July 1979. He found that storms with a V pattern had about 70% probability of producing severe weather, and that the median lead time from the onset of the V to the first severe weather was about 30 minutes. Adler et al. (1985) also presented similar evidence that the V feature is correlated with reported severe weather. They found that 75% of storms with the V feature had severe weather, but 45% of severe storm examined did not have this feature.

A notable classification was made by Adler and Mack (1986); they indicated that thunderstorms with thermal couplet may be classified according to thee types of thunderstorm tops:

- Class1: the IR cloud point is located with the cloud top and there is no close-in warm point;
- Class 2: similar to Class 1 except a warm point exists downwind of the cloud top.
- Class 3: cold and warm points exist and with the cold point displaced upstream of the cloud summit.

They found that thunderstorms could go through the three storm top classes during their lifetime.

*Corresponding author's address: Pao K. Wang, Department of Atmospheric and Oceanic Sciences, University of Wisocnsin-Madison, Madison, WI 53706.
Email: pao@windy.meteor.wisc.edu.

A more detailed analysis on satellite observation of V-Shape feature was performed by Heymsfield and Blackmer (1988). They studied nine different convective systems with different features from 1979 (five SESAME cases) to 1982 consisting of both isolated storms and squall lines comprised of supercell storms. The V-feature was present for all except one. On some of the days, the V was very well developed; on others it was poorly developed or very short-lived.

These investigators also performed studies to understand the mechanisms responsible for the formation of the enhanced-V. Heymsfield and Blackmer (1988) made a more comprehensive study on this subject and proposed a few conceptual models to describe the phenomenon. It would be desirable to use a numerical model to see if the proposed mechanisms can produce the V feature. However, previous numerical model studies were not conclusive mainly due to the lack of ice processes in the model microphysics (Schlesinger, 1984, 1988).

The present study attempts to use a numerical cloud model with more detailed microphysics (including the ice processes) to simulate a severe storm occurred in Montana in 1981 to see if the V feature and other important cloud top characteristics associated with severe thunderstorms as observed by previous investigators can be reproduced and, if so, to explain the mechanisms responsible for their formation.

2. DESCRIPTION OF THE CLOUD MODEL WISCDYMM

The cloud model utilized for the present study is the Wisconsin Dynamical/Microphysical Model (WISCDYMM), which is a 3D quasi-compressible, time-dependent, non-hydrostatic cloud model developed at the University of Wisconsin-Madison by the author's group. The governing equations and microphysical parameters are given in *Straka* (1989) and Johnson et al. (1994).

3. THE 2 AUG 1981 CCOPE SUPERCELL

The simulated storm for illustrating the plume-formation mechanism is a supercell that passed through the center of the Cooperative Convective Precipitation Experiment (CCOPE) (*Knight*, 1982) observational network in southeastern Montana on 2 August 1981. The storm and its environment were intensively observed for more than 5 h by a combination of seven Doppler radars, seven research aircraft, six rawinsonde stations and 123 surface recording stations as it moved east-southeastward across the CCOPE network. This storm case was chosen because it provides much detailed observational data for comparison with model results in dynamics and cloud physics, and the author's group has obtained successful simulations of it previously.

4. RESULTS AND DISCUSSIONS

The results of the simulation show that those important features can also be reproduced. An example of the results is shown in Fig. 1. Detailed descriptions of the model results and the mechanisms involved will be given at the time of the conference.

Acknowledgments. This work is partially supported by NOAA/NESDIS, NSF Grants ATM-9907761 ATM-9633424, and NASA Grant NAG5-7605.

REFERENCES

Adler, R. F., and R. A. Mack, 1986: Thunderstorm cloud top dynamics as inferred from satellite observations and cloud top parcel model. Journal of the Atmospheric Science, 43, 18, 1945-1960.

Heymsfield, G. M., R. H. Blackmer, and S. Sholtz, 1983a: Upper level structure of Oklahoma tornadic storms on May 2, 1979; Part 1: Radar and satellite observations. *Journal of Atmospheric Science*, **40**, 1740-1755.

Heymsfield, G. M., G. Szejwach, S. Sholtz, and R. H. Blackmer, 1983b: Upper level structure of Oklahoma tornadic storms on May 2, 1979; Part II: proposed explanation of "V" pattern and internal warm region in infrared observations. *Journal of Atmospheric Science*, **40**, 1756-1767.

Heymsfield, G. M., and R. H., Blackmer, 1988: Satellite-observed characteristics of Midwest severe thunderstorm anvils. Monthly Weather Review, 116, 2200-2224.

Johnson, D. E., P. K. Wang, and J. M. Straka, 1994: A study of microphysical processes in the 2 August 1981 CCOPE supercell storm. *Atmospheric Research*, **33**, 93-123.

Knight, C. A., Ed., 1982:The Cooperative Convective Precipitation Experiment (CCOPE), 18 May-7 August 1981. *Bull. Amer. Meteor. Soc.*, 63, 386-398.

Mack, R. A., A. F. Hasler, and R. F. Adler, 1983: Thunderstorm cloud top observations using satellite stereoscopy. *Monthly Weather Review*, **111**, 1949-1964.

McCann, D.W., 1983: The enhanced-V: a satellite observable severe storm signature. *Monthly Weather Review*, **111**, 887-894.

Negri, A. J., 1982: Cloud-top structure of tornado storms on 10 April 1979 from rapid scan and stereo satellite observations. *Bulletin of American Meteorological Society*, **63**, 10, 1151-1859.

Schlesinger, R. E., 1984: Mature thunderstorm cloud-top structure and dynamics: a three dimensional numerical simulation study. *Journal of Atmosferic Science*, **41**, 1551-1570.

Schlesinger, R. E., 1988: Effects of stratospheric lapse rate on thunderstorm cloud top structure in a three-dimensional numerical sinulation. Part I, Some basic and comparative experiments. *Journal of Atmosferic Science*, **45**, 1555-1570.

Straka, J. M., 1989: Hail growth in a highly glaciated central High Plains multi-cellular hailstorm. Ph.D. Diss., Dept. Meteorology, Universitiy of Wisconsin, Madison, 413 pp.

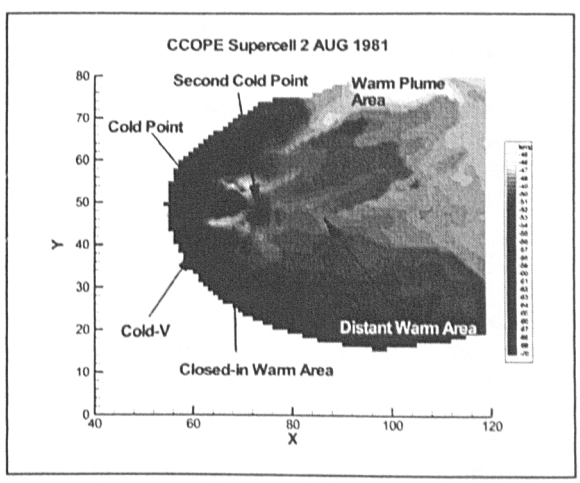

Fig. 1 Simulated cloud top temperature field of the CCOPE supercell of 2 Aug 1981, showing the V feature and other cloud top characteristics.

P3.55 A SATELLITE PERSPECTIVE OF THE PINE LAKE, ALBERTA TORNADO EVENT

A. Scott Bachmeier*, James P. Nelson III

Cooperative Institute for Meteorological Satellite Studies
University of Wisconsin-Madison

1. INTRODUCTION

Canada ranks second in the world for the number of tornadoes (behind the United States), with an average of about 80 per year (Newark, 1984). A significant number of these tornadoes often occur in the Prairies of western Canada (Alberta, Saskatchewan, and Manitoba).

A tornado occurred in the vicinity of Pine Lake in south-central Alberta (25 km southeast of Red Deer, CYQF, Fig. 1), from 00:45 to 01:15 UTC on 15 July 2000 (6:45 to 7:15 PM local time on 14 July). Twelve fatalities and 140 injuries resulted when the tornado moved across the Green Acres lakeside campground on the western shore of Pine Lake (producing F3 damage). This was the first fatal tornado event in Canada since the 31 July 1987 Edmonton, Alberta tornado. In addition to the tornado, this storm also produced golfball to baseball size hail. A chronology of the Pine Lake tornado event is available from Environment Canada (2000).

2. SYNOPTIC OVERVIEW

McCarthy (2001) describes synoptic conditions of the day in detail. A shortwave trough was moving eastward across British Columbia, producing a broad southwesterly flow across Alberta. The approach of a 50 ms^{-1} mid-upper level jet streak was enhancing deep layer wind shear over the region. Convection initially formed between 19:00 and 20:00 UTC over the foothills of the Rocky Mountains across southern and central Alberta, eventually moving northeastward across the plains. Surface observations showed evidence of a dryline across southwestern Alberta, but also suggested that a region of higher moisture existed east of the developing convection. A dewpoint of 61 F (16.1 C) was observed just ahead of the storm at Red Deer (CYQF) at 23:00 UTC, while farther to the east, the dewpoint at Coronation (CWCT) increased from 41 F (5 C) to 55 F (12.8 C) between 23:00 UTC and 00:00 UTC.

*Corresponding author: Scott Bachmeier, University of Wisconsin, Madison WI 53705;
E-mail: *scottb@ssec.wisc.edu*

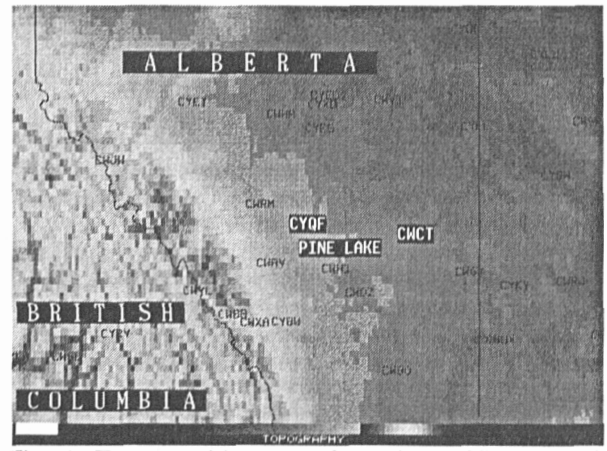

Fig. 1. Topographic map of southern Alberta and the surrounding region, showing station identifiers and the location of Pine Lake.

3. SATELLITE OBSERVATIONS

The two operational National Oceanic and Atmospheric Administration (NOAA) Geostationary Operational Environmental Satellite (GOES) were the eastern GOES-8 (centered at 75 W longitude) and the western GOES-10 (centered at 130 W longitude). Rapid Scan Operations (RSO) were activated for both GOES-8 and GOES-10 during the afternoon of 14 July, due to the potential for severe convection over the eastern US and also over Montana. During RSO periods, GOES imagery is available at 5-10 minute intervals (instead of the standard 15 minute interval imagery). In addition, GOES-11 (centered at 104 W longitude) had recently been launched, and was undergoing a Science Test where continuous RSO imagery was being generated during the July and August test period.

This event therefore provided a unique opportunity to view the development and life cycle of a high latitude tornadic supercell using multi-angle rapid-interval imagery from the 3 separate GOES platforms. A timely overpass of the NOAA-12 polar orbiting satellite also provided imagery of the developing convection prior to its producing damaging winds, large hail, and the Pine Lake tornado.

3.1 GOES-8 and GOES-10 imagery

Of the two operational GOES, the viewing geometry was most favorable from the western GOES-10 satellite. At 23:11 UTC, the GOES-10 10.7 micrometer InfraRed (IR) brightness temperature of the Pine Lake cell first became colder than -50 C, which was approximately the temperature of the tropopause (-51.5 C at 228 mb) on the 00:00 UTC 15 July Edmonton, Alberta rawinsonde report. A few images later (23:30 UTC, about 75 minutes prior to the Pine Lake tornado), an "Enhanced-V" cloud top signature became evident (Fig. 2), which often indicates convection that is producing or will soon produce damaging winds, large hail, or tornadoes (McCann, 1983).

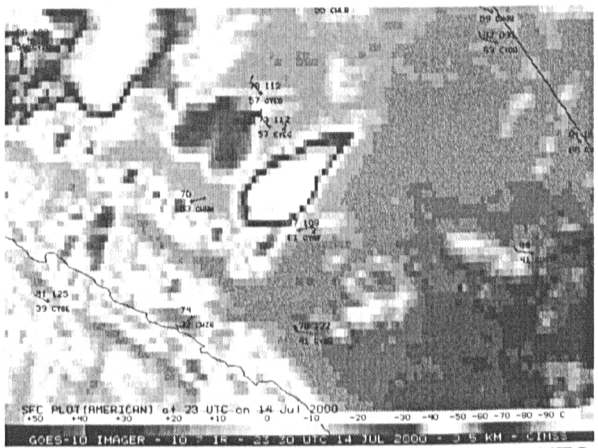

Fig. 2. GOES-10 10.7um IR image at 23:30 UTC, showing the initial "Enhanced-V" signature on the Pine Lake storm.

An animation of the GOES-10 visible imagery reveals that a small cloud element (a weak cell apparently unable to continue to organize and intensify) located just south and southeast of the Pine Lake storm appears to merge with the main cloud region around 23:30-23:40 UTC. Shortly after that time, the following is evident on the visible imagery:

-- a very large "shelf cloud" extends outward along the forward (eastern) edge of the Pine Lake cell.

-- the back edge of the storm becomes noticeably "brighter" on the visible imagery, indicating that the cell is becoming more "upright" leading to a greater degree of solar reflection off of the rear (western) edge of the storm. Subtle hints of shadowing from the "backsheared anvil" are also seen at this time.

The extreme viewing angle from the eastern GOES-8 satellite is less desirable, but an animation of that visible imagery also shows some interesting aspects of the Pine Lake storm:

-- the aforementioned "shelf cloud" along the leading edge is more obvious, since the view is not blocked by the overhanging anvil portion of the storm; the flanking line convection is well illuminated (Fig. 3).

-- the hazy region just to the rear of the cell after 00:15 UTC reveals that there was likely significant blowing dust produced by the strong rear flank downdraft to the south and southwest of Red Deer (CYQF).

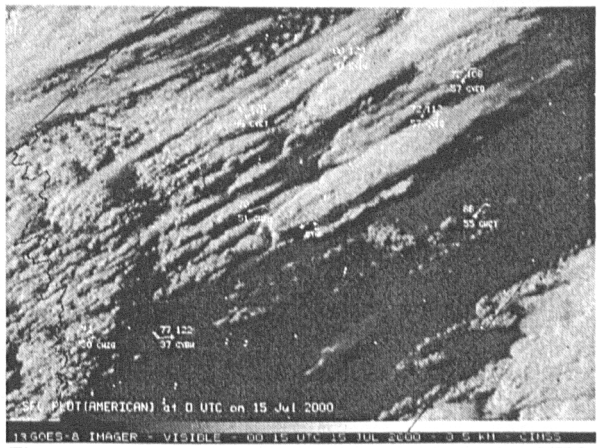

Fig. 3. GOES-8 visible image at 00:15 UTC, showing the shelf cloud along the leading edge of the storm, and flanking line convection along the southern edge.

Derived Product Imagery (DPI) from the GOES sounders are produced operationally on an hourly basis, and include total precipitable water (PW) and lifted index (LI). Unfortunately, the operational scan coverage of the GOES-10 Sounder only extended northward to about 50 North latitude, preventing the ability to monitor hourly stability or moisture parameters in the pre-convective environment across southern Alberta. The GOES-10 Sounder products did, however, hint that both an axis of instability and a moisture gradient extended from north-central Montana (where a severe thunderstorm watch had been issued at 23:30 UTC) northwestward into extreme southeastern Alberta and southwestern Saskatchewan (Fig. 4).

Total precipitable water derived from the High-resolution InfraRed Sounder (HIRS/3) on NOAA-15 (not shown) did indicate that a gradient of PW was in place across Alberta during the early afternoon overpass, with PW values around 1-7 mm in the west and 10-14 mm over eastern Alberta and western Saskatchewan.

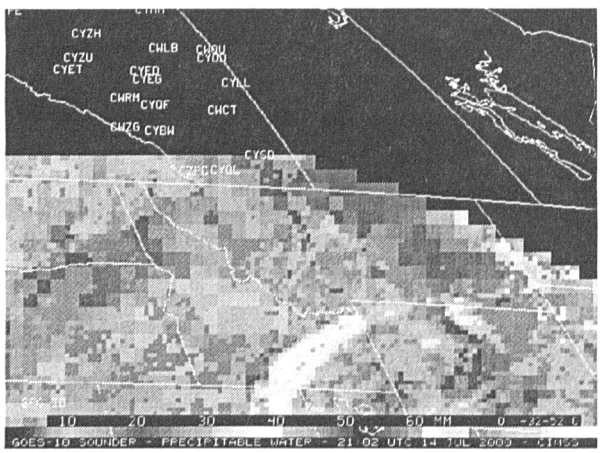

Fig. 4. GOES-10 sounder derived total precipitable water at 21:02 UTC.

3.2 NOAA-12 imagery

Visible and IR data from the 23:56 UTC overpass of the NOAA-12 polar orbiting satellite reveals finer detail in the cloud top and cloud top temperature structure (Fig 5), due to the higher resolution of the NOAA-12 AVHRR/2 instrument (1 km, versus the GOES IR resolution of 4 km). The NOAA-12 10.8 micrometer IR data also indicated colder cloud top temperatures within the "Enhanced-V" signature (-66 C, compared to -51 C measured by GOES-10 at 23:53 UTC).

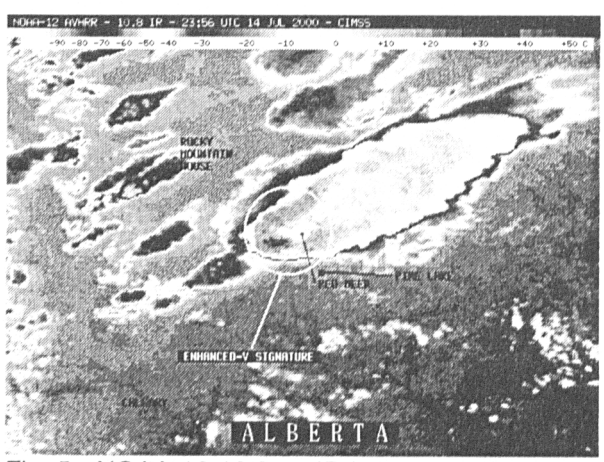

Fig. 5. NOAA-12 10.8um IR image at 23:56 UTC, showing the well-defined "Enhanced-V" signature.

3.3 GOES-11 imagery

The GOES-11 10.7-12.0 micrometer "split window" IR difference product (Fig. 6) shows evidence of a west-east oriented region of higher boundary layer moisture, along a Red Deer (CYQF) to Coronation (CWCT) line during the hours leading up to the development of the supercell that produced the Pine Lake tornado. This IR difference product highlights regions where the GOES-11 12.0 micrometer brightness temperatures are 5-6 K cooler than the corresponding GOES-11 10.7 micrometer brightness temperatures, due to attenuation by moisture pooled within the boundary layer (Chesters et al., 1983).

The Pine Lake supercell began to move to the right of the environmental (southwesterly) flow (Joe and Dudley, 2000), taking a more east-northeasterly path. The storms motion toward this region of increased boundary layer moisture may have played a role in the further intensification of the Pine Lake supercell prior to its producing large hail and the tornado.

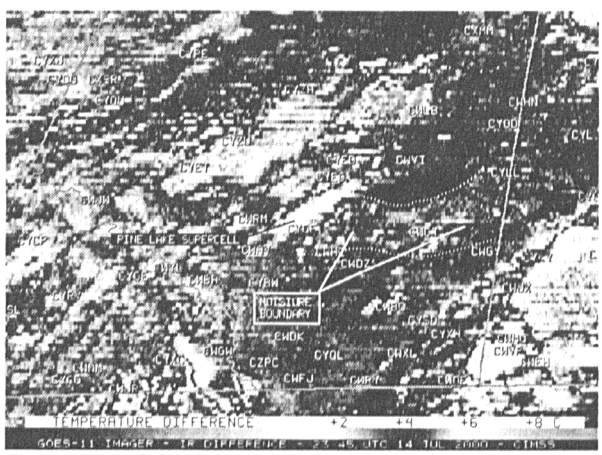

Fig. 6. GOES-11 split-window IR difference product at 23:45 UTC, showing the axis of higher boundary layer moisture in place to the east of the Pine Lake storm.

The Canadian National Radar Project site located at Carvel, Alberta (near Edmonton) collected radar data from the Pine Lake storm. Vertically Integrated Liquid (VIL) values increased dramatically (Joe, personal communication) around the time that the Pine Lake supercell encountered the axis of higher boundary layer moisture indicated by the GOES-11 split window IR difference product.

4. SUMMARY

The 14 July 2000 Pine Lake, Alberta tornado event was a unique opportunity to view a high latitude tornadic supercell using multi-angle rapid-interval imagery from 3 separate GOES platforms, as well as from NOAA polar orbiting satellites. Rapid Scan Operations imagery was available from GOES-8, GOES-10, and GOES-11, which showed several interesting aspects of the development and morphology of the convection across southern Alberta that day. In addition, a timely overpass of the NOAA-12 polar orbiter revealed striking detail in the Enhanced-V cloud top signature (20 minutes prior to the storm producing large hail, and 49 minutes prior to the Pine Lake tornado).

A west-east oriented axis of enhanced boundary layer moisture was evident across eastern Alberta using the GOES-11 split window IR temperature difference product. This feature was likely a key ingredient in the motion and intensification of the Pine Lake supercell.

Note: color versions of these GOES and NOAA satellite images (along with interactive Java animations) are available on the Cooperative Institute for Meteorological Satellite Studies (CIMSS) GOES Gallery at the following URL:

http://cimss.ssec.wisc.edu/goes/misc/000714.html.

5. REFERENCES

Chesters, D., L.W. Uccellini, and W. D. Robinson, 1983: Low-Level Water Vapor Fields from the VISSR Atmospheric Sounder (VAS) Split Window Channel. *J. of Climate and Appl. Meteor.*, **22**, 725-743.

Environment Canada, 2000: Tornado at Pine Lake, Alberta: A chronology. Web site: *http://www.ec.gc.ca/press/000715_n_e.htm*

Joe, P., and D. Dudley, 2000: A quick look at the Pine Lake storm. *CMOS Bulletin*, Nov. 2000, 1-11.

McCann, D.W., 1983: The enhanced-V, a satellite observable severe storm signature. *Mon. Wea. Rev.*, **111**, 887-894.

McCarthy, P., 2001: 14 July 2000, Pine Lake Tornado. Environment Canada Report, in press.

Newark, M.J., 1984: Canadian tornadoes. 1950-1979, *Atmosphere-Ocean*, **22**, 343-353.

P3.56

MCS DEVELOPMENT WITHIN CONTINENTAL-SCALE ELONGATED DRY FILAMENTS IN GOES WATER VAPOR IMAGES

Edward I. Tollerud, Fernando Caracena, Adrian Marroquin[1], and Steven E. Koch
NOAA Research-Forecast Systems Laboratory
Boulder, Colorado
[1][in collaboration with the Cooperative Institute for Research in the Atmosphere (CIRA), Colorado State University, Fort Collins, Colorado]

Jennie L. Moody and Anthony J. Wimmers
University of Virginia, Charlottesville, VA

1. INTRODUCTION

GOES water vapor images frequently show exceptionally dark filaments, ranging in size from short "dry slots" curling into cyclonic centers to equally narrow but very long regions extending longitudinally for many hundreds of kilometers. The implied midlevel dryness within these filaments suggests air with a history of subsidence. Furthermore, the largest of these longitudinal filaments indicate the presence of a jet stream immediately to the south, and recent studies show them to be closely collocated with similarly shaped filaments of enhanced potential vorticity ("PV streamers") on the cyclonic side of the jet. Occasionally there is dramatic convective development over the central United States within and toward the nose of the streamers/filaments. For instance, Caracena *et al.* (2000) and Tollerud *et al.* (2000) describe such a filament which persisted across the western U. S. for six days and spawned large mesoscale convective systems (MCSs) on four of those days (Fig. 1). As the winds and the contours of pressure on the 2 PV-unit surface on Figure 2 demonstrate, the filament coincides with an undulating PV surface that is slightly subsided relative to its surroundings over the southern borders of Utah and Colorado in the western U.S. To the east, three distinct regions of strongly lowered PV are found. The westernmost of these regions, over eastern Kansas, coincides with the western edge of a large MCS that produced heavy rainfall and flooding in the Kansas City area. The other two regions, one over southern Illinois and another extending from central Alabama into Georgia, are also associated with areas of convection. Both appear to be the result of residual midlevel PV from the previous day that drifted eastward overnight and redeveloped during the next heating cycle.

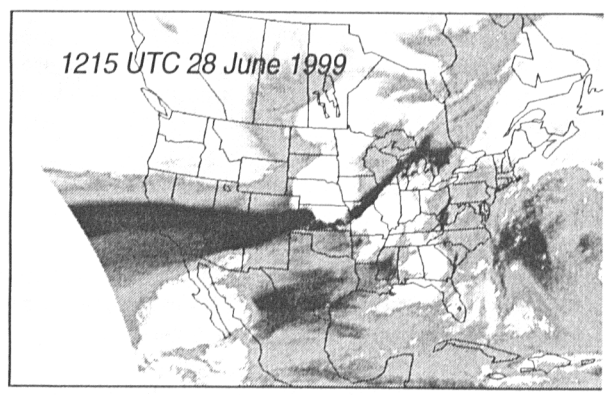

Fig. 1. GOES 8 water vapor image. Light colors indicate clouds and high water vapor content; black indicates low values of integrated water vapor. Figure taken from Caracena et al. (2000).

As this particular case of serial MCSs and a long-lived streamer suggest, filaments of this kind and the PV streamers they imply may have prognostic value as an indicator of likely MCS development. Previous studies of smaller-scale potential vorticity structures in Europe have reached the same conclusion. Appenzeller and Davies (1992) and Appenzeller *et al.* (1996), for instance, relate lee cyclogenesis to features of the upper level PV fields, and Massacand *et al.* (1998) suggest that the occurrence of PV streamers may be useful as precursor signals for heavy precipitation in the lee of the Alps. Mansfield (1994) describes a possible way to make operational model corrections using dry zones on water vapor imagery. Rodgers *et al.* (1988) present analyses and possible explanations of a large MCS that formed within a dry filament.

The value of this particular kind of mesoscale "trigger" is of course dependent on the frequency with which it occurs. Thus, a first step toward determining forecast utility for dry filaments in water vapor imagery is at least a qualitative assessment of their ubiquity. In this paper we follow water vapor

Corresponding author address: Edward Tollerud, NOAA/FSL, R/FS1, 325 Broadway, Boulder, CO 80305-3328. E-mail: tollerud@fsl.noaa.gov. Tel: 303-497-6127.

Fig.2. Atmospheric pressure (hPa) and winds on the 2-PV-unit (K $kg^{-1}s^{-1}10^{-6}$) surface at 1200 UTC 28 June 1999 as analyzed from Eta-Model initialization fields. Pressure contour intervals are 50 mb; white areas are above 300 hPa while areas of darkest shading are below 550 hPa.

imagery during several months of 2001 and present representative images of the exceptionally large or persistent filaments that also seemed related to significant MCS development. In addition to becoming a seasonal inventory of sorts, these cases also serve as a set of days for which future detailed analyses of the associated meteorological fields may help to explain the elusive physical mechanisms that relate the dry filament, the PV streamer, and subsequent MCS development.

2. MCS'S AND FILAMENTS DURING 2001

During the period April to July 2001, there were roughly six episodes of a persistent (two days or longer) continental-scale dry filament over the U.S. with associated MCS development. One of these episodes(July15-20)persisted for six days. Imagery for several of these cases are displayed in Figures 3-5.

The early-season (mid-April) example shown in Figure 3 extends essentially east-west across virtually the entire U.S. Its orientation and the coinciding PV contours are reminiscent of the 1999 case discussed in the Introduction and displayed on Figure 1. In contrast, the filament on 20 July (Fig. 4) has a pronounced latitudinal component, following the upper-level flow around the persistent midconti-

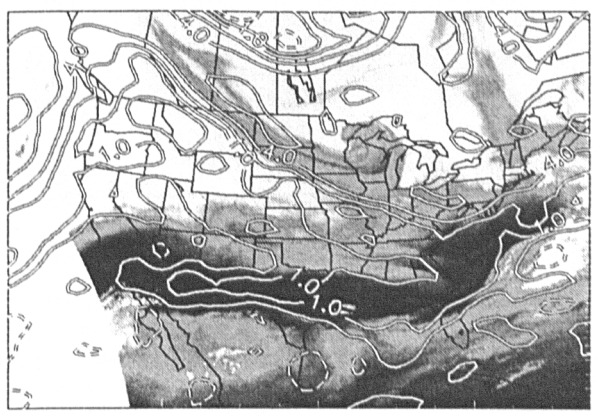

Fig. 3. As in Figure 1 except for 0000 UTC 16 April 2001. Contours of potential vorticity (PV units; K $kg^{-1}s^{-1}10^{-6}$) are superposed.

nent ridge that developed during this period. This streamer produced MCSs at its terminus in Minnesota and southern Canada for several consecutive nights.

The third example (Fig. 5), from 22 April, is displayed using altered water vapor (AWV; Moody *et al.*, 1999) imagery. The AWV is a derived product that represents a vertically weighted average of specific humidity at a fixed pressure layer in the mid-to-upper troposphere. The weighting function that represents the derived product's sensitivity to water vapor covers the pressure levels of approxi-

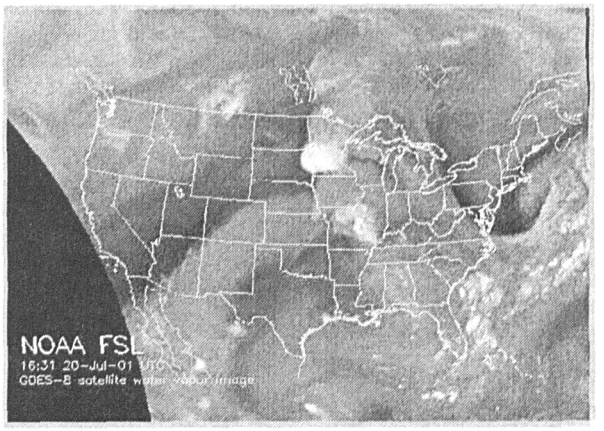

Fig. 4. GOES-8 water vapor imagery from 1630 UTC 20 July 2001.

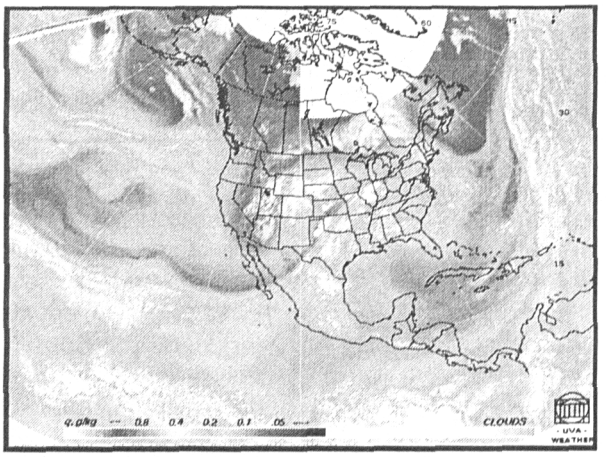

Fig. 5. Mid-to-upper tropospheric specific humidity at 0000 UTC 22 April 2001. See text for explanation.

mately 200 to 500 hPa, with a peak sensitivity at 400 hPa. It is developed from the water vapor channel and ancillary temperature fields from the 6-h MRF. In the color images, specific humidity varies logarithmically along a cool-to-hot colorscale, with a mask of high-level clouds in greyscale according to cloud-top temperature. The natural advantage of the AWV product is that it contains information on humidity variations at the same resolution as the water vapor channel, but does not carry the influences of atmospheric temperature and zenith angle that happen to compromise the interpretability of the image as a depiction of water vapor. The larger domain in the figure reveals that the filament is an extension of a much larger feature of the large-scale flow pattern. At the time of this observation, organized convection in the center of the thin filament is forming over Texas, Oklahoma, and Kansas.

3. TROPICAL STORM ALLISON

Figure 6 reveals another fascinating feature of water vapor and upper-level potential vorticity fields during 2001. Tropical Storm Allison (shown in the figure) and, to a lesser extent, Barry, were located downstream from regions of dry air with high PV. Although not as clearly a dry filament as the other examples, these regions were nonetheless prominent features during much of the lives of these storms. As with earlier studies of Hurricane Floyd, there is strong circumstantial evidence to suggest that the surprising longevity of and rainfall in these storms derived in part from the existence of these upstream regions. Confirmation of this hypothesis awaits closer analysis of the corresponding wind and thermodynamic fields.

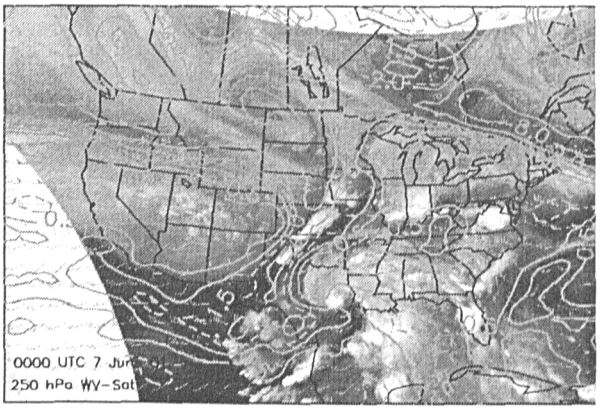

Fig. 6. GOES-8 water vapor imagery and 250 hPa potential vorticity (PV units; K $kg^{-1}s^{-1}10^{-6}$) at 0000 UTC 7 June 2001. Potential vorticity contours are shown at .5 PV-unit intervals.

4. CONCLUSIONS

In this paper we have discussed the possibility that MCSs form preferentially within long, narrow filaments of dry, and PV-rich, subsiding air. The examples shown do not in themselves, however, offer a pysical explanation for how this works. On the contrary, it might seem more likely, as Thiao *et al.* (1993) suggest, that MCSs would form at the terminus of filaments (more often called plumes) of *moist* air. A clue to how the MCSs might have evolved in the dry air is provided by the Fort Worth profile (Fig. 7) denoted by a white asterisk within the dry filament of Figure 8 shortly before a convective system developed. Lifting of parcels into the nearly adiabatic layer between 450 and 550 hPa could have been the critical factor leading to strong convective development, particularly in this region of very favorable vertical wind shear.

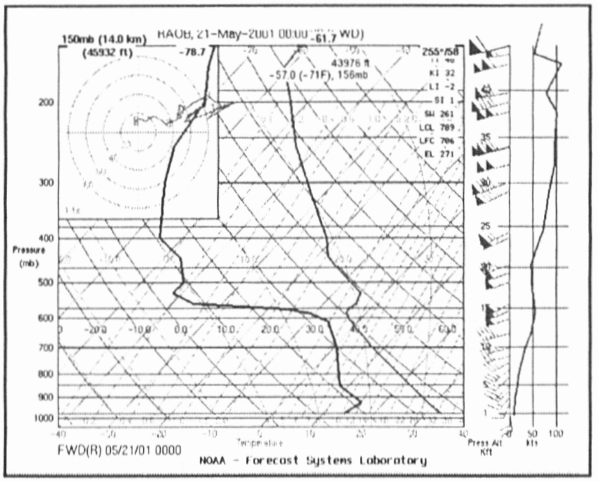

Fig.7. Radiosonde observation at 0000 UTC 21 May 2001 at Fort Worth, Texas.

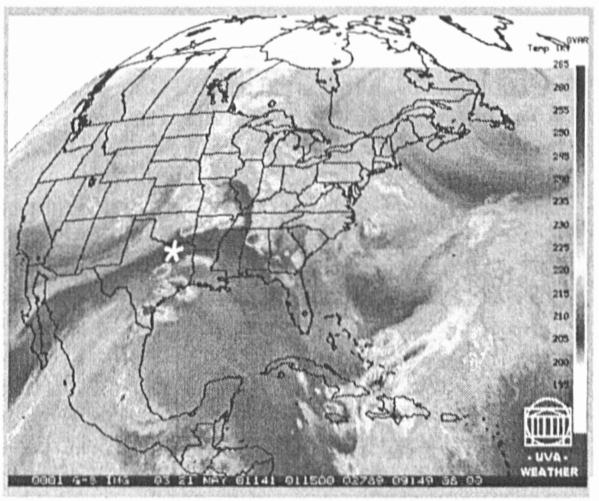

Fig. 8. GOES-East water vapor imagery at 0115 UTC 21 May 2001. White asterisk indicates location of radiosonde ascent made at Fort Worth, Texas (see Figure 7).

Among other mechanisms that may play a role in these cases of MCS development are dynamical processes involving jet interactions and potential vorticity (*e.g.*, circulations driven by superposed upper-level and low-level jetstreams; see Uccellini 1980). Another possibility is that the critical factor promoting MCS development is simply the dryness and location of the descending jet as it interacts with precipitation. Diagnostic analyses including potential vorticity budgets of these cases may help to resolve these possibilities. In any event, the cases inventoried here suggest the usefulness of dry filaments in water vapor imagery as precursors of MCS development.

Acknowledgments. We thank Nita Fullerton and Linda Wharton (FSL) for their helpful reviews.

5. REFERENCES

Appenzeller, C. and H.C. Davies, 1992: Structure of stratospheric intrusions into the troposphere. *Nature*, **358**, 570-572.

Appenzeller, C., H.C. Davies and W.A. Norton, 1996: Fragmentation of stratospheric intrusions. *J. Geophys. Res.*, **101 (D1)**, 1435-1456.

Caracena, F., A. Marroquin and E.I. Tollerud, 2000: A potential vorticity streamer and its role in the development of a week-long series of mesoscale convective systems. Part II: Mesoanalysis of a prominent storm in the series. Preprints *20th Conf. on Severe Local Storms*, Orlando, FL, Amer. Meteor. Soc., 497-500.

Mansfield, D.A., 1994: The use of potential vorticity in forecasting cyclones: operational aspects. *Proc. Int. Symposium on The Life Cycles of Extratropical Cyclones.* Bergen, Norway, Vol. III, 326-331.

Massacand, A.C., H. Wernli, and H.C. Davies, 1998: Heavy precipitation on the Alpine southside: An upper-level precursor. *Geophys. Res. Letters*, **25**, 1435-1438.

Moody, J.L., A.J. Wimmers, and J.C. Davenport, 1999: Remotely sensed specific humidity: Development of a derived product from the GOES Imager Channel 3. *Geophys. Res. Letters*, **26**, 59-62.

Rodgers, D.M., C. Girz Griffith and J.L. Torgerson, 1988: A GOES water vapor image dry slot and the formation of mesoscale convection. Preprints *15th Conf. on Severe Local Storms*, Boston, MA, Amer. Meteor. Soc., 267-271.

Tollerud, E. I., F. Caracena, and A. Marroquin, 2000: A potential vorticity streamer and its role in the development of a week-long series of mesoscale convective systems. Part I: Severe weather and precipitation. Preprints, *20th Conf. on Severe Local Storms*, Orlando, FL, Amer. Meteor. Soc., 335-338.

Thiao, W., R.A. Scofield, and J. Robinson, 1993: The relationship between water vapor plumes and extreme rainfall events during the summer season. *NOAA Tech. Report. NESDIS 67,* Washington D.C., Department of Commerce.

Uccellini, L. W., 1980: On the role of upper tropospheric jet streaks and leeside cyclogenesis in the development of low-level jets in the Great Plains. *Mon. Wea. Rev.*, **108**,1689-1696.

P3.57 OPERATIONAL CLOUD DETECTION IN GOES IMAGERY

Gary J. Jedlovec*
Global Hydrology and Climate Center
NASA/Marshall Space Flight Center, Huntsville, Alabama

and

Kevin Laws
Global Hydrology and Climate Center
University of Alabama - Huntsville, Huntsville, Alabama

1. INTRODUCTION

The accurate detection of clouds in satellite imagery is important in research and operational applications. Cloud cover influences the distribution of solar radiation reaching the ground where it is absorbed. Resulting fluxes of sensible and latent heat are critical to the accurate characterization of boundary layer behavior and mesoscale circulations that often lead to convective development. Therefore the spatial and temporal variation in cloud cover can greatly affect regional and localized weather processes.

NOAA's geostationary satellites play a key role in observing the spatial and temporal variations in cloud cover over much of North America and surrounding ocean regions. The nearly continuous viewing of the Imager and Sounder on the *GOES-East* and *West* satellites allows for the rapid temporal sampling of changes in cloud cover not captured by higher spatial resolution polar orbit instruments. While limited to 1km and 4km (or 8km from the Sounder) in the visible and infrared channels, respectively, the *GOES* Imager and Sounder are used by NOAA to generate real-time cloud products in support of their operational data requirements. Their cloud detection approach uses time and space dependent threshold tests involving inter-band comparisons, and comparisons to satellite-derived estimates of skin temperature and albedo (Hayden et al. 1996).

* *Corresponding author address: Gary J. Jedlovec, NASA/MSFC Global Hydrology and Climate Center, 320 Sparkman Drive, Huntsville, Alabama 35805; e-mail: gary.jedlovec@msfc.nasa.gov.*

Guillory et al. (1998) presented a new method for cloud detection using the shortwave and longwave window channels on the *GOES* Imager. The bi-spectral spatial coherence (BSC) method uses two spatial tests and one spectral threshold to identify clouds in *GOES* Imager or Sounder imagery. The BSC technique has been used operationally over the last several years at the Global Hydrology and Climate Center (GHCC) to support numerous climate research and modeling activities (Lapenta et al. 2001). The performance of the BSC method has been adequate during the day, however continued poor performance of the algorithm near sunrise / sunset and at night has prompted further research into the cloud detect problem. The focus of this conference paper and companion poster is to present some preliminary results of a modification to the BSC technique to improve the "round-the-clock" performance of the operational cloud detection algorithm used at GHCC. The paper describes the new algorithm and compares the results with the previous BSC approach and with the NOAA/NESDIS operational cloud product.

2. METHODOLOGY

The underlying principle of the original BSC approach is that the emissivity difference of clouds at 11 and 3.7 micrometers varies from that of the surface (land or ocean) and can be detected from channel differences. While the emissivity of clouds at 3.7 micrometers is considerably less than at 11 micrometers, reflected solar radiation at 3.7 micrometers makes the effective brightness temperatures (sum of emission and reflective components) quite large. The emissivity difference can be detected in the *GOES* 11 minus the 3.7 micrometer channel brightness temperature difference. During the day, this difference is a large (negative) number in

the presence of clouds and a small (positive or negative) number in non-cloudy regions. Thus, the transition region from a clear to a cloudy region is manifested in the 11 – 3.7-micrometer difference image as a discontinuity or edge. The BSC technique applies several spatial filters (standard deviation and adjacent pixel tests) to the difference image to first detect the cloud boundaries (edges) and then fill in the cloudy regions (Lecue 1997). This approach works pretty well from mid-morning through late afternoon, but its performance is reduced near sunrise and sunset.

2.1 *Bi-spectral ThresHold Approach*

Over the last year, considerable time was spent tuning the spatial filters in the BSC method to more effectively detect clouds under low sun angles without much success. However, analysis of the difference images in these cases (low sun angle) indicated that a subtle distinction existed between the cloudy and non-cloudy regions. The key was how to objectively detect these differences. The new Bi-spectral ThresHold (BTH) method was developed to do this.

The 11 – 3.7 micrometer brightness temperature differences under low solar angles are spatially and temporally variant. To capture this variation, a sequence of difference images for each time corresponding to the last 20 days is maintained. The historical difference images are used to determine two threshold images, one for positive differences and the other for negative differences, which represent the "expected" minimum difference value corresponding to clear regions. These minimum difference threshold images are used as an additional cloud check in the BSC algorithm. Therefore, the new bi-spectral threshold (BTH) approach uses the following methodology:

1) create 11 – 3.7 micrometer difference image
2) apply standard deviation test on difference image to detect clouds edges,
3) apply adjacent pixel test to fill in around cloud boundaries, and
4) use minimum difference threshold images as a final cloud check.

2.2 *Intercomparison*

To demonstrate the improvement of the new bi-spectral threshold (BTH) approach over its predecessor, the bi-spectral spatial coherence (BSC) method, a two-week period from July 2001 was selected for comparison. Each method was applied to hourly *GOES-8* Imager data on each day between 1100 and 2300 UTC. The resultant cloud images were inter-compared and differences were monitored. The NOAA/NESDIS operational cloud product from the *GOES-8* Imager was obtained for each day and time and used in the comparison as well.

2.3 *Validation*

To quantify the performance of the three different cloud detection methods (BTH, BSC, NOAA/NESDIS), fifteen eastern U.S. sites were selected for validation purposes based on unique topography including coastline, lakeshore, mountain range, urban/rural areas, and over open water. A trained meteorologist / satellite specialist used a time sequence of *GOES* visible and infrared images to subjectively determine the presence of clouds over a 32 km x 32 km area. If the area was partly cloudy, then the entire area was labeled as cloudy. This approach allowed for the overall cloud patterns and signatures from frontal structures, daytime cumulus fields and cirrus clouds to be identified. To further aid in the subjective cloud determination, eight of the fifteen sites selected were augmented Automated Surface Observing System (ASOS) stations (Unger 1992). The ASOS data not only provide the amount of cloud coverage, but also include cloud height, which has important implications when looking at reflective properties from different cloud regimes. A cloud – no cloud determination at each site, for each time on each day, provided the "ground truth" for the cloud validation. Each of the three satellite-derived cloud products were compared to this ground truth data and labeled in one of four ways: clear-correct (CLC), clear-incorrect (CLI), cloudy-correct (CDC), or cloudy-incorrect (CDI).

3. PRELIMINARY RESULTS

The dates for this initial study were 12 July through 26 July 2001. During this fifteen-day period, several days were not analyzed due to the loss of data, but there were several hundred verified points for each hour. The following results demonstrate the performance of the techniques for two representative times, namely, 1145 UTC and 1845 UTC. Performance at other times was similar and will be presented in the companion poster presentation. The results below are presented as the percentage correct and incorrect

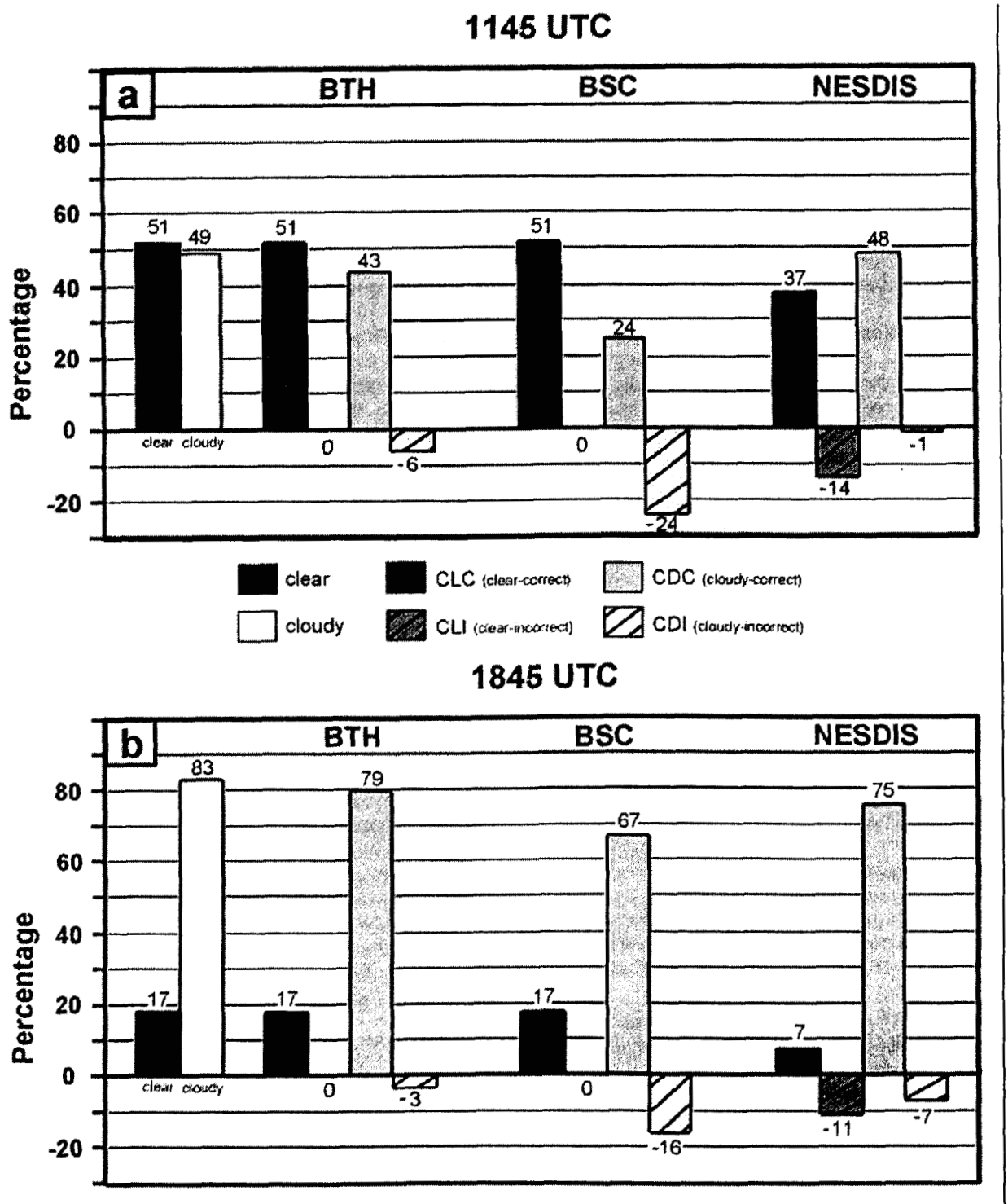

Figure 1. Statistical analysis comparing the three different cloud detection methods: Bi-spectral ThresHold (BTH), Bi-spectral Spatial Coherence (BSC), and NOAA/NESDIS. These results are based upon the initial study from 12-26 July 2001 for a) 1145 UTC and b) 1845 UTC.

for the clear and cloudy regions for all days combined. Each cloud mask technique is shown separately with the corresponding percentages. At 1145 UTC, nearly 50% of the validation points for these days were cloudy, while at 1845 UTC over 80% of the points contained some type of cloud.

Figure 1 presents the results for 1145 and 1845 UTC, respectively. The performance of the original BSC technique (currently used operationally at the Global Hydrology and Climate Center) is typical of the algorithms performance during the warm season. It can be seen that the algorithm tends to under-determine the clouds. While nearly all of the clear points are properly detected, 24% of the clouds go undetected at 1145 UTC. The BSC algorithms performance improves at 1845 UTC as the amount of undetected cloudy points falls to about 16%. This is significant because most of the ground truth points are cloudy at this time. The NESDIS operational product from the *GOES-8* Imager is used as a reference in this study. In contrast with the BSC technique, the NESDIS cloud algorithm seems to over determine clouds at both times. At 1145 UTC nearly all of the clouds are properly determined but about one-fourth (14%/51%) of the clear points are also improperly determined as clouds. This characteristic pattern exists at 1845 UTC as well although the amount of undetected cloudy points goes up a fair bit. Overall, the original BSC and NESDIS cloud products perform equally well in some regions but fail in others for their own separate reasons.

The results for the new BTH technique are also shown in the figures. Significant improvement over both the BSC and NESDIS techniques occurred for all times, including both times presented here. At 1145 UTC the BTH method detects the clear regions very well and only misses (under-determines) the clouds by about 6%. This is reduced down to just a few percent at 1845 UTC without degradation (over determination of clouds) in the clear regions.

4. DISCUSSION

The results of the new bi-spectral threshold (BTH) technique have been shown to offer improvements over existing techniques applied to *GOES* imagery for the detection of clouds. The running 20-day minimum difference threshold images used as part of the algorithm incorporate knowledge of the spatial and temporal changes in thermal characteristics of the surface which are important for cloud detection. In image form, these thresholds capture the spatially varying affects of solar illumination (as a function of time of day) and land use. The 20-day influence on the threshold images captures the seasonal variation in the solar illumination and land cover changes. Although it has only been tested on a limited number of days in one season, the new BTH method should perform quite well in other seasons as well.

Acknowledgments

This research was partially supported under the NOAA *GOES* Improved Measurements and Product Assessment Plan (GIMPAP). Jaime Daniels of NOAA/NESDIS provided the *GOES-8* cloud products.

References

Guillory, A. R., J. M. Lecue, G. J. Jedlovec, and B. N. Whitworth, 1998: Cloud filtering using a bi-spectral spatial coherence approach. 9th Conference on Satellite Meteorology and Oceanography, AMS, Paris, France, 374-376.

Hayden, C. M., G. S. Wade, and T. J. Schmit, 1996: Derived product imagery from GOES-8. *J. Appl. Meteor.*, **35**, 153-162.

Lapenta, W. M., R. J. Suggs, G. J. Jedlovec, R. T. McNider, and S. R. Dembek, 2001: Assimilation of GOES land surface temperature within a rapid update cycle format: Impact on MM5 warm season QPF. 11th Conference on Satellite Meteorology and Oceanography, AMS, Madison, WI (elsewhere in this preprint volume).

Lecue, J. M., 1997: The 'Cloud Map"method: A new cloud filtering algorithm. Research paper, IEEC, 14 pp, [Available from Gary Jedlovec, NASA/MSFC, SD60, Huntsville, AL 35812].

Unger, D. A., 1992: An evaluation of satellite sky cover estimates to complement ASOS observations. NOAA/NWS/OSD/TDL Office Note 92-13, 12 pp. [Available from NWS, Silver Spring, MD 20910.]

P3.58

A SATELLITE DIAGNOSTIC OF GLOBAL CONVECTION

Frederick R. Mosher*
Aviation Weather Center
Kansas City, Missouri

1. INTRODUCTION

The Aviation Weather Center (AWC) generates High Level Significant Weather forecasts covering 2/3 of the globe which include areas of convective activity that will affect jet aircraft. Verification of these forecasts requires an objective method of global monitoring of convective activity. In addition, a real time diagnostic of thunderstorm convective activity would be of great benefit to aircraft routing decisions. Both the verification of global thunderstorm forecasts and aircraft routing require continual monitoring over the entire globe with update rates of an hour or less. Thunderstorms can be detected directly using radar, remotely sensed lightning detection, and satellite microwave sensors. However, these detection techniques are either not available over the entire globe, or are not continually available. Algorithms for the indirect estimates of thunderstorm existence and intensity have been developed using geostationary satellite images. Over the past 30 years, a number of algorithms have been developed, especially for rainfall estimation. Many of these algorithms use infrared temperature thresholds (such as Arkin (1987) and Vicente (1998)) to determine the existence of thunderstorm clouds. Since cirrus clouds can also have temperatures colder than the thunderstorm's threshold, Rozumalski (2000) has shown that these techniques frequently produce erratic results. Other cloud classification techniques, such as Tag (2000) use a combination of thresholds, texture, and spectral response of various channels. However Shenk (1976) has shown that the ability of these cloud classification techniques to distinguish between thunderstorms and cirrus significantly degrades without the use of the visible channel, such as at night.

At the suggestion of Dennis Chesters (personal communications), the NASA GOES Project Scientist, a new approach to thunderstorm identification using satellite images has been undertaken. This technique uses the difference between the infrared 11 micron channel and the 6.7 micron water vapor channel. Since these two channels are on all the geostationary weather satellites, this technique has the potential for global applications of thunderstorm detection.

*Corresponding author address: Frederick R. Mosher Aviation Weather Center, 7220 NW 101st Terrace, Kansas City, MO 64153-2371; e-mail: Frederick.R.Mosher@noaa.gov

2. THUNDERSTORM DETECTION ALGORITHM

The algorithm is based on the temperature difference between the infrared channel and the water vapor channel.

2.1 Physical Basis of Algorithm

The physical concept behind the algorithm is that thunderstorms lift moisture and cloud particles to the top of the troposphere. Where there is active uplift, the infrared and water vapor channels will have the same temperature. The wind at the thunderstorm top will transport the cloud ice particles and moisture down wind. As the cloud ice particles advect away from the thunderstorm, they will gradually fall because of their size. The water vapor will also advect away from the thunderstorm, but will not fall. Hence in the cirrus clouds down wind of the thunderstorm, there should be a slight temperature difference between the infrared channel sensing the temperature of the cloud particles and the water vapor channel sensing the temperature of the water vapor in the air. In the current algorithm, areas are eliminated where the infrared channel is at least 1 degree C. warmer than the water vapor channel.

2.2 Algorithm Processing

The original version of the global thunderstorm algorithm used differences between the global composites of infrared and water vapor images. While the algorithm showed promise, there were problems in the overlap regions between satellites with false identification of cirrus as thunderstorms. Originally it was thought that these were caused by limb darkening differences between the two channels. However on closer examination it was found that the problems were caused by non-coincident pixels where one satellite was providing the infrared value in the composite and another satellite was providing the water vapor value. The algorithm was changed to first take the differences between the channels in the original satellite image projections, and then to remap and composite the differences into a global composite. This eliminated the false identification problems in the overlap regions.

The global composite is generated by remapping each satellite difference image into a Mercator projection with a parallax correction assuming a 10 km cloud top height. The parallax correction is accomplished by increasing the radius of the earth by 10 km in the navigation subroutines computing coordinate transformations. Image data close to the earth edge beyond approximately 77 degrees from the satellite

subpoint are excluded from the composite. Where there is overlap between satellites, the most timely data is selected for the composite.

2.3 Meteosat Overestimation

The requirement for space and time coincident differences of infrared and water vapor images is a problem with the Meteosat satellite. During the day time the visible and infrared channel data must share the same communications bandwidth, with the net result being that the water vapor image is sent only every 3 hours during daylight hours, and every ½ hour during the night hours. The infrared is continually sent every ½ hour. This results in an overestimation of convective cloud extent during the day time. In the areas covered by Meteosat the convective clouds have a 3 hour cycle where the thunderstorm clouds will appear to grow during the 3 hours, and then shrink back when a new water vapor image is obtained. This problem will be corrected in the coming years when a new generation of Meteosat satellites are launched. In the mean time, the decision was made to allow the overestimate of convective cloud extend in the regions covered by Meteosat rather than limit the data update to once every 3 hours.

2.4 Stability Filter

While thunderstorms are the most common phenomenon lifting clouds to the top of the troposphere, they are not the only lifting mechanisms which generate high clouds. Ageostrophic motions around jet streams cause cirrus clouds. Cyclone lifting mechanisms cause extensive cirrus shields around the mid latitude storms. The channel difference also picks up these cirrus clouds where they are being initially generated. Since these are not associated with thunderstorms, a filter is desired to remove them from the thunderstorm composite. Several meteorological filters have been tried. Warm advection at 250 mb showed some success in identification of jet stream cirrus, and positive vorticity advection at 250 mb showed some success in identification of mid latitude cyclone cirrus. However, a stability index filter appeared to have the most success in elimination of non-convective areas of active uplift. The global AVN forecast model 4 layer Lifted Index (LI) is being used in the current algorithm to eliminate areas not associated with convection. Areas with a positive LI of 1 or greater are eliminated from the composite. The most current gridded AVN model data are converted to an image in the same projection as the satellite image, and then used to eliminate areas not conducive to convection.

The use of the LI filter assumes that the AVN model has captured the state of the atmosphere correctly for the entire globe. Preliminary monitoring of the algorithm for areas incorrectly eliminated by the LI filter has shown few problems. The most common problem has been overrunning convection in the winter near warm fronts. The AVN 4 level LI does not appear to correctly capture the instability associated with these overrunning situations. The AVN model does appear to correctly identify areas of instability over the oceans as well as over land with various mesoscale forcing features.

2.5 Verification

During the development of the algorithm, remotely sensed lightning was used for ground truth of thunderstorm existence. The National Lightning Detection Network (NLDN) as described by Cummins (1998) was augmented with data from the Canadian Lightning Detection Network (CLDN), and network data from Japan, France, and Germany. Global Atmospheric, Inc. (GAI) processed these data with a long range detection algorithm described by Cramer (1999). Nierow (2000) showed these long range data to be useful with range of 2000-4000 km and location accuracy of 16-32 km.

An example of the satellite thunderstorm diagnostic is shown in figure 1. The infrared satellite is shown for the same area in figure 2 with an overlay of the lightning data detected for 60 minutes centered on the satellite data time. The example shows good subjective agreement between the satellite derived product and the lightning data.

A more formal verification is being undertaken utilizing the Real Time Verification System (RTVS) developed by the Forecast Systems Lab (FSL). The ground truth data will be the National Convective Weather Diagnostic (NCWD) described by Magenhardt (2000). Results of this verification study will be available next year.

3. Satellite Thunderstorm Diagnostic

The satellite thunderstorm diagnostic algorithm is routinely run every half hour at the AWC and is made available to AWC forecasters. Sectors are also generated for gif images that are posted to the web. Real time examples of the diagnostic can be seen on the AWC web page at:
http://www.awc-kc.noaa.gov/awc/experimnetal.html.
Sectors for the Atlantic, Pacific, Tropics, and the World are currently available, although other sectors could be generated.

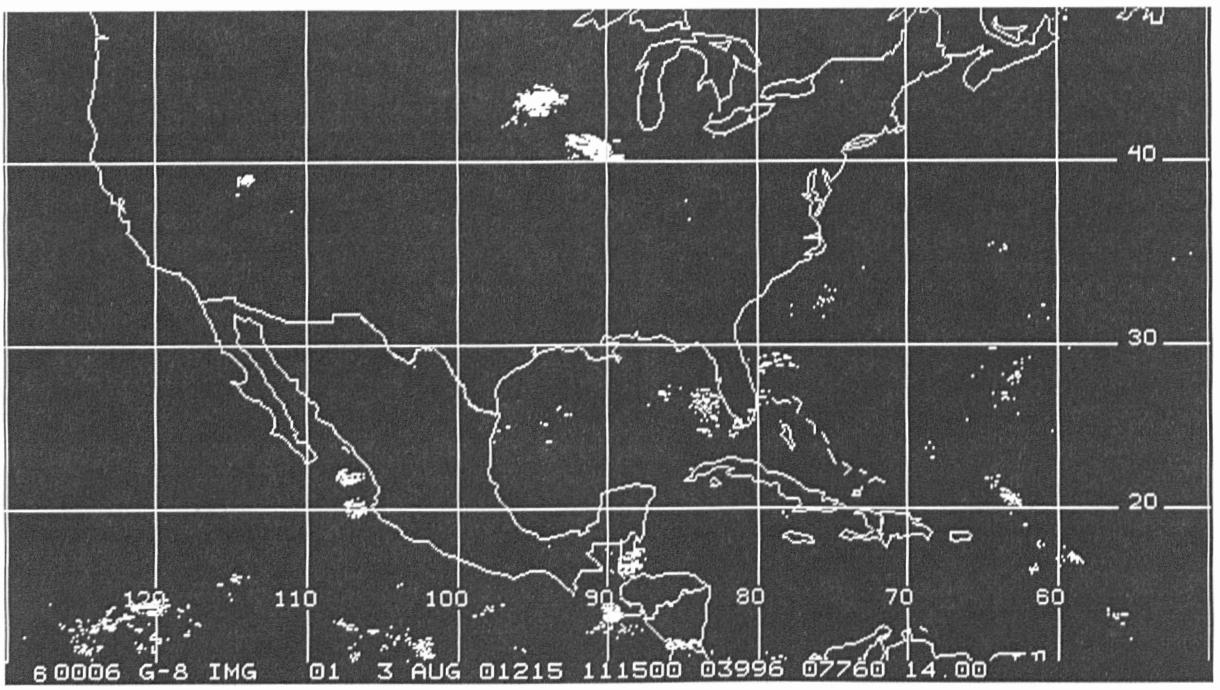

Figure 1
Satellite convective diagnostic showing sector over the US and adjacent ocean areas for August 3 at 11:15 UTC. Areas in white are active thunderstorms.

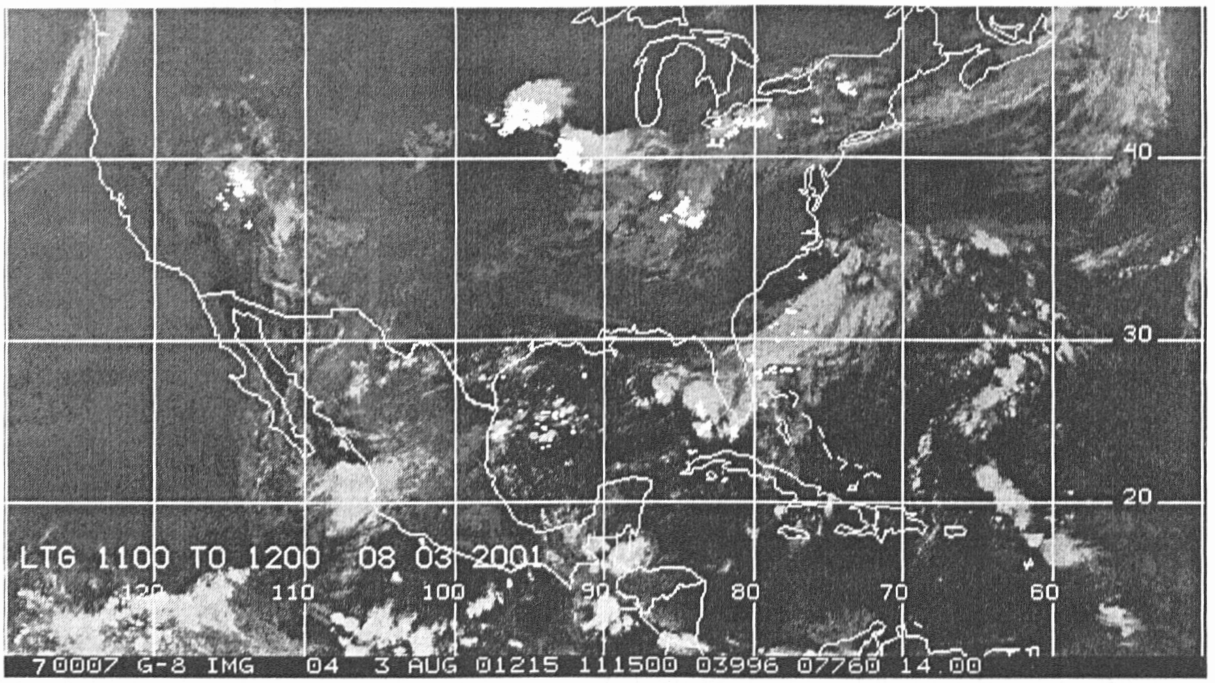

Figure 2
Infrared satellite image with lightning overlay in white. The lightning is for the one hour period centered on the time of the satellite image.

4. Summary

A global satellite based thunderstorm detection diagnostic has been developed using the temperature difference between the infrared and water vapor channels from geostationary satellite images. The physical concept behind the algorithm is that in areas of active uplift, the temperature of the clouds detected by the infrared channel will be the same as the temperature of the water vapor detected by the 6.7 micron channel. As the clouds advect away from the areas of uplift, the cloud particles will slowly fall, but the water vapor will not. This will result in the infrared channel being slightly warmer than the water vapor channel. In the current algorithm, pixels which have temperature differences of 1 degree C. or warmer are eliminated as non-thunderstorm. The temperature differences are remapped and combined into a global composite with a parallax correction of 10 km. Data beyond approximately 77 degrees from the satellite subpoint are eliminated from the composite. Where two satellites have overlap, the data from the more recent image is used in the composite. Since other phenomenon, such as ageostrophic motions around jet streams, can cause cloud formation at the top of the atmosphere, a filter of the AVN Lifted Index (LI) was applied to the data. Areas with a positive LI of 1 or greater are eliminated from the composite. Verification efforts have been started.

5. References

Arkin, Phillip A. and B.N. Meisner, 1987: The Relationship between Large-Scale Convective Rainfall and Cold Cloud over the Western Hemisphere during 1982-84. *Mon. Wea. Rev.*,**115**, 51-74.

Cramer, J.A. and K.L. Cummins, 1999: Long-range and Trans oceanic Lightning Detection. *Preprints, 11th International Conf. On Atmospheric Electricity,* Huntsville, Al. Amer. Meteor. Soc.,250-253.

Cummins, K.L., E.A. Brado, W.L. Hiscox, R.B. Pyle, A.E. Pfifer, 1998: A Combined TOA/MDF Technology Upgrade of the U.S. National Lightning Detection Network, *J. Geophys. Res.,* 103, 9035-9044.

Megenhardt, Dan, C.K. Mueller, N. Rehak, and G. Cunning, 2000: Evaluation of the National Convective Weather Forecast Product. *Preprints, 9th Conference on Aviation, Range, and Aerospace Meteorology,* Orlando, FL. Amer. Meteor. Soc.,171-176.

Nierow, A., R.C. Showalter, F. Mosher, J. Jalickee, and K. Cummins, 2000: Preliminary Evaluations of Using Lightning Data to Impove Convective Forecasting for Aviation. *Preprints, 16th International Conference on Interactive Information and Processing Systems (IIPS) for Meteorology , Oceanography and Hydrology,* Long Beach CA., Amer. Meteor. Soc., 174-177.

Rozumalski, Robert A. 2000: A Quantitative Assessment of the NESDIS Auto-Estimator. *Wea. Forecasting*, **15**, 397-415.

Shenk, William E., R.J. Holub, and R.A. Neff, 1976: A Multispectral Cloud Type Identification Method for Tropical Ocean Areas with Nimbus-3 MRIR Measurements. *Mon. Wea. Rev.* **104**, 284-291.

Tag, Paul M. , R.L. Bankert, and L.R. Brody, 2000: An AVHRR Multiple Cloud-Type Classification Package. *J. Appl. Meteor*,**3 9**,125-134.

Vicente, Gilberto A., R.A. Scofield, and W.P Menzel, 1998: The Operational GOES Infrared Rainfall Estimation Technique. *Bull. Amer. Meteor. Soc.*,**7 9**, 1883-1898.

P3.60

DERIVED CLOUD PRODUCTS FROM THE GOES-M IMAGER

Anthony J. Schreiner*
CIMSS/Univ. of Wisconsin, Madison, Wisconsin
Timothy J. Schmit
NOAA/NESDIS/ORA, Advanced Satellite Products Team, Madison, Wisconsin

1. INTRODUCTION

With the launch of the next in the series of geostationary platforms, Geostationary Operational Environmental Satellite (GOES) – M Imager, a modification in the suite of bands has been introduced. The current Imager obtains information from four infrared bands and one visible band (Menzel and Purdom, 1994). GOES-M continues the same number of bands, but initiates several changes. Table 1 summarizes those spectral changes.

Table 1. GOES Imager spectral widths for GOES-8 (similar for GOES-9 through GOES-11) and GOES-M. The units of wavelength are μm; the units for wavenumber are cm^{-1}.

GOES-8 Imager Bandwidths

Ch. No.	Wavelength Range	Central Wave-length	Wavenumber Range
1	0.53-0.72	0.64	13812-19048
2	3.78-4.03	3.91	2482.2-2647.7
3	6.47-7.03	6.75	1421.8-1544.5
4	10.21-11.20	10.69	892.5-979.1
5	11.54-12.47	11.97	802.1-866.2
6	---	---	---

GOES-M Imager Bandwidths

Ch. No.	Wavelength Range	Central Wave-length	Wavenumber Range
1	0.53-0.77	0.65	12970-18939
2	3.76-4.03	3.90	2481.9-2656.4
3	5.77-7.33	6.48	1363.3-1733.4
4	10.23-11.24	10.71	889.7-977.1
5	---	---	---
6	12.96-13.72	13.31	729.0-771.6

The GOES-M Imager includes a band centered at 13.3 μm and improves north-south spatial resolution of a spectrally modified 6.5 μm band. The addition of the 13.3 μm band comes at the expense of eliminating the 12 μm band on the Imagers. GOES-8 and GOES-M Imager spectral response functions are shown in Fig. 1. Note the elimination of the 12 μm band and the addition of the 13.3 μm band, in addition to the modified "water vapor" band.

With the current series of GOES Imagers cloud height or cloud top pressures from the GOES Imager are available using either the IR Window Technique (Schreiner, et al; 1993) or the IR Window-Water Vapor Intercept Technique (Nieman, et al; 1993). By including a "CO_2" band (13.3 μm) among the suite of Imager channels the opportunity for more frequent (than the GOES Sounder) and accurate cloud products (than the GOES Imager) is now possible using the CO_2 Absorption Technique (CAT) (Wylie and Menzel, 1999). The CAT will provide more accurate calculations of Effective Cloud Amount (ECA) than currently available from the GOES Imager, more frequent and timely Satellite Cloud Products (SCP) in support of the Automated Surface Observing System (ASOS), and hemispheric coverage of the CAT for input into numerical prediction models.

The objective of this paper is twofold. First, to briefly describe the changes on the GOES-M Imager. Second, to introduce the cloud product based on the Imager data.

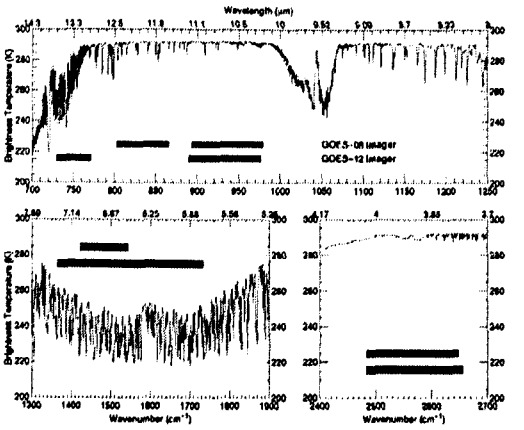

Fig. 1. Spectral ranges for the GOES-8 (top bars) and GOES-M (bottom bars) Imagers. A sample high spectral-resolution earth emitted spectra is also plotted.

* *Corresponding author address:* Anthony J. Schreiner, CIMSS, University of Wisconsin-Madison, 1225 W. Dayton St., Madison, WI 53706;e-mail: tonys@ssec.wisc.edu

2. INSTRUMENT CHANGES

The GOES-M "water vapor" band is spectrally wider than the current 6.7 μm band. The spectral width covers the region from 5.77 to 7.33 μm with a center wavelength of 6.5 μm (Table 1). The water vapor spectral response function was made spectrally wider to improve the signal-to-noise ratio, and thus compensate for the smaller Field Of View (FOV) on GOES-M than previous Imagers. The spectral shift will make it similar to the current European METEOSAT (METEOrological SATellite) "water vapor" band. The current Meteosat bandwidth for the "water vapor" band is 5.7 to 7.1 μm Schmetz et al., 1998). Radiative transfer calculations for a standard atmosphere show that the GOES-M band 3 will be approximately 2 K warmer than the current Imager band 3 onboard GOES-8. This difference is consistent for a variety of atmospheres (not shown) (Schmit et al., 2001).

The GOES-M 6.5 μm band will also have a higher north-south spatial resolution. It will change from approximately 8 km to 4 km at the sub-satellite point. On the GOES Imagers, the IGFOVs are over-sampled in the east/west direction by a factor of 1.75 providing an effective resolution in the east-west direction of 2.3 km (Menzel and Purdom, 1994).

Table 2. GOES-8 (top) and GOES-M (bottom) Imager spatial characteristics. Detector Instantaneous Geometric Field Of View (IGFOV) or footprint is in km at the sub-satellite point. The Sampled Subpoint Resolution (SSR) is also in km and is a finer resolution due to over sampling in the east-west direction. The spatial characteristics are listed as the east-west by north-south dimensions, respectively.

	GOES-8		
Ch.	Descr.	IGFOV	SSR
1	Visible	1.0 x 1.0	0.57 x 1.0
2	SW window	4.0 x 4.0	2.3 x 4.0
3	Water Vapor	8.0 x 8.0	2.3 x 8.0
4	LW window	4.0 x 4.0	2.3 x 4.0
5	Split window	4.0 x 4.0	2.3 x 4.0
6	CO_2	---	---

	GOES-M		
Ch.	Descr.	IGFOV	SSR
1	Visible	1.0 x 1.0	0.57 x 1.0
2	SW window	4.0 x 4.0	2.3 x 4.0
3	Water Vapor	4.0 x 4.0	2.3 x 4.0
4	LW window	4.0 x 4.0	2.3 x 4.0
5	Split window	---	---
6	CO_2	8.0 x 8.0	2.3 x 8.0

The 13.3 μm band, referred to as the GOES Imager band 6, will allow for cloud height determinations. This band is similar, although with a broader spectral response function, to band 5 on the current GOES Sounder (Menzel et al., 1998) (Fig. 2). Forward radiative transfer calculations for a standard atmosphere show the GOES-M Imager 13.3 μm band will have a slightly higher mean brightness temperature than the Sounder band 5 (Fig. 3). This difference of approximately 1.5 K exists for other atmospheres as well (not shown). The GOES-M 13.3 μm spatial resolution will be approximately 8 km in the north-south direction (Table 2).

The addition of the 13.3 μm band results in the elimination of the 12 μm band on the GOES-M/N/O/P Imager. For the GOES cloud product the 12 μm band is used for detecting the presence, or lack of clouds prior to determining the height and amount of cloud (Hayden, et al; 1996 and Schreiner et al; 2001).

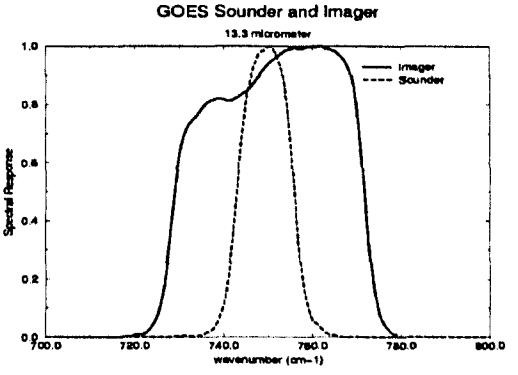

Fig.2. Normalized spectral response function for the GOES-M Imager 13.3 μm band and the corresponding Sounder band.

3. CLOUD PRODUCTS

Cloud products generated via the CO_2 absorption technique have been demonstrated from instruments on both geostationary and polar-orbiting platforms (Wylie and Wang, 1997; Wylie and Menzel, 1999; Schreiner et al., 2001). Cloud products derived from the GOES Sounder have been used to initialize numerical models (Bayler et al., 2001 and Kim et al., 2000). Improved products from the GOES-M Imager will include cloud top pressure, effective cloud amount and cloud top temperature. Fig. 4 shows the Cloud Top Pressure (CTP) derived image using only spectral bands from the GOES Sounder that will be available on the GOES-M Imager. This image has been compared to

one derived from the full set of Sounder bands used for deriving CTP. With a sample size of 3533, the bias (Sounder minus Imager derived CTP) was 20 hPa and the root mean square (rms) was 112 hPa.

With the addition of the 13.3 μm band on the GOES-M Imager, the Satellite Cloud Product (SCP) that complements the ground-based ASOS (Automated Surface Observing System) could be generated from the Imager rather than the Sounder (Schreiner et al., 1993). The SCP, based on GOES-M Imager data, could be available in a more timely fashion since the Imager coverage rate is much faster than the Sounder.

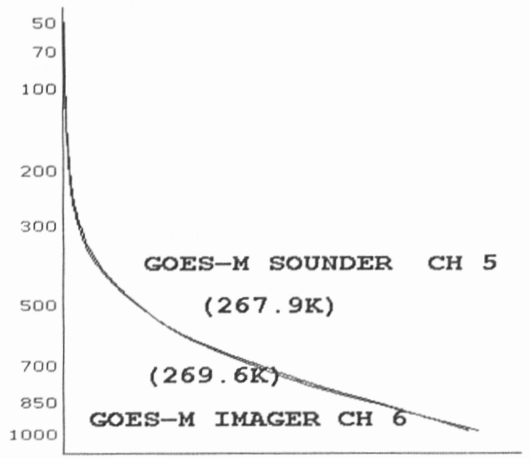

Fig. 3. Weighting function for both the 13.3 μm GOES-M Sounder and Imager bands for a standard atmosphere. The units of the ordinate are pressure (hPa).

An additional product available to the modeling community will be near-hemispheric cloud top information. Assuming the GOES-M schedule is similar to the current GOES-8 a hemispheric view of the earth will occur every three hours. Output from these processed data will provide cloud information in addition to clear, cloudy, and averaged brightness temperatures from 65N to 65S. An example of what such a cloud image may look like will be shown.

The loss of the 12 μm band will negatively impact the detection of low cloud. Currently, 11 minus 12 μm differences are used extensively to flag the presence of clouds at night. Without the 12 μm data, there will be more reliance on visible data during the day and 3.9 μm data during the night for cloud detection. The 13.3 μm data may also help to mitigate the loss of the 12 μm band for cloud detection. Experience with actual GOES-M data during the post-launch checkout will answer this question.

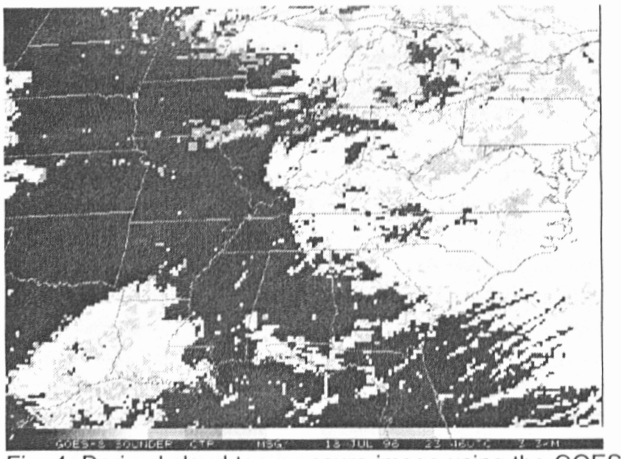

Fig. 4. Derived cloud top pressure image using the GOES Sounder 13.3 μm data and LW infrared window.

4. SUMMARY

Cloud products from the GOES-M Imager will benefit from the inclusion of a band centered at 13.3 μm. Among them are cloud height and effective cloud amount via the CO2 Absorption Technique. Quantitative coverage, both spatially and temporally, will increase. This will benefit the SCP for ASOS and the numerical modeling community.

In order to accommodate the 13.3 μm band, the 12 μm band was eliminated on the GOES-M Imager. This change may affect the ability to detect some clouds, especially low clouds at night. The 12 μm band, along with a host of other bands, will be included on the next generation series of GOES Imagers, beginning with GOES-R in the 2010 era.

5. REFERENCES

Bayler, G. M., R. M. Aune, and W. H. Raymond, 2001: NWP cloud initialization using GOES sounder data and improved modeling of non-precipitating clouds. *Mon. Wea. Rev.*, **128**, 3911-3920.

Hayden, C. M., G. S. Wade, and T. J. Schmit, 1996: Derived product imagery from GOES-8. *J. Appl. Meteor.*, **35**, 153-162.

Kim, D., and S.G. Benjamin, 2000: Assimilation of cloud-top pressure derived from GOES sounder data into MAPS/RUC. Preprints, *10th Conf. On Satellite Meteorology and Oceanography*, Long Beach, CA, Amer. Meteor. Soc., 110-113.

Menzel, W. P., F. C. Holt, T. J. Schmit, R. M. Aune, G. S. Wade, D. G. Gray, and A. J. Schreiner, 1998: Application of GOES-8/9 soundings to

weather forecasting and nowcasting, *Bull. Amer. Meteor. Soc.*, **79**, 2059-2078.

Menzel, W. P., and J. F. W. Purdom, 1994: Introducing GOES-I: The first of a new generation of geostationary operational environmental satellites, *Bull. Amer. Meteor. Soc.*, **75**, 757-781.

Nieman, S.J., J. Schmetz, and W.P. Menzel, 1993: A comparison of several techniques to assign heights to cloud tracers, *J. Appl. Meteor.*, **32**, 1559-1568.

Schmit, T.J., E.M. Prins, A.J. Schreiner, and J.J. Gurka, 2001: Introducing the GOES-M imager. Submitted to *Nat. Wea. Assoc. Digest.*

Schreiner, A. J., D. A. Unger, W. P. Menzel, G. P. Ellrod, K. I. Strabala, and J. L. Pellett, 1993: A comparison of ground and satellite observations of cloud cover. *Bull. Amer. Meteor. Soc.*, **74**, 1851-1861.

Schreiner, A. J., T. J. Schmit, and W. P. Menzel, 2001: Trends and observations of clouds based on GOES sounder data. Accepted by *J. Geophysical Res. --Atmospheres.*

Schmetz, J., H. Woick, S. Tjemkes, and J. Rattenborg, 1998: From Meteosat to Meteosat Second Generation, In Proceedings of the Ninth Conference on Satellite Meteorology and Oceanography, Paris, France, Amer. Meteor. Soc., 335-338.

Wylie, D. P., and P. H. Wang, 1997: Comparison of cloud frequency data for the High Resolution Infrared Radiometer Sounder and the Stratospheric Aerosol and Gas Experiment II. *J. of Geophys. Res.*, **102** (29), 29,893-29,900.

Wylie, D. P., and W. P. Menzel, 1999: Eight years of high cloud statistics using HIRS. *J. Climate*, **12**, 170-184.

P3.61 # UPPER TROPOSPHERIC MOISTURE ASSIMILATION USING GOES OBSERVATIONS

William H. Raymond*

Cooperative Institute for Meteorological Satellite Studies, University of Wisconsin, Madison, Wisconsin

and

Gary S. Wade

National Environmental Satellite, Data, and Information Service (NOAA), Madison, Wisconsin

1. RELATIVE HUMIDITY

Relative humidity is poorly sampled in both space and time by conventional atmospheric observations. Over the vast oceans, this lack of moisture information is particularly troublesome in numerical weather prediction. Clearly, this scarcity of moisture data enhances the potential value of satellite observations, especially data from the Geostationary Operational Environmental Satellites (GOES) which have good temporal and spatial characteristics. However, in the past, the accuracy of satellite information was compromised by the way the data were prepared for numerical weather prediction. Only in recent years has the true capability of satellite information been realized through the use of the raw observations. Radiance assimilation has been used successfully for some time with polar orbiting satellites employing the TOVS (TIROS Operational Vertical Sounder) instrument (see, McNally and Vesperini 1996; Andersson et al. 1994; Eyre et al. 1993). In contrast, direct assimilation of brightness temperatures from GOES continues to be tested and is now being partially implemented in operational forecasts. In this report the feasibility of a new direct moisture assimilation procedure is tested. The proposed procedure does not require any linearization or the use of an adjoint technique. The numerical optimization of the differences, between the forecast initial conditions (when processed by a forward radiative model) and the observed GOES satellite brightness temperatures for the water vapor channel 3 (6.7 micrometers), is incorporated directly to the CIMSS (Cooperative Institute for Meteorological Satellite Studies) Regional Assimilation System (CRAS) forecast model.

*Corresponding Author Address: William H. Raymond, University of Wisconsin, 1225 W. Dayton Street, Madison, Wisconsin 53706

2. CRAS ASSIMILATION SYSTEM

The CRAS is an improved version of the original Australian Bureau of Meteorology Research Centre's operational analysis (Mills and Seaman 1990), vertical mode initialization (Bourke and McGregor 1983), and semi-implicit forecast model (McGregor et al. 1978; Leslie et al. 1985). Our calculations use a horizontal grid spacing of 40 km on a 185 x 129 lattice, while the vertical sigma coordinate is subdivided into 30 levels. During each time step, the horizontal wind components, temperature, and mixing ratio fields are selectively smoothed using a 6th order implicit low-pass tangent filter (Raymond 1988), with a filter parameter set sufficiently large to provide only a limited amount of horizontal mixing. Because cloud and rainwater are horizontally discontinuous quantities, they are not filtered; nor, is horizontal diffusion applied. In our forecasts, cloud liquid water quantities appear to be of the proper magnitude (Raymond et al 1995) and the lack of horizontal mixing has so far not presented any numerical stability problems.

The version of the forecast model used in this study contains a nonlocal parameterization of dry turbulent mixing based on adjustment concepts, denoted by the acronym NTAC (Raymond 1999). This parameterization determines the nonlocal-mixing coefficients by examining a turbulent kinetic energy (TKE) equation. The mixing coefficients are zero when there is no turbulence.

The forecast model contains explicit

conservation equations for cloud, ice, and rainwater (Diak et al. 1992; Raymond et al. 1995). The explicit cloud physics parameterization uses a modified Kessler - type scheme (Kessler 1974); while, the ice physics, condensation, and fall velocity calculations are similar to those described in Asai (1965), Liu and Orville (1969), and Dudhia (1989). Liquid (ice) cloud and rainwater quantities are used in all calculations involving the virtual temperature, i.e., water loading is included. The parameterizations of deep cumulus convection use a modified Kuo scheme (Sundqvist et al. 1989). Clouds that cap the boundary layer are estimated by a shallow cumulus parameterization that is based on a nonlocal evaluation of TKE (Raymond 2000).

As suggested in the hybrid scheme described in Molinari and Dudek (1992), the convective cloud and rainwater are detrained to the grid scale cloud variables. By not instantaneously converting the convective rainwater directly into surface precipitation, the opportunity for (additional) evaporation is increased in the hybrid approach since the explicit cloud calculations contain both time dependent liquid water advection and rain water fallout calculations. Rain drag is included as a Rayleigh damping term to help control the production of excessive precipitation (Raymond and Aune 1998).

3. NUMERICAL APPROACH

For accuracy and efficiency, an iterative numerical approach is used to assimilate water vapor information from GOES channel 3 for numerical weather prediction purposes. Typically, one would modify the model (moisture and temperature) fields so that simulated (model) forward radiation calculations, at the wavelength corresponding to channel 3, agree with their remotely observed counter-parts. In the simplest approach, only the moisture would be modified. This assumes that the model temperature field is reliable. This assumption simplifies the calculations for this feasibility study. Additional channels are be added later.

The proposed assimilation procedure modifies only the moisture field in physical space, in contrast to the emphasis placed by many forecast centers on performing the data assimilation in radiance space. Both approaches allow the modelers to use their own background fields and to do the calculations whenever the schedule allows. Both approaches begin with meteorological fields that represent their best approximation of the atmosphere.

The upper tropospheric relative humidity is adjusted in the vertical column using weights determined by the forward radiative model. The adjustment procedure is combined with an optimization scheme so that the moisture field is modified until it reproduces the remotely observed brightness temperature field. The modifications (done in physical, not radiance, space) are retained separately, and can be quality controlled, and adjusted for biases and observational errors.

A schematic of the approach to be used is indicated in Fig 1. Note that the partitioning of changes made to the model moisture field, in physical space, is directly proportional to the observational weighting functions. Our iterative procedure uses an optimization scheme to require that the modifications, when expressed in brightness temperature, converge to the observed brightness temperatures. Additional details will be presented at the conference and/or in a formal publication.

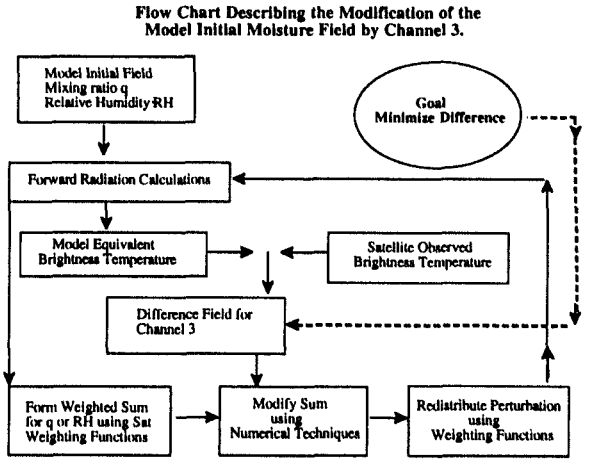

Fig. 1 Flow chart of the assimilation processes.

4. PRELIMINARY RESULTS

For the GOES water vapor channel 3, the correlation between observed brightness temperatures and model forecasts with and without GOES data, expressed in terms of brightness temperature using a forward radiative model, are displayed in Fig. 2. Note that the greatest benefit from using GOES data occurs

initially, in this example at 0000 UTC 18 Sep 2000, but some benefit exists throughout the forty-eight hour forecast, as indicated in Fig. 2. This benefit is believed to exist over the entire forecast partially because of the selective nature of the smoothing in the CRAS forecast model (Raymond 1988).

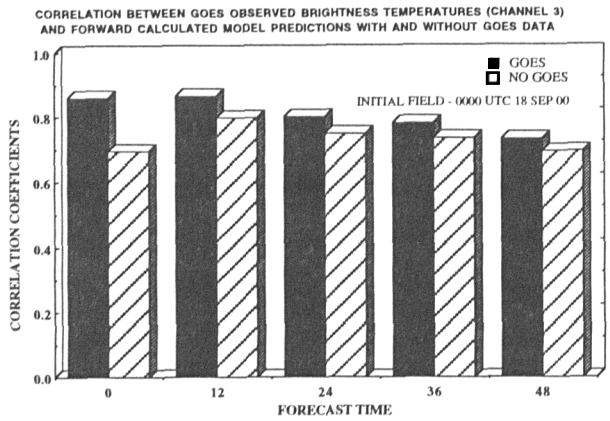

Fig. 2. Correlation of model forecasts, with and without GOES data, against observed brightness temperatures, from 0000 UTC 18 Sep 2000.

When viewed in terms of images, the benefits of the assimilation are readily apparent. Figs. 3 and 4 show the model brightness temperatures for the initial fields associated with the forward radiation calculations of channel 3, with and without GOES data, respectively. These can be compared against the actual GOES observations, which have been analyzed by a recursive filter and are presented in Fig. 5.

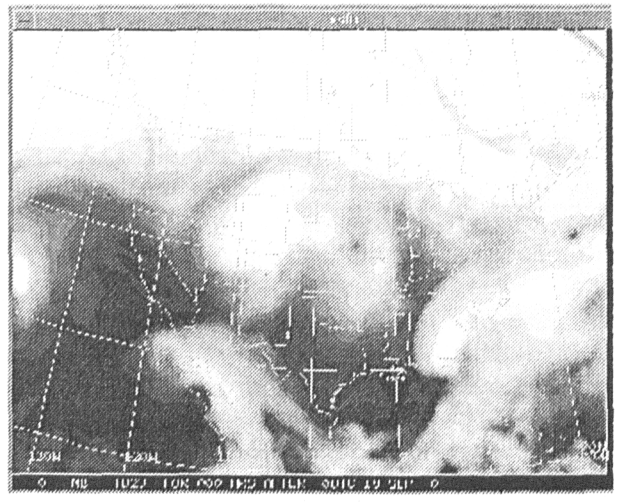

Fig. 3 Brightness temperature, with GOES data (0000 UTC 18 Sep 2000).

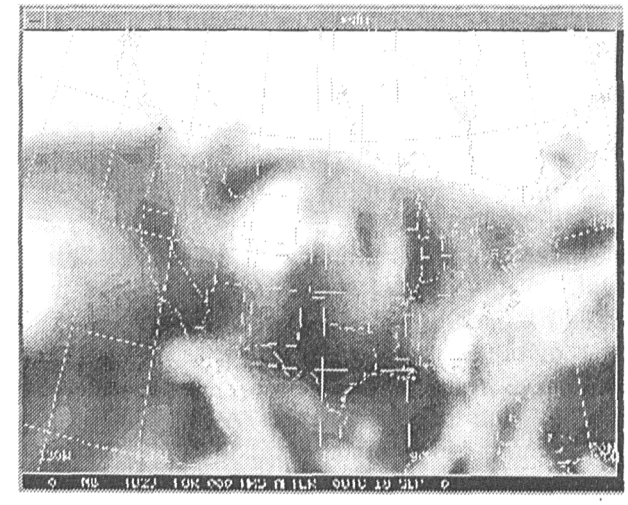

Fig 4. Brightness temperature, when no GOES data is used to create the initial model fields (0000 UTC 18 Sep 2000).

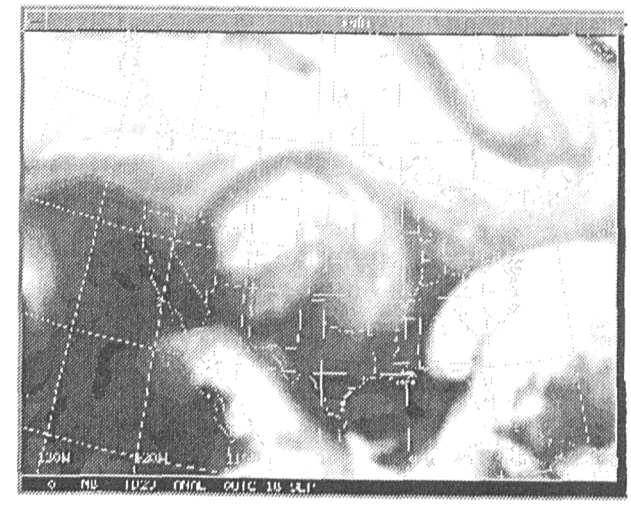

Fig 5. GOES observations analyzed to the model grid (0000 UTC 18 Sep 2000).

Particular features are better captured with the run including the GOES moisture observations, such as: the NW-SE dry slot through western James Bay; more cloud across South Dakota to eastern Illinois; sharper cloud edge gradient from Alabama to Kentucky; more distinct cloud in SW Gulf of Mexico; and less cloud in mid-Pacific (135W, 35N).

Results from an examination of an extended time period, 12-15 days, will be presented at the conference.

4. REFERENCES

Andersson, E., J. Pailleux, J. -N. Thepaut, J. R. Eyre, A. P. McNally, G. A. Kelly, and P. Courtier, 1994: Use of cloud-cleared radiances in three/four-dimensional variational data assimilation. *Q. J. R. Meteorol. Soc.*, **120**, 627-653.

Asai, T., 1965: A numerical study of the air-mass transformation over the Japan Sea in winter. *J. Meteor. Soc. Japan*, **43**, 1-15.

Bourke, W., and J. L. McGregor, 1983: A nonlinear vertical mode initialization scheme for a limited area prediction model. *Mon. Wea. Rev.*, **111**, 2285-2297.

Diak, G. R., D. Kim, M. S. Whipple, and X. Wu, 1992: Preparing for the AMSU. *Bull. Amer. Meteor. Soc.*, **73**, 1971-1984.

Dudhia, J., 1989: Numerical study of convection observed during the winter monsoon experiment using a mesoscale two-dimensional model. *J. Atmos. Sci.*, **46**, 3077-3107.

Eyre, J. R., G. A. Kelly, A. P. McNally, E. Andersson, A. Persson, 1993: Assimilation of TOVS radiance information through one-dimensional variational analysis. *Q. J. R. Meteorol. Soc.*, **119**, 1427-1463.

Kessler, E., 1974: Model of precipitation and vertical air currents. *Tellus*, **26**, 519-542.

Leslie, L. M., G. A. Mills, L. W. Logan, D. J. Gauntlett, G. A. Kelly, J. L. McGregor, and M. J. Manton, 1985: A high resolution primitive equation NWP model for operations and research. *Aust. Meteor. Mag.*, **33**, 11-35.

Liu, J. Y., and H. D. Orville, 1969: Numerical modeling of precipitation and cloud shadow effects on mountain-induced cumuli. *J. Atmos. Sci.*, **26**, 1283-1298.

McGregor, J. L., L. M. Leslie, and D. J. Gauntlett, 1978: The ANMRC limited-area model: consolidated formulation and operational results. *Mon. Wea. Rev.*, **106**, 427-438.

McNally, A. P., and M. Vesperini, 1996: Variational analysis of humidity information from TOVS radiances. *Q. J. R. Meteorol. Soc.*, **122**, 1521-1544.

Mills, G. A., and R. S. Seaman, 1990: The BMRC regional data assimilation system. *Mon. Wea. Rev.*, **118**, 1217-1237.

Molinari, J., and M. Dudek, 1992: Parameterization of convective precipitation in mesoscale numerical models: A critical review. *Mon. Wea. Rev.*, **120**, 326-344.

Raymond, W. H., 1988: High-order low-pass implicit tangent filters for use in finite area calculations. *Mon. Wea. Rev.*, **116**, 2132-2141.

Raymond, W. H., 1999: Nonlocal turbulent mixing based on convective adjustment concepts (NTAC). *Bound.-Layer Meteor.*, **92**, 263-291.

Raymond, W. H., 2000: Estimating moisture profiles using a modified power law. *J. Appl. Meteor.*, **39**, 1059-1070.

Raymond, W. H., and R.M. Aune, 1998: Improved precipitation forecasts using parameterized precipitation drag in a hydrostatic forecast model. *Mon. Wea. Rev.*, **126**, 693-710.

Raymond, W. H., W. S. Olson, and G. Callan, 1995: Diabatic forcing and initialization with assimilation of cloud and rainwater in a forecast model. *Mon. Wea. Rev.*, **123**, 366-382.

Sundqvist, H., E. Berge, and J. E. Kristjansson, 1989: Condensation and cloud parameterization studies with a mesoscale numerical weather prediction model. *Mon. Wea. Rev.*, **117**, 1641-1657.

P3.62

FUTURE SATELLITE INITIATIVES AT FLEET NUMERICAL METEOROLOGY AND OCEANOGRAPHY CENTER

Charles E. Skupniewicz*, J. Cornelius, J. Haferman, J. Vermeulen, and Y. Wang
Fleet Numerical Meteorology and Oceanography Center, Monterey, CA 93943-5501

1. INTRODUCTION

Fleet Numerical Meteorology and Oceanography Center (FNMOC), an echelon three command under the Commander, Naval Meteorology and Oceanography Command (CNMOC), is the Department of Defense's primary numerical prediction center for operational meteorological and oceanographic analysis and forecast products worldwide. Since areas of interest are constantly changing, and often centered in data sparse regions, the assimilation of satellite data into models is the highest priority of the Satellite Data Team at FNMOC. Second in priority is the dissemination of real time satellite data to CNMOC's worldwide regional centers, when direct sources of satellite data are not available, for use by on-site applications. While not a primary mission, visualization of satellite data, including fusion of data from multiple sources, is becoming increasingly important to the mission of the Satellite Data Team.

2. PRODUCTS - PRESENT AND FUTURE

Currently, FNMOC receives, processes, and/or distributes the following generic list of satellite products:

- microwave-derived wind, water, vapor, rain, and ice
- multi-channel sea surface temperature
- altimeter-derived wind/waves/sea height
- scatterometer-derived marine surface wind vectors
- feature tracking winds
- infrared, microwave sounder radiances
- multi-sensor 3-d cloud maps/snow cover
- visible, infrared, microwave imagery

*Corresponding author address: Charles E. Skupniewicz, FNMOC, 7 Grace Hopper Ave., STOP 1, Monterey, CA 93943-5501 skupniec@fnmoc.navy.mil

Since the types and sources of satellite data are wide ranging, FNMOC has become adept at processing all levels of satellite data and utilizing varied types of communication systems. This paper describes future satellite initiatives at FNMOC, which will enhance and expand the current list of products.

2.1 Special Sensor Microwave Imager Sounder (SSMIS)

The SSMIS will be the Defense Meteorological Satellite Program's (DMSP) next generation of passive microwave instruments. The sensor suite will be hosted on the F-16 platform, launched in January 2002. An important feature of this instrument package is the integration of the imager, temperature sounder, and moisture sounder. Another feature critical to modeling efforts at FNMOC is the sounder's ability to retrieve temperature up to 70 km altitude. A future release of the Navy Operational Global Atmospheric Prediction System (NOGAPS), which extends the upper boundary from 20 to 100 km, will depend heavily on these soundings.

FNMOC was integrally involved in algorithm and software development for the SSMIS, and a key participant in the validation and verification campaign. FNMOC will receive these data through a DOMSAT communication link, and process and distribute these data to Navy customers. FNMOC is the lead organization for passive microwave environmental products in the Shared Processing Program (SPP), which includes the National Environmental Satellite Data and Information Service (NESDIS), the Naval Oceanographic Office (NAVO), and the Air Force Weather Agency (AFWA). In that capacity, FNMOC will distribute derived products to the SPP community.

2.2 National Polar Orbiting Environmental Satellite System (NPOESS)

The NPOESS is the next generation of US-sponsored operational polar-orbiting environmental satellites. The Department of

Defense, Department of Commerce, and NASA have teamed to combine their respective polar-orbiting missions into one. As an NPOESS Processing Central, FNMOC has participated in NPOESS program definition, setting requirements for the environmental products. FNMOC contributed to the review of the system engineering and manufacturing development proposals, and is heavily involved in the Interface Data Processor Segment (IDPS) Advisory Team, which develops the Interface Control Documents (ICD) and defines the IDPS and NPOESS Processing Central responsibilities. FNMOC is also a member of the Microwave Operational Algorithm Team (MOAT), and will be involved in the risk reduction phase of the project.

2.3 Coriolis WindSat

The Coriolis WindSat program is a sensor risk-reduction/proof-of-concept for the NPOESS program. FNMOC participated in many aspects of the system design and review. A passive microwave polarimetric sensor (WindSat) will be flown on the Coriolis spacecraft launched on a Titan II rocket in the summer of 2002. FNMOC will serve as Payload Operation Center (POC) for the mission.

The primary mission is to derive marine surface wind vectors using Stokes vectors calculated from the polarimeter. The Naval Research Laboratory (NRL) is providing algorithms and software for transition to FNMOC operations. In addition to marine surface wind vector algorithms, software is being provided for water vapor, sea surface temperature, soil moisture, rain rate, ice and snow characteristics. As part of the operational demonstration, FNMOC will host the Coriolis Data Distribution System (CODDS), providing raw data to NRL for calibration and validation. FNMOC will also supply derived products to the CNMOC Regional Centers for analysis, and to NRL for possible assimilation into atmospheric models.

2.4 SeaWinds Scatterometer

FNMOC receives real-time ERS-2 and QuikScat SeaWinds scatterometer data made available from NESDIS over an ATM network in BUFR format. FNMOC is assimilating ERS-2 data into its NWP models operationally, and in the final stages of assimilation testing for SeaWinds data.

For the ERS-2 case, maximum likelihood estimates are calculated at FNMOC using the CMOD4 geophysical model function and a high wind speed adjustment. For the QuikScat case, we accept the Maximum Likelihood Estimate ranked solutions calculated at NESDIS. FNMOC has installed software used at NCEP (Peters et al., 1994) and adapted for use at FNMOC (Martin, 1997) to perform ambiguity removal (AR) using the NOGAPS surface wind fields. The ambiguous solutions are presented to the AR scheme, and the first choice is assimilated into NOGAPS. FNMOC is currently testing a similar AR approach for our regional models.

FNMOC is responsible for distributing real-time scatterometer data to the broader DOD meteorological and oceanographic community for use as direct observations. This is accomplished by transmitting processed data to regional centers' databases for use by on-site applications. FNMOC also produces a web product for data browsing. The resulting visual products are used for tropical cyclone targeting, operational forecasting, and other types of ocean weather analyses.

Improvements in the use of scatterometer data will largely be driven by a National Oceanic Partnership Program (NOPP) collaboration, currently under proposal review. FNMOC will install and test new geophysical model functions (GMF) as proposed and selected by the partners, and will make the NOPP products available to its remote customers for use in 'nowcasting' applications on a trial basis. Forecaster feedback will be requested, and dispersed among the NOPP collaborators. If added value is demonstrated, these products will be considered for operational production.

The upcoming launch of a second SeaWinds sensor on the Japanese Adeos-II satellite is eagerly anticipated, and FNMOC is positioned to receive and process these data as soon as they become available.

2.5 Radiance Assimilation

FNMOC is currently upgrading its data assimilation to a 3-dimensional variational scheme, the NRL Atmospheric Variational Data Assimilation Scheme. This system will enable the use of radiance data from atmospheric sounders (Baker et al., 2001). As demonstrated at other centers using these data, quality control and calibration is critical. FNMOC will monitor radiance data, and assume responsibility for calculation of bias corrections and updates as required. Maintenance and upgrade of forward

radiative transfer models will also become a major component of the satellite data assimilation efforts.

2.6 Feature-Tracking Winds

Feature Tracking Winds (FTWinds) algorithms observe the movement of cloud-edge features and water-vapor gradients from geostationary satellite imagery to derive atmospheric wind vectors. The Cooperative Institute for Meteorological Satellite Studies (CIMSS), University of Wisconsin, has been a leader in FTWinds research for many years. A version of their software is currently running at NESDIS, producing operational winds from the GOES satellites, and the algorithm has shown positive results in NOGAPS (Veldon et al., 1997).

Following the lead of NESDIS, FNMOC and the Air Force Weather Agency (AFWA) have established a cooperative project to use a C-portable version of the CIMSS software to produce FTWinds from the Japanese GMS satellite. Operational processing scripts were developed at FNMOC. An AFWA, FNMOC, and CIMSS integration team installed the software on hardware at AFWA, and the system is currently operational. Operational testing with Meteosat-5 and 7 are currently underway. Future plans call for applying this approach on the regional scale by using regional model background and customizing the quality control to particular regions.

2.7 Visualization

FNMOC has committed to a growing presence on the internet. Presentation of satellite data is migrating toward interactive, customized products, rather than predefined choices. Customer requirements now include fusion of satellite products with model fields and conventional data. Toward this goal, FNMOC has developed the Joint METOC Viewer, which provides satellite imagery with customized model and data overlays to a downloadable client over the internet (Skupniewicz and Huff, 2000). FNMOC has committed to operationally fielding the NRL Tropical Cyclone web page (Hawkins et al., 2001), which has become popular for satellite reconnaissance. Even more customization will be available in the upcoming release of MYWXMAP (Ravid et al., 2001). This system will allow users to create a custom area, imaged data product, and model background, all presented through a standard web browser.

3. SUMMARY

FNMOC is expanding its suite of satellite products to meet the growing challenges of environmental characterization and prediction for Navy operations.

4. REFERENCES

Baker, N.L., R. Daley, S.D. Swadley, E.H. Barker, J. Clark, J.S. Goerss, W.F. Campbell and K. Sashegyi, 2001: The Assimilation of Satellite Observations with the NRL Atmospheric-Variational Data Assimilation System (NAVDAS). 11th Conference on Satellite Meteorology and Oceanography, 15-18 October 2001, Madison, Wisconsin.

Hawkins, J.D., T.F. Lee, J. Turk, C. Sampson, J. Kent, and K. Richardson 2001: Real–Time Internet Distribution of Satellite Products for Tropical Cyclone Reconnaissance. Bulletin of the American Meteorological Society: Vol. 82, No. 4, pp. 567–578.

Martin, C.A. 1996: Operational Implementation of ERS Satellite Scatterometer Wind Retrieval and Ambiguity Removal. Masters Thesis, Naval Postgraduate School, Monterey, CA, December 1996.

Peters, C.A., V.M. Gerald, P.M.Woiceshyn, and W.H.Gemmill, 1994: Operational Processing of ERS-1 Scatterometer Winds: A Documentation OPC Contribution No. 96.

Ravid, E.V., K.Saylor and K-W. Stroh, 2001: CWxMAP – Customer-driven Interactive METOC Charts via the WWW. 17th Conference on Interactive Information and Processing Systems (IIPS) for Meteorology, Oceanography, and Hydrology, Albuquerque, New Mexico, 10-15 January, 2001.

Skupniewicz, C.E. and D. Huff (1999): Joint METOC Viewer Image Format. Proceedings of the15th International Conference on Interactive Information and Processing Systems (IIPS) for Meteorology, Oceanography, and Hydrology, Dallas, Texas, 10-15 January, 1999.

Velden, S. C., C. M. Hayden, S. J. Nieman, W. P. Menzel, S. Wanzong, and J. S. Goerss, 1997: Upper-Tropospheric Winds Derived from Geostationary Satellite Water Vapor Observations. Bull. Amer. Meteor. Soc. 78, 173-194.

P3.63 AN OPERATIONAL UNIFIED VALIDATION SYSTEM FOR SATELLITE DATA

Larry M. McMillin*
Hanjung Ding and Jiang Zhao
NOAA/NESDIS
Camp Springs, MD

1. INTRODUCTION

The National Environmental Satellite, Data, and Information Service (NESDIS) has developed a unified validation system. In this system, ground truth data are collected, stored in HDF, and matched with satellite data. This validation system was developed with support from the Atmospheric Infrared Sounder (AIRS) science team and from the Integrated Program Office (IPO). Two types of data are stored on the system.

Satellite data are matched with truth from a number of sources. These include ocean surface observations, aircraft reports, ARM/CART data, and rocketsondes. These data are used as individual or point measurements.

Radiosondes are included as a special type of measurement. The factor that makes radiosondes unique is that they are the start of complete specification of the atmospheric profile. In other words, radiosondes are matched with satellite observations, but other data are added to complete the specification of the atmospheric state at a given point. These include hourly surfaces observations that span the time and space between the satellite and the radiosonde, any aircraft reports, moisture measurements from the GPS system, ocean surface temperatures, rocketsonde data, upper atmospheric temperatures, and ozone data.

The system is designed to allow matching a single measure of 'truth" with multiple satellites. Currently it is being matched with TOVS data and with simulated AIRS data.

2. Current CAPABILITIES

Several types of analysis are available on the web site at orbit-net.nesdis.noaa.gov/crad/ipo. One is a time history of the accuracy of the operational retrievals. One difference between this system and the current operational system is that this system does not use the radiosondes to filter data. The operational system rejects profiles where the difference between the satellite and the radiosonde exceeds a limit, usually about 10K. We chose not to use that feature because we want to know the accuracy away from the radiosonde sites, even though we recognize that other factors such as forecast accuracy may cause a difference in accuracy that depends on closeness to a radiosonde. It should be noted that the differences that we show may be larger than the operational values for this reason.

One of the capabilities on the site is the ability to display the AIRCAR and ASDAR observations. For use as matches, we use fixed sites. There are two types of sites. One type consists of airports. We include an area of 300 km about the airport as this is the distance it takes an airplane to reach altitude. The other type consists of crossing points. We selected locations where flight paths frequently cross. This gives some vertical structure although it obviously is not as complete as an entire profile. One of the important features of these measurements is that they are more frequent than synoptic times. For this reason, they provide a greater chance for making timely matches.

The current system shows the locations of the aircraft observations. The AIRCAR observations are mostly over the North America while the ASDAR observations are centered over Europe. Both show the lower altitudes and higher temperatures that are centered on the airports surrounded by higher and lower values respectively. The plots show that, at the present, few moisture values are available. This is due to fact that the data shown are data that pass the quality tests for NCEP's model. Many of the moisture reports require corrections that are not made on a time schedule that is compatible with the forecast cycle. Accordingly, these observations do not show up on the file we access.

There is another entry for monthly error statistics. Results are available for TIROS-N, NOAA-6, NOAA-9, NOAA-10, NOAA-11, NOAA-12, and NOAA-14. For each satellite, results can be shown for day or night or both, land or sea or both, and clear or cloudy or both. One of the more obvious features of retrievals shown by this display is the annual cycle near the ground. The display shows the explained variance of the retrieval. A value of 1.0 is a perfect retrieval while a value of zero indicates no skill. The largest errors occur in the fall and the best retrievals are made during the summer. Accuracies are lower at 200 hPa and above 50 hPa. Over land, there is a seasonal pattern to the bias in the mid to lower troposphere (700 to 300 hPa). It is generally warm in the winter and cold in the summer.

* *Corresponding author address:* Larry McMillin, National Environmental Satellite Data and Information Service, Office of Research and Applications, Climate Research and Applications Division, 5200 Auth road, Room 810, Camp Springs, MD 20746; e_mail: Larry.McMillin@noaa.gov

This is consistent with retrieval studies which show that retrievals can be biased toward the mean value.

A third entry shows the match up error distribution. Errors are shown as a function of time, distance, and solar zenith angle for the same satellites and conditions described in the previous paragraph. Shown with the solar zenith angle is the error as a function of scan number. There is a general trend for errors to increase with time and distance over land, and less of a trend over water. There is also a trend for the lower atmospheric temperatures to be cold relative to radiosondes during the day and warm at night. This fits the expected pattern for retrievals to be biased toward the mean values and to not fully capture the extremes. The water vapor accuracy decreases with distance and time. But this pattern, at least for distance, is confused by the sampling. For the larger distances, the sample is smaller, decreasing the chance for the larger errors.

The block labeled "research report" shows an analysis of the error as a function of location. Since this is the difference between the satellite and the radiosonde, it is expected that some sites may be more representative than others. For example, near mountains, the two instruments frequently observe different atmospheres even though the two observations may be close in both time and space. This expectation is supported by the map which shows the average error level for each observation. Places like California and Denver have larger than expected errors. A tendency for larger errors near coasts was also noted. This is due to the frequent temperature differences between land and water and the resulting atmospheric response. These stations are not good candidates for use in validation studies.

3. FUTURE CAPABILITIES

Other capabilities are planned. One is to show the statistics of the radiosonde to aircraft differences in places where they are coincident. This is an important feature for validation studies because this type of data allows the accuracy of the 'truth" to be evaluated. As the accuracy of satellite retrievals increases, it is important that the accuracy of the 'truth" be considered. There are plans to use the GPS moisture to screen and correct radiosondes. The GPS total moisture has been shown to be nearly as accurate as the microwave radiometers which are used for this purpose at the ARMS sites. The GPS has the advantage of being located near many radiosonde sites. When this is the case, the GPS can be used to monitor/correct the radiosonde moisture retrievals.

The aircraft moisture sensors are important for upper atmospheric retrievals. Current radiosondes do not work well in cold temperatures with low moisture. Although the same sensors are currently used for aircraft measurements, the aircraft measurements have the advantage that the air is heated by compression. But these still have some calibration issues. More importantly, the network is being switched to a new sensor that will not have these problems.

One of the uses for these data is to tune out the systematic differences between observed and measured radiances to remove biases from the resulting retrievals. This is done by collecting a sample of measured and observed radiances. Then the difference is predicted from an estimate of the atmospheric state. For this type of correction, it is the general shape of the atmospheric profile, not the details that are needed. There are several possible sources of such data, including the microwave radiance, the measured radiances, and the calculated radiances. For AIRS, we are using the measured AIRS radiances. In some systems, this has an advantage over the calculated values in that the estimate of the correction does not change with iteration in an iterated solution. This advantage disappears when the cloud clearing is iterated along with the retrieval.

The regression has to be performed in a careful manner. Normal regression produces large coefficients with numerical artifacts. To stabilize the regression, we predict the difference between the measured and calculated radiance, not the measured radiance. These two approaches are equivalent when a full regression is done, but we constrain the regression by doing an eigenvector regression and using only a subset of the eigenvectors. An alternative is to perform a ridge regression which is equivalent to adding extra noise to the predictors to make the coefficients small. The correction is then added with the correct sign to the difference between the measured minus the calculated radiance at the point where the retrieval is done.

Predictors other than the radiance can be added. Some, such as latitude and longitude, should be related to the radiances and provide no new information. But others, such as solar zenith angle and scan position, can provide independent information and will probably be used. The scan dependent biases, in particular, are largely due to deficiencies in a particular instrument, and can't be reliably predicted before launch.

4. CONCLUSION

This paper describes a validation system that is being planned for use at NEDSIS. It is unique in that all the data are located on a single system using a single format to make accessing the data easy. It is also unique in that radiosonde data are matched with other sources of truth such as hourly surface observations, total water vapor soundings from the Global Positioning System (GPS), buoy data, aircraft data, ozone data, and upper atmospheric data from rocketsondes and limb sounders. These data are added to provide checks and adjustments for the radiosonde data and to provide a complete specification of the atmospheric state. Routine statics are available through a web site (orbit-net.nesdis.noaa.gov/crad/ipo). The data are also used to develop bias adjustments to remove systematic differences between measured and calculated radiances.

4.3 Estimating the Primary Analysis Variables, Temperature, Moisture and Wind from Space – Science and Cooperation

John Le Marshall
Bureau of Meteorology, Melbourne, Australia

1. INTRODUCTION

Errors in the estimation of wind, temperature and moisture from space-based observations have been reduced, particularly for regional applications, as the spatial, temporal and spectral resolution of the observations, data assimilation methods and computer power have improved. This paper describes progress, illustrating the advances with results derived from the use of recent, current and next generation operational sounding and image data. It presents examples of both the improvements in the estimation of the primary analysis variables and the resultant benefits to numerical weather prediction (NWP) from these improved data.

In particular, the importance of satellite direct readout is noted for providing timely data for regional applications where short data cut-off times are present. It also records the important role which shared community software plays in the utilisation of data from these operational satellite systems for both operations and research. It notes the important roles played by international collaboration, by the ITWG and by members of the wind community who attend the IWWs (International Wind Workshops). These two communities have been vital in the effective use of the operational satellite systems. The software they have produced and shared has been central in the use of satellite observations for operations and research on both global and regional scales.

2. BACKGROUND

Ever increasing improvements have been made in the observational capacity of earth observing satellites. Almost continuous improvements in the spatial, spectral and temporal resolution of the observations from these satellites have led to greater utility of the data. This paper provides evidence of the increasing benefits being derived from greater observational- power.

It concentrates on use of passive observations in the visible, infrared (IR) and microwave parts of the spectrum and examples are given of their increasing utility in particular for NWP. It also notes the impending availability of very high spatial, temporal and spectral resolution data, their ability to provide enhanced information about atmospheric state, and the anticipated benefit of this information in applications such as NWP. Examples used in this paper are drawn from the Southern hemisphere.

3. BENEFITS FROM INCREASING SPATIAL, TEMPORAL AND SPECTRAL RESOLUTION OBSERVATIONS

Improvements seen in operational forecasting capability, have been derived to a significant extent, from improved numerical modelling capability, improved data assimilation techniques, improved computing capacity and to a very significant extent improvements in the data base, particularly the remotely sensed data base. From the early 1970s, when images were used to provide the analyses for NWP, through the 1970s, with the introduction of first generation sounders and geostationary observations, and, later, through the 1980s, with the introduction of second generation sounders, increasing forecast accuracy has been recorded.

Imagery

Improvements due to imagery in the data base are not demonstrated here. Suffice it to say, weather systems over the southern oceans and other parts of the southern hemisphere, can go unnoticed in analysis (because of the sparsity of conventional data) if satellite imagery is not used.

Sounding Data

Improvements to regional and global forecast systems with the use of second generation sounding (TIROS Operational Vertical Sounder - TOVS) data are now well documented (eg. Bourke et al. 1982, Le Marshall et al. 1994) and these data have assumed an ever increasing role in the numerical analysis and prognosis. Improvements to the Australian Region forecast system are seen in Table 1.

Table 1: S1 Skill Score for local physical TOVS data assimilation forecasts (TOVS/RASP) and the matching control (NMOC) forecasts during the period 23UTC 17-12-92 to 11UTC 30-1-93.

System	Level	+12hr.	+24hr.	+36hr.
RASP	MSLP	32.2	41.0	49.5
TOVS/RASP	MSLP	30.3	37.8	45.1
RASP	500Hpa	15.4	21.2	28.7
TOVS/RASP	500Hpa	14.1	19.3	25.5
RASP	300Hpa	12.9	17.9	24.9
TOVS/RASP	300Hpa	12.2	16.9	23.0

This shows the S1 skill scores (Teweles and Wobus 1954) for a real time data impact experiment in December 1989 - January 1990. The experiment examined the benefits to the operational Australian Region forecast model resulting from the use of full resolution TOVS raw radiances, directly readout from satellite, via a physical retrieval scheme. This full physical retrieval scheme was subsequently implemented operationally. In the experiment the operational NMOC system was used as the control with the with the experimental system being identical but having TOVS radiances added to its data base. The 3 and 4 point S1 skill score gain seen in Table 1 with the use of TOVS is significant but expected given the lack of conventional data over the southern hemisphere.

A particular example, showing the impact of these TOVS data on the forecast track of tropical cyclone Bobby in February 1995 can be seen in Le Marshall and Mills (1995). Forecasts using the then operational Australian Region forecast model, the current operational model (LAPS), and the current operational model with TOVS, show that the track of Tropical Cyclone Bobby through Western Australia is only well-predicted through use of direct readout sounding data. Currently, real time TOVS data are not available operationally to the regional forecast system unless they are derived from direct readout, as a result of short cutoff times (about 1.5 hours).

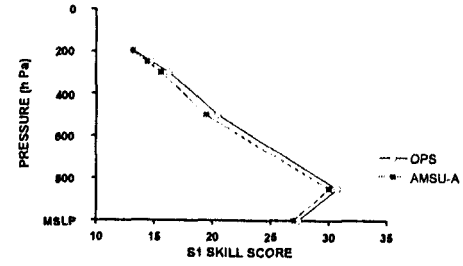

Figure 1. The S1 skill scores of 24 hour forecasts for Operations (OPS) and Operations using AMSU-A data (AMSU-A) in the Australian Region

The TOVS instrument used in the study above has been recently improved by the addition of spectral channels in the microwave. The new instrument, the Advanced TOVS, has greater spectral and spatial resolution and now carries a 20-channel HIRS,(High resolution InfraRed Sounder) and a 20-channel Advanced Microwave Sounding Unit (AMSU). The effect of addition of NOAA-15 ATOVS data to the operational Australian Region forecast scheme is seen in Fig. 1. In this experiment the operational NMOC system was used as the control, with the with the experimental

system being identical, but having NOAA-15 ATOVS AMSU-A radiances added to its data base. A gain in S1 skill score is seen throughout the troposphere, even though NOAA-15 direct readout at this stage was providing poor coverage due to data transmission problems from the satellite.

Atmospheric Motion Vectors

From the 1970s winds generated from tracking features in sequential geostationary satellite images have been used in NWP. Sequential imagery from the geostationary satellite, GMS-5, has been used to provide near-continuous wind observations over the Australian Region.

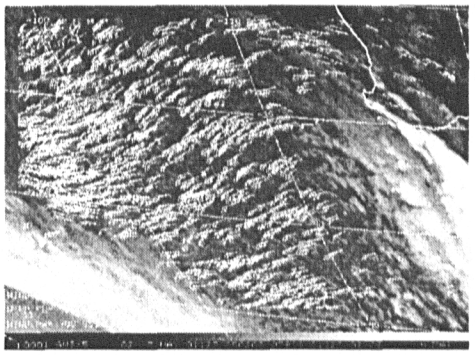

Figure 2. Atmospheric Motion Vectors 05UTC 7 May 2001

These data have been generated from observations in the high-resolution visible, visible, 11 μm infrared and 6.7 μm water vapour absorption bands as a result of the increased temporal and spectral resolution of GMS imagery available in the 1990s. The method for deriving these vectors is in Le Marshall et al.(1998b). An example of Cloud and water vapour motion vectors generated in real time South-west of Australia at 05UTC on 7 May 2001 is seen in Fig. 2.

The impact of these data on operational forecasts using intermittent assimilation techniques is well documented with the improvement in operational forecasts from using infrared, hourly and water vapour motion vectors being found in Le Marshall et al. 1998b,c.These works show increasing accuracy of the operational Australian Region forecast system with the incorporation of 11μm, hourly, visible and 6.7 μm image based winds. Recently another impact study has been completed illustrating the impact of using all winds simultaneously, with appropriate quality control.

The benefits of using these wind data with improving data assimilation techniques, namely continuous assimilation techniques such as 4-D variational assimilation have also been demonstrated. In a series of studies examining tropical cyclone track and intensity predictions significant gains in forecast track accuracy (Le Marshall and Leslie 1988) and a beneficial influence on intensity prediction (Le Marshall and Leslie 1999) have been found to result from use of the high resolution wind data. In the case of track forecasts it can be seen that by comparison with operational forecasts in general (Gordon et al., 1998), these forecasts illustrate the potential for greatly improved operational prediction.

4.THE HYPERSPECTRAL FUTURE

In early 2001, the launch of the first hyperspectral instrument to provide operational data (the AIRS) will be undertaken. To date this type of hyperspectral data has been available only from limited sources. Two instruments to provide such data from high altitude flights on NASA ER2 aircraft are the High resolution Interferometer Sounder (HIS) and the NAST-I (NPOESS Aircraft Sounding Testbed - Interferometer) instrument. These instruments are airborne interferometers, capable of taking full interferograms every few seconds and the related power spectra from these instruments have been used to produce temperature and moisture profiles (see eg. Smith et al. 1999). The temperature profiles have accuracies greater than 1 K with moisture accuracies of the order of 10%.

These interferometer data have been used in a series of 4-dimensional variational assimilation experiments, which, for the first time, are using hyperspectral data in high resolution studies. The first study (Le Marshall et al. 2001) involved the use of HIS data, taken over the Chesapeake Bay region in the United States in 1995 and using 1 km resolution, has involved documenting the impact of these data on initialisation using 4-D variational assimilation. A second study (Leslie et al. 2001) has been completed using NAST-I data around Andros Island on 13 September 1998, where the influence of these high resolution sounding data on initialised wind fields has been noted. Several new instruments providing remotely sensed data at higher spatial, temporal and spectral resolution will be flying in the near future, these include IASI, CrIS and GIFTS.

5. SCIENCE AND CO-OPERATION

There is little doubt that the science of satellite meteorology has progressed significantly as a result of international co-operation. Both research and operational atmospheric sounding from space have benefited from the International (A)TOVS Working Group (ITWG) which was formed in 1983 and has fostered free exchange of scientific information and software throughout the international sounding community. There not a single agency or group working in this area that has not benefited greatly from this exchange, which has addressed areas including radiative transfer, operational procedures and education and training The establishment of this group by the International Radiation Commission was certainly an excellent initiative.

In relation to sounding the atmosphere from space for wind, the International Wind Workshops have become fora for similar exchange of science and software. They are also fostering international co-operation and, as a result, are hastening the advance of this field.

The very worthwhile activities of these two groups have been supported principally by the WMO, the satellite operators and meteorological agencies. These important activities will continue because of their utility, efficiency and economy.

6. SUMMARY AND CONCLUSIONS

From the time of the launch of the first weather satellite on 1 April 1960, improving spatial, temporal and spectral resolution have led to improved characterisation of atmospheric state and improved predictions. The first weather satellites provided television images in the visible and IR (11 μm), allowing cloud picture interpretation to provide quantitative analyses in areas where there was otherwise no data.

Analyses and forecasts were substantially improved by the provision of sounding data in the thermal IR and microwave (eg. Smith et al. 1970, Le Marshall et al. 1994). Further improvements have been made through increases in the spatial and spectral resolutions associated with the ATOVS instrument on NOAA-15. These improvements in temperature and moisture sounding have been accompanied by the use of sequential imagery with increasing spatial, temporal and spectral resolutions to produce high resolution wind vectors (Le Marshall, 1996) which have also contributed to increased forecast accuracy. The increase in accuracy has been documented in terms of the improved data base. It should be noted that the timeliness of direct readout data processed here has allowed their use in operational NWP.

The improvement in observational capacity will be continued, early next year, with the launch of the Advanced Infrared Sounder (AIRS). This will be followed by the Infrared Atmospheric Sounding Interferometer (IASI), the Geostationary

Imaging Fourier Transform Spectrometer (GIFTS) and the Cross-track Infrared Scanner (CrIS). The benefits of this improved observational capacity will be enhanced by improving data assimilation methods such as 4-D variational assimilation and the availability of burgeoning computer power. These benefits will of course continue to be dependent on international cooperation and the sharing of ideas and software as fostered by groups such as the ITWG and IWW.

REFERENCES

Bourke, W. P., K. Puri and R. Seaman, 1982. Numerical weather prediction studies from the FGGE southern hemisphere data base. Mon. Wea. Rev.**110**, 1787-1800.

Gordon, A. W., R. Gude, R. Schwerdtfeger, and R. Byron-Scott, 1998. Dynamic Meteorology: A Basic Course, Arnold, London, 325 pp.

Le Marshall, J.F., P.A. Riley, B.J. Rouse, G.A. Mills, Z-J Wu, P.K. Stewart and W.L. Smith, 1994 : Real time Assimilation and Synoptic Application of local TOVS Raw Radiance Observations. Aust. Met. Mag., **43**, 153 - 166.

Le Marshall, J.F. and G. A. Mills, 1995. Tropical cyclone Bobby – a notable example of the impact of local TOVS data. Aust. Meteor. Mag. **44**, 293-29

Le Marshall, J.F. and L.M. Leslie, 1998. Tropical Cyclone Track Prediction - Using High Resolution Satellite Data with a New Methodology. Aust. Meteor. Mag. **47**, 261 - 266.

Le Marshall, J. N. Pescod, R. Seecamp, and C. Spinoso 1998b : Improved weather forecasts from continuous assimilation of high resolution satellite data. Proceedings of the Fourth International Winds Workshop, Saanenmoser, Switzerland, October, 1998.

Le Marshall, J. N. Pescod, R. Seecamp, K. Puri, C. Spinoso and R. Bowen 1998c : Local Estimation of GMS-5 Water Vapour Motion Vectors and their Application to Australian Region Numerical Weather Prediction. Aust. Meteor. Mag., **48**, 73 - 77.

Le Marshall,J.F and Leslie L.M., 1999. Modelling Tropical Cyclone Intensity. Aust. Meteor. Mag. **48**,. 147 -151.

Le Marshall, J., L.M. Leslie and C. Spinoso, 1996b. The impact of spatial and temporal distribution of satellite observations on tropical cyclone data assimilation : Preliminary results. Meteorology and Atmospheric Physics. **60**, 157 - 163.

Le Marshall, J.F., Leslie, L.M. and W.L. Smith. 2001. Initialisation Using High Spatial, Temporal and Spectral Resolution Satellite Observations. Accepted for publication in Adv. Space. Res.

Leslie, L.M., J.F. Le Marshall and W.L. Smith. 2001. Mesoscale Initialisation Using Advanced Sounder Data. Accepted for publication in Adv. Space. Res.

Smith, W.L. , H.M. Woolf and W. J. Jacob. 1970. A regression method for obtaining real time temperature and geopotential height profiles from satellite spectrometer measurements and its application to Nimbus 3 SIRS observations. Mon. Weath. Rev. **98**, 582-603.

Smith, W.L. et al.,1999. High spectral resolution sounding: latest results from aircraft and their implications for future satellite systems. Technical Proceedings of the Tenth International TOVS study conference, Boulder, Colorado, 27 January – 2 February, 1999. Report from Bureau of Meteorology. Melbourne.

Teweles, S. and H. Wobus, 1954. Verification of prognostic charts. Bull Amer Met. Soc., **35**, 455- 463.

P4.2 INTERCALIBRATION OF GEOSTATIONARY AND POLAR-ORBITING INFRARED WINDOW AND WATER VAPOR RADIANCES

Mathew M. Gunshor* [1], Timothy J. Schmit [2], and W. Paul Menzel [3]

[1] Cooperative Institute for Meteorological Satellite Studies
[2] NOAA/NESDIS/ORA/ASPT
[3] NOAA/NESDIS/ORA
Madison, Wisconsin

1. INTRODUCTION

Satellites traditionally used for weather monitoring have proven to be useful in environmental monitoring. Thus, the ability to compare the measured radiances from different instruments has become increasingly important. The Cooperative Institute for Meteorological Satellite Studies (CIMSS) has been intercalibrating five geostationary satellites (GOES-8, -10, METEOSAT-5, -7, GMS-5) with a single polar-orbiting satellite (NOAA-14 HIRS and AVHRR) on a routine, automated basis for over a year using temporally and spatially co-located measurements. The primary focus of this effort has been in comparing the 11-μm infrared window (IRW) channels. Similar efforts are being made for the 6.7-μm water vapor (WV) channels. The numerical methods for conducting the routine intercalibration are being updated. This includes updating the radiative transfer forward model used to estimate the differences in calculated brightness temperatures based on spectral differences between satellite instruments.

2. APPROACH

The technique for intercalibration has been developed at CIMSS over the past several years (Wanzong et al., 1998). Collocation in space and time (within +/- thirty minutes) is required. Data is selected within 10 degrees of nadir for each instrument in order to minimize viewing angle differences. Measured means of brightness temperatures of similar spectral channels from the two sensors are compared. In the IRW channel, data collection is restricted to mostly clear scenes with mean radiances greater than 80 $mW/m^2/ster/cm^{-1}$, and no additional effort is made to screen out clouds from the collocation area. In the WV channel there is no clear scene restriction applied. Data from each satellite are averaged to an effective 100-km resolution to mitigate the effects of different field of view (fov) sizes and sampling densities; HIRS under-samples with a 17.4 km nadir fov, AVHRR Global Area Coverage (GAC) achieves 4 km resolution by resampling, GOES imager over-samples 4 km in the east-west by 1.7 (Menzel and Purdom, 1994), and METEOSAT-5, METEOSAT-7, and GMS-5 have a nadir 5 km fov. Mean radiances are computed within the collocation area. Clear-sky forward calculations (using a global model for estimation of the atmospheric state) are performed to account for differences in the spectral response functions (Figures 1 and 2). The observed radiance difference minus the forward-calculated clear-sky radiance difference is then attributed to calibration differences.

Thus,

$$\Delta R_{cal} = \Delta R_{mean} - \Delta R_{clear}$$

For comparing a geostationary satellite to HIRS,

$$\Delta R_{cal} = [R^{GEO}_{mean} - R^{GEO}_{clear}] - [R^{HIRS}_{mean} - R^{HIRS}_{clear}]$$

where *GEO* indicates geostationary, *HIRS* indicates the HIRS instrument, *mean* indicates the mean measured radiance, and *clear* indicates the forward calculated clear-sky radiances. Conversion to temperatures for a comparison between a geostationary satellite to HIRS is accomplished by,

$$\Delta T_{HIRS} = [B^{-1}{}^{GEO}_{mean} - B^{-1}{}^{GEO}_{clear}] - [B^{-1}{}^{HIRS}_{mean} - B^{-1}{}^{HIRS}_{clear}]$$

* *Corresponding author address:* Mathew M. Gunshor, Univ. of Wisconsin-Madison, 1225 W. Dayton St., Madison, WI 53706.

where B^{-1} indicates converting radiance to brightness temperature using the inverse Planck Function. An identical method is used for calculating the temperature difference between a geostationary satellite and the AVHRR instrument (ΔT_{AVHRR}).

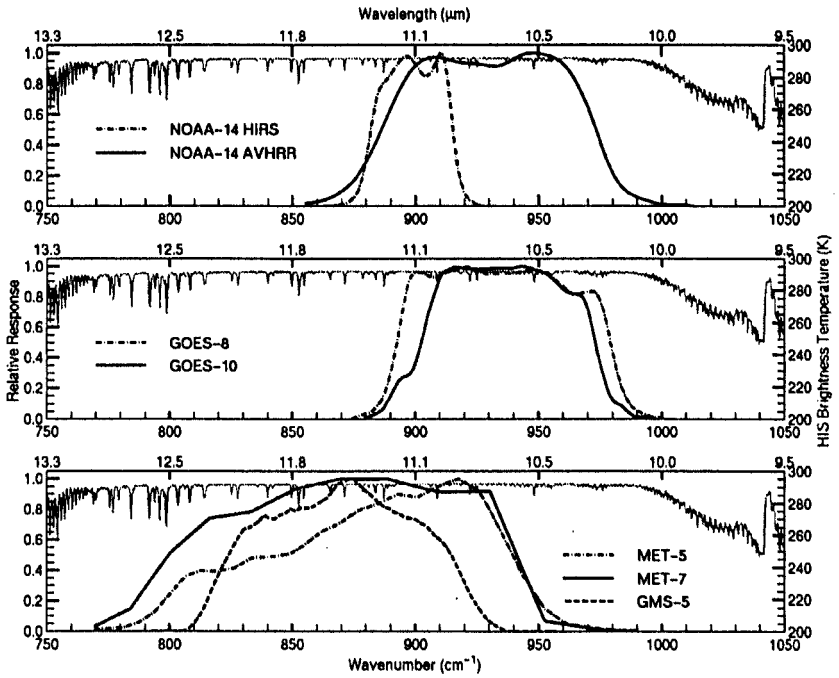

Fig. 1. Infrared Window Channel spectral response functions with a high spectral resolution earth emitted spectrum from a High-resolution Interferometer Sounder.

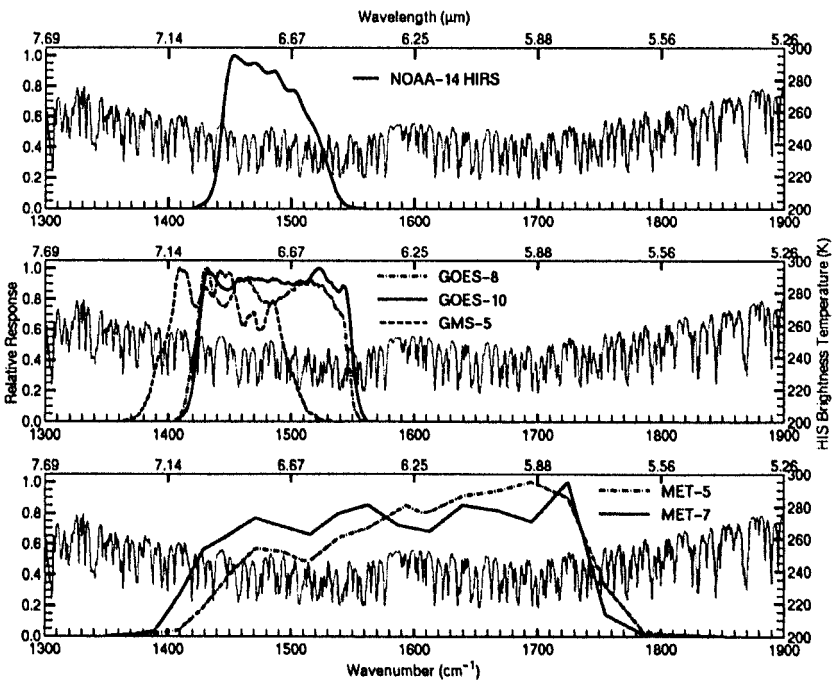

Fig. 2. Water Vapor Channel spectral response functions with a high spectral resolution earth emitted spectrum from a High-resolution Interferometer Sounder.

3. RESULTS

Intercalibration results for all five geostationary satellites covering the time period from January 2000 to July 2001 are shown in Table 1. The mean is the average of all cases for the indicated satellite and a negative sign indicates the measurements from the polar-orbiting instrument (HIRS or AVHRR) are warmer than those from the geostationary instrument. All five geostationary instruments on average are measuring colder temperatures than HIRS and AVHRR in the IRW channel; they measure warmer temperatures on average than HIRS in the WV channel. The standard deviation is the deviation about the mean. In the IRW channel the standard deviations for ΔT_{AVHRR} are lower than they are for ΔT_{HIRS}; the standard deviations for the WV channel comparisons are smaller than those in the IRW channel for ΔT_{HIRS}.

Table 1. January 2000 to July 2001 IRW (top) and WV (bottom) comparison of geostationary satellites and NOAA-14 HIRS and AVHRR.

Delta (geo – leo)		GOES-8 IRW	GOES-10 IRW	MET-5 IRW	MET-7 IRW	GMS-5 IRW
Number of Comparisons	ΔT_{HIRS}	29	227	240	291	119
	ΔT_{AVHRR}	29	227	240	291	119
Mean	ΔT_{HIRS}	-0.55 K	-0.31 K	-0.98 K	-1.12 K	-0.82 K
	ΔT_{AVHRR}	-0.35 K	-0.01 K	-0.34 K	-0.79 K	-0.59 K
Standard Deviation	ΔT_{HIRS}	0.84 K	1.21 K	1.25 K	0.88 K	1.19 K
	ΔT_{AVHRR}	0.32 K	0.43 K	0.64 K	0.65 K	0.73 K

Delta (geo – leo)		GOES-8 WV	GOES-10 WV	MET-5 WV	MET-7 WV	GMS-5 WV
Number of Comparisons	ΔT_{HIRS}	148	272	236	175	139
Mean	ΔT_{HIRS}	1.37 K	2.2 K	4.2 K	3.9 K	1.52 K
Standard Deviation	ΔT_{HIRS}	0.5 K	0.67 K	1.18 K	0.51 K	0.86 K

4. EFFECTS OF THE NEW APPROACH

The approach outlined in this paper is an updated version of the approach used at CIMSS for the past two years and reported at Coordination Group for Meteorological Satellites (CGMS) annual meetings. The first change is in the conversion from radiance to brightness temperature. The old approach used the slope of the Planck Function (dB/dT) while the new approach uses the inverse Planck Function. The second change is updating the forward model to PLOD/PFAAST. Although the results of these two changes are not differentiated here, the updating of the forward model reduced a small amount of error in the results, on the order of a tenth of a degree in some cases. Changing the method of conversion to brightness temperature proved to be a more significant alteration of the approach. For example, ΔT_{HIRS} in the IRW channel was less than 0.5 K for all instruments using the old approach. The results from the new approach do not appear as favorable as the results from the old approach, yet these results more fairly represent the actual differences between satellites and are more consistent with the results of other studies (Tjemkes et al., 2001).

5. CONCLUSIONS

Several conclusions can be drawn from the results in Table 1. The mean difference may suggest comparisons between HIRS and the geostationary

satellites are made difficult by the relatively narrow HIRS spectral response function (Figure 1) and large fov size compared to those of the other instruments. IRW results between AVHRR and all five geostationary instruments show smaller differences. For all geostationary instruments, comparison to HIRS is more favorable in the IRW channel than in the WV channel. This suggests a higher degree of difficulty to compare different instruments for the WV channel. This is possibly due to the widely different spectral responses (Figure 2), a higher degree of uncertainty in the calibration of this channel for some instruments, and the greater inhomogeneity of the atmospheric water vapor structure.

It is not possible, from this study, to determine which satellite is the most accurate or has the best calibration. It is only possible to compare them to each other. The mean differences of all five geostationary instruments appear to be calibrated to within approximately 1 K of each other.

The mean temperature differences in the IRW channel are small compared to those in the WV channel, but the standard deviations follow the opposite trend. Standard deviations in the IRW channel may be larger due to the greater variability in IRW radiances as compared to radiances in the WV channel. The IRW channel will measure surface effects as well as clouds and the range of radiances (and brightness temperatures) will be much greater than that of the water vapor channel, which only measures a small range of radiances (and brightness temperatures) from higher in the atmospheric column.

6. FUTURE WORK

There are two other changes to the technique being discussed. The first would be to use a Sea Surface Temperature (SST) for the surface temperature in the clear-sky forward model calculations. Currently the surface in the model calculations is considered to be the bottom layer of the atmospheric profile. This change is not expected to alter the results greatly, however it would produce slightly more accurate calculated clear-sky brightness temperatures, which may also mean more accurate ΔT calculations.

The second change involves the global atmospheric forecast model used to provide the atmospheric profiles for the forward model calculation. The results of an individual case are sensitive to changes in the moisture profile and this may be the greatest source of error in the intercalibration process. Efforts will be made to see that the most representative atmospheric model data available is used.

In addition to those changes, work has begun to transfer these comparisons from the research side to NESDIS operations. A goal of the CGMS is for all satellite operators to routinely produce similar statistics. There are plans for other polar-orbiting satellites to be compared, such as NOAA-15 or –16.

8. REFERENCES

Menzel, W. P. and J. F. W. Purdom, 1994: Introducing GOES-I: The first of a new generation of geostationary operation environmental satellites. Bull. Amer. Meteor. Soc., **75**, 757-781.

Tjemkes, S.A., M. König, H.-J. Lutz, L. van de Berg, and J. Schmetz, 2001: Calibration of Meteosat water vapor channel observations with independent satellite observations. J. Geophys. Res., **106**, 5,199-5,209.

Wanzong, S. W., W. P. Menzel, and G. Callan, 1998: Intercalibration of GOES, Meteosat, GMS, HIRS, and AVHRR infrared radiances. Report of the 9th Conference on Satellite Meteorology and Oceanography held 25 – 29 May, 1998 in Paris, France. AMS Publication.

P4.3 INTERCALIBRATION OF METEOROLOGICAL SATELLITE IMAGERS USING VIRS, ATSR-2 AND MODIS

Louis Nguyen*, Patrick Minnis
Atmospheric Sciences, NASA Langley Research Center, Hampton, VA

J. Kirk Ayers, and David R. Doelling
Analytical Services and Materials, Inc., Hampton, VA

1. INTRODUCTION

Global retrievals of surface, cloud and radiative properties from geostationary (GEO) and low-Earth-orbit (LEO) meteorological satellites require accurate calibration of their imagers. An accurate and consistent calibration increases the reliability and effectiveness of long-term monitoring of climate changes. More emphasis has been placed on calibrating the thermal infrared (IR) channel. The lack of on-board calibration in the visible (VIS) channel has prompted efforts to characterize the degradation of the VIS sensor using vicarious post-launch calibration techniques that measure bright stable desert targets from space and aircraft (e.g., Rao and Chen, 1996) or using satellite-to-to-satellite normalizations (e.g., Desmoreaux et al. 1993). While such inter-calibrations are valuable and widely used, the lack of a well-characterized calibration reference source and the lengthy time delay between updates have minimized their effectiveness in climate monitoring.

To address these shortcomings, this paper examines the use of research satellite imagers to provide stable calibration references for the visible (VIS, ~0.65 μm) channels and develops a method for rapid intercalibration of existing satellites. Calibration coefficients are determined for the Geostationary Operational Environmental Satellites (GOES-8 - GOES-10), Geostationary Meteorological Satellite (GMS-5), Meteosat-7, and the NOAA-14 Advanced Very High Resolution Radiometer (AVHRR). As a reference calibration source, this technique uses the self-calibrating sensors on the Tropical Rainfall Measuring Mission (TRMM) Visible Infrared Radiometers (VIRS) or the ERS-2 Along Track Scanning Radiometer (ATSR-2). GOES-8 is calibrated with VIRS and then its calibration is transferred to other GEO or LEO satellites. The absolute accuracy of this technique relies on the assumption that the on-board calibration is stable and well maintained. Minnis et al (2001) assessed the VIRS calibration using comparisons with other self-calibrated satellite sensors including the broadband Clouds and Earth's Radiant Energy System (CERES) scanners, the ERS-2 Along Track Scanning Radiometer (ATSR-2), and the Terra Moderate-resolution Imaging Spectroradiometer (MODIS). Thus, the VIRS data can be confidently used as the initial reference source.

*Corresponding author address: Louis Nguyen, NASA Langley Research Center, MS 420, Hampton, VA 23681-2199. Email: l.nguyen@larc.nasa.gov

3. METHODOLOGY

The general approach taken here is similar to the Desormeaux et al. (1993) method except that the data-matching constraints are less stringent and GOES-8, once calibrated against the VIRS, is used as a primary reference for calibration other satellites. GOES-8 is used because the degradation of the VIS channel is linear and well characterized, it has more 6 years of operational service, and its archived data are readily available.

The intercalibrations are performed between spatially and temporally matched averages of the data from the corresponding channels of two satellites. Additionally, the data are only selected if they have nearly the same values of viewing zenith θ and relative azimuth ϕ angle. For the GOES-8 calibration, VIRS is used as the reference calibration source. The GOES-8 data are matched with VIRS data taken within 15 minutes and have corresponding values of θ and ϕ that differ by less than 10°. Data taken in possible sunglint conditions are filtered out of the datasets. The reference radiance is normalized to the GOES-8 solar zenith angle θ_o and to a solar constant E_o of 526.9 $Wm^{-2}sr^{-1}\mu m^{-1}$. To account for the time and navigation differences, the radiances are averaged on a 0.5° grid to yield a pair of data points for each grid box.

Similarly, GEO satellites are also inter-calibrated with each other (GEO-to-GEO). For example, GOES-8 is used to calibrate GOES-10. Very close matches in time and space are possible because of the fixed views and regular imaging schedules. The GEO data are taken at local noon or midnight at the bisecting longitude between the two satellites. Local noon insures that all of the angles are nearly identical. The GEO data are matched to within 2 minutes. Because reflectance anisotropy may not be entirely symmetrical, average radiances at each 1° of latitude are computed for two 1° boxes that straddle the bisecting longitude. The regions used to cross-calibrate many of the various satellites are shown in Fig. 1.

In addition to the GEO-to-GEO matches, the GEO satellites are used to cross-calibrate with imagers like MODIS and AVHRR on Sun-synchronous satellites. Because TRMM is in a 35°-inclined orbit, the VIRS has few close matches with polar orbiters. However, it can frequently be collocated and bore-sighted with GEO

data to within a few minutes. Thus, GEOs can serve as calibration sources for other satellites. Calibrations between Sun-synchronous satellites follow the approach of Loeb (1997) who used the frequent polar overpasses of such orbiters to obtain well-matched data. Data are averaged on a 0.5° grid for GEO-to-GEO and GEO-to-LEO intercalibrations.

While the calibrations are performed for all channels that are spectrally similar, only IR (~11μm) and VIS channels are used here. The VIS brightness counts are regressed against the reference VIRS radiances L_V is

$$L_v = a(C - C_0) \qquad (1)$$

where a is the gain, C is the observed brightness count or squared count, and C_0 is the space count. The VIS regression forces the lines through the space count for the particular satellite. Although the VIS channel on each imager has a unique filter function, the bandwidth for most of the instruments is between 0.55 and 0.75 μm. The IR temperature is

$$T = b_1 T_0 + b_0, \qquad (2)$$

where b_1 and b_0 are the regression coefficients. The mean IR temperatures T_0 for each data point are computed in radiance and converted to T with the appropriate Planck function. Despite the spectral differences between the various IR channels, it is assumed that the equivalent blackbody temperatures should be the same for all of the sensors.

3. DATA

Matching GEO & LEO data are collected for a month at a time. A regression is then performed for each month of data. Data taken between 1994 and 2001 are used here. Table 1 shows an example of the monthly sampling used for each satellite calibration. GEO data were acquired from University of Wisconsin-Madison, AVHRR from the NOAA Satellite Active Archive, VIRS from NASA Langley DAAC, and ATSR-2 from the Rutherford Appleton Laboratory in Chilton, UK.

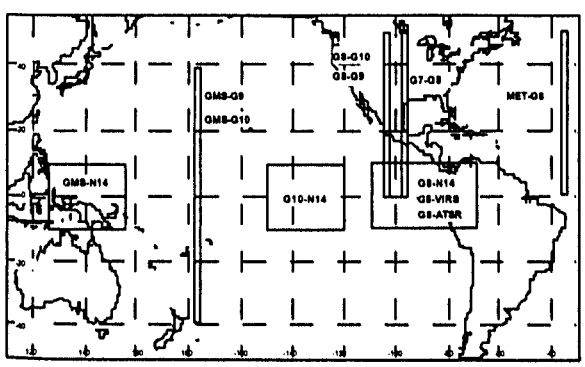

Fig. 1. Satellite intercalibration regions.

Satellites	Years	Total Mo.
VIRS - GOES8	1998-2001	23
GOES8 - ATSR2	1995-1999	12
GOES8 - N14	1995-2001	48
GOES8 - GOES9	1996-1998	14
GOES8 - GOES10	1998-2001	31
GOES8 - MET7	2000-2001	8
VIRS - GMS5	2000-2001	13

Table 1. Monthly calibration data by year.

3.1 VIRS

VIRS was launched on TRMM satellite at a 35° inclination and has been operating since late December 1997. The TRMM precessing orbit observes all local hours and viewing angle within a 45-day period. Channel 1 VIS (0.63μm) and 4 (IR) have a 2-km nominal resolution. The VIRS calibration is based on pre-launch and on-board procedures as reported by Barnes et al. (2000). As a reference source, the on-board system uses a solar diffuser plate that views the sun. The VIRS channel-1 radiances L_V are obtained the from Version-5 data, and the solar constant E_V is 531.7 $Wm^{-2}sr^{-1}\mu m^{-1}$. For comparisons with GOES, GMS, Meteosat-7, and ATSR-2, the L_V are normalized to equivalent GOES radiances by multiplying by the ratio of the GOES and VIRS solar constants (E_0 / E_V = 0.9923). The VIRS channel-1 reflectance is

$$\rho = \frac{L_v(\theta_v, \theta, \phi)}{E_0 \cos\theta_v \delta(day)}, \qquad (3)$$

where δ is the Earth-Sun distance correction factor.

3.2 AVHRR

NOAA-14 was launched into a near Sun-synchronous orbit on December 30, 194. The afternoon polar orbiter has an equatorial crossing time of 14:30 local time (LT). The orbit has since drifted to approximately 16:36 LT in early 2001. The AVHRR channel-1 VIS (0.67μm) and channel 4 IR (10.8μm) has a nominal spatial resolution of 1.1-km (High Resolution Picture Transmission, HRPT) and 4km (Global Area Coverage, GAC). In this study, the GAC datasets are used and matched with GOES-8 in the tropics.

3.2 Meteosat-7

The EUMETSAT Meteosat-7 was launched in September 1997 and is located at 0° where it became operational during June 1998. The Meteosat-7 Visible and Infrared Spin Scan Radiometer (VISSR) is a 3-channel 8-bit imager with a nominal resolution of 5 km (2.5-km VIS). The center wavelength of the VIS channel is 0.75 μm and the radiance varies linearly with the VIS count. Meteosat-7 and GOES-8 radiances are matched in ocean regions where the effect of the wide Meteosat-7 spectral response function is minimized.

3.3 GMS-5

The GMS-5 VISSR has a nominal 1.25-km resolution VIS channel and a 5-km IR channel. Matched data are obtained by averaging 0.5° grids over ocean regions. The IR temperature conversion uses a nonlinear lookup table. GMS-5, at 140°E, has provided data since June 1995. GMS-5 is calibrated directly with VIRS (Minnis et al., 2001) from March 2000 to March 2001. Farther examination of the GMS-5 calibration will be assessed with the GEO-to-GEO method from 1995 to 1999.

3.4 GOES-8, 9, 10

GOES-8 has been the primary GOES-East satellite since September 1994. GOES-9 operated as GOES-West at 135°W from January 1996 to July 1998. GOES-10, launched in April 1997, replaced GOES-9 in July 1998. The GOES imager has 1-km VIS and 4-km IR (10.7μm) channels (Menzel et al., 1994) with data taken at a 10-bit resolution. Simple averaging is used to degrade the VIS resolution to 4 km. GOES-9 and 10 are calibrated using GOES-8.

4. RESULTS

A scatterplot for the GOES-8 VIS calibration during July 2000 is shown in Fig. 2a with the regression fit forced through the space count, 31. The squared correlation coefficient is 0.993 and the data cover a large dynamic range. The standard error of the estimates using these fits is less than 10%. The IR scatterplot (Fig. 2b) shows a near perfect agreement between GOES-8 and VIRS with a gain of 1.001 and R^2=0.995. The IR gains from 1998 to 2001 are typical with a mean RMS error of 0.5% and a 0.4 K bias. Figure 3 shows that the GOES-8 VIS gain trends calibrated with VIRS (Os) and ATSR-2 (Xs) increase linearly with time consistent with a steady degradation of the instrument optics. The ATSR-2 trend line is consistent with VIRS to within 1%. Either calibration could be used as reference but VIRS was chosen as an absolute calibration for GOES-8 and other satellites because its VIS-channel filter is more like the operational satellites' than the ATSR-2 filter. For a given satellite, the post-launch calibration formula is

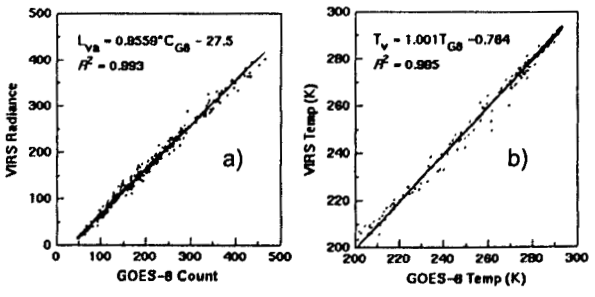

Fig 2. GOES-8 VIS & IR for July 2000. Radiance in $Wm^{-2}sr^{-1}\mu m^{-1}$.

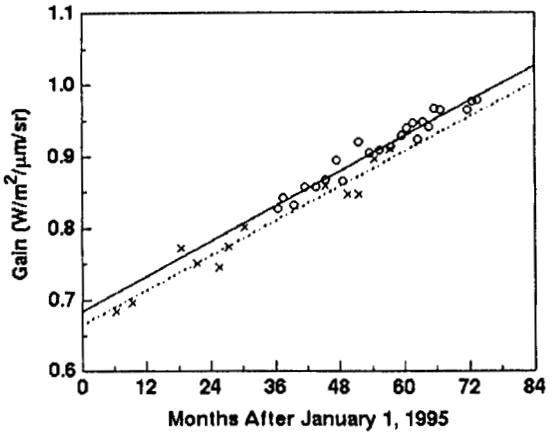

Fig 3. Monthly GOES-8 VIS gain trend from VIRS (O) and ATSR-2 (X). The solid (VIRS) and dotted (ATSR-2) lines are linear regression fit.

$$L_v = (\Delta g\, d + g_o)(C - C_o), \qquad (4)$$

where L_v is the normalized radiance, g_o is the initial gain, Δg is the trend, d is the days since the reference date (or launch date), C_o is the offset count, and C is the raw 8 or 10-bit count. For GMS-5, C is expressed as 8-bit squared counts. The calibration coefficients for several satellites are given in Table 2. The VIS reflectance can be calculated using (3).

The GOES gain trends in raw count are shown in figure 4. GOES-8 VIS count is 16.7% lower than GOES-9 in February 1996 and 28% lower than GOES-10 in March 1998. The VIS channel sensor on the GOES-8, 9 &10 degrade linearly at an annual rate of 7.5%, 5.8%, and 11.1% respectfully the first year after launch as calculated from Table 2. These rates are consistent with the 7.6% (GOES-8) and 4.9% (GOES-9) reported by Bermer et al. (1998) who uses star measurements for estimating the sensor degradation. The GMS-5 VIS sensor has an annual degradation rate of 1.4% (Minnis et al.). The NOAA-14 AVHRR VIS channel has a non-linear degradation (fig. 5) and the calibration equation is

$$L_{va}=(-3.139E\text{-}8d^2+9.318E\text{-}5d+0.6074)(C-41) \qquad (5)$$

where L_{va} is the radiance, C is 10-bit count, and d is the day after launch, 30 December 1994. The reflectance can be calculated using (3) and the NOAA-14 solar constant of 510.6 $Wm^{-2}sr^{-1}\mu m^{-1}$ instead of E_o. The calibration equation is not recommended for data after December 2001 since the trend is non-linear and the orbit is drifting into a terminator orbit. The calibration equation (5) for the period from 1995 to 1999 is ~7% greater than reported by Rao et al. (1996,1999), however, it is in good agreement with Vermote and El Saleous study as reported by Doelling et al.(2001). The Meteosat-7 calibration coefficients in Table 2 may not be as reliable for data from 1998 to 2000.

Satellite	g_o	Δg	C_o	Ref Date
GOES10	0.5234	1.5983E-4	34	04/25/97
GOES-9	0.5819	9.1929E-5	34	05/23/95
GOES-8	0.6497	1.3415E-4	31	04/13/94
GMS-5	0.00798	3.0301E-7	-30^2	03/19/95
MET-7	1.6846	6.1048E-4	6	09/02/97

Table 2. Calibration coefficients for equation (4). g_o and Δg in $Wm^{-2}sr^{-1}\mu m^{-1}$.

Presently, only data from 2001 were analyzed. The degradation rate is ~9% per year in 2001.

The IR channel comparisons from several satellites show that most sensors are relatively stable. The GOES-8/GOES-10 gains show no apparent trend and are stable from 1998 to 2001. The mean bias is –0.5 K with an RMS error of 0.6%. The GOES-8/GOES-9 gains are similar with RMS error of 0.4% and bias of 0.4 K. The GOES-8/NOAA-14 IR gains show a small trend in the NOAA-14 IR channel. In 1995, the IR channels were in excellent agreement. However, in 2001, the NOAA-14 cold temperatures (~210K) are 3 K lower than their GOES-8 counterparts.

To validate the cross calibration, a three-way calibration was performed. VIRS-to-GOES-8-to-NOAA-14 and VIRS-to-NOAA-14 calibration (Doelling et al., 2001) were performed. The two calibration slopes are within 1% showing that the method of using GOES-8 as a transfer medium is accurate and reliable.

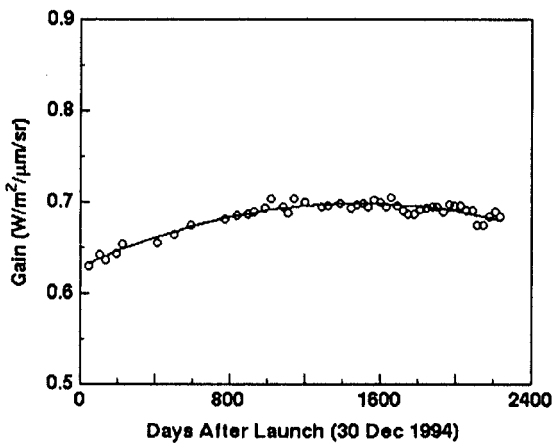

Fig 5. NOAA-14 AVHRR VIS channel gain trend in $Wm^{-2}sr^{-1}\mu m^{-1}$.

5. CONCLUSIONS

The method presented here provides a means for accurately calibrating satellite VIS channels in a timely fashion. This approach assumes that the VIRS sensors are well calibrated. Thus, any errors in the VIRS calibrations will be transferred to the other satellites.

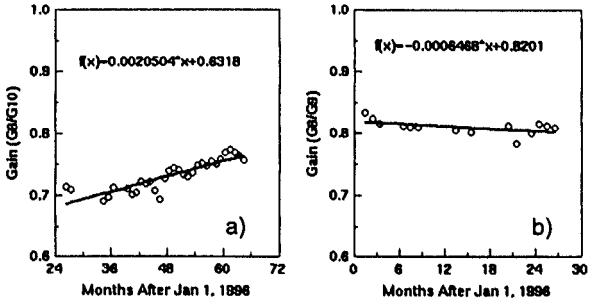

Fig 4. GOES-10 and GOES-9 VIS channel gain trends in count.

Independent validation of these results is an important part of this effort. Other new satellites and sensors will be examined and the validation of the VIS channels will continue. These calibrations provide the basis for consistent retrievals of cloud and surface properties and radiative fluxes from all of the different satellites used for climate monitoring. These techniques also permit rapid evaluation of the geostationary satellite data, thus paving the way for a near-real time analysis of radiative properties from these satellites.

References

Bremer, J.C., J.G. Baucom, H. Vu, M.P. Weinreb, and N. Pinkine, 1998: Estimation of long-term throughput degradation of GOES 8 & 9 visible channels by statistical analysis of star measurements. Proc. SPIE Conf. EOS (III), (Editor: W.L. Barnes), 3439, 145-154.

Desormeaux, Y., W. B. Rossow, C. L. Brest, and G. G. Campbell, 1993: Normalization and calibration of geostationary satellite radiances for ISCCP. *J. Atmos. Ocean. Tech.*, 10, 304-325.

Doelling, D. R., V. Chakrapani, P. Minnis, L. Nguyen, 2001: The Calibration of NOAA-AVHRR Visible Radiances with VIRS. *Proc. AMS 11th Conf. Atmos. Radiation*, Madison, WI, Oct 15–18.

Loeb, N.G., 1997: In-flight calibration of NOAA AVHRR visible and near-IR bands over Greenland and Antarctica. *Int. J. Remote Sens.*, 18, 477-490.

Menzel, W. P. and J. F. W. Purdom, 1994: Introducing GOES-I: The first of a new generation of Geostationary Operational Environmental Satellites. *Bull. Am. Meteorol. Soc.*, 75, 757-781.

Minnis, P., L. Nguyen, D. R. Doelling, D. F. Young, W. F. Miller, 2001: Rapid Calibration of Operation and Research Meteorological Satellite Imagers, Part I: Use of the TRMM VIRS or ERS-2 ATSR-2 as a Reference. *Submitted to J. Atmos. Ocean. Tech.*

Rao, C. R. N. and J. Chen, 1996: Post-launch calibration of the visible and near-infrared channels of the Advanced Very High Resolution Radiometer on NOAA-14 spacecraft. *Int. J. Remote Sens.*, 17, 2743-2747.

Rao, C. R. N., and J. Chen, 1999: Revised post-launch calibration of the visible and near-infrared channels of the Advanced Very High Resolution Radiometer on the NOAA-14 spacecraft, *Intl Jour. Remote Sens.*, 20, 3485.

P4.5 PHYSICAL DECOUPLING OF NEAR-INFRARED (3.9-μm) SOLAR AND THERMAL RADIATION COMPONENTS THROUGH SATELLITE OBSERVATIONS OF TOTAL SOLAR ECLIPSES

Steven D. Miller*
Naval Research Laboratory, Monterey

1. INTRODUCTION

This paper summarizes a method discussed at length by Miller (2001) whereby the solar and thermal radiation components of daytime near-infrared (NIR, 3.9 micron window) satellite imagery are separated from one another using the opportune passage of the moon in front of the sun, or "solar eclipse". Motivation for this research stems from the need to quantify uncertainties associated with cloud optical property retrievals. Owing to the spectral absorption properties of water, the magnitude of solar reflection in the NIR channel is a proxy for cloud droplet size (e.g., Nakajima and King 1990). The inverse models used to retrieve this parameter require knowledge of this shortwave component of the NIR signal exclusively; hence the undesired thermal component must be removed. This is achieved in practice by one of a variety of empirical, iterative, or physically based approximations. In any case, no direct estimate of the uncertainty of these approximations is available without a truth set.

At its point of maximum blockage, a solar eclipse is considered *total* if the solar disk is blocked completely by the moon (associated with the umbral shadow), *partial* if a portion of the disk is unblocked (associated with the penumbral shadow) and *annular* if the solid angle subtended by the moon as seen from the earth is less than that of the sun (producing a solar ring). In this study the total eclipse is used as a mechanism to temporarily remove the solar signal from a satellite scene, thereby providing the requisite truth data for validation of existing approximations.

2. DATA

The method requires multiple images of the same scene over a period of at least one hour. As such, the geostationary platform is best suited to this experiment. The Geostationary Operational Environmental Satellite (GOES) constellation includes a NIR window band (3.9 μm central frequency). Archived GOES data were obtained from the Cooperative Institute for Research in the Atmosphere (CIRA) at 30-minute intervals. Processing and analysis of the data was done using the Interactive Data Language (IDL; including the GVIEW package written by Kelly Dean of CIRA).

3. PROCEDURE

The umbral shadow traverses the earth's surface at speeds that can exceed 4 km/s. The GOES imager requires up to 26 minutes to complete a full-disk image. Consequently, the data near the equator in a nominal GOES image time of 1000 Z actually were collected near 1010 Z. While this offset holds only minor consequences for interpretation of most atmospheric phenomena, it presents a problem when determining the exact umbral shadow position in the image, which will have displaced anywhere from 300 to over 2000 km from its position at 1000 Z. Given the actual shadow positions as a function of time (from celestial geometry) and knowledge of scan line times in the imagery, the updated umbral shadow positions were determined via cost function minimization for all GOES imagery.

Decoupling of the thermal and solar signals was achieved by time-differencing the same registered scene prior to and during the passage of the umbral shadow. Due to the presence of the penumbral (partial eclipse) shadow, a temporal difference of approximately 1-hour was required to ensure full decoupling. This procedure hinges on the assumption that the thermal component of the scene remains relatively unchanged over the period. This will not apply to land surfaces, which may cool dramatically during a total eclipse. As the advection, formation and dissipation of most clouds occur typically on time scales less than 1-hour, the application is

* *Corresponding author address:* Steven D. Miller, Naval Research Laboratory, Monterey, CA 93943-5502;e-mail: miller@nrlmry.navy.mil

restricted largely to stratiform clouds (i.e., convective or rapidly advecting cloud elements are excluded). The thermal stability criterion imposed here was a 10.7 μm brightness temperature difference of less than 2.0° K.

As a further restriction, these clouds must occur within a relatively small region corresponding to the position of the umbral shadow in the GOES image series. While these restrictions narrow the possibilities considerably, the extensive and quasi-persistent coverage of marine stratocumulus on the eastern sides of the ocean basin high-pressure systems provides some hope for obtaining adequate case studies from any given eclipse traversing these domains.

4. CASE STUDY

A total eclipse occurring on 26 February 1998 began its track across the equatorial Pacific at 1546 Z, crossed Panama at 1728 Z, and terminated at 1909 Z of the northwestern coast of Africa. Its passage was observed by GOES-9 (135 W), GOES-K (106 W), and GOES-8 (75 W). As GOES-K offered the best coverage at lowest sensor zenith angles, its data were used for this analysis.

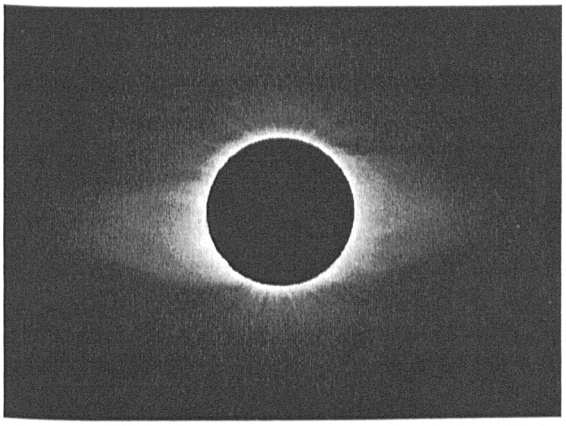

Fig. 1. The 26 February 1998 total solar eclipse (photograph by Fred Espanek).

Throughout history, solar eclipses have captivated the interest of scholars and laymen alike. Today, people from all corners of the world travel great lengths to witness these rare celestial events. The 1998 eclipse, which offered prime viewing near Central America, attracted a very large audience. A photograph of how this eclipse appeared to a surface observer (photograph by Fred Espenak) is shown in Figure 1. The solar corona, clearly visible here, often is accompanied by a spectacular display of solar prominences. Just prior-to and after totality, complicated light refraction and interference in the atmosphere sometimes will produce patterns of alternating light and shadow (called "shadow bands") moving across the surface and parallel to the direct-beam of the crescent Sun.

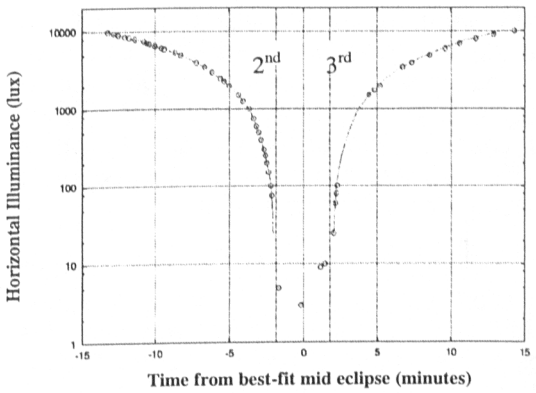

Fig. 2. Downwelling solar radiation measured at the surface during a total solar eclipse (from Mason and James 1998).

Mason and James (1998) use a luxmeter to measure changes in luminosity over the course of this eclipse. Results shown in Figure 2 indicate an effective removal of sunlight by the eclipse down to 4 orders of magnitude (below the calibration sensitivity of the GOES visible channel). The region between the "2nd and 3rd" annotations (in reference to contact points between the edges of the lunar and solar disks) corresponds to the period of total eclipse. At its lowest reading of 3 lux, the luminosity is approximately an order of magnitude greater than that of the full moon.

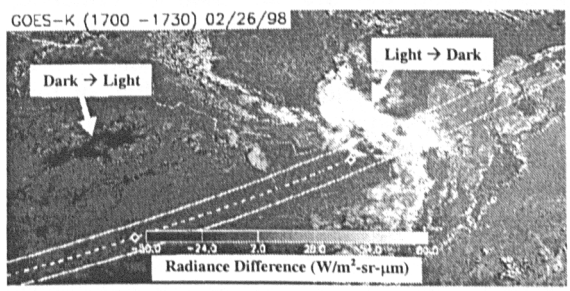

Fig 3. Example of image temporal differencing. Dark and bright clouds correspond to changes in the position of the umbral shadow over the interval.

An example of the image-differencing concept used for radiative decoupling is shown in Figure 3 for a portion of the eclipse track (indicated) near Central America. The image, shown here for the 0.65 μm visible channel, depicts changes in reflectance between 1700 and 1730 Z, with the umbral shadow approaching the region from the Southwest. Dark patches correspond to clouds that were within the umbral/penumbral shadow at 1700 Z but were again illuminated at 1730 Z, resulting in a negative reflectance difference over this period. In contrast, bright regions correspond to light-to-dark transitions. In the NIR channel (and under the assumption of thermal stability), this residual corresponds to the decoupled solar component.

An opportune deck of marine stratus (identified from visible and infrared imagery) located off the coast of Panama was within the track of the umbral shadow. A small fraction of these clouds dissipated during the approach of the total eclipse. While surface observers have noted marked cloud dissipation over the course of total eclipses in connection to increased low-level stability (John Weaver (CIRA), personal communication, 2000), this has not been verified as the responsible mechanism for the cloud dissipation observed in the current case study. The GOES-K pixels corresponding to clouds that passed the thermal stability test were used to compare against existing approximations as outlined in the following section.

5. RESULTS

Comparisons of eclipse-derived NIR albedo in the cloudy region were made against various levels of approximation. The crude approach of estimating the 3.9 μm thermal radiance based on the measured 10.7 μm brightness temperature and the Planck function was examined first. The primary shortfall of this technique is the erroneous assumption that cloud emissivities of the two channels are equivalent. With typical values near 0.7, the 3.9 μm cloud emissivity is much lower (less absorbing) than at 10.7 μm where corresponding emissivities approach unity (and the assumption of a blackbody emitter for optically thick clouds holds to a good level of approximation). Miller (2001) presents results from this comparison; they are omitted here for the sake of brevity.

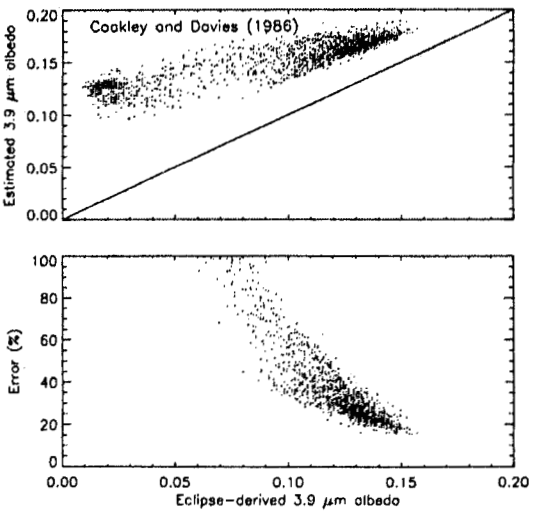

Fig. 4. Comparison between eclipse-derived and empirically derived (Coakley and Davies, 1986) 3.9 μm albedo.

The second comparison examined the performance of an empirical relationship developed between 3.7 μm and 11.0 μm Advanced Very High Resolution Radiometer (AVHRR) brightness temperatures measured at night (Coakley and Davies, 1986). The nighttime regression is then applied to 3.7 μm daytime imagery. The relationship follows as

$$I_{3.7}(thermal) = 1.59\text{E-}7 \times (I_{11.0})^{3.23} . \quad (1)$$

While superior to the former approximation, this relationship is limited in accuracy by any differences between the regression data and the daytime cloud fields to which it is applied. The results for this approach, plotted against the solar eclipse data, are shown in Figure 4. The best performance corresponded to optically thick (higher 3.9 μm albedo) clouds. To a lesser extent, differences between the GOES and AVHRR NIR and thermal-infrared channel spectral response functions also contribute to the observed discrepancies.

Lastly, a formulation based on fundamental principles of radiative transfer theory, following Kaufman and Nakajima (1986) and Kidder *et al.* (1998), was examined. Under the assumption of optically thick clouds (such that cloud transmittance may be neglected), the derived relationship assumes the form:

$$\rho_2 = \frac{I_2 - t_2' B_2(T_4)}{t_2^o \pi^{-1} F_o \mu_o - t_2' B_2(T_4)}, \quad (2)$$

where subscripts 2 and 4 correspond to GOES NIR and IR channels, respectively, t and t^0 are clear-atmosphere transmittances from cloud top to the satellite and sun, respectively, μ_0 is the cosine of the solar zenith angle, and $B(T)$ are the Planck blackbody radiances corresponding to temperature T.

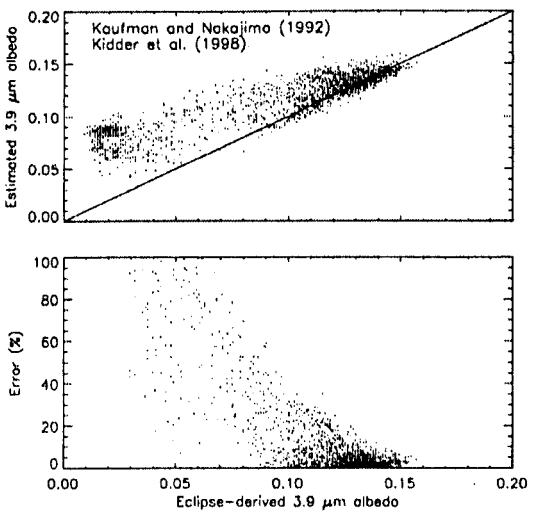

Fig. 5. Comparison of 3.9 μm albedo from Kaufman and Nakajima (1993) (and Kidder *et al.*, 1998) with eclipse-based results.

The comparison of this physically based approximation with eclipse data, shown in Figure 5, provides a quantitative assessment of its strengths and weaknesses. Errors were observed to fall below 5% for most optically thick clouds pixels (when the fundamental assumptions of the approximation are met) and increase systematically as the opacity assumption breaks down. With a GOES imager spatial resolution of 4 km, partly cloudy satellite pixels will also account for departures from the eclipse-derived truth data.

6. CONCLUSION

A natural experiment involving total solar eclipses and geostationary satellites was exploited as a means by which the shortwave and longwave components of a daytime NIR scene may be decoupled from one another. The 26 February 1998 total eclipse was examined to determine the NIR albedo of thermally stable clouds. Previous approximations of this retrieval-relevant quantity by various methods were assessed. It was found that the physically based method of Kaufman and Nakajima (1986) and Kidder *et al.* (1998) produced the closest agreement with the eclipse-derived results, provided the assumption of cloud opacity was met.

While this physical decoupling method is applicable only during on the rare occurrence of total solar eclipses, it represents a potentially useful tool for validating and quantifying the uncertainty of existing approximations.

7. REFERENCES

Coakley, J. A. Jr., and R. Davies, 1986: The effect of cloud sides on reflected solar radiation as deduced from satellite observations. *J. Atmos. Sci.*, **43**, 1025—1035.

Kaufman, Y. J., and T. Nakajima, 1993: Effect of Amazon smoke on cloud microphysics and albedo-analysis from satellite imagery. *J. Appl. Meteor.*, **32**, 729—744.

Kidder, S. Q., K. E. Eis, and T. H. Vonder Haar, 1998: New GOES imager system products suitable for use on field-deployable systems. In *Proceedings: BACIMO, AFRL, December 1995*, AFRL-VS-HA-TR-98-0103, Environmental Research Papers, No. 1217, 452—459.

Mason, J. W., and N. D. James, 1998: The total eclipse from Venezuela. *J. British Astronomical Assoc.*, **108**, 127—128.

Miller, S. D., 2001: Physical decoupling of the GOES daytime 3.9 μm channel thermal emission and solar reflection components using total solar eclipse data. *Int. J. Remote Sensing*, **22**, 9—34.

Nakajima, T. Y., and M. D. King, 1990: Determination of the optical thickness and effective particle radius of clouds from reflected solar radiation measurements. *J. Geophys. Res.*, **47**, 1878—1893.

8. ACKNOWLEDGEMENTS

The author is indebted to Tom Vonder Haar, Stan Kidder, Nick James, Fred Espenak, and Kelly Dean, for their helpful discussions, contributions of imagery, and assistance with software and data processing associated with this research. Travel and publication support from the Oceanographer of the Navy through the program office Space and Naval Warfare Systems Command, PMW-155, under program element 0603207N is gratefully acknowledged.

P4.6 ADVANCES IN THE BIAS CORRECTION OF SATELLITE RADIANCE DATA

William F. Campbell and Nancy Baker
Naval Research Laboratory, Monterey, California

1. INTRODUCTION

Satellite radiances provide essential coverage of data-poor regions, especially over the oceans and in the Southern Hemisphere. Data assimilation schemes such as optimal interpolation (OI) must convert radiance data into vertical temperature and moisture profiles by solving the so-called inverse problem, which is mathematically ill-posed. The ability to assimilate data in observation space, and avoid the inverse problem, is the principal advantage of three dimensional varational assimilation (3DVAR) over OI.

Like OI, 3DVAR blends forecasts, observations, and dynamical constraints to extend the spatial influence of incoming data. Many sources of error, both random and systematic, are present in the assimilation system. Random errors are handled within the framework of 3DVAR; systematic errors, or biases, are not. In order for 3DVAR to work well, biases must be minimized or eliminated.

Satellite radiance data is known to be biased. In particular, the brightness temperatures observed by the TIROS Operational Vertical Sounder (TOVS) suite of instruments (the High Resolution Infrared Sounder (HIRS) channels 1-7 and 10-15, the Microwave Sounding Unit (MSU) channels 2-4, and the Stratospheric Sounding Unit (SSU) channels 1-3) show bias relative to NOGAPS, the forecast model used operationally at NRL. The two principal sources of bias are due to the instruments themselves as they scan the atmosphere at different zenith angles (scan bias), and to inaccuracies in the fast radiative transfer model, whose biases differ depending on the thermodynamic properties of the underlying atmosphere (air-mass bias).

The scheme currently used at NRL is adapted from Eyre (1992). It employs a simple, global scan-bias correction, and a global linear regression against microwave brightness temperatures (MSU channels 2-4) to correct air-mass bias in all of the channels of the TOVS instruments. An improved scheme due to Harris & Kelly, 1999, takes into account the latitudinal dependence of both scan and air-mass bias. More importantly, air-mass bias correction is a function of four model forecast fields (1000-300 and 200-50 hPa thickness, surface skin temperature, and total column precipitable water), rather than observed radiances. The change in philosophy is significant. Harris & Kelly (1999) state that their scheme shifts the focus away from correcting the observations, towards correcting the forward operator (fast radiative transfer model), which is the main source of air-mass bias. The background fields essentially retune the forward operator to better match observations.

The Harris & Kelly (1999) scheme has been prototyped for use with the NRL Atmospheric Variational Data Assimilation System (NAVDAS) (Daley and Barker (2000)). Its performance has been tested against the currently operational Eyre scheme, and preliminary results are discussed below. Hybrid bias correction schemes and alternative quality control formulations have also been tested. Our primary goal is more general: to find and implement the best possible bias correction scheme for satellite radiance assimilation.

* *Corresponding author address:* William F. Campbell, Naval Research Laboratory, Monterey, CA, 93950; email: campbell@nrlmry.navy.mil

2. TESTBED ENVIRONMENT

In a 3DVAR or 4DVAR data assimilation system, bias correction is essential for all data types, not just satellite radiances. New instruments, such as scatterometers and hyperspectral sounders, will have different error characteristics, and thus require a flexible means of bias correction in order for their data to be assimilated. Our primary research goal is to design such a flexible, general bias correction system to accommodate future instrumentation.

We chose Matlab as the development environment for this system for a number of reasons: many statistical and visualization routines are built in; development of customized tools with graphical user interfaces is simple; and the resulting code can be transitioned to vectorized Fortran 90 in a straightforward fashion, then used for the quality assurance of operational code. A library of routines has been produced and tested against both the existing Eyre scheme and a Fortran implementation of the Harris & Kelly scheme (written by Dr. Edward Barker). A full-size test case has produced identical results, so we are confident that both the Fortran and Matlab codes are correct, as they were independently implemented.

3. PRELIMINARY RESULTS

We have run a suite of tests comparing the standard Eyre and Harris & Kelly models with a variety of hybrid models, varying the following parameters: number of regressions (one global or 18, one in each ten degree latitude band), data thinning, land-sea mask (standard one degree and one degree augmented by one degree), statistical outlier checking (none, three standard deviations, and two standard deviations), and scan correction (global, or by latitude band). Results were evaluated by considering the global root mean squared error in brightness

temperature, and the absolute value of the correlation between the predictors (brightness temperatures in the Eyre case, model variables in the Harris & Kelly case) and the difference between observed and forecast (or background) brightness temperatures.

An example of a run is given in figures 1 through 3. Two weeks of TOVS radiance data, available every six hours, were bias corrected using the standard Eyre scheme, and the Harris & Kelly scheme with Eyre-style data thinning, so that they end up looking at identical data after quality control. This represents a slight disadvantage for the Harris & Kelly scheme, as good data in the tropics and Northern midlatitudes is discarded. For comparison, results for each model with scan bias correction only are also presented. The Harris & Kelly scheme is superior in every channel in terms of root mean squared error, and in correlation as well (not shown).

In order to produce the optimum hybrid bias correction model, we must quantify the importance of each parameter and quality control factor. Observation of the temporal and spatial structure of residuals will guide us in the selection of additional predictors to further improve bias correction. In many channels, the correlation between predictors and predictands is quite low, so there is certainly room for improvement.

4. SUMMARY

Advances in bias correction will result in improved variational assimilation for many data types, thus enhancing resulting weather forecasts. The Harris & Kelly scheme appears superior to the Eyre scheme, and a hybrid Eyre/HK model holds promise for even greater improvement. Although many parameters and quality control factors go into the bias correction scheme, the most important factor will be finding new predictors that are highly correlated to observed bias. The methodology is sufficiently flexible and general to accommodate the assimilation of new data types as they become available.

5. REFERENCES

Daley, R., and E. Barker, 2000. *NAVDAS Source Book 2000*, NRL publication NRL/PU/7530—00-418, 155pp.

Eyre, J.R., 1992. A bias correction scheme for simulated TOVS brightness temperatures. ECMWF Tech. Memo. 186, 28pp.

Harris, B.A., and G. Kelly, 1999. A satellite bias correction scheme for radiance assimilation. *Quart. J. Roy. Meteor. Soc.*, in press.

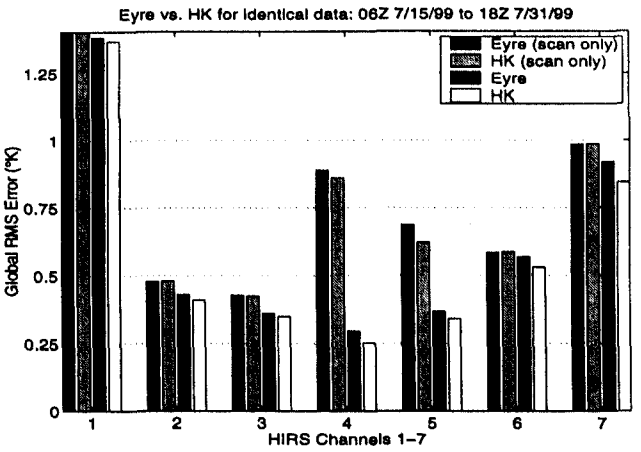

Figure 1. Comparison of RMS error in brightness temperatures of Eyre and Harris & Kelly schemes for HIRS channels 1-7.

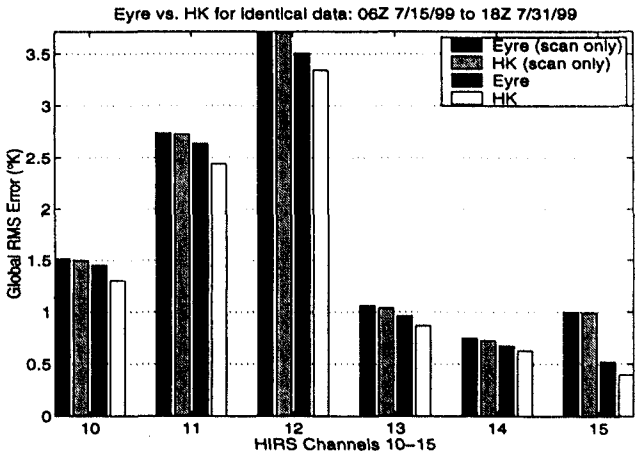

Figure 2. Same as figure 1, HIRS channels 10-15.

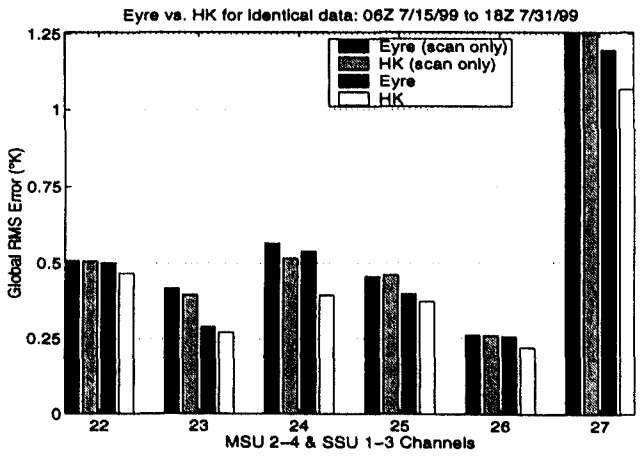

Figure 3. Same as figure 1, MSU channels 2-4 and SSU channels 1-3.

P4.8 CLOUD PROPERTIES FROM AMSU IN A SEMI-ARID REGION.

Amy M. Doherty*
CIMSS/University of Wisconsin, Madison, WI

1. ABSTRACT

To improve rain rate estimation from satellites, physically accurate radiative transfer models, or forward models, are needed to simulate the signal observed under different atmospheric conditions. A radiative transfer code developed by Dr. C. Kummerow, (University of Colorado), is used to simulate brightness temperatures from the Advanced Microwave Sounding Unit (AMSU). The code is run using typical parameters for Arizona, and comparisons of simulated brightness temperature are made with brightness temperature measurements taken during a field study in this region. Cloud properties are determined by minimising differences between simulations and measurements. Discussion of sensitivity tests and methods for tuning is presented along with analysis of performance. The future direction of this work is also discussed.

2. INTRODUCTION

Rain rate estimation in semi-arid regions can be improved using satellite instruments which give more complete information than the point measurements of rain gauges and do not require the expense of ground based radar. Geostationary satellites allow constant surveillance of a region but only carry IR and visible instruments, which estimate rain rate at the surface from measurements of cloud top parameters. Polar orbiting satellites carry microwave instruments that offer a more physically realistic rain rate estimate as they can see past the cloud top and detect the signal from the column of cloud. In order to develop a reliable method for estimating rain rate using the polar orbiting AMSU, an appropriate model is needed that can realistically simulate observed brightness temperatures.

3. DATA AND METHODS

The archived AMSU brightness temperatures and ancillary data for October 2000 were run through the International ATOVS Processing Package (IAPP) (Li *et al.*, 2000). This supplies atmospheric profiles of temperature, humidity and water vapour. The atmospheric profiles from the IAPP were then run through a precipitation code from Grant Petty from the University of Wisconsin (Petty, 2000), which generates profiles of precipitation rate for rain, snow and graupel. This code requires a number of input parameters related to the cloud microphysics, which are estimated based on realistic values for the area and season being considered and adjusted to give reasonable outputs. The original code from Grant Petty was changed slightly to follow closely the input temperature, pressure and relative humidity profiles from the IAPP.

The IAPP only produces results for non-precipitating fields of view, so the tuning was done for these cases, adjusting the variable parameters in the precipitation code to give output conditions of little or no rainfall at the surface.

The output from the precipitation code is input into the forward model. The inputs are profiles of temperature, pressure, relative humidity, liquid and ice cloud and rain rate for different hydrometeor types. The forward model is based on Eddington's second approximation (Kummerow, 1993). It assumes Mie scattering due to clouds and hydrometeors and calculates the upwelling radiance at the top of the atmosphere. The original code is from Chris Kummerow and it has been altered by Barbara Burns to use the water vapour absorption model of Liebe (1989) and to allow variable hydrometeor drop size distributions with different treatments for ice and water drops.

4. RESULTS

The calculated brightness temperatures were plotted against the measured brightness temperatures for each AMSU field of view. Ideally the scatter plot will follow a straight line. However the assumptions made about the cloud microphysics, both in the precipitation code and in the forward model, are not valid for all conditions and must be adjusted for the case in question in order to find the best fit to observations. Figure 1 shows a typical scatter plot for AMSU-B channel 4 for a field of view over Arizona in October 2000.

Over all, calculated brightness temperatures tended to be higher than observation, suggesting either over estimation of the temperature profile, underestimation of the water vapour, ice and liquid water content of the atmosphere or errors in the manner in which these parameters were treated by the forward model.

AMSU-B channel 1 is a surface channel and this displayed the most sensitivity to changes in surface temperature. AMSU-B channels 3-5, those centred

* *Corresponding author address:* Amy Doherty, 1225 West Dayton Street, Madison, WI 53706.
amyd@ssec.wisc.edu

on the 183.31 GHz water vapour band, were most sensitive to changes in the atmospheric moisture profile. Brightness temperatures also react as expected to changes in the ice cloud profile, with lower temperatures simulated as more ice is added. So in these respects the model is performing satisfactorily.

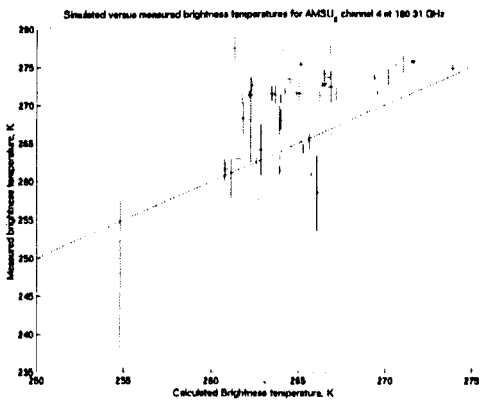

Figure 1: simulated versus measured brightness temperatures for a field of view over Arizona in October 2000. The line represents the ideal correlation between the two data sets.

Finer tuning of the variable parameters for the precipitation code and better parameterisation of ice cloud was therefore identified as the solution to improve agreement between measured and calculated brightness temperatures.

5. FUTURE WORK

This study is the first part of a larger research project that aims to improve rain rate estimation over semi-arid regions where precipitation is important for agriculture. The physically direct methods of microwave will be combined with the high temporal resolution of IR to give continuous rain rate estimates even when data from the microwave instruments is not available.

Many algorithms exist for estimation of precipitation from microwave sensors (e.g. Marzano *et al.* 1999; Panegrossi *et al.* 1998; Smith *et al.* 1998). Here the intention is to focus on semi-arid regions and by excluding other cases to some extent to overcome the difficulties of cloud microphysical parameterisation that face global models.

The forward model will be used in a physically based retrieval method to estimate rain rate from microwave measurements. This method will use a look up table created by the forward model that will relate sets of atmospheric parameters to a predicted brightness temperature. Then observed brightness temperatures will be used to retrieve the most likely atmospheric conditions from the look up table using a statistical technique. The results from this method will then be used to tune the IR estimate when coincident measurements are available

6. ACKNOWLEDGMENTS

I would like to thank Steve Ackerman, Grant Petty and Bryan Baum for their help and advice, everyone in my office for putting up with my questions and everyone else at SSEC who helped me. Dave Jones and Steve English from the UK Met Office, Barbara Burns from Aerojet and Chris Kummerow from the University of Colorado were also extremely helpful over email.

7. REFERENCES

Kummerow C. F., 1993: On The Accuracy of the Eddington Approximation for Radiative Transfer at Microwave Frequencies. *J. Geophys. Res,* **98,** 2757-2765.

Li, J., Wolf, W.W., Menzel, W.P., Zhang, W., Huang, H.-L., Achtor, T. H., 2000: Global Soundings of the Atmosphere from ATOVS Measurements: The Algorithm and Validation. *J. Appl. Meteor.*, **39,** No. 8, 1248-1268.

Liebe, 1989: MPM - An Atmospheric Millimeter-Wave Propagation Model. *Int J Infrared Milli.*, **10,** No. 6, 631-650.

Marzano, F. S., Mugnai, A., Panegrossi, G., Pierdicca, N., Smith, E. A., Turk, J., 1999: Bayesian Estimation of Precipitating Cloud Parameters from Combined Measurements of Spaceborne Microwave Radiometer and Radar. *IEEE Trans. Geosci. Remote Sensing,* **37,** No. 1, 596-613.

Panegrossi, G., Dietrich, S., Marzano, F. S., Mugnai, A., Smith, E. A., Xiang, X., Tripoli, G. J., Wang, P. K., Bapista, J. P. V. P., 1998: Use of Cloud Model Microphysics for Passive Microwave Based Precipitation Retrieval: Significance of Consistency between Model and Measurement Manifolds. *J. Atmos Sci.*, **55,** No. 9, 1644-1673.

Petty, G. W., 2000: Physical and Microwave Radiative Properties of Precipitating Clouds. Part 2: A Parametric 1-D Rain Cloud Model for Use in Microwave Radiative Transfer Simulations. *Submitted to J. Appl. Meteor.*

Smith, D. M., Kniveton, D. R., Barrett, E. C., 1998: A Statistical Modeling Approach to Passive Microwave Rainfall Retreival. *J. Appl. Met.*, **37,** 135-154.

P4.9

EFFECT OF CLOUD AND PRECIPITATION MICROPHYSICS ON AMSU MEASUREMENTS AS SIMULATED USING CLOUD RESOLVING MODEL OUTPUTS

Xiaofan Li[1] and Fuzhong Weng
NOAA/NESDIS/Office of Research and Applications, Camp Springs, Maryland

1. INTRODUCTION

Accurate knowledge of effects of cloud microphysics on satellite microwave sounding channel measurements is crucial for retrievals of temperature and moisture profiles in cloudy conditions. Such effects are usually unknown from observational analysis because of difficulties in obtaining cloud information such as vertical distributions of cloud hydrometeors. A cloud resolving simulation provides vertical profiles of cloud hydrometeors (Li et al. 1999). In this study, the AMSU-B responses to various cloud parameters are simulated using a radiative transfer model with the cloud resolving model outputs.

2. MODELS

The cloud resolving model outputs are used as the inputs of the radiative transfer model. The 2-D cloud resolving model includes prognostic equations for cloud hydrometeors, cloud microphysics and radiation parameterization schemes (Li et al. 2001). The model has been demonstrated to simulate tropical thermodynamic states and surface fluxes and rain rates well during the Tropical Ocean Global Atmosphere-Coupled Ocean Atmosphere Response Experiments (TOGA-COARE). A new fast and accurate microwave radiative transfer model (Liu and Weng 2001) includes scattering and polarization. The model is applied to compute the radiances at AMSU-B frequencies and bandwidths based on thermodynamic profiles and cloud information derived from the cloud resolving simulation on 2 pm 12 December 1992, when strong convection occurred. AMSU-B channel characteristics are summarized in Table 1.

Table 1 AMSU-B channel characteristics

Channel number	Center freq. (GHz)	No. of pass bands	Bandwidth per pass-band (MHz)	NEΔT (K)
16	89(0.9)	2	1000	0.37
17	150(0.9)	2	1000	0.84
18	183.31(1)	2	500	1.06
19	183.31(3)	2	1000	0.70
29	183.31(7)	2	2000	0.60

3. SENSIVITY TESTS

The radiative transfer model is first run with clouds. Strong convection occurs within 500-560 km, where surface rain rate has a maximum of 70 mm hour^{-1} (Fig. 1) The convection is associated with large total precipitable water, large horizontal wind shear, and large magnitudes of cloud hydrometeors, in particular raindrop (dark dashed) and graupel (light dashed). The convection causes large drop of brightness temperatures at AMSU-B frequencies, which are as low as 100K. The convection also causes zero total transmittance at Channels 16 and 17, whereas total transmittance is zero at channels 18-20 because of strong water vapor absorption.

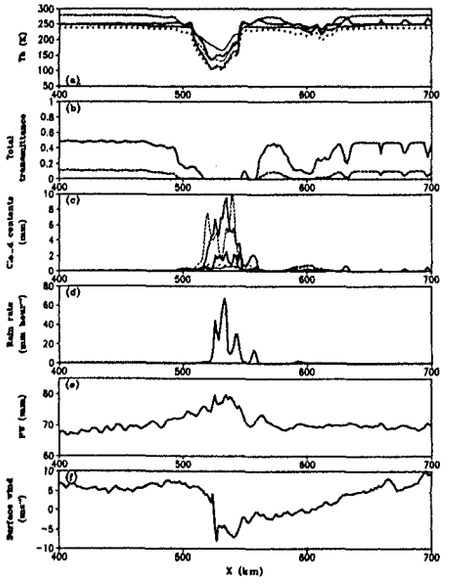

Fig. 1 Horizontal distributions of (a) brightness temperatures and (b) total transmittance for AMSU-B frequencies (dark solid: channel 16, dark dashed: channel 17, dot: channel 18, light solid: channel 19, light dashed: channel 20) simulated with clouds, (c) cloud hydrometeors (dark solid: cloud water, dark dashed: raindrop, dot: cloud ice, light solid: snow, light dashed: graupel), (d) surface rain rate, (e) total precipitable water, and (f) surface zonal wind.

The radiances at AMSU-B channels are used to retrieve vertical profiles of moisture. To examine effects of cloud hydrometeors on AMSU-B radiances, the raidative transfer model is run with clouds excluded. Fig. 2 shows the brightness temperatures (T_b) simulated with and without cloud hydrometeors

[1] Corresponding author address: Xiaofan Li, NOAA/NESDIS/ORA, 5200 Auth Road, Room 601, Camp Springs, MD 20746; e-mail: Xiaofan.Li@noaa.gov

versus total precipitable water (PW). The T_b increases with increasing PW slowly in the simulation without clouds whereas it decreases quickly in the simulation with clouds at channel 16. The T_b decreases with increasing PW in both simulations, but it decreases much quickly in the simulation with clouds than in the simulation without clouds at the other channels. These indicate dominant effects of clouds on AMSU-B radiances.

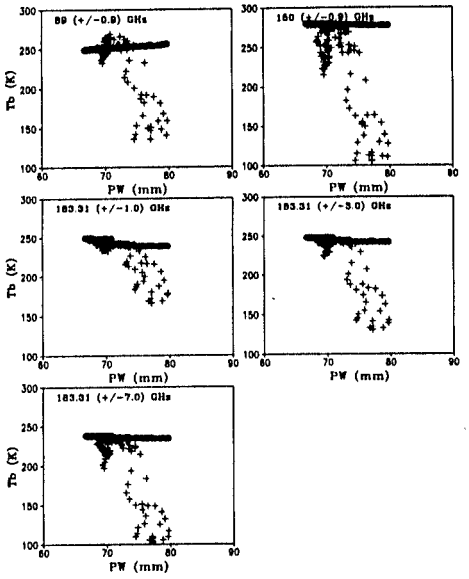

Fig. 2 Brightness temperatures simulated with (cross) and without (circle) cloud hydrometeors versus total precipitable water at AMSU-B channels.

To further examine which cloud hydrometeor has important impacts on the AMSU-B radiances, the radiative transfer model is run with thermodynamic profiles and each cloud hydrometeor profile. Fig. 3 displays T_b simulated with each cloud hydrometeor versus T_b simulated with all cloud hydrometeors. Cloud ice and graupel have much larger impacts on the radiances than do the other cloud hydrometeors for AMSU-B frequencies, indicating the importance of scattering effects of ice clouds.

Fig. 4 shows the T_b simulated with ice clouds and with clouds (water and ice clouds) as a function of the mixing ratio of vertically-integrated ice cloud hydrometeors ($q_i+q_s+q_g$). The T_b decreases as the mixing ratio increases from 0 to 5 mm at channels 16 and 17. When the mixing ratio is larger than 5 mm, the T_b barely changes in the simulation with ice clouds, whereas the T_b increases with increasing mixing ratio, indicating effects of water clouds in strong convection. At channels 18-20, ice clouds have dominant effects on the radiances. The water clouds tend to affect the radiances as the sub-frequencies increase. At channel 18, the radiances in both simulations are identical, indicating the negligence of water-cloud effects on this channel.

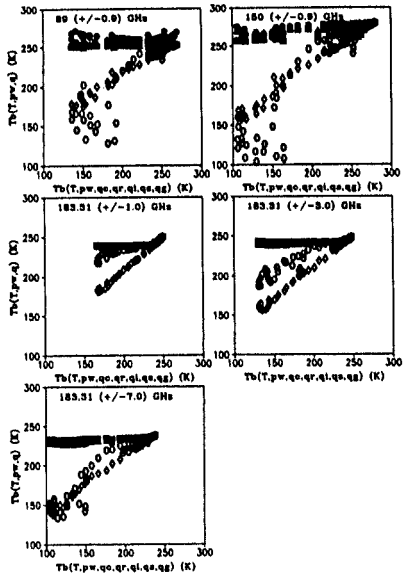

Fig. 3 Brightness temperatures simulated with each cloud hydrometeor (q) [cloud water (circle), raindrop (square), cloud ice (diamond), snow (triangle), graupel (oval)] versus those simulated with all cloud hydrometeors.

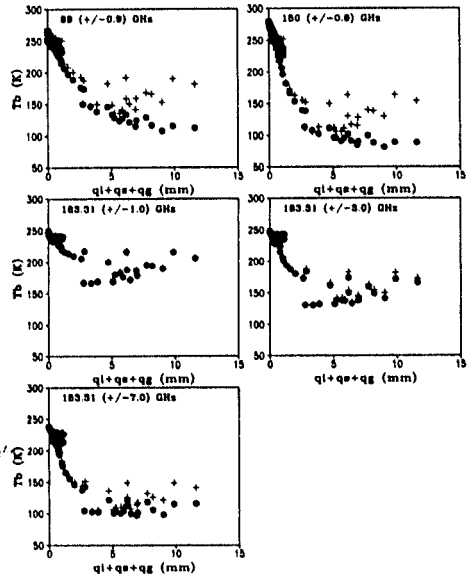

Fig. 4 Brightness temperatures simulated with ice cloud hydrometeors (circle) and all cloud hydrometeors (cross) as a function of mixing ratio of ice cloud hydrometeors ($q_i+q_s+q_g$).

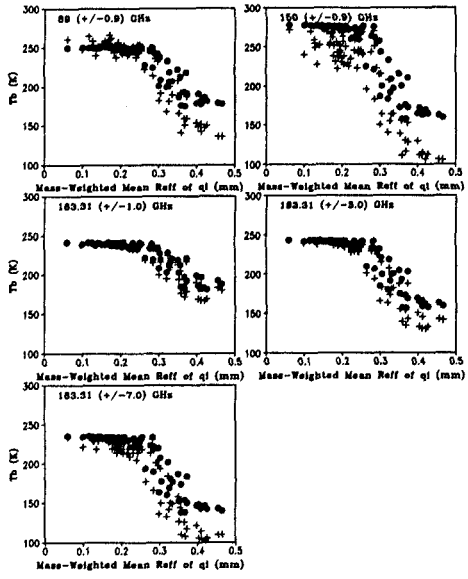

Fig. 5 Brightness temperatures simulated with cloud ice (circle) and with cloud hydrometeors (cross) versus mass-weighted mean effective radius of cloud ice.

The relationship between the brightness temperatures and mass-weighted mean effective radii of cloud ice and graupel is investigated since scattering is sensitive to the particle size of ice clouds. Both brightness temperatures simulated with cloud ice only and with cloud hydrometeors vary little when the effective radius of cloud ice is smaller than 0.25 mm, and they decrease as the effective radius goes from 0.25 to 0.5 mm (Fig. 5). This suggests that the other cloud hydrometeors do not have significant impacts on the AMSU-B radiances, and the effective radius of cloud ice can be retrieved with one of the AMSU-B radiances. Both brightness temperatures simulated with graupel only and with cloud hydrometeors vary little when the effective radius of cloud ice is smaller than 0.5 mm, and they decrease as the effective radius goes from 0.5 to 0.9 mm (not shown). Changes of T_b at channels 16 and 17 are similar, whereas decrease of T_b at channels 18-20 is slower in the simulation with graupel than that in the simulation with cloud hydrometeors, recommending that the T_b at channels 16 and 17 be used to retrieve the effective radius of graupel.

The brightness temperatures versus mixing ratio of cloud ice at each vertical level are analyzed to examine height dependence of the AMSU-B radiances on cloud ice in the simulation with cloud ice (Fig. 6). The variations of Tb at channels 16 and 17 are smaller than 5K, whereas those at channels 18-20 are larger than 10K. The cloud ice at higher levels has stronger impacts on the radiances than that at lower levels provided the same mixing ratios of cloud ice.

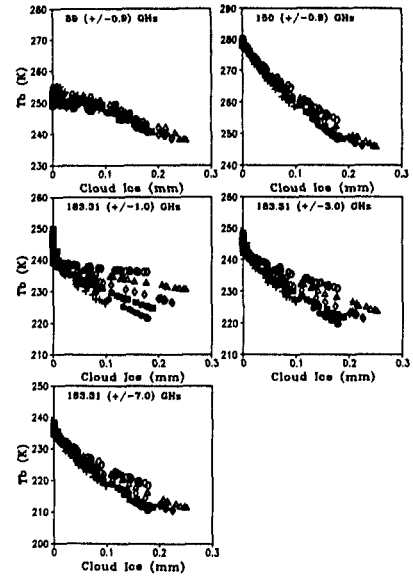

Fig. 6 Brightness temperatures versus mixing ratio of cloud ice at each vertical level in the simulation with cloud ice only (cross: 152 mb, circle: 175 mb, square: 199 mb, diamond: 225 mb, triangle: 253 mb, oval 282 mb)

4. CLOUD CONTAMINATION CORRECTION ON BRIGHTNESS TEMPERATURE

The brightness temperatures are largely affected by clouds. To physically retrieve moisture, the effects of clouds on the T_b should be removed. The clear-sky T_b in cloudy conditions at channels 16-17 is predicted using the T_b in cloudy conditions, total precipitable water, mixing ratio of vertically-integrated cloud ice and raindrop (liquid water path, LWP) because the PW and LWP are independently retrieved by the T_b at AMSU-A window channels. The linear regression model can be expressed by

$$T_b(T,pw)=A+B_1T_b(T,pw,qc,qr,qi,qs,qg) +B_2pw+B_3LWP. \quad (1)$$

The clear-sky T_b in cloudy conditions at channels 18-20 is predicted by the T_b in cloudy conditions, total precipitable water, mixing ratio of vertically-integrated cloud ice and snow and graupel (ice water path, IWP) because the IWP is independently retrieved by the T_b at channels 16-17. The linear regression model can be expressed by

$$T_b(T,pw)=A+B_1T_b(T,pw,q_c,q_r,q_i,q_s,q_g) +B_2pw+B_3IWP. \quad (2)$$

Here a, b_1, b_2, b_3 are regression coefficients, which are defined in Tables 2-3. q_c,q_r,q_i,q_s,q_g are respectively mixing ratios of cloud water, raindrop, cloud ice, snow, and graupel. T is an air temperature. Since the relationship between clear-sky and cloudy-sky T_b in weak convection differs from that in strong convection, Eq. (2) is derived for IWP> 0.5 mm and for IWP<0.5 mm separately (see Table 3).

Table 2 Coefficients of Eq. (1) and linear correlation coefficient R

Ch	A	B_1	B_2	B_3	R
16	215.7	-0.004	0.52	-0.055	0.94
17	288.3	0.004	-0.15	0.052	0.82

Table 3a Coefficients of Eq. (2) and linear correlation coefficient R for IWP >0.5 mm

Ch	A	B_1	B_2	B_3	R
18	238.1	0.019	-0.029	-0.070	0.65
19	248.8	0.003	-0.086	-0.036	0.58
20	243.1	-0.001	-0.105	-0.016	0.73

Table3b Coefficients of Eq. (2) and linear correlation coefficient R for IWP <0.5 mm

Ch	A	B_1	B_2	B_3	R
18	78.1	0.757	-0.261	2.423	0.97
19	203.7	0.297	-0.436	0.420	0.89
20	246.9	0.059	-0.341	-1.445	0.85

Fig. 7 shows clear-sky Tb versus predicted clear-sky T_b using Eqs. (1) and (2). The RMS between true and predicted T_b are less than 0.75 K and the linear correlation coefficients are larger than 0.8, indicating the models predict clear-sky T_b well.

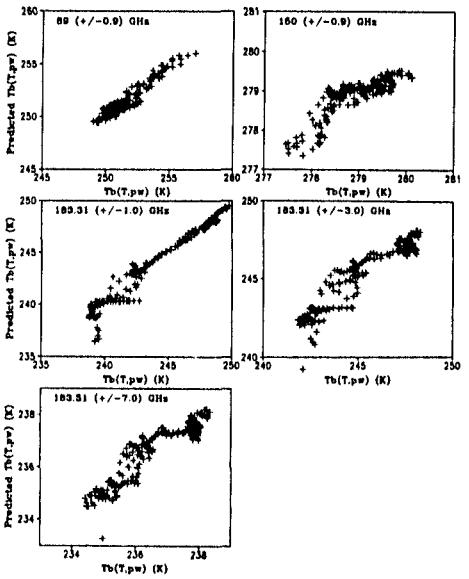

Fig. 7 C clear-sky Tb versus predicted clear-sky T_b using Eqs. (1) and (2) at AMSU-B Channels

5. Summary

A radiative transfer model including scattering and polarization is used to investigate the effects of cloud and precipitation microphysics on AMSU-B radiances. The thermodynamic profiles and profiles of cloud hydrometeors are obtained from a 2-D cloud resolving simulation over tropics during TOGA-COARE. The major results are summarized as follows.

1. Brightness temperature at channel 16 increases slowly (decreases quickly) with increasing total precipitable water in the simulation with clouds excluded (included). Brightness temperatures decrease much quickly with total precipitable water in the simulation with clouds than in the simulation without clouds. This indicates that the radiances in cloudy conditions need to be modified to eliminate cloud contamination in order to *physically* retrieve moisture.
2. The horizontal variations of AMSU-B radiances are mainly caused by the ice cloud hydrometeors.
3. Water clouds have more impacts on the radiances at channels 16 and 17 than on the radiances at channels 18-20. This suggests that the brightness temperatures at channels 18-20 are more adequate for retrieval of ice cloud properties.
4. Ice cloud hydrometeors have larger impacts on the radiances at upper levels than at lower levels. Thus, the radiances increase with decreasing height of top of ice clouds.
5. A linear regression model is developed to predict clear-sky brightness temperature to remove cloud contamination on the brightness.

Acknowledgments. Authors Dr. Q. Liu at CIRA, Colorado State University who helps us to run the radiative transfer model.

References

Li, X. C.-H. Sui, K.-M. Lau, and M.-D. Chou, 1999: Large-scale forcing and cloud-radiation interaction in the tropical deep convective regime. *J. Atmos. Sci.*, **56**, 3028-3042.

Li , X. C.-H. Sui, and K.-M. Lau, 2001: Cloud microphysics budget in the tropical deep convective regime. *J. Meteor. Soc. Japan*, Submitted.

Liu, Q., and F. Weng, 2001: Polarimetric two-stream radiative transfer model. *J. Atmos. Sci.*, Submitted.

P 4.11 COMBINING RADIO OCCULTATIONS AND IR / MW RADIANCES TO DERIVE TEMPERATURE AND MOISTURE PROFILES: A SIMULATION STUDY

Éva Borbás*[a], W. Paul Menzel**[b], and Jun Li*[a]
[a]Space Science and Engineering Center, University of Wisconsin / Madison,
[b]NESDIS/ Office of Research and Applications
1225 West Dayton St, Madison, Wisconsin

1. INTRODUCTION

Radiances from current polar orbiting infrared (IR) and microwave (MW) sounders are used to infer temperature and moisture profiles in the troposphere in a physical retrieval algorithm. Specifications of the tropopause and the surface are necessary boundary conditions in the profile retrieval. Good definition of the tropopause has been elusive via radiometric approaches. The Global Positioning System provides an opportunity to derive very accurate upper atmospheric temperature profiles (from 350 hPa up to 3 hPa) by using radio occultation (RO) techniques.

In this paper we show that the combination of radiometric (IR and MW) and geometric (RO) information yields improved tropospheric temperature and moisture profiles when compared to those inferred from either system alone. RO and IR/MW measurements are simulated from the NOAA/NESDIS NOAA88 global radiosonde data set. Retrievals are performed using a statistical regression approach. Simulation tests indicate that RO improves IR and MW retrievals of temperature and moisture in the upper troposphere and of temperature in the lower stratosphere. It remains to prove this with real data.

2. SIMULATION APPROACH

The NOAA88 radiosonde dataset was used to simulate IR and MW brightness temperatures, GPS refractivities, and GPS temperature profiles. The 7547 profiles are global in time and space and have been interpolated to 42 vertical levels. IR and MW data represent the Advance TIROS Operational Vertical Sounder (ATOVS) on polar orbiting NOAA satellites, which consists of three instruments: the High-resolution Infrared Radiation Sounder (HIRS), the Advanced Microwave Sounding Unit-A (AMSU-A), and the Advanced Microwave Sounding Unit-B (AMSU-B), which is a new five channel microwave humidity sounder.

A fast and accurate transmittance model called pressure-layer optical depth or pressure–layer fast algorithm for atmospheric transmittances (Hannon et al., 1996) was used to simulated ATOVS data. It has 42 pressure level vertical coordinates from 0.1 to 1050 hPa. Microwave surface emissivity is inferred from the AMSU-A 50.3 GHz window channel brightness temperature (Huang and Li, 1998). Random noise was added to simulate nominal instrument noise plus 0.2 K forward model noise.

Kursinski at al. (1997) estimated the different sources of error in the GPS refractivity profiles. These were used in our simulation studies. To simulate GPS profiles, 16 different pressure levels (from 42 levels) were chosen between 5 and 30 km. GPS temperature profiles were simulated from RAOB profiles simply by added randomly generated noises. To get refractivity (N) profiles, the following equation was used (Smith and Weintraub, 1953):

$$N = 77.6\frac{P}{T} + 3.73 * 10^5 \frac{P_w}{T^2}$$

where P is the atmospheric pressure (hPa), P_w is the water vapor partial pressure (hPa), T is the temperature (K) of the atmosphere. The noise of the refractivity profile was assumed to be 0.4 % in every level.

Surface temperature and humidity observations were defined as the lowest level values of the RAOB profiles. Random noise was placed at 0.5 K for the surface temperature and 10 % for the surface humidity (mixing ratio).

The temperature (K) and humidity (mixing ratio g/kg) profiles were related to simulated brightness temperatures and simulated GPS data using a statistical regression. Both linear and quadratic terms for brightness temperatures (HIRS, AMSU), refractivities (GPS), and surface observations (SFC) were included in the regression relationship. Regression coefficients were derived from 90 % of all profiles and tested in the remaining 10 %. Statistics of bias and rms differences were calculated for 1 km layers of temperature profiles and 2 km layers of humidity profiles up to 300 hPa. For humidity, rms and bias were normalized by the true value of the mixing ratio.

3. RESULTS

The impact of HIRS, AMSU, GPS, and SFC data on the temperature and humidity retrievals was studied. Six combinations were calculated:

(a) HIRS + SFC temp and humidity,
(b) HIRS + SFC and GPS refractivity profiles,
(c) HIRS + GPS,
(d) HIRS +AMSU (ATOVS) + SFC,
(e) ATOVS + GPS + SFC, and
(f) ATOVS + GPS

The rms errors of the retrievals obtained from these different combinations of information were compared to the original NOAA88 data. Figure 1 shows the differences of the rms errors for the temperature retrievals using the different combinations.

* *Corresponding author address*: Eva Borbas, SSEC, Univ. of Wisconsin/Madison, 1225 W. Dayton St., Madison, WI, 53706; email: Eva.Borbas@ssec.wisc.edu.

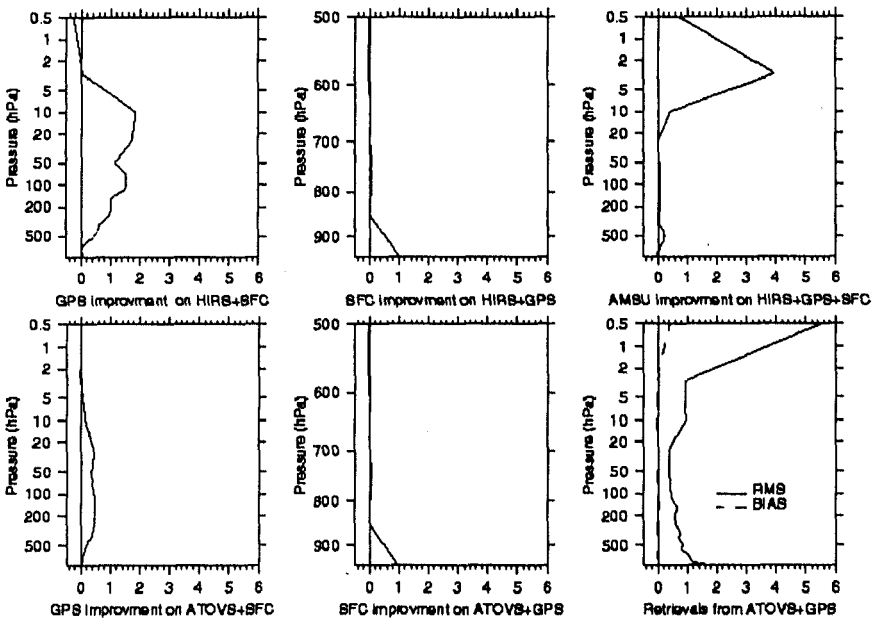

Figure 1: Temperature profile retrieval RMS differences using different data. Retrievals without AMSU (upper panels) and with (lower panels) are shown. The first column shows the improvement from addition of GPS information, second shows the effect of surface information on retrievals. The upper right panel shows the impact of AMSU (on HIRS and GPS). The lower right panel shows the bias and rms errors of the "best " case using ATOVS (AMSU+HIRS) and GPS.

GPS improves HIRS (as well as GOES sounder) temperature profile retrievals at the tropopause by 1.5 K, dropping off to 0.25 K at 570 hPa. In the stratosphere, this increases to about 2 K. This is consistent with the results of Wu et al (1998). GPS improves ATOVS (AMSU plus HIRS) temperature profile retrievals between the tropopause level and the stratosphere at 15 hPa by about 0.5 K. GPS improves HIRS moisture profile retrievals at 400 hPa by 3 % increasing to about 5 % at 700 hPa; ATOVS moisture profile retrievals are improved from 570 to 700 by about 4 % (not shown).

The sensitivity of the retrievals to GPS temperature versus refractivity as well as GPS noise were investigated. The rms and bias errors of retrievals using nominal, double, and triple GPS noise information were computed. The rms and bias differences incurred by using GPS temperature and GPS refractivity profiles in the regression computations reveal that even with triple noise both GPS temperature and refractivity profiles provide additional information and improve the temperature retrievals. However, humidity retrievals perform better using GPS refractivity profiles instead of temperature profiles.

The impact of using quadratic terms in the regression retrievals was studied as well. The regression relationship between temperature and moisture profile retrievals and IR/MW brightness temperatures and GPS refractivity profiles improves substantially when linear and quadratic terms are used.

4. SUMMARY AND FUTURE PLANS

In this study of simulated retrievals performed using a statistical regression approach, the combination of radiometric (IR and MW) and geometric (RO) information yields improved tropospheric temperature and moisture profiles when compared to those inferred from either system alone.

These simulation studies must now be repeated with real GPS and ATOVS data; furthermore, the independence of the validating data set must be ensured.

ACKNOWLEDGMENTS: This work was supported in part by NOAA cooperative agreement NAO7EC0676.

REFERENCES

Hannon, S., L.L. Strow, and W.W. McMillan, 1996: Atmospheric infrared fast transmittance models: A comparison of two approaches. *Proc. SPIE*, **2830**, pp. 94-105.

Huang, H.L. and J. Li, 1998: Determination of microwave emissivity from Advanced Microwave Sounder Unit measurements. *Proc. SPIE,* **3503**, pp. 233– 237.

Kursinski, E.R., G.A. Hajj, J. T. Schofield, R.P. Linfields, and K.R. Hardy, 1997: Observing Earth's atmosphere with radio occultation measurement using the Global Positioning System. *J. Geophys. Re.*, **102**, pp. 23,429-23,465

Smith, E.K., and S. Weintraub, 1952: The constants in the equation for atmospheric refractive index at radio frequencies. *J. Res. Natl. Bur. Stand.*, **50**, pp. 39-41.

Wu, X. and W.P. Menzel, W.L. Smith, 1998: Application of GPS occultations for deriving meteorological parameters. *Tenth Symp. on Meteor. Observing Instruments* held 11 – 16 Jan 1998 in Phoenix, AZ, AMS Publication, pp. J82-J85.

A SIMPLE DIAGNOSIS METHOD OF MOISTURE PROFILE FROM TMI/TPW

Tetsuo Nakazawa
Meteorological Research Institute, Japan Meteorological Agency

1. Introduction

Estimation of total precipitable water(TPW) over the globe by remote-sensing technique becomes very popular and practical. But to estimate the vertical profile of water vapor is still difficult. We will present a new relationship to estimate the vertical profile of water vapor, based on the statistical formula by Liu et. al (1991). The TPW data of the TRMM/TMI are used in this study, provided by Dr. Shibata at NASDA/EORC.

2. Relationship between surface humidity and lower TPW

Liu et. al (1991) documented that the lower TPW below 850 hPa (w*) is linearly correlated with the surface specific humidity qs. From his Fig. 10,

$$w_* = \frac{1}{g}\int_{p_*}^{p_s} q\,dp = 1.2931\times10^{-3} q_s, \qquad (1)$$

Assuming the following based on Smith(1966) below 850 hPa,

$$q = q_s\left(\frac{p}{p_s}\right)^{\lambda_s}, \qquad (2)$$

Here λ_s is the vertical profile parameter for specific humidity below 850 hPa.

From (1) and (2) we obtain that w_* is,

$$\frac{q_s}{g(\lambda_s+1)}\left\{p_s - p_*\left(\frac{p_*}{p_s}\right)^{\lambda_s}\right\} \qquad (3)$$

Substituting p_s =1013 hPa, p*=850 hPa and g=9.8 in (1) and (2), we calculate λ_s iteratively as

$$\lambda_s = 3.099 \qquad (4)$$

That is, from (2), below 850 hPa the specific humidity is proportional to the third power of the pressure.

Substituting (4) into (2), we also obtain

$$q_* = 0.5805 q_s, \qquad (5)$$

This indicates that the specific humidity at 850 hPa is about 60% of the surface specific humidity.

3. Estimation of vertical profile of specific humidity

By using Liu(1986)'s regressive formula to estimate the surface specific humidity from the TPW, we first estimate the surface specific humidity from the TRMM/TMI TPW.

We also assume (2) is applicable for the upper layer above 850 hPa.

$$q = q_*\left(\frac{p}{p_*}\right)^{\lambda_*}, \qquad (6)$$

Then the TPW, W, is written in the following.

$$W = \frac{p_*}{g}\left(\frac{q_*}{\lambda_*+1}\right) + w_*, \qquad (7)$$

In (7), as the unknown parameter is λ* only, we can easily get λ*, where λ* is the vertical profile parameter of specific humidity in the upper troposphere. There two parameters, λ_s and λ* will give us the simple estimation/ diagnosis method of vertical humidity profile.

Figure 1 is the monthly mean vertical moisture moisture profile parameter, λs (upper) and λ*(lower) obtained from TRMM/TMI in July, 1998.

Corresponding Author Address: Tetsuo Nakazawa
Meteorological Research Institute, 1-1 Nagamine, Tsukuba, Ibaraki 305-0052, Japan
E-mail: nakazawa@mri-jma.go.jp

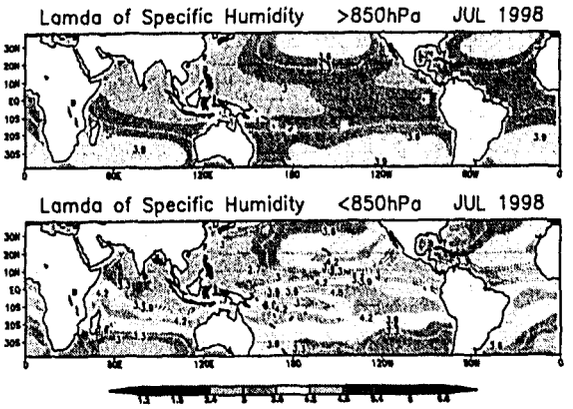

Fig. 1 Vertical Profile Parameter of specific humidity, λs (upper) and λ*(lower) from TRMM/TMI in July, 1998.

This figure shows that in the lower troposphere λs indicates homogeneous value between 3.0 and 3.9 with a slightly small number along the ITCZ and Asian Monsoon area. However, above 850 hPa the regions with larger and smaller λ* are separated. Here small λ corresponds small gradient of humidity decrease in height. In the lower figure we notice that the region with small λ* is associated with the ITCZ and the active Asian Monsoon region. The region with larger λ* may be associated with the area with cool SST over the tropics and sub tropical area.

4. Vertical Profile Parameter in Objective Analysis Data

We may estimate the vertical profile parameter in the same manner for the objective analysis data from JMA and NCEP.

Fig. 2 shows the result of JMA(a) and NCEP(b). First JMA. Comparing with Fig. 1 in the lower troposphere the value of λs is around 2, suggesting that more gradual decrease of moisture in the tropics. Also we find that large λs areas are detected off California and off North Africa. In most area λs and λ* are negatively correlated. When λ* is large, then λs is small at the same location.

NCEP in Fig. 2b has a different feature. There are large λs and small λ* regions.

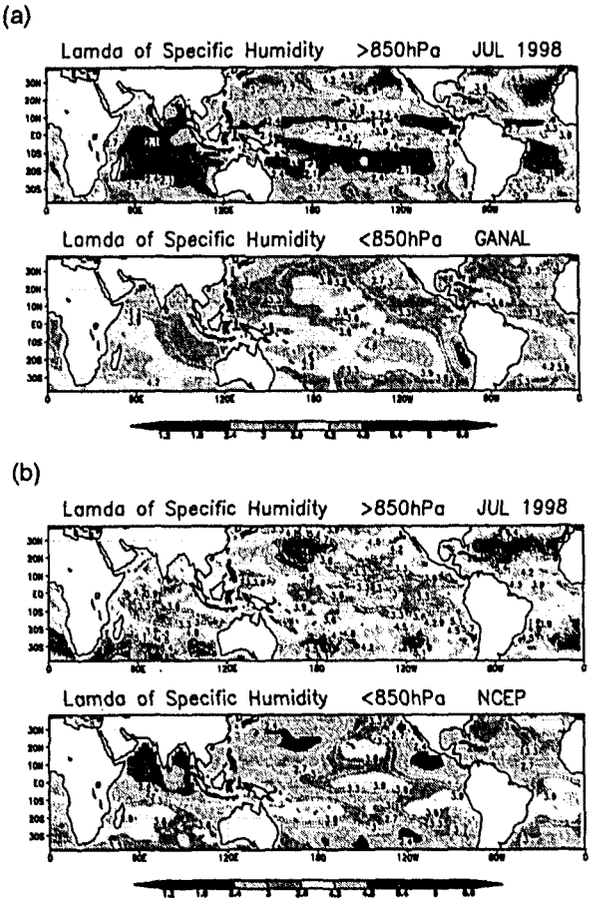

Fig. 2 Same as Fig.1, except for the objective analysis data of JMA(a) and NCEP(b).

5. Conclusion

We propose a simple diagnosis method to estimate the vertical mosture profile from the TRMM/TMI TPW data.

We found that vertical moisture profile parameter λ is small over the moisture abundant area, however, the value of λ is scattered in satellite data and objective analysis data.

References

Smith, W. L., 1966: Note on the relationship between total precipitable water and surface dew point. J. Appl. Meteor., 5, 726-727.

Liu, w. T., 1986: Statistical relation between monthly precipitable water and surface-level humidity over global ocean. Mon. Wea. Rev., 114, 1591-1602.

Liu, W. T., Tang, W and Niiler P. P., 1991: Humidity profiles over the ocean. J. of Climate, 4, 1023-1034.

P4.13

USE OF PASIVE MICROWAVE OBSERVATIONS IN A RADAR RAINFALL PROFILING ALGORITHM

Mircea Grecu and Emmanouil N. Anagnostou
University of Connecticut, Storrs, Connecticut

1. INTRODUCTION

One difficulty in estimating precipitation from active space borne instruments (space-borne radars) consists of the fact that frequencies greater than 10 GHz are usually used to limit the antenna size. At these frequencies, the active observations (radar reflectivity factors) are attenuated by rain and specific algorithms that explicitly correct for attenuation need to be employed for rain estimation (Iguchi and Meneghini, 1994). The estimation algorithms for such systems are generally based on the solution of a differential equation (Hitschfeld and Bordan, 1954) derived from the radar equation. It has been shown that two particular solutions may be obtained as a function of way the boundary conditions are set (Iguchi and Meneghini, 1994). A modality to set the boundary conditions is by assuming that the observed reflectivity factor at range zero is not affected by attenuation. Another one is by imposing that the particular solution derived from the general solution of the radar differential equation exhibits the same path integrated attenuation (PIA) as determined from different considerations. Such considerations may be surface return techniques (Iguchi and Meneghini, 1994), mirror image techniques (Meneghini and Atlas, 1989), or radiometer observations (Weinman et al., 1990; Smith et al., 1997). The particular solutions associated with each technique are not necessarily identical. However, if the PIA associated with a general solution is invariant to the way the boundary conditions are set, the particular solutions coincide (Iguchi and Meneghini, 1994). Consequently, two adjustments were proposed (in the attenuation-reflectivity relationships and in the radar constant) to make the particular solutions identical (Iguchi and Meneghini, 1994). The correction in the attenuation-reflectivity relationships, known as the α adjustment technique, is physically better sound in case of a well-calibrated radar because large variations in drop size distributions may cause significant changes in the attenuation-reflectivity relationships.

In this work, we formulate and investigate a combined algorithm for precipitation profile retrievals considering jointly passive and active observations. The formulation addresses some of the wants of previous approaches. It is based on a general solution of the radar differential equation that uses attenuation-reflectivity relationships parameterized as a function of an intercept coefficient N_0^*, in a normalized gamma drop-size distribution model (Testud et al., 2000). The reflectivity-rainfall rate (Z-R) relationships are also parameterized as a function of N_0^*. Using actual airborne radar observations, N_0^*-dependent precipitation profiles are used to simulate four different brightness temperatures (10.7, 19.35, 37.1, and 85.5 GHz) measured by the airborne radiometers. For each profile, the intercept N_0^* is estimated along with the cloud water content and few other variables such that the differences between simulated and the actually observed brightness temperatures are minimized. A bright-band model is included in both the radar and radiometer predictions to account for stratiform precipitation.

*Corresponding author: Dr. Mircea Grecu, University of Connecticut,261 Glenbrook Road, U-37, Storrs, CT 06269. E-mail: mgrecu@engr.uconn.edu

2. COMBINED RAIN PROFILING ALGORITHM

The profiling algorithm is based on the estimation of a set of variables consisting of the parameter δN_0^* that measures the departure of the intercept of the drop size distributions from the nominal values, the cloud water content, the ratio of snow content to graupel content, and two parameters describing the melting process in convective cores. We denote $\mathbf{X}_r$ their union state variable vector. The observations include a vector ($\mathbf{T}_B$) of radiometer brightness temperatures at the four frequencies, and vector ($\mathbf{Z}$) of attenuated observed reflectivities. The hydrometeor contents are determined uniquely from $\mathbf{Z}$ as a function of $\mathbf{X}_r$. Then the retrieved hydrometeor contents and $\mathbf{X}_r$ are used to predict the brightness temperatures by a non-polarized plane-parallel model based on the Eddigton approximation. An iterative procedure is devised to minimize the differences between the observed and predicted brightness temperatures. That is, an objective function of the type

$$F = \frac{1}{2}(T_B^M - T_B(Z^M, X_r))^T W_T^{-1}(T_B^M - T_B(Z^M, X_r)) + \frac{1}{2}(M_{x_r} - X_r)^T W_{X_r}^{-1}(M_{x_r} - X_r) \quad (2.1)$$

is minimized as a function of $\mathbf{X}_r$. Note that a term is introduced in Equation (2.1) to account for "a priori" knowledge on variable $\mathbf{X}_r$. $\mathbf{W}_{Xr}$ and $\mathbf{M}_{Xr}$ are estimated based on cloud model databases.

To minimize the objective function in (2.1), we use a gradient-based optimization technique that evaluates the function's gradient.

3. RESULTS AND CONCLUSIONS

The methodology was tested using data originating in the Kwajalein Experiment (KWAJEX). Specifically, we used data from the airborne radar (ARMAR) and one of the radiometers (AMPR) to investigate the rain profile retrieval algorithm described above. ARMAR, developed by NASA and JPL, provides data similar to those collected by the TRMM precipitation radar (PR). It operates at a frequency of 13.8GHz, which is the TRMM PR's frequency, and consists of downward pointing and scanning in the cross-track direction. The AMPR radiometer, developed by NASA and the Georgia Institute of Technology, collects data at four frequencies, i.e. 10.7, 19.35, 37.1, and 85.5GHz and resembles the TRMM Microwave Imager.

Figure 1 shows the PIAs estimated from a surface return technique and resulted from the application of the combined algorithm respectively. One may notice a fairly good agreement between the two estimates. Since the combined algorithm differs from a radar alone rain profiling algorithm just in the way the PIA and consequently the drop size distribution are estimated, it may be concluded the combined algorithm yields results consistent with radar only results but can mitigate situations when the PIA estimates from the surface return technique are not reliable. However, additional investigations including comparisons with independent estimates, such as ground radar estimates, need to be considered for a better characterization of the combined algorithm. The combined algorithm may be applicable to TRMM precipitation profile retrieval, provided that issues such as the reduction of radar and radiometer observations to a common grid and the extension of the algorithm to deal with different pointing vectors of the instruments are addressed.

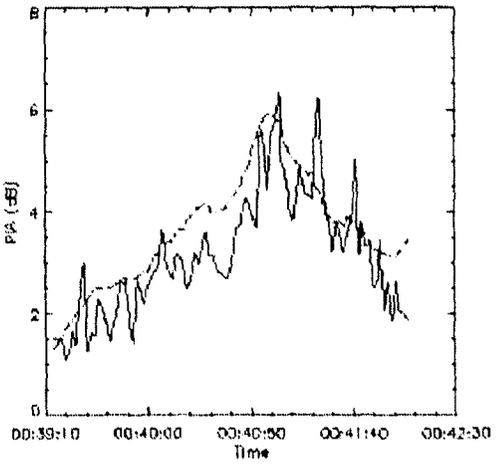

Figure 1. Surface return and combined algorithm retrieved PIA for the August 12, 1999 flight leg. The discontinuous line indicates the combined algorithm.

REFERENCES

Hitschfeld, W., and J. Bordan, 1954: Errors inherent in the radar measurement at attenuating wavelengths. *J. Appl. Meteor.*, **11**, 58-67.

Iguchi, T., and R. Meneghini, 1994: Intercomparison of single-frequency methods for retrieving a vertical rain profile from airborne or spaceborne radar. *J Atmos. Oceanic Technol.*, **11**, 1507-1516.

Meneghini, R., and D. Atlas, 1989: Simultaneous ocean cross section and rainfall measurements *Oceanic Technol.*, **3**, 400-413.

Smith, E. A., F. J. Turk, M. R. Farrar, A. Mugnai, X. W. Xiang, 1997: Estimating 13.8-GHz path-integrated attenuation from 10.7-GHz brightness temperatures for the TRMM combined PR-TMI precipitation algorithm. *J. Appl. Meteor.*, **36** (4): 365-388.

Weinman, J. A., R. Meneghini, and K. Nakamura, 1990: Retrieval of precipitation profiles from airborne radar and passive radiometer measurements: Comparison with dual-frequency radar measurements. *J. Appl. Meteor.*, **29**, 981-993.

Testud, J., S. Oury, and P. Amayenc, 2000: The concept of "normalized" distribution to describe raindrop spectra: A tool for hydrometeor remote sensing. *Physics and Chemistry of the Earth. Part B-Hydrology Oceans and Atmosphere*, **25**, 897-902.

P4.14

STRUCTURE AND CHARACTERISTICS OF PRECIPITATION SYSTEMS OBSERVED BY TRMM

Steven J. Goodman and Daniel J. Cecil[1]

NASA/MSFC and the National Space Science and Technology Center
Huntsville, Alabama
[1]University of Alabama in Huntsville

1. INTRODUCTION

Multi-sensor measurements from the suite of instruments on the Tropical Rainfall Measuring Mission (TRMM) satellite are providing useful information to investigate convective structures within varied convective regimes. Recent studies by Boccippio et al. (2000) and Nesbitt et al. (2000) have shown high correlations between lightning flash rates and microwave brightness temperatures, supporting the linkage between deep convection, convective mass (precipitation ice) flux, and lightning activity. Goodman et al. (2000) examined six supercells observed during a TRMM overpass in the later stages of the 3 May central Oklahoma tornado outbreak. They found the storms, each having reflectivity cores of 40 dBZ extending to a height in excess of 10 km, were dominated by in-cloud (IC) lightning, with periods of little or no cloud-to-ground (CG) lightning activity.

The goal of the present study is to begin a more comprehensive examination of the spectrum of storm types and their attributes worldwide, and as a function of season, location, and convective regime using the observed lightning, microwave scattering, and reflectivity signatures. A global, multi-year data set (1998-2000) is being assembled to further our understanding of convective processes in different climatological regimes. This paper reports on the initial examination of this data set.

Corresponding author address: Steven Goodman, NASA/MSFC Code: SD60, 320 Sparkman Dr., Huntsville, AL 35805

2. METHODOLOGY

TRMM provides total lightning (in-cloud plus cloud-to-ground) from the Lightning Imaging Sensor (LIS), passive microwave ice scattering from the TRMM Microwave Imager (TMI), and radar reflectivity profile information from the 14 GHz Precipitation Radar (PR). These sensor data are being cataloged for precipitation features observed by TRMM since its launch in November 1997 (Nesbitt et al., 2000). The precipitation features are defined by their surface rainfall or ice scattering signatures, with horizontal scales ~100-10,000 km^2. Additionally, convective scale (~100 km^2) storms are defined by the lightning data. Over the U.S. the national cloud-to-ground lightning observations (NLDN, Cummins et al., 1998) are used to also determine the ratio of in-cloud to cloud-to-ground lightning, where it is hypothesized these ratios are related to the vertical profile of reflectivity and concentration of precipitation-sized ice.

3. RESULTS

Figure 1 shows the global distribution of high flash rate storms January 1998-August 1999. The southeast U.S. has by far the greatest concentration of the highest flash rate storms (>30 flashes per min). Other extra-tropical (20-30 deg N and S) regions with these most intense storms are southeast South America, near the coast of South Africa, the Himalayas, and

southeast Australia. Some of the intense storms occur unexpectedly over the open ocean, and these will be the subjects of more detailed future study.

Figure 2 shows the minimum 37-GHz polarization-corrected temperature (PCT), an indicator of strong scattering from precipitation-sized ice. We note the greatest similarities between the ice scattering and highest flash rates occur in the extra-tropics. However, we note there are significant ice scattering signatures in northwestern Australia (Darwin area), central Africa, and Colombia not associated with the highest flash rates.

Table 1 is the result of a more detailed examination of the Nesbitt et al. (2000) TRMM (PR, TMI) database, U. S. only for all of 1999, and the associated LIS and NLDN flash rates. The table orders the storms by total flash rate. The top ten flash rates are from those storms observed in the TRMM orbits which produced the lowest 85 GHz or 37 GHz PCT in the 1999 sample of U.S. precipitation features.

This initial analysis shows the most electrically active 3 May Oklahoma tornado outbreak supercell (Stroud storm) examined by Goodman et al., 2000 is not even in the top ten of the highest flash rate storms of 1999, nor does the 3 May storm possess the lowest 85/37 GHz PCTs for the same year. Interestingly, all of the top-ranked intense electrical storms occur in the spring. The top ten flash rates in the table are from those storms observed in the orbits that produced the lowest TMI brightness temperatures, and thus may not necessarily represent the highest flash rate storms in the U.S during the year. One of the difficulties in examining these data in their present form is their classification as precipitation features, not as individual storms. Some of these extreme storms, such as the top-ranked N. Texas squall line of 17 May, are not isolated supercells, but may be multi-cellular complexes or even larger mesoscale convective systems.

The second ranked south Texas supercell does indeed seem to be a giant electrical storm, having an IC flash rate of 303 min^{-1} and IC:CG ratio of 61:1 during the overpass. Figure 3 shows a PR vertical cross-section of this storm, which produced 2.75" hail and straight-line wind damage. The storm has a tilted 40 dBZ PR reflectivity core extending to nearly 15 km altitude, and 50 dBZ echo extending above 11 km. At an earlier time, the NEXRAD-estimated storm top reached 19 km.

4. SUMMARY AND CONCLUSIONS

This study presents an initial examination of the global and regional characteristics of storms under a variety of convective regimes. The giant electrical storms sampled by TRMM are most common in the extra-tropics, specifically in the southeastern U.S. during the spring season. This study also provides a larger context for the 3 May 1999 TRMM observations of tornadic supercells, heretofore having produced the highest documented flash rates during TRMM's 3-yr of on-orbit operations.

The TRMM precipitation feature database developed by Nesbitt et al. (2000) has been expanded (S. Nesbitt, 2001, personal communication); from this database, those orbits containing the lowest 85 GHz and/or 37 GHz polarization corrected brightness temperatures were identified. Lightning clusters in the United States (where NLDN data is available) were identified using LIS data for 16 such orbits from 1999. The 3 May 1999 multi-cellular Stroud storm ranks 11th by total flash rate in this sample. Storms with the greater flash rates tend to also have lower brightness temperatures at both 85 GHz and 37 GHz. The ratios of IC to CG lightning in the 3 May storm is indeed unusually large, but not unique among storms with extreme flash rates. Some other storms with higher brightness temperatures and lower flash rates than those listed in Table 1 are also noted to have large ratios of intracloud to cloud-to-ground lightning.

5. REFERENCES

Boccippio, D. J., S. J. Goodman, and S. J. Heckman, Regional differences in tropical lightning distributions, J. Appl. Meteor., 39, 2223-2230, 2000.

Cummins, K. L., M. J. Murphy, E. A. Bardo, W. L. Hiscox, R. B. Pyle, A. E. Pifer, 1998: A combined TOA/MDF technology upgrade of the U.S. National Lightning Detection Network. J. Geophys. Res., 103, 9035-9044.

Goodman, S. J., D. Buechler, K. Driscoll, D. Burgess, and M. Magsig, Tornadic supercells on May 3 1999 viewed from space during an overpass of the NASA TRMM observatory, Preprints, 20th Conf. On Severe Local Storms, 11-15 September 2000, Orlando, FL, Am. Meteor. Soc., Boston, 638-641, 2000.

Nesbitt, S. W., E. J. Zipser, and D. J. Cecil, A census of precipitation features in the tropics using TRMM: Radar, ice scattering and lightning observations, J. Clim. 13, 4087-4106, 2000.

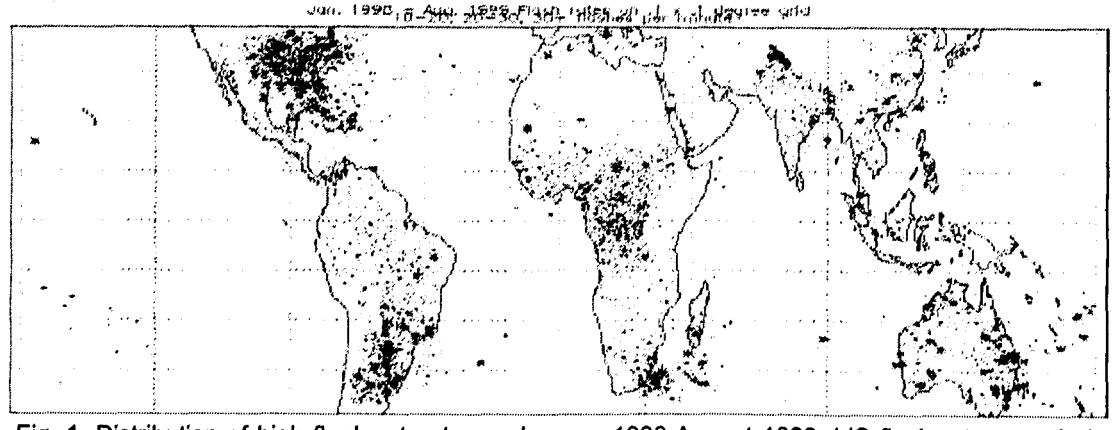

Fig. 1. Distribution of high flash rate storms January 1998-August 1999. LIS flash rate per min in 0.1 x 0.1 deg grid. Flash Scale: dot, 10-20/min; small star, 20-30/min; large star, >30/min.

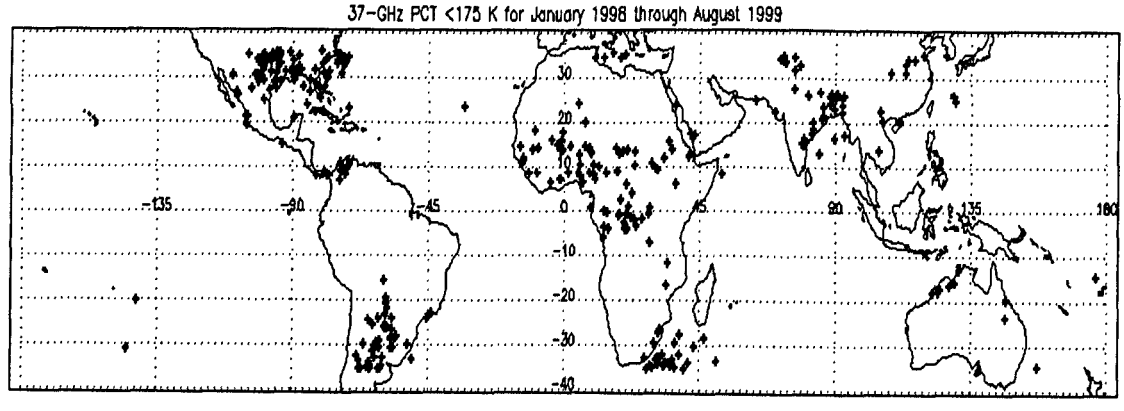

Fig. 2. Distribution of minimum TMI 37 GHz PCT<175K storms January 1998-August 1999.

Description	Time Date	Orbit	Min 85	Min 37	IC min^{-1}	CG min^{-1}	IC:CG
Part of N. TX squall line	2226 17 May	8453	60	95	524	85.5	6
S. TX isolated cell	0338 11 May	8346	55	119	303	5.0	61
Part of N. TX squall line	2049 17 May	8452	60	130	204	7.0	29
Part of N. TX squall line	2226 17 May	8453	57	135	173	18.5	9
SW OK multicell	0236 25 June	9055	64	142	165	17.0	10
Big Bend (Mex) multicell	0651 25 April	8096	64	125	156	21.0	7
Arkansas multicell	2226 17 May	8453	52	130	152	20.0	8
Part of N. TX squall line	2049 17 May	8452	65	135	161	8.0	20
NW Gulf squall line	0338 11 May	8346	60	137	125	31.0	4
SE TX multicell	2214 3 April	7759	63	140	145	9.5	15
Central OK Outbreak(Stroud)	**0403 4 May**	**8236**	**66**	**136**	**149**	**5.0**	**30**

Table 1. Flash rates and minimum polarization corrected brightness temperatures for extreme ice scattering events in the United States during 1999. Storms are sorted in descending order by total flash rate.

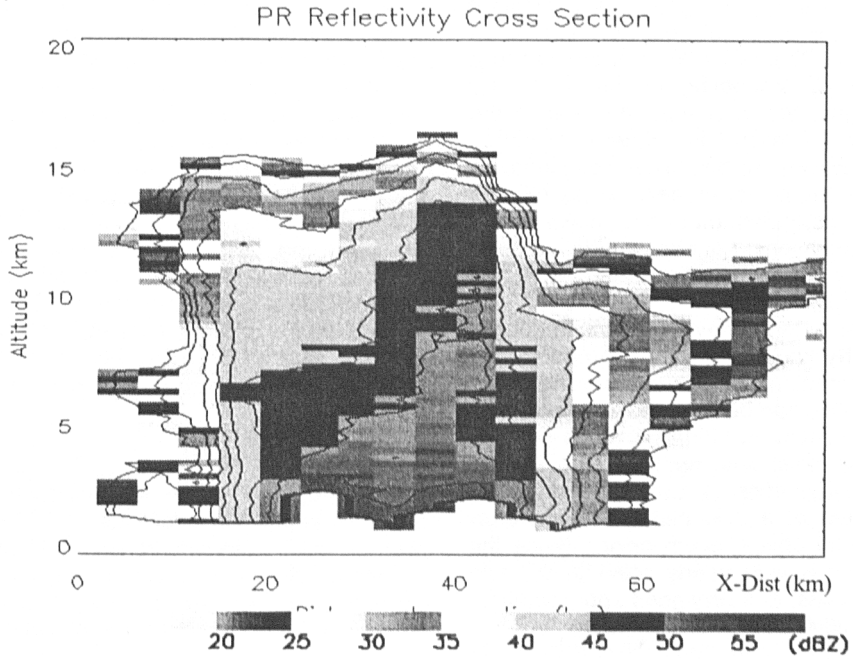

Fig. 3. PR cross-section through the south Texas supercell, TRMM orbit 8346, at 0338 UTC on 11 May 1999. Reflectivity contour interval every 5 dBZ.

P4.15 AN IMPROVED LEVEL-3 OCEANIC RAINFALL ALGORITHM FOR THE TRMM MICROWAVE IMAGER (TMI) AND THE ADVANCED MICROWAVE SCANNING RADIOMETER (AMSR)

T. T. Wilheit *, J. Huang, K.-W. Jin, D. H. Lee, J. L. Thomas-Stahle and R. Weitz
Texas A&M University, College Station, Texas

The present version of the Level-3 algorithm for oceanic rainfall retrieves monthly rainfall totals for 5° x 5° boxes. It is based on histograms of a linear combination of 19.35 (or 18) and 21 (22 or 23) GHz brightness temperatures. A histogram of brightness temperatures is computed from an assumed log-normal distribution of rain rates and a radiative transfer model. The parameters of the log-normal distribution are adjusted to achieve satisfactory agreement between the computed and observed histograms.

While there are many obvious shortcomings to this algorithm, it has performed extremely well both for TRMM and (when applied to the SSM/I) for the Global Precipitation Climatology Project.

In order to eliminate some of these shortcomings, in particular to enable the use of more of the available frequencies, a new algorithm has been developed. The success of the previous algorithm has established a high standard for determining that the new algorithm is, in fact, an improvement.

In this algorithm the rain-rates are computed using 10.7, 19.35 and 37 GHz. Each of the retrievals has a valid range of rain rates. Each also has a different spatial resolution because of the properties of microwave antennas. The rain rates are brought to a common resolution by smoothing to the 10.7 GHz resolution. The higher the frequency, the greater the sensitivity to rain relative to other interfering phenomena. However, at brightness temperatures above about 250 K, the retrievals become doubtful as they become overly dependent on poorly known details of the modeling assumptions. For each smoothed pixel, the highest frequency not contaminated with the doubtful retrievals is used.

Histograms of all of the retrievals at each frequency are accumulated. By knowing the most probable rain rate (0 mm/hr) any small offset due to modeling errors or instrument calibration can be detected and corrected. Offsets can occur because of modeling errors such as the non-precipitating cloud assumption or the surface emissivity or an instrumental calibration error. The modeling errors listed or a cold end calibration error would result in a total optical depth error. Since the absorption coefficient is very nearly linear in the rain rate at these frequencies, to a very good approximation, this results in an additive error in the rain rate.

It has been found that having the full range of frequencies has eliminated the need for the log-normal assumption. The monthly total rainfall is simply summed from the individual observations.

Comparisons of retrievals from this algorithm with rain gauges on small atolls are quite reasonable. Some small apparent artifacts in the retrievals from the present version are eliminated in this version.

* Corresponding author address: T. T. Wilheit, Department of Atmospheric Sciences, Texas A&M University, College Station, TX 77843-3150

P4.16 WHAT ARE THE BENEFITS OF COMBINING VISIBLE, INFRARED AND MICROWAVE SATELLITE DATA IN RETRIEVING CLOUD PHYSICAL PROPERTIES?

Thomas J. Greenwald* and Thomas H. Vonder Haar
Colorado State University, Fort Collins, Colorado

1. INTRODUCTION

Observing the physical properties of clouds from satellites remains an important component of integrated climate studies (Asrar et al. 2001). While data from both visible/infrared and microwave sensors contain cloud information, little attention has been paid to the value of combining these data to form a unified, synergistic retrieval approach. Lin et al. (1998), for example, combined visible/infrared and microwave data to examine cloud properties but performed retrievals separately in the respective wavelength regions.

With respect to retrievals of liquid water cloud properties, data from these different sensors are highly complimentary. Visible/infrared retrievals require assumptions about the droplet size distribution, whereas microwave retrievals are free of such assumptions because cloud absorption is independent of size distribution. Furthermore, microwave sensors can provide information on the atmospheric moisture content within clouds. The usually coarse resolution of satellite microwave data has prevented a synergistic approach to be put into practice. However, the improved spatial resolution of upcoming microwave sensors now makes this approach feasible.

The basic question we wish to address is whether microwave measurements can provide additional, beneficial information to retrievals of cloud optical depth and particle effective radius that have used exclusively visible/infrared measurements. This work is part of an effort to combine Global Imager (GLI) and Advanced Microwave Scanning Radiometer (AMSR) measurements from the soon to be launched Advanced Observing Satellite (ADEOS)-II to simultaneously estimate cloud, atmospheric and surface properties. Retrievals are limited here to clouds composed only of water droplets. As an early test of the retrievals, coincident MODerate-resolution Imaging Spectroradiometer (MODIS) and TRMM Microwave Imager (TMI) data are used as replacements for the GLI and AMSR.

2. DATA

MODIS is a multi-channel visible/IR imager that currently flies on NASA's Terra satellite (King et al. 1992). Both MODIS and GLI have 36 channels. Table 1 shows the MODIS channels of interest to this study in comparison to equivalent channels on the GLI. We used the MODIS 1 km product for all channels.

* *Corresponding author address:* Dr. Tom Greenwald, CIRA, Colorado State Univ., Fort Collins, CO 80523-1375; e-mail: greenwald@cira.colostate.edu.

TMI is 9-channel conical scanning microwave imager on the TRMM platform (Kummerow et al. 1998). The channels of interest here include the 10.65 GHz at vertical polarization (63 km resolution), 21.8 GHz at vertical polarization (23 km resolution), and 85.5 GHz at vertical polarization (5 x 7 km resolution). The 85.5 GHz channel was selected over the 37 GHz channels, which are also sensitive to liquid water, because they have higher spatial resolution and, in this case, greater sensitivity to liquid water. Table 2 shows selected TMI channels in comparison to equivalent channels on the AMSR.

TABLE 1. Comparison of spectral characteristics (in microns) between MODIS and GLI for selected channels.

MODIS		GLI	
Channel	Bandwidth	Channel	Bandwidth
1	0.62-0.67	22	0.60-0.72
20	3.66-3.84	30	3.55-3.88
31	10.78-11.28	35	10.3-11.3

TABLE 2. Comparison of spectral characteristics (in GHz) between TMI and AMSR for selected channels at vertical polarization.

TMI		AMSR	
Channel	Center Freq.	Channel	Center Freq.
1	10.65	3	10.65
5	21.8	7	23.8
8	85.5	11	89

3. METHODS

The retrieval approach is based on the concept of a cost function (Rodgers 1976) defined as

$$\Phi = (x-x_a)^T S_a^{-1}(x-x_a) + (y-f(x))^T S_y^{-1}(y-f(x))$$

where x is a vector of atmospheric, cloud, or surface parameters to be retrieved, x_a is a vector of a priori in-

formation for x, the matrix S_a corresponds to the errors associated with x_a, y is the vector of MODIS and TMI measurements, $f(x)$ is the vector of modeled measurements (i.e., forward radiative transfer calculations), and S_y is a matrix containing the combined error estimates of the measurements and forward model. The goal is to minimize Φ.

The strength of this method lies in providing the most probable estimate for x and is thus in a class of so-called "optimal" methods. It has the advantage of describing the retrieval errors in terms of the a priori data and the measurement and forward model errors, and it allows one to quantify the impact of different measurements on the retrievals, which is our goal here. In addition, this approach makes it much easier to include additional measurements at different wavelengths by simply lengthening the necessary vectors.

Ultimately, the retrieval vector x will include 9 parameters: cloud optical depth, cloud top temperature/height, droplet effective radius, cloud liquid water path, total precipitable water, sea surface skin temperature, and surface emissivity at all three microwave channels. We plan to incorporate 6 measurements (see Tables 1 and 2) into the observational vector y. However, early experiments will most likely start with fewer measurements and retrieved parameters and then work up to the full number of retrieved parameters.

The radiative transfer solver used in forward calculations of visible/IR radiances is the Spherical Harmonics Discrete Ordinate Method (SHDOM; Evans 1998). Cloud extinction and single-scatter albedo were estimated using the Modified Anomalous Diffraction Theory of Mitchell (2000). Simple assumptions were made regarding the scattering phase function. Initial plans are to assume a Henyey-Greenstein phase function, which is solely dependent on the asymmetry factor. The asymmetry factor is estimated from the parameterizations developed by Greenwald et al. (2001). Gas extinction is accounted for by the Optical Path TRANsmittance (OPTRAN) approach of McMillin et al. (1995).

For computing forward microwave radiances we used a model applied in our previous work (e.g., Greenwald et al. 1997) that solves the transmittance form of the radiative transfer equation for an absorbing/emitting atmosphere. Gas and cloud absorption are computing from the Millimeter-wave Propagation Model of Liebe et al. (1993).

4. CASE STUDY

Finding a suitable test case was limited to availability of coincident overpasses between Terra and TRMM. A good case of a marine stratocumulus system was found at 1016 UTC on 22 March 2000 off the east coast of southern Africa. Figures 1 and 2 show selected MODIS and TMI images, respectively.

Collocation was performed by collecting all MODIS data that fell within the footprint of the 85.5 GHz channel of the TMI. Only overcast 85.5 GHz footprints with warm clouds were considered for analysis. These situations were determined from MODIS visible and IR data.

5. RESULTS

Results will be presented at the conference.

6. ACKNOWLEGMENTS

Support was provided by the Department of Defense Center for Geosciences/Atmospheric Research grant DAAL01-98-2-0078 and the National Space Development Agency of Japan (NASDA) through an agreement under the ADEOS-II project.

7. REFERENCES

Asrar, G., J. A. Kaye, and P. Morel, 2001: NASA research strategy for earth system science: climate component, *Bull. Amer. Meteor. Soc.*, **82**, 1309-1329.

Evans, K. F., 1998: The spherical harmonics discrete ordinate method for three-dimensional atmospheric radiative transfer, *J. Atmos. Sci.*, **55**, 429-446.

Greenwald, T. J., C. L. Combs, A. S. Jones, D. L. Randel, and T. H. Vonder Haar, 1997: Further developments in estimating cloud liquid water over land using microwave and infrared satellite measurements, *J. Appl. Meteor.*, **36**, 389-405.

Greenwald, T. J., R. Hertenstein, and T. Vukicevic, 2001: Evaluation of a mesoscale model with explicit microphysics in simulating cloudy GOES imager measurements, submitted to *Mon. Wea. Rev.*

King, M. D., Kaufman, Y. J., Menzel, W. P., & Tanré, D. 1992, Remote sensing of cloud, aerosol, and water vapor properties from the Moderate Resolution Imaging Spectrometer (MODIS). *IEEE Trans. Geosc. and Remote Sens.*, **30**, 2-27.

Kummerow, C., W. Barnes, T. Kozu, J. Shiue, and J. Simpson, 1998: The tropical rainfall measuring mission (TRMM) sensor package, *J. Atmos. Oceanic Technol.*, **15**, 809-817.

Liebe, H. J., G. A. Hufford, and M. G. Cotton, 1993: Propagation modeling of moist air and suspended water/ice particles at frequencies below 1000 GHz, *Proc. Atmospheric Propagation Effects through Natural and Man-Made Obscurants for Visible to MM-Wave Radiation*, Palma de Mallorca, Spain, AGARD, 3.1-3.10.

Lin, B., P. Minnis, B. Wielicki, D. R. Doelling, R. Palikonda, D. F. Young, T. Uttal, 1998: Estimation of water cloud properties from satellite microwave, infrared and visible measurements in oceanic environments. Part 2: Results, *J. Geophys. Res.*, **103**, 3887-3905.

McMillin, L. M., L. J. Crone, M. D. Goldberg, and T. J. Kleespies, 1995: Atmospheric transmittance of an absorbing gas, 4. OPTRAN: A computationally fast and accurate transmittance model for absorbing gases with fixed and variable mixing ratios at variable viewing angles, *Appl. Opt.*, **34**, 6269-6274.

Mitchell, D. L., 2000: Parameterization of the Mie extinction and absorption coefficients for water clouds, *J. Atmos. Sci.*, **57**, 1311-1326.

Rodgers, C. D., 1976: Retrieval of atmospheric temperature and composition from remote measurements of thermal radiation, *Rev. Geophys. Space Phys.*, **14**, 609-624.

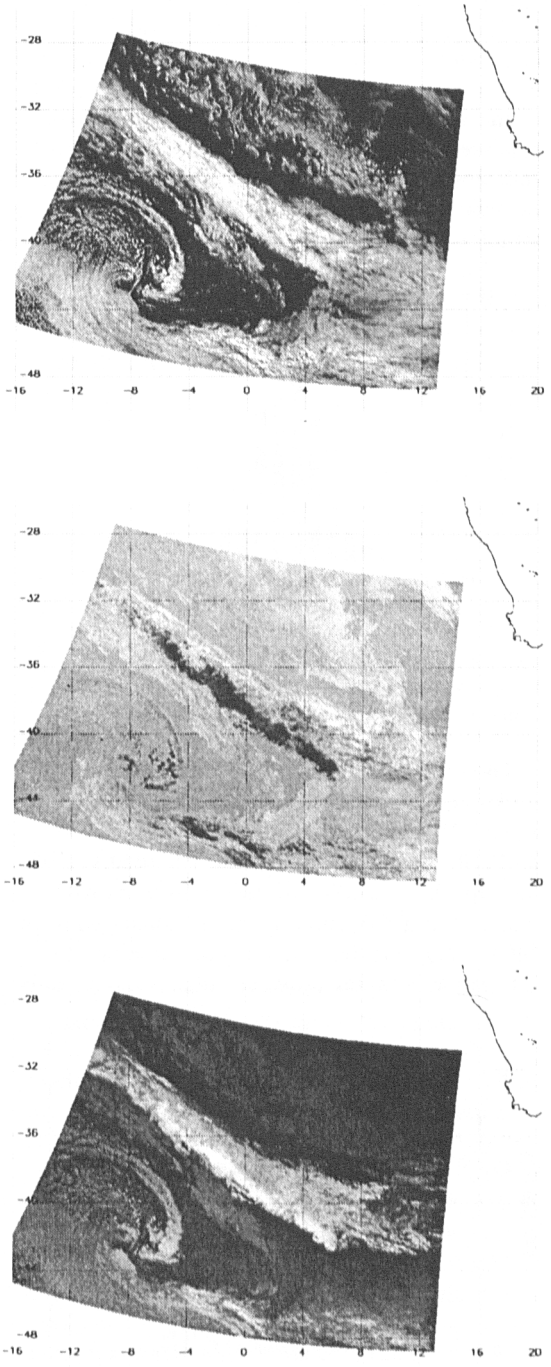

Fig 1. MODIS visible (top), near-infrared (middle), and infrared (bottom) images.

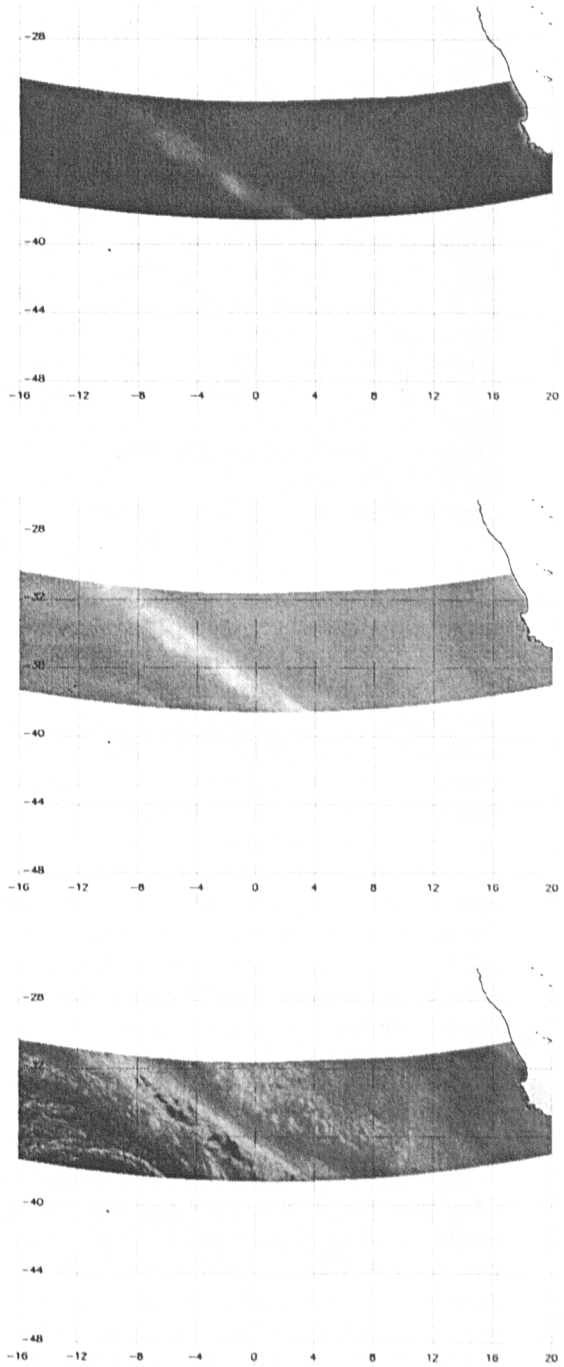

Fig 2. TMI 10.65 GHz (top), 21.8 GHz (middle), and 85.5 GHz (bottom) images.

P4.17 DETERMINATION OF LIQUID WATER PATH AND EFFECTIVE RADIUS FOR WATER CLOUDS USING MICROWAVE AND VISIBLE MEASUREMENTS

Guosheng Liu* and Hongfei Shao
Florida State University, Tallahassee, Florida
Mark Tschudi and Julie Haggerty
NCAR, Boulder, Colorado

1. INTRODUCTION

The radiative properties of water clouds are closely related to two cloud microphysical para - meters: liquid water path (LWP) and effective radius (r_e). For the same LWP, smaller water droplets will have larger optical depth i n the shortwave and reflect more solar radiation. The aerosol's indirect radi ative effect is the increase of cloud reflection by providing more cloud con - densation nuclei. In relation to INDOEX (Indian Ocean Experiment) project, the ultimate goal of this study is to assess the aerosol's effect on cloud microphysics and radiative properties. As a first step, we are developing retrieval algo rithms for LWP and r_e using data collected by AIMR (Airborne Imaging Microwave Radio meter) and MCR (Multi-Channel Radiometer). The AIMR is a cross -scanning, dual-frequency (37 and 90 GHz), dual polarization microwave radiometer. The MCR is a cross -scanning 7-channel radio - meter with wavelengths ranging from 0.64 μm to 10.8 μm although only the 0.64 μm channel was fully functional during the entire INDOEX experiment. Only the 0.64 μm channel is used in our retrieval algorithm at this moment. During the INDOEX intensive obser vation period (January through March of 1999), AIMR and MCR were deployed on NCAR C -130 air craft. Data were collected during 18 flights over Indian Ocean covering an area approximately from 10 ° S to 10° N and 65 to 75°E.

2. RETRIEVAL METHOD

The retrieval algorithm starts with determining LWP from AIMR microwave data first. Cloud height, cloud temperature and sea surface temp - erature are derived from other remote and in situ measurements onboard the aircraft. Detailed description of the LWP algorithm can be found in Liu et al. (2001). Fig. 1 shows the frequency distribution of retrieved "l iquid water path" for clear-sky regions, which provides the indication of the algorithm's systematic and random errors. It is seen that the frequencies peaks near zero, indicating no systematic error, and the standard deviation of the retrieved LWPs is 18 g m $^{-2}$, which is the indication of random error.

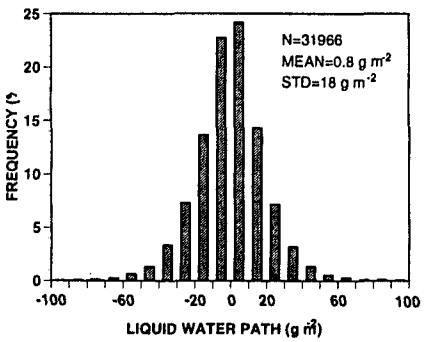

Fig. 1 Frequency distribution of retrieved LWP for clear -sky regions. The mean and standard deviation are indications of systematic and random errors.

The retrieval of effec tive radius is based on a lookup table generated by a radiative transfer model (Ricchiazzi et al. 1998) for various solar and instrument viewing angles. The inputs of the lookup table are LWP (retrieved from AIMR) and 0.64 μm reflection function (calculated from MCR). Fig. 2 is the frequency distribution of the difference between model calculated and actually

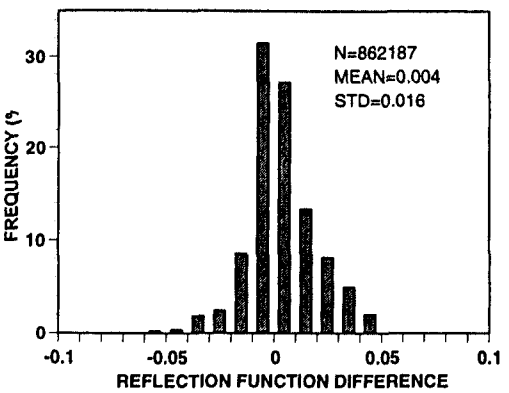

Fig.2 Frequency distribution of the difference between calculated and observed reflection function (0.64 μm) for clear-sky pixels. The mean and standard deviation are indications of systematic and random errors.

* Corresponding author address: Guosheng Liu, Florida State Univ., Dept. of Meteorology, Tallahassee, FL 32306-4520; e-mail: liug@met.fsu.edu

observed reflection function at 0.64 μm for clear-sky conditions. It is seen that the systematic error is near 0 and the random error is also small, ~0.016.

Fig. 3 is an example for explaining the lookup table method based measurements from 0653Z to 0658Z on Feb. 27, 1999. The curves are isolines for r_e calculated by radiative transfer model runs. From the observed values of LWP and reflection function, effective radius can be determined by interpolation. The small dots are actual observations at pixel scale and the large dots are averaged r_e at every 10 g m^{-2} LWP bin. On average, r_e increases with LWP from ~4 μm at LWP being a few g m^{-2} to ~12 μm when LWP is ~150 g m^{-2}. Scatters of the data at pixel level could be partially caused by the inhomogeneity of the cloud field.

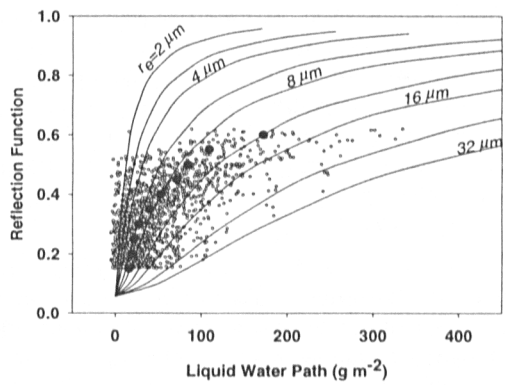

Fig. 3 Schematic diagram for retrieving effective radius from liquid water path and reflection function at 0.64 μm.

3. RESULTS

Figure 4 shows the retrieved LWP, observed radiance (I) at 0.64 μm, and retrieved r_e for a 5-minute flight on Feb. 27, 1999, based on the retrieval algorithms described above. The clouds are scattered cumulus with a depth of about 600 m within the boundary layer. Retrieved LWPs ranges from 0 to more than 300 g m^{-2}, while retrieved r_e is from 0 to ~20 μm. Bright clouds (high I values) generally correspond to greater LWP and larger r_e values. This example suggests that the retrievals are reasonable at least qualitatively although further validations using more quantitative methods are needed.

Using the LWP and r_e retrieved from all data collected during INDOEX, we are studying the relationship between LWP and r_e, and how this relationship is related to the aerosol concentration. Because deep cumulus clouds usually are associated with larger LWP and r_e, r_e generally

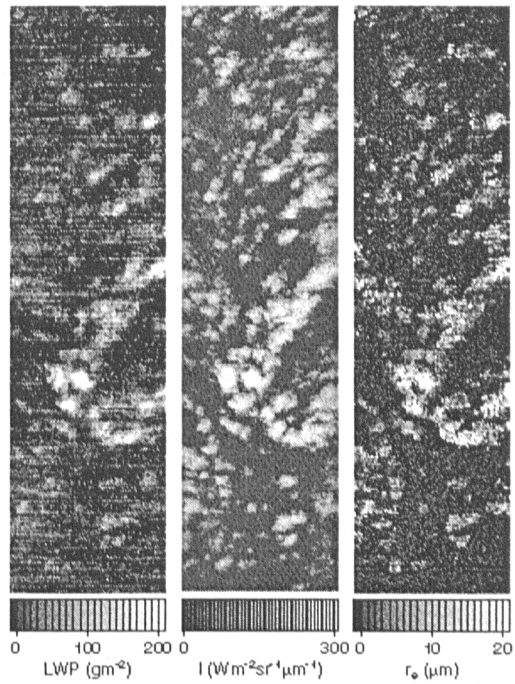

Fig.4 Retrieved LWP (left), observed reflected radiance at 0.64 μm (middle) and retrieved effective radius (right) for a 5-minute flight on Feb. 27, 1999. The area is roughly 12 km by 45 km.

increases with LWP. However, the rate of the increase (or the slope) is expected to be related to the number concentration of the water droplets, which, in turn, is a function of cloud condensation nuclei. By examining the slope, the aerosol's indirect effect on solar radiation may be assessed. Results based on this approach will be report at the conference.

Parallel to the data analysis using aircraft data, we are also conducting similar studies using simultaneously observed visible and microwave data from TRMM satellite. While aircraft observations provide detailed data at a fine resolution, satellite data cover a much broader area and much longer time period.

Acknowledgments. This research has been supported by NSF ATM-0002860.

References

Liu, G., J. A. Curry, J. A. Haggerty, and Y. Fu, 2001: Retrieval and characterization of cloud liquid water path using airborne passive microwave data during INDOX. J. Geophys. Res. (in press).

Ricchiazzi, P., S. Yang, C. Gautier, and D. Sowle, 1998: SBDART: A research and teaching software tool for plane-parallel radiative transfer in the Earth's atmosphere. Bull. Amer. Met. Soc., 79, 2101-2114.

P4.18

THE SENSITIVITY OF COMPUTED MICROWAVE BRIGHTNESS TEMPERATURES FROM PRECIPITATING CLOUDS TO MODELS OF SPHERICAL MIXED-PHASE HYDROMETEORS

BENJAMIN JOHNSON*, GRANT PETTY

[1]*Department of Atmospheric and Oceanic Sciences, University of Wisconsin-Madison, Madison, Wisconsin*

1. INTRODUCTION

Passive microwave remote sensing from satellites has become the primary basis for global monitoring of precipitation. Cold-cloud precipitation processes, dominant in midlatitude systems, are often composed of a variety of ice-phase and mixed-phase hydrometeors. Accurate models of the microwave optical properties of mixed- and ice-phase hydrometeors are critical to the success of physically based precipitation retrieval algorithms. To date, however, microwave radiative transfer calculations have generally relied on ad hoc assumptions about hydrometeor properties.

The research presented here consists of two primary components. A hydrometeor model, in which an effective medium approximation (Bruggeman 1935) is used for the computation of the average dielectric properties of an exponential size distribution of spherical mixed- and ice-phase hydrometeors; Mie theory is used for computation of the optical properties for the modeled hydrometeor ensemble. For the second component of the research a plane-parallel, polarized radiative transfer model (RT4) by Evans and Stephens (1995) is used to compute brightness temperatures of a semi-infinite layer of hydrometeors.

The ultimate objective of this work is to establish empirical constraints on hydrometeor properties assumed in radiative transfer models, based in part on comparisons between observed and simulated multichannel microwave radiances from current sensors, such as the Tropical Rainfall Measurement Mission (TRMM) Microwave Imager (TMI), the Advanced Microwave Scanning Radiometer (AMSR), and the Advanced Microwave Sounding Unit (AMSU).

* *Corresponding author address*: Benjamin Johnson, AOS Dept., UW-Madison, 1225 W. Dayton Street, Madison, WI 53706; e-mail: jbenjam@aos.wisc.edu

2. MODEL DESCRIPTION

2.1 *Hydrometeor Model*

Because we are interested in simulating the effects of the physical composition of mixed- and ice-phase hydrometeors on observed microwave brightness temperatures, it is necessary to incorporate some approximation of physical reality into the model. As a basic approximation, any hydrometeor can be represented by three volume fractions: liquid water f_{liq}, ice phase f_{ice}, and air f_{air}. Air volume fraction is represented by

$$f_{air} = (1 - f_{liq} - f_{ice}). \tag{2.1}$$

Water, ice, and air have significantly different dielectric functions. The dielectric function of a material determines how it interacts with a particular frequency of radiation. To simulate the dielectric function of a mixed-phase hydrometeor, the effective medium approximation of Bruggeman (1935) for two-components is used,

$$f_1 \frac{\varepsilon_1 - \varepsilon_{av}}{\varepsilon_1 + 2\varepsilon_{av}} + (1 - f_1) \frac{\varepsilon_2 - \varepsilon_{av}}{\varepsilon_2 + 2\varepsilon_{av}} = 0, \tag{2.2}$$

where f_1 is the ratio of the volume fraction of material 1 to material 2, and ε_1, ε_2 are the dielectric functions of materials 1 and 2 respectively. This is generalized to include three components by applying the two-component method (Eqn. 2.2) twice; first, to two of the components, and then to the average and the third component.

In this way, a single homogeneous spherical hydrometeor with an average dielectric function and expanded physical radius — an effect of the air component — can be used as a model of an actual hydrometeor having similar physical characteristics.

To model the properties of a ensemble of hydrometeor sizes, a simple two-parameter exponential size distribution is used,

$$N(D) = N_0 \exp(-\Lambda D), \tag{2.3}$$

where D is the liquid (or mass) equivalent particle diameter, Λ controls the size dependence of $N(D)$,

and thus the mass-weighted optical properties of the hydrometeors. N_0 can be computed by quantities such as rain-rate (in the case of rain) etc. In this case, we consider a reasonable fixed value of N_0 for simplicity, as is described later.

Using the Mie code based on Bohren and Huffman (1983), the optical properties of a single particle are determined. In particular, we are interested in the single scatter albedo (ϖ_0), asymmetry parameter (g), and mass extinction coefficient (κ). Averaging over the size distribution, "bulk" optical properties are obtained for the ensemble of hydrometeors.

2.2 *Radiative Transfer Model*

For microwave brightness temperature calculations, the one dimensional, polarized, plane-parallel model (RT4) described briefly in Evans and Stephens (1995) was used. Plane-parallel refers to the method in which the model layers are treated as being horizontally homogeneous and for our purposes infinite in extent. Polarized 4×4 phase matrices are calculated for each hydrometeor from Mie theory. It should be noted that while polarization is considered to be an important topic, the focus here is on the variation in the magnitudes of the brightness temperatures.

2.3 *Model Setup*

For the cases presented here, we assumed a semi-infinite layer of hydrometeors. The purpose of a semi-infinite layer is to obscure emission from the surface, and to provide brightness temperatures due to thermal emission from the layer of hydrometeors. By changing the model parameters, it is straightforward to observe the changes in the resultant brightness temperatures. It is possible to determine the relative sensitivity of the computed microwave brightness temperatures to those changes in the model parameters.

In particular, we focus here on how changing the volume fraction of ice, water, and air can affect the brightness temperature results. The purpose for doing this is to determine to what extent more simplistic treatment of hydrometeors are valid, or alternatively when a realistic treatment of hydrometeor composition becomes important.

3. EXAMPLE APPLICATIONS

3.1 *Hydrometeors*

A snowflake is an individual ice crystal grown by vapor deposition. As it falls in the atmosphere, it can collect other snowflakes and ice crystals forming a larger "clump" of crystals called an aggregate. Aggregates are thought to be important for the initiation of precipitation-sized-particle growth (Pruppacher and Klett 1997).

To model a snowflake aggregate and graupel using the hydrometeor model, somewhat subjective choices are made regarding the composition of the particle. Indeed, the individual aggregate is a loose collection of ice crystals; therefore, the volume fraction of ice compared to air will be low. For graupel, we expect a higher volume fraction of ice. Melting graupel would contain a small volume fraction of melted ice. Table 1 lists the choices for the model parameters for the three example cases.

	Water (f_{liq})	Ice (f_{ice})	Λ (cm^{-1})
Aggregate	0.0	0.2	25
Graupel 1	0.0	0.5	25
Graupel 2	0.1	0.4	25

Table 1: Volume fractions for selected hydrometeor simulations as examples. $1/\Lambda$ gives the mode diameter of the exponential size distribution.

In figure 1, the brightness temperature is plotted versus frequency for the three examples in table 1. Comparisons between the three curves show differences in the brightness temperature signatures, indicating that choices regarding the physical characteristics of hydrometeors, even in an ensemble, can potentially be important in algorithm applications.

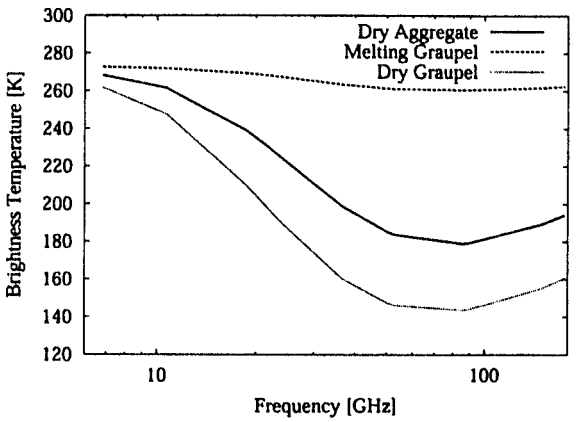

Figure 1: Simulated brightness temperature versus frequency for three example hydrometeors.

Of particular note is the effect of water. In figure 1, we find that the addition of 0.1 volume fraction water as compared to the dry graupel leads to a brightness temperature change as great as 100 K for the semi-infinite layer of hydrometeors. This is a potentially important source for error, and indicates

that the knowledge or assumptions regarding hydrometeor composition should be taken seriously.

Figure 2 explores the effects of water on the brightness temperature as a contour plot. The left axis shows the water volume fraction, and the right axis shows the corresponding ice volume fraction. In this case, there is no air present. The presence of even a small amount of liquid water significantly impacts the radiances from the layer of hydrometeors.

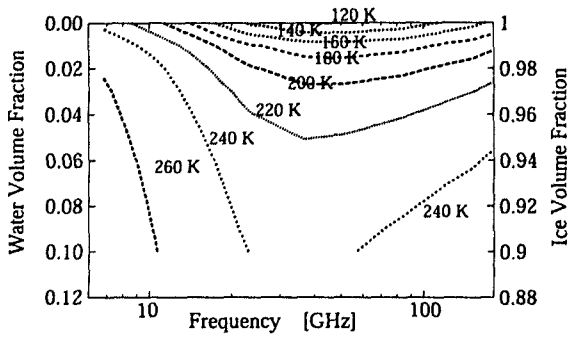

Figure 2: Contours of brightness temperature (K) for changing volume fraction of ice and water.

4. CONCLUSION

The model generated brightness temperatures for an semi-infinite layer of thermally emitting hydrometeors indicates that there is a strong sensitivity to the choices and assumptions of the physical properties of modeled hydrometeors. It was shown that small amounts of liquid water present can significantly impact the observed brightness temperature. Additionally, it can be seen that the effect of air component can have a lesser impact on the model brightness temperatures. These results illustrate the consequences of overly simplistic and/or ad hoc treatments of ice particles in algorithms or models.

Furthermore, the research presented here, a small sample of a more thorough sensitivity study in progress, will be used to improve current and future algorithms by providing empirical constraints through comparisons with observations and model simulations.

Future work will involve comparisons with actual data and empirical measurements of hydrometeors to more realistically constrain the range of model parameters. Additionally, shape considerations will be taken into account, along with polarization (vertical and horizontal). Actual measurements of the dielectric properties of hydrometeors would be greatly useful as a guide for decisions regarding model choices, especially with respect to the method of averaging dielectric constants.

5. REFERENCES

Bohren, C. F., D. R. Huffman, 1983: *Absorption and Scattering of Light by Small Particles.* Wiley-Interscience.

Bruggeman, D., 1935: Berechnung verschiedener physikalischer Konstanten von heterogenen Substanzen: I. Dielektrizitätskonstanten und Leitfähigkeiten der Mischkörper aus isotropischen Substanzen (Calculation of different physical constants of heterogeneous substances: I. Dielectric constants and conductivity of mixtures of isotropic substances). *Ann. Phys.*, **24**, 636-679.

Evans, K. F., G. L. Stephens, 1995: Microwave radiative transfer through clouds composed of realistically shaped ice crystals. Part II: Remote sensing of ice clouds. *J. Atmos. Sci.*, **52**, 2058-2072.

Kummerow, C., W. S. Olson, and L. Giglio, 1996: A simplified scheme for obtaining precipitation and vertical hydrometeor profiles from passive microwave sensors. *IEEE Trans. Geosci. Remote Sens.*, **34**, 1213-1232.

Pruppacher, H. R., J. D. Klett, 1997: *Microphysics of Clouds and Precipitation (2nd. Ed.).* Kluwer Academic Press.

P4.19 A NEAR-REAL TIME METHOD FOR DERIVING CLOUD AND RADIATION PROPERTIES FROM SATELLITES FOR WEATHER AND CLIMATE STUDIES

Patrick Minnis*, William L. Smith, Jr., David F. Young, L. Nguyen
Atmospheric Sciences, NASA Langley Research Center, Hampton, VA 23681

Anita D. Rapp, Patrick W. Heck
AS&M, Inc., Hampton, VA 23666

Sunny Sun-Mack, Qing Z. Trepte, Yan Chen
SAIC, Hampton, VA 23666

1. INTRODUCTION

As the dominant variable in atmospheric radiation and hydrological processes, clouds should be accurately represented in both weather and climate predictive models. The need to assimilate observed or validate predicted cloud properties in these models will rise with increasing model sophistication. The capability for deriving accurate cloud properties in a timely fashion is required to aid the improvement of these models and their forecasts. This capability has been realized to some extent in the CO_2-slicing product derived over the USA from Geostationary Operational Environmental Satellite (GOES) sounder data by the University of Wisconsin Cooperative Institute for Meteorological Satellite Studies. That gridded product is comprised of cloud cover, cloud-top pressure, and emissivity from each sounder image. Many of the latest mesoscale models, however, include parameterizations of relatively realistic cloud microphysical properties that vary with the conditions. To ensure that such models are accurately representing the hydrological and radiative budgets of the atmosphere in a given forecast, additional cloud parameters are required. Presumably, forecasts will improve if these energy and mass budgets are properly taken into account. Furthermore, initializing the model with a more accurate distribution of cloud water and its correct optical properties should also enhance forecast accuracy.

An approach has been developed for near-real-time derivation of cloud and radiation properties, including cloud fraction, height, optical depth, phase, particle size, albedo, outgoing longwave radiation OLR, and skin temperature, to facilitate research on cloud and radiation interactions by the Atmospheric Radiation Measurement (ARM) Program. This approach should have a wider application in the meteorological community. This paper presents the methodology and results from an initial implementation using data taken over the ARM Southern Great Plains (SGP) region.

*Corresponding Author Address: P. Minnis, MS420, NASA Langley Research Center, Hampton, VA 23681; e-mail: p.minnis@larc.nasa.gov.

2. DATA AND METHODOLOGY

The most logical choice for near-real time processing in mid-latitude and tropical regions is geostationary satellite data. GOES-8 1- and 4-km imager data (0.65 μm, VIS; 3.9 μm, SIR; 10.8 μm, IR; and 12.0 μm, SWC) taken every 15 to 60 min are ingested as they become available using the SSEC Man-computer Interactive Data Analysis System (McIDAS; Lazzara et al. 1999). The methods of Minnis et al. (2001) and Nguyen et al. (2001) are used to calibrate the VIS radiances and to monitor the thermal channel calibrations.

Determination of the cloud properties requires an array of various input data. Clear-sky VIS reflectance ρ_{cs} at a given time and location is computed by applying solar-zenith-angle *SZA* dependent albedo models and bidirectional reflectance models to a database of clear-sky zenith-sun albedos α_v resolved at 10' of latitude and longitude (Trepte et al. 1999). A similar database for the surface emissivity at 3.9, 10.8, and 12.0 μm is also maintained to help predict the clear-sky temperatures for these channels at any given time and location (e.g., Smith et al. 1999). Water-land percentage and elevation maps are used to determine the surface type and atmospheric thickness, respectively, for each grid location. Temperature and humidity profiles are interpolated from the gridded Rapid Update Cycle (RUC; Benjamin et al. 1994) analyses to match the analysis grid and image times. Surface skin temperature T_s is estimated from the RUC surface air temperature with an update of the technique used by Minnis et al. (1995a).

Each GOES-8 pixel is classified as clear or cloudy using a modified version of the cloud identification algorithm (e.g., Trepte et al. 1999) developed for the Clouds and Earth's Radiant Energy System (CERES). For each pixel, this method compares the observed VIS reflectance ρ, IR temperature T_4, and the SIR-IR brightness temperature difference *BTD* to several basic thresholds based on the predicted clear-sky values and their uncertainties for the grid box containing the pixel. In a simplified form, the clear-sky temperature T_{cs} for channel i is

$$B_i(T_{csi}) = \varepsilon_a B_i(T_{ai}) + (1-\varepsilon_{ai}) B_i(T_{si}) \qquad (1)$$

where B is the Planck function, ε_a and T_a are the atmospheric effective emissivity and effective temperature, respectively. The radiance for the apparent surface radiating temperature, T_{si}, is

$$B_i(T_{si}) = \varepsilon_i(\mu) B_i(T_s) + (1-\varepsilon_i)[L_{ai} + \chi_k S_i], \qquad (2)$$

where μ is the cosine of the viewing zenith angle *VZA*, L_a is the downwelling atmospheric radiance at the surface, χ_k is the bidirectional reflectance factor for surface type k, and S is the downwelling solar radiance at the surface. The atmospheric absorption and emission are computed using the correlated k-distribution coefficients, computed for the GOES channels as in Kratz (1995), in a simple radiative transfer model using the temperature and humidity in each of the RUC layers.

Cloud properties are computed for each pixel identified as cloudy using the visible infrared solar-infrared split window technique (VISST), which is an upgrade of the VIS-SIR-IR method described by Minnis et al. (1995b). VISST computes an array of VIS reflectances and SIR, IR, and SWC temperatures at the TOA for the specified *VZA*, *SZA*, and relative azimuth angle *RAZ* using model lookup tables (Minnis et al. 1998) in parameterizations that account for the contributions of the surface and atmosphere to the radiance in each channel. Solutions are computed iteratively for both liquid and ice clouds yielding effective droplet size r_e or effective ice crystal diameter D_e, optical depth τ, and cloud radiating temperature T_c. Phase is determined using several criteria including the value of T_c, the available solutions, and the consistency with the observed SWC temperature. Ice water path *IWP* or liquid water path *LWP* are computed from the particle size and optical depth.

The cloud radiating altitude z_c is determined by matching T_c with the same temperature in the RUC profile. Often, this altitude is close to the actual physical cloud-top height z_t. For diffuse clouds like cirrus, it corresponds to some height between cloud top and cloud base. Cloud thickness Δz is estimated using a set of empirical formulae developed from simultaneous radar, lidar, and satellite data taken during various field programs. These parameterizations also attempt to compute cloud-top height. Given Δz, cloud base height can be computed. Broadband shortwave albedo α_{sw} and OLR are computed for each pixel from narrowband-to-broadband relationships derived from ERBE data matched with GOES-6 imager data over the same domain (Minnis and Smith, 1998).

At night, the SIR-IR-SWC (SIRS) method is used to solve for the same parameters, except that no optical depths can be retrieved for clouds with $\tau > 10$. The IR temperatures change insignificantly for larger optical depths. Thus, for *SZA* > 78°, the information concerning *IWP* or *LWP* is limited.

Table 1. Pixel-level products derived from GOES-8.

Condition	All	Cloudy	Clear
SZA < 78°	ρ, ρ_{cs}, α_{sw} T_i, T_{cs} *OLR, SZA, VZA, RAZ*	T_c, z_c, z_t Δz, τ, phase r_e or D_e *LWP* or *IWP*	T_s, α_v
78° < *SZA* < 90°	ρ, ρ_{cs}, α_{sw} T_i, T_{cs} *OLR, SZA, VZA, RAZ*	T_c, z_c, If τ < 10: z_t, z_t, Δz, τ phase r_e or D_e *LWP* or *IWP*	T_s, α_v
SZA > 90°	T_i, T_{cs} *OLR SZA, VZA, RAZ*	T_c, z_c, If τ < 10: z_t, z_t, Δz, τ phase r_e or D_e *LWP* or *IWP*	T_s

For clear pixels, skin temperature is derived from the observed IR temperature for each clear pixel using (1) and (2). The clear-sky reflectances for each 10' region are adjusted for anisotropy and corrected to a zenith-sun albedo. If significantly different from the predicted value, the database is upgraded using the newly calculated albedo. Because the shortwave albedo and OLR are computed for each pixel, it is possible to determine the clear-sky albedo and OLR, parameters that can be used to compute cloud radiative forcing or to verify model inputs.

Table 1 lists the parameters that are included for each pixel in the output file. In addition to all of the derived parameters, the file includes the predicted clear-sky temperatures and reflectances. All of the cloud parameters are computed during the daytime (*SZA* < 78°), while the number of parameters computed during "twilight" (78° < *SZA* <90°) and at night are optical-depth limited as noted earlier. If the estimated value of τ exceeds 10, then default values are used for the phase and particle size. The cloud is assumed to act like a blackbody, so $T_c = T_4'$, which is the result after correcting T_4 for the atmosphere above the cloud level. This latter approach is the same as an IR-only method.

3. RESULTS AND DISCUSSION

An example of the derived parameters and imagery for 1845 UTC, March 14, 2000 is shown in Fig. 1. A relatively complex cloud field is passing through the region during this day. The VIS image shows relatively dim clouds over northern Colorado, heavy clouds over Missouri and north Texas and a line of clouds through central Oklahoma. These appear to be low clouds in the IR image, while the clouds in TX, MO, and CO are somewhat higher. The cloud mask (upper right corner) shows a large clear area over much of the western half and a smaller clear area over eastern OK and the Ozark

Plateau. Clear albedos vary between 15 and 23% while the albedos over cloudy areas range up to 80% in southeastern KS. Over the clouds in CO, α_{sw} reaches only 60%. The OLR varies from 165 Wm^{-2} over CO to 305 Wm^{-2} over the Texas panhandle.

Cloud heights range from 1 to 3 km over OK and northwestern MO to 11 km or more over CO and parts of AR. The liquid water clouds primarily correspond to $z_c <$ 4 km including a substantial amount of supercooled-liquid-water clouds (SCW) over northern MO and southern IA (see cloud mask). The values of r_e range from 6.5 μm to 18 μm. The values greater than 12 μm are typically found around the edges of the cirrus clouds where overlapping effects increase the value of r_e. *LWP*s as large as 250 gm^{-2} were observed over northern OK and in the SWC areas in MO. Cloud optical depths in these same areas reached 85 or more, while values of τ > 100 were derived for the ice clouds over southwestern MO and along the OK-TX border. Many of the cirrus cloud optical depths over AR and CO are less than 2. The values of D_e for the ice clouds are between 25 and 60 μm for many of the thinner clouds while the thicker clouds mostly have D_e between 75 and 135 μm. The *IWP* exceeds 400 gm^{-2} over central MO and northern TX while values less than 50 gm^{-2} are common for the thin cirrus clouds.

The values of r_e, τ, and *LWP* were recently validated for stratus clouds over the ARM SGP by Dong et al. (2001) who used radar, ceilometer, and shortwave and microwave radiometers to derive the same parameters retrieved from the GOES-8 data. For example, over the ARM central facility (indicated in the *IWP* plot in Fig. 1), the surface-derived values of r_e, τ, and *LWP* at 1845 UTC, March 14, 2001 are 8.5 μm, 30, and 175 gm^{-2} compared to 9.5 μm, 30, and 190 gm^{-2} from GOES-8. Overall, Dong et al. (2001) found that the satellite values of r_e, τ, and *LWP* were 1.4 μm larger, 2% less, and 5% greater than the respective surface-based values. Differences between the satellite and coincident aircraft values were of similar magnitudes. Validation of the other properties is underway.

The VISST code has been exercised in near-real time for several different experiments including the March 2000 ARM Cloud Intensive Observing Period. Although it is currently used to derive cloud properties in a near-operational mode for the ARM SGP domain, the algorithms are being continuously upgraded to minimize retrieval errors and expand the coverage area by developing solutions to some of the following problems. Regions of no-retrieval, like those seen in the cloud mask (Fig. 1), include pixels that were properly identified as cloudy, but have radiances that cannot be matched to the cloud model calculations. No retrievals occur for a variety of reasons such as poor background characterization (thin clouds), shadowing, or partially filled pixels. Multilayer clouds also affect the estimates of cloud microphysical properties and should be better characterized in the retrievals. For example, the large *IWP*s in Fig. 1 may be the result of a thick ice cloud over a water cloud. The two water paths should be quantified separately. Retrievals during twilight are more difficult than at other times of day because the small solar signal in the SIR balances the thermal signal rendering the channel nearly useless for retrievals. Uncertainties in all of the clear-sky variables can impact cloud detection and retrievals and should be reduced with improved databases. The frequency of retrievals and the domain size are computationally constrained by the large data volume. These and other issues are being addressed to improve the efficiency and accuracy of the algorithms so they can be applied confidently on a growing domain.

4. CONCLUDING REMARKS

Results from these analyses (click on ARM, SGP at http://www-pm.larc.nasa.gov) should be valuable for development of cloud climatologies, study of the relationships between clouds, the atmospheric state, and the local radiation budget, and derivation of icing diagnostics, as well as model validation and initialization. As the algorithms are upgraded, both the accuracy and area of analysis will continue increasing.

Acknowledgments
This research is supported by the Environmental Sciences Division of U.S. Department of Energy Interagency Agreement DE-AI02-97ER62341 under the ARM Program.

REFERENCES

Benjamin, S. G., K. J. Brundage, and L. L. Morone, 1994: The Rapid Update Cycle. Part I: Analysis/model description. Technical Procedures Bulletin No. 416, NOAA/NWS, 16 pp.

Dong, X., P. Minnis, G. G. Mace, W. L. Smith Jr, M. Poellot, and R. Marchand, 2001: Comparison of stratus cloud properties deduced from surface, GOES, and aircraft data during the March 2000 ARM Cloud IOP. Submitted to *J. Atmos. Sci.*

Kratz, D. P., 1995: The correlated *k*-distribution technique as applied to the AVHRR channels. *J. Quant. Spectrosc. Radiat. Transfer*, **53**, 501-517.

Lazzara, M. A., J. M. Benson, R. J. Fox, D. J. Laitsch, J. P. Rueden, D. A. Santek, D. M. Wade, T. M. Whittaker, and J. T. Young, 1999: The Man computer Interactive Data Access System: 25 years of interactive processing. *Bull. Amer. Meteor. Soc.*, **80**, 271-274.

Minnis, P., D. P. Garber, D. F. Young, R. F. Arduini, and Y. Takano, 1998.: Parameterization of reflectance and effective emittance for satellite remote sensing of cloud properties. *J. Atmos. Sci.*, **55**, 3313-3339.

Minnis P., et al., 1995b: Cloud optical property retrieval (Subsystem 4.3). CERES Algorithm Theoretical Basis Document, Volume III: Cloud analyses and radiance inversions (Subsystem 4), NASA *RP 1376 Vol. 3*, 135-176.

Minnis, P., L. Nguyen, D. F. Young, D. R. Doelling and W. F. Miller, 2001: Rapid calibration of Operational and research meteorological satellite imagers, Part I: Use of the TRMM VIRS or ERS-2 ATSR-2 as a reference. Submitted to *J. Atmos. Oceanic Technol.*

Minnis, P. and W. L. Smith, Jr., 1998: Cloud and radiative fields derived from GOES-8 during SUCCESS and the ARM-UAV Spring 1996 Flight Series. *Geophys. Res. Lett.*, **25**, 1113-1116.

Minnis P., W. L. Smith, Jr., D. P. Garber, J. K. Ayers, and D. R. Doelling, 1995a: Cloud properties derived from GOES-7 for Spring 1984 ARM Intensive Observing Period using Version 1.0.0 of ARM satellite data analysis program. NASA RP 1366, 58 pp.

Nguyen, L., P. Minnis, J.K. Ayers, and D. R. Doelling, 2001: Intercalibration of meteorological satellite imagers using VIRS, ATSR-2, and MODIS. *Proc. AMS 11th Conf. Sat. Meteorol. Oceanogr.*, Madison, WI, October 12 - 16.

Smith, W. L., Jr., P. Minnis, D. F. Young, and Y. Chen, 1999: Satellite-derived surface emissivity for ARM and CERES. *Proc. AMS 10th Conf. Atmos. Rad.*, Madison, WI, June 28 – July 2, 410-413.

Trepte, Q., Y. Chen, S. Sun-Mack, P. Minnis, D. F. Young, B. A. Baum, and P. W. Heck, 1999: Scene identification for the CERES cloud analysis subsystem. *Proc. AMS 10th Conf. Atmos. Rad.*, Madison, WI, June 28 – July 2, 1999, 169-172.

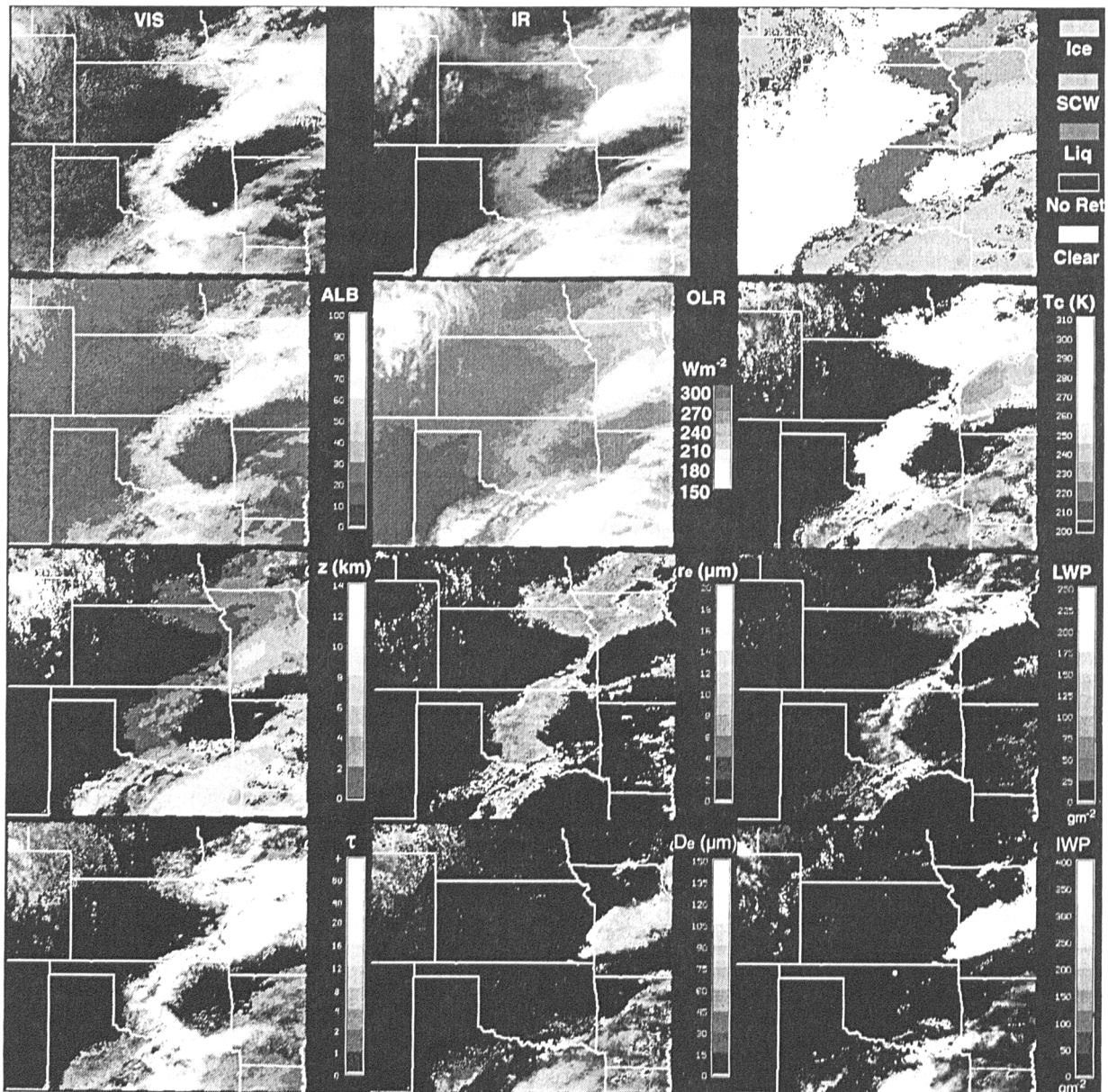

Fig. 1. Imagery and cloud and radiative properties from GOES-8 over ARM SGP domain (central facility indicated in IWP plot as a white square in north central Oklahoma), 1845 UTC, March 14, 2001.

P4.20

VALIDATION OF GOES AND MODIS ATMOSPHERIC PRODUCTS AND RADIANCES USING DEPARMENT OF ENERGY ATMOSPHERIC RADIATION (DOE ARM) MEASUREMENT DATA

Wayne F. Feltz*, Timonthy J. Schmit#, Jim Hawkinson, David Tobin, and Suzanne Wetzel-Seeman

Space Science and Engineering Center University of Wisconsin - Madison
Madison, Wisconsin

#NOAA/NESDIS/ORA Advanced Satellite Product Team (ASPT) Madison, Wisconsin, USA

1. INTRODUCTION

The Department of Energy (DOE) Atmospheric Radiation Measurement (ARM) Program (Stokes, 1994) has deployed a suite of ground-based in situ and remote sensing instrumentation to provide a long term (> 10 years) validation data set for General Circulation Models (GCM). The three DOE ARM measurement sites are named Southern Great Plains (SGP Oklahoma/Kansas region), North Slope of Alaska (NSA, near Barrow, Alaska), and Tropical Western Pacific (TWP). The main purpose of the ARM program is to improve knowledge of cloud radiative flux (shortwave and longwave) and to develop new GCM parameterizations to improve climate model forecasts. The ARM data sets have provided a unique high temporal resolution satellite validation source. The University of Wisconsin - Madison Space Science Engineering Center (SSEC) has a real-time direct broadcast downlink capability for the Geostationary Operational Environmental Satellites (GOES) and EOS-Terra data. The NOAA Cooperative Institute for Meteorological Satellite Studies (CIMSS) is producing atmospheric derived products from GOES and MODIS radiances, providing information about atmospheric stability, cloud properties, and moisture. ARM data sets are being used to validate GOES Total Precipitable Water (TPW), cloud tops, and atmospheric soundings derived from the GOES sounder. A best estimate temperature and moisture profile from the DOE ARM SGP site is being used to calculate radiance values for validation of GOES and MODIS radiance measurements. This paper will provide an overview of current DOE ARM measurements used for validation of these satellite products and recent conclusions.

2. GOES MOISTURE PRODUCT VALIDATION

The DOE ARM SGP site offers TPW measurements that allow for more precise validation of GOES retrievals than is possible with radiosondes. An operational microwave radiometer (MWR), located at the SGP central facility near Lamont, has demonstrated an accuracy of 0.7 mm under clear sky conditions (Liljegren 1995). All comparisons reported here are for clear sky cases. The MWR is tuned to the microwave emissions of the water vapor molecules in the atmosphere (Liljegren 1994) and measures TPW vapor every five minutes. The MWR measurements are completely independent of those from the GOES Sounder or radiosondes. These high temporal resolution MWR measurements enable validation of the GOES retrievals at times other than the conventional radiosonde launches (00 and 12 UTC). Of course, the MWR and GOES retrievals still differ in that one is a point measurement (although with an improved accuracy compared to radiosondes) and one a volumetric measurement.

TPW values computed from GOES-8 retrievals (Ma et al. 1999) and their corresponding first guess profiles were compared to the MWR TPW for a 29-day period between 20 March – 17 April 1998. The temporal resolution for GOES-8 was routine hourly profiling. Figure 1 shows a one-day comparison of TPW on 12 April 1998 between the MWR and GOES-8. While the first guess (diamonds), which was interpolated from 6-hourly forecasts, is relatively flat throughout the period, the GOES retrieval algorithm (pluses) produces nearly the same water vapor tendency patterns as measured by the MWR (dashed line). The satellite retrieval uses a 3 x 3 FOV matrix (equating to a 36 km x 45 km box at this geographic location), representing a volumetric profile over a larger horizontal area than the MWR (which represents the atmosphere directly above the instrument). Smooth temporal changes are generated by the GOES physical retrieval algorithm, even when the first guess experiences a discontinuity when switched from using forecasts from the 00 UTC to the 12 UTC model initialization times (e.g. near 18 UTC). These discontinuities could be minimized if the forecasts from the 06 UTC and 18 UTC initialization times were also used to build the first guess profiles for the GOES retrievals. The GOES retrievals follow the water vapor fluctuations between a local minimum of approximately 13 mm at 1130 UTC and a maximum of approximately 24 mm at 14 UTC; the temporally and spatially coarse

* *Corresponding author address*: Wayne F. Feltz, CIMSS/SSEC, 1225 West Dayton Street Room 238, Madison, WI, 53706; e-mail: wayne.feltz@ssec.wisc.edu.

radiosonde network did not capture these changes. Overall, GOES demonstrates skill in resolving the mesoscale water vapor fluctuations on this day.

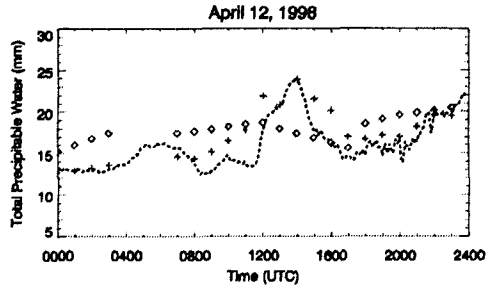

Figure 1: Microwave radiometer (dashed line), Eta model forecast (diamond symbols), and GOES-8 physical retrieval (plus symbols) total precipitable water vapor comparisons near Lamont, Oklahoma on 12 April 1998.

Figure 2 shows the improved agreement of the GOES physical retrieval algorithm (stars) versus the first guess (diamonds) when compared to the MWR measurements during the period 20 March to 17 April 1998. These data were derived by comparing all possible matches between GOES-8 retrievals and the MWR instrument. For the 364 matched values of MWR and GOES-8 shown in Fig. 2, the physical retrieval improves the first guess of TPW RMS from 2.21 to 1.80 mm and the bias from 0.83 to 0.40 mm. Even at greater TPW values, the GOES retrieval values compared better with microwave radiometer values (perfect agreement indicated by the diagonal line).

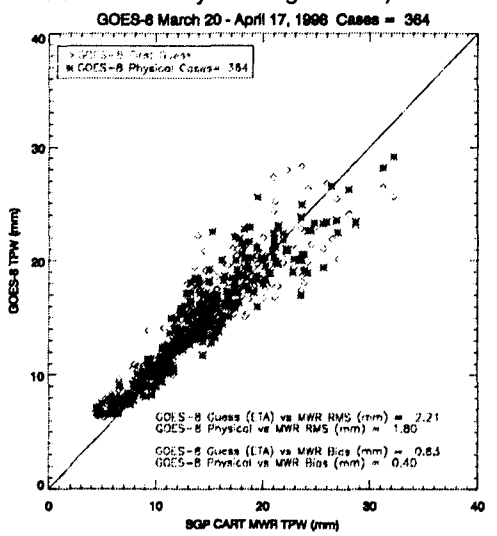

Figure 2: A scatter plot comparing MWR total water vapor values to the Eta model forecast (diamond symbols) and the GOES-8 physical retrieval (star symbols) values. RMS and bias for all matches are quantified in the lower right hand corner.

The DOE ARM microwave radiometer data has provided a valuable stable validation source for space-borne total precipitable water measurements at high temporal resolution. These data are also used to derive the post-launch tests for GOES (Daniels and Schmit 2001). Real-time TPW validation has been implemented at SSEC CIMSS UW-Madison to provide near instantaneous meteorological satellite product evaluation. More information about the evaluation of GOES TPW can be obtained in Schmit et al 2001.

3. GOES CLOUD TOP VALIDATION

A consensus cloud boundary product has been developed for the DOE ARM sites by using combined cloud information from the Microwave Millimeter Cloud Radar (MMCR) and MicroPulse Lidar (MPL). This product was used to validate hourly GOES sounder derived cloud top pressures for March 2000 at the central facility DOE ARM SGP near Lamont, Oklahoma. The DOE ARM cloud boundary data has a time resolution of 10 seconds and is determined over a narrow column of atmosphere over Lamont, Oklahoma. The GOES cloud product is derived from 3x3 FOV and provides an average cloud top pressure as well as minimum and maximum pressures. The technique for determining the GOES cloud top pressure is described in Schreiner et al. 2001. Due to the high temporal and spatial resolution of the DOE ARM cloud boundary product, five minute binning of this product on either side of an hourly GOES determined cloud top was done to minimize resolution discrepancies between the ground-based and space-borne cloud top determination. To simplify the comparison, multiple layered cloud scenes where removed from the samples. This was determined in the GOES 3x3 FOV by analysis of the minimum and maximum cloud top pressure altitude. Cloud top altitude differences of 2 km or less were used within the analysis generally providing uniform cloud top cases.

After accounting for spatial and temporal resolution differences and filtering multiple layer cloud cases, 73 matches between hourly GOES and 10 second MMCR/MPL cloud products were determined for March 2000 near Lamont, Oklahoma (Figure 3). A high correlation of 0.93 with an RMS of 930 meters was calculated. The two outliers in the figure are probably due GOES inability to detect very thin cirrus clouds with low emissivity/optical depth. This study will be expanded to use data for all months in the year 2000 to provide a more robust comparison and provide insight for GOES cloud top pressure altitude algorithm improvement. For more information on this study, view Hawkinson et al. 2001 (presented in these proceedings).

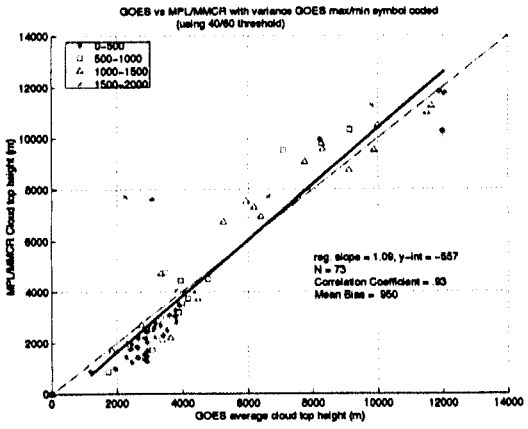

Figure 3: A scatter plot comparing DOE ARM ground-based MPL/MMCR and space-borne GOES derived cloud top altitude after resolution binning and multiple level clouds are removed. A correlation coefficient of 0.93 and a mean bias of 950 m was determined.

4. CONCLUSIONS

DOE ARM data have become an important validation sources for geostationary and polar orbiting satellite platform sounder instrumentation. GOES TPW and cloud top products are being extensively evaluated with the data. GOES cloud top estimates have shown a correlation of 0.93 and RMS differences of approximately one kilometer. The GOES moisture retrieval algorithm improves the precipitable water values from the ETA model first guess by 0.4 millimeters in both an RMS and mean statistical sense as compared the a DOE ARM microwave radiometer. A best estimate product for temperature and moisture derived from DOE SGP site Raman Lidar, AERI, MWR, and radiosonde information is currently providing a way to evaluate EOS Terra (and soon EOS Aqua) overpass radiance calibration (see Wetzel et al. 2001 in these conference proceedings). The DOE ARM NSA and TWP sites will be extensively used to evaluate cloud and thermodynamic retrievals for EOS AIRS and MODIS polar orbiting overpasses in the near future.

5. ACKNOWLEDGEMENTS

This research was supported by the NOAA Grant NA67EC0100. Data were obtained from the Atmospheric Radiation Measurement (ARM) Program sponsored by the U.S. Department of Energy, Office of Science, Office of Biological and Environmental Research, Environmental Sciences Division.

6. REFERENCES

Daniels, J. M., T. J. Schmit, 2001: GOES-11 Science Test: GOES-11 Imager and Sounder Radiance and Product Validations. NOAA Technical Report, In press.

Hawkinson, J., W. F. Feltz, T. Schmit, A. J. Schreiner, S. Ackerman, 2001: A Validation Study of the GOES Sounder Cloud Top Pressure Product Preprints, *Eleventh Conference on Satellite Meteor. And Oceanography,* 15-18 October, 2001, Madison, WI.

Liljegren, J. C., 1994: Two-channel microwave radiometer for observations of total column precipitable water vapor and cloud liquid water path. Preprints, *Fifth Symp. of Global Change Studies,* Nashville, TN.

------, 1995: Observations of total column precipitable water vapor and cloud liquid water using a dual-frequency microwave radiometer. *Microwave Radiometry and Remote Sensing of the Environment,* D. Solimini, Ed., Utrecht, VSP (Vista Science Press), 107-118.

Ma, Xia L., T. J. Schmit, W. L. Smith, 1999: A nonlinear physical retrieval algorithm—its application to the GOES-8/9 sounder. *J. Appl. Meteor.* **38**, No. 5, 501-513.

Menzel, W. P., F. C. Holt, T. J. Schmit, R. M. Aune, G. S. Wade, D. G. Gray, A. J. Schreiner, 1998: Application of GOES-8/9 Soundings to weather forecasting and nowcasting. *Bull. Amer. Meteor. Soc.* **79**, 2059–2078.

Schreiner, A.J., T.J. Schmit, and W.P. Menzel, 2001: Observations and trends of clouds based on GOES sounder data. Journal of Geophysical Research-Atmospheres, Accepted for publication March 2001.

Schmit, T. J., W. F. Feltz, W. P. Menzel, J. Jung, A. P. Noel, J. N. Heil, J. P. Nelson III, Gary S. Wade, 2001: Validation and use of GOES Sounder Moisture Information, Wea. And Fore., In Review.

Stokes, G. M., and S. E. Schwartz, 1994: The Atmospheric Radiation Measurement (ARM) program: Programmatic background and design of the cloud and radiation testbed. *Bull. Amer. Meteor. Soc.*, **75**, 1201-1221.

Wetzel-Seeman S., D. Tobin, L. E. Gumley, C. Moeller, W. P. Menzel, T. J. Schmit, M. Gunshor, 2001: Comparison of MODIS/TERRA radiances with GOES-8, GOES-10, and DOE ARM CART site. Preprints, *Eleventh Conference on Satellite Meteor. And Oceanography,* 15-18 October, 2001, Madison, WI.

P4.21 VALIDATION OF A GLOBAL CLOUD LIQUID WATER PRODUCT FROM AVHRR

Andrew K. Heidinger
NOAA/NESDIS Office of Research and Applications *

Quanhua Liu
Cooperative Institute for Research in the Atmosphere(CIRA)

1. INTRODUCTION

Imagers such as the Advanced Very High Resolution Radiometer (AVHRR) provide high spatial resolution data in spectral regions from the visible to the infrared window. Algorithms have become well-accepted that use a visible reflectance, a near-infrared reflectance and a brightness temperature from a thermal window channel to derive cloud optical depth, cloud particle size and cloud-top temperature. The work of Platnick and Valero(1995) provide a brief history of these algorithms up to 1995.

In this abstract, we present an algorithm which derives the statistical distribution of the cloud optical depth over a large region (a grid-cell) based on the statistical distribution of the visible reflectance and the mean values of other channel observations. This algorithm also estimates the mean cloud particle size and cloud-top temperature. The global validation of this algorithm is ongoing and this abstract serves as an illustration of its methods. One example retrieval is shown to highlight the type of information it provides.

The motivation to develop an algorithm such as this is that the pixel-scale retrievals of cloud properties are computationally expensive. The only pixel-scale processing needed for this algorithm is the application of a cloud mask and the accumulation of the grid-cell reflectance/radiance statistics. The goal of this work is develop an algorithm which can produce global cloud properties in real-time and can be used to efficiently reprocess the AVHRR data-record into new cloud climatologies which reflect ongoing improvements in cloud radiative transfer.

1 Methodology

Inspection of a single-layer cloud field within a grid-cell reveals that the cloud-top particle size and cloud top temperature typically do not vary significantly while the cloud optical depth can vary greatly. To illustrate this point, the results for a single grid-cell are analyzed. Fig. 1 shows the distribution of NOAA16 AVHRR GAC ch1 (0.63 μm) reflectance a stratus cloud field off the coast of California. Fig. 2 shows the ch1 values for one grid-cell that is outlined in Fig. 1. This grid-cell has a spatial resolution of 110 km which is the resolution of the AVHRR Pathfinder Atmospheres (PATMOS) data-set and is the resolution used for the global implementation of this algorithm. Plane parallel retrievals of the optical depth, τ, effective radius, r_e and the cloud-top temperature T_c where performed on each pixel determined to be cloudy. This resulted in over 600 retrievals for this one grid-cell. Fig. 3 shows the distributions of τ, r_e and T_c for this grid-cell. This distributions are normalized to have maximum of unity and the values of T_c are offset by 260 K to allow for plotting on the same axes.

Based on analysis of data as shown in Fig. 3, we make the assumption that a representative description of the cloudiness for a single cloud layer within a grid-cell can be given by the mean values of r_e and T_c and the distribution τ. The algorithm we have developed provides this information on global and real-time basis.

To model the statistical distribution of cloud optical depth in a grid-cell, $p(\tau)$, a modified Γ distribution is assumed and the form used is

$$p(\tau) = \frac{1}{\Gamma(\nu)} \left(\frac{\nu}{\bar{\tau}}\right)^{\nu} \tau^{\nu-1} \exp^{-\frac{\nu\tau}{\bar{\tau}}} \qquad (1)$$

where τ is the optical depth, ν is the width parameter, and $\bar{\tau}$ is the mean optical depth. The standard deviation of τ, σ_τ, is given by $\left(\frac{\bar{\tau}}{\nu}\right)^2$. The justification for the choice of the Γ distribution is given by inspection results similar to Fig. 3 and by the work of Barker et al. (1996) where many high spatial resolution cloud optical depth fields were produced from LandSat data using pixel-level retrievals. Barker et al. (1996) divided the LandSat scenes into three classes (A: Overcast Stratocumulus, B: Broken Stratocumlus, C: Scattered Cumulus). The ranges in $\bar{\tau}$ the for cases A,B and C were 5.6-20.5, 3.4-15.6,

* *Corresponding author address:* Dr. Andrew K. Heidinger, NOAA/NESDIS Office of Research and Applications, Washington, DC 20746-4304, USA; e-mail: andrew.heidinger@noaa.gov

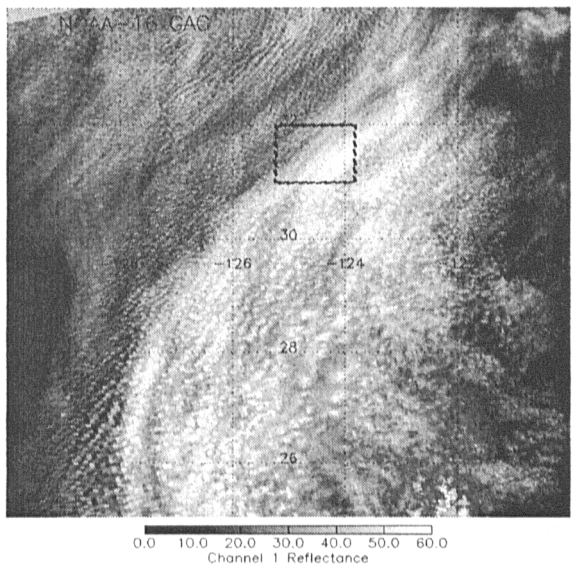

Figure 1: AVHRR Ch1 reflectance from NOAA-16 for a stratus cloud field off the coast of California

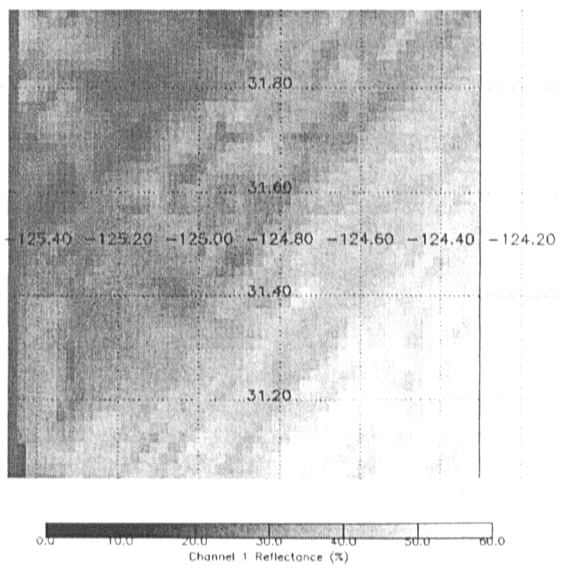

Figure 2: Variation of ch1 reflectance for grid-cell outlined in Fig. 1

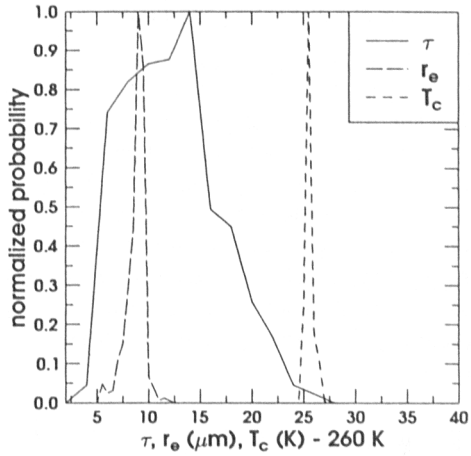

Figure 3: Histograms of pixel-level retrievals for τ, r_e, and T_c for grid-cell outlined in Fig. 1

1.0-12.1. The ranges in ν the for cases A,B and C were 1.6-22.5, 0.74-1.7 and 0.2 - 1.9. A similar study for non-boundary layer clouds has not been undertaken. However as long as the reflectance distributions from cloudy pixels are mono-model, a Γ distribution should adequately model the distribution of τ.

2 Retrieval Methodology

To retrieve the cloud parameters, a one-dimensional variational (1D-var) technique is used. In this retrieval 4 parameters are being estimated from 4 observations. A 1D-var approach was selected since more traditional iterative approaches such as applied by (Han et al. 1994) were found to offer no advantage in speed or in convergence. A 1D-var approach also offers the benefits of ensuring the retrievals are consistent with the forward models and the known uncertainty of the measurements.

The form of the 1D-var retrieval methodology used here is taken from Rodgers (1976). Using Rodger's notation, the vector of measurements, $\tilde{y}$, for this algorithm is given by

$$\tilde{y} = (R_1, R_{3a}, E_4, \sigma_1)$$

where R_1 is the mean channel 1 reflectance, R_{3a} is the mean channel 3a reflectance, E_4 is the mean channel 4 radiance, and σ_1 is the standard deviation of the channel 1 reflectance. The mean and

standard deviations are defined for all cloudy pixels of the same cloud type within a grid-cell.

The vector of estimated parameters, x, is defined as

$$\tilde{x} = (\bar{\tau}, r_e, T_c, \nu)$$

where $\bar{\tau}$ is the mean optical depth, r_e is the effective radius, T_c is the mean cloud-top temperature and ν is the width of $p(\tau)$. In addition, this retrieval method requires the definition of *a priori* estimates of $\tilde{x}$ which are derived based on representative values for each cloud type. The final solution is an optimal estimate of $\tilde{x}$ that reflects the uncertainties in the measurements, the forward models and the *a priori* parameters.

2.1 Forward Modeling

The goal of the forward models put forth here is to simulate the true behavior of cloud fields within grid-cells well enough to allow for meaningful estimation of their properties. Since global, faster than real-time processing is required of this algorithm, true radiative transfer models are approximated by lookup tables. The forward models described here are similar to the forward models used in pixel-scale retrievals except that the width of the τ distribution for a grid-cell, ν, is used. The forward models described below provide the vector, $\tilde{f}$, which contains the forward model estimate of $\tilde{y}$ and the kernel matrix, $\tilde{K}$ where each element contains $\frac{\partial f}{\partial x}$.

2.2 Modeling Solar Reflectance

To model the observed solar reflectance, a lookup table is computed using an adding/doubling model for the reflectance of an plane parallel cloud above a dark surface with no other atmospheric effects, R_c. Once the lookup tables for single layer plane parallel clouds are made, lookup tables with the additional dimensions of ν and surface reflectance, a_s, are made. To compute the top of atmosphere reflectance for a plane parallel cloud above a reflecting surface, the following expression taken from Chandrasekhar (1960) is used.

$$R = t_{ac}^m \left(R_c + \frac{T(\mu) a_s' T(\mu_o)}{1 - a_s' \alpha_{sph}} \right) \qquad (2)$$

where α_{sph} is the spherical albedo of the cloud layer, t_{ac} is the nadir transmission from the top of atmosphere to cloud-top, and m is the airmass factor $(\frac{1}{\mu} + \frac{1}{\mu_o})$. The terms $T(\mu)$ and $T(\mu_o)$ are the flux transmissions through the cloud layer (direct and diffuse) for a solar beam incident at zenith angles defined by μ and μ_o. The modified surface albedo,a_s', accounts for absorption between the cloud and the surface and is approximated as

$$a_s' = t_{bc}^m a_s$$

t_{bc} is the nadir transmission from the cloud to the surface.

The final mean reflectance for a distribution of optical depth, $\bar{R}(\bar{\tau}, \nu)$ is given by integrating (2) over the assumed $p(\tau)$ to give

$$\bar{R}(\bar{\tau}, \nu) = \int_0^\infty R_{pp}(\tau) p(\tau) d\tau \qquad (3)$$

with the standard deviation, σ_R being computed as

$$\sigma_R = \sqrt{\int_0^\infty \left(\bar{R}(\bar{\tau}, \nu) - R_{pp}(\tau) \right)^2 p(\tau) d\tau} \qquad (4)$$

The result of these computations are lookup tables for the mean and the standard deviation in reflectance as a function of the cloud properties, τ, r_e, ν, the surface reflectance, a_s, and the viewing geometry, $\mu, \mu_o, \phi_o - \phi$.

2.3 Modeling Thermal Emission

In a similar manner to modeling of solar reflectance, an adding/doubling model is used to compute the emissivity, ϵ_c and transmissivity, t_c, for an isolated isothermal cloud. The emissivities and transmissivites include the effects of scattering within the cloud layer. Values of the mean emissivity and transmissivity are computed using the plane parallel lookup tables and equation (3).

Once the lookup tables of emissivity and transmissivity are made as functions of $\bar{\tau}, \nu, r_e$ and θ, the cloud layer is embedded in a non-scattering atmosphere to model to the top of atmosphere radiance using the following relation.

$$E = E_{ac}(1 - t_{ac}^m t_c) + t_{ac}^m \left(\epsilon_c B(T_c) + t_c E_{clear} \right) \qquad (5)$$

where E_{clear} is the clear-sky radiance, E_{ac} is the emitted radiance from the layer above the cloud, and m is airmass for emitted radiation $(\frac{1}{\mu})$. To account for the lapse rate within the cloud, the cloud emissivity is redefined. Using a linear-in-depth variation of the emission through the cloud, a modified emissivity of the cloud, ϵ_c' can be computed to account for temperature variations using the following relation.

$$\epsilon_c' = \epsilon_c \left(1 - \frac{B_n}{B_o} e^{-\tau/\mu} + (1 - e^{-\tau/\mu}) \frac{(B_n - B_o)}{\tau B_o} \right.$$

where B_n and B_o are the black-body emitted radiances at the cloud top and cloud base.

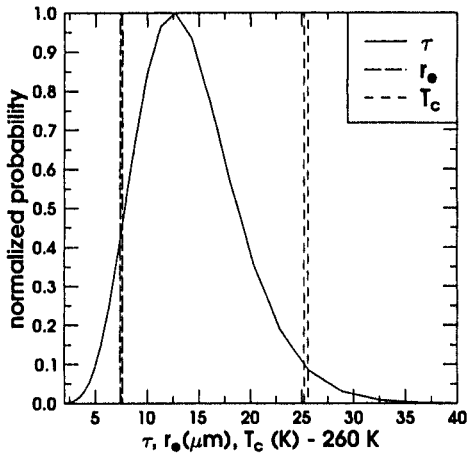

Figure 4: Results of grid-cell retrieval for τ, r_e, and T_c for grid-cell outlined in Fig. 1

3 Results

To illustrate how the retrieval works, the retrieval results for the grid-cell outlined in Fig. 1 are shown. This grid-cell consisted of only one layer of cloud. The pixel-level retrievals shown in Fig. 3 gave the values shown in Table 1. The values from the grid-cell retrieval are also shown in Table 1. The distribution of τ shown in Fig. 3 is computed from the retrieved values of $\bar{\tau}$ and ν.

	pixel	grid-cell
$\bar{\tau}$	13.5	12.6
ν	8.0	7.4
r_e	9.0	7.5
T_c	285.2	285.5

Table 1: Comparison of retrieved cloud properties using the grid-cell retrieval and the pixel-level retrieval for grid-cell outlined in Fig 1.

As the results in Table 1 indicate, differences can exist between the grid-cell and the pixel-level retrieval for some grid-cells. In this example, the mean effective radius from all the pixel-level retrievals in this grid-cell was 1.5 μm larger than the value estimated by the grid-cell retrieval. The differences between the two approaches do not appear to be biased in any one direction. Work is ongoing to understand the reason and physical meaning of the differences between the grid-cell and pixel-level retrievals.

4 Conclusions

A retrieval has been developed to produce real-time cloud products from AVHRR. A preliminary global implementation of this algorthm has already been performed using NOAA-16 AVHRR data. A global validation of these cloud products including the derived cloud liquid water path is being undertaken. This validation includes comparison with cloud properties from microwave sensors. Other areas of research include the optimal combination of the AVHRR products with those from microwave sensors. This work is supported by the NOAA/NASA Joint Center for Data Assimilation.

5 References

Barker, H. B. Wielicki, L. Parker, 1996: A parameterization for computing grid-averaged solar fluxes for inhomogeneous marine boundary layer clouds. Part II: Validation using satellite data. *J.Atmos. Sci.*, **53**, 2304- 2316.

Chandrasekhar, 1960: *Radiative Transfer.* Dover Publications Inc., 393 pp.

Platnick, S and F. P. J. Valero, 1995: A validation of a satellite cloud retrieval during ASTEX. *J. Atmos. Sci.*, **52**, 2985-3001.

Rodgers, C. D., 1996: Retrieval of atmospheric temperature and composition from remote measurements of thermal radiation. *Rev. Geophys. Space. Phys.*, **14**, 609-624.

P4.22

AEROSOL OPTICAL PROPERTY RETRIEVALS FROM VIS-SWIR DATA

J.W. Snow *, M.K. Griffin, H.K. Burke, and C.A. Upham
MIT Lincoln Laboratory, Lexington, Massachusetts

1. INTRODUCTION

Two over-land aerosol retrieval algorithms are compared – the current dense-dark vegetation (DDV) algorithm, and another using a general VIS-SWIR reflectance correlation and scatter-plot analysis, called here the vegetation scatter plot (VSP) technique. Comparisons of retrieved aerosol optical thickness values are made with concurrent AERONET measurements (Holben et al, 1998).

Data used in the retrievals are radiances from three bands of the DOE Multispectral Thermal Imager (MTI) (Kay et al. 1999). The DOE MTI is a well-calibrated 15-band pushbroom imager having the spectral and spatial parameters listed in Table 1. It is in a sun-synchronous 575 km orbit, 1300 local ascent, producing near-nadir images of 12x12 km^2.

Table 1. MTI Sensor Characteristics. Bands A, C, and O used in analyses.

Band	Band (μm)	Color	GSD
A	**0.45 – 0.52**	**Blue**	**5 m**
B	0.52 – 0.60	Green	5 m
C	**0.62 – 0.68**	**Red**	**5 m**
D	0.76 – 0.86	NIR	5 m
E	0.86 – 0.89	NIR	20 m
F	0.91 – 0.97	NIR	20 m
G	0.99 – 1.04	SWIR	20 m
H	1.36 – 1.39	SWIR	20 m
I	1.54 – 1.75	SWIR	20 m
O	**2.08 – 2.37**	**SWIR**	**20 m**
J	3.49 – 4.10	MWIR	20 m
K	4.85 – 5.05	MWIR	20 m
L	8.01 – 8.39	LWIR	20 m
M	8.42 – 8.83	LWIR	20 m
N	10.2 – 10.7	LWIR	20 m

The MTI data used here were taken with clear atmospheric conditions on 22 Aug 00 in the vicinity of Pilgrim Power Plant, Plymouth, MA. Fig 1 is the MTI Band O SWIR near-nadir image of the area.

Corresponding author address: J.W. Snow, MIT Lincoln Laboratory, 244 Wood St., Lexington, MA 02420-9108; e-mail: snow@ll.mit.edu.

MTI inter-band pixel registration is within 3 m and for the aerosol algorithm comparison each set of four contiguous Band A or C pixels is averaged to be equivalent to one coincident Band O pixel.

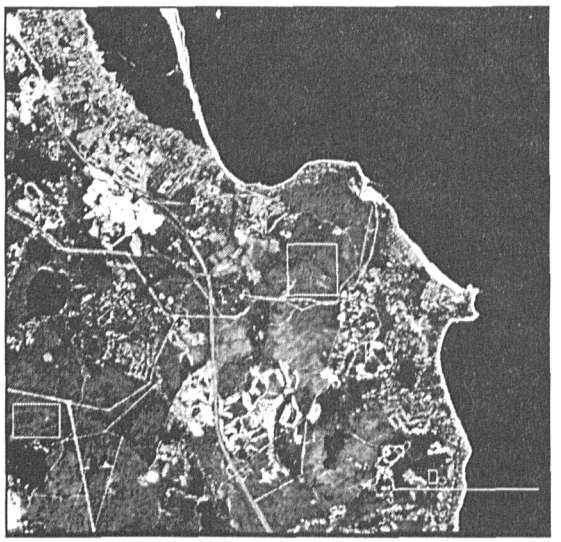

Figure 1. MTI SWIR Grey-Scale Radiance Image in the area of Plymouth, MA, at approximately 1315 local solar time on 22 Aug 2000.

A single cross-coast transect of measured radiances converted to top-of-atmosphere (TOA) reflectances ρ^{T}_{λ} by the standard procedure, is shown as Fig 2.

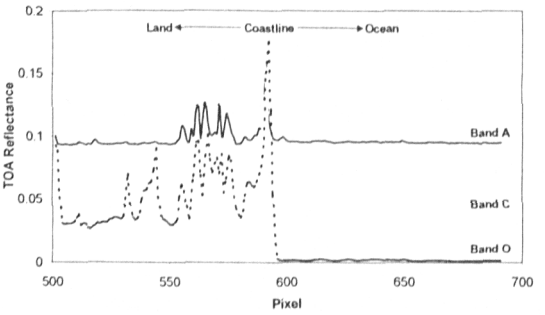

Figure 2. Cross-Coast Transect of TOA Reflectance for Bands A, C, and O from the MTI (ref. Fig 1).

The DDV method for specifying surface reflectance in aerosol retrievals over land is to identify dense-dark vegetation pixels and assign the VIS surface reflectances (blue and red) based upon top-of-atmosphere reflectance measured in the SWIR

window band (~2.2 μm), where aerosol attenuation is minimal (Kaufman et al. 1997). It requires the presence of narrowly defined dense-dark vegetation pixels, assignment of SWIR surface reflectance ρ^S_{swir} as equivalent to the measured TOA value ρ^T_{swir}, and specific relationships between surface reflectances for DDV – $\rho^S_{blue} = 0.25\ \rho^S_{swir}$ and $\rho^S_{red} = 0.50\ \rho^S_{swir}$. The DDV algorithm is the MTI program baseline for aerosol retrieval (Villeneuve and Borel, 1998).

Recent modification by Wen et al. (1999) widens the DDV definition allowing VIS and SWIR surface reflectances to be linearly related by locally adjustable coefficients, specific., $\rho^S_{blue} = \xi_{blue}\ \rho^S_{swir}$ and $\rho^S_{red} = \xi_{red}\ \rho^S_{swir}$. The ξ's are evaluated from analysis of scatter plots of TOA VIS versus SWIR reflectance data for various vegetated surfaces. This general VIS-SWIR surface reflectance model and scatter-plot analysis technique, referred to as VSP, enables more extensive over-land aerosol optical property retrievals.

This paper briefly summarizes both retrieval techniques, then defines the scatter-plot analysis formulas and an iterative procedure for retrieving aerosol optical properties using the VSP technique. Finally, both DDV and VSP algorithms are applied to MTI data for comparison.

2. REFLECTANCE COMPONENT EQUATION

Tropospheric aerosol property retrieval from TOA data involves solving some form of atmospheric RT equation. TOA reflectance is expressible as a sum of components – basically a 1-D (vertical in units of optical-thickness) boundary-value RT equation that places aerosols and water vapor together in the lower troposphere. It relates three reflectance components $\rho^{R,A,S}$, Rayleigh, aerosol, and surface, to the TOA measured reflectance ρ^T through various transmittances t^X. Specifically,

$$\rho^T_\lambda = t^G_\lambda [\rho^R_\lambda + t^R_\lambda (t^{W/2}_\lambda \rho^A_\lambda + t^A_\lambda t^W_\lambda \rho^S_\lambda)] \qquad (1)$$

Eq (1) is spectral, with effective wavelength indicated by the subscript. All transmittances are total (direct plus diffuse) and two-way. Specifically, $t^{G,R,A,W,W/2}$ are the total two-way transmittances due to fixed gases (esp. O_3 and CO_2 absorption), to Rayleigh molecules, aerosols, and to total-column and half-total-column water vapor content.

2.1 Thin Atmosphere Approximations

To apply Eq (1) in the inverse sense of retrieving aerosol optical properties requires expressions for ρ^A and t^A. For small aerosol optical thickness τ^A, the single-scattering approximation for aerosol reflectance is adequate, $\rho^A_\lambda = P(\Theta)\omega_\lambda\tau^A_\lambda/4\mu\mu_o$. The single-scattering phase function P(Θ) must be otherwise known. For the near-nadir MTI image in the Pilgrim Power Plant vicinity on 22 Aug 00, the scattering angle is $\Theta \equiv 147^o$. For non-smoke aerosols of modest amount ($\tau^A < 0.4$), the value P(147) = 0.215 is representative (Kaufman et al, 1997, fig 9, continental-urban aerosol, λ = 0.67 μm). Also, P(Θ) is assumed to have negligible spectral variation in the visible to near-infrared region.

Likewise for small τ^A, an approximation of the two-stream solution is used for the aerosol two-way total transmittance, viz., $t^A_\lambda \equiv 1-[1-\omega_\lambda(1-b)]m\tau^A_\lambda$, where $m = (1/\mu_o+1/\mu)$. The back-scattering fraction b has been measured for the tropospheric aerosol most common along the U.S. east coast, specific., b = 0.245 (Kaufman and Holben, 1996, fig 6). Also, measurements demonstrate little spectral variation in b, at least in the range $0.5 < \lambda < 1.0$ μm.

Incorporating these approximations for ρ^A_λ and t^A_λ, Eq (1) is the thin-atmosphere equation used here.

2.2 Aerosol Property Spectral Models

The multi-spectral application of Eq (1) involves band-to-band relationships for spectrally varying aerosol and surface properties. These spectral models are: the common Angstrom relationship, $\tau^A_j/\tau^A_k = (\lambda_k/\lambda_j)^\alpha$, a ω-model in water-vapor windows, $\omega_j = \omega_k - \beta\ \ln(\lambda_j/\lambda_k)$, and a surface reflectance coefficients model, $\xi_j = \gamma\ \xi_k$. The subscript k implies a reference band, esp. λ_k is a wavelength for which τ^A_k or ω_k is known or has a prescribed value.

Each spectral model includes a parameter: α the Angstrom exponent, β the aerosol absorption parameter [since for $\omega_k = 1$, $\beta \sim (1-\omega_j)$], and γ the surface reflectance parameter. While the Angstrom exponent α is familiar, β and γ are not. Depending on the multi-spectral algorithm, values of these parameters are assigned or result from the retrieval process. E.g., for the DDV algorithm, $\gamma = \xi_{red}/\xi_{blue} \equiv 2.000$, the ω-values (via ω_k and β) are assigned, and α results from the retrieval. For VSP, values for the three parameters are initially estimated and then, for γ and α, are optimally evaluated during the iterative retrieval process. Regarding assignment of β, the maximum value $\omega_k = 1$ occurs for most aerosol types within the range $0.40 \le \lambda_k \le 0.60$ μm; $\lambda_k = 0.475$ μm is selected. For moderately water-soluble aerosols at λ = 0.80 μm, $\omega_{0.80} = 0.940$ (d'Almeida et al, 1991, table A.9). The resulting value, used in both aerosol algorithms, is $\beta = 0.115$.

3. DENSE-DARK VEGETATION TECHNIQUE

The DDV land surface reflectance relationships, in MTI notation (Table 1), are $\rho^S_A = 0.25\ \rho^S_O$ and $\rho^S_C = 0.50\ \rho^S_O$. The selection of DDV pixels is critical to the technique. Thresholds on 2.2 μm reflectance of

$\rho^T_O < 0.05$, and uncorrected normalized difference vegetation index of NDVI > 0.50, are here used to identify the DDV pixels. Although the Band O aerosol effect is unknown, it is very small, and further, the two aerosol effects – reflectance and absorption – counteract each other resulting in a very small net aerosol effect, i.e., $\Delta\rho^T_O \leq \pm 0.0005$.

Inland about 1.5 km from the Pilgrim Power Plant is a coast-parallel 120 m wide strip that qualifies as strictly defined DDV. For this, the average value of ρ^T_O is 0.03307 and the uncorrected measured-radiance NDVI is 0.588. Estimation of VIS surface reflectances $\rho^S_{A,C}$ is from $\rho^T_O/\Pi_O = 0.03977$, where $\Pi_O \equiv t^G_O t^R_O t^W_O$. [All fixed-atmosphere transmittance and reflectance values are from MODTRAN-4 (Berk et al. 1999).] When reduced by slight Rayleigh reflectance the result is $\rho^S_O = 0.03959$, ignoring any unknown but small SWIR aerosol effects. Therefore, $\rho^S_C = 0.0198$ and $\rho^S_A = 0.0099$.

The evaluation of $\tau^A_{A,C}$ is then straightforward for single-scattering conditions, with the provision that realistic values of $\omega_{A,C}$ are available. Using the spectral ω-model in Sect 2.2, with $\beta = 0.115$, the values in Table 2 are generated. In turn, the thin-atmosphere form of Eq (1) provides $\tau^A_{A,C}$ in Table 2, with resulting Angstrom exponent of $\alpha = 0.05$.

TABLE 2. DDV Spectral Values

$\theta_o = 30.4°$, $\theta = 13.0°$, $\Theta = 147°$

Measured, Assigned ⟨ ⟩, Retrieved Quantities

λ	L^T	$(L^T$-to-$\rho^T)$	ρ^T	ρ^S	⟨ω⟩	τ^A
A	49.956	18.708	0.09345	0.0099	0.998	0.200
C	20.435	23.568	0.04816	0.0198	0.964	0.197
O	0.7142	463.14	0.03307	0.0396	----	----

Radiance $L(Wm^{-2}\,\mu m^{-1}\,sr^{-1})$; L-to-ρ factor x 10^4.

4. VEGETATION SCATTER-PLOT TECHNIQUE

The un-prescribed linear correlation between VIS and SWIR reflectance is, in MTI band notation, $\rho^S_A = \xi_A \rho^S_O$ and $\rho^S_C = \xi_C \rho^S_O$. In the retrieval of aerosol properties, values of the ξ's can vary considerably for different vegetated surfaces and still be useful.

In Fig 3 are scatter plots of individual pixel values of the MTI data – $\rho^T_{A,C}$ vs. ρ^T_O – for a 1 km^2 vegetated area that is not DDV. This area is the square near the center of Fig 1. The presumed linear surface reflectance correlations – ρ^S_A vs. ρ^S_O and ρ^S_C vs. ρ^S_O – are evident in the TOA reflectances since both Rayleigh and aerosol path-reflectance components are basically constants, independent of ρ^S, at least for small τ^A. Increasing $\rho^T_{A,C}$ with increased ρ^T_O is due to the concurrent increases in VIS surface reflectance components – but these as attenuated by aerosol, Rayleigh, and absorbing gas. As in Wen et al. (1999, fig 4), slopes decrease with increasing τ^A; the same is true for any attenuating constituent τ^X. Thus, in Fig 3 the slope of the blue (A) best-fit line is less than the red (C) line due mainly to $\tau^R_A > \tau^R_C$, as well as to $\xi_A < \xi_C$.

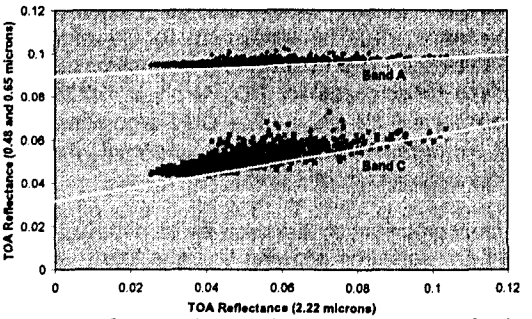

Figure 3. Scatterplots of MTI pixel values of TOA reflectances, $\rho^T_A : \rho^T_O$ and $\rho^T_A : \rho^T_O$, for contiguous 1 km^2 area of mixed vegetation (MTI pixel size 20 m^2). Slope and intercept values: $S_A = 0.0861$, $S_C = 0.3045$, $I_A = 0.0895$, $I_C = 0.0319$.

4.1 Slope and Intercept Formulas

The SWIR form of Eq (1), is just $\rho^T_O \equiv \Pi_O \rho^S_O$, since ρ^R_O and $\rho^A_O \equiv 0.000$, and t^R_O and $t^A_O \equiv 1.000$. So, to a good approximation, $\Pi_O = t^G_O t^W_O$, and, $\rho^S_O \equiv \rho^T_O / \Pi_O$. Since $\rho^S_j = \xi_j \rho^S_O$, then $\rho^S_j = \xi_j \rho^T_O / \Pi_O$. In the thin-atmosphere form of Eq (1), this enables evaluation of the slope and intercept values. In particular, the slope equations, $\Delta\rho^T_j/\Delta\rho^T_O \equiv S_j$, are

$$S_{j\,(j=A,C)} = \Pi^+_j \{1 - [1 - \omega_j(1-b)]\, m\, \tau^A_j\}\, \xi_j \qquad (2A)$$

where the symbol $\Pi^+_j \equiv [t^G_j t^R_j t^W_j / t^G_O t^R_O t^A_O t^W_O]$, the t^R_O and t^A_O values retained to improve accuracy.

The intercepts are ρ^T_j (at $\rho^S_O = 0.000$) $\equiv I_j$. The condition ρ^S_O = zero means that both ρ^S_A and ρ^S_C are also zero – yielding the intercept expressions,

$$I_{j\,(j=A,C)} = t^G_j \rho^R_j + t^G_j t^R_j t^{W/2}_j [P(\Theta)/4\mu\mu_o]\, \omega_j \tau^A_j \qquad (2B)$$

4.2 VSP Retrieval Procedure

The ratios and differences of the S's and I's are integral to the VSP technique. An outline of these, as used to derive needed parameters and aerosol properties themselves (* includes α, β, γ values), consists of the six quantities: $I_A/I_C \rightarrow \alpha$, $S_C/S_A \rightarrow \gamma$, $(I_C - I_A) \rightarrow \beta$, $S_j^* \rightarrow \xi_j$, $S_A^*/S_C^* \rightarrow \tau^A$, $(S_C^* - S_A^*) \rightarrow \omega$.

With measurement values for S_A, S_C, I_A, and I_C from the Fig 3 scatter-plot analyses and given values for $P(\Theta)$, b, and initially β, then Eqs (2A, B) constitute four equations in six unknowns: (τ^A_A, τ^A_C), (ω_A, ω_C), and (ξ_A, ξ_C). Introducing the three spectral models from Sect 2.2, with the objective of eliminating Band A quantities – Band C (red) containing more equally both the effects of aerosol scattering and absorption – then, α, β, γ replace the Band A values. But α and γ are estimated from ratios of

known quantities. Eqs (2A, B) are now solvable for t^A_C, ω_C, and ξ_C. The sequential steps of the multi-spectral retrieval procedure are in Fig 4.

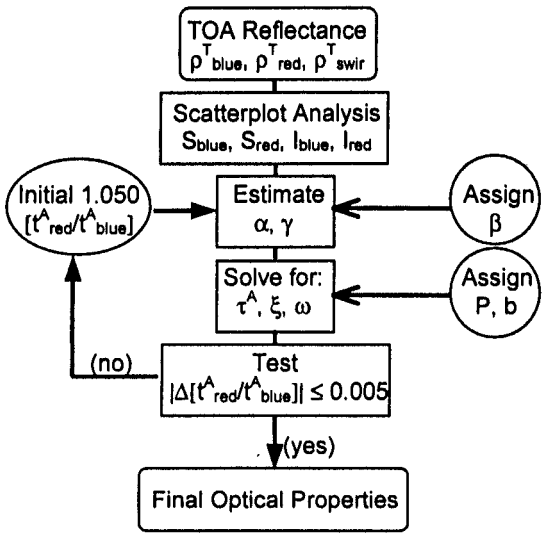

Figure 4. Aerosol Retrieval Using VSP Technique.

4.3 Application

The VSP technique is applied for three separate vegetated areas found in the 22 Aug 00 MTI image (two shown as squares in Fig 1). It is assumed that prevailing aerosol conditions are the same for all areas. The retrieval products are given in Table 3.

Table 3. VSP Computed Spectral Values; 3 Areas.

λ	ξ(λ)	γ	ω(λ)	β	τ(λ)	α
A	.129	3.06	.960	.115	.206	2.07
C	.395		.886		.112	
A	.155	2.93	.944	.115	.223	1.88
C	.455		.925		.128	
A	.069	3.27	.992	.115	.239	1.58
C	.226		.977		.150	

5. DISCUSSION

Two over-land VIS-SWIR aerosol retrieval algorithms, dense-dark vegetation (DDV) and vegetated scatter-plot (VSP), are discussed and applied to MTI data. Surface-based AERONET measurements are also used for comparison. Overall, as seen in Fig 5, good agreements are found. Both DDV and VSP retrieved τ^A_{blue} values are comparable with AERONET measurements. DDV value for τ^A_{red} is > 50% higher than the VSP or AERONET values, which implies a very different aerosol type. Of the two, VSP appears to capture the spectral variability in aerosol extinction, at least in the thin aerosol condition dealt with here.

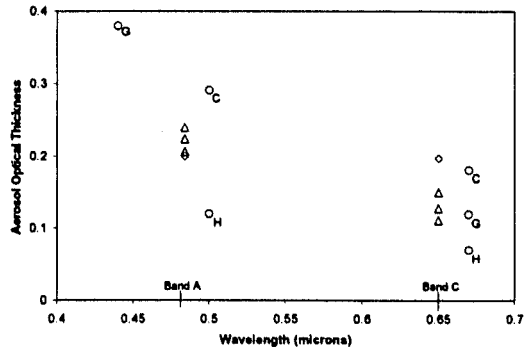

Figure 5. Comparison of retrieved and measured values of aerosol optical thickness from MTI data (◇ for DDV, Δ for VSP). Measurements from AERONET locations: Howland, ME (O_H), Cartel, VT (O_C), GISS, NY (O_G), are used for comparison. Based on the prevailing atmospheric conditions, these AERONET measurements are representative of the aerosol conditions at the Plymouth site.

6. REFERENCES

d'Almeida, G.A., P. Koepke, and E.P. Shettle, 1991: Atmospheric aerosols: global climatology and radiative characteristics. Deepak Pub., 561 pp.

Berk, A., and Coauthors, 1999: MODTRAN-4 User's Manual. AFRL, Hanscom AFB, 94 pp.

Holben, B.N., and Coauthors, 1998: AERONET – a federated instrument network – data archive for aerosol characteristics. *Rem. Sens. Envir.*, 1-16.

Kaufman, Y.J., and Coauthors, 1997: Operational remote sensing of tropospheric aerosol over land from EOS moderate resolution imaging spectro-radiometer. *J. Geophys. Res.*, **102**, 17051-17067.

Kaufman, Y.J., and B.N. Holben, 1996: Hemispherical backscattering by biomass burning and sulfate particles derived from sky measurements. *J. Geophys. Res.*, **101**, 19433-19445.

Kay, R.R., and Coauthors, 1999: An introduction to the DOE's multispectral thermal imager (MTI) project. *Proc. of 12th AIAA/USU Conf. Sat.*,1-11.

Villeneuve, P.V., and C.C. Borel, 1998: Scattering and absorption by aerosols, Los Alamos National Lab, LA-UR-98-306, 98-105.

Wen, G., S.C. Tsay, R.F. Cahalan, and L. Oreopoulos, 1999: Path radiance technique for retrieving aerosol optical thickness over land. *J. Geophys. Res.*, **104**, 31321-31332.

Acknowledgements: The authors wish to thank the project sponsor, Dr. Edward Howard of NOAA, for guidance and support. Also acknowledged is the MTI program office for providing data and additional sensor and algorithm information. AERONET data utilization is also greatly appreciated.

P4.23 THE CHESAPEAKE LIGHTHOUSE AND AIRCRAFT MEASUREMENTS FOR SATELLITES (CLAMS) EXPERIMENT

William L. Smith Jr.* [1], Thomas Charlock[1], Bruce Wielicki[1], Ralph Kahn[2], J. Vanderlei Martins[3], Charles Gatebe[4], Peter V. Hobbs[5], G. Carl Purgold[6], Jens Redemann[7], Lorraine Remer[8], Ken Rutledge[9]

[1]Atmospheric Sciences, NASA Langley Research Center, Hampton, VA
[2]Jet Propulsion Laboratory, California Institute of Technology, Pasadena, CA
[3]JCET, University of Maryland Baltimore County, NASA GSFC, Greenbelt, MD
[4]GEST, University of Maryland Baltimore County, NASA GSFC, Greenbelt, MD
[5]Dept. of Atmospheric Sciences, University of Washington, Seattle, WA
[6]Science Applications International Corporation, Hampton, VA.
[7]Bay Area Environmental Research Institute, San Francisco, CA.
[8]NASA Goddard Space Flight Center, Greenbelt MD.
[9]Analytical Services and Materials, Inc., Hampton, VA

1. INTRODUCTION

NASA has developed an Earth Observing System (EOS) consisting of a series of satellites designed to study global change from space. The EOS "flagship" is the EOS TERRA satellite, launched in December 1999, equipped with five unique sensors to monitor and study the Earth's heat budget and many of the key controlling variables governing the Earth's climate system. CLAMS, the Chesapeake Lighthouse and Aircraft Measurements for Satellites field campaign was conducted from NASA Wallops Flight Facility and successfully executed over the middle Atlantic eastern seaboard from July 10 – August 2, 2001. CLAMS is primarily a shortwave closure experiment designed to validate and improve EOS TERRA satellite data products being derived from three sensors: CERES (Clouds and Earth's Radiant Energy System), MISR (Multi-angle Imaging Spectro-Radiometer) and MODIS (MODerate Resolution Imaging Spectroradiometer). CLAMS is jointly sponsored by the CERES, MISR and MODIS instrument teams and the NASA GEWEX Global Aerosol Climatology Project (GACP). CLAMS primary objectives are to validate satellite-based retrievals of aerosol properties and vertical profiles of radiative flux, temperature and water vapor. Central to CLAMS measurement strategy is the Chesapeake Lighthouse, a stable sea platform located in the Atlantic Ocean, 13 miles east of Virginia Beach near the mouth of the Chesapeake Bay and the site of an ongoing CERES Ocean Validation Experiment (COVE). Six research aircraft were deployed to make detailed measurements of the atmosphere and ocean surface in the vicinity of COVE, over the surrounding ocean, over nearby NOAA buoys and over a few land sites. The measurements are used to validate and provide "ground truth" for simultaneous products being derived from TERRA data, a key step toward an improved understanding and ability to predict changes in the Earth's climate. One of the two CERES instruments on-board TERRA was programmed for Rotating Azimuth Plane Scans (RAPS) during CLAMS, increasing the CERES coverage over COVE by a factor of 10. Nine coordinated aircraft missions and numerous additional sorties were flown under a variety of atmospheric conditions and aerosol loadings. On one "golden day", July 17, all six aircraft flew coordinated patterns, vertically stacked between 100 ft and 65,000 ft over the COVE site as the TERRA satellite orbited overhead. A summary of CLAMS measurement campaign and a description of the platforms and measurements is given below.

*Corresponding author address: William L. Smith Jr., MS420, NASA LaRC., Hampton, VA 23666. (email:w.l.smith@larc.nasa.gov)

2. PLATFORMS

2.1 Surface Sites

An important component of the CERES program is to improve estimates of the Surface and Atmospheric Radiation Budget (SARB) over the globe (Charlock et al.,1997). COVE is a critical validation site for CERES SARB flux profiles and is the only continuously operating oceanic radiometric measurement station in the world meeting BSRN (Baseline Surface Radiation Network) calibration protocols. Validation of upwelling and net fluxes are less problematic at COVE than over land sites owing to the relative uniformity of the ocean surface. NASA LaRC has a 20 year agreement with the United States

Coast Guard for continuous access to this platform. CERES has installed and maintains a BSRN measurement station at COVE since August 1999 for broadband fluxes, supplemented with an MFRSR photometer and an AERONET (Cimel) sunphotometer for spectral aerosol optical thickness. A SP1A spectralphotometer scans downward to measure the angular distribution of reflected radiation by the sea or BRDF (bi-directional reflectance distribution function), an important boundary condition for satellite remote sensing. Additionally, numerous other radiometers are operating at COVE including Eppley pyranometers specially modified to account for thermal offset phenomena (Haeffelin, 2001), Kipp & Zonen radiometers, pyrgeometers, shadowband radiometers and a downward looking MFRSR. NOAA maintains a basic meteorology station at the lighhouse that includes wind and wave information.

During CLAMS a shortwave spectrometer measured downwelling irradiance from 350-2200 nm with 10 nm resolution and an MPLnet micro pulse lidar provided information on the vertical distribution of aerosols and clouds. A compliment of in-situ instruments including a nephelometer, an aphelometer, a condensation nuclei counter and a nucleopore filter collection system were deployed at COVE to measure aerosol radiative properties and chemical composition. In-situ oceanographic instruments were deployed by a team from the Old Dominion University (ODU) Ocean, Earth and Atmospheric Sciences Department to measure chlorophyll, color dissolved organic matter (CDOM), water column profiles of temperature and salinity. Spectral measurements of in-water absorption, attenuation and backscatter were obtained and water leaving radiance was measured with a SeaWIFS Airborne Simulator (SAS). At Wallops Flight Facility, the University of Wisconsin deployed an Atmospheric Emitted Radiance Interferometer (AERI) measuring longwave spectra from 3-25 μm to derive boundary layer temperature and humidity structure. A filter collection system similar to the one at COVE was deployed on top of a building on Wallops Island and an AERONET station was deployed in Oyster, Virginia near the lower end of Virginia's eastern shore. Wind and wave information from several NOAA ocean buoys are being used to help interpret CLAMS ocean optics measurements. Figure 1 depicts CLAMS operating area and the locations of the key surface sites. Radiosondes were launched daily from Wallops and COVE at 0 and 1200 UTC, near TERRA overpass time at roughly 1600 UTC and at other times coinciding with the aircraft measurements.

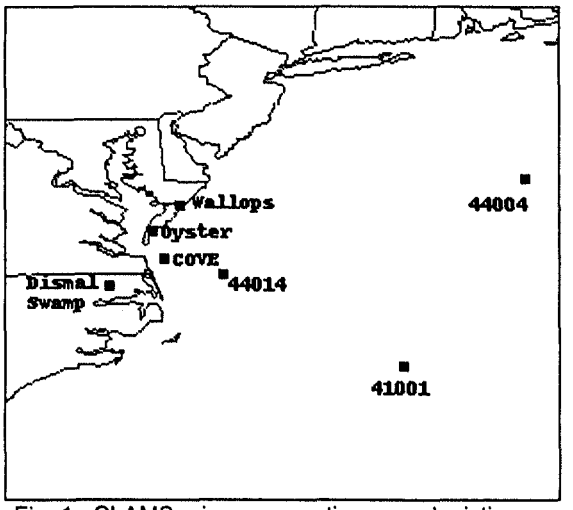

Fig. 1. CLAMS primary operating area depicting location of surface sites and NOAA buoys

2.2 Aircraft

Six research aircraft participated in CLAMS including NASA's ER-2 and OV-10, the University of Washington CV-580, the Proteus, a Cessna 210 and a Lear Jet. Figure 2 shows an altitude timeline for the aircraft operations conducted over COVE on July 17, 2001. All six aircraft participated on this day. The flight scenario shown in Fig. 2 is typical of most of CLAMS aircraft operations, although not all aircraft participated in every flight, the target area was moved to include offshore buoys or adjacent cloud free areas, and the timing of some of the profiles was altered for various reasons, mainly cloud avoidance.

The NASA ER-2 serving as a surrogate satellite, flew at 65 kft with airborne versions of MODIS (MAS: MODIS Airborne Simulator) and MISR (AirMISR). The Scanning High-resolution Interferometer Sounder (S-HIS) and the Advanced Visible/Infrared Imaging Spectrometer (AVIRIS) measured longwave and shortwave spectra, respectively. Typical flight patterns included a series of adjacent legs parallel to the solar plane to test new aerosol retrieval algorithms for sun-glint from MAS, daisy patterns for AirMISR BRDF and a single track parallel to the TERRA orbit track and centered over one of the surface sites (typically COVE or one of the NOAA Buoys). The latter track also provided multi-angle measurements of the target area with airMISR.

The University of Washington Convair 580 was the workhorse of CLAMS, instrumented to measure the physical and chemical properties of aerosols in-situ. The CV-580's instrument compliment included several nephelometers, an aphelometer, two FSSP's for small and large

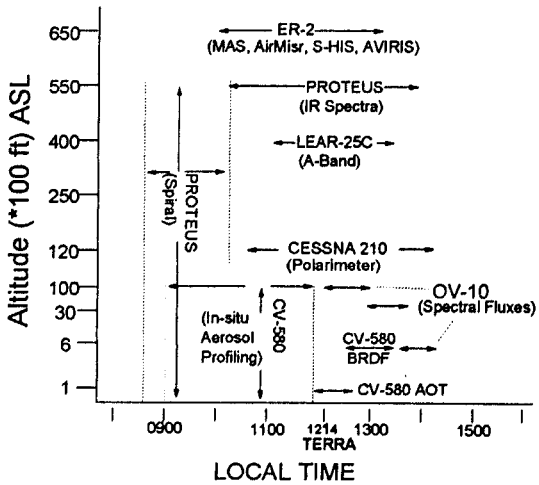

Fig. 2. Altitude timeline for CLAMS aircraft on July 17, 2001. The Terra overpass was at 1214 EDT.

particles, CN counters, an aerosol spectroreflectometer with a nucleopore filter collection system to measure aerosol absorption, teflon and quartz filter collection systems for measuring ionic and carbonaceous species. The CV-580 also deployed several radiometric instruments to measure spectral and broadband shortwave radiation, including the NASA Ames 14 channel Automated Airborne Tracking Sunphotometer (AATS-14) and the NASA Goddard Cloud Absorption Radiometer (CAR). The AATS-14 (Schmid et al., 2000) provides the aerosol optical thickness profiles while the CAR (King et al., 1986) provides the important lower boundary condition (BRDF), both critical for radiative closure studies and validation of AOT derived from the TERRA satellite and ER-2 airborne data. Although the CAR measurements are limited to the wind and sea conditions and solar geometries encountered during CLAMS, they will be useful for checking the validity of the long-term measurements of ocean BRDF being made at COVE under a much wider range and variety of conditions. The typical flight scenario for the CV-580 included BRDF patterns near the beginning and end of each mission, a 30-minute leg flown at 100ft centered at satellite overpass time to characterize the total column AOT and a detailed characterization of two to four aerosol layers. Each layer was sampled for 45 minutes alongwind and crosswind to ensure sufficient aerosol mass was collected on the filters. A quick ascent from the surface to 12 kft prior to the detailed characterization provided the flight scientist the information needed to determine what altitude and how many layers to characterize and also provide an AOT profile for closure studies.

A third key aircraft for CLAMS is the NASA LaRC OV-10 configured to measure upwelling and downwelling longwave (broadband) and shortwave (broadband and spectral) irradiances. The broadbands are manufactured by Eppley Laboratories, Inc. The spectral shortwave measurements are obtained with Analytical Spectral Devices Full Range (ASD-FR) spectrometers which measured irradiance from 350-2500 nm at 3-10 nm resolution (Kindel et al., 2001). The primary objectives of the OV-10 were to conduct low-altitude (100 and 600 ft) surveys of spectral and broadband flux to measure the spatial variability of ocean optics within the scale of a MODIS and MISR pixel; to help understand platform effects on the measurement of upwelling radiation at COVE; to determine how well COVE measurements represent the sea in general; and to determine the shortwave flux profile below 10 kft.

Three additional aircraft participated in CLAMS. The Proteus, owned by Scaled Composites, Inc., flew a payload that included NAST-I, NAST-M and FIRSC adding a longwave component to CLAMS. NAST-I is an interferometer measuring high resolution spectra from 3.3 to 18 μm to map sea surface temperature (SST) and atmospheric profiles of temperature and water vapor. NAST-M is a 17 channel scanning microwave radiometer used for temperature sounding through non-precipitating clouds and for deriving precipitation cell height. FIRSC is the Far-Infrared Spectrometer for Cirrus, a high resolution interferometer measuring from 70 to 1000 μm. Most of the Proteus flight hours were spent mapping at 55 kft but at times the Proteus conducted slow ascending and descending spirals over Wallops and COVE between 55 kft and the surface. A nine channel visible and near infrared Research Scanning Polarimeter (RSP) was flown on a Cessna 210. The Cessna 210 participated in CLAMS from July 10-22 making intensity and polarization measurements at 12 kft to retrieve aerosol properties and 200 ft to retrieve ocean optical properties. Finally, a new NASA Langley Airborne A-Band (765 nm) Spectrometer (LAABS) was flown for the first time during CLAMS on a Lear jet at 40 kft to demonstrate its capability for aerosol optical thickness retrievals. Both the RSP and an oxygen A-band similar to LAABS are being considered for future satellite platforms

3. SUMMARY

Table 1 summarizes the nine most successful CLAMS experiment days, the participating aircraft, flight locations, AOT from the COVE AERONET site, predominant sky conditions and the UTC time and associated wind conditions when the BRDF patterns

Date (2001)	Aircraft	Location	AOT (500nm)	Sky Cond.	BRDF-1 TIME(dir,spd)	BRDF-2 TIME(dir,spd)
10-Jul	1,2,4,5	COVE	0.23	Clear	1810(169,1.5)	2150(156,7.7)
12-Jul	1,2,3,4	COVE, E of Wallops	0.08	Scat. Cirrus		
14-Jul	1,2,4,5	COVE	0.08	few Cu	1605(305,8.2)	
17-Jul	1,2,3,4,5,6	COVE	0.47	Clear	1655(176,6.2)	
23-Jul	1	E of Wallops	0.06	Clear	1510(NA)	
26-Jul	1,2,4	COVE/Bouy 44014	0.17	Mostly Clear	1755(230,8.0)	
30-Jul	1,2,3,4	COVE/Buoy 44014	0.06	Low Clouds	1820(010,9.0)	1910(016,11.3)
31-Jul	1,2,3	Bouy 44004/ D.Swamp	0.08	broken Cu	1700(026,8.2)	1900(NA)
2-Aug	1,2,3	COVE	0.1	Clear	2010(116,3.1)	

Table 1. CLAMS primary experiment days with primary target area, COVE AOT sky conditions and time of BRDF (UTC) with associated wind direction (degrees) and speed (m/s). The participating aircraft are 1:CV-580, 2:OV-10, 3:ER-2, 4:Proteus, 5:Cessna, 6:Lear Jet.

were flown. July 2001 was anomalously cool and dry with lower aerosol amounts than normal. Nevertheless, a variety of aerosol conditions were encountered ranging from very clean (AOT<0.1) to moderate (AOT ~0.5) and a unique set of radiation and in-situ aerosol measurements were obtained to validate MODIS and MISR aerosols and test CERES SARB. Some of CLAMS experimental achievements include:

- Six MISR and MODIS aerosol retrieval validation experiments.
- Three MODIS 'glint' experiments.
- Two spatial variability experiments for MISR.
- Measurements of coastal, offshore and deep ocean BRDF(15 total; 8 uncontaminated by cloud) under a variety of sun angles and wind conditions for CERES, MISR and MODIS.
- Twelve OV-10 flights with spectral and broadband shortwave flux measurements under a variety of sun angles and wind conditions.
- Measurements demonstrating several new instrument technologies for future satellite platforms.
- July 17 was "Golden Day" with moderate aerosol and all six aircraft vertically stacked over the Chesapeake Lighthouse at TERRA overpass time.

Preliminary results will be shown at the conference. CLAMS data will be archived at the Atmospheric Sciences Data Center at NASA Langley and should become publicly available by August 2002.

References

Charlock, T. P., F. G. Rose, D. A. Rutan, T. L. Alberta, D. P. Kratz, L.H. Coleman, G. L. Smith, N. Manalo-Smith, and T. D. Bess, 1997: Compute Surface and Atmospheric Fluxes (System 5.0), CERES Algorithm Theoretical Basis Document. 84 pp. See http://asd-www.larc.nasa.gov/ATBD/

Haeffelin, M., S. Kato, A. M. Smith, C. K. Rutledge, T. P. Charlock and J. R. Mahan, 2001: Determination of the thermal offset of the Eppley precision spectral pyranometer. *Applied Optics*, 40, 472-484.

King, M. D., M. G. Strange, P. Leone and L.R. Blaine, 1986: Multiwavelength scanning radiometer for airborne measurements of scattered radiation within clouds. *J. Atmos. Oceanic Technol.*, 3, 513–522.

Kindel, B. C., Z. Qu and A. F. H. Goetz, 2001: Direct solar spectral irradiance and transmittance measurements from 350 to 2500 nm. *Applied Optics*, 40, 3483-3494.

Schmid, B., J. M. Livingston, P. B. Russell, P. A. Durkee, H. H. Jonsson, D. R. Collins, R. C. Flagan, J. H. Seinfeld, S. Gassó, D. A. Hegg, E. Öström, K. J. Noone, E. J. Welton, K. J. Voss, H. R. Gordon, P. Formenti, and M. O. Andreae, Clear sky closure studies of lower tropospheric aerosol and water vapor during ACE 2 using airborne sunphotometer, airborne in-situ, space-borne, and ground-based measurements, Tellus, B 52, 568-593, 2000.

P4.25

SIMULTANEOUS RETRIEVAL OF CLOUD HEIGHT AND EFFECTIVE EMISSIVITY FROM HYPERSPECTRAL RADIANCE MEASUREMENTS

Hung-Lung Huang, Xiangqian Wu, Jun Li, Paolo Antonelli, Roert O. Knuteson, EriK R. Olson, Kevin C. Baggett, and Brian J. Osborne.
Cooperative Institute for Meteorological Satellite Studies (CIMSS)
University of Wisconsin-Madison

1. INTRODUCTION

New instrumentation and innovative communication technology enable great advancement of development of the next generation weather satellite infrared profile sounding instrument that simultaneously achieves semi-continuous measurements in spectral, spatial, and temporal domains. While these instruments are been made and planned to be flown on the research (IMG, AIRS and GIFTS), and operational (CrIS, IASI and ABS) space-borne satellite systems. The new and improved processing algorithm must be developed to keep up with the unique features provided by these new observations. The most important and common feature of these spectral radiance data which posses not only improved spectral resolution (~ 0.25 to 1 wavenumber) but also semi-continuous sampling through out the infrared spectrum. For example, AIRS infrared sounding measurements has 1200 resolving power and achieve spectral data of every 0.4 wavenumber between cloud and surface sensitivity longwave window region of 700 to 1000 wavenumber. In this spectral region approximately 750 spectral radiances are available for retrieving spectrally related characteristics such as temperature profile, cloud and earth surface emissivity property. These measurements provide unprecedented opportunity when it compares to the current and past geostationary and polar orbiting weather satellite making measurements of less than 10 discrete piece of data in this part of infrared longwave region. In this paper, we are demonstrating a simple novel approach which takes the advantages of semi-continuous high spectral resolution radiances that are sensitivity to both cloud optical property of emission and cloud altitude geometry, and can be used to simultaneously retrieve cloud emissivity spectrum and altitude. Using a controlled simulation study, the Minimum Local Emissivity Variance (MLEV) approach can be fully demonstrated to be physical and the achieved accuracy can be quantified under variety of assumptions and atmospheric conditions.

Corresponding author address: Hung-Lung Allen Huang, Space Science and Engineering Center, University of Wisconsin-Madison, 1225 West Dayton Street, Madison, WI 53706; e-mail: AllenH@ssec.wisc.edu

2. Minimum Local Emissivity Variance (MLEV) Algorithm

Neglecting scattering processes, the infrared clear sky radiance measured by high spectral resolution instrument for a specific spectral channel within an instantaneous filed of view (IFOV) is

$$R_{clr}(\nu) = \varepsilon_s(\nu)B_s(\nu)\tau_s(\nu) - \int B(\nu)d\tau(\nu) + (1-\varepsilon_s) \int B(\nu)d\tau^*(\nu), \quad (1)$$

Where clear spectral channel radiance $R_{clr}(\nu)$ measured by high spectral resolution radiometer or interferometer; ν denotes spectral channel, ε_s is the surface emissivity; subscript s denotes surface; B is the Planck radiance; τ is the atmospheric transmittance function; $\tau^* = \tau_s^2/\tau$; and $\int$ indicates integration limit from surface to satellite altitude (~ 0 hPa). For complete cloud covered IFOV with opaque cloud (ε_c=1) at pressure P_c, the cloud radiance is

$$R_{cld}(\nu) = B_c(\nu)\tau_c(\nu) - \int B(\nu)d\tau(\nu), \quad (2)$$

Where subscript c denotes the cloud top, and $\int$ indicates integration limit from cloud pressure altitude P_c to0 hPa. The upwelling radiance R for a partially cloud-covered IFOV is

$$R(\nu) = (1 - N\varepsilon_c(\nu))R_{clr}(\nu) + N\varepsilon_c(\nu)R_{cld}(\nu), \quad (3)$$

Where the cloud emissivity spectrum $N\varepsilon_c(\nu)$ is modulated by the cloud fractional coverage N and the quantity $N\varepsilon_c(\nu)$ used through out this paper is referred to as the effective cloud emissivity spectrum. It can be shown that spectral region 750 to 950 wave number provides best sensitivity to both $N\varepsilon_c$ and P_c. Cold and isothermal condition provides unfavorable environmental factor towards retrieving $N\varepsilon_c(\nu)$ and P_c. The conduits between $N\varepsilon_c(\nu)$ and P_c can be explored through MLEV algorithm to optimize cloud signal (at least cloud detection) at these unfavorable condition since $N\varepsilon_c(\nu)$ and Pc can still provide complementary cloud sensitivities

Rewrite Eq. (3) one can reach

$$N\varepsilon_c(\nu) = (R(\nu) - R_{clr}(\nu)) / (R_{cld}(\nu) - R_{clr}(\nu)) \quad (4).$$

Which is the effective cloud emissivity spectrum that MLEV algorithm tries to derive simultaneously with cloud altitude. Besides the estimation of $R_{clr}(\nu)$ is the necessary input, $R_{cld}(\nu)$ need to be calculated by the guess of P_c. The fundamental principal of MLEV is to seek the optimal solution of $N\varepsilon_c(\nu)$ that exhibits the smallest local variation and its matching P_c claims to be the optimal altitude solution as well. Objective searches for the true combination of $N\varepsilon_c(\nu)$ and P_c becomes the focus of this MLEV paper. Finding the retrieved cloud emissivity spectrum that has the smallest variation will simultaneously determine the "correct" cloud altitude information. An objective procedure of MLEV is to minimize the averaged local variation of

$$\Sigma (N\varepsilon_c(\nu)\text{-Bar}(N\varepsilon_c(\nu)))^2 \quad (5),$$

where $\text{Bar}(N\varepsilon_c(\nu)) = (\Sigma (N\varepsilon_c(\nu))$ over ν-$\Delta\nu/2$ to $\nu+\Delta\nu/2)/\Delta\nu$ and $\Delta\nu$=5 cm^{-1}. Physical speaking, if cloud altitude is incorrect (under- or over- estimated), then $N\varepsilon_c(\nu)$ will displays molecular absorption spectral features which are relatively high frequency compared to cloud optical spectral feature. Thus, one can solve for that cloud altitude which minimizes the local variation of the derived cloud effective emissivity spectrum.

3. MLEV RESULTS

MLEV cloud height and effective emissivity spectrum retrievals are demonstrated using simulated GIFTS (Huang, et.al, 2000) longwave infrared measurements. A set of 177 continental U.S. profiles covering 10 to 35 north latitude and 90 to 110 west longitude over whole year of 2000 , which represent diverse atmospheric conditions coincident with GIFTS geographical coverage were selected for this demonstration. Forty combinations were formed from each profile by assigning four cloud heights (200, 300, 500, and 850 hPa corresponding to very high, high-, medium-, and low- level clouds) and ten effective emissivity (0.1, 0.2, 0.3, 0.4, 0.5, 0.6, 0.7, 0.8, 0.9, and 1.0 corresponding to low cloud cover/very transparent to overcast/ opaque cloudy conditions). The GIFTS longwave cloudy radiance spectra were simulated for all forty combinations of each profile. No spectral emissivity variation is introduced and GIFTS baseline measurement noise of 0.25 mw/sr.cm^{-1}.m^2 is randomly added to simulate real instrument measurements. Figure 1 displays MLEV cloud altitude root mean square error (RMSE) and bias as functions of cloud altitudes (four panels) and effective cloud emissivity (X- axis). MLEV algorithm shows little bias for all level of clouds and opaqueness. For very high and high clouds, retrieval RMSE of cloud altitude is around 30 hPa, except for transparent clouds ($N\varepsilon_c(\nu)$ is smaller than 0.2). For medium level cloud, the RMSE is about 10 hPa, except $N\varepsilon_c(\nu)$ is smaller than 0.2. For low cloud, RMSE is increased to ~ 50 hPa and large error for transparent clouds. Figure 2 is similar to figure 1 except for cloud emissivity MLEV retrieval RMSE of 800 and 900 cm^{-1}. Again, four-panel represents four different level of clouds simulated. Effective emissivity RMSE of both wavenumbers are shown as function of effective cloud emissivity as well. For medium and higher clouds the average RMSE of $N\varepsilon_c(\nu)$ is about 0.02 to 0.04 except

for very transparent cloud (when $N\varepsilon_c(\nu)$ is smaller than 0.2). For low cloud case, significant degraded performance of MLEV $N\varepsilon_c(\nu)$ is shown. At this cloud level about 0.2 of retrieved effective emissivity RMSE is shown. For comparison, CO_2 (Smith and Platt, 1978, Menzel et al., 1983) slicing cloud altitude retrieval using GOES sounder data (Menzel and Purdom 1994) and GIFTS MLEV retrieval cloud altitude RMSE is presented in figure 3. The cloud altitude information content of GIFTS and GOES demonstrates the needs of the prompt advancement of high spectral resolution instrument development.

The results shown in these three figures all assumes atmospheric uncertainties of 1.0 K for temperature profile, 1.0 K for surface skin temperature and 15 % for water vapor profile, respectively.

Figure 4 displays example MLEV derived emissivity spectra (high spectral resolution spectra collected during April 21, 1996 SUCCESS HIS field campaign) that depicts the fundamental principal of the MLEV (minimum variance of 1%) can be found when the cloud height is optimally determined. In another words, minimum variance of 1% is associated with optimal cloud altitude of 300 hPa is verified by Cloud Lidar System (CLS) 280 hPa cloud. Figure 5 demonstrates time series of the retrieval cloud height and its associated cloud emissivity at 900 1/cm. The single layer cloud heights determined by CLS are also overlaid to validate the MLEV can achieve optimal cloud height information, regardless of cloud transparency. Around record 210 (2112 Z) when cloud emissivity is near 20 % level, MLEV over estimated cloud height (retrieved too high). All other time period the MLEV is performed consistently with CLS measured, despite cloud emissivity varies from opaque (100 %) to semi-transparent (20%).

4. CONCLUSIONS

In summary, MLEV is a novel but simple technique that takes advantage of semi continuous sampling of cloud sensitive longwave infrared radiance measurements, simultaneously finding cloud altitude and effective emissivity spectrum. The optimal cloud altitude and emissivity spectrum solution is the one that yields the smallest local spectral variation of the derived emissivity spectrum. Since cloud absorbs, reflects, scatters, and radiates smoothly within local spectral region. Any abrupt high frequency feature exists in the retrieved emissivity spectrum is an indicative of suboptimal cloud altitude determination.

5. REFERENCES

Huang, H.-L., H.E. Revercomb, J. Thom, P.B. Antonelli, B Osborne, D Tobin, R. Knuteson, R. Garcia, S. Dutcher, J. Li, and W.L. Smith, 2000: Geostationary Imaging FTS (GIFTS) Data Processing: Measurement Simulation and Compression. SPIE Proceedings, 4151, Hyperspectral Remote Sensing of the Land and Atmosphere, 103-114.

Menzel, W.P., W.L. Smith, and T.R. Stewart, 1983: Improved Cloud Motion Wind Vector and Altitude Assignment Using VAS. J. Climate Appl. Meteor., 22, 377-384.

Menzel, W.P., J.F.W. Purdom, 1994: Introducing GOES-I: The First of a New Generation of Geostationary Operational Environmental Satellites. Bull. Amer. Meteor. Soc., 75, 757-781.

Smith, W. L., and C.M.R. Platt, 1978: Intercomparison of Radiosonde, Ground-bases Laser, and Satellite-deduced Cloud Heights. J. Appl. Meteor., 17, 1796-1802.

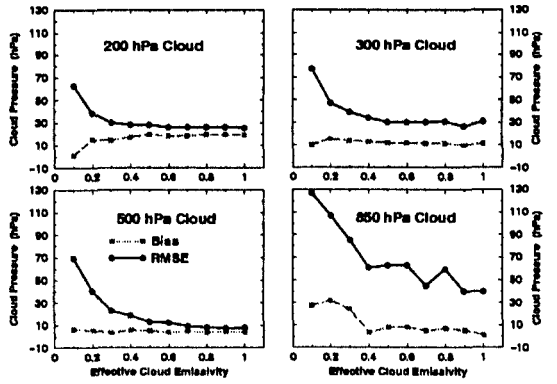

Figure 1, GIFTS MLEV cloud pressure retrieval RMSE and bias for cloud at level of 200, 300, 500, and 850 hPa.

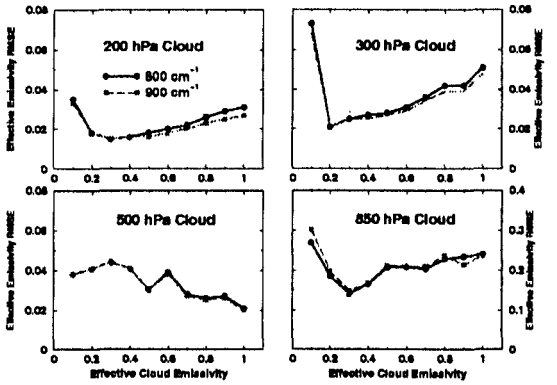

Figure 2, GIFTS MLEV retrieval of effective cloud emissivity RMSE of 800 and 900 cm^{-1} for cloud at level of 200, 300, 500, and 850 hPa..

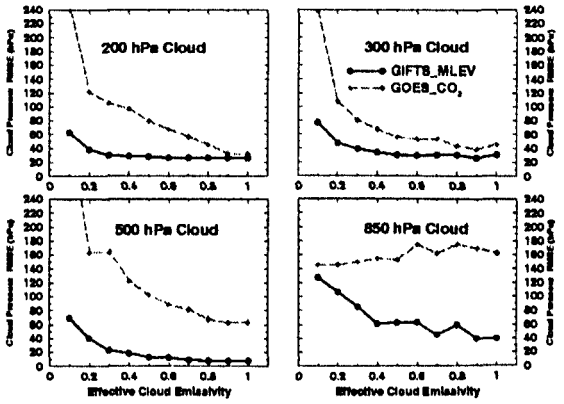

Figure 3, MLEV cloud pressure retrieval RMSE for GIFTS and GOES comparisons.

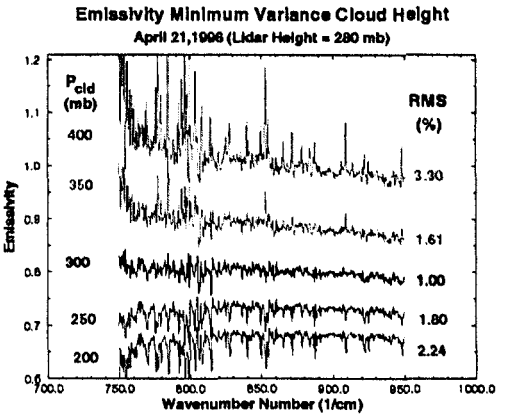

Figure 4, Retrieved local emissivity variance example for HIS data collected during April 21 of 1996 SUCCESS field campaign. Cloud Lidar System (CLS) identified single layer of cloud was located at 280 hPa.

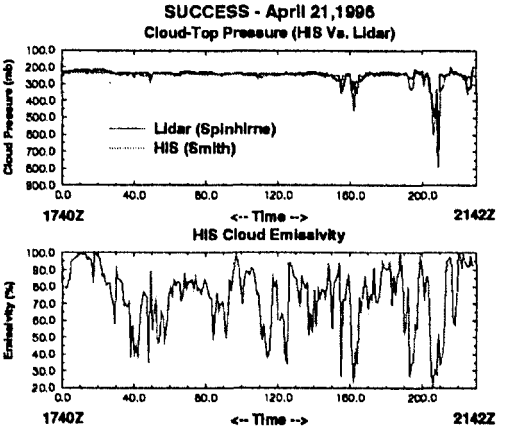

Figure 5, Time series of MLEV cloud altitude (upper panel) and effective emissivity (lower panel) for April 21, 1996 HIS measurements. Single layer cirrus cloud altitude determined by CLS is also overlaid for verification.

P4.26 **Retrieval of Cirrus Ice-Water Path, Particle Size, and Optical Thickness Using Thermal Infrared Satellite Data**

Robert P. d'Entremont
Satellite Meteorology Group
Atmospheric and Environmental Research, Inc.
131 Hartwell Ave., Lexington, MA 02421-3126

David L. Mitchell
Atmospheric Sciences Center
Desert Research Institute
2215 Raggio Parkway, Reno, NV 89512-1095

1. Introduction

Cirrus ice-water path (IWP) is estimated using a coupled algorithm that simultaneously retrieves IWP, ice-crystal particle size, emissivity, and cirrus temperature using radiances collected in the GOES mid-wave infrared (MWIR), water-vapor (WV), and thermal infrared (TIR) wavelengths, nominally at 3.9, 6.7, and 10.8 μm. From the standpoint of radiative transfer, cirrus IWP, emissivity, effective particle size, and effective temperature (defined here as the temperature of the radiative "center of mass" of the cirrus cloud) are interdependent. For this reason all these cloud attributes are being estimated simultaneously using a first-principles algorithm that numerically solves a set of simultaneous radiance equations.

The cirrus retrieval algorithm uses a simultaneous-solution approach to ensure physical consistency between satellite radiance measurements and theoretical radiative transfer calculations. The fundamental non-uniqueness of the relationship between measured radiance and cloud IWP, emissivity, particle size, and temperature at a single wavelength is resolved by forcing the retrieved parameters to be simultaneously consistent with theory and satellite observations at multiple infrared wavelengths. Retrievals are presented of cirrus cloud ice water path (IWP), effective diameter (D_{eff}) and optical depth (τ). Proof-of-concept retrievals are performed using GOES-8 thermal infrared satellite data.

2. Infrared Radiation Transfer in Cirrus

The cirrus analysis method is newly developed by AER and DRI. It is a thermal infrared (TIR) technique that retrieves the cirrus effective emissivity and temperature that simultaneously predict observed radiances in two or more TIR channels. Since the emissivity depends on absorption efficiency, IWP, and D_{eff}, a knowledge of the ice-crystal size distribution shape N(D) as a function of cirrus environmental temperature is required.

The approach has an explicit dependence of the retrievables not just on IWP and ice-crystal effective size D_{eff} but also on N(D) shape, including the slope parameter and dispersion of bi-modal modified gamma ice-crystal size distributions. These attributes have been related to temperature for tropical and mid-latitude cirrus using ARM and CEPEX in-situ aircraft observations. Comparisons between the ground- and satellite-based retrievals employing the same physics and methodology will reveal the sensitivity of IWP and D_{eff} on the vertical structure of cirrus cloud microphysics. In evaluating these differences, it may be possible to expand our retrieval confidence from small scales (e.g., using ground-based and aircraft data) to larger scales (e.g., satellite-based) for cloud radiative-forcing in climate models.

Analytic approximations to full geometric-scattering theory for non-spherical ice crystals have been developed for use in simulating MWIR, WV, and TIR bands. This section summarizes the theory and its application in our retrieval paradigm.

The infrared upwelling radiance $I_{\lambda,TOA}$ at wavelength λ in a non-scattering atmosphere and for a cirrus-filled pixel is well approximated by

$$I_{\lambda,TOA} = (1 - \varepsilon_\lambda) I_{\lambda,clr} + \varepsilon_\lambda B_\lambda(T_{cld}) , \quad (1)$$

where ε_λ is the cirrus emissivity at wavelength λ; $I_{\lambda,clr}$ is the TOA radiance that would be observed in an otherwise cloud-free pixel; and $B_\lambda(T_{cld})$ is the cirrus Planck blackbody radiance, a function of the cirrus effective emitting temperature T_{cld}. Neglecting cirrus reflectivity, absorption optical thickness τ_{abs} is related to cirrus emissivity ε via the expression $1 - \varepsilon = e^{-\tau}$. Cirrus effective temperature is a weak function of wavelength, and in general is not representative of the cirrus cloud top temperature. However, it helps diagnose the wavelength dependence of cirrus emissivity.

The overall retrieval paradigm is to write Eq. (1) for two wavelengths and solve them simultaneously using an iterative numerical approach. At first glance, Eq. (1) has two unknowns in emissivity ε and cirrus temperature T_{cld}, making such a solution possible in a strictly mathematical sense. In practice, the improper choice of the two wavelengths can make the solution unstable and poorly defined.

3. Ice-Crystal Size

Cirrus ice-crystal effective diameter D_{eff} is an important cloud attribute in our retrieval approach, and is directly related to ice water content (IWC). The effective photon path D_{eff} for the entire size distribution is defined as (Mitchell, 2000)

$$D_{eff} = 3 \, IWC / (2 \, \rho_i \, P_t) , \quad (2)$$

where IWC is the cirrus cloud ice water content (g cm^{-3}), and P_t is the total projected area of all ice crystals in the size distribution (with units of area per unit volume; e.g., $cm^2 \, cm^{-3} = cm^{-1}$). Projected area P_t is the geometric cross-sectional area per unit volume of a distribution of ice crystals with random orientations.

4. Absorption by Ice Clouds

If D_{eff} is the appropriate dimension for describing particle-radiation interactions for a size distribution, then it is natural to ask what the consequences might be if the absorption efficiency Q_{abs} were to be taken outside the integral for the absorption efficieny

$$\beta_{abs} = \int_0^\infty Q_{abs}(D,\lambda) \, P(D) \, N(D) \, dD ,$$

and solved for in terms of D_{eff}. This results in the following simple equation

$$\beta_{abs} = \underline{Q}_{abs} \, P_t , \quad (3)$$

where $\underline{Q}_{abs}$ is the absorption efficiency representing the entire size distribution; and where P_t is the geometric cross-sectional area of the entirety of ice crystals in the size distribution N(D).

Both the absorption coefficient β_{abs} and the cross-sectional area P_t of the size distribution are dependent on the amount and shape of the ice crystals that comprise the cirrus cloud. However, the absorption efficiency $\underline{Q}_{abs}$ is a normalized metric of absorption that depends only on crystal size, shape, wavelength, and refractive index. Thus if it is possible to compute β_{abs} and P_t for a "representative" unit volume of the actual ice-crystal size distribution, their ratio will yield that distribution's absorption efficiency. This forms the basis for computing cirrus TIR emissivities in our retrieval paradigm. Mitchell (2000) writes the absorption efficiency as

$$Q_{abs,ADA} = 1 - \exp(-8\pi \, n_i \, D_{eff} / 3\lambda) , \quad (4)$$

where $Q_{abs,ADA}$ is the absorption efficiency representing the entire size distribution based on the anomalous diffraction approximation (ADA) of van de Hulst (1981) and the concept of effective photon path. Equation (4) represents absorption due only to a particle's geometric cross section. It has been expanded by Mitchell (2000) to include the processes of internal reflection/refraction and photon "tunneling," which collectively are well approximated by

$$Q_{abs} = (1 + C_1 + C_2) \, Q_{abs,ADA} . \quad (5)$$

The leading term (the "1") on the right side of Eq. (5) represents absorption via the particle's cross section; the term C_1 represents absorption due to internal reflection/refraction; and C_2 is the photon tunneling term. Tunneling here is a process by which photons beyond the particle's geometric cross-section are absorbed, including large-angle diffraction and wave resonance

phenomena. Expressions for the constants C_1 and C_2 are given in Mitchell (2000) and are not repeated here, except to note that they depend only on ice-crystal particle size, shape, wavelength, and index of refraction.

Assuming no scattering at thermal wavelengths,

$$\varepsilon = 1 - \exp(-\tau_{abs} / \cos\theta_{sat}) , \qquad (6)$$

where θ_{sat} is the satellite zenith angle and τ_{abs} is the absorption optical depth. Dividing optical depth by the factor $\cos\theta_{sat}$ accounts for increased path length through the cirrus due to non-nadir views. For a cirrus cloud where the size distribution (SD) is invariant with in-cloud position, the absorption optical depth is given by

$$\tau_{abs} = \beta_{abs} \Delta z ,$$

where Δz is the cloud physical depth (from top to base) and β_{abs} is the absorption coefficient, defined by Eq. (3).

5. Ice Water Path

By definition, and assuming that IWC is the vertically averaged value,

$$IWP = IWC \, \Delta z$$

and Eq. (2) becomes

$$D_{eff} = 3 \, IWP / (2 \, \rho_i \, P_t \, \Delta z) , \qquad (7)$$

giving

$$IWP = 2 \, \rho_i \, D_{eff} \, \tau_{abs} / (3 \, \underline{Q}_{abs}) \qquad (8)$$

with the help of Eq. (3) solved for P_t. Substituting for τ_{abs} in (6) using (8), (6) can be rewritten as

$$\varepsilon = 1 - \exp(-3 \, IWP \, \underline{Q}_{abs} / 2 \, \rho_i \, D_{eff} \cos\theta_{sat}) .$$

Solving the above for IWP finally yields

$$IWP = -2 \, \rho_i \, D_{eff} \cos\theta_{sat} \ln(1 - \varepsilon) / (3 \, \underline{Q}_{abs}) . \qquad (9)$$

Note that D_{eff} appears both in the numerator and in the denominator, since $\underline{Q}_{abs}$ is dependent on particle size via Equation (4) for absorption efficiency (Mitchell, 2000).

Fortunately, we have exploited a means of estimating D_{eff} in tropical anvil and mid-latitude cirrus as a function of cirrus environmental temperature (Ivanova et al., 2000). The tropical scheme is based on 93 size distributions from tropical anvils observed during CEPEX and other field campaigns. The mid-latitude scheme is based on over 1000 in-situ measurements of cirrus taken during ARM and FIRE campaigns in the central U.S.

With a methodology to compute IWP, emissivity as a function of wavelength, and effective particle size as a function of cirrus environmental temperature, it is now possible to both simulate and solve a simultaneous set of equations as defined by Eq. (1) for two infrared bands using an iterative numerical approach. In application the clear-scene radiance estimate $I_{\lambda,clr}$ in Eq. (1) is made by averaging the radiances of nearby cirrus-free pixels (as determined by a pre-computed cloud mask) on a land-water background basis. Figure 1 illustrates graphically the process of retrieving cirrus emissivity and temperature. Effective particle size is tied to temperature, and also varies throughout the iteration process.

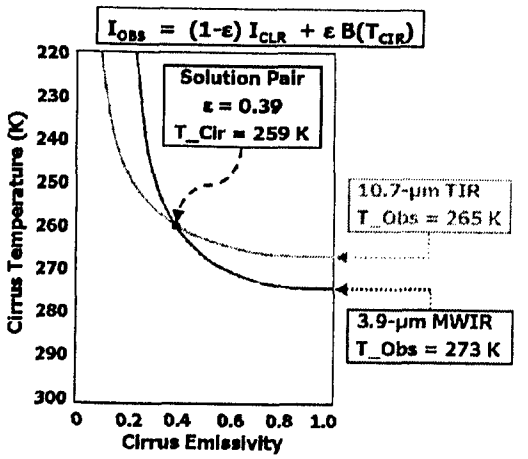

Figure 1. Plots of all mathematically possible pairs of cirrus temperature and emissivity for a given set of satellite radiance observations

In Figure 1 are plots of all mathematically possible pairs of cirrus temperature and emissivity for a given set of satellite radiance observations. The radiance observations correspond to an MWIR brightness temperature

of 273 K, and a TIR temperature of 265 K. Note that for a single wavelength the number of theoretically possible pairs (ε,T) is infinite. This ambiguity is resolved, however, by choosing the retrieved pair as that which satisfies satellite radiance observations at two infrared wavelengths simultaneously. This forms the fundamental basis of our retrieval paradigm.

6. Summary

Cirrus ice-water path (IWP) is estimated using a deterministic algorithm that simultaneously models the interdependent effects of IWP, ice-crystal particle size, emissivity, and cirrus temperature using radiances collected in nominal 3.9-μm MWIR, 6.7-μm WV, and 10.8-μm TIR wavelengths. The cirrus IWP retrieval algorithm uses a simultaneous-solution approach to ensure physical consistency between multispectral satellite radiance measurements and theoretical radiative transfer calculations.

Retrieval sensitivity studies indicate that, in general, IWP is underestimated and that the magnitude of the underestimation increases with increasing cirrus thickness. As cirrus thickness and/or IWP increases, the smaller crystals near the top of the cirrus have a larger cross section absorbing area than the larger crystals below. Being more efficient absorbers of upwelling energy, small crystals above tend therefore to "hide" or "subdue" the influence of the larger crystals below. Subsequently the upwelling infrared radiances are not maximally sensitive to the presence of the larger crystals, in turn causing IWP to be underestimated. However it has been shown that the consistent underestimate of IWP is not all bad because the error is systematic and repeatable, suggesting that thermal-IR retrievals of IWP can be adjusted according to our sensitivity results.

7. Future Plans

Retrievals will be performed of cirrus cloud ice water path (IWP), effective diameter (D_{eff}) and optical depth (τ) using our satellite-based technique and a newly developed cirrus analysis method that analyzes ground-based radar data.

The radar backscatter technique retrieves ice water content (IWC) as a function of the radar reflectivity factor, given information about the N(D) shape and dispersion, and power-law relations between crystal mass and size. Using ground-based radar backscatter returns it will be possible to integrate the IWC profile from cirrus base to cirrus top to obtain IWP, and compare the result with coterminous TIR retrievals of IWP and D_{eff}.

Proof-of-concept retrievals have been performed with satellite and in-situ data from two ARM cirrus IOPs during March 2000, using GOES-8 thermal infrared data and ground-based radar data. The retrievals coincide with in-situ measurements over the SGP ARM CART site, which will be used to test retrieval performance. Results will be presented at our poster.

References

Ivanova, D., D. L. Mitchell, W. P. Arnott, and M. Poellot, 2000: A GCM parameterization of bimodal size spectra for mid-latitude cirrus clouds. Proceedings, 13th International Conference on Clouds and Precipitation, Reno, Nevada, 14-18 August, 546-549.

Mitchell, D. L., 2000: Parameterization of the Mie extinction and absorption coefficients for water clouds. *Journ. Atmos. Sci.*, **57,** 1311-1326.

van de Hulst, H. C., 1981: *Light Scattering by Small Particles.* Dover, 470 pp.

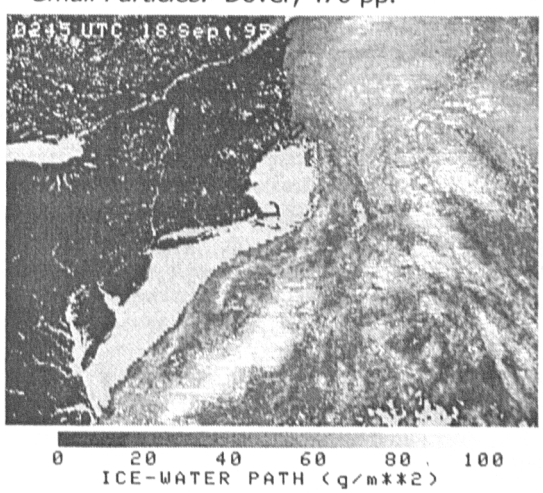

P4.28 Estimating thin cloud properties using an improved CO_2 slicing approach

Hong Zhang*
University of Wisconsin-Madison, Madison, Wisconsin
W. Paul Menzel
Office of Research and Applications, NOAA NESDIS, Madison, Wisconsin

1. INTRODUCTION

CO_2 slicing has been generally accepted as a useful algorithm for determining cloud top pressure (CTP) and effective cloud amount (ECA) for tropospheric clouds above 600 hPa. A modified CO_2 slicing algorithm was investigated wherein adjustments of both surface emissivity and cloud emissivity ratio are considered. To date, the technique has assumed that the surface emissivity is that of a blackbody in the long wavelength infrared radiances and that the cloud emissivities in spectrally close bands are approximately equal. In the modified CO_2 slicing algorithm, surface emissivity is adjusted according to the surface types and the ratio of cloud emissivities in spectrally close bands is adjusted away from unity according to radiative transfer calculations. The new CO_2 slicing algorithm was examined with MODIS Airborne Simulator (MAS) radiance measurements (King et al. 1996) over thin clouds and validated against Cloud Lidar System (CLS) (Spinhirne and Hart 1990) measurements of the same clouds; it was also applied to GOES Sounder (Menzel et al. 1998) data to study the overall impact on cloud property determinations.

2. MODIFIED CO_2 SLICING ALGOITHM

Infrared radiance measurements used in the CO_2 slicing algorithm are affected by surface emissivity and cloud emissivity considerations. For a specific infrared spectral band, the clear-sky upwelling radiance measured by the satellite within an instrument field-of-view (FOV) can be expressed as

$$R_{clr} = \varepsilon_s B_s \tau_s + \int_{P_s}^{P_0} B(T(p))d\tau + (1-\varepsilon_s)\tau_s \int_{P_0}^{P_s} B(T(p))d\tau^{\downarrow}$$

where surface emissivity ε_s is typically 0.95 over land and 0.99 over ocean for CO_2 slicing wavelengths.

The ratio of the deviations in cloud produced radiances R and corresponding clear-sky radiances R_{clr} for two spectral bands ν_1 and ν_2 viewing the same FOV are written as

$$\frac{\Delta R(\nu_1)}{\Delta R(\nu_2)} = \frac{R(\nu_1)-R_{clr}(\nu_1)}{R(\nu_2)-R_{clr}(\nu_2)}$$

$$= \frac{N\varepsilon_{c(\nu 1)}\{\int_{P_s}^{P_c}\tau(\nu_1,p)dB(\nu_1,p)+(1-\varepsilon_s)\tau_s(\nu_1)(B_s(\nu_1)-\int_{P_0}^{P_s}B(\nu_1,p)d\tau^{\downarrow}(\nu_1,p))\}}{N\varepsilon_{c(\nu 2)}\{\int_{P_s}^{P_c}\tau(\nu_2,p)dB(\nu_2,p)+(1-\varepsilon_s)\tau_s(\nu_2)(B_s(\nu_2)-\int_{P_0}^{P_s}B(\nu_2,p)d\tau^{\downarrow}(\nu_2,p))\}}$$

$$= \frac{N\varepsilon_{c(\nu 1)}}{N\varepsilon_{c(\nu 2)}} * \frac{RM(\nu_1)}{RM(\nu_2)}$$

When $|\Delta R(\nu_1)*RM(\nu_2) - \Delta R(\nu_2)*RM(\nu_1)* \frac{N\varepsilon_{c(\nu 1)}}{N\varepsilon_{c(\nu 2)}}|$ is minimum, the CTP has been determined. Given CTP, an ECA is evaluated from the infrared window (IRW) band using

$$ECA = N\varepsilon_{c(w)} = \frac{R(w) - R_{clr}(w)}{R_{bd}(w) - R_{clr}(w)}$$

In a sensitivity study (Zhang 2001), results show that the surface emissivity adjustment places the CO_2 slicing solution for high thin clouds lower in the atmosphere; a 2% surface emissivity change results in a change of about 15 hPa for CTP and a change of 1% for ECA. Furthermore, for high thin clouds (CTP = 300 hPa and ECA = 0.2), a 10% change of cloud emissivity ratio was found to cause about a 35 hPa change in CTP and a 1% change in ECA. Increasing the cloud emissivity ratio places the cloud lower in the atmosphere.

3. VALIDATION OF MODIFIED ALGORITHM

Possible cloud emissivity ratios for MAS bands observing thin high ice clouds were calculated using the Streamer model (Key and Schweiger 1998) wherein longwave ice cloud optical properties are based on Mie calculations using spherical particles at a relatively high spectral resolution. For MAS CO_2 band pairs (including ratios of measurements in spectral bands 14.2/13.7 and 13.7/13.2 microns), they range from 0.9 to 1.13, a few ratios vary from 0.75 to 0.9. For thin clouds, a mean cloud emissivity ratio of 1.05 works best for most of the CO_2 bands in the Streamer calculations.

MAS and CLS cloud heights of thin cirrus clouds were compared using data taken over Kansas and Oklahoma in the central United States on 16 April 1996. The MAS and CLS images are shown on the web address http://ltpwww.gsfc.nasa.gov/MAS/SUCCESShome.html and http://virl.gsfc.nasa.gov/~success/success.html

* Corresponding author address: Hong Zhang, CIMSS/SSEC, University of Wisconsin-Madison, 1225 West Dayton Street, Madison, WI 53706
email: hongz@ssec.wisc.edu

respectively. Figure 1 shows the comparison for single layer cloud observations from the CLS and MAS cloud retrievals for five cloud emissivity ratios (0.95, 1.025, 1.0, 1.05, and 1.075); the same value is used for all CO_2 spectral pair ratios. The distribution of cloud top height difference (CLS – MAS) is shown in 1000m intervals; at an altitude of 10 km in a U.S. standard atmosphere, 500 m corresponds to ~ 20 hPa. The best performance is found for a cloud emissivity ratio of 1.025, with about 60% of the comparisons within 500 m. Thin clouds are found to be very sensitive to the cloud emissivity and the CO_2 slicing technique with the cloud emissivity adjustment improves the agreement with the CLS observations.

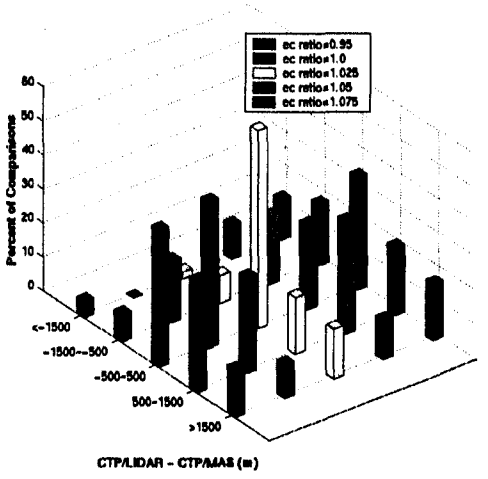

Figure 1: Comparisons of cloud top heights between from CLS and the MAS CO_2 slicing algorithm with different cloud emissivity ratio adjustments [0.95, 1.0 (no adjustment), 1.025, 1.05, and 1.075]. The MAS data is from single layer clouds and cloud top heights are greater than 4000 m on track 14 on April 16, 1996.

4. GOES-8 CASE STUDIES

The modified CO_2 slicing technique was applied to GOES-8 Sounder measurements. Figure 2 shows the scatter plot of CTP from the CO_2 slicing algorithm with non-unity cloud emissivity adjustment versus CTP from the CO_2 slicing algorithm with unity cloud emissivity. The data are from the GOES-8 Sounder on 13:46 UTC Feb. 14, 2001. (a) Comparisons for very thin clouds (ECA < 0.2) show a mean bias of approximately 11 hPa, and RMS (root mean square) difference of approximately 55 hPa. (b) For thin clouds (ECA between 0.2 and 0.5), the mean bias is around 8 hPa, and the RMS difference is approximately 22 hPa. (c) For thick clouds (ECA between 0.5 and 0.95), the mean bias is around 5 hPa, and the RMS difference is approximately 12 hPa. (d) For all cloud types, the mean bias is around 5 hPa, and the RMS difference is approximately 20 hPa. The associated ECA mean bias is 0.64% and RMS difference is 2%, approximately.

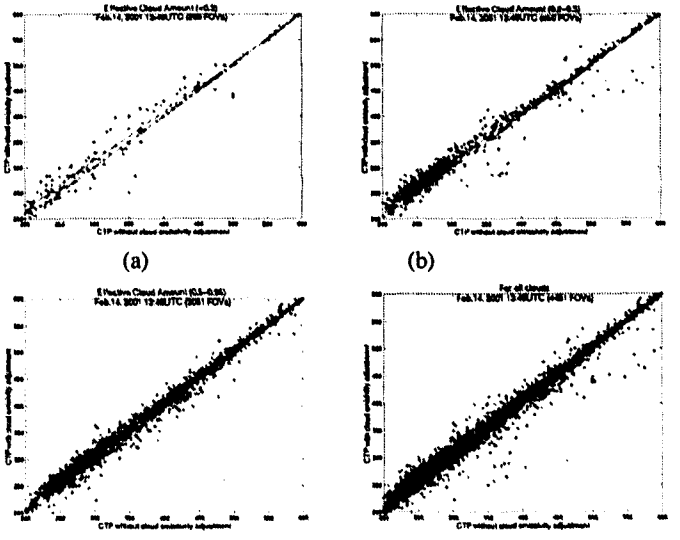

Figure 2: The scatter plot of GOES CTP using modified (y-axis) and original (x-axis) CO_2 slicing algorithm.

5. SUMMARY

The modified CO_2 slicing algorithm is found to be relatively insensitive to surface emissivity; there is a small effect on the cloud properties for thin cirrus and no effect for thick clouds. Adjusting the cloud emissivity ratio to 1.025 improves the cloud height product for high thin clouds and produces little change for thick and opaque clouds. For very thin clouds, the bias of differences is about 10 to 20 hPa and RMS difference is approximately 50 hPa; for thin clouds, there is about 10 hPa bias and RMS difference is approximately 30 hPa. The modified CO_2 slicing algorithm places the clouds lower in the troposphere.

REFERENCES

Key, J. and A.J. Schweiger, 1998: Tools for atmospheric radiative transfer: Streamer and FluxNet. *Computers and Geosciences*, 24(5), 443-451.

King, M. D., et al., 1996: Airborne scanning spectrometer for remote sensing of cloud, aerosol, water vapor and surface properties, *J. Atmos. Oceanic Technol.*, 13,777-794.

Menzel, W. P., Holt, F.C., Schmit, T. J. et al., 1998: Application of GOES-8/9 soundings to weather forecasting and nowcasting. *Bull Amer Meteor. Soc.*, 79, 2059-2077.

Spinhirne, J.D., and W. D. Hart, 1990: Cirrus structure and radiative parameters from airborne lidar and spectral radiometer observations, *Mon. Weather Rev.*, 118, 2329-2343.

Zhang, H., 2001: Estimating thin cloud properties using an improved CO_2 slicing approach. M.S. thesis, Dept. of AOS, University of Wisconsin-madison.

P 4.31

STATISTICAL DEPENDENCE OF CLOUD FRACTION AS A FUNCTION OF VIEW ANGLE DERIVED FROM MISR DATA

G. Zhao * and L. Di Girolamo
Department of Atmospheric Sciences, University of Illinois, Urbana, IL, USA

1. INTRODUCTION

Cloud fraction as a primary product reported in cloud climatologies plays an important role in monitoring and modeling our climate. However, cloud climatologies derived from satellites always suffer from an increase of cloud fraction with satellite viewing obliquely, which is largely a consequence of an increase in the amount of cloud-sides observed with viewing obliquity and pixel expansion with viewing obliquity. These two effects cannot be decoupled until now.

The Multi-angle Imaging SpectroRadiometer (MISR) on-board EOS-Terra is the first high-resolution imager to make global, near-simultaneous, multi-spectral, multi-angle radiometric measurements of the Earth (Diner et al. (1998)). Nine separate cameras provide viewing zenith angles at the surface that range from ± 70.5°. Each camera is designed to collect data at 275 m resolution over a 360 km swath. With this unique multi-angle viewing capability, MISR, for the first time, minimizes the effects of pixel expansion with view angle.

Cloud fraction is calculated from MISR's Radiometric Camera-by-Camera Cloud Mask (RCCM), which uses two observables to determine clear vs. cloudy that depend on whether the observations are made over water or land (Diner et al. (1999)). Over water, the observables are the bi-directional reflectance factor (BRF) in the 865nm channel at 1.1 km resolution and the standard deviation of the 4×4 array of 275-m-resolution 670 nm BRF found within 1.1 km spatially averaged measurements. Each observable is tested against three thresholds in order to classify the pixel as cloud with high confidence, cloud with low confidence, clear with low confidence, and clear with high confidence. Only MISR data over ocean is used to examine the statistical relationships of cloud fractions vs. view angle, since it is this part of the world where the RCCM is working best in the early part of the MISR mission.

Snow et al. (1985) analyzed multiple-view photographs taken from the Space Shuttle of several cloud scenes. However, there is only a very limited set of data from which statistically stable results cannot be calculated. Minnis (1989) analyzed coincident GOES East and GOES west data over the tropical Pacific Ocean. However, these results need to be verified from an independent source in order to determine the impact of the GOES pixel expansion and global applicability of the results. With MISR data, it is now possible to examine cloud fraction vs. view angle globally and (in principle) more accurately.

*Corresponding author address: Guangyu Zhao, Department of Atmospheric Sciences, University of Illinois at Urbana-Champaign, Urbana, IL 61801; email <gyzhao@atmos.uiuc.edu>

2. FEATURES SUMMARY

Figure 1 shows an ideal case in which cloud fractions smoothly increase as the view angle increases. But in reality, the function relating cloud fraction to view angle may become very complicated because of the following factors.

1) Sun-glint: Sun-glint causes the BRF to increase dramatically. As a result, the RCCM may overestimate clouds, if it is not working properly. If so, only one camera is contaminated by sun-glint at a time, which is shown as a spike on the curve of cloud fraction as a function of view angle.

2) Heavy Aerosols/thin clouds: In this situation the nadir RCCM may detect the scene as clear, but the oblique RCCM may detect it as cloudy, which leads to unrealistic behavior in cloud fraction vs. view angle.

3) Multi-layered clouds: It is possible that cloud fractions may decrease as view angle increases due to multi-layered clouds, as shown on Figure 2.

3. APPLICATION OF CLOUD FRACTION VS. VIEWING ANGLE

The importance of characterizing the cloud fraction dependence on view angle is embodied in its applications, which can be summarized as followings:

1) To validate the MISR cloud detection algorithm. If statistical results show that the changes of cloud fraction with view angle for a scene with fixed geometric parameters are not consistent with the ideal case, the RCCM threshold dataset is in need of improvement.

2) To identify heavy aerosols/thin clouds automatically. Whenever there is a big jump of cloud fractions between the nadir and 70.5° cameras (e.g. 50%), this scene will be marked as heavy aerosols/thin clouds. Further analysis of the scene can be performed to distinguish between heavy aerosols and thin clouds.

3) To calculate geometrical thickness of clouds. Statistical results may establish a function relating cloud geometrical thickness to the variation of cloud fractions with view angle.

4) To examine and reduce the biases in cloud climatologies derived from satellite radiometers that have large view angles (e.g., GOES, AVHRR, and MODIS)

5) To help reconcile the differences between surface-based cloud climatologies and satellite-based cloud climatologies.

4. STATISTICAL RESULTS

In the experiment presented here, 179 MISR orbits taken between April and May 2001 and limited to oceanic regions between 50°N and 50°S are examined. Total cloud fractions (including low confidence and high confidence clouds) for all the nine cameras are sorted into bins defined by the nadir cloud fraction over 5 MISR blocks (~360x640km^2). Two quality assessment criteria are applied to filter the data. One is that cloud fractions over 10 MISR blocks must increase with view angle, and the other is that abnormal behavior in cloud fraction vs. view angle is rejected. These two QA criteria totally filter out seventy percent of the data, which may be affected by those factors such as sun-glint and multi-layered clouds as mentioned before.

The final statistical results are shown on Figure 3. As expected, the larger the nadir cloud fraction is, the smaller the difference of cloud fractions between two adjacent cameras. Most importantly, cloud fraction vs. view angles is consistent with the ideal case.

Minnis (1989) also presented cloud fraction increases with view angle based on a substantial amount of GOES data. However, the variation of cloud fraction with view angle is smaller and less smooth in his results than the results shown on Figure 3. Furthermore, the maximum difference of cloud fraction with view angle in the Minnis resuts doesn't vary too much between different cloud fraction bins when compared to the results presented here.

5. CONCLUSION/FUTURE WORK

This study presents preliminary statistical relationships of cloud fraction vs. viewing zenith angle and its application. The accuracy of calculating the cloud fraction highly depends on the quality of the MISR cloud detection algorithm, which has not undergone validation yet. However, the validation of RCCM over ocean is nearly in maturity. The cloud fraction vs. view angle criteria are now taken as important quality assessment parameters to validate the MISR cloud detection algorithm.

In the future, statistical relationships between cloud fraction and view angle will be stratified by cloud type and geographic parameters (e.g., longitude, latitude). Studies on how to use cloud fraction vs. view angle to determine cloud geometrical thickness are underway.

6. REFERENCE

Diner, D. J., and co-authors, 1998: Multiangle Imaging SpectroRadiometer (MISR) description and experiment overview. *IEEE Trans. Geosci. Rem. Sens.* 36, 1072-1087.

Diner, D. J., Di Girolamo, L., and Clothiaux, E.E., 1999: MISR Level 1 cloud detection algorithm theoretical basis. *JPL* D-13397, *Rev.* B, Jet Propulsion Laboratory, Pasadena, CA, 38pp.

Minnis, P., 1989: Viewing zenith angle dependence of cloudiness determined from coincident GOES East and GOES West Data. *J. Geophys. Res.*, 94(D2), 2303-2320.

Snow, J. W. and co-authors, 1985: Space shuttle cloud photographs assist in correcting meteorological satellite data. *Eos Trans.* AGU, 66, 489-490.

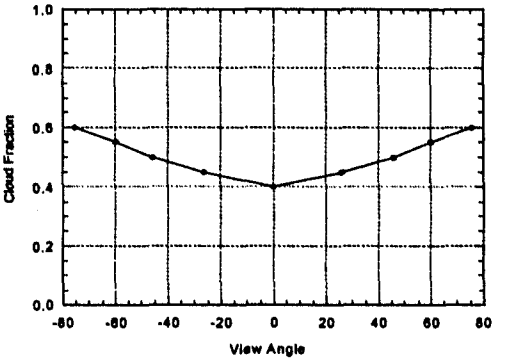

Fig. 1. Cloud fraction vs. view angle in an ideal case. The dots represent the 9 MISR view angles.

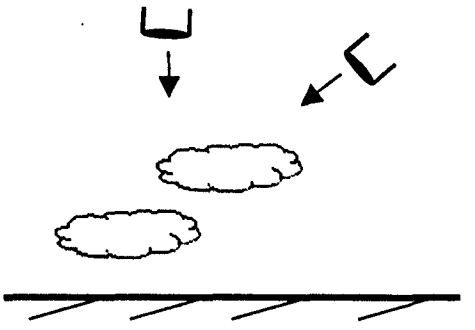

Fig. 2. An example of a scene in which cloud fraction decreases as view angle increases.

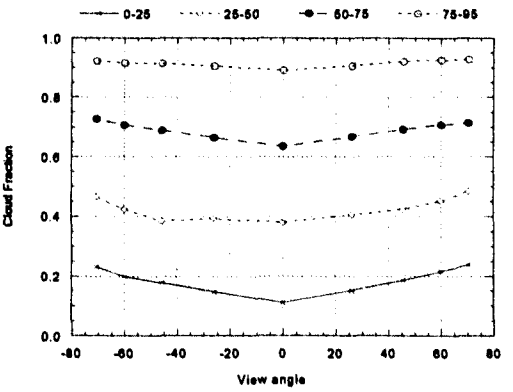

Fig. 3. The statistical relationship of cloud fraction vs. view angle is binned by the nadir cloud fraction.

P4.33 CONTRAIL COVER AND RADIATIVE PROPERTIES FROM HIGH-RESOLUTION SATELLITE DATA

Rabindra Palikonda*
Analytical Services and Materials, Inc., Hampton, VA

Patrick Minnis
Atmospheric Sciences Division, NASA Langley Research Center, Hampton, VA

Patrick W. Heck
Analytical Services and Materials, Inc., Hampton, VA

Sunny Sun-Mack, Qing Z Trepte
SAIC, Hampton, VA

Hermann Mannstein
DLR Institut für Physik der Atmosphäre, Oberpfaffenhofen, Germany

1. INTRODUCTION

Increasing jet air traffic and the coincident rise in jet engine efficiency have resulted in the apparent increase in cirrus cloudiness through the formation of persistent contrails. Minnis et al. (2000) found that cirrus cloud amounts have increased over most air traffic regions with the strongest trends over the USA where cirrus coverage rose by an average of 0.027 between 1971 and 1996. In order to evaluate the potential impact of these contrails on climate, it is necessary to determine the coverage and the radiative properties of contrails. This paper presents recent results from a continuing study of contrails using satellite data to determine contrail coverage and optical properties. Results are presented for selected areas of the USA during 1998 and 2001.

2. DATA

Images from daytime USA overpasses of the Terra 1-km Moderate Resolution Imaging Spectroradiometer (MODIS) and the NOAA-14 1-km Advanced Very High Resolution Radiometer (AVHRR) are analyzed for contrail coverage, optical depth, effective particle size, and longwave (LW) radiative forcing. Terra has an equatorial crossing time ECT of 1030 LT, while the NOAA-14 had an ECT of 1630 LT by 1998. AVHRR data taken during April and December 1998 over 4° regions around New York (41° N, 72° W) and Norfolk, Virginia (36° N, 76° W) were selected for intensive study (Fig. 1).

European Center for Medium-range weather Forecasting (ECMWF) 6-hourly analyses provide surface skin temperatures and 1° atmospheric profiles for calculating top-of-atmosphere (TOA) clear-sky temperatures. A global 10' monthly mean map of VIS albedo, Minnis, et al (2001), is used to estimate clear sky reflectance.

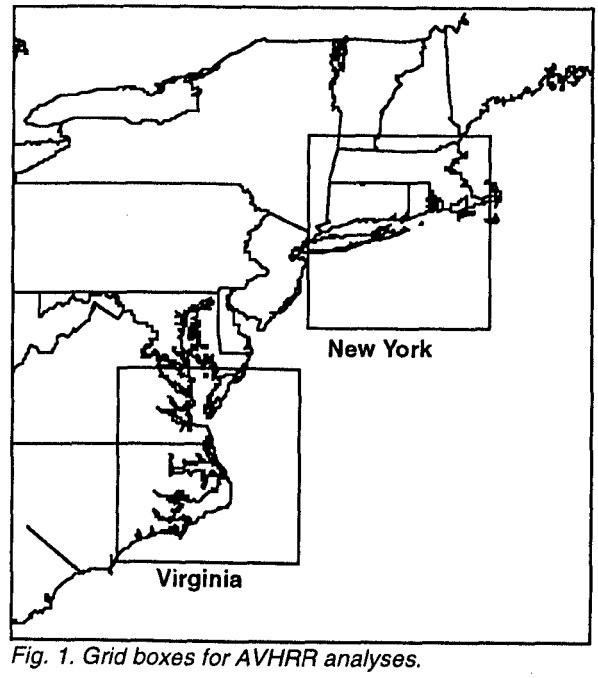

Fig. 1. Grid boxes for AVHRR analyses.

3. METHODOLOGY

3.1 Contrail Detection

Fresh linear contrails are detected using an image processing technique developed by Mannstein et al. (1999), which relies on the linear structure of contrails

Corresponding author address: R. Palikonda, AS&M, Inc., 1 Enterprise Pkwy., Hampton, VA 23666 USA
email: r.palikonda@larc.nasa.gov

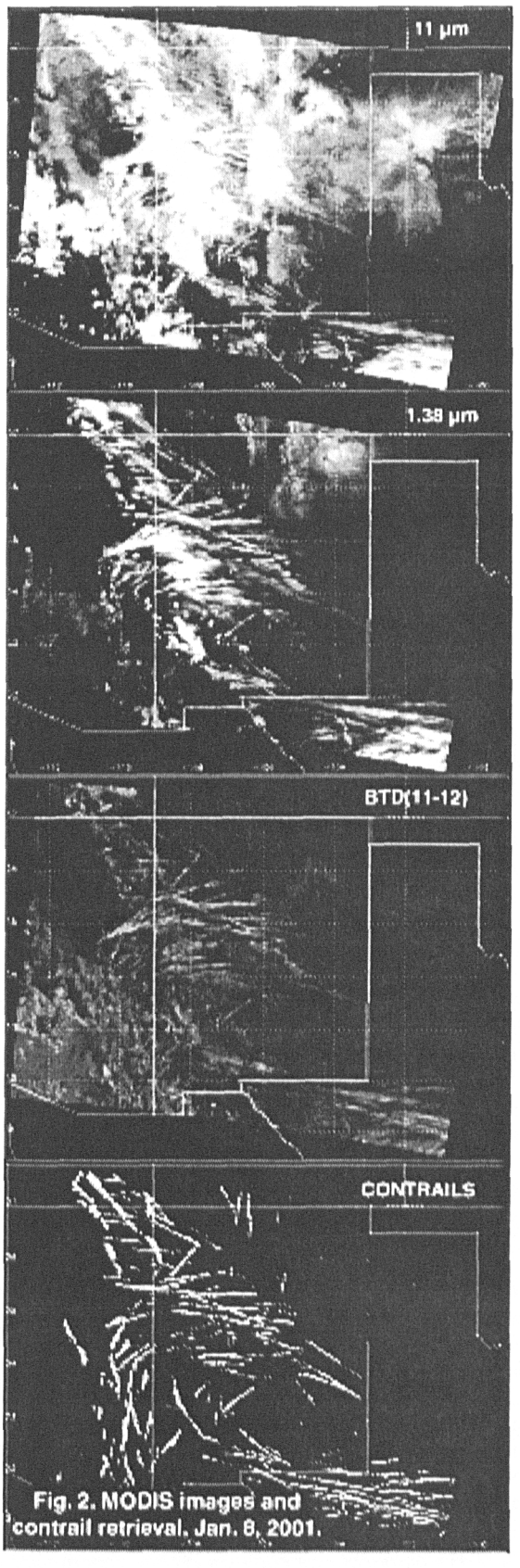

Fig. 2. MODIS images and contrail retrieval, Jan. 8, 2001.

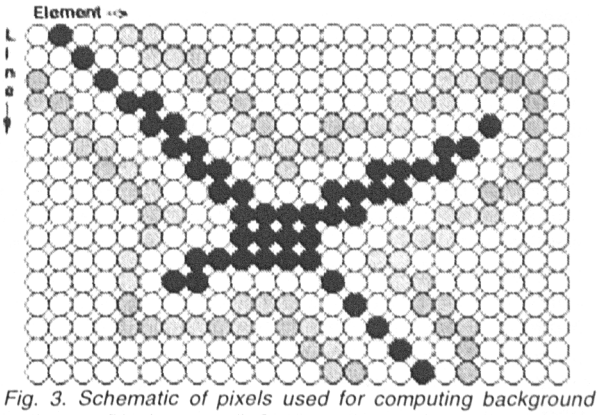

Fig. 3. Schematic of pixels used for computing background radiances. Black - contrail; Gray - background; white - unused.

and the emissivity difference between channel 4 (10.8 µm) and channel 5 (12.0 µm) for small ice crystals. The algorithm is applied to images of channel-5 brightness temperatures and the brightness temperature difference BTD between channels 4 and 5.

Figure 2 shows an example of MODIS images that were analyzed with this approach. The data were taken around 1742 UTC, January 8, 2001 over the southwestern USA. The 11-µm image shows a variety of cloud (white or gray) and surface (black or gray) including some linear structures. The 1.38 µm image, which is sensitive to reflecting surface in the upper atmosphere, shows a large number of linear features that were not evident in the 11-µm image. Similar features are also quite distinct in the BTD picture. The analysis algorithm applied to the BTD image yields the contrails in the bottom panel. Nearly all of the contrails are correctly identified in this case. A few contrails with N-S orientation are actually mountaintops, while some of the thicker contrails are too thin in the result.

3.2 Contrail Microphysical Properties

Cloud and contrail properties are derived using the Visible Infrared Solar-Infrared Split Window Technique (VISST), Minnis et al. (2001), to determine the microphysical properties. VISST is a 4 channel model-matching method for plane parallel clouds. It utilizes parameterizations of theoretical radiance calculations for 7 water and 9 ice crystal size distributions. The cloud properties, cloud height, temperature, emissivity, optical depth, phase, and effective particle size D_e are obtained by matching the model calculations to observations. Particle sizes are typically invalid for overlapped thin-over-thick clouds.

Additionally, for the contrail pixels the effective emissivity is calculated,

$$\varepsilon = [B(T) - B(T_b)] / [B(T_c) - B(T_b)], \quad (1)$$

following the approach of Meyer et al. (2001), where B is the Planck function at 10.8 µm, T is the observed channel 4 temperature, T_b is the background

temperature, and T_c is the contrail temperature. In this case T_c is assumed to be 224 K, a typical temperature suitable for contrail formation. The background radiance is calculated as the average radiance of all pixels at a distance of 2 pixels horizontally, vertically, or diagonally from a contrail pixel that is not adjacent to any other contrail pixels. The background pixels for a hypothetical pair of crossing contrails are shaded gray in Fig. 3. To ensure that the background pixels are below the contrail, $T_b > T_c$. Otherwise, T_b is invalid. If no pixels meeting these criteria are found, the mean background radiance, calculated for all other contrail pixels within the local 10' grid box, is used.

The optical depth τ for the contrails is also derived from the emissivity using the parameterization of Minnis et al (2001),

$$\varepsilon = 1 - \exp[\, a\, (\tau / \mu)^b], \qquad (2)$$

which accounts for the infrared scattering. In (2), μ is the cosine of the viewing zenith angle, and the coefficients, a = -0.458 and b = 1.033, are for an axi-symmetrical 20-μm hexagonal ice column. To minimize false detections, all contrails with $\tau > 1$ were eliminated from the processing. Although some actual contrails were observed with $\tau > 1$, the number eliminated is negligible.

3.3 Contrail Longwave LW Radiative Forcing

After the contrails are detected using the image processing technique, their LW forcing is computed directly from the observed radiances. The contrail LW forcing is given by

$$F = (Q_b - Q_c)\, f_c, \qquad (3)$$

where f_c is the contrail fraction and Q_c and Q_b are the LW fluxes for contrails and the background respectively. Broadband LW fluxes are calculated from the 10.8-μm radiances as described by Minnis and Smith (1998).

4. RESULTS

The contrails in Fig. 2 covered 22,644 km^2, or 5.8% of the region shown in the image. The distribution of contrail optical depths derived from (1) and (2) is shown in Fig. 4. Most of the contrails have τ between 0.05 and 0.2, although contrails with optical depths as large as 1.0 were observed. On average, τ = 0.14. In this case, F = 0.42 Wm^{-2}, which gives a unit forcing, $F_o = F / f_c$, of only 7.3 Wm^{-2}. The histogram of τ (Fig. 5) for the entire 1742-UTC MODIS image (~2.5 x 10^6 km^2) over the USA during Jan. 8, 2001 is nearly identical to that in Fig. 4 for the southwestern USA. The total contrail coverage was 9 x 10^4 km^2, or 3.6% of image. The mean τ and unit LW forcing are 0.13 and 4.9 Wm^{-2} for the entire image.

The distributions of optical depths from the AVHRR analyses in Figs. 6 and 7 show little seasonal and only slight regional differences. The histograms show more contrails with $\tau > 0.2$ than those from MODIS. In these cases, the mean optical depths over the New York and Virginia regions were 0.21 and 0.19 during April 1998 and 0.18 and 0.15 during December 1998, respectively

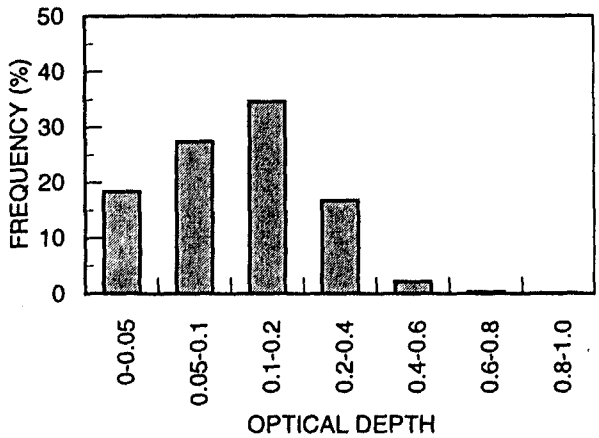

Fig. 4. Histogram of τ for contrails in Fig. 2.

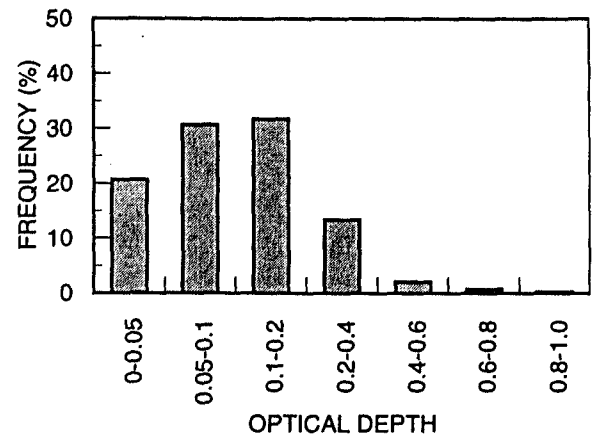

Fig. 5. Histogram of τ for contrails detected over USA in MODIS image taken at 1800 UTC, Jan. 8, 2001.

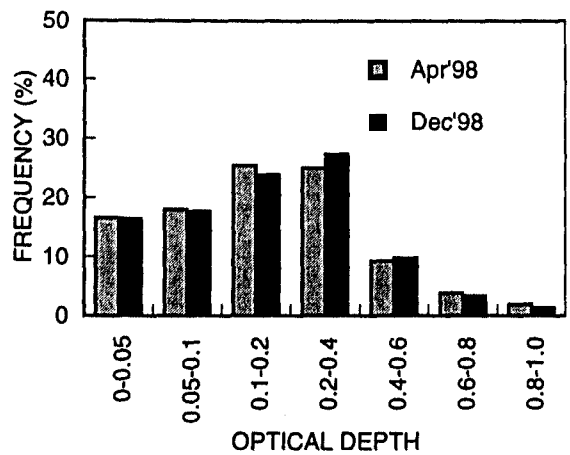

Fig. 6. Histogram of τ for contrails in New York region.

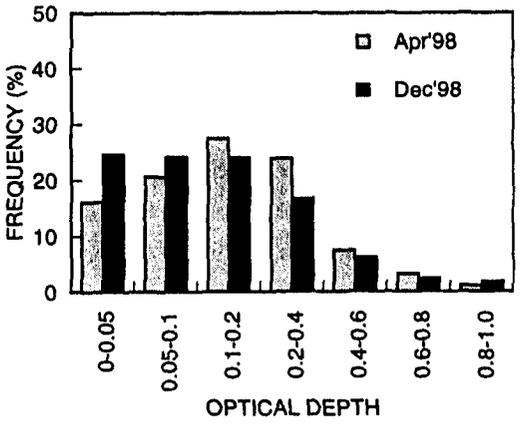

Fig. 7. Histogram of τ for contrails in Virginia region.

The respective mean contrail amounts are 0.50% and 0.26% during April and 0.52% and 1.05% during December. For all four datasets, the unit LW forcing is 8.8 Wm^{-2}. D_e was computed for the New York region using only those contrail pixels occurring over an otherwise cloud-free background. The resulting mean value is 37 μm.

5. DISCUSSION AND CONCLUSIONS

The contrail optical depths computed here are 20 to 90% larger than those from Meyer et al. (2001) for contrails over Europe, but are 50 to 70% less than those derived by Minnis et al. (2000) over the USA and the value of 0.3 used by Minnis et al. (1999) to simulate global contrail radiative forcing. The latter value was selected based on early estimates of τ that were derived from a few selected cases. Similarly, Minnis et al. (2000) only used contrails over clear backgrounds and a few selected days over the east coast of the USA. They derived τ using the visible channel, an approach that may bias the retrieval. The infrared method, which assumes a value of T_c, is a more reliable technique than the visible retrieval because of large uncertainties in the contrail scattering properties. The larger value relative to the Meyer et al. (2001) results is supported by model calculations (Ponater et al. 2001) that find τ over the USA is greater than over Europe because of temperature and moisture differences. The mean value of D_e is remarkably close to the 34-μm value used by Meyer et al. (2001).

The mean contrail coverage over the Virginia and New York regions, which is lower than expected from theoretical estimates, is probably underestimated. Using the same technique with NOAA-14 data, Meyer et al. (2001) estimated the contrail detection efficiency at 40%. If true for the AVHRR data used here, the average contrail coverage over the New York and Virginia regions respectively would be 1.3% and 1.6%, values that are closer to the January theoretical estimates of Ponater et al. (2001). The detection efficiency for these regions needs further examination. Visual examination of the MODIS retrievals indicate that the detection efficiency is much better than found for the AVHRR. The only contrails that were not detected appeared to be those that had already spread significantly.

The mean values of F_o are significantly less than the 28.7 Wm^{-2} from Minnis et al. (1999), primarily, because of the reduced optical depths. Adjusting for differences in τ yields global theoretical estimates of 12.4 and 16.6 Wm^{-2} for the MODIS and AVHRR results, respectively. These values are roughly twice those derived from the data. Remaining differences are likely due to the specific ambient cloud conditions, time of day, location, and the assumed model value of T_c.

The preliminary results shown here provide additional evidence that contrail radiative impacts are smaller than previously estimated. However, complete multi-seasonal analyses of both AVHRR and MODIS data taken over the USA are needed to determine the spatial and temporal distribution of contrails, their optical properties and shortwave and LW forcings as well as their relationships to the ambient conditions. Results from such studies are essential for confirming or improving predictions of future air traffic climate effects.

Acknowledgments

This research was supported by the NASA Office of Earth Science Pathfinder Dataset and Associated Science Program.

References

Mannstein, H., R. Meyer, and P. Wendling, 1999: Operational detection of contrails from NOAA-AVHRR data. *Intl. J. Remote Sens.*, **20**, 1641-1660.

Meyer, R. H. Mannstein, R. Meerkötter, U. Schumann, and P. Wendling, 2001: regional radiative forcing by line-shaped contrails derived from satellite data. Submitted *J. Geophys. Res.*

Minnis, P.,et al., 2001: A near-real time method for deriving cloud and radiation properties from satellites for weather and climate studies. *Proc. AMS 11th Conf. Satellite Meteor. and Oceanogr.*, Madison, WI, October 15-18.

Minnis, P., et al, 2000: Cirrus, contrails, and radiative forcing over the USA: their relationships to air traffic and upper tropospheric conditions. *Proc. European Workshop on Aviation, Aerosols, Contrails, and Cirrus Clouds*, Seeheim, Germany, July 10-12, 2000, Air Pollution Research Report 74, EUR 19428, European Commission, Brussels, 193-196.

Minnis, P., U. Schumann, D. R. Doelling, K. M. Gierens, and D. W. Fahey, 1999: Global distribution of contrail radiative forcing. *Geophys. Res. Lett.*, **26**, 1853-1856.

Minnis, P. and W. L. Smith, Jr.,1998: Cloud and radiative fields derived from GOES-8 during SUCCESS and the ARM-UAV Spring 1996 Flight Series. *Geophys. Res. Lett.*, **25**, 1113-1116.

Ponater, M., S. Marquart, and R. Sausen, 2001: Contrails in a comprehensive global climate model: parameterisation and radiative forcing results. Submitted, *J. Geophys. Res.*

P4.36 SURFACE EMISSIVITY DERIVED FOR INFRARED REMOTE SENSING FROM SATELLITES

Yan Chen, Sunny Sun-Mack
Science Applications International Corporation, Hampton, VA 23666

*Patrick Minnis, William L. Smith, Jr., David F. Young
Atmospheric Sciences, NASA Langley Research Center, Hampton, VA 23681

1. INTRODUCTION

Surface emissivity is essential for deriving the surface skin temperature from satellite-based infrared measurements and for estimating the emission of longwave radiation from the surface, an important component of the energy budget of the surface-atmosphere interface. It is also critical for cloud detection and retrieval of cloud properties. Brightness temperature differences *BTD* between 3.7 and 11-μm observations are often indicative of the presence or absence of clouds. For clear scenes, the *BTD* is due to differences in atmospheric absorption and in surface emissivity ε between the two channels. Cloud phase, optical depth, and particle size further affect the *BTD* in cloudy scenes. Retrieval of cloud phase and effective particle size often relies on the value of *BTD*, which for optically thin clouds is affected by the surface emission and, at 3.7 μm, the surface reflectance. Thus, the accuracy of cloud detection and particle size retrievals depends on the accuracy of the surface emissivity. The Clouds and Earth's Radiant Energy System (CERES, Wielicki et al. 1998) system is measuring broadband shortwave and longwave radiances and deriving cloud properties from various imagers to produce a combined global radiation and cloud property data set (Minnis et al. 1999). This paper presents the development and results of an analysis of satellite imager data taken at 3.7, 10.8, and 12.0 μm to derive a seasonally varying map of ε for use by CERES and other cloud retrieval algorithms.

2. DATA

ISCCP (International Satellite Cloud Climatology Project) DX Advanced Very High Resolution Radiometer (AVHRR) data taken during 1986 were used to obtain the clear-sky top-of-the-atmosphere (TOA) brightness temperatures T_i at 3.7, 10.8, and 12.0 μm, channels i = 3, 4, and 5, respectively. These data have a nominal resolution of 4 km but are sampled every 32 km. It is assumed that the ISCCP scene classification (Rossow and Schiffer 1999) is correct for all pixels and, therefore, the temperatures are uncontaminated by clouds. Six-hourly ECMWF (European Center Medium Range Weather Forecast) analyses provided at a resolution of 0.56° latitude and longitude were used to specify the vertical profiles of atmospheric temperature, humidity, and ozone. Linear interpolation was used to match the soundings to the satellite observation times. Standard atmospheric values were used for profiles of other absorbing gases such as NO_2 and CH_4.

*Corresponding author address: P. Minnis, MS 420 NASA Langley Res. Ctr., Hampton, VA 23681;
email: p.minnis@larc.nasa.gov

3. METHODOLOGY

The basic approach solves a set of simultaneous equations to obtain surface emissivity. The method requires observations from both daytime and nighttime over the same area.

The relationship between the TOA and surface radiances can be crudely represented as

$$B_i(T_i) = \varepsilon_{ai} B_i(T_{ai}) + (1-\varepsilon_{ai}) B_i(T_{si}) \quad (1)$$

where B is the Planck function, ε_a and T_a are the atmospheric effective emissivity and effective temperature, respectively. The radiance for T_{si}, the apparent skin radiating temperature, is determined using the correlated *k*-distribution method (Kratz 1995) with the atmospheric profiles to remove the molecular absorption. The *k*-distribution technique is used to compute the downwelling and upwelling radiation at each ECMWF layer over the entire band pass of the channel using the appropriate filter function for the particular satellite imager channel. Considering the downwelling atmospheric radiance at the surface L_a, the radiation balance at surface is

$$B_i(T_{si}) = \varepsilon_i B_i(T_{skin}) + (1-\varepsilon_i) L_{ai} \quad (2)$$

in the absence of solar radiation, where T_{skin} is the skin temperature and T_{si} is the effective radiating temperature of the surface. For simplicity, it assumed that ε_i does not depend on the viewing zenith angle VZA. Skin temperature can be expressed at night as

$$T_{skin} = B_i^{-1}[\{B_i(T_{si}) - L_{ai}\}/\varepsilon_i + L_{ai}], \quad (3)$$

where B_i^{-1} is the inverse Planck function. If the skin temperature is known, the emissivity can be solved for the remaining channels, e.g.,

$$\varepsilon_3 = [B_3(T_{s3}) - L_{a3}] / [B_3(T_{skin}) - L_{a3}]. \quad (4)$$

At night, both T_{s3} and T_{s4} can be derived using (2) and the emissivity ratio,

$$\varepsilon_3' = \varepsilon_3 / \varepsilon_4 = [B_3(T_{s3}) - L_{a3}] / [B_3(T_{s4}) - L_{a3}], \quad (5)$$

can be computed. If it is assumed that this ratio is a constant for a given surface, then the value of ε_3 can be determined from data taken during the daytime. However, the ratio is variable depending on L_{a3}, which changes with precipitable water *PW*. To account for this variation, the data can be fitted to an equation of the form

$$\varepsilon_3' = \varepsilon_{3o}' + a\,PW + b\,PW^2, \quad (6)$$

where ε_{3o}' is the baseline emissivity ratio and is generally close to the value obtained from (5) if $L_{a3} = 0$. The coefficients for (6) can be computed from data taken during the night for several different times to obtain a reasonable dynamic range in *PW*. During the daytime, the apparent surface temperature for channel 3 is

$$B_3(T_{s3}) = \varepsilon_3[B_3(T_{skin})] + \alpha_3[\chi S_3' + L_{a3}], \quad (7)$$

where χ is the anisotropic correction factor, α_3 is the surface albedo, and S_3', the solar radiation reaching the surface, is computed from the Earth-sun distance and solar-zenith-angle corrected solar constant attenuated by atmospheric absorption using the *k*-distribution method. According to the Kirchoff's law,

$$\alpha_3 = (1 - \varepsilon_3). \quad (8)$$

Using (4), (5), and (8) to substitute for the emitted component and the albedo on the right hand side of (7) and rearranging gives

$$\varepsilon_3 = 1 - \{B_3(T_{s3}) - \varepsilon_3'[B_3(T_{s4})] - (1 - \varepsilon_3')\,L_{a3}\}/\chi S_3'. \quad (9)$$

In this manner, ε_3 is derived using (9). The absorption coefficients used for the thermal component are applied to the observed 3.7-μm radiance to obtain $B_3(T_{s3})$. Although the atmospheric attenuation of the upwelling solar and emitted 3.7-μm radiances is slightly different for each component, the differences should have a negligible impact on the result. Knowing ε_3, T_{skin} can easily be solved from (7). Then, ε_4 and ε_5 are computed from (3).

This technique was tested theoretically using 3 different surface types with ε_3 ranging from 0.73 to 0.97 and ε_4 ranging 0.93 to 0.99 using 91 soundings to represent a large range of atmospheric conditions. The resulting values of ε_3 were within 1% of the original value for all of the cases with the largest errors occurring for the desert (0.73) case. RMS errors up to 3% were found for ε_4 with the greatest errors occurring for the desert case. The mean errors were all negligible. The theoretical calculations assumed an isotropic surface reflectance and no VZA dependence of ε.

The ISCCP data were analyzed by computing ε_3' for each clear nighttime pixel and averaging the results for every 1° latitude-longitude box for a given orbit. The corresponding value of *PW* was saved for each average. Because of insufficient sampling, however, a mean value of ε_3' was computed for each region and used instead of a fit to (6) to derive ε_3, ε_4, and ε_5 from the daytime data to obtain mean values and standard deviations for each region. The values of χ used in (9) were taken from the models used by Trepte et al. (1999). Those models are generally used for visible or broadband solar channels. Averages were also computed for each IGBP surface type (Table 1) and then used to fill in the results for regions with no data excepting deserts. During daytime, the value of T_3 was often not used because it saturated over desert areas due to high afternoon skin temperatures and highly reflective surfaces. Linear interpolation between the available months was used to obtain a more realistic estimate of emissivity for each desert region individually when no T_3 data were available. ISCCP DX data from January, April, June and October, 1986 were processed in this manner.

4. RESULTS

Figure 1 shows the distribution of ε_3 derived for January and June 1986. The gray scale starts at 0.700, but several desert areas have lower values. The heavily vegetated areas have values greater than 0.925 while intermediate values are found over less vegetated regions. The means for each of the IGBP types for the Northern Hemisphere are summarized in Table 2. The greatest seasonal variations occur in the lightly vegetated savannahs, grasslands, shrublands, and deserts. The most barren deserts like the Sahara do not show much seasonal variation. Some of the IGBP types, like tundra and deciduous needleleaf forests, are not well sampled and are not reliable. The ocean and snow categories are probably cloud contaminated and are not used for CERES.

Table 1. Surface type.

IGBP Type
1. evergreen needleleaf = conifer
2. evergreen broadleaf = conifer
3. deciduous needleleaf = deciduous
4. deciduous broadleaf = deciduous
5. mixed forests = 1/2 conifer + 1/2 deciduous
6. closed shrublands = mosaic
7. open shrubland = mosaic
8. woody savannas = grass
9. savannas = grass
10. grasslands = grass
11. permanent wetlands = 1/2 grass + 1/2 water
12. croplands = grass
13. urban = black body
14. mosaic = 1/2 grass + 1/2 mixed forest
15. snow/ice
16. barren/sparsely vegetated = desert
17. water
18. tundra = frost
19. coastline = 10% to 90% water

Table 2. Mean ε_3 for Northern Hemisphere.

IGBP	January	April	June	October
1	0.947	0.951	0.964	0.928
2	0.954	0.956	0.958	0.965
3	———	0.929	0.963	0.941
4	0.942	0.943	0.957	0.953
5	0.953	0.945	0.964	0.946
6	0.908	0.933	0.944	0.924
7	0.827	0.873	0.932	0.861
8	0.919	0.930	0.951	0.947
9	0.874	0.926	0.924	0.933
10	0.864	0.899	0.924	0.901
11	0.928	0.951	0.956	0.901
12	0.913	0.924	0.939	0.923
13	0.917	0.929	0.944	0.937
14	0.915	0.926	0.942	0.927
15	0.924	0.972	0.969	0.954
16	0.772	0.866	0.921	0.797
17	0.951	0.973	0.973	0.962
18	0.935	0.968	0.949	0.929
19	0.929	0.952	0.959	0.939

The values for ε_4 and ε_5 were generally much greater than their ε_3 counterparts. In some cases the values exceed unity, indicating errors in the retrievals.

To assess the results, the TOA channel-3 brightness temperatures were calculated using the emissivity maps, the observed values of T_4, and the ECMWF profiles. Two data sets were used: January 1986 ISCCP DX and January 1998 Visible Infrared Scanner (VIRS) data used by CERES. Differences between the predicted and observed values of T_3 are summarized in Tables 3 and 4. Except for snow, tundra, savannah, and open shrubland, the mean daytime errors are 1K or less and the standard deviations range between 2 and 4K. The nighttime results are biased by 1 to 5 K; the largest values occur over deserts. A diurnal variation in ε_3 was found by Minnis et al. (1998) that is roughly equivalent to the day-night differences seen in Table 3. The VIRS results are similar to those for AVHRR over heavily forested areas, but over other surface types, the predicted temperatures are generally much greater by 1 to 5K with much larger standard deviations. These differences indicate that ε_3 for the VIRS 3.7-μm channel is considerably greater than the corresponding AVHRR-based value. The source of these large differences is not readily apparent.

Table 3. T_3 errors using ε_3 for January 1986 DX data.

	ΔT (K)			
IGBP	Daytime		Nighttime	
	mean	std	mean	std
1	0.5	2.3	1.7	1.7
2	-0.6	3.4	0.2	3.0
3	—	—	—	—
4	0.4	2.8	1.4	2.1
5	0.5	2.4	1.4	1.7
6	0.8	2.8	1.9	2.0
7	3.9	5.5	3.1	3.0
8	0.7	2.9	1.3	2.2
9	2.0	3.9	1.7	2.3
10	1.3	4.1	3.0	3.3
11	0.6	2.2	1.0	1.9
12	0.4	3.0	1.9	2.6
13	-0.6	3.0	2.0	3.0
14	0.6	3.1	1.7	2.7
15	1.7	6.3	2.1	9.8
16	0.4	2.9	5.5	3.0
17	0.8	3.1	1.0	1.7
18	2.1	4.5	4.7	4.2
19	-0.4	3.9	1.3	3.0

Table 4. T_3 errors using ε_3 for Jan. 1998 VIRS data.

	ΔT (K)			
IGBP	Daytime		Nighttime	
	mean	std	mean	std
1	0.9	3.6	0.9	3.0
2	0.2	4.0	0.4	2.7
3	—	—	—	—
4	-1.1	4.2	-0.5	4.2
5	0.5	4.0	-0.4	3.5
6	-3.8	5.6	-1.5	3.6
7	-2.5	7.1	-2.6	4.0
8	-2.5	4.7	-0.7	3.0
9	-4.5	4.6	-1.1	2.8
10	-2.7	7.3	-1.8	4.3
11	1.3	4.8	0.7	3.7
12	-3.1	5.2	-0.4	3.2
13	-5.8	6.3	-1.9	4.6
14	-1.2	4.3	-0.1	3.4
15	8.3	7.6	-3.5	5.7
16	-2.1	5.5	-3.0	3.1
17	-0.7	3.0	0.7	1.2
18	-3.6	8.1	-3.2	5.2
19	-0.6	6.0	-1.7	5.0

5. CONCLUDING REMARKS

The results of the method applied here yield very reasonable daytime predictions of T_3 for the AVHRR data that were used in the original determination of the emissivities. The resulting bias in the nighttime data and even greater biases in the VIRS temperatures highlight the paucity of information about surface emissivity and the bidirectional reflectance characteristics at solar infrared (3.5 - 4.0 μm) wavelengths. The observed errors can arise for many different reasons: errors in the atmospheric profiles, large uncertainties in the anisotropic correction factors, spectral variability in surface emissivity, VZA-dependencies, small time and space scale changes of emissivity due to changes in surface moisture (e.g., dew), and residual cloud or ground fog contamination of the clear scenes. These and other factors will be explored to improve the determinations of surface emissivity for remote sensing.

References

Kratz, D. P., 1995: The correlated *k*-distribution technique as applied to the AVHRR channels. *J. Quant. Spectrosc. Radiat. Transfer*, **53**, 501--517.

Minnis, P., W. L. Smith, Jr., and D. F. Young, 1998: Surface emissivity derived from multispectral satellite data. Proc. *8th Annual ARM Sci. Team Mtg.*, Tuscon, AZ, March 23-27, 1998, 489-494.

Minnis, P., D. F. Young, B. A. Wielicki, P. W. Heck, S. Sun-Mack, and T. D. Murray, 1999. Cloud properties derived from VIRS for CERES. *Proc. AMS 10th Conf. Atmos. Rad.*, Madison, WI, June 28 – July 2, 21-24.

Rossow, W. B. and R. A. Schiffer, 1999: Advances in understanding clouds from ISCCP. *Bull Am. Meteor. Soc.*, **80**, 2261-2287.

Trepte, Q., Y. Chen, S. Sun-Mack, P. Minnis, D. F. Young, B. A. Baum, and P. W. Heck, 1999: Scene identification for the CERES cloud analysis subsystem. *Proc. AMS 10th Conf. Atmos. Rad.*, Madison, WI, June 28 – July 2, 1999, 169-172.

Wielicki, B. A., et al., 1998, Clouds and the Earth's Radiant Energy System (CERES): Algorithm overview. *IEEE Trans. Geosci. Remote Sens.*, **36**, 1127-1141.

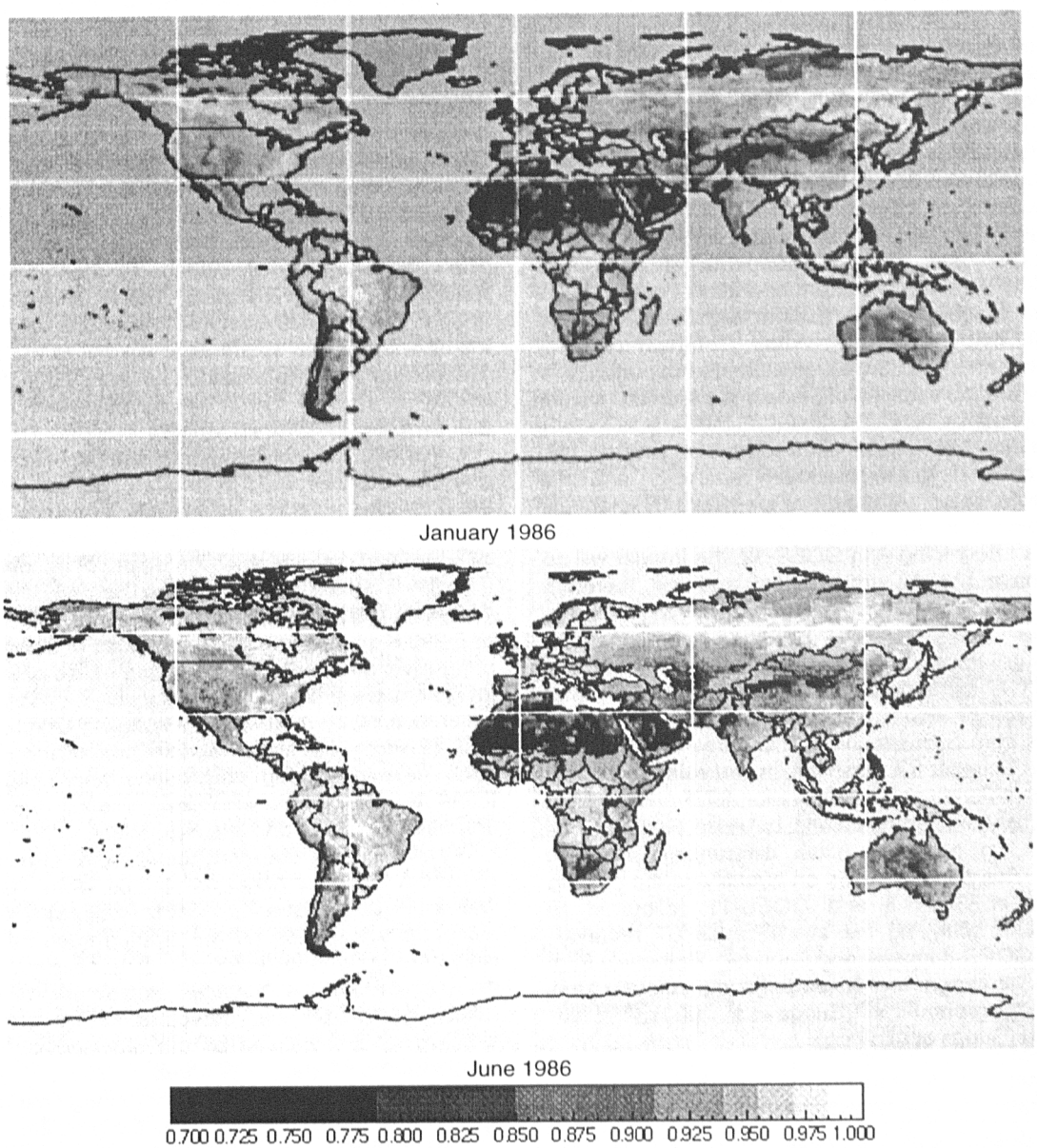

Fig. 1. Monthly mean 3.7-μm surface emissivities derived from AVHRR data during 1986.

P4.37 **INTER-COMPARISON OF GOES-8 IMAGER AND SOUNDER SKIN TEMPERATURE RETRIEVALS**

Stephanie L. Haines*
University of Alabama in Huntsville
Global Hydrology and Climate Center, Huntsville, AL

Ronnie J. Suggs and Gary J. Jedlovec
Global Hydrology and Climate Center
MSFC/NASA, Huntsville, AL

1. INTRODUCTION

Skin temperature (ST) (or land surface temperature) retrievals are currently made every hour from 1145 to 2345 UTC in support of near real-time modeling applications using Geostationary Operational Environmental Satellites (GOES) data at the Global Hydrology and Climate Center (GHCC). The GOES Imager or Sounder data are used in a physical split window technique (PSW) (Suggs et al. 1998) to derive skin temperature values over much of the United States. The frequency of the retrievals allows the data to be assimilated into numerical models to improve the accuracy of their forecasts (Lapenta et al. 1999). GOES-8 is the current eastern operational satellite and provides imagery of the eastern Continental United States (CONUS) every 15 minutes. The high temporal resolution of the GOES data provides the opportunity to study the diurnal variation of measured parameters such as skin temperature.

The PSW technique uses longwave infrared (IR) window channels to simultaneously retrieve ST and total precipitable water. At least two longwave IR channels are required from the Imager or the Sounder to make retrievals. Beginning with GOES-12, the Imager will no longer have the 12 μm channel and will therefore become obsolete with respect to the PSW retrieval technique. Once GOES-12 becomes operational, the Sounder will have to provide the data for ST retrievals. GOES-11 is currently in orbit ready to replace either GOES-8 or GOES-10 and will be able to provide retrievals from both sensors. This research compares Imager to Sounder ST retrievals, in particular the spatial resolution differences, in preparation for the loss of the 12 μm channel. Comparisons between GOES-8 and GOES-11, in particular noise differences, are also studied. This paper focuses on quantifying the striping observed in GOES-8 and GOES-11 calibrated IR images and analyzing the averaging of ST retrievals from the GOES-8 Imager and Sounder. Retrievals from the GOES-8 Imager and Sounder have previously been compared to ground-truth (Suggs et al. 2000) and inter-compared (Suggs et al. 2001).

* *Corresponding author address:* Stephanie L. Haines, UAH/ Global Hydrology and Climate Center, 320 Sparkman Dr, Huntsville, AL 35805.
E-mail: haines@atmos.uah.edu

2. BACKGROUND

2.1 Infrared On-Board Calibration

Temperatures on the GOES satellites vary diurnally by tens of degrees Kelvin. These large and rapid temperature changes cause the instruments' infrared responsivities to vary significantly (Weinreb 1996). The infrared channels of the Imager and Sounder are calibrated frequently during orbit to counteract the temperature changes. To calibrate their infrared channels, the Imager and Sounder view space and warm on-board blackbodies. The Sounder views space every 2 minutes and its blackbody every 20 minutes. The Imager needs to view space as often as possible to reduce the effect of 1/f noise. For routine imaging, the Imager views space every 36.6 seconds, and during a full disk image the space look interval is 2.2 seconds. The Imager views its blackbody every 30 minutes.

2.2 Striping in Infrared Images

The GOES satellites exhibit striping in both Imager and Sounder calibrated IR images. Stripes are seen in the East-West direction as a result of multiple detectors scanning the scene. Striping occurs on uniform scenes as a result of the differences in output of the detectors in a channel (Baucom and Weinreb 1996). Baucom and Weinreb (1996) state that for GOES-8 Imager channel 4 or 5 290 K scenes striping magnitudes of several tenths of a Kelvin are common. The main cause of striping in Imager scenes is low frequency, or 1/f, noise in the calibration of the detectors (Wack and Candell 1996). The 1/f noise causes a random drift of the output of each detector during calibrations and imaging and therefore the noises exhibited in each detector are unrelated (Baucom and Weinreb 1996).

The Sounder does not suffer from 1/f-noise drifts since the Sounder performs clamps while viewing its filter wheel at a frequency of 50Hz (Weinreb 1996). The complete explanation for the striping seen in Sounder calibrated images is unknown. It is believed that the main cause for the Sounder striping is the different responses of the four detectors to the changes in background flux caused by the changes of on-board temperatures (M. Weinreb 2001, personal communication). Also, the relatively long time between space looks (2-minutes) amplifies the problem.

Instrument noise (manifested as errors in radiances and systematic striping) plays a significant role in the accuracy of surface retrievals and often requires pixel averaging to reduce the affect of random noise.

3. METHODOLOGY

Striping errors were computed for both GOES-8 and GOES-11 from three days (July 25-27, 2000) of the GOES-11 science test. For each satellite results were computed for channels 4 and 5 from the Imager, and channels 7 and 8 from the Sounder. The GOES-11 satellite was launched on May 3, 2000 and positioned at 104W during the science test conducted from June 30, 2000 through August 13, 2000.

A method to quantify the striping in GOES Imager scenes is described in Baucom and Weinreb (1996). Their method selects 4 line x 7 element uniform regions from GOES-8 Imager calibrated IR scenes. The 14 pixels for each detector are averaged and the striping is defined as the difference between the two detector averages. For this study 10 line x 18 element uniform regions were selected from Imager scenes. Because of the pixel overlap in the sampling process, a 10 x 18 pixel Imager region corresponds to a square region of approximately 40 x 40 km at nadir. For the Sounder 4 lines x 4 elements (40 km by 40 km) pixel groups were selected. A region larger than that used by Baucom and Weinreb (1996) was selected so that the Imager region would be close in size to the smallest possible square Sounder region. The Sounder region requires at least four lines because of the four detectors utilized by the IR channels of the Sounder. Detector numbering throughout the study was selected randomly, since the detector numbers of the lines of a region were unknown.

The Imager striping is defined as the difference between the average brightness temperatures of the two detectors. Sounder striping is not defined by Baucom and Weinreb (1996) and, because of the different number of detectors, there is not a Sounder method equivalent to the Imager method. The Sounder striping in this research is defined as the average of the differences between brightness temperatures of adjacent detectors. The largest difference between adjacent detectors is also given.

Regions uniform with respect to the IR window brightness temperature values were selected manually and only those with standard deviations less than 1 K were retained. The standard deviation limit ensures that the chosen sectors have near constant brightness temperatures, with variation due to noise only. For each satellite sensor four regions were selected at three different times, giving a total of twelve regions for each channel. For each time, the root mean square (RMS) of the four striping errors was computed. Over the three images, the RMS error was averaged. This method is adapted from the method described by Wack and Candell (1996).

Retrieval statistics for GOES-8 Imager and Sounder were computed for a case study over a region covering much of the CONUS for a primarily clear-sky day on April 25, 2001. The standard deviations of the Imager and Sounder skin temperatures were computed for single pixel and 3x3 pixel averaging (with single pixel spacing) retrievals. The Imager and Sounder single pixel retrievals have 4 km and 10 km nominal spatial resolution, respectively.

4. RESULTS

4.1 Striping Comparisons

Visual inspection of calibrated IR GOES-8 and GOES-11 images reveals striping in the scenes from both satellites, with GOES-8 tending to exhibit a larger amount of striping. An exception to this general observation is the Imager channel 5 from GOES-11. For several, but not all, of the Imager channel 5 images viewed and analyzed during this research the GOES-11 striping was seen to be equal to or larger than the GOES-8 striping. This observation correlates to the findings presented by Wack and Candell (1996) that state that the channel 5 striping for GOES-11 can be expected to be similar to GOES-8 striping. The calculated GOES-11 Sounder channel-8 noise level is slightly higher than the noise level for the same channel on GOES-8 (Bachmeier et al. 2001), therefore Sounder channel 8 striping improvements should be expected to be negligible.

The computed average striping errors for the Imager and the Sounder instruments are presented in Tables 1 and 2, respectively. The Sounder striping errors are presented as the average of the differences between adjacent lines (error 1), and as the largest difference between adjacent lines (error 2). The average striping errors show improvement for GOES-11, with an average improvement factor of 1.4 from GOES-8 to GOES-11. The smallest improvement of a factor of 1.2, for the Imager channel 5, correlates well to previous observations. For the Sounder, channel 8 shows the smallest improvement factor, with a value of 1.3 (for both error computation methods) compared to channel 7 with improvement factors of 1.8 and 1.6 for striping errors 1 and 2, respectively.

Table 1. GOES-8 and GOES-11 Imager average striping errors.

Satellite	Band	Average Striping Error (K)
GOES-8	4	0.207
GOES-8	5	0.239
GOES-11	4	0.130
GOES-11	5	0.207

Table 2. GOES-8 and GOES-11 Sounder average striping errors.

Satellite	Band	Average Striping Error1 (K) (average of differences)	Average Striping Error2 (K) (largest difference)
GOES-8	7	0.250	0.389
GOES-8	8	0.177	0.316
GOES-11	7	0.138	0.243
GOES-11	8	0.137	0.246

Comparing the Imager average striping errors to the Sounder errors computed using the average differences indicates the striping is similar for the two instruments. However, comparing the Imager striping to the Sounder striping computed using the largest difference between adjacent detectors reveals larger Sounder striping. The largest difference between adjacent lines may be the best indication of striping within an image because this is the striping visually noticed. These results may indicate larger striping exhibited by the Sounder than the Imager, although the Imager striping is computed by averaging over several lines, and no averaging is performed during the Sounder computations. Even if the striping in the Sounder is less than in the Imager, the Sounder is at a disadvantage because of its coarser resolution.

Striping is known to increase with decreasing temperature and the Baucom and Weinreb (1996) study presents striping as a function of temperature. In general, the regions sampled for this case study had brightness temperatures in the range 290-300 K. Baucom and Weinreb (1996) study striping in terms of GVAR counts for GOES-8 imager channel 4 only, and they conclude that the mean GOES-8 Imager channel 4 striping for scenes at 300 K is between 0.11 and 0.18 K. Wack and Candell (1996) estimate GOES-8 Imager channel 4 striping at 0.14 K and channel 5 striping at 0.21 K. Comparisons of these published striping values to those presented in Tables 1 and 2 indicate that the striping values computed during this case study are larger than the published values. However, this case study was for a small sample of regions, and for a larger sector size. As the size of the sector increases, the probability of variations between detectors increases because of surface variations. The results from this case study display the same trends as the published results, with the Imager channel 5 having the larger striping value, and the GOES-11 Sounder exhibiting the expecting improvement.

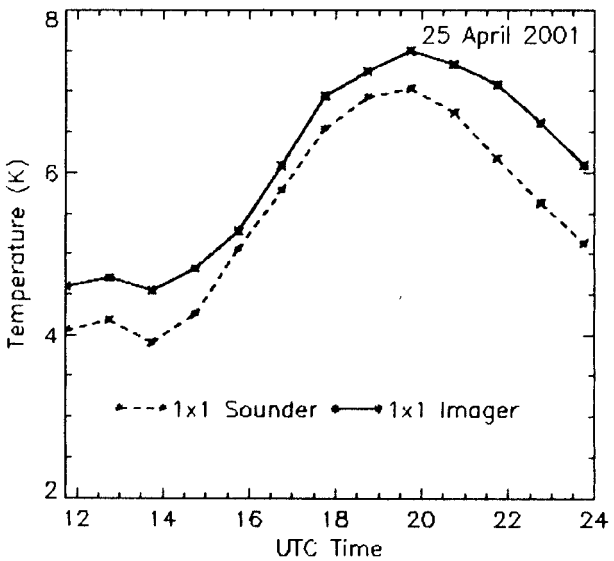

Figure 1. Standard deviation of single pixel ST retrievals from the GOES-8 Imager and Sounder over the CONUS domain.

4.2 GOES-8 Comparisons

Noise and striping within GOES images often requires averaging of retrievals. However, averaging reduces the spatial resolution of the retrievals and finer details of the natural variation are lost. It is therefore of interest to study the spatial variation of retrievals with varying degrees of pixel averaging. The standard deviation (SD) of ST within a domain reflects both the noise and natural variation. Figures 1, 2 and 3 show the SD of ST within a large subsection of the CONUS region for single pixel retrievals, Sounder single pixel retrievals and Imager 3x3 pixel averaged retrievals (with single pixel spacing), and 3x3 pixel averaged retrievals for both instruments, respectively.

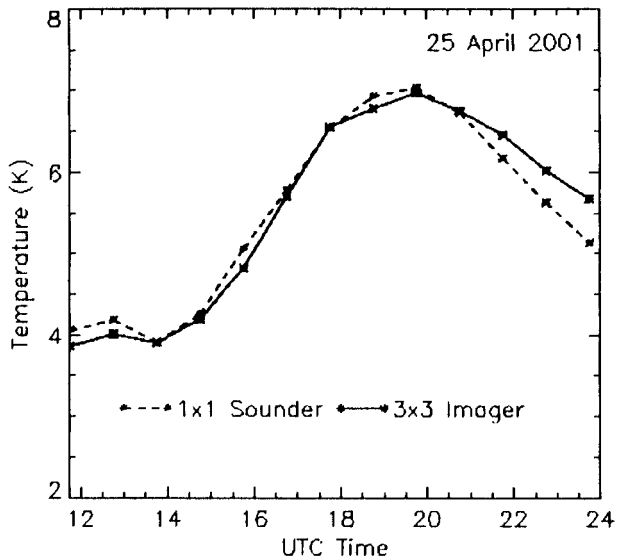

Figure 2. Standard deviation of GOES-8 Imager (3x3 pixel averaged retrievals) and Sounder (single pixel retrievals) ST over the CONUS domain.

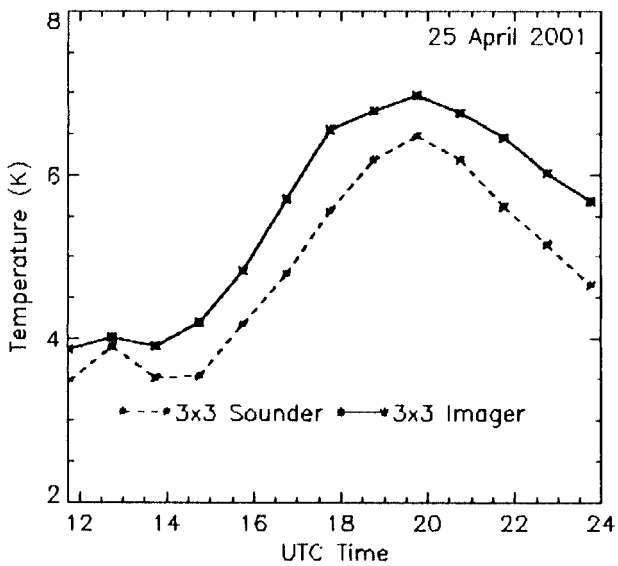

Figure 3. Standard deviation of 3x3 pixel averaged ST retrievals from the GOES-8 Imager and Sounder over the CONUS domain.

Comparing the SD of single pixel retrievals from the Imager and Sounder in Figure 1 reveals larger values for the Imager retrievals. This suggests that the Imager is detecting a higher degree of natural variation of ST across the region. Larger SD values for the Imager are expected because of the Imager's finer spatial resolution (4 km compared to the Sounder's 8 km resolution) and the 100% coverage by the Imager compared to only approximately 64% coverage by the Sounder. The Sounder has a field of view resolution of 8 km but samples only every 10 km, therefore only 64% of the pixel is sampled. Also, the Imager statistics are computed from a much larger number of pixels than the Sounder. The SD values from both instruments contain a noise component, and averaged retrievals can be expected to remove most of this noise.

Figure 2 shows the SD of ST sampled by the Imager and Sounder at similar sampled spatial resolutions. The Imager retrievals are still at single pixel spacing, but each pixel is the average of its surrounding 3x3 pixel box. The Imager retrievals are averaged and therefore both noise and natural variation components are reduced. The Imager and Sounder SD values are very close, with the only significant difference during the late afternoon hours. This observation suggests that for the same sampled spatial resolution single pixel Sounder retrievals detect a similar degree of natural variability as 3x3 pixel averaged Imager retrievals. However, the Sounder values still contain a striping and random noise component and therefore the natural variability detected by the Sounder should be less than that indicated in Figure 2.

Figure 3 shows the SD of ST for both Imager and Sounder averaged retrievals. As expected, the Sounder SD values have decreased from the single pixel results because of decreased components of both noise and natural variability. Also, the Imager again has the larger SD values for the same reasons as for those stated for Figure 1. Both Imager and Sounder 3x3 pixel averaged SD values have decreased by approximately 0.5 K from their single pixel SD values.

Retaining the 4 km spatial resolution of the Imager retrievals but performing averaging appears to reduce to striping and noise but preserve much of the natural variability of ST. At single pixel spacing, the Imager has approximately 15 pixels for every one Sounder pixel. The much higher number of pixels and the 100% coverage of the Imager are significant advantages over the Sounder. Statistics computed (not shown) for the same case study but with only the closest Imager pixel selected for each Sounder pixel (i.e. the Imager and Sounder statistics are computed using the same number of pixels) reveal similar SDs for 3x3 averaged retrievals. Therefore, the Imager's advantage is only retained at single pixel spacing. Images of retrievals produced using single pixel Sounder data often exhibit striping. Therefore averaging of Sounder retrievals is necessary to eliminate striping, but the sampled spatial resolution may be too coarse for some applications.

5. CONCLUSIONS

Current ST retrievals are produced using GOES-8 Imager data and assimilated into a forecast model. GOES-8 has passed it expected lifetime of five years and will be replaced soon by GOES-11 or GOES-12. Retrievals made from GOES-12 will need to be made using the Sounder because of the loss of the 12 μm channel from the Imager.

Comparisons of striping between GOES-8 and GOES-11 reveal decreased striping in some, but not all, cases from the newer satellite. The reduced striping will decrease the need for averaged retrievals, but it appears that striping will still be apparent.

Evaluations of the variability of ST across a region reveal components from both natural changes and noise. To reduce the striping noise, averaging of the retrievals is performed. Comparisons of GOES-8 Imager and Sounder SDs of ST reveal that the Imager retains the same variability with 3x3 pixel averaged retrievals as the single pixel Sounder retrievals. Single pixel Sounder retrievals contain noise from line-to-line striping, but averaged Sounder retrievals have a coarse resolution.

Acknowledgments. This work was partially supported under the GOES Improved Measurements and Products Assessment Plan (GIMPAP). GOES-11 data were supplied by Jaime Daniels at NOAA/NESDIS.

6. REFERENCES

Bachmeier S., M. Gunshor, J. Nelson, T. Schmit, T. Schreiner, D. Stettner, and G. Wade, cited 2001: CIMSS GOES-11 Science Test. [Available online from http://cimss.ssec.wisc.edu/goes/g11_report.]

Baucom, J.G. and M. Weinreb, 1996: Characteristics of E/W stripes in infrared images from the GOES-8 imager. *GOES 8 and Beyond*, E.R. Washwell, ed., Proc. SPIE 2812, 587-595.

Lapenta, W.M., R.J. Suggs, G.J. Jedlovec, and R.T. McNider, 1999: Impact of Assimilating GOES-Derived Land Surface Variables into the PSU/NCAR MM5. *Preprints, Workshop on Land-Surface Modeling and Applications to Mesoscale Models*, NCAR, Boulder, CO, 65-68.

Suggs, R.J., G.J. Jedlovec, A.R. Guillory, 1998: Retrieval of geophysical parameters from GOES: evaluation of a split window retrieval technique. *J. Appl. Meteor.*, **37**, 1205-1227.

Suggs, R.J., G.J. Jedlovec, W.M. Lapenta, and S.L. Haines, 2000: Evaluation of skin temperatures retrieved from GOES-8. *Preprints, 10th Conf. On Satellite Meteorology and Oceanography*, January 9-14, 2000, Long Beach, CA, 137-140.

Suggs, R.J., W.M. Lapenta, G.J. Jedlovec, and S.L. Haines, 2001: Intercomparison of GOES-8 Imager and Sounder Land Surface Temperature Retrievals. *Preprints, 11th Symposium on Meteorological Observations and Instrumentation*, January 14-19, 2001, Albuquerque, NM, 362-365.

Wack, E.C. and L.M. Candell, 1996: Simulation of GOES 8 Imager IR striping due to 1/f noise. *GOES 8 and Beyond*, E.R. Washwell, ed., Proc. SPIE 2812, 608-613.

Weinreb, M. 1996: Real-world calibration of GOES-8 and –9 sensors. *GOES 8 and Beyond*, E.R. Washwell, ed., Proc. SPIE 2812, 572-5

P4.38 AN AEROSOL-DEPENDENT ALGORITHM FOR REMOTELY SENSED SEA SURFACE TEMPERATURES FROM THE NOAA AVHRR

Nicholas R. Nalli*
CIRA, Colorado State University, Fort Collins, Colorado

Larry L. Stowe
NOAA/NESDIS/ORA, Washington, D.C.

1. INTRODUCTION

For two decades, global measurements of sea surface temperature (SST) have been produced by the National Oceanic and Atmospheric Administration (NOAA) using infrared (IR) data obtained from the Advanced Very High Resolution Radiometer (AVHRR) on board NOAA polar orbiting satellites (Walton *et al.*, 1998). The conventional retrieval algorithms provide a multichannel correction for IR attenuation due to molecular water vapor absorption under non-cloudy conditions. However for atmospheric conditions with anomalously high aerosol content (e.g., arising from dust, haze, biomass burning and volcanic eruptions), such algorithms lead to significant negative biases in SST due to unaccounted attenuation arising from aerosol absorption and scattering.

The standard multichannel SST (MCSST) relies on an observed quasi-linear statistical relationship between spectral window brightness temperatures and *in situ* measurements of "bulk" surface temperature obtained by oceanographic buoys (Walton *et al.*, 1998). Because of the nonlinear dependence of transmission on total absorber amount for the global range of water vapor, a nonlinear SST (NLSST) algorithm has also been implemented. However, it is difficult to separate the spectral signal caused by atmospheric aerosols from that caused by water vapor using only 2–3 channels in the IR. Although the empirical coefficients can account for the attenuation in a mean sense, they cannot account for anomalous aerosol loading. Hence the MCSST and NLSST equations lead to significant negative biases (i.e., $\overline{T_S' - T_S} < 0$, where T_S' and T_S are the retrieved and "true" SST, respectively) under such conditions without additional information.

This paper overviews a simple aerosol correction for AVHRR SST using measurements of visible solar reflectance at 0.63 and 0.83 μm in AVHRR channels 1 and 2, respectively (after Nalli and Stowe, 2001). A unique, globally comprehensive (both spatially and temporally) AVHRR matchup data sample is employed that includes retrievals of channel 1 aerosol optical depth (AOD). It is then empirically shown that the SST bias caused aerosols can be expressed as a parametric equation in two variables, these being the observed AVHRR channel 1 slant-path AOD, and the ratio of channels 1 and 2 normalized albedos. Based on these relationships, aerosol correction equations are derived for the daytime multichannel and nonlinear SST (MCSST and NLSST) algorithms. Separate sets of coefficients are utilized for two aerosol modes: Tropospheric (e.g., dust, smoke, haze) and Stratospheric/Tropospheric (e.g., following a major volcanic eruption). The elimination of cold biases in the AVHRR SST will greatly improve its utility for the general user community and in climate research.

2. DATA

Data used in our empirical analyses originate from the AVHRR Pathfinder Program, a collaborative effort led by NOAA and the National Aeronautics and Space Administration (NASA). Specifically, the AVHRR Pathfinder Atmospheres (PATMOS) and Oceans Pathfinder Matchup Database (PFMDB) data sets are merged to provide a unique PATMOS matchup data base. The two Pathfinder data sets are briefly described below.

2.1 Pathfinder Atmospheres (PATMOS)

PATMOS is a retrospective data set consisting of re-processed AVHRR 5-channel data mapped to a quasi-equal area grid (110 km)^2 over the time period spanning 1981–2000 (Stowe *et al.*, 2001). These data include the grid-cell means and standard deviations of AVHRR channels 1 and 2 (0.63 and 0.83 μm) normalized albedos, channels 3–5 (3.7, 11, 12 μm) radiances, and channel 1 AOD, τ_a, obtained from the 2nd Generation retrieval algorithm (Stowe *et al.*,

* *Corresponding author address:* Dr. Nicholas R. Nalli, Cooperative Institute for Research in the Atmosphere (CIRA), NOAA/NESDIS E/RA1, Washington, DC 20233, USA; e-mail: nick.nalli@noaa.gov

1997). The Clouds from AVHRR (CLAVR-1) cloud mask (Stowe *et al.*, 1999) is employed to obtain clear-sky statistics. Global observations were obtained under conditions of tropospheric haze, dust and smoke outflows from continents, as well as during the entire residence time of the Mt. Pinatubo (1991–93) stratospheric aerosol layer.

2.2 Pathfinder Matchup Database (PFMDB)

PFMDB is maintained on the internet by the NASA Jet Propulsion Laboratory (Kilpatrick *et al.*, 2001). It consists of global *in situ* observations taken by moored and drifting buoys that have been matched-up in space and time with AVHRR overpasses spanning 1985–1998. Of particular importance are the measurements of bulk surface temperatures, T_b, taken at depths on the order of 1 m. The matchup database also provides ancillary data used in our research, namely the NCEP Reynolds OISST extracted from the filtered weekly field.

3. METHOD

The magnitude of aerosol-induced attenuation in the IR will depend a number of factors, the more important ones being (1) the IR optical depth, (2) the effective temperature of the absorbing layer and (3) the particle size distribution. The latter of these provides information the relative proportions of extinction resulting from absorption and scattering. Assuming there is a correlation between AOD in the visible and IR, the channel 1 AOD can provide information about the first factor. However absorber temperature and particle size cannot be objectively inferred from AOD alone.

To put a constraint on the absorber temperature, it is necessary to first characterize the integrated aerosol content as belonging to one of two modes: Tropospheric and Stratospheric/Tropospheric (or Strato/Trop for short). This is to distinguish the difference in IR attenuation expected from absorbing layers confined to a relatively warm planetary boundary layer versus those found in the colder stratosphere after a major volcanic eruption.

Because the particle size distribution within either aerosol mode can exhibit considerable variation over time and space, the IR attenuation can also show variations independent of the AOD. Previous researchers (e.g., Haggerty *et al.*, 1990; May *et al.*, 1992) have suggested that the ratio of normalized reflectance measurements between channels 1 and 2, R_1/R_2, is sensitive to the particle size distribution. We therefore propose 2 predictors for modeling the SST depression

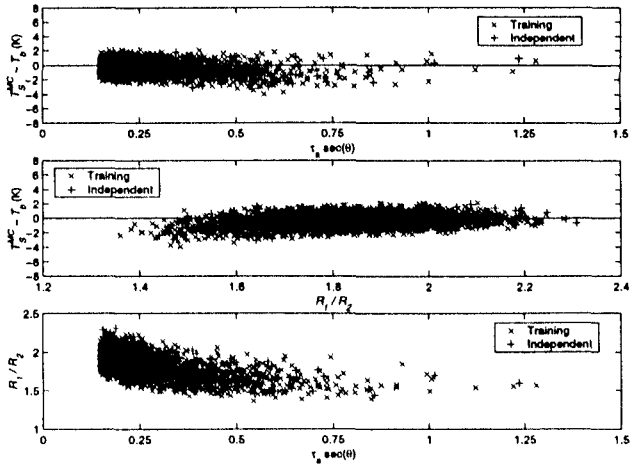

Figure 1: Regression parameter relationships, Tropospheric Mode: (top) δT_S and x_1, (middle) δT_S and x_2 and (bottom) x_2 and x_1. The training and independent data sets used for regression and validation are distinguished from one another using different symbols.

due to anomalous aerosol loading $\delta T_S \equiv T'_S - T_S$:

$$x_1 \equiv \tau_a \sec(\theta)\,, \quad (1)$$

$$x_2 \equiv R_1/R_2\,, \quad (2)$$

where parameters are given by the spatial mean values from PATMOS matchup grid-cells.

Because coefficients for operational SST algorithms are determined under background tropospheric aerosol conditions, it is necessary to estimate an AOD threshold for delineating background conditions from elevated levels. The PATMOS AOD background thresholds are taken to be $\tau_0^{\rm tropo} = 0.15$ and $\tau_0^{\rm strato} \simeq 0.10$ for the Tropospheric and Strato/Trop Modes, respectively.

4. STATISTICAL ANALYSIS

For the Tropospheric Mode, NOAA-14 data are taken from the years 1995–1998. For the Strato/Trop Mode, NOAA-11 data are taken during the Mt. Pinatubo residence time period of July 1, 1991 through 1992. Figures 1 and 2 show that the standard MCSST equation, derived under background aerosol conditions ($\tau_a < 0.15$), does not account for the attenuation caused by aerosols. For a given aerosol mode, the most simple model for the SST depression, $\delta T_S = T_S - T_b$, would be merely be a linear equation in x_1

$$\delta T_{S1} = a_0 + a_1\, x_1\,. \quad (3)$$

May *et al.* (1992) first demonstrated this relationship using a small sample of drifting buoy matchup data ob-

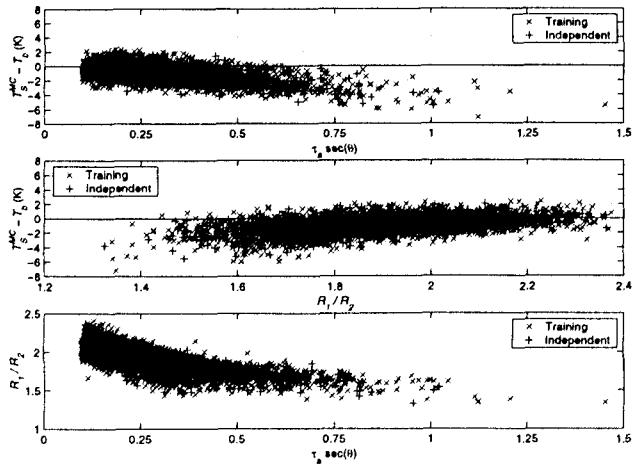

Figure 2: Same as Figure 1 except for the Strato/Trop Mode.

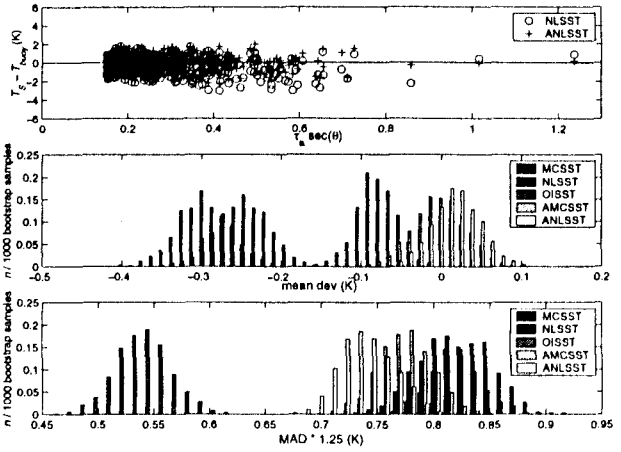

Figure 3: Aerosol corrected NLSST (ANLSST) statistics for Tropospheric aerosol mode, independent data set ($n = 612$): (top) scatterplot of retrieved NLSST and ANLSST minus buoy SST, (middle) statistical bootstrap histogram of bias error, and (bottom) scatter about the mean. For reference, bootstrap histograms of the NCEP Reynolds OISST are also shown.

tained off the coast of Africa from mid-June through September, 1990. To help account for tropospheric variations in aerosol particle size, we incorporate the albedo ratio predictor, x_2, allowing 3 potential expressions (linear, interaction and full quadratic) for the response surface δT_S in x_1, x_2 space. These are written as

$$\delta T_{S2} = a_0 + a_1 x_1 + a_2 x_2 , \quad (4)$$

$$\delta T_{S3} = a_0 + a_1 x_1 + a_2 x_2 + a_{12} x_1 x_2 , \quad (5)$$

$$\delta T_{S4} = a_0 + a_1 x_1 + a_2 x_2 + a_{12} x_1 x_2 + a_{11} x_1^2 + a_{22} x_2^2 . \quad (6)$$

The coefficients a_i and a_{ij} are derived using a training data subset (approximately 4/5) taken randomly from the quality controlled data samples. The remaining 1/5 of data are then reserved as an independent data set. The aerosol-corrected SST is then simply given by

$$T_S = T'_S - \delta T_S , \quad (7)$$

where T'_S can be given by either the MCSST or NLSST, and δT_S is calculated using any one of equations (3)–(6).

5. VALIDATION

To validate the regression models, independent data samples from both aerosol modes are used. Results using model equation (6) as an aerosol correction for the NLSST are displayed in Figures 3 and 4 for Tropospheric and Strato/Trop Modes, respectively.

The top panels in these figures show scatterplots of δT_S versus buoy SST obtained from the NLSST equation, along with the aerosol corrected value (ANLSST) obtained by subtracting equation (6). These plots demonstrate the ability of the quadratic algorithm to correct for aerosol attenuation under the global range of slant path AOD under both aerosol modes. Using the linear equation (3) yields very similar results on the Strato/Trop mode, but leads to significant positive bias for the Tropospheric mode at slant path AOD $\gtrsim 0.55$ as described above.

The middle and bottom panels of Figures 3 and 4 provide a statistical inference of the bias (mean deviation) and scatter (mean absolute deviation, MAD, scaled by a factor of 1.25) expected from the different SST algorithms using the Efron bootstrap method (i.e., random resampling with replacement). Results are shown for the standard MCSST and NLSST, the NCEP Reynolds OISST as given in the PFMDB, and the aerosol corrected MCSST and NLSST (AMCSST and ANLSST) using equation (6). Observable in the MCSST and NLSST are significant negative biases (middle panels) ranging from $[-0.35, -0.20]$ and $[-1.0, -0.85]$ for the Tropospheric and Strato/Trop Modes, respectively. The NCEP Reynolds OISST reduces the bias to within $[-0.12, -0.05]$ and $[-0.20, -0.10]$. The aerosol dependent equations, however, yield the best results, with bootstrap histograms nearly centered about zero for both modes. The aerosol corrected results also exhibit less scatter than the uncorrected as seen in the bottom panel. The reason the PATMOS derived SSTs show higher scatter than the NCEP Reynolds

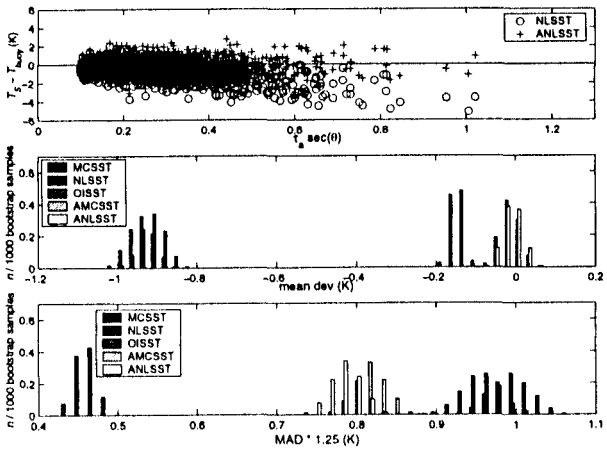

Figure 4: Same as Figure 3 except for the Strato/Trop aerosol mode ($n = 1092$).

OISST is because of precision loss in the IR channel brightness temperatures (Nalli and Stowe, 2001) and not because of the algorithm.

6. CONCLUSION AND FUTURE WORK

This research demonstrates empirically that AVHRR observations of normalized visible reflectance in channels 1 and 2 can be utilized to provide a correction for IR attenuation from elevated aerosol levels which otherwise lead to negative biases in remotely sensed sea surface temperature (SST). The Phase I daytime algorithms will be implemented for real-time and retrospective retrievals, including a PATMOS-based SST climatology. Subsequently, in Phase II, the 3rd Generation 2-channel AVHRR AOD retrieval will be used to better model the tropospheric aerosol correction under varying aerosol types and particle sizes.

ACKNOWLEDGEMENTS

This project is funded by the NESDIS Ocean Remote Sensing Program managed under Dr. A. Strong. We are grateful to Mr. A. Kidd, manager of the NOAA/NESDIS Satellite Active Archive, for providing access to the daily PATMOS data sets. We also thank Dr. B. Huang (UW-Madison) for informal correspondences about descriptive statistics.

REFERENCES

Haggerty, J. A., Durkee, P. A., and Wattle, B. J. (1990). A comparison of surface and satellite-derived aerosol measurements in the western Mediterranean. *J. Geophys. Res.*, **95**, 1547–1557.

Kilpatrick, K. A., Podestá, G. P., and Evans, R. (2001). Overview of the NOAA/NASA advanced very high resolution radiometer Pathfinder algorithm for sea surface temperature and associated matchup database. *J. Geophys. Res.*, **106**(C5), 9179–9197.

May, D. A., Stowe, L. L., Hawkins, J. D., and McClain, E. P. (1992). A correction for saharan dust effects on satellite sea surface temperature measurements. *J. Geophys. Res.*, **97**(C3), 3611–3619.

Nalli, N. R. and Stowe, L. L. (2001). Aerosol-dependent algorithms for remotely sensed sea surface temperatures from the NOAA AVHRR. *J. Atmos. Ocean. Tech.* In preparation.

Stowe, L. L., Ignatov, A. M., and Singh, R. R. (1997). Development, validation, and potential enhancements to the second-generation operational aerosol product at the National Environmental Satellite, Data and Information Service of the National Oceanic and Atmospheric Administration. *J. Geophys. Res.*, **102**(D14), 16,923–16,934.

Stowe, L. L., Davis, P. A., and McClain, E. P. (1999). Scientific basis and initial evaluation of the CLAVR-1 global clear/cloud classification algorithm for the advanced very high resolution radiometer. *J. Atmos. Ocean. Tech.*, **16**, 656–681.

Stowe, L. L., Jacobowitz, H., Ohring, G., Knapp, K., and Nalli, N. R. (2001). The advanced very high resolution radiometer Pathfinder Atmosphere (PATMOS) climate data set: Initial analyses and evaluations. *J. Climate.* Submitted May, 2001.

Walton, C. C., Pichel, W. G., Sapper, J. F., and May, D. A. (1998). The development and operational application of nonlinear algorithms for the measurement of sea surface temperatures with the NOAA polar-orbiting environmental satellites. *J. Geophys. Res.*, **103**(C12), 27,999–28,012.

P4.39
COMPARISONS OF OBSERVED AND SIMULATED MICROWAVE IMAGES OF EXTRATROPICAL CYCLONES

Jui-Yuan C. Chiu *
Purdue University, West Lafayette, Indiana

Grant W. Petty
University of Wisconsin - Madison, Madison, Wisconsin

1. INTRODUCTION

Satellite passive microwave observations are of interest for improving our understanding of surface rainfall and three-dimensional latent heating distributions over the globe. The Goddard Profiling Algorithm (GPROF) was selected for the Tropical Rainfall Measuring Mission (TRMM) to provide precipitation estimates on an operational basis from the TRMM Microwave Imager (TMI), and therefore GPROF has been optimized to obtain good performances in tropical regions. The performance of GPROF is partially determined by the representativeness of the cloud-radiation database. Currently, the database of GPROF is based on tropical and subtropical simulations. Since cloud and precipitation structures in the extratropics are quite different from those in the tropics, further evaluations of the relations between cloud structures and corresponding upwelling radiance at higher-latitude area will be beneficial for the GPROF applications.

The observational and model-simulated study of extratropical cyclones has experienced remarkable progress. Meteorological direct and indirect measurements have indicated natural variations in microphysical parameters. However, little modeling research has addressed how these uncertainties influence the mesoscale cloud and precipitation structure of oceanic midlatitude cyclones. In addition to the deficiencies of explicit moisture schemes themselves, the uncertainties may lead to significant errors in both cloud model and radiative transfer model. Furthermore, it still remains unknown how the errors and deficiencies affect retrieved rain rate and hydrometeor profiles obtained from a database-type algorithm.

The primary goal of the study is to systematically evaluate the impacts of microphysical parameters on simulated precipitation structures and microwave radiance of extratropical oceanic cyclone systems. The adopted approach utilizes the Pennsylvania State University-National Center for Atmospheric Research mesoscale model version 5 (MM5) and a backwards Monte-Carlo model as a common framework. Section 2 briefly describes the methodology, and results of the numerical experiments are shown in section 3. The conclusions will be given in section 4.

2. METHODOLOGY

An extratropical cyclone over the Atlantic in December 1992 was simulated at 36- and 12- km horizontal resolutions using MM5. These two nested domains both had 37 vertical levels and were run simultaneously for 48 hours. The model was initiated from ECMWF archived global analyses, and the lateral boundary conditions were updated at 12-h interval. Important physical processes in MM5 included the Blackadar planetary boundary parameterization and the Kain-Fritsch cumulus parameterization. A four dimensional data assimilation (FDDA) scheme was employed during the first 24-hr simulations.

Model-simulated dynamic and thermodynamic fields were verified using conventional objective measures, such as root-mean-square error, mean error, and skill scores. Sensitivities of the precipitation distribution to varying explicit moisture schemes were also examined. Two separate microphysics schemes in MM5 were employed: Tao

* *Corresponding author address*: Jui-Yuan C. Chiu, Purdue University, Dept. of Earth & Atmospheric Sciences, West Lafayette, IN, 47907; e-mail:chiuj@meso.aos.wisc.edu

scheme (Tao and Simpson, 1993; Lin et al., 1983), and Reisner2 (Reisner et al., 1998), which treated graupel density as a prognostic variable. Several numerical experiments were constructed and summarized in Table 1, and the paper will only emphasized on the effect of graupel species. The sensitivity test was evaluated by the noise/signal ratio (Li et al., 1995), and the variances of vertical distributions of hydrometeors were investigated by Empirical Orthogonal Function (EOF) analysis.

The employed Monte-Carlo model is a three-dimensional and time-reversed radiative transfer model with a specular lower boundary (see the details in Petty, 1994). It should be noted that the parameters in all numerical experiments were tuned only in MM5, and no parameters changes in the radiative transfer model. Simulated brightness temperatures were examined on horizontal distributions of cyclone structure and multi-channel relations comparing to a coincident Special Sensor Microwave Imager (SSM/I) overpass.

Experiment ID	Scheme	Key Parameters
STDG	Tao	ρ_g = 0.4, $N_{o,r}$ = 8.E6 $N_{o,g}$ = 4.E6, $N_{o,s}$=1.E8
HAIL	Tao	ρ_h = 0.9, $N_{o,r}$ = 8.E6 $N_{o,h}$ = 2.E5, $N_{o,s}$=1.E8
G-GH	Tao	ρ_g = 0.4, $N_{o,r}$ = 8.E6 $N_{o,g}$ = 4.E8, $N_{o,s}$=1.E8
G-GL	Tao	ρ_g = 0.4, $N_{o,r}$ = 8.E6 $N_{o,g}$ = 4.E4, $N_{o,s}$=1.E8
STDR	Reisner2	ρ_g = 0.4, $N_{o,r}$ = 8.E6 $N_{o,g}$ = 4.E6, $N_{o,s}$=2.E7
RR-1	Reisner2	ρ_g = 0.4, $N_{o,r}$ = 8.E6 $N_{o,g}$ = 4.E6, $N_{o,s}$=1.E8

Table 1: Numerical experiments tested in the study. The key parameters are the density of graupel ρ_g (g/cm^3), the intercept for rain $N_{o,r}$ (m^{-4}), the intercept of graupel $N_{o,g}$ (m^{-4}), and the intercept for snow $N_{o,s}$ (m^{-4}). STD means control or standard run. These changes are only made in MM5, not in the radiative transfer model. Detailed drop size distribution, fall speed relations, and all process parameterizations are described in Lin et al. (1983), Tao and Simpson (1993) and Reisner et al. (1998).

3. RESULTS

Validation of the MM5-simulated sea level pressure, temperature and water vapor fields at 36-km resolution using error measures (as described in section 2) suggested that simulations with varying explicit moisture schemes did not have appreciable differences (figures not shown). However, Reisner2 (STDR) tended to produce smaller rainy regions with larger stratiform but smaller convective surface rain rate than that of Tao scheme (STDG). Compared HAIL with STDG, the switch of graupel/hail regime did not make a significant difference. In addition, sensitivity tests demonstrated that Tao and Reisner2 were both sensitive to the slight change of microphysical parameters, but showed different reactions to the uncertainty of microphysical assumptions.

Results of the EOF analysis for vertical distributions indicated that the patterns of mean profiles and the first EOF component in all categories were close, except cloud ice. All experiments based on the Tao scheme (STDG, HAIL, G-GH and G-GL) produced much less cloud ice content than that in the STDR and RR-1. In addition, Reisner2 control run predicted more snow with a deeper layer, and the phenomenon would be amplified in the RR-1 run. Furthermore, the peak of mean graupel distribution from the Tao scheme was three times larger than the STDR and RR-1. The increase in $N_{o,g}$ (G-GH) levitated the peak level of the mean and first EOF snow profile associated with a smaller amount of snow content, while generating three times larger graupel density than the standard run. The increase of $N_{o,g}$ tended to produce more graupel at a higher vertical level, which may have been due to smaller graupel particles (corresponding to a larger intercept of drop size distribution) having less chance to convert to snow and accumulate at upper levels due to smaller terminal velocities.

The horizontal structures of calculated radiance from STDG and STDR were examined by comparing to the observed SSM/I brightness temperature (Figures not shown). Results revealed that these two microphysics schemes both produced separate rain bands and cold cores caused from high graupel content. The model-simulated background brightness temperatures at some places were too low compared to SSM/I, and they were a result of the less water vapor content

generated from MM5. In addition, calculated brightness temperature fields indicated that the simulations were able to represent multi-channel relations of actual observations (Figure 1, for the STDG experiment). The shift of larger polarization at the range of lower values of T_{22V}-T_{19V} (shown in Figure 1(d)-(f)) may be because the wind roughness effects were not accounted for in the current version of the Monte-Carlo model. Figure 2 revealed that the increase in the intercept for graupel decreased significantly both vertical and horizontal brightness temperatures at 85 GHz (around 20 K) due to a higher graupel content based on EOF analysis, while the G-GL run showed an increase at TB_{85V} to a lesser of degree.

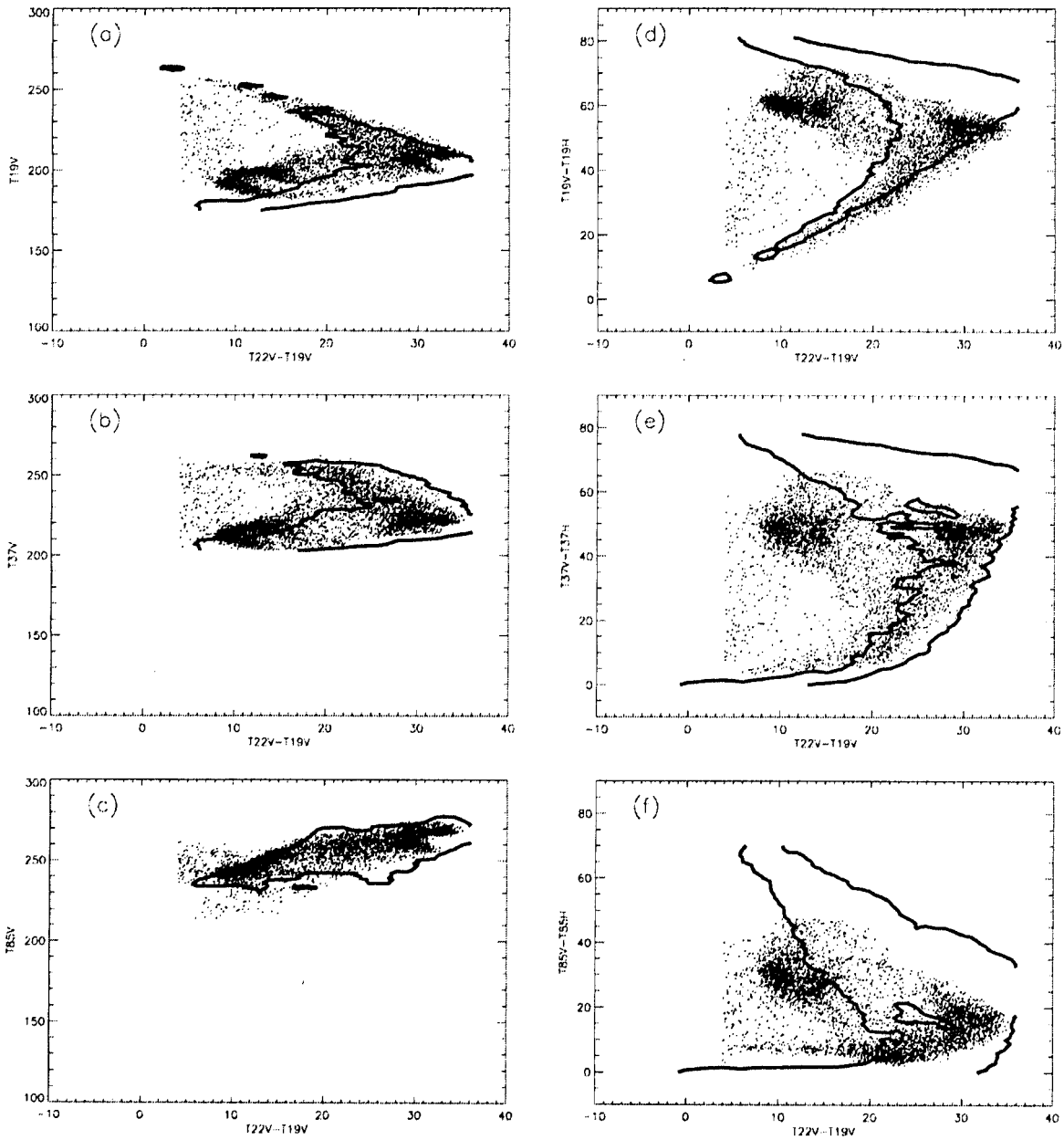

Figure 1: Multi-channel relations of SSM/I observations (dots) and simulated radiances (inside contour line). (a)-(c) depicts vertically polarized brightness temperature versus T22V–T19V. (d)-(f) depicts polarization differences versus T22V–T19V.

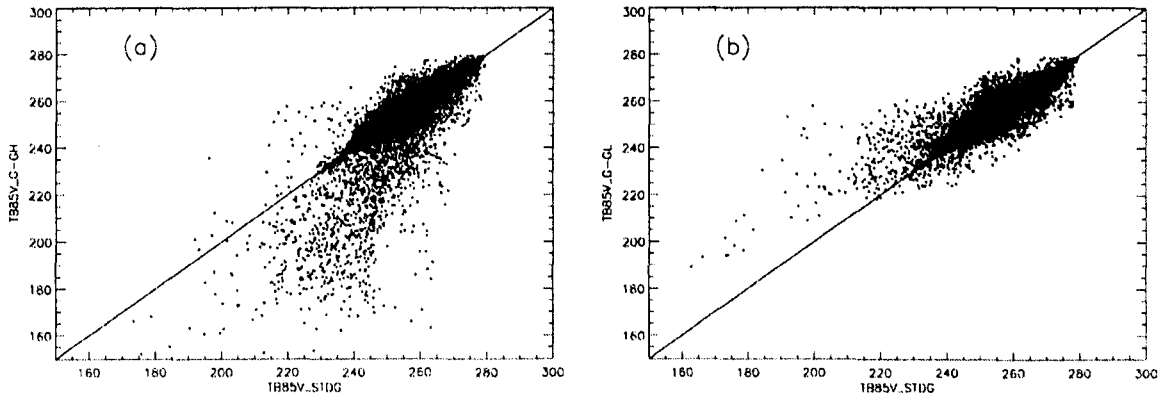

Figure 2: Inter-comparisons of T85V of STDG (control run) with (a) G-GH (larger $N_{0,g}$), and (b) G-GL (smaller $N_{0,g}$).

4. CONCLUSIONS

The study has shown that the model-simulated dynamic fields are not affected dramatically by various explicit moisture schemes and microphysical parameters in 48hr simulations for the oceanic midlatitude cyclone system. However, the variations of microphysics schemes have a significant impact on the hydrometeor fields and their corresponding simulated radiance. Results indicate that simulations could capture the main horizontal structure of the cyclone, and the multi-channel relations of simulated brightness temperatures are consistent with SSM/I data. In addition, the increase of the intercept for the graupel size distribution in the Tao scheme tends to produce larger graupel content at a higher vertical level, and then significantly decreases brightness temperatures at 85 GHz.

5. REFERENCES

Li, Q., R. L. Bras, and S. Islam, 1995: Growth and decay of error in a numerical cloud model due to small initial perturbations and parameter changes. *J. Appl. Meteor.*, **34**, 1622-1632.

Lin, Y.-L., R.D. Farley and H. D. Orville, 1983: Bulk parameterization of the snow field in a cloud model. *J. Clim. Appl. Meteor.*, **22**, 1065-1092.

Petty, G. W., 1994: Physical retrievals of over-ocean rain rate from multichannel microwave imagery. Part I: Theoretical characteristics of normalized polarization and scattering indices. *Meteor. Amos. Phys.*, **54**, 79-99.

Reisner, J., R. M. Rasmussen, and R. T. Bruintjes, 1998: Explicit forecasting of supercooled liquid water in winter storms using the MM5 mesoscale model. *Q. J. R. Meteo. Soc.*, **124**, 1071-1107.

Tao, W.-K., and J. Simpson, 1993: The Goddard Cumulus Ensemble Model. Part I: Model description. *Terr. Atmos. Ocean. Sci.*, **4**, 35-72.

5.4 COMBINING NEW SATELLITE TOOLS AND MODELS TO EXAMINE THE ROLE OF MESOSCALE INTERACTIONS IN FORMATION AND INTENSIFICATION OF TROPICAL CYCLONES

Joanne Simpson[1]
Goddard Space Flight Center/NASA, Greenbelt, Maryland
Elizabeth Ritchie,
Naval Postgraduate School, Monterey, California
W. Timothy Liu,
Jet Propulsion Laboratory/NASA, Pasadena, California
Christopher Velden,
University of Wisconsin, Madison, Wisconsin
Kurt Brueske,
Air Force Academy, Colorado Springs, Colorado
Harold Pierce,
Goddard Space Flight Center/NASA, Greenbelt, Maryland
Jeffrey Halverson,
University of Maryland, Baltimore County, Maryland

1. INTRODUCTION

This paper reports first results of an ongoing study of the formation (TD status) and early intensification of tropical cyclones using data from TRMM, AMSU and QuikSCAT, together with numerical model output, the NRL Web site (http://www.nrlmry.navy.mil/), and conventional data as available. Satellite tools such as these can examine tropical cyclones wherever they occur. We begin with Atlantic hurricanes because of a larger database and greater concern to the U.S. More than 50% of hurricanes originate from African waves often called "seedlings". We examined so far two African seedlings, both of which reached TD but only one intensified to a named hurricane (Floyd, 1999).

2. METEOROLOGICAL BACKGROUND

The formation of hurricanes has been a controversial problem, with few observations of mesoscale processes that might be important. It has been difficult to "catch" a hurricane forming with a fleet of instrumented aircraft. In the 1980's Ooyama (1982) and Schubert and Hack (1982) showed with models that the Rossby Radius of Deformation L_r had to be greatly decreased from its normal ~1500 km in the tropics for the latent heat released in convective systems to be retained locally, rather than being propagated away by gravity waves. This meant that the "background" vorticity had to be greatly increased above normal. High background vorticity is frequently found in monsoon troughs, making these the sites for development of most of the world's tropical cyclones (Greg Holland, personal communication). Our hypothesis is that there is an intermediate mesoscale step between high background vorticity and the formation of a Tropical Cyclone in many cases.

In 1997, Ritchie and Holland proposed that interaction of mesoscale vortices of dimension 200-500 km could be am important link in lowering the Rossby Radius, L_r. They had studied vortex models showing that when close together, two vortices may interact or "merge", with the weaker vortex giving up vorticity to the stronger and then shearing off in a pattern resembling a hurricane rainband.

Researchers (e.g. Menard and Fritsch, 1989) studying long-lived Mesoscale Convective Complexes (MCC's) over land discovered that the stratiform regions of such systems were an ideal environment for the growth of midlevel (4-8 km) elevation vortices on this scale. Miller and Fritsch (1991) and others found that these cloud systems lasted long enough (~24 hr) to allow the vortex to stabilize, so that when the stratiform anvil finally dispersed, the vortex remained coherent. Harr et al. (1996) documented that numerous similar systems in the tropical western Pacific also develop stable vortices on that scale. Because these mesoscale cloud systems permit developing vortices to remain stable with some reduction in L_r, they may provide important pre-conditions for the development of a tropical cyclone. Therefore we began testing a hypothesis concerning how these midlevel vortices might occasionally develop down to the surface with sufficient strength that increased fluxes of heat and moisture from the sea can begin the intensification cycle. The birth of one hurricane-force Tropical Cyclone, Oliver, was "caught" by two NASA aircraft off the east coast of Australia during TOGA COARE in 1993. The aircraft recorded the development, interaction and merger of two large Mesoscale Convective Systems (MCS's) that formed in association with midlevel vortices within a low-level monsoon cell (Simpson et al, 1997). A nearby island radar recorded the tracks of the two main mesoscale vortices by their rain echoes prior to and during the interaction of the mesoscale cloud

[1] Corresponding author address: Joanne Simpson, Mail Code 912, Goddard Space Flight Center/NASA Greenbelt, MD 20771;
email: simpson@agnes.gsfc.nasa.gov

systems. Results showed that the interaction both between the two midlevel vortices, and between the midlevel vortices and the low-level monsoon cell were important in the formation and development of a nascent eye in Oliver.

3. APPROACH

Our approach is to build a time sequence of three-dimensional mental pictures of each hurricane seedling studied. The goal is to understand and document the processes by which the system undergoes the observed changes between one and the next time interval. All observations available are used to build the time sequences. We used a global numerical model (NAVY NOGAPS) at 19 levels every 12 hr to describe the storms' environment and to tie the satellite observations together.

3.1 Use of Geosynchronous satellite data

The study benefited greatly from imagery from the GOES and Meteosat geosynchronous satellites. In particular, color-enhanced movie loops of the IR channel were used to depict early convective organization, overshooting towers preceding intensification, and detection of mid-level vortices. In addition, winds derived from the GOES and Meteosat multispectral imagery (Velden et al. 1998) and resultant vertical wind shear analyses (Gallina and Velden 2000) were useful in characterizing the shear environment during development.

3.2 New Satellite Technology, QuikScat, AMSU and TRMM and combinations available on the NRL Web Site

QuikSCAT has been the most revolutionary and most valuable for this study in that it provides winds at the sea surface as soon as the hurricane seedling moves off Africa. For this study, important QuikSCAT features are: its continuous 1,800-km swath that covers 93% of the global ocean in a single day; special products made with 12.5-km resolution for the hurricane seedling areas; and a wind range 3-30 m s^{-1} (Liu, 2001). Rain contaminated data are not discarded in this investigation of early development.

AMSU-A is a satellite-borne passive microwave radiometer capable of monitoring the three-dimensional structure and evolution of tropical cyclone warm cores. Two-dimensional vertical cross-sections were developed in an effort to relate temporal variability in observed mid-to-upper tropospheric warming to convection within the tropical cyclone inner core region. Radiometric noise and error associated with the retrieved temperatures limited our ability to discern nascent warming to a lower threshold of approximately +/-2K.

From TRMM we use the passive microwave data mainly in connection with the data sets on the Naval Research Laboratory's Web Site. The site makes available visible and infrared GOES data, together with the passive microwave (TMI) on TRMM and SSM/I, whenever overpasses with microwave sensors are made over tropical cyclones. A complete discussion of the Web Site products are found in Hawkins et al., 2001. Combinations of imagery are made with both the passive microwave sensors' high resolution channel (85 GHz) and with the 37 Hz channel of the TRMM TMI. The latter combination is made to enhance the low-level rainfall, which often develops with little ice scattering.

4. RESULTS AND DISCUSSION

Climatologically, more than half of Atlantic hurricanes originate in "seedlings" which move off Africa. QuikSCAT showed that for the 1999 season, the African monsoon trough frequently extended westward to 30° W and often reached as far north as 11-14° N. Calculated from the NAVY NOGAPS model, its "background vorticity" was frequently as large as 3 - 4 x 10^{-5} s^{-1}, the high value in the Australian monsoon trough at the birth of Oliver. It is clear that the background vorticity supplied by the extended monsoon trough over the ocean is likely to have reduced L_r adequately for vortices of 200-500 km to last long enough to merge and perhaps also for heat released by cumuli to be retained in the vortex. However, for African seedlings moving westward over the eastern Atlantic, life is not that easy.

Fig. 1 shows the Cape Verde sounding at 00 UTC on Sept. 4, 1999, when the pre-Floyd disturbance passed by to the south. Saturation in the lowest layer means low clouds, topped by a strong inversion and dry layer. The saturated layer from about 5 –7.5 km elevation indicates a middle cloud layer. Most noteworthy, if saturated air were forced upward through the inversion, it should be able to rise buoyantly since entrainment provides little drying above 400 mb.

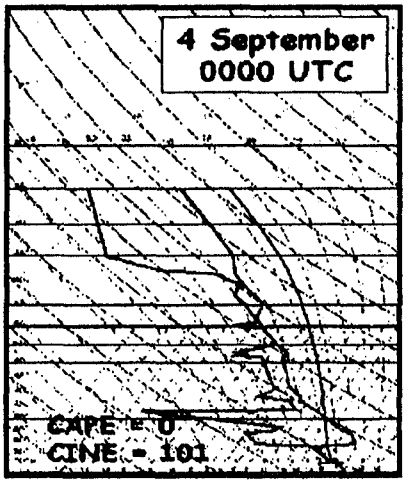

Fig. 1 Cape Verde Radiosonde for 00 UTC, Sept 4 1999. Typical for hurricane season.

4.1. The Birth and Early Life of Floyd 1999, September 2-5, 1999

Fig. 2 shows the track of Floyd plotted on underlying sea surface temperatures (SST's). The first circle indicates where the National Hurricane Center declared Floyd a TD, half way across the Atlantic on Sept 7. The x's follow the center of the vortex observed on QuikSCAT, combined with the infrared movie. The pre-Floyd disturbance moved off Africa on 2 Sept with a weak surface vortex signature in the scatterometer data and moderate convection organized into an MCS (area ~ 10,000 km^2) to the northeast of the center. It took another 5 days of struggling before Floyd was declared a TD.

During the first two days there was unfavorable wind shear greater than 7 ms^{-1} between the lower and upper air layers, which fell below 5 ms^{-1} on Sept 4 and thereafter. Also the SST's off Africa were marginal for development, less than about 27°C. However, the NOGAPS model showed the vortex was quite deep, extending down from 500 mb, with associated surface circulation of 4-6 ms^{-1} indicated by the scatterometer. Some convergence and low-level inflow was associated with the surface vortex so that the forcing was probably enough for a few cumulonimbus clouds to penetrate the inversion and form anvils. The IR image for 1925 UTC Sept 2 (not shown) had some towers up to 12-14 km, but the movie shows they disappeared in 12 hr or less. The rotational winds of the surface vortex seen in the scatterometer data weakened only slightly between Sep 3 and 4, although little convection developed close to the vortex center (black dot on Fig. 3). However, Figs 3a-d show an MCS that developed or redeveloped each day in the same relative location north of the vortex center. The anvils were large and long lasting enough to sustain the 200-500 km scale vortices. These could be the cause of the sustained, or slightly increased, strength of the surface vortex, especially if the vortex tilted north with height.

By Sept 5, there were two detectable midlevel vortices (Fig. 3d) in the IR movie. One was clearly associated with the MCS to the north of the surface circulation center and the other was a midlevel reflection of the surface circulation tracked by QuikSCAT. The two midlevel vortex centers merged during the 5th of Sept, intensifying the surface vortex winds by 2- 4 ms^{-1}. Fig 2 shows that pre-Floyd briefly crossed an ocean area with SST of only about 26°C during this merging time on Sept 5th. By late on Sept. 5 pre-Floyd again moved over increasing SST's. A pool of warmer θ_e air started appearing to the north of the system, partially built up by the swirling flow around the east and north side of the vortex itself.

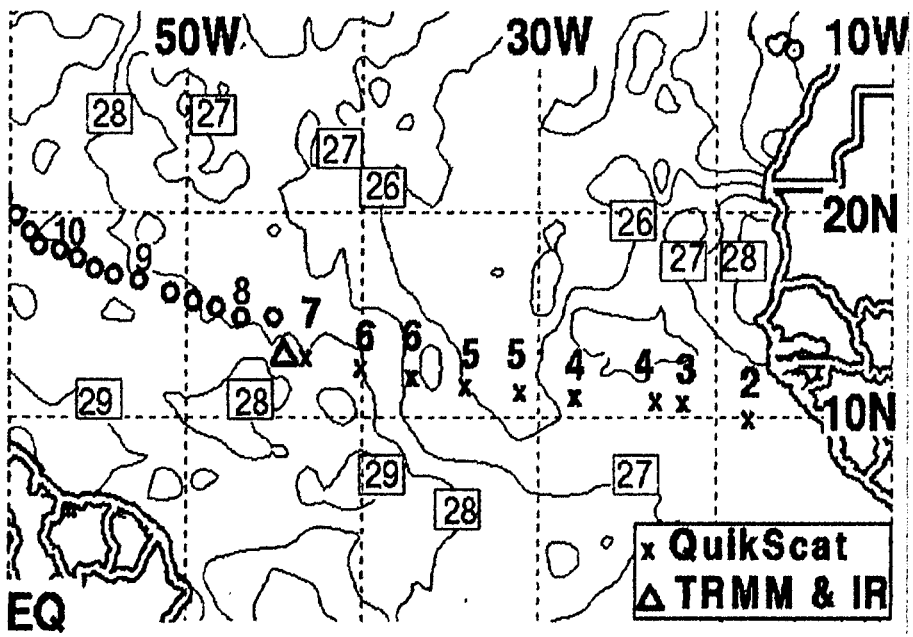

Fig. 2 Track of Floyd 1999 on background of Sea Surface Temperatures

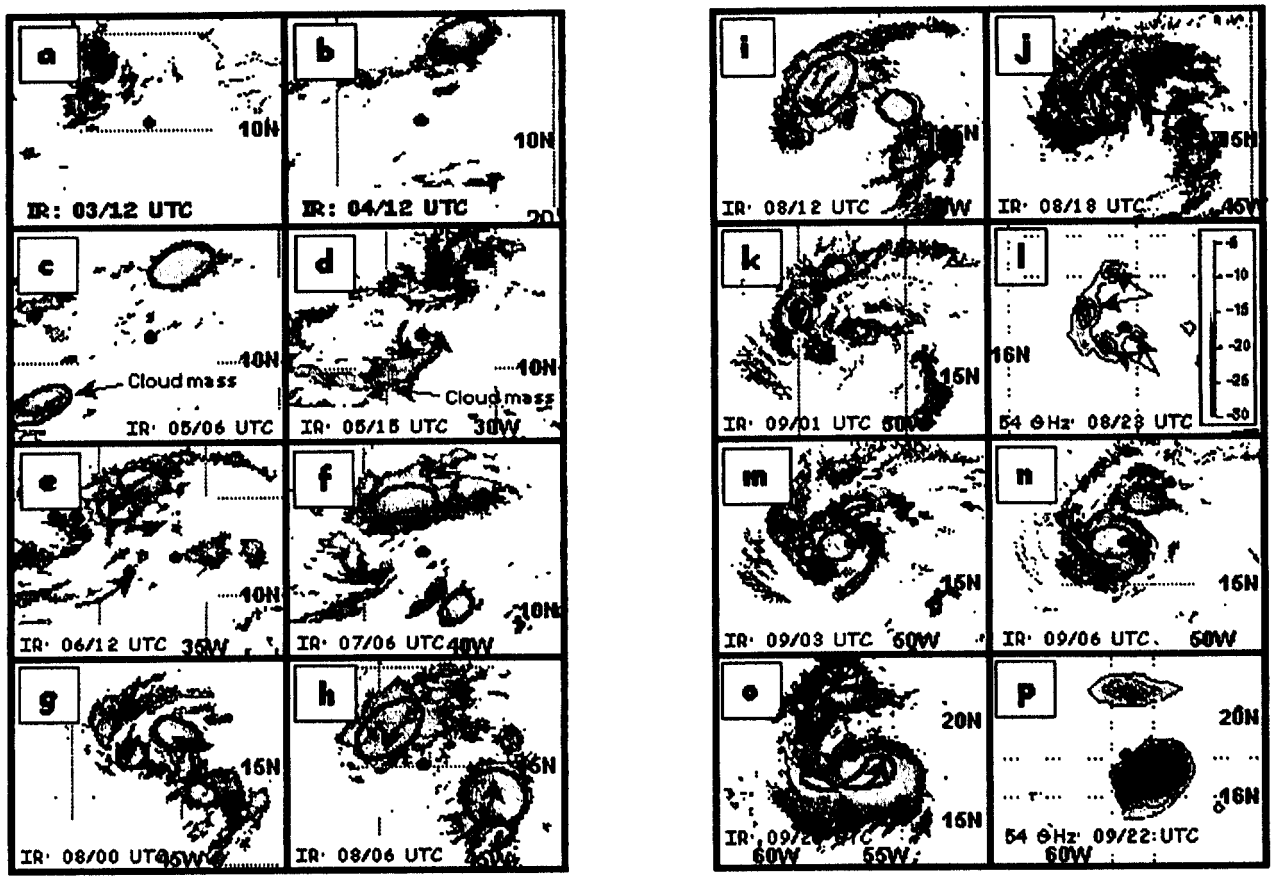

Fig. 3 Sequence of METEOSAT IR and AMSU-A 53.6 GHz images for early Floyd. Times, image type, on each panel. The thin black outlines indicate inferred vortices and black arrows show where cloud rotation was observed in the IR movies

4.2 Pre-Floyd's intensified convection and start of low-level incursion of high θ_e air, Sept. 6-9, 1999

By late on Sept. 6, pre-Floyd was moving over 28°C water. The scatterometer image shows two surface vortices merging. Taking into account the 1.3° northward jump on the track from 1950 UTC on the 5th to 0800 UTC on the 7th, events enacted a perfect merging scenario of these two vortices. By 0800 UTC on Sept.7, the QuikSCAT image showed a single vortex with an area of increased and highly sheared winds on its eastern edge. This is a perfect match with Ritchie's merging vortex model, a classic picture of a sheared losing vortex merged into the victor.

4.3. How Floyd Got the Hurricane Engine Started

The story of hurricane development is the story of successful interaction of many different scales of motion. The new technology which became available in the late 1990's (TRMM, AMSU, and QuikSCAT) has enabled us to observe and link together several interactions that previously had only fragmentary data to interpret. The NOGAPS model relates the vortex center to the field of θ_e. On Sept. 7, the vortex center was far from the high (above 252°K) θ_e air, while on Sept. 8, the center was on the edge of the high θ_e pool. On Sept. 9, the pool of 360°K air was in and to the north of the center, while 24 hours later, the highest energy air was found in the core of the storm. However, mesoscale processes are again required, both to build the bomb and to set it off.

By Sept. 6, the pre-Floyd circulation had moved over sea surface temperatures of higher than 28 C, which raised the θ_e of the inflowing air by increasing fluxes from the ocean to the lower air. This warming, moistening and destabilization of the air caused convection to be much more active, with multiple developments within about 4° of the center of the surface circulation (Figs 3 e, f). As existing mesoscale systems dissipated, new ones were already developing. The associated vortex mergers into the primary circulation resulted in an intensification of the surface swirling winds to greater than 8 ms^{-1} by late on the 7th of Sept, when Floyd was declared a TD by the National Hurricane Center. On the 8th, two substantial mesoscale systems began to develop, one to the east-southeast and one to the west-northwest of the center of the circulation. The two mesoscale convective systems rotated and merged over an 18-hr period (Figs 3,f-j) in a manner analogous to those for TC Oliver 1993. There was a hint of a nascent eye wall at 1800 UTC on 8 Sept. (Fig. 3 l) as the western

clouds wrapped around the center of circulation in a hook pattern also similar to that of Tropical Cyclone Oliver. In contrast to Oliver, however, another two days passed until Floyd intensified to hurricane strength. There was no marked drop in central pressure until mid-day on Sept. 9.

Fig. 4 shows storm relative winds, calculated from QuikSCAT data, on Sept. 8th and 9th. As late as Sept 8th at 2155 UTC when Floyd was already a Tropical Storm, the high θ_e air moves around the periphery of the storm (Fig. 4 top). On Sept. 9, Fig 4 (bottom) shows a region about 100 km across getting in to the core on the rear quadrants (from the east), setting the stage for the convective burst discussed later. On QuikSCAT the winds are now above 8 ms^{-1} out to a radius from center of more than 220 km and 6-8 ms^{-1} twice that far out. This means the ocean-air fluxes are already increased, causing the convection to be much more active within 400 km of the surface circulation center.

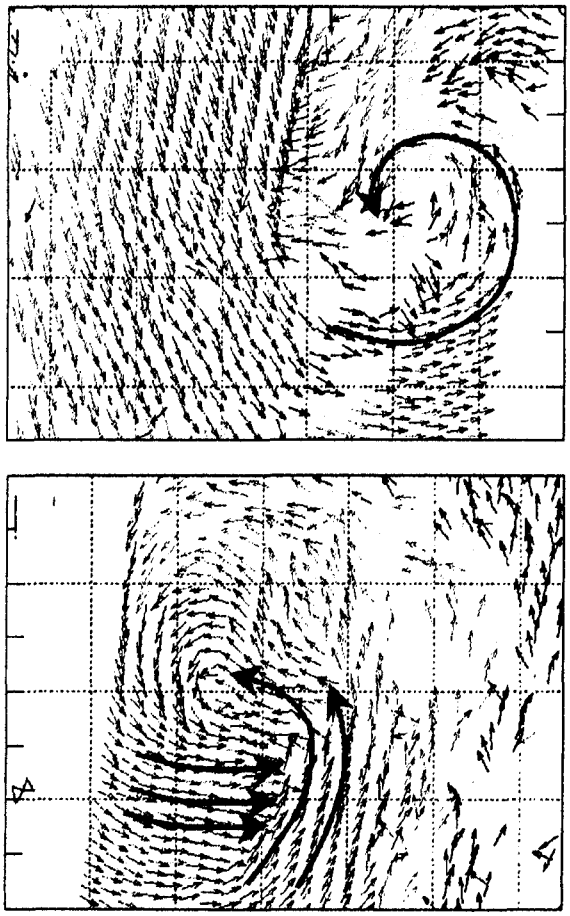

Fig. 4 QuikSCAT images for 2155 UTC Sept 8, 1999 (top) and 2130 UTC on Sept 9 (bottom)

4.4 Floyd's First Two Convective Bursts

Floyd's rapid intensification period commenced early on 9 Sept. with the sudden eruption of intense hot towers in the form of convective bursts (Fig. 5). Two bursts were identified through inspection of combined

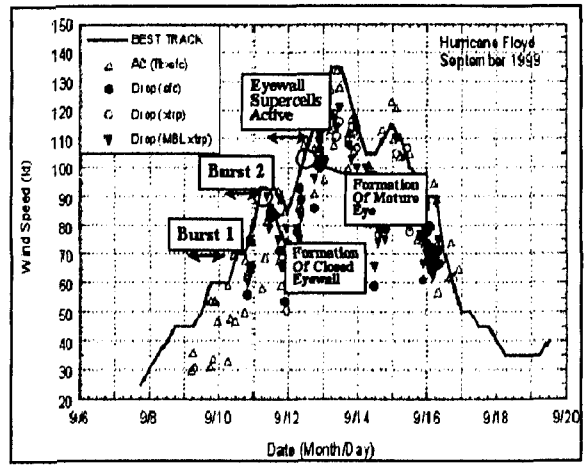

Fig. 5 Floyd's convective bursts, on windspeed and other events plotted against date/time.

GOES infrared and passive microwave imagery. We hypothesize that these convective bursts were essential for warm core development, the rapid deepening, and eye formation in Floyd, and they provide a crucial link between the forcing (i.e. convergence due to low-level wind surges) and vortex-scale intensification.

Figure 5 reveals that each burst was active for approximately 24 hours and followed in close succession during the period of most rapid vortex spin-up. Both of these bursts featured a cold, circular cirrostratus shield that expanded to 400-500 km diameter during maximum extent, with repeated eruption of overshooting hot towers occurring within the center of the cloudy mass. Minimum cloud top temperatures in the tallest overshoots approached –85 °C. Formation of a closed low-level eyewall occurred during the latter stage of Burst 2, when the storm's maximum sustained winds approached 50 ms^{-1} on 11 September.

4.5 Floyd's Warm Core Development

One of the most noteworthy aspects of Floyd's development was the length of time it took to develop a warm core in the upper levels. An upper-level warm core is necessary to support both the low central pressure and the strong winds at the surface. Despite the continued development of convection particularly throughout the period 6-8 September, it wasn't until the early hours of September 9 when the towers in the first convective burst carried the necessary high energy air to high levels that a warm core was finally observed to begin developing in AMSU-A data. At 2300 UTC on September 8, Floyd showed no significant warm core (not shown). By 1200 UTC on the 9th, after the first major hot tower eruption, a slight increase in the brightness temperature, which equates to ~ 1°C of real warming was observed. A

corresponding increase of surface winds then resulted in an increase in the ocean fluxes and thus the energy of the surface air that ascended in the second burst, so that by late on September 10th, the warm core had increased again to about a 2 °C equivalent maximum temperature anomaly (not shown). At that time, maximum winds had exceeded 36 m s^{-1} and a complete nascent eye wall exists. Finally by late on the 11th September, at the end of the second burst, warm core anomalies of about 7°C at 250 mb and 6.2°C at 150 mb were observed in the AMSU data. When computed hydrostatically this warm "core" would support a 31 mb reduction in the surface pressure relative to September 8. This is consistent with NHC's pressure data of 1000 mb on September 8 and 967 mb by the end of September 11. Figure 5 shows Floyd's intensification through September 13, and subsequent weakening, which is beyond the scope of this Chapter.

The explanation for the slow development of the warm core is found by examining the NOGAPS sequence of θ_e near the surface and in the mid-troposphere. A relationship found the 1960's between central pressure fall and increase in θ_e in the ascending undilute eyewall clouds, shows that the rising air in the eyewall clouds must increase its energy in terms of θ_e by 12 ° relative to the environment. In Floyd, this would mean a change from about 354K to about 366K. By late on September 11, the boundary layer θ_e was 380K, which sounds great. However, much dilution must have occurred in the towers of the convective bursts, because the mid-level θ_e was still only 346K. Since a mixture as large as 40 per cent of 346K air with 60 per cent rising 380K air from the low levels gives the required 366K for the pressure fall, our results are reasonable. The midlevel air encountered remained very dry and energy is being lost to moisten it, accounting for the very slow development of the Floyd warm core. For more on AMSU, see Brueske et al., 2001.

4.6 TD2, June 22-26, 2000

Experienced forecasters would not expect African seedlings to become hurricanes in June, owing to cool ocean waters and unfavorable soundings. However, we examined a vortex stronger than the pre-Floyd vortex when it left Africa, which came close to being named. It also traveled as far westward across the Atlantic Ocean as pre-Floyd (Fig. 6 compared with Fig. 2).

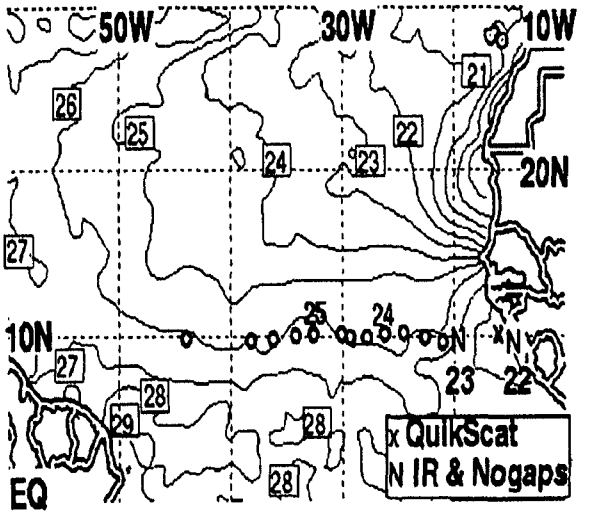

Fig. 6 Track of TD2, June 22-26, 2000 on background of Sea Surface Temperatures

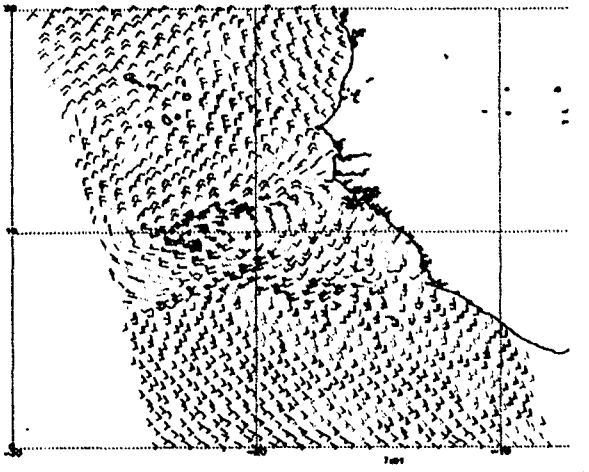

Fig. 7 QuikSCAT overlapping swaths at 0700 UTC June 23, 2000. Wind barbs in knots.

During the period 21-23 June 2000, the large-scale dynamic environment off the west coast of Africa appeared favorable for development. The vorticity in the monsoon trough zone was weaker than that for Floyd at the surface. However, it was much stronger at 700 mb, adequate to permit 200-500 km mesoscale vortices to persist. The ambient vertical wind shear was less than 6 ms^{-1}. The disturbance moving off Africa appeared deep, extending downwards from 500 mb in NOGAPS analyses, with an associated surface circulation of about 10 ms^{-1}. There was a confluence region ahead of the disturbance as shown in a later scatterometer image. The convergence in this region was as large as 20 x 10^{-6} s^{-1} for 23 June. A maximum value of 10 x 10^{-6} s^{-1} persisted over a large region throughout the disturbance (NOGAPS). The convergence was of great importance to the events that followed.

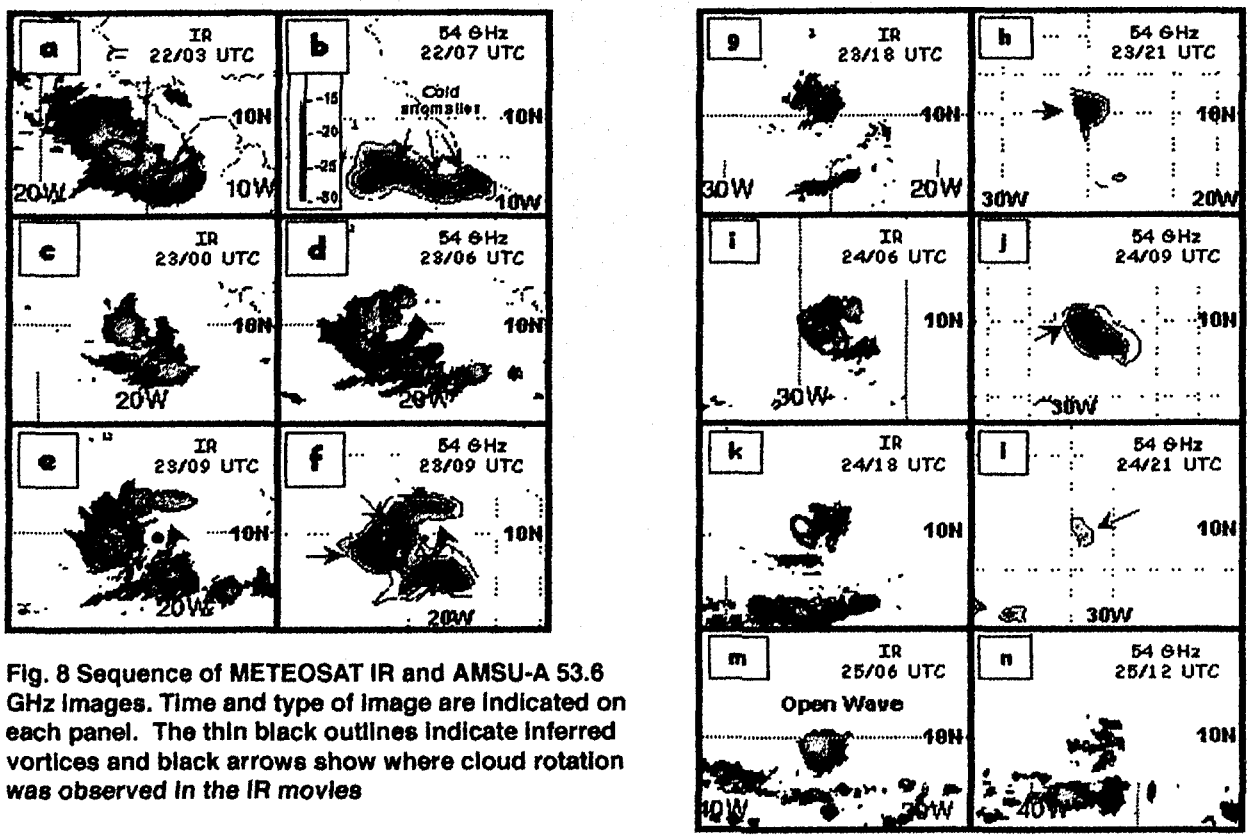

Fig. 8 Sequence of METEOSAT IR and AMSU-A 53.6 GHz images. Time and type of image are indicated on each panel. The thin black outlines indicate inferred vortices and black arrows show where cloud rotation *was observed in the IR movies*

Another important feature was a bulge of high sea surface temperatures (SST's) above 28°C just off the coast, as shown in Fig 6. This warm ocean area caused the low-level air to have unusually warm energy content, with a surface θ_e higher than 350 K. Warning notes are struck by the low mid-level θ_e of about 335° K, and particularly by the stable, dry atmospheric sounding at Dakar (not shown). It has a stronger inversion, no saturated layers, and a much drier air mass than does Fig 1. Thus a stronger "push" or upward forcing is required for penetrative clouds, and much more moistening of the environment would be necessary to "ripen" conditions enough for a convective burst.

The warm, moist low-level air, however, was given enough upward "push" by the convergence ahead of the seedling to create four or five convective towers simultaneously which reached higher than about 15 km as seen in the IR at 0845 UTC on 22 June. High towers became less numerous after that time. The last high tower was observed at 2250 UTC June 22. No cloud tops colder than 240°K, or about 13 km height were observed thereafter, with most clouds topping below 9 km. The main explanation for the diminishing strength and penetration of cumulonimbus towers is the decreasing energy θ_e of the low-level air as the TD moves westward on over the cooler ocean typical for June in this region. By 2250 UTC on the 22nd, the θ_e of the underlying air has decreased by 8°K. Also the dryness of the midlevel air in June dilutes cloud towers, killing their buoyancy. There was no evidence in the AMSU data for warming aloft as a result of convection associated with TD2.

Although convective towers failed to reach above 12-13 km after about 2250 on June 22, the TD2 vortex most closely approached hurricane wind speed and structure about 9 hr later, on the early morning of June 23 (Fig. 7). Fig. 8 shows this strengthening and organization was produced by the merging of midlevel vortices.

As TD2 first moved off Africa on June 22 (Fig 8a,b) convergence of high low-level θ_e air resulted in the development of several mesoscale convective systems with cold IR tops asymmetrically organized around the east and south of the center of the disturbance. The passive microwave images (not shown) reveal that the rain showers were more symmetrically distributed. However, the vertical wind shear increased during the day to more than 6 ms^{-1} from the east-southeast. As a consequence, the clouds became sheared and moved to the southwest of the circulation center. Although three vortices were identified with the aid of AMSU imagery, no merger was indicated in the cloud patterns.

By 2100 UTC on June 22, the wind shear had weakened, and the first of several new mesoscale convective systems developed just to the south of the surface circulation. As a result of lower θ_e in this region, there were fewer convective cells, and the associated stratiform anvils were smaller in extent (Fig 8c vs. Fig 8a). However, during the day of June

23, scatterometer imagery (Fig. 7) shows that TD 2 reached its peak winds close to 25 ms^{-1}. Moreover, combining the 85 GHz channels of the passive microwave instrument on TRMM (not shown) a configuration resembling a nearly closed hurricane eye appeared.

The mesoscale vortex interactions which produced this event are shown in Figs 8 (e-f). QuikSCAT imagery (Fig. 7) suggested that this vortex had winds above those required for a named storm. It also showed considerably strong rotation in the cloud systems. Forecasters resisted the pressure to name it because the high winds did not last for a 6-hr forecast interval. As the TD2 disturbance moved west of about 25° W late on June 23, the sea surface temperatures decreased to less than 26° C (Fig. 6) and both the low- and mid-level θ_e ahead of the disturbance had decreased. Some convection continued for more than 24 hours, but the tops were shallower (~12 km), Figs 8 l-m show the gradual decay. On June 25, TD2 had deteriorated to an open wave, after travelling more than 2500 km westward.

5.0 CONCLUDING REMARKS

The most important conclusion is that the new satellite instruments in combination have enabled us to show that mesoscale vortex interactions are extremely important in the development of hurricane seedlings originating in Africa. Vortex mergers enabled the Floyd seedling to travel far enough westward and live long enough to obtain an environment suitable for intensification.

For TD2 2000 thermodynamic conditions were unfavorable for intensification. But the system was able, by vortex merger, to reach near storm strength surface winds. Its prolonged life did not require intense deep convection. The main role that convection played was to provide the stratiform anvils making conditions suitable for the mesoscale midlevel vortices to last and to merge. This importance of dynamics in the early stages and relative unimportance of deep convection is quite contrary to most of the earlier ideas of Tropical Cyclone genesis, which usually start by discussing clusters of deep convective clouds.

6.0 ACKNOWLEDGMENTS

The authors are grateful to J. Hawkins and colleagues of the Naval Research Laboratory for providing easy access to IR and passive microwave satellite imagery and much additional help We are grateful to Dr. Scott Tyo for providing his expertise on image enhancement techniques. The work was supported by the NASA TRMM program, under Dr. Ramesh Kakar, NASA Headquarters Program Scientist and by the Office of Naval Research Marine Meteorology Program, under Dr. Robert Abbey, by the U.S. Air Force and its Department of Physics.

We are also grateful to Stacy Stewart and Miles Lawrence of the National Hurricane Center for much help and information and to G. Heymsfield and R.H. Simpson for many helpful discussions.

7.0 REFERENCES

Brueske, K.B. and C.S. Velden 2001:Satellite-based TC intensity estimation using the NOAA series AMSU. Conditionally accepted in *Mon. Wea. Rev.*

Gallina, G. and C.S. Velden, 2000: A quantitative look at the relationship between environmental vertical wind shear and TC intensity change utilizing enhanced satellite derived wind information. 24th Conf. Hurr. and Trop. Meteor., Ft. Lauderdale, FL, 256-257.

Gray, W. M., 1975: Tropical Cyclone genesis. Dep't. of Atmos. Sci. Paper No. 234, Colo. State Univ., Ft. Collins, CO, 121 pp.

Harr, P. A., M. S. Kalafsky, and R. L. Elsberry, 1996: Environmental conditions prior to formation of a midget tropical cyclone during TCM-93. *Mon. Wea. Rev.*, **124**, 1693-1710.

Hawkins, J., T. F. Lee, J. Turk, C. Sampson, J. Kent and K. Richardson, 2001: Real time Internet distribution of satellite products for Tropical Cyclone reconnaissance. *Bull. Amer. Met. Soc.*, **82**, 567-578.

Liu, W. T., 2001: Wind over troubled water, *Backscatter*, **12**, 10-14.

Menard, R. D., and J. M. Fritsch, 1989: A mesoscale convective complex-generated inertially stable warm core vortex. *Mon. Wea. Rev.*, **117**, 1237-1261.

Miller, D. and J. M. Fritsch, 1991: Mesoscale convective complexes in the western pacific region. *Mon Wea. Rev.*, **119**, 2978-2992.

Ooyama, K., V., 1982: Conceptual evolution of the theory and modeling of the tropical cyclone. *J. Met. Soc. Japan*, **60**, 369-380.

Ritchie, E. A. and G. J. Holland, 1997: Scale interactions during the formation of Typhoon Irving. *Mon. Wea, Rev.*, **125**, 1377-1396.

Schubert, W.H., J.J. Hack, P.L. Silvia Dias and S.R. Fulton, 1980: Geostrophic adjustment in an axisymmetric vortex. *J. Atmos. Sci.*, **37**, 1464-1484.

Simpson, J., E. A. Ritchie, G. J. Holland, J. Halverson, and S. Stewart, 1997: Mesoscale interactions in tropical cyclone genesis. *Mon. Wea. Rev.*, **125**, 2643-2661.

Velden, C.S., T.L. Olander and S. Wanzong, 1998: The impact of multispectral GOES-8 wind information on Atlantic tropical cyclone track forecasts in 1995. Part 1: Data set, methodology, description, and case analysis. *Mon. Wea. Rev.*, **126**, 1202-1218.

P5.2 NPOESS INSTRUMENTS: THE FUTURE OF METSAT OBSERVATIONS

John D. Cunningham, NPOESS Integrated Program Office, Silver Spring, MD 20910,
And
John M. Haas, and Hilmer Swenson, The Aerospace Corporation.

BACKGROUND

The past four decades have seen a tremendous growth in the use of weather satellites for both civilian and military applications. The maturation of visible-infrared imagery from geosynchronous and polar orbits has become familiar to vast television audiences and military planners as well as a wide array of geophysical, oceanographic, and atmospheric scientists.

The NOAA civilian polar orbiting satellites began in 1960 and evolved over time to become the POES (Polar-orbiting Operational Satellite) program. The military developed and operated their own distinct military operational satellites starting in 1965 under what became the Defense Meteorological Satellite Program (DMSP). During the Cold War, a dual system was required out of military necessity and differences between military and civilian user community needs.

Many government studies have been conducted to assess the value of converging the two systems into a single system. Most studies recommended retaining the separate systems. A 1993 tri-agency study by DoD, NOAA, and NASA recommended that a single converged system should replace the current separate systems. With the end of the Cold War, Congressional interest in saving money, and the increased cooperation between the nation's weather services, the concept of a converged system was included as an initiative in the Vice President's National Performance Review. A Presidential Decision Directive, signed in May of 1994, directed the convergence of the polar orbiting weather satellites systems into a single national system. An Integrated Program Office (IPO) within NOAA was established in October 1994 as a result of the signing of a tri-agency Memorandum of Agreement (MOA) in May 1994. The new converged system was identified as the National Polar-orbiting Operational Environmental Satellite System (NPOESS). The IPO was staffed with representatives of Department of Commerce, Department of Defense and NASA. Figure 1 is a notional system configuration.

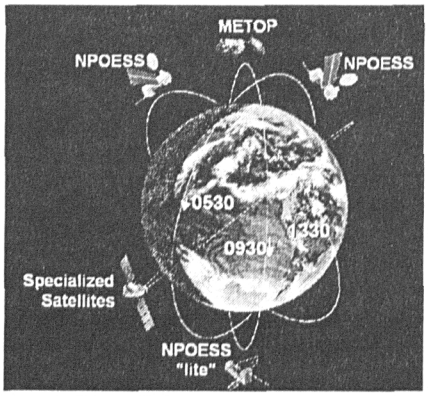

Figure 1. The NPOESS System Constellation

NPOESS is also charged to incorporate new technologies, especially from NASA, foster international cooperation, and, as the National Performance Review directed, save up to $ 1.3 B over operating separate systems. Current estimates indicate combined savings of greater than $ 1.8 B at this point.

NATIONAL IMPORTANCE

The goal of NPOESS is to dramatically improve the nation's space-based, remote sensing capabilities for Environmental Monitoring. Both the civilian and military sectors depend upon polar-orbiting, remotely sensed

weather data. Timely, accurate, and cost-effective public warnings and forecasts of severe weather events reduce the potential loss of human life, property, and agriculture, as well as advancing the national economy. NPOESS support of commercial and general aviation, agriculture, and maritime communities are aimed at increasing U.S. productivity. The NPOESS will allow DoD to shift the current tactical and strategic focus from "coping with and avoiding the weather" to "anticipating and exploiting" atmospheric and space environmental conditions. NPOESS has also "converged" the needs of the operational users with the needs of the science community in the case of the VIIRS (Visible Infrared Imaging Radiometer Suite). By addressing NASA scientific and climatic requirements as part of the VIIRS, important climatic data continuity is achieved while implementing NPOESS.

GETTING THERE

Over the next decade, NPOESS will evolve into the full operational capability as shown in Figure 2.

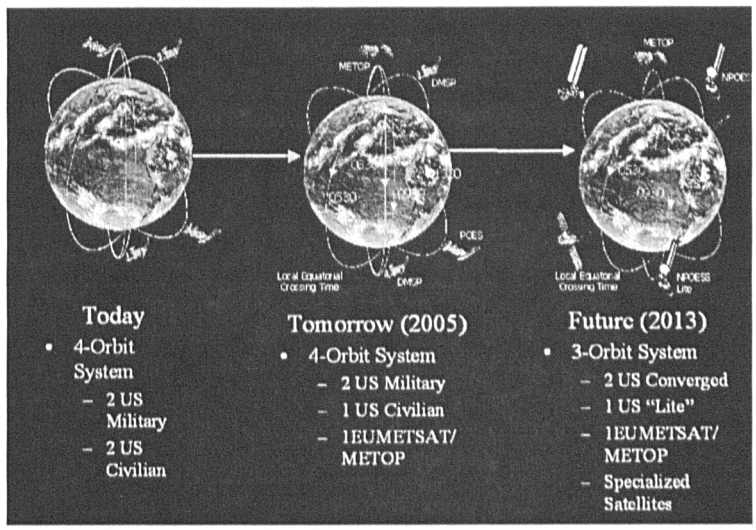

Figure 2. A Possible Evolution of the NPOESS Constellation

The IPO is currently managing two major types of competitive contractual programs: instrument development and Total System Program Responsibility. This means Figure 2 is more notional until a TSPR contractor is selected in 2002.

Currently, the U.S. operates two polar-orbiting systems with two Defense Meteorological Satellite Program (DMSP) spacecraft and two Department of Commerce Polar-orbiting Operational Environment Satellite (POES) platforms. By 2005, METOP will become operational to supplement the scheduled U.S. remaining satellites. In addition, a risk reduction effort, the NPOESS Preparatory Program (NPP), which is a joint NPOESS-NASA effort, will join the multinational operational satellites to provide data continuity for the NASA EOS program and risk reduction to the NPOESS program. NPP will be carrying three major NPOESS instruments: the VIIRS, the CrIS (Cross-track Infrared Sounder) and the NASA ATMS (Advanced Technology Microwave Sounder). NPP will help the IPO to assess the operability of the instruments as well as the C3 network and EDR (Environment Data Record Performance). Figure 3 is the planned NPOESS transition in more detail.

The Integrated program Office (IPO) is responsible for the operational deployment and operation of the NPOESS as early as 2008. The NPOESS will remain operational for at least ten years and provide global data for meteorological, oceanographic, and solar-geophysical users by disseminating the data to worldwide users. These data will be delivered in the form of Environmental Data Records (EDRs) in compliance with the Integrated

Operational Requirements Document (IORD),which incorporates the DOC and DoD operational mission requirements. Figure 4 relates the IORD EDRs to the NPOESS-developed instruments.

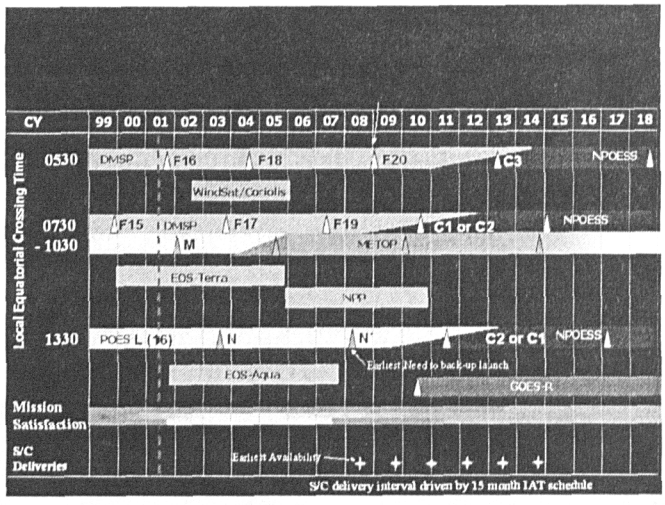

Figure 3 – The NPOESS Schedule

NPOESS INSTRUMENTS

The Requests for Proposal (RFPs) were released in April 1997 for the NPOESS sensor development effort. The IPO awarded nine sensor development efforts in July 1997. Because of the technical complexity and risk involved with these five particular payload suites below, two competitive contracts per sensor (except for GPSOS) were awarded to begin sensor development and risk mitigation. These sensors include: VIIRS - Raytheon; CMIS - Conical Microwave Imager/Sounder - Ball Aerospace and Boeing; CrIS - ITT; OMPS - Ozone Mapper/Profiler Suite - Ball Aerospace; GPSOS - Global Positioning System Occultation Sensor - Saab -Ericsson. Posters on VIIRS, OMPS, and CrIS will also be presented at this conference. All NPOESS instruments will provide capabilities well in excess of current operational sensors. The sensors and instruments on NPOESS will operate the breadth of the electromagnetic spectrum from 100 MHz to the UV for earth observations and into the X-ray region for the space environment.

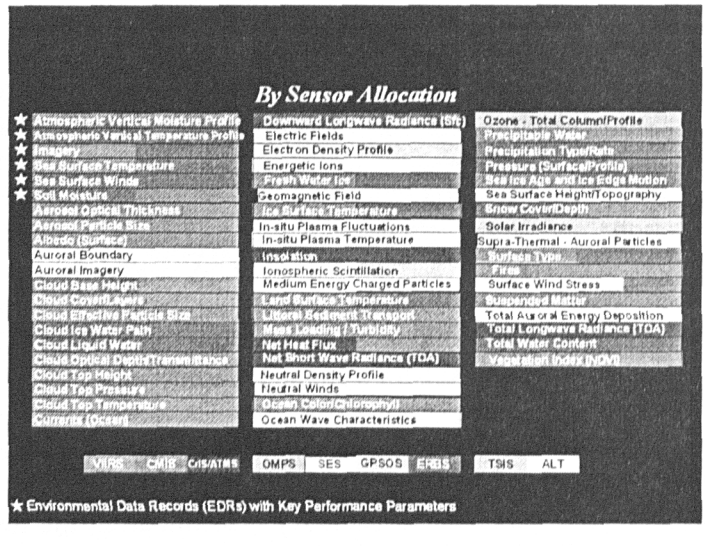

Figure 4 – EDR Allocation by NPOESS Sensor

NPOESS BENEFITS AND PROMISE

NPOESS will be providing an astonishing amount of environmental and climatic data from many advanced sensors beginning in the next few years. VIIRS alone will be capable of providing up to nearly 900 Gigabits of data per day. With the tight accuracy, precision, and uncertainty constraints of the EDRs, NPOESS will contribute to more accurate forecasts, which are critical to the protection of life, safety, and property. The military sector will also be well served with NPOESS data to central forecast centers and remotely located field terminals. Since weather permeates all aspects of military operations, NPOESS data will contribute to excellent situational awareness for unit commanders at many echelons. Situational awareness is critical to combat planning, air superiority and, ultimately, winning the war. Remote sensing has come far from the early 1960's to the end of the 20th century. Figure 5 contrasts the dramatic improvement over the last four decades. NPOESS will lead the way into the 21st century for operational and environmental remote sensing.

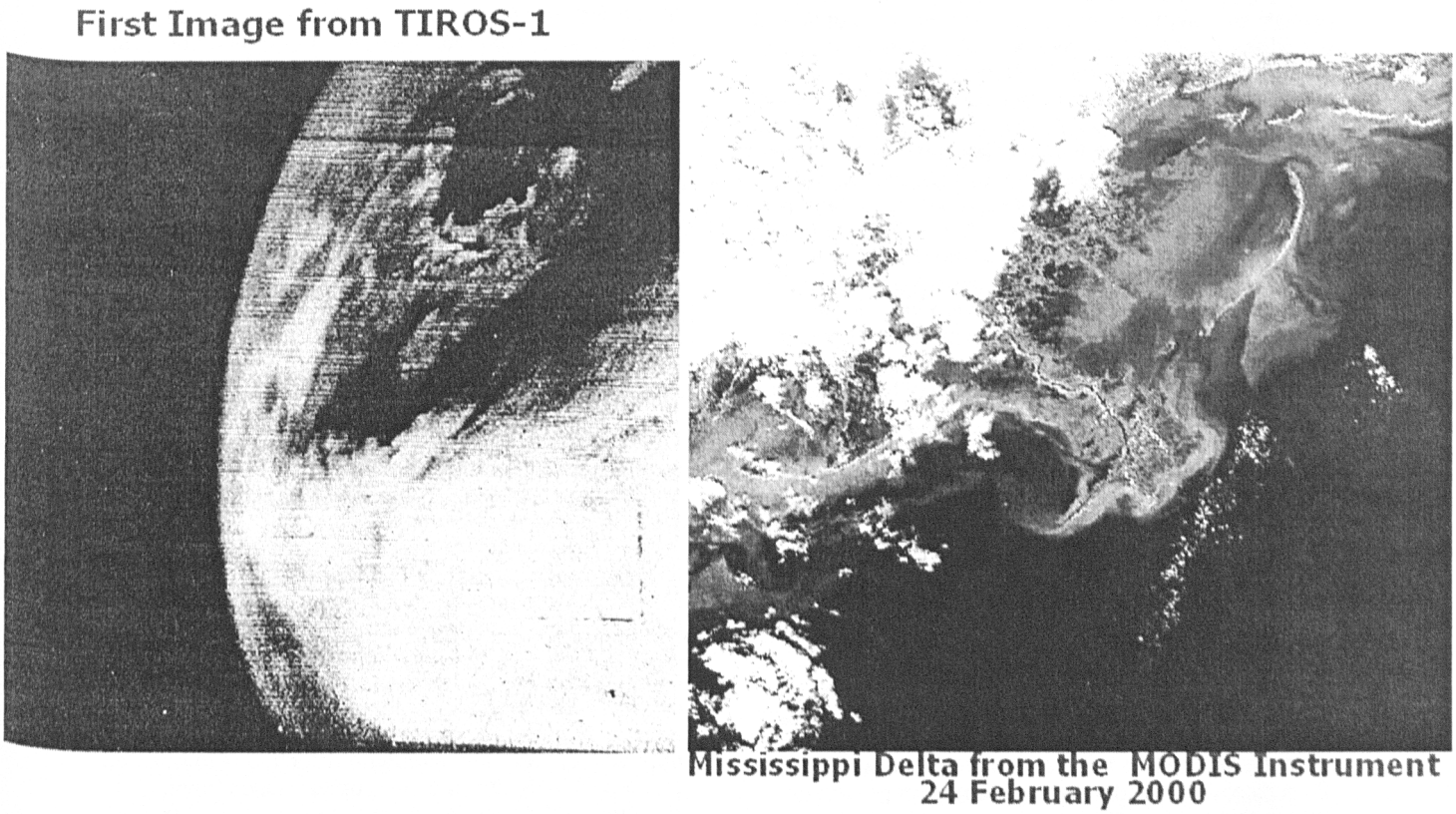

Figure 5. Past and Future Operational Capabilities

P5.3 RECOMMENDATIONS FROM THE GOES USERS' CONFERENCE

James J. Gurka* and Gerald J. Dittberner
National Environmental Satellite, Data and Information Service (NESDIS)
Office of Systems Development, Suitland, MD

1. INTRODUCTION

The GOES Users's conference was held from May 22 through 24, 2001 in Boulder Colorado, with close to 200 participants from government, the private sector, academia and the international community. It was organized by the National Oceanic and Atmospheric Administration (NOAA) with cooperation of the National Aeronautics and Space Administration (NASA), the American Meteorological Society (AMS), the National Weather Association, the World Meteorological Organization, and the National Institute of Standards and Technology.

The goals of the conference were: (1) to inform GOES users of plans for the next generation (GOES R Series) capabilities; (2) to provide information on the potential applications; (3) to determine user needs for new products, data distribution, and data archiving; (4) to assess potential user and societal benefits of GOES capabilities; and (5) to develop methods to improve communication between the National Environmental Satellite, Data, and Information Service (NESDIS) and the GOES user community. Sessions included: Planned and Potential Sensors for U.S. Geostationary Satellites; User Requirements, Applications, and Potential Benefits from Future GOES; Future International Geostationary Satellites; and Communications, Ancillary Services and Training Issues. The third day of the conference consisted of facilitated breakout sessions in which the user community was asked to provide input to ten questions on their future needs for products, services, data distribution, archiving, training and potential benefits of the next generation GOES to their operations and to society.

This paper will provide a summary of the recommendations provided by the GOES user community. It will also provide an outline of plans for a formal process of communication between NESDIS and GOES users, ensuring that the needs of the entire user community are considered in the design of future systems, products and services.

2. POTENTIAL BENEFITS

During the breakout sessions on the third day, the first question the participants were asked dealt with potential benefits to them and society as a whole. Specifically: "Considering the information presented during this conference regarding the potential benefits and service improvements of GOES, can you foresee additional savings in terms of life, injury avoidance or protection of property? Please indicate the three most important benefits to your program or to society."

Respondents indicated that planned improvements for the next generation GOES would lead to significant improvements in detection of atmospheric moisture and improved quality of satellite derived winds, leading to improved numerical model performance. This together with subjective use of the improved satellite data and products by forecasters, will result in more timely and accurate weather forecasts, including: improvements in tornado warnings; forecasts of hurricane landfall; forecasts of flooding; and forecast detail.

The improved forecasts in general will lead to preservation of life and property; improved quality of life due to better recreational planning; improved safety and economic benefits to commercial, military and general aviation; improved management of energy resources; improved planning and management of ground and marine based transportation; improved fisheries management; improved guidance for State Emergency Managers; cost savings for agricultural applications from better planning of watering, and application of pesticides, herbicides and fertilizers; improved management of water resources and flood control; and improved military operations due to improved forecasts for trafficability, weapons trajectories, ship and plane sorties for storm avoidance, and aircraft carrier operations.

3. DATA AND NEW PRODUCT NEEDS

The second and third questions in the breakout session, asked for the users' needs for real time data and for new products. The primary recurring themes in the user responses follow:

1) Twelve spectral channels should be a threshold requirement for the Advanced Baseline Imager (ABI). These channels should include the following: a) 0.64μ for daytime detection of clouds; b) 0.86μ for daytime detection of clouds, aerosols, vegetation and ocean properties; c) 1.375μ for daytime detection of thin cirrus; d) 1.6μ for distinguishing clouds from snow and water cloud from ice cloud (daytime only) e) 3.9μ for detection of fires, and nighttime detection of low clouds and fog; f) 6.15μ for detecting upper tropospheric moisture and determining upper level flow; g) 7.0μ for detecting mid tropospheric moisture and determining mid level flow; h) 8.5μ determining cloud phase, detecting sulfuric acid aerosols and determining surface properties; i) 10.35μ for determination of cloud particle size and surface properties; j) 10.7μ for detection of clouds, generating cloud drift winds, quantitative precipitation estimates and determination of low level

* Corresponding author address: James J. Gurka, NOAA/NESDIS, FB-4, room 3010B , 5200 Auth RD., Suitland, MD 20746-4304;
email: james.gurka@noaa.gov

water vapor; k) 11.2μ for detection of clouds, generating cloud drift winds, and determination of low level water vapor. l) 12.3μ for detection of volcanic ash, low level water vapor, and sea surface temperatures; and m) 13.3μ for determining cloud-top parameters and determining cloud heights for improved quality cloud drift winds.

2) In addition to the above listed channels, which should be considered absolutely essential, there was a strong recommendation for at least two additional channels: the 0.47μ and the 9.6μ. The 0.47μ channel would be valuable for detecting aerosols and haze in determining slant range visibility for aircraft operations. The 9.6μ channel would be important for detecting ozone and for the detection and forecasting of clear air turbulence. Beyond these channels, providing they would not result in major additional sensor complexity or expense, a 4.57μ channel would be useful for improved determination of precipitable water and a 14.2μ channel would be valuable for more accurate cloud top heights. However, these products will also be generated by the hyperspectral sounder on the GOES-R series.

3) Full disk imagery should be provided from the ABI every 5 minutes.

4) Calibration information and algorithms to generate products should be made available to the user community.

5) The sounder should be able to operate in a rapid scan mode.

6) Soundings are needed in cloudy areas. Conventional GOES clear air soundings should be supplemented either by a microwave sounder in geostationary orbit, or with GOES IR soundings above the clouds and polar microwave soundings.

7) Funding for research and development of new satellite products should be part of the satellite acquisition budget.

8) For developing new satellite products there should be improved collaboration between research and operations.

9) In operations there is a need for a blend of data and products from operational and research satellites.

10) Suggestions for new products include; a) atmospheric aerosols; b) cloud phase; c) cloud particle size; d) surface properties; e) improved satellite derived winds; f) moisture flux; g) improved quantitative precipitation estimates; h) improved volcanic ash product; i) improved products showing threat areas for atmospheric turbulence; j) cloud emissivity; j) improved low cloud and fog product; k) cloud layers; l) probability of rainfall for each pixel; m) improved sea surface temperature product; n) true color product; o) cloud optical depth; p) sulfur dioxide concentration (precursor to volcanic eruption); q) aircraft icing threat; r) ocean color; s) under (ocean) surface features (i.e. coral reefs); t) improved sea ice products; u) improved vegetation index; v) ozone layers; and w) surface emissivity.

4. SPACE WEATHER

The GOES program has included space environment measurements since its inception about a quarter-century ago, beginning with the launch of the Synchronous Meteorological Satellite (SMS-1 in 1974). These measurements have continued to grow in importance as the Nation's reliance on space and ground-based technology affected by the space environment accelerates, and as we embark upon an era of permanent human presence in space with the occupancy of the International Space Station. For GOES-R, the established requirements for observations of disk-integrated solar x-ray flux, disk integrated extreme ultraviolet flux, solar x-ray imaging, energetic charged particles, and the local magnetic field are basically similar to those set for the GOES N series. Proposed improvements include: Increasing the dynamic range of the Solar X-ray Imager (SXI) to better cover the full dynamic range of solar features and instrument modifications that may extend the measurements to other wavelengths; additional channels and increased cadence on the Solar Extreme Ultraviolet Sensor (EUVS) to obtain improved height resolution for thermospheric heating rates and ionization rates , and to monitor solar EUV flares; improved dynamic range and a lower threshold of the Solar X-Ray Sensor (XRS) so that the instrument will be able to monitor the solar x-ray flux even at low activity levels and to help in establishing secular (>10 year) trends in the solar x-ray flux and to extend the Energetic Particle Sensor (EPS) proton measurements down to 30 KeV to better monitor the bulk of Earth's ring current that contributes to spacecraft charging, and to meet specifications that were requested, but not met with the GOES N series. All of these improvements are important for data products that support systems and human activity affected by conditions in the space environment.

5. INSTRUMENT OF OPPORTUNITY

Each of NOAA's three-axis stabilized series of GOES satellites has a place reserved on the Earth-facing side for an Instrument of Opportunity (IOO). The IOO slot is a location for new technologies that provide space, time, and/or spectral resolution of the environment not possible with the preconceived Imager and Sounder. IOO's have been suggested to detect lightning, volcanic eruptions, ozone, sulfur dioxide, ocean color, vegetation and special weather events. To qualify as an IOO on GOES, the proposed instrument must: 1) have potential benefit to NOAA; 2) fit within the allocation constraints; 3) be independently funded, including pre-launch test equipment and the spacecraft accommodation costs; 4) be delivered two years before launch for integration and testing, and 5) not interfere with the existing launch schedule or the operational instruments.

Four of the breakout groups recommended a lightning mapper for an instrument of opportunity; four recommended a special event imager; and three recommended a microwave sounder. There was also a recommendation to provide baseline funding for spacecraft accommodation costs for an IOO.

6. DATA DISTRIBUTION

The current GOES transmits data with a rate of 2.1 Mbits per second. The GOES-R series, with thousands of bands on the sounder, as well as more channels on the imager with higher spatial and temporal resolution, the data rates will increase to 20 to 80 Mbits per second, depending on the amount of data compression used. Options include land line distribution, commercial satellite distribution, or rebroadcast from the GOES. The current L band broadcast may have to be changed to an X band transmission (which has problems with rain fade and low angle reception). This would require completely new reception equipment. The current L band is also the only approved method of transmission while the satellite is moving into position from a storage location. The conference participants were asked to convey their needs for data distribution and provide suggestions for optimum methods of distribution.

Some recurring themes among the user responses include: 1) there is a wide spectrum of user needs with different tiers of data access. There should be a full range of methods of reception to accompany the broad range of data requirements. 2) data distribution should be timely and have low cost and low data rate options available. 3) Data distribution options that should be considered include: a) commercial satellite broadcast; b) direct broadcast from GOES; c) Internet; d) dedicated land lines. e) data acquisition by users from a central location; and f) some combination of "a" through "e". 4) Re-use existing ground station assets and broadcast a subset of the ABI/ABS data streams from decommissioned GOES satellites.

7. DATA AND PRODUCT ARCHIVE NEEDS

The breakout groups recommended that a full spectrum of GOES products, ranging from raw data to highly processed products be available in an archive for applications ranging from the nowcasting scale to the climate scale. The products should be stored in a user friendly format, allowing for easy remote access at minimal cost to the user. The user must also have access to metadata, including information on data and product quality trends due to variations in instrument or satellite performance. Users should be able to browse, select and submit requests for products via the internet. Potential options for product distribution to the users include: File Transfer Protocol (FTP) for electronic transfer, CD-ROMs, and DVDs. Turnaround for most data requests should be less than 1 day, while one week should be allowed for extremely large requests (i.e. years worth of data).

8. NEW DATA INTEGRATION

Participants of the workshop provided several recommendations on ways to minimize the time required for integrations of the GOES-R data stream into operations: 1) leverage data from relevant instruments on other satellites to better understand GOES-R capabilities (i.e. use AIRS and GIFTS data to prepare for ABS; use MODIS to simulate ABI data); 2) provide correctly formatted sample data sets to the user community at least one year prior to the GOES-R launch; 3) requirements for operational algorithms should be identified by the spring of 2002; 4) operational algorithms should be developed 3 to 5 years prior to launch; 5) establish a working group to develop plans to provide sample data sets and for development of new operational algorithms; 6) NOAA should invest in education, training, research, and product development to ensure optimal use of GOES-R products shortly after launch; 7) provide an extended scientific checkout period following the GOES-R launch to allow use of current data and to ease the transition to new data sets. 8) NOAA should have in place a fully operational infrastructure for reception, distribution, processing, and archiving, ready for use with test data sets prior to the GOES-R launch.

8. EDUCATION OF USER COMMUNITY

To ensure maximum return on the investment in the next generation GOES, the breakout groups recommended a comprehensive education program for all levels of GOES users, including: forecasters, emergency managers, recreational users, academia, the media, industrial users, and commercial users. Education programs should be funded as part of the end-to-end GOES program budget.

Methods of education should include: 1) conferences and workshops; 2) web-based training; 3) teletraining; 4) CD-ROM or DVD based training; 5) brief segments on the Weather Channel; 6) educational packages appropriate for Congress, upper level management, and business leaders.

9. SUMMARY AND CONCLUSIONS

The GOES User's Conference was a good initial step for improving communication between NESDIS and the GOES User Community. Participants strongly supported a continuation of the process promoting a two way dialogue between GOES users and those planning the development of the next generation GOES. Recommendations for communication venues included: 1) regular conferences similar to the GOES Users' Conference; 2) formation of working groups to deal with specific issues; 3) provide a bulletin board for information exchange; 4) hold informational sessions at end-user conferences (e.g. NWA, CWSA, AMS, Space Weather Week); 5) provide an updated, focused, supported web site; 6) provide information via e-mail; 7) make an expert team available to all users and instrument developers.

In response to the user recommendations, a permanent working group has been established to deal with action items originating from the conference. Also, a bulletin board has been set up at: http://www.osd.noaa.gov/GOES/feedback/sign.asp for two way communication between NESDIS and the user community. Finally, plans for the next GOES User Conference are being prepared.

10. ACKNOWLEDGMENTS

The authors would like to thank all the participants of the GOES Users' Conference, especially the Program Committee, the speakers, participants of the breakout sessions, NIST personnel for logistic support, and all those who provided valuable suggestions for improving the future GOES program. The authors would also like to thank Dick Reynolds and Timothy J. Schmit for reviewing the manuscript.

P5.4

NOAA'S GOES SYSTEM - PLANS FOR NEW SENSORS

Gerald J. Dittberner[1]
National Oceanic and Atmospheric Administration (NOAA)
National Environmental Satellite, Data, and Information Service (NESDIS)
Suitland, Maryland

1. INTRODUCTION

The GOES mission is to maintain a continuous stream of data from two Geostationary environmental operational satellites. To satisfy this mission, the National Oceanic and Atmospheric Administration (NOAA) maintains operational satellites at the GOES-West position (GOES-10 at 135°W) and at the GOES-East position (GOES-8 at 75°W). Because the GOES Program competes in the United States' commercial launch services market, positions in the launch queue must be secured with typical lead times of 12 to 15 months. To reduce the risk of a break in service, NOAA uses the on-orbit spare concept. For example, NOAA launched GOES-10 as an on-orbit spare and on July 21, 1998, GOES-10 replaced GOES-9 as the operational GOES-West satellite when GOES-9 showed signs of imminent failure.

2. THE CURRENT SERIES: GOES-8, GOES-9, GOES-10, GOES-11, and GOES-M

The present GOES constellation consists of two operational satellites, GOES-8(I) and GOES-10(K); a fully capable on-orbit spare, GOES-11(L); and a limited-capability on-orbit spare, GOES-9(J). GOES-M was launched July 23, 2001 and at this writing (August 2, 2001) it is in the orbit raising phase. The five satellites in the GOES I through M series were produced by Space Systems/Loral. NOAA describes each satellite with a letter (e.g., I, J, etc.). Once it is successfully inserted into geostationary orbit, it is redesignated with a number (e.g., 8, 9, etc.).

2.1 *NOAA GOES-8*

GOES-8 was launched from Cape Canaveral April 13, 1994, is the operational satellite over the Americas and the Atlantic Ocean at 75°W, and continues to provide data more than two years beyond its nominal five year design life. It is the first GOES satellite stabilized in a three-axis pointing mode rather than as a spinner. It was designed this way to allow nearly instantaneous, properly navigated and registered data to track rapidly developing severe weather and so that the atmospheric Sounder instrument could stare long enough at one spot to provide a high signal to noise ratio. Instrumentation on GOES-8 consists of an Imager, a Sounder, and a Space Environmental Monitor (SEM) suite; along with a Data Collection System (DCS), weather facsimile (WEFAX) transponders, and Search and Rescue (SAR) receivers.

The Imager is a five channel imaging radiometer. Images are formed by scanning an array of detector footprints across the Earth from East to West, then back from West to East, from the top of the image to the bottom. An excellent description of both the Imager and Sounder can be found in Menzel and Purdom (1994). The visible channel consists of eight detectors mounted in a north-south line, each having a horizontal resolution of one km at nadir. Each scan covers an eight km swath. There are four infrared channels centered at 3.9, 6.7, 10.7, and 12.0 micrometers. Three of the IR channels consist of two four km detectors also mounted in a north-south line. The two detectors cover eight km each scan. One detector, the 6.7 micrometer channel, has one detector at eight km resolution. Thus, each scan produces eight lines of visible, two lines of IR in three channels and one line at 6.7 micrometers.

The Sounder instrument is a 19 channel discrete-filter radiometer that senses emitted radiances to measure the vertical distribution of temperature, moisture, cloud top temperatures, and ozone in the atmosphere. In addition to the one visible channel, there are seven longwave, five midwave, and six shortwave IR channels, all with horizontal resolution of 8.6 km at nadir. The Sounder stares at each field of view on the Earth for 0.1 to 0.4 seconds (commandable) and measures radiances in all 19 channels.

The Imager and Sounder each use a single scan mirror for East-West and North-South motion. Two motors are provided for each direction in the Imager design, one to move the mirror and one as backup. The Sounder has the same system design. On GOES-8, one of the Sounder East-West mirror motor windings failed in August 1994. Since that time, the backup motor has continued to provide data and no significant break in service has occurred.

Charged particles have rendered some of the memory in the Attitude and Orbit Control Electronics inoperable, although the backup electronics and remaining memory have allowed GOES-8 to continue to provide continuous operational data. Attitude and three-axis pointing are nominally controlled by two momentum wheels and one reaction wheel. Two of the three are required for operational control.

[1] *Corresponding author address:* Gerald J. Dittberner, NOAA/NESDIS/OSD1, 5200 Auth Road, FB4, Room 3301A, Suitland, MD 20746, e-mail: gdittberner@nesdis.noaa.gov

2.2 *NOAA GOES-9*

GOES-9, launched May 23, 1995 was the operational satellite over the Pacific Ocean at 135°W until July 21, 1998. At that time, both momentum wheels were exhibiting signs consistent with lubrication starvation in patterns similar to those seen in other momentum wheels just before failure. GOES-9 is believed to have only a few weeks of usable life left. It is presently in an on-orbit storage mode near 105°W, and serves as a limited-life spare if needed.

GOES-9 has the same instruments as GOES-8. In April 1996, the Imager mirror motor suffered the same problem with one of its East-West scan motors as the GOES-8 Sounder, but the GOES-9 Imager remains capable of providing data using its backup motor. Motors on subsequent Imagers and Sounders have been redesigned to eliminate this failure mode.

2.3 *NOAA GOES-10*

GOES-10 was launched April 25, 1997 as an on-orbit backup and was activated on July 21, 1998 to replace GOES-9 as GOES-West. GOES-10 has the redesigned East-West motors to eliminate the mirror motor problems faced on GOES-8 and GOES-9.

In May 1997, the solar array, which is designed to rotate once each day to keep itself pointed at the sun, slowed down and eventually stopped. However, innovative work by NOAA and NASA engineers led to turning the spacecraft into an upside down orientation (a yaw-flip maneuver) in which the solar array rotates backwards (Williams, 1998). This maneuver was highly successful in saving the spacecraft. Thanks to careful planning and preparation by the product production offices, data from GOES-10 were flowing within one day of activation and continues nominally as of this writing. Software was changed so that data from the instruments are provided to users as if the spacecraft were in the normal upright orientation. Users require no adjustments, and notice no difference in the GVAR data stream.

2.4 NOAA GOES-11

GOES-11, launched May 3, 2000, successfully completed its checkout phase and is now in place near 105° W as the fully capable on-orbit spare. Instrumentation on GOES-11 is the same as on the pervious three satellites.

2.5 *NOAA GOES M*

GOES-M was launched July 23, 2001 and is expected to complete its checkout about the time of this conference. GOES-M has the redesigned instrument motors and carry the same instrument complement as GOES-8, 9, 10, and 11, with two exceptions. The Imager on GOES-M will have its 12.0 micrometer channel replaced by a 13.3 micrometer channel to better determine the heights of mid-level steering winds and more accurately measure atmospheric and cloud optical properties. Also, the 6.7 micrometer channel resolution will be increased from eight km to four km .

GOES-M carries the first Solar X-Ray Imager (SXI) instrument, designed to provide images of the Sun in four X-Ray energy bands at intervals as frequently as once every few minutes. SXI data will provide the first continuous operational series of Solar X-Ray images and is expected to provide extremely valuable data during the Solar Maximum, expected to peak in 2000 or 2001.

3. NEXT: THE GOES-N SERIES

For the next series, instruments and spacecraft are being manufactured under separate contracts, each structured for two firm orders with two separate options for a third and a fourth, i.e., as a 2+1+1 procurement. Imager and Sounder instruments are under development by ITT Aerospace/Communications. Solar X-Ray Imagers are being produced by Lockheed-Martin Advanced Technology Laboratories and the spacecraft are being manufactured by Hughes Space and Communications. GOES-N will be launched in early 2003. The current launch schedule is provided in Table 1.

The four sets of Imagers and Sounders will be essentially the same as for the GOES I-M series. Imager channels remain the same as those on GOES-M, with a reduction in horizontal resolution from eight km to four km in the 13.3 micrometer channel on GOES-O, P, and Q. Sounder instruments will be the same filter-wheel based sounders. For SXI, current plans are to fly one on every other satellite so that there is always one operational unit in orbit.

Shortly before GOES-N is launched, analog WEFAX signals will be replaced by the digital Low Rate Information Transmission (LRIT) system. More information can be found in McClinton and Dittberner, 2001.

Satellites in the GOES N through Q series also have additional space, power, and data capacity for experimental sensors. Current candidates under consideration are instruments such as a Special Events Imager and a Volcanic Ash Mapper.

4. FUTURE: THE GOES-R SERIES

A number of studies are underway to help design the follow-on series of GOES sensors and satellites. A top level Program Development Plan (NESDIS, 1999) provides guidance for the next series. An important review of user requirements along with an analysis of potential benefits has been underway for more than two year. The first of a sequence of User Workshops was held in Boulder in September 2000. A description of this "Initial GOES-R+ User Workshop" 2000 can be found in Gurka and Dittberner, 2001a. A larger open user workshop was held in May, 2001 in Boulder. See

the companion paper at this conference: Gurka and Dittberner, 2001b.

Much has been learned about how these data enhance meteorological forecasting in the Weather Forecast Offices and increase forecast skill in numerical models. In fall 1997, Sounder data were first operationally assimilated into numerical models along with high spatial density wind information. GOES data make this an exciting time for meteorology.

An Advanced Baseline Imager (ABI) and Advanced Baseline Sounder (ABS) are planned for the GOES-R series. Engineering requirements were developed based on the 1999 National Weather Service needs (NWS Office of Meteorology, 1999), and passed to NOAA's System Acquisition Office and NASA for procurement activities. The ABI will have 8 to 12 channels, increased horizontal and higher coverage rates and be fully capable of operating through eclipse and keep out zones (Gurka and Dittberner, 2001). The ABS is expected to be an interferometer-type instrument closely modeled after the Geostationary Imaging Fourier Transform Spectrometer (GIFTS) being developed by NASA for its New Millennium Program (NMP). ABS procurement will follow ABI procurements by about six months. Spacecraft for remaining ABI/ABS instruments for GOES R through U will be procured with a new competitive contract.

5. PRODUCTS

In October 1997, GOES Sounder precipitable water started being used in the operational ETA numerical model runs. Starting in December 1997, high spatial density winds, derived from Imager IR and water vapor channels, were being used in the operational ETA model. Also, In 1997, the GOES fog product was distributed in the Advanced Weather Information Processing System (AWIPS). Forecasters in Weather Forecast Offices throughout the United States began using GOES-based winds, temperature and moisture soundings, and Derived Product Imagery (DPI) in daily forecast operations. Both forecasters and numerical models are benefitting from the use of GOES data.

In 2000, four Sounder Derived Product Imagery (DPI) products, one of the highest priority new product sets demanded by field forecasters, were made available operationally to the Advanced Weather Interactive Processing System (AWIPS) input site fro distribution.

6. SUMMARY

NOAA's GOES program continues to maintain the required flow of data from two operational satellites and has taken steps to ensure this continuity with an on-orbit spare philosophy. Instruments continue to evolve as meteorologists, atmospheric scientists, and engineers work with these data and discover new ways to provide better service to users. Emerging technologies are being examined to reduce costs and increase the information content of products provided.

7. REFERENCES

Gurka, J., and G. Dittberner, 2001a: The next generation GOES instruments: status and potential impact, Proceedings, AMS 5th Symposium on Integrated Observing Systems, Albuquerque, NM, January 15 - 19, 2001, 5pp.

Gurka, J., and G. Dittberner, 2001b: Recommendations from the GOES Users' Conference, Preprints, AMS 11th Conference on Satellite Meteorology and Oceanography, Madison, Wisconsin, October 15 - 19, 2001, 4pp.

McClinton, A. Jr., and G. Dittberner, 2001: GOES-N, The first of the next series - user community upgrades, Proceedings, AMS 17th Conference on Interactive Information Systems (IIPS) for Meteorology, Oceanography, and Hydrology, Albuquerque, NM, January 15 - 19, 2001, 2pp.

Menzel, P., and J. Purdom, 1994: Introducing GOES-I: The first of a new generation of Geostationary Operational Environmental Satellites, *Bull. Amer. Meteor. Soc.*, Vol. 75, No. 5, pp. 757-781.

National Weather Service Office of Meteorology, 1999: Operational Requirements Document for the Evolution of Future NOAA Geostationary Imagery, 31pp.

NESDIS, 1999: GOES-2010, Program Development Plan, April, 1999, 25 pp.

Williams, J.: Ingenuity turns eye back to the weather, *USA Today*, February 17, 1998, p. 10B.
GOES Launch Planning Schedule

Table 1. GOES Launch Schedule

Spacecraft	Spacecraft Availability	Planning Launch Date
GOES-N	Jan 2003	Jan 2003
GOES-O	Apr 2004	Apr 2005
GOES-P	Apr 2006	Apr 2007
GOES-Q/R	Apr 2010	Apr 2012

P5.5

CHANNEL SELECTION FOR THE NEXT GENERATION GEOSTATIONARY ADVANCED IMAGERS

Timothy J. Schmit
NOAA/NESDIS, Office of Research and Applications, Advanced Satellite Products Team (ASPT)

W. Paul Menzel
NOAA/NESDIS, Office of Research and Applications

Mathew M. Gunshor, James P. Nelson III
Cooperative Institute for Meteorological Satellite Studies (CIMSS)
University of Wisconsin-Madison

Madison, WI

1. INTRODUCTION

To keep pace with the growing need for GOES data and products, NOAA is evolving its geostationary sensor capabilities. The Advanced Baseline Imager (ABI) will be the next generation geostationary imager on GOES-R, beginning in 2010. As with the current GOES Imager, this instrument will be used for a wide range of both qualitative and quantitative applications. The ABI will include a number of improvements over the existing imager besides the additional bands. The ABI will improve the spatial coverage from nominally 4 to 2 km for the infrared bands, as well as almost a five-fold increase of the coverage rate (Gurka and Dittberner 2001). This imager will have a minimum of eight spectral bands and a maximum of twelve spectral bands. The minimum eight bands are similar to the five bands on the current GOES-8/11 Imagers (Menzel and Purdom 1994), plus a snow/cloud-discriminating 1.6 μm band, a mid-tropospheric 7.0 μm water vapor band, and a 13.3 μm band useful for determining cloud heights and amounts. This carbon dioxide-sensitive band is similar to that on the GOES-M and beyond series of Imagers (Schmit et al. 2001). The ABI bands were selected after considering NWS requirements, existing bands on the GOES Imagers and Sounders, bands on other future geostationary satellites, and bands on current and future polar-orbiting satellites. For example, the next generation METEOSAT (METEOrological SATellite) Second Generation (MSG), to be launched in 2002, will have 12 channels, including two water vapor channels centered at 6.2 and 7.3 μm (Schmetz et al. 1998).

The uses of the eight core bands, and the four additional bands, are briefly described in the following section.

Corresponding author address: Timothy J. Schmit, 1225 West Dayton Street, Madison, WI 53706; email: Tim.J.Schmit@noaa.gov.

2. ABI CHANNEL SELECTION

The 0.64 μm visible band is used for: daytime cloud imaging; snow and ice cover; detection of severe weather onset detection; low-level cloud drift winds; fog; smoke; volcanic ash, hurricane analysis; and winter storm analysis.

During the day, the 1.6 μm band can be used for: cloud/snow/ice discrimination; total cloud cover; aviation weather analyses for cloud-top phase (Hutchison 1999); and detecting smoke from low-burn-rate fires.

The shortwave IR window (3.9 μm) band has many uses: fog (Ellrod et al. 1998) and low-cloud discrimination at night; fire identification (Prins et al., 1998); volcanic eruption and ash detection; and daytime reflectivity for snow/ice.

The 6.15 μm and 7.0 μm bands will be used for upper and mid-tropospheric water vapor tracking; jet stream identification (Weldon et al., 1991); hurricane track forecasting; mid-latitude storm forecasting; severe weather analysis and for estimating upper level moisture (Soden et al., 1993; Moody et al., 1999).

The longwave infrared window (11.2 μm) band will provide day/night cloud analyses for general forecasting and broadcasting applications; precipitation estimates (Vicente et al., 1998); severe weather analyses; cloud drift winds (Velden et al. 1998a); hurricane strength (Velden et al. 1998b) and track analyses; cloud top heights; volcanic ash detection (Prata 1989); fog detection (in multi-band products); winter storms; and cloud phase/particle size estimates (in multi-band products).

The 12.3 μm band will offer nearly continuous cloud monitoring for numerous applications; low-level moisture determinations; volcanic ash identification detection (Davies and Rose 1998); Sea Surface Temperature measurements (Wu et al. 1999) and cloud particle size (in multi-band products).

The 13.3 μm band will be used for cloud top height assignments for cloud-drift winds;

cloud products for ASOS supplement (Schreiner et al. 1993; Wylie and Menzel 1999); tropopause delineation; and estimating cloud opacity.

Four bands have been proposed as additions to the core eight, with the goal of meeting NWS requirements and enhancing many products/applications. The 8.5 μm band, in conjunction with the 11.2 μm band, will enable detection of volcanic dust cloud containing sulfuric acid aerosols (Realmuto et al. 1997; Baran et al. 1993; Ackerman and Strabala 1994). In addition, the 8.5 μm band can be combined with the 11.2 and 12.3 μm bands to derive cloud phase (Strabala et al. 1994).

The 10.35 μm band will help to derive low-level moisture, cloud particle size and surface properties. Chung et al. (2000) showed how the 10 - 11 μm region is important for determining particle sizes of ice-clouds.

A visible band at 0.86 μm will help the detection of aerosols and vegetation. Characterizing aerosols and their optical properties is essential for improving a number of satellite products, for example land and sea surface temperatures. This band may enable localized vegetation stress monitoring, fire danger monitoring, and albedo retrieval. Other applications include suspended sediment detection (Aquirre-Gomez, 2000).

Finally, a near-infrared channel at 1.38 μm is proposed to detect very thin cirrus not detected by other bands. The 1.38 μm band is similar to a band on MODIS (MODerate resolution Imaging Spectroradiometer). Radiation from this band does not sense into the lower troposphere due to water vapor absorption and thus it provides excellent daytime sensitivity to very thin cirrus.

The spectral widths of the ABI infrared bands are shown both in Table 1 and Fig. 1. A number of these same bands were selected by NASA for the Advanced Geosynchronous Studies Imager (AGSI) (Hinkal et al. 1999).

Table 1. ABI channel selection. The four shaded bands denote the proposed additional bands.

Wavelength (μm)	Description
0.64 +/- 0.05	Visible
0.86 +/- 0.05	Visible
1.375 +/- 0.015	Near IR
1.61 +/- 0.03	Near IR
3.9 +/- 0.1	Shortwave IR
6.15 +/- 0.45	Water Vapor 1
7.0 +/- 0.2	Water Vapor 2
8.5 +/- 0.2	IR Window 1
10.35 +/- 0.25	IR Window 2
11.2 +/- 0.4	IR Window 3
12.3 +/- 0.5	IR Window 4
13.3 +/- 0.3	Carbon Dioxide

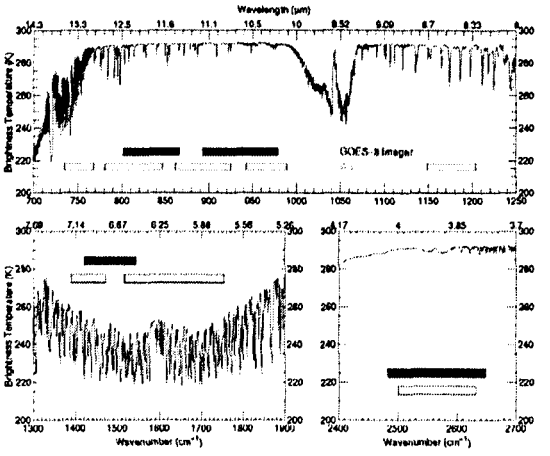

Fig. 1 The GOES-8 IR spectral bands (top bars) and the ABI IR spectral bands (lower bars). A high-spectral resolution earth-emitted spectra is also plotted.

The corresponding ABI weighting functions (for the IR bands) are shown in Fig. 2.

3. ABI SIMULATIONS BASED ON MODIS DATA

There are two main methods to simulate the expected signal from a future instrument. One method uses a radiative transfer model along with some estimate of the state of the atmosphere to calculate the expected (noise free) signal and then add noise. The second method, employed in this study, is to use higher-resolution data to simulate ABI. This method allows for more realistic simulations, especially of the clouds. Bands on the high-spatial resolution NASA MODIS data (Ackerman et al. 1998) have been used to simulate the ABI bands. The 10.35 μm band could not be simulated since there is no corresponding MODIS band.

The simulation of the ABI from MODIS data consists of two steps. First, apply a point spread function (PSF) to the MODIS data to account for diffraction and other blurring affects. PSF data were obtained from MIT/Lincoln Labs (personal communication, Edward Wack). Second, remap the MODIS 1 km to the ABI 2 km spatial resolution. No corrections were made to account for different spectral response functions between MODIS and ABI. Also, given the similarities between MODIS and ABI bit depth and instrument noise, no adjustments were made for either parameter.

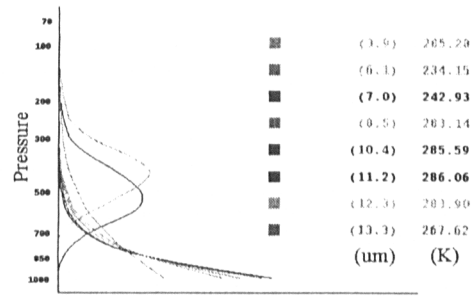

Fig. 2. The contribution weighting functions are plotted for each of the IR ABI bands for the standard atmosphere at a 40 degree local zenith angle.

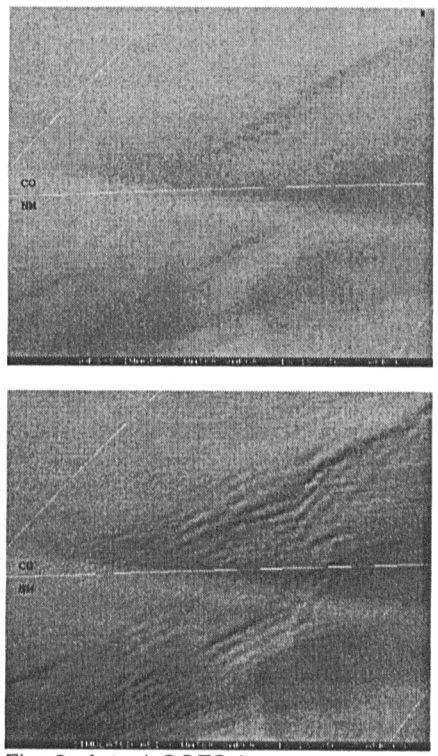

Fig. 3. Actual GOES Imager water vapor image (top) and the simulated ABI image (bottom). Both images are shown in the GOES projection. The gravity waves are clearly depicted in the ABI image. This case is from 7 April 2000, 1815 UTC.

Figure 3 shows current GOES and simulated ABI (from MODIS imagery) water vapor images in cloud free skies. These mountain waves over Colorado and New Mexico were induced by strong northwesterly flow associated with a pair of upper-tropospheric jet streaks moving across the elevated terrain of the southern and central Rocky Mountains. The mountain waves appear better defined over Colorado; in fact, several aircraft reported moderate to severe turbulence over that region.

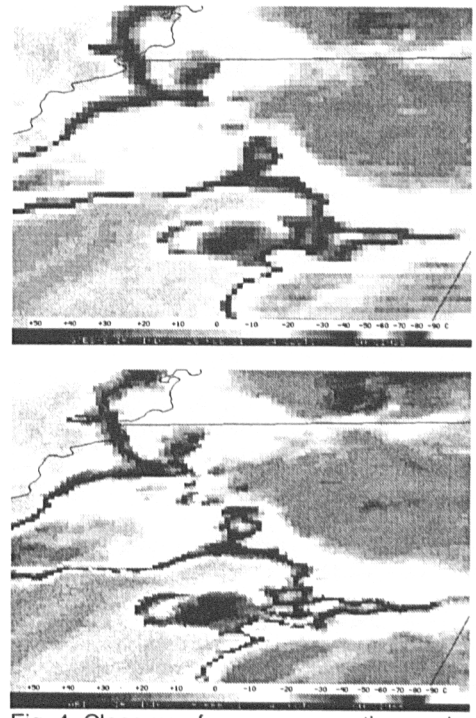

Fig. 4. Close-up of severe convection as depicted in the longwave IR window from 25 February 2001. GOES Imager (top) and simulated ABI (bottom) are shown.

Figure 4 shows GOES Imager and ABI close-ups of a severe thunderstorm. The details of the cold-tops are more evident in the ABI image. Additional comparisons are being made for a wide range of meteorological phenomena. These phenomena include wave clouds, severe convection, hurricanes, volcanoes, fires, lake ice, cloud phase and fog. For example, a thin ash plume from the Mt. Cleveland (Alaska) volcano was more readily identified in an 8.5 μm minus 11 μm image than in the traditional split window 11 minus 12 μm image.

4. SUMMARY

The ABI represents an exciting expansion in geostationary remote sensing capabilities, especially the 12 band version. Other improvements include faster coverage and improved spatial resolution. Even with 12 bands, the instrument could benefit from the addition of two more bands, at 0.47 μm and 9.6 μm. The 0.47 μm band would be used for aerosol detection and would enable daytime "true color" composites. The 9.6 μm band would monitor total ozone on space and time scales never before possible; MSG will also have such an ozone-sensitive band. Similar bands were proposed on the AGSI (Hinkal et al. 1999).

5. REFERENCES

Ackerman, S. A., K. I. Strabala, W. P. Menzel, R. A. Frey, C. C. Moeller, and L. E. Gumley, 1998: Discriminating clear sky from clouds with MODIS. *J. Geophys. Res.*, **103**, 32141-32157.

Ackerman, S. and K. I. Strabala, 1994: Satellite remote sensing of H2SO4 aerosol using the 8 to 12 μm window region: Application to Mount Pinatubo. *J. Geo. Res.*, **99**, 18,639-18,649.

Aquirre-Gomez, R., 2000: Detection of total suspended sediments in the North Sea using AVHRR and ship data. *Int. J. Remote Sensing*, **21**, 1583-1596.

Baran, A. J., J. S. Foot and P. C. Dibben, 1993: Satellite detection of volcanic sulfuric acid aerosol. *Geophys. Res. Letters*, **20**, 1799-1801.

Chung S., S. Ackerman, and P. F. van Delst, 2000: Model calculations and interferometer measurements of ice-cloud characteristics. *J. Appl. Met.*, **39**, 634-644.

Davies, M. A., and W. I. Rose, 1998: GOES imagery fills gaps in Montserrat volcanic cloud observations. *EOS, Transactions, American Geophysical Union*, **79**, 505-507.

Ellrod, G. P., R. V. Achutuni, J. M. Daniels, E. M. Prins, and J. P. Nelson III, 1998: An assessment of GOES-8 Imager data quality, *Bull. Amer. Meteor. Soc.*, **79**, 2509-2526.

Gurka, J. J., and G. J. Dittberner, 2001: The next generation GOES instruments: status and potential impact. Preprint Volume. 5th Symposium on Integrated Observing Systems. 14-18 January, Albuquerque, NM, Amer. Meteor. Soc., Boston.

Hinkal, S., Jenstrom, D.; Florez, J., Bremer, J. C.; Hersh, M.; Neuberger, D., and Kindsfather, R., 1999: Advanced Geosynchronous Studies Imager: Instrument system design. Earth Observing Systems IV, Proceedings of the Conference, Denver, CO, 18-20 July 1999. Bellingham, WA, Society of Photo-Optical Instrumentation Engineers (SPIE). SPIE Proceedings volume 3750, pp2-10.

Hutchison, K. D., 1999: Application of AVHRR/3 imagery for improved detection of thin cirrus clouds and specification of cloud-top phase. *J. Atmos. Oceanic Tech.*, **16**, 1885-1899.

Menzel, W. P., and J. F. W. Purdom, 1994: Introducing GOES-I: The first of a new generation of geostationary operational environmental satellites. *Bull. Amer. Meteor. Soc.*, **75**, 757-781.

Moody J. L., A. J. Wimmers, and J. C. Davenport, 1999: Remotely sensed specific humidity: development of a derived product from the GOES Imager channel 3, *Geo. Phys. Res. Let.*, **26**, 59-62.

Prins, E. M., J. M. Feltz, W. P. Menzel, and D. E. Ward, 1998: An overview of GOES-8 diurnal fire and smoke results for SCAR-B and 1995 fire season in South America, *J. Geophys. Res.*, **103** (D24), 31821-31835.

Prata, A. J., 1989: Observations of volcanic ash clouds in the 10-12 μm window using AVHRR/2 data. *Int. J. Remote Sens.*, **10**, 751-761.

Realmuto, V. J., A. J. Sutton, T. Elias, 1997: Multispectral thermal infrared mapping of sulfur dioxide plumes: A case study from the East Rift Zone of Kilauea Volcano, Hawaii, *J. Geophys. Res.*, **102**, 15,057-15,072.

Schmetz, J., H. Woick, S. Tjemkes, and J. Rattenborg, 1998: From Meteosat to Meteosat Second Generation, Proceedings, *Ninth Conference on Satellite Meteorology and Oceanography*, Paris, France, Amer. Meteor. Soc., 335-338.

Schmit, T. J., E. M. Prins, T. J. Schreiner, and J. J. Gurka, 2001: Introducing the GOES-M Imager. Submitted to the *National Weather Association-Digest.*

Schreiner, A. J., D. A. Unger, W. P. Menzel, G. P. Ellrod, K. I. Strabala, and J. L. Pellett, 1993: A comparison of ground and satellite observations of cloud cover. *Bull. Amer. Meteor. Soc.*, 74, 1851-1861.

Soden, B. J., and F. P. Bretherton, 1993: Upper tropospheric relative humidity from the GOES 6.7 μm channel: Method and climatology for July 1987. *J. Geophys. Res.*, **98**, 16669-16688.

Strabala, K. I., S. A. Ackerman, and W. P. Menzel, 1994: Cloud properties inferred from 8-12 μm data. *J. Appl. Meteor*, **33**, 212-229.

Velden, C. S., T. L. Olander, and S. Wanzong, 1998a: The impact of multispectral GOES-8 wind information on Atlantic tropical cyclone track forecasts in 1995. Part I: dataset methodology, description, and case analysis. *Mon. Wea. Rev.*, **126**, 1202–1218.

Velden, C. S., T. L. Olander, and R. M. Zehr, 1998b: Development of an objective scheme to estimate tropical cyclone intensity from digital geostationary satellite infrared imagery. *Wea. Forecasting*, **13**, 172–186.

Vicente, G. A., R. A. Scofield, and W. P. Menzel, 1998: The operational GOES infrared rainfall estimation technique, *Bull. Amer. Meteor. Soc.*, **79**, 1883–1898.

Weldon, R. B, and S. J. Holmes, 1991: Water vapor imagery -- interpretation and applications to weather analysis and forecasting, NOAA Technical Report NESDIS 57.

Wu, Xiangqian, W. P. Menzel, and Gary S. Wade, 1999: Estimation of sea surface temperatures using GOES-8/9 radiance measurements. *Bull. Amer. Meteor. Soc.*, **80** (6), 1127-1138.

Wylie, D. P., and W. P. Menzel, 1999: Eight years of high cloud statistics using HIRS. *J. Climate*, **12**, 170-184.

P5.6 CHANNEL SELECTION METHODS FOR INFRARED ATMOSPHERIC SOUNDING INTERFEROMETER RADIANCES

Nadia Fourrié *, **Florence Rabier**
METEO-FRANCE, Toulouse, France

1 INTRODUCTION

Advanced infrared sounders will provide thousands of radiance data at every observation location. Among other, the IASI (Infrared Atmospheric Sounding Interferometer) instrument will be onboard the first operational European polar-orbiting satellite METOP. IASI will cover the spectral range 645 cm^{-1} to 2760 cm^{-1}, with a spectral sampling of 0.25 cm^{-1}, leading to 8461 channels in each pixel. This number of individual pieces of information is not tractable in an operational Numerical Weather Prediction (NWP) context and we have investigated possibilities of choosing an "optimal" subset of data to be inserted in the assimilation. The issue of reducing the number of data to be used has been addressed in the context of optimal linear estimation theory, using simulated IASI data computed from a set of about 500 representative atmospheric profiles. The aim of this paper is to determine, among various methods of channel selection, the one which leads to the best analysis accuracy. The second step is to test the robustness of the chosen method in practice for all atmospheric conditions. In section 2 the experimental framework is described and the comparison of different channels selection methods is presented. In section 3, the results of a degraded non-optimal set of channels for all profiles are shown and finally section 4 concludes this preliminary study and discusses some perspectives.

2 CHOICE OF A CHANNEL SELECTION

2.1 Experimental framework

The general framework of this study is the linear optimal estimation theory in the context of NWP. The optimal analysed state x_a is given by $x_a = x_b +$

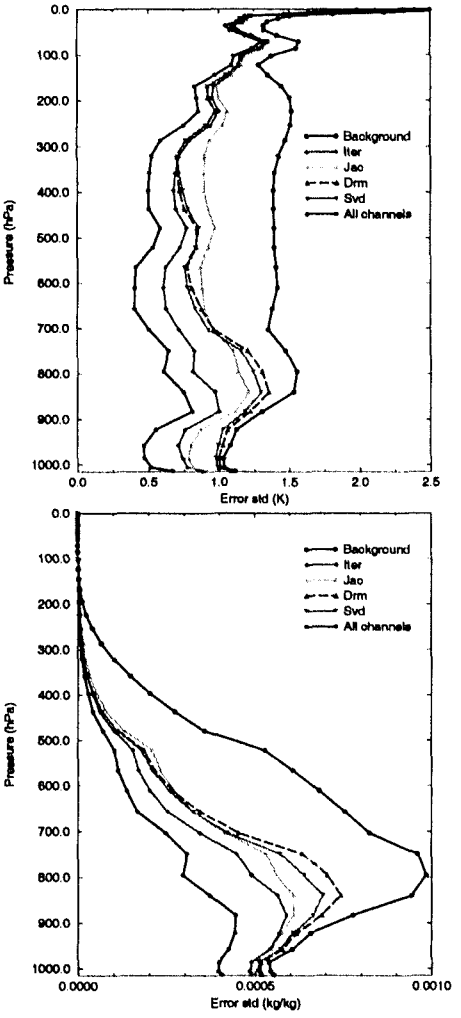

Figure 1: Standard-deviation of analysis errors averaged over 24 profiles, for various channel selections using 300 channels to retrieve T (top panel) and Q (bottom panel).

* Corresponding author address : CNRM/GMAP, Meteo France, 42 av. G. Coriolis, F-31057 Toulouse Cedex, email=Nadia.Fourrie@cnrm.meteo.fr

$\mathbf{K}(y-y_b)$, with x_b the background vector state, $\mathbf{K} = \mathbf{A}\mathbf{H}^{\mathrm{T}}\mathbf{R}^{-1}$, y the observation state, $y_b = \mathbf{H}x_b$. $\mathbf{H}$ is the tangent linear of the radiative transfer operator $\mathcal{H}$ ($\mathcal{H}(x) = \mathcal{H}(x_b) + \mathbf{H}(x - x_b)$). $\mathbf{A} = (\mathbf{B}^{-1} + \mathbf{H}^{\mathrm{T}}\mathbf{R}^{-1}\mathbf{H})^{-1}$ is the analysis error covariance matrix. $\mathbf{R}$ is the observation error covariance matrix and $\mathbf{B}$ is the background error covariance matrix.

One can introduce the so-called Data Resolution Matrix (**DRM**) which links the analysis to the true values in the observation space : $y_a - y_b = \mathbf{H}(x_a - x_b) \simeq \mathbf{HK}(y_t - y_b) = \mathbf{DRM}(y_t - y_b)$ (approximately when observations errors averaged out).

Some useful information theory concepts can be used to quantify the gain in information brought by the data. These are in particular the Degrees of Freedom Signal (DFS): $\mathrm{DFS} = \mathrm{Tr}\left(\mathbf{I} - \mathbf{AB}^{-1}\right)$, or the Entropy Reduction (ER): $\mathrm{ER} = -\frac{1}{2}\log_2 det(\mathbf{AB}^{-1})$. Both quantities give a global measure of the reduction of uncertainty brought by the analysis Rodgers (2000). For more detailed diagnostics of the quality of the analysis, one can use the standard-deviations of analysis errors (from the diagonal components of $\mathbf{A}$).

For this study we have used a set of 492 representative atmospheric profiles (temperature and humidity) from the SODA database (provided by F. Karcher, Météo France). IASI data have been simulated from each profile, using the fast radiative transfer model RTIASI (Matricardi and Saunders, 1999) over sea with a nadir-viewing angle, the scene being assumed to be cloud-free. The parameters to be retrieved are the temperature and the humidity profiles over the 43 RTIASI levels. The background error covariance matrix is typical of a state of art NWP model and has been built from the 60 level ECMWF covariance matrix representing short-range forecast errors.

2.2 Short methods description

For more details about the description of the methods tested is this study, see Rabier *et al.* (2001). A method based on the **DRM** picks up channels corresponding to the largest element of the **DRM**. Another one is based on Singular Value Decomposition (SVD) of the **DRM** (Prunet *et al.* (1998). The iterative method is based on Rodgers (1996) and consists in performing a series of successive analyses, each one using only one channel optimizing the ER at a time, the analysis error covariance matrix is updated and is used at the next step. The Jacobian Method is based on the jacobian matrix. For each retrieved parameter at each level in the vertical, one selects the channel among those peaking next to level with the largest ratio amplitude of the peak/width of the weighting function.

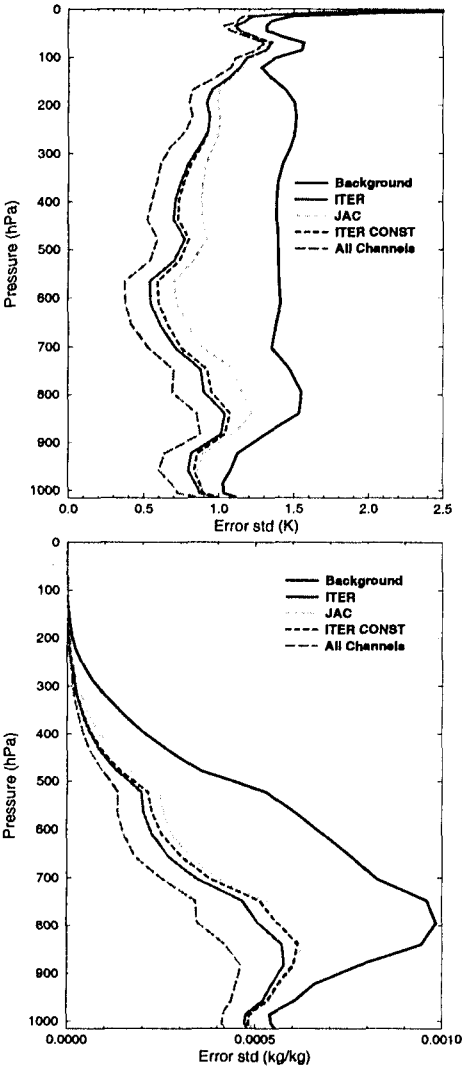

Figure 2: Standard-deviation of analysis errors averaged over 492 profiles, for various channel selections using 300 channels to retrieve T (top panel) and Q (bottom panel).

2.3 Results for various method

Before selecting some useful channels among all the spectrum, one has eliminated beforehand those located in the spectral bands of foreign gases (N_2O, CH_4, N_2O and CO). This pre-selection reduces the

total amount of channels from 8461 to 7227 for a given spectrum. For this study, 300 channels have been chosen as this number of pieces of information is assumed to be tractable for introduction in the operational assimilation system.

Results of the selection of 300 channels are presented in Figure 1 for the Biscarosse station (south west of France). The two best methods are the iterative and the Jacobian methods, the iterative being significantly better. This might be explained by the fact that the Jacobian method is not as optimal, being forced to optimize sequentially all 43 levels for temperature and humidity. In particular, the upper levels for Q have the same weight in the selection process as the lower levels for temperature for example. DRM and SVD methods lead to a good analysis accuracy in the stratosphere, but not in the troposphere. Both types of methods do not take into account the redundancy between channels in contrast to the two other methods (iterative and jacobian).

This premilinary study shows that only the iterative and the Jacobian methods can be considered as suitable methods to be used for the channel selection. The iterative method gives the best results and the Jacobian method gives slightly worse results but is much more economical.

3 DETERMINATION OF A NON-OPTIMAL SET OF CHANNELS

If one considers that the iterative method is too expensive to be performed for each atmospheric profile, one might consider two solutions: a Jacobian selection adapted to each profile or a "constant" selection based on off-line studies with the iterative method. The reduction of information content with the constant iterative selection is studied here. Firstly a constant channels selection is computed from a set of 492 different channel selection (corresponding to the SODA atmospheric profiles) provided by the iterative method. For each selection, one assigns a rank from 1 to 300 to each channel picked by the iterative selection, all the others having the largest possible rank corresponding to the number of channels on which the selection is performed. Then channels are selected according to their lower average rank, by in increasing order.

When applying this constant selection to the whole set of profiles, one loses around 0.7 units in terms of DFS compared to the optimal selection varying with each profile. This is about a third of the loss in terms of DFS when going from the iterative to the Jacobian method. Results in terms of analysis errors are shown in Figure 2. Comparing the iterative method with the "constant" iterative method one can see a degradation but the "constant" selection is still better than the jacobian method and could be used for operational purposes.

4 SUMMARY AND PERSPECTIVES

Advanced infrared sounders will provide thousands of radiances data at every observation location This number of individual pieces of information is not tractable in an operational NWP context and we wanted to investigate the possibilities of choosing an optimal subset of data to be inserted in the assimilation. Several methods have been tried to select a set of the most useful channels for each profile. Two methods are based on the Data Resolution Matrix, one method based on the Jacobian matrix selecting the channels with the most appropriate weighting function for retrieving each parameter at each level and one iterative method selecting sequentially the channels with largest information content and updating the error covariance matrix of the current analysis according this new information. The iterative method produces the best results, but at a larger cost than the Jacobian method. When deducing a constant selection from the iterative method applied to each profile, one obtains results of intermadiate quality between the ones provided by the optimal iterative method and the Jacobian method. The practical advantage of this method for operational purposes is that the same set can be used for various atmospheric profiles.

However, an obvious limitation is that the information content is known to depend on cloud amount (Eyre, 1990), on surface characteristics and scan angle. In addition, if IASI data have to lead to a very significant impact on the forecast, one should adress in more details the question of retaining the most information possible in sensitive atmospheric structures leading to major forecast failures (Rabier et al.,1996). For example, a preliminary study of cloud amount and levels of clouds in the sentitive areas for the 10th February 1997 12 UTC for the mean sea level pressure over the area [62.5N-52 N;20 W-0W] has been made. The fields of sensitivity to temperature have been squared and summed in order to get a unique horizontal field. The cloud amount and the top cloud temperature have been calculated from AVHRR data with the MAIA (Mask Avhrr for Inversion Atovs, La-

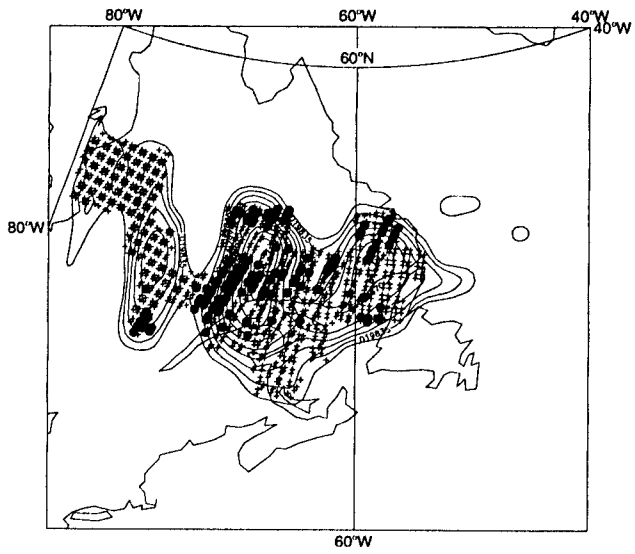

Figure 3: For 97/10/10 12 UTC, sensitive areas for a 48 hour-forecast of mean sea level pressure over the area [62.5N-52N;20W-0W] and cloudiness of simulated IASI pixel, crosses corresponding to cloudy pixel and dots to cloud free pixel.

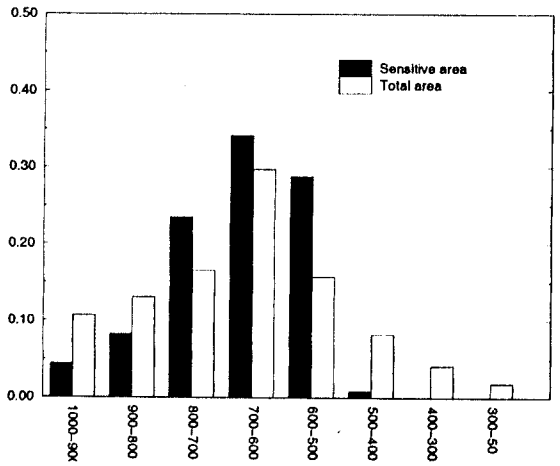

Figure 4: For 97/10/10 12 UTC, distribution (purcentage) of the vertical cloud levels (in hPa) in IASI pixels located in the sensitive area (87,2 % of cloudy pixels), compared to a whole IASI orbit (Total area, 94.6 % of cloudy pixels).

vanant et al, 1999) method. Figure 3 shows that there is only 12 % of cloud free pixels in the sensitive area for this date. Moreover, 34 % of clouds tops are located between 700 and 600 hPa and 28% between 600 and 500 hPa (Fig. 4). Sensitive areas, generally located in the low and mid-troposphere are thus broadly covered by clouds, reducing the gain of IASI for these atmospheric regions. The IASI channel selection study has to be followed by the optimization of the selection method to get upper-troposhere right and a study of the potential benefit of IASI in synergy with microwave instruments such as AMSU.

ACKNOWLEDGEMENTS

The authors thank Gwenaelle Hello and Tiphaine Labrot who have provided the sensitivity fields and the cloud parameters of IASI data.

REFERENCES

Eyre J.R., (1990) : The information content of data from satellite sounding systems: A simulation study, *Q. J. R. Meteorol. Soc.*,**116**, 401–434

Lavanant L., Legléau H., Derrien M., Levasseur S., Monnier G., Ardouin L., Brunel P. and Bellec B. 1999 : AVHRR Cloud Mask for Sounding Applications, *ITSC-10 proceedings*

Matricardi and Saunders, 1999 : A fast radiative transfer model for Infrared Atmospheric Sounding Interferometer radiances, *J. Appl. Optics*, **38**, 5679–5691

Prunet, P., Thépaut, J.-N. and Cassé, V., (1998) : The information content of clear sky IASI radiances and their potential for numerical weather prediction, *Q. J. R. Meteorol. Soc.*,**124**, 211–241

Rabier, F., Klinker, E., Courtier, P. and Hollingsworth, A., (1996) : Sensitivity of forecast errors to initial conditions, *Q. J. R. Meteorol. Soc.*,**122**, 121–150

Rabier F., Fourrié N., Chafaï D. and Prunet P., 2001 : Channel selection methods for infrared atmospheric sounding interferometer radiances, *Q. J. R. Meteorol. Soc.*, submitted

Rodgers, C. D., 1996 : Information content and optimisation of high spectral resolution measurements, *Optical Spectroscopic Techniques and Instrumentation for Atmospheric and Space Research II*, **SPIE, Volume 2830**, 136–147

Rodgers, C. D., 2000 : Inverse methods for Atmospheres: Theory and Practice, *World Scientific Publ., Singapore*, 238pp

P5.7 OPERATIONAL RADIANCE PRODUCTS FROM AIRS

Mitchell D. Goldberg* , Larry McMillin, Walter Wolf, Lihang Zhou, Yanni Qu, and Murty Divakarla
NOAA/NESDIS/ORA, Camp Springs, MD 20746

1. INTRODUCTION

In the early 21st century, new advanced infrared (IR) sounders will measure outgoing radiance from thousands of relatively narrow spectral intervals between 3 and 18 μm with near continuous spectral coverage. The spectral range includes the important 4.3 and 15 μm bands for temperature soundings, the 6.3 μm band for water vapor soundings and the 9.6 μm band for ozone soundings. The current operational polar-orbiting infrared instrument is the High resolution InfraRed Sounder (HIRS). HIRS measures outgoing infrared radiation within the same spectral region, however there are only 19 spectral intervals with much poorer spectral resolution. The combination of poor spectral resolution and relatively few spectral intervals (i.e. channels) result in the poor vertical resolution (3- 5 km in the troposphere) of current operational temperature and moisture soundings. The RMS accuracy of temperature from HIRS in 1 km layers within the troposphere is approximately 2 K , while moisture accuracy in 2 km layers is about 25 % (layer averaged mixing ratio). The National Weather Service (NWS) and the World Meteorological Office (WMO) requirement for soundings is temperature and moisture accuracy of less than 1 degree K per 1 km layers and 15 % per 2 km layers in the troposphere, respectively. High spectral resolution observations from advanced IR sounders will yield temperature and moisture profiles with vertical resolutions approaching 1 km in the lower troposphere and will have accuracies matching or exceeding NWS and WMO requirements. These observations are expected to yield significant improvements in forecast accuracy, which is the primary reason why Numerical Weather Prediction (NWP) centers are very interested in utilizing such data.

The first polar-orbiting high spectral resolution infrared sounder is the Advanced InfraRed Sounder (AIRS). The AIRS is part of the Earth Observing System (EOS) Aqua mission and is expected to be launched during 2002. Other future sounders include the Cross-track Infrared Sounder (CrIS) and the Infrared Atmospheric Sounding Interferometer (IASI). Those instruments will not be launched earlier than 2006. The EOS AIRS processing system will calibrate radiances from the instrument's raw counts, attempt to remove cloud contamination from AIRS field-of-views (fovs), and generate atmospheric sounding of temperature, moisture and ozone. The EOS processing system will not process AIRS data in near-realtime. There will be a delay of at least 24 hours and hence the EOS system does not serve those customers (i.e. NWP centers) needing the data in near-realtime. At NESDIS, with support from NASA and the Integrated Program Office, NWP AIRS products will be derived and distributed in near-realtime. The purpose of this paper is to describe the NWP AIRS radiance products. The major NWP centers will directly assimilate AIRS radiances. Because of communication restrictions, the AIRS radiance data is thinned by channel subsetting and eigenvector decomposition. A major topic of this paper is using principal component scores (PCS), which are coefficients of radiance eigenvectors as a form of data compression and noise filtering. PCS for compression of high spectral resolution infrared data is also discussed in Huang and Antonelli (2001).

*Corresponding author address: Mitchell D. Goldberg, NOAA/NESDIS, 5200 Auth Road, Room 810, Camp Springs, MD 20746, email:mitch.goldberg@noaa.gov

2. DESCRIPTION OF THE AIRS INSTRUMENT

The AIRS instrument is an array grating spectrometer which provides spectral coverage over the 3.74-4.61 μm, 6.20-8.22 μm, and 8.8-15.4 μm infrared wavebands at a nominal spectral resolution ($\lambda/\Delta\lambda$) of 1200. There are 2378 spectral samples (channels). Details are given in Aumann and Strow (2001). The AIRS is coupled with the Advanced Microwave Sounding Unit-A (AMSU-A) and the Humidity Sounder Brazil (HSB). HSB is similar to AMSU-B with no 89 Ghz channel. The set of sounding instruments scan the ground track in a synchronized pattern. For each AMSU footprint there are nine AIRS fovs which permit effective cloud clearing using the combined data sets; there are also nine HSB fovs at the AIRS locations. At a platform altitude of 705 km, the AIRS fov of 1.1 degrees provides a 13.5 km spatial footprint at nadir. The nearly contiguous along track sampling with +49.5 degrees of crosstrack scanning around nadir provides a full 1850 km swath width coverage every 2.67 seconds. Global coverage is obtained twice a day, except at regions very close to the equator. The ground based data processing system combines the data from AIRS, AMSU, and MHS to produce one temperature and moisture sounding for each AMSU footprint.

3. NWP AIRS PRODUCTS

Over the past decade the direct assimilation of atmospheric temperature and moisture retrievals in NWP model has been largely replaced with the assimilation of calibrated radiances. Nearly all of the major NWP centers around the world are requesting AIRS radiance

datasets. The initial constraint in providing AIRS NWP products is data size. AIRS/AMSU-A/HSB data is about 2 GB for a 100 minute orbit in comparison to the 8 MB per orbit from current operational sounding instruments. Of course a simple solution is to increase communication bandwidth. However, NWP centers presently cannot assimilate all the data for computational reasons and increasing bandwidth can be costly. The obvious solution is to thin the data to meet NWP data requirements. The AIRS/AMSU-A/HSB data will be thinned into three datasets. The following subsections describes each dataset. Each file contain a cloud indicator which is discussed in section 6. Also each file has ancillary information such as time, latitude, longitude, and satellite and solar viewing geometry. Note that full resolution (no thinning) level 2 retrieval products will also be available.

3.1 Thinned Radiance Data - Single FOV

The first data set contains data thinned by subsampling fovs and channels. A subset of about 250 channels from the center AIRS fov associated with every AMSU-A fov is extracted. (Note that the clearest fov may be selected instead of the center). All 15 AMSU-A channels and 4 HSB channels from the center HSB fov (coaligned with AIRS fov) are also included. The data is provided in BUFR in six minute segments. The size for each six minute granule is about 1 MB. An orbit's worth of data is about 16 MB. The channel selection is based on selecting channels with the sharpest Jacobians. Spectral purity is also taken into account. For example, we avoid significant water, ozone and other trace gas absorption when selecting temperature channels. The channel selection is tested by confirming that all channel radiances are satisfied by the retrieval even though only the subset is used in the retrieval algorithm.

3.2 Thinned Radiance Data – 9 FOVs

The number of channels in this dataset is the same as the single fov radiance dataset. The main difference is that instead of a single fov, all 9 AIRS and HSB fovs are included. Also instead of data from every AMSU-A fov, every seventh is used. The file size for a six minute granule is about 1.25 MB and one orbit's worth of data is about 20 MB. Having all 9 fovs allows cloud clearing of AIRS radiances.

3.3 Principal Component Data - Single FOV

The principal component data is thinned spatially in the same manner as the single fov radiance file. However, instead of approximately 250 AIRS channels, there are 200 principal component scores (PCS). There is a static file containing the principal components, which are also referred to, in the literature, as eigenvectors. All the AIRS channel radiances can be reconstructed to some level of accuracy by a matrix multiply of the eigenvectors and PCS. Details will be given in the section 5. A measure of how well the channels can be reconstructed is also provided. This measure, referred to as the reconstruction score, is a single value which gives an overall indication of how well the reconstructed radiances agree with the actual radiances. A reconstruction score of less than unity indicate that overall the radiances are reconstructed within the noise level of the observed radiances.

4. SIMULATIONS

In preparation of creating NWP AIRS products and to aid in the development and improvement of algorithms, AIRS/AMSU-A/HSB radiances are simulated using the NCEP six hour forecast for atmospheric state and the AIRS radiative transfer model developed by Hannon et al. (1996). In addition to the atmospheric states of temperature, moisture and ozone, the simulations also include variable surface emissivity and clouds.

5. PRINCIPAL COMPONENT ANALYSIS

Principal component (PC) (eigenvector) analysis was performed on data simulated for December 16, 2000. PC analysis finds K linear combinations of N radiances ordered from highest to lowest variance. For AIRS, N = 2378. PCS are the linear combinations computed from K eigenvectors and the N radiances. (The length of each eigenvector is N.) The first PCS will explain most of the variance, whereas the last PCS will explain virtually zero variance. The maximum number of principal components is N. However far fewer are needed to explain most of the variance. The analysis was performed on a covariance matrix of radiance normalized by expected instrumental noise, which we refer to as normalized radiances. From this point forward we will make reference to eigenvectors instead of principal components, however we will continue to use the term PCS. The eigenvectors are related to the covariance matrix by:

$$S = E \Lambda E^T \qquad (1)$$

where S is a NxN covariance matrix. E is the matrix of eigenvectors, and Λ is the diagonal matrix of eigenvalues. The principal component scores P are computed from:

$$P = E^T R \qquad (2)$$

where R is the vector of centered normalized radiances. The next equation is used to reconstruct the radiances from a truncated set of eigenvectors, E* and principal component scores P*

$$R^* = E^* P^* \qquad (3)$$

(E* is a NxK matrix and P* is a Kx1 vector.) R* is the normalized reconstructed radiance. To obtain the unscaled non-centered radiance, one must add the

ensemble mean normalized radiance used in generating the covariance matrix and multiply the sum by the noise.

Fig. 1 shows the explained variance of the data with respect to the number of eigenvectors. The explained variance is simply the accumulation of the eigenvalues normalized by the sum of all eigenvalues. The figure shows that nearly 100% of the variance is explained with only 10 eigenvectors. This number is often referred to as the number of independent pieces of information. However, 10 eigenvectors are insufficient to reconstruct the radiances within the noise level. Note there are two curves - one is based on eigenvectors generated from all sky conditions, the other for clear. The use of clear eigenvectors is discussed briefly in section 6. A better measure to determine the number of eigenvectors is to look at the square root of the eigenvalue, shown in Table 1. The square root of the eigenvalues is equivalent to the standard deviation of the principal component scores of the dependent ensemble. Since we are using normalized radiances, the square root of the eigenvalues can be interpreted as signal to noise. PCS can be thought of as superchannels since each one is a linear combination of all channels. The first PCS has the largest signal to noise ratio, which as shown in Table 1 is very large. When the eigenvalues fall below unity, the noise has larger contribution than the signal.

A reconstruction score can be defined as

$$RS = \left[1/n \sum_{i=1}^{N} (O_i - R_i)^2 \right]^{1/2} \qquad (4)$$

where O and R are the noise scaled observed and reconstructed radiances, respectively, for the ith channel and N is the total number of channels used in the principal component analysis. A reconstruction score of less than one indicates that root measure square (rms) difference over the number of reconstructed channels is within the noise level.

An important feature of eigenvector analysis is noise filtering. The contribution from the 62th PCS and greater is mainly noise. Our NWP product has 200 PCS. We selected 200 to assure that the radiances can be reconstructed within the noise level. AIRS has very low instrumental noise (most channels have noise less than 0.2 K for a scene at 250 K). For AIRS it will not be detrimental to reconstruct the radiances within the noise level (we recommend using no more than 70 PCS). However for the IASI instrument the noise is much larger, as shown in Fig. 2, in band 3 (wavenumbers greater than 2000 cm-1). Obviously we do not want to fit the IASI noise. Instead we want to filter most of the noise by using an optimal set of truncated eigenvectors. Fig. 3 shows the the difference between the reconstructed radiance and noise contaminated "observed" radiance for IASI band 3 using 50 eigenvectors. Also shown by the curve across the center of the figure (difficult to see without color) is the difference between the reconstructed radiance and noise-free radiance (The units on the ordinate are scaled by noise - so unity indicate that the reconstructed radiance is at the noise level.) The reconstructed radiance agree much better with the noise-free radiance spectrum

6. CLOUD DETECTION

The determination of cloud-free fovs is very important since currently only cloud-free radiances are assimilated by NWP models. Each NWP product file will have clear fov indicators. The approach we are currently using is to predict a single AIRS channel, at 4.18 um from AMSU-A channels 4, 5 and 6 using least square regression. The standard error of the regression solution is about 1.05 K. If the difference between the predicted AIRS and the observed AIRS is less than some threshold (e.g. 2.5 K), the fov may be clear. Additional tests such predicting shortwave channels from longwave also have to be passed. Work is still in progress. (Based on current simulations, we have a residual cloud error of about 0.5% clouds with a standard deviation of about 1% for fovs that are declared clear.) Values of all tests in addition to a cloud flag will be included in the product files. An additional test for detecting clouds is to use eigenvectors generated from clear data to reconstruct radiances. If the reconstruction score is large then the scene is not clear. The test works well, however it is not necessary because the other cloud detection tests are sufficient. We decided to generate only all-sky eigenvectors because we want to reconstruct all spectra - regardless of cloud amount.

7. SUMMARY

AIRS data will be provided in near-realtime to the NWP community. Specially tailored products files have been created to meet user requirements. One of the product files contain PCS of the radiances and seems to be very promising as a technique to reduce data rates to users without losing important information in the radiances. It also appears that PCS is effective in filtering noise from the measurements.

8. REFERENCES

Aumann, H.H. and L.L. Strow, 2001: AIRS, the first hyper-spectral infrared sounder in support of operational weather forecasting, *IEEE Aerospace Conference*, 10-17 March 2001.

Hannon, S E., L.L. Strow, W.W. McMillan, 1996: Atmospheric infrared fast transmittance models: a comparison of two approaches, *SPIE* 2830 , 94-105.

Huang, H-L and P. Antonelli, 2001: Application of Principal Component Analysis to High Resolution Infrared Measurement Compression and Retrieval, *J. Appl. Meteor.*, **40**, 3, 365-388

Table 1 SQUARE ROOT OF AIRS (RADIANCE/NOISE) EIGENVALUES

1	7497.60	19	14.68	37	3.38	55	1.25
2	1670.40	20	13.49	38	3.11	56	1.19
3	945.52	21	12.28	39	2.82	57	1.16
4	496.01	22	11.32	40	2.53	58	1.15
5	284.01	23	10.70	41	2.41	59	1.09
6	266.30	24	9.08	42	2.39	60	1.05
7	156.95	25	8.24	43	2.34	61	1.02
8	139.67	26	7.85	44	2.24	62	0.98
9	88.27	27	6.77	45	2.03	63	0.90
10	72.83	28	5.98	46	1.86	64	0.86
11	60.03	29	5.83	47	1.78	65	0.81
12	53.42	30	5.39	48	1.71	66	0.80
13	45.01	31	5.34	49	1.65	67	0.78
14	39.72	32	4.98	50	1.61	68	0.77
15	34.54	33	4.34	51	1.54	69	0.73
16	26.57	34	4.09	52	1.52	70	0.72
17	22.62	35	3.62	53	1.35	71	0.70
18	17.60	36	3.48	54	1.34	72	0.66

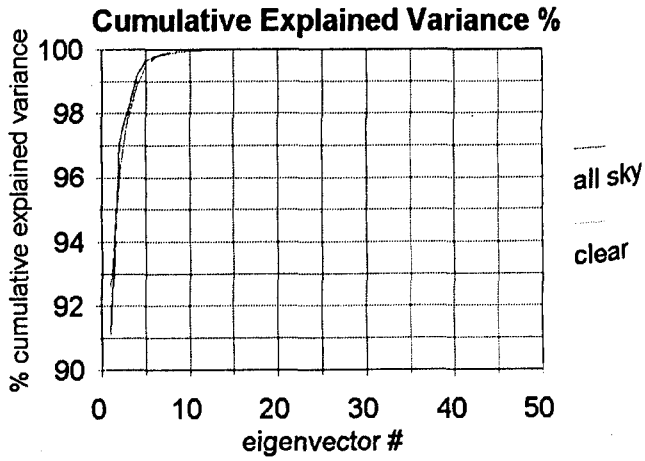

Fig. 1. Cumulative explained variance of principal components (eigenvectors).

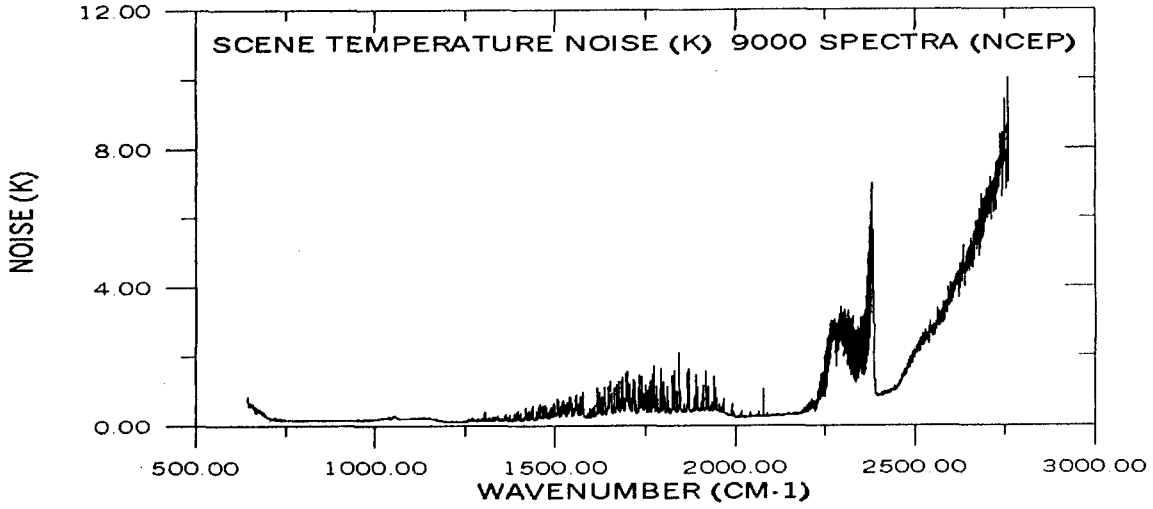

Fig. 2 IASI predicted noise at scene brightness temperature averaged from global ensemble of 9000 observations

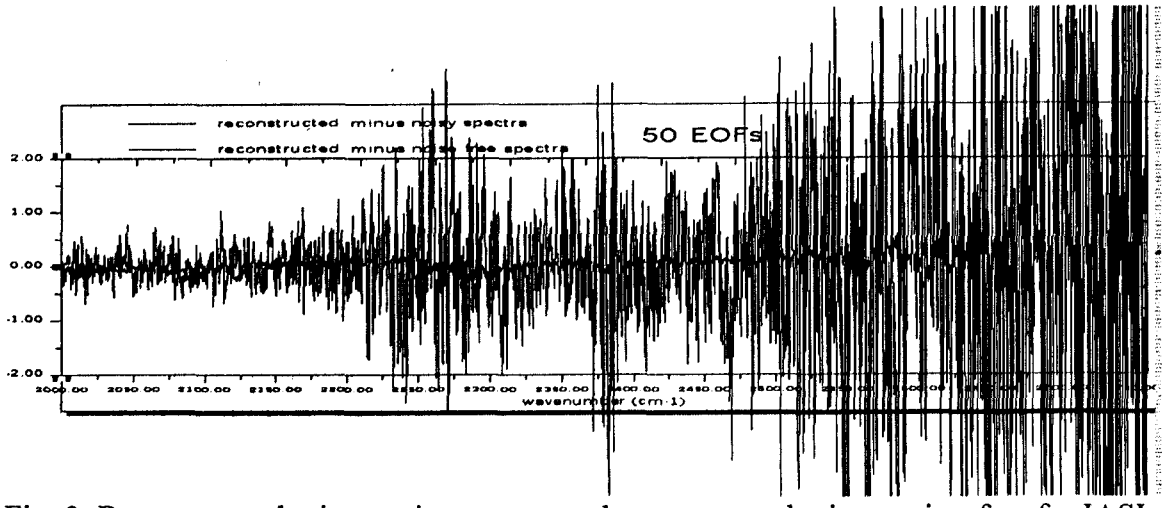

Fig. 3 Reconstructed minus noisy spectra and reconstructed minus noise_free for IASI Band 3 - reconstructed from 50 PCS.

P5.8 MEASUREMENT CONCEPT VALIDATION PLANS FOR GIFTS

Dave Tobin*, Chris Velden
Space Science and Engineering Center, University of Wisconsin-Madison

Nikita Pougatchev, William Smith
NASA Langley Research Center

1. Introduction

The Geosynchronous Imaging Fourier Transform Spectrometer (GIFTS) Indian Ocean METOC Imager (IOMI) is a combined NASA New Millennium Program, NOAA, and U.S. Navy mission. It represents a revolutionary step in satellite based remote sensing of atmospheric parameters. Using the combination of a Fourier Transform Spectrometer and Large Area Focal Plane Arrays, GIFTS will measure the Earth emitted infrared radiance at the top of atmosphere from geosynchronous orbit with an unprecedented combination of spectral, temporal, and spatial resolution and coverage. In its nominal Regional Sounding and Chemistry mode, GIFTS will measure the infrared spectrum in two bands (14.6 to 8.8 μm, 6.0 to 4.4 μm) at a spectral resolution of ~0.6 cm^{-1} for a 128 × 128 set of ~4-km *footprints* (a ~512 × 512 km area) every 11 seconds. The instrument will have the capability of taking successive measurements of such data to scan desired regions of the globe, and tradeoffs in the desired spectral resolution and spatial and temporal sampling can be performed. From these measurements, thermal and gaseous concentration profiles, cloud properties, wind field profiles, and numerous derived products can be retrieved.

Following launch in CY 2005, GIFTS will be positioned over or near the Continental United States for 12 to 18 months, and will then attain a position over the Indian Ocean for NAVY operations. This poster presents an overview of a "Measurement Concept Validation Plan" (MCVP), which describes the various tasks and data sources associated with the validation of the GIFTS Measurement Concept Objectives (see Section 2) under the scope of NASA's New Millennium Program (NMP) Earth Observing 3 (EO3) Mission. The goal of the resulting Measurement Concept Validation activities to occur while the sensor is stationed over CONUS is an accurate and timely assessment of the instrument performance and accuracies of the core GIFTS products for a representative set of observation conditions. In particular, this plan addresses validation in the areas of navigated and calibrated high spectral resolution radiances, *temperature and water vapor profile* retrievals, wind retrievals, carbon monoxide and ozone concentration retrievals, cloud property retrievals, and data compression.

While the NMP EO3 GIFTS program is primarily a technology validation program, the GIFTS Primary Measurement Concept Objective provides the driver for the required accuracies in the retrieved atmospheric parameters, the derived accuracies in the radiometric, spectral, and spatial accuracy of the measured radiance spectra, and the underlying instrument design. The goal of the MCVP is to define the various tasks and data sets that will be used to assess whether the desired accuracies in the primary GIFTS products are being attained. The plan therefore plays a critical role in the NASA NMP portion of the mission, detailing the various data to be collected, processed, and analyzed in order to validate the performance of the instrument and accuracy of the resulting products.

2. GIFTS Measurement Concept Objectives

The GIFTS Measurement Concept Objectives are divided into three groups: Primary, Secondary, and Applications Objectives. The Primary objective establishes the baseline instrument performance and operational requirements. The Secondary objectives fall within the measurement capability of the baseline GIFTS instrument and are considered a secondary priority with respect to mission operations and validation activities. The Applications objectives fall outside the scope of the funded NMP EO3 mission, require participation by organizations outside NMP, and as such are dependent upon funding by NASA, NOAA, or other organizations following the completion of the NMP technology and measurement concept validation.

For GIFTS, the Primary Measurement Concept Objective is to provide frequent, high spatial resolution temperature and water vapor sounding, allowing the vertical profile of wind velocity to be obtained by tracing the horizontal displacement of water vapor and cloud features. The Secondary objectives are to a) provide time-dependent ozone and carbon monoxide concentrations within layers of the troposphere and stratosphere, and b) to provide high temporal resolution measurements of radiative properties of clouds (augmented by a higher spatial resolution visible low-light-level camera to provide quasi-continuous imaging). The Applications objectives of GIFTS are numerous and are to a) enable demonstration of improvements in weather and climate observation, analysis and prediction, b) add to knowledge of the global water cycle and supporting research contributing to risk reduction from intense weather disasters, c) demonstrate the benefit to the commercial airline industry by using GIFTS data for better weather hazards forecasting that can reduce the risk to safe flight, as well as to reduce fuel costs through improved flight management as a result of increased availability of wind

* *Corresponding author address:* Dave Tobin, CIMSS/SSEC University of Wisconsin-Madison, Madison, WI 53706; email: dave.tobin@ssec.wisc.edu

data, and d) provide measurements that enhance other new Earth systems scientific investigations, especially the EOS Aqua and Aura and Earth Systems Science Pathfinder missions.

Various instrument parameters, geophysical products, and their required accuracies that are described in the EO-3 Mission Requirements Document (EMRD), the GIFTS-IOMI Mission Systems Requirements Document (GMSRD), and the GIFTS Instrument Requirements Document (GIRD). Tables 1 and 2 highlight the parameters and accuracies most relevant the MCVP efforts.

Under the scope of the NMP Measurement Concept Validation, this plan addresses the basic validation of the core GIFTS products relevant to the Primary Measurement Concept Objective as given above. This includes the validation of a) the navigation of the radiance data to Earth located geographic footprints, b) the spectral, radiometric, and spatial accuracy of the measured radiance spectra, c) the retrieved temperature and water vapor profiles, d) the retrieved wind fields, and e) the accuracy of the compressed data stream. These areas are chosen due to their direct relevance to the Primary Measurement Concept Objective; the navigation accuracy has a direct impact on the retrieved winds, the accuracy of the measured radiances impacts directly on the retrieved temperature, water vapor and resulting wind profiles, and the data compression assessment is relevant to the ability to perform such soundings operationally. This plan also addresses validation of the Secondary Measurement Concept Objectives regarding carbon monoxide and ozone concentrations and cloud properties.

3. Measurement Concept Validation Plans

The MCVP draws upon experience gained through previous and ongoing validation efforts of geostationary and polar orbiting (e.g. GOES, HIRS, IMG, AIRS, CrIS) and aircraft based (HIS, NAST-I, S-HIS) sounders. The plans also draw upon numerous advances in the instrumentation required for obtaining high quality validation data, as well as advances in the characterization of the accuracy of existing, traditional sources of validation data. In addition, due to the non-operational aspect of the NMP GIFTS mission, the validation will benefit from being able to influence, and in some cases, dictate the orbital positioning of the GIFTS satellite during the first 12 to 18 months in orbit. Additionally, specific observation sequences and spectral/temporal/spatial tradeoffs can be tailored for the purpose of validation.

The validation approaches are focused on comparisons of the GIFTS products to selected high quality validation data for GIFTS product accuracy assessment. A simple example is the comparison of GIFTS retrieved temperature profiles to those of coincident research grade radiosondes for a statistically representative set of conditions and resulting conclusions regarding the accuracy of the GIFTS retrieved profiles. The approaches include comparisons to data from ground based networks and high quality validation sites (e.g. ARM CART, Wind Profiler network), airborne observation networks (e.g. ACARS), other satellite based radiance sensors (e.g. AIRS, IASI) and retrievals (e.g. MOPITT, TES, AIRS), and data collected as part of a dedicated field campaign. While external data is the primary tool of these efforts, some validation can be performed using GIFTS data alone. This includes internal checks such as blackbody view analyses and specific pointing exercises. For example, analysis of spectra of the on-board calibration blackbodies can be used to assess the radiometric calibration and noise performance. Naturally, the resulting product accuracy assessments can be compared to the product accuracy goals. Logical outcomes are closure, or problem identification leading to feedback to the instrument, algorithm development and/or data processing efforts.

For the majority of this effort, the desired validation data are available from routine operations and as such do not require special arrangements for performing and/or obtaining the measurements. A notable exception are plans for a dedicated air and ground based field campaign in the Oklahoma ARM site domain approximately 4 months after launch.

Specific validation activities are planned for each validation area (navigation, radiance, temperature, water vapor, winds, carbon monoxide, ozone, cloud properties, and data compression). These approaches, the orbital geolocations and viewing sequences required to collect the appropriate data, and the analysis techniques are contained in the MCVP, and will be presented in detail at the poster presented at the conference.

4. Summary, and Other GIFTS Validation Efforts and Opportunities

The GIFTS Measurement Concept Validation Plan (MCVP) presents plans for assessing the basic instrument performance and product accuracy of GIFTS following the year after launch, under the scope of NASA's NMP EO3 mission. Details of this plan will be presented at the conference. As defined by the focus of the NMP program and its concentration on technology development and validation, the NMP funded efforts of the Measurement Concept Objectives validation are limited in scope. Generally, the NMP efforts will not require a relatively large percentage of the overall GIFTS data volume and are not intended to replace or duplicate additional efforts, which are more related to operational applications and use of the data. Rather, the NMP efforts are targeted in scope to provide enough data and analysis for a timely post-launch assessment of the accuracy of the core GIFTS products for a representative set of observation conditions. These efforts will occur during the first twelve months after launch while GIFTS is stationed in various positions over or near the continental United States.

These NMP MCV efforts will be supplemented by NOAA participation in the GIFTS program. This effort, the NOAA Demonstration of Operational Utility, will

Measurement Concept Objective	Parameter	Measurement Uncertainty (rms)	Reference
Primary Objective 1: Atmospheric profiles	Temperature	= 1 K for 1-km layers	EMRD, EO76
	Water vapor	= 20% for 2-km layers	EMRD, EO76
	Wind velocity	= 3 m/s for 2-km layers	EMRD, EO76
Secondary Objective 1: Ozone and Carbon monoxide concentrations	O_3 concentration	10-20% for 6-km mid-tropospheric layers 10-20% for three 6-11 km stratospheric layers	EMRD, EO68
	CO concentration	10-20% for three 3-8 km tropospheric layers	EMRD, EO68
Secondary Objective 2: Cloud Properties	Cloud mask	Cloud or clear, 3%	EMRD, EO68
	Cloud top height	20 mbar (pressure altitude)	EMRD, EO68
	Cloud top temperature	= 2 K	EMRD, EO68
	Cloud emissivity	10%	EMRD, EO68
	Cloud top phase	Ice or water, 10%	EMRD, EO68

Table 1. Level 2 product accuracy goals for the Regional Sounding and Chemistry (0.6 cm^{-1}) mode.

Parameter	Measurement Uncertainty	Reference
Radiometric Calibration		
Absolute	= 1.0 K (3σ) for T_{scene} = 190 K (LW)	GMSRD, MR595
	= 1.0 K (3σ) for T_{scene} = 240 K (SMW)	GMSRD, MR595
Reproducibility	= 0.2 K (3σ) for T_{scene}=190 K (LW) over 1 day	GMSRD, MR597
	= 0.2 K (3σ) for T_{scene}=240 K (LW) over 1 day	GMSRD, MR597
Radiometric Noise, NEN	= 0.2 mW/(m^2 sr cm^{-1}) (1σ) for T_{scene} = 280 K (LW)	GMSRD, MR586
	= 0.06 mW/(m^2 sr cm^{-1}) (1σ) for T_{scene} =280 K (SMW)	GMSRD, MR261
Spectral Calibration		
Knowledge	= 5 parts in 10^6 (3σ)	GMSRD, MR599
Reproducibility	= 1 part in 10^6 (3σ) over 30 days	GMSRD, MR608
Pointing		
Frame-to-Frame Pointing Knowledge	= 25 μrad over a 1 hour period	GMSRD, MR505
Pointing Stability	= 11.2 μrad (1s)	GMSRD, MR511
Pointing Jitter	= 11.2 μrad (1s)	GMSRD, MR512
Geolocation Knowledge	= 1 km at nadir	GMSRD, MR506
Geolocation Pointing Accuracy	= 50 km	GMSRD, MR513
Channel-to-Channel Knowledge	= 11.2 μrad (1s)	GMSRD, MR583

Table 2. Selected Level 1 product accuracy objectives for the Regional Sounding and Chemistry (0.6 cm^{-1}) mode.

nominally take place 6 months after launch to 18 months after launch. These efforts are similar to the NMP Measurement Concept Validation efforts but are distinguished by the larger scope and data volume associated with operational or quasi-operational use of the GIFTS data. Along with traditional validation (e.g. comparison with in-situ sensors) the NOAA efforts draw largely on the assimilation of the GIFTS data into numerical models to assess the impact of the data on predictions. NOAA involvement also plays a role in determining the desired orbital positions and resulting geographical areas and meteorological conditions observed by GIFTS. Details of these efforts are given in the *NOAA GIFTS Product Assurance Plan*.

Additionally, the NMP and NOAA validation efforts are expected to be supplemented by a solicitation for

proposals and resulting funding for further validation and algorithm development of the scientific products and goals of GIFTS. Specifically, this would provide additional funding for the Secondary and Applications Objectives Validation, as well as further validation of the Primary Objectives.

5. Acknowledgements

Thanks to the following for their contributions to the NMP GIFTS validation plans. UW: Hank Revercomb, Tim Schmit, Mat Gunshor, Jim Nelson, Brian Osborne, Bob Knuteson, and Allen Huang; UW/NOAA: Paul Menzel and Ralph Peterson; GIFTS Mission Operations Working Group: John Battcher, Charles Player, and Wayne Hicks; Space Dynamics Lab: Gail Bingham; GIFTS Project: Vickie Parsons, Wallace Harrison, and Jim Miller.

6. References

1. GIFTS Measurement Concept Validation Plan (MCVP, GIFTS-02-002).
2. EO-3 Mission Requirements Document (EMRD, GIFTS-01-002).
3. IOMI Mission Requirements Document (IMRD, GIFTS-01-003).
4. GIFTS-IOMI Mission System Requirements Document (GMSRD, GIFTS-01-008).
5. GIFTS Instrument Requirements Document (GIRD, GIFTS-04-001).
6. NOAA GIFTS Product Assurance Plan (GPAP)

P5.9 SIMULATION OF GIFTS DATA CUBES

Dave Tobin*, Kevin Baggett, Ray Garcia, Hal Woolf, Allen Huang, Bob Knuteson,
John Mecikalski, Erik Olson, Brian Osborne, Derek Posselt, Hank Revercomb
Space Science and Engineering Center, University of Wisconsin-Madison

1. Introduction

The Geosynchronous Imaging Fourier Transform Spectrometer (GIFTS) represents a revolutionary step in satellite based remote sensing of atmospheric parameters, and poses a challenge in terms of being able to process and understand the large amount of data it will collect. Using the combination of a Fourier Transform Spectrometer and Large Area Focal Plane Arrays, GIFTS will measure the Earth emitted radiance at the top of atmosphere from geosynchronous orbit. In its nominal operating mode, GIFTS will measure the infrared spectrum in two bands (a 14.6 to 8.8 μm longwave band and a 6.0 to 4.4 μm short/midwave band) at a spectral resolution of ~0.6 cm^{-1} for a 128x128 set of ~4 km footprints (a ~512 x 512 km area) every eleven seconds. Successive measurements of such data will be collected to cover desired regions of the globe. In terms of interferograms, the high rate data from the FPAs is numerically filtered and decimated to produce a raw "data cubes", consisting of a 128 × 128 array of 2048 point interferograms for the longwave band and a 128 × 128 array of 4096 point interferograms for the short/midwave band. These data are then passed through an on-board lossy data compression algorithm, and the raw and compressed data streams (as well as 512 × 512 arrays of visible data collected and associated metadata collected during the eleven seconds) are telemetered to the ground at a rate of ~65 Mb/s. In the project's formulation phase, these infrared "data cubes" have been simulated in order to support algorithm development efforts and instrument trade studies. In particular, the simulated data has been used to develop and test the lossy data compression algorithms, which operate on the numerically filtered and decimated interferograms. This poster presents an overview of the simulation methodology and gives some examples of the simulated GIFTS data.

2. Simulation Methodology

The simulated data includes radiometrically calibrated spectra, uncalibrated spectra, and uncalibrated interferograms, with or without various instrumental effects. These can be for Earth views or of views of the internal calibration blackbodies, and can be noise-free or including instrumental noise. The general simulation methodology includes three general steps: 1) creation of the atmospheric state on the appropriate temporal and spatial scales and resolution, 2) calculation of the high spectral resolution top-of-atmosphere (TOA) radiance spectra from the atmospheric state, and 3) inclusion of various instrumental effects. The following sub-sections describe these steps in more detail.

* *Corresponding author address:* Dave Tobin, CIMSS/SSEC University of Wisconsin-Madison, Madison, WI 53706; email: dave.tobin@ssec.wisc.edu

2.1. Generation of Atmospheric State

The atmospheric state parameters (profiles of temperature and gaseous absorber profiles, cloud properties, surface properties, and wind vectors) are generated using a high spatial resolution model. As opposed to observed quantities, the use of model data allows all variables to be known exactly when performing studies such as temperature retrieval studies using the simulated data. We use the University of Wisconsin Nonhydrostatic Modeling System (UW-NMS version 6a, released February 2000) developed by Greg Tripoli at UW-Madison. Input to the NMS model includes skin temperature, water vapor mixing ratio, ozone concentration, surface elevation, and liquid and ice water paths. A cloud-top height (set to the altitude at which the logarithm of the density of the cloud's liquid or ice content exceeds 0.25) is also input to the UW-NMS. Some features of the UW-NMS model include:

- Arbitrary spatial resolution in all directions
- Local spherical coordinate system in the horizontal
- Height coordinate system with step topography using a terrain following variable grid spacing near the ground
- Multiple two-way interactive grid nesting, with moveable inner grids
- Gridscale microphysics parameterization with cloud water, rain, pristine crystals, snow, aggregate crystals, and graupel
- Modified Emanuel convective parameterization scheme
- Long/Short wave radiation parameterization with clouds
- Diffusion based on TKE prediction.

For the GIFTS simulations, a 24 hour spin-up using a nested grid, with a 4km resolution inner grid, is performed using initial conditions from a global model. Forecasts are then performed with 15 to 30 minute time steps for a duration of several hours. The end result is realistic and coherent atmospheric state, surface, and cloud variables at 4km resolution for ~512 x 512 km areas with time steps of ~30 minutes. Larger spatial domains (~4 times larger) are also possible. Additional information on UW-NMS is available at http://mocha.meteor.wisc.edu/uw-nms.html.

2.2. Calculation of TOA radiance spectra

A forward model takes atmospheric state parameters (such as temperature, water vapor and other gas concentrations, and clouds) and derives satellite-altitude radiances. The major components

include computaion of the clear sky transmittances, cloudy sky transmisttances, and performing radiative transfer.

For the gaseous absorption, a clear sky fast model for GIFTS was generated by applying a PLOD regression (Hannon et al., 1996) to line-by-line calculations obtained with LBLRTM (Clough and Iacono, 1995), using HITRAN96 (Rothman et al.,1992) and the CKDv2.4 water vapor continuum module (Tobin et al., 1999). The line-by-line transmittances were mapped to the GIFTS spectral domain using a maximum optical path difference of ~0.87 cm, with an effective spectral resolution of approximately 0.6 cm^{-1}, and apodized (6th order Kaiser-Bessel) prior to performing the regression analysis.

Cloud effects are incorporated into the fast model via an optical thickness parameterization scheme developed by Dr. Yong Hu of NASA Langley Research Center:

$$OT_l = WP_l\left(C_0 r_{e,l}{}^{C_1} + C_2\right) \quad \text{(liquid cloud)}$$

$$OT_i = WP_i\left(C_0 r_{e,i}{}^{C_1} + C_2\right) \quad \text{(ice cloud)}$$

where C_0, C_1 and C_2 are parameterization coefficients, WP is the water path, and r_e is the effective radius of the cloud particle. Subscripts *l* and *i* denote liquid and ice cloud, respectively. The cloud transmittance is then

$$\tau_{cloud} = \exp(-OT).$$

Above the cloud level $\tau_{cloud} = 1$.

The clear and cloudy sky transmittance profiles are then multiplied and used along with the atmospheric temperature profiles and surface properties to compute the top-of-atmosphere radiances using the radiative transfer equation. The surface is represented as black (unit emissivity) with skin temperatures as given by the numerical model. At this point, the Kaiser Bessel apodization is removed from the calculated radiances, effectively producing top-of-atmosphere radiances with spectral resolution of that of an ideal (on-axis) FTS with a maximum optical path difference of ~0.87 cm.

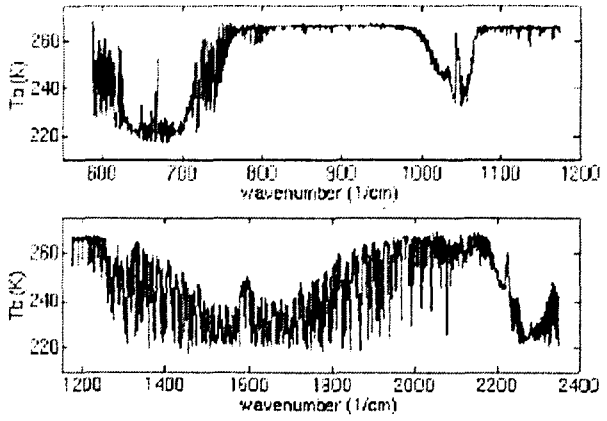

Figure 1. A sample TOA brightness temperature spectrum produced by the GIFTS fast model.

2.3. Instrumental Effects

A Fourier Transform Spectrometer (FTS) simulator has been developed to model the significant instrumental effects of the GIFTS interferometer on the top-of-atmosphere simulated radiances. For each pixel in the GIFTS focal plane array, the simulator produces an interferogram (or spectrum, if desired) of an Earth scene or calibration blackbody view. The instrumental effects included in the simulations are:

- Addition of background, instrument emission
- Application of the responsivity (gain)
- Application of the numerical filter
- Application of the complex phase due to beam splitter dispersion
- Inclusion of finite detector size, leading to self-apodization and ILS variations across the FPA.
- Inclusion of off-axis (from the FTS axis) detector, leading to different optical path difference sampling points for each FPA pixel.
- Inclusion of pixel-to-pixel offset and gain variations
- Inclusion of pixel operability
- FTS axis not aligned with FPA center
- Inclusion of random (thermal) detector noise
- Inclusion of photon generated noise
- Inclusion of integrated circuit readout noise
- Inclusion of quantization noise

Any, all, or none of the effects can be included depending on the particular use of the simulated datacube. Particular effects which are not currently included are:

- Phase variations across the FPA
- Non-linear detector response
- Interferometric (scan mirror tilt and velocity variation) noise
- Diffraction and jitter blur
- Consecutive data cube spatial misalignment

The logic behind the inclusion/exclusion of each effect, and how the effects were simulated will be presented at the conference. In addition, two GIFTS project documents, references 1 and 2, describe the simulation process in detail. Reference 1 gives an overview of the simulations and information (times, locations, meteorology) of the data cubes simulated to date, and Reference 2 gives details on the simulated instrumental noise.

2. Examples of Simulated Data Cubes

The following three figures show examples of the simulated data cubes. Figure 2 shows the dramatic effect of the variation of optical path difference point sampling in the interferogram domain for the off-axis FPA pixels. This is due to the different optical path differences which are experienced for beams of light which propagate through the FTS at different angles with respect to the FTS axis. In this figure, the top panel shows the interferfogram values for zero optical path difference (ZPD), which are not affected by the off-axis angles. The x and y axes are pixel indices (ranging from 1 to 128) representing the horizontal spatial dimensions. The z-axis represents the interferogram value and is proportional to the total energy reaching the

FPA for each pixel. The lower values are due to clouds. (Note the direction of the z-axis limits). The bottom panel of Figure 2 shows the interferogram values for the same Earth scene but for an optical path difference of ~0.6 cm. In this case, the off-axis OPD sampling causes the underlying signal to vary smoothly. This effect is easily removed using ground-based computing hardware and algorithms, but is a challenge to the on-board compression algorithms.

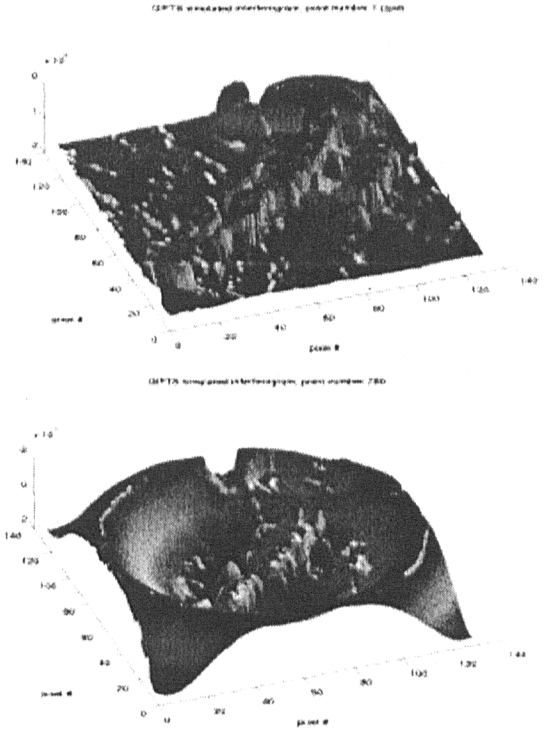

Figure 2. Effects of off-axis OPD sampling, as discussed in the text. Top panel: interferogram values for ZPD; bottom panel: interferogram values near the CO_2 resonance region (~0.6 cm).

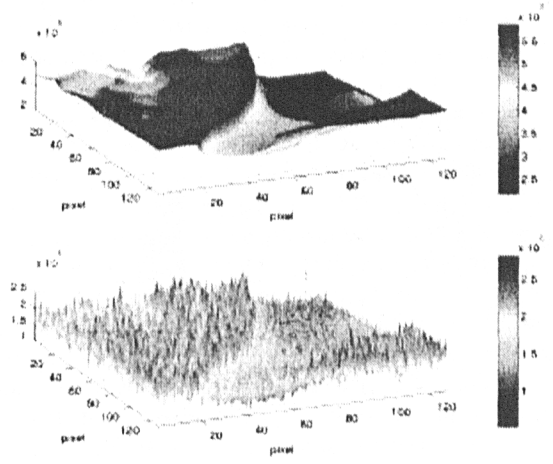

Figure 3. Effect of FPA pixel-to-pixel gain and offset variability, as discussed in the text.

Figure 3 shows the effect of pixel-to-pixel variations in the FPA detector gains and offsets. This is due to the inherent variability in the characteristics of individual pixels within the FPA. The top panel shows the (uncalibrated) interferogram values without the effects included, and the bottom shows the interferograms, but with variable offsets and gains applied. Pre-launch characterization of the FPAs and on-board blackbody and space views will allow for these effects to be removed via the radiometric calibration, but this is an effect that the on-board compression algorithms need to account for.

The last example (Figure 4) shows the ~1650 cm^{-1} calibrated brightness temperatures for data cubes produced for three time steps (00:00, 00:30, 01:00 UTC) for the upper Midwest region. This shows the variability in time and space of the mid to upper level water vapor and clouds present in the model runs.

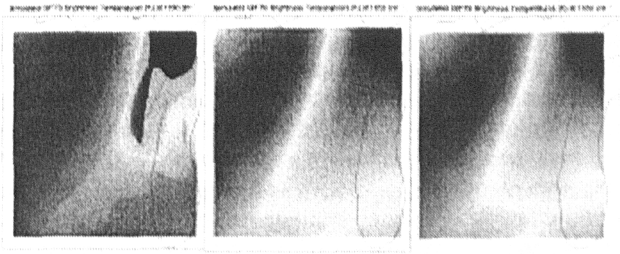

Figure 4. ~1650 cm-1 brightness temperatures for simulated cubes of the upper Midwest region at 0000, 0030 and 0100 UTC on 3 April 2000.

3. Acknowledgements

Thanks to Gail Bingham, John Elwell, and Alan Thurgood of the Space Dynamics Lab, Utah State University for their contributions to this work. Thanks to the supporting GIFTS Project personnel including Mike Blythe, Wallace Harrison, and Jim Miller.

4. References

GIFTS Simulated Compression Algorithm Dataset Description Document, UW-GIFTS 04-005 ver. 2.0, 29 May 2001.

Signal and Noise Relationships for GIFTS Simulated Datacubes, UW Tech. Note 07-001, ver. 3.0, 26 July 2001.

Clough S. A. and M. J. Iacono, 1995: Line-by-line calculations of atmospheric fluxes and cooling rates. 2: Applications to carbon dioxide, ozone, methane, nitrous oxide and the halocarbons, *J. Geophys. Res.*, **100**, 16519–16535.

Rothman, L. S. et al., 1992: The HITRAN Molecular Database: Editions of 1991 and 1992,*J. Quant. Spectrosc. Radiat. Transfer,* **48**, 469–507.

Hannon, S., L. L. Strow, and W. W. McMillan, "Atmospheric infrared fast transmittance models: A comparison of two approaches," in *Proceedings of SPIE Conference 2830*, 1996.

Tobin, D. C. et al., 1999: Downwelling spectral radiance observations at the SHEBA ice station: Water vapor continuum measurements from 17 to 26 μm, *J. Geophys. Res.*, **104**, 2081-2092.

P5.11 APPLICATION AND DESIGN OF SATELLITE INFRARED SPECTRAL IMAGING RADIOMETERS WITH UNCOOLED MICROBOLOMETER ARRAY DETECTORS

James D. Spinhirne
NASA Goddard Space Flight Center/912, Greenbelt, MD 20771

Redgie S. Lancaster
Goddard Earth Science and Technology Center, University of Maryland, Baltimore County
1000 Hilltop Circle, Baltimore, MD 21250

Kevin R. Maschhoff
BAE System, Lexington, MA 02421

1. INTRODUCTION

Uncooled array detectors offer a number of advantages for space borne infrared array imaging. The elimination of detector cooling requirements can significantly reduce the size, cost and power requirements systems. Integration of the instrument to a spacecraft is much simplified due to reduced thermal management requirements. An array of detectors permits imaging without mechanical scanning. In addition an array may be exploited to provide information on the angular distribution of radiation simultaneously to spectral radiance. The potential limitation of uncooled infrared detectors is reduced sensitivity. Other issues are stability and calibration.

Over the last five years the use of infrared imaging radiometers based on uncooled microbolometer array detectors has been studied and tested. A prototype instrument was flown as a hitchhiker experiment on the space shuttle in 1997 (Spinhirne et al., 1999). The performance and application of data has been extensively studied. The hitchhiker experiment is now followed by a project to develop an engineering model of an operational imaging radiometer for low earth orbit. In addition the use of uncooled infrared array detectors for geosynchronous and other satellite applications has significant potential.

2. IR DETECTOR

The uncooled microbolometer array detector (UMAD) is a large-format (328x246 and above) device providing good sensitivity ($D^* \sim 5x10^9$ $cmHz^{1/2}/Watt$) in the thermal IR at room temperature. These detectors were developed in the late 1980's and early 1990's, at the Honeywell Sensor and System Development Center, using silicon micro-machining techniques to produce a monolithic array of silicon microbolometers and CMOS readout circuitry. In 1993 Honeywell demonstrated a nearly theoretical level reduction in noise with frame averaging, suggesting UMADs would display similar noise reduction with frame integration techniques and spatial averaging. In 1994 Honeywell licensed UMAD detector technology to others companies who are now providing low-cost commercial versions of these devices (Wood and Foss, 1993). Detector arrays of 640x480 size and larger are now available.

3. ISIR

The Infrared Spectral Imaging Radiometer (ISIR) program developed an infrared radiometer that flew as part of the hitchhiker complement onboard space shuttle mission STS-85 in August 1997. The ISIR instrument was the first earth observing radiometer to include UMAD technology and was built to address the applicability of these detectors as space-borne radiometric sensors. During mission STS-85 the ISIR instrument was used to obtain radiometric imagery of clouds, land, and ocean in several narrow spectral bands in the thermal infrared and provided measurements of cloud-top temperature, classification, and cloud droplet size.

The basic goal for a low earth orbit imager is one with possibly incremental increases in spatial or spectral resolution or number of bands over current AVHRR instruments. A compact imaging radiometer that offered such capabilities would find application on any number of possible multisensor missions. Hence, the ISIR instrument included thermal IR channels centered at 8.6 um, 10.8 um, and 12.0 um each with an approximate 1 um passband. A broadband channel spanning the wavelength range of 7–12 um was also included in ISIR. ISIR obtained ¼ km resolution from shuttle orbit. The AVHRR instrument uses single element detectors to provide imagery with 0.12K resolution for a 300K scene in the infrared channels (Kramer, 1994). The instantaneous field of view provides an approximate resolution of up to 1 km at nadir.

Prior to the ISIR program, no real assessment had been made of the spectral-radiometric performance of UMADs. All previous tests of sensitivity had been done broadband. ISIR used an early prototype device and the measurements shown here are not reflective of state-of-the-art devices. The measurements show an NEDT of 80mK for the broadband case current production devices offer a performance ranging between 30–50mK.

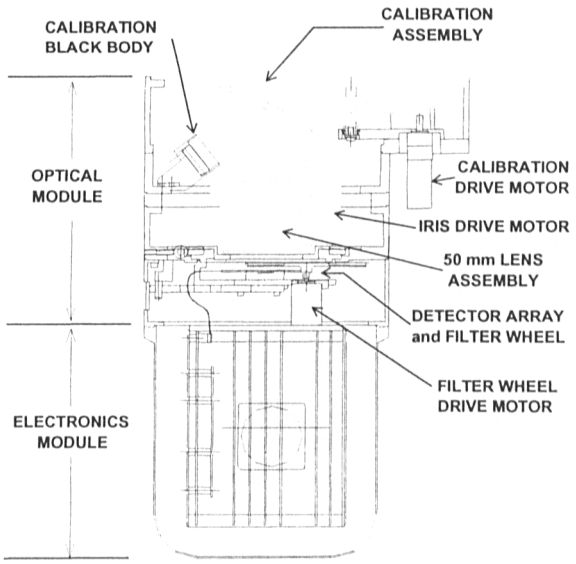

Fig. 1. Design of the Infrared Spectral Imaging Radiometer (ISIR) instrument.

A schematic of the ISIR instrument is shown in Figure 1. Frame averaging is used to obtain the 0.12K sensitivity requirement. Time delay integration (TDI) is employed in ISIR to continuous imaging of 320 pixel cross track. Images are acquired at 30 Hz and successive rows of detectors are integrated in a time-delayed sequence, adding the signals from the pixel elements that originate from the same earth location. Hence, TDI requires that the image motion due to the forward motion of the platform across one pixel row and the frame readout rate be synchronized. In the absence of correlated noise, TDI improves the signal-to-noise ratio by the square root of the number of pixels used in the averaging process. For ISIR the spectral bands were selected by filters mounted on a rotating filter wheel. Radiance calibration was through an internal black body target that was viewed as part of the imaging sequence. Laboratory measurements and analysis of ISIR on orbit data in comparison to airborne radiometers demonstrate that a 0.12 K brightness temperature accuracy was obtained.

Shown in Figure 2 is an example of 10.7 um imagery collected during the ISIR shuttle flight of STS-85. This figure includes a compilation of 6 individual image frames. Each of these frames was acquired while operating in a mode that used 40 pixels in the TDI process and the images were registered during post-processing. Additionally, these data have been calibrated in units of brightness temperature and a color scale indicating the range of observed temperatures is shown. Cooler temperatures of course tend to indicate higher cloud-tops but this is dependent upon the optical depth of the cloud under consideration. Measurement on ST-85 included some direct cloud height measurements by the Shuttle Laser Altimeter.

The image data were collected at a rate sufficient to provide overlap from one image to the next. This allows for a relative registration to be performed wherein one component of an image pair is selected as the reference to which the other component image is registered. Image-processing techniques are used to determine the relative translation of each image and a geometric transformation based on the determined displacement is applied. An alternative approach to registering the data is to do so based upon the altitude, orientation, and forward motion of the spacecraft. However, this is less practical because clouds at different altitudes require different transformations and thus registration requires apriori knowledge of cloud height.

4. COVIR

The Compact Visible and Infrared Radiometer (COVIR) instrument is being developed with the goal of providing an operational imager for small satellite missions dedicated to earth and climate monitoring (Lancaster et al., 2001). Small satellite missions continue to increase in priority at NASA as they hold the potential for improved

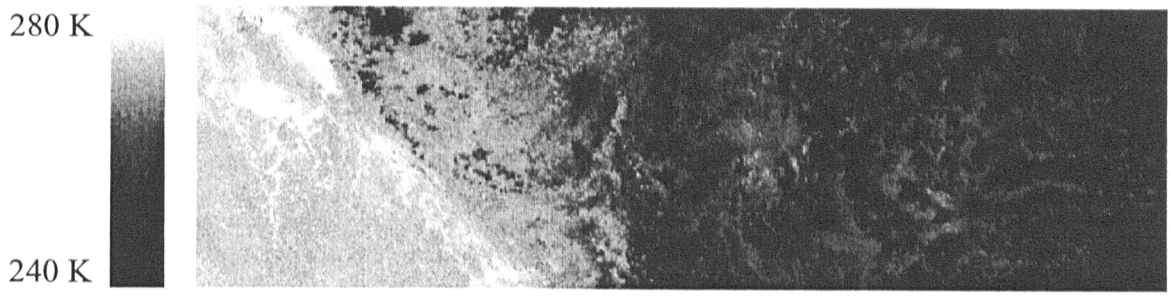

Fig. 7. Imagery acquired with the ISIR instrument of an optically thick cloud scene spanning several kilometers in altitude.

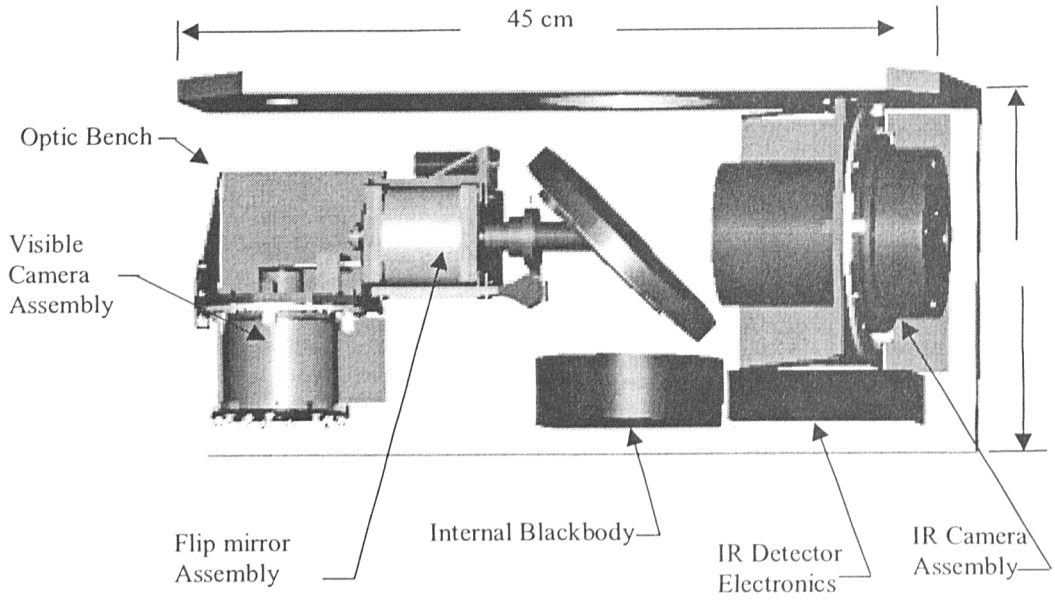

Fig. 3. A solid body model of the Compact Visible and Infrared Radiometer.

temporal coverage of the earth environment through multiple missions and an opportunity for increased scientific yield through the deployment of different complements of mission instrumentation.

The spectral selection for ISIR was achieved with the use of a filter wheel. Using this approach the scene imaged onto the entirety of the detector was sampled simultaneously in a single channel and sequentially in each of the four channels. Although the COVIR instrument operates on this same principle it departs from this approach by incorporating a strip filter array within the UMAD detector package. Hence, as the instrument platform advances the image scene moves sequentially from one filter to the next. An instantaneous field of view (IFOV) of 15 degrees is contained in the cross-track direction of the detector and 11 degrees in the along-track direction.

The design of COVIR consists of one visible and one infrared camera, a flip-mirror mechanism and internal blackbody for calibration, and the optics bench support structure on which they are mounted. A solid-body model of these subsystems is shown in Figure 3. The view toward the Earth is made through the top direction. For ease of accommodation the optics bench consists of a structural "L" bracket on which all components remain mounted to the sidewall regardless of the platform. The primary subsystem of the COVIR instrument is the infrared camera. It is built around a Lockheed Martin Infrared Systems (LMIRS) SIM200 imaging module incorporating a LAM 2D-class infrared focal plane array. This imaging module includes the UMAD in its package on a focal plane front-end board, a video signal processing and control card, and a power supply card. The IR is imaged through a fast, F/0.8, 55mm focal-length compound lens is made up of one zinc selenide and two germanium optical elements. This configuration provides an IFOV of 0.833 mrad/pixel; equivalent to ¼ km ground resolution when operated at Shuttle orbit altitude and ½ km resolution when placed in polar orbit at 600 km altitude. A flip mirror mechanism is used to provide rapid two point calibrations. This mirror is mounted at 45 degrees to the motor shaft of a single-axis direct drive stepping motor. The mirror is made up of a lightweight aluminum foam core that has been plated with nickel, polished, and coated with gold for high reflectivity in the IR bands. This mirror rotates 90 degrees and settles in less than ¼ second. During normal operation the mirror will be regularly rotated to view the Earth, a port for viewing cold space, or an internal blackbody. When viewing the Earth scene the pointing is repeatable to within 20 urads. Regardless of the target the number of optics in the optical path remains constant.

The internal blackbody assembly of COVIR provides a source for frequent two-point calibrations when combined with views to cold space. For proper calibration of the imagery data, knowledge of the temperature of this blackbody must be achieved to within an accuracy of 0.1°C, and uniformity must be maintained across an approximate 15cm aperture. A two-phase, copper/water sinter wick device developed by the semi-conductor industry for cooling high heat density IC's is used as the iso-thermalizing baseplate for the blackbody assembly. To this baseplate a honeycomb structure is epoxied and painted with a high-emittance black paint. Experimentation with straight-cut and bias-cut honeycomb structures, as well as flat and glossy black paints has shown little dependence of the performance of this blackbody on

these parameters. These same laboratory measurements have also shown that this novel design to a spacecraft blackbody does indeed provide the required radiometric accuracy.

Operation of the visible camera included in COVIR departs significantly from the approach taken with the infrared camera. Whereas the IR camera is a pushbroom imager that uses a 2-D array, the visible camera employs continual readout of four linear arrays. In order for the visible imagery to be used together with that of the infrared camera in a multi-spectral analysis, the two sets of data must be registered to within about ¼ pixel. This means that the pixels of the two detectors must share common fields of view and that the readout of the visible detector must be clocked to the infrared detector. The visible camera optics have been designed to provide the same 0.833 mrad/pixel IFOV for the 21 um pixels of the visible detector and only the center 327 of them are used to build up continual imagery. Ten pixels on both ends of the linear arrays are masked to provide a dark current reference.

The COVIR electrical system consists of the electronics assembly and drive motors along with the necessary wiring connectors and cable harnesses to connect these subassemblies to each other. The microbolometer array detector that is the heart of the infrared camera is supplied with various associated electronics. The objective of COVIR is to produce an engineering model radiometer. As such, these associated electronic cards remain in their commercial format, meeting military specification, and no effort has been made to optimize or limit the circuitry included on them for space flight. For a free-flyer mission much of the IR camera circuitry would be removed to reduce the associated risk of failure of parts that are not pertinent to this application. Combined, the COVIR electronics assembly consists of 7 printed-circuit boards and three camera-electronics signal processing boards. The printed circuit boards include a TDI processing board, a house keeping and digital I/O board, and a board for control of various heaters and TEC power supplies. Also, there is the visible camera interface board, a control DSP board and a power supply board.

5. GEOSYNCHONOUS

Uncooled infrared array detectors have significant potential for imaging radiometer applications from geosynchronous orbit. Small instruments could be developed for specialized and general applications that require higher resolution or more rapid repeat imaging. Large-format UMAD arrays offering 1024 x 1024 pixels are now being developed (Tsao et al. 1999). An issue is whether sufficient sensitivity can be obtained for geosynchronous applications. Studies indicate that with frame averaging, similar to that demonstrated for our LEO instruments but direct rather than TDI, sufficient sensitivity for cloud observations can be readily obtained. The influence of correlated noise is a limiting factor, but such pattern noise can be largely eliminated by masking and dither techniques. An additional requirement, as for LEO applications is a fast optical design. System studies indicate that practically sized instruments are possible. A special study has been made on an imager for rapid detection of volcanic eruptions.

6. SUMMARY

The use of uncooled infrared detectors for space borne imaging has been demonstrated by the shuttle ISIR hitchhiker experiment. The Compact Visible and Infrared Radiometer instrument is now being developed at the NASA Goddard Space Flight Center with the goal of providing an operational design for visible and infrared imagery for small satellite missions dedicated to earth and climate monitoring. Use of an uncooled microbolometer array detector as a pushbroom multiwavelength image sensor allows the size, cost, and weight of the instrument to be reduced through the elimination of a cooler. The COVIR instrument is being developed as part of the NASA Instrument Incubator Program (IIP) as an engineering model. The goal of the IIP is to develop laboratory prototype instruments that can be rapidly upgraded to meet flight standards and integrated into a spacecraft. The target spacecraft for the COVIR instrument is a sun synchronous, polar orbiting earth satellite at a nominal altitude of 600 km. The COVIR instrument may be tested on a shuttle flight in 2003. Although it is not being developed expressly as a shuttle instrument, a flight provides an ideal opportunity to test the instrument capabilities under space flight conditions.

REFERENCES

Kramer, H.J., 1994: *Observation of the Earth and Its Environment*, Berlin: Springer-Verlag.

Lancaster, R. S., K. Manizade, S. P. Palm and J. D. Spinhirne, 2001:The compact visible and infrared radiometer (COVIR) for earth and climate monitoring, IEEE Aerospace Conference Extended Abstract Volume, Big Sky.

Spinhirne, J. D., V. S. Scott, J. Cavanaugh, S. P. Palm, K. Manizade, J. W. Hoffman and R. C. Grush, 1998: Preliminary space flight results from the uncooled infrared spectral imaging radiometer (ISIR) on shuttle mission STS-85, 1.

Tsao, H. R., K. R. Maschhoff, W. Watson, J. W. White, 1999: A space instrument application of an uncooled infrared microbolometer array, IEEE Aerospace Conference Extended Abstract Volume, Big Sky.

Wood, R.A. and N.A. Foss, 1993: Micromachined Bolometer Arrays, *Laser Focus World*, 101-106.

P5.12 A Proposed Multiangle Satellite Dataset Using GEO, LEO and Triana

Helen Y. Yi *
Analytical Services and Materials, Inc., Hampton, VA

Patrick Minnis and Louis Nguyen
Atmospheric Sciences, NASA-Langley Research Center, Hampton, VA

D. R. Doelling,
Analytical Services and Materials, Inc., Hampton, VA

1. INTRODUCTION

Simultaneous multi-angle viewing of the Earth has recently been achieved with multi-angle satellite instruments such as POLDER (Polarization and Directionality of the Earth's Reflectance), MISR (Multi-angle Imaging Spectro-Radiometer) and the ATSR2 (Along Track Scanning Radiometer). These multi-viewing instruments on polar orbiting satellites are useful for estimating several parameters including cloud height, optical depth and phase. However, due to orbital constraints and matching difficulties, the applicability of data from multi-angle instruments on a single satellite and the dual views from paired satellites has been limited in angular coverage and temporal sampling.

The Triana satellite with the Earth Polychromatic Imaging Camera (EPIC) is designed for insertion into a Lissajous orbit around the L1 point (Valero et al. 1999). EPIC is an imager with a nominal resolution of 8 km at nadir and 10 channels that include several solar bands common to many operational and research meteorological satellites, such as 0.645-μm visible (VIS) channel. Images of the Earth will be taken with 3 or more EPIC channels every 15 minutes. Thus, every Earth-viewing low Earth orbit (LEO) or geostationary Earth orbit (GEO) satellite imager observing the sunlit Earth will have the potential for viewing the same location as Triana to within ± 7.5 minutes. Because of Triana's orbit, the EPIC will view 83 to 98% of the sunlit Earth at a scattering angle varying between 165° and 177°. However, most views from other satellites are at scattering angles between 60° and 170°. Since reflectances in the back-scattering direction are very sensitive to features such as cloud particle shape (e.g., Chepfer et al. 2001) or surface canopy structure, the EPIC will provide a unique contribution to Earth remote sensing.

Radiance measurements from the Triana EPIC will be continuously matched with operational and research satellite data to create a new source of data for multi-angle studies of the Earth and atmosphere. This paper describes the development of the proposed multi-angle dataset and applies it to currently available datasets. The Triana dataset is simulated using Moderate Resolution Imaging Spectroradiometer (MODIS) on the Terra satellite. The simulated Triana EPIC data are then matched with several GEO satellites (GOES-East, GOES-West, and GMS-5) and LEO satellites, including MODIS and the AVHRR (Advanced Very High Resolution Radiometer) on NOAA-12, NOAA-14, 15, and 16. A technique is developed to collocate and nearly simultaneously match visible images from Triana with current available satellites to build new multi-angle, multi-satellite VIS imagery. The imager data from each satellite will be matched to the Triana's EPIC view within 5-15 minutes. This methodology will also be useful for combining currently available datasets.

2. METHODOLOGY

2.1 Image Matching and Extracting

The first steps in creating the matched dataset are image selection and pixel extraction. Programs were developed for the Man-computer Interactive Data Analysis System (McIDAS; Lazzara et al. 1999) to search through all available satellite image files organized in the Abstract Data Distribution Environment (ADDE) to find matching

* *Corresponding author address:* Helen Y. Yi, Analytical Services and Materials, Inc., Hampton, VA 23666; email: y.yi@larc.nasa.gov.

images. The criteria for pairing images include common regions, time t, and tolerant time difference Δt. The matched simultaneous measurements of Triana, all GEOs and LEOs are defined as collocated measurements made within $\pm\Delta t$ = 5-15 minutes of specific time t. For VIS data, the solar zenith angle SZA is specified to be less than 90°. Each pixel's latitude and longitude are obtained from the navigation information of each satellite. If the pixel is located in a matching region, its SZA, view zenith angle VZA, relative azimuth angle RAZ and scattering angle SCA are calculated. The most current calibrations (e.g., Minnis et al. 2001) are used to convert the observed pixel's brightness count or radiance to reflectance. These values are stored into an intermediate file, designated the Multi-View Dataset (MVD) Level 0.

2.2 Image Gridding and Merging

The SZA, VZA, RAZ, SCA and reflectance of matching pixels are averaged into a grid box, such as 0.2° latitude by 0.2° longitude. These grid-averaged variables from a given satellite are output into a Hierarchical Data Format (HDF) file, which organizes all values from one satellite as an independent group. The dataset is called the Multi-View Dataset Level 1 (MVD1).

2.3 Structure of MVD HDF File

Figure 1 shows the structure of a multi-view angle dataset. The MVD1 is written in standard HDF using HDF-defined data models, such as the Scientific Data Set (SDS), the Vdata, and the Vgroup model. Each HDF Vgroup acts like a container that holds all information associated with one satellite.

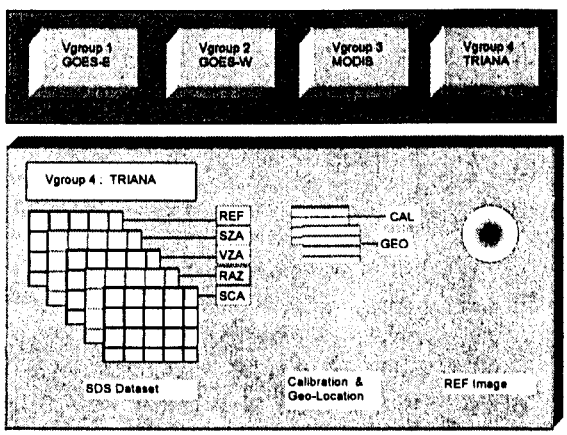

Figure. 1. Schematic structure of MVD1.

3. EXAMPLE DATA

An example data set is created here to simulate the process for Triana.

3.1 Simulated Triana EPIC Earth Views

The 5 MODIS visible channels (0.466 μm, 0.554 μm, 0.647 μm, 0.857 μm and 0.904 μm) are used to simulate hourly Triana EPIC views on September 7, 2000. The MODIS images are analyzed with the CERES cloud retrieval algorithms to define each pixel according to surface type and state of cloudiness. Anisotropic correction factors are applied to each pixel according to the amount of cloudiness and underlying surface type to compute the spectral albedo. Thus, each pixel has a record of angles, scene type, and albedo. These pixels are then used to simulate the view from Triana.

Since Triana will orbit around the L1 point in an elliptical path that takes it from within 4° to as far as 15° from the L1 position, its orbital parameters can be specified for nearly any conditions that satisfy those constraints. The simulation here uses a satellite position of 10° north and 10° east of L1 in the simulation. The latitude and longitude of the Sun nadir point (same as the L1 sub-point) varies with time. For example, at 1800 UTC, the sun nadir point is at 5.84°N and 90.53°W. Thus the Triana's nadir point at 1800 UTC is at 15.84°N and 80.53° west. The simulated Triana view has an 8-km resolution at its nadir point. To simulate the view to any location, the SZA, VZA, and RAZ are first computed for the Triana view and the reflectance for those angles is computed for each MODIS pixel by applying directional and bidirectional reflectance models to the albedo for each pixel. The models depend on the scene type. The size and latitude-longitude boundaries for each Triana pixel are then computed with spherical geometry to account for growth of the pixel with VZA. The reflectance for each Triana pixel is then computed by averaging the reflectance for each of the MODIS pixels as computed for the Triana angles. Although a nearly complete 24-h Triana dataset has been simulated (see http://www-pm.larc.nasa.gov/, click on Triana) the simulated Triana dataset for matching is initially computed only for the time of the actual MODIS data

obviating the need for the directional reflectance models. With these simulated Triana chunks, it is now possible to perform the matching process with other satellites.

3.2 GEOs, LEOs and MODIS data

GOES-8 (east), GOES-10 (west), NOAA-14 AVHRR and MODIS image data were collected for September 7, 2000. All four datasets, including the simulated Triana data were calibrated to each other using the results of Minnis et al. (2001) and the approach of Nguyen et al. (1999).

4. RESULTS

The ARM SGP (Southern Great Plains) region (105°W - 91°W, 30°N - 40°N) is used to demonstrate the multi-view angle, multi-satellite dataset. Figure 2 shows, from top to bottom, the VIS reflectances (left column) and scattering angles (right column) at 1800 UTC, September 7, 2000 for GOES-E, GOES-W, MODIS and the simulated Triana EPIC. The latter image for EPIC has an almost constant scattering angle between 166° and 167°. GOES-E also has a near retro-reflection scattering angle between 160° to 163° for the selected region. The scattering angles for GOES-W are between 128° to 131°. The MODIS scattering angles vary from 100° to 150°.

Typically, clouds are more reflective in the backscatter and forward scatter directions than in the cross-scatter (~90°) direction or near nadir. Clear land surfaces are most reflective in the retro direction, except at large SZAs. The results in Fig. 2 confirm these general characteristics. The clear and cloudy areas for both GOES-E and Triana are noticeably brighter than either MODIS or GOES-W. Because MODIS has more views near nadir, it is darker than GOES-W. The consistency between the GOES-E and simulated Triana images conforms the approach used to simulate the upcoming Triana imagery. Careful examination of the images reveals the presence of some geolocation differences between various cloud features. These are due primarily to time differences and to parallax effects due to cloud altitude.

5. FUTURE RESEARCH

The results shown here represent the beginning of this process. A useable hourly matched multi-angle satellite dataset will be produced prior to the Triana launch. Those datasets will be used for some initial scientific studies. Concurrently, we will develop methods to account for the spatial and temporal mismatch of cloud fields because of (1) movement between image times, (2) parallax due to cloud, and (3) navigation errors for each pixel. To solve those problems, we will correlate the pixels for the entire image chunk initially, and then progress to correlations of pixels having similar temperatures rather than a single set of pixel shifts for each image.

The dataset derived with this technique will be used to determine cloud phase, particle shape, and height. The dataset will also be made available to the scientific community for other studies. An application package with a GUI interface will be developed to let users browse and analyze the Multi-View Angle Dataset much easier.

Acknowledgments
The NASA Triana Program supported this research.

References

Chepfer, H., P. Minnis, D. F. Young, L. Nguyen, and R. F. Arduini, 2001: Retrieval of cirrus cloud ice crystal shapes using visible reflectances from dual-satellite measurements. Submitted to *J. Geophys. Res.*

Lazzara, M. A., J. M. Benson, R. J. Fox, D. J. Laitsch, J. P. Rueden, D. A. Santek, D. M. Wade, T. M. Whittaker, and J. T. Young, The Man computer Interactive Data Access System: 25 years of interactive processing. *Bull. Amer. Meteor. Soc.*, **80**, 271-274, 1999.

Minnis, P., L. Nguyen, D. R. Doelling, D. F. Young, and W. F. Miller, 2001: Rapid calibration of Operational and research meteorological satellite imagers, Part I: Use of the TRMM VIRS or ERS-2 ATSR-2 as a Reference. Submitted to *J. Atmos. Oceanic Technol.*

Nguyen, L., P. Minnis, J.K. Ayers, W.L. Smith, Jr. and S.P. Ho, 1999: Inter-calibration of geostationary and polar satellite data using AVHRR, VIRS, and ATSR-3 data, Proc AMS 10th Conf. Atmos Rad., Madison, WI, June 28 – July 2, 1999.

Valero,F.P.J., J. Herman, P. Minnis, W.D. Collins, R.Sadourny, W. Wiscombe, D.Lubin, and K. Ogilvie, 1999: Triana – a Deep Space Earth and Solar Observatory, NASA background report, December. (Available at http://triana.gsfc.nasa.gov/home)

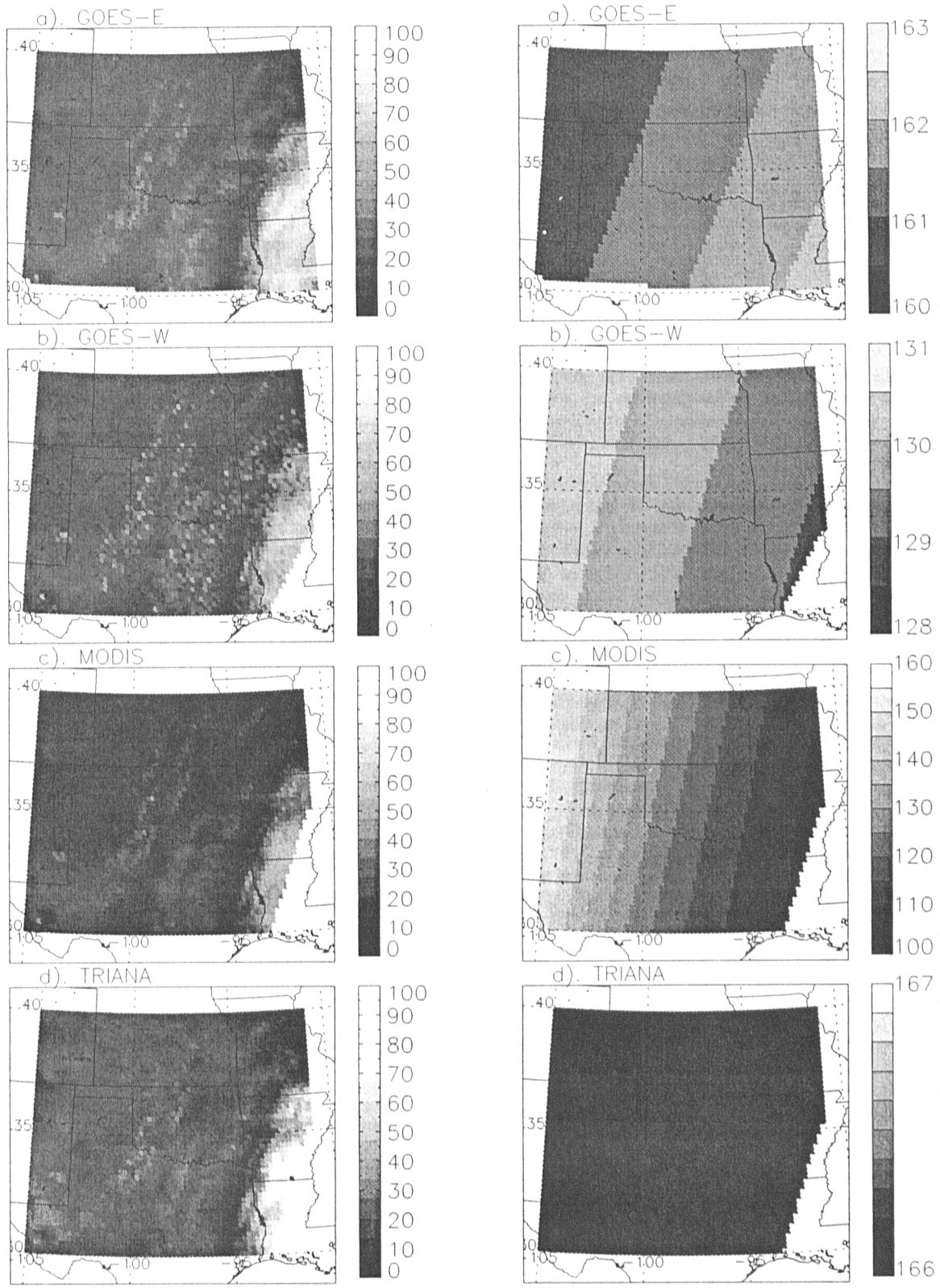

Figure 2. Matched satellite VIS imagery (left) and scattering angles (right, in degree), 1800 UTC, September 7, 2000.

P5.13 Cloud Detection from MISR using a Band-Differenced Angular Signature

Michael Wilson and Larry Di Girolamo
University of Illinois at Urbana-Champaign
Urbana, IL

1. Introduction

Cloud detection has historically been prone to more uncertainty in the polar regions than other regions of the earth. Low-level clouds and snow have similar radiation properties in visible and near-infrared channels, especially in nadir views. Since satellites have historically used nadir views for cloud detection, large errors in cloud detection for snow and ice covered regions have been typical. However, through the use of the Multi-angle Imaging SpectroRadiometer (MISR) on-board EOS Terra, coincident nadir and non-nadir visible/near-IR radiation measurements are now a possibility, which has the potential to circumvent the errors that have plagued previous satellite measurements.

MISR provides multi-angle coverage of the earth at nine specific angles: 0°, ±26.1°, ±45.6°, ±60°, and ±70.5°. This is done using 9 separate cameras, four of which view in the forward direction with respect to the satellite orbital track, one which views at nadir, and four which view in the aft direction. Each camera has four spectral channels: the blue band, the green band, the red band, and the near-infrared band (443 nm, 555 nm, 670 nm, and 865 nm respectively). MISR operates in a push broom fashion, with a cross-track resolution of 275 m, and a swath width of approximately 360 km (For more information on the specifications of MISR, see Diner et. al., 1998).

The ability of MISR to make multi-angle measurements of the same scene creates new opportunities for cloud detection in the polar regions. While clouds, snow and ice may all appear to be approximately the same in nadir views, in non-nadir views, the radiative scattering properties have a much larger contrast. This led Di Girolamo and Davies (1994) to develop the Band-Differenced Angular Signature (BDAS), which will be shown to be effective at cloud detection for the polar regions.

The BDAS technique utilizes both the capability of MISR to measure at multiple angles and the capability of MISR to measure at multiple wavelengths. The BDAS takes the difference between the 443 nm and the 865 nm for two cameras: the camera at 60 degrees measuring forward scattered radiation, and the camera at 70.5 degrees measuring forward scattered radiation. Once the wavelengths have been differenced, the 70.5 degree band-differenced result is subtracted from the 60 degree band-differenced result, to create the BDAS.

Corresponding Author Address: Michael Wilson
105 S. Gregory St., Urbana, IL 61801
email: Wilson@atmos.uiuc.edu

The BDAS works due to differences in the forward-scattering properties of clouds and surface features. For example, figure 1 shows that clouds and surface features are very similar for the differenced wavelength between the blue and near-ir channels, except in the forward-scattered direction. In addition, the BDAS is sensitive to molecular scattering contributions above cloud tops. Longer path lengths through the molecular atmosphere tend to lead to higher levels of scattered blue light reaching the MISR sensor. Higher clouds shorten the path length that solar radiation takes through the atmosphere, and thereby reduces the amount of atmospherically-scattered blue light that reaches each MISR camera, compared to longer wavelengths. As a result, the BDAS is sensitive to higher clouds. Figure 1 shows that the differenced-wavelength value tends to increase towards the more oblique angles in the forward-scattered direction for clear conditions, while it decreases for cloudy regions. Therefore, the contrast between clouds and surface features can be measured by taking the slope of the lines between the most oblique cameras (i.e. differencing the two most oblique cameras). The results of Figure 1 are qualitatively consistent with the theoretical results of Di Girolamo and Davies (1994).

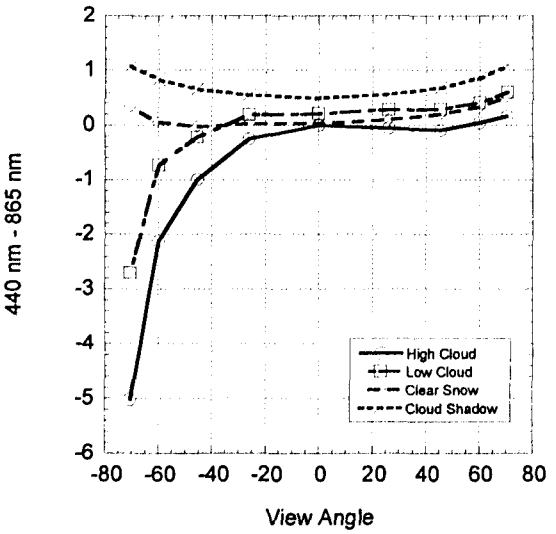

Figure 1: Demonstration of Difference between Blue and IR bands with respect to scattering angle. Negative values of view angle represent the forward-scattered direction. Positive values of view angle represent the back-scattered direction. This example was taken from MISR orbit 6865 over Antarctica. The symbols are positioned at the 9 MISR view angles.

2. Method

Seven scenes over the Greenland land mass were chosen for this particular study (see table 1).

Greenland was chosen because of the presence of a constant ice sheet over the region, especially during the summer. Since MISR can only operate in daylight conditions, scenes were chosen during the summer, so that enough daylight would be present for analysis.

Orbit #	Block #	Date	Average SZA
2713	28	Jun 21, 2000	53.405
3006	22	Jul 11, 2000	61.895
3455	37	Aug 11, 2000	51.165
3458	20	Aug 11, 2000	71.175
3459	17	Aug 11, 2000	74.760
3470	29	Aug 12, 2000	60.830
3475	12	Aug 12, 2000	81.070

Table 1: Orbit number, block number, observation date, and average solar zenith angle for the block of the MISR data used in this study.

Four consecutive blocks were chosen for each scene, based upon the availability of valid data, limited oceanic presence, and existence of surface and cloud features in each scene. Each block covers approximately 360 km cross-track, and 128 km along-track. Since MISR has multiple camera angles, it has the unique ability to determine stereo heights of objects in any scene. This effect can be visually achieved by placing all nine terrain-projected images of a scene into an animated sequence. In this sequence, surface features remain still for all nine images, while higher level features (such as clouds) move between scenes. This novelty of MISR allowed for the creation of a truth set, which greatly aided in determining appropriate thresholds for the BDAS and individual cameras in this study.

Once the animated scenes were developed, one block from each group of four was chosen for thresholding purposes. Multiple blocks could have been taken from each scene for thresholding, but by choosing only one block from each scene, any dependence based on scene choice was minimized. The BDAS was compared to the near-IR reflectance of the nadir and the most oblique camera in the forward-scattered direction for cloud detection. Thresholds were set manually for each individual scene.

This method did not take into account changes in the solar zenith angle between scenes. Within each scene, the solar zenith angle did not vary by more than three degrees. However, between all seven scenes, the solar zenith angle varies by over thirty degrees. Such a drastic change in solar zenith angle does have an effect on the chosen threshold for a given scene, as is illustrated by figure 2. In this figure, each case is placed in order according to the chosen BDAS threshold. A trend appears to be present between increased solar zenith angle and increased choice for a threshold.

The quality of each threshold was also checked to determine whether cloudy and clear pixels could adequately be separated by any given threshold. This factor became critical in the nadir near-IR thresholding cases, where as many as four of the seven cases had major misclassification errors that could not be reduced with any applied threshold.

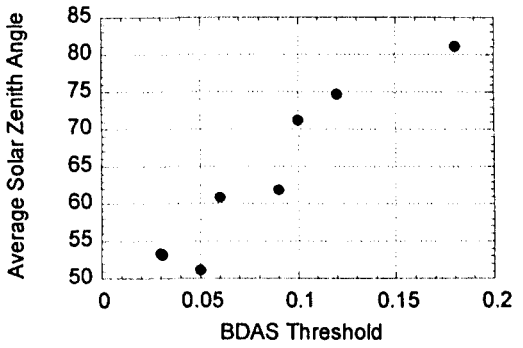

Figure 2: Solar Zenith Angle vs. BDAS Threshold. Note that as the chosen BDAS threshold increases, the average solar zenith angle also tends to increase.

3. Results

The BDAS technique and the near-IR thresholding for the most oblique camera (hereafter referred to as the oblique thresholding technique) appear to be statistically similar. Figure 3 shows the cloud fractions for each scene, using a manually determined threshold. All of the methods seem to show the general amount of cloud cover, but the oblique threshold technique and the BDAS technique tend to be similar, while the nadir values are more different. In addition, the manual thresholds applied to the nadir cameras were poor for over half of the cases, due to very bright surface features and dim clouds. Therefore, the BDAS and the oblique thresholding method appear to be much better suited to polar cloud detection than the traditional nadir thresholding method.

The graphs seem to indicate that the BDAS and the oblique thresholding method are very similar. However, the scenes have more differences than the graphs indicate. For example, in the case of orbit 3455, block 37 (see figure 4a), the oblique thresholding method can not detect clouds on the left side of the image, without misclassifying some clear region as cloud on the right side of the image (figure 4b). This occurs because the clouds on the left side of the image have a lower oblique camera near-IR value than the clear regions on the right side of the image. The BDAS threshold can create a proper threshold for both sides of the image, but some regions in the interior of large clouds get misclassified as clear (figure 4c). While the cloud fraction difference is just above 6% between the two types, the quality of those thresholds is quite different. The nadir near-IR thresholding techniques are very different from both the oblique near-IR thresholds and the BDAS thresholds (figure 4d). The contrasts between clouds, snow, and ice are minimized in the nadir images, which leads to the largest chance of cloud misclassification. The quality of the nadir thresholds is much lower than for either the BDAS thresholds or the oblique near-IR thresholds. Figure 4 represents the worst performance of the seven scenes examined.

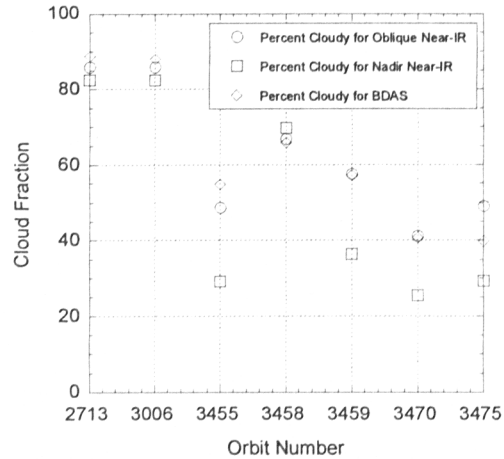

Figure 3: The percentage of each scene that was classified as cloudy by each manually determined threshold.

4. Conclusion

Cloud detection through visible and near-infrared channels has been error-prone in the polar regions due to the similar radiative properties of snow and ice in the nadir viewing directions. Through the use of MISR, however, polar cloud detection can be improved. Oblique cameras in the forward-scattering directions tend to measure stronger contrasts between surface and cloud features than do nadir measurements.

Nadir images tended to have more cloud misclassification for any manually applied threshold, compared to the oblique thresholds and BDAS thresholds. Since the thresholds do depend on solar zenith angle, future studies should explore the relationship between chosen threshold and average solar zenith angle. A threshold range dependent on solar zenith angle may give a more accurate representation of the true cloud cover in the arctic and antarctic.

The cloud fractions seem to indicate that oblique near-IR thresholding methods and BDAS thresholding methods are approximately equal in their ability to determine cloud cover. However, the near-IR method tends to miss some clouds, while the BDAS method tends to miss small parts of clouds. The result is a small difference between cloud fractions, but for different reasons. The nadir thresholds were of significantly worse quality on average, even when cloud fractions were similar, because much more misclassification occurred using the nadir method than for either the oblique or BDAS method. Cameras at non-nadir angles have much more potential than nadir cameras for cloud detection in polar regions, due to the different scattering properties of clouds and surface features in the forward scattering direction. This study shows that non-nadir measurements are more reliable than nadir measurements. In addition, the BDAS method has the ability to detect more clouds than near-IR thresholding on the oblique cameras. However, seven scenes are not enough to draw strong statistical conclusions. Therefore, more study must be done in order to create an automatic thresholding method for the polar regions.

References:

Diner, D. J. and co-authors, 1998: Multi-angle Imagine SpectroRadiometer (MISR) description and experiment overview. *IEEE Trans. Geosci. Remote Sens.* 36, 1072-1087.

Di Girolamo, L. and R. Davies, 1994: A Band-Differenced Angular Signature Technique for Cirrus Cloud Detection. *IEEE Trans. Geosci. Remote Sens.* 32, 890-896.

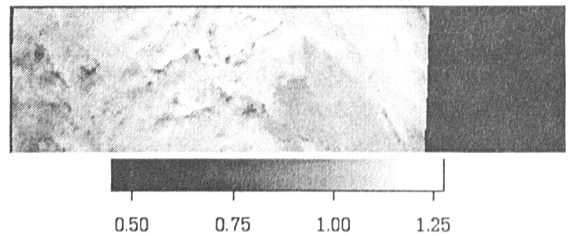

Figure 4a: Orbit 3455, Block 37, oblique near-IR image.

Figure 4b: Orbit 3455, Block 37, with an oblique near-IR threshold of 1.0. All white regions are cloudy, all black regions are clear.

Figure 4c: Orbit 3455, Block 37, with a BDAS threshold of 0.05. All white regions are cloudy, all black regions are clear. Semi-vertical stripes are no retrieval. Note that the striped regions were not used in the calculation of the BDAS cloud fractions.

Figure 4d: Orbit 3455, Block 37, with a NADIR near-IR threshold of 0.79. All white regions are cloudy, all black regions are clear.

Blank Page

Blank Page

P5.16 HIGH SPECTRAL RESOLUTION LIDAR VALIDATION OF MODIS DERIVED CLOUD PHASE AND ALTITUDE

R. E. Holz Univ. of Wisconsin, Madison, WI 53706,
S. Nasiri, R. E. Kuehn, R. Frey, B. Baum, and E. W. Eloranta

Introduction

To retrieve cloud optical thickness and particle size from satellite measurements, one must first have some idea of the cloud phase, that is, whether the cloud is composed of ice or water or some combination of both. Furthermore, little work has previously been performed to infer cloud phase in operational satellite data products. This is changing with the advent of data from the MODIS (Moderate resolution Imaging Spectro radiometer) on the NASA Terra platform. An operational MODIS cloud product concerns the inference of cloud thermodynamic phase. The phase retrieval (ice, water, mixed, or uncertain) is based on analysis of measurements at 8.5 and 11 microns, and thus is applicable for both daytime and nighttime data. The problem addressed here is upon the comparison of the satellite cloud phase product with independent determinations of cloud phase measured with the University of Wisconsin High Spectral Resolution Lidar (HSRL).

HSRL Background

The HSRL provides vertical profiles of backscatter cross-section, extinction cross-section, and depolarization. The HSRL divides the return signal into separate molecular and particulate scattering profiles. The Rayleigh scattering by molecules is used as a calibration target that provides robust recovery of cross section measurements. Residual depolarizations in the receiver are very small and a small receiver field of view (110 micro-radians) minimizes depolarization caused by multiple scattering. Thus, the HSRL depolarization signal allows easy distinction between scattering from spherical water droplets that induce little depolarization and ice crystals, which are non-spherical, and thus highly depolarizing. Clouds with depolarization greater then 25% consist of ice while depolarization less then 15% are generally water clouds or aerosols.

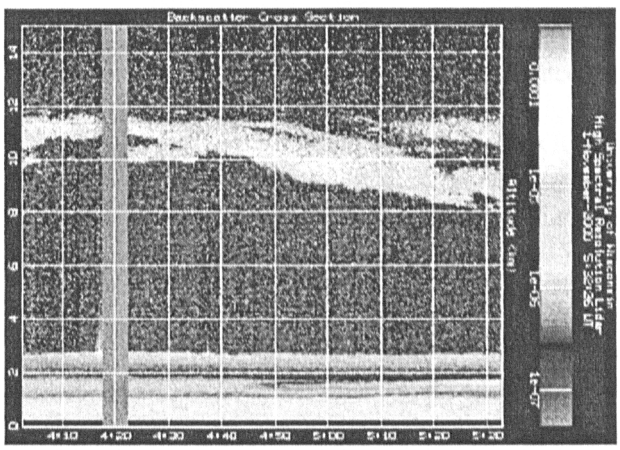

Figure 1. Plot of the aerosol backscatter cross-section. The X and Y-axis represent Time and Altitude. The shading corresponds with backscatter cross-section.

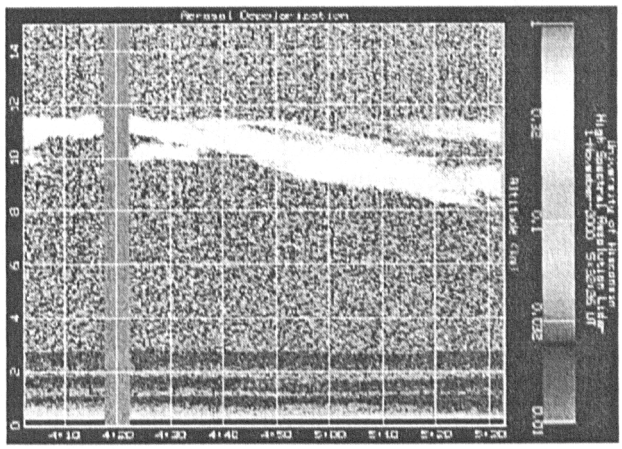

Figure 2. Plot of aerosol depolarization from the same data as Figure 1. Notice the highly depolarizing ice cloud (light shaded) and the thin water cloud below (dark shading).

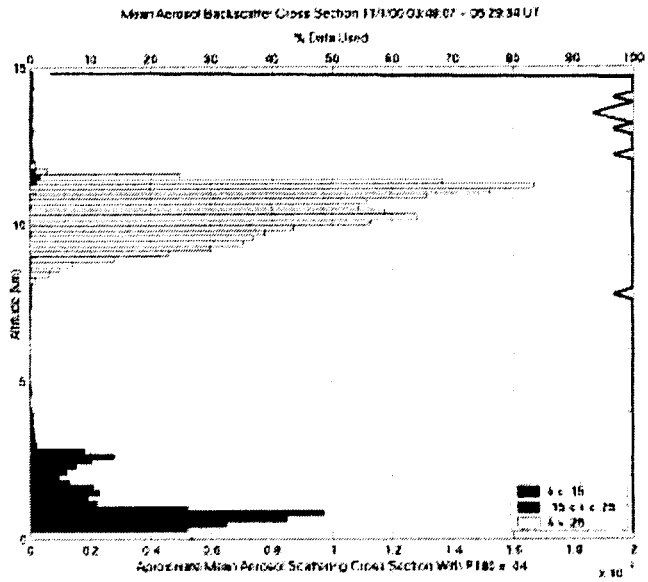

Figure 3. The aerosol scattering cross-section and depolarization for the entire data set generated from 3 minute averaged data with 165-meter vertical resolution. Depolarization values are divided into 3 ranges consisting of d < 0.15 (black), 0.15 <d < 0.25(gray), and d > 0.25 (light shading). Depolarization less then 0.15 are generally water droplets or aerosol. Depolarization greater then 0.25 are ice clouds. The black line represents the percent of the 3 minute averaged profiles used in the figure.

Results

This paper uses HSRL measured cloud phase and cloud altitudes acquired over Madison, Wisconsin to validate simultaneous, co-located MODIS retrievals. Data is taken starting 1-2 hours before the TERA overpass and continues 1-2 hours after the over-flight. Figures 1-3 are examples of HSRL-derived data products used for MODIS comparisons. Figure 1 and 2 show a vertical cross section of the backscatter cross-section and depolarization for February 20th, 2001. Notice that figure 2 consists of ice clouds from 8–12 km with depolarization's greater then 25% and an aerosol layer from the surface to 3 km with low depolarizations.

Figure 3 is the estimated scattering cross-section and depolarization averaged across the entire data-taking period of the 20th of February 2001. The length of each bar represents the mean of the scattering cross-sections measured during the data collection period that has a molecular scattering error <2%. The black line shows the percent of the data used at each altitude. The scattering cross section is computed using the measured particulate backscatter cross section, ß' and an estimated backscatter phase function of $P(180)/4\pi=0.04$. The value of 0.04 is derived from a 1-year climatology of HSRL lidar data. The approximate scattering cross section is then equal to: ß'/0.04. Each bar is divided into colored segments based on depolarization. The length of the segment is determined by the fraction of the measurements weighted by the scattering cross-section. The plot was developed to be representative of MODIS satellite that has 1 km resolution compared to the 1-meter resolution of the HSRL. Averaging the HSRL data decreases the spatial resolution that better correlates with 1 km MODIS data. Figure 3 clearly shows an ice cloud at 8-12 km and a layer with low depolarizations from the surface to 3 km.

The HSRL measurements will be compared with simultaneous Modis cloud phase results in the presentation.

P5.17 CLOUD TOP ANALYSIS USING CLOUD MODEL SIMULATIONS AND SATELLITE OBSERVATIONS

Stefano Natali[1], Pao K. Wang[2] and Hsin-mu Lin[2]

[1]University of Ferrara, Dept. of Physics, Ferrara, I-44100, Italy
[2]Dept. of Atmospheric and Oceanic Sciences, University Of Wisconsin-Madison, Madison, WI 53706

1. INTRODUCTION

A central issue in the study of impact of convective systems related to strong phenomena is the understanding of their complex structure and evolution. Such systems are often related to high precipitation rate, strong winds and hailfall. Satellite observations and cloud microphysical model (CMM) simulations have proven to be effective in the study of this kind of phenomena. These two approaches, even different, complement themselves in the description of convection, providing an observative approach joins with a theoretical one.

A peculiar characteristic of cloud top of deep convective system has been defined as Enhanced-V or V-Shape; different studies have been performed so far to describe and explain this feature (e.g. Heymsfield et al, 1983ab). McCann (1983) accumulated V statistics from half-hourly enhanced IR data from April to July 1979. He found that storms with a V pattern had about 70% probability of producing severe weather, and that the median lead time from the onset of the V to the first severe weather was about 30 minutes. Adler et al. (1985) also presented similar evidence that the V feature is correlated with reported severe weather. They found that 75% of storms with the V feature had severe weather, but 45% of severe storm examined did not have this feature.

Different studies have been previously performed making use of satellite data, radar observations, conventional data and, in few cases, of numerical model simulations. Among them, Heymsfield and Blackmer (1988) treated in the more complete way this subject, also proposing a conceptual model to describe the phenomenon. But, for used numerical models, it was difficult to reproduce all observed features. This was mainly due to the lack of ice processes inside the model microphysics (Schlesinger, 1984, 1988).

Now that improvement in satellite technology, model refinement and computational resources get observational and simulation approaches to have almost the same spatial resolution, with reasonable computational time, a complete combined study is feasible.

The aim of this work is to merge satellite and numerical model approaches in the study of some features related to cloud top structure. An approach that considers both satellite observations and cloud three dimensional microphysical model simulations seems to be a good way in order to learn more about physics of convective systems and to improve image interpretation significance.

To perform this study two events have been selected, from their intensity, the availability of data on which compare satellite derived parameters and their previous model simulations. These events have been observed by geostationary and polar platforms and simulated by Wisconsin Dynamical-Microphysical Model (WISCDYMM).

Corresponding author's address: Stefano Natali, University of Ferrara, Dept. of Physics, Ferrara, I-44100, Italy; E-Mail: natali@fe.infn.it.

2. PREVIOUS STUDIES ON ENHANCED V

2.1 *Satellite approach*

For almost ten years across eighties, different studies making use of satellite data have been focused on the V-Shape study and analysis; this was mainly due to the facility to detect this feature from the first infrared (IR) geostationary satellite data.

Heymsfield and Blackmer (1988) performed a complete analysis on satellite observation of V-Shape feature. Most of the terms used in analyzing IR data are shown in Figure 1. The cold area (CA) is a region of embedded low equivalent black body temperature (EBBT) associated with the convective updrafts and top of the storms. CA is typically at the vertex of the V. The close-in warm area (CWA) is defined as an embedded region of higher temperature ≤50 Km downwind of the cold area. Often the CWA has a distinct EBBT maximum, although sometimes is only a degree warmer than the overall anvil temperatures. The Distant Warm Area (DWA) is defied similarly to the CWA, except it is further downwind. Usually DWAs are more transient than the CWAs and often do not have a maximum of EBBT.

A notable classification was made by Adler and Mack (1986); they indicated that thunderstorms with thermal couplet (CA and CWA) might be classified according to three types of thunderstorm tops:
Class1: the IR coldest point is located with the cloud top and there is no close-in warm point;
Class 2: similar to Class 1 except a warm point exists downwind of the cloud top.
Class 3: cold and warm points exist and with the cold point displaced upstream of the cloud summit.

They found that thunderstorms could go through the three storm top classes during their lifetime.

2.2 *CMM simulations*

Some cloud microphysical models have been tested in order to reproduce and study the dynamical Mack (1986) made numerical calculation using one

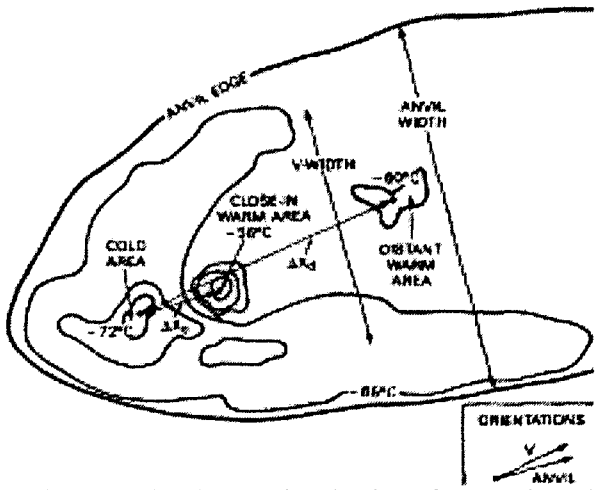

Figure 1: Terminology for cloud top features based on 23:34 UTC 2 May 1979 GOES IR image (Heymsfield and Blackmer, 1988).

processes involved in V-Shape formation. Adler and dimensional cloud model to simulate the overshooting cloud top. Their approach was based on a one-dimensional parcel model (Schlesinger, 1984). They concluded that the warm point occurs due to the subsistence and overshooting on the downward side; moreover they said that cirrus observed above the anvil (Fujita 1982) is an effect of this process, not the cause of the distinct warm point.

Schlesinger (1984, 1988) used a three-dimensional cloud model without ice processes to examine origins of air in the cold and warm points. The resulting cloud top analysis reproduced both thermal couplet and V (U) shape of the cold area; the V-Shape was found to be parallel to the cloud top horizontal wind field and cloud-top height/temperature was found consistent with Adler and Mack class 2 and class 3 systems. Moreover class 3 systems looked favored by marked stratospheric inversion, while class 2 looked favored by no stratospheric inversion.

3. DATA AND ALGORITHMS

Two events have been selected accounting for their evolution, previous simulations and available data amount. One of them had already been studied (analyzed and simulated, see Lin 2000), while the other has been selected because of its evolution and the high quality of available satellite data. Table 1 describes event specifics, available simulations and data.

Table 1. Data availability for selected events

Event Location	Date	Data available
Montana (CCOPE project)	8/2/1981	Simulation, GOES-4
Nashville (TN)	5/25/2000	Simulation, GOES-8, MODIS

The observational dataset for the CCOPE event consists of GOES-4 images in both Visible and Infrared spectra, starting at 21:45 UTC of 8/2/81 to 04:15 of 8/3/81. The time resolution is 30 minutes, while spatial resolution for infrared images is about 4x7 Km.

The observational dataset for the second event consists of GOES-8 images (channels 1, 2, 3, 4, 5) from 23:00 UTC of 5/24/00 to 08:00 UTC of 5/25/00, with temporal resolution from 15 to 3 minutes and spatial resolution from 1x1 Km (ch. 1) to 2x4 Km (others), and MODIS overpass at 04:30 UTC, with spatial resolution from 250 m (bands 1 and 2) to 1 Km (bands 8-36).

The microphysical model used in this work is a reviewed version of the WISCDYMM model developed in 1989 (Starka, 1989). The theoretical framework of the WISCDYMM is a non-hydrostatic, three dimensional, time-dependent cloud model. The WISCDYMM utilizes six different types of water substance: water vapor, cloud droplets, cloud ice crystals, rain drops, snow, crystals and aggregates and graupel/hail. There are a total of 38 microphysical processes incorporated in the model including nucleation, condensation, evaporation, freezing, melting,

For this study the hail parameterization model (HPM) version of the WISCDYMM, (inverse exponential size distributions for rain, snow and graupel/hail, and monodispersed distributions for cloud water and cloud ice) has been used (see Straka 1989 for a complete description).

A compromise between simulations definition (spatial and temporal) and computational resources, sets spatial resolution at 1 km, and temporal resolution at 2 minutes. A horizontal grid spacing of 1 Km and vertical spacing of 0.5 Km over 20 Km depth and over a 56x56 Km horizontal domain is found to adequately resolve the dynamics of all storms here analyzed (there are 8 to 12 grid points across the main features of the cloud in the CCOPE storm).

4. RESULTS

4.1 *CCOPE Case*

In order to identify cloud top on cloud model output, three substances have been considered and analyzed: Relative Humidity respect to ice (RHi), snow content (qs) and ice content (qi). A graphical comparison has shown that 90% RHi is the best field value to identify the cloud top. Temperature field has been considered over this iso-surface above 8 Km level.

A 3 dimensional animation of the evolution of this surface showed a well defined cold V-Shape pattern, with a warm area downwind. As for Adler and Mack class 3 systems, the cloud top coldest point is displaced respect to the highest one. Horizontal distances vary from 0 Km to 6 Km during evolution. Sometimes there is superposition between them. Height differences range from 0 Km to 3.5 Km. These differences are more evident in the first part of the event evolution, while in the final part (steady state and dissipation) points tend to be closer in height. There are no preferred displacement directions: the relative position of coldest point respect to the highest point is spread around the highest one during the event evolution. This is in contrast to what observed by Adler and Mack about

class 3 systems, which observed coldest point downstream respect to the highest point.

A further analysis was performed comparing coldest point and warm area values and their relative positions. The warm area maxima range from 223 K to 229 K (maxima inside a warm pool), and distances between CAs and CWAs vary from 1.4 to 20 Km. Warm areas are always located downwind respect to the coldest point. The almost constant CWA value is in good agreement with that observed by Heymsfield and Blackmer even though values are a little bit warmer (around –45 C) than observed before (-56 to –60 C). CA evolution has a variation rate (up to 16 degrees) larger than observed by Heymsfield and Blackmer (10 degrees). Distances retrieved by model analysis resulted shorter than observed by Heymsfield and Blackmer using satellite data (lower than 20 Km compared with 21-44 Km), but larger than values simulated by Schlesinger (up to 10 Km)

Satellite analysis involved EBBT field. IR 11 μm images show, at the early stage (21:45 UTC) a growing cell with a warm area inside a cold cloud top. This structure went to a V-Shaped cold area in the following images (22:15, 22:45). A cold minimum grew in the southern arm, becoming the coldest point at 23:45. After that, the V-Shape feature was present till 00:45, but the coldest point wasn't located on the vertex. After 00:45 it became more like a cold ring around a warm inner area, and after 2:15, no warm areas could be identified on the EBBT field.

Comparison between simulated and observed CWAs shows very similar values, while CA analysis suffers of the coarse satellite resolution: simulated values are generally 10 K colder than observed ones, with a peak of 18 K at 2:15 UTC. Despite to these differences, the trend of both curves is almost the same, showing a good agreement in the cold point genesis. Distances report almost the same problem as CA points: in fact the trend is almost the same in observations and simulations, but with different magnitude.

4.2 *Nashville Case*

A complete analysis using simulations and observations has been made on this event. A detailed analysis comparing GOES 8 and MODIS quasi-simultaneous observations has been made as well. Moreover, even though current event is not directly related to CCOPE case, these two events have certain common characteristics which worth to be analyzed. First, they both show a well-developed V-Shape feature, second their spatial dimension is comparable (around 30 Km linear dimension of updraft area and around 120 Km anvil area) as well as temporal evolution (around 4 hours); at last they show very peculiar feature on cloud top simulation and observation. Comparison between their lifetime as seen by simulation of CCOPE case and observations (GOES and MODIS) of Nashville case shows high similarity between the evolution of these two events. Cold and warm patterns can be identified on both observations and simulation; shapes and dimensions are similar as well as their duration. Moreover, the availability of MODIS and GOES data almost at the same time allows evaluating how the spatial resolution improvement affects the cloud top observation. Figure 2 shows the most complete instant we have in term of data availability: GOES images (channel 4, 4:32 UTC, remapped onto MODIS high-resolution grid is shown in figure 2 a)) and MODIS data (band 31, 4:30 UTC, figure 2 b)). Computed synchronization gave model output results after 90 minutes simulation (see figure 2 c)). In MODIS image it's easy to identify a well-developed cold V shaped area (dark area). There are two coldest areas: the biggest one is close to the V vertex, while the second smaller cold area is located toward the system center. Due to its lower resolution, GOES image shows a V-Shape structure but cannot identify this second cold point.

MODIS image describes in a great detail both cold and warm areas. Warm area is placed between the V arms, with two warmer areas deeply penetrating in the inner part of the cold vertex area just around the smallest minimum. This behavior is in great accord to that showed by cloud model simulation: a cold "tongue" extended from the V vertex to the center of the system surrounded by a warm 'U' shaped area.

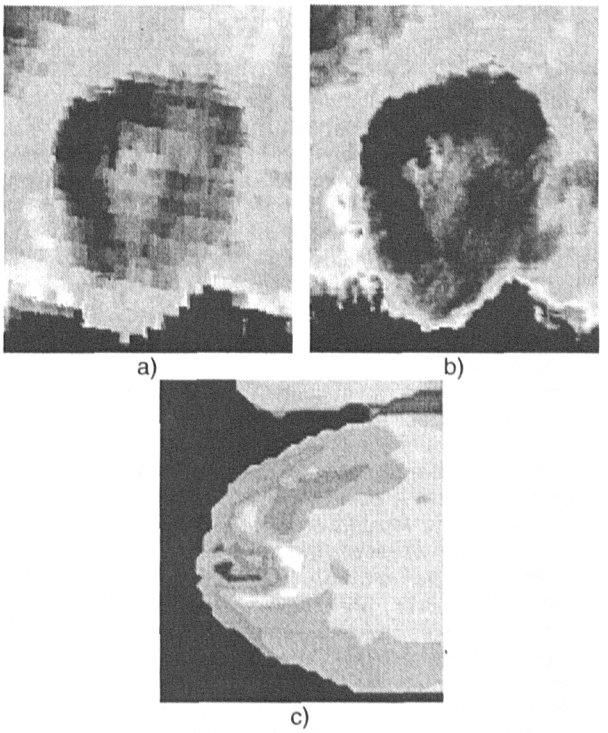

Figure 2. a): GOES-8 11 μm EBBT field colder than 235 K at 04:32 UTC of May 25 2000. b): MODIS 11 μm EBBT image for 4:30 UTC. c): cloud model output: temperature field plotted over cloud top as identified by 90% RHi isosurface (90 min. simulation X-Y view of CCOPE case).

CA and CWA points identified on model outputs are generally warmer than CA and CWA in EBBT satellite pictures. CA differences range from 0.3 to 10 degree, while CWA differences are more similar around 17

degrees (from 15 to 19 degrees). Moreover, MODIS observation for 4:30 UTC shows a CWA quite close to GOES observation while CA value is colder than GOES value of about 11.6 degrees (199.5 K GOES EBBT, 187.9 K MODIS EBBT). This, in accord to that observed by Negri (1982), comes from different sensor spatial resolutions: even though GOES channel 4 resolution is about 2 by 4 Km, MODIS band 31 resolution is 1 by 1 Km. This means that in one GOES pixel there are 8 MODIS pixels and this accounts for more than 10 K EBBT difference. Distances are generally shorter in model outputs respect to satellite observations (in both GOES and MODIS observations). Distances are closer at the early stages but the more the system develops the more the distances in GOES observations grow. This could be due to the coarse resolution as well, since closer warm areas in model output are generally too small to be detected by geostationary satellites.

6. CONCLUSIONS

The cloud top structure proposed by Heymsfield and Blackmer (1988) has been observed in all two cases. Even if distant warm areas have not been investigated, CAs and CWAs have been found in both observations and simulations. Their evolution has been found consistent to which proposed by previous studies. The high resolution of both of them (observations and simulations) has provided a detailed description of the cloud top area just above the updraft. Some new features have been identified in cloud model simulation and seen in high-resolution satellite observations as well.

Model simulations have been run, analyzed and some interesting conclusions have been carried out. The high spatial (1 Km) and temporal (2 minutes in this case) resolutions have enabled to study simulated cases in great detail. The most notable observed characteristics are related to the 'U' shape of the closest warm area and a second minimum that appears downwind respect to the cold V vertex. The 'U' shaped warm area showed peculiar characteristics: two maxima placed over the 'arms', and penetration on the colder part just around a cold tongue. The second cold point has been found located at the end of this cold tongue, extended downwind from the V vertex.

Newer satellite-borne sensors provided better spatial, temporal and spectral resolution respect previous studies. Moreover, among them (GOES-4, GOES-8 and MODIS) improvement due to better resolutions could be clearly evaluated. Cloud top features identified by CMM analysis cannot be observed in GOES-4 images (resolution around 4x7 Km) and in GOES-8 images (2x4 Km), while they are clearly present on MODIS images (1x1 Km resolution). Even if we cannot be sure that a better resolution could see something more than GOES-4 images, for the GOES-8 case we can see the improvement of cloud top features identification provided by MODIS data (see figure 2). In this case a comparison between cloud simulations and MODIS 11 μm channel shows a very similar pattern for both cold and warm area, confirming the high quality of model simulation processes, satellite sensor and selected approach.

6. ACKNOWLEDGEMENTS

This work has been funded in part by a fellowship provided by University of Ferrara, "Ufficio Programmazione e Sviluppo", "Borse di Studio di Perfezionamento all'Estero".

7. REFERENCES

Adler, R. F., and R. A. Mack, 1986: Thunderstorm cloud top dynamics as inferred from satellite observations and cloud top parcel model. *J. Atmos. Sci.*, **43**, 18, 1945-1960.

Fujita, T. T., 1982: Principle of stereographic height computations and their application to stratospheric cirrus over severe thunderstorm. *J. Meteor. Soc. Japan*, **60**, 355-368.

Heymsfield, G. M., R. H. Blackmer, and S. Sholtz, 1983a: Upper level structure of Oklahoma tornadic storms on May 2, 1979; Part 1: Radar and satellite observations. *J. Atmos. Sci.*, **40**, 1740-1755.

Heymsfield, G. M., G. Szejwach, S. Sholtz, and R. H. Blackmer, 1983b: Upper level structure of Oklahoma tornadic storms on May 2, 1979; Part II: proposed explanation of "V" pattern and internal warm region in infrared observations. *J. Atmos. Sci.*, **40**, 1756-1767.

Heymsfield, G. M., and R. H., Blackmer, 1988: Satellite-observed characteristics of Midwest severe thunderstorm anvils. *Mon. Wea. Rev.*, **116**, 2200-2224.

Lin, H. M., 2000: The microphysical characteristics of summer time thunderstorm in subtropics and High Plains from 3-D model simulation. Ph.D. Diss., Dept. of Atmospheric and Oceanic Sciences, Universitiy of Wisconsin, Madison, 287 pp.

McCann, D.W., 1983: The enhanced-V: a satellite observable severe storm signature. *Mon. Wea. Rev.*, **111**, 887-894.

Negri, A. J., 1982: Cloud-top structure of tornado storms on 10 April 1979 from rapid scan and stereo satellite observations. *Bull. Amer. Meteor. Soc.*, **63**, 10, 1151-1859.

Schlesinger, R. E., 1984: Mature thunderstorm cloud-top structure and dynamics: a three dimensional numerical simulation study. *J. Atmos. Sci.*, **41**, 1551-1570.

Schlesinger, R. E., 1988: Effects of stratospheric lapse rate on thunderstorm cloud top structure in a three-dimensional numerical sinulation. Part I, Some basic and comparative experiments. *J. Atmos. Sci.*, **45**, 1555-1570.

Straka, J. M., 1989: Hail growth in a highly glaciated central High Plains multi-cellular hailstorm. Ph.D. Diss., Dept. Meteorology, Universitiy of Wisconsin, Madison, 413 pp.

P5.18 NIGHTTIME CLOUD OVERLAP USING MODIS DATA

Monica K. Harkey*
Cooperative Institute for Meteorological Satellite Studies, University of Wisconsin-Madison

Bryan A. Baum
NASA/Cooperative Institute for Meteorological Satellite Studies, University of Wisconsin-Madison

Clouds play an important role in our weather and climate. Formed as water vapor condenses onto tiny particles of dust, soot, or chemical compounds, clouds change the radiative heating of our planet, which in turn drives the conditions in which the clouds form. As global climate models (GCMs) are extremely sensitive to cloud parameterization, we need to study clouds to better understand how they affect our world, to better our modeling, and in turn, the prediction of changing weather and climate.

To improve our knowledge of clouds, the International Satellite Cloud Climatology Project (ISCCP) was conceived. ISCCP uses data at two wavelengths, 0.6 and 11 microns, from international geostationary and polar orbiters to retrieve information every three hours on cloud top temperature and pressure, cloud optical thickness (only in daytime), and cloud type (also only in daytime), for example (Rossow and Schiffer, 1999). To retrieve the cloud properties, several assumptions are made. Each pixel is assumed to be wholly cloudy or clear, and if cloudy, there is only one cloud layer. Until 1992, all clouds were treated as a distribution of water droplets having an effective radius of 10 microns. Clouds at night are assumed to be opaque, which results in cloud top pressures being high by about 75 hPa. Since an ice model (a "fractal polycrystal" with an effective radius of 30 microns) has been introduced, nighttime cloud top pressures have been corrected such that they are only about 45 hPa too high. The wavelengths ISCCP uses have difficulty detecting high, optically thin cirrus clouds, perhaps missing 5-10% of cirrus because the radiance threshold is too high for detecting them (Rossow and Schiffer, 1999). This problem is exacerbated at nighttime, since during the day both wavelengths are available, but at night only the 11 micron channel is available. Considering that infrared optical thicknesses are about half the value of visible optical thicknesses, this makes ISCCP's detection of thin cirrus at nighttime tenuous at best.

A more sensitive method uses the High resolution Infrared Radiation Sounder (HIRS) on the National Atmospheric and Oceanic Administration (NOAA) polar orbiting satellites. Wylie and Menzel (1999) describe a CO_2 slicing technique that uses radiation from wavelengths from 13 to 15 microns to calculate cloud level, optical thickness, and effective emissivity. Effective cloud amount (the cloud fraction multiplied by the cloud emittance) is also inferred from a ratio of the radiance of the observed cloud to the radiance of an opaque cloud at the same level. A cloud at levels less than 3 km is assumed to be opaque, since the wavelengths used cannot detect radiation that far down into the atmosphere--there is a high signal-to-noise ratio below 3 km. Another assumption made is that there is only one cloud layer in each field of view--if there is a scene with multiple cloud layers, the method retrieves a mean height and emissivity.

GCMs have different assumptions about how to treat cloud overlap. Hogan and Illingworth (2000) used 71 days of cloud data over the United Kingdom from a 94 GHz high vertical resolution radar to investigate how GCMs treat cloud overlap. The most common cloud overlap assumption used in GCMs is the "maximum-random" assumption, such as discussed in Chou et al. (1998). There are also other assumptions for cloud association used in GCMs. These include random overlap, in which clouds are assumed to be randomly distributed horizontally at each level; mixed overlap, in which all clouds are randomly overlapped except for convective clouds, which are maximally overlapped; full overlap, in which all clouds are overlapping as much as possible; and combinations of these overlap assumptions. In the maximum-random assumption, vertically continuous clouds are assumed to be maximally overlapped, while clouds separated by levels without clouds are assumed to have random overlap. Tian and Curry (1989) noted that the maximum overlap assumption closely followed observations of vertically continuous cloud scenes. From their high-resolution radar data, Hogan and Illingworth found that for vertically continuous clouds, when the separation between cloud layers increases, the random overlap assumption fits better than the maximum overlap assumption. Most GCMs assume maximum overlap for all vertically continuous clouds, no matter how far they are apart from other layers. However, the GCM assumption of random overlap for vertically non-continuous clouds is in agreement with their data. Which assumption is used in a GCM affects the results of the model (Weare, 2001, also Chen, 2000), making the basis of the assumption critical for radiative feedback and heating calculations and other sensitivities.

In a remarkable collaboration among 19 different GCMs, Cess et al. (1990) found that in a simulated climate change, the variation of the global sensitivity parameter of the GCMs is almost three times more than the variation of the clear-sky sensitivity parameter. Since the global sensitivity parameter is shown to be linearly related to the cloud feedback parameter, cloud feedback is the source of the variation among the GCMs. Six years later, in a follow up paper (Cess, 1996) found that the

* *Corresponding author address*: Monica K. Harkey, Cooperative Institute for Meteorological Satellite Studies,University of Wisconsin-Madison, 1225 W Dayton, Madison WI 53706; email: monicah@ssec.wisc.edu

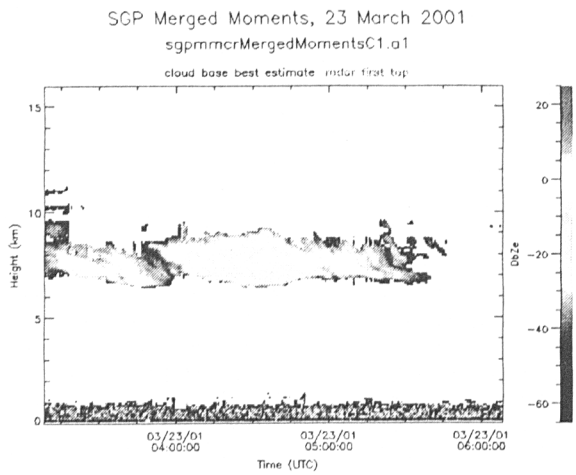

Fig. 1. Radar/LIDAR composite showing cloud layers.

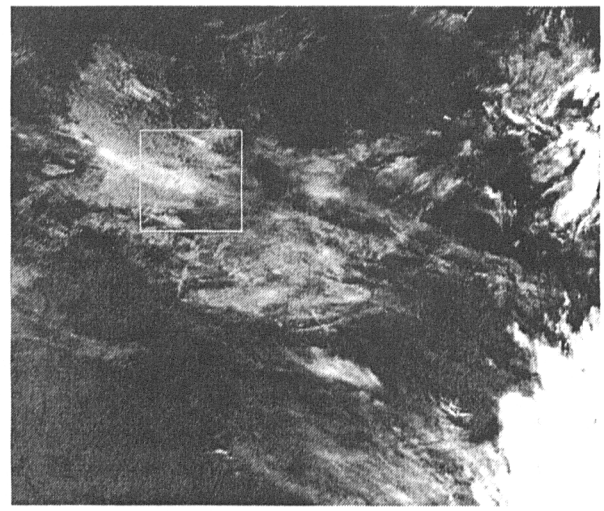

Fig. 2. Scene from MODIS overpass at 5:35 UTC over ARM SGP site. 11 micron brightness temperatures are shown, with white being the lowest and black being the highest values.

variation among the GCMs decreased because a few of the models had changed aspects of their cloud parameterizations, such as cloud optical properties. However, there still is a range of the cloud feedback parameter of about 1.2 among the GCMs. This range suggests that as there is so little agreement among a large number of climate models, more research needs to be done in cloud parameterizations. An important aspect of cloud parameterizations is the treatment of overlapping cloud layers.

The focus of this work is the detection of overlapping clouds at nighttime using three IR bands of MODIS data: 3.78, 8.5, and 11 microns. Samples of MODIS granules are chosen for detailed analysis over the Department of Energy's (DOE) Atmospheric Radiation Measurement Clouds and Radiation Testbed (ARM CART) at the southern great plains (SGP) site that were found to have cloud overlap by radar and lidar data. Single-layer clouds are modeled using a discrete ordinate radiative transfer model (DISORT). An algorithm is applied to subtract out the modeled single-layered clouds from the satellite data, leaving pixels that are potentially of overlapping clouds. We assume that there are no more than two cloud layers in each region used in this study. This assumption is supported Tian and Curry (1989) in general, and more specifically by ARM data. We also limit our cases to scenes with optically thin cirrus (11 micron optical thickness is less than 2), which ISCCP has difficulty detecting. Our approach may prove to be even more useful than previous studies in the formation of GCM parameters and assumptions, because of the resolution of the MODIS instrument. The channels used in our study (20, 29, and 31, corresponding to 3.78, 8.5, and 11 microns) all have resolutions of 1 km.

Surface-based observations are provided by Drs. Ken Sassen and Jay Mace of the Facility of Atmospheric Remote Sensing, at of the University of Utah. Additionally, they have compiled cloud data using lidar and radar measurements over the various ARM sites. Figure 1 shows such data--at the time of the 23 March 2001 MODIS overpass over the ARM SGP site at 4:35 UTC, there is a low cloud with a top at about 1 km, and the high cloud is between 7 and 9 km in altitude. Part of that MODIS granule is shown as Fig. 2, with a box around the sample data set. This image was obtained using Interactive Visualizer and Image Classifier (IVICS) software developed by Todd Berendes of the National Space Science Technology Center. With IVICS, a sample dataset was taken that had two cloud layers along with potentially overlapping cloud pixels. The two cloud layers were modeled in DISORT. We found that the low cloud was a water cloud at 272 K with particles having an reff of 4 um. The high cloud corresponded to the cold cirrus model, at a temperaure level T = 228 K. Figure 3 shows the sampled data set with the DISORT-derived curves for each cloud layer.

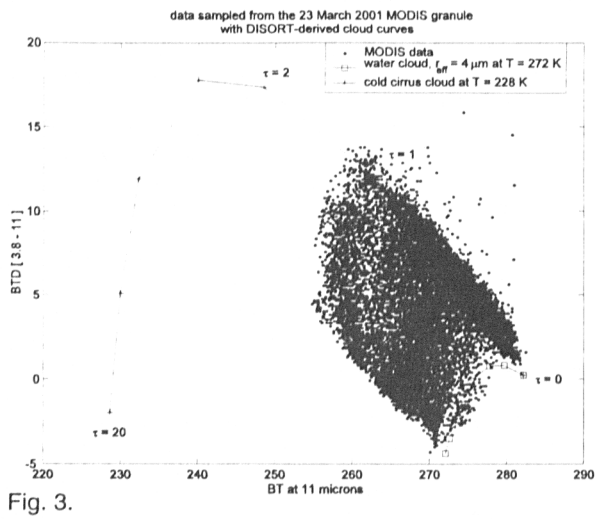

Fig. 3.

We have been able to reasonably identify the individual cloud layers in order to isolate the potentially overlapping cloud pixels. Our goal is to show that our method of nighttime cloud overlap identification using MODIS data is unique and very useful, as cloud climatology projects such as ISCCP and the HIRS CO_2 slicing technique assume, among other things, only one cloud layer per field of view, and cloud overlap is a critical aspect of cloud parameterizations needed in GCMs.

REFERENCES

Cess, R. D., et al., 1990: Intercomparison and interpretation of climate feedback processes in 19 atmospheric general circulation models. *Journal of Geophysical Research*, **95**, 16,601-16,615.

Cess, R. D., et al., 1996: Cloud feedback in atmospheric general circulation models: An update. *Journal of Geophysical Research*, **101**, 12,791-12,794.

Chou, M. D. et al., 1998: Parameterizations for cloud overlapping and shortwave single-scattering properties for use in general circulation and cloud ensemble models. *Journal of Climate*, **11**, 202-214.

Hogan, R. J., and A. J. Illingworth, 2000: Deriving cloud overlap statistics from radar, *Quarterly Journal of the Royal Meteorological Society*, **126**, 2903-2909.

Rossow, W. B., and R. A. Schiffer, 1999: Advances in understanding clouds from ISCCP, *Bulletin of the American Meteorological Society*, **80**, 2261-2287.

Tian, L., and J. Curry, 1989: Cloud overlap statistics, *Journal of Geophysical Research*, **94**, 9925-9935.

Wylie, D. P., and W. P. Menzel,: 1999. Eight years of high cloud statistics using HIRS, *Journal of Climate*, **12**, 170-184.

P5.20

HIGH SPATIAL RESOLUTION SURFACE AND CLOUD TYPE CLASSIFICATION FROM MODIS MULTI-SPECTRAL BAND MEASUREMENTS

Jun Li, Zhongdong Yang, Hung-Lung Huang
Cooperative Institute for Meteorological Satellite Studies (CIMSS)
University of Wisconsin-Madison, Madison, WI

W. Paul Menzel
NOAA/NESDIS, Office of Research and Applications, Madison, WI

Richard A. Frey, and Steven A. Ackerman
Cooperative Institute for Meteorological Satellite Studies (CIMSS)
University of Wisconsin-Madison, Madison, WI

1. INTRODUCTION

A method was developed for automated classification of surface and cloud types using Moderate-Resolution Imaging Spectroradiometer (MODIS) radiance measurements. The MODIS cloud mask (Ackerman et al. 1998) is used to define the training sets. Surface and cloud type classification is based on the maximum likelihood (ML) classification method. Classified results then define training sets for another iteration. Iterations end when the number of pixels switching classes becomes smaller than a predetermined number or when other criteria are met. The final class mean gravity values in the spectral domain are used for class identification and a final 1 km resolution classification map is generated for a MODIS granules. This classification procedure refines the cloud mask algorithm, and enables further applications such as clear atmospheric profile or cloud parameter retrievals from MODIS radiance measurements or from the combination of MODIS and other sounder systems such as the Atmospheric Infrared Sounder (AIRS). The advantages of this method are the automated surface and cloud classification independent of radiance or brightness temperature threshold criteria, and interpretation of each class based on the radiative spectral characteristics of different classes. This paper describes the ML classification algorithm and presents daytime MODIS classification and identification results.

The classification results are compared with the cloud mask image, visible image, infrared window image and other sources of observations for the initial validation.

Corresponding author address: Jun Li, Space Science and Engineering Center, University of Wisconsin-Madison, 1225 West Dayton Street, Madison, WI 53706; e-mail: JunL@ssec.wisc.edu

2. MODIS CLASSIFICATION ALGORITHM

2.1 MODIS cloud mask algorithm

MODIS measures radiances in two visible bands at 250 m spatial resolution, in five more visible bands at 500 m resolution, and the remaining 29 visible and infrared bands at 1000 m resolution. Radiances from 14 spectral bands (bands 1 and 2, bands 5 and 6, bands 18-21, bands 26 and 27, band 29, bands 31 and 32, band 35) are used in the MODIS cloud mask algorithm (initial classification) to estimate whether a given view of the Earth surface is obstructed by clouds or optically thick aerosol and whether a clear scene is affected by cloud shadows (Ackerman et al. 1998).

The MODIS cloud mask provides fifteen classes. Those classes are the primary input as the initial classification of the iterative classification procedure. They are: Class 1: Confident clear water (bit fields 1~2 = 1 1, bit fields 6~7 = 0 0); Class 2: Confident clear coastal (bit fields 1~2 = 1 1, bit fields 6~7 = 0 1); Class 3: Confident clear desert or semi-arid ecosystems (bit fields

1~2 = 1 1, bit fields 6~7 = 1 0); Class 4: Confident clear land (bit fields 1~2 = 1 1, bit fields 6~7 = 1 1); Class 5: Confident clear snow or ice (bit fields 1~2 = 1 1, bit 5 = 0); Class 6: Shadow of cloud or other clear (bit fields 1~2 ≠ 1 1, bit 10 = 0); Class 7: Other confident clear; Class 8: Possible clear with cirrus detected by solar bands (bit fields 1~2 ≠ 1 1, bit 9 = 0); Class 9: Possible clear with cirrus detected by infrared bands (bit fields 1~2≠1 1, bit 11=0); Class 10: High clouds detected by CO_2 bands (bit fields 1~2 ≠ 1 1, bit 14 = 0); Class 11: High clouds detected by 6.7 micron band (bit fields 1~2 ≠ 1 1, bit 15 = 0); Class 12: High clouds detected by 1.38 micron band (bit fields 1~2 ≠ 1 1, bit 16 = 0); Class 13: High clouds detected by 3.7 micron and 12 micron bands (bit fields 1~2 ≠ 1 1, bit 17 = 0) at nighttime only; Class 14: Other clouds or possible clouds; and Class 15: Undecided (bit 0 = 0). The above classes will provide basic surface and cloud type information

2.2 Maximum likelihood classification algorithm based on the MODIS cloud mask

Data classification or clustering is an important part of data analysis and image segmentation; the method tries to analyze data and identify several groups or clusters. A group or cluster is a class of data that has similar appearances (i.e., for MODIS images, it can be a particular surface type or cloud cover). Basic data clustering does not need any external information for its completion. The clustering algorithm can be described by the following steps:
(1) Classify the MODIS measurements using the MODIS cloud mask, calculate the mean vector and covariance matrix of each class within the MODIS cloud mask;
(2) Calculate the distances between the vector of each pixel and all the class mean vectors and assign the pixel to the nearest class;
(3) Update the class mean vector and covariance matrix of each class after all pixels have been reassigned to the nearest classes;
(4) Analyze the separability of the classes produced and merge or split some classes if necessary. For example, if the distance between a pixel and its nearest class is too large, this pixel will form a new class in the remaining iterations; on the other hand, if the distance between two classes is too small, then these two classes will be merged into one class. In this paper, this procedure was not implemented in order to remain the surface and class type index of the MODIS cloud mask in the ML classification.
(5) Repeat steps 2 - 4 until convergence criteria are met. In this paper, if the summit of off-diagonal for each class in the classification matrix (Li et al. 2001) is less than 6%, the iterations end. In general, 6 ~ 7 iterations allow a final ML classification result.

3. FEATURE SELECTION FOR MODIS SURFACE AND CLOUD TYPE CLASSIFICATION

There are three types of features in the MODIS classification. All the features are determined for 1km resolution. More spectral bands are used for surface and cloud type classification than used for cloud masking.

(1) *Spectral band radiances*

Radiances provide the primary spectral information of different scene and cloud types. MODIS visible bands 1-7, bands 17-29, and bands 31-35 are used in the daytime classification. The visible images are all mapped to the IR spatial resolution of 1km.

(2) *Variance images*

A variance image is constructed for each of the visible images and infrared longwave window images. In the visible variance images, the value attributed to each 1km pixel is the local standard deviation (LSD) of FOVs within the 1km area (for example, the standard deviation is computed from 4 by 4 values (FOVs) for bands 1 and 2, and from 2 by 2 FOVs for bands 3-7). Visible variance images are used as the features in the ML classification procedure, this guarantees that all the information used in the classification is restricted in the 1km resolution pixel. In the associated visible images, edges of different classes still present large variances, low visible variances are associated with cirrus clouds and relatively high variances with low stratiform clouds.

(3) *Brightness temperature difference images*

Studies show that differences between two infrared spectral bands are very useful for detecting clouds. For example, large positive brightness temperature (BT) differences in 8 minus 11 microns indicate the presence of cirrus clouds, for clear conditions, the 8 minus 11 micron BT difference will usually be negative due to stronger atmospheric water vapor absorption at 8 microns than at 11 microns. Most clouds appear positive values in the BT difference (8.6 minus 11 micron) image.

In order to save computation time, the simple Euclidean distance is used in the ML classification procedure. A weighting factor for each feature is used to scale the magnitude in the distance calculation (Li et al. 2001).

4. RESULTS

Figure 1 shows the band 2 (left panel) and its variance (right panel) images of an African Sahel/desert scene at 0935UTC 05 November 2000, indicating the clouds in the southern part of the granule. The MODIS cloud mask algorithm sometimes has difficulties in desert area since the VIS reflectances are usually higher over the desert than over clear land, and sometimes clear desert is not well separated from low clouds in the cloud mask algorithm. Twelve classes are obtained from the cloud mask algorithm and the ML classification in this case. The details for each class can be found in a recent paper (Li et al. 2001).

Figure 2 shows the cloud mask map (left panel) and classification map (right panel) for this case. In the cloud mask algorithm, the drought lake mentioned above was misidentified (classified as clouds) but is slightly recognized by the ML classification. Some striped lines existed in the cloud mask due to the use of band 36 in the cloud mask algorithm; band 36 was not used in the ML classification. The cloud coverage from the cloud mask is very close to that of classification results although there are significant cloud type changes (e.g., less high clouds in the classification than the cloud mask). However, the cloud mask has more clear desert than the classification.

The initial classification results from the cloud mask may be sensitive to the thresholds in some regions, especially when desert exists. In order to test the sensitivity of both the cloud mask and classification algorithms to the thresholds used in the cloud mask, the thresholds were changed in the cloud mask algorithm. Some arid and semi-arid zones were purposefully misidentified vegetated land, where visible band thresholds are lowered. The cloud mask then misinterpreted the brighter than expected surface reflectances as clouds. Figure 3 is the cloud mask map (left panel) with altered thresholds and its corresponding classification map (right panel). In the cloud mask algorithm, many desert pixels are changed to lower clouds due to the change of thresholds; however, those low cloud pixels are correctly reclassified as desert after the classification. Although there are some differences for the desert/land separation between the two classifications (see figures 2 and 3), the clear/cloud separation is almost the same in both classifications. This offers some reassurance that the classification is relatively insensitive to the thresholds used in the cloud mask algorithm.

5. CONCLUSIONS

A maximum likelihood classification initialized from the cloud mask algorithm was used to classify the scenes and clouds. The VIS and IR 1km resolution spectral information and visible spatial information are used in the classification. Results of applying both radiances and local variances confirm the usefulness of these parameters for cloud/clear separation, as well as for separation between the cloud types or clear types. The 1 km resolution classification map improves the 1 km cloud mask derived from the MODIS cloud mask algorithm in some situations. Combined use of the cloud mask and cloud classification improves identification of clear skies in the MODIS imagery as well as cloud types.

6. REFERENCES

Ackerman, S. A., K. I. Strabala, W. P. Menzel, R. A. Frey, C. C. Moeller, and L. E. Gumley, 1998: Discriminating clear sky from clouds with MODIS. *J. Geophys. Res.*, 103, D24, 32141-32157.

Li, J., Z. Yang, H.-L. Huang, W. P. Menzel, R. A. Frey, and S. A. Ackerman, 2001: High spatial

resolution surface and cloud type classification from MODIS multi-spectral band measurements, *J. Geophys. Res.* (submitted)

Water (Black)

Land (Blue)

Desert (Green)

Mid-low clouds (While)

Mid-high clouds (Yellow)

High clouds (Red)

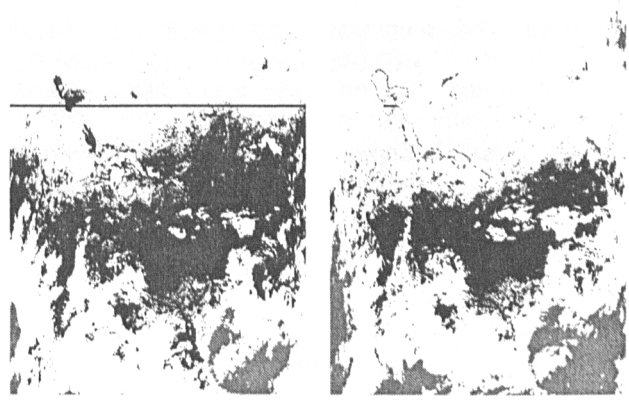

Figure 2 shows the cloud mask map (left panel) and classification map (right panel) for this case. In the cloud mask algorithm, the drought lake mentioned above was mis-identified (classified as clouds) but is slightly recognized by the ML classification (color image, see the left color bars)

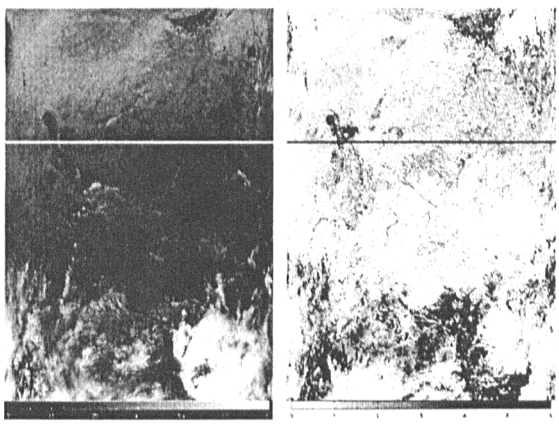

Figure 1,the MODIS band 2 (left panel) and its variance (right panel) images of an African Sahel/desert scene at 0935UTC 05 November 2000, indicating the clouds in the southern part of the granule.

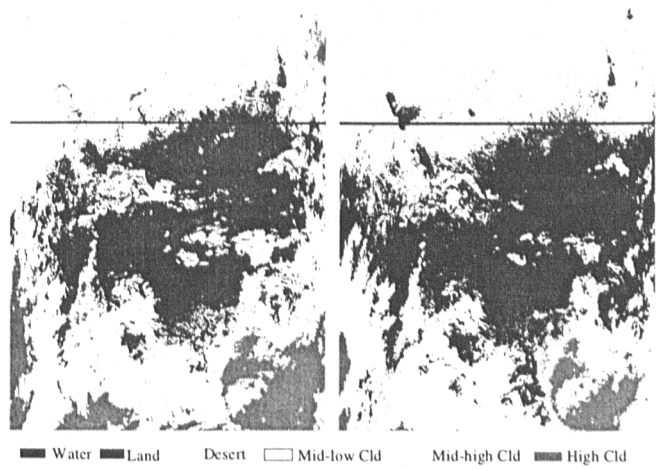

Figure 3, the cloud mask map (left panel) with altered thresholds and its corresponding classification map (right panel).

P5.21 LAND SURFACE ALBEDO, NADIR BRDF-ADJUSTED REFLECTANCE, AND BRDF PRODUCTS FROM THE MODERATE RESOLUTION IMAGING SPECTRORADIOMETER (MODIS)

Crystal B. Schaaf*, Feng Gao, Alan H. Strahler, Wolfgang Lucht, Xiaowen Li, Xiaoyang Zhang, Yufang Jin, Elena Tsvetsinskaya, Jan-Peter Muller, Philip Lewis, Michael Barnsley, Gareth Roberts, Christopher Doll, Shunlin Liang, David Roy, and Jeffery L. Privette

Department of Geography and Center for Remote Sensing, Boston University Boston, MA, USA
Potsdam Institut für Klimafolgenforschung (PIK), Potsdam, Germany.
Department of Geomatic Engineering, University College London,United Kingdom
Department of Geography, University College London, United Kingdom
Department of Geography, University of Wales Swansea, Swansea, United Kingdom
Research Center for Remote Sensing, Beijing Normal University, Beijing, China.
Department of Geography, University of Maryland, College Park, MD, USA
NASA/Goddard Space Flight Center, Greenbelt, MD, USA

1. INTRODUCTION

Provisional albedo, bidirectional reflectance and nadir surface reflectance products of the Earth's land surfaces from the MODerate resolution Imaging Spectro-radiometer (MODIS) on board NASA's Terra spacecraft have been available from the EROS Data Center (EDC) since November 2000. Atmospherically corrected, cloud cleared, surface reflectances are used to produce 1km gridded MODIS Bidirectional Reflectance Distribution Function (BRDF), Nadir BRDF-Adjusted surface Reflectance (NBAR), and Albedo Products (MOD43B1, MOD43B3 and MOD43B4) every 16 days (Lucht et al., 2000). The operational MODIS BRDF/Albedo algorithm relies on multidate surface reflectance data and a semiempirical kernel-driven BRDF model (RossThickLiSparseReciprocal) to determine a global set of parameters describing the BRDF of the land surface. These one kilometer gridded parameters are then used to determine both global directional hemispherical reflectance (direct beam or "black sky albedo" at local solar noon), and bihemispherical reflectance (diffuse or "white-sky albedo") for the first seven spectral bands of MODIS and three broad bands of interest to modelers. The parameters are also used to obtain the Nadir BRDF-Adjusted surface Reflectances (NBAR) for the seven spectral bands (at the mean solar zenith angle of the period). The quality of these products is currently being evaluated by the MODIS science team and validation scientists.

**Corresponding author address*: Crystal Schaaf, Department of Geography, Boston University, 675 Commonwealth Ave, Boston,MA 02215; email: schaaf@bu.edu.

2. PROTOTYPING with AVHRR

Prior to launch, the operational MODIS BRDF/Albedo algorithm was tested with multidate AVHRR data to see if consistent BRDF parameters and albedos could be produced that reflected the true phenological cycles of the underlying surface. A sequence of over 4 months of daily AVHRR data of New England from July to October 1995 were used for this prototyping exercise. The daily data were broken into 16 day periods, and laboriously calibrated, geolocated, and cloud cleared following the methods described in (d'Entremont et al.,1999). The data were then atmospherically corrected using the 6S code (Vermote et al,1997a;b) with standard atmospheres and visibility information from the eleven meteorological stations in the region. The data were finally transformed into the ISG projection and formatted to simulate a MODIS input tile (with, of course, only the two solar spectral channels that are available from the AVHRR). BRDF parameters were retrieved for each pixel in the scene and used to obtain albedo and nadir reflectance measures. The resulting red and NIR spectral white-sky albedos obtained over the latter portion of the period are displayed in Figure 1. Over the summer months, the values remained fairly consistent with higher NIR (and lower red) albedos occurring over the forested portions of Vermont, New Hampshire and New York and lower NIR (and higher red) spectral values occurring over the urban and suburban areas. However, a change is seen sweeping over the scenes as autumn (late September) approaches, with the northern areas producing increased red spectral albedos as the deciduous forests senesce into a typically spectacular New

England fall with peak colors on October 8th and then abruptly changing to high red (and low NIR) values as the region experiences leaf drop a week later.

3. OPERATIONAL MODIS PRODUCTS

As MODIS Terra operationally captured the New England autumn September – October 2000, a companion series of white-sky albedo images were produced (Figure 2). During this period, the data products were available to the public as beta products. A full aerosol correction was not yet being applied to the data and a uniform default optical depth was used globally. Despite these obvious limitations, Figure 2 indicates that the MODIS derived albedos captured the senescence of the predominantly deciduous and mixed forests of the region. Foliage color peaked on October 20th in 2000 and leaf drop had occurred by October 26th (slightly later than in 1995). Note the slightly higher albedo values (~5%) which are attributed to the poor aerosol correction used with the MODIS beta products and the differences in channel width between MODIS and AVHRR.

4. SUMMARY

While the results discussed are only from a small regional study, they are representative of the temporal consistency of the MODIS BRDF/Albedo products. Six months worth of Nadir BRDF-Adjusted Reflectances have already been used to produce the first provisional MODIS Land Cover product (Friedl et al., 2000). Furthermore, the BRDF/Albedo global products from November 2000 onward are currently being reprocessed to obtain a consistent year running from November 2000 through October 2001. This will allow us to more accurately capture annual phenological cycles across the globe and monitor the greenup and the senescence of various deciduous vegetation canopies. Active field validation programs are currently underway at the Beltsville Agricultural Research Center (BARC) in Maryland, at the Barton Bendish agricultural site in East Anglia, at the Mongu, Zambia woodland site and the Skukuza, South Africa savanna site (both part of the Southern African Regional Science Initiative – SAFARI), and at the Liangchen, Shunyi and Yucheng agricultural sites in China.

5. REFERENCES

d'Entremont, R. E., C. L. Barker Schaaf, W. Lucht, and A. H. Strahler, 1999: Retrieval of red spectral albedo and bidirectional reflectance using AVHRR HRPT and GOES satellite observations of the New England region, J. Geophys. Res., **D-104**, 6229-6239.

Friedl, M., Muchoney, D., McIver, D., Gao, F., Hodges, J., and Strahler, A., 2000: Characterization of North American Land Cover from NOAA-AVHRR Data Using the EOS- MODIS Land Cover Classification Algorithm. Geophys. Res. Let., **27**, 977-980.

Lucht, W., C.B. Schaaf, and A.H. Strahler, 2000: An Algorithm for the retrieval of albedo from space using semiempirical BRDF models, IEEE Trans.Geosci. Remote Sens., **38,** 977-998.

Vermote, E. F., N. El Saleous, C. O. Justice, Y. F. Kaufman, J. L. Privette, L. Remer, J. C. Roger, and D. Tanre, 1997a:, Atmospheric correction of visible to middle infrared EOS-MODIS data over land surfaces: Background, operational algorithm, and validation, J. Geophys. Res., **D-102**, 17131-17141.

Vermote, E. F., D. Tanre, J. L. Deuze, M. Herman, and J. J. Morcrette, Second simulation of the satellite signal in the solar spectrum: an overview,1997b: IEEE Trans. Geosci. Remote Sens., **35**, 675-686.

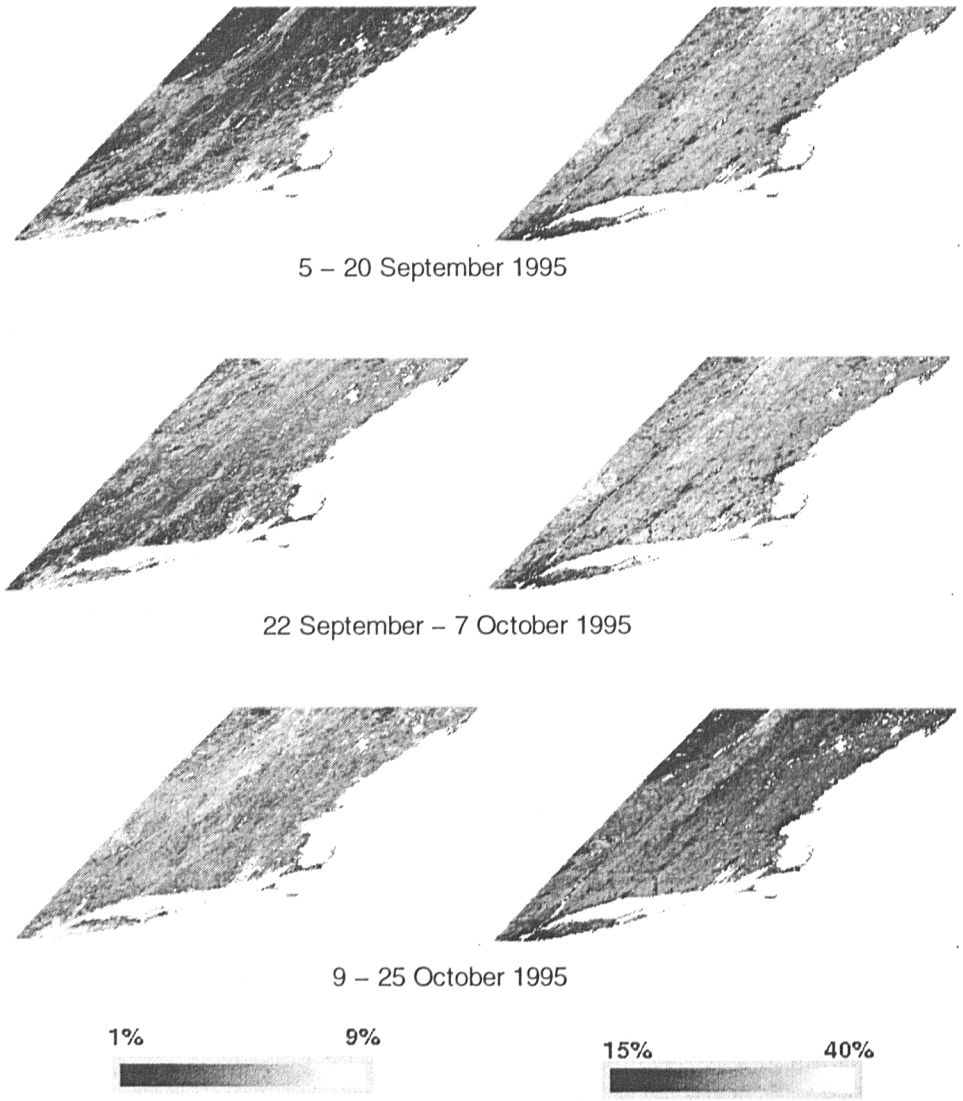

Figure 1. NOAA AVHRR red band (left) and NIR band (right) spectral white–sky albedo for New England during autumn 1995.

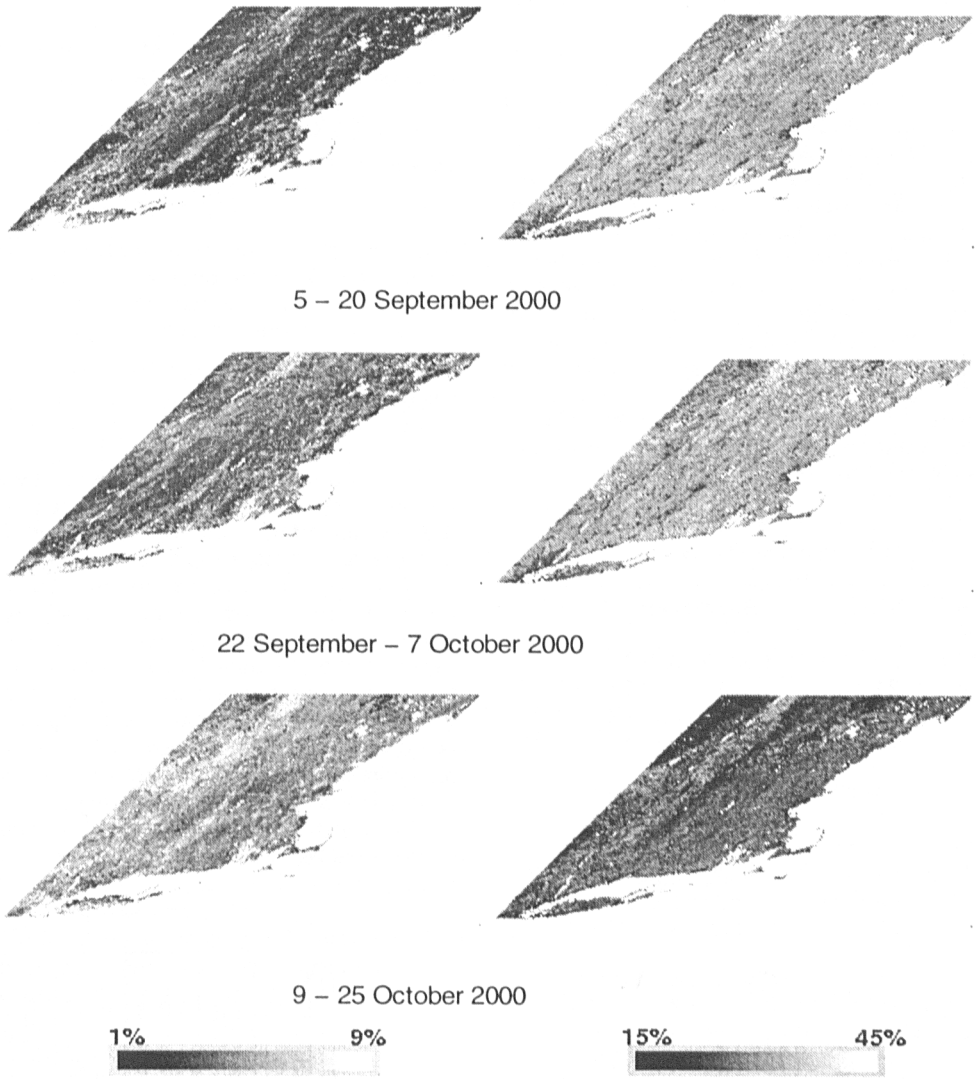

Figure 2. Terra MODIS red band (left) and NIR band (right) spectral white–sky albedo for New England during autumn 2000.

P5.22

MODIS STATISTICAL STRUCTURE FUNCTION ANALYSIS

Tomoko Koyama*, Donald W. Hillger, and Thomas H. Vonder Haar
Cooperative Institute for Research in the Atmosphere/Department of Atmospheric Science
Colorado State University, Fort Collins, Colorado

1. Introduction

The Moderate Resolution Imaging Spectroradiometer (MODIS) is the key instrument aboard the Terra (EOS AM-1) satellite. Terra MODIS views the entire Earth's surface every 1 to 2 days, acquiring data in 36 spectral bands (0.4 μm - 14.5 μm). It not only has more bands than the heritage instruments like the AVHRR or the HIRS, but also better resolution such as 250, 500 and 1000 m at nadir. It provides key observations important to study of atmosphere, oceans, and land surfaces with emphasis on interactions between each of the systems. The goal of this study is to estimate noise levels of the MODIS Thermal Emissive Bands (TEB) using spatial structure analysis. The target bands are bands 20 to 36 except band 26 (see Table 1 below).

TABLE 1
MODIS Spectral Bands

Primary Use	Band	Bandwidth (μm)
Surface/Cloud	20	3.8819 - 3.6915
Temperature	21	4.0343 - 3.9505
	22	4.0158 - 3.9287
	23	4.1008 - 4.0139
Atmospheric	24	4.5191 - 4.4280
Temperature	25	4.5921 - 4.4999
Water Vapor	27	6.8868 - 6.6461
	28	7.5078 - 7.1831
	29	8.7066 - 8.3574
Ozone	30	9.8956 - 9.5946
Surface/Cloud	31	11.2797 - 10.7591
Temperature	32	12.3009 - 11.7779
Cloud Top	33	13.5217 -13.2127
Altitude	34	13.8475 -13.5217
	35	14.0795 - 13.7504
	36	14.3421 - 14.0558

2. Methodology

Statistical structure function was used by Gandin (1963) in an objective analysis technique.

*Corresponding author address: Tomoko Koyama, Dept. of Atmospheric Science, Colorado State University, Fort Collins, CO 80523;
e-mail: koyama@cira.colostate.edu

The structure function (STR) of quantity f at each of the two points $\hat{r}_1$ and $\hat{r}_2$ is given by:

$$STR(\hat{r}_1,\hat{r}_2) = N^{-1}\sum\left[f'(\hat{r}_1) - f'(\hat{r}_2)\right]^2$$

where

$$f'(\hat{r}) = f(\hat{r}) - \bar{f}(\hat{r})$$

and $\bar{f}$ is the mean over time for N observations at each point. This function approaches twice the inherent variance of the measuring system as the data separation approaches zero.

$$STR(\rho = 0) = 2\sigma^2$$

When scalar separation distance can be expressed as:

$$\rho = \left|\hat{r}_1 - \hat{r}_2\right|$$

Estimates of STR(0) can be obtained by extrapolating the structure values to zero separation, and structure-derived uncertainties as a result do not included any type of bias or systematic error.

For the error estimation, two assumptions are required, no cloud contaminated and spatially homogeneous field. When these conditions are satisfied, the structure function will be independent of the position and orientation of the pair of observations. Each 1-km resolution band has a ten-element linear detector array. Thus, along line (Track-direction) analysis shows a single detector performance, whereas along element (Scan-direction) gives us structure values of the entire array of detectors for each band (see Figure 1 below).

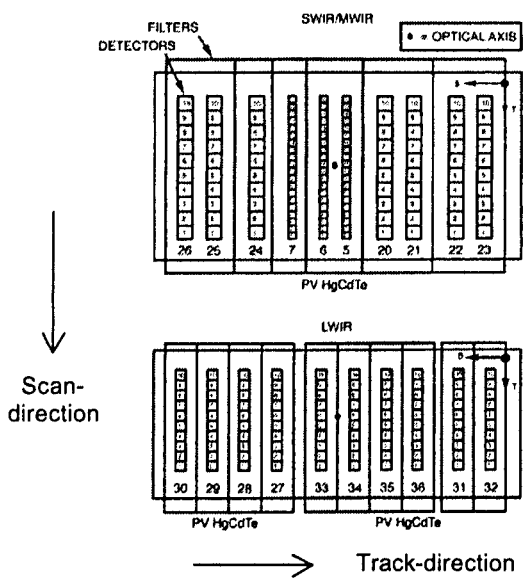

Figure 1. Focal plane

3. Data

Two data products of MODIS are used in this study.

3.1 Calibrated radiances1 km (MOD021KM)

Three "Calibrated radiances 1 km" datasets are used for this study. They contain calibrated and geolocated radiances for 36 bands generated from MODIS Level 1A sensor counts. They are generated and distributed from NASA/GSFC and the target bands have 1-km resolution at nadir. Several cloud-free areas (51 x 51 grid size) for the structure function analysis from each data set were determined on a McIDAS system. Cloud clearing was performed manually using all bands.

3.2 Cloud mask (MOD35_L2)

Because different cloud types reflect and emit radiant energy differently, we can use MODIS' unique data set to distinguish between water, snow, and ice clouds. To satisfy the assumption for the structure function analysis, cloud mask product is used as ancillary information. MODIS cloud mask is more than a simple yes/no decision. Only two flags from the cloud mask product are used in this study. The first one identifies the algorithm success, and the second one describes the cloud obstruction.

Figure 2 shows statistical information of one analysis area (51 x 51 grids), mean equivalent blackbody temperature and its standard deviation. Solid lines show the whole coverage results, and the other lines show one-dimensional results having the same center position. Percentages in the legend are confident/probably clear grid ratio derived from the cloud mask product. A homogeneous and uniform observation field is required for the structure function analysis; on the other hand, a real observation field will never achieve such a perfect condition. However, the variability of this scene is small enough and standard deviations could be regarded as the maximum errors of the analyzed region.

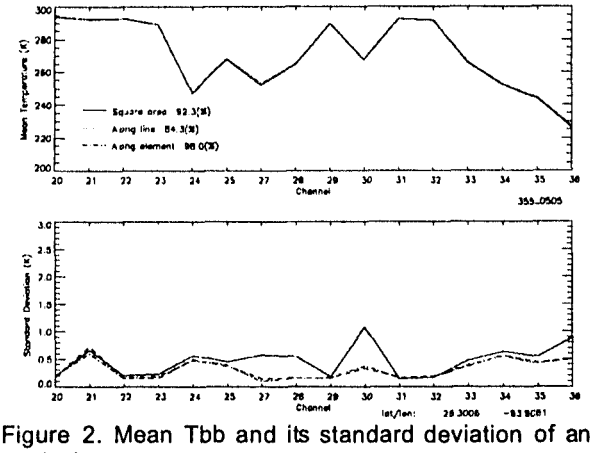

Figure 2. Mean Tbb and its standard deviation of an analysis area

4. Trade-off problem – Extrapolating the structure function

It is critical to find a fitted function to extrapolate the structure function to zero distance for the error evaluation. The coefficient of determination (C.O.D.) as an indicator is introduced to get appropriate estimations in this study. The C.O.D. varies from 0 to 1 and reveals how closely the trend line fits to the actual data. By decreasing the spatial sampling area, a trend line fits to observations better. Therefore, there is a trade-off problem to extrapolate the structure value at zero separation distance to determine error values:

- Does the trend line fit to the observation points well?
- Does the fitted curve show the inherence of the whole analysis area sufficiently?

Figure 3 shows three kinds of fitting curves (polynomial functions) as the result of six different C.O.D.s as the thresholds. The black points in the following figures are the structure function values for a case of the band 31, Track-direction analysis. Also, solid, dotted, and dashed lines show the second, the third, and the fourth order polynomials respectively. From the figures, we can see higher C.O.D. as a threshold can give us more uniform error estimation. The numbers that appears in the upper left part of the graphs are the number of points that were used to achieve the C.O.D. from left to right, the numbers correspond to the second, third and fourth order polynomials, respectively.

5. What makes the error bigger?

Because of the MODIS design, striped images can be found on several band's scenes, which would affect the result of Scan-direction analysis. This effect could be caused by:

1) Non-Functioning Detectors
2) Incomplete knowledge of sensor response across scan Thermal Emissive Bands (bands 20-36, except band 26)
3) Non-uniform channel to channel response within a band (bands 20-25)

and so on. Also, radiance error might exist due to Optical cross-talk from band 31 into band 32 through 36 optical leak causes scattering off a spectral filter edge. For the difference between Scan-direction and Track-direction analyses, we have to consider characterization of the instrument spatial response profile or line spread function (LSF), causing image blur with most bands (See Figure 4).

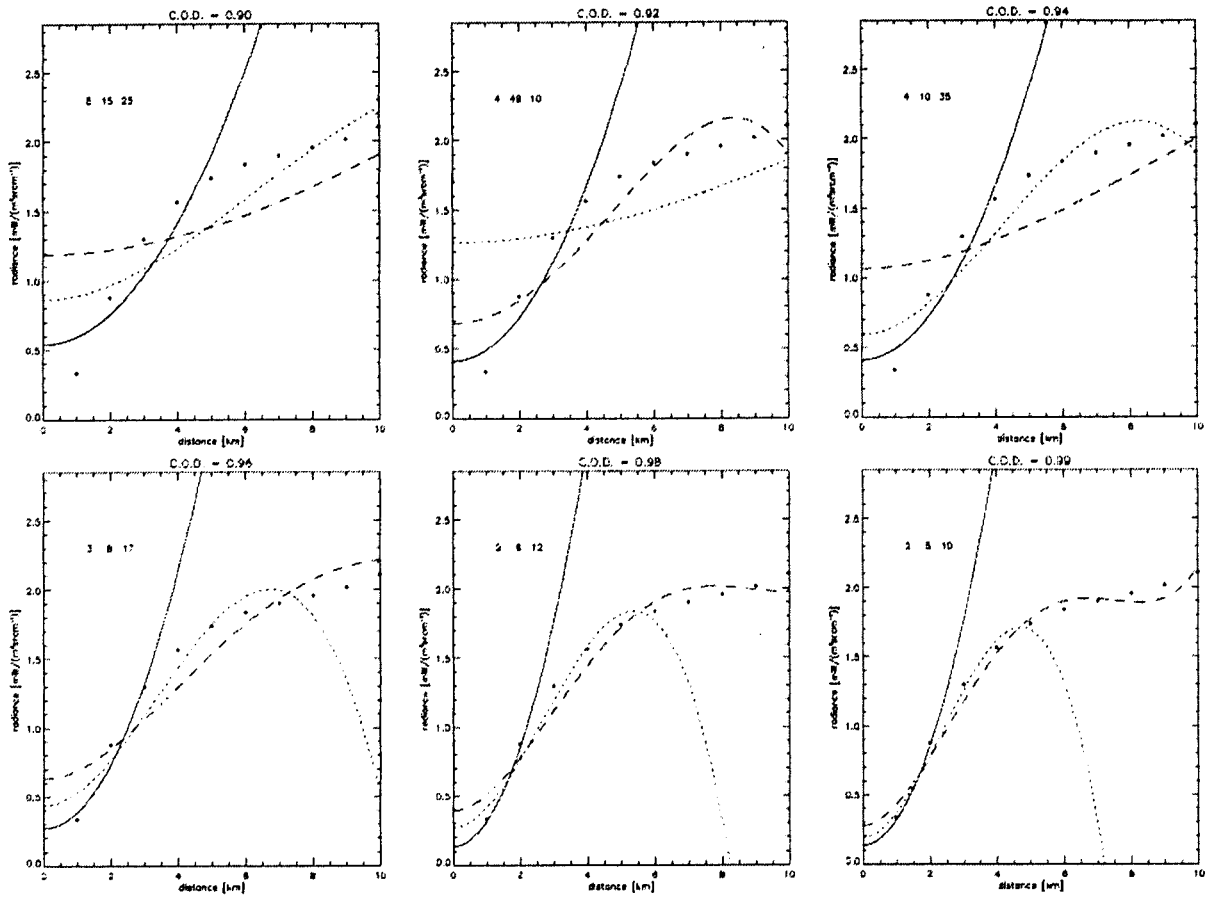

Figure 3. Structure function values and the fitting curves by different C.O.D.s

6. Preliminary results

Table 2 shows Noise-equivalent temperature difference (NE?T) values of the pre-launch study and those derived from the structure function analysis. "Spec" column shows the required MODIS sensitivities, and "Line" and "Element" are the results from Track-direction and Scan-direction analysis respectively. "Pre-launch" testing program was executed on the MODIS Protoflight Model (PFM). Those values are estimates taken from channel 5 (the fifth detector, in the middle of each ten detector array) of each band. Thus, the NE?T values do not include the effects of striping.

The two values of "Line" and "Element" columns show the minimum and the maximum values of the 6 smallest values from 60 case studies. Due to the digitization limit, there are unavoidable errors at the asterisked 0.000. But they are very small numbers (.0001 - .0062 K, assuming typical Earth scene for each band). Shadowed boxes are "striped" images recognized evidently.

In general, the shorter wavelength bands show larger errors than the pre-launch values. There are several reasons that cause the uncertainty as mentioned before. However, the attraction of this technique is that it does not require comparisons with another data source to estimate errors.

7. Acknowledgement

Mr. Chris Moeller at CIMSS, University of Wisconsin provided McIDAS formatted MODIS Calibrated radiances 1km and useful information about the research. This work was supported by NOAA Grant NA17RJ122B.

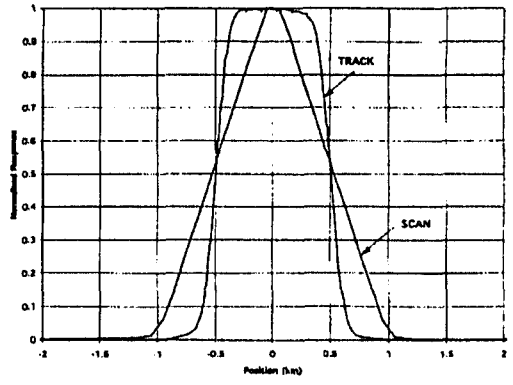

(a)

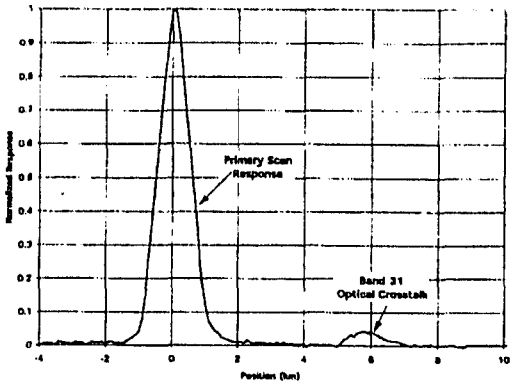

(b)

Figure 4. Typical LSF's for MODIS. (a) Band 10, channel 6. (b) Band 35 has a ~5% leak in the region of band 31 in the scan direction.

8. References

Ackerman, S. A., K. I. Strabala, W.P. Menzel, R. A. Fray, C.C. Moeller, and L. E. Gumley, 1998: Discriminating clear sky from clouds with MODIS. J. Geophys. Res., 103, 32141-32157.

Barnes, W. L., T. S. Pagano, and V.V. Salomonson, 1998: Prelaunch characteristics of the Moderate Resolution Imaging Spectroradiometer (MODIS) on EOS-AM1. IEEE Trans. Geosci. Remote Sensing, 36, 1088-1100.

Gandin, L.S., 1963: Objective analysis of meteorological fields. Translated from Russian, Israel Program for Scientific Translation, Jerusalem, 242pp.

Hillger, D.W., and T. H. Vonder Haar, 1979: An analysis of satellite infrared soundings at the mesoscale using statistical structure and correlation functions. J.Atmos. Sci., 36, 287-305.

Hillger, D.W., and T. H. Vonder Haar, 1988: Estimating noise levels of remotely sensed measurements from satellites using spatial structure analysis. J. Atmos. Ocean. Tech., 5, 206-214.

MCST, 2000: MODIS Level 1b Product User's Guide. MCST Document #MCM-PUG-o1-U-DNCN

9. World Wide Web links

MODIS Web page:
http://ltpwww.gsfc.nasa.gov/MODIS/MODIS.html
MODIS Characterization Support Team (MCST):
http://mcstweb.gsfc.nasa.gov/
DAAC Data Sets:
http://eosdata.gsfc.nasa.gov/data/dataset/index.html

Table 2

NE?T comparison (K)

Band	Spec	Line	Element	Pre-launch
20	0.05	0.260 ~ 0.415	0.248 ~ 0.401	0.027
21	2.00	0.336 ~ 0.520	0.405 ~ 0.617	0.155
22	0.07	0.246 ~ 0.405	0.280 ~ 0.405	0.027
23	0.07	0.215 ~ 0.363	0.249 ~ 0.382	0.025
24	0.25	0.054 ~ 0.112	0.000* ~ 0.099	0.126
25	0.25	0.129 ~ 0.212	0.000* ~ 0.163	0.060
27	0.25	0.011 ~ 0.054	0.100 ~ 0.147	0.097
28	0.25	0.010 ~ 0.162	0.000* ~ 0.131	0.043
29	0.05	0.150 ~ 0.363	0.000* ~ 0.298	0.020
30	0.25	0.113 ~ 0.205	0.200 ~ 0.448	0.086
31	0.05	0.151 ~ 0.392	0.000* ~ 0.331	0.026
32	0.05	0.135 ~ 0.387	0.000* ~ 0.381	0.039
33	0.25	0.097 ~ 0.217	0.198 ~ 0.348	0.135
34	0.25	0.081 ~ 0.133	0.099 ~ 0.139	0.200
35	0.25	0.082 ~ 0.121	0.108 ~ 0.126	0.232
36	0.35	0.000* ~ 0.148	0.181 ~ 0.223	0.457

P5.23
Simulation of GOES-M 5-band Imager Using MODIS Data For Volcanic Ash

Donald W. Hillger*
NOAA/NESDIS/ORA/RAMMT
CIRA / Colorado State University
Fort Collins CO

James Clark
NOAA/NESDIS/OSDPD/SSD
Satellite Analysis Branch
Camp Spring MD

1. Introduction

The next three satellites in the GOES series, GOES-M through O, with the first to be launched in 2001, will have slightly-changed Imager instruments, with a new band at 13.3 μm (Schmit et al 2001). The new band was introduced to improve cloud height determinations. Unfortunately this band is not an additional band. Instead, it replaces the 12.0 μm band currently used, along with the GOES longwave infrared band at 11 μm, to identify volcanic ash. This technique was pioneered by Prata (1989), but has been applied by many (Oppenheimer 1998; Ellrod et al 2001).

To simulate the effect of the new band on usage of GOES for volcanic ash detection, selected bands of Moderate Resolution Imaging Spectroradiometer (MODIS) data were used. Table 1 lists the GOES Imager band number arrangement. The new 13.3 μm band will be called band 6 even on the new 5-band arrangement (bands 1 through 4 and 6). The current 12.0 μm band will continue to be called band 5, to avoid confusion between band numbers on current and new versions of the GOES Imager.

Table 1: Simulation of GOES-M Imager using MODIS bands

GOES Imager		MODIS	
Band number	Central wavelength (μm)	Band number	Central wavelength (μm)
1	0.65	1	0.645
2	3.9	22	3.96
3	6.7	27	6.7
4	10.7	31	11.0
5	12.0	32	12.0
6	13.3	33	13.3

Table 1 also lists the MODIS bands that correspond to the six bands available between the two versions of the GOES Imager. MODIS contains 36 bands, and six of those bands have central wavelengths that correspond to the six GOES bands (bands 1, 22, 27, 31, 32, and 33 respectively). In general the MODIS bandwidths are narrower than those of the equivalent GOES bands, but simulating both the current and new bands using MODIS minimizes any differences this may cause.

2. Analysis Using Principal Components

To determine the effect of the change from band 5 to band 6 on GOES-M, that band was substituted into a volcanic ash product used operationally by the Washington Volcanic Ash Advisory Center (VAAC). That product consists of Principal Component Image (PCI) analysis of the three GOES thermal infrared bands (bands 2, 4, and 5). PCI analysis creates images that explain all of the variance in the original bands by separating the common from the difference information in the original bands (Hillger* 1996; Hillger and Ellrod 2001). PCI-1 contains the common signal from the three GOES bands that are input, generally cloud/no-cloud information. The band 2/4 (shortwave/longwave) difference usually seen in PCI-2 is useful for detecting volcanic hot spots, and the band 4/5 (split window) difference usually seen in PCI-3 is good for detecting volcanic ash.

Two test versions of the PCIs were generated, one using simulated current-GOES bands 2, 4, and 5;

* Corresponding author address: Dr. Donald W. Hillger, NOAA/NESDIS/RAMMT, CIRA/Colorado State University, Fort Collins CO 80523-1375. E-mail: hillger@cira.colostate.edu

and the other using simulated GOES-M bands 2, 4, and 6. The case for this study was a large eruption of ash on 20 December 2000 from the Popocatepetl volcano (hereafter abbreviated Popo, 19.02°N, 98.62°W) at 5426 m elevation near Mexico City. For this case MODIS data were available at 1715 UTC from the polar-orbiting EOS AM-1/Terra satellite. The MODIS data were analyzed at 2 km spatial resolution (at nadir) and afterward remapped into a GOES projection at 4 km resolution to match the ash analyses that are available for verification.

Figure 1 is an analysis issued by the Washington VAAC (Operations 1999) giving the extent of the ash plume based on GOES multi-spectral imagery for 1715 UTC. This analysis time matches the time of the MODIS imagery that was analyzed using PCIs. The ash extends mainly east and south of the volcanic source, to as far away as the Yucatan Peninsula. In the ash analysis the plume is given in two parts, at different flight levels (FL250 [25,000 ft / 7600 m] and FL320 [32,000 ft / 9800 m]). These levels were estimated by effectively matching the derived vector motion of the ash as seen in GOES imagery to the appropriate height levels from the Mexico City upper-air sounding and a model sounding. The extent of the ash in this analysis is a guide for the simulated GOES analyses to follow.

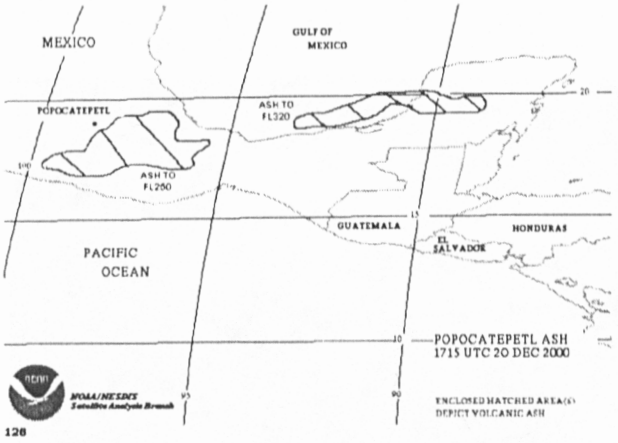

Figure 1: Volcanic ash analysis for 1715 UTC on 20 December 2000 for Popocatepetl volcano near Mexico City. Analysis based on GOES multi-spectral imagery by the Satellite Analysis Branch (SAB) Washington VAAC.

There was no volcanic hot spot detected for Popo for this case since clouds obscured the volcanic vent. Otherwise PCI-2 is often effective for detecting hot spots or thermal anomalies. Since PCI-2 is generally a longwave vs. shortwave band difference, the change from band 5 to band 6 does not cause a significant change in this PCI. Similarly PCI-1, since it shows the overall cloud setting common to all three infrared bands (and not any of the volcanic features that are often seen only in image differences), does not change much. Therefore the remainder of the discussion will focus on PCI-3, a product that will change primarily from a band 4/5 difference to a band 4/6 difference, with much less contribution from GOES band 2.

Figure 2 contains PCI-3 as it is now available from a simulation of current GOES Imager bands 2, 4, and 5. This multi-spectral image product generally depicts the volcanic ash very well. Ash is seen as white, in contrast to the image background and other image features. The ash is concentrated mainly to the east and southeast of Popo where there is a maximum in the ash signal. A secondary maximum exists to the east over the Yucatan Peninsula. Some ash can be seen connecting the two maxima, but that ash has much less contrast to the background of the image.

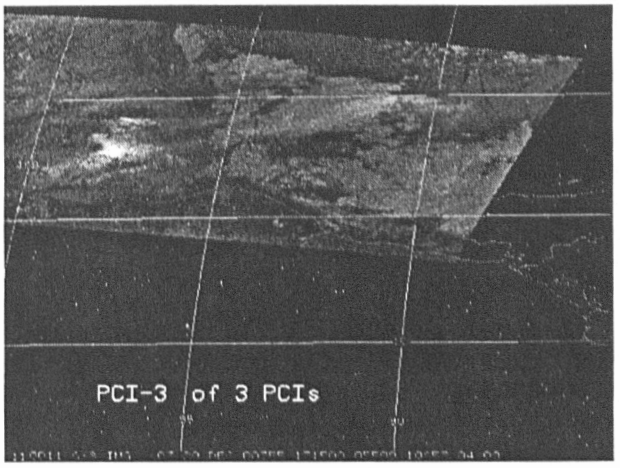

Figure 2: PCI-3 of three PCIs that were generated from a simulation of the three thermal infrared bands of GOES-8 through 11 (bands 2, 4, and 5) using MODIS data for 1715 UTC on 20 December 2000 over Popocatepetl volcano near Mexico City. PCI-3 shows the ash plume as white by heavily utilizing GOES band 5.

For comparison, Figure 3 is PCI-3 generated from simulated GOES bands 2, 4, and 6 in place of bands 2, 4, and 5 used in Figure 2. In this figure the densest part of the ash plume can still be seen east and south of Popo, including ash at the far eastward extent over the Yucatan. However, the immediate difference compared to the current version of PCI-3 in Figure 2 is the lessened contrast of the ash to the image background and the more significant contribution from clouds. These cloud features tend to obscure the ash

plume except at locations where the ash concentration is the greatest. The secondary maximum east off the coast of Yucatan easily seen in Figure 2 is hard to discern in this new image due to low clouds underlying the ash. This cloud contamination is a major drawback to this three-band product with the change in bands planned for GOES-M.

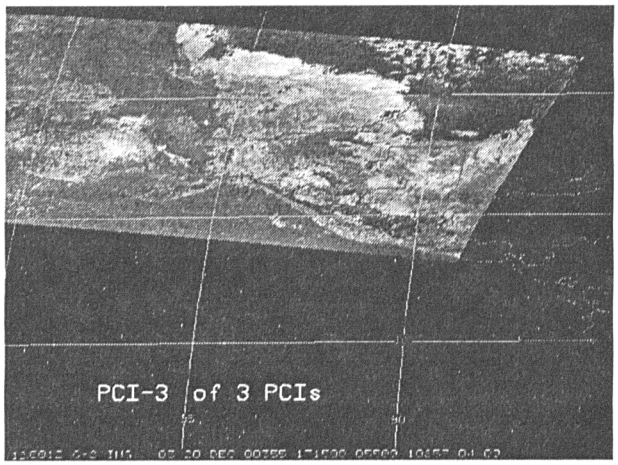

Figure 3: Same as Figure 2 except generated from a simulation of the three thermal infrared bands of GOES-M through O (bands 2, 4, and 6). PCI-3 shows only the parts of the ash plume where the ash is most concentrated, when compared to the current version of PCI-3 in Figure 2, and also suffers from contamination by low clouds.

In an attempt to isolate the cloud problem, the contributions of the bands to the current and new versions of the three-band product will be examined. Table 2 gives the contributions of the GOES bands to the PCIs for both current and new simulations of this volcanic ash case. In the new version of PCI-3, band 2 contributes 11% of the explained variance, compared to approximately 0% for the current version of PCI-3. If it is assumed that the cloud contamination is due to the increased contribution from GOES band 2 in PCI-3, the immediate thought for fixing the cloud contamination is to eliminate band 2 from the analysis to generate a two-band (band 4/6) difference image that may not suffer from this low-cloud contamination. The reasoning is that PCI-3 generated from current GOES bands 2, 4, and 5 is basically a two-band difference with little or no contribution from GOES band 2. When generated, the two-band difference is nearly identical to PCI-3 in Figure 2 and is therefore not shown.

Figure 4 is a two-band difference generated from simulated bands 4 and 6. This image product shows the ash plume only very faintly southeast of Popo where the ash concentration is the greatest. The two-band difference is not as good for ash detection as the three-band product in this case and continues to have significant cloud contamination. The clouds therefore are not due to the contribution from band 2, but are inherent in the difference between bands 4 and 6. Band 6 was added to detect clouds, the kind that are contaminating both the two-band and the three-band products in attempts to see volcanic ash. That cloud signal comes at the expense of detection of ash that is easily accomplished with the current split window bands. It is at least some consolation that PCI-3 generated from the new combination of bands (Figure 3), although inferior for ash detection to PCI-3 generated from the current combination of bands (Figure 2), is far superior to a two-band difference that uses the new band 6 (Figure 4).

Table 2: Contributions of MODIS-simulated GOES infrared bands to PCIs used for Volcanic Ash Detection

PCI	GOES-8 through 11 bands			GOES-M through O bands		
	Explained Variance (%) and Sign (negative contributions in parentheses) of GOES Band Contributions					
	2	4	5	2	4	6
1	46	26	27	37	22	41
2	54	(20)	(26)	52	~0	(48)
3	(~0)	**53**	**(47)**	(11)	**78**	(11)

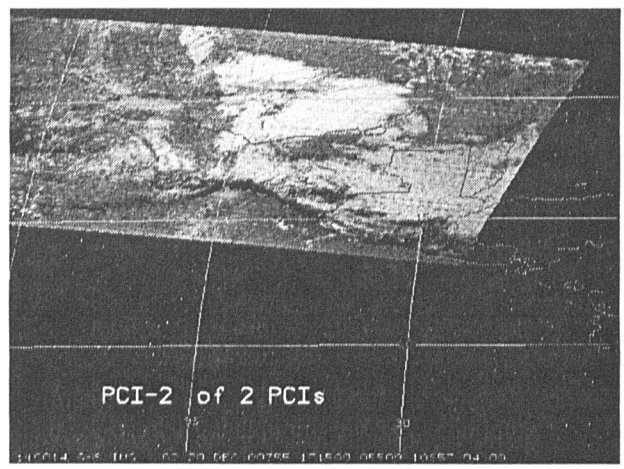

Figure 4: A two-band (band 4/6) difference image generated from a simulation of the two longwave infrared bands of GOES-M through O using MODIS data for 1715 UTC on 20 December 2000 over Popocatepetl volcano near Mexico City. This image product is far inferior for volcanic ash detection compared to the three-band product in Figure 3.

3. Summary and Conclusions

This study provided a simulated case using MODIS data where a two-band volcanic ash product (when differenced with GOES band 4) is not suitable for ash detection with the new GOES-M band 6 substituted for the current-GOES band 5. Rather, a three-band product of GOES-M bands 2, 4, and 6 depicts the ash plume better, although not as well as a similar three-band product generated from the current set of GOES infrared bands. The choice for the ash analyst is to either generate PCIs directly from the new set of GOES-M thermal infrared bands or utilize similarly-configured combinations of the three bands, as suggested by the assessed contributions of the bands to PCI-3. However the main drawback of the new band 6 remains, a greatly increased chance of contamination by clouds that can obscure the extent of the ash plume, causing decreased ability to monitor diffuse ash and increased chance of false ash detection.

Acknowledgements

The MODIS data for this study were provided by Chris Moeller of the CIMSS at the University of Wisconsin in Madison. Funding for this study is made available through NOAA Grant NA67RJ0152.

4. References

Ellrod, G.P., B.H. Connell, and D.W. Hillger, 2001: Improved volcanic ash detection using multi-spectral infrared satellite data. Submitted to *Journal of Geophysical Research: Solid Earth.*

Hillger, D.W., 1996: Meteorological analysis using principal component image transformation of GOES imagery. *International Radiation Symposium - IRS'96: Current Problems in Atmospheric Radiation,* (W.L. Smith and K. Stamnes, Editors; A. Deepak Publishing), 19-24 August, Fairbanks AK, 480-483.

Hillger, D.W., and G.P. Ellrod, 2001: Detection of unusual atmospheric and surface features by employing Principal Component Image transformation of GOES imagery, *Tenth Conference on Satellite Meteorology and Oceanography*, AMS, 9-14 January, Long Beach CA, 461-464.

Oppenheimer, C., 1998: Volcanological applications of meteorological satellites, *International Journal of Remote Sensing*, 19, 2829-2864.

Operations of the Washington Volcanic Ash Advisory Center, 1999: *Third Caribbean/South American Regional Air Navigation Meeting,* International Civil Aviation Organization, October 05-15, 5-p.

Prata, A.J., 1989: Observations of volcanic ash clouds in the 10-12 μm window using AVHRR/2 data, *International Journal of Remote Sensing*, 10, 751-761.

Schmit, T.J., E.M. Prins, A.J. Schreiner, and J.J. Gurka, 2001: Introducing the GOES-M Imager, Submitted to *National Weather Association Digest.*

P5.26

CORRELATED NOISE MODELING FOR SATELLITE RADIANCE SIMULATION

Thomas J. Kleespies *
David Crosby
NOAA/NESDIS, Camp Springs, Maryland

1. INTRODUCTION

This work is motivated by an Observing Systems Simulation Experiment in which NESDIS is collaborating with NCEP/EMC and the NASA Data Assimilation Office. The immediate goal is to determine the incremental improvement on the forecast of a Doppler Wind Lidar instrument over present day observing systems. In order for the current satellite instruments to be accurately simulated, it is necessary to model instrument noise, both independent and correlated. This paper presents such a method, and notes a high level of correlation in the inter channel noise in one of the High Resolution Infrared Sounder (HIRS) instruments.

2. METHODOLOGY

A number of standard methods of modeling correlated noise are available. We chose one such method presented in Searle (1982). Let S be the sample covariance matrix from the measured noise, then the vector of simulated correlated noise is given by

$$Y = G\sqrt{\Lambda}X \qquad 1)$$

where G is the eigenvectors of S, $\sqrt{\Lambda}$ is a matrix whose diagonal is composed of the square root of the eigenvalues of S, X is a vector of gaussian random numbers with mean 0 and variance 1 .

* *Corresponding author address:* Thomas J. Kleespies, E/RA1 Room 810 WWB, NOAA/NESDIS, 5200 Auth Road, Camp Springs MD 20746; email: Thomas.J.Kleespies@noaa.gov

The sample of the measured noise is from HIRS space calibration observations for an entire day. An example of inter channel noise correlation for NOAA 11 is given in figure 1, which is the scatter diagram of channel 10 versus channel 15 space looks.

The gaussian random numbers are computed using Box and Muller (1958),

$$x = (-2\ln U_1)^{1/2}\cos(2\pi U_2) \qquad 2)$$

where U_1 and U_2 are numbers drawn from a uniform random distribution. We used the FORTRAN RAN function for this purpose. A realization of size 100,000 was applied and the inter channel correlation coefficients were computed. Results for selected channel pairs are presented in Table 1.

3. CONCLUSIONS

We have presented a method for simulating correlated noise and applied it to radiances from the NOAA 11 HIRS instruments. This method accurately reproduces the observed correlation structure. The NOAA 11 HIRS exhibits inter channel noise correlations that approach 0.5 . This fact has implications for the use of off diagonal elements in the observational error covariance matrix used in variational data assimilation.

4. REFERENCES

Box, G. E. P. and M. E. Muller, 1958: A note on the generation of random normal deviates. Annals of Mathematical Statistics, 29, pp 610-611.

Searle, S. R., 1982: Matrix Algebra Useful for Statistics, Ch. 13, Wiley&Sons.

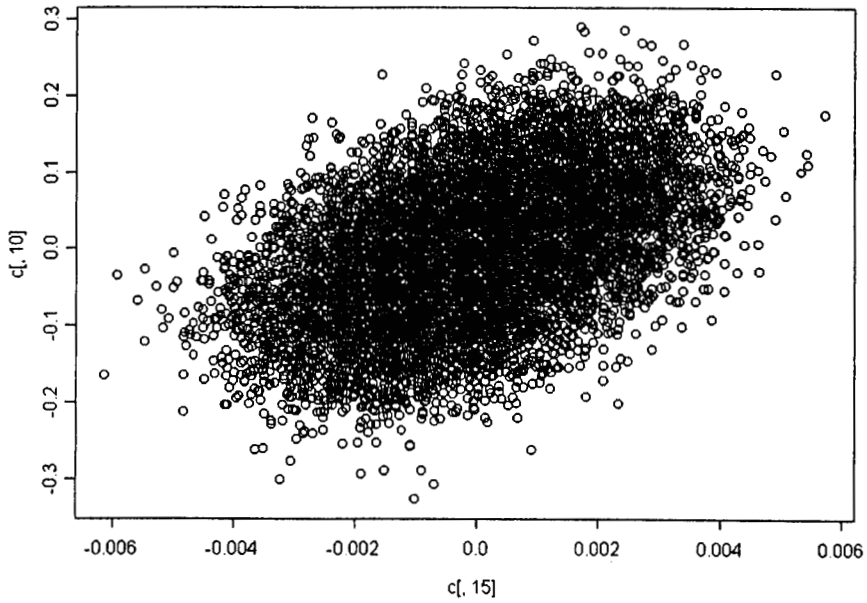

Figure 1. HIRS 11 Space calibration radiances, Ch 10 versus Ch 15, n=16032, r=.492 units are mw /(cm^2 sr cm^{-1})

NOAA 11 N=100000 Chan	Chan	Observed r	Simulated r
6	4	0.487	0.481
9	2	0.408	0.410
9	8	0.428	0.430
11	5	0.483	0.481
11	8	-0.409	-0.413
12	10	-0.434	-0.436
13	4	-0.417	-0.418
14	10	-0.438	-0.438
14	11	0.475	0.474
15	10	0.492	0.495
15	11	-0.417	-0.416
15	14	-0.462	-0.464
17	4	0.416	0.415
17	13	-0.411	-0.411

Table 1. Correlation coefficient for selected channels of NOAA 11 HIRS observed and simulated space calibration observations.

P5.27 CERES/ARM VALIDATION EXPERIMENT (CAVE)

David A. Rutan[1], Fred G. Rose[1], Natividad Smith[1], and Thomas P. Charlock[2]
1. Analytical Services & Materials Inc., Hampton VA
2. NASA Langley Research Center, Atmospheric Sciences Competency, Hampton, VA

1. Introduction

The Clouds and the Earth's Radiant Energy System (CERES) project (Wielicki et al. 1996) is a series of broadband scanning radiometers measuring total (0.3-∞ μ m), reflected (0.3-5.0 μ m), and window (8-12 μ m) energy. The instruments, on board the Tropical Rainfall Measurement Mission (TRMM) and Earth Observing System (EOS) Terra and Aqua satellites, measure radiation at the Top Of the Atmosphere (TOA). Another goal of CERES is to compute the Surface and Atmospheric Radiation Budget (SARB) of the vertical column for each footprint. Inputs for these calculations include cloud optical properties (determined by higher resolution imagers), atmospheric profiles of pressure, temperature, relative humidity (ECMWF), ozone (NCEP), and a characterization of the column loading of aerosols by a chemical transport model that assimilates aerosol sources and sinks (Collins et al., 2001). With these inputs and global maps estimating spectral variation of surface albedo and emissivity (see: http://tanalo.larc.nasa.gov:8080/surf_htmls/SARB_surf.html), a modified 1-D radiative transfer code (Fu & Liou, 1993), (on line at: http://srbsun.larc.nasa.gov/flp0300/) computes broadband shortwave (SW), longwave (LW), and window IR fluxes within the atmosphere. Given the large number of input variables, the global scope of the problem, and the natural variability of the atmosphere there is an obvious need for validation of the fluxes as calculated.

2. CERES/ARM Validation Experiment (CAVE)

The formal product for the SARB consists of radiative fluxes at the surface, 500hPa, 200hPa, 70hPa and TOA. TOA computations are compared directly with CERES observations. Given the un-availability of in-situ flux observations within the atmosphere we turn to validation at the surface. The sites selected for the CERES "ARM" Validation Experiment (CAVE) are indicated in Figure 1.

Corresponding author: David A. Rutan
1 Enterprise Pkwy Suite 300 Hampton, VA 23666
(757)827-4629; d.a.rutan@larc.nasa.gov

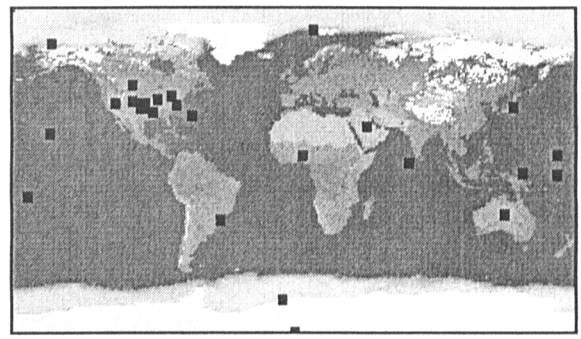

Figure 1. Locations of CAVE sites.

All CAVE sites subscribe to traceable calibration protocols. Consistent with the CERES goal of relating radiation to climate change, CAVE sites observe and record several radiation fields almost continuously for the long-term. Many CAVE sites have auxiliary measurements useful for validating inputs of radiative transfer computations and for validating diagnostic quantities like aerosol radiative forcing. The goal of CAVE is to make available via the World Wide Web an informal, continuous record of radiation and meteorological data having:

(1) TOA broadband observations from the CERES instruments collocated in space and time with,

(2) surface broadband flux measurements.

Where available CAVE includes other variables such as meteorological records of surface temperatures, humidity and winds; as well as aerosols and, if available, temperature T(z) and humidity q(z) profiles. A pilot form of this project is developed more thoroughly in the CERES/ARM/GEWEX or CAGEX experiment (Charlock and Alberta, 1996). (See http://www-cagex.larc.nasa.gov/cagex/) The CAVE record begins on January 1, 1998 shortly after the CERES instrument on the TRMM satellite first began taking data. Depending upon the surface site, the data sets will be continuous and kept nearly up to date.

3. The Data

The basic CAVE philosophy is to supply currently available high quality surface observations of broad band fluxes over a wide variety of scene types around

the globe then collocate in time, CERES observations with the surface sites. To keep the data sets small a standard time step of 1/2 hour and time span of 1 month per file is chosen. Surface data is averaged into continuous 1/2 hour intervals and placed into the Surface, Aerosol, & Meteorology (SAM) files. Intermittent "snap-shot" CERES observations are placed into the nearest 1/2 hour intervals in a similar format. Though this causes a large number of time steps for a CERES data file to be empty, it facilitates comparison of TOA values with surface observations. Ancillary data sets (aerosols etc.) are placed within the same 1/2 hour format as the surface and TOA files. The participating groups from which we receive the bulk of radiometric fluxes and surface observations are: The Atmospheric Radiation Measurement Program (ARM), Climate Monitoring & Diagnostics Laboratory (CMDL), NOAA Surface Radiation Research Branch, SURFRAD data, and the Baseline Surface Radiation Network (BSRN). Other groups supplying data include NASA Langley Research Center's Chesapeake Lighthouse CERES Ocean Validation Experiment (COVE), the National Renewable Energy Resources Laboratory (NREL) Saudi Solar Village, NASA Goddard Spaceflight Center's Aerosol Network (AERONET) and the Indian Ocean Experiment (INDOEX). A number of other researchers have contributed their time and talent in supplying ancillary data such as aerosol information, profile data and cloud amounts. Their contributions are noted on the web site.

Along with observations, several calculated fields are added to the CAVE files. We have adjusted surface SW radiometer data, where possible, to provide a more accurate flux record. For example, measurements of diffuse shortwave with the shaded Eppley pyranometers are susceptible to offsets of several Wm^{-2} due to thermal IR exchange between the detector and dome (Dutton et al., 2000). This first order correction for the "night offset" at ARM SGP and other CAVE sites is noted when provided. Many CAVE files include supplementary estimates of cloud cover based on temporally intensive surface SW radiometric data (Long and Ackerman, 2000). These data can be used to validate classifications of sky conditions from satellites and models.

4. Visualization

Several plotting routines are made available at the CAVE web site for easy visualization of the data sets. These routines are web based and require no downloading of programs or data to execute. The "SAMPLOT" routine will read any site/month of available surface data (a SAM file), plot a summary table showing the contents and basic statistics, and can produce a postscript image of any of the available data within the file. A similar plotting capability exists for the TOA CERES files called "CERESPLOT". Finally, a page is provided to summarize the Long/Ackerman cloud fraction data made available in the SAM files. This plotting routine reads the SAM files for any available time period and plots a summary graph of the cloud amount.

5. Profile Data

The sparsest data set within the CAVE data base is the atmospheric profile data. Recently a set of radiosonde data from the ARM/SGP central facility (CF) was added to the CAVE data base for 1998 and 1999. This data takes thrice daily balloon sondes from ARM and places them into files based on the 1/2 hour CAVE format. Between sonde launches, 1/2 hour intervals are filled via interpolation. Humidity profiles are scaled to the Microwave Radiometer precipitable water observed for that time. CAVE files contain a number of single variables and profiles of geopotential height, pressure, temperature, water vapor mixing ratio and ozone (updated daily) from NCEP.

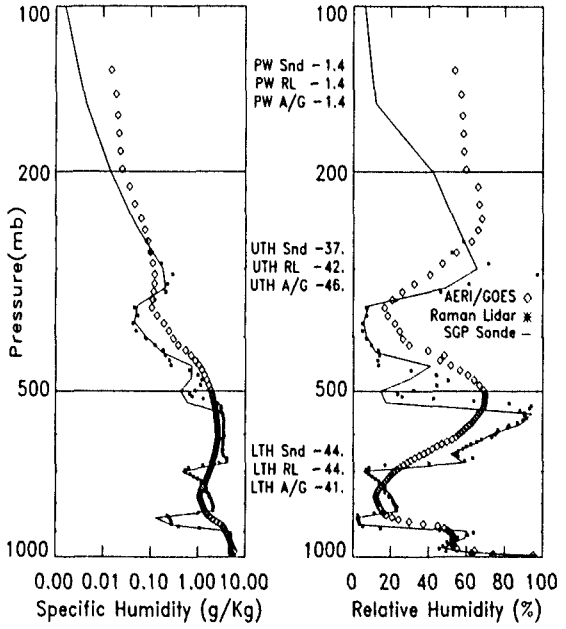

Figure 2. Humidity profile comparisons at ARM/SGP Central Facility.

To test these files, atmospheric profile data from two independent sources, the Raman Lidar (RL) and AERI/GOES (AG) at the ARM central facility are retrieved and compared to the CAVE sonde files. The ARM value added product from which the RL and AG data are taken is: "sgp10rlprofmr1turnC1.c1". It contains all the RL mixing ratio retrievals and the AG

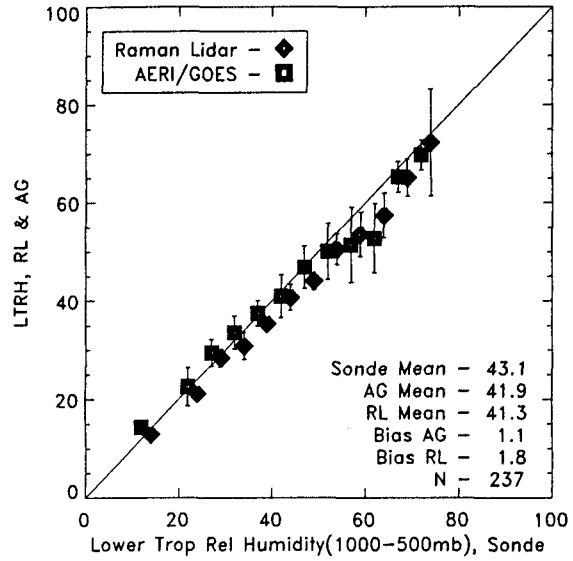

Figure 3. Comparison of mean (1 σ) Raman Lidar & AERI/GOES Lower Tropospheric Relative Humidity (1000-500mb) for Jul through Oct 1998 at the ARM/ SGP central facility.

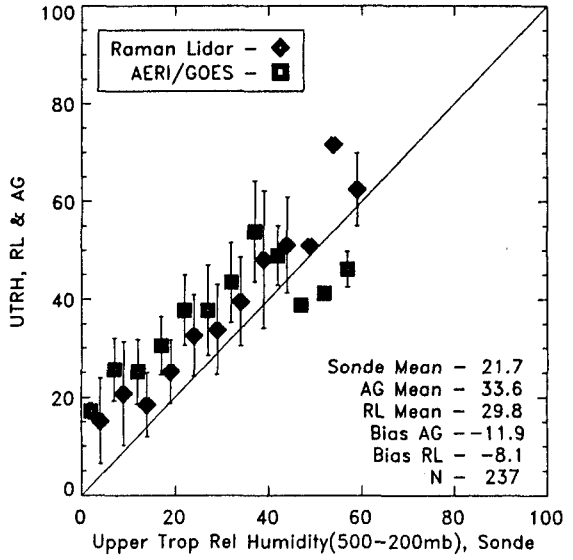

Figure 4. Comparison of mean (1 σ) Raman Lidar & AERI/GOES Upper Tropospheric Relative Humidity (500-200mb) for Jul through Oct 1998 at the ARM/SGP central facility.

temperature and water vapor profiles (Turner et al. 2000). The RL and AG data are archived every 10 minutes. The temperature profiles from the AG product compare well with the sondes. The following plots focus on water vapor. Figure 2 shows the specific humidity and relative humidity profiles for the three products at ~6:30AM Local Time, Oct. 22, 1998. The micropulse lidar and ceilometer at the CF both show a cloud base of just under 5 km at this time. Water vapor shows considerable structure in the lower troposphere (1000-500mb) and the sonde and RL track each other closely while the AG product provides data that is smoother. All three provide total precipitable waters of 1.3cm and lower tropospheric relative humidity near 44%. In the upper tro-

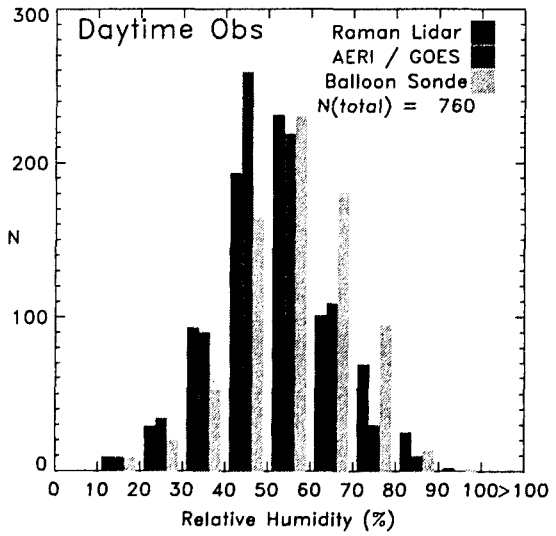

Figure 5. Comparison of daytime 1000mb-850mb integrated relative humidity for ARM/SGP Central Facility Balloon Sonde, Raman Lidar and AERI/GOES for Jul-Oct 1998.

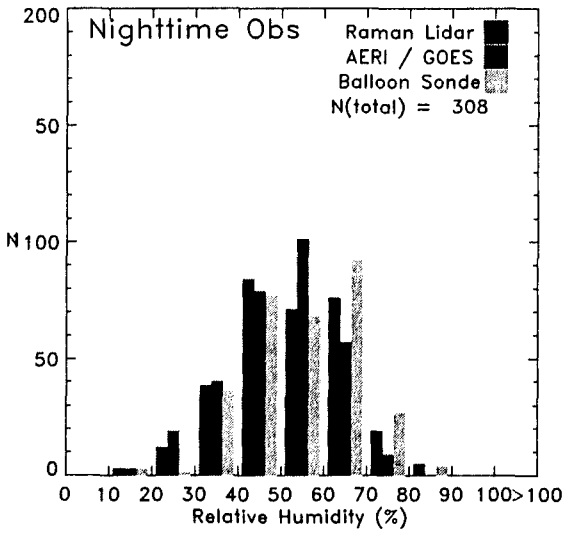

Figure 6. Comparison of nighttime, 1000mb-850mb integrated relative humidity for ARM/SGP Central Facility Balloon Sonde, Raman Lidar and AERI/GOES for Jul-Oct 1998.

posphere (500-200mb), retrievals appear less certain for all three. The upper tropospheric humidity shows close agreement in the mean between the RL and the sonde, around 22% where the AG shows a value of 36%. This is only a single case.

To summarize the comparisons statistically, profiles were processed for Jul., Aug., Sep. and Oct. 1998. In Figure 3, 1/2 hour averages of Lower Tropospheric Relative Humidity (LTRH) are binned by 5% ranges and compared to sonde LTRH if the observations are within +/- 4 hours of a balloon launch. Data points are retained only if all three methods retrieve a result for both LTRH and UTRH (CAVE data includes interpolated profiles). Since the RL does not provide much data above 500mb during the day this plot shows primarily night time data. Figure 3 shows that the RL and AG and Sonde data match well in the lower troposphere. Figure 4 shows the same summary but for Upper Tropospheric Humidity (500-200mb). Both the RL and the AG show significantly more water vapor in the upper troposphere though the RL has a slightly smaller bias with respect to the sonde humidities.

Figures 5 and 6 show histograms of the all sky relative humidity integrated between 1000mb and 700mb for the four month period (+/- 2 hours of balloon launch) during day and night respectively. One finds daytime distribution peaks vary. Sonde and RL data are more moist, peaking between 50% and 60% RH while AG is driest peaking between 40% and 50% RH. The distributions show that as the humidity increases, the sonde shows more moisture than the ground based retrieval methods. During the night, Figure 6, the RL and sonde data show twin peaks while AG retains a more normal distribution. The current schedule for launching balloons at the ARM CF is ~5:30AM, 2:30PM and 6:00PM local time. It is possible that the sonde data is biased high due to this type of sampling. The effect of the sampling requires further study.

The addition of these profile data to the CAVE data base enhances the data set for the running of radiation transfer models. It is planned to add these profiles continuously for the ARM Central Facility and for the ARM TWP sites.

6. Web Availability

The CAVE data is made available via ftp over the world-wide-web. The home-page describing the various data sources and supplying the programs to read the data is found at: **http://www-cave.larc.nasa.gov/cave/**

Surface and TOA data for the first eight months of 1998, the CERES/TRMM time period, are available. Surface observations from a number of sites up through 2001 are also available and CERES TOA footprint data from the Terra satellite, Version 1 are available from Mar 2000 through May 2001.

7. Acknowledgments

This work was supported by the Earth Science Enterprise of NASA through Langley Research Center by contract to AS&M. CERES data are provided by the Langley Research Center's Atmospheric Sciences Data Center (ASDC).

8. References

Charlock, T. P., and T. L. Alberta, 1996: The CERES/ARM/GEWEX Experiment (CAGEX) for the Retrieval of Radiative Fluxes with Satellite Data. Bull. Am. Met. Soc., 77, 2673-2683.

Collins, W. D., P. J. Rasch, B. E. Eaton, B. V. Khattatov, J-F.Lamarque, and C. S. Zender, 2001: Simulating aerosols using a chemical transport model with assimilation of satellite aerosol retrievals: Methodology for INDOEX. J. Geophys. Res., vol. 106, 7313--7336.

Dutton, E. G., J. J. Michalsky, T. Stoffel, B. W. Forgan, J. Hickey, D. W. Nelson, T. L. Alberta, and I. Reda, 2000: Measurement of broadband diffuse solar irradiance using current commercial instrumentation with a correction from thermal offset errors. J. Atmos. Oceanic Technol., 18, 297-314.

Fu, Q. and K.N. Liou, 1993: Parameterization of the radiative properties of cirrus clouds. J. Atmos. Sci., 50, 2008-2025.

Long, C. N. and T. P. Ackerman, 2000: Identification of clear skies from broadband measurements and calculation of downwelling shortwave cloud effects. J. Geophys. Res., 105, 15,609-15,626.

Turner D.D. , W.F. Feltz, and R.A. Ferrare 2000: Continuous water vapor profiles from operational active and passive remote sensors, Bull. Amer. Meteor. Soc., 81, 1301-1317, 2000.

Wielicki, B. A., B. R. Barkstrom, E. F. Harrison, R. B. Lee, G. L. Smith, and J. E. Cooper, 1996: Clouds and the Earth's Radiant Energy System (CERES): An Earth Observing System Experiment. Bull. Amer. Meteor. Soc., 77 853-868.

P5.28

INTERCOMPARISON OF CERES SCANNING AND ERBS WFOV NON-SCANNING RADIOMETERS

David A. Rutan[1], G. Louis Smith[2], Robert B. Lee III[3] and Takmeng Wong[3]

1. Analytical Services and Materials, Inc.
2. Virginia Polytechnic Institute and State University
3. Atmospheric Sciences Division, Langley Research Center, NASA

1. INTRODUCTION

Flight Models 1 and 2 (FM-1, FM-2) of the Clouds and Earth's Radiant Energy System (CERES) scanning radiometers (Barkstrom, 1990) are now operating aboard the TERRA spacecraft which was placed in orbit December 18, 1999. The instruments began scanning the Earth in February 2000 and have provided over a year of data thus far. The Proto-Flight Model (PFM) CERES flew aboard the Topical Rainfall Measuring Mission (TRMM) in November 1997 and provided data for eight months. Though operation was curtailed due to a problem (corrected on TERRA) PFM returned to operation for intercomparisons with Terra FM-1 and FM-2 (Haeffelin et al., 2000)

The Earth Radiation Budget Experiment (ERBE) Wide Field-of-View (WFOV) radiometers aboard the Earth Radiation Budget Satellite (Luther et al., 1986; Barkstrom and Smith, 1986) have operated since November 1984 and maintained a high level of precision (Paden et al., 2000). Green et al. (1990) developed a method for comparing nonscanning WFOV radiometer results with scanning radiometer results demonstrating accuracy at the level of 1% to 2% between ERBE scanners and ERBE WFOV radiometers. Bess et al. (1997) applied the Green method and software to compare the Scanner for Radiation Balance (ScaRaB) results (Kandel et al., 1998) with the ERBS WFOV radiometer. Rutan et al. (1999) compared a sample of CERES data with ERBS data. The ERBS WFOV radiometers thus serve as a transfer standard for these scanning radiometers. The present paper makes a more extensive comparison of CERES/TRMM with ERBS.

After 15 years of ERBS operation, in October 1999 following a routine calibration, the elevation drive which rotated the radiometers to look at the Sun failed after returning the radiometer to Earth-viewing position. After this time calibrations could no longer be done. WFOV data after that occurrence are not regarded as well-calibrated. The present work also compares ERBS and CERES FM-2 aboard TERRA as part of an effort to reestablish the calibration of ERBS WFOV after the October 1999 anomaly.

Corresponding author address: David A. Rutan, Analytical Services and Material, Inc., 1 Enterprise Parkway, Hampton, VA 23666 USA
d.a.rutan@larc.nasa.gov

2. TRMM/ERBS INTERCOMPARISON

The method of comparing scanning and WFOV radiometer results is described by Green et al. (1990). The WFOV measures total and shortwave flux at ERBS altitude. The scanner measures radiances at the TRMM or TERRA spacecraft. Data are used from points where orbits cross and both spacecraft pass this point within ten minutes. Radiances as measured by the scanner are used to compute radiances from all points within the FOV of the WFOV radiometer by use of bidirectional reflectance distribution models for shortwave radiances and limb-darkening models for longwave radiation. These radiances are then integrated to compute the flux as measured by the WFOV radiometer. The computation is done for both shortwave and total radiation.

Nighttime longwave radiation is measured by the total channel for both scanner and WFOV. Figure 1 shows the comparison for nighttime flux. The bias is 1.7 $W\text{-}m^{-2}$(0.8%). The slope difference of 0.04 gives a difference of 2 $W\text{-}m^{-2}$ over the measurement range of 50 $W\text{-}m^{-2}$, so that the line of best fit matches at the lower range but differs by 3.7 $W\text{-}m^{-2}$ (1.4%) at the top of the range.

Figure 2 shows the comparison for shortwave results. The WFOV has a bias of 2.4 $W\text{-}m^{-2}$ (1.5%) higher than the scanner. The slope is 0.97 so that the line of best fit for the two instruments agree at 80 $W\text{-}m^{-2}$, which is the lower end of the measurement range. The scatter for shortwave is significantly greater than that for the longwave. This is attributed to the greater variation of shortwave BRDFs as compared to longwave directional models. During daytime the longwave results for each instrument are given by the difference of total and shortwave results. Figure 3 shows the comparison

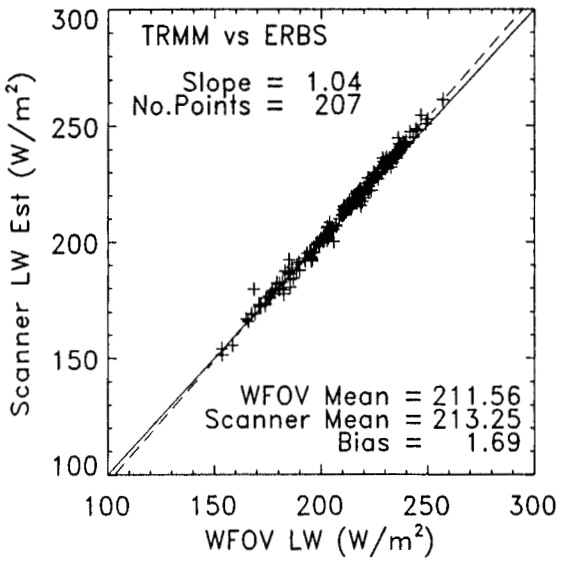

Figure 1: WFOV compared to CERES/TRMM scanner estimate of nighttime longwave radiation.

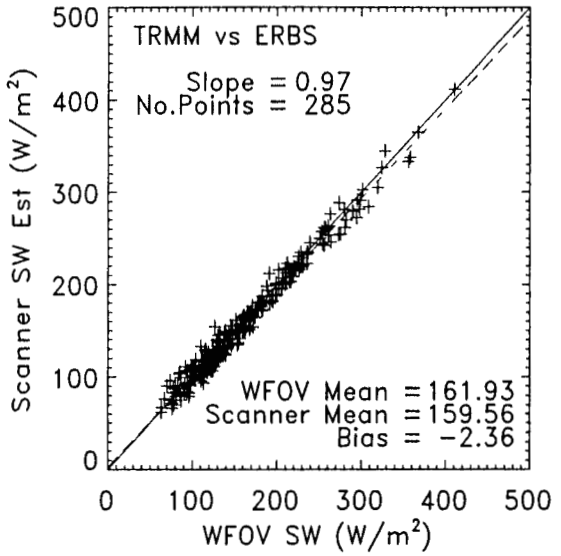

Figure 2: WFOV compared to CERES/TRMM scanner estimate of shortwave radiation.

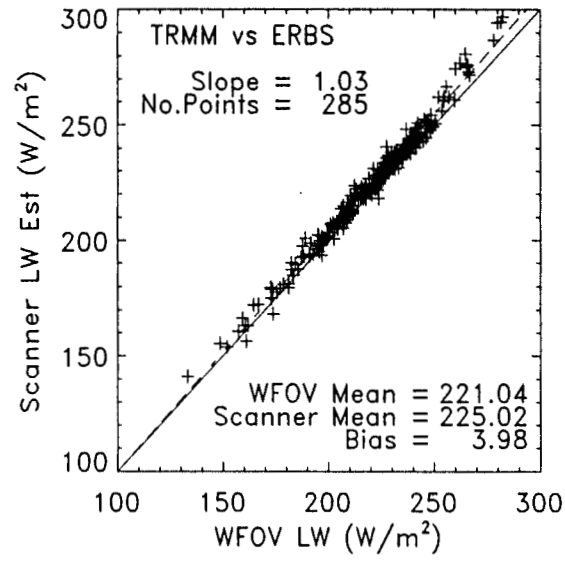

Figure 3: WFOV compared to CERES/TRMM scanner estimate of daytime longwave radiation.

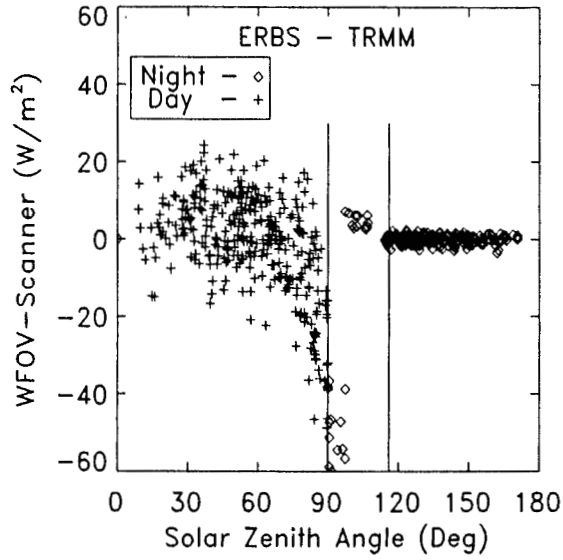

Figure 4: Shortwave WFOV minus CERES/ TRMM estimate as a function of solar zenith angle.

of CERES/TRMM results with ERBS measurements for daytime. The bias of 4 W-m^{-2} (1.8%) is consistent with the shortwave and night longwave biases. The slope is 1.03, so that the line of best fit agrees at the lower range of the measurements as for the shortwave and nighttime longwave results. The differences of results as function of solar zenith angle of the subsatellite point of ERBS are a useful diagnostic and are shown by fig. 4 for short wave measurements. As ERBS approaches the terminator (solar zenith angle of 90°) scanner results increasingly exceed WFOV measurements because the BRDFs are not accurate for large solar zenith angles. Thus, results are not used for solar zenith angles greater than 80°. This limitation is unfortunate as it reduces the range available for comparison.

Figure 5 shows the longwave flux as measured by ERBS WFOV radiometers minus the flux at ERBS computed from the CERES/TRMM scanner

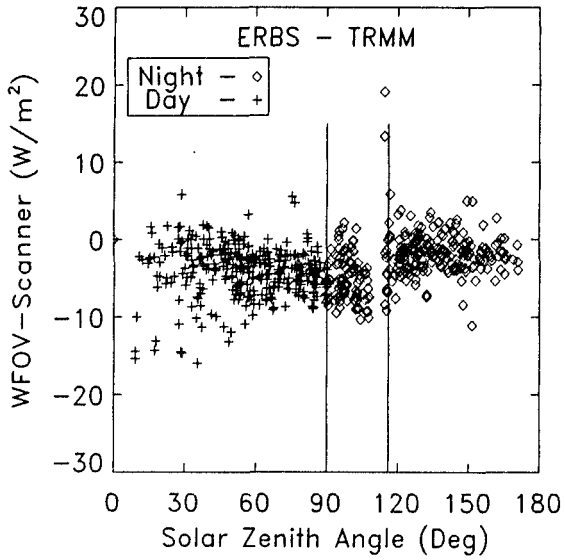

Figure 5: Longwave WFOV minus CERES/ TRMM estimate as a function of solar zenith angle.

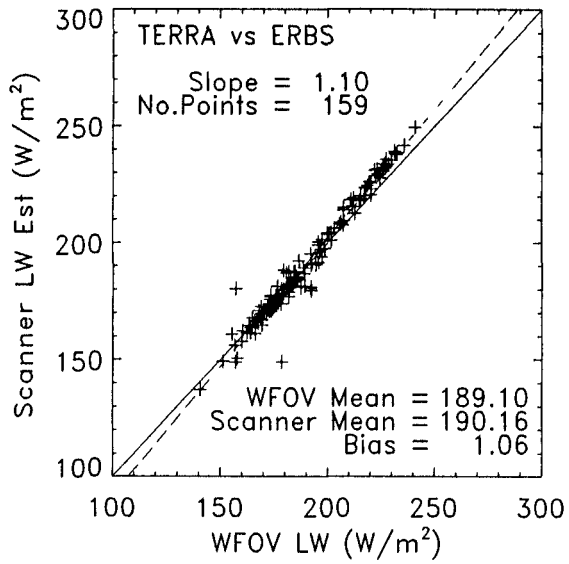

Figure 6: WFOV compared to CERES/Terra estimate of nighttime longwave radiation.

as a function of solar zenith angle. During the day there is a slight downward trend with solar zenith angle, but otherwise the results are as expected.

3. TERRA/ERBS INTERCOMPARISON

Terra is in a Sun-synchronous orbit crossing the Equator at 10:30 AM going south, so that the orbits of ERBS and Terra intersect with local times between 9:00 and 12:00 and over a latitude range between 57° north and south. Comparisons are shown here for March through July 2000 using edition 1 CERES/Terra data. Figure 6 shows the comparison of fluxes at the ERBS spacecraft computed using CERES FM-2 data with WFOV measurements for longwave radiation at night. The WFOV mean is 190.2 W-m^{-2} and FM-2 has a relative bias of 1.06 W-m^{-2}(<1%). Although the means compare quite well, the slope is 1.10 W-m^{-2} resulting in a difference of 3 W-m^{-2} at the lower limit but 7 W-m^{-2} at the upper limit of measurements. Figure 7 shows the comparison for shortwave radiation. The slope is 1.00, but the bias of the shortwave FM-2 relative to ERBS is 20 W-m^{-2}(9%). The daytime longwave comparison is shown in fig. 8. The scanner mean is higher than the WFOV mean by 6.2 W-m^{-2}(3%) and the slope is 1.08. The ERBE WFOV does not agree with Terra as well as any of the other comparisons made before the October 1999 drive failure. Figure 9 shows the differences between the ERBS/WFOV and FM-2 as a function of solar zenith angle. The difference is mostly random, without a noticeable dependence on solar zenith angle and is not understood now.

4. CONCLUDING REMARKS

Comparisons of CERES/TRMM with ERBS WFOV measurements are consistent to better than 1% for nighttime longwave fluxes, 1.5% for shortwave fluxes and 2% for daytime longwave fluxes. Whereas the ERBS WFOV compares well with ERBE scanners, ScaRaB and CERES/TRMM scanners, after the drive failure of October 1999 calibration checks have not been made for the WFOV. Thus, information is not available to account for degradation of the dome of the shortwave channel. It is hoped than in late 2001 a pitchover maneuver can be made with the ERBS spacecraft so that offsets and gains can be determined for the WFOV radiometer channels.

5. ACKNOWLEDGEMENTS

This work was supported by the Earth Science Enterprise of NASA through Langley Research Center by contract to AS&M and by cooperative agreement NCC1-405 with Virginia Polytechnic Institute and State University. Data were provided by the Langley Distributed Active Archive Center.

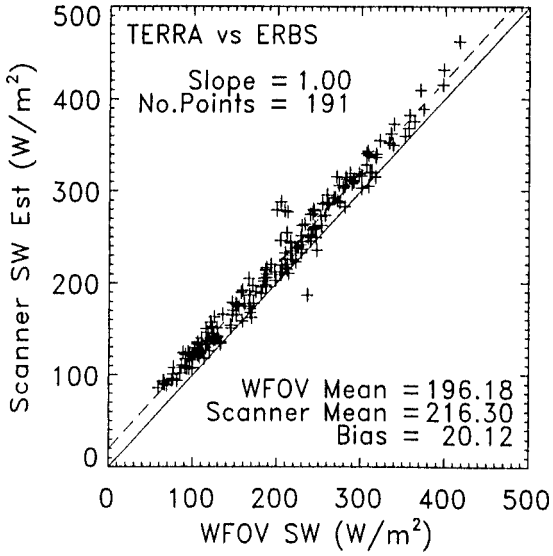

Figure 7: WFOV compared to CERES/Terra estimate of shortwave radiation.

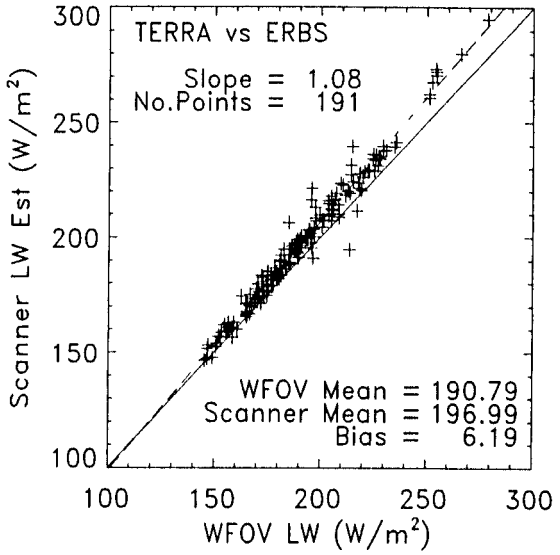

Figure 8: WFOV compared to CERES/Terra estimate of daytime longwave radiation.

6. REFERENCES

Barkstrom, B. R., 1990: Earth radiation budget measurements pre-ERBE, ERBE, and CERES, Long-Term Monitoring of the Earth's Radiation Budget, Bruce R. Barkstrom, Editor, Proc. SPIE 1299, 52-60.

Barkstrom, B. R. and G. L. Smith, 1986: The Earth Radiation Budget Experiment Science and Implementation, *Rev. of Geophys., 24*, 379-390.

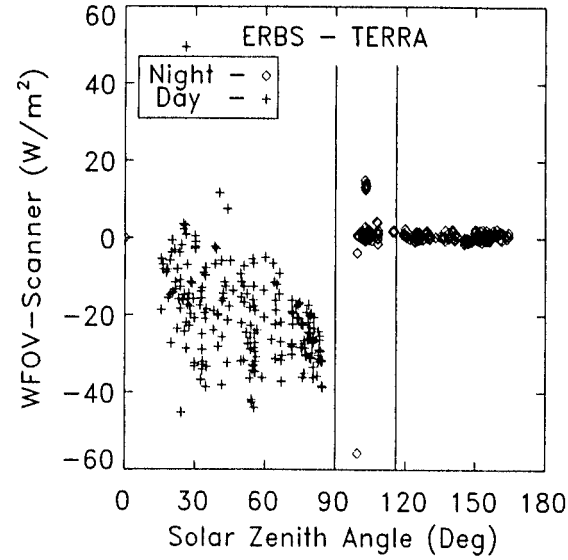

Figure 9: Shortwave WFOV minus CERES/ Terra estimate as a function of solar zenith angle.

Bess, T. D., G. L. Smith, K. A. Bush and D. A. Rutan, 1999: "Intercomparison of ScaRaB and ERBS monthly mean radiation fluxes," 60-63, Proc. 10th Conf. Atmos. Rad., American Met. Soc., Madison, Wisc. June.

Green, R. N., F. B. House, P. W. Stackhouse, X. Wu, S. A. Ackermann, W. L. Smith and M. J. Johnson, 1990: Intercomparison of scanner and nonscanner measurements for the Earth radiation budget experiment (ERBE), *J. Geophys. Res., 95,* 11,785-11,798.

Haeffelin, M., B. A. Wielicki, and K. J. Priestley, 2000: Direct comparisons of radiances measured by independent contemporary ERB instruments, *Proc. Internat. Rad. Symp.*

Kandel, R., M. Viollier, L. A. Pakhomov, V. A. Golovko, E. Raschke, R. Stuhlmann, and the international ScaRaB Scientific Working Group (ISSWG), 1998: The ScaRaB Earth radiation budget data set, *Bull. Amer. Met. Soc., 78,* 765-783.

Luther, M. R., J. E. Cooper and G. R. Taylor, 1986: The Earth Radiation Budget Experiment nonscanning instrument, *Rev. of Geophys., 24,* 391-399.

Paden, J., R. B. Lee III, D. K. Pandey, G. L. Smith, R. S. Wilson and K. J. Priestley, 2000: Validation and analysis of Earth radiation budget active cavity radiometric data (1984-1999), *Proc. SPIE, 4168,* 86-96, Barcelona, Spain.

Rutan, D. A., G. L. Smith, T. P. Charlock, and R. N. Green. 1999: Early intercomparison of CERES and ERBE results, Proc. 3rd Symp. on Integ. Obs. Sys., Dallas, Texas.

P5.29 The Calibration of NOAA AVHRR Visible Radiances with VIRS

David R. Doelling, Venkatesan Chakrapani
Analytical Services & Materials Inc., Hampton, VA

Patrick Minnis and Louis Nguyen
NASA Langley Research Center, Hampton, VA

1. INTRODUCTION

There is a long history of Advanced Very High Resolution Radiometer (AVHRR) derived products that rely on accurate visible channel radiances. Currently AVHRR instruments lack onboard calibration for channels 1 (0.65 μm) and 2 (0.87 μm). Operationally, these channels are calibrated using a stable desert surface target as a reference to account for degradation of the sensors (Rao and Chen 1999 and 1996; http://psbsgi1.nesdis.noaa.gov:8080/EBB/ml/niccal.html). Adjustments usually consist of a gain change that varies linearly with the day since launch of the particular satellite. Two NOAA satellites with AVHRR are usually operating at any given time: one is an afternoon (1330 or 1430 local equator crossing time (ECT)) and the other morning (0730 ECT) Sun-synchronous orbit. Operational calibrations are only performed for the afternoon orbiter. Degradation rates have been computed for NOAA-9 (Loeb 1997); 9, 10, and 11 (Masonis and Warren 2001); and 14 (Tahnk and Coakley 2001) using polar snow targets. For detection of long term trends in remotely sensed parameters and to detect changes in surface or cloud properties over a given location, it is critical to have consistent calibrations over the record of observations from satellite imagers. The polar intercalibration technique can be used to determine the relative degradation between any two satellites. Thus, given enough overlap, a single calibration reference can be transferred from one satellite pair to the next to provide a consistent calibration for all available AVHRR data. This paper presents preliminary gain comparisons of sequential afternoon and morning satellites from NOAA-9 to NOAA-15 and they are normalized to a well-calibrated reference satellite imager.

Recently launched scanning radiometers, including the Moderate Resolution Imaging Spectroradiometer (MODIS), Visible Infrared Scanner (VIRS) and Along Track Scanning Radiometer (ATSR-2) use solar diffusers to calibrate their visible radiances. If these calibrations are reliable and the spectral response functions similar, then one could inter-calibrate VIRS, MODIS and ATSR-2 with AVHRR. It has been shown that VIRS has a stable visible calibration when compared with ATSR-2, MODIS, and other geostationary satellites (Minnis et. al. 2001). This paper uses the VIRS data as a reference for the NOAA-14 AVHRR visible channel that will be used to intercalibrate the AVHRRs on the other NOAA satellites. The direct AVHRR-VIRS calibrations are compared with an indirect 3-way calibration using matched VIRS and Geostationary Operational Environmental Satellite (GOES-8) data and AVHRR-GOES calibration. This 3-way calibration provides an estimate of the uncertainty resulting from a given satellite-to-satellite calibration transfer.

* *Corresponding Author Address*: D. R. Doelling, AS&M Inc., 1 Enterprise Parkway, Hampton, VA 23666; e-mail: d.r.doelling@larc.nasa.gov

2. NOAA Cross-Calibration Method

AVHRR Global Area Coverage (GAC) data were used for each satellite. To minimize errors, only coincident, collocated and angle-matched radiances were used to compare visible radiances from different satellite platforms. The best opportunities for meeting such criteria for a pair of afternoon and morning polar orbiters occur over polar regions. Their ground tracks only intersect at 80° north (1000 LST) or south (2200 LST) latitude 14 times a day. During the 8-day satellite repeat cycle, the time difference between the morning and afternoon satellite intersections ranges from 0 up to 45 minutes, the time required to complete half an orbit. Daytime intersections occur in the Northern Hemisphere from February until November; while during the remainder of the year the daytime intersections occur over the Southern Hemisphere. For this study, two days (8 days apart) of intersections are used, when the time difference is less than 2.5 minutes. These days straddle Dec. 23, Apr. 23, June 23, and Aug. 23. The solar zenith angles *(SZA)*, 77°, 67°, 57° and 67°, vary interannually by less than 3° for each month, despite the gradual precession of the ECT for each satellite.

For each intersection, several matched data points were created by computing the average 10-bit visible count over selected areas defined by a nominal radius of 50 km from the center of each matched region to minimize the effects of any navigation errors from either one or both of the satellites. These averages are based on approximately 150 pixels from each satellite. Usually, the counts are linearly related to radiance. For the one exception, NOAA-15, the dual-gain counts were first converted to radiances and then converted to NOAA-14 equivalent counts with the nominal calibration to provide a linear fit between counts and gain.

Several data points are possible for each intersection because the satellites cross at an angle of

~60° (or 120°). In addition to the matching nadir point, the viewing zenith angles *(VZA)* between the two satellites are equal at four different locations, one in each of the quadrants defined by the crossing orbital ground tracks. To differentiate between the matched *VZA*s in the oblique and acute crossing-angle quadrants, the lines between the ground track and the matching regions in the acute angle quadrants are referred to as the along-track. Similarly, the lines in the oblique-angle quadrants are denoted as cross-track lines. The radius was increased with *VZA* to ensure that at least 150 pixels were included in each data point. Only non-overlapping matched regions with *VZA* < 6° for along track and *VZA* < 17° in the cross-track were used for the off-nadir points. This matching approach results in more than one data point for each quadrant because the matched *VZA*s vary continuously with distance from the ground-track intersection. Although the relative azimuth angles *(RAZ)* differ for each satellite, the impact should be relatively small because the *VZA* are so small.

Figure 1 shows scatter plots of NOAA-11 and 12 channel 1 data of the off-nadir and nadir points from taken during December 1991 near the South Pole. Regressions were performed for each dataset using the force-fit and Principal Components (PC) methods. The force-fit technique holds the offset or space count constant at 41 and derives the slope from the mean radiances. The PC fit is essentially the first-order principal component and computes the minimum distance perpendicular to the line, thereby taking into account errors in both variables. The PC gain and offset for the data in Fig. 1a are 0.950 and 0.74 with the correlation coefficient r^2 = 0.994. The force-fit gain is 0.940 for 224 samples. The corresponding PC statistics for the nadir points are 0.887, 11.24, and 0.975 while the force-fit gain is 0.939 for 25 samples. The cross- and along-track points increased the dynamic range and the PC slope was similar to the force fit unlike the nadir case and the offset was near zero. Note the force fits in Fig. 1a and b are nearly the same.

Figure 2 shows the relative trend lines using both techniques applied to data from channels 1 and 2 for the five morning and afternoon satellite combinations. The trend lines have been normalized so that the mean of both the nadir and cross & along track monthly points is unity for the five satellite combinations. The trend line describes, for each satellite pair X-Y, the ratio of the gain drift of satellite Y to the gain drift of satellite X. Thus the first set of lines in the top panel of Fig. 2 is for the ratios of the NOAA-10 to the NOAA-9 gains. Gaps in time series are found for January and December 1995 and Dec 1989. Those data were not used because the PC offset was greater than 20 counts suggesting too much noise in the data. The PC gain and offset drifts usually occur in tandem with one coefficient offsetting the effect of the other. The force fit is not really affected by any apparent space count drifts. The relative gain for the South Pole data often differs from that from the North Pole. These pole-to-pole changes are mostly balanced by changes in the offsets. The reason for the hemispherical variation may be related to differences in the *RAZs*.

The force fit plots in Fig. 2 show that the nadir and cross- and along-track trend lines are nearly identical except for NOAA-12 and 14. This suggests that the cross and along track points do not bias the slope and that the *VZA* limitations eliminate most of the impact from differing *RAZs*. The off-nadir PC and force-fit slopes for NOAA-12/NOAA-14 are systematically below the nadir counterparts. This anomaly may be due to different geometry between the two satellites relative to the other four pairs. More study is required to understand these differences.

Overall, the relative gain trends appear to be linear. Negative trends indicate that the newer satellite is degrading faster than the older satellite. The only positive trends occur for the NOAA-9/NOAA-10 combination and for the NOAA-14/NOAA-15 channel 2 gains. Masonis and Warren (2001) found that NOAA-10 degraded in a cyclical fashion with the gain decreasing before November 1988 and increasing afterwards. Although channels 1 and 2 do not degrade in the same fashion, they generally degrade in the same direction relative to the other satellite. The exception again is for the NOAA-14/NOAA-15 combination. These relative gain drifts will be compared with published calibrations such as Masonis and Warren (2001) and Brest et. al. (1997) for verification.

3. VIRS and NOAA-14 Inter-calibration

Absolute values for each of the gains will be assigned by first normalizing the NOAA-14 gains to the VIRS, then transferring the gains using the relative trend lines in Fig. 2. VIRS is operating on the Tropical Rainfall Measuring Mission (TRMM) satellite that was launched in November 1997 into a 35° precessing orbit. To effect the matching of NOAA-14 and VIRS, an orbital prediction routine was used to locate intersections within 15 min for the NOAA-14 and TRMM ground tracks. A 40 x 60 - 0.5° latitude-longitude grid was centered on each of the intersection coordinates rounded to the nearest 0.5°. The number of regions meeting the following criteria were determined for each selected intersection: *VZA* difference < 7.5°, *RAZ* difference < 15°, and no sunglint. All regions with *SZA* > 72° and fewer than 20 matches were rejected. NOAA-14 was launched in Dec. 1994 with a 1340 ECT and gradually precessed to an ECT of 1705 by August 1, 2001. The typical *SZA* for the matched regions varied from ~40° in 1998 to almost 70° in 2001. Fits based on the later datasets with higher *SZA*s have smaller dynamic ranges and more scatter about the regression line.

Monthly scatter plots of NOAA-14 counts and VIRS radiances were fitted using the force-fit and PC regression methods. Figure 3 shows the resulting points

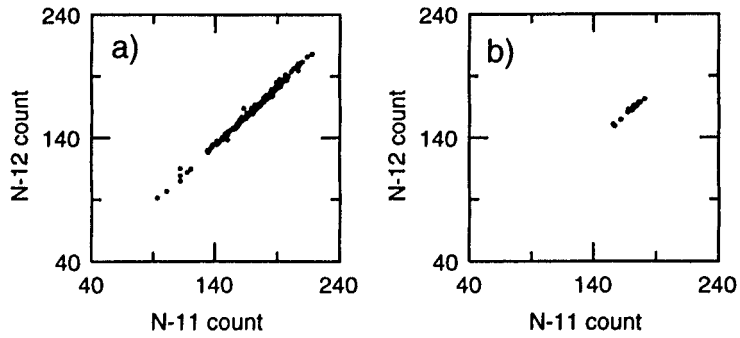

Fig. 1. a) A scatter plot of the NOAA-11 and NOAA-12 channel 1 count of cross & along track (off nadir) points for the month of Dec. 1991. b) same as a) except for nadir points only.

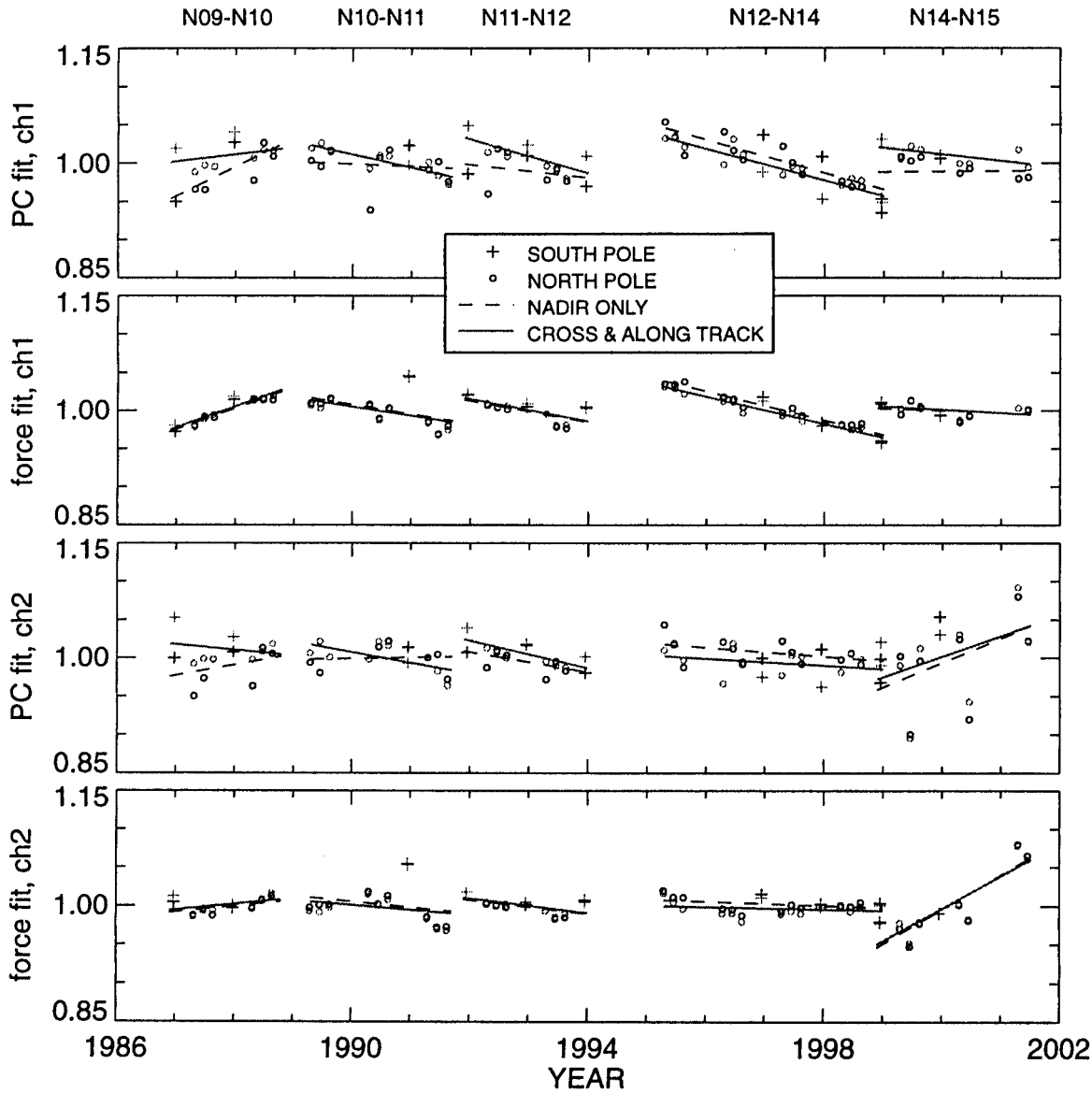

Fig. 2. The relative gain ratio of the two NOAA satellites, which are labeled on top, based on monthly regressions using the PC and force fit method for channels 1 and 2. The trend lines are also plotted. Cross & along track points and the associated trend line are shown in solid gray.

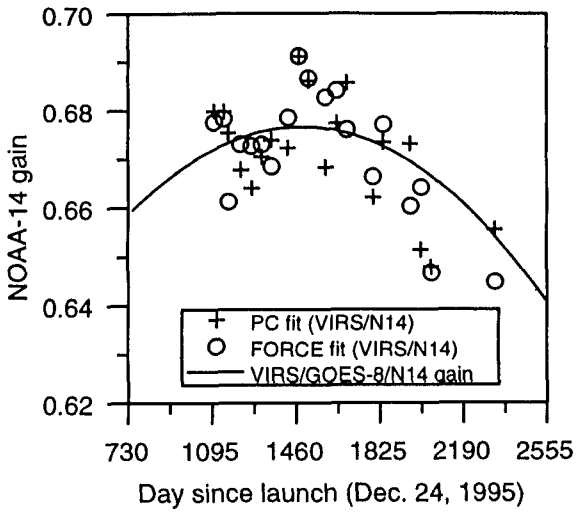

Fig. 3. Monthly NOAA-14 AVHRR visible channel gains derived from VIRS as a function of time. The VIRS/GOES-8/NOAA-14 trend line is shown.

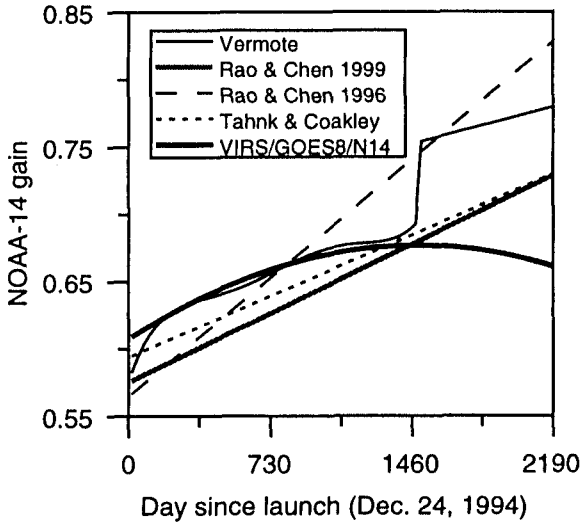

Fig. 4. Comparison of NOAA-14 AVHRR visible channel gains as a function of time.

and the NOAA-14 gain as derived from cross-calibrating VIRS with GOES-8 and GOES-8 with NOAA-14 (Nguyen et al. 2001). The monthly points follow the same type of trend as the GOES-8 based fit, thus validating the three-way circular calibration. The gain from both the points and trend line decreases after mid-2001. This behavior may be a result of the decreasing dynamic range or to some actual changes in the instrument. This trend needs further examination.

The NOAA-14 gain trend line is compared with other estimates in Fig. 4. The operational calibration (Rao and Chen 1996) was used until November 1998 when Rao and Chen (1999) provided a revised version. The coefficients are available at the web site noted earlier. The trend line from Tahnk and Coakley (2001) is based on the radiometrically stable ice sheet of Antarctica as "truth". The Vermote and El Saleous (1999) fit is based on clear ocean and cloud views. This fit can be found at http://www.dar.csiro.au/rs/CalWatch. Most of the gains are close to each other until 1999, and then diverge. The gains derived here are the only ones that decrease after 2000, but they are also the only ones with data taken after 1999. The VIRS/GOES-8/NOAA-14 gain is similar to that of before 1999. After 1999 an extrapolation was used for the Vermote and Saleous (1999) fit. Minnis et al. (2001) confirm the excellent agreement between the Vermote and Saleous (1999) and the VIRS-based fit using data taken during 1995. The wide range of fits seen in Fig. 4 suggest that any surface or cloud properties derived using NOAA-14 could have large uncertainties depending on the particular calibration that was used for the visible channel. Thus, it is important that the most accurate gain should be determined for the entire NOAA-14 period.

4. CONCLUDING REMARKS

This method presents a way to validate existing NOAA AVHRR visible calibrations and sequentially transfer a calibration from one satellite to the next. To further validate the derived trend lines, ATSR-2/NOAA-14 and MODIS/NOAA-14 monthly gains will also be obtained using the polar orbiting matching methods. The VIRS calibration will then be applied to all of the AVHRRs on the NOAA satellites from NOAA-9 through NOAA-16.

Acknowledgements
This research is supported by the Environmental Sciences Division of U. S. Department of Energy Interagency Agreements DE-AI02-97ER62341 and ITF-214216-A-Q1 under the ARM program.

References

Brest, C. L., W. B. Rossow, and M. D. Roiter, 1997: Update of Radiance Calibrations for ISCCP. *J. Atmos. Oceanic Technol.*, **14**, 1091-1109.

Loeb, N. G., 1997: In-flight calibration of NOAA AVHRR visible and near-IR bands over Greenland and Antarctica. *Intl Jour. Remote Sens.*, **18**, 477-490.

Minnis, P., L. Nguyen, D. R. Doelling, D. F. Young, and W. F. Miller, 2001: Rapid Calibration of operational and research meteorological satellite imagers, Part 1: Use of the TRMM VIRS or ERS-2 ATSR-2 as a reference. Submitted to *J. Atmos. Oceanic Technol.*

Masonis, S. J., and S. G. Warren, 2001: Gain of the AVHRR visible channel as tracked using bidirectional reflectance of Antarctic and Greenland snow. *Intl Jour. Remote Sens.*, **22**, 1495-1520.

Nguyen, L., P. Minnis, J. K. Ayers and D. R. Doelling, 2001: Intercalibration of meteorological satellite imagers using VIRS, ATSR-2 and MODIS. *Proc. AMS 11th Conf. Satellite Meteorl. Oceanogr.*, Madison, WI, Oct. 12-16.

Rao, C. R. N., and J. Chen, 1996: Post launch calibration of the visible and near-infrared channels of the Advanced Very High Resolution Radiometer on the NOAA-14 spacecraft. *Intl Jour. Remote Sens.*, **17**, 2743-2747.

Rao, C. R. N., and J. Chen, 1999: Revised post-launch calibration of the visible and near-infrared channels of the Advanced Very High Resolution Radiometer on the NOAA-14 spacecraft. *Intl Jour. Remote Sens.*, **20**, 3485.

Tahnk, W. R. and J. A. Coakley, Jr., 2001: Improved calibration coefficients for NOAA-14 AVHRR visible and near-infrared channels. *Intl Jour. Remote Sens.*, **22**, 1269-1283.

Vermote, E. and N. Z. El Saleous, 1999: private communication.

P5.30 USING POLARIMETRIC TWO-STREAM RADIATIVE TRANSFER MODEL TO STUDY MICROWAVE POLARIMETRIC SIGNATURES

Quanhua Liu [1,2], and Fuzhong Weng[2]
[1] CIRA, Colorado State University, Fort Collins, Colorado
[2] NOAA/NESDIS/ Office of Research and Applications, Camp Springs, Maryland

1. INTRODUCTION

There are growing needs to study polarimetric signatures at microwave frequencies for developing a physical retrieval algorithm of sea surface wind vector. In particular, the upcoming satellite sensors such as WindSAT/Coriolis and Conical Microwave Imager Sounder (CMIS) of U.S. National polar-orbiting Environmental Satellite System (NPOESS) will have full Stokes vector at low frequencies in addition to the polarization measurements at higher frequencies. The full polarimetric signatures allow us to derive both sea surface wind speed and direction which are very helpful for weather forecast and climate monitoring. The polarimetric two-stream radiative transfer model used here is extremely fast so that the model can be used in data assimulation and for physical retrievals of operational products. It is shown that the brightness temperature within the range of satellite viewing angle calculated from the polarimetric two-stream model differs from that obtained from the sixteen-stream model by no more than 1 K for various atmospheric and surface conditions including precipitation. Simulations show all four components of Stokes vector are sensitive to the sea surface wind direction. The variation of the first and second components (intensity and polarization) to the sea surface wind direction is about 2 K. The variation of the third component of Stokes vector can reach up to 4 K. The dependence of the sensitivity on wind direction and speed as well as frequency is discussed. The polarimetric signatures are also beneficial to other products such as sea surface wind speed and total precipitable water. The improvement to those products is discussed.

2. POLARIMETRIC TWO-STREAM RADIATIVE TRANSFER MODEL

The advantages using two-stream model are its analytical and fast solution of a radiative transfer equation. For a scalar two-stream model the asymmetry factor of the phase function is used to take into account the multiple scattering. For a polarimetric two-stream model, two additional parameters are introduced to solve the polarimetric radiative transfer equation. The new parameters are the phase polarization factor q_0 and phase polarization asymmetry factor q_1 defined as follows:

$$q_0 = \int_{-1}^{1} [P_{rr}(\cos\Theta) - P_{ll}(\cos\Theta)] d\cos\Theta \quad (1)$$

$$q_1 = \int_{-1}^{1} [P_{rr}(\cos\Theta) - P_{ll}(\cos\Theta)] \cos\Theta d\cos\Theta \quad (2)$$

where p_{ll} and p_{rr} are the parallel and perpendicular components of the phase matrix, respectively. Liu and Simmer (1996) showed that q_0 is smaller than one and it is directly related to the polarization difference. Detailed discussions on this model are found in Liu and Weng (2001).

The solution of the third and fourth components of Stokes vector must be zero because of a lack of the source. However, the atmosphere can still modify the surface polarimetric properties through the absorption and scattering. As demonstrated in the previous studies (Yueh 1997), the third and fourth components can be also generated by the small and large surface roughness of ocean. Thus, these U and V components are affected by the boundary conditions of a Stokes emissivity vector and a bistatic reflectivity matrix (Weng 1992).

3. VALIDATION

The polarimetric two-stream radiative transfer model is tested against the sixteen-stream model. Within the range of satellite viewing angles, the microwave brightness temperatures from the two-stream are accurate (< 1 K). The simulated brightness temperatures from the polarimetric two-stream model are compared with the SSM/I measurements under clear sky conditions. The SSM/I and surface observations over Atlantic ocean were matched up during ICE experiment in 1989. The temporal difference is less than 1 hour whereas the spatial

* Corresponding author address: Quanhua Liu, CIRA/CSU, NOAA/NESDIS/ORA, 5200 Auth Road, Camp Springs, MD 20746

difference is within 30 km. Surface observations include buoy surface wind, temperature and radiosonde data. Surface measurements are used as inputs to the polarimetric two-stream model. Figures 1-3 display simulated brightness temperatures vs SSM/I measurements at 22 GHz and 37 GHz. In general, the rms error is near 4 K and the bias is less than 2 K. These errors and biases would be significantly reduced if the effect of wind direction can be included in the simulations. As indicated earlier (Yueh 1997), the wind direction can induce a variation of ± 1 K for the vertically polarized brightness temperature and ± 3 K for the horizontally polarized brightness temperature under clear sky conditions. Unfortunately, the azimuthal direction of SSM/I data was not stored in the matchup data.

4. DISCUSSION

The new polarimetric two-stream model is valided and ready for many applications.

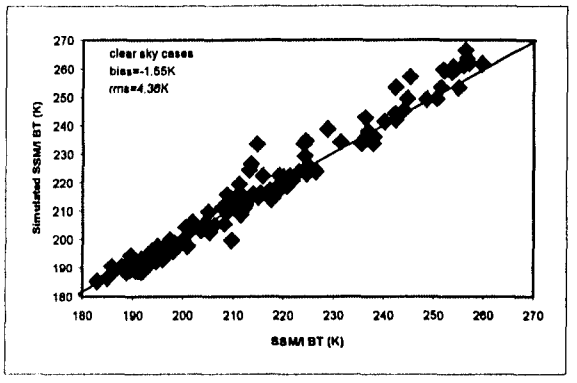

Figure 1. Comparisons of the vertically polarized brightness temperature at 22 GHz.

The polarimetric two-stream model runs fast. For a cloudy atmosphere, the polarimetric two-stream model is about 100 ~ 1000 times (depending on number of the cloud layers) faster than the detailed radiative transfer calculation. The computation efficient enables us to perform the physical retrieval for the microwave sensors and the data assimilation.

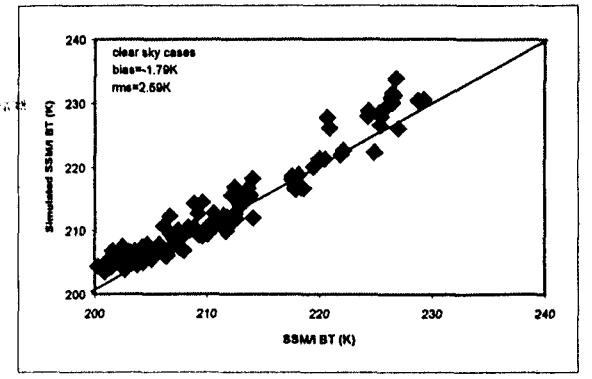

Figure 2. Comparisons of the vertically polarized brightness temperature at 37 GHz.

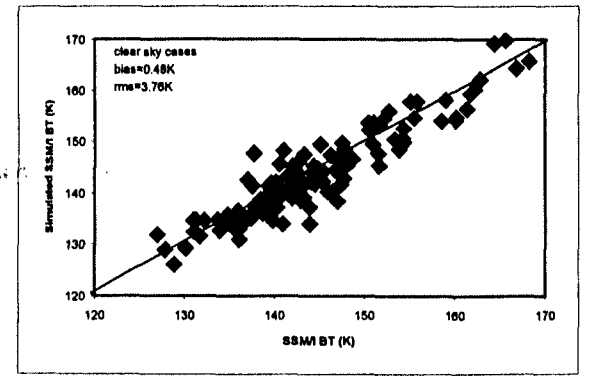

Figure 3. Comparisons of the horizontally polarized brightness temperature at 37 GHz.

5. REFERENCE

Liu, Q., and C. Simmer, 1996: Polarization and intensity in microwave radiative transfer. *Contri. Atmos. Phys.*, 69, 535-545.

Liu, Q., and F. Weng, 2001: A polarimetric two-stream radiative transfer, submitted to Journal of Atmospheric Sciences.

Weng, F., 1992: A multi-layer discrete-ordinate method for vector radiative transfer in a vertically-inhomogeneous, emitting and scattering atmosphere I: Theory. *J. Quant. Spec. Radiat. Trans.*, 47, 19-33.

Yueh, S., 1997: Modeling of wind direction signals in polarimetric sea surface brightness temperatures. *IEEE Trans. Geosci. Remote Sensing*, 35, 1400-1418.

P5.31

A TEST OF THE PETTY AND KATSAROS (1994) INCIDENCE ANGLE CORRECTION IN A FORWARD MODEL

Clay B. Blankenship*
Naval Research Laboratory, Monterey, California

1. INTRODUCTION

In microwave radiative transfer (RT) models, upwelling brightness temperatures (TB's) over an ocean background are generally computed by following the path of a single beam of radiation with specular reflection off a horizontal plane surface. While models generally allow for the variation of surface emissivity with surface roughness, another effect is often neglected. The upwelling radiation at zenith angle θ actually includes contributions from a range of incidence angles, due to the variation of surface slope within the field of view. Petty and Katsaros (1994) derived a parameterization (at Special Sensor Microwave Imager (SSM/I) frequencies and view angle) for an effective sky radiation angle θ' which could be used as the angle of a single beam of downwelling radiation in an RT model. This parameterized incidence angle is tested in this paper.

2. PROCEDURE

The Petty and Katsaros (PK) incidence angle correction was tested using simulations in the following manner. A set of 20 different atmospheres (together with surface temperature and wind speed) was compiled. These were taken from NOGAPS model atmospheres at various points around the globe. In nine of the cases, clouds were assigned (with total cloud liquid water ranging up to 0.2 mm) and the relevant levels were saturated. Simulated SSM/I TB's were calculated with the downwelling radiation angle set to 1) the upwelling radiation angle θ (simple reflection off a horizontal plane), and 2) the corrected sky radiation angle θ'. Table 1 gives values for the mean TB's for each channel with each computation method. In all cases the corrected TB is higher since the PK correction always gives a lower (less steep) incidence angle and hence a greater optical depth.

Table 1. Mean calculated brightness temperatures before and after the Petty and Katsaros correction.

Channel	Mean TB (Original)	Mean TB (Corrected)	Difference
19V	200.4 K	201.6 K	1.2 K
19H	140.8	143.9	3.0
22V	226.4	227.4	1.0
37V	217.8	218.8	1.0
37H	160.2	164.9	4.7
85V	257.7	257.9	0.2
85H	224.7	228.9	4.2

*Corresponding author address: Clay B. Blankenship, Naval Research Laboratory, 7 Grace Hopper Ave., Monterey, CA 93943; e-mail:blankens@nrlmry.navy.mil.

Next, for each atmosphere, simulated retrieved values of precipitable water (PW) and surface wind speed (SWS) were computed from the Environmental Data Record (EDR) algorithms of the SSM/I Algorithm Specification Document (Raytheon Systems Company, 2000). The SWS algorithm is more fully described by Goodberlet et al. (1990). The EDR algorithms were derived by regression with buoy-observed SWS and radiosonde-observed PW. Because these algorithms were empirically derived from relationships between TB and observed parameters in the real atmosphere, they provide a test for RT models. Inputting a more realistic set of TB's into the EDR algorithms is expected to more closely reproduce the model EDR values. Results from this experiment are shown in Table 2.

Table 2. Results from simulated retrievals for uncorrected and corrected brightness temperatures.

	Surface Wind Speed [m/s]	Precipitable Water [cm]
Mean	9.53	2.88
Bias(Original)	-2.54	-0.01
Bias(Corrected)	0.27	0.03
Standard Deviation of Error (Original)	0.85	0.25
Standard Deviation of Error (Corrected)	1.31	0.26
RMS Error (Original)	2.67	0.24
RMS Error (Corrected)	1.30	0.25

3. RESULTS AND ANALYSIS

The PK correction improved the RMS error for SWS from 2.67 m s^{-1} (40% of the mean) to 1.30 m s^{-1} (21% of the mean). The correction had very little effect on the retrieved PW. This can be explained because 1) proper retrieval of SWS is dependent on accurate modeling of surface effects, and 2) the PW EDR uses channels less affected by the incidence angle correction.

Most of the improvement in SWS is due to the reduction of a systematic bias in the uncorrected TB's, so it is possible that the correction is just compensating for another systematic error in the RT model. However, given the systematic TB correction and the fact that the EDR algorithm for SWS is a linear combination of Tb's, a systematic change in retrieved EDR values is

expected. This experiment shows that the effective incidence angle correction given by Petty and Katsaros (1994) does introduce a significant improvement to simulated retrievals of SWS.

4. REFERENCES

Goodberlet, M., C. T. Swift, and J. Wilkerson, 1990, Ocean Surface Wind Speed Measurements of the Special Sensor Microwave/Imager (SSM/I), *IEEE Trans. Geo. Rem. Sens.*, **28**, 823-828.

Petty, G. W. and K. B. Katsaros, 1994, The Response of the SSM/I to the Marine Environment. Part II: A Parameterization of the Effect of the Sea Surface Slope Distribution on Emission and Reflection, *J. Atmos. Ocean. Tech.*, **11**, 617-628.

Raytheon Systems Company, 6 January 2000, SSM/I Algorithm Specification Document AS-32268-100.

P5.32 KCARTA : A FAST PSEUDO LINE-BY-LINE RADIATIVE TRANSFER CODE WITH SCATTERING

Sergio De Souza-Machado*, L. Larrabee Strow,
Howard E. Motteler and Scott E. Hannon
University of Maryland Baltimore County, Baltimore, MD 21250 USA

1. INTRODUCTION

Line-by-line radiative transfer algorithms are the basis for fast forward models used in the retrieval of atmospheric parameters from satellite measured radiances. As we begin the era of high-spectral resolution infrared sounding the availability of accurate, fast, and easy-to-use line-by-line models will become even more important. High-spectral resolution sensors, compared to the present wide-band filter-based sounders, will stress the accuracy of the line-by-line models. This is especially true for channels in-between spectral lines where difficult to model line-wing effects dominate. Note that these channels are also the best choices for sounding since they have sharper weighting functions than channel sitting on the top or sides of spectral lines.

We have previously developed a highly compressed pre-computed database of monochromatic atmospheric optical depths that is accurate, relatively small (600 Mbytes), and easy to use, Strow et al. (1998). We call the radiative transfer algorithm that uses this compressed database *kCARTA*, DeSouza-Machado et al. (1997), which stands for the k-Compressed Atmospheric Radiative Transfer Algorithm. The original version of the *kCARTA* optical depth database used *GENLN2* Edwards (1992) to generate the database.

Although *GENLN2* does include first-order CO_2 line-mixing, it does not include a physically-based model for P/R-branch CO_2 line-mixing or duration-of-collision effects, both of which are important for temperature sounding. Subsequently, we developed our own line-by-line code (in MATLAB) that includes all of these important effects, DeSouza-Machado et al. (1999). However, because accurate transmittance calculations of line-mixing and duration-of-collision effects using physically-based models is much more complicated, and far slower, than standard line-by-line calculations, this line-by-line code is quite slow, which is one reason we developed the *kCARTA* compressed look-up table approach.

Radiances computed using *kCARTA* are as accurate as those computed with a line-by-line code since our lossy compression algorithm procedure introduces errors well below spectroscopy errors. *kCARTA* can also provide very fast temperature and gas amount radiance Jacobians for sensitivity studies and retrieval algorithms.

In this paper we present an overview of the capabilities of *kCARTA* and introduce a new version that includes three scattering algorithms, *RTSPEC* Deeter and Evans (1998), *DISORT* Stamnes et al. (1998), and our own *TWOSTREAM* scattering code. The speed and relative simplicity of our compressed database allows us to easily interface it to other codes with almost no performance penalty. *DISORT* is interfaced to *kCARTA* primarily to easily test the accuracy of other scattering approximations, since it is often too slow for many monochromatic applications.

2. OVERVIEW OF *kCARTA*

The *kCARTA* database currently spans 605 to 2830 cm^{-1} at a point spacing of 0.0025 cm^{-1}. Each of these 0.0025 cm^{-1} points is an average of five points on a 0.0005 cm^{-1} grid centered about each 0.0025 cm^{-1} grid point. Thus *kCARTA* is not truely monochromatic, although for both existing and planned satellite instruments, it can be considered monochromatic for all practical purposes. The compressed optical depths are tabulated for 11 temperatures covering all possible atmospheric conditions. The default layering of the atmosphere is 100 layers, which are the same as those used for the *AIRS* (Atmospheric InfraRed Sounder, Aumann and Pagano (1994)) fast forward model Hannon et al. (1996).

Generation of monochromatic transmittances from

*Corresponding author address : S. DeS-M, Dept. of Physics, 1100 Hilltop Circle, UMBC, Baltimore MD 21250; email: sergio@umbc.edu

this database for an arbitrary Earth atmosphere temperature, pressure and gas amount profile is more than an order of magnitude faster than using a line-by-line code. Interpolation to arbitrary profile layering in temperature and pressure can be done using the compressed version of the optical depths, leading to significant compute savings. Both up- and down-welling radiance computations are possible, although limb-viewing is not supported.

kCARTA serves as the *AIRS* "Reference Forward Model" and is used to generate the *AIRS* fast forward model Hannon et al. (1996) and to validate the *AIRS* radiance products.

For a downward looking instrument in a clear sky, the surface and layer emission terms are automatically included in the radiative transfer calculation. In addition, reflected background thermal and solar terms can also be included. The reflected thermal contribution is accurately computed at each spectral point by using a diffusive angle that varies with the layer to ground absorption, instead of $\arccos(3/5)$ at each layer. The program can either assume a plane parallel atmosphere, or include effects on the satellite viewing angle due to the curvature of the earth.

While uncompressing the database, *kCARTA* can compute the gas amount *and* temperature radiance Jacobians very rapidly DeSouza-Machado et al. (1997). Jacobians are very useful in analyzing which part of the atmosphere the radiance is most sensitive to a change in the amount of one of its constituents and/or temperature.

Radiative fluxes can also be computed by computing radiance intensities at various angles for each layer. The speed of *kCARTA* makes it an attractive alternative to other existing "line by line" codes for radiance and flux calculations.

3. SCATTERING

If an atmosphere is to be modeled more realistically, the effects of clouds and/or aerosols should be included. For infrared applications, especially for small particle clouds, relatively simple scattering approaches can be quite accurate. The speed gain with a simple two-stream approach, for example, is extremely important for a pseudo-monochromatic codes such as *kCARTA* and it's application to the high-spectral resolution radiances that will be measured by *AIRS*.

The radiative transfer equation to be solved is Deeter and Evans (1998); Liou (1980) :

$$\mu\frac{dI(\nu)}{d\tau_e} = I(\nu) - B(\nu,T)(1-\omega_0) - \frac{\omega_0}{2}\int_{-1}^{+1} I(\nu,\tau_e,\mu\prime)P(\mu,\mu\prime)d(\mu\prime) - \frac{\omega_0}{4\pi}\pi F_{sun}P(\mu,-\mu_{sun})e^{-\tau_e/\mu_{sun}}$$

This involves an integral over the intensities at various angles, weighted by a phase function P. I is the radiance at viewing angle $\arccos(\mu)$, $B(T)$ is the Planck radiance at temperature T, ω_0 is the single scattering albedo and F_{sun} is the incident solar flux. Depending on the number of stream angles intensities used to evaluate the integral, one has a n stream solution to the problem.

kCARTA has been interfaced with two well known scattering packages, *DISORT* Stamnes et al. (1998) and *RTSPEC* Deeter and Evans (1998). *DISORT* can include the effects of solar beam scattering but is quite slow. *RTSPEC* uses two streams to compute the solution, and is very fast; however it does not include the effects of solar beam scattering. Our *TWOSTREAM* scattering package includes solar beam scattering and is fast.

Similar to *DISORT* and *RTSPEC*, *TWOSTREAM* uses an exponential-in-tau layer temperature variation in the cloudy layers, while it uses an average layer temperature in the clear layers. Background thermal is also included for a down-looking instrument. *TWOSTREAM* computes the reflection, transmission, emission and beam coefficients for the cloud by adding together the coefficients for the individual cloud layers. As interfaced, the three scattering codes assume that the cloud particles are spheres (Mie scattering); however more general routines could be used to compute the phase function, single scattering albedo and asymmetry factor for other particle shapes, and used in any of the three algorithms.

Figure 1 shows a comparison run of the three scattering codes in the infrared for a nighttime down-looking instrument for a 1 km thick cirrus cloud. One can see that the three agree very well with each other, even though *DISORT* uses more than two streams, as compared to *RTSPEC* and *TWOSTREAM* that each use two. The main use of this code will be in the window regions, where the agreement is quite good. *RTSPEC* is a little more accurate than our *TWOSTREAM* code, but as stated earlier, *RTSPEC* cannot do solar scattering.

On a Linux PC *kCARTA* can compute the clear-sky up-welling radiance from 605 to 2830 cm^{-1} in approximately 5 minutes using the 100 *AIRS* layers. Introducing a 3-layer cloud, our *TWOSTREAM* algorithm takes about 20% more time than the clear-sky calculation.

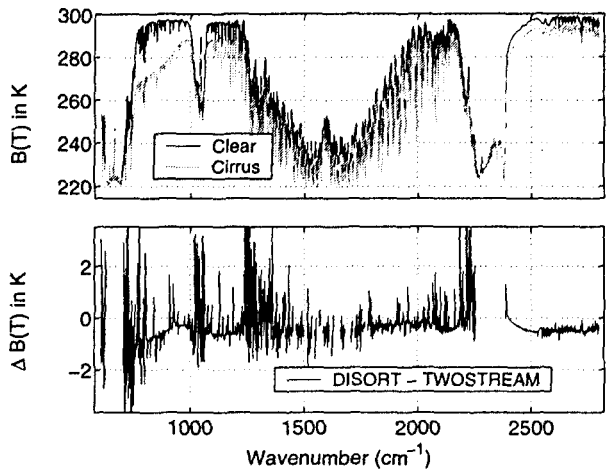

Figure 1: Clear sky vs cloudy sky computations, from Ground to TOA. A 1 km thick cirrus cloud is at 10 km in a US Standard Atmosphere, with average particle size of 10 μm and IWP = 2 g/m^2

Our initial use of this new capability of *kCARTA* will be to measure cirrus cloud properties using *AIRS*, and using a new high-resolution radiometric interferometer we are presently installing on Mauna Lao in Hawaii.

4. CONCLUSIONS

kCARTA is a fast pseudo line-by-line code which offers the user many desirable features. It provides very fast line-by-line accuracies, and the accuracy of its spectroscopic database has been extensively compared against *GENLN2*, although with the inclusion of P/R-branch line-mixing and duration-of-collision effects *kCARTA* will now produce somewhat different radiances than *GENLN2* in some CO_2 regions. Analytic temperature and gas amount clear sky Jacobians are rapidly computed. The computed radiances include the solar contribution as well as an accurate estimate of the background thermal. The package can allow the user to include the effects of scattering as well, with three package choices being available. The three packages give roughly the same results for the same conditions.

5. ACKNOWLEDGMENTS

This work was supported in part by NASA grant number 05-5-28108.

References

Aumann, H. H. and R. J. Pagano: 1994, Atmospheric Infrared Sounder on the Earth Observing System. *Optical Engineering*, **33**.

Deeter, M. and K. Evans: 1998, A hybrid eddington-single scattering radiative transfer model for computing radiances from thermally emitting atmospheres. *J.Quant.Spectrosc.Radiat.Transfer*, **60**, 635–648.

DeSouza-Machado, S., L. Strow, and S. Hannon: 1997, kCompressed atmospheric radiative transfer algorithm (kCARTA). *Satellite Remote Sensing of Clouds and the Atmosphere*, Proceedings of the European Symposium on Aerospace Remote Sensing #3220, Europto Series, Institute of Electrical Engineers, London, Great Britain.

— 1999, Improved atmospheric radiance calculations using CO_2 P/R branch line mixing. *Satellite Remote Sensing of Clouds and the Atmosphere*, Proceedings of the European Symposium on Aerospace Remote Sensing #3867, Europto Series, Florence, Italy.

Edwards, D.: 1992, GenIn2: A general line–by–line atmospheric transmittance and radiance model. *NCAR Technical Note 367+STR*, National Center for Atmospheric Research, Boulder, Colo.

Hannon, S., L. L. Strow, and W. W. McMillan: 1996, Atmospheric infrared fast transmittance models: A comparison of two approaches. *Proceedings of SPIE Conference 2830, Optical Spectroscopic Techniques and Instrumentation for Atmospheric and Space Research II.*

Liou, K.: 1980, *An Introduction to Atmospheric Radiation.* Academic Press.

Stamnes, K., T. S-C., W. W., and K. Jayaweera: 1998, Numerically stable algorithm for discrete ordinate method radiative transfer in multiple scattering and emitting layered media. *Appl. Opt.*, **27**, 2502–2509.

Strow, L., H. Motteler, R. Benson, S. Hannon, and S. De Souza-Machado: 1998, Fast computation of monochromatic infrared atmospheric transmittances using compressed look-up tables. *J. Quant. Spectrosc. Rad. Trans.*, **59**, 481–493.

P5.35

NOAA/NESDIS Operational Advanced-TOVS (ATOVS) Polar Orbiter Sounding Products

Anthony L. Reale
NOAA/NESDIS,Suitland, Maryland

Americo S. Allegrino
Raytheon Information Technology and Scientific Services, Lanham, Maryland

1.0 INTRODUCTION

Since 1979, the NESDIS operational sounding products from NOAA's polar orbiting satellites have provided a continuous suite of infrared and microwave radiation sounder measurements, and derived temperature and moisture sounding products on a global scale. These data represent a unique source of global, atmospheric, weather information, with a demonstrated positive impact on Numerical Weather Prediction (NWP) forecasts, NOAA's primary mission for sounding products. In May, 1998, the ATOVS instrument configuration onboard NOAA-15 was successfully deployed, followed by NOAA-16 in September, 2000. ATOVS consists of the new 15-channel Advanced Microwave Sounding Unit-A (AMSU-A), the new 5-channel AMSU-B for atmospheric moisture, the HIRS/3 and the AVHRR /3. ATOVS sounding products from NOAA-15 were operationally implemented by NESDIS in April, 1999 (Reale et al. 1999a and 1999b). AMSU-B processing was delayed until May, 2000 (Chalfant et al.1999 and Reale et al. 2000b). This report summarizes the ATOVS sounding product systems and scientific algorithms operated by NESDIS.

2.0 ATOVS SCIENTIFIC ALGORITHMS

Two product systems are currently operated, **ATOVS-A,** which processes sounding products using the HIRS, AMSU-A and AVHRR radiometers (Reale et al. 2000a), and **ATOVS-B,** which processes (moisture) sounding products using the AMSU-B radiometer (Chalfant et al. 1999). The scientific procedures for each system are comprised of two primary subsystems for **Orbital** and **Offline** support processing, respectively.

2.1 Orbital Processing

The orbital processing system consists of five steps:

- Preprocessing
- Radiance Temperature Adjustments
- Contamination Detection
- First Guess Computation
- Retrieval Computation

Preprocessing for each orbital system is done on the raw, level-1b satellite data. Preprocessing steps include the application of the calibration coefficients and, the computation of the radiance and radiance temperature measurements. In addition, preprocessing for ATOVS-B includes the correction of AMSU-B measurements for Radio Frequency Interference (RFI) from data transmitters onboard NOAA-15 (Atkinson 1999 and 2000). AMSU-B data from NOAA-16 have no RFI.

Limb adjustments are then applied to the calibrated, radiance temperature measurements from HIRS/3, AMSU-A and AMSU-B (Wark 1993 and Allegrino et al. 1999. The limb corrected measurements for AMSU-B are also adjusted to remove perceived bias relative to radiative transfer model calculations (Fleming et al. 1991).

The contamination detection step is done separately for microwave and infrared sensor data. Microwave contamination detection primarily consists of identifying localized anomalies in AMSU sounding channels sensitive in the lower troposphere typically due to precipitation and large ice particles (Grody et al. 1999). Infrared measurements are screened for cloud contamination by methods described in Ferguson and Reale, 2000.

The first guess computation is uniquely determined for each ATOVS-A and ATOVS-B sounding using a library search technique (Goldberg et al. 1988). The first guess libraries consist of collocated radiosonde and satellite observations, which are directly accessed during orbital processing and updated daily.

The matrix equation for the library search is given in (1):

$$D = (R - R_k)^t \; B^{-1} \; (R - R_k) \qquad (1)$$

where the subscript t indicates the matrix transpose and

D: scalar closeness parameter,
B: sounding channel radiance covariance matrix
R: adjusted, observed radiance temperature vector
R_k: adjusted, library radiance temperature vector

The first guess temperature, moisture and radiance temperature profiles for a given sounding are computed by averaging the 10 closest collocations; that is, those with the smallest "D". Radiosonde averages are used for temperature and moisture, and the adjusted measurements from the sounder are averaged for radiance temperature.

In the retrieval step, the general form of the retrieval equation is given by (2):

$$T - T_g = C\,(R - R_g) \qquad (2)$$

where T and R are product and measurement parameters, the subscript "g" an apriori estimate, and C is the solution.

The ATOVS-A retrieval method is the Minimum-Variance-Simultaneous (MVS) solution (Smith et al. 1984 and Fleming et al. 1986) given by matrix equation (3):

$$\begin{aligned} T - T_g &= S A^t (A S A^t + N)^{-1} (R - R_g) \qquad (3) \\ &= X \quad (\quad Y \quad)^{-1} (R - R_g) \end{aligned}$$

where the subscript t indicates the matrix transpose, and:

T: final soundings products vector, (151),
T_g: first guess products vector, (151)
S: first guess covariance matrix, (151 x 151),
A: sounder channel weighting matrix, (35 x 151),
N: measurement noise covariance matrix, (35 x 35),
R: observed radiance temperature vector
R_g: first guess radiance temperature vector
X,Y: pre-computed retrieval operator components.

The product vector (T) contains 100 levels of atmospheric temperature (1000 mb to .1 mb), 50 levels of moisture (1000 mb to 200 mb), and the surface level. The dimension 35 for the A and N matrices denotes all the ATOVS channels; not all are used. The first guess and observed channels used in the retrieval solution, depend on the sounding type.

The ATOVS-B retrieval utilizes an ordinary least squares solution of equation 2, where:

T: water vapor mixing ratio sounding products vector
T_g: first guess mixing ratio vector
C: statistical regression coefficients
R: observed radiance temperature vector
R_g: first guess radiance temperature vector

The product vector (T) includes 15 levels of atmospheric moisture (1000 to 300 mb). Two sets of regression coefficients are available, for sea and non-sea soundings respectively.

The original calibrated sounder measurements, the adjusted sounder measurements, the first guess information, the derived temperature and moisture soundings and the appended ancillary data (i.e. cloud mask, AVHRR, SST, etc.) are operational products that are routinely distributed to users. The dedicated links for these data are NOAA-EMC, the United Kingdom Meteorological Office (UKMO) (Bracknell, England), the Global Telecommunications System (GTS) and the Shared Processing Network (SPN).

2.2 Offline Processing

The offline systems contribute the tuning and validation functions required to maintain the scientific integrity of the sounding products. Offline systems routinely compile and maintain data sets comprised of

- Satellite Radiance Databases
- Satellite and Radiosonde Collocations
- Coefficients

The Satellite Radiance Database Sets are separately maintained for HIRS/3, AMSU-A and AMSU-B radiometer data. These data sets contain adjusted and non-adjusted radiance temperature measurements for the respective instruments, typically spanning the latest 30 to 60 days. Each data set is updated at the conclusion of orbital processing at about a 50% sub-sampling rate, excluding polar-redundant and high terrain (>1000m) observations.

Collocated radiosonde and satellite observations are extensively used in the derivation and validation of the operational sounding products. The steps to compile and utilize collocated radiosonde and satellite observations include the radiosonde collocation processing and, updating the Matchup Data Bases (MDB) and the First Guess Libraries.

In the radiosonde collocation process, the radiosonde reports are processed daily. Accepted radiosonde reports are candidates for collocation with satellite data. A collocated radiosonde and satellite observation is compiled if the candidate radiosonde and satellite sounding data meet the criteria described in Tilley et. al., 2000.

The Matchup Data Bases (MDB), supporting the ATOVS-A and ATOVS-B products systems, respectively, provide the longer term data sets of radiosonde and satellite data collocations used for the tuning and validation of derived sounding products (Tilley et al. 2000 and Reale et al. 1990). Each MDB is updated daily. The ATOVS-A system maintains separate MDB's for clear and cloudy collocations, which are stratified among 23 geographical categories. On the other hand, the ATOVS-B system maintains a single MDB where collocations are stratified by sea and non-sea.

The First Guess Libraries are updated daily based on the MDBs, and directly accessed during orbital processing. The first guess libraries have about half of the capacity of the MDBs, with an additional requirement that the vertical extent of a candidate radiosonde report be complete from (at least) 950 mb

to 50 mb for ATOVS-A, and from 950 mb to 400 mb for ATOVS-B, respectively. A new approach based on a statistical regression of the collocated AMSU-A measurements (Goldberg 1999) was deployed for NOAA-15 during April 2000 to extend each radiosonde from the highest report level to .1 mb. The downward extension of a radiosonde is only required if the first significant level is between 950 and 1000 mb, and is done using a weighted, averaged, lapse rate and constant dewpoint depression for temperature and moisture, respectively, based on the lowest reported levels.

Various offline systems also compute coefficients for the derivation of operational sounding products. Coefficients are required for limb adjustment, cloud detection (Ferguson and Reale, 2000), the first guess (Goldberg et al. 1988), the retrieval (Fleming et al, 1986 for ATOVS-A and Goldberg et al. 1998 for ATOVS-B), AMSU-B radiance bias adjustment (Fleming et al. 1991 and McMillin et al. 1989, using the approach of Crone et al. 1996), and, RFI correction (AMSU-B for NOAA-15). Except for limb adjustment and RFI correction, all coefficients are updated weekly.

3.0 RESULTS

The scientific monitoring and evaluation of operational sounding products is maintained on a continuous basis at NESDIS. The primary evaluation strategy is the vertical accuracy statistics. Vertical accuracy statistics, based on satellite minus radiosondes differences computed from collocations stored on the MDB, are illustrated in Figures 1 and 2. These provide estimates of the expected performance of NESDIS operational soundings on a global scale. Figure 1 shows differences for ATOVS-A clear temperature soundings from the 60N to 60S latitude belt. Figure 3 shows differences for ATOVS-B moisture soundings for the 30N to 30S latitude belt. The thicker curves for each plot are for the final soundings, and the thinner lines for the corresponding first guess profiles, respectively. Figure 2 provides mean and standard deviation differences in degrees K, whereas the Figure 3 plots are percent differences in water vapor mixing ratio (g/kg), with the mean profiles used to compute percentages shown along the inside of the left axis. Pressure (mb) and sample size are indicated along the left and right vertical axis for all plots.

Figure 1 indicates that satellite minus radiosonde differences approach 2.5 K (RMS) near the surface and troposphere, 1.5 K in the middle troposphere where the sounders are most reliable, and about 2.0 K in the stratosphere. Little or no bias is present except at the tropopause. Figure 2 indicates expected uncertainties for moisture near the surface to be about 15 percent in the tropics. However, when multiplied by the mean mixing ratio values, the actual differences in water mixing ratio units is about 2 g/kg in the tropics. The steady increase in the percentage uncertainty of moisture with height is also attributable to the relatively low mixing ratio values aloft. Factoring in the spatial and temporal windows for each collocation, the inherent variability of moisture measurements, and radiosonde moisture errors, the accuracy estimates shown in Figure 2 are reasonable.

Significantly improved accuracy of the final soundings (thick curves) compared to the guess (thin curves) in Fig. 1 confirms the scientific approach, in particular, the consistency of the first guess radiance temperature and temperature observations provided for the retrieval step (Fleming et al. 1986).

4.0 FUTURE PLANS

The primary scientific activity planned over the next year is the merging of the ATOVS-A and B systems into a single, simultaneous, temperature and moisture products generation system. This will include studies to replace the library search with a statistical regression technique based on AMSU, and if successful, the replacement of pre-computed with real-time retrieval operators. Referred to as System-2002, the proposed upgrade would result in dual sounding products, consisting of climate oriented first guess information, and real-time weather oriented derived products, the later optimized for assimilation into NWP. There are also new requirements to provide ATOVS processing fall back contingencies, particularly in the event of a HIRS sounder failure.

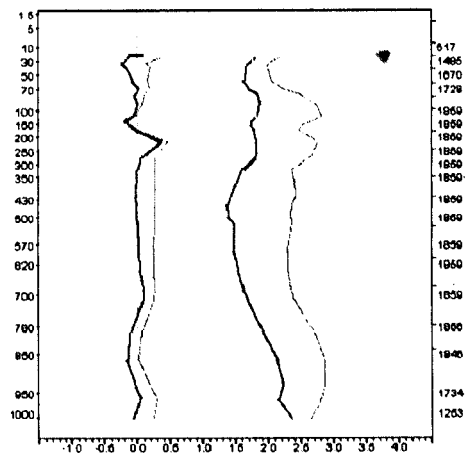

Figure 1: ATOVS-A Clear Statistics

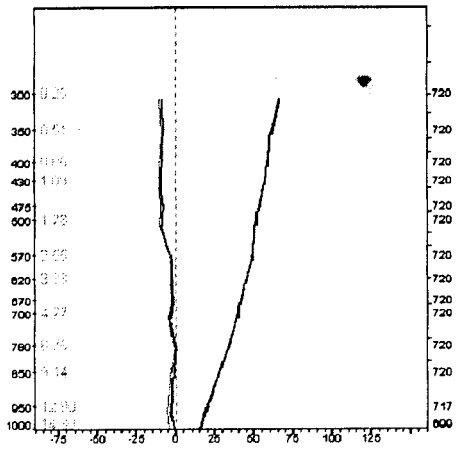

Figure 2: ATOVS-B Tropical Statistics

5.0 REFERENCES

Allegrino, A., A.L. Reale, M.W. Chalfant and D.Q.Wark, 1999: Application of limb adjustment techniques for polar orbiting sounding data. Technical Proceedings of the 10th International TOVS Study Conference, Jan 26- Feb 2, Boulder, Colorado, USA., 1-10.

Atkinson, N.C., 2000: Calibration, monitoring and validation of AMSU-B. 33rd Committee on Space Research (COSPAR) Scientific Assembly, Warsaw, 16-23 July, to be published in Advances in Space Research.

Atkinson, N.C., 1999: Calibration and in-orbit performance of AMSU-B. Technical Proceedings of the ECMWF/EUMETSAT Workshop on Use of ATOVS Data for NWP Assimilation, 2-5 November, 105-108.

Chalfant, M.W., A. Reale, and F. Tilley, 1999: Status of NOAA Advanced Microwave Sounding Unit-B products. Technical Proceedings of the 10th International TOVS Study Conference, Jan 26- Feb 2, Boulder, Colorado, USA., 60-71.

Crone, L.J., L.M. McMillin, and D.S. Crosby, 1996: Constrained Regression in satellite meteorology. Journal of Applied Meteorology, AMS, Vol 35, No. 11, 2023-2035.

Ferguson, M.P., and A.L. Reale, 2000: Cloud detection techniques in NESDIS Advanced-TOVS sounding products systems. 10th Conference on Satellite Meteorology and Oceanography, 9-14 January, Long Beach, Ca., 252-254.e

Fleming, H.E., et. al., 1991: The forward problem and corrections for the SSM/T satellite microwave temperature sounder. IEEE Transactions on Geoscience and remote Sensing, Vol. 29, No. 4, 571-584.

Fleming, H.E., D.S. Crosby, and A.C. Neuendorffer, 1986: Correction of satellite temperature retrieval errors due to errors in atmospheric transmittances. Journal of Climate and Applied Meteorology, Vol 25, No. 6, 869-882.

Goldberg, M.D., 1999: Generation of retrieval products from AMSU-A: methodology and validation Technical Proceedings of the 10th International TOVS Study Conference, Jan 26- Feb 2, Boulder, Colorado, USA., 219-229.

Goldberg, M, J. Daniels and H. Fleming, 1988: A method for obtaining an improved initial approximation for the temperature/moisture retrieval problem. Preprints, 3rd Conference on satellite Meteorology and Oceanography, Anaheim, Ca, 16-19.

Goldberg, M.D., A. Reale and G. Kratz, 1998: The use of pattern recognition to derive SSM/T2 moisture retrievals. Adv. Space res., Vol. 21, 385-398.

Grody, N., et. al., 1999: Applications of AMSU for obtaining water vapor, cloud liquid water, precipitation, snow cover and sea ice concentration. Technical Proceedings of the 10th International TOV Study Conference, Jan 26- Feb 2, Boulder, Colorado, 230-240.

McMillin, L.M., L.J. Crone and D.S. Crosby, 1989: Adjusting satellite radiance by regression with an orthogonal transformation to a prior estimate. Jour. Appl. Meteor., Vol 28, No 9, 969-975.

Reale, A.L., M.W. Chalfant, and L.M. Wilson, 2000a: NESDIS advanced TOVS sounding products. 10th Conference on Satellite Meteorology and Oceanography, 9-14 January, Long Beach, Ca., 259-262.

Reale, A.L., M.W. Chalfant, and F.H. Tilley, 2000b: NESDIS moisture sounding products from AMSU-B and SSM/T2. 10th Conference on Satellite Meteorology and Oceanography, 9-14 January, Long Beach, Ca., 263-266.

Reale, A., M. Chalfant and L. Wilson, 1999a: Scientific status of NOAA advanced TOVS sounding products. Technical Proceedings of the 10th International TOVS Study Conference, Jan 26- Feb 2, Boulder, Colorado, USA., 437-448.

Reale, A., M. Chalfant and L. Wilson, 1999b: Scientific status of NESDIS advanced TOVS sounding products. Technical Proceedings of the ECMWF/EUMETSAT Workshop on Use of ATOVS Data for NWP Assimilation, 2-5 November, 1999, 153-160.

Reale, A., H. Fleming, D. Wark, C. Novak, M. Gelman, F. Zbar, J. Neilon, and H. Bloom, 1990: Baseline upper air network final report. NOAA Technical Report NESDIS 52, U.S. Dept. Of Commerce, Washington D.C., 57 pp.

Smith, W.L., H.M. Woolf, C.M. Hayden, D.Q. Wark, A.J. Schreiner and J.F. LeMarshall, 1984: The physical retrieval TOVS export package. Proc. Of the First International TOVS Study Conference, Madison, Wi., Cooperative Institute for Meteorological Satellite Studies, 227-278.

Tilley, F.H., M.E. Pettey, M.P. Ferguson, and A.L. Reale, 2000: Use of radiosondes in NESDIS advanced-TOVS (ATOVS) sounding products. 10th Conference on Satellite Meteorology and Oceanography, 9-14 January, Long Beach, Ca., 255-258.

Wark, D.W., 1993: Adjustment of TIROS operational vertical sounder data to a vertical view. NOAA Technical Report NESDIS-64, U.S. Dept. Of Comm., Washington D.C., 36 pp.

P5.36

DERIVING ATMOSPHERIC TEMPERATURE AND HUMIDITY PROFILES FROM AMSU-A AND AMSU-B MEASUREMENTS USING NEURAL NETWORK TECHNIQUES

Lei Shi *
SeaSpace Corporation, Poway, California

1. INTRODUCTION

The Advanced Microwave Sounding Unit (AMSU) is an operational microwave sounder aboard the new generation of the National Oceanic and Atmospheric Administration (NOAA) polar orbiting satellites. Currently there are two satellites in this series, NOAA-15 and NOAA-16, carrying the AMSU platform. The AMSU platform is composed of three separate radiometers referred to as AMSU-A1, AMSU-A2, and AMSU-B. Collectively AMSU-A1 and AMSU-A2 are named AMSU-A. Table 1 lists the AMSU channel frequencies based on the values specified in Goodrum et al. (1999). The AMSU modules are cross-track, line scanned instruments. The AMSU-A sensor scans in a stepped-scan mechanism and covers 30 discrete scene resolution cells in each scan line. The cell at nadir has a resolution of 50 km. The AMSU-B sensor samples 90 contiguous scene resolution cells in a continuous fashion. The cell at nadir has a resolution of 16.3 km. The 20-channel AMSU represents a significant improvement in both horizontal and vertical resolutions from previous satellite microwave sounding instruments. The AMSU-A channels are designed to provide measurement for deriving atmospheric temperature profiles, while the AMSU-B channels, together with a number of the AMSU-A channels, are designed for deriving atmospheric humidity profiles. In this study, the retrievals of both temperature and humidity profiles from AMSU-A and AMSU-B measurements using neural network techniques are examined.

Though the AMSU sensors were not on board the NOAA satellite series until the NOAA-15, similar microwave temperature sounder have been flown on the Defense Meteorological Satellite Program (DMSP) satellites for more than 20 years. An investigation of using neural network technique to derive atmospheric temperature based on the DMSP Special Sensor Microwave Temperature Sounder (SSM/T1) was carried out by Butler et al. (1996). Their study showed that neural networks yield excellent results in retrieving temperature profiles together with tropopause temperature and pressure estimates.

Table 1. AMSU-A and AMSU-B channel frequencies.

Instrument	Ch. Num.	Channel Frequency (MHz)	Bandwidth (MHz)
AMSU-A2	1	23,800	251.02
	2	31,400	161.20
AMSU-A1	3	50,300	161.14
	4	52,800	380.52
	5	53,596+/-155	168.20
	6	54,400	380.54
	7	54,940	380.56
	8	55,500	310.34
	9	57,290.344	310.42
	10	57,290.344+/-217	76.58
	11	57,290.344+/-322.2+/-48	35.11
	12	57,290.344+/-322.2+/-22	15.29
	13	57,290.344+/-322.2+/-10	7.93
	14	57,290.344+/-322.2+/-4.5	2.94
	15	89,000	1998.98
AMSU-B	16	89,000+/-900	1000
	17	150,000+/-900	1000
	18	183,310+/-1000	500
	19	183,310+/-3000	1000
	20	183,31+/-7000	2000

Recently, Shi (2001) examined the retrieval of atmospheric temperature profiles from NOAA-15 AMSU-A measurements. Backpropagation neural networks were applied on both regional direct acquisition and global recorded AMSU-A data. The retrievals yielded good results in the atmospheric temperature profiles. For the global data retrieval case, the root-mean-square (rms) deviation of temperature retrieval was 3.2°C at the

* Corresponding author address: Lei Shi, SeaSpace Corporation, 12120 Kear Place, Poway, CA 92064.

surface, only 1.0 to 1.2°C in the mid-troposphere, less than 1.5°C around the tropopause, and between 1.0 and 1.5°C in the stratosphere. However, though global data coverage was considered, only data from a northern-hemisphere winter (and thus southern-hemisphere summer) season were examined. The resulting neural network structure may not work as well for the atmospheric conditions not represented by the profiles in the neural network training set. In the current study, global NOAA-16 AMSU-A data from March 2001 are supplemented to the neural network training set used in Shi (2001) to enhance the representation of the temperature conditions between the winter and summer seasons.

Backpropagation neural networks are also applied in the current study to derive the atmospheric humidity profiles from the AMSU measurements. A retrieval scheme is developed to derive the specific humidity at the surface and at pressure levels from 1000 to 100 hPa. In the retrieval scheme, channels 10 to 14 of AMSU-A are excluded as their weighting functions peak well above the 100 hPa level. The AMSU-A channel 15 is also excluded because it centers at the same frequency as that of the AMSU-B channel 16. All five channels of AMSU-B are used in the retrieval.

2. TEMPERATURE PROFILE RETRIEVAL

To build the neural network training structure, two series of global AMSU-A data are collected. The first series is taken from NOAA-15 during 9-13 January 2000, and the second series is taken from NOAA-16 during 17-23 March 2001. The AMSU-A data are processed into brightness temperatures. The analysis data corresponding to these two periods from the National Centers for Environmental Prediction (NCEP) global model Global Data Assimilation System (GDAS) at 0000, 0600, 1200, and 1800 UTC are used to construct the training set. The NCEP data consist of the temperature values at the surface and at the pressure levels of 1000, 975, 950, 925, 900, 850, 800, 750, 700, 650, 600, 550, 500, 450, 400, 350, 300, 250, 200, 150, 100, 70, 50, 30, 20, and 10 hPa. The neural network training set is built based on the subset of AMSU-A data that are within 0.5 h of the four NCEP analysis times and the subset of NCEP analysis data that are within the corresponding AMSU-A coverage. The collocation of AMSU-A and NCEP data is performed by matching each NCEP grid dataset with the closest AMSU-A pixel in the corresponding pass. A total of 40902 matched patterns are generated.

Backpropagation neural networks are used in developing the retrieval scheme. A presentation of the backpropagation theory, architectures, and applications can be found in Chauvin and Rumelhart (1995). A commercial pachage NeuroShell 2 (Ward Systems Group, Inc. 1996) is employed in the network training. A backpropagation neural network is a computer model composed of individual processing elements called neurons. A network consists of multiple layers of neurons interconnected with other neurons in the different layers. These layers are referred to as input layer, hidden layer, or output layer. Each layer is generally fully connected to the layers below and above.

For the temperature profile retrieval, there are 15 neurons in the input layer. They correspond to the brightness temperatures (in kelvin) of AMSU-A channels 1-12, channel 15, secant of AMSU-A sensor viewing angle, and position of the pixel in a scan line. AMSU-A channels 13 and 14 are excluded from the input structure because their weighting functions peak at around 4 hPa and 2 hPa pressure levels, respectively, much higher than the top retrieval level of 10 hPa. The number of neurons in the output layer is the number of the output variables in the retrieval. They correspond to the temperatures at 26 pressure levels and the surface temperature.

Different backpropagation architectures with different layers and transfer functions are examined. A five-layer network, with one input layer, three hidden layers, and one output layer, is chosen based on the improved performance compared to four-layer and three-layer networks. It is found that using a hyperbolic tangent function to propagate to each of the three hidden layers and a logistic transfer function to propagate to the output layers gives the optimum network performance for the type of data studied. The definition of the hyperbolic tangent transfer function is

$$f(x) = \tanh(x), \qquad (1)$$

and the definition of the logistic transfer function is

$$f(x) = \frac{1}{1+\exp(-x)}. \qquad (2)$$

The numbers of neurons in the hidden layers are adjusted and the best network performance is obtained by setting 46, 50, and 51 neurons, respectively, for the three hidden layers.

Among the total of 40902 collocated patterns, 20% (8180) are randomly extracted to construct a testing set, and another 20% are randomly extracted and set aside as a validation set for later statistical studies. As a result, there are 24542

patterns remaining in the training set. A backpropagation network is trained by "supervised learning". The network is presented with a series of pattern pairs, each consisting of an input pattern and an output pattern, in random order until predetermined convergence criteria are met. At this time the network presents the input elements in the testing set and retrieves the output elements. Then the retrieved output elements are compared with the output elements in the testing set, and the averaged root mean square deviation of all the output elements are computed. The network parameters are saved if the averaged rms deviation is less than that computed previously. This process is repeated until no improvement is found for a specified number of test trials.

Using the saved network parameters, the retrievals corresponding to each input pattern in the validation set are calculated. The rms deviation is computed using the output pattern in the validation data set as truth data. Fig. 1 illustrates the resulting rms deviations of the temperature profiles. The figure shows that the rms deviations are between 1.5 and 2.5°C at the near surface levels of 800 – 1000 hPa, and are between 0.8 and 1.5°C at the levels above. The vertical pattern of the temperature rms deviations is similar to that shown in Shi (2001). At the surface, the rms value is 4.1°C. This relatively large value is mostly due to broader temperature range and more complex radiative properties at the surface.

3. SPECIFIC HUMIDITY PROFILE RETRIEVAL

The similar retrieval technique is investigated to derive the specific humidity profile based on the winter series of NOAA-15 data described in the previous section. Both the AMSU-A and AMSU-B data are processed into brightness temperatures. The AMSU-B bias caused by radiation interference are corrected. Specific humidity profiles are derived from NCEP GDAS analyses of temperature and dew-point temperature profiles. The AMSU channel brightness temperatures are then collocated with the corresponding specific humidity profiles at the four GDAS analysis times. The collocation is performed by matching each NCEP grid dataset with the closest AMSU-A pixel and the AMSU-B pixels within the AMSU-A footprint. Only the AMSU data that are within 0.5 h of the four NCEP analysis times are considered. The collocation generated 47844 matched patterns. Among these collocated data, 20% (9568) are randomly extracted to construct a testing set for use during the network training phase. Another 20% are randomly extracted to construct a validation dataset. The remaining 28708 patterns are used to build the neural network training set for the specific humidity retrieval.

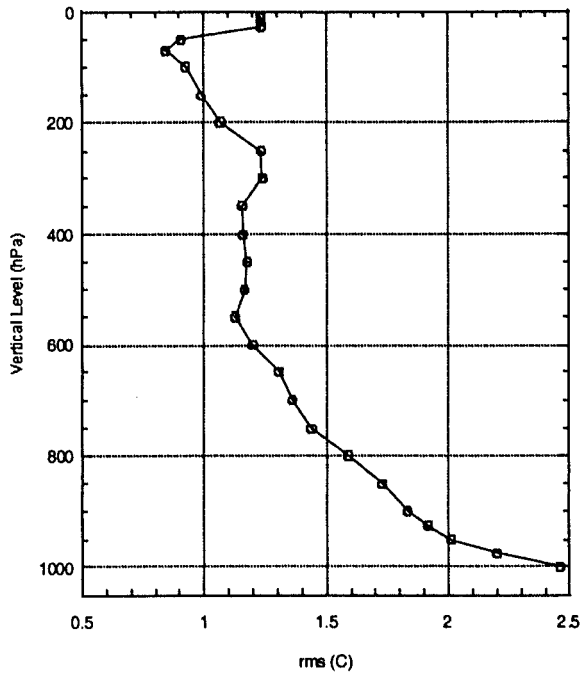

Fig. 1. The rms deviations of temperature retrieval.

It is found that five-layer backpropagation network structures with the same transfer functions as that used for the temperature retrieval also perform well for the specific humidity retrieval. Best performance is obtained by setting 63 neurons to each of the three hidden layers. In this network structure, there are 16 input elements in the input layer. They are the brightness temperatures of AMSU-A channels 1-9, five AMSU-B channels, secant of AMSU-B sensor viewing angle, and position of AMSU-B sample in a scan line. There are 22 elements in the output layer. They are specific humidity values at the surface and at the pressure levels of 1000, 975, 950, 925, 900, 850, 800, 750, 700, 650, 600, 550, 500, 450, 400, 350, 300, 250, 200, 150, and 100 hPa.

Similar to the temperature neural network training, the network is trained by randomly

presenting the input and output pairs from the training set. When the predetermined convergence criteria are met, a specific humidity retrieval is performed using the input data from the testing set. The retrieved elements are compared with the output elements in the testing set. The process is repeated and the network parameters that generated smallest averaged rms deviation among the comparisons are saved to build a computer model of the neural network.

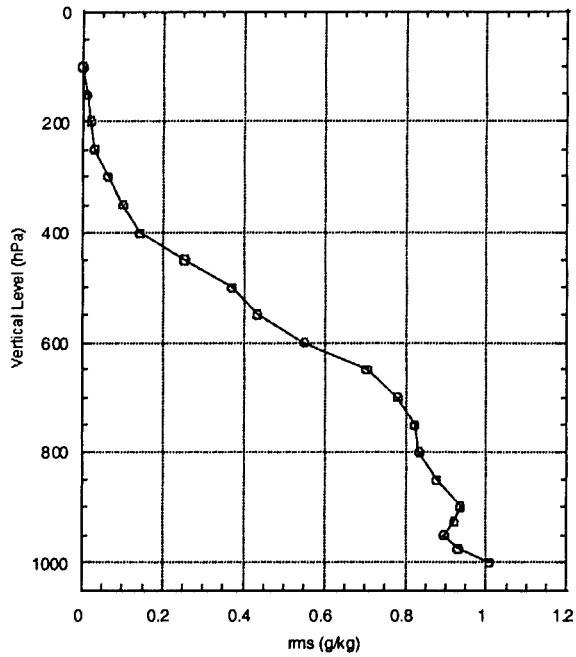

Fig. 2. The rms deviations of specific humidity retrieval.

This neural network model is applied to the data in the validation dataset. The rms deviations of specific humidity at all the levels are computed assuming the outputs in the validation dataset as truth data. The computed rms deviations of the specific humidity at the standard pressure levels are shown in Fig. 2. In the near-surface layer, the rms values range from 1 g/kg at the 1000 hPa level to about 0.8 g/kg at 700 hPa. The values decrease steadily toward the upper atmosphere. At the surface, the rms value is 1.1 g/kg.

Acknowledgments. I would like to thank Robert Bernstein for helpful suggestions and Greg DeCow for assistance in data collection.

REFERENCES

Butler, C. T., R. v. Z. Meredith, and A. P. Stogryn, 1996: Retrieving atmospheric temperature parameters from DMSP SSM/T-1 data with a neural network. *J. Geophys. Res.*, **101**, 7075-7083.

Chauvin, Y. and D. E. Rumelhart, 1995: *Backpropagation: Theory, Architectures, and Applications.* Lawrence Erlbaum Associates, Hillsdale, New Jersey, 561 pp.

Goodrum, G., K. B. Kidwell, and W. Winston, 1999: NOAA KLM user's guide. National Oceanic and Atmospheric Administration, Suitland, MD.

Shi, L., 2001: Retrieval of atmospheric temperature profiles from AMSU-A measurement using a neural network approach. *J. Atmos. Ocean. Tech.*, **18**, 340-347.

Ward Systems Group, Inc., 1996: NeuroShell 2. Ward Systems Group, Inc., 5 Hillcrest Drive, Frederick, MD21702.

P5.37

AN OPTIMAL-ESTIMATION ALGORITHM FOR WATER VAPOR PROFILING USING AMSU

Darren S. McKague[1]*, R. J. Engelen[2], J. M. Forsythe[1] , S. Q. Kidder[1], and T. H. Vonder Haar[1,2]

[1]Cooperative Institute for Research in the Atmosphere (CIRA), Colorado State University, Fort Collins, CO

[2]Department of Atmospheric Science, Colorado State University, Fort Collins, CO

1. INTRODUCTION

Retrievals of water vapor profiles are required for applications ranging from numerical weather forecasting to climate modeling and climate change studies. As these fields advance, there is an increasing need for weather and climate water vapor studies over complex, cloudy conditions (e.g. Lietzke et al. (2001)). The Advanced Microwave Sounding Unit (AMSU), first flown on board the NOAA-15 satellite in 1998, provides global water vapor measurements in clear and cloudy skies. This broad capability makes it a key instrument for water vapor retrievals. This paper describes an algorithm for the retrieval of water vapor profiles from AMSU. The algorithm has the ability to simultaneously retrieve water vapor profiles, temperature profiles, and microwave surface emissivities. This ability allows for more accurate water vapor retrievals, as is shown using simulated data.

2. ALGORITHM DESCRIPTION

The retrieval algorithm is a physically based iterative optimal-estimation scheme adapted from the method of Engelen and Stephens (1999). The algorithm can take data from AMSU-B, from AMSU-B and AMSU-A combined, or from SSM/T-2. A variety of parameters can be retrieved including profiles of water vapor mixing ratio, joint water vapor and temperature profiles (including surface temperature), and water vapor and temperature profiles along with microwave surface emissivities.

The retrieval scheme requires an a priori guess of the water vapor and temperature profiles as well surface emissivities at the relevant microwave frequencies. This is used to constrain a non-linear iterative optimal-estimation scheme which uses the method of Rogers (1976) to minimize the cost function Φ to find the optimal solution x, where:

$$\Phi=(x-x_a)^T S_a^{-1}(x-x_a)+\{y-F(x)\}^T S_y^{-1}\{y-F(x)\}$$

where x is the vector of parameters to be retrieved, x_a is the a priori vector, y is the set of observations, F(x) is a forward radiative transfer model used to compute radiances given x, and S_a and S_y are the error covariance matrixes of the a priori data and the observations, respectively. The vector of retrieval parameters may include the profile of water vapor mixing ratio alone, or may include the temperature profile and surface emissivities as well. The a priori error covariance matrix includes the variances of and correlations between the retrieval parameters, thus providing a constraint on the solution from a priori knowledge. The error covariance matrix of the observations includes forward model errors and uncertainty in the observed radiances.

For the forward radiative transfer, monochromatic microwave brightness temperatures were computed using numerical integration of the radiative transfer equation for a plane parallel, absorbing atmosphere together with Liebe's MPM92 (Liebe and Hufford 1993) model of microwave atmospheric attenuation. The Rayleigh-Jeans distribution was used for the source function.

3. AMSU SIMULATIONS

To test the retrieval scheme, simulations of AMSU observations have been created. 100 mid-latitude ocean profiles from the NOAA-88 profile data set have been input to the radiative transfer model to calculate AMSU-A and AMSU-B brightness temperatures. Independent random noise was added to each of the simulated brightness temperatures in order to simulate random sensor uncertainty. The noise was assumed to be Gaussian with a standard deviation set to the temperature sensitivity (NEDT) of the appropriate AMSU channel. Table 1 presents the characteristics used to simulate the AMSU instruments. The temperature of the lowest level of the NOAA-88 profile was taken as the surface temperature. This surface temperature, together with a randomly chosen surface wind speed taken from the SSM/I sea surface wind speed cal/val distribution, were input to the ocean surface model of Yueh (1997) to

* Corresponding author address: Darren S. McKague, Colorado State University / Cooperative Institute for Research in the Atmosphere (CIRA), Fort Collins, CO 80523; e-mail mckague@cira.colostate.edu.

compute microwave emissivities at the appropriate frequencies.

The first guess for the retrieval algorithm was obtained by adding noise to the original NOAA-88 profile. The noise was assumed to be Gaussian with the parameters presented in Table 2 and is correlated using the correlation matrix calculated from the entire set of NOAA-88 mid-latitude ocean profiles.

The a priori error covariance matrix S_a was computed using the errors of the first guess in Table 2 along with the correlations for the retrieval variables calculated from the entire set of NOAA-88 mid-latitude ocean profiles. The error covariance matrix for the observations, S_y, was computed using the AMSU characteristics in Table 1. The AMSU channels were assumed to be uncorrelated. Forward model error was not included in Sy, since the effects of forward model error should be negligible for simulated data where the simulations use the same forward model as the retrieval scheme.

	Channel	Frequency (GHz)	NEDT (K)
AMSU-A	1	23.8	0.3
	2	31.4	0.3
	3	50.3	0.4
	4	52.8	0.25
	5	$53.596 \pm .115$	0.25
	6	54.4	0.25
	7	54.94	0.25
	8	55.5	0.25
	9	$57.290344 = f_0$	0.25
	10	$f_0 \pm .217$	0.4
	11	$f_0 \pm .3222 \pm .048$	0.4
	12	$f_0 \pm .3222 \pm .022$	0.6
	13	$f_0 \pm .3222 \pm .010$	0.8
	14	$f_0 \pm .3222 \pm .0045$	1.2
	15	89.0	0.5
AMSU-B	1	89.0	0.8
	2	150.0	0.8
	3	183.31 ± 1.0	0.8
	4	183.31 ± 3.0	0.8
	5	183.31 ± 7.0	0.8

Table 1. AMSU characteristics used in simulations.

Parameter	Std. Deviation	Source
Water Vapor Mixing Ratio	0.0005-2.1 g/kg (see figure 2)	English (1999)
Temperature	3.0 K	Nutter et al. (1999)
Emissivity	.01	2 m/s wind speed and 3.0 K surface temperature uncertainty

Table 2. Magnitude of first guess errors.

4. RESULTS

The algorithm has been used to retrieve profiles from the simulated data for a number of different cases. One set of cases uses AMSU-B data, while the other uses both AMSU-A and AMSU-B for the same set of 100 profiles. Retrievals of water vapor profiles only, joint retrievals of temperature and water vapor profiles, and joint temperature, water vapor and emissivity retrievals have been run. For AMSU-A, three emissivities are retrieved with the 50-60 GHz channels grouped into one emissivity. For AMSU-B, three emissivities are retrieved with all of the channels centered around 183 GHz grouped into one emissivity. For each of the 100 profiles, the appropriate brightness temperatures have been simulated and input to the retrieval scheme for each retrieval case described above. An example of a retrieved mixing ratio profile for both AMSU-B and AMSU-A data retrieving water vapor, temperature, and surface emissivities simultaneously is shown in Figure 1. The retrieved profiles are then compared to the original and an rms error as well as a mean bias has been computed for each level of the profile. Table 3 contains the profile averaged rms error, bias, and maximum bias for the data set broken down by retrieval case.

Figures 2 through 4 show the water vapor mixing ratio profile errors for the AMSU-B retrievals for water vapor profile retrieval only, temperature and water vapor profile retrieval, and temperature and water vapor profile along with surface temperature and surface emissivity retrieval respectively. With just AMSU-B data, the retrieval should be sensitive primarily to the water vapor. However, a reduction in retrieval error, particularly in retrieval bias, is seen in going from water vapor only to water vapor, temperature, and emissivity retrievals. While there is some temperature and emissivity information in the AMSU-B channels, this improvement of the water vapor retrievals by simultaneously retrieving temperature and surface emissivity along with water vapor is in large part due to the constraint provided by the a priori error covariance matrix S_a. If only the water vapor profile is retrieved, then the water vapor profile must compensate for first guess errors in temperature profile and surface properties. This compensation shows up primarily as bias in the retrieval that disappears as the retrieval of a temperature profile and surface emissivities are added. The a priori error covariance matrix helps to constrain the temperature and emissivity retrievals by correlating them to the retrieved water vapor profile. Some residual bias from the retrieval scheme remains even when water vapor, temperature, and emissivity are retrieved.

Figures 5 through 7 show the three different retrieval cases with both AMSU-B and AMSU-A data. The water vapor retrieval errors for all three cases are reduced in going from the water vapor retrieval only to the water vapor, temperature, and emissivity simultaneous retrieval. With both AMSU-B and AMSU-A data, both water vapor and temperature profiles can be directly retrieved, thus further improving the water vapor profile retrieval. As shown in Table 3, the AMSU-B and AMSU-A water vapor retrievals do better (i.e. have lower

mean rms error and lower bias compared to truth) than the AMBU-B retrievals when temperature is simultaneously retrieved. The water vapor only retrieval, though, is better using just the AMSU-B data. The AMSU-A data don't contain much direct information about water vapor. Without the temperature retrieval, the effect of the AMSU-A data is to add noise to the retrieval.

Data	Retrieval Type	Mean RMS Error (g/kg)	Mean Abs. Bias (g/kg)	Max. Abs. Bias (g/kg)
AMSU-B	Water Vapor Only	.33	.08	.20
	Water Vapor + Temperature	.28	.06	.19
	Vapor + Temp + Emissivity	.23	.03	.08
AMSU-B and AMSU-A	Water Vapor Only	.37	.10	.32
	Vapor + Temperature	.25	.03	.11
	Vapor + Temp + Emissivity	.18	.02	.06

Table 3. Statistics for the water vapor mixing ratio retrievals averaged over the profile levels. Mean and maximum biases are for the absolute value of the bias.

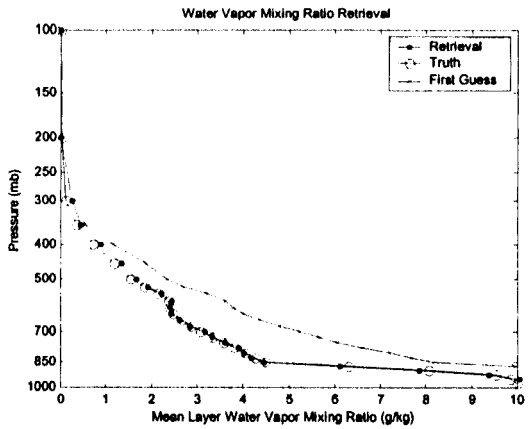

Figure 1. Retrieved, true, and first guess water vapor mixing ratio profiles from AMSU-B and AMSU-A data for a simultaneous water vapor, temperature and surface emissivity retrieval.

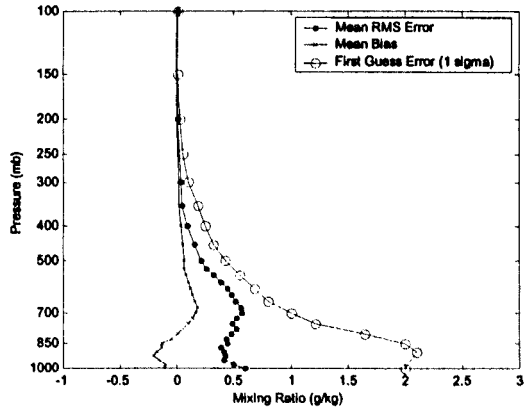

Figure 2. Errors from AMSU-B retrieval of water vapor mixing ratio. Only water vapor was retrieved.

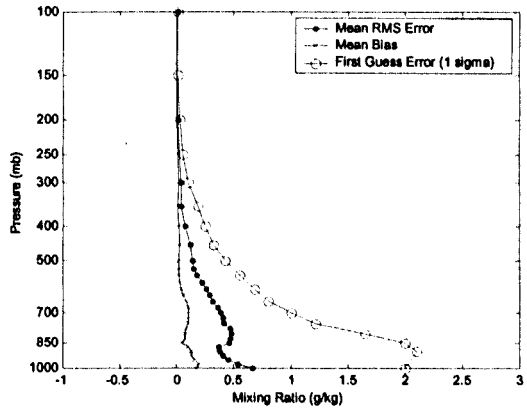

Figure 3. Errors from AMSU-B retrieval of water vapor mixing ratio. Water vapor and temperature profiles were retrieved simultaneously.

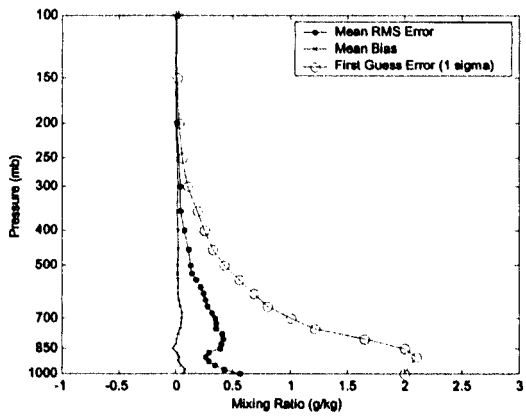

Figure 4. Errors from AMSU-B retrieval of water vapor mixing ratio. Water vapor and temperature profiles as well as surface emissivities were retrieved simultaneously.

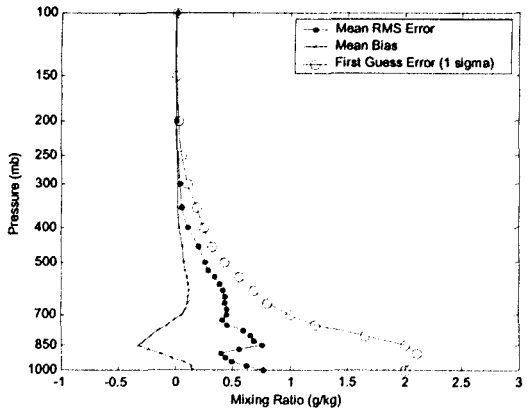

Figure 5. Errors from AMSU-B and AMSU-A retrieval of water vapor mixing ratio. Only water vapor was retrieved.

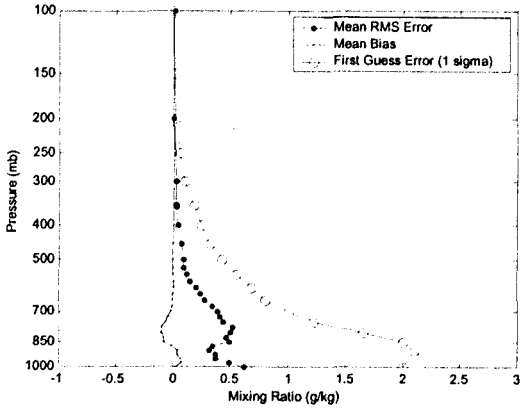

Figure 6. Errors from AMSU-B and AMSU-A retrieval of water vapor mixing ratio. Water vapor and temperature profiles were retrieved simultaneously.

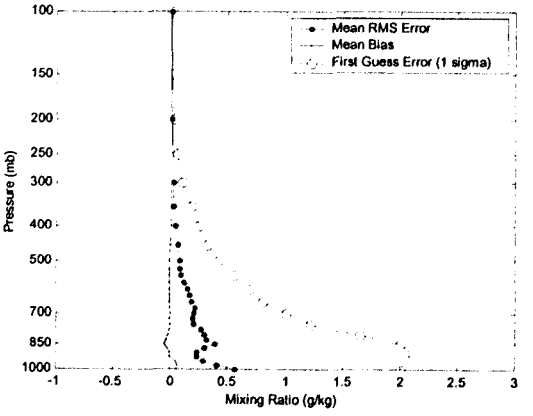

Figure 7. Errors from AMSU-B and AMSU-A retrieval of water vapor mixing ratio. Water vapor and temperature profiles as well as surface emissivities were retrieved simultaneously.

5. CONCLUSIONS AND FUTURE WORK

An algorithm for the retrieval of water vapor profiles from AMSU has been presented. The algorithm is quite general, in that it can be applied to data from AMSU as well as other satellite platforms such as SSM/T-2 and the upcoming SSM/IS instrument, which should become available in 2002. Water vapor profiles can be retrieved with or without profiles of temperature profiles and surface emissivities. It was shown using simulated AMSU-A and AMSU-B measurements that, even with AMU-B measurements alone, water vapor retrieval performance is improved for the case of simultaneous water vapor, temperature, and emissivity retrievals. Future work will concentrate on applying the algorithm over land and to cloudy conditions.

6. ACKNOWLEDGMENTS

This research was supported by the DoD Center for Geosciences at CIRA/CSU under grant #DAAL01-98-2-0078 from the Army Research Laboratory.

7. REFERENCES

Engelen, R. J. and G. L. Stephens, 1999: Characterization of water-vapour retrievals from TOVS/HIRS and SSM/T-2 measurements. *Q. J. R. Meteor. Soc.*, **125**, 331-351.

English, S. J., 1999: Estimation of temperature and humidity profile information from microwave radiances over different surface types. *J. Appl. Meteor.*, **38**, 1526-1541.

Liebe, H. J. and G. A. Hufford, 1993: Models for atmospheric refractivity and radio-wave propagation at frequencies below 1 THz. *Int. J. Infrared and Millimeter Waves*, **77**, 437-471.

Lietzke, C. E., C. Deser, and T. H. Vonder Haar, 2001: Evolutionary structure of the eastern Pacific double ITCZ based on satellite moisture profile retrievals. *J. Clim.*, **14**, 743-751.

Nutter, P. A. and J. Manobiano, 1999: Evaluation of the 29-km Eta Model, Part I: Objective verifica-tion at three selected stations. *J. Amer. Meteor. Soc.*, **14**, 5-17.

Rodgers, C. D., 1976: Retrieval of atmospheric temperature and composition from remote measuremetn of thermal radiation. *Rev. Geophys. Space Phys.*, **14**, 609-624.

Yueh, S. H., 1997: Modeling of wind direction signals in polarimetric sea surface brightness temperatures. *IEEE Trans. Geosc. Rem. Sens.*, **35**, 1400–1418.

P5.38

RETRIEVAL OF ATMOSPHERIC INVERSIONS USING GEOSTATIONARY HIGH-SPECTRAL-RESOLUTION SOUNDER RADIANCE INFORMATION

Jun Li
Cooperative Institute for Meteorological Satellite Studies (CIMSS)
University of Wisconsin-Madison

Timothy J. Schmit
NOAA/NESDIS, Office of Research and Applications, Advanced Satellite Products Team (ASPT)

Hung-Lung Huang, and Harold M. Woolf
Cooperative Institute for Meteorological Satellite Studies (CIMSS)
University of Wisconsin-Madison, Madison, WI

1. INTRODUCTION

The era of high-spectral-resolution radiance measurements from the geostationary perspective is approaching. The first instrument to usher in this new era is the experimental Geosynchronous Imaging Fourier Transform Spectrometer (GIFTS), which is to be followed by an operational Advanced Sounder Baseline (ABS). The advanced sounders will have thousands of channels with widths on the order of single wavenumbers, while the current GOES Sounder (Menzel and Purdom, 1994) has only 18 bands with widths on the order of tens of wavenumbers. High-spectral-resolution sounder measurements from geostationary orbit will allow for monitoring the evolution of temperature and moisture inversions in clear skies. The current GOES sounder radiance measurements are, in general, not able to depict atmospheric inversion structure because of their lower spectral-resolution. Being able to characterize inversions is important for many reasons, including the detection of severe weather potential and possible fog formation, numerical model initialization, and sounding retrieval. High-spectral-resolution sounder radiances, as well as current GOES sounder radiances, will be simulated, with instrument noise included, for a number of radiosonde profiles with varying inversion strengths. A physical retrieval algorithm will be employed to retrieve temperature and moisture profiles with both sounders. The retrievals will be compared to the true profiles that were used to create the radiances in order to determine the strength of an inversion that can be retrieved from both current and the next-generation geostationary radiances.

Corresponding author address: Jun Li, Space Science and Engineering Center, Uiniversity of Wisconsin-Madison, 1225 West Dayton Street, Madison, WI 53706; e-mail: JunL@ssec.wisc.edu

2. RETRIEVAL SIMULATIONS

A fast and accurate transmittance models called Pressure Layer Optical Depth (PLOD) or Pressure layer Fast Algorithm for Atmospheric Transmittances (PFAAST) (Hannon et al. 1996) is used for the Advanced Baseline Sounder (ABS) or Cross-track Infrared Sounder (CrIS) (Bloom, 2001) simulations. The calculations are made at 101 pressure levels (0.01–105 kPa) and take into account the satellite zenith angle, absorption by well-mixed gases (including nitrogen, oxygen, and carbon dioxide), water vapor (including the water vapor continuum), and ozone.

A two-step algorithm, a Principle Component Regression (PCR; Huang and Antonelli 2001) followed by a non-linear physical retrieval method (Li and Huang 1999; Li et al. 2000), will be adopted for retrieval of atmospheric temperature and moisture profiles from ABS or CrIS simulated radiances which are added with the instrument noise. The regression retrieval serves as the first guess (or background) in the physical retrieval. PCR uses the projections of the predictor

variables (brightness temperature) onto a subset of principle components. Once a first guess is obtained from a numerical model forecast or generated from the regression technique described above, a non-linear iterative procedure is applied to the radiative transfer equation to further improve the profiles. Approximately half of the channels (optimal channels) are used in the physical retrieval procedure.

A data set containing more than 6000 global radiosonde profiles between 65S and 65N latitude is used for ABS retrieval simulation. 90% of the profiles are used for training - to create the regression coefficients, while the remaining 10% of the profiles are used to test the retrieval performance. The radiative transfer calculations of the ABS spectral band radiances are performed for each profile from the training data set to provide a temperature-moisture-ozone profile/ABS radiance pair for use in the statistical regression analysis. The ABS instrument noise is added into the calculated spectral band radiances. The eigenvector or Empirical Orthogonal Function (EOF) regression equation is then generated based on these calculated radiances and the matching atmospheric profiles. To complete the regression retrieval, the regression equation can be applied to the ABS independent radiances to obtain the estimated atmospheric profile retrieval, the regression retrieval is further updated with the nonlinear physical retrieval procedure. Comparison between the true and retrieved profiles gives the accuracy of retrieval performance.

3. RESULTS

Figure 1 shows an example of CrIS brightness temperature spectra and GOES band brightness temperatures (lower panel) calculated from profile with low level temperature inversion. The ABS Technical Requirement Document (TRD) noise (upper panel) is included in the CrIS radiances, while the GOES-8 spec noise is added in the GOES radiances. It can be see that the temperature inversion signal is well depicted by the CrIS spectra, while it is smoothed by the GOES brightness temperatures due to the low spectral resolution of the current GOES sounder. Figure 2 shows the true atmospheric temperature profile used in the simulation, the CrIS and GOES retrieved temperature profiles. Since CrIS spectra is able to well reflect the atmospheric inversion signal, significant improvement of CrIS low level temperature retrieval over the GOES sounder retrieval is found.

Figure 3 is the 1km vertical resolution temperature RMS (left panel) and 2km vertical resolution water vapor mixing ratio RMS (right panel) from the 605 independent profile retrievals with EOF regression physical procedures. There is substantial improvement of physical retrieval procedure over the EOF regression procedure for the boundary layer temperatures, while the accuracy of moisture retrievals is significantly improved from the physical procedure over the EOF regression procedure (2 ~ 5% improvement for atmospheric water vapor mixing ratio). Figure 4 shows the residual RMS from the EOF regression first guess profiles, the physical retrieval profiles, along with instrument noise (NEDT RMS). It can be seen that the EOF regression first guess fits the radiances very well (the residual is close to the instrument noise) in the longwave CO_2 region, this is due to the fact that CO_2 absorption region's radiances are more linear to atmospheric temperature profile since there is only CO_2 absorption in that region. For the longwave window region and the midwave water vapor region, the radiances are highly nonlinear to the water vapor mixing ratio. The regression first guess is not able to fit the observed radiances, while the nonlinear physical approach can reduce the first guess residual to the noise level in those spectral regions.

4. CONCLUSIONS

Retrievals from simulated CrIS radiances with the ABS TRD noise indicates that

(1) Nonlinear physical retrieval procedure improves eigenvector regression derived first guess profile, especially for atmospheric moisture profile;
(2) Simulations from CrIS radiances demonstrates that the next GOES advanced sounder (ABS) meets the NWS requirement for atmospheric profile products (1K of temperature for 1km vertical resolution and 15% of

water vapor mixing ratio for 2km vertical resolution);

(3) The ABS is able to depict the atmospheric temperature inversion structure on which the current GOES sounder has limited information.

5. REFERENCES

Bloom, H. J., 2001: The Cross-track Infrared Sounder (CrIS): A sensor for operational meteorological remote sensing, Technical Digest of Optical Remote Sensing of the Atmosphere, 74-76, February 5-8, 2001, Coeur d'Alene, Idado.

Hannon, S., L. L. Strow, and W. W. McMillan, 1996: Atmospheric infrared fast transmittance models: A comparison of two approaches. *Proceedings of SPIE*, 2830, 94-105.

Huang, H. L., and Antonelli, 2001: Application of principal component analysis to high-resolution infrared measurement compression and retrieval, *J. Appl. Meteor.* 40, 365-388.

Li, J., and H. L. Huang, 1999: Retrieval of atmospheric profiles from satellite sounder measurements using the discrepancy principle. *Appl. Optics*, 38, 916-923.

Li, J., W. Wolf, W. P. Menzel, W. Zhang, H.-L. Huang, and T. H. Achtor, 2000: Global soundings of the atmosphere from ATOVS measurements: the algorithm and validation. *J. Appl. Meteor.* 39, 1248 - 1268.

Menzel, W. P., and J. F. W. Purdom, 1994: Introducing GOES-I: The first of a new generation of geostationary operational environmental satellites. *Bull. Amer. Meteor. Soc.*, **75**, 757-781.

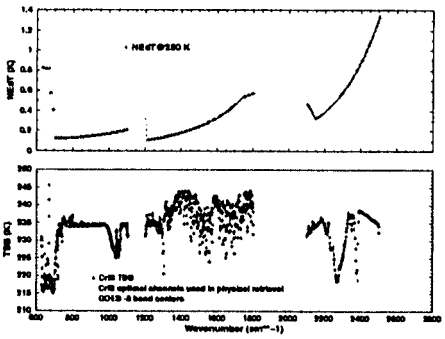

Figure 1, CrIS brightness temperature spectra and GOES band brightness temperatures (lower panel) calculated from profile with low level temperature inversion. The ABS TRD noise (upper panel) is included in the CrIS radiances, while the GOES-8 spec noise is added in the GOES radiances.

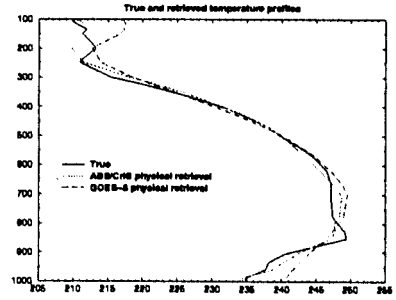

Figure 2, the true atmospheric temperature profile used in the simulation, along with the CrIS and GOES retrieved temperature profiles.

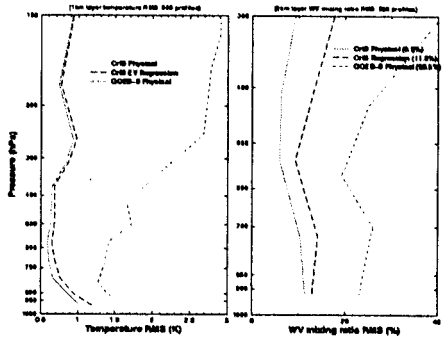

Figure 3, 1km vertical resolution temperature RMS (left panel) and 2km vertical resolution water vapor mixing ratio RMS (right panel) with EOF regression physical procedures (CrIS and GOES).

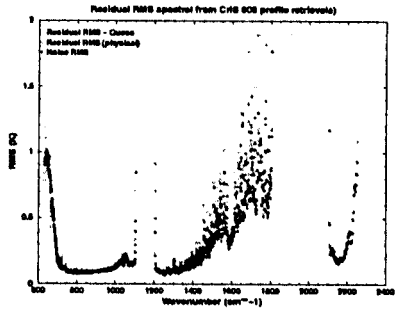

Figure 4, the CrIS residual RMS from the EOF regression first guess profiles, the physical retrieval profiles, along with instrument noise (NEDT RMS).

P5.39 SSMIS UPPER ATMOSPHERE SOUNDING CALIBRATION AND VALIDATION PLANS

Steven D. Swadley *
METOC Consulting
Marine Meteorology Division, Naval Research Laboratory, Monterey, California

1. Introduction

The Defense Meteorological Satellite Program (DMSP) is presently scheduled to launch the first of five Special Sensor Microwave Imager/Sounder (SSMIS) in November 2001. The SSMIS is a joint United States Air Force/Navy multi-channel passive microwave sensor that combines and extends the current imaging and sounding capabilities of three separate DMSP microwave sensors, SSM/T, SSM/T-2 and SSM/I. Built by Aerojet, the SSMIS measures the earth's upwelling partially-polarized radiances in 24 channels covering a wide range of frequencies (19–183 GHz) in an SSM/I-type conical scan geometry (53 degree earth incidence angle), maintaining uniform spatial resolution, polarization purity and common fields-of-view for all channels across the entire swath.

The DMSP System Program Office (SPO) in conjunction with the Office of Naval Research (ONR) is conducting a comprehensive end-to-end calibration/validation (Cal/Val) of the first SSMIS, to begin shortly after launch. The Naval Research Laboratory has been selected to lead the technical efforts of the Cal/Val with support and guidance from DMSP and ONR.

The SSMIS Upper Atmosphere Sounding (UAS) capabilities offer a unique opportunity to provide real-time stratospheric and mesospheric temperature observations. However, supporting measurements for the calibration and validation of the sensor and retrieved soundings are quite limited in comparison to tropospheric and lower stratospheric sounding sensors. A wide reaching combination of lidar, rocketsonde and NWP model fields will be used to calibrate the SSMIS UAS channels and retrieved temperature profiles. Plans for the utilization of these data sources and their limitations are presented.

2. SSMIS Sensor Characteristics

The SSMIS hardware characteristics and retrieval algorithms for the temperature and humidity retrievals have been described in Swadley and Chandler (1991, 1992). A thorough discussion of the background theory and approach to the SSMIS mesospheric temperature retrievals are discussed in Stogryn (1989a, 1989b). Figure 1 and Table 1. describe the SSMIS scan geometry and channel characteristics.

Figure 1. SSMIS scan geometry

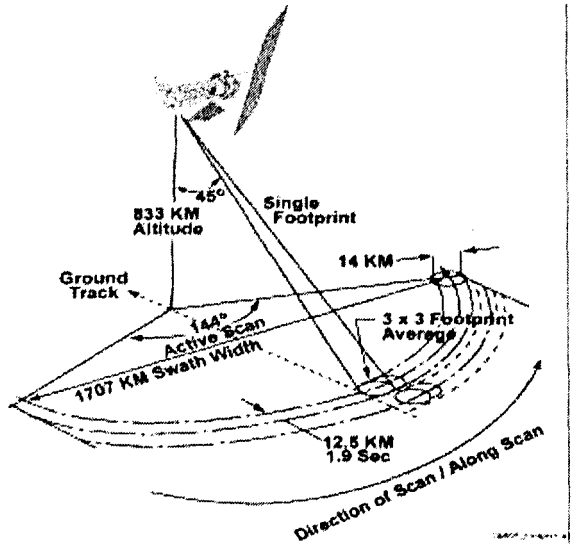

3. SSMIS Calibration and Validation Plans

The Cal/Val approach taken for the SSMIS is divided into four major phases. In Phase I, the foremost task is the calibration of the instrument itself. This includes the instrument health, general operation and verification that it is working as designed and within specification. It also includes calibration of the sensor-related algorithms and of the absolute power level at the input to the feed-horn (antenna temperature) and the correction for antenna reception pattern effects to obtain the absolute brightness temperature of the scene. The calibration of the SSMIS instrument and verification that the accurate absolute scene brightness temperatures are being measured is the essential first step of the Cal/Val Plan. The verification of the Doppler shift correction in the SSMIS hardware will also be carried out.

The second step of Phase I involves validation of the retrieval algorithms encoded in the GPS used

* *Corresponding author address:* Steven D. Swadley, METOC Consulting, Marine Meteorology Division, NRL, Monterey, CA 93943; e-mail: swadley@nrlmry.navy.mil

Table 1. SSMIS channel characteristics.

Ch. No.	Center Frequency (GHz)	Pass Band (MHz)	Polarization	NE?T (K)
1	50.3	400	H	0.4
2	52.8	400	H	0.4
3	53.596	400	H	0.4
4	54.4	400	H	0.4
5	55.5	400	H	0.4
6	57.29	350	*	0.5
7	59.4	250	*	0.6
8	150.0	1500	H	0.88
9	183.31±6.6	2500	H	1.2
10	183.31±3	100	H	1.0
11	183.31±1	500	H	1.25
12	19.35	400	H	0.7
13	19.35	400	V	0.7
14	22.235	400	V	0.7
15	37.0	1500	H	0.5
16	37.0	1500	V	0.5
17	91.655	3000	V	0.9
18	91.655	3000	H	0.9
19	63.283248 ±0.285271	3	V+H	2.4
20	60.792668 ±0.357892	3	V+H	2.4
21	60.792668 ±0.357892 ±0.002	6	V+H	1.8
22	60.792668 ±0.357892 ±0.0055	12	V+H	1.0
23	60.792668 ±0.357892 ±0.016	32	V+H	0.6
24	60.792668 ±0.357892 ±0.050	120	V+H	0.7

to derive the EDR products. A team of specialists selected for their experience and expertise in microwave radiometer remote sensing and their knowledge of the particular EDR will be conducting the initial assessment. Depending on the results of the early EDR assessment, recommendations will be made for Phase II efforts that range from simple refinement of the algorithm coefficients to the development of new algorithms to bring the EDR performance within specification.

The Cal/Val for the upper air sounding channels represents a unique challenge because it is the first time such observations will be made and there is very limited independent data on which to base a comparison of either SDRs or EDRs. Therefore, we have developed a combined approach, Figure 2. Raw sensor data is transformed by the GPS calibration algorithm into SDRs, which are subsequently converted to sounding EDRs by the GPS retrieval algorithm. The collection of "ground truth" or validation data sources consisting of coincident rocketsondes, Lidar observations and NWP analysis fields are then processed and compared with the SSMIS sounding EDRs to form the validation component. The cycle is completed when the "ground truth" is used as input to the forward model to generated SDRs, which may then be compared to the calibration component. Clearly, a successful upper air Cal/Val depends on having an intimate knowledge of the sensor-related performance parameters (e.g. Doppler correction), an understanding of the approximation and limitations of radiative transfer theory, thorough knowledge of the retrieval algorithms and their performances and an in-depth understanding of the errors occurring in the validation data.

Figure 2. Schematic of the SSMIS Cal/Val approach

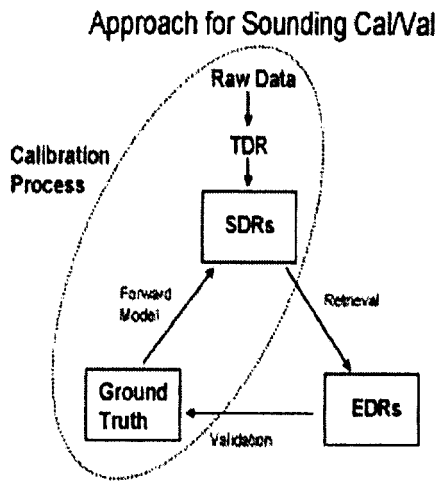

The SSMIS UAS retrieval error can be decomposed into several components (see e.g. Rodgers (1996); Burns (1998)). These include the brightness temperature measurement error, the error in the forward model used to generate simulated brightness temperatures and regression coefficients, errors due to the simplifying approximations made in the algorithm, and the error due to the limited samples contained in the RAOB/ROCOB/LIDAR profile database used to derive the UAS algorithm coefficients. The measurement error can be estimated from the predicted calibration accuracy and NE?T; the actual measurement error will be determined from the calibration phase. Quantifying the other errors as far as possible prior to launch will facilitate identifying the part of the UAS algorithm

responsible for residual discrepancies with the validation data.

Immediately after launch, the first step toward UAS validation will be a qualitative assessment of the retrieved temperature profiles by a meteorologist. Such large-scale qualitative assessments are important as they provide an overall impression of algorithm performance and indicate possible deficiencies. For this purpose the SSMIS upper atmosphere retrievals will be gridded to and 1.0 degree spherical coordinate system. Ascending and descending passes will be analyzed separately to limit diurnal/semi-diurnal effects. The gridded retrievals then will be examined for the classic meteorological patterns of horizontal and vertical variations expected for the hemisphere and time of year of observation. The large-scale temperature features of the stratosphere will be verified. Qualitative assessment of smaller scale features must also differentiate real meteorological from noise effects. This qualitative view of UAS performance will provide a meteorological context for the quantitative statistics to be derived from comparison with the validation data. Figures 3 and 4 demonstrate some of the analysis tools available to the SSMIS Cal/Val Team for such qualitative assessments.

Comparisons of the SSMIS gridded upper atmosphere temperatures with NWP temperature analyses from operational centers (FNMOC, ECMWF and NCEP) will also aid in this initial qualitative assessment. The temperature analyses will also be used as background profiles for input into the forward radiative transfer models

Figure 3. Temperature profile comparisons from ECMWF, NOGAPS and ATOVS.

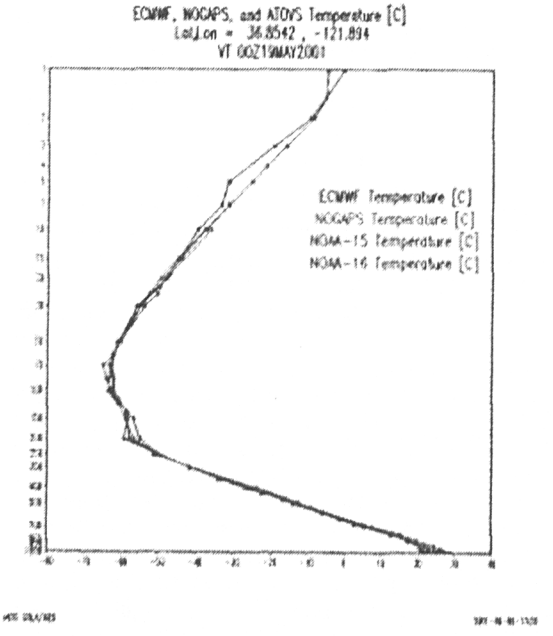

Figure 4. Global comparisons of the NOGAPS and ATOVS temperatures at hPa.

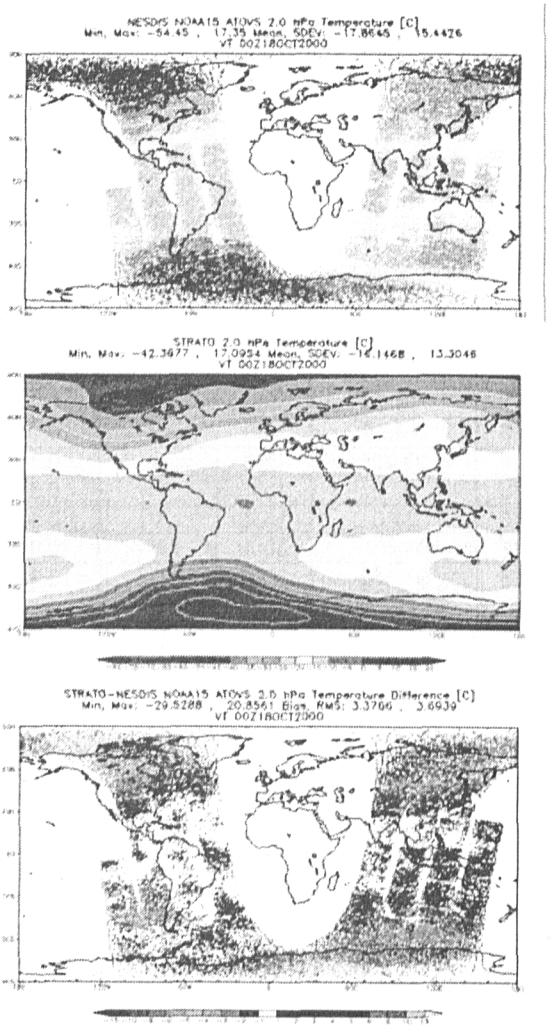

4. Upper Atmosphere Observation Campaigns

The primary sources of temperature profiles in the altitudes 30-80 km are Rayleigh LIDAR and ROCOBs. These observations will be combined with RAOBs to form profiles extending to the surface. Profiles will be assembled throughout the Cal/Val period, with several intensive observation periods (IOPs) for intercomparison of the validation data sources. Analysis fields from NWP models will be used to supplement the RAOB/ROCOB/LIDAR databases to provide a firmer basis for statistical analyses on a global scale.

The SSMIS Cal/Val team has made plans for three lidar IOPs and one coincident ROCOB/LIDAR IOP in direct support of the upper atmosphere sounding calibration and validation Phase I efforts. These campaigns are detailed in Table 2. They include IOPs using a Rayleigh lidar at the NASA JPL Table Mt. Facility (TMF) and a combined

Raman and Rayleigh lidar facility at Mauna Loa, HI (MLO) (Leblanc, et. al. 1998); the Geophysics Institute (GI) of the University of Alaska Fairbanks's Poker Flat Research Range (PFRR) lidar observatory (Cutler, 2000); and the Aerospace Mobile lidar observatory deployed at the Pacific Missile Range Facility (PMRF).

Table 2. SSMIS Upper Atmosphere Observational campaigns

Team	Site	Dates	Lidar	Rocob
NASA/JPL	TMF	Feb '02	X	
NASA/JPL	MLO	Oct '02	X	
Geophys. Institute U. of A.	PFRR	Jan-Apr '02	X	
PMRF and Aerospace	PMRF	Jan-Apr '02	X	X

Once the measurement and retrieval error statistics have been derived through the intercomparisons, the analysis framework used to characterize the UAS retrieval error sources will be applied. This allows the total observed retrieval error to be broken down into its components. With the errors associated with measurement, forward model, and database already quantified, an estimate of the error due to the algorithm formulation itself can be obtained. The relative magnitude of these contributors then indicates where improvements to the retrieval system are required. A proposal for algorithm improvement and/or development of alternative algorithms (e.g. physical-statistical retrievals), and associated validation studies, will be produced, and will form the basis for the efforts in Phase II of the SSMIS Cal/Val.

5. Summary

The SSMIS upper atmosphere sounding calibration and validation effort has been presented. The level of effort in Phase II of the calibration and validation will be determined by the results of Phase I. Results of the SSMIS Upper Atmosphere Sounding Calibration and Validation efforts will be presented at a future AMS conference.

6. Acknowledgements

The author wishes to thank Col. Randy Odle, Director of the Defense Meteorological Satellite Program, Dr. Robert McCoy of the Space, Space and Remote Sensing Office of Naval Research, and Gene Poe, SSMIS Cal/Val Team Leader for support and encouragement in the development of the overall SSMIS Cal/Val Plan. The author also wishes to thank Barbara Burns (Aerojet), John Wessel (Aerospace), Stuart McDermid and Thierry Leblanc (NASA JPL), Richard Collins (Geophysics Institute, University of Alaska), Stu Burley and Judy Batis (PMRF) and Francis Schmidlin (NASA WFF) for the planning of the lidar and rocketsonde campaigns. Finally the SSMIS Cal/Val team would like to express gratitude to John Hennessey and Tony McNally (ECMWF) for providing ECMWF temperature analyses.

7. References

Burns, B.A., 1998: Characterization of Retrieval Errors for Microwave Temperature and Humidity Sounders. *Proc. COST 712 Workshop on Microwave Radiometry for Atmospheric Research and Monitoring*, 9-11 February 1998, Noordwijk, The Netherlands, pp. 103-116, 1998.

Cutler, L.J., R.L. Collins, K. Mizutani and T Itabe, 2000: Rayleigh Lidar Observations of Mesospheric Inversion layers at Poker Flat,-Alaska 67° N, 147 ° W., *Geophys. Res. Lett.* Accepted 2000.

Leblanc,T., I.S. McDemid, P. Keckhut, A. Hauchecorne, C.Y. She and D.A. Krueger, 1998: Temperature climatology of the middle atmosphere from long-term lidar measurements at middle and low latitudes. . *J. Geophys. Res.*, **103**, D14, 17,191-17,204.

Rodgers, C.D, R.J. Wells, R.G. Grainger and F.W. Taylor, 1996: Improved stratospheric and mesospheric sounder validation: General approach and in-flight radiometric calibration. *J. Geophys. Res.*, **101**, D6, 9775-9793.

Stogryn, A., 1989a: The magnetic field dependence of brightness temperatures at frequencies near the O_2 microwave absorption lines. *IEEE Trans. Geosci. Rem. Sens.*, **22**: (3), 279-289.

Stogryn, A., 1989b: Mesospheric temperature sounding with microwave radiometers. *IEEE Trans. Geosci. Rem. Sens.*, **22**: (3), 332-338.

Swadley, S.D. and J. Chandler, 1991: The Defense Meteorological Program's Special Sensor Microwave Imager/Sounder (SSMIS). Preprints Seventh Symposium on Meteorological Observations and Instrumentation, New Orleans, LA.

Swadley, S.D. and J. Chandler, 1992: The Defense Meteorological Program's Special Sensor Microwave Imager/Sounder (SSMIS): Hardware and Retrieval Algorithms. Preprints Sixth Conference on Satellite Meteorology and Oceanography, Atlanta, GA.

5.40 AIR FORCE WEATHER AGENCY SPECIAL SENSOR MICROWAVE IMAGER/SOUNDER PROCESSING

David M. Paal, Thomas J. Kopp *
HQ Air Force Weather Agency, Offutt AFB, Nebraska

1. INTRODUCTION

The Special Sensor Microwave Imager/Sounder (SSMI/S) system is a passive, conical-scanning, microwave radiometer system operating on the Defense Meteorological Satellite Program's (DMSP) satellites S16-20. The satellites will be placed into sun synchronous orbits at a approximate altitude of 833 kilometers (km). The sensor integrates the Special Sensor Microwave Imager (SSMI), the T-1 temperature sounder and T-2 moisture sounder into one with higher resolution than the old sensors and also includes an upper air sounding capability that probes atmospheric temperatures up to 73 km. The Ground Processing Software (GPS) takes the measured raw sensor data and produces calibrated and Earth-located Sensor Data Records (SDRs) and a variety of Environmental Data Records (EDRs). The SDRs and EDRs are then stored in Air Force Weather Agency (AFWA) databases for users to retrieve as needed and further processed and displayed for forecaster use.

2. SYSTEM SPECIFICS

The radiometer system rotates about a vertical axis on a conical angle of 45 degrees from nadir. This scan pattern, combined with a constant angle of incidence on the Earth of 53.1 degrees result in an increased clear field of regard and swath width (compared to SSMI (Raytheon, 1999)) shown in Table 1 below. Other enhancements include smaller and constant-size beam footprints (beam width: 0.4-1.9 degrees) for all sounding channels, reduced Noise Equivalent Difference in Temperature for all channels and beam averaging.

Table 1 Sensor Comparison

Sensor	Field of Regard	Swath Width
SSM/I	102.8 degrees	1400 km
SSMI/S	144-degrees	1707 km

The sensor collects data to the aft of nadir for a morning ascending node spacecraft orbit, and collects data forward of nadir for a morning descending node spacecraft orbit. The system passively measures brightness temperatures of the Earth's surface and the intervening atmosphere at 24 discrete frequencies from 19 to 183 GHz and in various altitude regimes. (To 55 km with 19 frequency channels and to 110 km with 6 channels for the upper air temperature sounding) (GenCorp, 2001).

* Corresponding author address: Captain David M. Paal, HQ AFWA/SCSS, Dr. Thomas J. Kopp, HQ AFWA/SCS, 106 Peacekeaper DR STE 2N3, Offutt AFB, NE 68113-4039; e-mail: david.paal@afwa.af.mil; thomas.kopp@afwa.af.mil.

2.1 Data Parameters

These measurements will provide retrievals of data parameters up to 30 km (basic system) and 73 km (with upper air sounding). It will measure surface properties like wind speeds, cloud liquid water, rain rates, surface temperature, and sea-ice with a 15 km field of view. Tropospheric temperature, and humidity soundings as well as stratospheric temperature soundings will be measured with a 38 km field of view. The soundings will measure temperature, geopotential heights, relative humidity, absolute humidity, and water vapor mass at mandatory pressure levels. The new mesospheric temperature soundings will be taken with a 75 km field of view.

3. GROUND PROCESSING

After telemetering the acquired frequency channel data to AFWA, the measured raw data is processed by using matrix inversion algorithms. The GPS produces calibrated and Earth-located Sensor Data Records (SDRs). The GPS then uses the sensor data from a combination of frequencies to compute a variety of Environmental Data Records (EDRs) for storage in databases at AFWA. The GPS also produces Temperature Data Records (TDRs) and Lower and Upper Air Soundings (LASs and UASs respectively).

The EDRs include: Air Temperature Profiles; Humidity Profiles; Ocean Surface Wind; Rain Over Land/Ocean; Cloud Water Over Ocean; Soil Moisture; Ice Concentration; Ice Age; Ice Edge and Snow Edge; Water Vapor Over Ocean; Surface Type; Snow Water Content; and Surface Temperature Over Land.

The GPS also performs verification and validation of the retrieved data and updates the inversion algorithms by comparison between the EDRs and other observed values (mainly RAOBS) to maintain high retrieval accuracy and correct the lower temperature bias error to no more than 1K from 10 to 1,000 Mb.

4. DISPLAY AND FORECASTING USES

Forecasters from AFWA will use Satellite Data Handling System (SDHS) display programs and the SDR and EDR data to perform tropical cyclone fixing and analysis. Other forecasters in AFWA will use the same SDHS programs and SSMI data and various EDRs for locating fronts over oceans and other limited observation regions. Table 2 shows the SSMI/S channels and their associated frequency and data type. Presently, only channels 1-18 will be used by the SDHS display programs for use by AFWA forecasters. However, the SDHS programs have the ability to add the remaining channels in the future as applications are built for the data.

Table 2 SSMI/S 24 Channels

Channel	Frequency	Data Type
1	50.300 GHz H	T1 Temperature
2	52.800 GHz H	T1 Temperature
3	53.596 GHz H	T1 Temperature
4	54.400 GHz H	T1 Temperature
5	55.500 GHz H	T1 Temperature
6	57.290 GHz V	T1 Temperature
7	59.400 GHz V	T1 Temperature
8	150.000 GHz H	T2 Water Vapor
9	183.310 ± 7 GHz H	T2 Water Vapor
10	183.310 ± 3GHz H	T2 Water Vapor
11	183.310 ± 1GHz H	T2 Water Vapor
12	19.350 GHz H	SSMI
13	19.350 GHz V	SSMI
14	22.235 GHz V	SSMI
15	37.000 GHz H	SSMI
16	37.000 GHz V	SSMI
17	91.665 GHz V (replaces 85 GHz)	SSMI
18	91.665 GHz H (replaces 85 GHz)	SSMI
19	63.283248 ± 0.285271 GHz H+V	Upper Air Sounding
20	60.792668 ± 0.357892 GHz H+V	Upper Air Sounding
21	60.792668 ± 0.357892 ± 0.002 GHz H+V	Upper Air Sounding
22	60.792668 ± 0.357892 ± 0.0055 GHz H+V	Upper Air Sounding
23	60.792668 ± 0.357892 ± 0.016 GHz H+V	Upper Air Sounding
24	60.792668 ± 0.357892 ± 0.050 GHz H+V	Upper Air Sounding

H-Horizontal, V-Vertical

Meteorological Modelers will also use these databases to improve current Numerical Weather Prediction models such as Surface Temperature and Snow Depth models.

The Real-Time Hurricane Forecast Center/Florida State University Department of Meteorology currently uses SSMI TDR data to initialize its global atmospheric model and to produce a precipitation forecast. The Center also uses the TDR data to conduct research for a variety of projects and products. The Center will use TDR data from SSMI/S when it becomes available.

Future Variational NWP models could exploit SDRs for direct radiance assimilation.

5. SUMMARY

After the DMSP satellite with the SSMI/S sensor onboard is launched, AFWA will begin processing the 24 channels of raw sensor data into calibrated and Earth-located SDRs and EDRs. The new sensor will provide a larger swath width and clear field of regard as well as higher resolution data than the current SSMI, T-1 and T-2 sensors provide. AFWA will use the GPS to provide the higher resolution SSMI/S data to all of its customers, from the research community to the Forecasters and Meteorological Modelers within AFWA.

6. REFERENCES

GenCorp Aerojet, 2001: Software Requirements Specification for the Ground Processing Software of the Special Sensor Microwave Imager/Sounder, GenCorp Aerojet, Azusa, California 91702-0296, p. 1

Raytheon, 1999: Special Sensor Microwave/Imager User's Interpretation Guide, Fourth Edition (Revision A), Raytheon Systems Company, April 1999

P5.41 IMAGERY INTERPRETATION OF MICROWAVE OBSERVATIONS BY AMSU AND TMI OVER A COMPLEX TROPICAL REGION

Benjamin Ruston*, Thomas H. Vonder Haar, and John Forsythe
Center for Geosciences / Atmospheric Research at the Department of Atmospheric Science at Colorado State University, Fort Collins, Colorado

1. INTRODUCTION

Satellite microwave radiometers have been used for over thirty years to observe the earth and derive atmospheric parameters. The number of meteorological satellites in orbit with microwave capabilities continues to increase, with new satellites featuring better spatial resolution, and wider spectral range. From the new array of radiometers, an age with multiple calibration procedures is becoming possible, and an effective microwave radiance shell surrounding the Earth can be constructed. A simple first step towards this goal is to compare co-temporal observations from the AMSU and TMI instruments, which provide over 25 channels of various frequencies and polarizations. In this study, we present current theory and technique to interpret microwave imagery over the Malaysian-Indonesian region, emphasizing utility to forecasting. The area has widely varying features including mountain terrain, rain forest, swampland, lakes, and surrounding ocean. We demonstrate and discuss how physical parameters such as soil moisture, precipitation, cloud liquid water, and total column water vapor create differences in brightness temperatures across the microwave spectrum.

Microwave radiometers on weather satellites currently span the frequency range of 10 - 183 GHz. The resolution of microwave radiometers is diffraction limited, meaning that lower frequency observations require a larger physical antenna to have the same ground resolution as higher frequency observations. However, lower frequency microwave data has advantages because the atmosphere is more transparent, allowing better remote sensing of the surface.

When examining microwave imagery additional considerations should include knowledge of the terrain being evaluated, and resolution of the instrument being used. The difference in soil moisture between a desert, and a river basin creates noticeable differences in lower frequencies. Detailed maps including topography are useful because of temperature gradients due to terrain height. Lower instrument resolution will begin to average affects of clouds, or surface features such as small bodies of water. Keeping these non-atmospheric affects in mind, we begin to explore atmospheric affects due to gases (oxygen and water vapor), and liquid and ice water.

*Corresponding author address: Benjamin Ruston, CSU, Dept. of Atmos. Science, Ft. Collins, CO 80523 Ruston@cira.colostate.edu

2. EMISSION CHARACTERISTICS

Interpretation of microwave imagery begins with an examination of the sources of the radiation. Microwave radiation reaching space from the Earth-atmosphere system is a combination of emission and scattering. Emitters in the 10 to 183 GHz range include the land and ocean surface, water vapor, water and ice clouds, and precipitation. Scattering occurs at the land and ocean surface, and in clouds. Thin ice clouds composed of small ice crystals (e.g. cirrus) are essentially transparent in the microwave, especially at frequencies below 50 GHz. The fact that microwave remote sensing and atmospheric retrievals can be performed in the presence of clouds is a driving force behind satellite microwave radiometry. Microwave data can also retrieve parameters not typically sensed with visible or infrared data, such as sea surface wind speed. Microwave radiometers can also be built with low noise values. These three features, ability to perform in clouds, ability to retrieve unique environmental parameters, and stable calibration ensure that satellite microwave remote sensing will play and larger and increasingly important role in atmospheric science.

2.1 Surface

By definition, a blackbody has a uniform emission efficiency (emissivity) of one throughout all frequencies. No body on Earth is a perfect blackbody and as a consequence the variation of emissivity with frequency is a property utilized in microwave imagery interpretation. When a body has an emissivity of one the temperature derived from the radiance will correspond to the temperature of the body. However, an emissivity of 0.5 will make a body at 300 K radiate like a blackbody of 150 K. Dry land has a high emissivity, often greater than 0.9, while increasing soil moisture or a moist canopy of vegetation will drive the emissivity of the surface down. For example, at low (< 30GHz) frequencies a desert has a much greater emissivity than swampland, so even if the surface temperatures are identical, microwave brightness temperatures will show the desert as warmer than the swampland. The emissivity of land is greatly variable at a single frequency, with the greatest differences at frequencies of 10 - 30 GHz, which are used to detect soil moisture, or infer properties of the vegetative canopy (Schmugge, 1985). Many parameters such as dew, rainfall, vegetation type, soil type, and urbanization effects affect land emissivity over the globe. As a consequence land surfaces exhibit highly temporally and spatially variant emissivity patterns.

Ocean emissivity is not highly variable at a single frequency, with temperature, salinity, and wind speed determining the emission. Lower microwave frequencies are used to find sea surface temperature (Stogryn, 1967), and wind speed (Williams, 1969; Hollinger, 1971; and Webster et al., 1976). The ocean emissivity also varies steadily over frequency; at lower frequencies (< 20 GHz) the ocean's emissivity is about 0.4 and increases with increasing frequency. This large discrepancy in emissivity at low frequencies causes a difference in radiance over ocean and land, allowing for easy land detection.

Polarization is of paramount importance in microwave remote sensing, unlike visible and infrared measurements. The sea surface is highly polarized, while land surfaces exhibit low polarization, with some exceptions like desert sand and ice. Atmospheric effects case the outgoing radiation to space to become less polarized. Atmospheric retrievals exploit this change in the polarizations signal. Vertical and horizontal polarization measurements are typically sufficient to retrieve a wide range of phenomena. Fully polarimetric (Stokes) vector measurements may be required to sense sea surface wind direction (Yueh, S. H., 1997). For a microwave instrument without a constant viewing angle, such as the cross-track scanning AMSU, each field of view has a mixture of vertical and horizontal polarizations. This is benefit of a conical scanning instrument. The incident angle is constant which simplifies surface effects. Measurements from any field of view in a conical instrument can be combined to create composites of features like surface emissivity (Jones and Vonder Haar, 1997). Such compositing is not easily accomplished with a cross-track instrument.

2.2 Atmosphere and Clouds

The atmosphere's gaseous extinction increases with frequency in the microwave regime due to the water vapor continuum. Superimposed over this gradual increase are strong absorption bands due to water vapor, and oxygen. In a clear atmosphere, the absorption and reemission by these gases can be detected.

To examine the effect of cloud liquid water and ice, we used the Goddard Cumulus Ensemble (GCE) model created at Goddard Space Flight Center (Tao and Simpson, 1993). Brightness temperatures were derived from the cloud profiles taken from this model using a plane parallel radiative transfer model with the Eddington approximation and explicit Mie calculations (Kummerow, 1993). The underlying surface was a specular ocean surface with a temperature of 300 K, with the emissivity calculation following the models of Stogryn (1967) and Hollinger (1971). We have prepared five cases of varying properties: a clear sky case, a non-precipitating cloud, two precipitating clouds of varying precipitation rates, and finally a cloud with little rain and a high ice content. These five cases are presented in Figure 1, and a synopsis of their properties in Table 1.

TABLE 1

CASE	Surface Rain Rate (mm/hr)	Column Water Vapor (mm)	Column Precip Liq + Cld Water (mm)	Column Precip Ice + Cld Ice (mm)
Clear	0.000	67.693	0.000	0.000
No Rain Cld	0.000	71.570	1.180	0.000
Lt Rain	1.148	71.481	2.108	0.000
Hvy Rain	19.347	74.821	2.017	1.162
Ice Cld	0.214	67.746	1.380	2.831

In general, the presence of clouds and rainfall obscure the gaseous absorption peaks. Three regimes across the frequency range can be loosely defined, liquid water emission, ice scattering, and a third regime where liquid water emission and ice scattering compete. The first regime is from 10 GHz to the water vapor band at 22 GHz. Emission by liquid water warms the brightness temperatures above the cold ocean surface. As more and larger raindrops are found the warming at lower frequencies increases more dramatically. The non-precipitating cloud had much higher low-level water vapor than the clear or ice cloud case and displayed a warmer background due to the vapor emission.

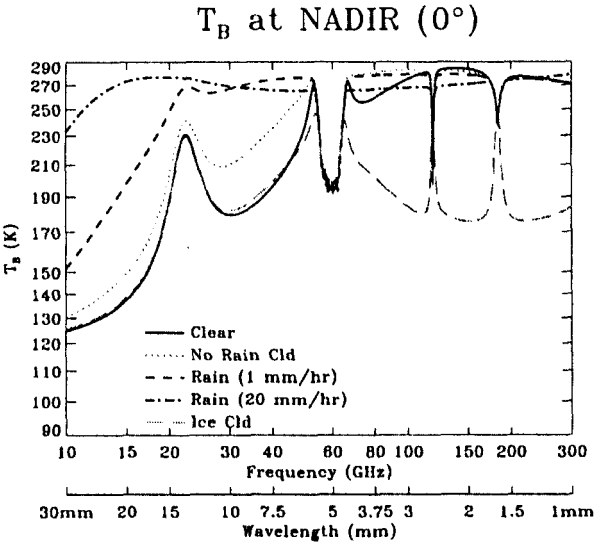

FIGURE 1: Profile of brightness temperature with respect to frequency for five cases. Vertical cloud profiles are from the Goddard Cumulus Ensemble model.

Between the water vapor absorption peak at 22 GHz and the oxygen band and around 60 GHz the liquid water emission, and ice scattering begin to compete. This is displayed well in the two precipitating cloud cases where, the brightness temperature profile for the heavily raining case begin to grow cooler than the lightly raining case, due to the scattering by precipitation size ice. Also notice the ice cloud begins to drop below the clear sky case.

At frequencies greater than 80 GHz precipitation-size ice increases scattering and dominates the

brightness temperature. For the two precipitating cloud cases notice though the heavily raining case is colder than the lightly raining by around 30 GHz it doesn't grow colder than the ocean background until above 80 GHz. With the largest scattering signature found in the ice cloud which strongly depresses the brightness temperature. At the center of the large oxygen absorption band around 60 GHz; all cases have the same brightness temperature, because this portion of the spectrum is sensitive to the upper levels of the atmosphere. However, in the wings of this absorption band the band brightness temperature come from lower in the atmosphere until enough liquid water makes the atmosphere sufficiently opaque.

3. IMAGERY INTERPRETATION

On September 13, 1999 the TRMM Microwave Imager (TMI) and Advanced Microwave Sounding Unit (AMSU) instruments both had descending passes over the Indonesian region of Borneo and Celebes within minutes of each other. The TMI instrument is a conical scanner, at a constant scan angle of 53° allowing for polarized channels. Imagery from four channels in TMI was chosen for presentation, the 10.65V, 19.35H, 37.0H, and 85.5V GHz. Two sounding channels were selected from the AMSU instruments, centered at 50.3 GHz and 183.3±7 GHz. Infrared imagery at 10.8 μm from both the Visible Infrared Scanner (VIRS) and the Advanced Very High Resolution Radiometer (AVHRR) is also presented. From this selection of channels we can make determinations about the land and ocean boundaries, see resolution issues between channels and satellites, and determine objectively some surface features, heavily raining clouds, and clouds with large column ice content. This provides a good example of issues encountered by a real-time user of microwave imagery, such as a forecaster.

TABLE 2

Channel Frequency (GHz)	EFOV (km)	NEΔT (K)
10.65V	63 × 37	0.63
19.35H	30 × 18	0.47
37.0H	16 × 9	0.31
50.3	48 × 48 (1.9°) 79 × 148 (57.6°)	0.219
85.5V	7 × 5	0.52
183.3±7	16 × 16 (0.6°) 27 × 53 (59.2°)	0.60

The imagery resolution in both the AMSU and TMI instruments increases with increasing frequency (see Table 2). This is demonstrated by the fuzzy edges seen around the islands and clouds at 10.65V GHz, which can be contrasted with the well-defined land edges at 85.5V GHz. The infrared channel on AVHRR has a 1 km resolution at nadir and corresponds to ~28,000 GHz. The draw back however to the greater resolution in the infrared is that the emissivity differences are lost.

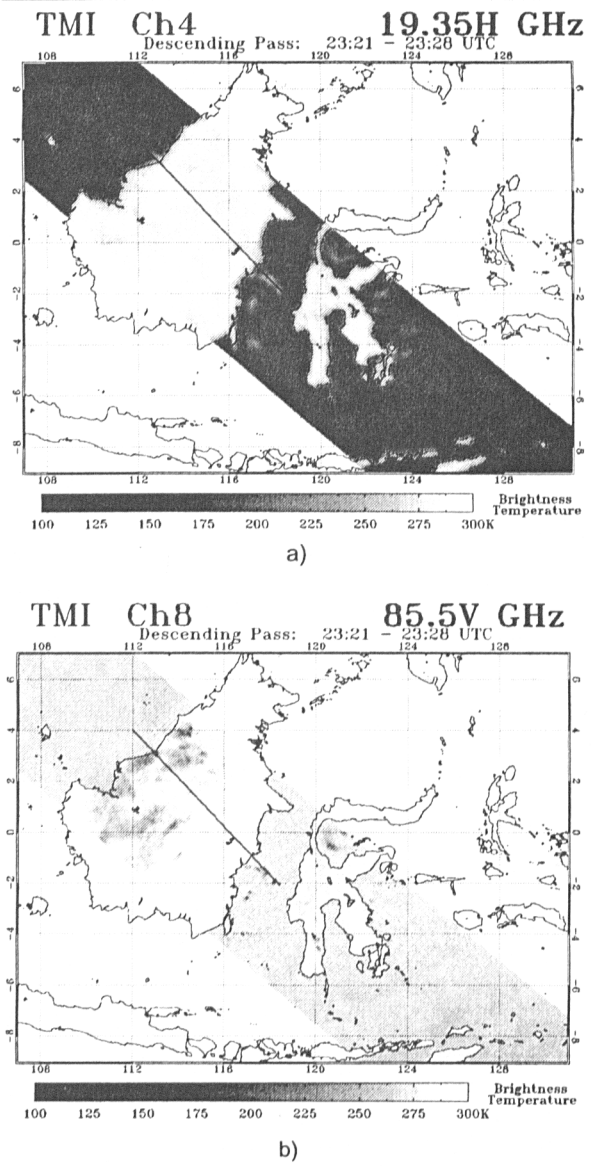

FIGURE 2: Images from the TRMM microwave imager (TMI) at two frequencies: a) 19.35H and b) 85.5V GHz.

In the two lower frequency channels on the TMI at 19.35H and 10.65V GHz, the land-ocean contrast is a dominant feature. The land surface variations reveal swampland around the small lakes at 112E and 116E in Borneo and identification of river basins is possible as well. These two swampland regions have lower brightness temperatures due to the lower emissivity of the land surface. The emissivity change is due to soil moisture content, and vegetation. Channels at 19.35H and 10.65V GHz cannot easily distinguish clouds over

land, unless extremely large raindrops are present. Over ocean however clouds are more easily detected due to the cold ocean background. These channels are sensitive again to the larger precipitation size particles. The 19.35H GHz channel has increased sensitivity to water vapor not present in the lower frequency channel. The clouds that are apparent in both the 19.35H, and the 10.65V channel have very large water drops, and are precipitating heavily. Those that are present in only the 19.35 GHz may be thicker clouds with smaller precipitation particles. There may be heavy rain on the sub-pixel scale that is undetected due to the sensor resolution (refer to Table 2); this is referred to as the beam-filling problem (Kummerow and Giglio, 1994). Examining the cloud field in both the infrared images and in these two microwave channels gives an idea of which clouds, over the ocean, are precipitating heavily.

The two TMI channels centered at 37.0H and 85.5V GHz begin to give highly resolved cloud boundaries over both ocean and land, and are both referred to as imaging channels due to relative minima in the extinction due to the water vapor continuum. At these frequencies the total column water vapor is extremely important. In the tropics the high column water vapor dominates the signal, and these channels become sensitive to changes in this total. While in a polar scene with low column water vapor the channels become sensitive to liquid water (Petty, 1992). In our scene the 37.0H GHz channel has a greater contribution due to liquid water, while the 85.5V GHz channel is still dominated by the water vapor emission and sensitivity to liquid water is small. Where precipitation size ice exists the radiation at 85.5V GHz is scattered by these particles. This scattering reduces the radiance at the satellite sensor and creates lower brightness temperatures. Over land, radiation at 85.5V GHz frequency is due to scattered surface radiation, while over the ocean the scattered radiation is due to water vapor and liquid water emission. The sensitivity to ice scattering makes the 85.5V GHz channel very useful for detecting precipitation size ice.

In summary, the variation of brightness temperature across the microwave spectrum allows interpretive analysis of the land surface (swampland and river basin identification). Clouds appear quite differently through the microwave spectrum with large liquid precipitation particles warming the lower frequencies, and precipitation-size ice scattering, and dominating by 80 GHz. Images using color enhancements can emphasize the land surface brightness temperature variation, atmospheric liquid emission, and ice scattering. These images can be used to make real-time determinations about areas of precipitation, intensity of precipitation, and amount of precipitation size ice.

(on-line at: http://cassiopeia.cira.colostate.edu/AMS2001/)

4. ACKNOWLEDGEMENTS

We appreciate the assistance of Dr. Christian Kummerow, Stan Kidder, and Andy Jones who provided technical assistance and suggestions.

This research, conducted at CIRA/CSU, has been supported by the United States Department of Defense Center for Geosciences / Atmospheric Research, Cooperative Agreement DAAL01-98-2-0078. We also acknowledge partial support from the Ball CMIS team via STC-METSAT.

5. REFERENCES

Hollinger, J. P., 1971: Passive Microwave Measurements of Sea Surface Roughness. *IEEE Trans. Geosci. Electron., GE-9*, pp. 169.

Jones, A. S., and T. H. Vonder Haar, 1997: Microwave Surface Emittance Over Land Using Coincident Microwave and Infrared Satellite Measurements. *Journal of Geophysical Research*, **102**, D12, 13609-13626.

Kidder, S. Q., and Vonder Haar, T. H., 1995: Satellite Meteorology: An Introduction. *Academic Press*, San Diego.

Kummerow, C., and L. Giglio, 1994: A Passive Microwave Technique for Estimating Rainfall and Vertical Structure Information from Space. Part I: Algorithm Description. *Journal of Applied Meteorology*, **33**, 1, pp. 3 - 18.

Kummerow, C., 1993: On the Accuracy of the Eddington Approximation for Radiative Transfer in the Microwave Frequencies. *Journal of Geophysical Research*, **98**, D2, pp. 2757-2765.

Petty, G. W., Katsaros, K. B., 1992: The Response of the SSM/I to the Marine Environment. Part I: An Analytic Model for the Atmospheric Component of Observed Brightness Temperatures. *Journal of Atmospheric and Oceanic Technology*, **9**, 6, pp. 746 - 761.

Prigent, C., Rossow, W. B., and E. Matthews, 1997: Microwave Land Surface Emissivities estimated from SSM/I Observations. *Journal of Geophysical Research*, **102**, D18, pp.21867-21890.

Schmugge, T., 1985: Remote Sensing of Soil Moisture. *Hydrological Forecasting*. John Wiley & Sons Ltd., Chichester, pp. 101 - 124.

Stogryn, A., 1967: The Apparent Temperature of the Sea at Microwave Frequencies. *IEEE Transactions on Antennas and Propagation*, **AP-15**, 2, pp. 278-286.

Tao, W.-K., and J. Simpson, 1993: The Goddard Cumulus Ensemble Model. Part I: Model Description. Terrestrial. *Atmospheric Oceanic Sciences*, 4, pp. 35-72.

Webster, W. J., Wilheit, T. T., Ross, D. B, and P. Gloersen, 1976: Spectral Characteristics of the Microwave Emission From a Wind-Driven Foam-Covered Sea. *Journal of Geophysical Research*, **81**, 18, pp. 3095-3099.

Williams, G. F., 1969: Microwave Radiometry of the Ocean and the Possibility of Marine Wind Velocity Determination from Satellite Observations. *Journal of Geophysical Research*, **74**, 18, pp. 4591-4594.

Yueh, Simon H., 1997: Modeling of Wind Direction Signals in Polarimetric Sea Surface Brightness Temperatures. *IEEE Transaction on Geoscience and Remote Sensing*, **35**, 6, pp. 1400 - 1418.

P5.42 EURAINSAT: EUROPEAN SATELLITE RAINFALL ANALYSIS AND MONITORING AT THE GEOSTATIONARY SCALE

Vincenzo Levizzani[1*], Peter Bauer[2], Andrea Buzzi[1], Donald E. Hinsman[3], Alexander Khain[4], Chris Kidd[5], Frank S. Marzano[6], Francesco Meneguzzo[7], Alberto Mugnai[8], J. Pedro V. Poiares Baptista[9], Franco Prodi[1,10], James F. W. Purdom[11], Daniel Rosenfeld[4], Johannes Schmetz[12], Eric A. Smith[13], Francesco Tampieri[1], F. Joseph Turk[14], Gilberto A. Vicente[13,15]

[1]ISAO-CNR, Bologna, Italy, [2]ECMWF, Reading, UK, [3]WMO, Geneva, Switzerland, [5]Univ. Birmingham, UK, [6]Univ. L'Aquila, Italy, [7]LaMMA, Firenze, Italy, [8]IFA-CNR, Roma, Italy, [9]ESA-ESTEC, Nordwijk, The Netherlands, [10]Univ. Ferrara, Italy, [11]NOAA-NESDIS, Camp Springs, MD, [12]EUMETSAT, Darmstadt, Germany, [13]NASA-GSFC, Greenbelt, MD, [14]NRL, Monterey, CA, [15]QSS Group, Inc, Seabrook, MD

1. INTRODUCTION

The latest generation sensors on board the Geostationary Operational Environmental Satellites (GOES) (Menzel and Purdom, 1994) and the upcoming METEOSAT Second Generation (MSG) (see Fig. 1) Spinning Enhanced Visible and Infrared Imager (SEVIRI) (Schmetz et al., 1998) significantly enhance the ability of sensing cloud microstructure and precipitation forming processes (Levizzani et al., 2000) from a geostationary platform. A potential exists for improved instantaneous rainfall measurements from space by combining infrared (IR) and visible (VIS) observations with passive microwave (MW) measurements.

IR and VIS satellite rainfall estimates have long since been available and suffered from the difficulty in associating cloud top features to precipitation at ground level. They were used for climate purposes or combined with radar measurements for nowcasting (e.g. recent examples by Amorati et al., 2000; Porcù et al., 1999; Vicente et al., 1998).

Physically-based passive MW methods were developed mainly using data from the Special Sensor Microwave/Imager (SSM/I) and are based on several different physical principles (see for example Smith et al., 1998; Wilheit et al., 1994). Limitations of MW algorithms include the relatively large footprint and the low earth orbits not suitable for most of the operational strategies.

Combined MW and IR algorithms using SSM/I radiometric data were first oriented to monthly averages over wide areas (e.g. Adler et al., 1993) or to global products as it is for the Global Precipitation Climatology Project (GPCP) (Huffman et al., 2001), although the need for instantaneous combined estimations was recognized already some time ago (e.g. Levizzani et al., 1996). Several methods exist (Sorooshian et al., 2000; Todd et al., 2001; Turk et al., 1999) that make use of IR and MW at various degrees of complexity and targeting different rainfall regimes. Some of these are running operationally, granting that their validation requires additional work in the years to come. In particular, global rapid-update estimates with near real-time adjustment of the thermal IR co-localized with MW-based rainrates are operationally very promising (Turk et al., 1999).

The algorithms for the Tropical Rainfall Measuring Mission (TRMM) Precipitation radar (PR) require a special mention given the novelty and potential of the active instruments for future missions: an example is the TRMM algorithm 2A-25 (Iguchi et al., 2000). Combined MW and rain radar algorithms are relatively new and were developed for the TRMM Microwave Imager (TMI) and the PR (e.g. TRMM algorithm 2B-31, Haddad et al., 1997).

Finally, rainfall and humidity assimilation, and microphysical parameterizations for Local Area Models (LAM) and General Circulation Models (GCM) open up the road to very effective operational meteorological applications that incorporate the verification of model output (Turk et al., 1997).

2. EURAINSAT: THE PROJECT

EURAINSAT is a project partially funded by the European Commission with the aim of developing new satellite rainfall estimation methods at the geostationary scale for an operational use in short and

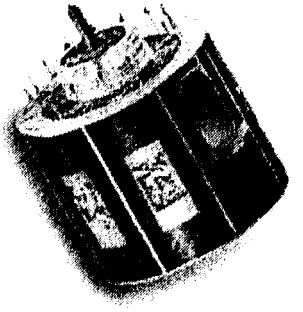

FIG. 1. Artist impression of the Meteosat Second Generation spacecraft (courtesy of EUMETSAT).

*Corresponding author address: V. Levizzani, ISAO-CNR, via Gobetti 101, I-40129 Bologna, Italy; e-mail: v.levizzani@isao.bo.cnr.it

very short range weather monitoring and forecasting. It will exploit the new channels in the VIS, near IR and IR of the MSG SEVIRI that will be launched in middle 2002. The project started in January 2001 and will last until December 2003.

The consortium has two objectives in mind: 1) contribute to improving the knowledge of clouds and precipitation formation processes using meteorological satellite sensors, and 2) make available new precipitation products for weather analysis and forecasting. SEVIRI will in fact provide better multispectral measurements for the identification of the physical processes of cloud formation and evolution. The 15 min image repetition time is also more compatible with the time responses of cloud systems.

The following key geographic areas and major meteorological events were adopted:

- Flood-producing episodes (e.g. Northwestern and Southern Italy);
- Several cases involving the presence/absence of ice, polluted air masses and maritime conditions;
- Influence of orography, e.g. the Alps during the Mesoscale Alpine Programme (MAP) Special Observing Period (SOP) (Bougeault et al., 2001);
- Sustained light rain and "insignificant" rain cases (very difficult to detect from satellite) in UK and Northern Europe;
- Tropical and sub-tropical cases over Africa, where the Niger catchment was selected given the relatively regular ground raingage network;
- A climatological window over Europe (30-60 N, 15 W-20 E).

The project has gathered together a substantial part of the satellite rainfall community and in this sense has already reached an important milestone. This is particularly true considering that the team actively participates into the development of scenarios and concept for the future Global Precipitation Measurement (GPM) Mission. More information on EURAINSAT and its findings can be gained at the web site *http://www.isao.bo.cnr.it/~eurainsat/*.

3. MULTISPECTRAL MICROPHYSICAL CHARACTERIZATION OF CLOUD PROCESSES

A method was developed by Rosenfeld and Lensky (1998) to infer precipitation-forming processes in clouds based on multispectral satellite data. The method was originally based on the Advanced High Resolution Radiometer (AVHRR) imagery on polar orbiting satellites (Lensky and Rosenfeld, 1997). The forthcoming MSG SEVIRI is expected to enhance the capabilities of extracting cloud physical properties (Watts et al., 1998) more relevant for cloud genesis and evolution and not anymore limited by the insufficient number of passages. The effective radius (r_e) of the particles and the cloud optical thickness are extracted and used for radiative transfer calculations that define the cloud type and improve its characterization. Precipitation forming processes are inferred using also data from the AVHRR, The TRMM VIS and IR Sensor (VIRS) and the Moderate-resolution Imaging Spectroradiometer (MODIS) on board NASA's Terra spacecraft.

Microphysically "maritime" clouds grow in very clean air with small cloud condensation nuclei (CCN) and droplet concentrations, which produce very efficient coalescence and warm rain processes. "Continental" clouds normally grow, on the contrary, in polluted air having large CCN and droplet concentrations, i.e. the coalescence is relatively inefficient. The better knowledge of cloud microstructure and precipitation forming processes will facilitate the development of a new generation of improved passive MW rainfall algorithms. The importance of the cloud characterization method has recently been demonstrated by observing the effects of forest fire (Rosenfeld, 1999), urban pollution (Rosenfeld, 2000) and desert dust aerosols (Rosenfeld et al., 2001) in inhibiting precipitation formation processes.

4. RAINFALL ESTIMATION METHODS

4.1 MW Methods

Many methods have been proposed for detecting rainfall from MW satellite sensors. Simple methods using polarization-corrected brightness temperatures (e.g. Kidd, 1998) have been proposed together with more physical approaches that rely upon microphysical characterization by

- stratifying clouds into different microphysical types and examining how much of the variability in the bias of MW rainfall estimation is explained by the microphysical characterization;
- developing a library of passive MW signatures from different cloud types, and
- using a microphysical cloud classification for improving cloud radiative transfer modeling based on statistical multivariate generators of cloud genera.

The scheme of Mugnai et al. (1993) and Smith et al. (1992) is a good example of such methods, especially in the very complex environment of severe storm microphysics. Cloud modeling and MW radiative transfer has been recently applied to stratiform rainfall by Bauer et al. (2000). Panegrossi et al. (1998) have shown the importance of testing the physical initialization and the consistency between model and measurement manifolds.

4.2 Combined Multispectral and MW Methods

Cloud microphysical information, when combined with MW measurements, can lead to improvements in satellite-based rainfall measurements, especially from clouds in the extra tropics and over land (e.g. Bauer et al., 1998). EURAINSAT concentrates on exploiting SEVIRI data in the VIS, near IR and water vapor (WV) for cloud characterization and screening within a rapid cycle of rainfall estimation based on SSM/I, TMI and geostationary IR data. Data from MODIS serve the

purpose of simulating data from MSG SEVIRI during the pre-launch phase. Moreover, the project shares in the cloud-related work from the MODIS team (King et al. 1997).

Two are the main research lines:

- Develop new MSG-MW rainfall algorithms incorporating the observed cloud microstructure and precipitation forming processes. State of the art cloud (Khain et al., 2000) and radiative transfer modeling will be instrumental to detailed cloud and rainfall type discrimination.
- Introduce such methods into rapid update rainfall cycles for near real time rainfall estimations over oceans and land with the widest possible area coverage. Mid-latitude Europe, the Mediterranean basin, North Africa, the Middle East and equatorial and tropical African regions are the main targets for operational and climatological applications. Applications to the Mediterranean have been reported by Meneguzzo et al. (1998).

5. APPLICATIONS

Applications embrace, among others, water availability, global change studies, nowcasting, hydrogeological disaster management, agriculture and famine reduction, and monitoring of remote areas.

Data assimilation procedures that improve cloud and humidity characterization in current analysis schemes for LAMs are at hand. Most important are the sensitivity to the orography and the modeling of moist processes (Buzzi et al., 1998). Cloud parameterization using information from multispectral methods is foreseen as a main goal. Extensive rainfall model output verification is another important task that can only be possible using satellite data with enhanced physical content such as those provided by the SEVIRI-MW proposed scheme.

MW signatures of precipitation, as given by a space-borne multi-frequency radiometer, have been shown to be the base for estimating the path attenuation in K-band satellite communications (Marzano et al., 2000) and opening the door to potential rainfall fade mitigation approaches.

ACKNOWLEDGMENTS

EURAINSAT is a shared-cost project (contract EVG1-2000-00030) co-funded by the Research DG of the European Commission within the RTD activities of a generic nature of the Environment and Sustainable Development sub-programme (5th Framework Programme). The authors acknowledge their mother institutions that strongly supported the formation of the project's science team.

REFERENCES

Adler, R. F., A. J. Negri, P. R. Keehn, and I. M. Hakkarinen, 1993: Estimation of monthly rainfall over Japan and surrounding waters from a combination of low-orbit microwave and geosynchronous IR data. *J. Appl. Meteorol.*, **32**, 335-356.

Amorati, R., P. P. Alberoni, V. Levizzani, and S. Nanni, 2000: IR-based satellite and radar rainfall estimates of convective storms over northern Italy. *Meteor. Appl.*, **7**, 1-18.

Bauer, P., L. Schanz, R. Bennartz, and P. Schlüssel, 1998: Outlook for combined TMI-VIRS algorithms for TRMM: lessons learned from the PIP and AIP projects. *J. Atmos. Sci.*, **55**, 1714-1729.

————, A. Khain, A. Pokrovsky, R. Meneghini, C. Kummerow, F. S. Marzano, and J. P. V. Poiares Baptista, 2000: Combined cloud–microwave radiative transfer modeling of stratiform rainfall. *J. Atmos. Sci.*, **57**, 1082-1104.

Bougeault, P., P. Binder, A. Buzzi, R. Dirks, R. Houze, J. Kuettner, R. B. Smith, R. Steinacker, and H. Volkert, 2001: The MAP Special Observing Period. *Bull. Amer. Meteor. Soc.*, **82**, 433-462.

Buzzi, A., N. Tartaglione, and P. Malguzzi, 1998: Numerical simulations of the 1994 Piedmont flood: role of orography and moist processes. *Mon. Wea. Rev.*, **126**, 2369-2383.

Haddad, Z., E. A. Smith, C. Kummerow, T. Iguchi, M. Farrar, S. Darden, M. Alves, and W. Olson, 1997: The TRMM 'Day-1' radar/radiometer combined rain-profile algorithm. *J. Meteor. Soc. Japan*, **75**, 799-808.

Huffman, G. J., R. F. Adler, M. M. Morrissey, D. T. Bolvin, S. Curtis, R. Joyce, B. McGavock, and J. Susskind, 2001: Global precipitation at one-degree daily resolution from multisatellite observations. *J. Hydrometeorol.*, **2**, 36-50.

Iguchi, T., T. Kozu, R. Meneghini, J. Awaka, and K. Okamoto, 2000: Rain-profiling algorithm for the TRMM precipitation radar. *J. Appl. Meteorol.*, **39**, 2038-2052.

Khain, A., M. Ovtchinnikov, M. Pinsky, A. Pokrovsky, and H. Krugliak, 2000: Notes on the state-of-the-art numerical modeling of cloud microphysics. *Atmos. Res.*, **55**, 159-224.

Kidd, C., 1998: On rainfall retrieval using polarization-corrected temperatures. *Int. J. Remote Sensing*, **19**, 981-996.

King, M. D., S.-C. Tsay, S. E. Platnick, , M. Wang, and K.-N. Liou, 1997: Cloud retrieval algorithms for MODIS: optical thickness, effective particle radius, and thermodynamic phase. *MODIS Algorithm Theoretical Basis Doc.*, ATBD-MOD-05 and MOD-06, 79 pp.

Lensky, I. M., and D. Rosenfeld, 1997: Estimation of precipitation area and rain intensity based on the microphysical properties retrieved from NOAA AVHRR data. *J. Appl. Meteorol.*, **36**, 234-242.

Levizzani, V., F. Porcù, F. S. Marzano, A. Mugnai, E. A. Smith, and F. Prodi, 1996: Investigating a SSM/I microwave algorithm to calibrate METEOSAT infrared instantaneous rainrate estimates. *Meteorol. Appl.*, **3**, 5-17.

————, P. P. Alberoni, P. Bauer, L. Bottai, A. Buzzi, E. Cattani, M. Cervino, P. Ciotti, M. J. Costa, S. Dietrich, B. Gozzini, A. Khain, C. Kidd,

F. S. Marzano, F. Meneguzzo, S. Migliorini, A. Mugnai, F. Porcù, F. Prodi, R. Rizzi, D. Rosenfeld, L. Schanz, E. A. Smith, F. Tampieri, F. Torricella, F. J. Turk, G. A. Vicente, and G. Zipoli, 2000: Use of the MSG SEVIRI channels in a combined SSM/I, TRMM and geostationary IR method for rapid updates of rainfall. *Proc. 1st MSG-RAO Workshop*, ESA SP-452, 63-66.

————, J. Schmetz, H. J. Lutz, J. Kerkmann, P. P. Alberoni, and M. Cervino, 2001: Precipitation estimations from geostationary orbit and prospects for METEOSAT Second Generation. *Meteorol. Appl.*, **8**, 23-41.

Marzano, F. S., J. F. Turk, P. Ciotti, S. Di Michele, and N. Pierdicca, 2000: Combined use of spaceborne polar-orbiting microwave and geo-stationary infrared radiometers for estimating rainfall attenuation along earth-satellite links. *Proc. 1st Int. Workshop on Radiowave Propagation Modelling for SatCom Services at Ku-band and above*, ESA WPP-146, 189-196.

Meneguzzo, F., S. Migliorini, G. A. Vicente, L. Bottai, B. Gozzini, and G. Zipoli, 1998: Satellite rainfall estimates in real time in the Mediterranean countries. Verifications in Tuscany. *Proc. ICAM-98, 25th Int. Conf. Alpine Meteor.*, Turin, 14-19 Jul, 2-7.

Menzel, W. P., and J. F. W. Purdom, 1994: Introducing GOES-I: the first of new generation of Geostationary Operational Environmental Satellites. *Bull. Am. Meteor. Soc.*, **75**, 757-781.

Mugnai, A., E. A. Smith, and G. J. Tripoli, 1993: Foundations for statistical-physical precipitation retrieval from passive microwave satellite measurements. Part II: Emission-source and generalized weighting-function properties of a time-dependent cloud-radiation model. *J. Appl. Meteorol.*, **32**, 17-39.

Panegrossi, G., S. Dietrich, F. S. Marzano, A. Mugnai, E. A. Smith, X. Xiang, G. J. Tripoli, P. K. Wang, and J. P. V. Poiares Baptista, 1998: Use of cloud model microphysics for passive microwave-based precipitation retrieval: significance of consistency between model and measurement manifolds. *J. Atmos. Sci.*, **55**, 1644-1672.

Porcù, F., M. Borga, and F. Prodi, 1999: Rainfall estimation by combining radar and infrared satellite data for nowcasting purposes. *Meteorol. Appl.*, **6**, 289-300.

Rosenfeld, D., 1999: TRMM observed first direct evidence of smoke from forest fires inhibiting rainfall. *Geophys. Res. Lett.*, **26** (20), 3105-3108.

————, 2000: Suppression of rain and snow by urban and industrial air pollution. *Science*, **287**, 1793-1796.

————, and I. M. Lensky, 1998: Satellite-based insights into precipitation formation processes in continental and maritime convective clouds. *Bull. Am. Meteor. Soc.*, **79**, 2457-2476.

————, Y. Rudich, and R. Lahav, 2001: Desert dust suppressing precipitation: a possible desertification feedback loop. *PNAS*, **98**, 5975-5980.

Schmetz, J., H. Woick, S. A. Tjemkes,, and M. Rattenborg, 1998: From METEOSAT to METEOSAT Second Generation (MSG). *Prepr. 9th Conf. Satellite Meteorol. Oceanography*, AMS, 335-338

Smith, E. A., A. Mugnai, H. J. Cooper, G. J. Tripoli, and X. Xiang, 1992: Foundations for statistical-physical precipitation retrieval from passive microwave satellite measurements. Part I: Brightness-temperature properties of a time-dependent cloud-radiation model. *J. Appl. Meteorol.*, **31**, 506-531.

————, J. E. Lamm, R. F. Adler, J. Alishouse, K. Aonashi, E. C. Barrett, P. Bauer, W. Berg, A. Chang, R. Ferraro, J. Ferriday, S. Goodman, N. Grody, C. Kidd, D. R. Kniveton, C. Kummerow, G. Liu, F. S. Marzano, A. Mugnai, W. Olson, G. Petty, A. Shibata, R. Spencer, F. Wentz, T. Wilheit, and E. Zipser, 1998: Results of the WetNet PIP-2 project. *J. Atmos. Sci.*, **55**, 1483-1536.

Sorooshian, S., K.-L. Hsu, X. Gao, H. V. Gupta, B. Imam, and D. Braithwaite, 2000: Evaluation of PERSIANN system satellite–based estimates of tropical rainfall. *Bull. Am. Meteor. Soc.*, **81**, 2035–2046.

Todd, M. C., C. Kidd, D. Kniveton, and T. J. Bellerby, 2001: A combined satellite infrared and passive microwave technique for estimation of small-scale rainfall. *J. Atmos. Oceanic Technol.*, **18**, 742-755.

Turk, F. J., G. D. Rohaly, and P. Arkin, 1997: Utilization of satellite-derived tropical rainfall for analysis and assimilation into a numerical weather prediction model. *Prepr. 22nd Conf. Hurricanes and Tropical Meteor.*, AMS, 310-311.

————, G. D. Rohaly, J. Hawkins, E. A Smith, F. S. Marzano, A. Mugnai, and V. Levizzani, 1999: Meteorological applications of precipitation estimation from combined SSM/I, TRMM and infrared geostationary satellite data. In *Microwave Radiometry and Remote Sensing of the Earth's Surface and Atmosphere*, P. Pampaloni and S. Paloscia Eds., VSP Int. Sci. Publ., 353-363.

Vicente, G. A., R. A. Scofield, and W. P. Menzel, 1998: The operational GOES infrared rainfall estimation technique. *Bull. Am. Meteor. Soc.*, **79**, 1883-1898.

Watts, P. D., C. T. Mutlow, A. J. Baran, and A. M. Zavody, 1998: Study on cloud properties derived from Meteosat Second Generation observations. *Final Rep. EUMETSAT ITT No. 97/181*, 344 pp.

Wilheit, T. T., R. F. Adler, S. Avery, E. Barrett, P. Bauer, W. Berg, A. Chang, J. Ferriday, N. Grody, S. Goodman, C. Kidd, D. Kniveton, C. Kummerow, A. Mugnai, W. Olson, G. Petty, A. Shibata, E. A. Smith, and R. Spencer, 1994: Algorithms for the retrieval of rainfall from passive microwave measurements. *Remote Sens. Rev.*, **11**, 163-194.

P5.43 MICROWAVE SURFACE AND PRECIPITATION PRODUCTS SYSTEM (MSPPS) – AN APPLICATION OF AMSU DATA TO THE RETRIEVAL OF SURFACE GEOPHYSICAL PRODUCTS

Huan Meng*, D. A. Moore, L. Zhao, R. R. Ferraro**, F. Weng**, and N. Grody**
QSS Group, Inc., Lanham, Maryland

1. MSPPS PRODUCTS

The MSPPS project was motivated by a group of NOAA/NWS/NCEP scientists who had a demand for near-real-time surface and precipitation products derived from data collected by the Advanced Microwave Sounding Unit (AMSU). These products are especially helpful in regions with cloud cover, where visible and infrared instruments have decreased capability. Table 1 lists the currently available operational products, their respective associated instrument (AMSU-A or AMSU-B), and their respective product retrieval surface (land, ocean, or global). Algorithms for additional products such as snow depth and soil moisture are in development.

TABLE 1

PRODUCT	AMSU-A	AMSU-B
Total Precipitable Water	Ocean	
Cloud liquid Water	Ocean	
Sea Ice Concentration	Ocean	
Emissivity (23.8, 31.4, 50.3 GHz)	Land	
Surface Temperature†	Land	
Rain Rate		Global
Ice Water Path		Global
Snow Cover		Land

†Experimental product

2. SYSTEM STRUCTURE

The MSPPS system takes Level-1B* data from AMSU instruments carried onboard both NOAA-15 and NOAA-16 satellites, and generates and outputs products as Level-2 swaths and Level-3 grid maps. Figure 1 shows a flowchart of the MSPPS operational system.

The standard output data format for the project is NASA's HDF-EOS. The near-real-time Level-2 data includes an HDF-EOS swath and a binary swath. The Level-3 data are composed of a near-real-time 16th mesh polar stereographic map and a global geographic map; both maps are in HDF-EOS format. MSPPS output data are used for research and application purposes both within NOAA and by external agencies.

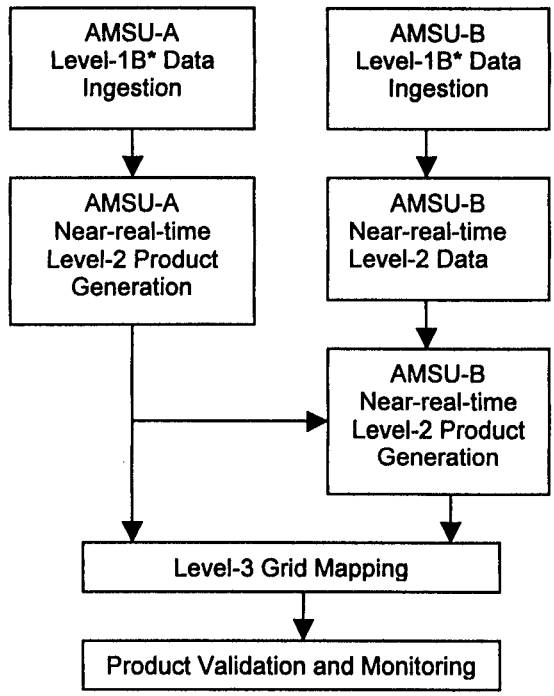

FIGURE 1. MSPPS System Flowchart

3. PRODUCT VALIDATION AND MONITORING

MSPPS products are currently undergoing an extensive validation process involving a comparison with products from other sources (radiosonde, radar, models, other satellites, *etc.*) using images, statistics, and case studies. Since its inception, the project has led to the development of many visualization tools enabling algorithm and system performance monitoring. The MSPPS project web site, http://orbit-net.nesdis.noaa.gov/arad2/MSPPS, is a comprehensive source of information about the project. Located there are daily-generated products, comparisons with other independent data (images, animations, statistical plots, *etc.*), and query engines for past results. The web site also includes such information as introduction to the project, the product algorithms, project data format, and links to various MSPPS-related sites.

* Corresponding author address: Huan Meng, Rm 703F, WWBG, NOAA/NESDIS/ORA, 5200 Auth Road, Camp Springs, MD 20746; e-mail: Huan.Meng@noaa.gov.
** NOAA/NESDIS/ORA, Camp Springs, Maryland

P5.45

MOTIVATING THE USE OF REMOTELY-SENSED DATA SOURCES FOR ESTIMATING CONVECTIVE MOMENTUM TRANSPORTS

John R. Mecikalski[1]

Cooperative Institute for Meteorological Satellite Studies
Space Science and Engineering Center
University of Wisconsin - Madison

1 MOTIVATION

The goal of this study is to estimate convective momentum transport (CMT) of deep, moist convection using remotely-sensed data sources. These data include aircraft and ground-based vertically-looking Doppler radar data, Weather Surveillance Radar–1988 Doppler data, Tropical Rainfall Measuring Mission (TRMM) Precipitation Radar (PR) reflectivities, as well as cloud-derived winds from geostationary satellite. Up to now, little to no work has considered such data sets for studying CMT, owing perhaps to the relative inadequacy or unavailability of them for accomplishing this task. With the inception of the TRMM PR data in 1997, and upward- (Disdrometer) and downward- (ER-2 aircraft-based Dopplers, EDOP) looking Doppler radars, the time has come to begin evaluating how well these types of instruments measure component terms in the three-dimensional momentum budget. Given the operational capabilities of TRMM [its follow-on satellite system, the Global Precipitation Mission (GPM) slated for 2008] and the WSR-88D system, and the importance of correctly parameterizing CMT in general circulation models, the motivation is high for this work.

Critical issues that must addressed when using radar data for measuring CMT is the sometimes weak correlation between hydrometeor (fall) motion and wind velocities, as well as the sometimes inconsistent relationships between precipitation core orientation, convective updrafts and CMT. In the case of Doppler data, this task is made somewhat easier given velocity information; for TRMM, our goal is to develop parameterizations that utilize reflectivity information alone. Assessing conditions in the ambient environment is critical, and therefore any parameterization will certainly rely on data from model analysis fields. In light of these issues, the main effort here is to assess precisely *how useful are these data for assessing component terms in the budget equations, assuming first that they are probably incapable of measuring all necessary components.*

The goals of this note, and the accompanying poster, therefore are as follows:

1. Given the respective resolutions and attributes of each data set, identify how they may be used to evaluate CMT,
2. Provided a numerical model-generated budget of convection (considered as "truth"), use the radar data in an attempt to compute selected budget terms,

This analysis has as it's overall goal the use of TRMM PR data within a CMT parameterization for operational, regional-scale CMT evaluations.

2 DATA

The Doppler data used for this research were collected during the TExas FLorida UNderflight–B (TEFLUN-B) and the Large-scale Biosphere Atmosphere (LBA) TRMM validation experiments conducted in August-September 1998 and February 1999, respectively. Calibrated Rd-69 Disdromet Disdrometer (Joss-Waldvogel Disdrometer) 915 MHz data are provided by the NOAA Aeronomy Laboratory as collected at the Triple-N-Ranch, Florida (see Gage et al. 2000). The EDOP data are also provided by the NOAA Aeronomy Laboratory. The EDOP is an X-band 9.6 GHz radar with two fixed antennas (one with a nadir view). The nominal vertical resolution of the Disdrometer and EDOP data are 105 and 70 m, respectively, with one minute time resolutions (Heymsfield et al. 2000). TRMM PR data (Level 1C) has resolutions of 250 m in the vertical and 4 km in the horizontal. The WSR-88D radar data used for this work has a vertical resolution between 100 and 500 m. All numerical budget experiments were conducted using the University of Wisconsin - Nonhydrostatic Modeling System's (UW-NMS) regional and mesoscale model.

Figure 1 shows a time-height cross section of Disdrometer data for 22 August 1998, one "high-priority" day during TEFLUN-B chosen in this analysis. The figure illustrates several important components of cumulonimbus cloud structure that this analysis will key in on for assessing CMT. One main feature, denoted by the horizontal strip of high-reflectivity centered on 4-4.5 km, is the freezing level within this particular thunderstorm.

[1] *Corresponding author*: John R. Mecikalski, Cooperative Institute for Meteorological Satellite Studies, University of Wisconsin - Madison, 1225 West Dayton Street, Madison, WI 53706. email: *johnm@ssec.wisc.edu*

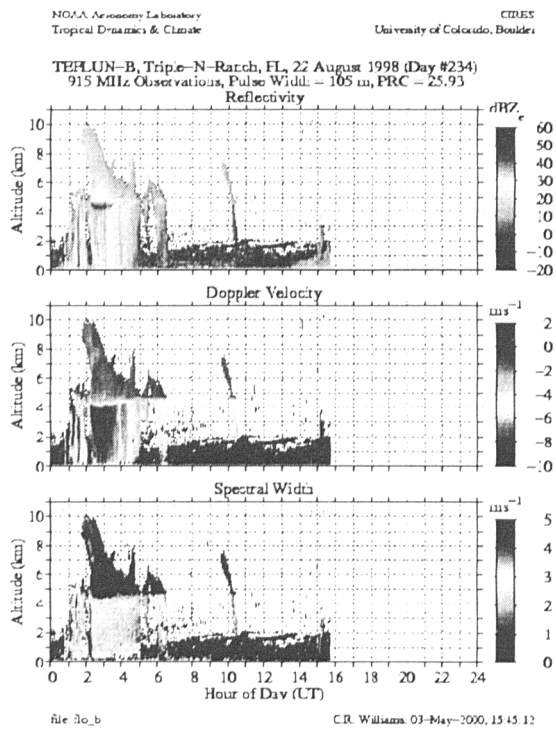

Figure 1: Disdrometer data collected at the Triple-N-Ranch, Florida on 22 August 1998.

Other features, using the freezing level as a reference, are the (liquid) precipitation fall streaks from the freezing level downward (as well as below the cloud base, denoted by roughly by the level of horizontally-continuous -10 to +10 dBZ$_e$ returns below about 2 km). Another feature is the character of radar returns above the freezing level, which denote frozen hydrometers, and to some extent, cloud draft characteristics. Our analysis methods focus in on these resolved features in the data. Figure 2 presents EDOP data for convection near the Triple-N-Ranch on 23 August 1998 near 1900 UTC. Similar features are seen in Fig. 2 as in Fig. 1, yet we note that since these data are collected above storm top, the tops of the convection appear better resolved with more high (above 10 km) cirrus clouds being measured in EDOP versus Disdrometer data.

3 TECHNIQUES OF ANALYSIS

A general assumption, made for the Disdrometer data only, is that these data can only describe a storm's *line-normal* component of momentum. This is the case as the storm should move over a stationary ground-based site along the line of motion described by the mean shear vector over the storm's depth. The same assumption cannot be made regarding the EDOP data, since the ER-2 aircraft intersects a storm at an angle quite independent of storm motion. It may be assumed for the

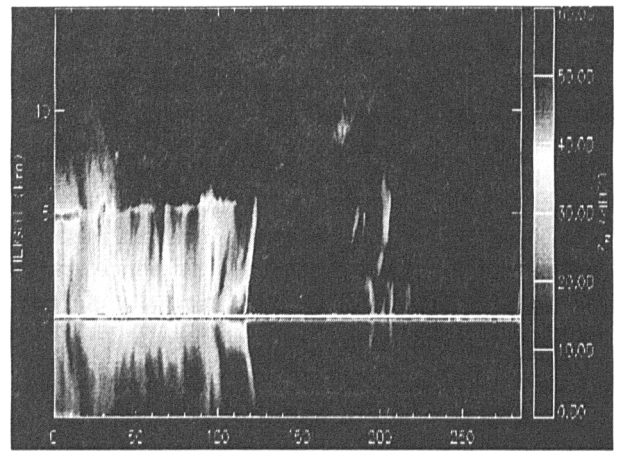

Figure 2: ER-2 Aircraft Doppler (EDOP) data collected near the Triple-N-Ranch, Florida on 23 August 1998 centered on 1900 UTC.

EDOP data however, that the ER-2 moves at a horizontal ground-relative speed that is much higher (by an order of magnitude) than storm motion, and therefore provides a reasonable "snapshot" of CMT properties. Thus, provided one has aircraft motion information accompanying the EDOP data for a particular storm, the data's relevance for determining either the $u-$ and/or $v-$budget components can be determined.

Returning to the Disdrometer data, we may expect that a storm's structure may evolve somewhat as it passes over the ground-based instrument, yet its CMT properties should be somewhat constant. An exception would be in cases where a significant outflow feature, not associated with the storm over the instrument, would affect the precipitation fall characteristics of the measured storm (to influence an estimate of CMT by a storm's downdrafts). If storm motion is exceptionally slow (<5 ms^{-1}), there is a possibility that significant storm evolution may occur during the sampling period.

For WSR-88D, which has yet to be analyzed, we are challenged to evaluate how the Doppler velocities can be used surrounding a radar site. This entails treating the velocities as a function of radial direction from single Doppler radar. Once this is determined, similar processing methods can be applied using these data as used with the other two Doppler data sources.

TRMM PR data has quite different characteristics compared to the Doppler data. Figure 3 presents a east-west slice though a mature mesoscale convective system as measured by TRMM PR. Highlighted is the general updraft slope for this system in this snapshot image. A risky assumption when using these data for CMT evaluations is that the updrafts are along the long-axis of the deepest precipitation cores, in this case, tilted slightly toward the east. The squall line-parallel slice (not shown) shows nearly vertical updrafts with no tilt.

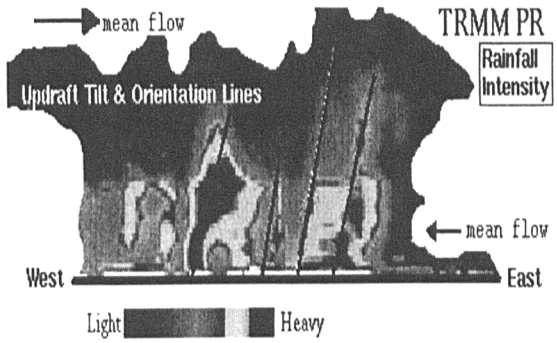

Figure 3: TRMM Precipitation Radar image slice through a mature squall line. This slice is nearly perpendicular to a north-south oriented line.

Given the lower resolutions of these data compared to the Doppler instruments, we will be significantly challenged to evaluate CMT properties much beyond the gross characteristics. However, by using relationships developed from the Doppler data, there is reason to be optimistic that satellite-based radar systems will some day provide a significant level of CMT information.

Figure 4 presents the UW-NMS momentum budgets for convection modeled at 2 km resolution centered on 28° N and 81° W, over the Triple-N-Ranch for the TEFLUN-B experiment valid at 0000 UTC 22 August 1998. The flux and domain-averaged form of the zonal momentum budget used here is as in LeMone and Jorgensen (1991). The convection on this day was generally transporting momentum down the mean shear gradient, decelerating the low-level (below 8 km), increasing mid-level easterlies, and increasing westerly flow at cloud top between 12 and 16.5 km.

4 BUDGET TERM CALCULATIONS

Routines to automatically measure the hydrometeor fall slope angles relative to Earth from radar reflectivities have been constructed. Figure 5 presents the automated tagging of precipitation core slopes for Disdrometer data the period 1300-1600 UTC 21 August 1998. The black lines denote the highest reflectivity cores and are used to relate hydrometeor fall motions and estimated hydrometeor sizes to estimate perturbation line-normal wind. Routines to relate Doppler velocities to both air (convective draft) and hydrometeor motions are constructed, and for convection on 22 August 1998, momentum flux terms ($\overline{u'w'}$) and ($\overline{v'w'}$) have been computed.

The following list provides a specific overview of our algorithm for using radar data to compute CMT flux terms. This procedure currently is based on our processing of EDOP, 915 MHz Disdrometer-calibrated radar, and TRMM PR data.

- Evaluate Doppler velocities (w_D) from the vertically-pointing Disdrometer and EDOP data sets. Evaluate w_D as a mean over a layer (400-1000 m deep).
- Using reflectivity information, seek an estimate of drop (i.e. hydrometeor) size, $\bar{D}$. As a first attempt, use relationships based on the Marshal-Palmer distribution (e.g., Spilhaus 1948) to determine $\bar{D}$. Then, estimate terminal partical velocity, w_T from $\bar{D}$.
- Compare w_T with w_D and estimate w'. Do this by evaluating whether or not hydrometeors are being pushed downward in a downdraft or being held in suspension by an updraft.
- Evaluate the slope of the falling precipitation (Fig. 5). From the vertically-looking Dopplers, this is done by measuring the difference in scan times between the top and bottom of a precipitation core (or the vertically-oriented fall paths of larger hydrometeors from a cumulus). For 915 MHz profiles, a storm is always moving toward the stationary instrument and the slope can be easily measured. For EDOP, knowledge of aircraft motion is required, while for TRMM, three-dimensional cubes of PR data are used to evaluate the slopes.
- Using UW-NMS storm motion vector components and the precipitation fall slopes, evaluate line-normal wind v_{LN}, taking into account how far the precipitation falls due to storm motion alone.
- Evaluate the actual u' and v' winds from v_{LN} and storm motion vector components.

Clearly, estimating w, and more importantly w', presents one large challenge from each data type, as it did for early researchers of CMT using aircraft measurements (see LeMone et al. 1983; Zipser et al. 1981). This is especially true for TRMM PR. Using the UW-NMS model results as truth, we find that simply assuming $w = \sqrt{2CAPE}$, where CAPE is the convective available potential energy (Emanuel 1994), overestimates the vertical motions for this Florida convection by a factor of two. Disdrometer and EDOP velocity information provides a much better "first guess" estimate of w. If we assume that $w \approx w'$, as it should be for the deepest updrafts (which transport the most momentum), a reasonable estimate of the eddy flux terms ($u'w'$) and ($v'w'$) should be attainable when TRMM PR measurements are used alone in this processing. Relationships between rain and ice particle sizes and environmental winds, developed from the ground- and aircraft-based radar systems, will be used to convert TRMM PR data into useful information to draft velocities.

5 ANALYSIS RESULTS

Employing the analysis procedure outlines above with Disdrometer radar, first CMT results are becoming available. Compared to the budgets of Fig. 4, our results are able to estimate the sign and relative magnitudes of

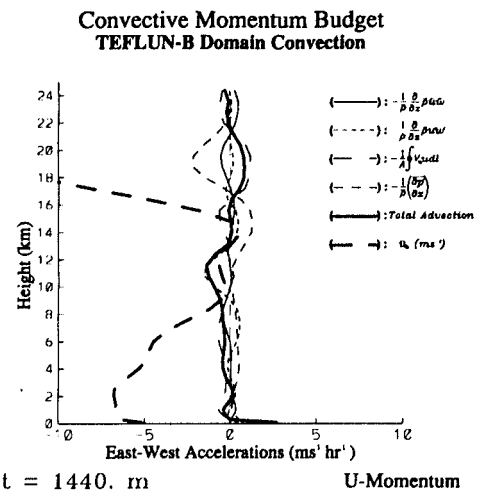

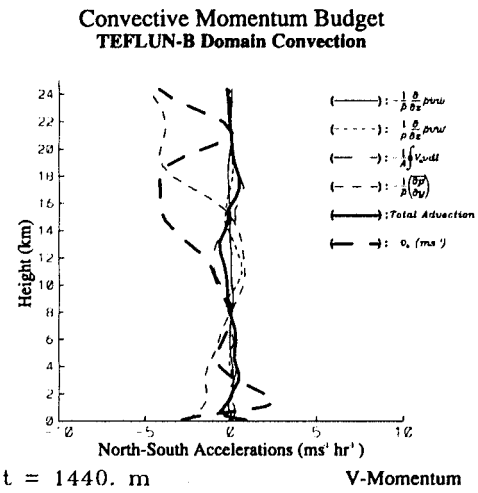

Figure 4: The zonal (top) and meridional (bottom) momentum budgets for convection occurring over east-central Florida at 0000 UTC 22 August 1998 during TEFLUN-B. Budget terms are as in Eq. 1 as in text.

the CMT flux terms $\partial(\overline{u'w'})/\partial z$ and $\partial(\overline{v'w'})/\partial z$. These are exciting results, but much checking and assessment is currently being done to verify our analysis preocedure. The more fully scrutinized results will be presented at the conference.

Given our preliminary work, ongoing work is the construction of a CMT parameterization which relies on TRMM PR radar data as much as possible, while incorporating atmospheric data from model analysis fields (e.g., ECMWF). As a way of corroborating the radar-CMT estimated fluxes, we will very soon begin processing geostationary satellite-derived winds as available at CIMSS. Using these data, our algorithms will provide better estimate of CMT fluxes at the cumulonimbus cloud top level. This is an important level for obtaining these information considering that CMTs tend to maximize near the tropopause in many mature convective systems. We hope to expand our analyses to begin processing QuickSat surface winds for oceanic convection. These information will aid in the assessment of downdrafts as they impinge on the water surface.

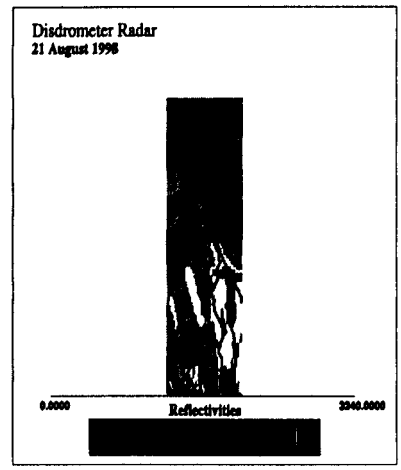

Figure 5: Results (vertical black lines) of an automated algorithms to tag the highest reflectivity cores within profiling and aircraft-based radars (the Disdrometer and EDOP), for use with TRMM PR. These data are presented as a time–height cross section. See text for discussion on how these information are used.

This research is supported by NASA TRMM Grant NAG5-9673.

6 BIBLIOGRAPHY

Emanuel, K. A. 1994: *Atmospheric Convection.* Oxford University Press, 580 pp.

Gage, K. S., C. R. Williams, P. E. Johnston, W. L. Ecklund, R. Cifelli, A. Tokay, and D. A. Carter, 2000: Doppler radar profilers as calibration tools for scanning radars. *J. Appl. Meteor.*, **39**, 2209–2222.

Heymsfield, G. M., B. Geerts, and L. Tian, 2000: TRMM preciptation radar reflectivity profiles as compared with high-resolution airborne and ground-based radar measurements. *J. Appl. Meteor.*, **39**, 2080–2102.

LeMone, M. A. and D. P. Jorgensen 1991: Precipitation and kinematic structure of an oceanic convective system. Part II: Momentum transport and generation. *Mon. Wea. Rev.*, **119**, 2638–2653.

Mecikalski, J. R., and G. J. Tripoli, 2001: The influence of upper tropospheric inertial stability on the cumulus transport of momentum. In Press. *Quart. J. Roy. Meteor. Soc.*

Spilhaus, A. F., 1948: Drop size, intensity and radar echo of rain. *J. Meteorol.*, **5**, 161–164.

Zipser, E. J., R. J. Meitin, and M. A. LeMone, 1981: Mesoscale motion field associated with a slowly moving GATE convective band. *J. Atmos. Sci.*, **38**, 1725–1750.

P5.48

COMPARISON OF INSTANTANEOUS TMI AND PR RAINFALL DATA FROM THE TRMM SATELLITE

John Stout*
George Mason University
Center for Earth Observing and Space Research
Fairfax, VA 20330

Robert Meneghini
NASA/Goddard Space Flight Center
Greenbelt, MD

Abstract – **Results are presented from analysis of the Tropical Rainfall Measuring Mission (TRMM) data from the perspective of comparisons of precipitation retrievals between instruments. The instruments specific to this study are the Precipitation Radar (PR) and the TRMM Microwave Imager (TMI).**

1. Introduction

The joint U.S./Japanese Tropical Rainfall Measuring Mission (TRMM) satellite was launched from Tanegashima Island, Japan on November 27, 1997 for the purpose of gaining insight into tropical precipitation processes. The satellite includes two microwave precipitation sensors: the TRMM Microwave Imager (TMI) and the Precipitation Radar (PR). The TMI is an enhanced version of the SSM/I passive microwave radiometer. In contrast, the PR is an active microwave sensor which provides profiling information. An in-depth discussion on the specifics of the complete TRMM sensor package can be found in Kummerow et al. (1998). The work presented here focuses exclusively on the microwave instruments.

Data from the TRMM satellite is processed at the TRMM Science Data and Information System (TSDIS) using retrieval algorithms provided by the Joint TRMM Science Team consisting of U.S. and Japanese scientists and the National Space Development Agency of Japan (NASDA). TRMM data is processed through a series of levels creating data products that are passed on to the National Aeronautics and Space Administration (NASA) Goddard Distributed Active Archive Center (GDAAC) for public distribution. Periodically, the entire set of mission data is reprocessed with improved algorithms. Version 5 data are currently being produced.

Data products are created from the level 0 (raw binary packets) through level 3 (temporal and spatial rainfall averages). Level 1 data consist of geolocated, instantaneous field of view (IFOV) sensor measurements such as brightness temperatures (TMI) or reflectivity (PR). Level 2 data consist of retrievals of physical parameters, such as rainfall rate, at IFOVs similar to level 1. Level 2 rainfall products are very large; a single orbit of level 2 PR rainfall data is 257MB in size. The storage needed to access a large amount of this instantaneous data is typically not available to individual researchers. The TSDIS algorithm testing system allows for the online storage of several months of level 2 TRMM data. This allows the analysis of the instantaneous data over long periods of time and the ability to generate statistics not found in the standard TRMM level 3 products.

One of the roles performed by TSDIS is the analysis of the TRMM algorithms in cooperation with the TRMM science team. In an attempt to verify the standard TRMM algorithms and instruments, TSDIS has conducted several simple statistical studies. For example, comparisons of PR and TMI rainfall retrievals provide some insight into the strengths and weaknesses of the respective algorithms and instruments. Note the distinction here between these consistency studies and traditional validation, which assumes an independent, more trusted, data set. This paper presents results from some of these consistency studies.

2. Method

Investigators (Kummerow et al., 2000) have compared zonal monthly averages of the PR rainfall rate algorithm (PR rain) and the TMI rainfall rate algorithm (TMI rain) to assess their bulk accuracy. (The TRMM IDs of PR rain and TMI rain are 2A25 and 2A12.) In contrast, this work compares 2-dimensional distributions (TMI vs. PR) of instantaneous rainfall rate in order to explore the behaviour of PR rain and TMI rain during August 1998. The influence of surface type is investigated since TMI rain uses a different algorithm for ocean, land, and coast. TMI rain uses a 0.25 × 0.25 degree grid to determine surface type and records this for each pixel in the TMI rain product. The influence of rain type is also investigated since PR rain uses different reflectivity vs. rain (Z-R) relations depending on whether the rain type is stratiform or convective. The rain type used by PR rain is recorded in the PR qualitative product (TRMM ID 2A23).

* Corresponding author address: John E. Stout, GSFC, Code 902, Greenbelt, MD 20771

To make pixel to pixel comparisons, a common set of pixel locations was constructed using two resolutions: fine and coarse. To construct the fine resolution data set, first the 760 km wide TMI swath was reduced to match the 215 km wide PR swath. Second, the ~4 km PR IFOVs were mapped into the TMI rain coordinate system (4.6 km × 13.9 km pixels). PR rain IFOVs were averaged. PR rain type IFOVs were combined using majority rule to decide between stratiform and convective, with ties thrown out. The resulting common set of pixels is at the TMI rain pixel resolution.

To assess the effect of resolution size, a second data set was constructed. This coarse resolution data set was constructed using a larger box size: 5 along track by 13 cross track TMI rain pixels, creating a box 69 km along track and 60 km cross track.

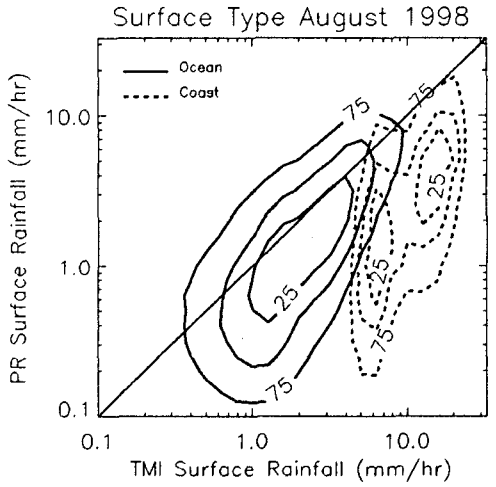

Fig. 1. Joint probability distribution of TMI Surface Rainfall Rate vs. PR Surface Rainfall Rate plotted on a logarithmic scale. Bin size is one decibel of rainfall rate (mm/hr). Contour interval is conditional cumulative probability of 25%. For example, the bins inside the contour labeled 75% contribute 75% of the total rain volume of pixels that are raining in both TMI and PR. Solid contours are ocean pixels at fine resolution (4.6 km × 13.9 km). Dashed contours are coast pixels at fine resolution. Version 5 data were used.

3. Results

The influence of surface type on surface rainfall rate is explored in Fig. 1, which shows two TMI vs. PR distributions. One is the distribution of ocean pixels, which is somewhat oriented along the 1-1 line with a slight majority of pixels having higher TMI than PR rain, in agreement with comparisons of zonal monthly averages (Kummerow, et al., 2000). The other

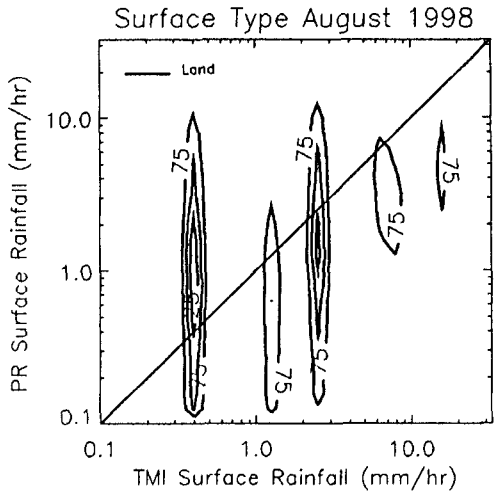

Fig. 2. Same as Fig. 1 except solid contours are land pixels at fine resolution.

distribution, of coast pixels, shows a weak relationship between PR and TMI rain. A large majority of coast pixels have higher TMI than PR rain. In fact, the mean TMI rain was twice as high as the mean PR rain for coast pixels. The TMI coast distribution includes very few rain rates lower than 4 mm/hr and a double peak. The double peak may be due to one peak for stratiform and another for convective conditions (Kummerow, personal communication). There is a large overlap between the ocean and coast PR distributions, but only a small overlap between the ocean and coast TMI distributions. The land distribution (Fig. 2) shows a very weak relationship between TMI and PR rain. In addition, the TMI distribution is strongly quantized, i.e., the TMI land algorithm has a strong preference for specific rainfall rates.

The influence of rain type determined by PR is investigated in Fig. 3, which shows two distributions of surface rainfall rate: stratiform rain pixels and convective rain pixels. To remove the influence of surface type, only ocean pixels were included. The stratiform distribution is somewhat oriented along the 1-1 line, but the convective distribution is well off the 1-1 line. The convective distribution extends into higher rain rates than the stratiform distribution, as expected. Interestingly, stratiform pixels usually have higher TMI rain than PR rain, but convective pixels usually have lower TMI rain than PR rain. In fact, the ratio of the TMI mean rainfall rate over the PR mean rainfall rate is 1.3 for stratiform pixels and 0.62 for convective pixels.

The above results used the fine resolution data set, but a TMI to PR comparison for assessing accuracy would average over a larger box since the observations used to create a TMI rain pixel have footprints as large as 37 km × 63 km (Kummerow et al., 1998). Fig. 4 shows the

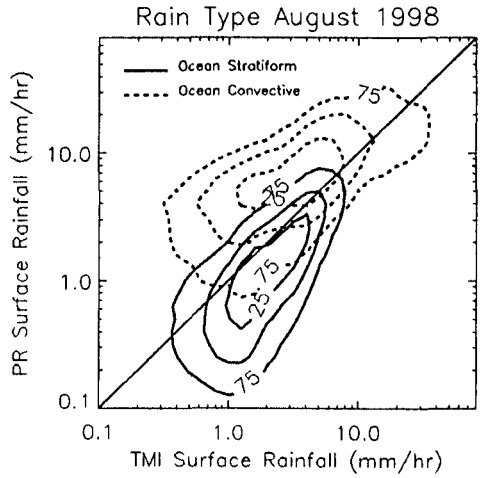

Fig. 3. Same as Fig. 1 except solid contours are ocean stratiform pixels. Dashed contours are ocean convective pixels.

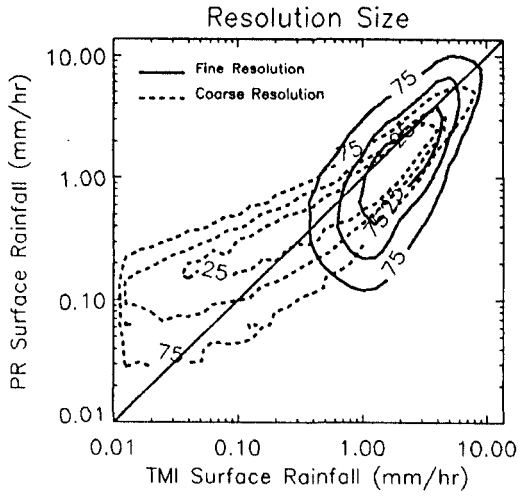

Fig. 4. Same as Fig. 1 except solid contours are ocean pixels at fine resolution (4.6 km x 13.9 km). Dashed contours are ocean pixels at coarse resolution (60 km x 69 km).

influence of resolution size on the TMI to PR comparison. To remove the influence of surface type, only ocean pixels were included. The TMI PR relationship at surface rainfall rates above 1 mm/hr is stronger for the coarse resolution than for the fine resolution. The relationship at lower rain rates is poor for the coarse resolution, but those rain rates contribute little to total rainfall volume. To assess the contribution to total rainfall volume, the product of rainfall rate and frequency for each bin is shown in Fig. 5. The rainfall rate used was the average of the TMI and PR rainfall rates for the joint bin. The correlation between TMI and PR rainfall rates is higher for the coarse resolution than the fine resolution data set.

4. Conclusions

Some of the results of the analysis presented here are being studied for possible improvement of the TRMM production algorithms. These types of statistics are provided by TSDIS as an ongoing effort to improve the TRMM algorithms. As precipitation retrieval algorithms and the instruments themselves become more complex, e.g. a possible Global Precipitation Mission (GPM), the need for simple algorithm consistency studies is expected to continue.

Acknowledgments. The authors thank the members of the TRMM PR science team, J. Awaka, T. Iguchi and T. Kozu and a member of the TRMM TMI science team, C. Kummerow, for providing valuable insight into the TRMM algorithms. We also thank E. Stocker, J. Kwiatkowski, and TSDIS for providing the encouragement and facilities to perform this work.

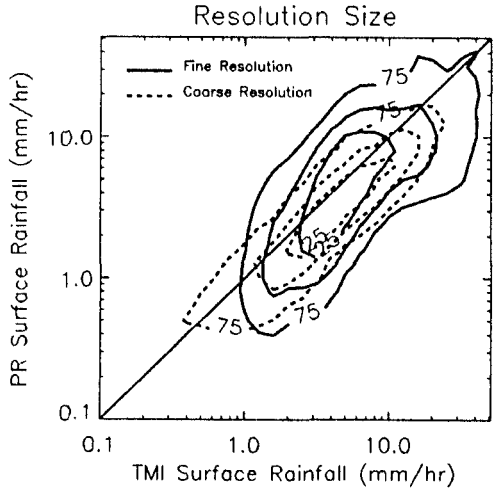

Fig. 5. Same as Fig. 4 except joint distribution of contribution to total rain volume is plotted.

REFERENCES

Kummerow, C., W. Barnes, T. Kozu, J. Shuie, and J. Simpson, 1998: The Tropical Rainfall Measuring Mission (TRMM) Sensor Package. *J. Atmos. Oceanic Technol.*, **15**, 809-817.

Kummerow, C., et al., 2000: The status of the Tropical Rainfall Measuring Mission (TRMM) after Two Years in Orbit. *J. Appl. Meteor.*, **39**, 1965-1982.

P 5.50 EVOLUTION OF THE NOAA/NESDIS SSM/I LAND RAINFALL ALGORITHM INTO THE TRMM AND AMSR ERA

Jeffrey R. McCollum[1,2] * and Ralph R. Ferraro [1]
[1] NOAA/NESDIS Office of Research and Applications, Camp Springs, MD, USA
[2] Cooperative Institute for Climate Studies, University of Maryland, College Park, MD, USA

1. INTRODUCTION

The primary source of microwave satellite data for rainfall estimation from the late 1980's to the late 1990's was the SSM/I data from the Defense Meteorological Satellite Program satellites. At the time of this writing, microwave data were available from additional sensors on board other satellite platforms. Among these are the TMI, launched late 1997, the Advanced Microwave Sounding Unit (AMSU) on board NOAA-K, launched in 1998, and the AMSR-E, scheduled to be launched on board the Earth Observing System (EOS) Aqua satellite in December, 2001. In comparison with the SSM/I, these new sensors have in general better resolution and more channels, which will provide more accuracy for satellite rainfall estimation.

This study focuses on the development of the land components of the instantaneous rainfall rate algorithms for current microwave sensors. The new algorithms use the Goddard Profiling Algorithm (GPROF; Kummerow et al. 1996) and build upon previous versions (Kummerow et al. 2001), accounting for the different frequencies and resolutions of the new microwave data. The development is done using SSM/I and TMI data, as only those data existed at the time of this study, but an algorithm for AMSR-E data is also created.

2. GPROF

The Version 5 TMI 2A12 algorithm (Kummerow et al. 2001) was created to produce rain rate estimates similar to those of the Ferraro and Marks (1995) NOAA/NESDIS algorithm. This was done by selecting from the entire library of cloud model output (~3000-4000 profiles) a profile database for the algorithm comprised of only 30 profiles with the same rainfall rate to 85 GHz vertically-polarized (TB85V) brightness temperature as in the NOAA/NESDIS algorithm. These 30 profiles span the range of possible rain rates. In the algorithm, TB85V is used as the only profile selection criterion, as opposed to matching multiple frequencies as is done for the oceanic estimates. This procedure can be used to force the GPROF to reproduce any relationship between rainfall rate and brightness temperature, as long as the profiles with that relationship can be found in the original cloud model output database and span the range of possible rain rates.

There have been many microwave land rainfall estimation methods that use more sophisticated physics for rainfall rate estimation than the simple rain rate vs. TB85V relationship, but there has been no conclusive evidence to show that any of these algorithms produce better results (Conner and Petty 1998; Ebert et al. 1996). The more simple NOAA/NESDIS algorithm has been used for many years for different weather and climate applications and is considered reliable, so we are continuing to base our operational algorithms on the more well-understood physical principles and make relatively incremental changes to previous versions so that the user community can continue to use our algorithms with confidence and understanding.

3. METHODOLOGY

Prior to 1998, calibration of the rainfall rate (RR) to brightness temperature (TB) relationship was usually done using ground-based radar-rainfall estimates, often calibrated with rain gauges. The main disadvantage of this method is that the fraction of land with well-calibrated radar coverage is low, so biases may result from global application of the ground radar-based relationship. With the launch of TRMM, there has been a continuous record of coincident radar rainfall estimates and microwave TB's covering the tropics available for RR calibration. In addition, these co-located data can be used to calibrate relationships between PR-estimated convective rainfall percentage and microwave convective rainfall predictors.

For each TMI pixel corresponding to a 0.1 grid box of the 3G68Land product, several convective rainfall predictors were extracted and tested for their utility in estimating the convective percentage estimated by the PR. These methods are taken from previous work and are listed here:

(1) Spatial standard deviation (STDEV), as in Grecu and Anagnostou (2001);

(2) Brightness temperature minima as developed by Prabhakara et al. (1999);

(3) Polarization, from Olson et al. (2001)

(4) Brightness temperatures, as in Grecu and Anagnostou (2001)

These parameters were used to develop an empirical equation for the probability of convection, P(C), based on the values of the predictors. P(C) was used to estimate RR as a function of TB85V using the following equation:

$$RR(TB85) = RRconv(TB85V)\ P(C) + RRstrat(TB85V)\ (1\text{-}P(C)) \quad (1)$$

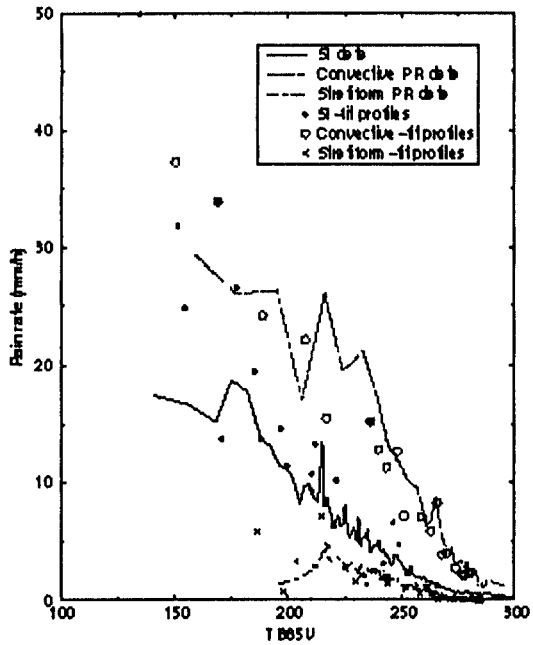

The convective rain rate (RRconv(TB85V)) and the stratiform rain rate (RRstrat(TB85V)) functions were also determined from 3G68Land data. The data were grouped to the nearest integral value of TB85V, and the mean PR RR for each bin was determined for both convective and stratiform classifications. To use the results in the GPROF framework, we found those profiles having similar relationships between RR and TB85V. Figure 1 shows the results. Note the large difference between convective and stratiform RRs for a given TB85V; this is why an estimate of the convective vs. stratiform nature of the rainfall may reduce uncertainty in the RR estimate significantly. Also included are the profiles and data from the Version 5 algorithm, based on the Ferraro and Marks (1995) NOAA/NESDIS scattering index (SI; Grody 1991) algorithm. It is shown later that there is more stratiform than convective rainfall in the data, giving P(C) values less than 0.5, so the rainfall rates are in the vicinity of the Version 5 estimates. Thus, the change from Version 5 to Version 6 will only be significant when the CPI gives enough information for the convective or stratiform RR to be given high weight, and at the high rain rates, which are infrequent and have high uncertainty.

4. RESULTS

The TMI rain estimates from using the new profiles to estimating RR from Eq. (3) were first compared with the PR estimates to check whether the estimates are unbiased with respect to the PR rainfall. The 3G68Land data from Oct. 2000 through Feb. 2001 were used again to compare rainfall estimates. Table 1 shows that for these sample data the new (V6) algorithm is nearly unbiased with respect to the PR.

	Africa (mm/d)	South America(mm/d)
V5	2.01	6.53
V6	1.46	5.11
PR	1.55	5.16

Table 1. Mean daily rainfall estimate for October, 2000 through February, 2001.

The PR rain rate algorithm is still undergoing changes similar to those of the TMI algorithm, so the PR may also be biased globally. The best test of unbiasedness of the TMI algorithm is a long-term comparison with the Global Precipitation Climatology Project (GPCP; Huffman et al. 1997) monthly rainfall product, as this product uses rain gauge data with extensive quality control to reduce the satellite bias over land. It is reasonable to assume that the relationship between RR and TB varies regionally, so it is useful to plot zonal means to observe the variation of bias with climate. Figure 2 displays the zonal rainfall profiles for the three rainfall products.

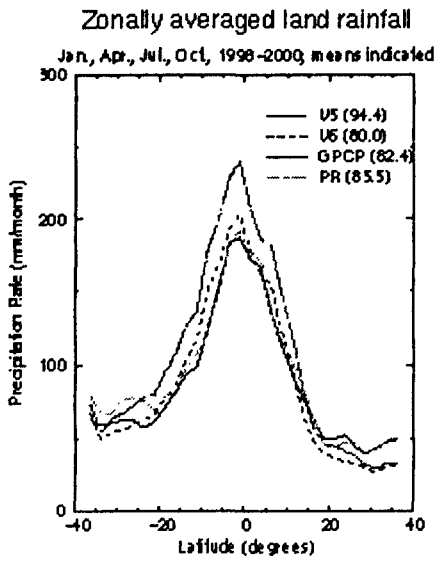

5. APPLICATION TO OTHER SENSORS

We compared TMI and SSM/I from January through May, 2001. We applied the V6 TMI algorithm to SSM/I data and found that the SSM/I monthly rainfall estimates were lower than those from the TMI. There were 2 reasons for this. First, the zonal profiles of estimated P(C) were lower than those from the TMI, presumably due to differences in resolution and spatial sampling pattern between the two sensors. With all other factors the same, this would lead to lower RR's. The index used to estimate P(C) was adjusted by a multiplicative factor using trial and error to match the TMI convective probabilities. However, the rain rates were still low, suggesting another cause of underestimation, so we investigated the resolution difference between the TMI and SSM/I.

The ~ 7 km x 5 km resolution of the TMI is 4 to 5 times smaller than that of the ~12.5 km x 12.5 km SSM/I resolution. From spatial sampling theory, a sampled distribution will be wider (have more variance) when a continuous field (in this case 85 GHz TB's) is sampled at higher resolution. Empirical data (not shown) shows that the distribution of TMI TB's is wider than that of SSM/I, although the difference is so small it isn't obvious whether it has an effect on rainfall estimates. So the values were multiplied by an approximation of the RR corresponding to each TB using the formula:

$$RR = 55 - 0.2\,(TB85V) \qquad (2)$$

taken from Fig. 1. This product approximates the accumulated rainfall contributed by the range of brightness temperatures. The TMI curve (not shown) has about 20% more area, which is equivalent to 20% more accumulated rainfall. Thus, the same RR vs. TB relationship should not be used for both of these sensors with different resolutions.

Rather than attempting to re-calibrate the RR vs. TB relationship for SSM/I, we simply tried increasing the CPI by a higher multiplicative factor, which results in higher rainfall rates. After some trial and error, we found that a 50% increase in the CPI results in a good match of mean rainfall between SSM/I and TMI. The zonal rainfall profiles (not shown) of SSM/I and TMI after the CPI adjustment are quite similar. The F13 SSM/I satellite observes more rainfall due to it's local observing times of approximately 6:30 am and pm, in comparison with the approximate 10:30 am/pm F14 observing times. The same trends in SSM/I and TMI estimated convective probabilities are observed, but the SSM/I probabilities are now higher. Again, these probabilities are estimated for the purposes of more accurate rain rates and while the uncertainty of the quantitative estimated probabilities is assumed to be high, we are not concerned about it.

One other issue concerning the adaptation from TMI to SSM/I is the 85V no-rain threshold. Using the 270K TMI threshold, the SSM/I rain area is lower than the TMI rain area, again due to resolution differences. With it's larger pixel size, the SSM/I can observe low rainfall rates at a higher brightness temperature from the non-raining areas within the pixel. Therefore the no-rain threshold was increased to 280K, which yields an excellent correspondence in the zonal profiles of rain area (not shown).

The AMSR has a similar resolution to the TMI, so the TMI rain rate calibration should be applicable to AMSR. However, the 85 GHz sampling strategy is different, so the convective probabilities may differ. It is difficult to predict whether this will bias the rainfall rate estimates; this will require further study.

6. DISCUSSION

The GPROF framework is being used to incorporate the changes to the new algorithms for a variety of reasons. For several years (1987 - 96), the SSM/I was the only passive microwave sensor that was operating. Beginning with TRMM (1997) and AMSU (1998), we are now in an era with multiple sensors in operation. Hence, the need for a "unified" retrieval algorithm that incorporates the best features of several existing

algorithms, as well as one that is built in a framework that allows for continual enhancements is highly desirable. We have adopted this philosophy and believe that the development of a unified land based retrieval algorithm for use with a variety of passive microwave sensors has several advantages.

First, the same underlying physical assumptions (i.e., hydrometeor profiles, radiative transfer, etc.) are consistent. This allows for a more direct approach for evaluating and ultimately improving the retrieval process. These improvements can all be incorporated via the cloud model database and surface type/climate zone classification in the land retrieval module. The second advantage is that the module will be fully portable to other sensors, and will be suitable for operational/production use. This point cannot be stressed enough, as user friendly code is critical for a 24-hour a day, 7 day a week operation. Experience with SSM/I, TMI, and AMSU shows that even the smallest change to a software module can cause havoc in an operational environment. Finally, the implemented code will be the same for both land and water. This will greatly simplfy the algorithm flow, thus enhancing our confidence that the code will work as intended.

7. SUMMARY AND CONCLUSIONS

A microwave land rainfall algorithm has been created for operational use for the TMI, SSM/I, and AMSR instruments. The major improvement of this algorithm over previous versions is the elimination of the global high bias. This was done using coincident TMI and PR data to derive relationships between RR and TB85V for both convective and stratiform rain. In addition, the PR-estimated convective percentage was used to calibrate the relationship between the probability of convection and microwave predictors of convection. The resulting rainfall estimates compare quite well with GPCP estimates, which are considered as the most unbiased global rainfall estimates.

After slight modifications to account for different resolutions and sampling patterns, the algorithm was applied to SSM/I data to produce similar rain estimates. With the launch of AMSR on the Aqua satellite, we will also be able to test modifications to the algorithm to permit the use of AMSR data. The experience with these three microwave satellites will be carried over to future microwave satellites that are launched in support of the GPM mission so that the data from the different satellites can be merged into a global product made up of unbiased estimates with respect to one another.

REFERENCES

Anagnostou, E.N., and C. Kummerow, 1997: Stratiform and convective classification of rainfall using SSM/I 85-GHz brightness temperature observations. *J. Atmos. Ocean. Tech.*, **14**, 570-575.

Conner, M.D., and G.W. Petty, 1998: Validation and intercomparison of SSM/I rain-rate retrieval methods over the continental United States. *J. Appl. Meteor.*, **37**, 679-700.

Draper N.R., and H. Smith, Applied Regression Analysis, 2nd ed., John Wiley, New York, 1981.

Ebert, E.E., 1996: Results of the 3rd Algorithm Intercomparison Project (AIP-3) of the Global Precipitation Climatology Project (GPCP). BMRC Research Report No. 55, Melbourne, Victoria, Australia.

Ferraro, R.R., and G.F. Marks, 1995: The development of SSM/I rain rate retrieval algorithms using ground based radar measurements. *J. Atmos. Ocean. Tech.*, **12**, 755-770.

Grecu, M., and E.N. Anagnostou, 2001: Overland precipitation estimation from the TRMM passive microwave observations. *J. Appl. Meteor.*, **40**(8), 1367-1380.

Grody, N.C., 1991: Classification of Snow Cover and Precipitation Using the Special Sensor Microwave Imager. *J. Geophys. Res.*, **96**, 7423-7435.

Huffman, G.J., R.F. Adler, P. Arkin, A. Chang, R. Ferraro, A. Gruber, J. Janowiak, A. McNab, B. Rudolf, and U. Schneider, 1997: The Global Precipitation Climatology Product (GPCP) Combined Precipitation Data Set. *Bull. Am. Meteorol. Soc.*, **78**, 5-20.

Kummerow, C., W.S. Olson, and L. Giglio, 1996: A simplified scheme for obtaining precipitation and vertical hydrometeor profiles from passive microwave sensors. *IEEE Trans. on Geosci. and Rem. Sen.*, **34**, 1213-1232.

----------, Y. Hong, W.S. Olson, S. Yang, R.F. Adler, J. McCollum, R. Ferraro, G. Petty, and T.T. Wilheit, 2001: The evolution of the Goddard Profiling Algorithm (GPROF) for rainfall estimation from passive microwave sensors. *J. Appl. Meteor.*, in press.

Olson, W.S., C.D. Kummerow, Y. Hong, and W.K. Tao, 1999: Atmospheric latent heating distributions in the tropics derived from satellite passive microwave radiometer measurements. *J. Appl. Meteor.*, **38**, 633-664.

Prabhakara, C., R. Iacovazzi, Jr., J. A. Weinman, and G. Dalu, 2000: A TRMM microwave radiometer rain rate estimation method with convective and stratiform discrimination, *J. Met. Soc. Japan*, **78**, 241-258.

P5.52 CO AND CH4 COLUMN RETRIEVAL FROM THE SCANNING HIGH RESOLUTION INTERFEROMETER SOUNDER (S-HIS)

Kenneth Vinson*, Henry Revercomb, H. Ben Howell, and Robert Knuteson
Space Science and Engineering Center, University of Wisconsin-Madison, Madison, WI

This study presents a new technique for the retrieval of CO and CH4 column amounts from high spectral resolution Fourier Transform Spectrometer (FTS) data. Results are presented from aircraft flights of the Scanning-High-resolution Interferometer Sounder (S-HIS). Case study results are presented from ER-2 underflights of the Terra satellite over controlled fires during the NASA SAFARI experiment in South Africa.

1. INTRODUCTION

In the ongoing effort to understand the composition, chemistry, and distribution of pollutants in the troposphere, it is important to have accurate measurements of gases such as Carbon Monoxide (CO) and Methane (CH4). Such measurements had been historically isolated and sometimes inaccurate. With the launch of the MOPITT instrument on board the NASA TERRA satellite in December 1999 there is now the potential for global CO and CH4 measurements. To help ensure accuracy of these measurements we have utilized data from an airborne Fourier Transform Spectrometer (FTS) to produce measurements of CO and CH4 optical depth along a flight path over a region of interest. These optical depths were obtained using an algorithm developed at the University of Wisconsin Space Science and Engineering Center (UW-SSEC) and applied to data gathered by the UW-SSEC Scanning HIS instrument (S-HIS) during a field experiment. The SAFARI-2000 mission in South Africa included flight paths coincident with overpasses of the NASA TERRA spacecraft and controlled fires. The MOPITT instrument on board the TERRA spacecraft is specifically designed to measure CO and CH4 column amounts. (Drummond, 1992) The optical depths obtained via the algorithm performed on S-HIS data may therefore be used in the validation of MOPITT CO and CH4 measurements as well as potential products of the NASA AIRS instrument on the EOS Aqua platform.

2. THEORETICAL DEVELOPMENT

In this section we present a treatment of the physical and mathematical aspects of the method used to derive optical depths. The primary assumptions are stated and justified.

The technique to be applied to the observations from the S-HIS instrument is one developed for the NASA SAFARI experiment to map CO distribution from fires.

* Corresponding Author Address: Kenneth H. Vinson, University of Wisconsin, Space Science and Engineering Center, 1225 W. Dayton St., Madison, WI 53706-1612; email: kenneth.vinson@ssec.wisc.edu

The method makes use of high spectral resolution emission lines observed by the S-HIS spectrometer to derive an optical depth using weak absorption lines. It is less sophisticated than a full profile retrieval approach, but is very useful for a survey result of localized events.

A ratio of on-line to off-line emission for selected lines of the gas of interest provides a measure of the gas amount. The selected wavenumbers are displayed in the table below.

Gas	On-line wn's	Off-line wn's
CO	2150.80	2151.77
	2154.667	2153.698
	2158.05	2159.02
	2158.52	2164.80
	2165.29	2166.75
	2165.77	2168.193
	2169.157	2170.126
	2172.54	2173.506
	2173.02	
CH4	1230.0	1230.96
	1240.62	1240.14
	1241.11	1241.59

The form of the equation to be used can easily be derived from a single-layer atmosphere approximation;

$$N_v^{Obs} = t_v \cdot N_v^{Surf} + N_v^{Atm} + t_v \cdot N_v^{\mathrm{Re}\,fl}$$

$$t_v = \exp[-\tau_v] \; and \; \tau = optical\ depth$$

$$Assume: N_v^{\mathrm{Re}\,fl} = 0; N_v^{Atm} = B_v(\overline{T_{Atm}})$$

where N^{Obs} is the S-HIS observed upwelling spectral radiance at an altitude of 20 km, t_v is the atmospheric transmission for wavenumber v, N^{Surf} is the emission from the surface, N^{Atm} is the atmospheric emission, N^{Refl} is the contribution from surface reflection, and B is the Planck emission function at a temperature $\overline{T_A}$ which approximates the mean atmospheric temperature. Neglecting the reflected radiance and substituting for the atmospheric emission leads to:

$$N_v^{Obs} \cong t_v \cdot N_v^{Surf} + B_v(\overline{T_{Atm}})$$

We then rearrange terms and split equation (2) into separate expressions for the on-line and off-line radiance.

$$t_{on} \cdot N_{on}^{Surf} = N_{on}^{Obs} - B_{on}(\overline{T_{Atm}})$$

$$t_{off} \cdot N_{off}^{Surf} = N_{off}^{Obs} - B_{off}(\overline{T_{Atm}})$$

We further assume that the surface emitted radiance is equal for both on-line and off-line spectral channels.

$$Assume: N_{on}^{Surf} = N_{off}^{Surf}$$

We may then divide equations (3) and (4) to obtain a ratio. We then use our earlier expression in equation (1) relating transmission to optical depth and substitute it,

$$Thus:$$

$$\frac{t_{on}}{t_{off}} = \frac{\exp(-\tau_{on})}{\exp(-\tau_{off})} = \frac{N_{on}^{Obs} - B_{on}(\overline{T_{Atm}})}{N_{off}^{Obs} - B_{off}(\overline{T_{Atm}})}$$

Take the natural log of both sides and the resulting expression becomes:

$$\Delta\tau = \tau_{on} - \tau_{off} = -\ln\left[\frac{N_{on}^{Obs} - B_{on}(\overline{T_{Atm}})}{N_{off}^{Obs} - B_{off}(\overline{T_{Atm}})}\right]$$

This result allows us to plot time series of changes in the optical depth of target gases. These results would be vulnerable to any dramatic change in the path distance between the emitter and the detector. The results therefore may be sensitive to conditions of heavy haze or cloud cover. Fortunately, there were also present on the ER-2 during the SAFARI experiment a cloud LIDAR system and an imaging system the MODIS Airborne Simulator (MAS). Data from these instruments were used to find clear sky regions on which to perform analysis of CO and CH4 optical depth.

3. DESCRIPTION OF EQUIPMENT

Scanning HIS Description

The Scanning HIS (S-HIS) is an advanced version of the HIS ER-2 instrument (Smith et al. 1987/89, Revercomb et al. 1988a), developed between 1996 and 1998 with the combined support of the US DOE, NASA, and the NPOESS Integrated Program Office. It has flown in seven field campaigns beginning in 1998 and has proven to be very dependable and effective. The continuous spectral coverage from 3.3 to 16.7 μm at 0.5 cm^{-1} resolution is illustrated in Figure 1 by a sample spectrum from the SAFARI-2000 mission in South Africa. This coverage is divided into three bands with separate detectors (two photoconductive HgCdTe and one InSb) to achieve the required noise performance. The bands use a common field stop to ensure accurate spatial co-alignment. The longwave band provides the primary information for temperature sounding for cloud phase and particle size. The midwave band provides the primary water vapor sounding information and further cloud property information. The shortwave band provides information on cloud reflectance and augments sounding information.

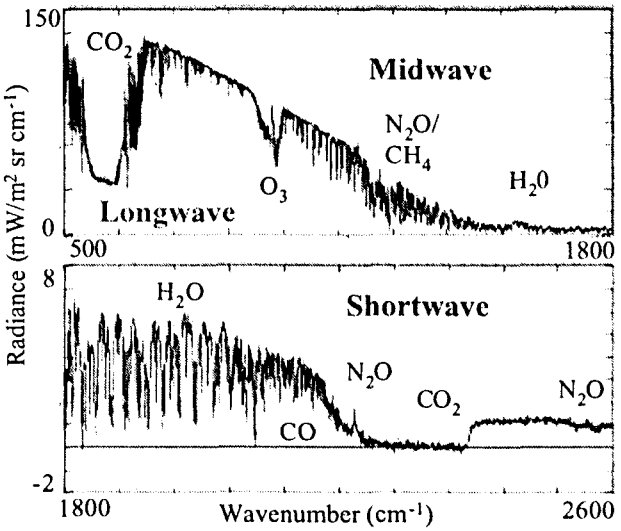

Figure 1. Sample Scanning HIS spectrum from NASA SAFARI-2000 mission. The three different spectral bands are color-coded. There is overlap between the longwave and the midwave band that is useful for diagnostics.

The optical design is very efficient, providing useful signal-to-noise performance from a single 0.5 second dwell time. This allows imaging with 2-3 km resolution to be accomplished by cross-track scanning. Onboard reference blackbodies are viewed as part of each cross-track scan, providing updated calibration information every 20-30 seconds. The rapid sampling frequency of the S-HIS allows cross-track imaging at 2 km resolution with a swath width on the ground of 30-40 km, as illustrated in Figure 2, or a nadir only mode with overlapping fields of view.

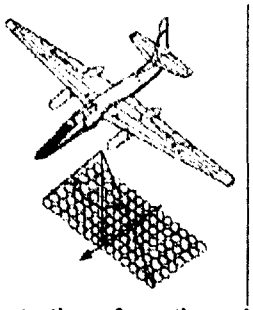

Figure 2. Illustration of swath angle and size subdivided into cells representing individual scans.

4. RESULTS

In this study we used data from several flights during the SAFARI field experiment when the NASA ER-2 was based in Pietersburg, South Africa. We focused our efforts on the flight of 7 September 2000. This was a daylight flight of the ER-2 which included three passes over a controlled fire set by SAFARI personnel. The times for the overpasses are summarized below:

First Overpass (North to South):
08:18:30 UTC to 08:23:36 UTC

Second Overpass (South to North):
08:41:30 UTC to 08:47:28 UTC

Third Overpass (North to South):
09:02:10 UTC to 09:08:30 UTC

The SHIS instrument was in nadir only mode for this flight obtaining a single spectrum from a 2 km field of view every 0.5 seconds along the aircraft flight path. Figure 3 is an image of the ER-2 flight track superimposed on a Meteosat image recorded very near the times of interest.

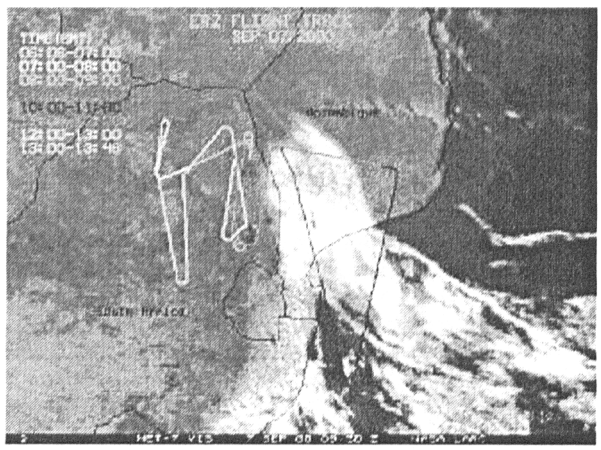

Figure 3. ER-2 flight track over Meteosat image.

It was expected that, as a primary combustion product, an increase in CO column density, and thus optical depth, would be observed during the data period when the ER-2 overflew the fire. The results obtained from our algorithm are consistent with this expectation. A significant peak in the CO optical depth is apparent in the SHIS data in each of the overpasses coincident in time with the controlled fire. This peak is also present in the brightness temperature for the nearby window region. The peak increase of the CO optical depth in the first overpass is ~40% over the background. The peak increase in the second and third overpasses is ~100% over the background level.

A verification of the cloud-free scene apparent in the MAS image of the target area can be observed in the optical depth of methane during the fire overpasses. The methane optical depth was not observed to vary significantly over all three overpasses of the fire site. This uniformity of methane optical depth can also be seen as an indicator that the mean atmospheric temperature assumed in our algorithm is sufficiently constant over the area of interest.

Figure 4 is a MODIS Airborne Simulator (MAS) view of the fire region during the first overpass (north to south). The target fire, with its attendant smoke plume, can be clearly observed near the center of the image. A larger, older burn scar can be seen near the top of the image. The SHIS observation path passes directly down the center of the MAS image. MAS images such as the one in Figure 4 were crucial to identifying the regions of interest present in SHIS SAFARI data.

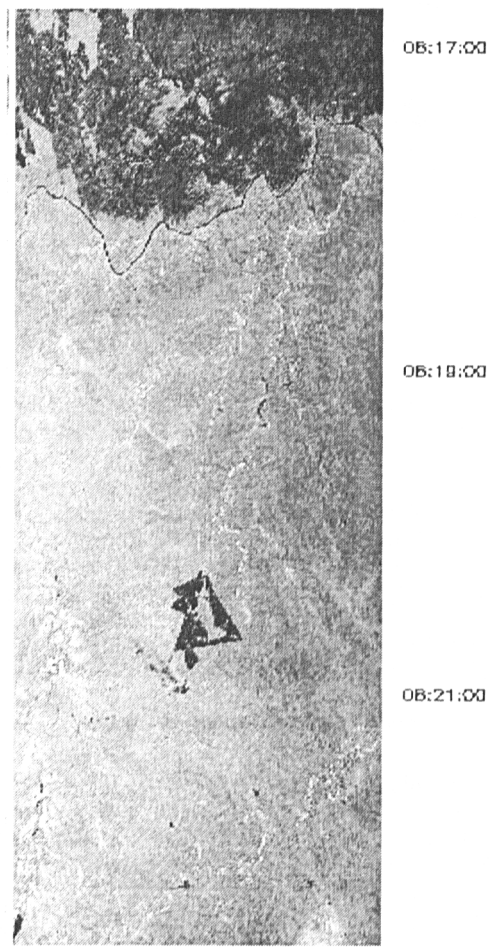

Figure 4. MAS view of fire region.

The results of the optical depth algorithm for CO and CH4 are plotted in Figure 5 with accompanying brightness temperatures for the 4 micron window region. In each of the three optical depth graphs CO is the top line and CH4 is the bottom line.

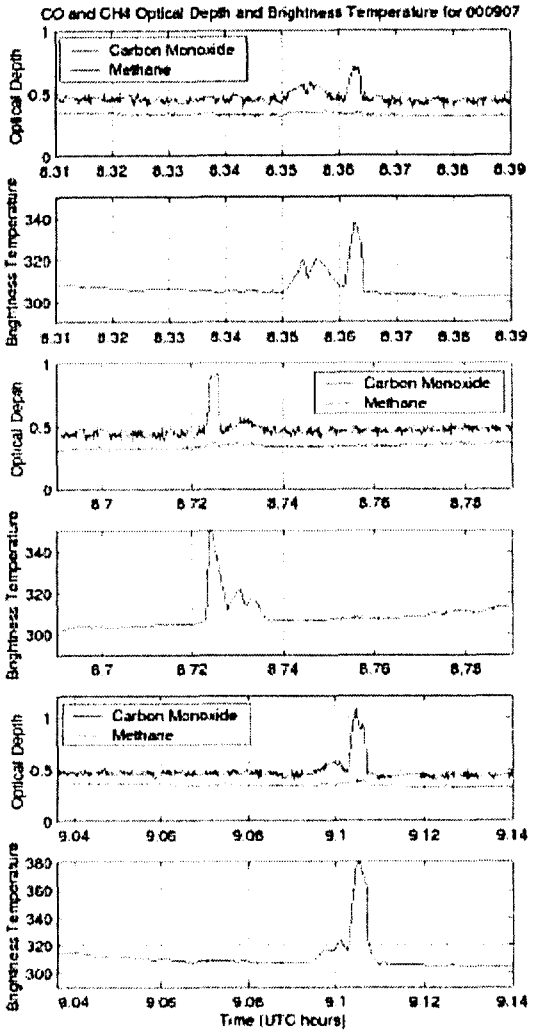

Figure 5. Derived optical depth results from S-HIS for three ER-2 overpasses of a controlled fire on 7 September 2000. Derived Carbon Monoxide and Methane optical depths are compared with the observed brightness temperature from the 4 micron region of S-HIS.

5. SUMMARY

A new technique is presented to derive trace gas column optical depth from high spectral resolution upwelling infrared emission spectra. The technique has been applied to accurately calibrated observations of the University of Wisconsin Scanning HIS instrument. Results have been presented showing a doubling of carbon monoxide optical depth over controlled fires observed by the S-HIS on the NASA ER-2 during the NASA SAFARI experiment. Future work includes validation of this technique and extension of it to the EOS AIRS instrument on the Aqua spacecraft platform.

6. REFERENCES

Drummond, J.R., 1992: Measurements of Pollution in the Troposphere (MOPITT), in *The Use of EOS for Studies of Atmospheric Physics*, J.C. Gille and G. Visconti, Eds., pp. 77-101, North-Holland, Amsterdam (1992)

King, M. D., W. P. Menzel, P. S. Grant, J. S. Myers, G. T. Arnold, S. E. Platnick, L. E. Gumley, S. C. Tsay, C. C. Moeller, M. Fitzgerald, K. S. Brown and F. G. Osterwisch, 1996: Airborne scanning spectrometer for remote sensing of cloud, aerosol, water vapor and surface properties. J. Atmos. Oceanic Technol., 13, 777-794.

McMillan, W.W., Strow, L.L., Smith, W.L., Revercomb, H.E., Huang, 1996: The detection of enhanced carbon monoxide abundances in remotely sensed infrared spectra of a forest fire smoke plume. Geophys. Res. Lett., 23(22):3199-3202.

Revercomb, H.E., D.D. LaPorte, W.L. Smith, H. Buijs, D.G. Murcray, F.J. Murcray, and L.A. Sromovsky, 1988a: High-Altitude Aircraft Measurements of Upwelling IR Radiance: Prelude to FTIR from Geosynchronous Satellite. Mikrochimica Acta [Wien], II, 439-444.

Revercomb, H.E., V.P. Walden, D.C. Tobin, J. Anderson, F.A. Best, N.C. Ciganovich, R.G. Dedecker, T. Dirkx, S.C. Ellington, R.K. Garcia, R. Herbsleb, R.O. Knuteson, D. LaPorte, D. McRae, and M. Werner, 1998: Recent results from two new aircraft-based Fourier transform interferometers: The Scanning High-resolution Interferometer Sounder and the NPOESS Atmospheric Sounder Testbed Interferometer, 8th International Workshop on Atmospheric Science from Space using Fourier Transform Spectrometry (ASSFTS), Toulouse, France, 16-18 November 1998.

Smith, W.L., H.M. Woolf, H.B. Howell, H.-L. Huang, and H.E. Revercomb, 1987/1989: The Simultaneous Retrieval of Atmospheric Temperature and Water Vapor Profiles - Application to Measurements with the High-resolution Interferometer Sounder (HIS). RSRM '87:Advances in Remote Sensing Retrieval Methods, A. Deepak, H. Fleming, J. Theon (Eds.). A. Deepak Publishing, Hampton, Virginia.

P 5.53 The Role of *A Priori* Information in the Retrieval of CO Profiles from Terra-MOPITT Measurements

Shu-peng Ho, John C. Gille, David P. Edwards, Jean-Luc Attie, Merritt N. Deeter, Juying Warner, Gene L. Francis and Daniel Ziskin

National Center for Atmospheric Research, Boulder, Colorado

1. INTRODUCTION

Anthropogenic activities have significant impacts on biogeochemical cycles. To better understand the changes occurring in the atmosphere and to clearly distinguish natural from anthropogenic influences, it is extremely important to monitor the temporal and spatial distributions of gases and identify their sources and sinks. Carbon monoxide (*CO*) is one of the key tropospheric trace species. With roughly a 2 month lifetime, and with diverse sources, both natural and anthropogenic (CH_4 oxidation, *NMHC* oxidation, biomass burning, fossil fuel burning etc.), *CO* can serve as a useful tracer of atmospheric transport. *CO* also affects the concentration of the hydroxyl radical (*OH*), which is involved in much of the chemistry in the troposphere. However, *OH* has an extremely short lifetime and is difficult to measure. Therefore, the ability to continuously monitor CO from space should provide an important window on tropospheric chemistry.

To measure the spatial and temporal variation of the *CO* profile and total column amount in the troposphere, the Measurements of Pollution In The Troposphere (*MOPITT*) instrument was launched in 1999 on board the NASA Terra satellite. *MOPITT* is an eight-channel gas correlation radiometer; each channel generates an average (*A*) signal and a difference (*D*) signal (Drummond, 1992). The *A* signals are sensitive to the background emissions, while the *D* signals are sensitive to the target gas vertical distribution. *MOPITT* measurements can resolve the vertical distribution of tropospheric *CO* in 3-4 layers with a 22X22 km horizontal resolution.

The *MOPITT* operational retrieval is based on the Maximum Likelihood (*ML*) method (Pan et al., 1998; Rodgers, 2000). The *ML* retrieval algorithm seeks the statistically most likely *CO* profile consistent with both the observed radiances and *a priori* information. The role of the *a priori* mean profile and covariance matrix is to constrain the retrieved profile to fall within the range of physically realistic solutions (based on variability statistics of a selected set of observed in-situ profiles). The relative weighting of the *a priori* information and information from the measured radiances in the retrieved profile is controlled directly by the *a priori* covariance matrix and measurement error covariance matrix.

The operational *MOPITT CO* retrieval currently uses a fixed global *a priori*. This approach was adopted initially to ensure that observed geographical variations in the retrieval results are due to information in the measured radiances rather than features of the *a priori*. Studies (Hansen et al.,1995; Pan, et al., 1998) have confirmed that the choice of *a priori* affects the accuracy of the retrievals. There is some question as to whether the use of a global *a priori* is an adequate representation of the seasonal variation in the *CO* profiles for diverse locations. Furthermore, only limited regional surface observations and aircraft measurements from field experiments are available for the construction of the *MOPITT* global *a priori*. The purpose of this paper is to quantify the sensitivity of the retrieval to the use of a fixed global *a priori* in the *ML* method. We conduct simulation experiments to explore the impact of using a fixed global *a priori* on the *MOPITT CO* retrievals. This is further illustrated using an alternative criterion to dynamically choose an *a priori* error covariance matrix (the *DAP* method) which constrains the *CO* retrievals using primarily measurement errors. The method will be described in section 2. The simulated *CO* profiles retrieved from the *DAP* method are compared to *CO* profiles retrieved from the *ML* method in section 3.

Corresponding author address : Dr. Shu-Peng Ho, Atmospheric Chemistry Division, NCAR, PO BOX 3000 Boulder, Colorado, 80307-3000.
E-mail address: spho@ucar.edu, Tel: (303)497-2922

2. DATA and the DYNAMIC *A PRIORI* Method

MOPITT has four *CO* thermal channels, two *CO* solar reflectance channels and two CH_4 solar reflectance channels. Characteristics of the *MOPITT* channels are described in Drummond (1992). The radiative transfer equation (RTE) for the upwelling *MOPITT A* and *D* signals for each channel is described in Pan et al., (1998). The *MOPITT* transmittance model (Edwards, et al., 1999) is used in this study to simulate *MOPITT* radiances while the mixing ratio of target and interfering gases, viewing geometry, vertical thermal profiles and surface emissivity and temperature are

used as inputs. If the measurement errors can be described approximately by a Gaussian distribution, then a regularized estimate of the state vector *X* (*CO* vertical profile, surface skin temperature and emissivity) is given by the minimizer of the penalty function (O'Sullivan and Wahba 1985; Wahba, 1990):

$$J(X)=\{Y^m-F(X)\}^T E^{-1}\{Y^m-F(X)\}+(X-X^b)^T C_\gamma^{-1}(X-X^b) \quad (1)$$

In Eq. (1), Y^m is a vector of *MOPITT* radiances, X^b is the initial guess profile; *F(X)* is the radiative transfer model described in Pan et al., (1998); *E* is the expected covariance matrix of measurement errors and the forward model errors; C_γ is the first guess expected error covariance matrix used to constrain the solution, and is defined as γ^*C where *C* is the *a priori* error covariance matrix for *CO* profiles, surface skin temperature and emissivity. *C* is generated from *CO* profiles collected from field campaigns (see Section 3), while γ is a smoothing parameter, which balances the fit to the observations (first term in Eq. (1)) and the fit to the *a priori* (the second term in Eq. (1)). In the case of the *ML* method, the *C* is a statistical constraint based on other measurements and does not vary. This is equivalent to setting γ equal to unity.

Since the *RTE* is nonlinear, the optimal state parameters must be found iteratively. The Newtonian nonlinear iteration method (O'Sullivan and Wahba, 1985) is applied here such that

$$X_{n+1}=X_0+C_{\gamma n}K_n^T(K_nC_{\gamma n}K_n^T+E)^{-1}\{\delta Y_n^m+K_n(X_n-X_0)\} \quad (2)$$

where δY_n^m indicates the differences between the observed and calculated radiances, X_0 (=X^b) is a vector of the first guess state profile generated from the mean of all *CO* profiles, and *K* is the weighting function matrix defined by $\partial Y = K\partial X$. The normalized radiance residual is defined as

$$R_{n+1}=\left(\frac{1}{nch}\sum_{k=1}^{nch}\{Y_k^m-F_k(X_{n+1})\}^2/\mathrm{var}_k\right)^{1/2} \quad (3)$$

where *k* is an index of channel number, *nch* is the total number of channels used in the retrieval, and var_k is the diagonal term of the error covariance matrix *E*, which is specified from differences between calculated and measured radiances. In each iteration, the discrepancy principle (Morozov, 1966) provides smoothing parameters so that the residual norms are close to *a priori* upper bounds for the *A* and *D* signals respectively. The *a priori* upper bound for *A* or *D* signals is defined as

$$\sigma = \left(\frac{1}{nch}\sum_{k=1}^{nch}\eta_k^2/\mathrm{var}_k\right)^{1/2} \quad (4)$$

where η^2_k is the square of the instrument noise plus the square of the forward model errors in channel *k*. The error is assumed to be random for each channel. Here the measurement noise is known from the calibration. The forward model error is assumed to be 2% of the instrument noise for each channel for the determination of σ. If $R_{n+1} > \sigma$, then the solution is assumed to be over-constrained, and γ will be increased for the next iteration. If $R_{n+1} < \sigma$, then the solution is assumed to be under-constrained, and γ will be decreased. For each iterative step, a value of γ for A signals and a value of γ for D signals are determined. The iteration stops when the absolute value of the difference between R_{n+1} and σ is less than a reasonable small number, assumed to be 0.05σ. However, because the *CO* vertical distribution may not be completely resolved by *MOPITT*, retrieval results may not meet the required criterion after several iterations. In this case, the solution having the smallest difference between R_{n+1} and σ is selected. The retrieval results with R_{n+1} larger than 0.5σ are discarded. The initial value of γ, γ_0, is taken as 10. By using this method, reasonable γ can be found, and the retrieved *CO* profiles and total column will be an inverse solution of the radiative transfer equation in the sense of minimizing the penalty function. In summary, in *ML*, we assume *C* is known completely and is held constant in the retrieval. In *DAP*, *C* is allowed to vary but the forward model and instrument noise become the constraint.

3. RETRIEVAL RESULTS

To show how different *a priori* background covariance matrices affect the retrieval results, simulated retrieval experiments have been conducted. A total of 525 *CO* profiles with ancillary temperature and water vapor vertical distributions were collected from 10 different geophysical locations for varied seasons (Wang, et al., 1999). The *CO* profiles with odd index numbers are separated from those with even index numbers. The 263 *CO* profiles with odd index number are used as a training set and the other 262 *CO* profiles are used as a test set. The *a priori* covariance matrix (*C*) is generated from the training set. The square roots of the diagonal terms of *C* for the training set are shown in Fig. 1. In real *MOPITT* retrievals, because of various limitations of the training set profiles (poor representation of some geographical areas and

seasonal variability, etc.) this *a priori* matrix cannot be assumed to perfectly represent global *CO* variability. In this study, *CO* profiles measured from Carr, Colorado and during the Pacific Exploratory Mission in the Western Pacific Region (PEMWEST) phase B (Wu, et al., 1997) are used to generate alternative *a priori* matrices (*CARR C* and *PEM-B C*). As shown in Fig.1,

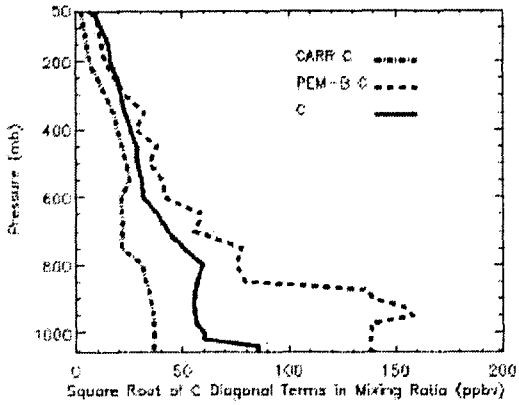

Fig. 1. The square roots of the diagonal terms of CO vertical profiles for a priori covariance matrices C, CARR C and PEM-B C.

the *CO* variations for different vertical levels over Carr (*CARR C*) is less than those for *PEM-B* and is used to represent the model *CO* ensemble or local observed *CO* ensemble. The *a priori* matrix, *PEM-B C*, is used to represent cases of over-estimated background errors for both the *ML* and *DAP* algorithms. In these studies, the *ML* a priori mean profile is held constant.

The retrieval results for all three *a priori* matrices for both *ML* and *DAP* methods are shown in Figs. 2(a) and 2(b) respectively. For all retrieval experiments, the instrument noises for the *A* and *D* signals and forward model error are randomly added to the forward calculated *MOPITT* radiances. The mean of the training set is used as the initial profile for all retrievals. Because the *CO* profiles are divided into the testing set and the training set, the STD of the *CO* training set (Fig. 1) could quantify the *CO* variations for different vertical levels for the testing set (not shown). Under the condition that the measurement errors and the *a priori* distribution are well known and are well-represented by a Gaussian distribution, the *ML* method will provide the best estimates of the state parameters (*ML* with *C* cases) by minimizing the penalty function (Wahba, 1985) (Fig. 2). However, in real global *MOPITT* retrievals, this detailed knowledge of the background error covariance matrix may not be available. Some retrieval results may be under-constrained by the *a priori* matrix like *PEM-B C* (over-represented cases). Some retrieval results may be

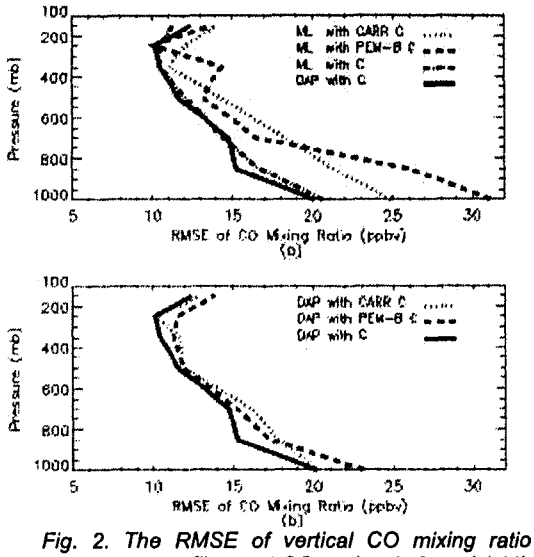

Fig. 2. The RMSE of vertical CO mixing ratio between the true profiles and CO retrievals from (a) ML method and (b) DAP method by using C, CARR C and PEM-B C as the a priori covariance matrices.

over-constrained by the *a priori* matrix like *CARR C* (under-represented cases), where a small *a priori* matrix (smaller standard deviation) will decrease the relative magnitude between KCK^T and E in Eq. (2) and the *CO* retrieval will be more tightly constrained by the *a priori*. The *RMSE* (Root Mean Square of Errors) of all *CO* profiles, and the *RMS* (Root Mean Square) values of true fractional CO column error for *ML* with *PEM-B C*, *ML* with *CARR C*, *ML* with *C* and *DAP* with *C* are listed in Table 1.

	ML with PEM-B	ML with CARR C	ML with C	DAP with C
RMSE all CO levels (ppbv)	18.8004	16.3173	13.7083	13.6843
RMSE of true fractional CO column error (%)	6.8	6.18	4.72	4.71

Table 1. RMSE (Root Mean Square of Errors) of all CO profiles and the RMS (Root Mean Square) values of true fractional CO column error for ML with PEM-B C, ML with CARR C, ML with C and DAP with C cases.

On the other hand, *CO* profiles retrieved with the *DAP* method are less affected by a pre-chosen *a priori* covariance matrix (Fig. 2(b)) than those retrieved

from the *ML* method. In the *DAP CO* retrieval, the relative magnitude between KCK^T and E in Eq. (2) is dynamically adjusted to satisfy the criteria mentioned in Section 2 according to the initial profile (X_0), the instrument and forward model noises (E), the vertical resolution of *MOPITT* measurements (K), the estimated background error (C) and the true *CO* profile. The γ found from the smallest difference between radiance residuals (defined in Eq. (3)) and *a priori* upper bound (defined in Eq. (4)) (Fig. 3(b)) can provide reasonably good *CO* retrievals (Fig. 3(a)). However, to be useful practically in an operational sense, the *DAP* method would require greater characterization of the measurement errors (both radiance noise and forward model) than is currently available for the *MOPITT* instrument.

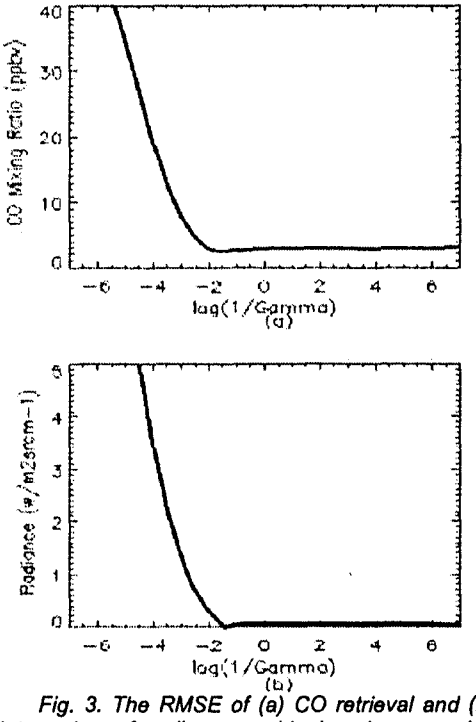

Fig. 3. The RMSE of (a) CO retrieval and (b) absolute value of radiance residuals minus a priori upper bound (abs(R-ô)) changed with different γ value for D signal.

4. CONCLUDING REMARKS

The role of the *a priori* covariance matrix in the retrieval algorithm is to provide extra background information about the retrieval parameters, to constrain the retrieval results by truncating the instrument errors and forward model errors from the measurement information, and to stabilize the matrix inversion. Our studies show that *ML* retrievals produce the smallest retrieval errors when the simulation profiles are statistically consistent with the selected *a priori* matrix. When processing *MOPITT* real operational data by using the *ML* method, however, the fixed covariance generated from limited regional surface observations and aircraft measurements from field experiments may not be optimum. Compared with the *ML*, retrievals from the *DAP* method are less affected by the pre-chosen *a priori* covariance matrix. However, this method requires good characterization of the measurement error. In the future, when *MOPITT* processing has stabilized and we better understand the measurements and associated error sources, work will begin on the implementation of a variable *a priori* that depends on location and season. This will be tested thoroughly with data from validation sites and field campaigns.

5. REFERENCE

Edwards, D. P., C. Halvorson, and J. C. Gille., 1999: Radiative transfer modeling for the EOS Terra satellite Measurement of Pollution in the Troposphere (MOPITT) Instrument, *J. Geophys. Res.* **104**, 16755-16775.

Hansen, P. C. 1995, Rank-deficient and discrete ill-posed problems, Ph. D. dissertation. Technical University of Denmark.

Morozov, V. A., 1966: On the solution of functional equation by the method of regularization, *Sovit Math.* Dokaldy, **7**, 414-417.

O'Sullivan, F., G. Wahba 1985 : A cross validated Baysian retrieval algorithm for non-linear remote sensing, *J. Comput. Physics.* **59**, 441-455.

Pan, L., J. C. Gille, D. P. Edwards, P.L. Bailey, and C. D. Rodgers, 1998: Retrieval of tropospheric Carbon Monoxide for the MOPITT Experiment, *J. Geophys. Res.*, **103**, 32277-32290.

Rodgers, Clive 2000: Inverse Methods for Atmospheric Sounding : Theory and Practice. World Scientific.

Wahba, G. 1985: A comparison of GCV and GML for choosing the smoothing parameter in the generalized spline smoothing problem, *Ann. Statist.* **13**, 1378-1402

Wahba, G. 1990 : Spline Models for Observational Data, SIAM. CBMS-NSF Regional Conference Series in Applied Mathematics, V. 59.

Wang, Jinxue, Deeter, M., Gille, J. Bailey, P. Retrieval of Tropospheric Carbon Monoxide Profiles from MOPITT: Algorithm Description and Retrieval Simulation. SPIE 44-th Annual Meeting, 18-23, 1999, Denver, Colorado

Wu, Z., R. E. Newell, Y. Zhu, B. E. Anderson, E. V. Browell, G. L. Gregory, G. W. Sachse, J. E. Collins Jr. Atmospheric Layers Measured from the NASA DC-8 during PEM-West B and Comparison with PEM-West A. *J. Geophys. Res.*, **102**, 28353-28365.

P5.55 APPLICATION OF MODIS DATA FOR DERIVING OCEAN SURFACE CURRENTS

R.L. Bernstein* and K.S. Prasad
SeaSpace Corporation, Poway, CA 92064

1. INTRODUCTION

Geostationary satellite imaging sensors have been used for over 25 years to derive atmospheric wind vectors, based on the displacement of visible and/or thermal infrared features in time-sequential imagery. Typically, a two- or three-image sequence, separated by 30 minutes, using 5-km resolution sensor data, is the basic input. If the sensor data is perfectly earth-located, the "least count" of this process is 5000 m / 1800 s or approximately 3 m/s, and this determines the limiting accuracy of the derived wind speeds and direction.

In principle, a similar approach for deriving ocean surface currents could be employed, using for example NOAA, polar orbiting satellites AVHRR sensor. Attempts to infer near-surface current velocities from sequential CZCS images have been made using techniques similar to the feature tracking described for AVHRR data. When examining time series of SST images, it is tempting to assume that feature displacement is an estimate of surface water velocity. The most basic approach is to identify common features between successive images and estimate velocity from the horizontal displacement. Similar techniques were employed to develop velocity maps over the Oyashio Front (Vastano and Borders, 1984). Emery et al. (1986) adapt techniques used in satellite registration, cloud motion detection, and ice motion to develop an objective method for feature tracking. Displacement velocities derived from AVHRR and CZCS images compared well with coincident drifter velocities (Svejkovsky, 1988). La Violette (1990) uses similar methods for estimating surface velocities for the Alboran Sea. While a number of published papers have described results from such an approach, in practice it has seen limited operational usage, for a variety of reasons including: restriction of thermal infrared (sea surface temperature) features; earth-location inaccuracies in AVHRR due to spacecraft attitude uncertainties; six-hour time separation between overpasses, which increases likelihood of cloud cover moving over features that were successfully imaged in the first overpass, thus eliminating the required minimum two-image time sequence.

The advent of the MODIS sensor, now flying on the NASA EOS Terra satellite (overpass time 10:30 AM/PM), and also on its sister satellite Aqua, scheduled for launch in late 2001 (overpass time 1:30 AM/PM), opens up new opportunities to apply the displacement technique for deriving ocean currents. MODIS has both thermal infrared and ocean color channels. In addition, the Oceansat-1 OCM and Orbview-2 SeaWiFS ocean color sensors provides data at local noon, exactly midway between Terra and Aqua.

The earth location accuracy of MODIS is better than 200 m, i.e. considerably smaller than the 1000 m resolution of the ocean color channels of MODIS and SeaWiFS. The "least count" for surface currents using these sensor inputs is determined by the sensor spatial resolution and the time separation. Focusing for the moment only on Terra/Aqua, which will be separated by three hours (10,000 s), the least count will be 1000 m / 10 000 or 0.1 m/s (10 cm/s). This should be sufficient for determining surface flow of major ocean currents with useful accuracy.

In this paper we show an example of surface currents derived from a sequence of MODIS and OCM chlorophyll imagery from the Gulf of California.

*Corresponding author address: R. L. Bernstein, SeaSpace Corporation, 12120 Kear Place, Poway, CA 92064; e-mail: rbernstein@seaspace.com

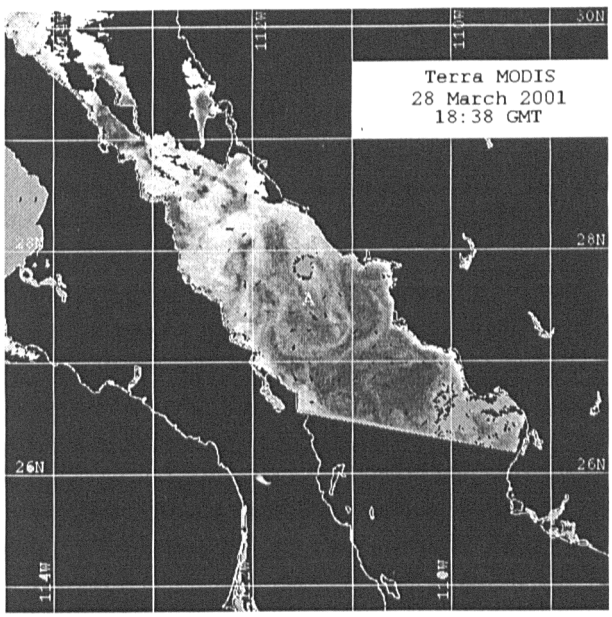

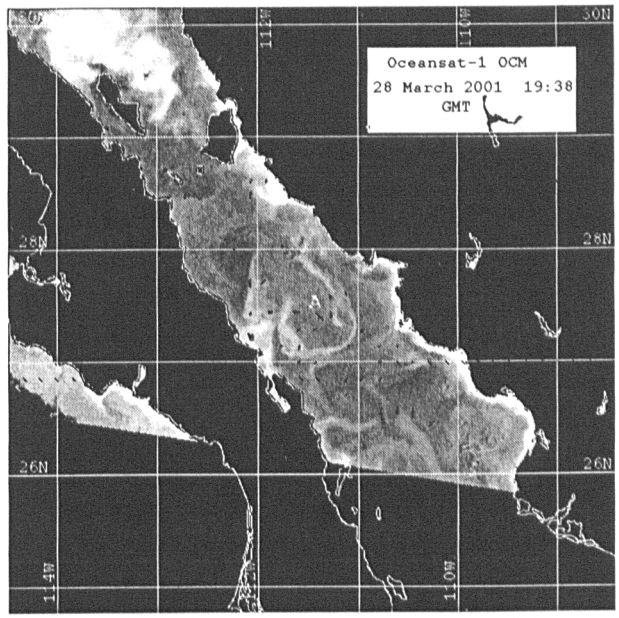

2. METHODS

2.1 Satellite image pairs

We used a pair of satellite overpasses acquired over San Diego, California on 28 March, 2001 for demonstrating our feature displacement technique. The first overpass was Terra MODIS at 18:38 GMT and the second image for the time sequence was Oceansat-1 OCM at 19:38 GMT. These images had a time seperation of approximately 3600 s. TeraScan image processing software was employed to acquire and process all data sets. Both images were processed to level 2 ocean chlorophyll using standard SeaWiFS-type atmospheric correction algorithms. Details of level 0 to level 2 processing of MODIS data can be found in the extended abstract P1.18 (Prasad and Bernstein, same volume).

Both the water-leaving radiance at 443 nm and the chlorophyll concentration provide good ocean features for tracking currents. Because the MODIS sensor has no tilt mechanism in the along track direction, data in the reflective bands often get obscured by sun glint. This is evident in the ocean chlorophyll image generated from MODIS where data is masked in the area covering 29 to 30 N of the Gulf of California. However, there were strong circulation features in both the OCM and MODIS images in the Southern part of the Gulf that were useful for our feature displacement study.

The selected images from OCM and MODIS were accurately earth-located and remapped to a rectangular map projection. A Terascan function *imcorr* was employed for automated generation of vectors from the images. The function essentially correlates neighborhoods from the *reference* image (Fig. 2 OCM image) with slightly larger corresponding neighborhoods in the *search* image (Fig.1 MODIS image) and saves the offset vectors. The values that are automatically computed from the two images were *latitude, longitude* of the reference image, *latitude + delta-latitude, longitude + delta-longitude* position of the search image. If the *reference* image is older than the *search* image, the vectors thus generated indicate motion. Correlation strengths for the vectors are also computed as part of the output.

3. RESULTS

The vectors generated due to displacement of features between the reference and search image are shown in black on both images. The OCM image was displayed using TeraVision, a visualization tool for displaying terascan data sets. TeraVision has tools to accurately compute the distance and bearing between any two points in an image. Maximum correlation strength was obtained from vector "A" which showed a displacement of 6500 m. The feature marked A was displaced from 27 25.75 N 111 24.22 W to 27 23.16 N 111 22.28 W (bearing 151.367 deg). As discussed earlier, the OCM and MODIS images were separated by 3600 s and a

6500 m displacement was computed by *imcorr*. This translates approximately to a 55 cm/s velcocity of the displaced ocean chlorophyll feature due to surface currents in that region. This study demonstrates that this approach does provide useful levels of surface current mapping capability, when flow speeds are in excess of 50 cm/s. The availability of SeaWiFS, OCM, MODIS, Terra/Aqua will provide an additional factor of improvement in the "least count"; additionally, as is also the case with geostationary winds, a three-image sequence will permit significantly better quality control checks on displacement-derived surface currents.

4. REFERENCES

Emery, W.J., A.C. Thomas, M.J. Collins, W.R. Crawford and D.L. Mackas. 1986: An objective method for computing advective surface velocities from sequential infrared satellite images. *J. Geophys. Res.*, **91,** 12,865-12878.

La Violette, P.E., J. Tintore and J. Font. 1990: The surface circulation of the Balearic Sea. *J. Geophys. Res.*, **95,** 1559-1568.

Svejkovsky, J. 1988: Sea surface flow estimation from advanced very high resolution radiometer and coastal zone color scanner imagery: a verification study. *J. Geophys. Res.*, **93,** 6735-6743.

Vastano, A.C., and S.E. Borders. 1984: Sea Surface motion over an anticyclonic eddy on the Oyashio front. *Remote Sens. Environ.*, **16,** 87-90.

P5.56 STATISTICAL CHARACTERISTICS OF QUIKSCAT "REAL-TIME" OCEAN SURFACE WIND VECTOR RETRIEVALS

William H. Gemmill
NOAA/National Weather Service/NCEP/Environmental Modeling Center

1. INTRODUCTION

QuikSCAT was launched in June 1999 with a SeaWinds Ku-band scatterometer on board and ocean surface wind vector retrievals from it became available in "real-time" (within three hours of observation) for operational use during February 2000, at NCEP.

It is a customary practice at NCEP to evaluate the timeliness of availability and the quality of every new data set before using them in operational models. The specification criteria for satellite ocean surface wind retrievals require that the RMS speed errors should be less than 2 m/s for winds up to 20 m/s and no more than 10% for wind speeds above 20 m/s. The RMS errors for direction should be less than 20 degrees, The design of QuikSCAT's antenna system is different from the ones used for previous scatterometers. It uses two antennas at different look angles to scan the ocean surface. The radar design suggests that there are three regions of the swath where the accuracy may deteriorate; two regions are located along the outer 200km edges of the swath where only one scanning antenna can retrieve measurements, and the third region is near nadir where the viewing angles are small, suggesting that wind direction may be less accurate.

It is well known that the backscatter in the Ku-band will be affected by atmospheric attenuation due to rain and cloud liquid water as well as being subjected to distortions at the ocean surface due to rain. In addition, the wind retrievals suffer from the well-known directional ambiguity problem because the inversion process from backscatter measurements to wind vector is not unique and may provide up to 4 vector solutions which are ranked in order of their Most Likelihood Estimate (MLE). But the MLE is not always adequate to select the "best" wind retrieval. The procedure applied to reduce errors in determining the "best" wind vector was to use the 6-hour forecast from NCEP's global forecast model. The closest of the first two MLE solutions to the forecast wind field is selected as the "nudged" solution. The nudged solutions are used to initialize a 7X7 median filter which is applied at each QuikSCAT cell to provide for consistency in the wind vector retrievals over the swath.

This poster presents the statistical results of the evaluations carried out during the Spring of 2001 to determine the quality of QuikSCAT data. Two types of evaluations have been carried out; 1) collocated fixed buoy wind data with "real-time" QuikSCAT wind retrievals from 2001/03/06 to 2001/04/30. Collocation in time is within +/- 3hours and in space within 50km. and 2) ocean model surface wind field analyses (from NCEP's global data assimilation system) matched with QuikSCAT swath data from 2001/03/06 to 2001/04/11. Collocation in time is +/- 1.5 hours.

2. FIXED BUOY COMPARISON STATISTICS

From the scatter diagrams of buoy data vs QuikSCAT data (excluding the edge data), it can be observed that the data do not meet specifications (figure 1). The overall statistics seem to suggest that data are close to the specifications with an RMS speed difference of 2.13 m/s and directional RMS of 25.0 degrees. But, there are many satellite retrieved wind speed outliers that are much higher than the buoy data. In an attempt to improve the quality of the retrievals only those retrieval with a probability of rain flag set to 0, were examined. A probability of rain flag (Huddleston and Stiles, 2000) is included as part of the retrieval data. There was a substantial improvement of the wind speeds for these data, but there did not appear to be much difference in the wind direction. Unfortunately, the process also eliminated many of the high wind cases. To determine the influence of rain contamination on the retrievals, only those retrievals with a probability of rain greater than 10% were compared (excluding the outer edges).

*Corresponding author's address:
William Gemmill, Ocean Modeling Branch, NOAA/NWS/NCEP/EMC, 5200 Auth Road, Rm 207, Camp Springs, MD 20746.

*OMB Contribution No. 203

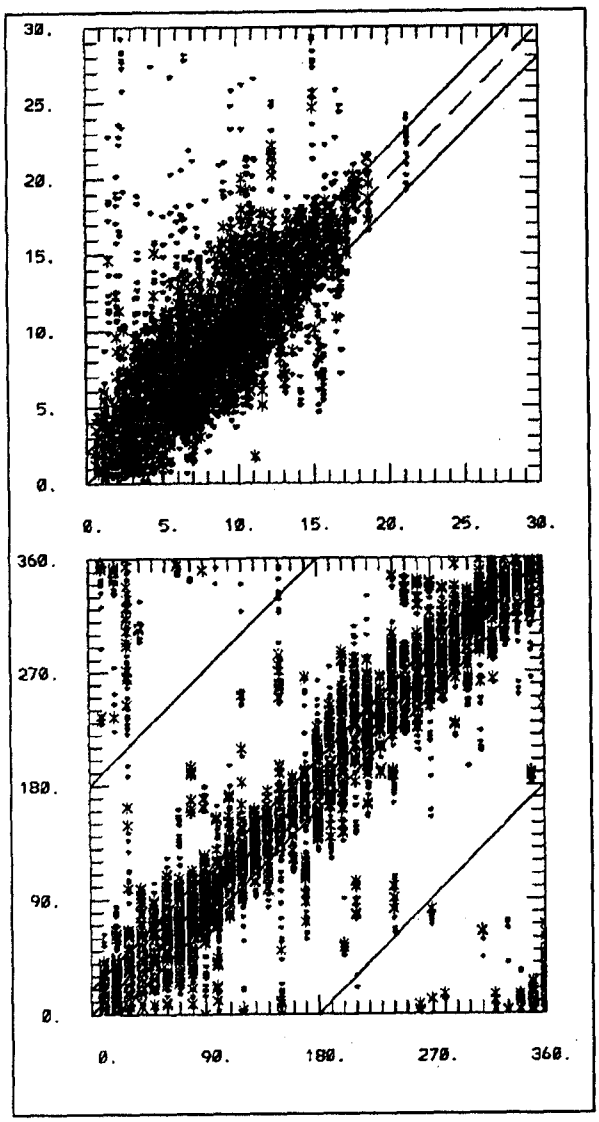

Figure 1. Scatter plots for buoy (horizontal) vs QuikSCAT (vertical) speeds (m/s) (top panel) and directions (degrees) (bottom panel) for all data.

PR	0.0	0.0<0.1	> 0.10	ALL
SPEED BIAS	0.21	0.76	3.98	0.50
SPEED RMS	1.53	2.02	6.71	2.13
DIREC-TION RMS	23.4	25.8	40.1	25.0

Table 1. QuikSCAT vs buoy collocated match-up errors by probability of rain (PR) category. With speed in m/s and direction in degrees. Bias = QuikSCAT - buoy.

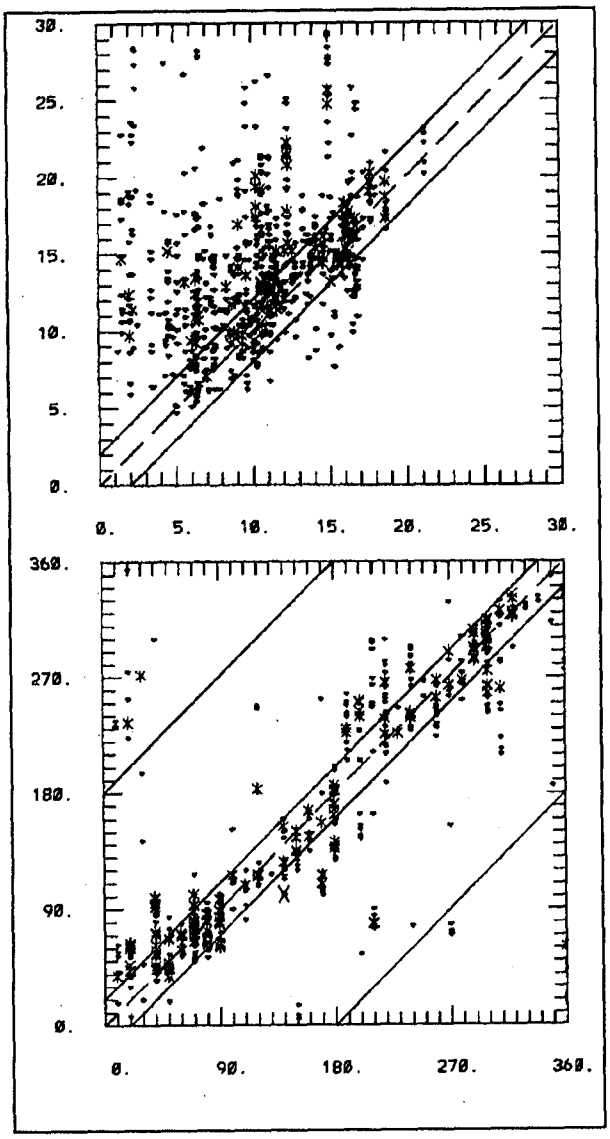

Figure 2. Scatter plots for bouy (horizontal) vs QuikSCAT (vertical) speeds (m/s) (top panel) and directions (degrees) (bottom panel) for data with probability of rain > 10%.

It is clear from figure 2 that the impact of rain on the retrievals is large on both speed and direction (figure 2). The results of rain on the accuracy of wind retrievals are summarized in Table 1.

3. MODEL ANALYSES COMPARISON STATISTICS

This part of the evaluation is designed to determine the sensitivity of errors across the swath due to cell location.

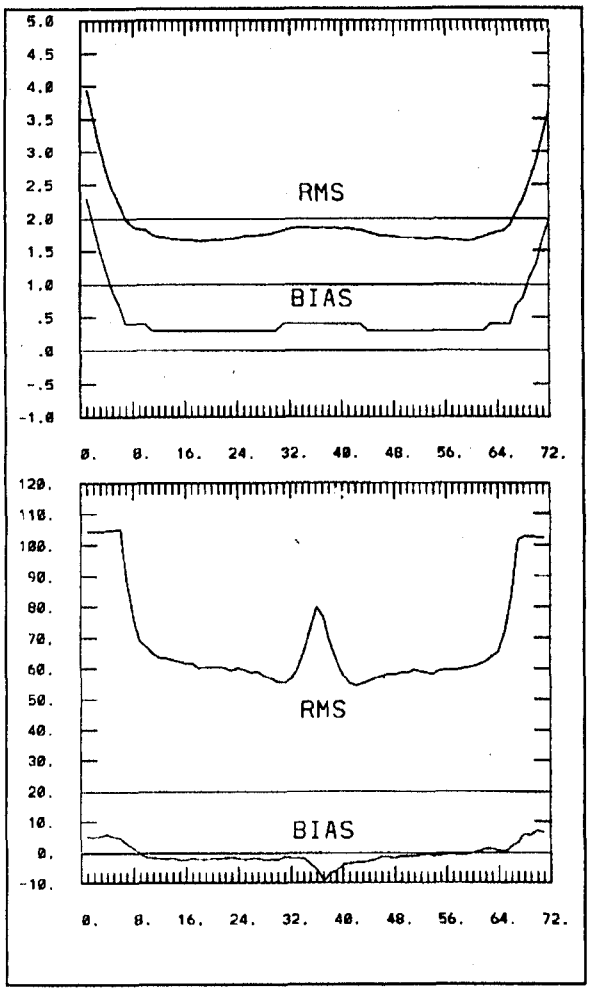

Figure 3. Graph of differences between QuikSCAT swath vs interpolated global model analysis (vertical) and cell number (across) for speed (m/s) (top panel) and direction (degrees) (bottom panel) for all data based the MLE selection.

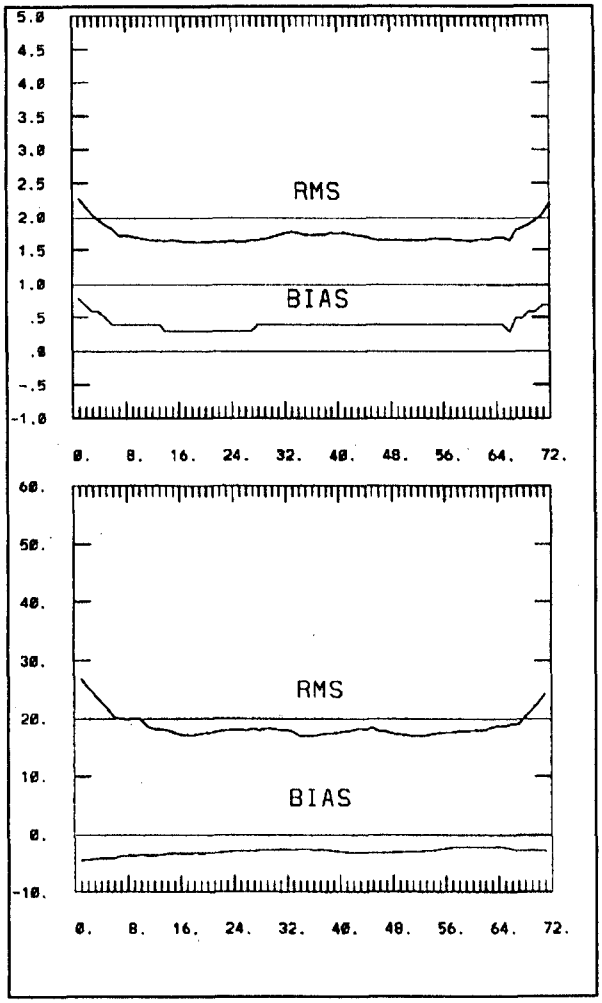

Figure 4. Graph of differences between QuikSCAT swaths vs interpolated global model analysis (vertical) and cell number (across) for speed (m/s) (top panel) and direction (degrees) (bottom panel) for data based the nudged and filtered selection.

A comparison of the MLE wind vector selections across the entire swath with the surface wind vectors from the NCEP's Global Model shows that the speed accuracy deteriorates on the outer edges where only one antenna scans, and near nadir, although the values are still close to the 2 m/s specification. But the MLE is incapable of selecting "good" directions anywhere across the swath (figure 3).

The comparison of the "nudged and filtered selected wind vector s shows there is a dramatic improvement in the wind speeds along the edge although the interior part of the swath is nearly the same (figure 4). The speeds now meet the specification across most of the swath. But, the "nudged" direction solution shows the most significant improvement across the entire swath. The directions meet specifications across the swath except for the deterioration along the edges.

Comparisons were made to determine whether or not there was an impact of rain on the vector retrievals

When the probability of rain assigned to the wind retrieval is zero, the wind speed differences are remarkably constant (rms 1.4 m/s) across the

swath. The directional differences were not quite as good (RMS 20 degrees), and poorest near the edges.

Since rain contamination causes problems with the retrievals, a comparison was made with those winds whose retrievals were assigned a probability of rain greater than 10% (figure 5) These retrievals definitely show that there are serious problems with rain contamination. The speed RMS differences across the swath were 3.8 m/s, and the satellite wind speeds were bias by 2.4 m/s. The directional RMS across the swath was near 20 degrees.

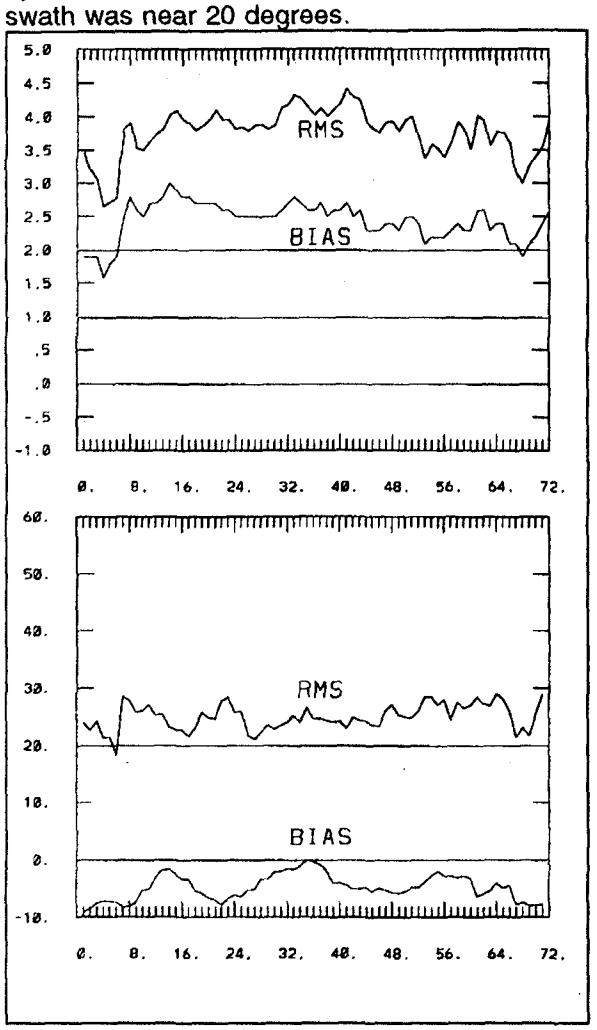

Figure 5. Graph of differences between QuikSCAT swath vs interpolated global model analysis (vertical) and cell number (across) for speed (m/s) (top panel) and direction (degrees) (bottom panel) for data, excluding edges, based on the nudged and filtered selections with a probability of rain greater than 10%.

Wind retrievals were compared with rain probabilities between 0.0 and 0.1, to complete the examination. There is a deterioration of wind speeds but the wind directions are slightly better than the probability of rain of 0.0 cases.

PR	0.0	0 < 0.1	> 0.1	ALL	MLE
SPEED BIAS	-.02	0.85	2.44	0.41	0.50
SPEED RMS	1.42	1.94	3,.78	1.75	2.01
DIREC-TION RMS	19.7	17.3	25.1	18.9	71.1

Table 2. QuikSCAT vs model analyses collocated match-up errors by probability of rain (PR) category, including MLE estimates. With speed in m/s and direction in degrees. Bias = QuikSCAT - analysis.

4. CONCLUSIONS

The above evaluations suggest that the comparison of QuikSCAT data to model analyses (without QuikSCAT data) was better than to buoys. But there are several differences in the data used as "ground" truth, and the space and time windows employed.

Based on these evaluations, the following conclusions can be made: QuikSCAT ocean surface wind vector data meet the accuracy specifications only if retrievals are eliminated for cells along the outer 200km edges of the swath and for cells with a rain probability of greater than 10%.

But, unfortunately, nudging and filtering may remove too much independent information and force the retrieved winds to be too similar to the model wind. Rain contamination often occurs in wind retrievals in weather active regions (storms and fronts), so that reliable retrievals are often not available where they are needed most.

REFERENCES:

Huddleston, J.M., and B.W. Stiles, 2000: Multidimensional Histogram (MUHD) Overlay, Products Description. Ver. 1, Jet Prop. Lab., Cal Inst. Tech, 4p.

Kenneth Holmlund
EUMETSAT, Darmstadt. Germany

1. INTRODUCTION

The European geostationary satellite Meteosat will within roughly a year be replaced by Meteosat Second Generation (MSG). The key Meteosat products that are also derived with MSG are the Atmospheric Motion Vector (AMV) field products. MSG will provide imagery data every 15-min. over the visible portion of the Earth with a sampling distance of 3 km enabling an improvement in the quality of the derived vectors. Furthermore MSG will observe the atmosphere in several spectral bands, amongst others two water vapor absorption channels at 6.3 and 7.2 μm and a CO_2 absorption channel. These channels will for the first time operationally enable the application of the IR/WV and IR/CO_2 ratioing methodologies simultaneously, thus providing more accurate estimates of the cloud heights. Further new channels like the 3.9 μm channel and High Resolution Visible channel at 1 km resolution are expected to improve especially the tracking of low-level clouds.

The new capabilities of MSG have also initiated the development of a new generation of AMV retrieval algorithms. This paper will present the MSG AMV extraction scheme especially high-lighting the changes with respect to the current Meteosat AMV scheme and the expected areas of improvements. Results demonstrating the capabilities of the new AMV retrieval scheme with data from existing geostationary satellites are also presented.

2. THE METEOSAT SECOND GENERATION

Meteosat Second Generation (MSG) is a spin-stabilized satellite in geosynchronous orbit. The spin rate is 100 rpm and with the new SEVIRI instrument the satellite will provide global imagery every 15-min. The sampling distance of SEVIRI is 3 km (1 km for High-resolution visible (HRVIS) data) and the radiometric resolution is 0.25 K. Figure 1 presents the EBBT as observed at the top of the atmosphere for Mid-latitude summer together with the infrared spectral band coverage of the MSG SEVIRI instrument. As a comparison the spectral coverage of the GMS-5 (Geostationary Meteorological Satellite, maintained by the Japan Meteorological Agency), GOES-8 (Geostationary Operational Environmental Satellite, maintained by National Oceanographic and Atmospheric Administration/National Environmental Satellite, Data and Information Service) sounder and GOES-8 imager are included.

Corresponding author address: Kenneth Holmlund, EUMETSAT, Am Kavalleriesand 31, 64295 Darmstadt, Germany; e-mail: holmlund@eumetsat.de.

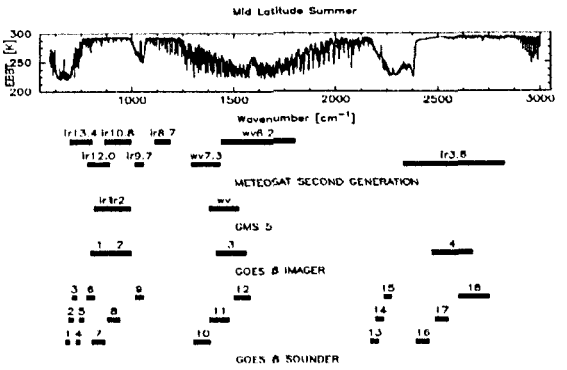

Figure 1. The EBBT as observed at the top of the atmosphere for Mid-latitude summer together with the infrared spectral band coverage of the MSG SEVIRI as well as the GMS-5, GOES-8 sounder and imager.

Table 1 presents the current baseline channels for AMV extraction. The table also incorporates an extended set of channels that are highly likely to provide significant and improved data, but for which there is currently no experience. It is foreseen that the AMV-products derived from these channels are not declared operational at Day-1 (First day of operational dissemination), but at a later stage when a complete validation and assessment of the quality of the derived vectors has been performed.

Table 1. The AMV channels and target type. HLC, MLC and LLC refer to high, medium and low-level clouds, respectively.

Baseline channels:		
Band	Central wavelength	Prime targets
IR	10.8 μm	Clouds
IR	6.2 μm	HLC/Moisture
IR	7.3 μm	HLC/MLC/Moisture
VIS	0.6 μm	LLC over sea
VIS	0.8 μm	LLC over land
Extended channels:		
IR	9.7 μm	Clouds/ozone
IR	3.9 (8.7) μm	LLC at night
HRVIS	0.8 μm	LLC over sea

3. THE ATMOSPHERIC MOTION VECTOR EXTRACTION SCHEME

The Atmospheric Motion Vector (AMV) extraction scheme will in general retrieve the AMVs in a similar fashion to the current operational extraction scheme at EUMETSAT (e.g. Schmetz et. al., 1993, Buhler and Holmlund, 1993). The main components are the following; 1) Target extraction; 2) Image enhancement; 3) Tracking ;4) Height Assignment; 5) Quality control.

In the following sections several examples are presented. These are based on the new AMV extraction scheme, currently employed at EUMETSAT for development and verification purposes. This system is able to digest various kinds of image data and for these examples simulated MSG data has been used. The simulated data is based on calibrated Meteosat-6 IR, WV and VIS data that has been re-sampled to the MSG SEVIRI resolution.

3.1 *Target extraction*

The main major change to the current operational AMV extraction scheme at EUMETSAT is the target extraction. Currently the AMVs are extracted on an equidistant grid (baseline 32*32 pixels) with a target size equivalent to the grid size. In the new scheme the target size and extraction grids are controlled separately. Furthermore the exact location of the target is not fixed and centered at the grid location but optimized in a search area around the grid-location. The main two reasons for this approach are; 1) Better and more stable targets for tracking, e.g. the target area contains at least a certain minimum amount of the clouds at the highest level locally and 2) Avoidance of extraction of targets in multi-layered cloud situations that have proven to be difficult to handle. These conclusions were already indicated by Holmlund (1995) and by the necessity to introduce complex image enhancement procedures (Hoffman, 1990). A variable target extraction scheme is already used operationally at NOAA/NESDIS and has proven to be reliable (e.g. Nieman et. al., 1997). The EUMETSAT target extraction scheme investigates the following features of each location:

- Contrast
- Local standard deviation
- Number of pixels with high local standard deviation
- Entropy
- Cloud configuration
- Land/Sea (water) distribution
- Overlap control

Suitable targets are typically targets that have the highest contrast and largest amount of standard deviation (highest entropy) within the optimization area. Furthermore multilayered cloud situations should be avoided and a minimum amount of cloudy/clear sky pixels are required for respective target type. Coastal regions are avoided in the IR and VIS channel, as the coastal feature might have an impact on the tracking. Finally the overlap between targets is restricted in order to avoid vectors to be derived that contain a large amount of pixels from the same cloud (clear sky feature). This will minimize the impact of correlated errors by reducing the horizontal dependency between neighboring targets. Currently the baseline overlap is limited to 30 %

Figure 2 shows the impact of the variable target extraction. In order to visualize the performance of the location optimization a low-density grid was used. It can be seen in figure 1 that the target locations are preferably extracted along strong gradients in the coldest parts of the satellite imagery data.

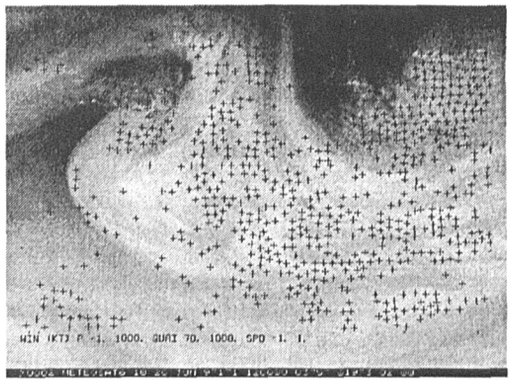

Figure 2. Low-density targets extracted from MSG water vapor data simulated by data from Meteosat-6.

3.2 *Image enhancement*

The image enhancement is equivalent to the current methodologies applied at the Meteorological Product Extraction facility (MPEF) for the current Meteosat-satellites (Schmetz et. al., 1993). The only important difference is the derivation of mean radiances of identified scenes used in the image enhancement. In the current operational scheme the mean radiances are based on a multi-dimensional histogram analysis. For MSG pixels in the target area will be clustered and averaged according to the results from a pixel based multi-channel analysis scheme.

3.3 *Tracking*

The tracking of the targets is generally the task that uses the largest amount of computer resources in any AMV extraction scheme. Therefore several various alternatives have been explored in order to minimize the computational load. Generally the following methodologies have been employed; 1) Use of additional data for first guess estimates of the displacements; 2) In cases where several consecutive vector fields are derived the search area is after the initial matching reduced for any subsequent derivation; 3) Sequential derivation of matching surfaces with full surface calculated only at locations indicated by a low resolution matching surface. The first approach is often relying on NWP data and is therefore not recommended as flow with a large discrepancy to the NWP field might not be derived correctly. The second approach is better introduces however some limitations on the timely variation on the vectors and is implicitly invoking a quality control (by limiting the search area) that preferably is performed at a later stage. The third alternative is generally the most promising and for current satellite data and resolution it has been shown that the results are agreeing up to 97% of a full matching surface. As the available processing capacity has in the past years increased tremendously the

requirement for a limited calculation of matching surfaces has decreased and therefore the calculation of the full matching surface was regarded to be feasible. Three basic matching methods have been implemented 1) Cross-correlation in the time domain, 2) Cross-correlation in the Fourier domain and 3) Sum of Squared Distances. The detailed description of the implementation of these methods is given in Dew and Holmlund (2000). Figure 3 shows an example of a water vapor vector field derived with the current software version using simulated MSG image data.

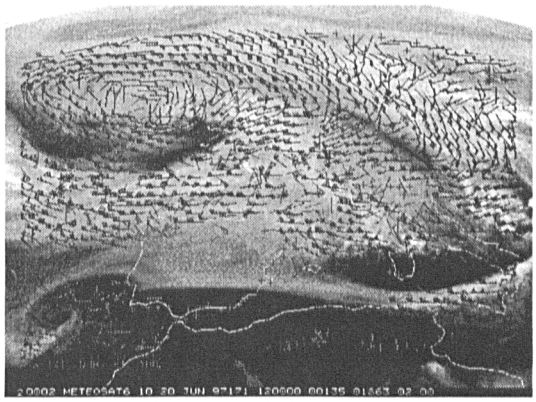

Figure 3. Water vapor vector field with water vapor imagery data from 20 June 1997.

3.4 *Height assignment*

The height assignment of AMVs is currently the most challenging task in the AMV extraction schemes. Broken clouds, multi-layered cloud targets, low level targets (requiring cloud base height assignment) and height assignment of clear sky targets, do all require their special attention. The biggest problems however are generally encountered with semi-transparent clouds.

With the advent of MSG it will for the first time be possible to operationally derive the correct height for semi-transparent clouds using two operationally established methodologies simultaneously; the semi-transparency correction utilizing the WV and IR channel (e.g. Schmetz 1993) and the CO_2-ratioing method (Eyre and Menzel, 1989, Nieman et. al. 1997). Nieman et. al. (1993) showed that for high level clouds the mean pressure difference of the estimated cloud height is of the order of 20 hPa and the RMS difference is ca 80 hPa between the two methods. The implementation of these methods contains the following new features:

- channel dependant noise is included in the calculations
- refined selection of pixels or groups of pixels depending on the characteristics of the pixels and the neighboring pixels
- various possibilities to extract background/surface information (real observations, history of previous observations, forecast, climatology)

Figure 4 presents an example of extracted IR vectors with their respective height over the South Atlantic. The delineation between high (above 400 hPa) (dark gray), medium (between 440 and 700 hPa) (black) and low (below 700 hPa) level vectors (light gray) looks realistic and has been verified against operational heights derived from Meteosat-6 data. It should be noted that as these results are based on simulated MSG data based on the Meteosat-6 IR, WV and VIS data, no CO_2-channel is present and therefore only the semi-transparency correction method has been applied to the thin high level clouds.

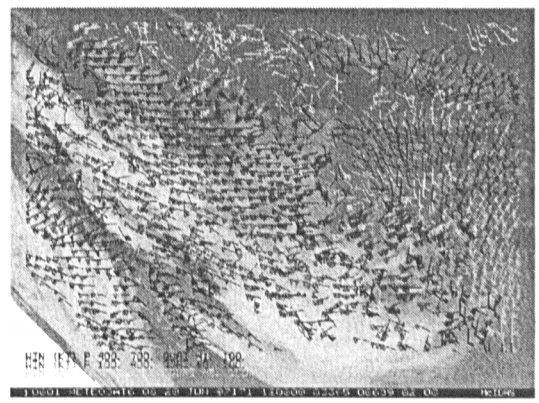

Figure 4. AMVs derived from simulated MSG images over the South Atlantic. The image data has been simulated from Meteosat-6 data from 20 June 1997 1200 GMT. High (above 400 hPa) level vectors are in light gray, medium (between 400 and 700 hPa) level vectors in black and low level (below 700 hPa) vectors in light gray.

3.5 *Automatic quality control*

The automatic quality control is based on the same principals currently used operationally (Holmlund, 1998). The scheme has been further improved with latest experiences with current operational AMVs and the new capabilities provided by MSG. The baseline Automatic Quality Control (AQC) tests are based on:

- local consistency (horizontal)
- speed consistency (in time)
- direction consistency (in time)
- vector consistency (in time)
- background consistency (currently against NWP)
- inter-channel consistency

The extraction cycle of the baseline AMV product consists for MSG of three vector fields. All vector fields contribute to the consistency calculations enabling a better estimation of the vector reliability.

3.6 *Final product*

The AMV fields can be derived continuously, however the current baseline is that a final product should be extracted once every hour. The baseline

product derivation is therefore set up to extract three intermediate AMV fields from four consecutive images during one hour. The targets are extracted from the first image in the sequence and are then followed in time throughout the other three images. The final vector components (speed, direction, height, temperature and quality) are based on a weighted mean of the intermediate vectors. The current baseline is however that the intermediate fields all have the same weight.

4. DEVELOPMENT APPROACH

4.1 *Pre-launch activities*

The development of the MSG MPEF AMV scheme is based on previous experience with the Meteosat-satellites. It further incorporates the knowledge gained at the previous International Winds Workshops (e.g. IWWS 5) as well as information exchange during co-operation amongst the various AMV extraction centers. Finally results from various studies have been incorporated as well as in-house development activities. The development of the operational software has been given to industry and is based a formal Algorithm Specification Document and on in-house prototyping of all essential parts. The performance of the prototype code has been verified with comparisons against not only the operational extraction schemes but also with detailed case studies

4.2 *Post-launch activities*

The main goal for all activities is to ensure that the derived software is capable to produce from the first day of operations products that are at least as good as the current operational products. As MSG incorporates a completely new instrument with new channels and performance the tuning of the configuration parameters will be an essential activity. Therefore it is foreseen that during commissioning of the satellite an early access to image data is granted to the MSG MPEF in order to tune all algorithms (not only the AMV-scheme). The use of real MSG data is also likely to identify possible problems in the software implementation and might also identify some shortcomings in the current baseline methodologies. The MSG MPEF is designed to be modular such that it will be possible to incorporate new software modules or to replace existing modules with improved modules if necessary.

5. CONCLUSIONS

The Atmospheric Motion Vector (AMV) extraction scheme for Meteosat Second Generation (MSG) has been introduced. The new scheme is based on well-established operational algorithms enhanced with new concepts utilizing the foreseen new capabilities of the satellite. It is expected that the AMVs will be extracted in up to 7 image channels, with a target size of 80 km and an extraction grid of 50 km. The vectors will be disseminated hourly over the GTS. With the new capabilities of MSG it is expected that the quality of the AMV-products will improve, especially with respect to height assignment due to the new channels (especially the CO_2-channel). The launch of MSG is currently expected in mid 2001.

6. REFERENCES

Buhler Y. and K. Holmlund, 1993: The CMW Extraction Algorithm for MTP/MPEF. *Proc. Second Int. Winds Workshop*, Tokyo, Japan, 205-217.

Dew, G. and K. Holmlund, 2000: Investigations of Cross-Correlation and Euclidian Distance Target Matching Techniques In the MPEF Environment. *Proc. Fifth Int. Winds Workshop*, Lorne, Australia, EUMETSAT, 235 243.

Eyre J. and P. Menzel, 1989: Retrieval of Cloud Parameters from Satellite Sounder Data: A Simulation Study. *J. Appl. Meteor.*, **28**, 267-275.

Hoffman, J., 1990: The Use of Spatial Coherence Method for Cloud Motion Wind retrieval. *Proc. 8th Meteosat Scientific users Meeting*, Norröping, Sweden, EUMETSAT EUM P 05, 97-100.

Holmlund K., 1995: Half Hourly Wind Data From Satellite Derived Water Vapour Measurements. *Adv. Space Res.*, **16**, (10)59-(10)68.

Holmlund, K, 1998: The Utilization of Statistical Properties of Satellite-Derived Atmospheric Motion Vectors to Derive Quality Indicators. *Wea. Forecasting*, **13**, 1093-1104.

IWWS 5, 2000: *Proc. Fifth Int. Winds Workshop*, Lorne, Australia, EUMETSAT, 298 pp.

Kelly, G., 1993: Numerical experiments using Cloud Motion Winds at ECMWF, *Proc. On Developments in the use of Satellite Data in Numerical Weather Prediction*, Reading, UK, ECMWF, 331-348.

Nieman S. J., Schmetz J. and W. P. Menzel, 1993: A Comparison of Several Techniques to Assign Heights to Cloud Tracers. *J. Appl. Meteor.*, **32**, 1559-1568.

Nieman, S.J., W. P. Menzel, C. M. Hayden, D. Gray, S. T. Wanzong, C. S. Velden, J. Daniels, 1997: Fully Automated Cloud-Drift Winds in NESDIS Operations, *Bull. Amer. Meteor. Soc.*, **78**, 1121-1133.

Schmetz J., K. Holmlund, J. Hoffman, B. Strauss, B. Mason, V. Gärtner, A. Koch and L. van de Berg, 1993: Operational Cloud-Motion Winds from Meteosat Infrared Images. *J. Appl. Meteor.*, **32**, 1206-1225.

P5.59

FURTHER STUDY OF DERIVING SEA SURFACE TEMPERATURE FROM FUTURE GOES

Xiangqian Wu*
Cooperative Institute for Meteorological Satellite Studies
University of Wisconsin, Madison, Wisconsin

Alain Brisson, Pierre Le Borgne, Anne Marsouin
Météo-France, CMS

W. Paul Menzel
NOAA/NESDIS, Madison, Wisconsin

1. Introduction

On July 23, 2001, a new Geostationary Operational Environmental Satellite (GOES-M) was successfully launched into orbit, which will become GOES-12 once commissioned. For the Imager instrument on this and the following GOES satellites, the 12 μm channel has been replaced with a 13.3 μm channel. This poses challenges to both the correction of atmospheric absorption and the detection of clouds that are crucial to deriving sea surface temperature (SST) from GOES Imager. Following previous discussion (Wu and Menzel 2000), we further address these challenges in this poster.

2. Atmospheric Correction

Radiation from sea surface is subject to absorption by the overlaying atmosphere before it reaches a sensor on satellite. To accurately determine SST, the atmospheric absorption must be properly accounted for. Two approaches are often used simultaneously: selecting a spectral channel that is least affected by atmospheric absorption and correcting for the remaining absorption.

GOES Imager provides two "window" channels (at 3.9 and 11 μm) where atmospheric absorption is weak (Menzel and Purdom 1994). The atmosphere is often more transparent at 3.9 μm, however the reflected solar radiation at 3.9 μm is neither negligible nor well predictable. Therefore GOES SST is derived primarily from the 3.9 μm channel at night and from the 11 μm channel during day (Wu et al 1999).

To correct for the remaining atmospheric absorption in either window channels, a third channel is needed, typically at 12 μm, where atmospheric absorption is stronger than that at 11 μm channel (McMillin and Crosby 1984). These combinations of channels, the "split-window" of 11 and 12 μm during day and the "dual-window" of 3.9 and 11 or 12 μm (or "triple-window") at night, have been used successfully for decades to derive SST from satellite measurements (McClain et al 1985).

Without the 12 μm channel on future GOES Imagers, atmospheric correction becomes difficult during day but remains virtually unchanged at night. Current focus is thus to ensure SST production at night from GOES-M and beyond while exploring new ways to retrieve SST during day. A regression algorithm is used to correct for atmospheric absorption. In the past, regression coefficients were derived from collocations of GOES Imager measurements and buoy SST. Alternatively, regression coefficients can also be derived from simulated GOES measurements. Using MODTRAN 3.5 and a set of 402 carefully selected cloud free radiosonde profiles that are representative of the world oceans, two algorithms were derived for GOES-M nighttime SST (see François et al 2001 for more details):

$$\text{(A)}\ SST=(a+bS_\theta)T_{3.9} + (c+dS_\theta)(T_{3.9}-T_{11}) + eS_\theta + f$$
$$\text{(B)}\ SST=(a+bS_\theta)T_{11} + (c+dS_\theta)(T_{3.9}-T_{11}) + eS_\theta + f$$

*Corresponding author: Dr. Xiangqian Wu, CIMSS, 1225 W. Dayton St., Madison, WI 53706. fredw@ssec.wisc.edu

where S_θ = sec(θ)-1, θ is satellite zenith angle, $T_{3.9}$ and T_{11} are brightness temperature in °C for the 3.9 and 11 μm channels, respectively, and coefficients are listed in Table 1. The residuals are 0.37°K for both algorithms, assuming noise of 0.12°K for 11 μm and 0.15°K for 3.9 μm band and error in mixing ratio profile is 1 g/cm^2.

Table 1. Coefficients for algorithms (A) & (B)

Alg.	A	b	C	D	E	F
(A)	1.024	0.008	0.139	0.095	2.239	1.747
(B)	1.024	0.008	1.164	0.103	2.239	1.747

3. Cloud Detection

As nighttime SST retrieval becomes more important for GOES-M and beyond, it is imperative to consider another aspect of nighttime SST retrieval, the detection of clouds.

Most clouds are bright in the visible spectrum, making them easily identifiable during day over the dark ocean as background. At night, thick high clouds stand out in infrared spectrum because they are cold. The emissivity of fog and low strata at 3.9 μm is lower than that at 11 μm so that T_{11}-$T_{3.9}$, normally positive because atmosphere is more transparent at 3.9 μm, becomes negative. Thin cirrus can be detected in two ways: its scattering property can cause large difference between T_{11} and T_{12}, and its 3-D distribution, often highly inhomogeneous, can cause large local variation in radiance. Finally, broken or partially filled cloud scenes are expected to significantly increase the $T_{3.9}$-T_{12} difference because $(dR/dT_b)_{3.9} > (dR/dT_b)_{12}$. Although there are more tests available at night, nighttime cloud detection has always been more difficult.

Without the 12 μm channel, the T_{11}-T_{12} test for thin cirrus can no longer be made. The $T_{3.9}$-T_{12} test for partial/broken cloud can be replaced by a $T_{3.9}$-T_{11} test. Since the varying atmospheric water vapor loading can alter the $T_{3.9}$-T_{11} difference in clear scene, a measure of that loading is needed to establish the threshold for the partial/broken cloud test. Although T_{11} was used by some authors (Saunders and Kriebel 1988 and, more recently, Závody et al 2000), we have been using T_{11}-T_{12} as a measure of total water vapor in an atmospheric column to avoid mistakes in regions where SST is high but atmosphere is relatively dry. Without the 12 μm channel, it will be more difficult to set the threshold properly. Note that the detection of broken/partial clouds at night is complicated anyway, especially for a field of view (FOV) partially filled with strata.

The addition of the 13.3 channel should enhance cloud detection at night. According to the radiative transfer theory, T_{13} for a clear FOV is cooler than T_{11} by about 20K, varying with lapse rate and water vapor profile, because of CO_2 absorption at 13.3 μm. For a cloud contaminated FOV, the T_{11}-T_{13} difference will be reduced, depending on the height, optical thickness, and fractional coverage of the cloud. In the limit, the difference approaches to zero when the FOV is filled with sufficiently high and thick clouds.

We tested this theory with MODIS data that has all the current and future GOES Imager channels (Fig. 1). From an image taken during daytime, we first detect clouds with visible channel as a reference (upper panel). Two experiments follow to detect cloud without the visible channel, one with T_{11} only (middle panel) and one with T_{11} and T_{13} (lower panels). T_{11} alone can detect most of the clouds, but the last few percent of cloudy pixels are the most difficult to identify without losing a lot of clear pixels. In that context, T_{13} is very helpful. The results of using T_{11} and T_{12} are similar to that using T_{11} alone (not shown). We could not use $T_{3.9}$ for this image because of solar contamination. Preliminary results at night suggest that T_{11}-T_{13} is as effective as $T_{3.9}$ for detecting low clouds but more effective for detecting other type of clouds, including the broken/partial clouds. Overall, it seems that for nighttime cloud detection, the 13.3 μm channel is more useful that the 12 μm channel.

4. Summary

The current GOES SST algorithm is reviewed to assess the impact of losing the 12 μm channel from GOES-M and beyond. Although atmospheric correction will be difficult during day, it remains the same at night. Regression coefficients for two nighttime SST retrieval algorithms have been derived from simulated GOES-M measurements. On the other hand, this shifted emphasis on

nighttime SST prompted an examination of nighttime cloud detection since it has been a challenge in nighttime SST retrieval. It was found that the addition of the 13.3 μm channel would be very helpful to ensure high quality of nighttime SST production.

5. References

François, C., A. Brisson, P. Le Borgne, and A. Marsouin, 2001: Definition of a radio-sounding database for sea surface Brightness temperature simulations: Application to SST retrieval algorithm determination. *Rem. Sens. Env.* (Submitted)

McClain, E. P., W. G. Pichel, and C. C. Walton, 1985: Comparative performance of AVHRR-based multichannel sea surface temperatures. *J. Geophys. Res.*, **90**, 11,587-11,601.

McMillin, L. M., and D. S. Crosby, 1984: Theory and validation of the multiple window sea surface temperature technique. *J. Geophys. Res.*, **89**(C3), 3655-3661.

Menzel, W. P., and J. F. W. Purdom, 1994: Introducing GOES-I: The first of a new generation of Geostationary Operational Environmental Satellites. *Bull. Amer. Meteor. Soc.*, **75**, 757-780.

Saunders, R. W., and K. T. Kriebel, 1988: An improved method for detecting clear sky and cloudy radiances from AVHRR data. *Int. J. Rem. Sens.*, **9**, 123-150. Correction: **9**, 1393-1394.

Wu, X., W. P. Menzel, and G. S. Wade, 1999: Estimation of sea surface temperatures using GOES-8/9 radiance measurements. *Bull. Amer. Meteor. Soc.*, **80**, 1127-1138.

Závody, A. M., C. T. Mutlow, and D. T. Llewellyn-Jones, 2000: Cloud clearing over the ocean in the processing of data from the Along-Track Scanning Radiometer (ASTR). *J. Atmos. Oceanic Tech.*, **17**, 595-615.

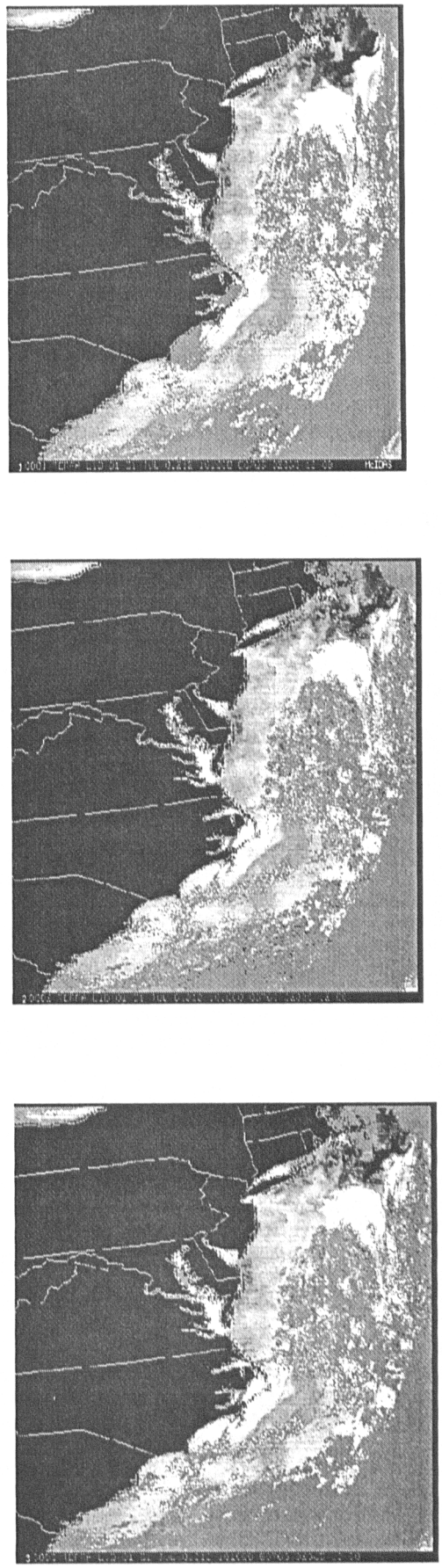

Figure 1: Cloud detection with visible (upper), T_{11} only (middle), and both T_{11} and T_{13} (lower).

P5.60 **INFRARED LAND SURFACE EMISSIVITY RETRIEVAL FROM HIGH-SPECTRAL RESOLUTION UPWELLING RADIANCE**

Robert Knuteson*, Brian Osborne, Henry Revercomb, and David Tobin
Space Science and Engineering Center, University of Wisconsin-Madison

William L. Smith
NASA Langley Research Center, Hampton, VA

This study will presents techniques for the retrieval of infrared land surface temperature and emissivity from high spectral resolution upwelling radiances. Results will be presented from aircraft flights of the Scanning High-resolution Interferometer Sounder (S-HIS) and the NPOESS Atmospheric Sounder Testbed – Interferometer (NAST-I). Case studies will be presented from ER-2 underflights of the Terra satellite at the Southern Great Plains ARM site in Oklahoma and over surface features during the NASA SAFARI experiment based in South Africa.

1. INTRODUCTION

The University of Wisconsin Space Science and Engineering Center (UW-SSEC) is developing techniques for the retrieval of infrared land surface temperature and emissivity from high spectral resolution upwelling radiances. These techniques are being used in support of the validation of the NASA Atmospheric InfraRed Sounder (AIRS) on the Aqua platform, but also have application to future satellite instruments, e.g. the NPOESS Cross-track Infrared Sounder (CrIS) and the Geostationary Infrared Fourier Transform Spectrometer (GIFTS).

Remote sensing of the earth's surface with high spectral resolution data has the potential to allow the separation of land surface skin temperature and emissivity while providing a significantly better atmospheric "correction" than low resolution infrared emission measurements. However, the relatively large field of view of many of the proposed satellite instruments (15 km or more) complicates the validation of the satellite measurements over sites where there is significant sub-pixel variability in land type.

The wide array of state-of-the-art instrumentation at the DOE Southern Great Plains (SGP) Cloud and Radiation Testbed (CART) site makes it a unique facility for the validation of atmospheric sounding products derived from satellite measurements. The site extends across a 250 km square region in Oklahoma and Kansas dominated by rural agricultural land use with significant variability on scales less than 1 km. This paper describes the use of ground-based and aircraft-based observations near the SGP CART central facility to characterize the surface properties important for IR thermal emission at the SGP site. The techniques are also applied to the measurements made in southern Africa during the recent NASA SAFARI experiment.

* corresponding author address: Robert Knuteson, 1225 W. Dayton St., University of Wisconsin-Madison, Madison, WI 53706; robert.knuteson@ssec.wisc.edu.

2. THEORY

The radiative transfer equation used to model the upwelling infrared radiance at the top of the atmosphere under cloud free conditions can be written as

$$N_\nu^{\uparrow} = \int B_\nu(T(P))\,d\tau_\nu + \tau_\nu^{tot} \cdot e_\nu \cdot B_\nu(T_S) + \tau_\nu^{tot} \cdot (1 - e_\nu) \cdot \overline{N}_\nu^{\downarrow} \qquad (1)$$

where N_ν is the upwelling radiance (up arrow) or the downwelling flux (down arrow) at wavenumber ν, B_ν is the Planck radiation distribution function at each atmospheric temperature profile value T(P), τ_ν is the atmospheric transmittance profile, and e_ν is the surface emissivity. The first term of the radiative transfer equation is the contribution of the atmospheric emission to the upwelling radiation. The second term is the contribution of the surface emission transmitted through the total atmospheric column. The third term is the surface reflection term under the approximation of a lambertian surface.

Two limiting cases are useful to consider. When the observer is near the surface the contribution from the atmospheric upwelling emission can be neglected and the total transmittance can be set to unity for all wavelengths. In this case, equation (1) can be written in the form

$$e_\nu = \frac{N_\nu^{\uparrow} - \overline{N}_\nu^{\downarrow}}{B_\nu(T_S) - \overline{N}_\nu^{\downarrow}} \text{ [near surface only]} \qquad (2)$$

When the atmosphere is relatively dry, the atmospheric emission and absorption in the microwindows between absorption lines can be neglected and downwelling radiance at the surface can be set to zero. In this case, equation (1) can be written in the form

$$e_\nu \cong \frac{N_\nu^{\uparrow}}{B_\nu(T_S)} \text{ [clean microwindows only]} \qquad (3)$$

3. OBSERVATIONS

Three sets of observations are described in this paper; a ground based survey of the ARM SGP site in November 2000, the ARM/FIRE Water Vapor Experiment (AFWEX) in Nov.-Dec. 2000, and the NASA SAFARI experiment in Aug. 2000.

The November 2000 ARM land surface emissivity survey was conducted by personnel from the University of Wisconsin-Madison during the period 29-30 November 2000 to improve our understanding of the variability of surface emissivity in the vicinity of the SGP ARM site central facility. This was the first of several planned surveys designed to capture the seasonal changes of surface emissivity on scales useful to characterize the sub-pixel variability needed to support satellite validation activities. The surface measurements are made with the UW Scanning-Atmospheric Emitted Radiance Interferometer (S-AERI) (Knuteson, et al., 1999). The survey approach was the following; 1) spectral data were collected with the S-AERI at a variety of land types, 2) a corresponding cataloging of land cover found along roads near the CART site was undertaken, and 3) a combination of the observed spectral library and statistical information on the fraction of field types along the survey route was used to determine a weighted emissivity average.

Figure 1 shows the S-AERI sensor deployed vertically sixteen feet above ground level where it is able to make slant view measurements (at 60 degrees) of the surface and the atmosphere. The S-AERI measurements of upwelling and downwelling radiance are used in equation (2) along with the additional constraint that the emissivity should be smoothly varying across atmospheric emission lines (Bower, et al., 1999). Shown in figure 2 are the results from a 22 mile North-South survey illustrating the measured emissivities of pasture, wheat, and bare soil and the weighted average emissivity spectrum along the survey line.

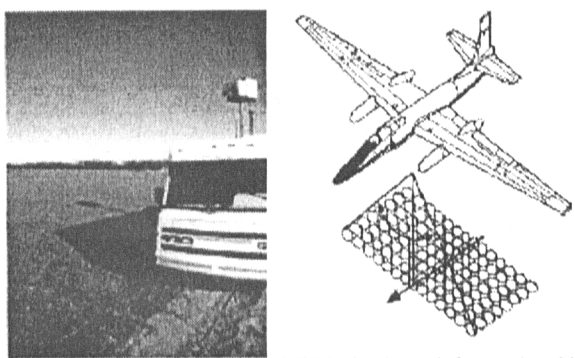

Figure 1. The Scanning-AERI deployed from the UW research vehicle near the ARM SGP site (left). Illustration of S-HIS and NAST-I crosstrack scan (right).

The AFWEX experiment (Nov-Dec 2000, SGP ARM stie) provided an excellent dataset for satellite validation studies under cloud-free conditions. During the AFWEX experiment, the UW S-HIS was operating from the NASA DC-8 aircraft flying at altitudes between 8 and 12 km while the LaRC NAST-I operated from the Proteus aircraft at about 15 km altitude. The atmospheric state is particularly well characterized by instrumentation on the NASA aircraft in addition to ground-based lidars and radars. Observations from 30 March 2000 02:30 UT for the S-HIS and 02:45 UT for the NAST-I are used in this analysis. During this time period the UW S-AERI was operating in surface scanning mode at the DOE SGP central facility. Comparison of the results derived form these observations are given in the next section.

The Scanning-HIS (S-HIS) is an advanced version of the HIS ER-2 instrument, developed between 1996 and 1998 with the combined support of the US DOE, NASA, and the NPOESS Integrated Program Office (Revercomb, et al., 1999). It has flown in seven field campaigns beginning in 1998 and has proven to be very dependable and effective. The continuous spectral coverage from 3.3 to 16.7 μm at 0.5 cm^{-1} resolution is divided into three bands with separate detectors (two photoconductive HgCdTe and one InSb). The bands use a common field stop to ensure accurate spatial co-alignment. The mid-wave band provides the primary water vapor sounding information. The optical design is very efficient, providing useful signal-to-noise performance from a single 0.5 second dwell time. This allows imaging with 2-3 km resolution to be accomplished by cross-track scanning. Onboard reference blackbodies are viewed as part of each cross-track scan, providing updated calibration information every 20-30 seconds. The rapid sampling frequency of the S-HIS allows cross-track imaging at 2 km resolution with a swath width on the ground of 30-40 km, as illustrated in Figure 1, or a nadir only mode with overlapping fields of view.

The NPOESS Atmospheric Sounder Testbed – Interferometer (NAST-I) is an aircraft instrument built by MIT-Lincoln Labs and operated by NASA Langley Research Center. The UW is responsible for on-board and ground calibration of the NAST-I. The NAST-I is of similar design to the S-HIS and has similar spectral and spatial coverage but higher spectral resolution.

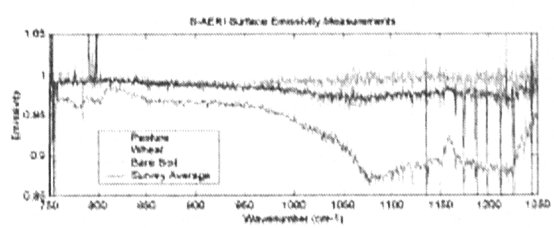

Figure 2. The measured surface emissivity of pasture, wheat, and bare soil near the DOE ARM site in Oklahoma overlaid with the weighted average emissivity as determined by the North/South survey results (39% pasture; 55% wheat; 6% bare soil).

The third observation set is from the NASA SAFARI experiment based in South Africa during Aug-Sept.

2000. The S-HIS flew onboard the NASA high altitude ER-2 aircraft during SAFARI and collected over 90 hours of upwelling radiance spectra on 14 different flights over a variety of surface types. Numerous coincident aircraft underflights of the Terra platform were obtained. The S-HIS data presented in this paper are from the flight of 27 August 2000 over the Okavanga Delta region of Botswana.

4. RESULTS

The approach taken in this paper is to find the weight of the three main surface types which provide the best fit to the average aircraft observations. A best fit weighting of 35% pasture, 40% wheat, and 25% bare soil is shown in figure 3 compared with the average NAST-I aircraft observations. The NAST-I relative emissivity is given in the lower panel of figure 3. In precisely the same manner, a weighting of 45% pasture, 40% wheat, and 15% bare soil was found to be a best fit to the S-HIS observations on this day. The comparison of weighted surface emissivity and aircraft S-HIS relative emissivity is shown in figure 4. The relative emissivity of both the NAST-I and S-HIS has been set equal to 0.99 at 823 cm^{-1} for consistency with the ARM survey results.

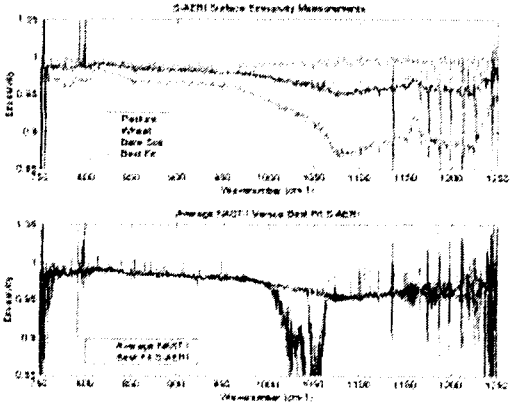

Figure 3. A best fit weighted average of the ground-based S-AERI measurements (35% pasture; 40% wheat; 25% bare soil) shown in the upper panel is overlaid in the lower panel on the average north/south nadir measurements of the NAST-I at 55,000 feet in the vicinity of the ARM SGP central facility. The feature at 1000-1080 cm^{-1} in the aircraft observations is due to absorption by ozone in the path from the aircraft to the ground. The numerous spikes in the data are due to water vapor and carbon dioxide absorption lines where the approximation leading to equation (3) is not valid. The spikes are pointed up because of the presence of a nocturnal surface inversion at the time of the measurements.

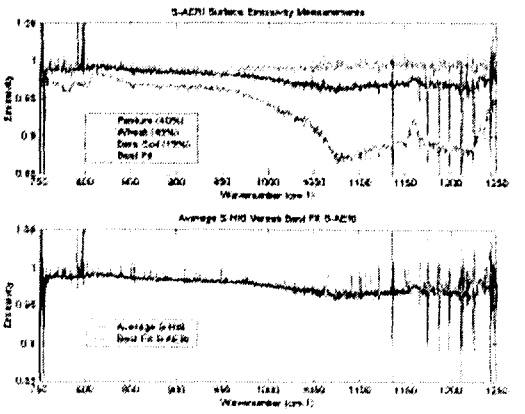

Figure 4. Best fit of a linear combination (40% pasture, 45% wheat, 15% bare soil) of surface emissivity types to surface relative emissivity derived from the Scanning-HIS aircraft observations made from the NASA DC-8 at 25,000 feet. The flight path of the DC-8 was in the vicinity of the ARM SGP central facility but along a different ground path than the PROTEUS. Notice the lack of ozone absorption at this lower altitude though water vapor absorption lines are still present.

For a simultaneous fit of surface temperature and emissivity from the aircraft observations, we can use equation (2) where an calculation has been used to correct for the atmospheric emission. We vary the skin temperature until the deived emissivity is no longer contains gaseous absorption features (Smith, 1996). This is referred to as the online/offline technique. This fit appears to be biased low by an error in the calculated radiance representing the atmospheric emission either due to spectroscopy or water amount.

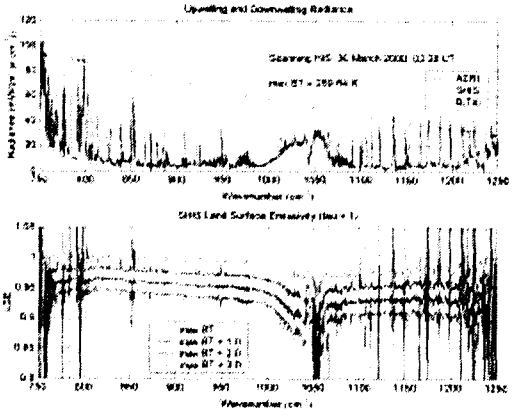

Figure 5. The S-HIS and AERI observations used in the online/off-line fitting technique are shown in the upper panel. The lower panel shows a range of skin temperature values. The best fit is the one which minimizes the spectral line variations of the derived emissivity.

Measurements of the Okavanga Delta region of southern Africa obtained by the UW S-HIS instrument aboard the NASA high altitude ER-2 aircraft are shown in figure 6. The cooler water-filled swamp is surrounded by the high temperature Kalahari desert region. This example illustrates the importance of considering non-black surface types which in this case produce an apparent brightness temperature variation reaching 5 K between 10 and 8 μm. Further analysis of this data is underway to obtain the associated surface emissivity and skin temperature maps.

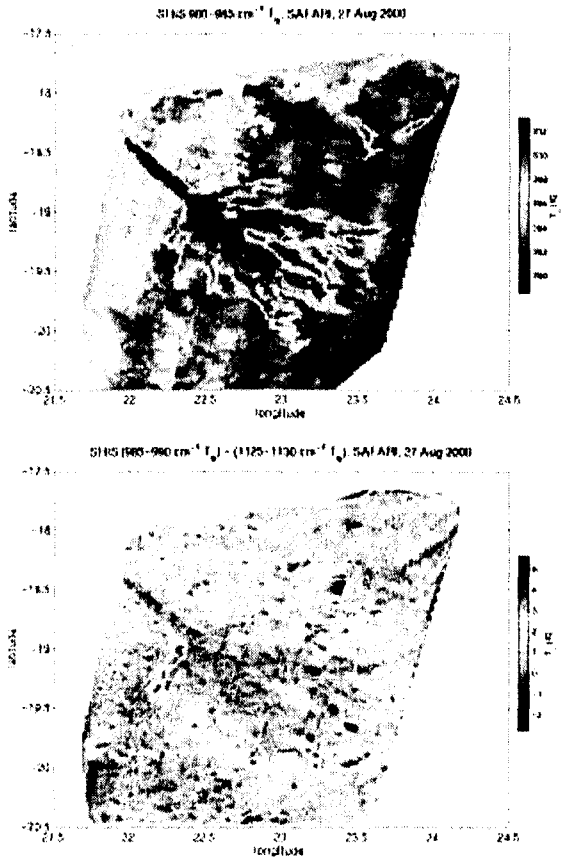

Figure 6. The upper panel is a 10 μm microwindow brightness temperature image created from Scanning-HIS data of the Okavanga Delta in southern Africa. The lower panel shows the temperature contrast in two sets of microwindows (10-8 μm).

5. SUMMARY

The results show that aircraft observations of spectral emissivity in the vicinity of the ARM SGP central facility are generally consistent with a linear combination of bare soil and vegetated emissivity measured in a ground-based site survey. Several factors may influence the differences between the ground-based and aircraft measurements. Nadir aircraft views are being compared with surface measurements made at a view angle of 60 degrees from nadir. The aircraft fields of view do not exactly overlap with the ground survey so that a different fraction of bare soil and vegetated soil types can be expected. Moreover a comparison of the S-HIS results from figures 4 and 5 suggests that the absolute emissivity magnitude derived from the online/offline technique is sensitive to the accuracy of the atmospheric correction; either due to spectroscopy errors or water vapor amount uncertainties.

A more comprehensive analysis of the NAST-I and S-HIS data is anticipated which will extend the results of the ARM LSE Survey to a larger area of the ARM SGP site. Additional measurements at the ARM site at different times of the year will help to characterize the seasonal variation of the land surface emissivity and thus improve our characterization of this site for satellite validation.

6. ACKNOWLEDGEMENTS

This work was performed for the AIRS science team under NASA contract NAS5-31375.

7. REFERENCES

Bower, Nicholas, Robert O. Knuteson, and Hank E. Revercomb, 1999: High spectral resolution land surface temperature and emissivity measurement in the thermal infrared. Conference on Atmospheric Radiation: A Symposium with tributes to the works of Verner E. Suomi, 10th, Madison, WI, 28 June-2 July 1999 (preprints). Boston, MA, American Meteorological Society.

Knuteson, Robert O., Fred A. Best, Wayne F. Feltz, Ray G. Garcia, H. Ben Howell, Hank E. Revercomb, David Tobin, and Von Walden, 1999: UW High Spectral Resolution Emission Observations for Climate and Weather Research: Part II Groundbased AERI. Conference on Atmospheric Radiation: 10th, Madison, WI, 28 June-2 July 1999 (preprints). Boston, MA, American Meteorological Society.

Revercomb, Hank E., R. O. Knuteson, F. A. Best, D.D. LaPorte, S. A. Ackerman, N.N. Ciganovich, R.G. Dedecker, T.P. Dirkx, S.D. Ellington, W.F. Feltz, R.A. Herbsleb, H.B. Howell, R.K. Garcia, J.F. Short, D.C. Tobin, P. van Delst, V.P. Walden, M. Werner, and H.M. Woolf, 1999: UW High Spectral Resolution Emission Observations for Climate and Weather Research: Part I Airborne. Conference on Atmospheric Radiation: 10th, Madison, WI, 28 June-2 July 1999 (preprints). Boston, MA, American Meteorological Society.

Smith, William L., R. O. Knuteson, H. E. Revercomb, W. Feltz, H. B. Howell, W. P. Menzel, N. Nalli, Otis Brown, James Brown, Peter Minnett, Walter McKeown, 1996: Observations of the infrared radiative properties of the ocean - implications for the measurement of sea surface temperature via satellite remote sensing. *BAMS*, **77**, 41-51.

P5.61

QUALITY CONTROL AND PRELIMINARY DATA ANALYSIS OF THE INTERFEROMETRIC MONITOR FOR GREENHOUSE GASES (IMG) DATA SET

Robin L. Tanamachi
University of Wisconsin – Madison, Madison, WI

Von P. Walden
University of Idaho, Moscow, ID

Steven A. Ackerman and Robert O. Knuteson
University of Wisconsin – Madison, Madison, WI

1. INTRODUCTION

The Interferometric Monitor for Greenhouse Gases (IMG) is a Michelson–type, Fourier transform interferometer that collected upwelling terrestrial infrared radiance data aboard the polar–orbiting ADEOS satellite between October 1996 and June 1997. IMG measured raw uncalibrated interferograms, which are transformed into calibrated brightness temperature and radiance spectra. This paper describes the application of quality control procedures to both the IMG spectra and interferograms. The paper also presents some preliminary scientific findings.

2. ASSESSMENT OF IMG DATA QUALITY

The IMG instrument was developed by the Japan Resources Observation System Organization (JAROS) and was the first polar–orbiting interferometer since the Infrared Interferometric Spectrometer (IRIS) on board Nimbus 4 in 1970–1971. Kobayashi *et al.* (1999) described the technical details of the IMG instrument and its observation pattern.

The instrument obtains eight measurements as part of a measurement sequence: six measurements of upwelling radiance from the underlying earth and atmosphere and two calibration measurements from deep space and an onboard blackbody, assumed to have unit emittance ($\varepsilon = 1$). The latter two measurements are used for calibrating the six earth views. The measurements are taken simultaneously over three different spectral bands: 2500 – 3000 cm^{-1} (3.3 – 4.3 μm); mediumwave, 2000 – 2500 cm^{-1} (4.0 – 5.0 μm); and longwave, 700 – 2000 cm^{-1} (5.0 – 14.0 μm). Only the longwave band is considered in this study.

Two primary data sets were used for analysis here:

- **Level 0B:** Raw, uncalibrated interferograms for 23,089 IMG sequences meeting National Space Development Agency of Japan (NASDA) data quality criteria (Kobayashi *et al.*, 1998). These interferograms were corrected for detector nonlinearity in Band 3 by NASDA.
- **Level 1N3:** Calibrated, brightness temperature spectra for Band 3 for the same 23,089 sequences available as level 0B interferograms. The calibration was performed by Dr. Ryouichi Imasu of the National Institute for Resources and the Environment of Japan (NIRE).

From the Level 1N3 data set, a summary product consisting of spectrally averaged brightness temperatures over 27 different channels was created. Channels were selected for their utility in scientific studies, as denoted in Table 1.

Table 1. The 27 channels selected for the Level 1N3 summary product.

Channel	Wavenumber (cm^{-1})	Wavelength (μm)	Description
1	685 – 690	14.49 – 14.60	upper level temperature
2	695 – 710	14.08 – 14.39	cloud top altitude
3	710 – 725	13.79 – 14.08	cloud top altitude
4	725 – 742	13.47 – 13.79	cloud top altitude
5	742 – 758	13.19 – 13.47	cloud top altitude
6	784 – 785	12.74 – 12.76	inversion channel
7	787 – 789	12.67 – 12.70	background channel
8	830 – 835	11.98 – 12.05	desert aerosols
9	870 – 875	11.43 – 11.49	cloud properties (particle size & emission)
10	980 – 985	10.15 – 10.20	cloud properties (particle size & emission)
11	1000 – 1075	10.00 – 9.30	total ozone
12	1125 – 1130	8.85 – 8.89	window
13	1175 – 1180	8.47 – 8.51	desert aerosols
14	1302 – 1305	7.66 – 7.68	methane
15	1330 – 1335	7.49 – 7.52	desert aerosols
16	1575 – 1577	6.34 – 6.35	upper level water/temperature
17	1590 – 1595	6.27 – 6.29	mid level water/temperature (with accurate forward model)
18	1449.28 – 1529.05	6.54 – 6.9	MODIS channel 27
19	1336.90 – 1392.76	7.18 – 7.48	MODIS channel 28
20	1149.43 – 1190.48	8.4 – 8.7	MODIS channel 29
21	1012.15 – 1043.84	9.58 – 9.88	MODIS channel 30
22	886.52 – 927.64	10.78 – 11.28	MODIS channel 31
23	815.00 – 849.62	11.77 – 12.77	MODIS channel 32
24	741.29 – 758.15	13.19 – 13.49	MODIS channel 33
25	725.16 – 741.29	13.49 – 13.79	MODIS channel 34
26	709.72 – 725.16	13.79 – 14.09	MODIS channel 35
27	694.93 – 709.72	14.09 – 14.39	MODIS channel 36

Corresponding author address: Robin L. Tanamachi, Space Science & Engineering Center, University of Wisconsin – Madison, 1225 W. Dayton St., Madison, WI 53706; e–mail: robint@ssec.wisc.edu

Initial efforts to derive scientific products from the Level 1N3 summary product were promising. However, the appearance of nonphysical brightness temperatures in some of the spectra led to the development of automated process for data quality screening (Tanamachi 2001). All of the Level 1N3 brightness temperature spectra were checked for series of potential problems, based on defined thresholds, variances and differences of the channels shown in Table 1. Table 2 gives a summary of the data-quality checks that were performed. Spectra are flagged in the summary product by assigning a data-quality flag between 0 and 5, where a value of 0 denotes a spectrum that passes all the checks and a positive value between 1 and 5 denotes the particular check that the spectrum has failed.

Table 2. Data quality flags incorporated into the L1N3 summary product.

Check No.	*Description*
0	Spectrum passed Checks 1 -5
1	Spectrum fails if Ch. 12 – 13 brightness temperature difference > 2.0 K
2	Spectrum fails if Ch. 10 brightness temperature is either > 350 K or < 170 K
3	Spectrum fails if Ch. 23 brightness temperature variance > 7.0 K
4	Spectrum fails if Ch. 22 brightness temperature variance > 7.0 K
5	Spectrum fails if Ch. 21 – 20 brightness temperature difference > 0.0 K and latitude < 65 N or S

Spectra with a positive data-quality flag are eliminated from subsequent scientific analysis. Out of 138,534 total spectra (23,089 total sequences x 6 earth observations per sequence), 33,310 spectra (24.0%) received a positive data-quality flag. Therefore, 76.0% of the spectra were retained for the scientific analysis discussed in Section 3.

The significant fraction of flagged Level 1N3 set led to an investigation of the quality of the Level 0B interferograms from which the spectra were produced. This was motivated, in part, by the fact that a problem with any of three interferograms (the earth and its corresponding calibration views, space or warm blackbody) could be the reason why a particular Level 1N3 brightness temperature spectrum fails a Level 1N3 data-quality check. Three types of interferograms were identified, which could potentially lead to erroneous spectra:

- **Decentralized ZPD:** Interferograms that display a highly decentralized zero path difference (ZPD). These result in spectra with impossibly high radiances or brightness temperatures. Less than 1% of the Level 0B interferograms displayed this feature.
- **Asymmetric ZPD region:** Interferograms with an asymmetry generally apparent at the second maximum outwards from the ZPD on either side. These result in highly nonphysical spectra. Approximately 1.0% of IMG interferograms displayed this feature.
- **Random noise bursts:** Interferograms displaying erratic and often asymmetric noise patterns. The actual effect of the noise bursts on calibrated radiances is still being investigated.

The detection of interferograms with decentralized ZPDs and asymmetric ZPD regions is fairly straightforward. However, the detection and flagging of noise bursts in interferograms is much more difficult. This is due to the random location of the noise, as well as the fact that the magnitude of the noise is variable.

3. PRELIMINARY DATA ANALYSIS

The Level 1N3 summary product, screened for data quality, is now used to derive preliminary scientific products from the IMG data set.

3.1 *Land Surface Emissivity*

Different types of land cover possess different spectral emissivity signatures. By estimating surface emissivity in clear scenes, emissivity distribution profiles can be generated for different biomes (Wittich 1997).

According to Knuteson et. al. (2001), under cloud-free conditions in spectral microwindows, the surface emissivity e_ν at all altitudes can be approximated by

$$e_\nu \simeq \frac{N_\nu\uparrow}{B_\nu(T_s)} \qquad (1)$$

where $N_\nu\uparrow$ is the observed upwelling radiance spectrum, B_ν is Planck's function, and T_s is the surface temperature.

The method developed by Knuteson et. al. (2001) involves lowering the spectral resolution of the longwave L1N3 brightness temperature spectra for all the IMG sequences contained in a specific geographic area. This is accomplished by fitting lines through the mean brightness temperatures in four selected microwindows: 820–825 cm^{-1}, 960–962 cm^{-1}, 1202–1204 cm^{-1}, and 1231–1233 cm^{-1}. The low-resolution brightness temperature spectra are then converted into observed radiances. Emissivity spectra e_ν are derived using Eqn. (1) relative to the microwindow with the maximum observed radiance, which is assumed to have unit emissivity ($e = 1$).

Since this method works on the assumption of a clear-sky view, a tri-spectral cloud-clearing/data quality control method was applied after the emissivity derivation. The three wavelengths selected for this tri-spectral method were 820 cm^{-1} (12.0 μm), 980 cm^{-1} (10.3 μm), and 1200 cm^{-1} (8.3 μm). This technique assumes that ice and water clouds have an emissivity signature characterized by $e_{820} < e_{980}$. Therefore, data points were labeled "clear" if $e_{980} - e_{820} < 0$. An additional criterion on the $e_{980}-e_{820}$ difference was used to screen out data of poor quality; the data were labeled "good" if $e_{980} - e_{820} > -0.1$. Emissivity histograms were then derived for the subset of data labeled both "clear" and "good" (Fig. 1).

The L1N3 data was used to derive surface emissivity profiles over three test areas in Africa (each with longitudinal span 12 °E – 30 °E): the Sahara Desert (latitudinal span 15 °N – 30 °N), the Sub-Saharan transition belt (5 °N – 15 °N), and the Congolese rain forest (5 °S – 5 °N). Fig. 1 shows two interesting results that yield confidence in using IMG

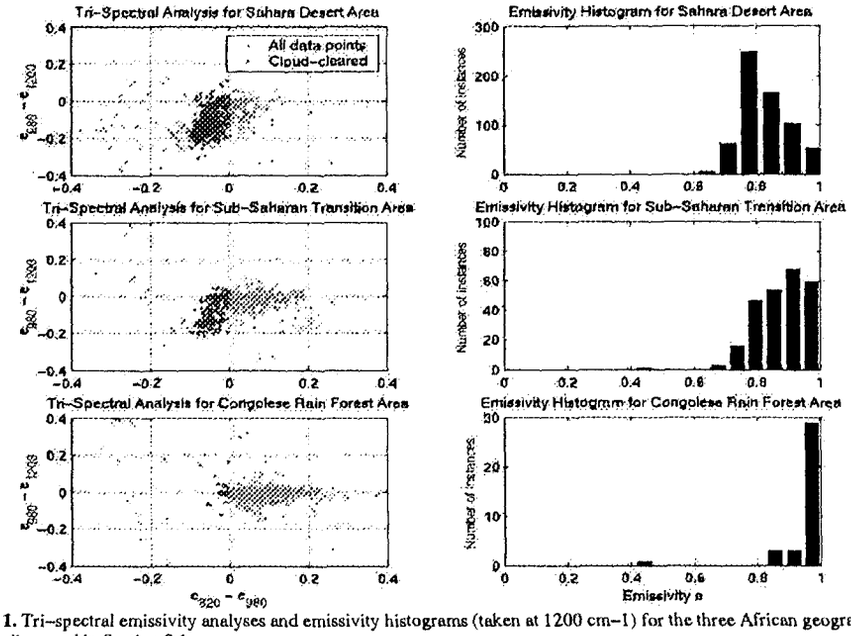

Figure 1. Tri-spectral emissivity analyses and emissivity histograms (taken at 1200 cm-1) for the three African geographic regions discussed in Section 3.1.

data for studies of land-surface emissivity. Firstly, the tri-spectral emissivity analyses (left column) show that cloudiness gradually increases from the Sahara desert southward to the Congolese rain forest, as expected. Secondly, the surface emissivities (right column) also increase from 0.80 over the Sahara Desert, to 0.90 over the sub-Saharan transition zone, to near unity over the Congolese rain forest.

3.2 *Convective Clouds*

Ackerman (1996) discussed High Resolution Interferometer Spectrometer (HIRS) observations of negative brightness temperature differences between 900 cm^{-1} (11 μm) and 1490 cm^{-1} (6.7 μm) observations ($BT_{11} - BT_{6.7}$). Ackerman (1996) presents evidence that these negative brightness temperature differences of less than −5 K can be indicative of either a nocturnal inversion over a snow-covered surface or a high cloud.

Using Ackerman (1996) as a guideline, frequency of occurrence of $BT_{11} - BT_{6.7} < -5$ K was investigated using the IMG data set. The analysis was applied to SSEC's L1N3 summary product Channels 22 (886.52 – 927.64 cm^{-1}) and 18 (1449.28 – 1529.05 cm^{-1}). Fig. 2 shows the percent frequency of $BT_{11} - BT_{6.7} < -5$ K over the entire duration of the IMG campaign.

A majority of these instances from the IMG data occur over Antarctica and Greenland, two areas that are continually covered by ice. IMG appears to be detecting a large number of surface inversions over snow-covered ground, in agreement with Ackerman (1996).

Ackerman (1996) also showed enough instances of $BT_{11} - BT_{6.7} < -5$ K in the HIRS data to delimit the Intertropical Convergence Zone (ITCZ).

This identifying characteristic of the ITCZ was not apparent in similar studies using the IMG data. One possible explanation to account for this feature is the high spatial resolution of the HIRS data relative to that

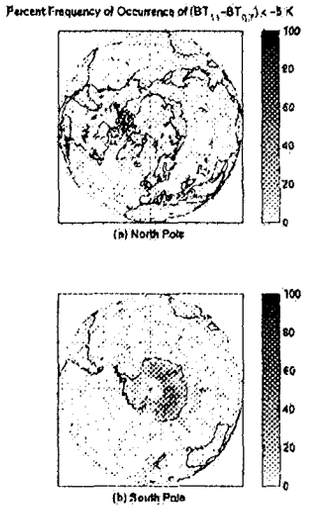

Figure 2. Percent frequency of occurrence of the 11 – 6.7 μm observations being less than −5 K during the IMG campaign, over (a) the North Pole, and (b) the South Pole. The gray bars on the right are the percentage scale.

of the IMG data. (While $BT_{11} - BT_{6.7} < -5$ K is indicative of active convection over the tropics, it may not detect anvils or other cold clouds with little internal convection because these typically have $BT_{11} - BT_{6.7} \sim 0$ K. $BT_{11} < 230$ K is typical of a cold high cloud in the tropical regions, and should be visible in the IMG spatial sampling.) IMG fails to capture the desired ITCZ signal, indicating that the IMG spatial sampling over the tropics may be too coarse for large scale studies of convective features.

3.3 *Polar Clouds*

Walden et al. (1998) detailed a method for diagnosing the presence or absence of cloud cover over cold polar regions. This method is applied to the IMG

L1N3 summary product using Channels 6 (784 – 785 cm^{-1}) and 7 (787 – 789 cm^{-1}). $BT_{Ch.\ 6} - BT_{Ch.\ 7} > 0$ is indicative of a clear scene, while $BT_{Ch.\ 6} - BT_{Ch.\ 7} < 0$ is indicative of a cloudy scene.

Fig. 3 shows the geographical coverage of 'clear' scenes over the polar regions. The most noticeable differences lie in the lack of clear scenes over the northern Atlantic Ocean and the Antarctic Ocean, as well as the increases density of clear scenes over the ice covered region of Antarctica.

Although the spatial sampling of IMG data may not be sufficient for large scale investigation of circulations over the tropics, the polar orbit of the ADEOS satellite yields better IMG coverage over the poles.

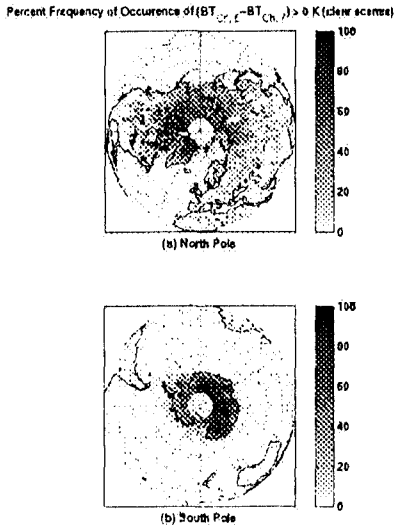

Figure 3. Percent frequency of occurrence of $BT_{Ch\ 6} - BT_{Ch\ 7}$ greater than 0 K (i.e. clear scenes) over (a) the North Pole, and (b) the South Pole. The gray bars on the right are the percentage scale.

4. CONCLUSIONS

The IMG instrument measured a large number of upwelling terrestrial radiance spectra over its 8–month lifetime. Data quality issues still exist with this data set and are manifested in both the calibrated spectra and the raw interferograms. We are continuing to develop algorithms that select IMG interferograms that can be used for proper calibration of IMG spectra.

In spite of the data quality issues, the following conclusions can be drawn from preliminary data analysis:

1. The spatial coverage of the IMG data appears to be adequate for large–scale studies of circulation features over the polar regions, but inadequate over the tropical regions.
2. The IMG data is useful for detecting clear skies over the polar regions because of its high spectral resolution, which makes the narrow surface inversion signal visible in the brightness temperature spectra.
3. The IMG data is useful for studies of land–surface emissivity, as demonstrated by the preliminary study of north central Africa.

These results show that the IMG data set has scientific value once its data quality issues are more thoroughly addressed.

5. ACKNOWLEDGEMENTS

We acknowledge Dr. Ryouichi Imasu of the National Institute for Resources and Environment of Japan (NIRE) for supplying his calibrated data set and for many helpful discussions regarding the calibration of IMG spectra.

6. REFERENCES

Ackerman, S. A., 1996: Global Satellite Observations of Negative Brightness Temperature Differences between 11 and 6.7 microns. *J. Atmos. Sci*, **53**, 2803–2812.

Knuteson, R. O., B. Osborne, J. Short, H. Revercomb, D. Tobin, S. Nasiri, 2001: Progress Towards a Characterization of the Infrared Emissivity of the Land Surface in the Vicinity of the ARM SGP Central Facility: Surface (S–AERI) and Airborne Sensors (NAST–I/S–HIS). Presentation to the 11th Annual ARM Program Science Team Meeting, 19–23 March 2001, Atlanta, GA.

Kobayashi, Hirokazu, T. Ogawa, H. Shimoda, A. Shimota, K. Kondo, S. Kadokura, C. Yoshigahara, Y. Uehara, I. Yoshida, 1998: IMG, precursor of the high–resolution FTIR on the satellite. Proceedings of the International Society for Optical Engineering (SPIE), **3501**, 23 – 33.

Kobayashi, H., A. Shimota, K. Kondo, E. Okumura, Y. Kameda, H. Shimoda, T. Ogawa, 1999: Development and evaluation of the interferometric monitor for greenhouse gases: a high–throughput Fourier–transform infrared radiometer for nadir Earth observation. *Appl. Optics*, **38**, 6801 – 6807.

Revercomb, H. E., H. Bujis, H. B. Howell, D. D. LaPorte, W. L. Smith, L. A. Sromovsky, 1988: Radiometric Calibration of IR Fourier Transform Spectrometers: solution to a problem with the High–Resolution Interferometer Sounder. *Appl. Optics*, **27**, 3210 – 3218.

Tanamachi, R. L. Data Quality Control and Preliminary Data Analysis from the Interferometric Monitor for Greenhouse Gases (IMG) Data Set [thesis]. Madison, WI: University of Wisconsin – Madison; 2001. 32 pgs.

Walden, V. P., D. C. Tobin, and H. E. Revercomb, 1998: "Creation of a Web–Based Archive of IMG Data Over the Arctic." International Arctic Research Center (IARC) Final Report, available from authors.

Walden, V. P., R. Imasu, R. Tanamachi, H. E. Revercomb, and D. C. Tobin, 2001: Spectral and radiometric validation of the Interferometric Monitor for Greenhouse Gases (IMG) between 5 and 14 micrometers. In production.

Wittich, K.–P., 1997: Some simple relationships between land–surface emissivity, greenness and the plant cover fraction for use in satellite remote sensing. *Int. J. Biometeorol.*, **41**, 58–64.

P5.63

Calibration and Initial Results from the OSSEs for NPOESS

M. Masutani*, J. S. Woollen*, J. Terry+, S. J. Lord*,
T. J. Kleespies#, G. D. Emmitt**, S. A. Wood**, S. Greco**,
J. C. Derber*, R. Atlas+, M. Goldberg#

*NOAA/NWS/NCEP/EMC, +NASA/GSFC/DAO,
#NOAA/NESDIS, **Simpson Weather Associates
http://www.emc.ncep.noaa.gov/research/osse

1. INTRODUCTION

The future National POES System (NPOESS) is scheduled to fly during the 2007-2010 period. For the next 10 years, a considerable amount of effort must take place to define, develop and build the suite of instruments which will comprise the NPOESS. The forecast impact of current instruments can be assessed by Observing System Experiments (OSEs), in which already existing observations are denied or added to observations from a standard data base. However, the impact of future instruments must be assessed with experiments using simulated observations. These experiments are known as Observing System Simulation Experiments (OSSEs).

This project is a collaboration among, the National Centers for Environmental Prediction (NCEP), NASA/Data Assimilation Office (DAO), Simpson Weather Associates (SWA), and the National Environmental Satellite, Data and Information Service (NESDIS). Through this collaboration, the data assimilation and modeling communities can be involved in instrument design and can provide information about the expected impact of new instruments. Furthermore, through the OSSEs, operational data assimilation systems will be ready to handle new data in time for the launch of new satellites. This process involves preparation for future data volumes in operations, the development of the data base and data-processing (including formatting) and a quality control system. All of this development will accelerate the operational use of data from the future instruments (Lord et al. 1997).

2. THE NATURE RUN

For the OSSE, a long integration of an atmospheric general circulation model (GCM) is required to provide a "true atmosphere" for the experiment. This is called the "nature run" (NR). The nature run needs to be sufficiently representative of the actual atmosphere and but different from the model used for the data assimilation. The observational data for existing instruments is simulated from NR and impact tests are performed for both real and simulated data.

Corresponding authors address: Michiko Masutani, NOAA/NWS/NCEp/EMC, 5200 Auth Rd. Camp Springs, MD 20746. E-mail: michiko.masutani@noaa.gov.

For this project, the nature run was provided by the European Centre for Medium-Range Weather Forecasts (ECMWF). The description and evaluation of the nature run is provided. (Becker et al., 1996.) A one month model run was made at resolution T213 and 31 levels starting from 5 February 1993. The version of the model used for the nature run is the same as for the ECMWF reanalysis.

The nature run was found to be representative of the real atmosphere but with a few exceptions (Masutani et al. 1999a,1999b). Low level marine stratocumulus required some adjustment. A localized warm SST in southern hemisphere in real data was not included in the nature run. This SST could potentially cause some inconsistent results in OSSE verification results.

3. SIMULATION OF OBSERVED DATA

Details of procedures to simulate observational data are described in Masutani et al. (1999b) and Lord et al. (2001a, 2001b). These papers are available at the OSSE web site. In this paper, simulation of Atmospheric Infrared Sounder (AIRS) and cloud motion vectors (CMV, Velden et al. 1998) are mainly described. AIRS is scheduled to be included in the NPOESS Preparatory Project (NPP) instrument suite.

NASA/DAO is taking the lead for the simulation of realistic conventional observations, including CMV and ACARS. The initial simulation uses real observational data distributions available in February 1993.

Doppler wind lidar (DWL) wind data are produced as line-of-sight (LOS) winds by SWA using their Lidar Simulation Model (LSM). Bracketing sensitivity experiments are being performed for various DWL concepts to bound the potential impact (Lord et al. 2001a). Scanning, and various data sampling strategies are being tested with these experiments. No measurement error is assigned for these initial tests but will be added in the future. Strategies for systematic errors are discussed by Emmitt (2000).

3.1 *Simulation of cloud motion vector*

The CMV available in 1993 were generally obtained by manual tracking and thus were limited in numbers compared to what is available today. The experiments being presented in this paper used the locations of actual CMVs assimilated in 1993 to pick a wind observation from the nature run. While this approach may be reasonable for the first few days of NR, the locations of clouds suitable for CMVs from NR are different in the out days of NR compared to the actual conditions in 1993. Thus a new CMV simulation algorithm has been developed by NASA/DAO and SWA that will identify NR clouds that would be

suitable for motion vectors. This algorithm also assigns both random and systematic error (e.g., navigation, slow bias, height assignment) to the CMVs to insure a more realistic data quality for the OSSE calibration.

The locations of CMV observations, unlike most conventional observations, are derived from cloud and water vapor feature in the atmosphere. A good correlation of the CMV observations locations with the cloud information from NR will add realism to the simulated data for NPOESS OSSE's. An estimate of this correlation was made by determining the distribution of cloud fractions, derived from the model first guess from a real data assimilation, in the vicinity of real CMV observations. This is done separately for several tropospheric layers. These statistics provide statistical constraints for determining the simulated CMV locations when using cloud fractions from NR. Other constraints, internal to the overall wind retrieval process, are also considered. These include: latitude cut-offs; filtering of CMV's based on topography; discrete levels for height assignment; and a nominal count of observations by layer. To obtain realistic simulated CMV locations while maintaining a resolution comparable to real CMV observations, two methods are being developed. One method begins with a fixed grid at a resolution approximating the horizontal spacing of real CMV observations. The grid points are then filtered using the above constraints. The second method, which may be of more practical with higher density observations, involves the creation of a large "pool" of real CMV observation locations which are randomly sampled until the representative distribution is achieved, again, based on the above constraints. A procedure for introducing a correlated height assignment error is also being developed since these errors contribute significantly to overall CMV observational error (Merrill et al. 1991). The height assignment error is assumed to be associated with large-scale atmospheric features (Schmetz and Holmlund, 1992) which are capable of being resolved by NR; therefore one or more NR parameters will likely be used for this procedure.

3.2 *Simulation of AIRS radiances*

The AIRS simulation package was originally developed by Evan Fishbein of JPL. The simulation (i.e. forward calculation) is based on radiative transfer code developed by Larrabee Strow (UMBC). The package was modified by Walter Wolf to generate thinned radiance datasets in the BUFR format. The effort to provide AIRS data to NWP centers in near-realtime is being led by Mitch Goldberg (NESDIS). Because the AIRS instrument will not be launched until 2002, the NESDIS AIRS near-realtime system is currently based on simulated data. The NCEP AVN six-hour forecasts are used to specify the state variables needed for the forward calculation. The simulation package runs in real-time and products (thinned radiances and retrievals) are produced in near-realtime. This same package is being used to generated AIRS radiances for the OSSE (Goldberg et al. 2001).

4. DATA ASSIMILATION SYSTEM

The data assimilation system at NCEP is based on the "Spectral Statistical Interpolation" (SSI) of Parrish and Derber (1992), which is a three-dimensional variational analysis (3-D var.) scheme. The TOVS level-1b radiance (T1B) is used (McNally et al., 2000, Derber and Wu 1998) for data assimilation and the March 1999 version of NCEP's operational Medium Range Forecast (MRF) and data assimilation system are used for the data impact test. LOS winds from DWL are directly used in the data assimilation.

The following upgrades of the NCEP operational data assimilation system are in progress.

- Development of situation-dependent background error covariances for global and regional systems (Purser and Parrish, 2000).
- Bias correction of background field.
- Improved moisture background error covariances.
- Development of cloud analysis system.

Data from NPP/NPOESS instruments, quickscat observations, GCP radio-occultation observation, GIFTS, DMSP (SSM/IS), and imager radiances (MODIS, GOES, AVHRR) are all planned to be included at a later time.

5. OSSE CALIBRATION

OSSE calibrations are performed for existing instruments by comparing the simulated and real impact tests (Lord 2001a, Lord 2001b). Assessments for future instruments will be performed by comparing relative impacts from the calibration experiments. Denial of RAOB wind (R_wind), RAOB temperature (R_temp), and T1B with various combinations are tested. The analysis with all conventional data and T1B is used as control (CTL). The results show generally satisfactory agreements between real and simulated impacts.

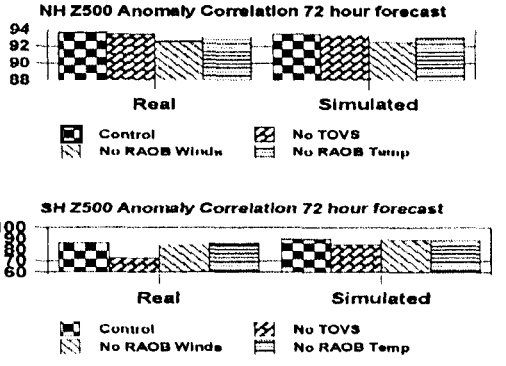

Fig.1

Anomaly correlations for 500hPa height fields for 72 hour forecast skill for the experimentss without T1B (NTV), experiments without R_wind (1BNWIN), experiments without R_temp (1BNTMP) are presented in Fig.1. The forecast skills are verified against experiments with all data (CTL). The geographical distribution of RMSE from the CTL are presented in Lord et al. (2001b). For both real and simulated experiments, 1BNWIN shows least skill in the northern hemisphere (NH) and globally less skill compare to 1BNTMP showing R_wind have more impact compared to R_temp in both simulation and real. The geographical distribution shows that the impact of R_wind

is slightly weaker in simulation and the impact of R_temp is slightly stronger in the simulation.

In the NH, T1B shows impact over the Pacific for both the real and simulated analysis, where the RMSE between CTL and NTV is larger in the simulation (Lord et al. 2001b). In the 72 hour forecast the impact of T1B spreads out over the NH and NTV shows a similar magnitude of impact compared to 1BNTMP. One of the reasons for the larger impact of T1B in simulation is the lack of measurement error in the simulated data. Under-estimation of the cloud effect in the simulation is another possible reason for the large impact in simulation.

In the southern hemisphere (SH) T1B has the largest impact. Although simulated T1B is supposed to be too good and a stronger impact is expected, the skill reduction in NTV is far larger in real experiments. It is noted that there is a localized large warm SST in south Pacific in the end of February. However, SST in NR is fixed through the period. The impact of this difference is being evaluated.

In the tropics, a large analysis impact of R_temp in the low troposphere. This large analysis impact is partially related to the bias between the NCEP model and NR. Including a bias correction in the data assimilation may be required for reliable OSSEs. (Purser and Derber, 2001).

In order to test sensitivity to observational error, the difference between observation and analysis (o-a) from the real data assimilation is used as the error for the simulated data. This error will give a large-scale correlated error. With (o-a) error, the rejection statistics of simulated experiments become closer to those for real data. With random error too little data are rejected by quality control.

Another deficiency noted was caused by envelope orography. It was found that the large portion of surface data in the real world are located in underground in NR. As results there are much less surface data in the simulation. It is necessary to test with equal number of surface data for simulation and real.

6. SOME INITIAL RESULTS FROM THE OSSE FOR DWL WINDS

Among many candidate instruments for the OSSE, DWL winds heve been simulated by SWA. According to the strategy for bracketing sensitivity experiments (Lord 2001a, Lord 2001b), scanning or non-scanning, various wave lengths and the number of LOS per measurement, are being tested. Sensitivity to weight in the data assimilation is also being tested. For the first four days of assimilation, 14 combinations of DWL with TIB and conventional data were compared. Assimilation for the total one month period has been conducted for selected cases.

DWL data improved the wind fields globally at all levels for all experiments. Major improvement are over tropics while Marseille et al. (2001) showed major impact in SH but did not use T1B data. T1B data are included in this paper and large improvements are achieved by T1B in the SH. The results also show an advantage of a scanning instrument over a non-scanning instrument in the upper troposphere. The number of measurements an indication of observation quality, becomes more important in the lower troposphere. The analysis impact is sensitive to the weight of observations in the assimilation.

DWL winds also need to be evaluated with both the current data distribution and the anticipated future data distribution corresponding to when the DWL data will be used. For this reason, simulated data from at least one advanced sounder (e.g., AIRS), a scatterometer (e.g., ASCAT) and at least the current ACARS data, must be added in the future. More realistically distributed, high-density, CMV data also need to be included.

7. FUTURE PLANS

The calibration will be continued to gain further confidence in OSSE. Various techniques for adding systematic errors will be tested. The simulation procedure of T1B requires further evaluation, including the formulation of observational errors.

In addition to a DWL and AIRS., the Cross Track Infrared Sounder (CrIS), Conically-scanning Microwave Imager/Sounder (CMIS), and the Advanced Technology Microwave Sounder (ATMS) have been proposed as candidate instruments to be tested by OSSEs. We are proceeding to develop appropriate forward models for these instruments.

In order to make reliable recommendations, the techniques for creating simulated observation need to be refined. Addition of large-scale spatially correlated error and systematic error in simulated data may alter the results.

OSSEs also need to be tested with an upgraded techniques for data handling and data assimilation system. Since the amount of data involved in the future instruments increases drastically, effective super-observations to reduce the sizes of data sets needs to be studied (Purser et al. 2001). Including an adaptive correction for the bias in the data assimilation will also be tested (Purser and Derber, 2001).

Future instruments need to be tested with 2001 and future data distributions since the 1993 data distribution is outdated. An alternative NRs for the same period and summer time have also been generated by NASA/DAO and can be used to investigate additional atmospheric regimes. NRs to test northern summer time response is important especially to study the impact on tropical storm prediction.

The evaluation metrics will be expanded to include diagnostics of strength and position of cyclones and jets and a study of extreme events, as well as standard forecast skill scores. Cost-benefit and flight planning will also be studied.

ACKNOWLEDGMENT

We received much assistance from the Data Services Section and Dr. Anthony Hollingsworth of ECMWF in supplying the nature run. Throughout this project NOAA/NWS/NCEP, NASA/DAO and NOAA/NESDIS staffs provided much technical assistance and advice. Especially, we would like to thank W. Yang, R. Treadon, Y. Zhu, W.-S. Wu, M. Iredel, D. Keyser, W. Collins, and R. Kistler of NCEP, G. Brin, S. Bloom and N. Wolfson of DAO, and V. Kapoor, P. Li and W. Wolf of NESDIS. We would like to thank Evan Fishbein of JPL for providing simulation code for AIRS data. Drs. E. Kalnay, W. Baker, J. Yoe and R. Daley provided expert advice. We appreciate the constructive comments from members of the OSSE Review Panel. This project is sponsored by the Integrated Program Office (IPO) for NPOESS and by the NOAA Office of Atmospheric Research (OAR) and the NOAA National Environmental Satellite, Data and Information Service (NESDIS). We thank Drs. Stephen Mango and Alexander

MacDonald, and John Gaynor, Jim Ellickson and John Pereira for their support and assistance in this project.

REFERENCES

Becker, B. D., H. Roquet, and A. Stofflen 1996: A simulated future atmospheric observation database including ATOVS, ASCAT, and DWL. *BAMS*, **10**, 2279-2294.

Derber, J. C. and W.-S. Wu, 1998: The use of TOVS cloud-cleared radiances in the NCEP SSI analysis system. *Mon. Wea. Rev.*, **126**, 2287 - 2299.

Emmitt, G. D., 2000: Systematic errors in simulated Doppler wind lidar observations. http://www.emc.nceo.noaa.gov/resarch/osse/swa/sys_errors.htm

Goldberg, Mitchell D. , Larry McMillin, Walter Wolf, Lihang Zhou, Yanni Qu, and Murty Divakarla, 2001: Operational radiance products from AIRS, AMS 11th Conference on Satellite Meteorology and Oceanography 15-18 October 2001, Madison, Wisconson

Lord, S. J., E. Kalnay, R. Daley, G. D. Emmitt, and R. Atlas 1997: Using OSSEs in the design of the future generation of integrated observing systems. Preprint volume, 1st Symposium on Integrated Observation Systems, Long Beach, CA, 2-7 February 1997.

Lord, S.J., M. Masutani, J. S. Woollen, J. C. Derber, R. Atlas, J. Terry, G. D. Emmitt, S. A. Wood, S. Greco, T. J. Kleespies, 2001a: Observing System Simulation Experiments for NPOESS, *AMS Preprint volume the Fifth Symposium on Integrated Observing Systems. 14-19 January 2001, Albuquerque, NM*

Lord, S.J., M. Masutani, J. S. Woollen, J. C. Derber, R. Atlas, J. Terry, G. D. Emmitt, S. A. Wood, S. Greco, T. J. Kleespies, 2001b: Observing System Simulation Experiments for NPOESS, *AMS Preprint volume the 14th Conference on Numerical Weather Prediction, 30July-2August 2001, Fort Lauderdale, Florida.* 167-171.

Marseille, G. J., A. Stoffelen, F. Bouttier, C. Cardinali, S. de Haan and D. Vasiljevic, 2001: Impact assessment of a doppler wind lider in space on atmospheric atalysies and Numerical weather prediction. KNMI, Contract No.13018/98/NL/GD.

Masutani, M., J.C. Woollen, J.C. Derber, S. J. Lord, J. Terry, R. Atlas, S. A. Wood, S. Greco, G. D. Emmitt, T. J. Kleespies 1999a: "Observing System Simulation Experiments for NPOESS", AMS Preprint volume for the 13th Conference on Numerical Weather prediction. September 1999, Denver Colorado,1-6.

Masutani, M. K. Campana, S. Lord, and S.-K. Yang 1999b: Note on Cloud Cover of the ECMWF nature run used for OSSE/NPOESS project. *NCEP Office Note* No.427

McMillin, L. M., L. Crone and T. J. Kleespies, 1995: Atmospheric transmittance of an absorbing gas. 5: Improvements to the OPTRAN approach. *Appl. Opt.* **34** (36) 1995.

McNally, A. P., J. C. Derber, W.-S. Wu and B.B. Katz, 2000: The use of TOVS level-1 radiances in the NCEP SSI analysis system. *Q.J.Roy. Metorol. Soc.* , **129**, 689-724.

Merrill, R. T., W. P. Menzel, W. Baker, J. Lynch, and E. Legg, 1991. A report on the recent demonstration of NOAA's upgraded capability to derive cloud motion satellite winds. *Bull. Amer. Meteor. Soc.*, **72**, 372-376.

Parrish, D. F. and J. C. Derber, 1992: The National Meteorological Center's spectral statistical interpolation analysis system. *Mon. Wea. Rev.*, **120**, 1747 - 1763.

Purser, R. J. and J. C. Derber, 2001: Unified Treatment of measurement bias and correlation in variational analysis with consideration of the preconditioning problem. *AMS Preprint volume for the 14th Conference on Numerical Weather prediction. July 2001, Fort Lauderdale, Florida.* 467-470.

Purser, R. J. and D. F. Parrish, 2000: A Bayesian technique for estimating continuously varying statistical parameters of a variational assimilation. *NCEP Office Note 429.* (Also submitted to Meteor. And Appl. Phys.)

Purser, R. J., D.F. Parrish and M. Masutani 2001:Meteorological observational data compression; an alternative to conventional "Super-Obbing". *NCEP Office Note* 430.

Saunders, R.W., M. Matricardi and P. Brunel, 1998: An improved radiative transfer model for assimilation of satellite radiances *Q. J. Roy. Meteor. Soc.* **124**.

Schmetz, J. and K. Holmlund, 1992. Operational cloud motion winds from METEOSAT and the use of cirrus clouds as tracers. *Adv. Space Res.*, **12**, 95 - 103.

Velden, C. S., T. L. Olander and S. Wanzong, 1998: The impact of multispectral GOES-8 wind information on Atlantic tropical cyclone track forecasts in 1995. Part 1: Dataset methodology, description and case analysis. *Mon. Wea. Rev.*, **126**, 1202-1218.

6.2 THE GEOSYNCHRONOUS IMAGING FOURIER TRANSFORM SPECTROMETER (GIFTS)

W. Smith*, F.Harrison, D. Hinton, J. Miller, M. Bythe, and D. Zhou
. NASA Langley Research Center, Hampton, VA

H. Revercomb, F. Best, H. Huang, R. Knuteson, D. Tobin, and C. Velden
University of Wisconsin, Madison, WI

G. Bingham, R. Huppi, A. Thurgood, L Zollinger, and R. Epslin
Utah State University, Logan, Utah

R. Petersen
National Oceanic and Atmospheric Administration, Camp Springs Md.

The Geosynchronous Imaging Fourier Transform Spectrometer (GIFTS) combines a number of advanced technologies to observe atmospheric weather and chemistry variables in four dimensions. Large area format Focal Plane detector Arrays (LFPAs) provide near instantaneous large area coverage with high horizontal resolution. A Fourier Transform Spectrometer (FTS) in front of the LFPAs enables atmospheric radiance spectra to be observed simultaneously for all detector elements thereby providing high vertical resolution temperature and moisture sounding information. The fourth dimension, time, is provided by the geosynchronous satellite platform, which enables near continuous imaging of the atmosphere's three-dimensional structure. The key advance that GIFTS achieves beyond current geosyncronous capabilities is that the water-vapor winds will be altitude-resolved throughout the troposphere. GIFTS, will be launched in 2005, as NASA's third New Millennium Program (NMP) Earth Observing (EO-3) satellite mission, and will serve as the prototype of sounding systems to fly on future operational geosynchronous satellites. After a one year validation period in view of North America, the GIFTS will be repositioned to become the Navy's Indian Ocean METOC Imager (IOMI).

1. Introduction

A new era is about to begin in hyper-spectral remote sensing, namely the implementation of hyper-spectral remote sounding systems. The Geosynchronous Imaging Fourier Transform Spectrometer (GIFTS), selected for flight demonstration as NASA's New Millennium Program (NMP) Earth Observing-3 (EO-3) mission, combines new and emerging sensor and data processing technologies to acquire geophysical measurements that lead to revolutionary improvements in meteorological observations and forecasting. The NOAA, Navy, and Air Force are partners with NASA in the GIFTS program; the NOAA will provide the ground processing system to demonstrate the operational utility of the data, the Navy will provide the spacecraft and support the operation of GIFTS after the NMP phase of the program as its Indian Ocean METOC Instrument (IOMI), and the Air Force will provide the launch of the GIFTS-IOMI satellite to geosynchronous orbit using a new Delta IV rocket multiple payload launch capability developed under their Space Test Program (STP).

The GIFTS uses large area format focal plane (LFPA) infrared (IR) detector arrays (128 x 128) in a Fourier Transform Spectrometer (FTS) mounted on a geosyncronous satellite to gather high spectral resolution (0.6 cm $^{-1}$) and high spatial resolution (4-km footprint) Earth infrared radiance spectra over a large geographical area (512-km x 512-km) of the Earth within a 10-second time interval. A low visible light level camera provides quasi-continuous imaging of clouds at 1-km footprint spatial resolution. Extended Earth coverage is achieved by step scanning the instrument field of view in a contiguous fashion across any desired portion of the visible Earth. The radiance spectra observed at each time step are transformed to high vertical resolution (1-2 km) temperature and water vapor mixing ratio profiles using rapid profile retrieval algorithms. These profiles are obtained on a 4-km grid and then converted to relative humidity profiles.

Images of the horizontal distribution of relative humidity for atmospheric levels, vertically separated by approximately 2 km, are constructed for each spatial scan. The sampling period will range from minutes to an hour, depending upon the spectral resolution and the area coverage selected for the measurement. Successive images of clouds and the relative humidity for each atmospheric level are then animated to reveal the motion of small-scale thermodynamic features of the atmosphere, providing a measure of the wind velocity distribution as a function of altitude. The net result is a dense grid of temperature, moisture, and wind profiles which can be used for atmospheric analyses and operational weather prediction. O_3 and CO features observed in their spectral radiance signatures, provide a measure of the transport of these pollutant and greenhouse gases. It is the unique combination of the Fourier transform spectrometer and the large area format detector array (i.e., an imaging interferometer), and the geosyncronous satellite platform, that enables the revolutionary wind profile and trace gas transport remote sensing measurements.

2. The GIFTS Instrument

The optical layout of the GIFTS instrument is shown in Figure 1. The imaging FTS produces the interferometric patterns for spectral separation of scene radiation reaching the detector arrays. To limit the background signal, the FTS is cooled by the first stage of the cryocooler to <150 K. The high data rates generated by the focal plane arrays (FPAs) are reduced by loss-less compression techniques and then passed to the telemetry system by low-power, low-volume, next-generation electronic components.

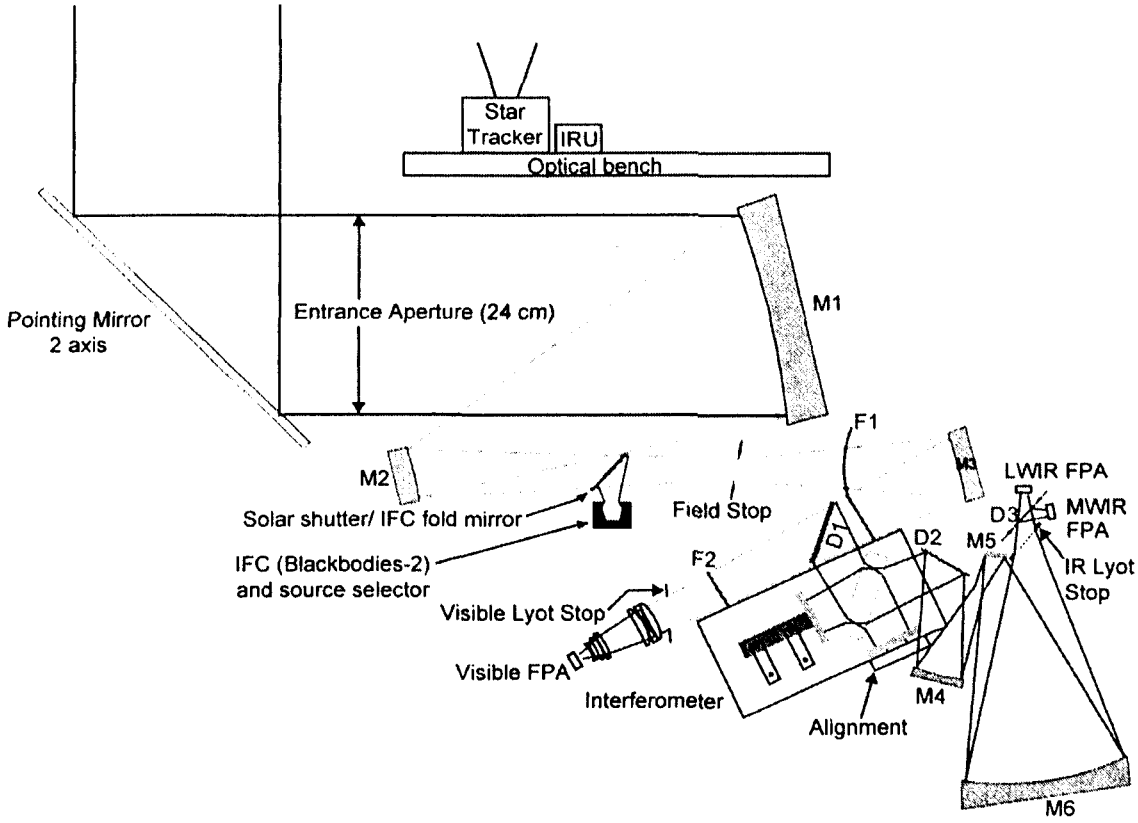

Figure 1. Schematic of GIFTS Sensor Module

GIFTS will view areas of the Earth with a linear dimension of about 500-km, anywhere on the visible disk, for a period between 0.125 and 10.0 sec, depending on the data application (i.e., imaging or sounding). GIFTS uses two detector arrays within a

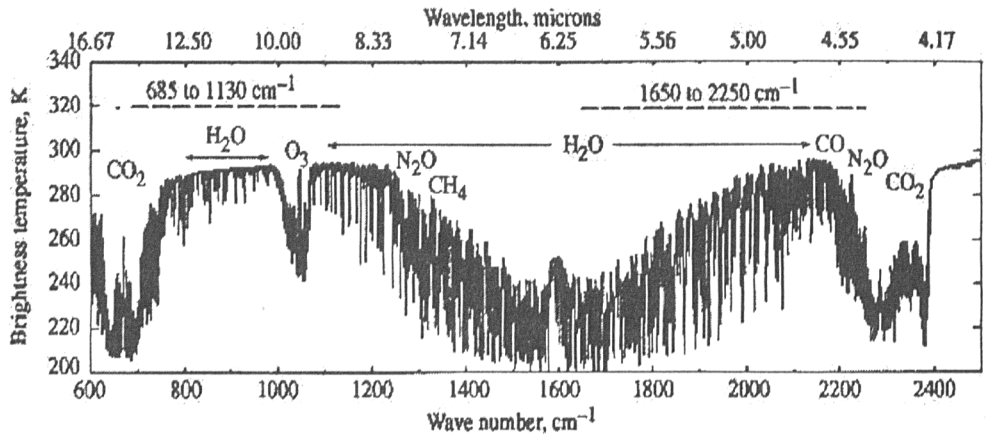

Figure 2: GIFTS spectral coverage with 2 detector arrays with the spectral regions of key radiatively active atmospheric trace gases.

Michelson interferometer to cover the spectral bands, 685 to 1130 cm $^{-1}$ and 1650 to 2250 cm $^{-1}$ (Figure 2), to achieve a wide range of spectral resolutions (figure 3). These spectral characteristics are optimized to achieve all technology/scientific validation objectives of GIFTS, as well as the sounding accuracy desired for a future operational sounding system. The Michelson interferometer, or FTS, approach for geosyncronous satellite applications allows spectral resolution to be easily traded for greater area coverage or higher temporal resolution. The 4-km footprint size of the IR LFPAs enable sounding to the ground under most broken-to-scattered cloud situations and resolving small scale atmospheric water vapor and cloud features required for wind profiling.

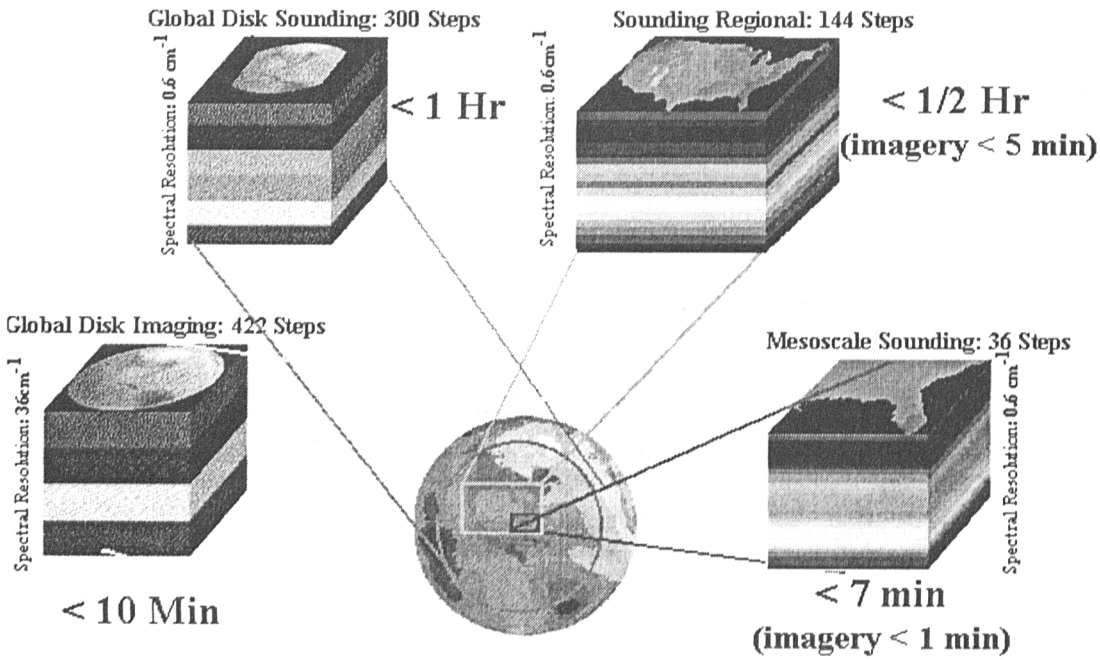

Figure 3. Example operating modes for GIFTS

Figure 3 shows the area coverage, measurement frequency, spectral resolution, and geophysical measurement for example modes of operation for GIFTS. Quasi-continuous imagery of localized areas and minute-interval imagery of large-scale areas can be achieved. Relatively high spectral resolution (36 cm $^{-1}$) full disk imagery will be obtained in less than 10 min. High vertical resolution soundings and atmospheric chemistry measurements of GIFTS require 0.6 cm $^{-1}$ spectral resolution and a longer stare time, thereby reducing the area coverage and/or frequency of observation relative to the imagery mode of operation. Nevertheless, GIFTS will cover a major portion of the visible disk with high vertical resolution soundings in less than one hour; and regions the size of CONUS and surrounding oceans will be observed with a half hourly frequency. This feature is important for obtaining wind profiles from geosyncronous temperature and moisture sounding data.

The sounding performance of GIFTS (figure 4) has been determined by radiance simulation.

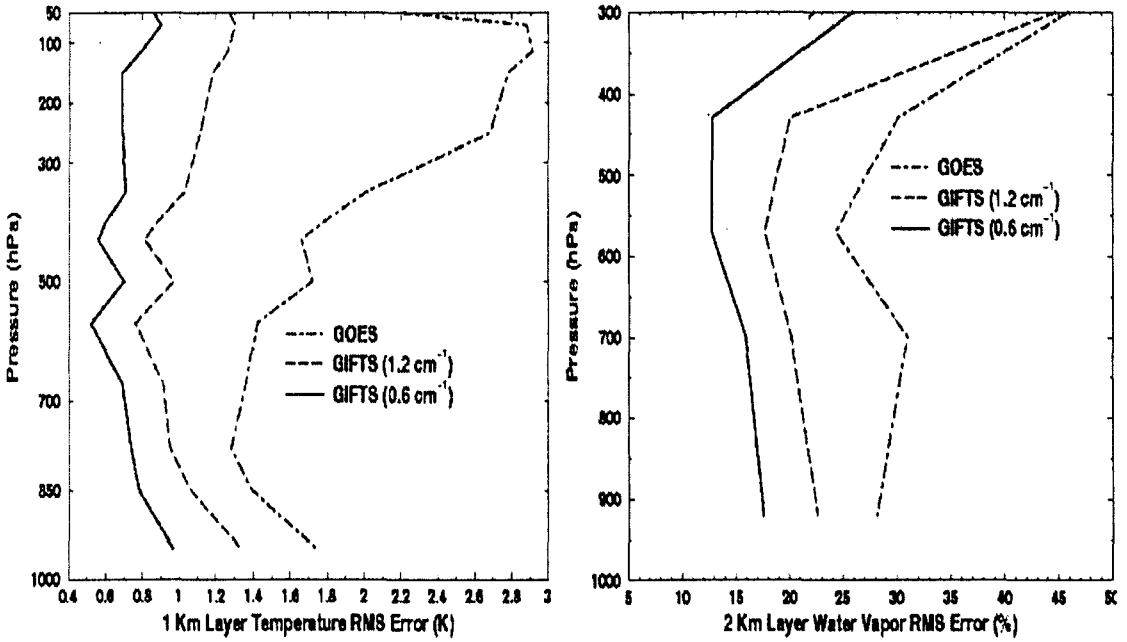

Figure 4: RMS temperature and mixing ratio profile errors for 2 different GIFTS spectral resolutions compared to those associated with the current GOES sounder

The significance of the lower spectral resolution (i.e., 1.2 cm^{-1}) sounding mode is that twice the area coverage, or a doubling of the refresh rate, can be achieved by sacrificing the vertical resolution and, consequently, the accuracy of the sounding products. The radiometric noise and accuracy requirements for the retrieval of temperature and water vapor in the highest spectral resolution (0.6 cm^{-1}) mode with a 10 sec dwell time are: (1) Noise Equivalent Radiance (NEN) in the LW spectral band (685-1130 cm $^{-1}$) <0.2 mW/m^2 sr cm $^{-1}$; (2) NEN in the SW/MW spectral band (1650-2250 cm $^{-1}$) <0.06 mW/m^2 sr cm $^{-1}$; and (3) absolute calibration accuracy better than 1 K brightness temperature for Earth scene brightness temperatures > 190 K for the LW and >240 K for the SW/MW band. Periodic views of onboard references and cold space will be used to realize this high calibration accuracy. Achieving these radiometric requirements for the primary high spectral resolution sounding mode is sufficient to insure the performance of other GIFTS imaging and lower vertical resolution sounding modes. The only other necessary constraints are that the time required to point the field-of-view to an adjacent region on Earth be less than 1 sec and that the

pointing knowledge be better than 0.4 km for wind determination.

3. Aircraft Demonstrations of Measurement Capability

A high spectral resolution (0.25cm-1) and high spatial resolution scanning interferometer sounding system, called the NPOESS Aircraft Sounding Testbed-Interferometer (NAST-I) has been built and flown to provide experimental observations needed to finalize the specifications and to test proposed designs and data processing algorithms for the Cross-track scanning Infrared Sounder (CrIS) to fly on the National Polar-orbiting Operational Satellite System (NPOESS). Because of the selection of the GIFTS to fly on the Earth Observing Three (EO-3) satellite, the data collected by the NAST-I has become an important source of information to test the design characteristics and data processing algorithms for GIFTS as well. NAST-I is a passive infrared (IR) Michelson interferometer that scans the Earth and atmosphere from an aircraft, such as the high-altitude NASA ER-2 research airplane and the Scaled Composites, Incorporated, (SCI) Proteus aircraft. The NAST-I, measures thermal radiation contiguously across the spectral region 3.5-16 microns with a spectral resolution of 0.25 cm^{-1}, which is sufficient for simulating the full spectral measurement capabilities of both the CrIS and the GIFTS. NAST also spatially scans the earth beneath the aircraft with 1-3 km spatial resolution, depending on aircraft altitude, thereby providing three-dimensional images of spectral radiance, and derived products, similar to that to be obtained by the GIFTS. Unlike the GIFTS, however, the NAST-I does not use large focal plane arrays to achieve its imaging capability; instead, it uses a cross-track scanning mirror and the motion of the aircraft to produce a similar result. The NAST retrieval results to be shown were obtained using the eigenvector regression retrieval method as applied to high spectral resolution interferometer data. In this technique, a training sample of historical radiosonde data is used to simulate radiance spectra for the NAST instrument. Eigenvectors are computed; and regression equations, which relate the eigenvector amplitudes to the radiosonde temperature and water vapor values, are derived, assuming a variable number of eigenvectors for the representation of the spectral radiance information. Appropriate random instrumental noise is added to the simulated radiance data set, and retrievals are performed for all cases as a function of the number of eigenvectors. The optimal number of eigenvectors is selected as that number which minimizes the RMS retrieval error for the historical radiosonde data set. This number ranges between 20 and 200, depending upon the variance associated with the historical data set used (such as regional or global, seasonal or annual). The regression equations for the optimal set are then applied to real NAST-I radiance measurements. Since all the radiative transfer calculations and eigenvector decomposition analysis is done "off-line" to the actual data processing, the algorithm is extremely fast when applied to real data. Because of both it's speed and accuracy, the eigenvector retrieval method will be used for the real-time processing of GIFTS data. Figure 5 shows a derived temperature profile and a cross-section for atmospheric relative humidity in the vicinity of Andros Island Bahamas. The spatial detail of the retrieved humidity distribution is particularly noteworthy. Most of the fine scale vertical details shown in the radiosonde validation data are displayed by the NAST soundings.

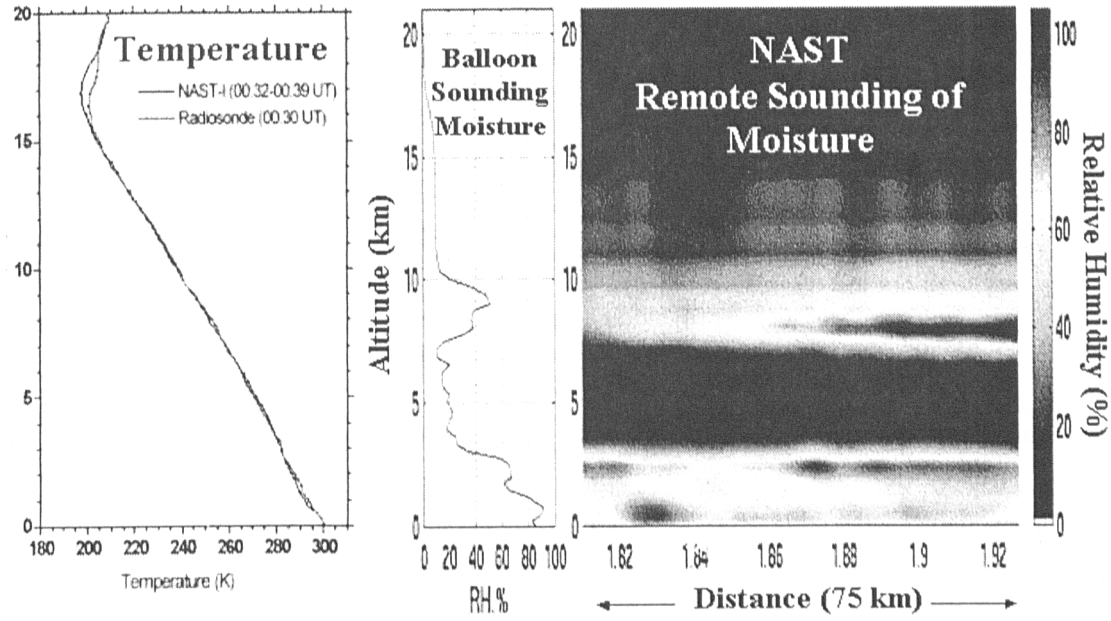

Figure 5: Retrieved and radiosonde Temperature profiles and a 75 km. vertical cross-section of atmospheric relative humidity near Andros Island Bahamas, on September 11, 1998.

More recent results obtained with NAST-I aboard the Proteus flying over a scattered Cirrus deck demonstrate that GIFTS should be able to sound below most scattered-to-broken cloud decks. Figure 6 shows the GOES IR image with the flight track superimposed for the case being presented.

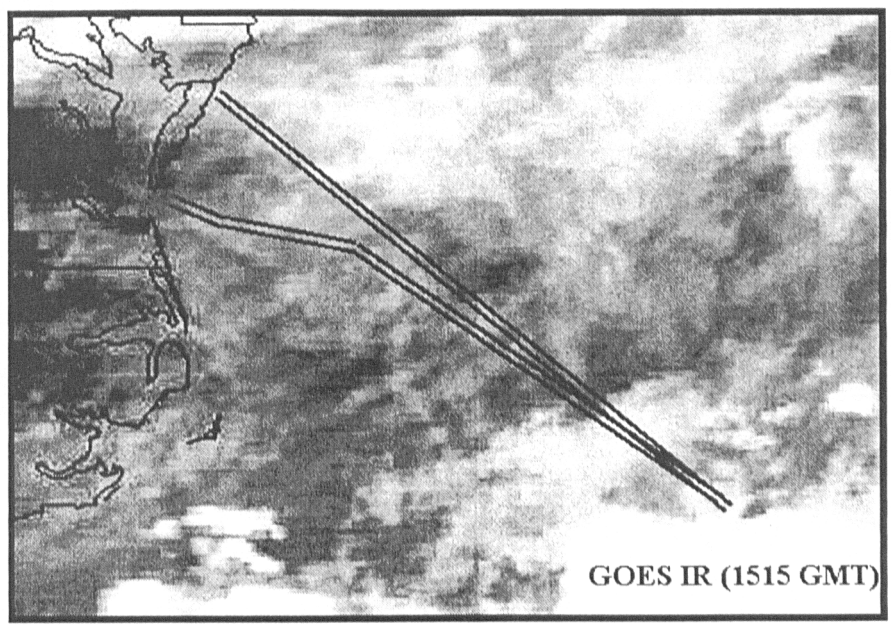

Figure 6: GOES IR image of Cirrus cloud cover associated with Proteus flight track for 07/12/01.

Figure 7 shows the vertical cross-sections of temperature and moisture retrieved along the flight tracks over the Cirrus cloud cover. The vertical streaks in this plot are due to the attenuation by the Cirrus cloud, which can be seen in the cloud image shown at the bottom of this chart. The moisture cross-section indicates that the top of the Cirrus cloud is at about the 9 km level and extends downward to about the 6 km level. Below 6 km, there is a layer of dry air extending down to a marine boundary layer of moisture whose top is at 2 km at the northern end of the track and extends upward to the Cirrus level at the southern end of the track (the middle of figure 7) where deep convection is occurring. As can be seen from figure 7, the GIFTS should be able to resolve and track the movement of important moisture features below a scattered and semi-transparent Cirrus cloud deck. The result is analogous to viewing an object through a window with partially open Venetian blinds. Further validation of this conclusion is shown by the comparison of the retrievals at the northern end of the cross-section with the nearby Wallops Island radiosonde observation, as shown in figure 8 below. It is further noted that since the lower tropospheric water vapor feature signal is inherent in the spectral radiance data for partially cloudy and semi-transparent Cirrus cloud situations, "cloud-clearing" techniques can be used to filter out any cloud artifacts (i.e., the Venetian blinds) from the water vapor imagery prior to the specification of wind profiles from the GIFTS data. This result is a very important finding in support of the use of the GIFTS passive wind sounding technique for achieving high density wind profiles extending into the lower troposphere under the Cirrus shield that exists in the vicinity of active storm systems (e.g., the hurricane environment).

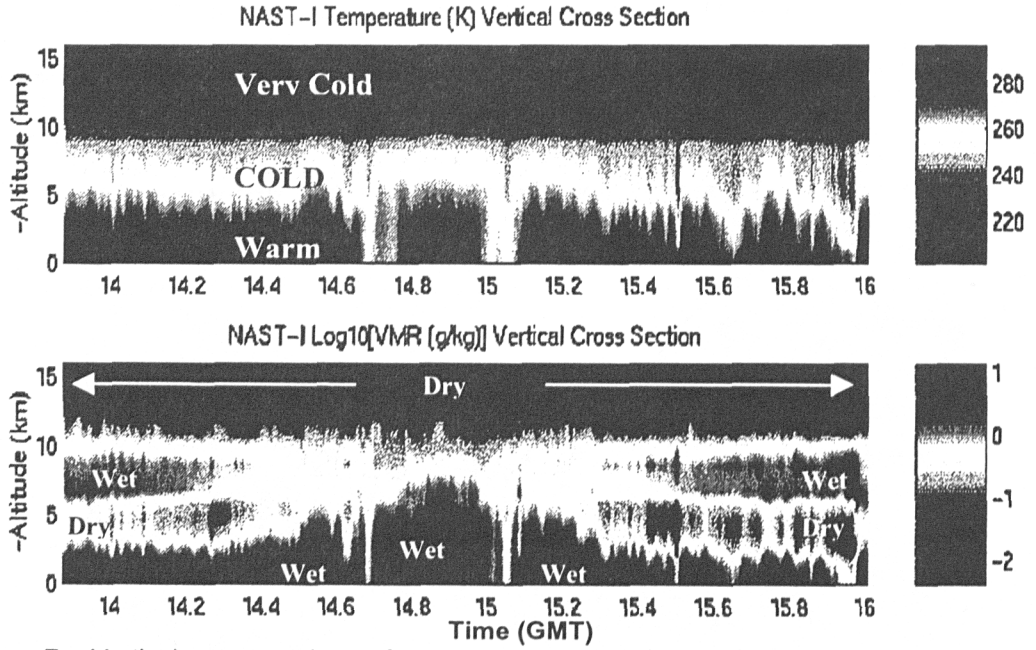

Figure 7: Vertical cross-sections of temperature and moisture observed by NAST-I along the flight track shown in Figure 6.

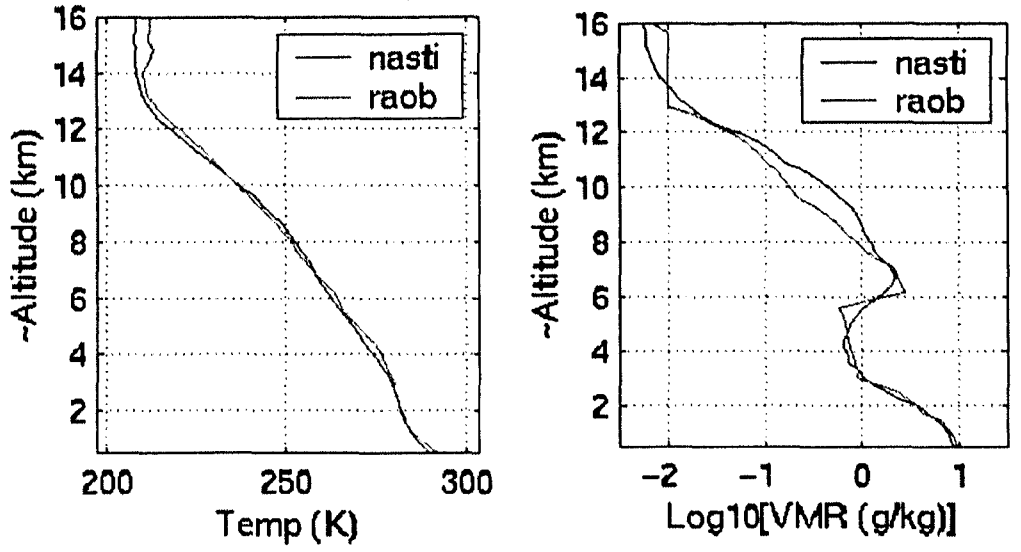

Figure 8: Comparison of Clear air NAST sounding with the Wallops radiosonde (7/12/01).

4. Summary

The first hyper-spectral imaging spectrometer designed for atmospheric sounding, GIFTS, will be orbited aboard a geosynchronous satellite to usher in a new era of high space and time resolution measurements of the atmosphere. Such measurements will lead to revolutionary improvements in our ability to forecast weather and climate. Observations with an airborne Michelson interferometer flying aboard the NASA ER-2 and the SCI Proteus aircraft validate the approach being used to achieve the scientific objectives of the GIFTS-IOMI mission.

5. References

W.L. Smith, H.E. Revercomb, and G. Bingham, 2000: Geostationary Fourier Transform Spectrometer (GIFTS) – The New Millenium Earth Observing-3 Mission. *Current Problems in Atmospheric Radiation*, A. Deepak Publishing, Hampton, Virginia.

Smith, W. L., H. B. Howell, and H. M. Woolf, 1979: The use of interferometric radiance measurements for sounding the atmosphere. J. Atmos. Sci., 36, 566-575.

Smith, W. L., H. E. Revercomb, D. D. LaPorte, L. A. Sromovsky, S. Silverman, H. M. Woolf, H. B. Howell, R. O. Knuteson, and H.-L. Huang, 1990: GHIS - The Goes High Resolution Interferometer Sounder. J. Appl. Meteor., 29, 1189-1204.

Stewart, T. R., C. M. Hayden, and W. L. Smith, 1985: A note on water vapor wind tracking using VAS data on McIDAS. Bull. Amer. Meteor. Soc., 66, 1111-1115.

Velden, C.S., C. M. Hayden, S.J. Nieman, W.P. Menzel, S. Wanzong and J. S. Goerss, 1997: Upper-tropospheric winds derived from geosyncronous satellite water vapor observations. Bull. Amer. Meteor. Soc., 78, 173-195.

Cousins, D and W. L. Smith, 1997: National Polar-Orbiting Operational Environmental Satellite System (NPOESS) Airborne Sounder Testbed Interferometer (NAST-I). SPIE International Symposium on Optical Science, Engineering, and Instrumentation, San Diego, CA, 27 July - 1 August.

Smith, W. L. et al., NAST-I: results from revolutionary aircraft sounding spectrometer, *Proc.SPIE*, 3756, 2–8, 1999.

Zhou, D.K., W.L. Smith, and A.M. Larar, 2000: Temperature and Moisture Retrieval Algorithm Development for the NAST Interferometer. *Current Problems in Atmospheric Radiation*, A. Deepak Publishing, Hampton, Virginia.

6.3

METEOSAT SECOND GENERATION (MSG): CAPABILITIES AND APPLICATIONS

Johannes Schmetz, Paolo Pili, Alain Ratier, Sergio Rota and Stephen Tjemkes
EUMETSAT, Am Kavalleriesand 31, D-64295 Darmstadt, Germany

1. INTRODUCTION

Meteosat Second Generation (MSG) is the new generation of European geostationary meteorological satellites MSG (Meteosat Second Generation). It has capabilities greatly enhanced over the current Meteosat series. The twelve channel imager, called SEVIRI (*Spinning Enhanced Visible and Infrared* Imager), observes the full disk of the Earth with an unprecedented repeat cycle of 15 minutes. Pixels are sampled with a distance of 3 km and the high resolution visible (HRV) channel even has 1 km sampling distance. The spectral channels, at 3.9, 6.2, 7.3, 8.7, 9.7, 10.8 ,12.0 and 13.4 μm and at 0.6, 0.8 *and 1.6 μm, draw on experience* from existing satellites, thus providing continuity of services and facilitating the development of novel operational applications. Thermal IR channels have an onboard calibration and for the solar channels an operational vicarious procedure is developed aiming at an accuracy of 5%. The core operational meteorological products are derived by the Meteorological Product Extraction Facility (MPEF) at EUMETSAT in Darmstadt. Other products will be derived in Satellite Application Facilities (*SAF*), *a decentralised part of the* Applications Ground Segment. As additional scientific *payload MSG carries a* Geostationary Earth Radiation Budget (GERB) instrument. The MSG system is established under a cooperation between ESA and EUMETSAT. The MSG Programme consists of a series of three identical satellites, which will provide *observations and services over at least 12 years. The* first launch of MSG is scheduled for 2002.

A novelty of MSG is the full disk imaging at time intervals of 15 minutes. Studies have shown that this has great potential to improve wind products mainly used for global Numerical Weather Prediction (*NWP*). The repeat cycle also provides unprecedented multi-spectral observations of rapidly changing phenomena (e.g. deep convection) and provides novel insight into rapid changes in cloud microphysics. Ongoing studies reveal the potential for monitoring atmospheric instability.

Corresponding author: Johannes Schmetz, EUMETSAT, Am Kavalleriesand 31, D-64295 Darmstadt, Germany, email: schmetz@eumetsat.de

2. THE SEVIRI INSTRUMENT

The primary mission of MSG is the continuous observation of the Earth's full disk. This is achieved with the Spinning Enhanced Visible and Infrared Imager (SEVIRI) imaging radiometer, a twelve channel imager observing the Earth-atmosphere system with a spatial sampling distance of 3 km in eleven channels. A high-resolution visible (HRV) channel covers half of the full disk with a 1 km spatial sampling. The actual field of view of the channels is about 4.8 km and 1.67 km.

A repeat cycle of 15 *minutes for full-disk imaging* provides unprecedented multi-spectral observations of rapidly changing phenomena (e.g. deep convection) and provides better and more numerous wind observations from the tracking of cloud features. Rapid scans of limited latitude belts are possible with shorter time intervals.

The imaging is performed by combining the satellite spin with the rotation (stepping) of the scan mirror. The images are taken from South to North and East to West. The nominal spin rate is 100 revolutions per minute. The spin axis is nominally parallel to the *North-South axis of the Earth. The scan from South to* North is achieved with 1250 E-W scans; this provides 3750 image lines for channels 1 through 11 (see Table 1) since 3 detectors for each channel are used for the imaging. For the HRV (channel 12) 9 detectors sweep the Earth for one line scan. The number of line scans is programmable such that shorter repeat *cycles can be performed. A full disk image is obtained* within about 12 minutes (see Figure 1). This is followed by the calibration of thermal IR channels (see section 2.2).

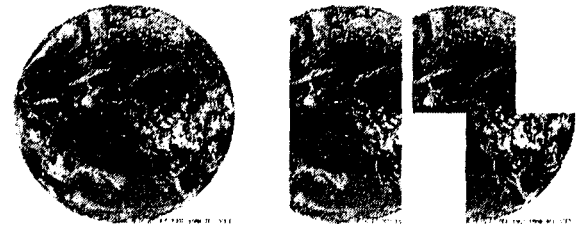

Figure 1: Coverage of MSG for the repeat cycle of 15 minutes for channels 1 through 11 (ref. Table 1). The High resolution Visible (HRV), i.e. channel 12, *covers only half the Earth in E-W, however the* area of imaging can be selected.

Channel No.		Channel Spectral Band in µm		
		λ_{cen}	λ_{min}	λ_{max}
12	HRV	Broadband (silicon response)		
1	VIS0.6	0.635	0.56	0.71
2	VIS0.8	0.81	0.74	0.88
3	NIR1.6	1.64	1.50	1.78
4	IR3.9	3.90	3.48	4.36
5	WV6.2	6.25	5.35	7.15
6	WV7.3	7.35	6.85	7.85
7	IR8.7	8.70	8.30	9.1
8	IR9.7	9.66	9.38	9.94
9	IR10.8	10.80	9.80	11.80
10	IR12.0	12.00	11.00	13.00
11	IR13.4	13.40	12.40	14.40

Table 1: Spectral channel characteristics of SEVIRI providing central, minimum and maximum wavelength of the channels.

Most SEVIRI spectral channels build upon the heritage from other satellites which has the great advantage that the operational user community can readily use existing know-how to utilise SEVIRI radiance observations. The heritage of channels can be summarised as follows:

VIS0.6 and VIS0.8: Known from the Advanced Very High Resolution Radiometer (AVHRR) of the polar orbiting NOAA satellites. Essential for cloud detection, cloud tracking, scene identification, aerosol and land surface and vegetation monitoring.

NIR1.6: Discriminates between snow and cloud, ice and water clouds, and provides aerosol information.

IR3.9: Known from AVHRR. Primarily for low cloud and fog detection (Eyre et.al., 1984). Also supports measurement of land and sea surface temperature at night. For MSG, the spectral band has been broadened to higher wavelengths to improve signal-to-noise ratio.

IR6.2 and IR7.3: Continues mission of Meteosat broadband water vapour channel for observing water vapour and winds. Enhanced to two channels peaking at different levels in the troposphere. Also support height allocation of semitransparent clouds.

IR8.7: Known from the High resolution Infra Red Sounder (HIRS) instrument on the polar orbiting NOAA satellites. The channel provides quantitative information on thin cirrus clouds and supports the discrimination between ice and water clouds.

IR9.7: Known from HIRS and current GOES satellites. Ozone radiances could be used as an input to Numerical Weather Prediction (NWP). As an experimental channel, it will be used for tracking of ozone patterns that should be representative for wind motion in the lower stratosphere. The evolution of the total ozone field with time can also be monitored.

IR10.8 and IR12.0: Well-known split window channels (e.g. AVHRR). Essential to measure sea- and land-surface and cloud top temperatures.

IR13.4: CO_2 absorption channel known from former GOES VAS instrument. It improves height allocation of tenuous cirrus clouds (Menzel et al., 1983). In cloud free areas, it will provide temperature information from the lower troposphere that can be used to infer static instability.

2.1 Radiometric Performance

The radiometric requirements for SEVIRI specify: i) short term error or noise, ii) mid-term drift error, and iii) bias or long-term drift error.

The short term error or noise requirement includes all factors affecting the radiometry during one nominal repeat cycle (15 minutes duration) and applies to in-orbit conditions at End Of Life (EOL). These are essentially: random noise, stability of temperature of detectors, crosstalk and straylight, stability of gain. Table 2 provides the measured performance of SEVIRI on MSG-1 and the specified requirements. Measured performance is based on tests complemented by a prediction of in-flight performances. Except for channel NIR1.6, the predicted in-orbit radiometric performances at EOL are better than the requirements. Thus excellent radiometric image quality can be expected.

The mid-term drift requirement limits the variation of the mean radiometric error in a sequence of nominal images. The requirement for the warm channels is a maximum drift over 1 day (i.e. 96 nominal repeat cycles) of less than 0.1% of the maximum of the dynamic range. The requirement for the cold (i.e. the thermal IR with cooled detectors) channels is a maximum drift between two on-board calibrations of less than 0.05K (or 0.1K for WV6.2 and WV7.3) at the maximum temperature of the dynamic range. The ground tests have shown that the worst case applies to channel IR12.0 requiring an on- board calibration every 10 images. It should, however, be noted that the baseline design of SEVIRI enables to perform one calibration per image cycle.

Channel	Short term radiometr error performances	Short term radiometric error requirements
HRV	0.93 at 1.3 W/(m² sr µm)	1.07 at 1.3 W/(m² sr µm)
VIS0.6	0.37 at 5.3 W/(m² sr µm)	0.53 at 5.3 W/ (m² sr µm)
VIS0.8	0.37 at 3.6 W/(m² sr µm)	0.49 at 3.6 W/(m² sr µm)
NIR1.6	0.25 at 0.75W/(m² sr µm)	0.25 at 0.75 W/(m² sr µm)
IR3.9	0.24K at 300K	0.35K at 300K
WV6.2	0.40K at 250K	0.75K at 250K
WV7.3	0.48K at 250K	0.75K at 250K
IR8.7	0.17K at 300K	0.28K at 300K
IR9.7	0.24K at 255K	1.5K at 255K
IR10.8	0.15K at 300K	0.25K at 300K
IR12.0	0.22K at 300K	0.37K at 300K
IR13.4	0.30K at 270K	1.80K at 270K

Table 2: Noise equivalent radiances and temperatures for the channels of the SEVIRI instrument on MSG-1 compared with the requirements. Values for the thermal IR channels refer to a focal plane temperature of 95K.

The bias and long-term drift requirement specifies the absolute radiometric error (i.e. the difference between the measured radiance and the actual radiance at the input of the instrument). Tests confirmed that the performance for all thermal IR channels is about 0.5 K for typical warm scene temperatures of 300 to 335 K (see also following section on calibration).

2.2 SEVIRI Calibration

The thermal IR channels of SEVIRI are calibrated with an on-board blackbody (Pili, 2000). The relationship between digital counts and the observed radiance is assumed to be linear:

$$C(L) = g\,L(\lambda, T) + C_0$$

Where C(L) is the digital count output from SEVIRI, $L(\lambda, T)$ the measured radiance, λ the wavelength (in practice a spectral interval), T the effective blackbody temperature of an observed scene, g the gain (or calibration coefficient) and C_0 the offset. The assumption of a linear relationship between counts and radiance is valid since small non-linearity are corrected for on ground before applying the linear calibration procedure.
SEVIRI uses the deep space as cold source and an internal blackbody as warm source for the calibration. While the deep space view is obtained by viewing through the complete optical path of the instrument the blackbody is moved into the optical path avoiding the front optics. This design necessitates a correction to be applied to the blackbody calibration considering the optical properties of the front optics, whose characteristics have been measured before launch and whose temperature is monitored continuously. The blackbody can also be heated to allow for the determination of the correction factor. Overall a calibration performance better of about 0.5 K is expected for all thermal IR channels (Pili, 2000).

The solar channels (channels 1 –3 and 12) do not have an on-board calibration but have to rely on a vicarious method based on radiance observations over well-characterised targets (clear-sky desert, clear-sky ocean and optically thick high level clouds) and radiative transfer simulations (Govaerts et al., 2000). This new method of solar channel calibration will achieve an accuracy of the about 5% after the first year of operations as the characterisation of targets improves and quality control parameters will become better tuned.

3. MSG PRODUCTS

The derivation of level 2.0 meteorological products, is performed within the Applications Ground Segment (AGS) which consists of:
1) a central Meteorological Products Extraction Facility (MPEF)
2) a network of satellite Application Facilities (SAF) located at National Weather Services and other institutions of EUMETSAT member states.

3.1 Products from the Central MPEF

The Scenes Analysis (SCE) is the first step and an intermediate product of the MSG MPEF which is further used in the derivation of other products requiring either cloudy or clear pixels. The results of Scenes Analysis algorithm will provide per pixel and repeat cycle:
i) Identification of cloudy and clear pixels and a cloud mask, ii) Identification of scene type for each pixel, iii) Radiances at the top of the atmosphere.
The Scenes Analysis algorithm is based on threshold techniques (e.g. Saunders and Kriebel, 1988). Advantage is taken of the 15 minute repeat cycle by using results of the previous image as first guess in the current image. SCE and Cloud Analysis are described in more detail by Lutz (1999).

Cloud Analysis (CLA) is based on the Scenes Analysis results and provides on a scale of 100 km x 100 km (or better) information about cloud cover, cloud top temperature, cloud top pressure/height and cloud type and phase. An important objective of the Cloud analysis product is to support the generation of the Atmospheric Motion Vectors (AMV). Therefore an intermediate product for each pixel and repeat cycle, which provides the necessary internal input to the Atmospheric Motion Vectors, is derived, but not disseminated. This intermediate (pixel scale) Cloud Analysis is also used for the Cloud Top Height product. It also provides input to the statistical information contained in the off-line Climate Data Sets product.
Cloud Top Height (CTH) is a derived product image, which provides the height of the highest cloud at a super-pixel resolution of 3x3 pixels. This product is for use in aviation meteorology. It provides the heights with a vertical resolution of 300 meter.
Clear Sky Radiance (CSR) gives mean radiances (in $Wm^{-2}\ sr^{-1}\ (cm^{-1})^{-1}$) for cloud-free pixels. Operational NWP centres will use CSR products from the MSG infrared channels in their analyses. The benefit will emerge with the advent of 4-d variational data assimilation systems that have the capability to utilise the frequent time observations from geostationary orbit (e.g. Munro et al., 1998).
Tropospheric Humidity (TH) provides estimates of layer-mean relative humidity for two tropospheric layers. One layer humidity (between about 600 and 200 hPa) is based on 6.3 µm clear sky radiances; this product is also known as UTH (upper tropospheric humidity) from the current Meteosat MPEF. The mean relative humidity of a second layer (between 850 and 350 hPa) uses clear sky 7.3 µm and is named MTH (mid-tropospheric humidity). The algorithm follows the improved UTH retrieval presented in Schmetz et al. (1995).

Atmospheric Motion Vectors (AMV) are the most important product for numerical weather prediction. The tropospheric AMVs will be derived from cloud and water vapour motion using primarily the 0.6 or 0.8 μm channel, the 10.8 μm channel and the 6.2 and 7.3 μm channels, respectively. The capabilities to extract lower stratospheric displacements vectors from ozone will also be exploited.
The product is based on conceptually validated ideas and methods (e.g. Schmetz at al., 1993 and Holmlund, 2001). An important feature, already implemented in the current Meteosat products, is the improved automatic quality control using quality indicators (Holmlund, 1998). The MSG algorithm also features novel concepts, such as i) a wind vector assignment to the exact target position, ii) improved target selection and enhancement, iii) improved quality control which benefits from the fact that wind fields from a single repeat cycle are used to derive a spatially dense final AMV product, iv) improved height assignment for semitransparent cloud tracers.
ISCCP Data Set (IDS) continues the support to the International Satellite Cloud Climatology Programme (ISCCP) providing three different data formats.
High Resolution Precipitation Index (HPI) continues the support to the Global Precipitation Climatology Project (GPCP) and provides the frequency of pixels for classes of brightness temperatures. Since it is indicative of convective (tropical) rainfall the product is confined to the latitudes between 40°S and 40°N.
Climate Data Set (CDS) provides statistical information about the scene classes in a processed segment (nominally 32x32 pixels). It is a concise summary of the radiances observed in a segment and potentially very useful for climatological studies of cloud and radiation fields.
Global Instability Index (GII) is an air mass parameter indicating the stability of the atmosphere at a scale of about 30 km. It is closely related to products from the SAF for Nowcasting and Very Short Range Forecasting, except that the GII is derived globally and disseminated. Based on successful applications and experience by NOAA/NESDIS with GOES lifted index products (Menzel et al., 1998) the idea for the GII emerged. Two algorithms are currently foreseen for the GII product i) a physical retrieval (Ma et al., 1999) and ii) an artificial neural network. Details on GII product are provided in this issue (König et al., 2001).
Total Ozone Product (TOZ) uses the 9.7 μm channel, other SEVIRI channels and correlative data and is derived with a regression algorithm (Orsolini and Karcher, 2000). The ozone observations are useful input for monitoring and forecasting UV radiation at the ground level. Preliminary studies show that ozone observations at high temporal and spatial resolution may provide useful information about the winds in the upper troposphere and lower stratosphere, although the derivation of dense vector fields seems difficult. Alternatively, the ozone observations can be assimilated into a numerical model with a suitable multivariate data assimilation system in which the forecast includes a prognostic equation for ozone (e.g. Riishojgaard, 1996).

3.2 Products from Sattellite Application Facilities (SAF)

Satellite Application Facilities (SAF) are specialised development and processing centres within the EUMETSAT Applications Ground Segment. Utilising specialised expertise in Member States, they will complement the production of meteorological products derived from satellite data at EUMETSATs Central Facilities (the MPEF) and will also distribute user software packages. There are currently seven SAFs. Links to relevant web pages are provided via the EUMETSAT web page www.eumetsat.de/SAF/. A generic list of products, relevant ot the use of MSG, from the Ocean and Sea Ice SAF, the SAF for Land Surface Analysis and the Climate SAF reads as follows:
- Examples of products from the Ocean and Sea Ice SAF include i) Atlantic Sea Surface Temperature, ii) Surface radiative fluxes over the Atlantic, iii) Sea Ice (Polar Atlantic): ice edge/cover, thickness/age.
- Examples of products from the Climate SAF are i) Sea Surface Temperature and sea ice cover, ii) Cloud parameters, iii) Surface radiation budget components, iv) Radiation budget components at TOA, v) humidity products.

- Examples of targeted products from the Land Analysis SAF are i) Vegetation parameters and biophysical indicators, ii) Snow cover, iii) Land Surface Temperature, emissivity and moisture, iv) Short wave and long wave radiation parameters.

Some SAF products are composites and based on multi-mission data including MSG data as one source. It is also noted that the SAF on Nowcasting and Very Short Range Forecasting develops software for a suite of products that can be derived from MSG. The software will be made available for local implementation.

3.3 Development Toward New Applications

The improvement of products will be a continuous task. Several improvements are already planned. For instance, Tjemkes and Watts (2000) report on a research study which investigates new ways to perform a scenes analysis. The new method uses 'optimum estimation' Rodgers (1976) as novel way to infer simultaneously a set of cloud parameters and possibly surface features. This Enhanced Cloud Product (ECP) derives the following cloud micro-physical properties from SEVIRI observations: Optical Thickness, Mean Particle Radius, Cloud Top Temperature, Cloud Top Pressure, and Cloud Phase.

An area for improvement are the Atmospheric Motion Vectors (Holmlund, 2001) where two products will complement the current Day-1 baseline products:

i) Ozone Motion Vectors describe the displacement of total ozone features and include a height assignment of the derived vectors. In the baseline of the MSG-MPEF the use of total ozone product derived from observations in the IR 9.6 channel for the derivation of displacement vectors in the stratosphere was not foreseen. ii) Low Level Winds over Land and Ocean will be an enhancement of the current low-level wind products. It gives the displacement of low level clouds derived from HRVIS, 0.6, 0.8 and 3.9 μm observations. In order to improve the quality of the low level wind field over land a new target selection, image enhancement, and cloud height and tracking procedures are developed that utilise the full capabilities of the SEVIRI instrument. Initial study results are encouraging (Szantai et al., 2000).

MSG will also provide new potential for observing components of the hydrological cycle which undergo rapid changes. Convective cloud processes related to thunderstorms or frontal systems require an appropriate monitoring with a high temporal repeat cycle. Cloud glaciation and precipitation formation occur rapidly and imagery from current geostationary satellites at the 30 minute time scale seem to be inadequate for capturing the transient processes that influence precipitation formation. The change in time of cloud microphysical state as observable from multispectral imagery may provide useful information on the formation of precipitation. Recent work by Rosenfeld and Lensky (2000) shows that microphysical processes, relevant to precipitation, can be observed with multispectral satellite imagery.

MSG also provides novel perspectives for applications over land (see EUMETSAT-SAI Report, 1999) because of its multispectral imagery in the visible, near-infrared and thermal infrared bands. The quantitative application of the visible and near-infrared bands will be facilitated through the development of an accurate operational vicarious calibration (Govaerts, 2000a). An interesting application is the monitoring of the land surface reflectance. The utility of such a product has been demonstrated by Pinty et al. (2000a and b) who derive a Meteosat surface albedo (i.e. confined to the spectral band of the VIS channel of the current generation of Meteosat satellite) with an algorithm accounting for water vapour and ozone absorption, aerosol scattering and surface anisotropy.

4. GERB

The Geostationary Earth Radiation Budget Experiment (GERB) is a visible-infrared radiometer for Earth radiation budget studies (Harries, 2000). It makes accurate measurements of the shortwave (SW) and longwave (LW) components of the radiation budget at the top of the atmosphere. It is the first ERB experiment from geostationary orbit. It measures the solar waveband from 0.32 – 4 μm and the total from 0.32 – 30 μm. The LW from 4 – 30 μm is obtained through subtraction. With a nominal pixel size of about 45 by 40 km (NS x EW) at nadir view it obtains an absolute accuracy better than 2.4 $Wm^{-2}ster^{-1}$ (< 1%) in the SW and better 0.4 $Wm^{-2}ster^{-1}$ for the SW. The channel co-registration with respect to SEVIRI is 3 km at the subsatellite point. The cycle time for full disk is 5 minutes for both channels (15 minutes for full radiometric performance). The derivation of products from GERB is described by Dewitte et al. (2000).

5. CONCLUDING REMARKS

The Meteosat Second Generation (MSG) system will significantly enhance the observation capabilities for rapidly changing phenomena such as cloud and water vapour structures. These will help nowcasting, short range forecasting and numerical weather prediction through improved and more frequent products. The capabilities of MSG are also expected to be of great value to research in various disciplines. Notably investigations of convective phenomena will benefit from the operational 15 minute repeat cycle. It will be a major challenge to enhance the utilisation of the multispectral image data in weather forecasting (e.g. NWP and Nowcasting). Images do contain a wealth of information on cloud and humidity structures which can be used to improve the corresponding analyses of humidity and cloud; however this has only an impact on the very short range forecast unless the wind and mass fields get also adjusted in consistent way. Sequences of images do contain information on dynamical development, which currently is hardly used in a quantitative manner. Future developments of models resolution, the ability of models to represent humidity and cloud features together with the development of 4-d assimilation systems may provide the basis for improved utilisation of the satellites image data (Eyre, 2001).

The current network of Satellite Application Facilities provides the basis for a wide use of the capabilities of MSG in various disciplines in meteorology. More information on MSG is available on the EUMETSAT webpage under www.eumetsat.de (go to Meteosat Second Generation) and www.eumetsat.de/saf/.

6. REFERENCES

Eyre, J., Brownscombe, J. L., Allam, R. J., 1984: Detection of fog at night using Advanced Very High Resolution Radiometer (AVHRR) imagery. Meteorological Magazine, 113, 1984.

Eyre, J., 2001: Planet Earth seen from space: Basic concepts. In seminar proceedings on 'Exploitation of the new generation of satellite instruments for numerical weather prediction. ECMWF Seminra, 4 – 8 September 2000, p. 5 –19.

Dewitte, S., N. Clerbaux, L. Gonzalez, A. Hermans, A. Ipe, A. Joukoff and G. Sadowski, 2000: Generation of GERB unfiltered radiances and fluxes. Proceedings of the 2000 EUMETSAT Meteorological Satellite Data Users' Conference, Bologna, EUM-P29, p. 72 – 78.

EUMETSAT and SAI, 1999: Meteosat Second Generation Opportunities for Land Surface Applications. Report compiled by J. Cihlar, A. Belward and Y. Govaerts, EUM SP 01, pp. 67.

Govaerts, Y. A. Arriaga and J. Schmetz, 2000a: Operational vicarious calibration of the MSG/SEVIRI solar channels. To appear in Advances in Space Research.

Harries, J.E., 2000: The Geostationary Earth radiation Budget experiment: Status and Science. *Proceedings* of the 2000 EUMETSAT Meteorological Satellite Data Users' Conference, Bologna, EUM-P29, p. 62 – 71.

Holmlund, K., 1998: The utilisation of statistical properties of satellite-derived atmospheric motion vectors to derive quality indicators. Wea. Forecasting, 13, 1093 –1104.

Holmlund, K., 2001: Atmospheric Motion Vectors with Meteosat Second Generation, This issue.

König, M., S. Tjemkes and J. Kerkmann, 2001: Atmospheric instability parameters derived from MSG SEVIRI observations. This issue.

Lutz, H J, 1999: Cloud processing for Meteosat Second Generation. EUMETSAT Technical Department, Technical Memorandum No. 4, pp. 26.

Ma, X.L., T. Schmit and W.L. Smith, 1999: A non-linear retrieval algorithm – its application to the GOES-8/9 sounder. J. Appl. Meteorol., 38, 501 – 513.

Menzel, W.P., W.L.Smith and T.R. Stewart, 1983: Improved cloud motion wind vector and altitude assignment using VAS. Journal of Climate and Applied Meteorology, 22, 377-384.

Menzel, W.P., F.C. Holt, T.J. Schmit, R.M. Aune, A.J. Schreiner, G.S. Wade and D.G. Gray, 1998: Application of GOES-8/9 soundings to weather forecasting and nowcasting. Bull. Am. Meteor. Soc., 79, 2059 - 2077.

Munro, R., G. Kelly, M. Rohn and R. Saunders, 1998: Assimilation of Meteosat radiance data within the 4dvar system at ECMWF. Proceedings of the 4th International Winds Workshop, Saanenmöser, Switzerland, 20 – 23 October 1998, EUM Publication P 24, 299 – 306.

Orsolini, Y.J. and F. Karcher, 2000: Total-ozone imaging over North America with GOES-8 infrared measurements. Q. J. R. Meteorol. Soc., 126,1557 – 1561.

Pili, P., 2000: Calibration of SEVIRI. Proceedings of 'The 2000 EUMETSAT Meteorological Satellite Data Users' Conference', Bologna, Italy, 29 May – 2 June 2000, EUM P-29, p. 33 – 39.

Pinty, B., Roveda, F., Verstraete, M.M., Gobron, N., Govaerts, Y., Martonchik, J.V., Diner, D.J., and Kahn, R.A. (2000a) Surface albedo retrieval from Meteosat: Part 1: Theory, Journal of Geophysical Research, Vol. 105, 18099-18112.

Pinty, B., Roveda, F., Verstraete, M.M., Gobron, N., Govaerts, Y., Martonchik, J.V., Diner, D.J., and Kahn, R.A. (2000b) Surface albedo retrieval from Meteosat: Part 2: Applications, JGR, Journal of Geophysical Research, Vol.105, 18113-18134.

Riishojgaard, L. P. On four-dimensional variational assimilation of ozone data in weather prediction models. Q. J. R. Meteorol. Soc., 122, 1545-1571, 1996.

Rodgers, C., 1976: Retrieval of atmospheric temperature and composition from remote measurements of thermal radiation. Rev. Geophys. And Space Physics.

Rosenfeld, D., and I.W. Lensky, 2000: Satellite-based insights into precipitation formation processes in continental and maritime clouds. Bull. American Meteorol. Soc., 79, 2457 –2476.

Saunders R.W. and K.T. Kriebel, 1988: An improved method for detecting clear sky and cloudy radiances from AVHRR data. Int. J. Remote Sensing, 9, 123-150.

Schmetz J., K. Holmlund, J. Hoffman, B. Strauss, B. Mason, V. Gaertner, A. Koch and L. van de Berg, 1993: Operational cloud motion winds from Meteosat infrared images, J. Appl. Met, 32, 1206-1225.

Schmetz, J., C. Geijo, W.P. Menzel, K. Strabala, L. van de Berg, K. Holmlund and S. Tjemkes, 1995: Satellite observations of upper tropospheric relative humidity, clouds and wind field divergence. Beitr. Phys. Atmosph., 68, 345 - 357.

Szantai, A., F. Desalmand, M. Desbois and P. Lecomte, 2000: Tracking low-level clouds over Central Africa on Meteosat images. Proceedings of 'The 2000 EUMETSAT Meteorological Satellite Data Users' Conference', Bologna, Italy, 29 May – 2 June 2000, EUM P-29, p. 813 – 820.

Tjemkes, S.A. and J. Schmetz, 1997: Synthetic Satellite Radiances using the Radiance Sampling Method, J. Geophys. Res., Vol. 102(D2), 1807-1818.

Tjemkes, S. and P. Watts, 2000: Cloud properties from Meteosat. Proceedings of the 2000 EUMETSAT Meteorological Satellite Data Users' Conference, Bologna, EUM-P29, p. 314 – 317.

Velden, C. S., D. Stettner and J. Daniels, 2000: Wind vector fields derived from GOES rapid-scan imagery. Proceedings of the 10th Conference on Satellite Meteorology and Oceanography. 9 – 14 January 2000, Long Beach California, American Meteorological Society, p. 20 - 23.

Dr Donald E. Hinsman *
Senior Scientific Officer
WMO Satellite Activities Office

1. INTRODUCTION

The Thirteenth World Meteorological Congress, (Cg-XIII) held in May 1999 recognized that a need existed for WMO to convene direct discussions with operators of environmental satellites to address policy and important funding issues. WMO agreed that, because of the long-term nature of most issues and the expected large investments required, such a dialogue would be mutually beneficial between appropriate high-level representatives of WMO and operators of environmental satellites. In particular, WMO felt that it should receive advice from those entities that were providing satellite systems that required major investment in order to meet WMO Member needs, including those missions of a research nature not normally included in the space-based component of the World Weather Watch's (WWW) Global Observing System (GOS). WMO thought it appropriate to have discussions with those satellite operators who had the capability, or would have the capability, to provide data, products and services in support of WMO Programmes and international projects and activities sponsored by WMO. WMO also recognized that satellite operators needed to receive WMO approved requirements to help justify the necessary financial investments. As a result, WMO agreed to the establishment of Consultative Meetings on High-Level Policy on Satellite Matters and endorsed the guidelines for such meetings (WMO No. 915)

The First Consultative Meeting on High-Level Policy on Satellite Matters was held at the World Meteorological Organization (WMO) Headquarters in Geneva, Switzerland from 22 to 23 January 2001. The recommendations from the First Consultative Meeting were insightful and will have a profound impact on WMO. The immediate impact will be an expansion of the space-based component of the GOS to include relevant Research and Development satellite missions which will enable WMO Members to provide improved meteorological and hydrological services due to the availability of new satellite data, product and services. The recommendations have already been formally endorsed by the WMO Executive Council at its fifty-third session held in June, 2001 and activities related to their implementation have commenced.

Corresponding author address: D.E. Hinsman, World Meteorological Organization, Case postale No. 2300, 1211 Geneva 2, Switzerland; e-mail: hinsman@www.wmo.ch

2. PRESENT SPACE-BASED COMPONENT OF THE GLOBAL OBSERVING SYSTEM

Before, reviewing the specific recommendations endorsed by the WMO Executive Council, it is appropriate to first consider the present configuration of the space-based component of the GOS. There are two major constellations in the current space-based component of the GOS (see Figure 1). One constellation is the various geostationary satellites, which operate in an equatorial belt and provide a continuous view of the weather from roughly 70°N to 70°S. At present there are satellites at 0° longitude and 63°E (operated by the European Organisation for the Exploitation of Meteorological Satellites - EUMETSAT), a satellite at 76°E (operated by the Russian Federation), a satellite at 105°E (operated by the People's Republic of China), a satellite at 140°E (operated by Japan), and satellites at 135°W and 75°W (operated by the USA).

The second constellation in the current space-based GOS comprises the polar-orbiting satellites operated by the Russian Federation, the USA and the People's Republic of China. The METEOR-3 series has been operated by the Russian Federation since 1991. The polar satellite operated by the USA is an evolutionary development of the TIROS satellite, first launched in April 1960. The present NOAA series, based on the TIROS-N system, has been operated by the USA since 1978. FY-1C, the third in the series of China's polar-orbiting satellites, is now operational. These spacecraft provide coverage of the polar regions beyond the view of the geostationary satellites and fly at altitudes of 850 to 900 km.

The ability of geostationary satellites to provide a continuous view of weather systems make them invaluable in following the motion, development, and decay of such phenomena.

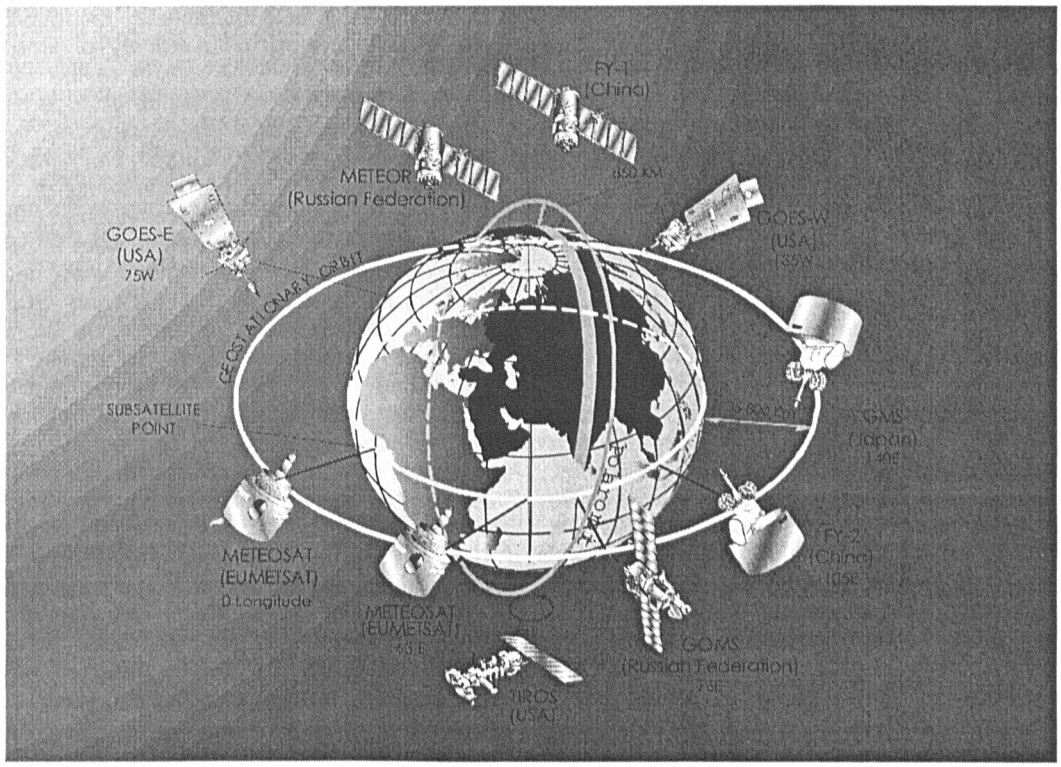

Figure 1, Present space-based component of the Global Observing System

Even such short-term events such as severe thunderstorms, with a life-time of only a few hours, can be successfully recognized in their early stages and appropriate warnings of the time and area of their maximum impact can be expeditiously provided to the general public. For this reason, its warning capability has been the primary justification for the geostationary spacecraft. Since 71 per cent of the Earth's surface is water and even the land areas have many regions which are sparsely inhabited, the polar-orbiting satellite system provides the data needed to compensate the deficiencies in conventional observing networks. Flying in a near-polar orbit, the spacecraft is able to acquire data from all parts of the globe in the course of a series of successive revolutions. For these reasons the polar-orbiting satellites are principally used to obtain: (a) daily global cloud cover; and (b) accurate quantitative measurements of surface temperature and of the vertical variation of temperature and water vapour in the atmosphere. There is a distinct advantage in receiving global data acquired by a single set of observing sensors. Together, the polar-orbiting and geostationary satellites constitute a truly global meteorological satellite network.

3. THE FUTURE SPACE-BASED COMPONENT OF THE GLOBAL OBSERVING SYSTEM

As part of the preparations for the First Consultative Meeting on High-Level Policy on Satellite Matters, a review of the support provided by the present Research and Development (R&D) satellite missions to WMO Programmes was made. The review highlighted the significant contributions already made by R&D satellite missions in support of WMO Programmes. WMO was convinced of the value in articulating the positive impacts experienced by its Members in utilizing data from R&D satellite missions. Feedback from the operational user community to the satellite agencies was identified as crucial and pivotal in highlighting the potential value of R&D data. In order to maximize the usefulness of R&D data, early involvement of the users was deemed essential. It was recognized that one of the

benefits from utilizing R&D satellite data would be a learning process for future systems. Additionally, it would be necessary, where appropriate, to identify impacts on operations within the NMHSs as well as to find where limitations to data access to R&D data occurred. WMO stressed that access to R&D data should be expanded by the satellite operators with the expectation that the impact in operational use would be increased.

Thus, WMO reaffirmed the need to develop persuasive arguments related to the impacts of satellite data justified through feedback from the operational user community. In doing so, it agreed to prepare a report that would be a synthesis of input from the operational user communities on the utility of existing R&D data including persuasive arguments related to their impacts from R&D satellite missions. Furthermore, it suggested that an active interaction between R&D satellite agencies with missions planned for the near-future and perspective operational users be established. Furthermore, it suggested that an active interaction between R&D satellite agencies with missions planned for the near-future and perspective operational users be established.

In recognizing that there were substantial differences between operational meteorological and Research and Development satellite missions, WMO developed and endorsed the *Guidelines for requirements for observational data from operational and R&D satellite missions* (see Chapter 4) in order to provide operational users a measure of confidence in the availability of operational and R&D observational data, and data providers with an indication of its utility.

WMO recognized that there was an increasing convergence between research and operational requirements for the space-based component of the GOS and that it should seek to establish a continuum of requirements for observational data from R&D satellite missions to operational missions. These requirements should be prioritized in the light of both scientific priorities and practicalities and cross-mapped against the needs of the scientific disciplines and Earth system components embraced by WMO, including areas such as the atmosphere, oceans and hydrology, observations needed to improve the monitoring and forecasting/prediction of weather and climate, and impacts of weather and climate variability on natural, social and economic resources. The establishment and maintenance of this continuum of requirements would require a vigorous interactive dialogue fostered by WMO amongst data users, operational satellite providers and R&D agencies. Commitments to address these requirements would allow an evolution of the space-based component of the GOS that would help characterize the total Earth and climate system on a variety of time and space scales and would also provide for the effective transition of research to operational platforms based on the progression of scientific understanding and maturity of required technologies. The global monitoring of water resources (water cycle), ecosystems (carbon cycle), snow and ice and others were important categories in which observations were needed to improve prediction models and address global impacts. Issues and questions related to research categories such as these had proceeded well beyond the research domain and reflected items raised by policy makers and the general public. Consequently, such research categories were becoming, *de facto*, operational needs that would have to be addressed. The existing operational meteorological satellites in geostationary and low earth orbit (LEO) were the best starting point for defining an evolutionary and flexible architecture for the future GOS. WMO envisaged that such a system should be flexible enough to: (1) accommodate proven and existing operational meteorological and other related environmental observations and services; (2) enhance these capabilities based on evolution of scientific understanding and technological innovations; and (3) adopt new and mature capabilities and provide the associated services mandated by emerging requirements.

WMO also reviewed possible configurations for the space-based component of the GOS that included R&D missions as well as the existing constellations of environmental geostationary and near-polar-orbiting satellites. In reviewing the basis for the need to propose new configurations, WMO recalled the requirements setting process within WMO. It noted that it followed a process that resulted in a hierarchical set of requirements. At the highest level, WMO was guided by its Long-term Planning Process. The Fifth Long-term Plan was the current plan and spanned the time frame 2000 to 2009. WMO also noted, that in the nearer term, its four year Programme and Budget contained guidance, objectives, opportunities and challenges that were based on the long-term objectives. WMO recalled that detailed observational requirements for the various application areas found within the WMO and supported programmes were available. Furthermore, the Commission for Basic System in meeting its mandate to provide the basic infrastructure for all WMO Programmes was already considering a redesign of the GOS.

WMO recalled that the Rolling Review of Requirements (RRR) process had been formally approved by the Commission for Basic Systems. The RRR process had four distinct steps: a compilation and review of observational requirements resulting in a consolidated set of observational requirements unique to an application area, development of expected performances for both *in situ* and satellite-based observing systems, an objective comparison of how well the requirements were met by the observing systems, and a Statement of Guidance that was an evaluation of the objective comparison by experts in the various application areas. WMO has conducted and published three such Statements of Guidance as WMO Satellite Activities Technical Documents (TD No. 913, TD No. 992, TD No. 1052).

In view of the existing process within WMO to provide a hierarchical set of requirements, WMO felt that the most appropriate manner to satisfy the full suite of present requirements, while recognizing the capabilities of both operational meteorological and Research and Development satellites, would be to expand the present definition of the space-based component of the GOS to include Research and Development satellites, complementing the existing two operational meteorological satellite constellations (geostationary and near-polar-orbiting). Enhancements to the overall space-based component of the GOS would be incremental as new contributions from the R&D satellites were realized. WMO agreed that the expansion of the definition should be through a resolution by WMO constituent bodies, especially the Commission for Basic Systems, thus formalizing the high-level system requirements that would provide the necessary observational data for WMO and supported programmes.

Therefore, WMO at the fifty-third session of its Executive Council requested the Commission for Basic Systems to review, as a matter of urgency, the space-based component of the GOS with a goal of defining an overall system that included appropriately identified R&D satellite missions. The Commission should be guided by the WMO process for its hierarchical set of requirements in order to ensure that the new space-based component would be justified by WMO needs.

WMO also encouraged its Commission for Basic Systems to be forward looking in proposing enhancements to the space-based component of the Global Observing System. It should account for the differences between operational environmental satellites and R&D satellites. There were different levels of maturity within the various R&D satellites. Flexibility and adaptability must be included into the new design. Those Research and Development space agencies that have or will have satellite missions contributing to WMO Programmes and supported Programmes have been approached to establish a dialogue towards including their missions into the space-based component of the GOS.

WMO suggested that CBS review and make appropriate changes to the definitions as contained in the Guide and Manual for the GOS for the present polar-orbiting and geostationary satellites. The changes should be flexible enough to: (1) accommodate proven and existing operational meteorological and other related environmental observations and services; (2) enhance these capabilities based on the evolution of scientific understanding and technological innovations; and (3) adopt new and mature capabilities and provide the associated services mandated by emerging requirements such as, but not limited to:

- Improved understanding of the structure and dynamics of the atmosphere through, for example, soundings of temperature and humidity, improved wind profiles and better rainfall estimates;
- Improved knowledge of the ocean structure and circulation through, for example, operational surface wind vectors and ocean surface topography;
- Better knowledge of the chemistry of the atmosphere, for example, through measurement of ozone, carbon dioxide, and other trace gases;
- Better understanding of the changes in the terrestrial and marine ecosystems and their role in the carbon cycle;
- Improved knowledge of the cycling of water and energy through the earth system to enable better management of global fresh water resources;
- Increased emphasis on calibrated instruments with a view to a better understanding of climate change;
- Improved global coverage from geostationary orbit using at least six operational spacecraft;
- Improved detection and monitoring of hazardous atmospheric phenomena such as fog and volcanic ash.

4. GUIDELINES FOR REQUIREMENTS FOR OBSERVATIONAL DATA FROM OPERATIONAL AND R&D SATELLITE MISSIONS

As noted earlier, there are substantial differences between Research and

Development and operational meteorological satellite missions, e.g., data access, data continuity and data policy. The following are the *Guidelines for Requirements for Observational Data from Operational and R&D Satellite Missions* as agreed upon by the fifty-third session of the WMO Executive Council. The Guidelines serve to provide a basis for using Research and Development satellite data within an operational context.

Preamble

Whilst there is a distinction between operational and research satellite programmes, there is an increasing convergence between their requirements for the space-based component of the Global Observing System and WMO should seek to establish a continuum of requirements for observational data from R&D satellite missions to operational missions. These requirements should be prioritized in the light of both scientific priorities and practicalities and cross-mapped against the needs of the scientific disciplines and Earth system components embraced by WMO, including areas such as the atmosphere, oceans and hydrology, observations needed to improve the monitoring and forecasting and prediction of weather and climate, and impacts of weather and climate variability on natural, social and economic resources. The establishment and maintenance of this continuum of requirements require a vigorous interactive dialogue fostered by the WMO amongst data users, operational satellite providers and R&D agencies. Commitments to address these requirements should allow an evolution by the space-based component toward a comprehensive Global Observing System that should help characterize the total Earth and climate system on a variety of time and space scales and should also provide for the effective transition of research to operational platforms based on the logical progression of scientific understanding and maturity of required technologies. The global monitoring of water resources (water cycle), ecosystems (carbon cycle), snow and ice and others are important categories in which observations are needed to improve prediction models and address global impacts. Issues and questions related to research categories such as these have proceeded well beyond the research domain and reflect items raised by policy makers and the general public. Consequently, such research categories have become, *de facto*, operational needs that should be addressed. The existing operational meteorological satellites in geostationary and low earth orbit (LEO) are the best starting point for defining an evolutionary and flexible architecture for the future Global Observing System. It is envisaged that such a system should be flexible enough to: (1) accommodate proven and existing operational meteorological and other environmental observations and services; (2) enhance these capabilities based on evolution of scientific understanding and technological innovations; and (3) adopt new and mature capabilities and provide the associated services mandated by emerging requirements.

Guidelines

1. In order to maximize the impact of data from operational and R&D missions and the associated expenditures in resources (manpower and financial) by operational users, there should be agreed upon guidelines in the form of requirements that must be met by space agencies responsible for potential R&D missions that would contribute to the space-based component of the Global Observing System. These requirements need further definition but, as a preliminary set, should include considerations relating to:

(a) Data dissemination;
(b) User preparation for R&D data; and
(c) Data continuity for sufficient periods of time.

2. The agreed Guidelines for the Requirements for operational and R&D missions that contribute to the space-based component of the Global Observing System are, in outline, that:

(a) Data dissemination should be:

(i) Available to WMO Members taking into consideration user and provider data policies;
(ii) In data formats (standardized where possible but well publicised in all cases to allow data access);
(iii) Timely;
(iv) Readily accessible from supported infrastructures (capabilities beyond current GTS capabilities must be established) (If possible, use the existing dissemination procedures of the meteorological satellite operators);
(v) Based on a dialogue, encouraged and facilitated by WMO, between users and satellite agencies concerning data dissemination on a regional basis;

(b) User preparation for R&D data implies that:

(i) Resources to enable use of research data must be provided;

(ii) Training new users of new data and products must be organized and financially supported;

(iii) On-line training systems, such as the Virtual Laboratory concept, should be used;

(iv) International working groups should be used as fora for information;

(v) Spending on technology must be supplemented with resources for utilization;

(vi) WMO programmes using satellite data should put in place systems to provide early operational evaluations and feedback to satellite operators concerning the utility and benefits they have derived from usage of the data;

(vii) WMO should encourage activities that focus on a dialogue between users and the satellite agencies concerning data usage on a regional basis;

(c) Data continuity for sufficient periods of time requires that:

(i) A clear path for research capabilities to be adopted by operational agencies must be identified;

(ii) Political high level agreements must be encouraged;

(iii) More active participation of research satellite agencies in operational coordination and planning groups must be encouraged and expanded;

(iv) Opportunities need to be fostered for satellite remote sensing capabilities to evolve;

(v) R&D satellite operators must identify and confirm an intention to provide data for an identified period of time;

(vi) There be continuity of calibration of data sets (bias estimations);

(vii) Responsibility for long-term maintenance of data sets be identified.

REFERENCES

WMO Executive Council, fifty-second session, Geneva, 16-26 May 2000, WMO-No. 915, Annex II, pg 67.

Preliminary Statement of Guidance Regarding How Well Satellite Capabilities Meet WMO User Requirements in Several Application Areas, WMO TD No. 913 (SAT-21).

Statement of Guidance Regarding How Well Satellite Capabilities Meet WMO User Requirements in Several Application Areas, WMO TD No. 992, (SAT-22).

Statement of Guidance Regarding How Well Satellite and *In Situ* Sensor Capabilities Meet WMO User Requirements in Several Application Areas, WMO TD No. 1052 (SAT-26).

P3.49 **Meandering Sea Surface Temperature of April 2001**

Serge Hagan-Deschamps, MSC, Dartmouth, NS, Canada

NOAA Sea Surface Satellite Imagery Composites for storm watch

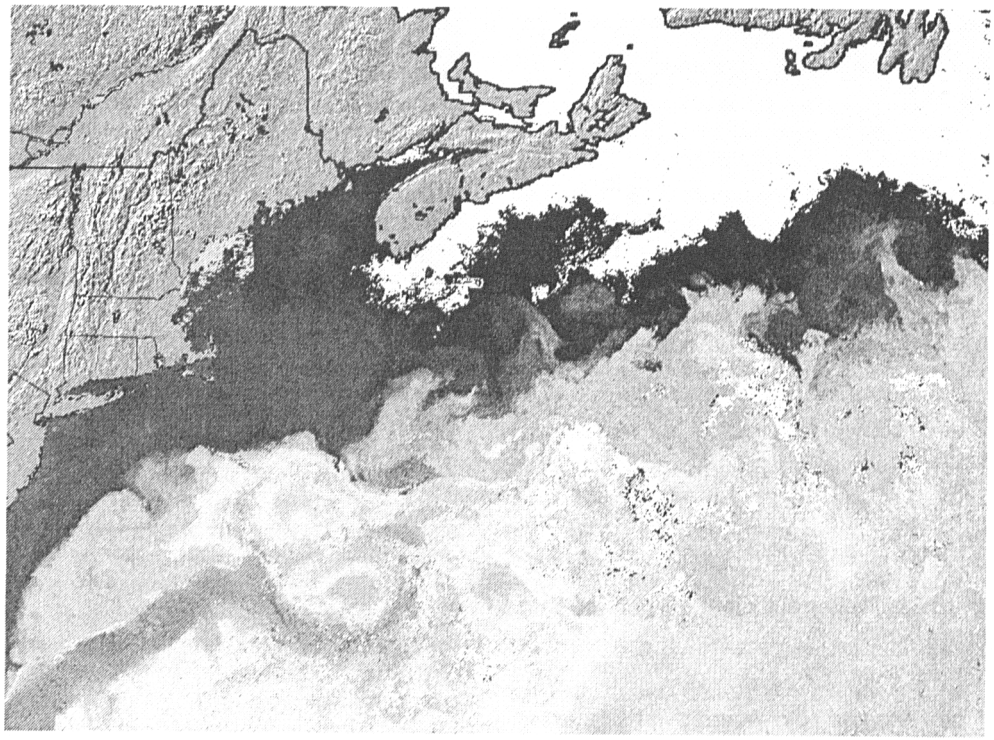

Ocean Feature Analysis for April 17, 2001

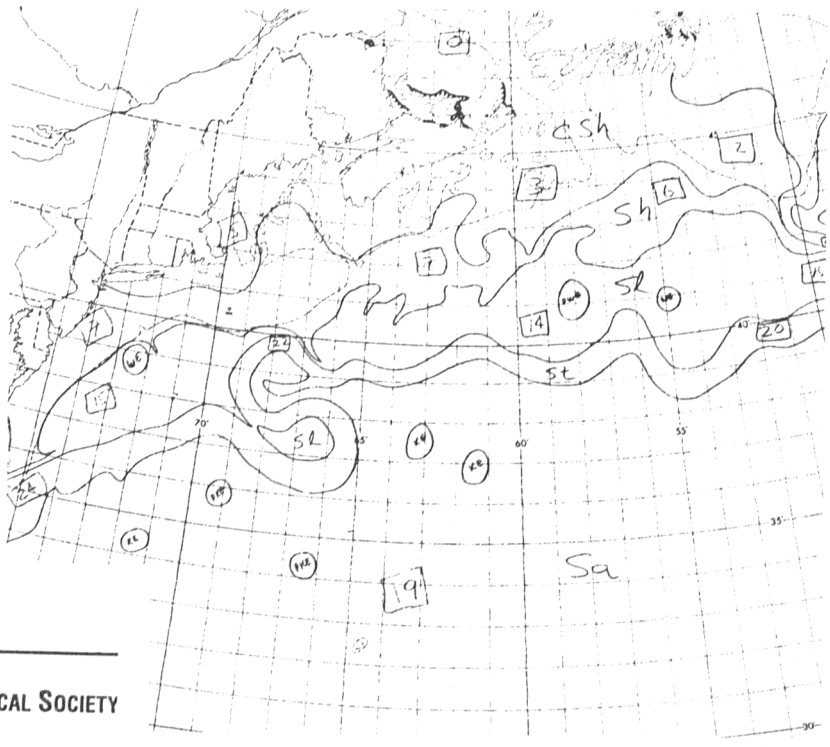

Sea Surface Temperature Analysis

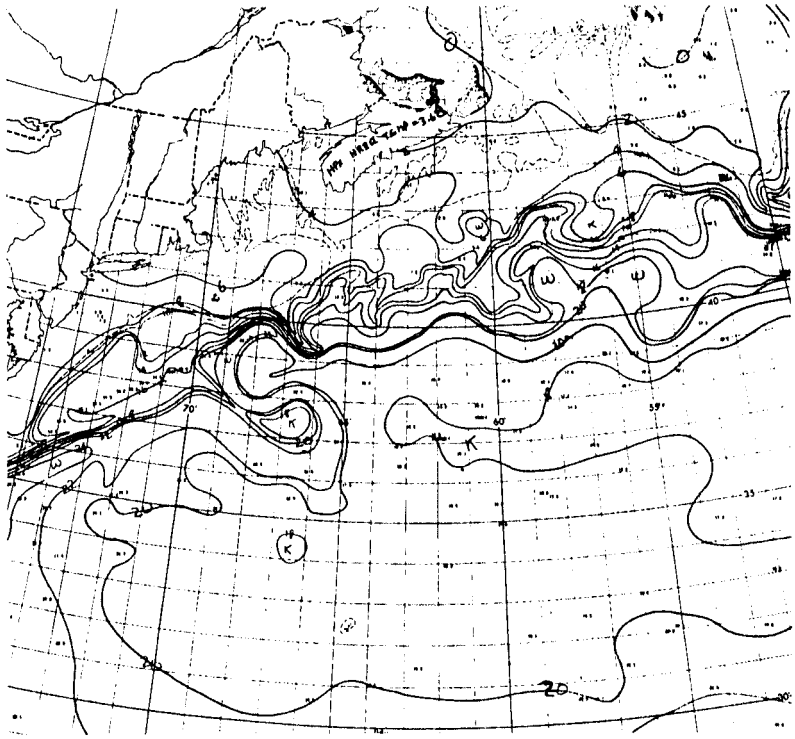

P2.24 WATER VAPOR TRANSPORT OVER THE PACIFIC OCEAN DURING EL NIÑO AND LA NIÑA: A SATELLITE APPROACH

B.J. Sohn[1], Seong-Chan Park[1], Franklin R. Robertson[2], and Eric A. Smith[3]

[1]School of Earth and Environmental Sciences
Seoul National University, Seoul, Korea
E-mail: sohn@snu.ac.kr

[2]Global Hydrology and Climate Center (GHCC), NASA/MSFC
Huntsville, AL

[2]NASA Goddard Space Flight Center
Greenbelt, MD

1. INTRODUCTION

One of important problems of the atmospheric water budget is the role of water vapor transport in atmospheric circulation whose convergence provides, in part, spatial distribution of heating due to the latent heat release. Considering that spatial distribution of the heating is a main forcing driving the atmospheric circulation over the tropics, the examination of water vapor transport would bring in better understanding of atmospheric circulation. However, little attention is given to what extent of mean or extreme climate is contributed by water vapor transport or vice versa, in particular, associated with long term widespread droughts or floods.

Recent advent of PMW measurements from space such as Special Sensors for Microwave Imager (SSM/I) on board DMSP satellite and TMI on board TRMM satellite provides atmospheric water budget parameters, i.e., water vapor, cloud liquid water, and precipitation to investigate water budget within the atmosphere. Satellites also offer global spatial coverage with consistent quality and high temporal sampling which lead to an improved estimation of latent heat flux and to an improved climatology with remote sensing techniques (Chou et al., 1995; Schulz et al., 1997).

Thus, it is now possible to carry out a purely satellite-based water budget over the global oceans, which in essence, captures all of the important water budget components and transport features. In this study, we will construct atmospheric branch of hydrologic cycle by combining estimates of precipitation and evaporation from recent spaceborne sensors, without requiring information on the wind and moisture profiles over the globe.

*Corresponding Author's Address: Dr. B.J. Sohn
School of Earth and Environmetal Sciences
Seoul National University, Seoul, 151-742, Korea.
E-mail:sohn@snu.ac.kr

2. BACKGROUND AND METHODOLOGY

The balance equation for the vertically integrated total water in an atmospheric column can be expressed by:

$$\frac{\partial(W + W_C)}{\partial t} + div(Q + Q_C) = E - P \qquad (1)$$

where $W+W_c$ and $Q+Q_c$ are the column integrated total water and horizontal water transport vector, respectively. Often, transports related to condensation terms are small, thus, eq (1) is simplified over specified time and space domains:

$$[\frac{\partial(W + W_c)}{\partial t}] + [divQ] = [E - P] \qquad (2)$$

Traditionally, large-scale water vapor transport [Q] has been derived directly from circulation statistics in which transport processes are often depicted by mean and eddy motions (Peixoto and Oort, 1992). Detailed and accurate calculations of three-dimensional moisture transport terms over the globe are required. Notably, the lack of systematically spaced conventional measurements of meteorological variables over oceans has hindered understanding of the distribution and transport of water vapor. This motivates the use of indirect calculation methods. Assuming the rate of changes of precipitable water and condensates is small over a sufficiently long time period, horizontal divergence of water vapor is balanced by the evaporation minus precipitation, [E-P], i.e.:

$$divQ = [E\text{-}P] \qquad (3)$$

Introducing water vapor transport potential function (Φ) and separating water vapor transport into rotational (Q_R) and divergent (Q_D) components, we can solve water vapor transport, i.e.:

$$divQ = [E\text{-}P] = \nabla^2\Phi \qquad (4)$$

$$[Q_D] = -\nabla\Phi \qquad (5)$$

Eqs. (4) and (5) are solved on a complete global domain using the spectral method. The divergent

component of water vapor transport then will be examined in conjunction with tropical circulation changes associated with SST variations during El Niño and La Niña periods.

3. Data Sets

For solving Eqs. (4) and (5), we need [E-P] information. Precipitation data for seven year (1988-94) mean climatology are derived from SSM/I measurements. But, for the transport calculation of El Nino and La Nina periods, we use precipitation data from combination of different data sources, i.e., monthly average unclipped TRMM Microwave Imager (TMI) estimate, monthly SSM/I, pentad geostationary infrared (IR) estimates, and the monthly accumulated Climate Assessment and Monitoring System (CAMS) or Global Precipitation Climatology Centre (GPCC) rain gauge analysis. They are obtained from NASA GSFC data distribution center.

The evaporation (E) is estimated from the bulk aerodynamic method, i.e.:

$$E = \rho C_E(U-U_s)(q_s-q) \qquad (6)$$

where ρ is air density, C_E is bulk transfer coefficient, U is the wind speed at the reference height and U_s is the ocean surface current, and q and q_s are specific humidity at the reference height and ocean surface, respectively. We used Chou's algorithm (Chou et al., 1995) with inputs of SST, specific humidity and wind speed at 10 m above the sea surface, air temperature at 2 m above the surface. In this study, 10 m wind speed is derived from SSM/I products (Wentz, 1992). Humidity at the surface layer is also estimated from SSM/I measurements by applying the relationship of surface humidity - lowest 500 m boundary layer water vapor (Schulz et al., 1993).

Since the SSM/I-derived evaporation is only available over oceans, boundary conditions along the continental outline are required for solving Eq. (5). Instead of specifying boundary conditions NCEP data provide [E-P] distributions over the land so that potential function in Eq. (5) can be solved in the entire global domain.

4. Seven Year (1988-94) Mean Atmospheric Moisture Transport

a. Satellite-derived Atmospheric Moisture Transport

Satellite-derived seven year January, February, March (JFM) mean P, E, and Q_D with Φ and divQ_D are displayed in Fig. 1a-c, respectively. Prominent features found in the precipitation map (Fig. 1a) include local maxima over the intertropical convergence zone (ITCZ) north of equator over the eastern Pacific, and western Pacific maritime continent and southeastern Asia, and over the South Pacific convergence zone (SPCZ). Also noted is a precipitation zone over the northern hemispheric storm tracks over the midlatitudes of the North Pacific and Atlantic Ocean.

Seven year JFM mean evaporation was estimated from SSM/I brightness temperature measurements using Chou (1993) retrieval algorithm -- Fig. 1b. The maximum evaporation rates are found over the North Pacific off the East Asian continent and over the east coast off North America. They are due to dry and cold air advection from the continent eastward onto the warm oceans during the winter period. Evaporation rates larger than 6 mm/day are also found in the subtropical trade wind zones over the North Pacific and Atlantic Ocean. In the Southern Hemispheric oceans, it is found that the more zonal distribution with relatively large values over the subtropical latitudes. Spatial variations of E are much smaller than those of P, indicating that spatial distributions of fresh water flux (E-P) are mainly controlled by precipitation.

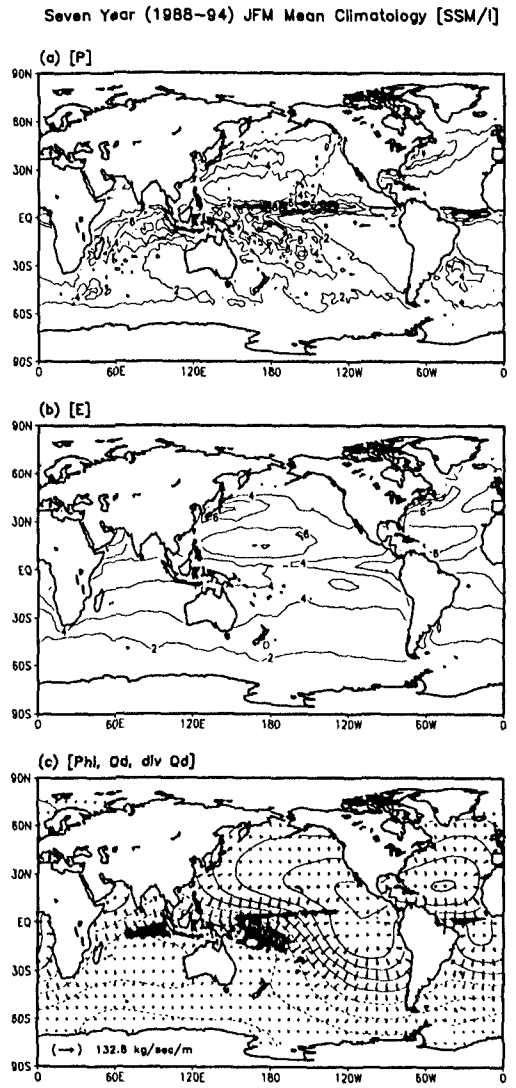

Fig. 1: Satellite-derived seven year JFM mean (a) precipitation [P], (b) evaporation [E], and (c) the resultant divergent component of water vapor transport [Q_D] with its potential function [Φ], and flux divergence [div Q_D]

The resultant divergent component of water vapor transport (Q_D) is illustrated in Fig. 1c, with its potential function [Φ], and divergence [div Q_D]. The transport vector field shows southward transport over most of oceans except north of 30°N, with a maximum at 10°N. Due to the cross-equatorial moisture flux and weak northward transport over the North Pacific and North Atlantic, the northern hemispheric subtropical oceans form moisture source regions, in which evaporated moistures are carried onto deep moisture sink convective regions by the lower tropospheric branch of the Hadley circulation.

b. NCEP-evaluated Atmospheric Moisture Transport

Seven year mean climatology is also obtained from NCEP reanalysis data (results are not shown). Compared to SSM/I estimates, large-scale features agree well but differences are significant over some areas. In the ITCZ, magnitudes are smaller and heavy rain areas (>6mm/day) are broader. Similar behaviors are found over the SPCZ region. In comparison to weak precipitation within the subtropical high, NCEP precipitation field shows stronger rain rate, especially over the eastern Pacific of the Southern Hemisphere. Heavier rain rates are also found in the midlatitude storm tracks of the Northern Hemisphere.

NCEP evaporation also shows good agreement with SSM/I estimates, e.g., a minimum in the cold tongue over the equatorial eastern Pacific, high evaporation features over the subtropical oceans and over the North Pacific and the North Atlantic off the continents. However, differences in magnitude are noticeable over the subtropical North Pacific and the southeastern Pacific off the Peruvian coast.

Moisture transport vector field derived from NCEP E-P field shows similar patterns to that found in the SSM/I derived transport vector field.

c. Zonal and Meridional Mean Transport

Mean meridional moisture transports from SSM/I and NCEP analyses, averaged only over oceans, are given in Fig. 2. It is evident that predominant southward transports occur throughout the tropics and the Southern Hemisphere, with a maximum of 67 kg s^{-1} m^{-1} for SSM/I and 51 kg s^{-1} m^{-1} for NCEP at about 10°N, leading to net water vapor flux into the Southern Hemisphere during the January to March season. It is of interest to note that there is a local minimum of southward transport (or poleward transport) around 15°S latitude. This is due to slight equatorward transport over the Indian Ocean and the southwestern Pacific off Australian continent around 15°S, which then contributes moisture flux convergence over the equatorial western Pacific and Indian Ocean. Thus, the deficit of moisture (precipitation excess) between 10°N and 10°S is compensated by the moisture convergence due to dominant southward transport associated with returning low branch of the Hadley circulation.

The corresponding east-west moisture transport, averaged over the equatorial belt from 10°N to 10°S, is displayed Fig. 3. Most of the equatorial Pacific west of about 110°W shows westward transport with a maximum of 45 kg s^{-1} m^{-1} around 160°W whose magnitude is comparable to north-south component. Distributions of east-west transport result in moisture divergence between 110°W and 160°W and convergence over the western Pacific, consistent with expected from the east-west Walker circulation.

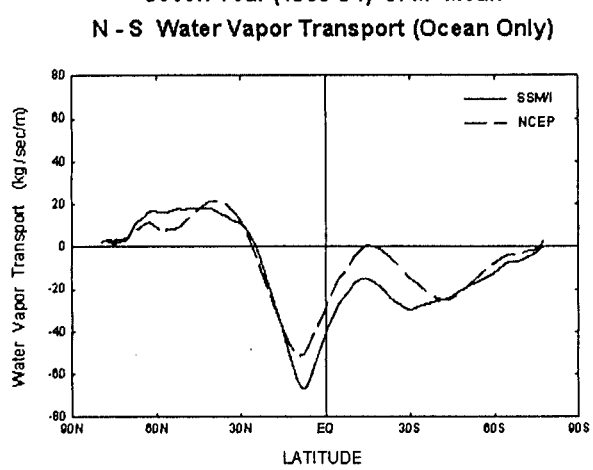

Fig. 2: Mean meridional moisture transports from SSM/I and NCEP reanalyses, averaged only over oceans.

5. Interannual Variability of Moisture Transport

In order to investigate the behavirors of water vapor transport during El Nino and La Nina we first examine SST variations during the ENSO period (not shown) from the seven year (1988-94) JFM mean SST climatology. The anomalous SST for JFM 1998 is similar to that found in typical ENSO SST anomalies, showing positive anomalies with maximum up to 3°C over most of equatorial central-eastern Pacific and a negative anomalies surrounding the positive anomaly area, with a horse-shoe shape over the western Pacific and the adjacent subtropics in both hemispheres. Sharp contrasts are noticed during the La Nina period. Most of the tropical central to eastern Pacific shows negative anomalies, in which the maximum up to -2°C is located near the dateline, representing the reestablishment of the tongue of cold surface water over the eastern Pacific.

Precipitation, evaporation, and associated moisture transport for JFM 1998 are obtained for the prevailed El Nino event. The precipitation pattern shows increased rainfall over the central Pacific, especially west of the maximum SST anomaly, with large reduction in rainfall in the South Pacific convergence zone and in the tropical western Pacific.

Compared to seven year mean climatology, the

distribution evaporation shows substantially increased moisture flux over subtropical oceans, especially in the North Pacific. Taken together, stronger Hadley-type circulation connecting more vigorous upward motion in the equatorial region to more intensified sinking motion over the North Pacific is expected.

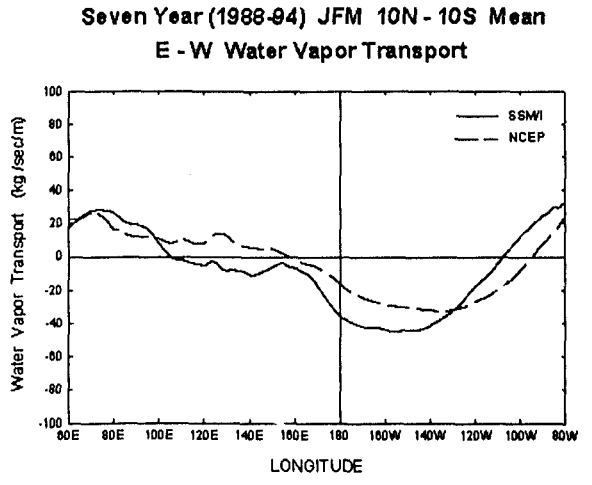

Fig. 3 The east-west moisture transports from SSM/I and NCEP reanalyses, averaged over the equatorial belt from 10°N to 10°S.

The corresponding water vapor transport field reveals that there exist a dominant east-west coupled water vapor transport, in which moisture is transported from the eastern Pacific into the western Pacific warm pool region, associated with the enhanced Walker circulation during the La Niña. But transport magnitude appears to be smaller, compared to that exited during the El Nino.

Moisture transport anomalies from seven year mean climatology with potential function and transport-induced flux convergence anomalies are given in Fig. 4. Results indicate that there are distinct differences in water vapor transport anomalies between the El Niño and the La Niña. During the El Niño period, anomalous vapor transports whose magnitudes are comparable to found in the mean field take places in the eastern half of the tropical Pacific, with strong eastward vapor transport from the date line to the equatorial eastern Pacific and equatorward transport from the subtropics of both hemispheres.

Although the general circulation of the atmosphere is driven by differential heating due to radiation energy and heat transfer from surface, orography and rotational effect, it is relatively simple to understand the time-averaged flow in the tropics because of the thermally direct circulation (Gill, 1980). There are number of studies modeling the circulation over the tropics in particular, in response to SST changes. Lindzen and Nigam (1987) showed that the boundary layer flow is much tied to the SST gradient, with an incorporation with deep convection. Modeling the moist stability diagnosed on the basis on SST, a number of studies successfully explained the position of circulation as an SST-driven phenomenon with low-level convergence and convection over warmer area (Held, 1982; Neelin and Held, 1987). Moisture transport generated by the dynamical response to the SST anomalous forcing and interactions with circulation tend to enhance the transport, maintaining a more vigourous hydrological cycle associated with enhance and Walker circulations.

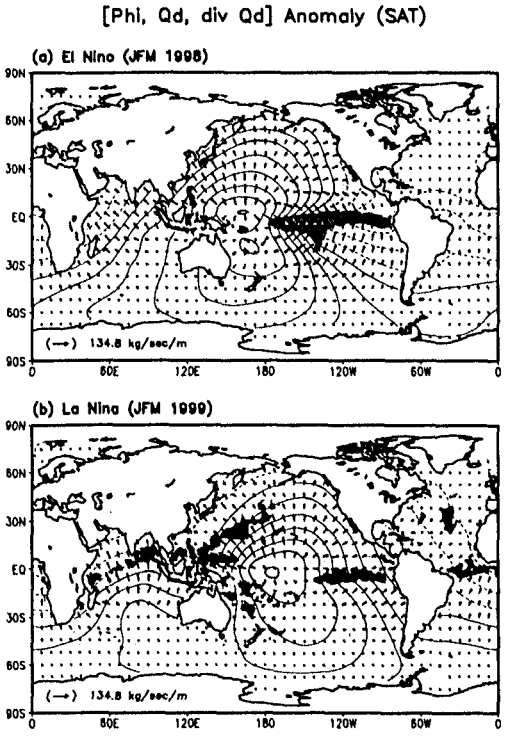

Fig. 4: Water vapor transport anomalies for (a) El Nino and (b) La Nina.

Acknowledgement

This reaseach has been supported by Minisitry of Science and Technology of Korea [Grant number: I-00-007]

References

Chou, S.-H., R.M. Atlas, C.-L. Shie, and J. Ardizzone, 1995: Estimates of surface humidity and latent heat fluxes over oceans from SSM/I data. *Mon. Wea. Rev.*, **123**, 2405-2425.

Gill, A.E., 1980: Some simple solutions for heat-induced tropical circulation. *Quart. J. Roy. Meteor. Soc.*, **106**, 447-462.

Lindzen, R.S., and S. Nigam, 1987: On the role of surface sea surface temperature gradients in forcing low-level winds and convergence in the Tropics. *J. Atmos. Sci.*, **44**, 2418-2435.

Peixoto, J.P., and A.H. Oort, 1992: *Physics of Climate*. American Institute of Physics, New York, 520 pp.

Schulz, J., J.M. Meywerk, S. Ewald, and P. Schluessel, 1997: Evaluation of satellite-derived latent heat fluxes. *J. Clim.*, **10**, 2782-2795.

P3.8 # THE IMPACT OF SATELLITE WINDS ON TWO VERSION OF NCEP GLOBAL DATA ASSIMILATION AND FORECAST SYSTEMS

Xiujuan Su*[1], John Derber[2], Stephen Lord[2]
1. Science Applications International Corp, Camp Springs, Maryland

2: EMC/NCEP, Camp Springs, Maryland

1. INTRODUCTION

Low density satellite winds from EUMETSAT, GMS and INSAT as well as high density GOES cloud drift infrared and water vapor cloud top winds are used operationally at NCEP. These winds provide valuable information for initializing numerical model over regions where conventional observations are unavailable. In this study, we compared the impacts of satellite winds to forecasts using two versions of the data assimilation and model forecast systems used in NCEP.

2. THE SYSTEM and EXPERIMENTS

The experiments were conducted with two T62L28 (192x94 horizontal grid and 28 vertical levels) versions of NCEP global assimilation and forecast system. Forecasts were run twice daily during the August 1-31, 2000 period. The first system is the older version of the T62 operational system (circa October, 2000), and the second is the operational system since 2001 May. The primary difference between the two versions is a change to the convective parameterization and the prediction of cloud liquid water in the second version. These changes have resulted in the significant improvement in the tropical wind field. The experiments presented here are the control run (CONT), which includes all satellite winds in the data assimilation, no satellite winds (NOSTW), and QI-thinning which thins GOES high density winds according to QI (QI) quality mark developed in EUMETSAT (Hulmlund, 1998). The QI-thinning was developed to reduce the correlated errors of satellite winds. We used 2^0x2^0 boxes with tops and bottoms at 100, 150, 200, 250, 300, 350, 400, 500, 600, 700, 750, 800, 850 mb. One observation of satellite winds with the highest QI value was chosen in a box.

3. THE RESULTS

The results of experiments are presented in Table 1 and Table 2.

Table 1. The test scores the first system

		2-day	3-day	4-day	5-day
	CONT	94.7	88.6	79.4	67.0
NH-500	QI	94.7	88.6	79.3	67.1
	NOSTW	94.7	88.6	79.7	68.1
	CONT	95.0	89.0	83.0	75.2
SH-500	QI	95.0	89.2	83.2	75.1
	NOSTW	95.0	89.4	82.8	73.9
	CONT	3.910	4.560	5.051	
TR-850	QI	3.882	4.541	5.033	
	NOSTW	3.952	4.627	5.151	
	CONT	7.066	8.348	9.373	
TR-200	QI	6.971	8.358	9.327	
	NOSAT	7.105	8.452	9.394	

In the Table 1, NH-500 and SH-500 represent the North Hemisphere (20^0 -80^0 N) and the South Hemisphere (20^0 -80^0S) forecast 500 mb geopotential height anomaly correlation score (%) compared with its own analysis. TR-850 and TR-200 represent the tropical (20^0 N -20^0 S) wind vector RMS error (m/s) against its own analysis at 850mb and 200mb, respectively. Note that comparison of forecast wind field with rawinsonde observation produced results consistent with Table 1.

The results (CONT vs. NOSAT) show that the satellite winds have little impact on the forecast skill for the mid-latitude 500 mb heights (the impact is in the third decimal place). However, the satellite winds slightly improve the tropical wind forecasts. The difference between 850 mb and 200 mb vector RMS values with and without satellite winds in the tropics is less than 2% averaged over experiment period (August 1-31, 2000). The QI-thinning has an additional small impact with the effects negligible in the mid-latitude heights and up to a 2% improvement in the tropical RMS error compared to the control run.

*** Corresponding author address: Xiujuan Su EMC/NOAA, 5200 Auth Rd., Camp Springs, MD 20746; e-mail: Xiujuan.Su@noaa.gov**

Table 2. The test scores for the second system

	2-day	3-day	4-day	5-day
CONT	95.4	90.1	81.6	70.1
NH-500 QI	95.4	90.0	81.4	69.9
NOSTW	95.4	89.9	81.2	69.9
CONT	95.1	89.4	83.4	75.8
SH-500 QI	95.1	89.5	83.4	75.6
NOSAT	95.1	89.6	83.8	76.7
CONT	3.824	4.270	4.558	
TR-850 QI	3.845	4.301	4.596	
NOSAT	3.798	4.255	4.575	
CONT	7.158	8.157	8.903	
TR-200 QI	7.152	8.135	8.888	
NOSTW	7.266	8.278	8.955	

Comparing Tables **1** and **2**, produced over the same period with the first system the overall test scores for the second system are better than those for the first system, except wind vector RMS differences 200 mb in the tropics on the second forecast day. The results for the second system show that the impacts of using all satellite winds are much smaller on the tropical wind vector RMS at 200mb with a negative impact on the tropical wind vector RMS at 850mb for the two and three day forecast. The impact of satellite wind on the geopotential height forecasts, if any, is also in the third decimal place, except for the South Hemisphere at forecast day 5 (0.758 (control) vs. 0.767 (no satellite winds)). For the upgraded model/data assimilation system, the impact of the satellite wind is much smaller than in the older systems, because the useful signal in the data is smaller while the errors in the data are the same.

The impact of thinning is more complicated in the new model. The thinning almost has no impact on the geopotential height forecast field, negative impact on the 850mb tropical wind vector RMS, and a slightly positive impact on the 200mb tropical wind vector RMS (Table 2).

4. CONCLUSIONS

The impact of using satellite-derived winds (or any other data) in a forecast/data assimilation system is complicated and system dependent. The impact is smaller for the system whose overall performances on forecast are better. Further analyses are needed to explore the problem of improving the use of satellite winds by the operational forecast systems. Future improvements in the use satellite winds are expected to result over improved satellite wind quality and improved data assimilation methods.

References

Holmlund, K., 1998: The utilization of sttistical properties of satellite-derived atmospheric motion vectors to derived quality indicators. Weather and Forecasting, **13**, 1093-1104

P3.26 VALIDATION OF GMS BRIGHTNESS TEMPERATURE DIFFERENCE TECHNIQUE FOR ESTIMATE OF CUMULONIBUS IN TYPHOON BY TRMM PR DATA

Kotaro Bessho*, Yoshinobu Tanaka and Tetsuo Nakazawa
Meteorological Research Institute, Tsukuba, Japan

1. INTRODUCTION

TRMM is considered as a powerful tool for watching tropical cyclones such as a typhoon. From a image of TRMM PR, 3-D structure of precipitational area of typhoon is easily understood. The distribution of rain area and wind field are also found widely by TRMM TMI. But TRMM is one of LEO satellites and it can observe the typhoon only two or three times a day. Because of this reason, it is needed to use both Geostationary Meteorological Satellite (GMS) and TRMM for analysis of typhoons still now.

For the analysis of typhoon using GMS images, it is important to understand typhoon intensity which has strong connection to cumulonimbus (Cb) in typhoon. For the estimate of typhoon intensity, infrared image of GMS are used as Dvorak technique (Dvorak, 1984). Because there is a possibility that low brightness temperature area consists of cirrus from Cb in typhoon, the typhoon intensity can be estimated from the condition or shape of low brightness temperature area. This technique is depend on the cirrus, which has indirect connection to typhoon intensity. If Cb in typhoon connected directly to its intensity can be detected from GMS image, the accuracy of the technique will be improved.

Using TRMM PR image, Cb in typhoon can be found easily. But because of its low observational frequency and narrow observational area, TRMM cannot estimate typhoon intensity continuously.

Recently new algorithm to identify Cb has been developed using Brightness Temperature Difference (BTD) between brightness temperature of infrared channel (BTir) and that of water vapour channel (BTwv) (Ackerman,1996; Kurino,1997; Schmetz *et al.*,1997). Velden and Olander (1998) showed the possibility of this method to estimate tropical cyclone intensity more precisely.

This paper presents a result of validation of this new technique using TRMM PR data. Firstly, images of GMS BTD are compared with that of TRMM PR. Secondly, superiority of BTD to BTir is shown about the sensitivity to rain intensity. Lastly, BTD is classified into every 1 K. Then the grid points number, which include Cb in TRMM PR data, is accounted in each classified BTD, and some statistical elements are calculated. Using these elements, the range of BTD, in which Cb can be detected efficiently, is confirmed.

* *Corresponding author address:* Kotaro Bessho, Meteorological Research Institute, Tsukuba, Japan 305-0052; e-mail: kbessho@mri-jma.go.jp.

2. DATA

GMS data were collected in CD-ROM of 'Monthly Report of Meteorological Satellite Center' made by Japan Meteorological Agency (JMA). The GMS data are limited to the domain from 20ºN to 50ºN latitude and from 120ºE to 150ºE longitude. Spatial resolution of GMS data is 0.06º and time resolution is one hour. TRMM PR data were obtained from NASA and rain rate in 2A25 data set was used. The best track data of typhoon were derived from Regional Specialized Meteorological Centre Tokyo analysis. This comparison were done using the data in 1998 and 1999.

There were 83 cases in which TRMM observed typhoons in this period over this domain. Among them, 19 cases were chosen when typhoon centers were included in GMS data domain, and TRMM passed the centers within 10 minutes of GMS observation.

3. TECHNIQUE FOR ESTIMATING Cb USING BTD

BTD between BTir and BTwv of GMS are defined as below,

$$BTD = BTir - BTwv.$$

According to Schmetz *et al.*(1997), BTir over Cb or dense cirrus which reached to stratosphere shows only the cloud top temperature. On the other hand BTwv includes both cloud top temperature and the radiation from the water vapour in the stratosphere. So BTwv is usually higher than BTir over the Cb or dense cirrus overshooting the stratosphere. If BTD is negative, it can be guessed that there are Cb or dense cirrus at that negative BTD area.

4. COMPARISON OF GMS IMAGES IN TYPHOON REX AND TYPHOON VIRGIL

Fig. 1(a) shows image of BTir and BTD in Typhoon Rex observed by GMS at 22:31(UTC) 30 Aug. 1998. The area, in which BTD is below 0 K (BTD<0), is found near the surroundings of typhoon's eye located at 31ºN and 143ºE. There is another BTD<0 area concentrated in the east side of the eye. And in the south eastern part of typhoon, line shaped BTD<0 area are scattered. BTD<0 area surrounding the eye corresponds to eyewall of typhoon. BTD<0 areas in the east to south eastern part of typhoon also corresponds to rain bands which are surrounding the outer side of the typhoon. Fig. 1(b) shows the image of rain intensity at the altitude of 4.0 km observed by TRMM PR at 22:22(UTC) 30 Aug. 1998. Strong rain intensity areas are found at the surrounding of the eye and the east to south eastern part of typhoon. These areas show Cb clusters. Comparing Fig. 1(a) with 1(b), it is easy understood that BTD<0 areas corresponds to Cb qualitatively.

Fig. 2(a) shows image of BTir and BTD in Typhoon Virgil observed by GMS at 03:37(UTC) 27

Aug. 1999. The typhoon's eye is located at 28.5ºN and 146ºE. The cloud cluster is found only the south western part of the eye. Most part of the cluster is covered by the area of BTD below -1 K. Fig. 2(b) shows the image of rain intensity at the altitude of 4.0 km observed by TRMM PR at 03:31(UTC) 27 Aug. 1999. There are few rain falling areas in the PR image. BTD<0 area (including BTD<-1) does not corresponds to strong rain intensity area. From the judgment of the life cycle of this typhoon, BTD<-1 area shows dense cirrus cloud. This Virgil case is different from Rex case in Fig.1, and BTD<0 area does not means Cb in this case.

5. COMPARISON OF BTD AND RAIN INTENSITY GRID BY GRID

In previously mentioned 19 cases, BTD of GMS images and rain intensity of TRMM PR are compared grid by grid. Grids of PR data were interpolated to match with grids of GMS data. In each cases the domain of comparison is a rectangle (6º lat.×6º lon.) in which each typhoon's eye is centered.

Fig. 3(a) shows comparisons between BTD and rain intensity at the altitude of 4.0 km at all 73,506 grids in all cases. All grid points are found from -10 K to 50 K in BTD. Especially from -5 K to 10 K in BTD there are grid points which have strong rain intensity above 10 mm/hr. According to referenced papers, grid points of BTD<0 mean Cb. But from this figure, it is supposed that grid points include Cb in the case of not only negative BTD but also positive BTD.

Fig. 3(b) shows comparison between BTir of GMS and rain intensity. All grid points are found widely from 195 K to 295 K in BTir. Grid points which have strong rain intensity above 10 mm/hr are distributed from 195 K to 260 K in BTir. The range of the BTir is wider than that of BTD. From the comparison between the range of BTD in Fig. 3(a) and BTir in (b), it is found that BTD coincide to strong rain intensity grid points at narrower temperature range than BTir.

6. CLASSIFIED BTD AND Cb

Table1 shows classified BTD and grid number of rain points, Cb points, Cb POD (Probability Of Detection) and Cb hit rates.

Rain points mean the cases in which the points have rain intensity above 0.5 mm/hr at the altitude of 4.0 km. Cb points mean the cases in which the points have rain intensity above 5.0 mm/hr from the altitude of 3.0 km to 5.0 km continuously. Cb POD means the percentage of grid number of Cb points in the classified BTD to all grid numbers of Cb points in the whole domain. Cb hit rates means the percentage of grid number of Cb points to grid number of rain points in the classified BTD.

In this table, Cb POD above 10 % is found in classified BTD from -1 K to +3 K. Cb hit rates above 20 % is also found in classified BTD below +1 K. So BTD below -1 K show high percentage of including Cbs in that classified BTD (Cb hit rates), but catch few Cbs in whole domain (Cb POD). In the meanwhile, BTD above +1 K has many Cbs in the domain (Cb POD), but the percentage of including Cbs in the classified BTD is low (Cb hit rates). In conclusion, when BTD from -1 K to +1 K is used, it can detect Cb efficiently.

From this table and Fig. 1, it is validated that BTD from -1 K to +1 K can identify Cb in typhoon at high percentage. And from this table and Fig.2, it is supposed that BTD below -1 K does not show Cb, it identify dense cirrus. But this guess is not confirmed yet.

7. SUMMARY

Cb has a direct relation to typhoon intensity. This study showed that BTD from -1 K to +1 K can identify Cb in typhoon efficiently. And BTD is also more sensitive to strong rain intensity in typhoon than BTir which is now used to estimate the typhoon's intensity. BTD has a potential to become a very useful tool for objective estimation of typhoon intensity

In future, the reliability of this BTD technique will be improved using new data in wider domain for validation. And this technique will be applied to objective estimation of typhoon intensity.

8. REFERENCES

Ackerman, S. A., 1996: Global satellite observation of negative brightness temperature differences between 11 and 6.7μm. *J. Atoms. Sci.*, 53, 2803-2812.

Dvorak, V. F., 1984: Tropical cyclone intensity analysis using satellite data. *NOAA Technical Report NESDIS*, **11**, 47pp.

Kurino, T., 1997: A rainfall estimation with the GMS-5 infrared split-window and water vapour measurements. *Meteorological Satellite Center Technical Note*, 33, 91-101.

Schmetz, J., S. A. Tjemkes, M. Gube and L. van de Berg, 1997: Monitoring deep convection and convective overshooting with METEOSAT. *Adv. Space Res.*, 19, 433-441.

Velden, C. S. and T. L. Olander, 1998: Bispectral satellite technique for delineating intense convection: Applications to tropical cyclones. Preprints, *23rd Conference on Hurricanes and Tropical Meteorology*, 458-461.

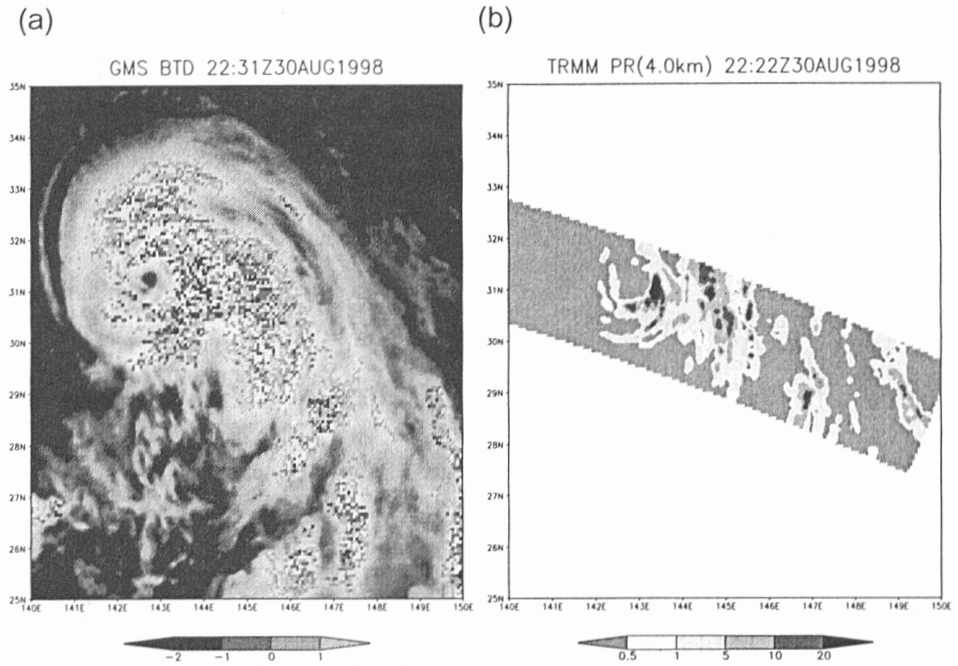

Fig. 1 (a) Image of BTD (K) in Typhoon Rex observed by GMS at 22:31(UTC) 30 Aug. 1998.
(b) Image of rain intensity (mm/hr) in same typhoon at the altitude of 4.0 km observed by TRMM PR at 22:22(UTC) 30 Aug. 1998.

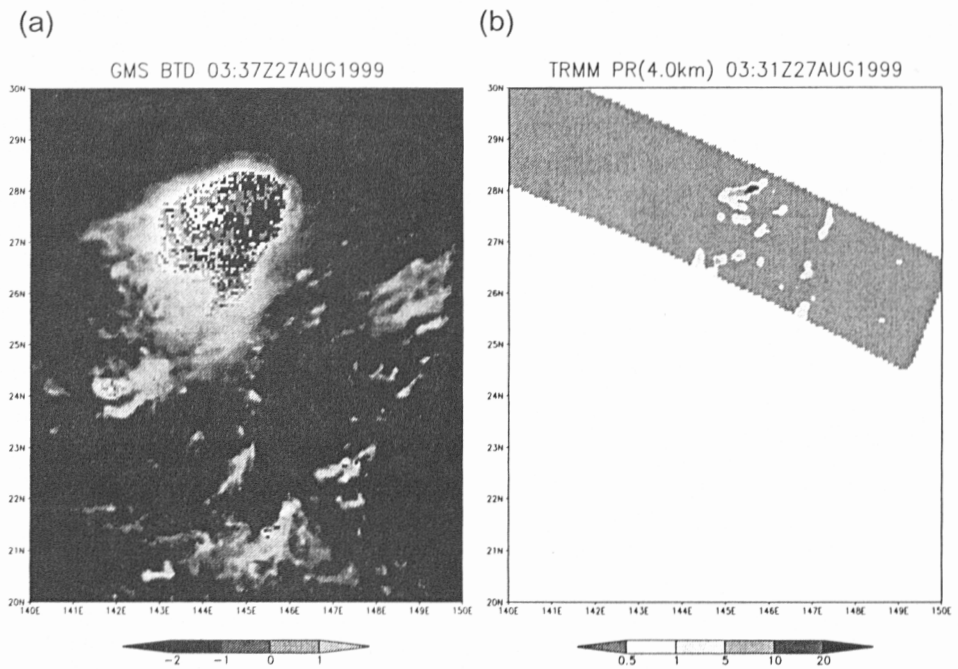

Fig. 2 (a) Image of BTD (K) in Typhoon Virgil observed by GMS at 03:27(UTC) 27 Aug. 1999.
(b) Image of rain intensity (mm/hr) in same typhoon at the altitude of 4.0 km observed by TRMM PR at 03:31(UTC) 27 Aug. 1999.

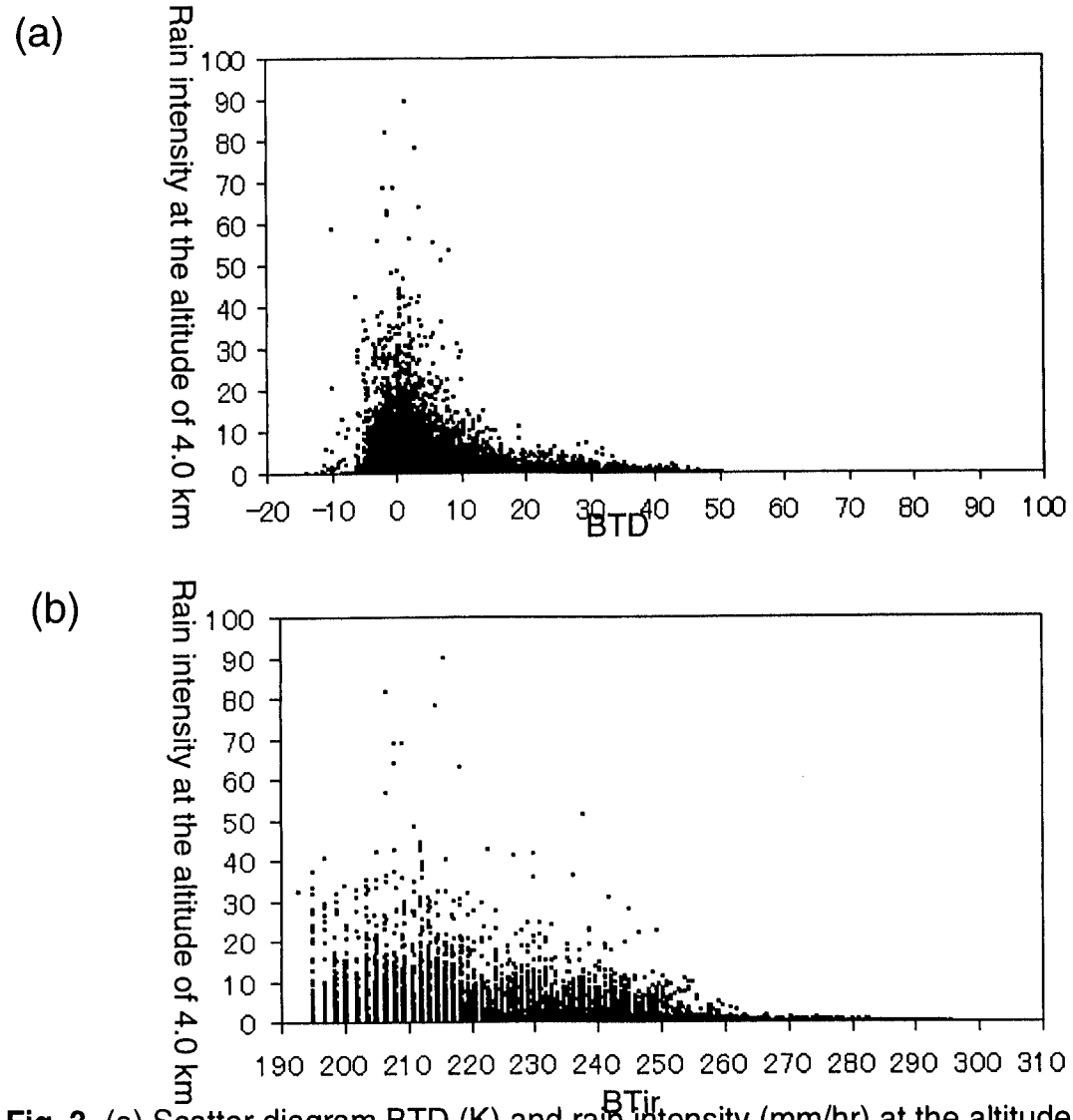

Fig. 3 (a) Scatter diagram BTD (K) and rain intensity (mm/hr) at the altitude of 4.0 km. (b) Scatter diagram BTir (K) and rain intensity (mm/hr) at the altitude of 4.0 km.

□□□□□□□□□□□□	□5□□4	□4□ - 3	-3□ - 2	-2□ - 1	-1□ 0	0 □ 1
Grid num. of Rain points	95	234	483	766	1460	2320
Grid num. of Cb points	36	64	96	205	331	554
Cb POD□□□	1.3	2.2	3.4	7.2	11.6	19.4
□□□□Cb hit rates□□□	37.9	27.4	19.9	26.8	22.7	23.9

1□ 2	2 □ 3	3 □ 4	4 □ 5	5 □ 6	6 □ 7	7 □ 8	8 □ 9	9 □ 10
2450	2446	1594	1183	919	754	683	553	424
410	379	196	144	93	56	73	57	37
14.3	13.3	6.9	5.0	3.3	2.0	2.6	2.0	1.3
16.7	15.5	12.3	12.2	10.1	7.4	10.7	10.3	8.7

Table. 1 Classified BTD, grid number of rain points, Cb points, Cb POD and Cb hit rates

DIRECTORY OF ACRONYMS

A

AER	Atmospheric Environmental Research Inc.
AES	Atmospheric Environment Service
ANL	Argonne National Lab.
AL	Aeronomy Lab.
AOML	Atlantic Oceanographic and Meteorological Labs.
APL	Applied Physics Lab.
ARC	Ames Research Ctr.
ARL	Air Resources Lab.
ARS	Agricultural Research Service
AS&M	Analytical Services and Materials, Inc.
ATDD	Atmospheric Turbulence and Diffusion Division
AWS	Air Weather Service

B

BMRC	Bureau of Meteorology Research Centre

C

CAC	Climate Analysis Ctr.
CAPS	Center for Analysis and Prediction of Storms
CDC	Climatic Diagnostics Ctr.
CETP	Centre d'études des Environnements Terrestre et Planétaires
CIAMS	Cooperative Inst. for Applied Meteorological Studies
CICESE	Centro de Investigación Científica y de Educación Superior de Ensenada
CIMMS	Cooperative Inst. for Mesoscale Meteorological Studies
CIMSS	Cooperative Inst. for Meteorological Satellite Studies
CIRA	Cooperative Inst. for Research in the Atmosphere
CIRES	Cooperative Inst. for Research in the Environmental Sciences
CIRP	Cooperative Institute for Regional Prediction
CMDL	Climate Modeling Diagnostics Lab.
CNR	Consiglio Nazionale delle Ricerche
CNRM	Centre National de Recherches Meteorologiques
COAPS	Center for Ocean-Atmsopspheric Prediction Studies
COLA	Ctr. for Ocean-Land-Atmosphere Studies
COMET	Cooperative Program for Operational Meteorology, Education and Training
CPC	Climate Prediction Ctr.

C (Continued)

CRPA	Centre de Recherches en Physique de l'Atmosphere
CRPE	Centre de Recherches en Physique de l'Environnement
CSIR	Council for Scientific and Industrial Research
CSIRO	Commonwealth Scientific and Industrial Research Organization

D

DOC	Dept. of Commerce
DOE	Dept. of Energy
DOT	Dept. of Transportation
DRI	Desert Research Inst.
DLR	Deutsches Zentrum fuer Luft-und Raumfahrt
DWD	Deutscher Wetterdienst

E

EC	Environment Canada
ECMWF	European Centre for Medium Range Weather Forecasts
EMC	Environmental Modeling Ctr.
EPA	Environmental Protection Agency
ETH	Eidgenössische Technische Hochschule
ETL	Environmental Technology Lab.

F

FEMA	Federal Emergency Management Agency
FNMOC	Fleet Numerical Meteorology and Oceanography Ctr.
FSL	Forecast Systems Lab.

G

GFDL	Geophysical Fluid Dynamics Lab.
GHCC	Global Hydrology and Climate Center
GISS	Goddard Inst. for Space Studies
GOES	Geostationary Operational Environmental Satellite
GLERL	Great Lakes Environmental Research Lab.
GSFC	Goddard Space Flight Ctr.

H

HRD	Hurricane Research Division
HRC	Hurricane Research Ctr.

I

IARC	International Arctic Research Center
IGCR	Institute for Global Change Research
INPE	Instituto Nacional de Pesquisas Espaciais
ISWS	Illinois State Water Survey

DIRECTORY OF ACRONYMS

J

JCET	Joint Center for Earth Systems Technology
JISAO	Joint Inst. for the Study of Atmosphere and Oceans
JPL	Jet Propulsion Lab.
JSFC	Johnson Space Flight Ctr.

K

KNMI	Koninklijk Nederlands Meteorologisch Instituut

L

LANL	Los Alamos National Lab.
LLNL	Lawrence Livermore National Lab.
LRC	Langley Research Ctr.

M

MIT	Massachusetts Inst. of Technology
MRI	Meteorological Research Inst.
MSC	Meteorological Service of Canada
MSFC	Marshall Space Flight Ctr.

N

NASA	National Aeronautics and Space Administration
NCAR	National Ctr. for Atmospheric Research
NCDC	National Climatic Data Ctr.
NDBC	National Data Buoy Center
NCEP	National Centers for Environmental Prediction
NESDIS	National Environmental Satellite Data Information Service
NOAA	National Oceanic and Atmospheric Administration
NPS	Naval Postgraduate School
NRL	Naval Research Lab.
NSF	National Science Foundation
NSSL	National Severe Storms Lab.
NWS	National Weather Service
NWSFO	National Weather Service Forecast Office

O

OAR	Office of Atmospheric Research
ONR	Office of Naval Research
ORA	Office of Research and Applications
ORNL	Oak Ridge National Lab.
OSF	Operation Support Facility

P

PAAWC	Prairie Aviation and Arctic Weather Centre
PAGE	Program for the Advancement of Geoscience Education
PMEL	Pacific Marine Environmental Lab.
PNNL	Pacific Northwest National Lab.
PSPC	Prairie Storm Prediction Center

R

RSMAS	Rosenstiel School of Marine and Atmospheric Science

S

SAIC	Science Applications International, Corp.
SIO	Scripps Inst. of Oceanography
SMHI	Swedish Meteorological & Hydrological Institute
SPC	Storm Prediction Center
SSAI	Science Systems Applications, Inc.
SUNY	State Univ. of New York

T

TDL	Tech. Development Lab.
TPC	Tropical Prediction Center

U

UCAR	University Corporation for Atmospheric Research
UMIST	Univ. of Manchester Inst. of Science and Technology
USDA	U.S. Department of Agriculture
USGS	U.S. Geological Survey
USRA	Universities Space Research Assn.

W

WHOI	Woods Hole Oceanographic Inst.
WMO	World Meteorological Organization

SATELLITE METEOROLOGY & OCEANOGRAPHY CONFERENCE SERIES

DATE	LOCATION	CONFERENCE NAME
25–29 June 1984	Clearwater Beach., FL	(First) Conference on Satellite Meteorology / Remote Sensing and Applications
13–16 May 1986	Williamsburg, VA	Conference on Satellite Meteorology/Remote Sensing and Applications
31 January–5 February 1988	Anaheim, CA	Third Conference on Satellite Meteorology & Oceanography
16–19 May 1989	San Diego, CA	Fourth Conference on Satellite Meteorology & Oceanography
3–7 September 1990	London, England	Fifth Conference on Satellite Meteorology & Oceanography
5–10 January 1992	Atlanta, GA	Sixth Conference on Satellite Meteorology & Oceanography
6–10 June 1994	Monterey, CA	Seventh Conference on Satellite Meteorology & Oceanography
28 January–2 February 1996	Atlanta, GA	Eighth Conference on Satellite Meteorology & Oceanography
25–29 May 1998	Paris, France	Ninth Conference on Satellite Meteorology & Oceanography
9–14 January 2000	Long Beach, CA	10th Conference on Satellite Meteorology & Oceanography
15–18 October 2001	Madison, WI	11th Conference on Satellite Meteorology & Oceanography

GLOSSARY OF METEOROLOGY

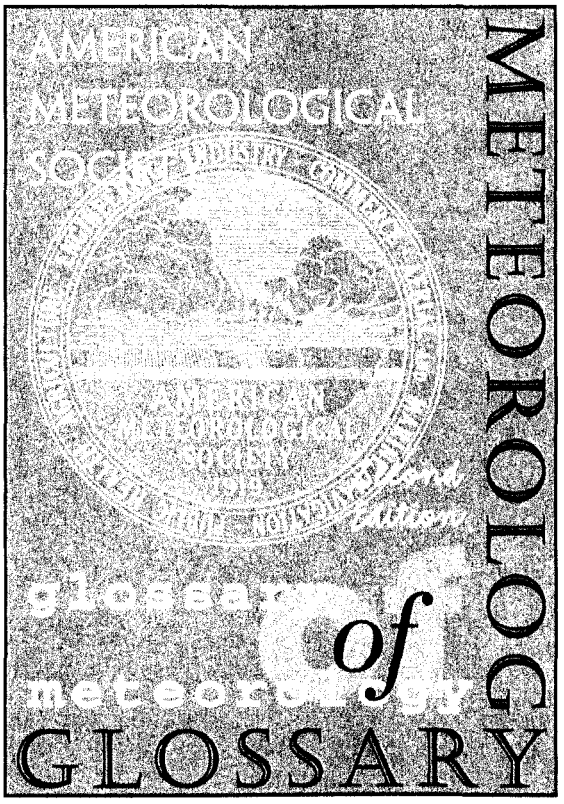

Second Edition

Forty-one years ago, the AMS published the *Glossary of Meteorology*. Containing 7900 terms, more than 10,000 copies have been sold over four decades through five printings. It is a tribute to the editors of the first edition that it has withstood the test of time and continued to be among the leading reference sources in meteorology and related sciences.

Now, over five years in the making, the second edition is available. The volume contains over 12,000 terms, including those from "new" disciplines, such as satellite meteorology and numerical weather prediction. In addition, related oceanographic and hydrologic terms are defined.

The *Glossary of Meteorology*, Second Edition, was produced by an editorial board comprised of 41 distinguished scientists and the participation of over 300 contributors. The CD-ROM version is compatible with Windows, Macintosh, and most UNIX platforms, and features hyperlinked cross-references.

depolarization

electrojets

WSR-88D

zero-plane displacement

arroyo

circulation theorem

ISBN 1-878220-34-9, approx. 850 pp., hardbound. To place an order, refer to the pricing chart below and submit your prepaid orders to: ***Order Department, AMS, 45 Beacon Street, Boston, MA 02108-3693***; call **617-227-2425** to order by phone using Visa, Mastercard, or American Express; or send e-mail to **amsorder@ametsoc.org.** Please make checks payable to the **American Meteorological Society.**

ORDERS BEING ACCEPTED NOW!

HARDBOUND BOOK	**CD-ROM**
$80 List	$95 List
$55 AMS Members	$65 AMS Members
$30 AMS Student Members	$35 AMS Student Members